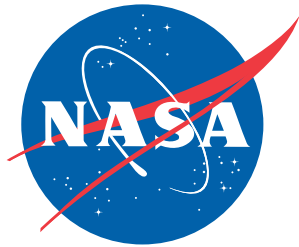


NASA/TM-2020-220582



# **Wind Tunnel Investigation of the Supersonic Stage Separation Aerodynamics of a Generic 0.0175-Scale Bimese Two-Stage-to-Orbit Reusable Launch Vehicle Configuration**

*Gary E. Erickson*  
*Langley Research Center, Hampton, Virginia*

---

April 2020

## NASA STI Program . . . in Profile

Since its founding, NASA has been dedicated to the advancement of aeronautics and space science. The NASA scientific and technical information (STI) program plays a key part in helping NASA maintain this important role.

The NASA STI program operates under the auspices of the Agency Chief Information Officer. It collects, organizes, provides for archiving, and disseminates NASA's STI. The NASA STI program provides access to the NTRS Registered and its public interface, the NASA Technical Reports Server, thus providing one of the largest collections of aeronautical and space science STI in the world. Results are published in both non-NASA channels and by NASA in the NASA STI Report Series, which includes the following report types:

- **TECHNICAL PUBLICATION.** Reports of completed research or a major significant phase of research that present the results of NASA Programs and include extensive data or theoretical analysis. Includes compilations of significant scientific and technical data and information deemed to be of continuing reference value. NASA counter-part of peer-reviewed formal professional papers but has less stringent limitations on manuscript length and extent of graphic presentations.
- **TECHNICAL MEMORANDUM.** Scientific and technical findings that are preliminary or of specialized interest, e.g., quick release reports, working papers, and bibliographies that contain minimal annotation. Does not contain extensive analysis.
- **CONTRACTOR REPORT.** Scientific and technical findings by NASA-sponsored contractors and grantees.

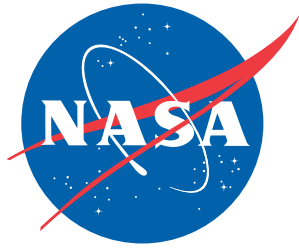
- **CONFERENCE PUBLICATION.** Collected papers from scientific and technical conferences, symposia, seminars, or other meetings sponsored or co-sponsored by NASA.
- **SPECIAL PUBLICATION.** Scientific, technical, or historical information from NASA programs, projects, and missions, often concerned with subjects having substantial public interest.
- **TECHNICAL TRANSLATION.** English-language translations of foreign scientific and technical material pertinent to NASA's mission.

Specialized services also include organizing and publishing research results, distributing specialized research announcements and feeds, providing information desk and personal search support, and enabling data exchange services.

For more information about the NASA STI program, see the following:

- Access the NASA STI program home page at <http://www.sti.nasa.gov>
- E-mail your question to [help@sti.nasa.gov](mailto:help@sti.nasa.gov)
- Phone the NASA STI Information Desk at 757-864-9658
- Write to:  
NASA STI Information Desk  
Mail Stop 148  
NASA Langley Research Center  
Hampton, VA 23681-219





# **Wind Tunnel Investigation of the Supersonic Stage Separation Aerodynamics of a 0.0175-Scale Bimese Two-Stage-to-Orbit Reusable Launch Vehicle Configuration**

*Gary E. Erickson  
Langley Research Center, Hampton, Virginia*

National Aeronautics and  
Space Administration

Langley Research Center  
Hampton, Virginia 23681-2199

April 2020

The use of trademarks or names of manufacturers in the report is for accurate reporting and does not constitute an official endorsement, either expressed or implied, of such products or manufacturers by the National Aeronautics and Space Administration.

Available from:

NASA STI Program / Mail Stop 148  
NASA Langley Research Center  
Hampton, VA 23681-2199  
Fax: 757-864-6500

# Table of Contents

|   |    |
|---|----|
| Abstract.....   | 1  |
| Introduction.....   | 1  |
| Nomenclature.....   | 3  |
| Experimental Program .....  | 5  |
| Wind Tunnel Facility and Test Conditions.....   | 7  |
| Test Conditions .....   | 7  |
| LGBB Model Description.....   | 7  |
| Model Details.....  | 7  |
| Model Transition Grit Patterns .....  | 8  |
| Model Control System, Support Hardware, and Test Procedures .....                         | 9  |
| Model Control System Modifications.....   | 9  |
| Support System Hardware and Setup .....   | 9  |
| Traverse and Axial Support Calibration Procedures .....                                   | 10 |
| Experimental Test Space and Model Positioning .....                                       | 11 |
| Stage Separation Model Installation Procedure.....  | 11 |
| Instrumentation for LGBB Model Stage Separation Testing .....                             | 13 |
| Force and Moment Measurements.....  | 13 |
| Strain-gauge balances .....   | 13 |
| Balance check loadings.....   | 14 |
| Balance zeroes histories.....   | 14 |
| Model Chamber and Base Pressure Measurements .....  | 14 |
| Pitch Angle Measurements .....  | 15 |
| Accelerometer instrumentation.....  | 15 |
| Sting deflection measurements .....   | 15 |
| Roll Angle Measurements .....   | 16 |
| Miniature Video Camera Monitoring .....   | 16 |
| Additional Corrections.....   | 16 |
| Flow Angularity.....  | 16 |
| Model Attitude Tares .....  | 16 |
| Balance Temperature Stabilization .....   | 16 |
| Data Quality Assessment .....   | 17 |
| Within-Test Force and Moment Data Repeatability .....                                     | 17 |
| Post-Test Tunnel-to-Tunnel Force and Moment Data Reproducibility .....                    | 17 |
| Post-Test Experiment-to-CFD Force and Moment Comparisons.....                             | 18 |
| Data Processing Information .....   | 18 |
| Check Point Analysis.....   | 19 |
| Data Format .....   | 19 |
| Run Log .....   | 19 |
| Discussion of Results.....  | 20 |
| UPWT Test 1739 Overview .....   | 20 |
| UPWT Tests 1741 and 1745 Data Plots .....   | 20 |
| 3-D Scatter Plots .....   | 21 |
| Force and moment coefficients at Mach = 2.3, 3.0, and 4.5, $\Delta\alpha = 0^\circ$ ..... | 21 |
| Color Contour Plots .....   | 22 |
| Force and moment coefficients at Mach = 2.3, 3.0, and 4.5, $\Delta\alpha = 0^\circ$ ..... | 22 |
| Relative angle-of-attack comparisons, Mach = 3.0 .....                                    | 22 |
| Influence Plots .....   | 23 |
| Force and moment coefficients at Mach = 2.3, 3.0, and 4.5, $\Delta\alpha = 0^\circ$ ..... | 23 |

|  |    |
|--|----|
| Force and moment coefficients at Mach = 3.0, $\Delta\alpha = 0^\circ$ and $5^\circ$ .....                          | 23 |
| Surface pressure coefficients at Mach = 2.3, 3.0, and 4.5, $\Delta\alpha = 0^\circ$ .....                          | 24 |
| Isolated Orbiter Data Repeatability .....  | 24 |
| Isolated Booster Data Repeatability .....  | 24 |
| Proximity Force and Moment Measurements on Belly-to-Belly Configuration .....                                      | 25 |
| Mach = 2.3, $\Delta\alpha = 0^\circ$ .....   | 25 |
| Mach = 3.0, $\Delta\alpha = 0^\circ$ .....   | 27 |
| Mach = 4.5, $\Delta\alpha = 0^\circ$ .....   | 27 |
| Mach = 2.3, 3.0, and 4.5; $\Delta\alpha = 5^\circ$ .....   | 28 |
| Proximity and Isolated Aerodynamic Characteristics on Belly-to-Belly Configuration, $\Delta\alpha = 0^\circ$ ....  | 29 |
| Mach = 2.3 .....   | 29 |
| Mach = 3.0 .....   | 29 |
| Mach = 4.5 .....   | 30 |
| Relative Angle-of-Attack Effects on Interference Aerodynamics, Mach = 3.0 .....                                    | 30 |
| Orbiter aerodynamic characteristics .....  | 30 |
| Booster aerodynamic characteristics .....  | 30 |
| Mach Number Effects on Proximity Aerodynamics, $\Delta\alpha = 0^\circ$ .....                                      | 31 |
| Orbiter aerodynamic characteristics .....  | 31 |
| Booster aerodynamic characteristics .....  | 31 |
| Interference Effects on Belly-to-Belly and Back-to-Belly Configurations, Mach = 3.0, $\Delta\alpha = 0^\circ$ .... | 32 |
| Orbiter aerodynamic characteristics .....  | 32 |
| Booster aerodynamic characteristics .....  | 32 |
| Isolated Orbiter Surface Static Pressure Measurements .....  | 33 |
| Mach = 2.3, 3.0, and 4.5 .....   | 33 |
| Orbiter Surface Static Pressure Distributions on Belly-to-Belly Configuration, $\Delta\alpha = 0^\circ$ .....      | 33 |
| Mach = 2.3 .....   | 33 |
| Mach = 3.0 .....   | 34 |
| Mach = 4.5 .....   | 34 |
| Orbiter Individual Surface Static Pressure Measurements, $\Delta\alpha = 0^\circ$ .....                            | 34 |
| Mach = 2.3 .....   | 34 |
| Mach = 3.0 .....   | 35 |
| Mach = 4.5 .....   | 36 |
| Relative Angle-of-Attack Effect on Orbiter Surface Pressure Distributions, Mach = 3.0 .....                        | 36 |
| Mach Number Effect on Orbiter Surface Static Pressure Distributions, $\Delta\alpha = 0^\circ$ .....                | 36 |
| Mach Number and Relative Angle-of-Attack Effects on Orbiter Surface Pressure Distributions.....                    | 37 |
| Summary .....  | 37 |
| References .....   | 38 |
| Appendix A .....   | 41 |
| Appendix B .....   | 42 |
| Appendix C .....   | 43 |
| Appendix D .....   | 44 |
| Appendix E .....   | 45 |
| Tables .....   | 46 |
| Figures .....  | 61 |

## Abstract

*A wind tunnel investigation was conducted of the supersonic stage separation aerodynamics of a generic two-stage-to-orbit bimaneuvering wing-body configuration in the NASA Langley Research Center Unitary Plan Wind Tunnel. Proximity and isolated model testing was conducted at Mach numbers of 2.3, 3.0, and 4.5 and a unit Reynolds number of 2.0 million per foot using 0.0175-scale models of the Langley Glide-Back Booster concept designated as the orbiter and booster in belly-to-belly and back-to-belly configurations. Longitudinal forces and moments were obtained on both models and surface static pressure measurements were obtained on the orbiter model at 328 relative proximity locations and at relative angles of attack of 0 degrees and 5 degrees. The test results supported a larger effort to develop and validate experimental and computational tools applicable to the design and simulation of stage separation and abort procedures for reusable launch vehicles composed of multiple bodies, including winged bodies. An initial proof-of-concept experiment featuring low-cost uninstrumented models was conducted to verify an emerging automated model control system and new support system hardware, and to identify potential model and support system blockage and unsteady aerodynamics/model dynamics prior to committing to higher-fidelity instrumented models. This investigation led to upgrades in the facility stage separation hardware, calibration and testing techniques and capabilities, and data analysis and documentation methodologies that have been extended to the more recent NASA Constellation and Space Launch System crew and cargo launch vehicle programs. A virtual diagnostics interface methodology was used to facilitate the design of the stage separation support hardware, to position the models in the test section, and to define the experimental test space. Advances in the facility automated model positioning system established a foundation for the development of a continuous-sweep data acquisition technique that is responsible for significant productivity improvements to the current NASA Space Launch System test program. The automated model positioning capability was leveraged to conduct a companion statistically-designed stage separation experiment requiring randomization of the relative proximity positions of the orbiter and booster models. The respective zones of influence and interference effects of the orbiter and booster were identified from three-dimensional scatter plots, contour and influence maps, and two-dimensional plotting methods. The highly-nonlinear, shock-dominated aerodynamic characteristics of the orbiter and booster in the Unitary Plan Wind Tunnel exhibited good agreement with independent test data obtained in a NASA Marshall Space Flight Center wind tunnel and with computational fluid dynamics predictions using a compressible, three-dimensional flow solver and an inviscid, unstructured Cartesian method.*

## Introduction

Studies of the aerodynamics of separating bodies have been performed for decades, and experimental and computational tools currently

exist to generate and utilize this type of data. One problem that has received significant attention in the literature is that of store separation from aircraft [1]. The aerodynamic characteristics of

the relatively small-sized store is influenced by the proximity of the aircraft, but those of the aircraft aerodynamics are virtually unaffected. A similar example is the separation of the X-15 research vehicle from the B-52 carrier aircraft [2]. Here, the aerodynamic characteristics of the relatively smaller X-15 vehicle were influenced by the proximity of the B-52 aircraft but not vice-versa. Significant stage separation interference effects were encountered during the NASA Hyper-X program [3] to demonstrate airbreathing hypersonic flight, where the X-43 on a Northrop-Grumman Innovations Systems Pegasus rocket encountered aerodynamic anomalies during launch from a B-52 carrier aircraft. The other class of stage separation problem involves separation of two or more vehicles or bodies of comparable size, where the aerodynamic characteristics of all components are significantly disturbed from nominal conditions. In some cases, the integrity of only one vehicle or body may be of importance, such as the staging of multi-stage expendable launch vehicles, and the integrity of only the upper stages is of primary concern post-separation. The expended stages need only to move away safely from the upper stages before their eventual disintegration. Examples of multi-stage expendable launch vehicles include the Ares I crew launch vehicle and Ares V cargo launch vehicle from the NASA Constellation program [4] and the crew and cargo launch vehicles under development in the ongoing NASA Space Launch System (SLS) program [5]. For multi-stage reusable launch vehicles, the integrity of some or all stages is important post separation. The NASA Space Shuttle [6] was a partially reusable low earth orbital spacecraft system, featuring recoverable solid rocket boosters (SRBs) and expendable external tank. The SpaceX Falcon 9, Falcon 9 Heavy, and Starship launch vehicles are examples of fully-reusable launch system concepts, where the first stage returns to the launch site shortly after the separation event, and the second stage returns to the launch pad following orbital realignment with the launch site and atmospheric reentry [7]. SpaceX routinely lands first stages, either on land or on drone ships

in the ocean. However, the company has not yet pursued plans to reuse the second stage.

Some of the earliest studies of parallel separation of similar-sized lifting stages was initiated by the United States Air Force in 1959-1960 in their reusable booster studies [8]. NASA followed in the early 1960s as the nation began its quest for a reusable launch vehicle system. References 9-12 document extensive proximity testing on both simple shapes and typical two-stage-to-orbit (TSTO) configurations at supersonic and hypersonic conditions to develop the necessary experimental tools to generate aerodynamic proximity data as well as to understand the nature of support interference effects. The data generated from these studies were then input into a six-degree-of-freedom simulation program in order to simulate resulting flight trajectories. Although the final design that emerged as the Space Shuttle in the early 1970s did not have parallel lifting stages, the methodologies developed in these early separation studies established an important foundation for future stage separation work.

In the 1980s, post-Shuttle development, NASA continued to examine earth-to-orbit space transportation concepts to cover a wide range of mission requirements, which included system analysis studies of TSTO fully reusable systems [13,14]. Following the accidental loss of the Space Shuttle Challenger on ascent in 1986, a focused program employing experimental and system analysis tools was initiated to examine Shuttle Orbiter boost-phase abort scenarios, that is, separation of the orbiter from the external tank on ascent. The majority of activity related to reusable launch vehicle development in the 1990s focused on single-stage-to-orbit (SSTO) concepts in hopes of improving safety and reliability and reducing cost. A renaissance in stage separation research occurred in the late 1990s and early 2000s when it was realized that the technologies needed for the development of reusable SSTO vehicles were not yet available, and the NASA Next Generation Launch Technology (NGLT) program identified stage separation as one of the critical technologies needed for successful

development and operation of NASA's next generation multistage reusable launch vehicles. NASA initiated a comprehensive stage separation tool development activity that included wind tunnel testing and the development and validation of computational fluid dynamics (CFD) and engineering level tools [15]. A product of a NASA small launcher vehicle concept study [16] was used as the baseline vehicle in this tool development activity, and this generic bimese reusable booster concept was referred to as the Langley Glide-Back Booster (LGBB). Figure 1 illustrates the bimese LGBB concept in a belly-to-belly configuration. A TSTO vehicle in which the booster and the orbiter have the same outer mold lines is called a bimese vehicle, that is, the external geometries of both vehicles are identical. While it is possible that there could be various sizing and arrangements of these stages, it was assumed that a bimese, belly-to-belly (or back-to-belly) wing-body TSTO configuration would provide a worst case in wing-to-wing proximity effects known to provide significant aerodynamic interference. The expectation was that if the tools can be exercised and validated for a bimese, belly-to-belly configuration, other flow fields of lesser complexity and loading would also be amenable to analysis, recognizing that proximity effects are extremely configuration dependent. Products of this NASA stage separation tool development and validation program included supersonic proximity testing in the NASA Langley Research Center Unitary Plan Wind Tunnel (NASA LaRC UPWT) [17] and in the NASA Marshall Space Flight Center Aerodynamic Research Facility 14-Inch Trisonic Wind Tunnel (NASA MSFC ARF TWT) [18], hypersonic stage separation testing in the NASA LaRC Mach 6 Tunnel [19], development and validation of Euler and Navier-Stokes computational fluid dynamics (CFD) tools to simulate steady and dynamic stage separation and abort scenarios [20], and engineering tools for simulation and analysis of staging maneuvers for TSTO bimese reusable launch vehicles [21]. The current report provides a detailed account of the supersonic stage separation testing described in reference 17, which was conducted in the NASA LaRC UPWT using 0.0175-scale LGBB orbiter

and booster models from 10 January 2002 to 15 November 2002. The LGBB stage separation testing in UPWT described in this report encompassed three test entries designated UPWT Tests 1739, 1741, and 1745 that were conducted at Mach numbers of 2.3, 3.0, and 4.5 and a unit Reynolds number of 2.0 million per foot. UPWT Test 1739 was a proof-of-concept investigation featuring uninstrumented LGBB orbital and booster models. UPWT Tests 1741 and 1745 featured higher-fidelity models instrumented with internal strain-gauge balances and surface static pressure instrumentation, and included proximity and isolated model testing. A subset of proximity data was obtained in UPWT Test 1741 as part of a statistically-designed stage separation experiment using response surface methods, and this work is documented in a separate report in reference 22. The stage separation hardware design and installation (aided by a virtual diagnostics interface methodology described in reference 23), calibration and testing techniques, and automated model control system upgrades featured in this investigation provided a foundation for more recent stage separation experiments in UPWT. These advanced stage separation investigations featured a 0.01-scale model of the Ares I crew launch vehicle (model description provided in reference 24) and 0.009-scale models of the SLS crew and cargo configurations featuring separation of the core and two solid rocket boosters (SRBs) with simulated plumes from the booster separation motors (BSMs) [25,26].

## Nomenclature

|                      |   |
|----------------------|---|
| <i>AMS</i>           | angle measurement system                            |
| <i>ARF</i>           | Aerodynamics Research Facility                      |
| <i>ASCII</i>         | American Standard Code for Information Interchange  |
| <i>ATS</i>           | Automated Test Sequence                             |
| <i>AF</i>            | axial force, pounds (lbs)                           |
| <i>b<sub>w</sub></i> | reference span, 6.525 inches (in.)                  |
| <i>BDDU</i>          | balance dynamic display unit                        |
| <i>Betfwd</i>        | UPWT traverse system forward screw position, counts |
| <i>Betaft</i>        | UPWT traverse system aft screw position, counts     |
| <i>Block</i>         | UPWT nozzle block setting, in.                      |

|                      |  |                        |  |
|----------------------|--|------------------------|--|
| <i>BMC</i>           | UT-39A balance moment center (MS 7.525 for LGBB orbiter model); UT-55 balance moment center (MS 8.676 for LGBB booster model) (See Fig. 13.) | <i>MSFC</i>            | Marshall Space Flight Center   |
| <i>BL</i>            | model butt line, in.   | <i>NASA</i>            | National Aeronautics and Space Administration  |
| <i>BSM</i>           | booster separation motor   | <i>NDE</i>             | nondestructive examination   |
| <i>csv</i>           | comma separated value  | <i>NF</i>              | normal force, lbs  |
| <i>C<sub>A</sub></i> | axial force coefficient,<br>$\frac{AF}{q(S_w)}$  | <i>NFDEFL</i>          | normal force deflection constant (angular) for booster model, deg/lb                                 |
| <i>C<sub>N</sub></i> | normal force coefficient,<br>$\frac{NF}{q(S_w)}$   | <i>NFINCH1</i>         | normal force deflection constant (translational) for booster model, in/lb                            |
| <i>C<sub>m</sub></i> | pitching moment coefficient,<br>$\frac{PM}{q(S_w)L}$   | <i>NFINCH2</i>         | normal force deflection constant (translational) for orbiter model, in/lb                            |
| <i>C<sub>p</sub></i> | surface static pressure coefficient,<br>$\frac{p - p_{inf}}{q}$  | <i>NF2DEFL</i>         | normal force deflection constant (angular) for orbiter model, deg/lb                                 |
| <i>CFD</i>           | computational fluid dynamics   | <i>NF1.2</i>           | normal force of booster model after balance interactions and wind-off zeroes computations, lbs       |
| <i>CL</i>            | confidence limit (also centerline)   | <i>NF2.2</i>           | normal force of orbiter model after balance interactions and wind-off zeroes computations, lbs       |
| <i>CLV</i>           | crew launch vehicle  | <i>NGLT</i>            | Next Generation Launch Technology  |
| <i>d</i>             | LGBB body diameter, 1.441 in.  | <i>OML</i>             | outer mold line  |
| <i>DAS</i>           | data acquisition system  | <i>OD</i>              | outer diameter, in.  |
| <i>DESL</i>          | data engineering scripting language  | <i>psfa</i>            | pounds per square foot absolute  |
| <i>Dewpt</i>         | tunnel air dewpoint, degrees Fahrenheit (°F)   | <i>psia</i>            | pounds per square inch absolute  |
| <i>FS</i>            | full scale   | <i>p<sub>inf</sub></i> | freestream static pressure, psfa   |
| <i>h</i>             | vertical distance from floor to lower front edge of balance calibration fixture with applied load, in.                                       | <i>PM</i>              | pitching moment, inch-pounds (in-lbs)  |
| <i>h<sub>o</sub></i> | vertical distance from floor to lower front edge of balance calibration fixture with no applied load, in.                                    | <i>PMDEFL</i>          | pitching moment deflection constant (angular) for booster model, deg/in-lb                           |
| <i>H<sub>o</sub></i> | stagnation pressure, psfa  | <i>PMINCH1</i>         | pitching moment deflection constant (translational) for booster model, in/in-lb                      |
| <i>L</i>             | LGBB model reference length, 13.125 in.  | <i>PMINCH2</i>         | pitching moment deflection constant (translational) for orbiter model, in/in-lb                      |
| <i>LaRC</i>          | Langley Research Center  | <i>PM2DEFL</i>         | pitching moment deflection constant (angular) for orbiter model, deg/in-lb                           |
| <i>LGBB</i>          | Langley Glide-Back Booster   | <i>PM1.2</i>           | pitching moment of booster model after balance interactions and wind-off zeroes computations, in-lbs |
| <i>mV</i>            | millivolts (mV)  | <i>PM2.2</i>           | pitching moment of orbiter model after balance interactions and wind-off zeroes computations, in-lbs |
| <i>Mach</i>          | freestream Mach number   |                        |  |
| <i>Mode</i>          | UPWT operating mode  |                        |  |
| <i>MRC</i>           | moment reference center, MS 8.925 in. (See Fig. 6.)  |                        |  |
| <i>MS</i>            | model station, in.   |                        |  |



|                            |   |
|----------------------------|---|
| <i>Power</i>               | Tunnel power requirement, megawatts (MW)  |
| <i>PRT</i>                 | platinum resistance thermometer   |
| <i>q</i>                   | freestream dynamic pressure, psfa   |
| <i>Q-Flex</i>              | gravity sensing servo accelerometer   |
| <i>Re</i>                  | unit Reynolds number, per foot (/ft)  |
| <i>sif</i>                 | standard interface file   |
| <i>Sting</i>               | distance between booster MRC and support system point of rotation, in.  |
| <i>Sting2</i>              | distance between booster model MRC and midpoint between forward and aft traverse screws, in.                    |
| <i>Strut2</i>              | axial strut encoder output, counts  |
| <i>S<sub>w</sub></i>       | LGBB reference area, 19.184 square inches (in <sup>2</sup> ) (0.1132 square feet (ft <sup>2</sup> ))            |
| <i>SLS</i>                 | Space Launch System   |
| <i>SRB</i>                 | solid rocket booster  |
| <i>SSTO</i>                | single-stage-to-orbit   |
| <i>SVS</i>                 | single vector system  |
| <i>T<sub>0</sub></i>       | stagnation temperature, °F  |
| <i>Traverse</i>            | traverse location, computed by taking the average of the <i>Betfwd</i> and <i>Betaft</i> encoder output, counts |
| <i>TS</i>                  | test section  |
| <i>TSTO</i>                | two-stage-to-orbit  |
| <i>TWT</i>                 | Trisonic Wind Tunnel  |
| <i>UPWT</i>                | Unitary Plan Wind Tunnel  |
| <i>ViDi</i>                | virtual diagnostics   |
| <i>WL</i>                  | model water line, in.   |
| <i>x</i>                   | axial distance from front edge of balance calibration fixture and model MRC, in.                                |
| <i>x<sub>offset</sub></i>  | offset obtained from calibration of axial support strut calibration, in.  |
| <i>x<sub>setpt</sub></i>   | wind-on relative axial distance between LGBB orbiter and booster models, in. (See Fig. 12.)                     |
| <i>x<sub>slope</sub></i>   | slope obtained from calibration of axial support strut calibration, in./count                                   |
| <i>z<sub>aero</sub></i>    | translational and rotational increments to the relative vertical distance caused by aerodynamic loads, in.      |
| <i>z<sub>initial</sub></i> | wind-off relative vertical distance between LGBB orbiter and booster models, in.                                |

|                           |  |
|---------------------------|--|
| <i>z<sub>offset</sub></i> | offset obtained from calibration of main support system traverse mechanism, in.  |
| <i>z<sub>setpt</sub></i>  | wind-on relative vertical distance between LGBB orbiter and booster models, in. (See Fig. 12.)   |
| <i>z<sub>slope</sub></i>  | slope obtained from calibration of main support system traverse mechanism, in./count   |
| $\alpha$                  | booster model angle of attack, degrees (deg)   |
| $\theta$                  | angular deflection due to loading, deg   |
| $\mu V$                   | microvolts   |
| $\Delta$                  | denotes delta coefficient value; in data repeatability analysis, $\Delta$ s are obtained by interpolating in each run to the nominal values of the independent variable, then averaging and subtracting the averages from the interpolated data; also used to denote relative angle of attack between orbiter and booster models |

#### *Subscripts*

|                |   |
|----------------|---|
| <i>booster</i> | booster model coefficient                             |
| <i>orbiter</i> | orbiter model coefficient                             |
| <i>setpt</i>   | setpoint  |
| <i>101-108</i> | orbiter model centerline pressure orifice designation |
| <i>201-204</i> | orbiter model right wing pressure orifice designation |
| <i>301</i>     | orbiter model left wing pressure orifice designation  |

## Experimental Program

As a first step in developing experimental stage separation tools across the speed regime, proximity testing was initiated at supersonic conditions using the generic LGBB two-stage reusable launch vehicle concept. The assumption was the bimese TSTO configuration would provide a worst case in wing-to-wing proximity effects, known to provide significant aerodynamic interference. The expectation was that if the tools could be exercised and validated for the selected configuration, other flow fields of

lesser complexity and loading would also be amenable to analysis. Initial screening data were generated in the NASA MSFC 14-Inch ARF TWT [27] with a more extensive program conducted in the NASA LaRC UPWT. Examples of schlieren flow visualization images acquired in the NASA MSFC testing of 0.01-scale LGBB orbiter and booster models at Mach = 2.99 [18] are shown in Fig. 2, which reveal the complex shock-dominated flow field during this stage separation experiment. In the near-docking or mated conditions, mutual interference is characterized by a channel-like flow between the bodies, and the bow shock waves of each body impinge on the other resulting in multiple reflections. As the bodies move apart due to axial or vertical displacement or relative angle of attack, the channel-like flow is not observed. Instead, mutual interference is mainly determined by bow shock impingements and their reflections. Clearly, two-body proximity testing is a more complex undertaking than single-body testing. While issues such as instrumentation and model accuracy, flow modeling limitations (for example, viscous effects), and tunnel performance (flow quality/uniformity) are just as relevant, other factors may present even greater problems for two-body systems. Aerodynamic proximity increments may be very small compared with full-scale aerodynamic loads (but nevertheless important with respect to vehicle stability and control characteristics in a separation maneuver) and highly nonlinear and configuration-dependent. Support interference and positioning accuracy are of extreme concern with the hardware required to locate one model in proximity to another. The testing described in this report address these issues in order to assess the ability to generate credible static separation data for like-scale, two-stage configurations with existing testing infrastructure in UPWT. The testing was considered exploratory in nature, with the intent of establishing a better understanding of testing methodologies in this facility and the flow physics related to these configurations.

The requirements for the stage separation experiment in UPWT included a planar test grid defined by the relative axial and vertical

displacements of the orbiter and booster models that extended to approximately two body lengths in the axial direction and one body length in the vertical direction. This test grid was intended to encompass typical stage separation trajectories at the selected supersonic Mach numbers of 2.3, 3.0, and 4.5. Additional requirements included changes to the relative angle of attack between the orbiter and booster models and the ability to simulate belly-to-belly (that is, wing-to-wing) and back-to-belly (wing-to-fuselage) configurations. Figure 3 illustrates test grid matrices that encompass all of these requirements, where the orbiter model is assumed to be in a fixed position while the booster model undergoes translations to discrete setpoint locations in the axial direction (defined by  $x_{setpt}$  in inches (in.)) and the vertical direction (defined by  $z_{setpt}$  (in.)), rotation to a specified relative angle of attack (defined by  $\Delta\alpha$  in degrees ( $^{\circ}$ )), and roll rotation of the booster model from a belly-to-belly to back-to-belly orientation. Table I lists the nominal values of the relative axial and vertical locations expressed in inches and in nondimensional terms using the LGBB model reference length,  $L$ , of 13.125 inches. A total of 328 grid points was specified at a relative angle of attack of  $0^{\circ}$ . To provide sufficient clearance when the booster model angle of attack was  $5^{\circ}$ , data were not acquired at the minimum relative vertical separation. Consequently, the number of grid points was reduced to 299. Three distinct phases of the experiment were defined by the acquisition of proximity aerodynamic forces and moments on the orbiter and booster models, force and moment measurements on the isolated booster, and proximity surface static pressure measurements on the orbiter. The results from the MSFC ARF TWT testing in reference 18 suggested isolated orbiter data could be acquired without removing the booster model, provided the latter was translated sufficiently downstream of the orbiter. Orbiter and booster model stage separation interference aerodynamic increments could then be estimated by subtracting the isolated force and moment and surface pressure measurements from the respective proximity aerodynamic data.

The conceptual two-stage reusable launch vehicle configuration, the desired stage separation test parameters, and the experimental facility have been identified in this section. The synthesis of the wind tunnel, test article, support hardware, testing procedures, and instrumentation are described in the following sections.

## **Wind Tunnel Facility and Test Conditions**

The NASA LaRC UPWT is a continuous-flow, variable pressure supersonic wind tunnel. The tunnel contains two test sections, that are approximately 4 feet by 4 feet by 7 feet long. Each test section encompasses only part of the Mach number range of the tunnel. The nozzle ahead of each test section consists of an asymmetric sliding block that allows continuous Mach number variation during tunnel operations from 1.47 to 2.86 in the low Mach number test section (TS 1) and 2.3 to 4.63 in the high Mach number test section (TS 2). Unit Reynolds numbers from 1.0 to 5.0 million per foot can be routinely run with a capability to attain 6.0 million per foot on a transient basis. The basic model support mechanism is a horizontal wall-mounted strut that is capable of forward and aft travel of over 3 feet in the streamwise direction. A main sting support attached to the strut can traverse laterally  $\pm 20$  in. and can provide yaw capability of  $\pm 12^\circ$ . Forward of the main sting support is the angle-of-attack mechanism that provides pitch motion from  $-15^\circ$  to  $+30^\circ$ . A roll mechanism can be installed ahead of the pitch mechanism to provide continuous roll motion over a nearly  $360^\circ$  range. The stage separation investigation described in this report was conducted exclusively in TS 2 and utilized all of the facility support system capabilities to mount and position the booster model relative to the orbiter model throughout the experimental test space. Photographs of the LGBB orbiter and booster models installed in UPWT TS 2 during proof-of-concept testing in Test 1739 are shown in Fig. 4. A complete description of the facility and test section calibration information are contained in Ref. [28].

## **Test Conditions**

Table II shows the average freestream conditions used in UPWT Tests 1739, 1741, and 1745 in TS 2. Testing was performed at Mach = 2.3, 3.0, and 4.5 at a unit Reynolds number of 2.0 million per foot. The stagnation temperature was 125 °F at Mach = 2.3 and 3.0 and 150 °F at Mach = 4.5. A unit Reynolds number of 2.0 million per foot was selected for all runs because of the reduced facility power requirements and the increased margin of safety in the event of undesired model and balance dynamics caused by unsteady aerodynamics or unplanned flow unstart conditions. It is noted that Reynolds number sensitivity assessments were conducted in UPWT supersonic aerodynamics ascent testing of advanced launch vehicles in reference 29, where test data were obtained at unit Reynolds numbers ranging from 2.0 million to 5.0 million per foot. These assessments validate testing at the selected value of the Reynolds number to conserve power and avoid dynamic overloads without compromising the integrity of the aerodynamic data.

The tolerances for the tunnel condition set points for the total pressure and temperature were typically  $\pm 5$  pounds per square foot absolute (psfa) and  $\pm 2$  degrees Fahrenheit (°F), respectively. The tunnel air dew point was maintained at sufficient levels to minimize water vapor condensation effects during all phases of the test. The dewpoint set points for each Mach number are also tabulated in Table II. The tolerance for the dew point set point was  $+0$  °F to any value less than the set point. The automated tunnel control system allowed data acquisition only when the total pressure, temperature, and dew point were simultaneously within tolerances.

## **LGBB Model Description**

### **Model Details**

The LGBB is a generic wing-body configuration that was developed by NASA Langley Research Center's Vehicle Analysis Branch for in-house multistage launch vehicle system analysis studies. The ability to leverage

this earlier work was the primary driver in the selection of this particular wing-body configuration. The virtual diagnostics (ViDi) interface methodology described in Ref. [23] was used to provide simplified three-dimensional (3-D) renderings of the LGBB orbiter and booster models in the UPWT test section that assisted in the sizing of the models, their positioning in the test section, and the design of new support hardware for the orbiter model. An example of a ViDi rendering of the LGBB models is shown in Fig. 5. The ViDi methodology has been applied to all subsequent stage separation tests in UPWT for model and support system hardware design and setup and for real-time and post-test data visualization. The selected model scale was 0.0175, which corresponded to a reference length,  $L$ , of 13.125 in. measured from the tip of the nose to the base of the body (engine exit plane), reference span,  $b_w$ , of 6.526 in., reference diameter,  $d$ , of 1.441 in., and reference area,  $S_w$ , of 19.184 square inches (in<sup>2</sup>) or 0.1332 square feet (ft<sup>2</sup>). A sketch of the model and the corresponding reference dimensions are provided in Fig. 6. The wing/strake was an NACA 2300 series airfoil at a 6-degree dihedral angle. The strake was swept 81.1 degrees, and the wing sweep was 45.3 degrees. The wing's forward-swept trailing edge was a full-span elevon pair separated by a center body flap. The configuration had a centerline vertical tail with a leading-edge sweep angle of 45 degrees. The tail airfoil section, including trailing-edge rudder, was an NACA 0013 airfoil, and its span was 1.928 in. The baseline LGBB vehicle included a swept canard with an NACA 64A012 airfoil, located on the forward part of the fuselage. However, canards were not used in the two-stage bimese configuration in the current investigation. Detailed drawings of the 0.0175-scale LGBB orbiter and booster models are provided in Appendix A.

Two 0.0175-scale aluminum models of the LGBB configuration were fabricated for proof-of-concept testing in UPWT Test 1739. These models were previously shown installed in TS 2 in Fig. 4. These low-cost, uninstrumented models were used to explore the stage separation

aerodynamic environment throughout the test grid matrix, to confirm the integrity of the support system hardware, and to modify and validate the testing procedures to simulate the desired supersonic staging maneuvers. Two 0.0175-scale stainless steel LGBB models were fabricated for the production testing in UPWT Tests 1741 and 1745. Photographs of these models installed in the test section are included in Fig. 7. Additional photographs taken during the model/instrumentation/support system build-up, calibration, installation, and testing processes are included in Appendix B. Both models accepted internal six-component strain gauge balances for force and moment measurements. The orbiter model featured a total of 13 lower surface static pressure orifices, with 8 orifices distributed along the fuselage centerline, 4 orifices in a chordwise row at midspan on the right wing, and a single orifice at midspan on the left wing. Details of the pressure orifice layout are shown in Fig. 8, Table III, and in Appendix A. The booster model was installed on the main tunnel support system and included the centerline vertical tail. The outer mold line (OML) of the orbiter model was identical to the booster model. However, the orbiter model upper fuselage was modified to include a V-notch where the vertical tail would be installed to allow entry of a swept horizontal blade strut mounted to the tunnel side wall. The blade strut simulated a nonmetric vertical tail, allowed the installation of a six-component balance in the orbiter model, and provided an internal instrumentation trench for the routing of the balance instrumentation wire bundle and model surface and cavity pressure lines.

### Model Transition Grit Patterns

The wind tunnel models included standard experimental techniques for tripping the boundary layer in an effort to force the boundary layer to transition from laminar to turbulent, since the wind tunnel Reynolds number was significantly less than the actual flight Reynolds number. Selected patterns of artificial surface roughness in the form of distributed carborundum grit particles were applied to the model nose, wings, and vertical tail as shown in Fig. 9. Per UPWT standard practices [28], a 0.10-inch wide

ring consisting of #40 grit was applied 1.2 in. aft of the nose of each model. Strips of 0.01-in. wide #40 grit were also applied 0.28 in. aft of the wing leading edges. A similar grit strip was applied at the same distance from the leading edge of the booster model vertical tail. The approximate average height for the #40 grit particles was 0.0187 inches. No rigorous determination of the state of the model boundary layers was possible within the scope of the tests.

## **Model Control System, Support Hardware, and Test Procedures**

### **Model Control System Modifications**

The UPWT wind tunnel was an excellent facility for adaptation to proximity testing due to the existing fore/aft/lateral translation and angular rotation capability of its main support strut. The translation capability was originally designed to position a model in the test section for testing at a fixed location. However, the tunnel capabilities were modified to enable model positioning within  $\pm 0.005$ -in. tolerance during a tunnel run. Significant modifications were made to the automated model control system (also referred to as the automated test sequence (ATS) system) to attain the desired setpoint accuracy at as high a movement speed as possible to minimize tunnel run time. In the event of undesirable model dynamics caused by mutual aerodynamic interference between the models, the control system included an automated home position option, whereby the booster model was simultaneously moved to the positive extreme in the relative axial location and minimum vertical separation distance and relative angle of attack. Additional modifications included the input and automation of a predetermined matrix of proximity locations, typically conducted in a move-pause mode from the maximum to minimum axial separation distances at a fixed vertical separation distance. This approach allowed manual intervention in the event of undesired model dynamics when the models were in close proximity. The modifications to the ATS system algorithms facilitated the implementation of statistically-designed experimental methods

[22] in a separate phase of UPWT Test 1741 that required data acquisition at randomized combinations of the translational and rotational setpoints. The control system modifications were also a key factor in the development of a continuous-sweep data acquisition technique that has yielded significant improvements in test productivity at UPWT [30].

### **Support System Hardware and Setup**

Proximity testing of the LGBB bimese reusable launch system configuration was accomplished by installing the booster model onto the main sting support featuring a standard straight sting, mechanized roll coupling, and the main strut assembly, while the orbiter model was installed on a fixed horizontal blade strut mounted to the test section sidewall. This setup was previously shown in the model installation photographs in Figs. 4 and 7. The traverse and rotational capabilities of the main support system allowed positioning of the booster model in the test section to within  $\pm 0.050$  in. of the relative axial and vertical distance setpoints and to within  $\pm 0.1^\circ$  of the relative angle-of-attack setpoints. With the ability to accurately move the booster model in the test section, only an orbiter model mounted in the test section at a fixed attitude and location was required to perform proximity testing in UPWT. This allowed separation testing to be initiated in the facility with a minimum of hardware costs. A custom horizontal blade strut was designed and fabricated for mounting to the test section sidewall, because of constraints in attaching support hardware to the ceiling or floor of the test section. Detailed drawings of the blade strut are provided in Appendix C. The all-stainless-steel support strut consisted of two major pieces: a rectangular mounting plate and a fixed-angle blade strut. The interface between the two parts included a series of holes for  $\pm 3^\circ$  angular adjustment in increments of  $0.1^\circ$ . The strut arm was a wedge-slab-wedge shape at a  $30^\circ$  sweep angle designed to withstand aerodynamic loads with minimum interference. The strut was designed to receive a designated LaRC six-component strain-gauge balance to which the orbiter model was mounted for aerodynamic measurements. A channel with cover plate was

incorporated in the strut design to allow routing of the balance wiring and surface static pressure and cavity pressure lines from the orbiter model and through the tunnel sidewall for external connections to the wind tunnel instrumentation and data system. The standard sidewall insert with multiple optical-quality windows was replaced with a solid sidewall with a small rectangular viewport in order to install the blade strut. This precluded the use of the facility schlieren flow visualization system during the stage separation testing. Later stage separation experiments using larger models featured a horizontal strut installation downstream of the test section sidewall insert that allowed the use of the facility schlieren system [31]. The fixed horizontal blade strut positioned the orbiter model centerline 18 inches from the test section sidewall at pitch and yaw angles of  $0^\circ$  and a roll angle of  $-90^\circ$  (wings vertical). A slot was machined into the lee side of the orbiter in place of the vertical tail to accommodate the blade strut entry into the model. The booster model was rolled  $+90^\circ$  to a wings-vertical orientation to simulate a belly-to-belly arrangement of this bimese TSTO configuration. The mechanized roll coupling allowed the booster model to be rolled  $-90^\circ$  to simulate a back-to-belly configuration, whereby the vertical tail of the booster was removed and replaced with an off block. The ViDi system [23] assisted in the sizing and positioning of the orbiter and booster models in the test section, including the offset of the orbiter model from the sidewall, and the design of the horizontal blade strut to ensure the orbiter model would not encounter aerodynamic interference from its own bow shock at Mach = 2.3, 3.0, and 4.5. The overall test setup is illustrated in Fig. 10.

### **Traverse and Axial Support Calibration Procedures**

Calibration of the traverse support was necessary for determining the belly-to-belly or back-to-belly separation distance between the orbiter and booster models. The sting and blade strut deflection calibrations described in a later section are also taken into account to compute the final relative vertical translation distance,  $z_{setpt}$ , in

inches. The methodology behind these computations is described in Appendix D. The traverse calibration was performed by measuring the distance between the tunnel sidewall and a flat section on the main sting body at various traverse locations with a height gauge. The forward and aft screws were set to an equal number of counts to achieve a zero angle-of-attack condition at the booster model. Moving the traverse in the same direction, measurements were taken at six different points to determine a calibration slope expressed in terms of inches per count. The models were aligned nose-to-nose in the axial direction and the sting-mounted booster model was moved to the near-docking position (minimum separation distance) corresponding to a belly-to-belly separation of 0.41 in. and a relative vertical translation of 0 in. The traverse setting offset computed from the calibrated traverse mechanism slope in combination with the 0.41-in. separation distance were used in the data processing to yield a computed relative vertical setpoint value of 0 in. The computation of the relative vertical separation distance also had to account for changes in the relative angle of attack from  $0^\circ$  to  $5^\circ$ . This required the determination of an additional offset in the computations based on the sting length and angle. This offset was determined based on the measured distance from the booster model moment reference center (MRC) to the midpoint between the forward and aft traverse screws on the main sting body and the computed angle from the forward and aft traverse screw counts. The validity of this in situ calibration method was verified in several static (wind-off) measurements. The data processing method was additionally modified to account for wind-on aeroelastic deflections of the booster and orbiter balance and support systems, as described in Appendix D.

Calibration of the axial support mechanism was necessary for determining the axial separation distance between the two models. The calibration was performed by measuring the distance between the front of the balance box (a fixed part of the tunnel structure) and the front edge of the main support strut at various strut

locations using a digital height gauge. An axial support mechanism slope was computed, and an offset value was determined when the booster and orbiter models were aligned nose-to-nose. An additional term was included in the data system computations to account for changes to the booster model angle of attack via the traverse mechanism. Several static measurements verified the validity of the axial position calculations.

### Experimental Test Space and Model Positioning

The proximity grid point matrices featuring 328 and 299 discrete locations of the booster model relative to the orbiter model at relative angles of attack of  $0^\circ$  and  $5^\circ$ , respectively, were previously shown in Fig. 3. Figure 11 illustrates the overall model setup superimposed on the test grid matrix. The three model test parameters in this experiment were the relative axial distance,  $x_{setpt}$ , relative vertical distance,  $z_{setpt}$ , and relative angle of attack,  $\Delta\alpha$ , of the orbiter and booster models, as illustrated in Fig. 12. The relative axial and vertical distances were measured in inches between the respective moment reference centers (MRCs) of the orbiter and booster models, and the relative angle of attack was the total included angle between the models. Changes to these parameters were accomplished exclusively through the translation and rotation of the booster model relative to the fixed orbiter model. A near-docking or mated position of the orbiter and booster models was previously shown in the model installation photographs in Fig. 7. This position corresponded to  $x_{setpt} = z_{setpt} = 0$  in. and  $\Delta\alpha = 0^\circ$ . At this position, the models were axially aligned, and the minimum vertical spacing between the bellies of each model was 0.41 in. This spacing was established from static and wind-on verification testing as a reasonable buffer to account for small-amplitude model dynamics and booster angles of attack up to  $2.5^\circ$ . Prior to production testing, the relative angle-of-attack requirement was increased to  $5^\circ$ . As a result, a more conservative minimum spacing of approximately 1.066 in. was established, corresponding to  $z_{setpt} = 0.656$  in., at a relative angle of attack of  $5^\circ$ . The relative axial distance,

$x_{setpt}$ , was varied from a minimum of 0 in. to a maximum of 28 in. at all  $z_{setpt}$  locations (except at  $z_{setpt} = 0.656$  in. as noted below) that corresponded to a range of approximately 2.13 model body lengths, where the model reference length,  $L$ , was 13.125 in. measured from the model nose to the engine exit plane (not the trailing edge of the centerline body flap). The relative axial distance was varied from a minimum of 0 in. to a maximum of 14 inches at  $z_{setpt} = 0.656$  in. that corresponded to a range of approximately 1.07 model body lengths. The relative vertical distance,  $z_{setpt}$ , was varied from 0 in. to 13.13 in. at  $\Delta\alpha = 0^\circ$  and from 0.656 inches to 13.13 inches at  $\Delta\alpha = 5^\circ$ , corresponding to a range of approximately 1 model body length. The relative angle of attack,  $\Delta\alpha$ , was  $0^\circ$  and  $5^\circ$ . The positioning of the booster model in the test section was corrected for deflections caused by aerodynamic loads. An in situ calibration technique described in the previous section and documented in Appendix D was used to determine the relative axial and vertical distances accounting for axial and traverse support mechanism translations, traverse mechanism rotation, and aeroelastic or mechanical deflections of the booster and orbiter models, balances, and support systems due to aerodynamic loads. Test section flow angularity estimates were not obtained in this investigation, and the impact of nonuniformities in the flow angle throughout the test section core is discussed in a later section and in Ref. [17].

### Stage Separation Model Installation Procedure

All models, sting and blade strut hardware, uninstrumented (“dummy”) balances, instrumented (“live”) balances, balance calibration blocks, and custom dowel pins and keys were subject to nondestructive examinations (NDE), quality assurance inspections, detailed check fits and build-up, and required calibrations prior to the test entries. Separate installations were required in UPWT TS 2 for Test 1739 and Tests 1741/1745, since aluminum models installed on dummy balances were used in Test 1739 and higher-fidelity stainless steel models

installed on live balances were used in Test 1741 and Test 1745. A comprehensive, step-by-step installation check list was applied in Tests 1739, 1741, and 1745. This process included the determination of all roll coupling-to-balance, horizontal strut-to-balance, and balance-to-model misalignment angles, which were obtained in a systematic manner during the instrumentation and model installation process in the test section. These misalignment angles were used in the Euler rotation computations as part of the data processing. The dummy balances and the live balances used in Tests 1739, 1741, and 1745 were fit to precision calibration blocks that accommodated NASA LaRC angle measurement system (AMS) packages as described in Ref. [32]. The stainless steel 0.0175-scale LGBB orbiter and booster models also featured attachment points for leveling blocks to which the AMS packages were mounted. Similarly, AMS packages were mounted to the horizontal blade strut and to the main tunnel support system (knuckle plate). The AMS measurements were used to verify alignment of the balances and models in roll and yaw. The booster model pitch angle was adjusted using the twin-screw arrangement of the main support strut, whereas angular alignment of the orbiter model with respect to the internal balance, blade strut, and tunnel coordinate system was verified by independent measurements outside the test section and during the installation of the horizontal blade strut and base plate to the test section sidewall. A digital height gauge was also used to independently verify the model alignments with respect to the tunnel coordinate system and to each other. Snap gauges and micrometers were used to measure and verify the selected combinations of relative axial and vertical separation distances at relative angles of attack of  $0^\circ$  and  $5^\circ$ , and the measured results were compared to the computed positions from the wind tunnel data acquisition system (DAS). These check measurements also included the application of known load combinations to both models to ensure that sting deflections were correctly accounted for in the calculations of the relative axial and vertical translations and the relative angle of attack.

The 0.0175-scale LGBB orbiter model used in UPWT Tests 1741 and 1745 incorporated a NASA LaRC 0.80-inch diameter, internally-mounted six-component strain-gauge balance designated UT-39A. The model and balance assembly was installed to the custom blade strut mounted to the test section sidewall and secured with a key and draw nut. The 0.0175-scale LGBB booster model used in UPWT Tests 1741 and 1745 incorporated a NASA LaRC 0.80-inch diameter, internally-mounted six-component strain-gauge balance designated UT-55. The NASA LaRC UT-39B balance was designated as a back-up to the UT-39A and UT-55 balances. The booster model and balance assembly was installed on a NASA LaRC sting designated UPWT 350-15B and secured with a key and draw nut. Details of the UT-39A and UT-55 primary balances and the UT-39B back-up balance are provided in the next section. The UPWT 350-15B sting was installed in the UPWT mechanized roll coupling and secured with set screws. The roll coupling with digital encoder was attached to the model support system using a taper fit and key and draw nut arrangement. The roll coupling could be continuously rolled from approximately  $0^\circ$  to  $+345^\circ$ , where a positive roll angle was defined as a clockwise rotation from the perspective of an observer situated aft of the model and looking upstream. The main support system was capable of pitch and yaw rotations and axial and lateral translations. Detailed quality assurance inspections were performed on both instrumented models to verify critical dimensions and to establish a repeatable model-to-balance installation process. This process also included the application of a prescribed torque to the balance front-end expanders and the insertion of custom dowel pins to secure the models to internal sleeves and to the balances. The balance strain gauge and platinum resistance thermometer (PRT) wire bundles were routed through an instrumentation trench in the blade strut and through the center bore of the 350-15B sting. The balance wiring was terminated with UPWT-compatible connectors to enable a rapid connection to the tunnel instrumentation cable system. The PRT wires were soldered in place to the corresponding tunnel wiring.



Static pitch and roll runs were performed with the booster model to ensure the integrity of the external pressure tube bundle without crimping. The instrumentation cable and tubing bundle exiting near the base of the horizontal blade strut was routed through metal conduit and secured to the tunnel sidewall before passing through a sealed access hole for external connections.

Fouling strip circuits were also installed on the strut and sting extending into the aft end of each model during Tests 1741 and 1745. Sufficient clearance was provided between the V-notch in the upper fuselage of the orbiter model and the blade strut to avoid fouling. Fouling of the models with the supporting hardware was not observed at any time during the stage separation testing.

## **Instrumentation for LGBB Model Stage Separation Testing**

### **Force and Moment Measurements**

#### ***Strain-gauge balances***

Six-component force and moment data were measured simultaneously on the orbiter and booster models using the internally-mounted strain-gauge balances designated UT-39A and UT-55, respectively. The UT-39B balance was reserved as a back-up and was check fit with custom dowel pins to both models. Outline diagrams and design loads of the balances are provided in Appendix E. Figure 13 illustrates the UT-39A and UT-55 balances installed in the orbiter and booster models and the corresponding axial and vertical transfer distances from the balance moment centers (BMCs) to the moment reference center (MRC). The balances were selected based on their compatibility with the LGBB model size and expected loads during the stage separation testing. Each balance featured a front-end expander arrangement as depicted in the balance diagrams in Appendix E to facilitate installation of the balance to custom balance sleeves in the orbiter and booster models. A gear mechanism was engaged via a custom wrench to initially secure the expander within the sleeve of each model. After insertion of precision dowel

pins, a torque wrench was used to apply a prescribed final torque to the expander assembly. The torque was periodically checked on each model throughout the testing.

Custom hardware was fabricated for the balances to allow automated calibrations on the NASA LaRC Single-Vector System (SVS) [33] using statistically-designed experimental techniques applied to the calibration and data analysis processes. The SVS calibration and data analysis methodologies allowed the determination of balance interactions that could not be derived from more conventional one-factor-at-a-time calibration techniques. The improved calibration results are important, since aerodynamic proximity increments may be very small compared with full-scale aerodynamic loads, but nevertheless significant with respect to the vehicle stability and control characteristics in a separation maneuver. In addition, the proximity increments may be highly nonlinear and configuration-dependent. The parallel-voltage balances featured electrical leads of 10-foot lengths terminated in 19-pin Nanonics connectors that were compatible with the facility balance connectors. Each balance featured a single on-board PRT to monitor the temperature during the testing. Wind-on preheat runs were typically conducted to minimize balance thermal gradients and associated electrical zero shifts, and the convergence of the PRT output to a stable value was a factor in determining the duration of these preheat runs. The tunnel was returned to static conditions after each preheat run for the acquisition of hot wind-off electrical zeroes prior to conducting production wind-on runs.

Acquisition of the orbiter and booster model forces and moments from the strain-gauge balances and the orbiter body and wing surface static pressures from individual pressure transducers was performed in a move-pause mode with a sampling rate of 30 samples per second for 2 seconds for a total of 60 samples per data point. Acquisition of the model cavity pressure measurements using an electronic scanner module were obtained with a sampling

rate of 15 samples per second for 2 seconds for a total of 30 samples per data point.

Balance Dynamic Display Units (BDDUs) were used to display the real-time dynamic response of the orbiter and booster model balances throughout the testing and to provide prescribed visual and audible cues if any balance component reached 80 percent or 100 percent of the balance design loads. Testing of the booster model at relative vertical displacements near the outer extreme of the stage separation grid matrix was precluded at  $Mach = 2.3$  and  $\Delta\alpha = 5^\circ$  because of the dynamic response of the UT-55 axial force component on the BDDU display.

The UT-39A and UT-55 balance accuracies expressed in terms of 95 percent confidence limits (CLs) based on the full SVS calibrations performed on June 4, 2001 and July 25, 2001, respectively, are shown in Table IV. The balance calibration accuracies in percent full-scale (FS) were converted to microvolts ( $\mu V$ ) and pounds (lbs) or inch-pounds (in-lbs) as shown in Table IV. The microvolt values served as bounds with which to assess the stability of the wind-off balance zeroes in Tests 1741 and 1745. The values expressed in lbs and in-lbs were used to assess the balance static loadings during the installation and calibration processes. The values in lbs or in-lbs were also used to estimate 95 percent confidence limits for the mean normal force, axial force, and pitching moment coefficients corresponding to the test conditions in UPWT TS 2. The coefficients in Table V provided upper and lower confidence limits for the within-test data repeatability analyses and assessments of stage separation proximity aerodynamic coefficients and interference increments that are presented in this report. It is noted that these bounds are estimated from a balance calibration performed in a controlled laboratory environment. In contrast, the balance measurements in a wind tunnel are obtained in a dynamic testing environment that is subject to many sources of random variation and, possibly, known or unknown systematic variation.

### ***Balance check loadings***

Check loadings of all six components on the UT-39A and UT-55 balances were performed during the installation process in Tests 1741 and 1745. Axial force loads using calibrated weights were applied to the balances and calibration fixtures assembled in a vertical pedestal. Detailed check loads to the other five balance components were applied to the balances and calibration fixtures during the sting deflection calibration processes. Check loads were also applied to the model using a hand-held, digital force gauge.

### ***Balance zeroes histories***

The initial and final wind-off balance zeroes that bracketed a run series were closely monitored and documented throughout the testing. The balance zero histories were an important factor in determining the scheduling and duration of preheat wind-on runs during Tests 1741 and 1745.

### **Model Chamber and Base Pressure Measurements**

The orbiter model used in Tests 1741 and 1745 incorporated a total of 13 lower surface static pressure orifices, with eight orifices distributed along the body centerline, four orifices in a chordwise row on the right wing midspan, and a single orifice on the left wing midspan. Details of the model pressure orifice locations were provided in the previous section LGBB Model Description and in Fig. 8, Table III, and Appendix A. The 0.040-inch outer diameter (OD) stainless steel pressure lines were terminated with flexible tubing with fused ends near the base of the orbiter model for dedicated force and moment measurements. Flexible tubing jumpers were connected to 0.040-inch OD stainless steel tubing from the model and to stainless steel tubing routed through the instrumentation trench in the horizontal blade strut for the dedicated pressure measurements phase of testing. Two 0.040-inch OD stainless steel pressure tubes were also positioned inside the bore of the orbiter model fuselage for cavity pressure measurements. The UT-39A balance,

PRT wire, and pressure tubing bundle exiting near the strut base mounting plate were routed outside the tunnel through a sealed access hole in the solid side wall. This required a slight modification to the base plate to fully expose the access hole. The model surface static pressure lines were then soldered to 0.060-inch OD stainless steel tubes and connected to individual 5 pounds per square inch absolute (psia) Druck transducers. The model cavity pressure lines were connected to a 5 psia electronic pressure scanner module. Two pressure lines were also installed within the bore of the booster model fuselage for cavity pressure measurements, and these tubes were routed externally along the sting and main support system and through an access hole in the ceiling to the external electronic pressure scanner module. Note that the orbiter and booster model cavity pressures were acquired throughout the testing, but cavity pressure corrections were not applied to the aerodynamic data presented in this report.

The manufacturer-specified uncertainty as a percent of full-scale is  $\pm 0.1$  percent for the Druck transducers ( $\pm 0.005$  psia or  $\pm 0.72$  psfa). The stated uncertainty was used to estimate upper and lower 95 percent confidence limits for the orbiter model surface static pressure measurements at Mach = 2.3, 3.0, and 4.5. Table VI presents a list of measurement accuracies expressed in terms of the static pressure coefficient for the test conditions in UPWT Tests 1741 and 1745.

Continuity and leak checks were performed on all 13 model pressure lines and 4 model cavity pressure lines using a vacuum gauge. The initial and final wind-off “pumpdown” zeroes with the pressure in the test section reduced to approximately 300 psfa provided a within-test static check of the orbiter model surface pressure and orbiter and booster model chamber pressure measurements. This procedure was useful in checking the functionality of the Druck pressure transducers and electronic pressure scanner module and identifying crimped pressure tubing. The presence of cracks or leaks in the pressure tubing (none detected during the testing) could

only be ascertained, however, by a comparative analysis of the wind-on pressure responses.

## **Pitch Angle Measurements**

### ***Accelerometer instrumentation***

The primary type of instrumentation in use at UPWT for pitch angle measurement is a gravity-sensing servo accelerometer (Q-Flex). The current testing featured an accelerometer installed in a protective housing on the knuckle component of the model support system with corrections applied to account for aeroelastic or mechanical deflections of the model, balance, and sting assembly.

### ***Sting deflection measurements***

The corrections applied to account for aeroelastic or mechanical deflections of the model, balance, sting, and strut assemblies due to aerodynamic loads were based on in-tunnel sting and balance deflection calibrations. A precision calibration block was installed on the UT-55 balance in the test section, and AMS packages were installed on the calibration block and the main sting support knuckle plate. Calibrated weights were applied at prescribed locations on the calibration block using calibration knife edges and load arms, and the angular deflections due to normal force, pitching moment, side force, yawing moment, and rolling moment were determined. A digital height gauge was also used to measure the linear deflections for all load combinations measured from the lower front edge of the calibration block.

A modified calibration process was used to measure the deflection characteristics of the horizontal blade strut and UT-39A balance. The blade strut and base plate were removed from the test section sidewall and mounted to predrilled holes in the steel floor outside the test section. This allowed a determination of angular and linear deflections due to applied normal force and pitching moment, since these calibrations were precluded with the balance and strut mounted to the test section sidewall. The blade strut and balance were reinstalled on the sidewall, so that side force and yawing moment deflection

calibrations could be conducted. A rolling moment deflection calibration was not considered necessary. Note that only the normal force and pitching moment deflection calibration results were used in Tests 1741 and 1745 due to the symmetry in the test setup and flow conditions. Table VII summarizes the deflection calibration results. As expected, the angular and linear deflection constants of the horizontal blade strut and UT-39A assembly were significantly less than the corresponding deflection constants for the 350-15B sting and UT-55 balance assembly. These results were used in the data processing computations to determine the wind-on relative axial and vertical translation and relative angle-of-attack setpoint values.

### **Roll Angle Measurements**

The UPWT mechanized roll coupling with digital encoder provided the primary measurement for the booster model roll angle. The roll coupling was calibrated using AMS packages installed on the UT-55 balance calibration block and the main support system knuckle plate.

### **Miniature Video Camera Monitoring**

Although a video camera mounted inside the tunnel to the main tunnel support system was not an instrument for acquiring quantitative measurements, it was an important safety tool and a key component in the stage separation test setup for monitoring the status of the orbiter and booster models during wind-on operation. A miniature camera in a protective housing was mounted to the knuckle plate of the main sting support system, and its field-of-view encompassed both models under all possible test conditions. The video output was continuously recorded and displayed in the wind tunnel control room throughout UPWT Tests 1739, 1741, and 1745. The installed video camera was previously shown in the model installation photographs in Fig. 7.

## **Additional Corrections**

### **Flow Angularity**

Given the exploratory nature of this investigation, the force and moment data obtained in UPWT Tests 1741 and 1745 were not corrected for nonuniform flow angularity within the test section. The location and orientation of the LGBB orbiter model was fixed throughout the testing. In contrast, the booster model was positioned throughout the test grid matrix encompassing a significant region of the test section in the longitudinal and lateral directions. Consequently, the booster model traversed regions of potentially varying flow nonuniformity at each Mach number. Isolated booster model results obtained at selected locations within the test grid matrix in Test 1741 revealed nonrandom variation in the force and moment measurements that were of the same order of magnitude, or exceeded, the bounds defined by the UT-55 balance calibration accuracies. These trends were a factor leading to a follow-on test (Test 1745), where runs of the isolated booster model were conducted in full axial sweeps at all relative vertical locations at Mach = 2.3, 3.0, and 4.5. The acquisition of proximity and isolated booster model forces and moments at common locations within the entire experimental space mitigated the potential effects of flow nonuniformity and enhanced the estimation of stage separation aerodynamic interference increments.

### **Model Attitude Tares**

Model attitude tares were obtained to account for the effects of the orbiter and booster model weights on the strain gauge balance responses as a function of the model attitude.

### **Balance Temperature Stabilization**

The UT-39A and UT-55 balances featured a single onboard PRT for temperature monitoring purposes. The PRT output was used in combination with wind-on preheat runs to achieve stable balance temperatures prior to the acquisition of wind-off electrical zeroes at the outset of a production run series. The balance temperatures were continuously monitored

during wind-on runs to determine the necessity for acquiring updated electrical zeroes. An automated program was also executed during off-shift hours to continuously monitor and record the balance temperatures. This information was useful in determining the need for, and duration of, wind-on preheat runs at the beginning of the next shift.

## **Data Quality Assessment**

### **Within-Test Force and Moment Data Repeatability**

Data quality was monitored throughout the UPWT testing and post-test by employing several available methods. To verify that data were repeating within the quoted balance accuracies, multiple repeat runs were obtained throughout the test program for the orbiter and booster in the isolated conditions and at numerous proximity positions. The results presented in this report focus on the isolated orbiter and booster model data repeatability.

The position and orientation of the LGBB orbiter model was fixed on the sidewall-mounted horizontal blade strut. Within-test repeatability of the UT-39A balance forces and moments was evaluated using data acquired when the booster model was positioned approximately two body lengths aft of the orbiter model at any given vertical separation distance. Under these conditions, the orbiter model was unaffected by the presence of the booster model, thereby providing numerous repeat data points corresponding to the isolated orbiter model.

Given the constant aft location of the booster model relative to the orbiter model throughout the test matrix and the resulting proximity effects, the orbiter model and its fixed sidewall support strut were removed to obtain isolated data on the booster model. In a typical single-body wind tunnel test program in UPWT, the model is kept as close as possible to the center of rotation of the tunnel so that at all model attitudes, test data are acquired in the same location within the tunnel test core. While the booster model angle of attack only varied a maximum of  $5^\circ$  throughout the test program, by virtue of the proximity test matrix,

the spatial location of the model in the tunnel varied by 28 in. in the streamwise direction and over 13 in. in the spanwise direction, thereby introducing a potential source of variation in the test results by acquiring data in different regions of the tunnel flow field. Prior to testing, it was thought that this variation would be random and small in magnitude (relative to balance accuracies). Isolated booster data repeatability was checked in Test 1741 with multiple runs at four locations in the proximity matrix spanning its spatial extent (that is, minimum and maximum  $x_{setpt}$  and  $z_{setpt}$ ). Results from these runs (not presented in this report) showed the variation of the longitudinal aerodynamic coefficients for the isolated booster to be on the order of, and in some cases larger than, the balance accuracies and not random. That is, the coefficient data were repeatable within balance accuracies at a single location in the tunnel (as was seen for the orbiter model at its fixed location), but not over the entire test region. Thus, in a subsequent separate test entry (Test 1745), repeat isolated booster data were acquired at each of the 328 spatial locations at Mach = 3.0 to better understand and characterize the variation, which was greater in the spanwise direction than the streamwise direction, and larger near the extreme spanwise positions as the booster model moved closer to the test section sidewall.

### **Post-Test Tunnel-to-Tunnel Force and Moment Data Reproducibility**

A complementary test program was conducted in the NASA MSFC blow-down 14-inch ARF TWT using 0.01-scale LGBB orbiter and booster models for a Mach number range of 2.74 to 4.96 [18]. The availability of the MSFC results provided an opportunity to conduct a post-test assessment of tunnel-to-tunnel reproducibility of the stage separation data. Reference 17 provided several comparisons of data obtained on the LGBB bimese orbiter and booster in a belly-to-belly configuration in UPWT (Mach = 3.0) and in the TWT (Mach = 2.99) with corresponding unit Reynolds numbers of 2.0 and 5.0, respectively. Very good agreement was generally observed in trend and magnitude of the observed normal force and pitching moment interference increments (that is, proximity value minus isolated value).

This agreement is illustrated in Fig. 14 that compares the proximity and isolated booster normal force and pitching moment coefficients corresponding to a common vertical separation distance,  $z_{setpt}$ , equivalent to 0.10 body length,  $L$ . The number of data points from the MSFC facility were limited, since the relative axial and vertical translations and relative angle of attack were manually set prior to each run.

### Post-Test Experiment-to-CFD Force and Moment Comparisons

Another post-test data quality assurance method used in UPWT Tests 1741 and 1745 featured comparisons of the experimental data obtained at Mach = 3.0 to CFD predictions using an overset grid Navier-Stokes flow solver and a Cartesian grid Euler method [20]. The OVERFLOW code is a high-fidelity, compressible, three-dimensional flow solver that solves the time-dependent, Reynolds-averaged Navier-Stokes equations using multiple overset structural grids. The Cart3D code is an inviscid, unstructured Cartesian solver and is a versatile analysis package for conceptual/preliminary aerodynamic design. Figure 15 compares the longitudinal aerodynamic coefficients of the booster and orbiter models obtained in experiment and from the OVERFLOW and Cart3D methods in an axial setpoint sweep at the minimum vertical separation distance and Mach = 3.0. The OVERFLOW-measured viscous force components and vertical tail components were added to the Cart3D and experimental results, respectively. The level of agreement between the experimental and computational sources is very good, except in the booster normal force coefficient during the aft translation. This is a region of large interference between the two vehicles, although the difference between the experimental and predicted results is currently unexplained.

The Cart3D Euler method was used to evaluate a large number of relative axial and vertical locations of the booster and orbiter vehicles. This allowed the creation of color contour plots of normal force, axial force, and pitching moment coefficients for the booster and

orbiter vehicles at Mach = 3.0, as shown in Fig. 16 [20]. The CFD contour plots are shown here for reference, since similar experimental contour plots are shown from UPWT Test 1741 in the Discussion of Results section of this report. Clearly indicated are the relative zones of influence between the vehicles, with the orbiter returning to undisturbed (isolated) conditions over much of the relative axial and vertical setpoint space. Also indicated are the effects of interference following Mach lines, in the  $+x_{setpt}/L$  and  $+z_{setpt}/L$  directions for the booster and in the  $-x_{setpt}/L$  and  $+z_{setpt}/L$  directions for the orbiter. The contour plots for the booster exhibit some dissipation with increased relative separation distances, although Reference 20 cites possible dissipation due to the resolution of the matrix along with the linear interpolation that was applied between points.

### Data Processing Information

The aerodynamic coefficient data have been processed in the body and stability axis systems. Model layouts with dimensional details and the BMC and MRC locations and transfer distances were previously shown in Figs. 6 and 13. The final offline data were processed using the UPWT Test SLATE Matlab-based data acquisition and processing system [34] at an MRC location corresponding to model station (MS) 8.925 in. or 68 percent of the model reference length,  $L$ , of 13.125 in. measured from the nose of the orbiter and booster models.

The data processing used the full pretest calibrations of the UT-39A and UT-55 balances dated June 4, 2001 and July 21, 2001 that were conducted using the NASA LaRC SVS system and statistically-designed experimental and data analysis techniques.

The constants used to process the force and moment data to coefficient form included the reference area and reference lengths determined from the LGBB model drawings in Appendix A. Other constants that were used in the data processing programs include the calibration

slopes and offsets determined from the in-tunnel calibrations of the main support system Q-Flex accelerometer, roll coupling, axial and traverse mechanisms, Druck pressure transducers, electronic pressure scanner, and balance/support system deflections. The roll coupling-to-balance, strut-to-balance, and model-to-balance misalignment angles that were determined during the installation process in the test section were also included in the data processing. The data have been not been corrected for base or cavity pressure measurements.

### Check Point Analysis

Independent detailed check points were performed to verify the facility data processing methods. These check points consisted of automated and manual, step-by-step computations beginning with the voltage outputs from the wind tunnel and model instrumentation and culminating in the computations of the final forces, moments, and pressures and their respective coefficients. Software applications that were independent of the online and offline data processing systems were used to perform the more complex operations, including the balance force and moment calculations with all interactions, attitude tares, Euler rotations, and rotation and translation to the selected model coordinate systems. An independent data reduction specialist performed frequent verification checks of the data processing program by computing the aerodynamic coefficients using data engineering scripting language (DESL) software [35]. The manual and automated computations verified the facility data processing methods.

### Data Format

Separate electronic data files were provided for UPWT Tests 1741 and 1745. The data files were in binary standard interface file (sif) and American Standard Code for Information Interchange (ASCII) comma-separated variable (csv) formats.

## Run Log

The final run logs for UPWT Tests 1741 and 1745 are presented in Tables VIII to X, corresponding to dedicated force and moment measurements in Test 1741, dedicated pressure measurements in Test 1741, and dedicated force and moment measurements in Test 1745, respectively. The run log format mirrors the test grid matrices previously presented in Fig. 3. Each module in the run log corresponds to relative axial location sweeps at all values of the relative vertical location for a fixed combination of Mach number, relative angle of attack, and orbiter-to-booster configuration (belly-to-belly or back-to-belly). The run number is listed in the right-hand column in each module, with increasing run number from top to bottom. Within each run number, the data points acquired in a move-pause mode are presented in a row with increasing point numbers from right to left. Each data point corresponds to a specific combination of the relative axial and vertical setpoint locations,  $x_{setpt}$  and  $z_{setpt}$ , respectively, that are presented as a standard coordinate system along the horizontal and vertical “axes” of each module. The sequencing of runs and points is consistent with the manner in which the testing was performed, specifically, a run series was initiated at the extreme value of the relative vertical setpoint, and data were acquired within a run starting at the extreme value of the relative axial setpoint and progressing forward toward the minimum relative axial setpoint. This approach was based on model, instrumentation, and facility safety considerations to provide sufficient time to respond to undesired unsteady aerodynamics and/or model/balance/support system dynamics and to return the booster model to a safe home position as defined in the next section. In addition, conducting the runs and acquiring data points in consistent directions avoided potential hysteresis effects associated with the traverse and axial support system mechanisms.

Testing was conducted at Mach = 2.3, 3.0, and 4.5 in UPWT Tests 1741 and 1745. All runs were performed at a unit Reynolds number of 2.0 million per foot.

## Discussion of Results

### UPWT Test 1739 Overview

A proof-of-concept test was conducted in UPWT Test 1739 using low-cost uninstrumented orbiter and booster models installed on dummy balances to qualitatively assess the model behavior throughout the stage separation test grid matrix at Mach = 2.3, 3.0, and 4.5. Installation photographs of the uninstrumented models in UPWT TS 2 were previously shown in Fig. 4. This diagnostic entry also allowed an assessment of the stage separation support system hardware and modifications that were made to the facility calibration procedures and the automated model control system algorithms to ensure accurate positioning of the booster model relative to the orbiter model. The gains in the automated control system were tailored during this entry to allow the booster model to establish a desired setpoint without overshooting. A procedure was established whereby the booster model was moved in an axial sweep starting at the extreme aft  $x_{setpt}$  location and progressing forward in a move-pause mode to the minimum  $x_{setpt}$  location. The model would then automatically return to the extreme aft  $x_{setpt}$  location in preparation for the next run. This procedure was done at all relative vertical locations starting at the outermost value of  $z_{setpt}$  and moving inward toward the minimum  $z_{setpt}$  location. For operational safety purposes, a home position was also established for the booster model in the event of undesired proximity aerodynamics effects and model/balance/support system dynamics. In this case, the booster model would automatically move to the extreme aft  $x_{setpt}$  location to maximize the separation from the orbiter model. Test 1739 revealed benign model and support system behavior throughout the test grid matrix at all Mach numbers and verified the custom calibration and testing procedures and the modifications to the automated model control system. These results established confidence in advancing to the installation of the higher-fidelity stainless-steel models with live instrumentation for the proximity and isolated model testing in Tests 1741 and 1745.

### UPWT Tests 1741 and 1745 Data Plots

Data plots created using statistical data analysis software [36] and DESL scripts [35] are presented in the following sections that represent an extensive sampling of the stage separation proximity and isolated orbiter and booster model test results obtained in UPWT Tests 1741 and 1745. Photographs of the 0.0175-scale LGBB orbiter and booster models installed in UPWT TS 2 were previously shown in Fig. 7. Qualitative data visualization is provided in three formats, which include 3-D scatter plots, color contour maps, and color influence plots corresponding to the body axis normal force, axial force, and pitching moment coefficients ( $C_N$ ,  $C_A$ ,  $C_m$ ) of the LGBB orbiter and booster models and, on a selected basis, the surface static pressure coefficients ( $C_p$ ) on the orbiter model throughout the stage separation test grid matrix. A majority of results focus on the LGBB models in a belly-to-belly configuration at Mach = 2.3, 3.0, and 4.5 and relative angles of attack,  $\Delta\alpha$ , of  $0^\circ$  and  $5^\circ$ . Test results obtained with the LGBB models in a back-to-belly configuration are presented on a limited basis. The remaining plots are more conventional two-dimensional (2-D) representations of the proximity and isolated aerodynamic coefficients and surface static pressure coefficients. The longitudinal aerodynamic responses are typically plotted against the relative axial separation distance,  $x_{setpt}$ , in inches at selected relative vertical separation distances,  $z_{setpt}$ , in inches at Mach = 2.3, 3.0, and 4.5 for relative angles of attack of  $0^\circ$  and  $5^\circ$ . Individual orbiter surface static pressure coefficients are plotted in a similar manner, whereas the entire distribution of pressure coefficients on the windward fuselage centerline are plotted against the model station (MS) at selected combinations of  $x_{setpt}$  and  $z_{setpt}$ . Several plot series include the isolated orbiter and booster coefficients as a reference. As needed, computed aerodynamic coefficient increments (proximity minus isolated data ( $\Delta C_N$ ,  $\Delta C_A$ ,  $\Delta C_m$ )) are plotted. The majority of 2-D plots depict the upper and lower 95 percent confidence limits for the strain-gauge balance and static pressure transducer measurements based on the respective



instrumentation calibrations in order to better assess the variability in the experimental data.

### 3-D Scatter Plots

#### *Force and moment coefficients at Mach = 2.3, 3.0, and 4.5, $\Delta\alpha = 0^\circ$*

Figure 17 presents 3-D scatter plots of the orbiter normal force, axial force, and pitching moment coefficients versus the relative axial and vertical locations,  $x_{setpt}$  and  $z_{setpt}$ , respectively, at Mach = 2.3 and  $\Delta\alpha = 0^\circ$ . The LGBB orbiter and booster models are in a belly-to-belly configuration. There are two plots for each aerodynamic component, representing two different views of the data cloud. The first view corresponds to an observer situated near the lower right quadrant of the test grid matrix (that is, near the maximum relative axial position and minimum relative vertical position) and looking diagonally across the test space. The second view corresponds to an observer situated near the upper right quadrant of the test grid matrix (that is, near the maximum relative axial and vertical positions) and looking diagonally across the test space. The first plot for each aerodynamic component reveals a relatively confined region of the test grid matrix at the smaller values of the relative axial and vertical locations (where the booster is closer to the orbiter model) characterized by systematic variation in the data with marked positive and negative peaks. The aerodynamic response outside of this region rapidly converges to undisturbed levels where the interference effects of the booster model have dissipated. The perspective of these plots is roughly aligned with the bow shock system generated by the booster model. The second plot for each aerodynamic component also shows the large region of undisturbed responses, but the data points appear randomly scattered in the region of the test grid matrix where the booster effects on the orbiter model are significant. In these plots, the perspective is at an oblique angle to the Mach lines emanating from the booster model.

Figure 18 presents similar 3-D scatter plots of the longitudinal aerodynamic responses for the booster model at Mach = 2.3 and  $\Delta\alpha = 0$  degrees.

In this case, the first plot for each aerodynamic coefficient exhibits apparent random data scatter throughout the entire experimental space when viewed from the lower right quadrant of the test grid. However, viewing the data from the upper right quadrant reveals discernible patterns characterized by significant peaks and valleys in the data cloud. The lack of any discernible planar regions of constant response suggests the booster model remains in the influence of the orbiter model throughout the experimental space. This perspective is more aligned with the bow shock system emanating from the orbiter model. These initial data plots demonstrate the importance of data rotation in 3-D space. Changing the viewpoint for the 3-D scatterplots is an effective exploratory technique, since it can reveal patterns that are easily obscured unless the cloud of data points is viewed from an appropriate angle.

Figures 19 and 20 feature the 3-D scatter plots for the orbiter and booster models at Mach = 3.0, and the corresponding scatter plots at Mach = 4.5 are presented in Figs. 21 and 22, respectively. The data trends at the higher supersonic Mach numbers are similar to those observed at Mach = 2.3 in Figs. 17 and 18. A qualitative assessment of the data clouds indicates the region of influence of the booster model on the orbiter model diminishes at the higher Mach numbers (Figs. 19 and 21). The booster model responses at Mach = 3.0 suggest the influence of the orbiter model persists throughout the experimental space (Fig. 20). At Mach = 4.5, however, a small region of undisturbed aerodynamic response is manifested along the outer region of the test grid (Fig. 22), where the booster model is presumed to be positioned outside of the shallower bow shock from the orbiter at this highest test Mach number.

Scatter plots of the individual surface static pressure coefficients on the windward surface of the orbiter exhibit trends similar to those observed in the orbiter force and moment coefficients. Consequently, 3-D surface pressure coefficient scatter plots are not shown in this report.

## Color Contour Plots

### *Force and moment coefficients at Mach = 2.3, 3.0, and 4.5, $\Delta\alpha = 0^\circ$*

Figure 23 presents color contour plots of the orbiter proximity normal force, axial force, and pitching moment coefficient responses within the entire test grid matrix at Mach = 2.3 and  $\Delta\alpha = 0^\circ$ . Linear interpolation between data points was used to define the contours. Each point in the test grid matrix is indicated by a small black dot in the contour plots. The format of these plots is similar to the Cart3D CFD color contour plots previously shown in Fig. 16. The region of significant proximity effects of the booster on the orbiter is confined to a relatively small region in the lower left quadrant of each plot, with the orbiter aerodynamic responses returning to undisturbed, or isolated, conditions over much of the experimental space. The color contours of the booster proximity force and moment responses in Fig. 24 are consistent with the observed multiple peaks and troughs that were prominent features in the 3-D scatter plots in Fig. 18. The interference effects of the orbiter on the booster persist throughout the experimental space. In addition, the effects of aerodynamic interference follow Mach lines in the orbiter and booster contour plots in Figs. 23 and 24 in a manner similar to the CFD contour maps in Fig. 16.

The color contour plots of the orbiter and booster proximity aerodynamic responses at Mach = 3.0 are shown in Figs. 25 and 26, respectively, and the corresponding plots at Mach = 4.5 are presented in Figs. 27 and 28. The color contours of the orbiter proximity aerodynamic responses at Mach = 3.0 and 4.5 in Figs. 25 and 27, respectively, reveal diminished regions of aerodynamic interference due to the presence of the booster model as the Mach number is increased. The irregularities in the contour shading in the central portion of the orbiter axial force coefficient response in Fig. 27 are attributed to UT-39A balance electrical zero shifts during the run series. These shifts were within the balance calibration accuracies. However, the ranges of axial force coefficient that define the contour color palette are sufficiently sensitive to display this anomaly.

The contour plots of the booster proximity aerodynamic responses at Mach = 3.0 in Fig. 26 are similar to those observed at Mach = 2.3 in Fig. 24, and the booster model appears to remain in the influence of the orbiter model at all points within the test grid matrix. The significant interference effects of the orbiter on the booster persist at Mach = 4.5 in Fig. 28, although each component plot reveals a region of undisturbed aerodynamic response along the outer region of the experimental space, where the booster model is outside of the shallower orbiter bow shock at Mach = 4.5. The contour plots at Mach = 2.3, 3.0, and 4.5 in Figs. 23 through 28 reveal relative zones of influence between the vehicles that follow Mach lines of increased sweep as the Mach number increases.

### *Relative angle-of-attack comparisons, Mach = 3.0*

Figure 29 compares the color contour plots corresponding to the proximity effects on the orbiter model at Mach = 3.0 and relative angles of attack,  $\Delta\alpha$ , of  $0^\circ$  and  $5^\circ$ . For each aerodynamic coefficient, a common color palette is used for both  $\Delta\alpha$  settings in order to ascertain differences in the contour maps due to a change in the relative angle of attack. The differences in the contour plots in Fig. 29 are subtle, but reveal a reduced region of significant interference effects of the booster on the orbiter and a slightly more rapid return to the undisturbed aerodynamic response at  $\Delta\alpha = 5^\circ$ . Within the smaller region of influence, however, the color shading suggests higher local incremental effects when the booster model is at an angle of attack of  $5^\circ$ . It is speculated that the more intense response within a smaller region of influence is caused by a change in the booster bow shock strength and position relative to the orbiter. The spurious values of the incremental axial force response at  $\Delta\alpha = 0^\circ$  in Fig. 29(b) are attributed to anomalies in the UT-39A balance electrical zeroes that are well within the balance calibration accuracies.

The interference effects on the booster model at Mach = 3.0 and  $\Delta\alpha = 0^\circ$  and  $5^\circ$  are illustrated in Fig. 30. The relative angle of attack of  $5^\circ$  was achieved by changing the booster angle of attack, while the orbiter remained fixed. Compared to

the orbiter model, it was more important to compute the increments between the booster proximity and isolated booster aerodynamic responses in order to better isolate response changes due to the relative angle of attack. The data obtained in axial sweeps of the isolated booster at all relative vertical positions in Test 1745 were subtracted from the corresponding booster proximity data in similar axial sweeps in Test 1741. A common color palette was also used for each booster model response coefficient at  $\Delta\alpha = 0^\circ$  and  $5^\circ$ . Similar to the results obtained on the orbiter model in Fig. 29, the differences in the booster model contour plots at  $\Delta\alpha = 0^\circ$  and  $5^\circ$  are typically subtle. The shading of the contours for the incremental normal force and pitching moment coefficients suggest a more significant interference effect with the booster model at an angle of attack of  $5^\circ$ . The opposite effect appears to occur in the incremental axial force coefficient response. Within the resolution of the contour plots, it is difficult to quantify any sensitivity of the positioning of the booster model aerodynamic response peaks and troughs to a change in relative angle of attack.

### **Influence Plots**

#### ***Force and moment coefficients at Mach = 2.3, 3.0, and 4.5, $\Delta\alpha = 0^\circ$***

Figure 31 shows qualitative influence plots for the longitudinal aerodynamic coefficients of the orbiter model in proximity to the booster model at Mach = 2.3, 3.0, and 4.5 and  $\Delta\alpha = 0^\circ$ . The shaded regions denote areas where the orbiter aerodynamic coefficients are *not* affected by the booster. The shaded interference-free regions were determined from the detailed force and moment data plots presented in later sections of this report and, specifically, by assessing the values of the relative axial and vertical location setpoints where the aerodynamic responses converged to the isolated booster conditions within the 95 percent confidence intervals from the UT-39A balance calibration accuracies. The influence plots reveal large regions of the test grid matrix where the influence of the booster on the orbiter is negligible. At a given Mach number, these regions are virtually identical for the normal force and pitching moment coefficient responses.

The region of undisturbed flow is slightly less for the axial force coefficient response. Increasing the Mach number produces larger regions of undisturbed flow as the booster bow shock angle becomes shallower at the higher Mach numbers.

The test results from UPWT Tests 1741 and 1745 indicate the booster model remains in the influence of the orbiter model within the entire experimental space at Mach = 2.3 and 3.0. The 3-D scatter plots and color contour plots at Mach = 4.5 shown previously in Figs. 22 and 28, respectively, suggest there is a limited region within the test grid matrix where the booster model aerodynamic responses return to undisturbed conditions. Figure 32 shows the qualitative influence plots of the booster proximity aerodynamic coefficients at Mach = 4.5. The shaded regions denote areas where the booster aerodynamic coefficients are *not* affected by the orbiter. The booster proximity normal force and pitching moment coefficients were estimated to have the same region of undisturbed flow, starting in a narrow band along the inboard forward edge of the test grid matrix and extending outboard in a widening strip to encompass most or all of the outermost measurement stations. The booster proximity axial force coefficients exhibit a similar trend, although the region of undisturbed flow is slightly broader. Similar to the orbiter model assessment, the shaded regions were determined from the detailed force and moment data plots presented in later sections of this report by assessing the values of the relative axial and vertical location setpoints where the aerodynamic responses converged to the isolated booster conditions within the 95 percent confidence intervals from the UT-55 balance calibration accuracies.

#### ***Force and moment coefficients at Mach = 3.0, $\Delta\alpha = 0^\circ$ and $5^\circ$***

Figure 33 shows qualitative influence plots for the longitudinal proximity aerodynamic coefficients of the orbiter model at Mach = 3.0 and  $\Delta\alpha = 0$  degrees and 5 degrees. Increasing the relative angle of attack from  $0^\circ$  to  $5^\circ$  results in a slight forward and inboard expansion of the region of undisturbed flow conditions, which is

consistent with the color contour plots shown previously in Fig. 29.

### ***Surface pressure coefficients at Mach = 2.3, 3.0, and 4.5, $\Delta\alpha = 0^\circ$***

Figure 34 shows qualitative influence plots for the orbiter model surface static pressure coefficients in proximity to the booster model at Mach = 2.3, 3.0, and 4.5 and  $\Delta\alpha = 0^\circ$ . The shaded regions denote areas where the orbiter surface pressure coefficients are *not* affected by the booster. The shaded interference-free regions were determined from the detailed pressure coefficient data plots presented in later sections of this report and, specifically, by assessing the values of the relative axial and vertical location setpoints where the surface pressure responses converged to the isolated booster conditions within the 95 percent confidence intervals from the Druck pressure transducer calibration accuracies. The qualitative results shown in Fig. 34 reveal interference-free zones that expand with increasing Mach number in a manner similar to the results previously shown in Fig. 31 corresponding to the orbiter longitudinal aerodynamic coefficients.

### **Isolated Orbiter Data Repeatability**

Figures 35 to 37 present plots of the orbiter normal force, axial force, and pitching moment coefficients versus the relative vertical location,  $z_{setpt}$ , at Mach = 2.3, 3.0, and 4.5, respectively, for all relative axial locations corresponding to  $x_{setpt} = 28$  in. The orbiter model is considered to be in undisturbed, or isolated, flow conditions when the booster model is located at the most extreme aft setpoint at all  $z_{setpt}$  stations. The upper and lower 95 percent confidence limits based on the UT-39A balance calibration accuracies are included in all plots. The results indicate the isolated orbiter longitudinal aerodynamic coefficients are repeatable within the balance accuracy limits at each Mach number. The discontinuity in the orbiter axial force coefficient at Mach = 4.5 in Fig. 37 is attributed to a balance electrical zero shift arising from a thermal gradient on the balance at the higher operating temperature. The variability in the axial force coefficient is well within the bounds

of the balance component calibration accuracy limits.

Test data obtained in UPWT Tests 1741 and 1745 at Mach = 2.3, 3.0, and 4.5 indicated the orbiter model returned to undisturbed flow conditions when the booster model was at relative axial locations greater than one body length aft of the near-docking position at relative angles of attack of  $0^\circ$  and  $5^\circ$ . This trend was observed at all relative vertical locations within the test grid matrix. As a result, numerous data points were available for inclusion in an alternate data repeatability analysis of the isolated orbiter longitudinal aerodynamic characteristics. Data points at relative axial locations within the range  $x_{setpt} = 24$  in. to 28 in. were extracted from all runs at Mach = 2.3, 3.0, and 4.5,  $\Delta\alpha = 0^\circ$  and  $5^\circ$ , and in the belly-to-belly configuration. Figures 38 to 40 plot these data versus the run number at Mach = 2.3, 3.0, and 4.5, respectively, for the orbiter model normal force, axial force, and pitching moment coefficients. The average of these points is shown as a solid black line, and the UT-39A balance accuracy upper and lower limits are represented as dashed red lines in each plot. All data points are bounded by the 95 percent confidence limits derived from the NASA LaRC SVS UT-39A balance calibration, and these results established confidence in the repeatability of the isolated orbiter longitudinal aerodynamic characteristics.

### **Isolated Booster Data Repeatability**

The location and orientation of the LGBB orbiter model was fixed throughout the testing. In contrast, the booster model was positioned throughout the test grid matrix encompassing a significant region of the UPWT test section in the longitudinal and lateral directions. Consequently, the booster model traversed regions of potentially varying flow nonuniformity at each Mach number. Isolated booster model results were obtained in three non-sequential repeat runs consisting of relative axial location sweeps at all relative vertical locations within the experimental space in Test 1745. Figure 41 shows the repeatability of the data obtained in the three axial sweeps at Mach = 3.0

and  $\alpha = 0^\circ$ . Each plot corresponds to a fixed relative vertical position, and plots are shown for all values of  $z_{setpt}$  from 0 in. to 13.13 in. The incremental normal force, axial force, and pitching moment coefficients,  $\Delta C_N$ ,  $\Delta C_A$ , and  $\Delta C_m$ , are plotted versus the relative axial location,  $x_{setpt}$ , in inches. The delta coefficients were obtained using a third-order polynomial fit to the data, interpolating in each run to the nominal values of the independent variable ( $x_{setpt}$ ), then averaging and subtracting the averages from the interpolated data. The upper and lower 95 percent confidence limits from the UT-55 balance calibration are also shown for each balance component. The isolated booster model incremental normal force and pitching moment coefficients exhibit good repeatability at a given relative vertical position, are randomly scattered about the mean, and are bounded at all measurement stations by the corresponding balance accuracy limits. The axial force coefficient exhibits systematic variation that approaches, or exceeds, the balance accuracy limits. Specifically, the third run in each series is offset from the first two runs, which suggests an electrical zero shift in the balance axial force component. It is noted that the axial force coefficient data are plotted using an expanded scale, and the balance accuracy limits correspond to less than  $\pm 5$  microvolts ( $\pm 5$  uV) based on a full-scale axial force gauge output of  $\pm 5.24$  millivolts ( $\pm 5.25$  mV). For comparison, the quoted UPWT DAS accuracy is  $\pm 2$  uV. As a result, the systematic variation exhibited in the axial force data is considered statistically significant but not practically important.

The isolated booster model data repeatability at Mach = 3.0 is further examined by plotting the longitudinal aerodynamic coefficients obtained in one of the three repeat runs versus the relative axial location,  $x_{setpt}$ , at all values of the relative vertical position,  $z_{setpt}$ , as shown in Fig. 42. Each aerodynamic component features two plots, since the values of  $z_{setpt}$  are partitioned for clarity with one intermediate  $z_{setpt}$  location bridging the two plots. The results indicate that the data variability approaches or exceeds the UT-55 balance

accuracy limits as the booster model traverses the aft and outer regions of the test grid matrix.

The same plot format previously used in Fig. 41 is applied in Fig. 43 to display the isolated booster model incremental aerodynamic coefficients at three selected relative vertical positions at Mach = 3.0. The purpose of these plots is to compare three runs acquired at increasing  $z_{setpt}$  intervals, with  $z_{setpt} = 0$  in. as a common reference, in order to better isolate the source of the data variability. The results reveal systematic variation between the three runs that typically exceeds the balance accuracy limits. In addition, the data variability increases as the interval between the three  $z_{setpt}$  stations increases. The increased data variability as the booster model traverses the range of relative vertical location may be associated with a change in the local flow angle across the test section, particularly as the booster model moves closer to the tunnel wall (although the booster model is positioned more than one body length away from the sidewall at the outer edge of the test grid matrix). The data obtained on the isolated booster model in Test 1745 were incorporated into the data plotting and analysis in this report, such that the booster proximity aerodynamic coefficients obtained in relative axial location sweeps were always compared to the corresponding isolated data obtained at the same relative vertical position.

### **Proximity Force and Moment Measurements on Belly-to-Belly Configuration**

***Mach = 2.3,  $\Delta\alpha = 0^\circ$***

#### **Orbiter proximity aerodynamic characteristics**

Plots of the longitudinal proximity aerodynamic coefficients of the orbiter model in the baseline belly-to-belly configuration at Mach = 2.3 and  $\Delta\alpha = 0^\circ$  are shown in Fig. 44. The proximity normal force, axial force, and pitching moment coefficients are plotted versus the relative axial location,  $x_{setpt}$ , at selected values of the relative vertical separation location,  $z_{setpt}$ .

Two measures were implemented to enhance the visualization of the data for each aerodynamic component. The results obtained at the fifteen  $z_{setpt}$  locations were partitioned into two plots with a common run at an intermediate  $z_{setpt}$  location bridging the two plots. Color-coding of the data points was also applied to distinguish each axial sweep. The UT-39A upper and lower 95 percent confidence limits from the balance calibration are shown in all plots. The orbiter proximity data shown in Fig. 44 were acquired by axial movement of the booster model relative to the fixed orbiter model, ranging from the near-docking position at  $x_{setpt} = 0$  in. to the extreme aft location at  $x_{setpt} = 28$  in. A docked or mated condition corresponds to the relative position of the orbiter and booster in the presence of vehicle attach hardware (not simulated in these tests). The orbiter proximity effects at  $z_{setpt} = 0$  in. are nonlinear within approximately the first twelve inches of axial separation between the models. The orbiter proximity data converge to interference-free conditions at this  $z_{setpt}$  location when the booster model MRC is approximately one body length aft of the near-docking position ( $x_{setpt} = 0$  in.). The MSFC schlieren flow visualization images at Mach = 2.99 previously shown in Fig. 2 revealed a complex flow-field interaction between the orbiter and booster models, including bow shock interactions and multiple shock reflections when the models were in close proximity. The orbiter model is only partially exposed to the booster model bow shock within a limited combination of the relative axial and vertical locations in the test grid matrix. The zone of influence of the booster on the orbiter diminishes in both dimensions as the vertical separation of the booster model increases, and this effect is discussed in more detail later in this paragraph. The nonlinear behavior of the orbiter proximity aerodynamic coefficients and the limited zone of influence of the booster on the orbiter were manifested in the qualitative data visualization previously shown in the 3-D scatter plots, color contour plots, and influence plots in Figs. 17, 23, and 31, respectively. The data in Fig. 44 in combination with the UT-39A upper and lower balance accuracy bounds were used to estimate the relative axial location where the

orbiter aerodynamic coefficients converged to interference-free conditions at each relative vertical spacing. These estimates were the basis for the color-coded influence plots in Fig. 31. It is not possible from the UPWT balance measurements alone to correlate all data trends with specific flow features. However, the nonlinear behavior centered about the peak values of the orbiter normal force and pitching moment coefficients is consistent with the advance of the booster bow shock toward the orbiter strake and its subsequent passage over the wing, and the associated induced pressure rise on the strake and wing windward surfaces. For reference, the locations of the apex of the strake, MRC, strake-wing intersection, and trailing edge of the body flap correspond to model stations (MS) 6.968, 8.925, 10.179, and 13.617, respectively, that were previously illustrated in Fig. 6. It is conjectured that the shock-induced pressure rise causes the positive increments to the orbiter normal force coefficient and the negative (nose-down) increments to the pitching moment coefficient, since the wings are located entirely aft of the MRC. The induced pressure rise and impingement location of the booster bow shock on the orbiter model are sensitive to the relative vertical location,  $z_{setpt}$ . A gradual dissipation of the shock-induced pressure rise is expected as the vertical spacing between the models increases. At a fixed relative axial location, increased vertical spacing will promote an aft shift in the booster bow shock impingement on the orbiter. The traversal of the bow shock across the orbiter strake and wing occurs at smaller values of the relative axial location, and the range of relative axial locations within which the bow shock affects the orbiter diminishes. These effects are apparent in the orbiter proximity data shown in Fig. 44, which include reduced magnitude and forward displacement of the peak interference effects in axial sweeps at increased values of the relative vertical position. In addition, the orbiter data converge to interference-free conditions at lower values of the relative axial location,  $x_{setpt}$ . Interpretation of the cyclic behavior of the orbiter proximity axial force coefficient in Fig. 44(c) is more problematic. These trends may be associated with shock-induced flow separation on

the orbiter strake and wing as the booster bow shock traverses these surfaces during a relative axial location sweep.

#### **Booster proximity aerodynamic characteristics**

Basic plots of the longitudinal proximity aerodynamic coefficients of the booster model in the belly-to-belly configuration at  $Mach = 2.3$  and  $\Delta\alpha = 0^\circ$  are shown in Fig. 45 using the same format applied to the orbiter proximity data in Fig. 44. The UT-55 upper and lower 95 percent confidence limits from the balance calibration are shown in all plots. The booster proximity aerodynamic effects are highly nonlinear throughout the entire experimental space at  $Mach = 2.3$ , with the normal force and pitching moment coefficients changing signs several times as the booster moves aft relative to the orbiter. The largest values of the longitudinal proximity effects occur in the first several inches of streamwise separation, although significant aerodynamic responses persist through the test grid matrix. Interference magnitudes are clearly larger than the UT-55 balance accuracy limits shown in each plot. Unlike the orbiter model, the booster model is partially or fully embedded within the orbiter zone of influence at all combinations of the relative axial and vertical locations. At small separation values, the flow-field region between the models is quite complex, likely dominated by multiple shock reflections and regions of flow separation. A typical axial sweep will cause a forward traversal along the booster of aerodynamic flow discontinuities emanating from the orbiter nose, strakes, and wings (bow shock and oblique shocks, for example). Sufficient translation of the booster in the axial direction results in the booster nose traversing the orbiter bow shock such that the entire booster model is embedded in the orbiter zone of influence. As a result, the proximity normal force, axial force, and pitching moment coefficients exhibit multiple local maxima and minima within an axial sweep. Pitching moment proximity effects are quite significant in magnitude and trend, resulting in changes in trim and stability levels that must be accounted for by vehicle control surface capability. The trends that

are visible in the booster data presented in Fig. 45 were also apparent in the 3-D scatter plots and color contour maps of the booster force and moment data in Figs. 18 and 24 that revealed prominent nonlinearities and other interference effects, including multiple local maxima and minima, following Mach lines.

$$Mach = 3.0, \Delta\alpha = 0^\circ$$

#### **Orbiter proximity aerodynamic characteristics**

Basic plots of the longitudinal proximity aerodynamic coefficients of the orbiter model in the belly-to-belly configuration at  $Mach = 3.0$  and  $\Delta\alpha = 0^\circ$  are presented in Fig. 46. The orbiter proximity aerodynamic data trends are similar to those described in the previous section in Fig. 44 corresponding to  $Mach = 2.3$ . The data indicate that the zone of influence of the booster on the orbiter longitudinal aerodynamic coefficients diminishes, and the orbiter proximity coefficients converge to undisturbed (isolated) conditions sooner in an axial sweep than at  $Mach = 2.30$ . These trends were previously revealed in the 3-D scatter plots, color contour maps, and influence plots in Figs. 19, 25, and 31, respectively.

#### **Booster proximity aerodynamic characteristics**

Basic plots of the longitudinal proximity aerodynamic coefficients of the booster model in the belly-to-belly configuration at  $Mach = 3.0$  and  $\Delta\alpha = 0^\circ$  are presented in Fig. 47. The nonlinear proximity effects that persisted through the experimental space at  $Mach = 2.3$  in Fig. 45 are also apparent in the data at  $Mach = 3.0$  and are consistent with the trends observed in the 3-D scatter plots and contour maps in Figs. 20 and 26, respectively.

$$Mach = 4.5, \Delta\alpha = 0^\circ$$

#### **Orbiter proximity aerodynamic characteristics**

Basic plots of the longitudinal proximity aerodynamic coefficients of the orbiter model in the belly-to-belly configuration at  $Mach = 4.5$  and  $\Delta\alpha = 0^\circ$  are presented in Fig. 48. The orbiter

proximity aerodynamic data show a decreasing region of influence of the booster model as the shock angles become shallower and are positioned closer to the bodies at Mach = 4.5. The orbiter longitudinal aerodynamic coefficients return to isolated values at smaller values of  $x_{setpt}$  with increasing Mach number. The qualitative data visualization in Figs. 21, 27 and 31 corresponding to the 3-D scatter plots, color contour maps, and influence plots, respectively, reveal similar trends.

#### **Booster proximity aerodynamic characteristics**

Basic plots of the longitudinal proximity aerodynamic coefficients of the booster model in the belly-to-belly configuration at Mach = 4.5 and  $\Delta\alpha = 0^\circ$  are presented in Fig. 49. Nonlinear proximity effects are manifested in the booster normal force, axial force, and pitching moment coefficients in Fig. 49. However, the shallow angle of the orbiter bow shock promotes an expanding region of interference-free conditions along the forward and outer regions of the experimental space, where the booster model is positioned upstream of the orbiter bow shock. This region is estimated from the distributions of the booster aerodynamic coefficients beginning at  $x_{setpt} = 3.281$  in. for the normal force and pitching moment coefficients and beginning at  $x_{setpt} = 1.969$  in. for the axial force coefficient, where the data exhibit a partial or full return to isolated conditions. The test results indicate a return to undisturbed flow at all test grid points within the outer three relative vertical locations corresponding to  $z_{setpt} = 10.500, 11.810, \text{ and } 13.130$  in. The data presented in Fig. 49 are consistent with the 3-D scatter plots and contour maps in Figs. 22 and 28, respectively, and were the basis for the influence plots previously presented in Fig. 32.

*Mach = 2.3, 3.0, and 4.5;  $\Delta\alpha = 5^\circ$*

#### **Orbiter proximity aerodynamic characteristics**

For completeness, the longitudinal proximity aerodynamic coefficients of the orbiter model in the belly-to-belly configuration at Mach = 2.3,

3.0, and 4.5 obtained with a relative angle of attack,  $\Delta\alpha$ , of  $5^\circ$  are shown in Figs. 50 to 52, respectively, without detailed analysis. The minimum  $z_{setpt}$  separation distance was 0.656 in. at  $\Delta\alpha = 5^\circ$  that was a conservative test safety measure to provide sufficient clearance between the models. Note that test data were not obtained at  $z_{setpt} = 11.81$  in. and 13.13 in. at Mach = 2.3 and  $\Delta\alpha = 5^\circ$  in Fig. 50 because of an observed UT-55 balance axial force dynamic response on the BDDU that approached 100 percent of full-scale output. All data trends that were described with a relative angle of attack of  $0^\circ$  in Figs. 44, 46, and 48 at Mach = 2.3, 3.0, and 4.5, respectively, are applicable to the data at  $\Delta\alpha = 5^\circ$ . The results presented in Figs. 50 to 52 were used to estimate the regions of interference-free conditions within the test grid matrix at each Mach number. The estimates derived from the data at Mach = 3.0 in Figs. 46 and 51 at Mach = 3.0 were used to compare the zones of influence associated with  $\Delta\alpha = 0^\circ$  and  $\Delta\alpha = 5^\circ$  in the qualitative influence plots previously shown in Fig. 33. Increasing the relative angle of attack to  $5^\circ$  was accomplished by a rotation of the booster model on the main sting support system. In general, the booster proximity data revealed an increase in the local force and moment coefficient peaks that occurred at smaller values of the relative axial location. A return to isolated conditions also occurred at smaller  $x_{setpt}$  values. The latter trend was demonstrated in the qualitative influence plots at Mach = 3.0 in Fig. 33. These results suggest the booster bow shock strength and position relative to the orbiter model were sensitive to the relative angle of attack. Detailed comparisons of the orbiter aerodynamic proximity and interference increments due to a change in the relative angle of attack are presented in a later section.

#### **Booster proximity aerodynamic characteristics**

The longitudinal proximity aerodynamic coefficients of the booster model in the belly-to-belly configuration at Mach = 2.3, 3.0, and 4.5 obtained with a relative angle of attack,  $\Delta\alpha$ , of  $5^\circ$  are shown in Figs. 53 to 55, respectively, without detailed analysis. Test data were not obtained at



$z_{setpt} = 11.81$  in. and  $13.13$  in. at  $Mach = 2.3$  and  $\Delta\alpha = 5^\circ$  in Fig. 53 because of an observed UT-55 balance axial force dynamic response on the BDDU that approached 100 percent of full-scale output. The booster proximity aerodynamic coefficients that are plotted in Figs. 53 to 55, and the data obtained on the isolated booster at  $\Delta\alpha = 5^\circ$  in Test 1745 were used to compute booster aerodynamic interference increments at  $\Delta\alpha = 5^\circ$ . These results are compared to corresponding interference increments that were computed for the booster model at  $\Delta\alpha = 0^\circ$  in a later section.

### **Proximity and Isolated Aerodynamic Characteristics on Belly-to-Belly Configuration, $\Delta\alpha = 0^\circ$**

#### ***Mach = 2.3***

##### **Orbiter aerodynamic characteristics**

Comparisons of the longitudinal proximity and isolated aerodynamic coefficients of the orbiter model in the belly-to-belly configuration at  $Mach = 2.3$  and  $\Delta\alpha = 0^\circ$  are presented in Fig. 56. The aerodynamic coefficients are plotted as a function of the relative axial location,  $x_{setpt}$ , at all values of the relative vertical location,  $z_{setpt}$ . The isolated orbiter coefficients correspond to the values obtained with the booster translated to the extreme aft location ( $x_{setpt} = 28$  in.) at each relative vertical location. These values are represented as solid red lines spanning the respective  $x_{setpt}$  ranges at each  $z_{setpt}$  location. The upper and lower bounds of the UT-39A balance accuracies are also included in each plot. The data comparisons show the significant nonlinear interference effects encountered by the orbiter in proximity to the booster. The interference effects are confined to a relatively small subspace within the test grid matrix, however, and the convergence of the proximity data to the isolated orbiter values is clearly illustrated in a pseudo 3-D manner by a rapid scan through the data plots at all  $z_{setpt}$  locations.

##### **Booster aerodynamic characteristics**

Comparisons of the longitudinal proximity and isolated aerodynamic coefficients of the

booster model in the belly-to-belly configuration at  $Mach = 2.3$  and  $\Delta\alpha = 0^\circ$  are presented in Fig. 57. The aerodynamic coefficients are plotted as a function of the relative axial location,  $x_{setpt}$ , at all values of the relative vertical location,  $z_{setpt}$ . The isolated booster data were acquired in Test 1745 with the orbiter model and horizontal blade strut support hardware removed from the test section. Axial sweeps of the isolated booster model were conducted at all relative vertical locations. The upper and lower bounds of the UT-55 balance accuracies are included in all plots. A review of all data plots corresponding to  $z_{setpt} = 0$  in. to  $z_{setpt} = 13.13$  in. reveals highly nonlinear interference effects that persist throughout the experimental space. The interference increments are generally significantly greater than the UT-55 balance accuracies and exhibit only a minor dissipation as the booster model traverses through the test grid matrix.

#### ***Mach = 3.0***

##### **Orbiter aerodynamic characteristics**

Comparisons of the longitudinal proximity and isolated aerodynamic coefficients of the orbiter model in the belly-to-belly configuration at  $Mach = 3.0$  at  $\Delta\alpha = 0^\circ$  are presented in Fig. 58. The plot format is the same as that used at  $Mach = 2.3$  in Fig. 56. The trends observed at  $Mach = 3.0$  are similar to those obtained at  $Mach = 2.3$ . A progressive review of the data plots at  $z_{setpt} = 0$  in. to  $z_{setpt} = 13.13$  in. indicates the zone of influence of the booster on the orbiter diminishes at the higher Mach number.

##### **Booster aerodynamic characteristics**

Comparisons of the longitudinal proximity and isolated aerodynamic coefficients of the booster model in the belly-to-belly configuration at  $Mach = 3.0$  and  $\Delta\alpha = 0^\circ$  are presented in Fig. 59. The plot format is the same as that used at  $Mach = 2.3$  in Fig. 57. Increasing the Mach number to 3.0 does not affect the aerodynamic interference trends that were observed in Fig. 57 at  $Mach = 2.3$ . The test results suggest that the booster model remains in the influence of the

orbiter model throughout the entire experimental space.

### ***Mach = 4.5***

#### **Orbiter aerodynamic characteristics**

Comparisons of the longitudinal proximity and isolated aerodynamic coefficients of the orbiter model at  $Mach = 4.5$  and  $\Delta\alpha = 0^\circ$  are presented in Fig. 60. The plot format is the same as that used at  $Mach = 2.3$  and  $3.0$  in Figs. 56 and 58, respectively. A progressive review of the data plots at  $z_{setpt} = 0$  in. to  $z_{setpt} = 13.13$  in. indicates the nonlinear interference effects are limited to a small subset of the  $x_{setpt}$ - $z_{setpt}$  experimental space where the booster and orbiter models are in close proximity.

#### **Booster aerodynamic characteristics**

Comparisons of the longitudinal proximity and isolated aerodynamic coefficients of the booster model in the belly-to-belly configuration at  $Mach = 4.5$  and  $\Delta\alpha = 0^\circ$  are presented in Fig. 61. The plot format is the same as that used at  $Mach = 2.3$  and  $3.0$  in Figs. 57 and 59, respectively. The nonlinear interference effects on the booster remain significant at  $Mach = 4.5$ . However, there are several plots that reveal a partial or full return to interference-free conditions beginning in a narrow zone near the forward edge of the experimental space at  $z_{setpt} = 1.969$  in. (for the axial force coefficient) or  $z_{setpt} = 3.281$  in. (for normal force and pitching moment coefficients) and expanding at increased relative vertical spacing to include all test grid points at  $z_{setpt} = 10.500$ ,  $11.810$ , and  $13.130$  in. The return to isolated conditions is the result of the booster model being situated upstream and out of the zone of influence of the orbiter model bow shock wave.

### **Relative Angle-of-Attack Effects on Interference Aerodynamics, Mach = 3.0**

#### ***Orbiter aerodynamic characteristics***

Figure 62 compares the longitudinal aerodynamic coefficients of the orbiter model in the belly-to-belly configuration in axial sweeps at

$Mach = 3.0$  and relative angles of attack,  $\Delta\alpha$ , of  $0^\circ$  and  $5^\circ$ . The minimum vertical separation distance was  $0.656$  in. ( $z_{setpt} = 0.656$  in.) to provide sufficient clearance between the orbiter and booster models at  $\Delta\alpha = 5^\circ$ . A relative angle of attack of  $5^\circ$  was obtained by changing the attitude of the booster model mounted to the main sting support system. Isolated orbiter coefficients are shown as solid blue lines that allow a comparison of the interference effects at the two relative angles of attack. This was a valid approach, since the orbiter model location and attitude were fixed throughout the testing. For reference, the upper and lower limits of the UT-39A balance accuracies are shown in each plot. The peak normal force and pitching moment coefficients are higher and occur sooner in the axial sweeps at  $z_{setpt} = 0.656$ ,  $1.313$ ,  $1.969$ , and  $2.625$  in. when the relative angle of attack is increased from  $0^\circ$  to  $5^\circ$ . In addition, the data at  $\Delta\alpha = 5^\circ$  return to undisturbed conditions slightly sooner in comparison to the  $\Delta\alpha = 0^\circ$  case. This trend was previously illustrated in the qualitative influence plot in Fig. 33 that showed a slight expansion of the interference-free zone at a relative angle of attack of  $5^\circ$ . These results suggest there are changes to the booster model bow shock strength and impingement location on the orbiter model at  $\Delta\alpha = 5^\circ$ . It is speculated that an increase in the booster bow shock strength promotes a corresponding increase in the interference effects on the orbiter model. The rotation of the booster causes a small aft displacement of the bow shock impingement location on the orbiter. As a result, the booster bow shock will clear the orbiter model slightly sooner in a given axial sweep.

#### ***Booster aerodynamic characteristics***

An assessment of the interference effects on the booster caused by a change to the relative angle of attack required an account of the direct effects of an angle-of-attack change on the booster longitudinal aerodynamic coefficients. Incremental aerodynamic coefficients were computed by subtracting the isolated booster coefficients obtained in Test 1745 in axial sweeps at  $\alpha = 0^\circ$  and  $5^\circ$  from the corresponding booster proximity coefficients obtained in Test 1741 in

axial sweeps at relative angles of attack of  $0^\circ$  and  $5^\circ$ . This approach provided improved estimates of the interference effects on the booster caused by a change to the relative angle of attack. The incremental normal force, axial force, and pitching moment coefficients,  $\Delta C_N$ ,  $\Delta C_A$ , and  $\Delta C_m$ , are plotted versus the relative axial location,  $x_{setpt}$ , in inches in Fig. 63 at Mach = 3.0 and vertical spacing from  $z_{setpt} = 0.656$  in. to  $z_{setpt} = 13.13$  in. The delta coefficients were obtained using a third-order polynomial fit to the data, interpolating in each run to the nominal values of the independent variable ( $x_{setpt}$ ), and computing the differences through the applicable range of  $x_{setpt}$  in increments of one inch. The delta coefficients shown in Fig. 63 indicate an increase in the relative angle of attack generally increases the peak normal force and pitching moment interference increments, particularly when the models are in close proximity. These effects diminish somewhat with increased vertical spacing between the models. Similarly, the initial peaks in the incremental normal force and pitching moment coefficients occur at slightly smaller  $x_{setpt}$  values in a given axial sweep. However, this trend is not universally applicable to the additional maxima and minima that occur in the aerodynamic responses at larger separation distances between the models. The booster model remains in the influence of the orbiter model throughout the experimental space at  $\Delta\alpha = 0^\circ$  and  $5^\circ$ . In addition, the overall trends of the booster interference increments, including the cyclic aerodynamic responses with multiple maxima and minima, are not sensitive to the relative angle of attack change at Mach = 3.0.

### **Mach Number Effects on Proximity Aerodynamics, $\Delta\alpha = 0^\circ$**

#### ***Orbiter aerodynamic characteristics***

Figure 64 shows the effects of the Mach number on the orbiter proximity aerodynamic coefficients in axial sweeps at all values of the relative vertical location,  $z_{setpt}$ , and a relative angle of attack,  $\Delta\alpha$ , of  $0^\circ$ . The overall levels of the proximity aerodynamic coefficients typically decrease as the Mach number increases. Increasing the Mach number decreases the peak

values of the proximity aerodynamic coefficients that occur when the orbiter and booster models are in close proximity. In addition, the maximum aerodynamic responses occur at smaller values of the relative axial location as the Mach number increases. Furthermore, the proximity aerodynamic coefficients return sooner to undisturbed conditions at the higher Mach numbers. The latter effects were inferred from the 3-D scatter plots (Figs. 17, 19, and 21), color contour maps (Figs. 23, 25, and 27), and influence plots (Fig. 31). The induced effects of the booster bow shock wave on the orbiter decrease with increased supersonic Mach number. The shallower angle of the booster bow shock changes the impingement location on the orbiter at a given relative spacing such that the shock-induced pressure rise on the orbiter strakes and wings occurs sooner in a relative axial sweep. The booster bow shock also traverses aft of the orbiter model at smaller  $x_{setpt}$  values because of the more oblique shock angles at the higher Mach numbers.

#### ***Booster aerodynamic characteristics***

Figure 65 shows the effects of the Mach number on the booster proximity aerodynamic characteristics in axial sweeps at all values of the relative vertical location,  $z_{setpt}$ , and a relative angle of attack,  $\Delta\alpha$ , of  $0^\circ$ . The booster model traverses a complex and varying flow field throughout the test grid matrix arising from multiple shock impingement, shock reflections, and possible shock-induced flow separation. The complex nature of the proximity flow field was previously shown in the schlieren images obtained in the MSFC TWT at Mach = 2.99 in Fig. 2. It is speculated that the multiple sign changes in the booster proximity normal force and pitching moment coefficients are caused by the successive passage across the booster wings, strakes, and moment reference center (MRC) of a varying combination of the orbiter bow shock, the oblique shocks from the orbiter strakes and wings, and reflected shocks. One trend that is inferred from the data in Fig. 65 is analogous to a phase shift effect, where the cyclic patterns of the booster proximity aerodynamic coefficients at a given vertical spacing exhibit axial displacements

as the Mach number increases. The booster traverses the zone of influence of the orbiter in a different manner, since the shock angles become shallower at the higher Mach numbers. For example, at small separation distances at Mach = 4.5, more of the booster model is upstream of the orbiter bow shock than at Mach = 2.3. Larger axial displacements from the mated position are required at the higher Mach number to position the booster entirely within the orbiter zone of influence and for impingement of the complex system of shocks and reflected shocks to traverse specific locations on the booster. An extreme example is at the larger vertical separation distances, where the entire booster is in undisturbed conditions at Mach = 4.5, but a major portion of the booster is in the orbiter zone of influence at Mach = 2.3.

### **Interference Effects on Belly-to-Belly and Back-to-Belly Configurations, Mach = 3.0, $\Delta\alpha = 0^\circ$**

#### ***Orbiter aerodynamic characteristics***

A back-to-belly configuration was simulated by rolling the booster model -90 degrees. In this orientation, the top side of the booster faced the belly of the orbiter. The booster vertical tail was removed and replaced with a tail-off block. Figure 66 compares the longitudinal aerodynamic coefficients of the orbiter model in the belly-to-belly and back-to-belly configurations in axial sweeps at Mach = 3.0 and a relative angle of attack,  $\Delta\alpha$ , of  $0^\circ$ . Isolated orbiter coefficients are shown as solid blue lines that allow a comparison of the interference effects on both configurations. As previously stated, this was a valid approach, since the orbiter model location and attitude were fixed throughout the testing. For reference, the upper and lower limits of the UT-39A balance accuracies are shown in each plot.

The test results shown in Fig. 66 reveal slightly higher peak aerodynamic responses, and aft displacements where these peaks occur, with the back-to-belly configuration. In addition, there are typically minor differences in the axial locations where the data return to undisturbed conditions. A possible explanation for the small

increments to the interference effects are correspondingly small changes to the booster bow shock strength and its position relative to the orbiter. Specifically, a slight increase in the shock strength and a forward displacement of the shock impingement location on the orbiter may be caused by rolling the drooped nose of the booster model to a  $-90^\circ$  orientation. The data plots in Fig. 66 are limited to  $z_{setpt}$  locations of 0 in. to 6.563 in., since there were negligible differences between the two configurations at all other values of the vertical separation.

#### ***Booster aerodynamic characteristics***

An assessment of the interference effects on the booster caused by a change to the booster roll angle orientation relative to the orbiter required a modified analysis. This approach accounted for isolated booster model runs conducted in Test 1745 at roll angle orientations of  $+90^\circ$  and  $-90^\circ$ . Incremental aerodynamic coefficients were computed by subtracting the isolated booster coefficients in axial sweeps at  $\alpha = 0^\circ$  from the corresponding booster proximity coefficients obtained in axial sweeps of the belly-to-belly and back-to-belly configurations at  $\Delta\alpha = 0^\circ$  in Tests 1741 and 1745. The incremental normal force, axial force, and pitching moment coefficients,  $\Delta C_N$ ,  $\Delta C_A$ , and  $\Delta C_m$  are plotted versus the relative axial location,  $x_{setpt}$ , in inches in Fig. 67 at Mach = 3.0 and vertical separation locations from  $z_{setpt} = 0$  in. to  $z_{setpt} = 13.13$  in. The delta coefficients were obtained using a third-order polynomial fit to the data, interpolating in each run to the nominal values of the independent variable ( $x_{setpt}$ ), and computing the differences through the applicable range of  $x_{setpt}$  in increments of one inch. Note that the sign of the delta coefficients for the body-axis normal force and pitching moment coefficients for the booster in the back-to-belly configuration was reversed to provide a direct comparison to the corresponding delta coefficients in the belly-to-belly arrangement.

The booster interference effects in Fig. 67 are measurably different for the belly-to-belly and back-to-belly configurations. The low-wing design of the LGBB configuration increases the

vertical separation of the strakes, wings, and body flap relative to the orbiter in the back-to-belly arrangement. The change in vertical spacing promotes a downstream shift in the impingement locations of the complex system of shock waves on the booster. This causes corresponding shifts in the booster interference coefficient curves in Fig. 67 similar to that described in a previous section on Mach number effects. This trend persists throughout the entire experimental space at Mach = 3.0.

### **Isolated Orbiter Surface Static Pressure Measurements**

#### ***Mach = 2.3, 3.0, and 4.5***

A plot of the isolated orbiter static pressure coefficients distributed along the centerline of the body lower surface at Mach = 2.3, 3.0, and 4.5 is shown in Fig. 68. Details of the pressure orifice locations were previously shown in Fig. 8, Table III, and Appendix A. The isolated pressure distributions were obtained with the booster model translated to the extreme aft location ( $x_{sept} = 28$  in.) in the test grid matrix at all Mach numbers. The Mach number effect on the orbiter pressure measurements is very small. These results were repeatable within the 95 percent confidence intervals of the Druck pressure transducer measurement accuracy (repeatability analysis not included in this discussion), and these results are included for reference in the majority of surface static pressure plots in the following sections.

### **Orbiter Surface Static Pressure Distributions on Belly-to-Belly Configuration, $\Delta\alpha = 0^\circ$**

#### ***Mach = 2.3***

Plots of the orbiter lower surface centerline pressure distributions at Mach = 2.3 obtained on the belly-to-belly configuration with  $\Delta\alpha = 0^\circ$  are shown in Fig. 69. The plot format features the surface static pressure coefficient,  $C_p$ , versus the model station (MS) location in inches of the eight pressure orifices distributed along the belly of the orbiter model. Each plot contains multiple color-coded curves corresponding to specific relative

axial locations,  $x_{sept}$ , at a fixed relative vertical location,  $z_{sept}$ . There are two plots for each  $z_{sept}$  location that partition the full range of  $x_{sept}$  locations for improved data visualization. For reference, the isolated orbiter pressure distribution is presented in each plot as a solid black line. The upper and lower limits of the Druck pressure transducer calibration accuracies are also included in each plot.

The first pressure orifice location is approximately 0.3 in. aft of the orbiter model nose, and it is insensitive to changes in the relative axial and vertical spacing of the models. The  $C_p$  values at this discrete measurement location are coincident with the isolated orbiter value, which indicates this location near the orbiter nose is in undisturbed flow conditions everywhere within the experimental space. Two features can be readily derived from the data, within the resolution of the centerline pressure distributions: (1) the approximate length along the orbiter centerline, beginning from the nose, where the surface pressures correspond to interference-free conditions and (2) the approximate location of booster bow shock impingement on the orbiter. A typical pressure distribution is characterized by pressure coefficient values tracking along the isolated orbiter curve starting from the nose, followed by a pressure rise to a local maximum that occurs downstream of the booster bow shock impingement. For example, at  $x_{sept} = 2$  in. and  $z_{sept} = 0$  in., the  $C_p$  values track along the isolated orbiter curve along the first two inches of the model. There is a subsequent rise in the surface pressures to a local maximum at approximately four inches aft of the model nose. A similar trend occurs at  $x_{sept} = 4$  in., where undisturbed flow conditions exist along the first four inches of the model, followed by a maximum  $C_p$  value approximately six inches aft of the model nose. A rapid scan through the 2-D data plots from the minimum vertical spacing ( $z_{sept} = 0$  in.) to the maximum  $z_{sept}$  location of 5.25 in. shown in Fig. 69 illustrates the extent of the interference-free zone and the traversal of the booster bow shock pressure signature along the orbiter model. The data shown in Fig. 69 in conjunction with the

$C_p$  data obtained at Mach = 3.0 and 4.5 shown in the next two sections of this report were used to construct the influence plot previously shown in Fig. 34.

### ***Mach = 3.0***

Plots of the orbiter lower surface centerline pressure distributions at Mach = 3.0 obtained on the belly-to-belly configuration are shown in Fig. 70. The plot format is the same as that shown in the previous section at Mach = 2.3. Test results are presented for relative vertical locations ranging from  $z_{setpt} = 0$  in. to  $z_{setpt} = 4.594$  in. only, since all pressure data at greater relative spacings converge to undisturbed conditions. The data trends at Mach = 3.0 are similar to those observed at the lower supersonic Mach number and are presented without additional discussion.

### ***Mach = 4.5***

Plots of the orbiter lower surface centerline pressure distributions at Mach = 4.5 obtained on the belly-to-belly configuration are shown in Fig. 71 using the same format as that used at Mach = 2.3 and 3.0 in Figs. 69 and 70, respectively. Test results are presented for relative vertical locations ranging from  $z_{setpt} = 0$  in. to  $z_{setpt} = 3.281$  inches only, since all pressure data at greater relative spacings converge to undisturbed conditions. The trends in the surface pressure distributions observed at Mach = 2.3 and 3.0 are unchanged at Mach = 4.5. The data clearly show the expanding region of interference-free conditions at the highest test Mach number.

## **Orbiter Individual Surface Static Pressure Measurements, $\Delta\alpha = 0^\circ$**

### ***Mach = 2.3***

An alternate assessment of the orbiter lower surface static pressure measurements obtained at all 13 pressure orifice locations with the belly-to-belly configuration and  $\Delta\alpha = 0^\circ$  is presented in the following sections. The  $C_p$  values obtained at each of the discrete pressure orifice locations on the belly centerline and left and right wing lower surfaces are plotted in axial ( $x_{setpt}$ ) sweeps at

selected values of the relative vertical location,  $z_{setpt}$ . There were eight equally-spaced orifices on the orbiter centerline starting at MS 0.300 in. (near the nose) and ending at MS 13.300 in. (center of aft body flap). A total of four equally-spaced orifices were located in a chordwise row on the right wing midspan at butt line (BL) 1.632 in., and a single orifice was located on the left wing midspan (BL -1.632 in.) at a location that mirrored the second orifice location on the right wing. For reference, the isolated orbiter  $C_p$  value obtained at the selected pressure orifice location featured in a given plot is shown as a solid black line. The upper and lower limits corresponding to the 95 percent confidence intervals from the pressure transducer calibrations are included in each plot.

Figure 72 presents plots of the eight individual surface static pressure coefficients on the orbiter lower surface centerline in axial sweeps at relative vertical spacings from  $z_{setpt} = 0$  in. to  $z_{setpt} = 4.594$  in. All pressure coefficient responses were consistent with undisturbed flow conditions at the larger vertical separation distances. The axial sweep range was limited to one body length ranging from  $x_{setpt} = 0$  in. to  $x_{setpt} = 13.13$  in., since the orbiter surface pressure responses returned to interference-free conditions at larger relative axial locations. The pressure coefficients are distinguished by a number designation ranging from 101 to 108 to denote their order in the centerline distribution. The corresponding model stations (in inches from the orbiter nose) for pressure orifices 101 to 108 are MS = 0.300, 2.157, 4.014, 5.871, 7.729, 9.586, 11.443, and 13.300, respectively. Interference effects can be estimated by comparing the proximity pressure coefficients to the reference isolated orbiter pressure coefficient in each plot.

The data corresponding to the first pressure orifice location in Fig. 72 reveal interference-free conditions at all locations in the experimental space, since the proximity pressure coefficients are coincident with the isolated orbiter pressure coefficient response. The first indication of an induced effect of the booster bow shock on the orbiter pressure coefficients occurs in the near-

docking position ( $x_{setpt} = 0$  in.,  $z_{setpt} = 0$  in.) at the second orifice location. Pressure responses at the orifices downstream of this location also exhibit interference effects, since they are all within the zone of influence of the booster bow shock. The pressure coefficient quickly returns to undisturbed conditions when the booster model is translated aft to  $x_{setpt} = 2$  in. at the minimum vertical separation distance ( $z_{setpt} = 0$  in.). At this relative axial position, the pressure coefficient at the third orifice location exhibits a positive peak to denote the impingement of the booster shock at/near this location on the orbiter. The pressure coefficient at the third orifice location returns to undisturbed conditions when the booster model moves aft to  $x_{setpt} = 4$  in. The aft progression of the booster bow shock pressure signature in the axial sweep at  $z_{setpt} = 0$  in. is apparent at the remaining five orifice locations in Fig. 72. In each case, the peak pressure response is followed by a rapid return to interference-free conditions as the shock passes aft of the orifice location. At a booster model aft translation distance equivalent to one body length ( $x_{setpt} = 13.13$  in.), the pressure coefficient data at the last orifice location marks the passage of the booster bow shock aft of the orbiter model. The orbiter pressure coefficient responses at orifice locations 104 to 108 reveal successive  $C_p$  maxima within the axial sweep at  $z_{setpt} = 0$  in. that may reflect the additional induced effect of a reflected shock wave at this minimum vertical separation distance. The MSFC TWT schlieren image at Mach = 2.99 corresponding to the near-docking position previously shown in Fig. 2 clearly showed a “shock train” within the region between the orbiter and booster models. Within the resolution of the current pressure measurements, there is no evidence of similar successive  $C_p$  maxima at increased vertical separation distances from  $z_{setpt} = 0.656$  in. to  $z_{setpt} = 4.597$  in. As the booster model moves away from the orbiter model in the vertical direction, the location of the booster bow shock impingement on the orbiter shifts downstream. As a result, the peak pressures marking the passage of the bow shock and the return to interference-free conditions occur sooner in the axial sweep. At the largest relative vertical location shown in Fig. 72

( $z_{setpt} = 4.597$  in.), only the pressure responses from the last two orifices reveal interference effects at the beginning of the axial sweep, followed by a rapid return to undisturbed flow conditions. In general, the magnitudes of the peak pressure coefficients diminish at the larger vertical separation distances, within the resolution of the coarse distribution of pressure measurement locations. This trend is consistent with a reduction in booster model bow shock strength at increased distances from the booster.

For completeness, the surface static pressure measurements obtained on the right and left wing lower surfaces are presented in Fig. 73. Four orifices were distributed in a chordwise row at midspan on the right wing corresponding to MS 10.717, 11.293, 11.869, and 12.444 in. The pressure coefficients are distinguished by a number designation ranging from 201 to 204 to denote their order in the chordwise distribution. A single orifice was located at midspan on the left wing at MS 11.293 in., which mirrored the second orifice location on the right wing, and the corresponding number designation for this pressure coefficient was 301. The trends in the orbiter wing pressure coefficients as the booster model navigates the  $x_{setpt}$ - $z_{setpt}$  experimental space are similar to those exhibited by the orbiter body centerline pressure coefficients. The surface pressure responses at the aft two pressure orifice locations 203 and 204 capture successive  $C_p$  maxima at the minimum vertical separation distance ( $z_{setpt} = 0$  in.) that are consistent with the induced effects of the booster bow shock and a reflected shock previously inferred from the orbiter body centerline pressure coefficients in Fig. 72. The pressure coefficients at the single orifice location 301 on the left wing show good agreement with the mirror orifice location 202 on the right wing that demonstrates the symmetry of the proximity flow field at Mach = 2.3.

### ***Mach = 3.0***

The  $C_p$  values obtained at each of the discrete pressure orifice locations on the belly centerline and left and right wing lower surfaces at Mach = 3.0 are plotted in axial ( $x_{setpt}$ ) sweeps at selected values of the relative vertical location,

$z_{setpt}$ , in Figs. 74 and 75. The trends observed at Mach = 3.0 are similar to those described in the previous section at Mach = 2.3. Specifically, the orbiter surface pressure response to the progression of the booster bow shock along the body and wings, the conjectured induced effects of a reflected shock, and the return to interference-free conditions as functions of the relative axial and vertical locations in the experimental space are similar at the higher Mach number.

### ***Mach = 4.5***

The  $C_p$  values obtained at each of the discrete pressure orifice locations on the belly centerline and left and right wing lower surfaces at Mach = 4.5 are plotted in axial ( $x_{setpt}$ ) sweeps at selected values of the relative vertical location,  $z_{setpt}$ , in Figs. 76 and 77. The shallower shock angle at Mach = 4.5 expands the region of interference-free conditions that is indicated by a return of the orbiter pressure coefficients to undisturbed conditions at smaller values of the relative axial and vertical locations in Figs. 76 and 77. The induced effects of a reflected shock are more subtle at the aft four orifice locations along the body centerline (orifices 105, 106, 107, and 108) and at the aft orifice location on the left wing (orifice 204). In general, the maximum shock-induced  $C_p$  values diminish at Mach = 4.5 compared to the results obtained at the lower supersonic Mach numbers.

### **Relative Angle-of-Attack Effect on Orbiter Surface Pressure Distributions, Mach = 3.0**

Plots of the orbiter lower surface centerline pressure distributions obtained on the belly-to-belly configuration at Mach = 3.0 and relative angles of attack of  $0^\circ$  and  $5^\circ$  are shown in Fig. 78. The plot format features the distribution of the lower surface static pressure coefficient,  $C_p$ , versus the model station (MS) location (in inches) along the centerline of the orbiter model. Each page contains three plots corresponding to specified relative axial and vertical locations,  $x_{setpt}$  and  $z_{setpt}$ . For example, Figs. 78(a) and 78(b) compare the centerline pressure

distributions at  $\Delta\alpha = 0^\circ$  and  $5^\circ$  at nominal  $x_{setpt}$  values of 0, 2, 4, 6, 8 and 10 in. at a fixed  $z_{setpt}$  value of 0.656 in. Similar pairs of plots are presented for  $z_{setpt} = 1.313, 1.969, 2.625, 3.281,$  and  $3.938$  in. The isolated orbiter pressure distribution obtained at Mach = 3.0 and the upper and lower limits of the pressure transducer calibration accuracies are included in each plot.

The test results indicate that changing the relative angle of attack from  $0^\circ$  to  $5^\circ$  causes an aft displacement of the booster bow shock-induced pressure peaks at a given  $x_{setpt}$  location and, in general, a small increase in the peak magnitudes. In addition, a return of the entire centerline pressure distribution to undisturbed flow conditions occurs sooner in an axial sweep. These trends were attributed in a previous section to small changes to the strength and position of the booster bow shock relative to the orbiter as a result of a rotation of the booster in the pitch plane.

### **Mach Number Effect on Orbiter Surface Static Pressure Distributions, $\Delta\alpha = 0^\circ$**

The effect of the Mach number on the orbiter lower surface centerline proximity pressure distributions obtained on the belly-to-belly configuration at  $\Delta\alpha = 0^\circ$  are shown in Fig. 79. The plot format features the distribution of the lower surface static pressure coefficient,  $C_p$ , versus the model station (MS) location (in inches) along the centerline of the orbiter model. Each page contains three plots corresponding to specified relative axial and vertical locations,  $x_{setpt}$  and  $z_{setpt}$ . For example, Figs. 79(a) and 79(b) compare the centerline pressure distributions at Mach = 2.3, 3.0, and 4.5 at nominal  $x_{setpt}$  values of 0, 2, 4, 6, 8 and 10 in. at a fixed  $z_{setpt}$  value of 0 in. Similar pairs of plots are presented for  $z_{setpt} = 0.656, 1.313, 1.969, 2.625, 3.281,$  and  $3.938$  in. It was previously shown in Fig. 68 that the isolated orbiter pressure distributions exhibited only small changes at Mach = 2.3, 3.0, and 4.5. Consequently, the proximity results in Fig. 79 are representative of the sensitivity of the surface pressure interference effects to changes in the test Mach number.



The data in Fig. 79 typically show an aft shift in the peak shock-induced  $C_p$  values and a reduction in peak magnitudes as the Mach number increases from 2.3 to 4.5. These trends are not universally applicable, because of pressure distribution resolution limitations. Increasing the Mach number also causes the pressure coefficients to return to undisturbed conditions at smaller values of the relative axial and vertical locations within the experimental space. These trends are attributed to the shallower shock angles and reduced shock strength at the orbiter model surface at the higher Mach numbers.

### **Mach Number and Relative Angle-of-Attack Effects on Orbiter Surface Pressure Distributions**

The plots presented in this section provide a combined assessment of the effects of the Mach number and the relative angle of attack on the orbiter lower surface centerline pressure distributions obtained on the belly-to-belly configuration. The plot format features the distribution of the lower surface static pressure coefficient,  $C_p$ , versus the model station (MS) location (in inches) along the centerline of the orbiter model. Each page contains three plots comparing the pressure distributions at  $\Delta\alpha = 0^\circ$  and  $5^\circ$ , and each plot is associated with a corresponding Mach number. The data in all three plots on a given page were obtained at a fixed combination of the relative axial and vertical locations,  $x_{setpt}$  and  $z_{setpt}$ . For example, Figs. 80(a) to 80(d) compare the centerline pressure distributions for  $\Delta\alpha = 0^\circ$  and  $5^\circ$  at Mach = 2.3, 3.0, and 4.5 at nominal  $x_{setpt}$  values of 0, 4, 8 and 12 in. and a fixed  $z_{setpt}$  value of 0.656 in. The next four pages display similar plots corresponding to  $z_{setpt} = 1.919$  in. (Figs. 80(e) to 80(h)). Data obtained at  $z_{setpt} = 3.281$  in. are plotted in the final four pages in Figs. 80(i) to 80(l). The isolated orbiter pressure distributions and 95 percent confidence intervals from the pressure transducer calibrations are included for each Mach number.

The results presented in Fig. 80 indicate that increases in the relative angle of attack and the

Mach number typically promote aft shifts in the location of the booster bow shock-induced pressure peaks and a more rapid return to undisturbed flow conditions at a given combination of the relative axial and vertical locations. An increase in the relative angle of attack generally causes an increase in the maximum  $C_p$  levels, whereas the opposite effect occurs as the Mach number is increased. The mechanisms affecting the booster bow shock impingement location and strength at the orbiter model include the rotation of the booster model in the pitch plane and the shallower shock wave angles at the higher Mach numbers.

### **Summary**

A wind tunnel investigation was conducted of the supersonic stage separation aerodynamic characteristics of a generic bimese two-stage-to-orbit reusable launch vehicle configuration. Force and moment and surface static pressure measurements were obtained on 0.0175-scale models of the Langley Glide-Back Booster concept in the NASA Langley Research Center Unitary Plan Wind Tunnel at Mach numbers of 2.3, 3.0, and 4.5 and a unit Reynolds number of 2.0 million per foot. The test results supported a larger effort to develop and validate experimental and computational tools applicable to the design and simulation of stage separation and abort procedures for reusable launch vehicles composed of multiple bodies, including winged bodies. The UPWT stage separation testing resulted in improvements to model and support system hardware design and installation processes, in-tunnel calibrations, testing procedures and capabilities, and data visualization and analysis methods. An exploratory test was conducted using uninstrumented models to ensure operational safety, evaluate qualitative proximity aerodynamic responses, and verify new support hardware and automated model positioning techniques. Follow-on testing using instrumented models provided an extensive longitudinal force and moment and surface static pressure database on the bimese LGBB concept in belly-to-belly and back-to-belly configurations at simulated supersonic separation and abort

conditions through large ranges of axial and vertical separation distances and selected relative angles of attack. The orbiter and booster models exhibited highly nonlinear aerodynamic responses as a result of a complex system of shock waves, reflected shocks, and possibly shock-induced flow separation. The zone of influence of the booster on the orbiter was limited to a relatively small region of the experimental space, whereas the booster remained in the orbiter zone of influence throughout the test grid matrix, except at the highest test Mach number of 4.5. The stage separation interference effects were sensitive to the Mach number, relative angle of attack, and roll angle orientation of the booster relative to the orbiter. The UPWT data exhibited good agreement with previous testing conducted in the NASA Marshall Space Flight Center 14-Inch Trisonic Wind Tunnel and with computational fluid dynamics methods using a compressible, three-dimensional Reynolds-averaged Navier-Stokes flow solver OVERFLOW and an inviscid, unstructured Cartesian Euler flow solver CART3D at Mach = 3.0. The UPWT stage separation testing of the LGBB models established a foundation for more efficient and complex testing of advanced launch vehicles in this facility, including continuous-sweep data acquisition, booster separation motor plume separation, and multi-body stage separation and abort simulation at supersonic speeds.

## References

1. Dillenius, M. F. E., Perkins, S. C., and Nixon, D.: *Pylon Carriage and Separation of Stores*. AIAA Progress in Astronautics and Aeronautics: Tactical Missile Aerodynamics – General Topics, M. J. Hensch, ed., Vol. 141, 1992.
2. Taylor, R. T., and Alford, W. J., Jr.: *A Wind Tunnel Investigation of the Carry Loads and Mutual Interference Effects of 1/40-Scale Models of the X-15 and B-52 Airplanes in Combination*. NASA TM X-184, December 1959.
3. Woods, W. C., Holland, S. D., and DiFulvio, M.: *Hyper-X Stage Separation Wind-Tunnel Test Program*. AIAA 2000-4008, August 2008.
4. Hall, R. M., Holland, S. P., and Blevins, J. A.: *Aerodynamic Characterization of a Modern Launch Vehicle*. AIAA 2011-10, January 2011.
5. Pinier, J. T., Herron, A., Gomez, R. J.: *Advances in the Characterization of NASA's Space Launch System Aerodynamic Environments*. AIAA 2019-3397, June 2019.
6. Craig, M. K. and Dresser, H. S.: *Shuttle Booster Separation Aerodynamics*. NASA CP 2283, Shuttle Performance: Lessons Learned, Part 1, pp 139-158, J. P. Arrington and J. J. Jones, ed., October 1983.
7. Klotz, I.: *Recycling Rockets*. Aerospace America, pp 32-39, September 2017.
8. *The U.S. Air Force in Space 1945 to the Twenty-First Century*. Proceedings Air Force Historical Foundation Symposium, Andrews AFB, Maryland, published by Washington, D.C.: USAF History and Museums Project, United States Air Force, R. C. Hall and J. Neufeld, ed., ISBN 13: 9780160496660, September 1995.
9. Decker, J. P.: *Aerodynamic Separation Characteristics of Conceptual Parallel-Staged Reusable Launch Vehicle at Mach 3 to 6*. NASA TM X-1051, January 1965.
10. Decker, J. P. and Gera J.: *An Exploratory Study of Parallel-Stage Separation of Reusable Launch Vehicles*. NASA TN D-4765, October 1968.
11. Decker, J. P.: *Aerodynamic Interference Effects Caused by Parallel-Staged Simple Aerodynamic Configurations at Mach Numbers of 3 and 6*. NASA TN D-5379, August 1969.
12. Decker, J. P. and Wilhite, A. W.: *Technology and Methodology of Separating Two Similar Size Aerospace Vehicles Within the Atmosphere*. AIAA 75-29, January 1975.

13. Naftel, J. C., Wilhite, A. W., and Cruz, C. I.: *Analysis of Separation of a Two-Stage Winged Launch Vehicle*. AIAA 96-0195, January 1986.
14. Naftel, J. C. and Wilhite, A. W.: *Aerodynamic Separation and Glideback of a Mach 3 Staged Orbiter*. AIAA 90-0223, January 1990.
15. Murphy, K. J., Buning, P. G., Pamadi, B. N., Scallion, W. I., and Jones, K. M.: *Overview of Transonic to Hypersonic Stage Separation Tool Development for Multi-Stage-to-Orbit Concepts*. AIAA 2004-2595.
16. Pamadi, B. N., Tartabini, P. V., and Starr, B. R.: *Ascent, Stage Separation, and Glideback Performance of a Partially Reusable Small Launch Vehicle*. AIAA 2004-0876, January 2004.
17. Murphy, K. J., Erickson, G. E., and Goodliff, S.: *Experimental Stage Separation Tool Development in NASA Langley's Unitary Plan Wind Tunnel*. AIAA 2004-4727, August 2004.
18. Bordelon, W. J., Jr., Frost, A. L., and Reed, D. K.: *Stage Separation Wind Tunnel Tests of a Generic Two-Stage-to-Orbit Launch Vehicle*. AIAA 2003-4227, June 2003.
19. Murphy, K. J. and Scallion, W. I.: *Experimental Stage Separation Tool Development in NASA Langley's Aerothermodynamics Laboratory*. AIAA 2005-6127, August 2005.
20. Buning, P. G., Gomez, R. J., and Scallion, W. I.: *CFD Approaches for Simulation of Wing-Body Stage Separation*. AIAA 2004-4838, August 2004.
21. Pamadi, B. N., Neirynck, T. A., Covell, P. F., Hotchko, N. J., and Bose, D.: *Simulation and Analyses of Staging Maneuvers of Next Generation Reusable Launch Vehicles*. AIAA 2004-5185, August 2004.
22. Erickson, G. E.: *Estimation of Supersonic Stage Separation Aerodynamics of Winged-Body Launch Vehicles Using Response Surface Methods*. NASA/TM-2010-216196, February 2010.
23. Schwartz, R. J. and Fleming, G. A.: *Advanced Visualization of Experimental Data in Real Time Using LiveView3D*. AIAA 2006-3302, June 2006.
24. Pinier, J. T.: *Ares I and Ares I-X Stage Separation Testing*. Journal of Spacecraft and Rockets, Vol. 9, No. 5, pp 842-852, September-October 2012.
25. Wilcox, F. J., Jr., Pinier, J. T., and Chan, D.T.: *Space Launch System Booster Separation Aerodynamic Testing in the NASA Langley Unitary Plan Wind Tunnel*. AIAA 2016-0796, January 2016.
26. Winski, C. S., Danehy, P. M., Watkins, A. N., Shea, P., Meerooff, J., Lowe, K. T., and Houlden, H.: *Space Launch System Booster Separation Supersonic Powered Testing with Surface and Off-Body Measurements*. AIAA 2019-3505, June 2019.
27. Simon, E. H.: *The George C. Marshall Space Flight Center's 14x14 Inch Trisonic Wind Tunnel Handbook*. NASA TM X-64624, November 1971.
28. Jackson, C. M., Jr., Corlett, W. A., and Monta, W. J.: *Description and Calibration of the Langley Unitary Plan Wind Tunnel*. NASA TP 1905, August 1981.
29. Erickson, G. E. and Wilcox, F. J., Jr.: *Ares I Aerodynamic Testing at the NASA Langley Unitary Plan Wind Tunnel*. AIAA 2011-0999, January 2011.
30. Falman, B. E. and Wilcox, F. J., Jr.: *Overview of the Continuous Sweep Data Acquisition Capability at the Langley Unitary Plan Wind Tunnel*. NASA Langley Research Center whitepaper, 2010.
31. Erickson, G. E.: *Overview of Supersonic Aerodynamics Measurement Techniques in the NASA Langley Unitary Plan Wind Tunnel*. NASA/TM-2007-214894, August 2007.
32. Crawford, B. L.: *Angle Measurement System (AMS) for Establishing Model Pitch and Roll*

*Zero, and Performing Single Axis Angle Comparisons.* AIAA 2007-1162, January 2007.

33. Parker, P. A., Morton, M., Draper, N., and Line, W.: *A Single-Vector Force Calibration Method Featuring the Modern Design of Experiments (Invited).* AIAA 2001-0170, January 2001.
34. Cramer, C. J., Wright, J. D., Simmons, S. A., Bobbitt, L. E., and DeMoss, J. A.: *A Description of the Development, Capabilities, and Operational Status of the Test SLATE Data Acquisition System at the National Transonic Facility.* AIAA 2015-0623, January 2015.
35. Vigyan, Inc. 1999: *Vigyan's DESL: Data Engineering Scripting Language.* <https://www.vigyan.com/desl>, viewed 6 March 2020.
36. Carver, R. H.: *Practical Data Analysis with JMP, Third Edition.* SAS Institute Inc., Cary, NC, USA, October 2019.

## Appendix A

Please follow the [link](#) to the detailed drawings of the 0.0175-scale LGBB booster and orbiter models.

## **Appendix B**

**Please follow the link to additional photographs showing the model, instrumentation, and support system hardware build-up, calibration, and installation processes in UPWT Test Section 2.**

## Appendix C

Please follow the link to the detailed drawings of the horizontal blade strut assembly for the 0.0175-scale LGBB orbiter model.

## Appendix D

Please follow the [link to the calibration procedures for the LGBB orbiter and booster relative axial and vertical positions](#).



## **Appendix E**

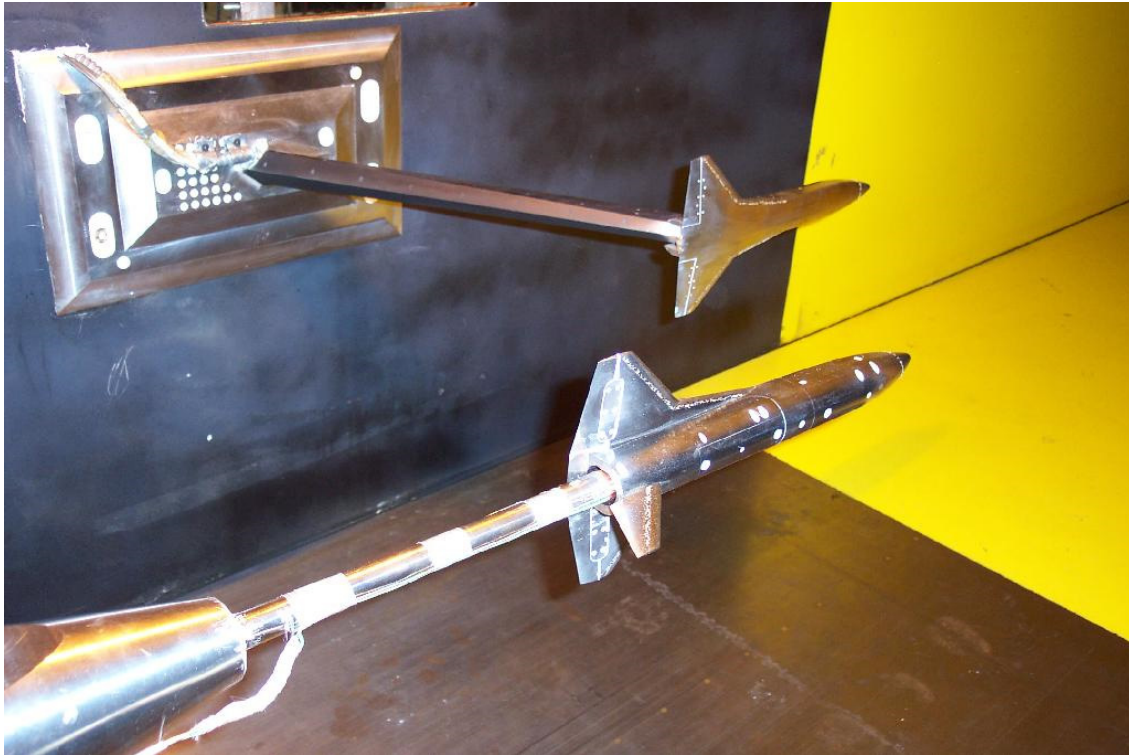
**[Please follow the link to the UT-39A and UT-55 balance outline drawings and design loads.](#)**

Table I. Axial and vertical setpoint locations in LGBB model stage separation test grid matrix.

| $x_{setpt}$ ,<br>inches | $x_{setpt}/L$ | $z_{setpt}$ ,<br>inches | $z_{setpt}/L$ |
|-------------------------|---------------|-------------------------|---------------|
| 0                       | 0             | 0                       | 0             |
| 1                       | .076          | 0.656                   | .05           |
| 2                       | .152          | 1.313                   | .10           |
| 2.625                   | .2            | 1.969                   | .15           |
| 4                       | .305          | 2.625                   | .20           |
| 5.25                    | .4            | 3.281                   | .25           |
| 6                       | .457          | 3.938                   | .30           |
| 7                       | .533          | 4.594                   | .35           |
| 7.875                   | .6            | 5.250                   | .40           |
| 9                       | .686          | 6.563                   | .50           |
| 10                      | .762          | 7.875                   | .60           |
| 10.5                    | .8            | 9.188                   | .70           |
| 12                      | .914          | 10.500                  | .80           |
| 13.13                   | 1.00          | 11.810                  | .90           |
| 14                      | 1.067         | 13.130                  | 1.00          |
| 15                      | 1.143         |                         |               |
| 16                      | 1.219         |                         |               |
| 17                      | 1.295         |                         |               |
| 18                      | 1.371         |                         |               |
| 19                      | 1.448         |                         |               |
| 20                      | 1.524         |                         |               |
| 21                      | 1.6           |                         |               |
| 22                      | 1.676         |                         |               |
| 23                      | 1.752         |                         |               |
| 24                      | 1.829         |                         |               |
| 25                      | 1.905         |                         |               |
| 26                      | 1.981         |                         |               |
| 27                      | 2.057         |                         |               |
| 28                      | 2.133         |                         |               |

$L$  (LGBB model reference length) = 13.125 inches

*Table II. Average freestream conditions in UPWT Test Section 2 for 0.0175-scale LGBB model Tests 1739, 1741, and 1745. (Tunnel operating information and model installation photograph are shown for reference.)*



| <i>Condition Number</i> | <i>Mach</i> | <i>Mode</i> | <i>Block (in.)</i> | <i>Power (MW)</i> | <i>H<sub>o</sub> (psfa)</i> | <i>T<sub>o</sub> (°F)</i> | <i>Re (1/ft)</i>      | <i>q (psf)</i> | <i>p<sub>inf</sub> (psfa)</i> | <i>Dewpt (°F)</i> |
|-------------------------|-------------|-------------|--------------------|-------------------|-----------------------------|---------------------------|-----------------------|----------------|-------------------------------|-------------------|
| 1                       | 2.30        | II          | 126.58             | 28.94             | 1445                        | 125                       | 2.0 x 10 <sup>6</sup> | 427.9          | 115.55                        | -27               |
| 2                       | 3.00        | III         | 178.13             | 27.93             | 2083                        | 125                       | 2.0 x 10 <sup>6</sup> | 357.2          | 56.70                         | -21               |
| 3                       | 4.50        | IV          | 218.07             | 23.22             | 4666                        | 150                       | 2.0 x 10 <sup>6</sup> | 228.2          | 16.12                         | -6                |

Table III. Orbiter model surface static pressure measurement locations.

| <b>Orifice Number</b> | <b>Location</b><br>(All orifices are on lower surface.) | <b>MS</b><br>(in.) | <b>BL</b><br>(in.) |
|-----------------------|---|--------------------|--------------------|
| 101                   | Body Centerline   | 0.300              | 0.000              |
| 102                   | Body Centerline   | 2.157              | 0.000              |
| 103                   | Body Centerline   | 4.014              | 0.000              |
| 104                   | Body Centerline   | 5.871              | 0.000              |
| 105                   | Body Centerline   | 7.729              | 0.000              |
| 106                   | Body Centerline   | 9.586              | 0.000              |
| 107                   | Body Centerline   | 11.443             | 0.000              |
| 108                   | Body Centerline   | 13.300             | 0.000              |
| 201                   | Right Wing Midspan                                      | 10.717             | 1.632              |
| 202                   | Right Wing Midspan                                      | 11.293             | 1.632              |
| 203                   | Right Wing Midspan                                      | 11.869             | 1.632              |
| 204                   | Right Wing Midspan                                      | 12.444             | 1.632              |
| 301                   | Left Wing Midspan                                       | 11.293             | -1.632             |

Table IV. UT-39A and UT-55 balance design loads and calibration accuracies.

| <b>UT-39A Balance</b> |                     |   |  |   |
|-----------------------|---------------------|---|--|---|
| <b>Component</b>      | <b>Design Loads</b> | <b>Accuracies</b><br>(percent FS,<br>95 percent CL) | <b>Accuracies Expressed</b><br><b>in Balance Voltage</b> | <b>Accuracies Expressed</b><br><b>in Forces and</b><br><b>Moments</b> |
| NF                    | ±150 lbs            | ±0.06   | ±4.9 μV  | ±0.09 lbs   |
| AF                    | ±30 lbs             | ±0.19   | ±18.6 μV   | ±0.057 lbs  |
| PM                    | ±200 in-lbs         | ±0.07   | ±5.0 μV  | ±0.14 in-lbs  |

| <b>UT-55 Balance</b> |                     |   |  |   |
|----------------------|---------------------|---|--|---|
| <b>Component</b>     | <b>Design Loads</b> | <b>Accuracies</b><br>(percent FS,<br>95 percent CL) | <b>Accuracies Expressed</b><br><b>in Balance Voltage</b> | <b>Accuracies Expressed</b><br><b>in Forces and</b><br><b>Moments</b> |
| NF                   | ±150 lbs            | ±0.10   | ±6.7 μV  | ±0.15 lbs   |
| AF                   | ±20 lbs             | ±0.09   | ±4.7 μV  | ±0.018 lbs  |
| PM                   | ±200 in-lbs         | ±0.05   | ±3.5 μV  | ±0.10 in-lbs  |

Table V. UT-39A and UT-55 balance calibration accuracies expressed as aerodynamic coefficients. (Coefficients are based on test conditions at a unit Reynolds number of 2.0 million per foot.)

| <b>UT-39A (Orbiter Model)</b> |                         |                         |                         |
|-------------------------------|-------------------------|-------------------------|-------------------------|
| <b>Mach</b>                   | <b><math>C_N</math></b> | <b><math>C_A</math></b> | <b><math>C_m</math></b> |
| 2.30                          | +/-0.00158              | +/-0.00100              | +/-0.00019              |
| 3.00                          | +/-0.00189              | +/-0.00120              | +/-0.00022              |
| 4.50                          | +/-0.00296              | +/-0.00187              | +/-0.00035              |

| <b>UT-55 (Booster Model)</b> |                         |                         |                         |
|------------------------------|-------------------------|-------------------------|-------------------------|
| <b>Mach</b>                  | <b><math>C_N</math></b> | <b><math>C_A</math></b> | <b><math>C_m</math></b> |
| 2.30                         | +/-0.00263              | +/-0.00032              | +/-0.00013              |
| 3.00                         | +/-0.00315              | +/-0.00038              | +/-0.00016              |
| 4.50                         | +/-0.00493              | +/-0.00059              | +/-0.00025              |

Table VI. Orbiter model pressure measurement uncertainties expressed in terms of the static pressure coefficient (95 percent confidence limits (CL) about the mean response).

| <b>Mach</b> | <b><math>q</math><br/>(psf)</b> | <b><math>C_p</math> uncertainty, <math>\Delta C_p</math><br/>(95 percent CL)</b> |
|-------------|---------------------------------|--|
| 2.30        | 427.9                           | $\pm 0.001682$   |
| 3.00        | 357.2                           | $\pm 0.002017$   |
| 4.50        | 228.2                           | $\pm 0.003151$   |

$$\Delta C_p = \Delta p/q = [0.001 * (5 \text{ psi}) * 144 \text{ sq.in/sq.ft.}]/q = 0.72 \text{ psf}/q$$

Table VII. Sting and strut deflection calibration constants with UT-55 and UT-39A balances.

| <i>UPWT 350-15B Sting with UT-55 Balance Deflection Constants</i> |                    |
|---|--------------------|
| NFDEFL  | 0.019023 deg/lb    |
| PMDEFL  | 0.004980 deg/in-lb |
| NFINCH1   | 0.005066 in/lb     |
| PMINCH1   | 0.004980 in/in-lb  |

| <i>Horizontal Blade Strut with UT-39A Balance Deflection Constants</i> |                    |
|--|--------------------|
| NFDEFL2  | 0.001565 deg/lb    |
| PMDEFL2  | 0.002759 deg/in-lb |
| NFINCH2  | 0.000437 in/lb     |
| PMINCH2  | 0.000163 in/in-lb  |

(a)  $Mach = 2.30$ ,  $\Delta\alpha = 0^\circ$  and  $5^\circ$

x - Not attainable due to axial limit breeches on the sting-mounted balance



(b)  $Mach = 3.00$ ,  $\Delta\alpha = 0^\circ$  and  $5^\circ$

Run

 $X/L$ 

Run

$$X/L$$



Table VIII. Concluded.

(c) Mach = 4.50,  $\Delta\alpha = 0^\circ$  and  $5^\circ$

| Mach = 4.50, Δα = 0° |      |        |  |  |  |  |  |  |  |  |  |  |  |  |  |  |  |  |  |  |  |  |  |  |  |  |  |  |  | Run |  |  |  |  |  |  |  |  |  |  |  |  |  |  |  |  |  |  |  |  |  |  |  |  |  |  |  |  |  |  |  |  |  |  |  |  |  |  |  |  |  |  |  |  |  |  |  |  |  |  |  |  |  |  |  |  |  |  |  |  |  |  |  |  |  |  |  |  |  |  |  |  |  |  |  |  |  |  |  |  |  |  |  |  |  |  |  |  |  |  |  |  |  |  |  |  |  |  |  |  |  |  |  |  |  |  |  |  |  |  |  |  |  |  |  |  |  |  |  |  |  |  |  |  |  |  |  |  |  |  |  |  |  |  |  |  |  |  |  |  |  |  |  |  |  |  |  |  |  |  |  |  |  |  |  |  |  |  |  |  |  |  |  |  |  |  |  |  |  |  |  |  |  |  |  |  |  |  |  |  |  |  |  |  |  |  |  |  |  |  |  |  |  |  |  |  |  |  |  |  |  |  |  |  |  |  |  |  |  |  |  |  |  |  |  |  |  |  |  |  |  |  |  |  |  |  |  |  |  |  |  |  |  |  |  |  |  |  |  |  |  |  |  |  |  |  |  |  |  |  |  |  |  |  |  |  |  |  |  |  |  |  |  |  |  |  |  |  |  |  |  |  |  |  |  |  |  |  |  |  |  |  |  |  |  |  |  |  |  |  |  |  |  |  |  |  |  |  |  |  |  |  |  |  |  |  |  |  |  |  |  |  |  |  |  |  |  |  |  |  |  |  |  |  |  |  |  |  |  |  |  |  |  |  |  |  |  |  |  |  |  |  |  |  |  |  |  |  |  |  |  |  |  |  |  |  |  |  |  |  |  |  |  |  |  |  |  |  |  |  |  |  |  |  |  |  |  |  |  |  |  |  |  |  |  |  |  |  |  |  |  |  |  |  |  |  |  |  |  |  |  |  |  |  |  |  |  |  |  |  |  |  |  |  |  |  |  |  |  |  |  |  |  |  |  |  |  |  |  |  |  |  |  |  |  |  |  |  |  |  |  |  |  |  |  |  |  |  |  |  |  |  |  |  |  |  |  |  |  |  |  |  |  |  |  |  |  |  |  |  |  |  |  |  |  |  |  |  |  |  |  |  |  |  |  |  |  |  |  |  |  |  |  |  |  |  |  |  |  |  |  |  |  |  |  |  |  |  |  |  |  |  |  |  |  |  |  |  |  |  |  |  |  |  |  |  |  |  |  |  |  |  |  |  |  |  |  |  |  |  |  |  |  |  |  |  |  |  |  |  |  |  |  |  |  |  |  |  |  |  |  |  |  |  |  |  |  |  |  |  |  |  |  |  |  |  |  |  |  |  |  |  |  |  |  |  |  |  |  |  |  |  |  |  |  |  |  |  |  |  |  |  |  |  |  |  |  |  |  |  |  |  |  |  |  |  |  |  |  |  |  |  |  |  |  |  |  |  |  |  |  |  |  |  |  |  |  |  |  |  |  |  |  |  |  |  |  |  |  |  |  |  |  |  |  |  |  |  |  |  |  |  |  |  |  |  |  |  |  |  |  |  |  |  |  |  |  |  |  |  |  |  |  |  |  |  |  |  |  |  |  |  |  |  |  |  |  |  |  |  |  |  |  |  |  |  |  |  |  |  |  |  |  |  |  |  |  |  |  |  |  |  |  |  |  |  |  |  |  |  |  |  |  |  |  |  |  |  |  |  |  |  |  |  |  |  |  |  |  |  |  |  |  |  |  |  |  |  |  |  |  |  |  |  |  |  |  |  |  |  |  |  |  |  |  |  |  |  |  |  |  |  |  |  |  |  |  |  |  |  |  |  |  |  |  |  |  |  |  |  |  |  |  |  |  |  |  |  |  |  |  |  |  |  |  |  |  |  |  |  |  |  |  |  |  |  |  |  |  |  |  |  |  |  |  |  |  |  |  |  |  |  |  |  |  |  |  |  |  |  |  |  |  |  |  |  |  |  |  |  |  |  |  |  |  |  |  |  |  |  |  |  |  |  |  |  |  |  |  |  |  |  |  |  |  |  |  |  |  |  |  |  |  |  |  |  |  |  |  |  |  |  |  |  |  |  |  |  |  |  |  |  |  |  |  |  |  |  |  |  |  |  |  |  |  |  |  |  |  |  |  |  |  |  |  |  |  |  |  |  |  |  |  |  |  |  |  |  |  |  |  |  |  |  |  |  |  |  |  |  |  |  |  |  |  |  |  |  |  |  |  |  |  |  |  |  |  |  |  |  |  |  |  |  |  |  |  |  |  |  |  |  |  |  |  |  |  |  |  |  |  |  |  |  |  |  |  |  |  |  |  |  |  |  |  |  |  |  |  |  |  |  |  |  |  |  |  |  |  |  |  |  |  |  |  |  |  |  |  |  |  |  |  |  |  |  |  |  |  |  |  |  |  |  |  |  |  |  |  |  |  |  |  |  |  |  |  |  |  |  |  |  |  |  |  |  |  |  |  |  |  |  |  |  |  |  |  |  |  |  |  |  |  |  |  |  |  |  |  |  |  |  |  |  |  |  |  |  |  |  |  |  |  |  |  |  |  |  |  |  |  |  |  |  |  |  |  |  |  |  |  |  |  |  |  |  |  |  |  |  |  |  |  |  |  |  |  |  |  |  |  |  |  |  |  |  |  |  |  |  |  |  |  |  |  |  |  |  |  |  |  |  |  |  |  |  |  |  |  |  |  |  |  |  |  |  |  |  |  |  |  |  |  |  |  |  |  |  |  |  |  |  |  |  |  |  |  |  |  |  |  |  |  |  |  |  |  |  |  |  |  |  |  |  |  |  |  |  |  |  |  |  |  |  |  |  |  |  |  |  |  |  |  |  |  |  |  |  |  |  |  |  |  |  |  |  |  |  |  |  |  |  |  |  |  |  |  |  |  |  |  |  |  |  |  |  |  |  |  |  |  |  |  |  |  |  |  |  |  |  |  |  |  |  |  |  |  |  |  |  |  |  |  |  |  |  |  |  |  |  |  |  |  |  |  |  |  |  |  |  |  |  |  |  |  |  |  |  |  |  |  |  |  |  |  |  |  |  |  |  |  |  |  |  |  |  |  |  |    |
|----------------------|------|--------|--|--|--|--|--|--|--|--|--|--|--|--|--|--|--|--|--|--|--|--|--|--|--|--|--|--|--|-----|--|--|--|--|--|--|--|--|--|--|--|--|--|--|--|--|--|--|--|--|--|--|--|--|--|--|--|--|--|--|--|--|--|--|--|--|--|--|--|--|--|--|--|--|--|--|--|--|--|--|--|--|--|--|--|--|--|--|--|--|--|--|--|--|--|--|--|--|--|--|--|--|--|--|--|--|--|--|--|--|--|--|--|--|--|--|--|--|--|--|--|--|--|--|--|--|--|--|--|--|--|--|--|--|--|--|--|--|--|--|--|--|--|--|--|--|--|--|--|--|--|--|--|--|--|--|--|--|--|--|--|--|--|--|--|--|--|--|--|--|--|--|--|--|--|--|--|--|--|--|--|--|--|--|--|--|--|--|--|--|--|--|--|--|--|--|--|--|--|--|--|--|--|--|--|--|--|--|--|--|--|--|--|--|--|--|--|--|--|--|--|--|--|--|--|--|--|--|--|--|--|--|--|--|--|--|--|--|--|--|--|--|--|--|--|--|--|--|--|--|--|--|--|--|--|--|--|--|--|--|--|--|--|--|--|--|--|--|--|--|--|--|--|--|--|--|--|--|--|--|--|--|--|--|--|--|--|--|--|--|--|--|--|--|--|--|--|--|--|--|--|--|--|--|--|--|--|--|--|--|--|--|--|--|--|--|--|--|--|--|--|--|--|--|--|--|--|--|--|--|--|--|--|--|--|--|--|--|--|--|--|--|--|--|--|--|--|--|--|--|--|--|--|--|--|--|--|--|--|--|--|--|--|--|--|--|--|--|--|--|--|--|--|--|--|--|--|--|--|--|--|--|--|--|--|--|--|--|--|--|--|--|--|--|--|--|--|--|--|--|--|--|--|--|--|--|--|--|--|--|--|--|--|--|--|--|--|--|--|--|--|--|--|--|--|--|--|--|--|--|--|--|--|--|--|--|--|--|--|--|--|--|--|--|--|--|--|--|--|--|--|--|--|--|--|--|--|--|--|--|--|--|--|--|--|--|--|--|--|--|--|--|--|--|--|--|--|--|--|--|--|--|--|--|--|--|--|--|--|--|--|--|--|--|--|--|--|--|--|--|--|--|--|--|--|--|--|--|--|--|--|--|--|--|--|--|--|--|--|--|--|--|--|--|--|--|--|--|--|--|--|--|--|--|--|--|--|--|--|--|--|--|--|--|--|--|--|--|--|--|--|--|--|--|--|--|--|--|--|--|--|--|--|--|--|--|--|--|--|--|--|--|--|--|--|--|--|--|--|--|--|--|--|--|--|--|--|--|--|--|--|--|--|--|--|--|--|--|--|--|--|--|--|--|--|--|--|--|--|--|--|--|--|--|--|--|--|--|--|--|--|--|--|--|--|--|--|--|--|--|--|--|--|--|--|--|--|--|--|--|--|--|--|--|--|--|--|--|--|--|--|--|--|--|--|--|--|--|--|--|--|--|--|--|--|--|--|--|--|--|--|--|--|--|--|--|--|--|--|--|--|--|--|--|--|--|--|--|--|--|--|--|--|--|--|--|--|--|--|--|--|--|--|--|--|--|--|--|--|--|--|--|--|--|--|--|--|--|--|--|--|--|--|--|--|--|--|--|--|--|--|--|--|--|--|--|--|--|--|--|--|--|--|--|--|--|--|--|--|--|--|--|--|--|--|--|--|--|--|--|--|--|--|--|--|--|--|--|--|--|--|--|--|--|--|--|--|--|--|--|--|--|--|--|--|--|--|--|--|--|--|--|--|--|--|--|--|--|--|--|--|--|--|--|--|--|--|--|--|--|--|--|--|--|--|--|--|--|--|--|--|--|--|--|--|--|--|--|--|--|--|--|--|--|--|--|--|--|--|--|--|--|--|--|--|--|--|--|--|--|--|--|--|--|--|--|--|--|--|--|--|--|--|--|--|--|--|--|--|--|--|--|--|--|--|--|--|--|--|--|--|--|--|--|--|--|--|--|--|--|--|--|--|--|--|--|--|--|--|--|--|--|--|--|--|--|--|--|--|--|--|--|--|--|--|--|--|--|--|--|--|--|--|--|--|--|--|--|--|--|--|--|--|--|--|--|--|--|--|--|--|--|--|--|--|--|--|--|--|--|--|--|--|--|--|--|--|--|--|--|--|--|--|--|--|--|--|--|--|--|--|--|--|--|--|--|--|--|--|--|--|--|--|--|--|--|--|--|--|--|--|--|--|--|--|--|--|--|--|--|--|--|--|--|--|--|--|--|--|--|--|--|--|--|--|--|--|--|--|--|--|--|--|--|--|--|--|--|--|--|--|--|--|--|--|--|--|--|--|--|--|--|--|--|--|--|--|--|--|--|--|--|--|--|--|--|--|--|--|--|--|--|--|--|--|--|--|--|--|--|--|--|--|--|--|--|--|--|--|--|--|--|--|--|--|--|--|--|--|--|--|--|--|--|--|--|--|--|--|--|--|--|--|--|--|--|--|--|--|--|--|--|--|--|--|--|--|--|--|--|--|--|--|--|--|--|--|--|--|--|--|--|--|--|--|--|--|--|--|--|--|--|--|--|--|--|--|--|--|--|--|--|--|--|--|--|--|--|--|--|--|--|--|--|--|--|--|--|--|--|--|--|--|--|--|--|--|--|--|--|--|--|--|--|--|--|--|--|--|--|--|--|--|--|--|--|--|--|--|--|--|--|--|--|--|--|--|--|--|--|--|--|--|--|--|--|--|--|--|--|--|--|--|--|--|--|--|--|--|--|--|--|--|--|--|--|--|--|--|--|--|--|--|--|--|--|--|--|--|--|--|--|--|--|--|--|--|--|--|--|--|--|--|--|--|--|--|--|--|--|--|--|--|--|--|--|--|--|--|--|--|--|--|--|--|--|--|--|--|--|--|--|--|--|--|--|--|--|--|--|--|--|--|--|--|--|--|--|--|--|--|--|--|--|--|--|--|--|--|--|--|--|--|--|--|--|--|--|--|--|--|--|--|--|--|--|--|--|--|--|--|--|--|--|--|--|--|--|--|--|--|--|--|--|--|--|--|--|--|--|--|--|--|--|--|--|--|--|--|--|--|--|--|--|--|--|--|--|----|
| Z setpoint           | 1.00 | 13.130 |  |  |  |  |  |  |  |  |  |  |  |  |  |  |  |  |  |  |  |  |  |  |  |  |  |  |  |     |  |  |  |  |  |  |  |  |  |  |  |  |  |  |  |  |  |  |  |  |  |  |  |  |  |  |  |  |  |  |  |  |  |  |  |  |  |  |  |  |  |  |  |  |  |  |  |  |  |  |  |  |  |  |  |  |  |  |  |  |  |  |  |  |  |  |  |  |  |  |  |  |  |  |  |  |  |  |  |  |  |  |  |  |  |  |  |  |  |  |  |  |  |  |  |  |  |  |  |  |  |  |  |  |  |  |  |  |  |  |  |  |  |  |  |  |  |  |  |  |  |  |  |  |  |  |  |  |  |  |  |  |  |  |  |  |  |  |  |  |  |  |  |  |  |  |  |  |  |  |  |  |  |  |  |  |  |  |  |  |  |  |  |  |  |  |  |  |  |  |  |  |  |  |  |  |  |  |  |  |  |  |  |  |  |  |  |  |  |  |  |  |  |  |  |  |  |  |  |  |  |  |  |  |  |  |  |  |  |  |  |  |  |  |  |  |  |  |  |  |  |  |  |  |  |  |  |  |  |  |  |  |  |  |  |  |  |  |  |  |  |  |  |  |  |  |  |  |  |  |  |  |  |  |  |  |  |  |  |  |  |  |  |  |  |  |  |  |  |  |  |  |  |  |  |  |  |  |  |  |  |  |  |  |  |  |  |  |  |  |  |  |  |  |  |  |  |  |  |  |  |  |  |  |  |  |  |  |  |  |  |  |  |  |  |  |  |  |  |  |  |  |  |  |  |  |  |  |  |  |  |  |  |  |  |  |  |  |  |  |  |  |  |  |  |  |  |  |  |  |  |  |  |  |  |  |  |  |  |  |  |  |  |  |  |  |  |  |  |  |  |  |  |  |  |  |  |  |  |  |  |  |  |  |  |  |  |  |  |  |  |  |  |  |  |  |  |  |  |  |  |  |  |  |  |  |  |  |  |  |  |  |  |  |  |  |  |  |  |  |  |  |  |  |  |  |  |  |  |  |  |  |  |  |  |  |  |  |  |  |  |  |  |  |  |  |  |  |  |  |  |  |  |  |  |  |  |  |  |  |  |  |  |  |  |  |  |  |  |  |  |  |  |  |  |  |  |  |  |  |  |  |  |  |  |  |  |  |  |  |  |  |  |  |  |  |  |  |  |  |  |  |  |  |  |  |  |  |  |  |  |  |  |  |  |  |  |  |  |  |  |  |  |  |  |  |  |  |  |  |  |  |  |  |  |  |  |  |  |  |  |  |  |  |  |  |  |  |  |  |  |  |  |  |  |  |  |  |  |  |  |  |  |  |  |  |  |  |  |  |  |  |  |  |  |  |  |  |  |  |  |  |  |  |  |  |  |  |  |  |  |  |  |  |  |  |  |  |  |  |  |  |  |  |  |  |  |  |  |  |  |  |  |  |  |  |  |  |  |  |  |  |  |  |  |  |  |  |  |  |  |  |  |  |  |  |  |  |  |  |  |  |  |  |  |  |  |  |  |  |  |  |  |  |  |  |  |  |  |  |  |  |  |  |  |  |  |  |  |  |  |  |  |  |  |  |  |  |  |  |  |  |  |  |  |  |  |  |  |  |  |  |  |  |  |  |  |  |  |  |  |  |  |  |  |  |  |  |  |  |  |  |  |  |  |  |  |  |  |  |  |  |  |  |  |  |  |  |  |  |  |  |  |  |  |  |  |  |  |  |  |  |  |  |  |  |  |  |  |  |  |  |  |  |  |  |  |  |  |  |  |  |  |  |  |  |  |  |  |  |  |  |  |  |  |  |  |  |  |  |  |  |  |  |  |  |  |  |  |  |  |  |  |  |  |  |  |  |  |  |  |  |  |  |  |  |  |  |  |  |  |  |  |  |  |  |  |  |  |  |  |  |  |  |  |  |  |  |  |  |  |  |  |  |  |  |  |  |  |  |  |  |  |  |  |  |  |  |  |  |  |  |  |  |  |  |  |  |  |  |  |  |  |  |  |  |  |  |  |  |  |  |  |  |  |  |  |  |  |  |  |  |  |  |  |  |  |  |  |  |  |  |  |  |  |  |  |  |  |  |  |  |  |  |  |  |  |  |  |  |  |  |  |  |  |  |  |  |  |  |  |  |  |  |  |  |  |  |  |  |  |  |  |  |  |  |  |  |  |  |  |  |  |  |  |  |  |  |  |  |  |  |  |  |  |  |  |  |  |  |  |  |  |  |  |  |  |  |  |  |  |  |  |  |  |  |  |  |  |  |  |  |  |  |  |  |  |  |  |  |  |  |  |  |  |  |  |  |  |  |  |  |  |  |  |  |  |  |  |  |  |  |  |  |  |  |  |  |  |  |  |  |  |  |  |  |  |  |  |  |  |  |  |  |  |  |  |  |  |  |  |  |  |  |  |  |  |  |  |  |  |  |  |  |  |  |  |  |  |  |  |  |  |  |  |  |  |  |  |  |  |  |  |  |  |  |  |  |  |  |  |  |  |  |  |  |  |  |  |  |  |  |  |  |  |  |  |  |  |  |  |  |  |  |  |  |  |  |  |  |  |  |  |  |  |  |  |  |  |  |  |  |  |  |  |  |  |  |  |  |  |  |  |  |  |  |  |  |  |  |  |  |  |  |  |  |  |  |  |  |  |  |  |  |  |  |  |  |  |  |  |  |  |  |  |  |  |  |  |  |  |  |  |  |  |  |  |  |  |  |  |  |  |  |  |  |  |  |  |  |  |  |  |  |  |  |  |  |  |  |  |  |  |  |  |  |  |  |  |  |  |  |  |  |  |  |  |  |  |  |  |  |  |  |  |  |  |  |  |  |  |  |  |  |  |  |  |  |  |  |  |  |  |  |  |  |  |  |  |  |  |  |  |  |  |  |  |  |  |  |  |  |  |  |  |  |  |  |  |  |  |  |  |  |  |  |  |  |  |  |  |  |  |  |  |  |  |  |  |  |  |  |  |  |  |  |  |  |  |  |  |  |  |  |  |  |  |  |  |  |  |  |  |  |  |  |  |  |  |  |  |  |  |  |  |  |  |  |  |  |  |  |  |  |  |  |  |  |  |  |  |  |  |  |  |  |  |  | </ |

Table IX. Final run log for UPWT Test 1741, Phase II, orbiter surface static pressure measurements.

(a)  $Mach = 2.30$ ,  $\Delta\alpha = 0^\circ$  and  $5^\circ$

| Mach = 2.30, Δα = 0°  |        |        |      |      |       |      |      |      |      |       |      |      |      |      |       |      |      |      |      |      |      |      |      |      |      |      |      | Run  |      |      |        |
|-----------------------|--------|--------|------|------|-------|------|------|------|------|-------|------|------|------|------|-------|------|------|------|------|------|------|------|------|------|------|------|------|------|------|------|--------|
| Z setpoint            | 1.00   | 13.130 |      |      |       |      |      |      |      |       |      |      |      |      |       |      |      |      |      |      |      |      |      |      |      |      |      | N/A  |      |      |        |
|                       | 0.90   | 11.810 |      |      |       |      |      |      |      |       |      |      |      |      |       |      |      |      |      |      |      |      |      |      |      |      |      | N/A  |      |      |        |
|                       | 0.80   | 10.500 |      |      |       |      |      |      |      |       |      |      |      |      |       |      |      |      |      |      |      |      |      |      |      |      |      | N/A  |      |      |        |
|                       | 0.70   | 9.188  |      |      |       |      |      |      |      |       |      |      |      |      |       | 4350 | 4349 |      |      |      |      |      |      |      |      |      |      | 195  |      |      |        |
|                       | 0.60   | 7.875  |      |      |       |      |      |      |      |       |      |      | 4354 | 4353 | 4352  | 4351 |      |      |      |      |      |      |      |      |      |      |      | 196  |      |      |        |
|                       | 0.50   | 6.563  |      |      |       |      |      |      |      |       | 4360 | 4359 | 4358 | 4357 | 4356  | 4355 |      |      |      |      |      |      |      |      |      |      |      | 197  |      |      |        |
|                       | 0.40   | 5.250  |      |      |       |      |      | 4369 | 4368 | 4367  | 4366 | 4365 | 4364 | 4363 | 4362  | 4361 |      |      |      |      |      |      |      |      |      |      |      | 198  |      |      |        |
|                       | 0.35   | 4.594  |      |      | 4381  | 4380 | 4379 | 4378 | 4377 | 4376  | 4375 | 4374 | 4373 | 4372 | 4371  | 4370 |      |      |      |      |      |      |      |      |      |      |      | 199  |      |      |        |
|                       | 0.30   | 3.938  | 4395 | 4394 | 4393  | 4392 | 4391 | 4390 | 4389 | 4388  | 4387 | 4386 | 4385 | 4384 | 4383  | 4382 |      |      |      |      |      |      |      |      |      |      |      | 200  |      |      |        |
|                       | 0.25   | 3.281  | 4409 | 4408 | 4407  | 4406 | 4405 | 4404 | 4403 | 4402  | 4401 | 4400 | 4399 | 4398 | 4397  | 4396 |      |      |      |      |      |      |      |      |      |      |      | 201  |      |      |        |
|                       | 0.20   | 2.625  | 4423 | 4422 | 4421  | 4420 | 4419 | 4418 | 4417 | 4416  | 4415 | 4414 | 4413 | 4412 | 4411  | 4410 |      |      |      |      |      |      |      |      |      |      |      | 202  |      |      |        |
| 0.15                  | 1.969  | 4437   | 4436 | 4435 | 4434  | 4433 | 4432 | 4431 | 4430 | 4429  | 4428 | 4427 | 4426 | 4425 | 4424  |      |      |      |      |      |      |      |      |      |      |      | 203  |      |      |      |        |
| 0.10                  | 1.313  | 4451   | 4450 | 4449 | 4448  | 4447 | 4446 | 4445 | 4444 | 4443  | 4442 | 4441 | 4440 | 4439 | 4438  |      |      |      |      |      |      |      |      |      |      |      | 204  |      |      |      |        |
| 0.05                  | 0.656  | 4465   | 4464 | 4463 | 4462  | 4461 | 4460 | 4459 | 4458 | 4457  | 4456 | 4455 | 4454 | 4453 | 4452  |      |      |      |      |      |      |      |      |      |      |      | 205  |      |      |      |        |
| 0.00                  | 0.000  | 4479   | 4478 | 4477 | 4476  | 4475 | 4474 | 4473 | 4472 | 4471  | 4470 | 4469 | 4468 | 4467 | 4466  |      |      |      |      |      |      |      |      |      |      |      |      | 206  |      |      |        |
| Z/L                   | inches | 0      | 1    | 2    | 2.625 | 4    | 5.25 | 6    | 7    | 7.875 | 9    | 10   | 10.5 | 12   | 13.13 | 14   | 15   | 16   | 17   | 18   | 19   | 20   | 21   | 22   | 23   | 24   | 25   | 26   | 27   | 28   | inches |
|                       |        | 0.00   | 0.08 | 0.15 | 0.20  | 0.30 | 0.40 | 0.46 | 0.53 | 0.60  | 0.69 | 0.76 | 0.80 | 0.91 | 1.00  | 1.07 | 1.14 | 1.22 | 1.30 | 1.37 | 1.45 | 1.52 | 1.60 | 1.68 | 1.75 | 1.83 | 1.90 | 1.98 | 2.06 | 2.13 | X/L    |
| -----X setpoint-----  |        |        |      |      |       |      |      |      |      |       |      |      |      |      |       |      |      |      |      |      |      |      |      |      |      |      |      |      |      |      |        |
| Mach = 2.30, Δα = +5° |        |        |      |      |       |      |      |      |      |       |      |      |      |      |       |      |      |      |      |      |      |      |      |      |      |      |      | Run  |      |      |        |
| Z setpoint            | 1.00   | 13.130 |      |      |       |      |      |      |      |       |      |      |      |      |       |      |      |      |      |      |      |      |      |      |      |      |      | N/A  |      |      |        |
|                       | 0.90   | 11.810 |      |      |       |      |      |      |      |       |      |      |      |      |       |      |      |      |      |      |      |      |      |      |      |      |      | N/A  |      |      |        |
|                       | 0.80   | 10.500 |      |      |       |      |      |      |      |       |      |      |      |      |       |      |      |      |      |      |      |      |      |      |      |      |      | N/A  |      |      |        |
|                       | 0.70   | 9.188  |      |      |       |      |      |      |      |       |      |      |      |      |       | 4487 | 4486 |      |      |      |      |      |      |      |      |      |      | 207  |      |      |        |
|                       | 0.60   | 7.875  |      |      |       |      |      |      |      |       |      |      | 4491 | 4490 | 4489  | 4488 |      |      |      |      |      |      |      |      |      |      |      | 208  |      |      |        |
|                       | 0.50   | 6.563  |      |      |       |      |      |      |      |       | 4497 | 4496 | 4495 | 4494 | 4493  | 4492 |      |      |      |      |      |      |      |      |      |      |      | 209  |      |      |        |
|                       | 0.40   | 5.250  |      |      |       |      |      | 4506 | 4505 | 4504  | 4503 | 4502 | 4501 | 4500 | 4499  | 4498 |      |      |      |      |      |      |      |      |      |      |      | 210  |      |      |        |
|                       | 0.35   | 4.594  |      |      | 4518  | 4517 | 4516 | 4515 | 4514 | 4513  | 4512 | 4511 | 4510 | 4509 | 4508  | 4507 |      |      |      |      |      |      |      |      |      |      |      | 211  |      |      |        |
|                       | 0.30   | 3.938  | 4532 | 4531 | 4530  | 4529 | 4528 | 4527 | 4526 | 4525  | 4524 | 4523 | 4522 | 4521 | 4520  | 4519 |      |      |      |      |      |      |      |      |      |      |      | 212  |      |      |        |
|                       | 0.25   | 3.281  | 4546 | 4545 | 4544  | 4543 | 4542 | 4541 | 4540 | 4539  | 4538 | 4537 | 4536 | 4535 | 4534  | 4533 |      |      |      |      |      |      |      |      |      |      |      | 213  |      |      |        |
|                       | 0.20   | 2.625  | 4567 | 4566 | 4565  | 4564 | 4563 | 4562 | 4561 | 4560  | 4559 | 4558 | 4557 | 4556 | 4555  | 4554 |      |      |      |      |      |      |      |      |      |      |      | 214  |      |      |        |
| 0.15                  | 1.969  | 4581   | 4580 | 4579 | 4578  | 4577 | 4576 | 4575 | 4574 | 4573  | 4572 | 4571 | 4570 | 4569 | 4568  |      |      |      |      |      |      |      |      |      |      |      | 215  |      |      |      |        |
| 0.10                  | 1.313  | 4595   | 4594 | 4593 | 4592  | 4591 | 4590 | 4589 | 4588 | 4587  | 4586 | 4585 | 4584 | 4583 | 4582  |      |      |      |      |      |      |      |      |      |      |      | 216  |      |      |      |        |
| 0.05                  | 0.656  | 4609   | 4608 | 4607 | 4606  | 4605 | 4604 | 4603 | 4602 | 4601  | 4600 | 4599 | 4598 | 4597 | 4596  |      |      |      |      |      |      |      |      |      |      |      | 217  |      |      |      |        |
| 0.00                  | 0.000  |        |      |      |       |      |      |      |      |       |      |      |      |      |       |      |      |      |      |      |      |      |      |      |      |      |      | N/A  |      |      |        |
| Z/L                   | inches | 0      | 1    | 2    | 2.625 | 4    | 5.25 | 6    | 7    | 7.875 | 9    | 10   | 10.5 | 12   | 13.13 | 14   | 15   | 16   | 17   | 18   | 19   | 20   | 21   | 22   | 23   | 24   | 25   | 26   | 27   | 28   | inches |
|                       |        | 0.00   | 0.08 | 0.15 | 0.20  | 0.30 | 0.40 | 0.46 | 0.53 | 0.60  | 0.69 | 0.76 | 0.80 | 0.91 | 1.00  | 1.07 | 1.14 | 1.22 | 1.30 | 1.37 | 1.45 | 1.52 | 1.60 | 1.68 | 1.75 | 1.83 | 1.90 | 1.98 | 2.06 | 2.13 | X/L    |
| -----X setpoint-----  |        |        |      |      |       |      |      |      |      |       |      |      |      |      |       |      |      |      |      |      |      |      |      |      |      |      |      |      |      |      |        |

(b)  $Mach = 3.00$ ,  $\Delta\alpha = 0^\circ$  and  $5^\circ$

Run

N/A  
N/A  
N/A  
171  
172  
173  
174  
175  
176  
177  
178  
180  
181  
182  
183

Run

N/A  
N/A  
N/A  
184  
185  
186  
187  
188  
189  
190  
191  
192  
193  
194  
N/A

$$Mach = 4.50, \Delta\alpha = 0^\circ$$

| Mach = 4.50, Δα = +5° |        |        |      |      |       |      |      |      |      |       |      |      |      |      |       |      |      |      |      |      |      |      |      |      |      |      |      | Run  |      |      |        |
|-----------------------|--------|--------|------|------|-------|------|------|------|------|-------|------|------|------|------|-------|------|------|------|------|------|------|------|------|------|------|------|------|------|------|------|--------|
| Z setpoint            | 1.00   | 13.130 |      |      |       |      |      |      |      |       |      |      |      |      |       |      |      |      |      |      |      |      |      |      |      |      |      |      | N/A  |      |        |
|                       | 0.90   | 11.810 |      |      |       |      |      |      |      |       |      |      |      |      |       |      |      |      |      |      |      |      |      |      |      |      |      |      | N/A  |      |        |
|                       | 0.80   | 10.500 |      |      |       |      |      |      |      |       |      |      |      |      |       |      |      |      |      |      |      |      |      |      |      |      |      |      | N/A  |      |        |
|                       | 0.70   | 9.188  |      |      |       |      |      |      |      |       |      |      |      |      |       |      |      |      |      |      |      |      |      |      |      |      |      |      | N/A  |      |        |
|                       | 0.60   | 7.875  |      |      |       |      |      |      |      |       |      |      |      |      |       |      |      |      |      |      |      |      |      |      |      |      |      |      | N/A  |      |        |
|                       | 0.50   | 6.563  |      |      |       |      |      |      |      |       |      |      |      |      |       |      |      |      |      |      |      |      |      |      |      |      |      |      | N/A  |      |        |
|                       | 0.40   | 5.250  |      |      |       |      |      |      |      |       |      |      |      |      |       |      |      |      |      |      |      |      |      |      |      |      |      |      | N/A  |      |        |
|                       | 0.35   | 4.594  |      |      |       |      |      |      |      |       |      |      |      |      |       |      |      |      |      |      |      |      |      |      |      |      |      |      | N/A  |      |        |
|                       | 0.30   | 3.938  | 4727 | 4726 | 4725  | 4724 | 4723 | 4722 | 4721 | 4720  | 4719 | 4718 | 4717 | 4716 | 4715  | 4714 |      |      |      |      |      |      |      |      |      |      |      |      |      | 225  |        |
|                       | 0.25   | 3.281  | 4741 | 4740 | 4739  | 4738 | 4737 | 4736 | 4735 | 4734  | 4733 | 4732 | 4731 | 4730 | 4729  | 4728 |      |      |      |      |      |      |      |      |      |      |      |      |      | 226  |        |
| 0.20                  | 2.625  | 4755   | 4754 | 4753 | 4752  | 4751 | 4750 | 4749 | 4748 | 4747  | 4746 | 4745 | 4744 | 4743 | 4742  |      |      |      |      |      |      |      |      |      |      |      |      |      | 227  |      |        |
| 0.15                  | 1.969  | 4769   | 4768 | 4767 | 4766  | 4765 | 4764 | 4763 | 4762 | 4761  | 4760 | 4759 | 4758 | 4757 | 4756  |      |      |      |      |      |      |      |      |      |      |      |      |      | 228  |      |        |
| 0.10                  | 1.313  | 4783   | 4782 | 4781 | 4780  | 4779 | 4778 | 4777 | 4776 | 4775  | 4774 | 4773 | 4772 | 4771 | 4770  |      |      |      |      |      |      |      |      |      |      |      |      |      | 229  |      |        |
| 0.05                  | 0.656  | 4797   | 4796 | 4795 | 4794  | 4793 | 4792 | 4791 | 4790 | 4789  | 4788 | 4787 | 4786 | 4785 | 4784  |      |      |      |      |      |      |      |      |      |      |      |      |      | 230  |      |        |
| 0.00                  | 0.000  |        |      |      |       |      |      |      |      |       |      |      |      |      |       |      |      |      |      |      |      |      |      |      |      |      |      |      | N/A  |      |        |
| Z/L                   | inches | 0      | 1    | 2    | 2.625 | 4    | 5.25 | 6    | 7    | 7.875 | 9    | 10   | 10.5 | 12   | 13.13 | 14   | 15   | 16   | 17   | 18   | 19   | 20   | 21   | 22   | 23   | 24   | 25   | 26   | 27   | 28   | inches |
|                       |        | 0.00   | 0.08 | 0.15 | 0.20  | 0.30 | 0.40 | 0.46 | 0.53 | 0.60  | 0.69 | 0.76 | 0.80 | 0.91 | 1.00  | 1.07 | 1.14 | 1.22 | 1.30 | 1.37 | 1.45 | 1.52 | 1.60 | 1.68 | 1.75 | 1.83 | 1.90 | 1.98 | 2.06 | 2.13 | X/L    |
| -----X setpoint-----  |        |        |      |      |       |      |      |      |      |       |      |      |      |      |       |      |      |      |      |      |      |      |      |      |      |      |      |      |      |      |        |



Table X. Final run log for UPWT Test 1745, isolated booster force and moment measurements.

(a) Mach = 3.00,  $\alpha = 0^\circ$  and  $5^\circ$

| Mach = 3.00, α = 0° |      |        |  |  |  |  |  |  |  |  |  |  |  |  |  |  |  |  |  |  |  |  |  |  |  |  |  |  |  |  |  | Run |  |  |  |  |  |  |  |  |  |  |  |  |  |  |  |  |  |  |  |  |  |  |  |  |  |  |  |  |  |  |  |  |  |  |  |  |  |  |  |  |  |  |  |  |  |  |  |  |  |  |  |  |  |  |  |  |  |  |  |  |  |  |  |  |  |  |  |  |  |  |  |  |  |  |  |  |  |  |  |  |  |  |  |  |  |  |  |  |  |  |  |  |  |  |  |  |  |  |  |  |  |  |  |  |  |  |  |  |  |  |  |  |  |  |  |  |  |  |  |  |  |  |  |  |  |  |  |  |  |  |  |  |  |  |  |  |  |  |  |  |  |  |  |  |  |  |  |  |  |  |  |  |  |  |  |  |  |  |  |  |  |  |  |  |  |  |  |  |  |  |  |  |  |  |  |  |  |  |  |  |  |  |  |  |  |  |  |  |  |  |  |  |  |  |  |  |  |  |  |  |  |  |  |  |  |  |  |  |  |  |  |  |  |  |  |  |  |  |  |  |  |  |  |  |  |  |  |  |  |  |  |  |  |  |  |  |  |  |  |  |  |  |  |  |  |  |  |  |  |  |  |  |  |  |  |  |  |  |  |  |  |  |  |  |  |  |  |  |  |  |  |  |  |  |  |  |  |  |  |  |  |  |  |  |  |  |  |  |  |  |  |  |  |  |  |  |  |  |  |  |  |  |  |  |  |  |  |  |  |  |  |  |  |  |  |  |  |  |  |  |  |  |  |  |  |  |  |  |  |  |  |  |  |  |  |  |  |  |  |  |  |  |  |  |  |  |  |  |  |  |  |  |  |  |  |  |  |  |  |  |  |  |  |  |  |  |  |  |  |  |  |  |  |  |  |  |  |  |  |  |  |  |  |  |  |  |  |  |  |  |  |  |  |  |  |  |  |  |  |  |  |  |  |  |  |  |  |  |  |  |  |  |  |  |  |  |  |  |  |  |  |  |  |  |  |  |  |  |  |  |  |  |  |  |  |  |  |  |  |  |  |  |  |  |  |  |  |  |  |  |  |  |  |  |  |  |  |  |  |  |  |  |  |  |  |  |  |  |  |  |  |  |  |  |  |  |  |  |  |  |  |  |  |  |  |  |  |  |  |  |  |  |  |  |  |  |  |  |  |  |  |  |  |  |  |  |  |  |  |  |  |  |  |  |  |  |  |  |  |  |  |  |  |  |  |  |  |  |  |  |  |  |  |  |  |  |  |  |  |  |  |  |  |  |  |  |  |  |  |  |  |  |  |  |  |  |  |  |  |  |  |  |  |  |  |  |  |  |  |  |  |  |  |  |  |  |  |  |  |  |  |  |  |  |  |  |  |  |  |  |  |  |  |  |  |  |  |  |  |  |  |  |  |  |  |  |  |  |  |  |  |  |  |  |  |  |  |  |  |  |  |  |  |  |  |  |  |  |  |  |  |  |  |  |  |  |  |  |  |  |  |  |  |  |  |  |  |  |  |  |  |  |  |  |  |  |  |  |  |  |  |  |  |  |  |  |  |  |  |  |  |  |  |  |  |  |  |  |  |  |  |  |  |  |  |  |  |  |  |  |  |  |  |  |  |  |  |  |  |  |  |  |  |  |  |  |  |  |  |  |  |  |  |  |  |  |  |  |  |  |  |  |  |  |  |  |  |  |  |  |  |  |  |  |  |  |  |  |  |  |  |  |  |  |  |  |  |  |  |  |  |  |  |  |  |  |  |  |  |  |  |  |  |  |  |  |  |  |  |  |  |  |  |  |  |  |  |  |  |  |  |  |  |  |  |  |  |  |  |  |  |  |  |  |  |  |  |  |  |  |  |  |  |  |  |  |  |  |  |  |  |  |  |  |  |  |  |  |  |  |  |  |  |  |  |  |  |  |  |  |  |  |  |  |  |  |  |  |  |  |  |  |  |  |  |  |  |  |  |  |  |  |  |  |  |  |  |  |  |  |  |  |  |  |  |  |  |  |  |  |  |  |  |  |  |  |  |  |  |  |  |  |  |  |  |  |  |  |  |  |  |  |  |  |  |  |  |  |  |  |  |  |  |  |  |  |  |  |  |  |  |  |  |  |  |  |  |  |  |  |  |  |  |  |  |  |  |  |  |  |  |  |  |  |  |  |  |  |  |  |  |  |  |  |  |  |  |  |  |  |  |  |  |  |  |  |  |  |  |  |  |  |  |  |  |  |  |  |  |  |  |  |  |  |  |  |  |  |  |  |  |  |  |  |  |  |  |  |  |  |  |  |  |  |  |  |  |  |  |  |  |  |  |  |  |  |  |  |  |  |  |  |  |  |  |  |  |  |  |  |  |  |  |  |  |  |  |  |  |  |  |  |  |  |  |  |  |  |  |  |  |  |  |  |  |  |  |  |  |  |  |  |  |  |  |  |  |  |  |  |  |  |  |  |  |  |  |  |  |  |  |  |  |  |  |  |  |  |  |  |  |  |  |  |  |  |  |  |  |  |  |  |  |  |  |  |  |  |  |  |  |  |  |  |  |  |  |  |  |  |  |  |  |  |  |  |  |  |  |  |  |  |  |  |  |  |  |  |  |  |  |  |  |  |  |  |  |  |  |  |  |  |  |  |  |  |  |  |  |  |  |  |  |  |  |  |  |  |  |  |  |  |  |  |  |  |  |  |  |  |  |  |  |  |  |  |  |  |  |  |  |  |  |  |  |  |  |  |  |  |  |  |  |  |  |  |  |  |  |  |  |  |  |  |  |  |  |  |  |  |  |  |  |  |  |  |  |  |  |  |  |  |  |  |  |  |  |  |  |  |  |  |  |  |  |  |  |  |  |  |  |  |  |  |  |  |  |  |  |  |  |  |  |  |  |  |  |  |  |  |  |  |  |  |  |  |  |  |  |  |  |  |  |  |  |  |  |  |  |  |  |  |  |  |  |  |  |  |  |  |  |  |  |  |  |  |  |  |  |  |  |  |  |  |  |  |  |  |  |  |  |  |  |  |  |  |  |  |  |  |  |  |  |  |  |  |  |  |  |  |  |  |  |  |  |  |  |  |  |  |  |  |  |  |    |
|---------------------|------|--------|--|--|--|--|--|--|--|--|--|--|--|--|--|--|--|--|--|--|--|--|--|--|--|--|--|--|--|--|--|-----|--|--|--|--|--|--|--|--|--|--|--|--|--|--|--|--|--|--|--|--|--|--|--|--|--|--|--|--|--|--|--|--|--|--|--|--|--|--|--|--|--|--|--|--|--|--|--|--|--|--|--|--|--|--|--|--|--|--|--|--|--|--|--|--|--|--|--|--|--|--|--|--|--|--|--|--|--|--|--|--|--|--|--|--|--|--|--|--|--|--|--|--|--|--|--|--|--|--|--|--|--|--|--|--|--|--|--|--|--|--|--|--|--|--|--|--|--|--|--|--|--|--|--|--|--|--|--|--|--|--|--|--|--|--|--|--|--|--|--|--|--|--|--|--|--|--|--|--|--|--|--|--|--|--|--|--|--|--|--|--|--|--|--|--|--|--|--|--|--|--|--|--|--|--|--|--|--|--|--|--|--|--|--|--|--|--|--|--|--|--|--|--|--|--|--|--|--|--|--|--|--|--|--|--|--|--|--|--|--|--|--|--|--|--|--|--|--|--|--|--|--|--|--|--|--|--|--|--|--|--|--|--|--|--|--|--|--|--|--|--|--|--|--|--|--|--|--|--|--|--|--|--|--|--|--|--|--|--|--|--|--|--|--|--|--|--|--|--|--|--|--|--|--|--|--|--|--|--|--|--|--|--|--|--|--|--|--|--|--|--|--|--|--|--|--|--|--|--|--|--|--|--|--|--|--|--|--|--|--|--|--|--|--|--|--|--|--|--|--|--|--|--|--|--|--|--|--|--|--|--|--|--|--|--|--|--|--|--|--|--|--|--|--|--|--|--|--|--|--|--|--|--|--|--|--|--|--|--|--|--|--|--|--|--|--|--|--|--|--|--|--|--|--|--|--|--|--|--|--|--|--|--|--|--|--|--|--|--|--|--|--|--|--|--|--|--|--|--|--|--|--|--|--|--|--|--|--|--|--|--|--|--|--|--|--|--|--|--|--|--|--|--|--|--|--|--|--|--|--|--|--|--|--|--|--|--|--|--|--|--|--|--|--|--|--|--|--|--|--|--|--|--|--|--|--|--|--|--|--|--|--|--|--|--|--|--|--|--|--|--|--|--|--|--|--|--|--|--|--|--|--|--|--|--|--|--|--|--|--|--|--|--|--|--|--|--|--|--|--|--|--|--|--|--|--|--|--|--|--|--|--|--|--|--|--|--|--|--|--|--|--|--|--|--|--|--|--|--|--|--|--|--|--|--|--|--|--|--|--|--|--|--|--|--|--|--|--|--|--|--|--|--|--|--|--|--|--|--|--|--|--|--|--|--|--|--|--|--|--|--|--|--|--|--|--|--|--|--|--|--|--|--|--|--|--|--|--|--|--|--|--|--|--|--|--|--|--|--|--|--|--|--|--|--|--|--|--|--|--|--|--|--|--|--|--|--|--|--|--|--|--|--|--|--|--|--|--|--|--|--|--|--|--|--|--|--|--|--|--|--|--|--|--|--|--|--|--|--|--|--|--|--|--|--|--|--|--|--|--|--|--|--|--|--|--|--|--|--|--|--|--|--|--|--|--|--|--|--|--|--|--|--|--|--|--|--|--|--|--|--|--|--|--|--|--|--|--|--|--|--|--|--|--|--|--|--|--|--|--|--|--|--|--|--|--|--|--|--|--|--|--|--|--|--|--|--|--|--|--|--|--|--|--|--|--|--|--|--|--|--|--|--|--|--|--|--|--|--|--|--|--|--|--|--|--|--|--|--|--|--|--|--|--|--|--|--|--|--|--|--|--|--|--|--|--|--|--|--|--|--|--|--|--|--|--|--|--|--|--|--|--|--|--|--|--|--|--|--|--|--|--|--|--|--|--|--|--|--|--|--|--|--|--|--|--|--|--|--|--|--|--|--|--|--|--|--|--|--|--|--|--|--|--|--|--|--|--|--|--|--|--|--|--|--|--|--|--|--|--|--|--|--|--|--|--|--|--|--|--|--|--|--|--|--|--|--|--|--|--|--|--|--|--|--|--|--|--|--|--|--|--|--|--|--|--|--|--|--|--|--|--|--|--|--|--|--|--|--|--|--|--|--|--|--|--|--|--|--|--|--|--|--|--|--|--|--|--|--|--|--|--|--|--|--|--|--|--|--|--|--|--|--|--|--|--|--|--|--|--|--|--|--|--|--|--|--|--|--|--|--|--|--|--|--|--|--|--|--|--|--|--|--|--|--|--|--|--|--|--|--|--|--|--|--|--|--|--|--|--|--|--|--|--|--|--|--|--|--|--|--|--|--|--|--|--|--|--|--|--|--|--|--|--|--|--|--|--|--|--|--|--|--|--|--|--|--|--|--|--|--|--|--|--|--|--|--|--|--|--|--|--|--|--|--|--|--|--|--|--|--|--|--|--|--|--|--|--|--|--|--|--|--|--|--|--|--|--|--|--|--|--|--|--|--|--|--|--|--|--|--|--|--|--|--|--|--|--|--|--|--|--|--|--|--|--|--|--|--|--|--|--|--|--|--|--|--|--|--|--|--|--|--|--|--|--|--|--|--|--|--|--|--|--|--|--|--|--|--|--|--|--|--|--|--|--|--|--|--|--|--|--|--|--|--|--|--|--|--|--|--|--|--|--|--|--|--|--|--|--|--|--|--|--|--|--|--|--|--|--|--|--|--|--|--|--|--|--|--|--|--|--|--|--|--|--|--|--|--|--|--|--|--|--|--|--|--|--|--|--|--|--|--|--|--|--|--|--|--|--|--|--|--|--|--|--|--|--|--|--|--|--|--|--|--|--|--|--|--|--|--|--|--|--|--|--|--|--|--|--|--|--|--|--|--|--|--|--|--|--|--|--|--|--|--|--|--|--|--|--|--|--|--|--|--|--|--|--|--|--|--|--|--|--|--|--|--|--|--|--|--|--|--|--|--|--|--|--|--|--|--|--|--|--|--|--|--|--|--|--|--|--|--|--|--|--|--|--|--|--|--|--|--|--|--|--|--|--|--|--|--|--|--|--|--|--|--|--|--|--|--|--|--|--|--|--|--|--|--|--|--|--|--|--|--|--|--|--|--|--|--|--|--|--|--|----|
| Z setpoint          | 1.00 | 13.130 |  |  |  |  |  |  |  |  |  |  |  |  |  |  |  |  |  |  |  |  |  |  |  |  |  |  |  |  |  |     |  |  |  |  |  |  |  |  |  |  |  |  |  |  |  |  |  |  |  |  |  |  |  |  |  |  |  |  |  |  |  |  |  |  |  |  |  |  |  |  |  |  |  |  |  |  |  |  |  |  |  |  |  |  |  |  |  |  |  |  |  |  |  |  |  |  |  |  |  |  |  |  |  |  |  |  |  |  |  |  |  |  |  |  |  |  |  |  |  |  |  |  |  |  |  |  |  |  |  |  |  |  |  |  |  |  |  |  |  |  |  |  |  |  |  |  |  |  |  |  |  |  |  |  |  |  |  |  |  |  |  |  |  |  |  |  |  |  |  |  |  |  |  |  |  |  |  |  |  |  |  |  |  |  |  |  |  |  |  |  |  |  |  |  |  |  |  |  |  |  |  |  |  |  |  |  |  |  |  |  |  |  |  |  |  |  |  |  |  |  |  |  |  |  |  |  |  |  |  |  |  |  |  |  |  |  |  |  |  |  |  |  |  |  |  |  |  |  |  |  |  |  |  |  |  |  |  |  |  |  |  |  |  |  |  |  |  |  |  |  |  |  |  |  |  |  |  |  |  |  |  |  |  |  |  |  |  |  |  |  |  |  |  |  |  |  |  |  |  |  |  |  |  |  |  |  |  |  |  |  |  |  |  |  |  |  |  |  |  |  |  |  |  |  |  |  |  |  |  |  |  |  |  |  |  |  |  |  |  |  |  |  |  |  |  |  |  |  |  |  |  |  |  |  |  |  |  |  |  |  |  |  |  |  |  |  |  |  |  |  |  |  |  |  |  |  |  |  |  |  |  |  |  |  |  |  |  |  |  |  |  |  |  |  |  |  |  |  |  |  |  |  |  |  |  |  |  |  |  |  |  |  |  |  |  |  |  |  |  |  |  |  |  |  |  |  |  |  |  |  |  |  |  |  |  |  |  |  |  |  |  |  |  |  |  |  |  |  |  |  |  |  |  |  |  |  |  |  |  |  |  |  |  |  |  |  |  |  |  |  |  |  |  |  |  |  |  |  |  |  |  |  |  |  |  |  |  |  |  |  |  |  |  |  |  |  |  |  |  |  |  |  |  |  |  |  |  |  |  |  |  |  |  |  |  |  |  |  |  |  |  |  |  |  |  |  |  |  |  |  |  |  |  |  |  |  |  |  |  |  |  |  |  |  |  |  |  |  |  |  |  |  |  |  |  |  |  |  |  |  |  |  |  |  |  |  |  |  |  |  |  |  |  |  |  |  |  |  |  |  |  |  |  |  |  |  |  |  |  |  |  |  |  |  |  |  |  |  |  |  |  |  |  |  |  |  |  |  |  |  |  |  |  |  |  |  |  |  |  |  |  |  |  |  |  |  |  |  |  |  |  |  |  |  |  |  |  |  |  |  |  |  |  |  |  |  |  |  |  |  |  |  |  |  |  |  |  |  |  |  |  |  |  |  |  |  |  |  |  |  |  |  |  |  |  |  |  |  |  |  |  |  |  |  |  |  |  |  |  |  |  |  |  |  |  |  |  |  |  |  |  |  |  |  |  |  |  |  |  |  |  |  |  |  |  |  |  |  |  |  |  |  |  |  |  |  |  |  |  |  |  |  |  |  |  |  |  |  |  |  |  |  |  |  |  |  |  |  |  |  |  |  |  |  |  |  |  |  |  |  |  |  |  |  |  |  |  |  |  |  |  |  |  |  |  |  |  |  |  |  |  |  |  |  |  |  |  |  |  |  |  |  |  |  |  |  |  |  |  |  |  |  |  |  |  |  |  |  |  |  |  |  |  |  |  |  |  |  |  |  |  |  |  |  |  |  |  |  |  |  |  |  |  |  |  |  |  |  |  |  |  |  |  |  |  |  |  |  |  |  |  |  |  |  |  |  |  |  |  |  |  |  |  |  |  |  |  |  |  |  |  |  |  |  |  |  |  |  |  |  |  |  |  |  |  |  |  |  |  |  |  |  |  |  |  |  |  |  |  |  |  |  |  |  |  |  |  |  |  |  |  |  |  |  |  |  |  |  |  |  |  |  |  |  |  |  |  |  |  |  |  |  |  |  |  |  |  |  |  |  |  |  |  |  |  |  |  |  |  |  |  |  |  |  |  |  |  |  |  |  |  |  |  |  |  |  |  |  |  |  |  |  |  |  |  |  |  |  |  |  |  |  |  |  |  |  |  |  |  |  |  |  |  |  |  |  |  |  |  |  |  |  |  |  |  |  |  |  |  |  |  |  |  |  |  |  |  |  |  |  |  |  |  |  |  |  |  |  |  |  |  |  |  |  |  |  |  |  |  |  |  |  |  |  |  |  |  |  |  |  |  |  |  |  |  |  |  |  |  |  |  |  |  |  |  |  |  |  |  |  |  |  |  |  |  |  |  |  |  |  |  |  |  |  |  |  |  |  |  |  |  |  |  |  |  |  |  |  |  |  |  |  |  |  |  |  |  |  |  |  |  |  |  |  |  |  |  |  |  |  |  |  |  |  |  |  |  |  |  |  |  |  |  |  |  |  |  |  |  |  |  |  |  |  |  |  |  |  |  |  |  |  |  |  |  |  |  |  |  |  |  |  |  |  |  |  |  |  |  |  |  |  |  |  |  |  |  |  |  |  |  |  |  |  |  |  |  |  |  |  |  |  |  |  |  |  |  |  |  |  |  |  |  |  |  |  |  |  |  |  |  |  |  |  |  |  |  |  |  |  |  |  |  |  |  |  |  |  |  |  |  |  |  |  |  |  |  |  |  |  |  |  |  |  |  |  |  |  |  |  |  |  |  |  |  |  |  |  |  |  |  |  |  |  |  |  |  |  |  |  |  |  |  |  |  |  |  |  |  |  |  |  |  |  |  |  |  |  |  |  |  |  |  |  |  |  |  |  |  |  |  |  |  |  |  |  |  |  |  |  |  |  |  |  |  |  |  |  |  |  |  |  |  |  |  |  |  |  |  |  |  |  |  |  |  |  |  |  |  |  |  |  |  |  |  |  |  |  |  |  |  |  |  |  |  |  |  |  |  |  |  |  |  |  |  |  |  |  |  |  |  |  |  |  | </ |

(b)  $Mach = 3.00$ ,  $\alpha = 0^\circ$ , first and second repeat sets

Run

[illegible]

Run

[illegible]

(c)  $Mach = 2.30$  and  $4.50$ ,  $\alpha = 0^\circ$

|            |        | Mach = 2.30, $\alpha = 0^\circ$ |      |      |       |      |      |      |      |       |      |      |      |      |       |      |      |      |      |      |      |      |      |      |      |      |      |      |      | Run  |        |      |      |      |      |      |      |      |      |      |      |      |      |      |      |      |      |      |      |      |      |      |     |
|------------|--------|---------------------------------|------|------|-------|------|------|------|------|-------|------|------|------|------|-------|------|------|------|------|------|------|------|------|------|------|------|------|------|------|------|--------|------|------|------|------|------|------|------|------|------|------|------|------|------|------|------|------|------|------|------|------|------|-----|
| Z setpoint | 1.00   | 13.130                          |      |      |       |      |      |      |      |       |      |      |      |      |       |      |      |      |      |      |      |      |      |      |      |      |      |      | 2920 | 2919 | 2918   | 2917 | 2916 | 130  |      |      |      |      |      |      |      |      |      |      |      |      |      |      |      |      |      |      |     |
|            | 0.90   | 11.810                          |      |      |       |      |      |      |      |       |      |      |      |      |       |      |      |      |      |      |      |      |      |      |      |      |      |      | 2933 | 2932 | 2931   | 2930 | 2929 | 2928 | 2927 | 2926 | 2925 | 2924 | 2923 | 2922 | 2921 | 131  |      |      |      |      |      |      |      |      |      |      |     |
|            | 0.80   | 10.500                          |      |      |       |      |      |      |      |       |      |      |      |      |       |      |      |      |      |      |      |      |      |      |      |      |      |      | 2946 | 2945 | 2944   | 2943 | 2942 | 2941 | 2940 | 2939 | 2938 | 2937 | 2936 | 2935 | 2934 | 132  |      |      |      |      |      |      |      |      |      |      |     |
|            | 0.70   | 9.188                           |      |      |       |      |      |      |      |       |      |      |      |      |       |      |      |      |      |      |      |      |      |      |      |      |      |      | 2963 | 2962 | 2961   | 2960 | 2959 | 2958 | 2957 | 2956 | 2955 | 2954 | 2953 | 2952 | 2951 | 2950 | 2949 | 2948 | 2947 | 133  |      |      |      |      |      |      |     |
|            | 0.60   | 7.875                           |      |      |       |      |      |      |      |       |      |      |      |      |       |      |      |      |      |      |      |      |      |      |      |      |      |      | 2982 | 2981 | 2980   | 2979 | 2978 | 2977 | 2976 | 2975 | 2974 | 2973 | 2972 | 2971 | 2970 | 2969 | 2968 | 2967 | 2966 | 2965 | 2964 | 134  |      |      |      |      |     |
|            | 0.50   | 6.563                           |      |      |       |      |      |      |      |       |      |      |      |      |       |      |      |      |      |      |      |      |      |      |      |      |      |      | 3003 | 3002 | 3001   | 3000 | 2999 | 2998 | 2997 | 2996 | 2995 | 2994 | 2993 | 2992 | 2991 | 2990 | 2989 | 2988 | 2987 | 2986 | 2985 | 2984 | 2983 | 135  |      |      |     |
|            | 0.40   | 5.250                           |      |      |       |      |      |      |      |       |      |      |      |      |       |      |      |      |      |      |      |      |      |      |      |      |      |      | 3037 | 3036 | 3035   | 3034 | 3033 | 3032 | 3031 | 3030 | 3029 | 3028 | 3027 | 3026 | 3025 | 3024 | 3023 | 3022 | 3021 | 3020 | 3019 | 3018 | 3017 | 3016 | 3015 | 3014 | 136 |
|            | 0.35   | 4.594                           |      |      | 3064  | 3063 | 3062 | 3061 | 3060 | 3059  | 3058 | 3057 | 3056 | 3055 | 3054  | 3053 | 3052 | 3051 | 3050 | 3049 | 3048 | 3047 | 3046 | 3045 | 3044 | 3043 | 3042 | 3041 | 3040 | 3039 | 3038   | 137  |      |      |      |      |      |      |      |      |      |      |      |      |      |      |      |      |      |      |      |      |     |
|            | 0.30   | 3.938                           | 3093 | 3092 | 3091  | 3090 | 3089 | 3088 | 3087 | 3086  | 3085 | 3084 | 3083 | 3082 | 3081  | 3080 | 3079 | 3078 | 3077 | 3076 | 3075 | 3074 | 3073 | 3072 | 3071 | 3070 | 3069 | 3068 | 3067 | 3066 | 3065   | 138  |      |      |      |      |      |      |      |      |      |      |      |      |      |      |      |      |      |      |      |      |     |
|            | 0.25   | 3.281                           | 3122 | 3121 | 3120  | 3119 | 3118 | 3117 | 3116 | 3115  | 3114 | 3113 | 3112 | 3111 | 3110  | 3109 | 3108 | 3107 | 3106 | 3105 | 3104 | 3103 | 3102 | 3101 | 3100 | 3099 | 3098 | 3097 | 3096 | 3095 | 3094   | 139  |      |      |      |      |      |      |      |      |      |      |      |      |      |      |      |      |      |      |      |      |     |
| 0.20       | 2.625  | 3151                            | 3150 | 3149 | 3148  | 3147 | 3146 | 3145 | 3144 | 3143  | 3142 | 3141 | 3140 | 3139 | 3138  | 3137 | 3136 | 3135 | 3134 | 3133 | 3132 | 3131 | 3130 | 3129 | 3128 | 3127 | 3126 | 3125 | 3124 | 3123 | 140    |      |      |      |      |      |      |      |      |      |      |      |      |      |      |      |      |      |      |      |      |      |     |
| 0.15       | 1.969  | 3180                            | 3179 | 3178 | 3177  | 3176 | 3175 | 3174 | 3173 | 3172  | 3171 | 3170 | 3169 | 3168 | 3167  | 3166 | 3165 | 3164 | 3163 | 3162 | 3161 | 3160 | 3159 | 3158 | 3157 | 3156 | 3155 | 3154 | 3153 | 3152 | 141    |      |      |      |      |      |      |      |      |      |      |      |      |      |      |      |      |      |      |      |      |      |     |
| 0.10       | 1.313  | 3209                            | 3208 | 3207 | 3206  | 3205 | 3204 | 3203 | 3202 | 3201  | 3200 | 3199 | 3198 | 3197 | 3196  | 3195 | 3194 | 3193 | 3192 | 3191 | 3190 | 3189 | 3188 | 3187 | 3186 | 3185 | 3184 | 3183 | 3182 | 3181 | 142    |      |      |      |      |      |      |      |      |      |      |      |      |      |      |      |      |      |      |      |      |      |     |
| 0.05       | 0.656  | 3238                            | 3237 | 3236 | 3235  | 3234 | 3233 | 3232 | 3231 | 3230  | 3229 | 3228 | 3227 | 3226 | 3225  | 3224 | 3223 | 3222 | 3221 | 3220 | 3219 | 3218 | 3217 | 3216 | 3215 | 3214 | 3213 | 3212 | 3211 | 3210 | 143    |      |      |      |      |      |      |      |      |      |      |      |      |      |      |      |      |      |      |      |      |      |     |
| 0.00       | 0.000  | 3267                            | 3266 | 3265 | 3264  | 3263 | 3262 | 3261 | 3260 | 3259  | 3258 | 3257 | 3256 | 3255 | 3254  | 3253 | 3252 | 3251 | 3250 | 3249 | 3248 | 3247 | 3246 | 3245 | 3244 | 3243 | 3242 | 3241 | 3240 | 3239 | 144    |      |      |      |      |      |      |      |      |      |      |      |      |      |      |      |      |      |      |      |      |      |     |
| Z/L        | inches | 0                               | 1    | 2    | 2.625 | 4    | 5.25 | 6    | 7    | 7.875 | 9    | 10   | 10.5 | 12   | 13.13 | 14   | 15   | 16   | 17   | 18   | 19   | 20   | 21   | 22   | 23   | 24   | 25   | 26   | 27   | 28   | inches |      |      |      |      |      |      |      |      |      |      |      |      |      |      |      |      |      |      |      |      |      |     |
|            |        | 0.00                            | 0.08 | 0.15 | 0.20  | 0.30 | 0.40 |      |      |       |      |      |      |      |       |      |      |      |      |      |      |      |      |      |      |      |      |      |      |      |        |      |      |      |      |      |      |      |      |      |      |      |      |      |      |      |      |      |      |      |      |      |     |

| Mach = 4.50, α = 0° |                      |        |      |       |      |      |      |      |       |      |      |      |      |       |      |      |      |      |      |      |      |      |      |      |      |      |      | Run  |      |      |      |      |      |     |
|---------------------|----------------------|--------|------|-------|------|------|------|------|-------|------|------|------|------|-------|------|------|------|------|------|------|------|------|------|------|------|------|------|------|------|------|------|------|------|-----|
| Z setpoint          | 1.00                 | 13.130 |      |       |      |      |      |      |       |      |      |      |      |       |      |      |      |      |      |      |      |      |      |      |      |      |      |      | 3329 | 3328 | 3327 | 3326 | 3325 | 149 |
|                     | 0.90                 | 11.810 |      |       |      |      |      |      |       |      |      |      |      |       |      |      |      |      |      |      |      |      |      |      |      |      |      |      |      |      |      |      |      | 150 |
|                     | 0.80                 | 10.500 |      |       |      |      |      |      |       |      |      |      |      |       |      |      |      |      |      |      |      |      |      |      |      |      |      |      |      |      |      |      |      | 151 |
|                     | 0.70                 | 9.188  |      |       |      |      |      |      |       |      |      |      |      |       |      |      |      |      |      |      |      |      |      |      |      |      |      |      |      |      |      |      |      | 152 |
|                     | 0.60                 | 7.875  |      |       |      |      |      |      |       |      |      |      |      |       |      |      |      |      |      |      |      |      |      |      |      |      |      |      |      |      |      |      |      | 153 |
|                     | 0.50                 | 6.563  |      |       |      |      |      |      |       |      |      |      |      |       |      |      |      |      |      |      |      |      |      |      |      |      |      |      |      |      |      |      |      | 154 |
|                     | 0.40                 | 5.250  |      |       |      |      |      |      |       |      |      |      |      |       |      |      |      |      |      |      |      |      |      |      |      |      |      |      |      |      |      |      |      | 155 |
|                     | 0.35                 | 4.594  |      |       |      |      |      |      |       |      |      |      |      |       |      |      |      |      |      |      |      |      |      |      |      |      |      |      |      |      |      |      |      | 156 |
|                     | 0.30                 | 3.938  | 3492 | 3491  | 3490 | 3489 | 3488 | 3487 | 3486  | 3485 | 3484 | 3483 | 3482 | 3481  | 3480 | 3479 | 3478 | 3477 | 3476 | 3475 | 3474 | 3473 | 3472 | 3471 | 3470 | 3469 | 3468 | 3467 | 3466 | 3465 | 3464 | 157  |      |     |
|                     | 0.25                 | 3.281  | 3734 | 3733  | 3732 | 3731 | 3730 | 3729 | 3728  | 3727 | 3726 | 3725 | 3724 | 3723  | 3722 | 3721 | 3720 | 3719 | 3718 | 3717 | 3716 | 3715 | 3714 | 3713 | 3712 | 3711 | 3710 | 3709 | 3708 | 3707 | 3706 | 158  |      |     |
|                     | 0.20                 | 2.625  | 3521 | 3520  | 3519 | 3518 | 3517 | 3516 | 3515  | 3514 | 3513 | 3512 | 3511 | 3510  | 3509 | 3508 | 3507 | 3506 | 3505 | 3504 | 3503 | 3502 | 3501 | 3500 | 3499 | 3498 | 3497 | 3496 | 3495 | 3494 | 3493 | 159  |      |     |
|                     | 0.15                 | 1.969  | 3550 | 3549  | 3548 | 3547 | 3546 | 3545 | 3544  | 3543 | 3542 | 3541 | 3540 | 3539  | 3538 | 3537 | 3536 | 3535 | 3534 | 3533 | 3532 | 3531 | 3530 | 3529 | 3528 | 3527 | 3526 | 3525 | 3524 | 3523 | 3522 | 160  |      |     |
|                     | 0.10                 | 1.313  | 3579 | 3578  | 3577 | 3576 | 3575 | 3574 | 3573  | 3572 | 3571 | 3570 | 3569 | 3568  | 3567 | 3566 | 3565 | 3564 | 3563 | 3562 | 3561 | 3560 | 3559 | 3558 | 3557 | 3556 | 3555 | 3554 | 3553 | 3552 | 3551 | 161  |      |     |
|                     | 0.05                 | 0.656  | 3608 | 3607  | 3606 | 3605 | 3604 | 3603 | 3602  | 3601 | 3600 | 3599 | 3598 | 3597  | 3596 | 3595 | 3594 | 3593 | 3592 | 3591 | 3590 | 3589 | 3588 | 3587 | 3586 | 3585 | 3584 | 3583 | 3582 | 3581 | 3580 | 162  |      |     |
|                     | 0.00                 | 0.000  | 3637 | 3636  | 3635 | 3634 | 3633 | 3632 | 3631  | 3630 | 3629 | 3628 | 3627 | 3626  | 3625 | 3624 | 3623 | 3622 | 3621 | 3620 | 3619 | 3618 | 3617 | 3616 | 3615 | 3614 | 3613 | 3612 | 3611 | 3610 | 3609 | 162  |      |     |
| Z/L                 |                      |        |      |       |      |      |      |      |       |      |      |      |      |       |      |      |      |      |      |      |      |      |      |      |      |      |      |      |      |      |      |      |      |     |
| inches              | 0                    | 1      | 2    | 2.625 | 4    | 5.25 | 6    | 7    | 7.875 | 9    | 10   | 10.5 | 12   | 13.13 | 14   | 15   | 16   | 17   | 18   | 19   | 20   | 21   | 22   | 23   | 24   | 25   | 26   | 27   | 28   |      |      |      |      |     |
|                     | 0.00                 | 0.08   | 0.15 | 0.20  | 0.30 | 0.40 | 0.46 | 0.53 | 0.60  | 0.69 | 0.76 | 0.80 | 0.91 | 1.00  | 1.07 | 1.14 | 1.22 | 1.30 | 1.37 | 1.45 | 1.52 | 1.60 | 1.68 | 1.75 | 1.83 | 1.90 | 1.98 | 2.06 | 2.13 |      |      |      |      |     |
|                     | <i>X setpoint</i> </ |        |      |       |      |      |      |      |       |      |      |      |      |       |      |      |      |      |      |      |      |      |      |      |      |      |      |      |      |      |      |      |      |     |

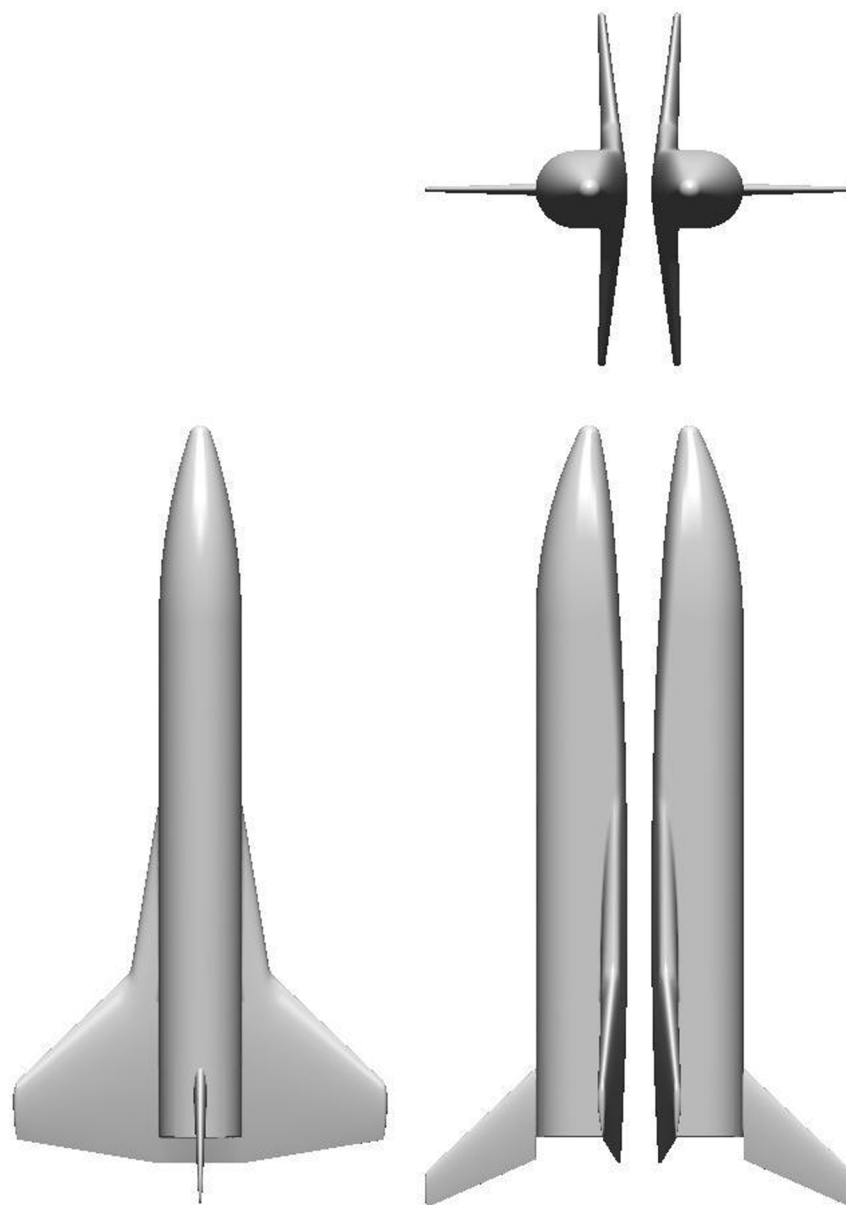


Table X. Concluded.

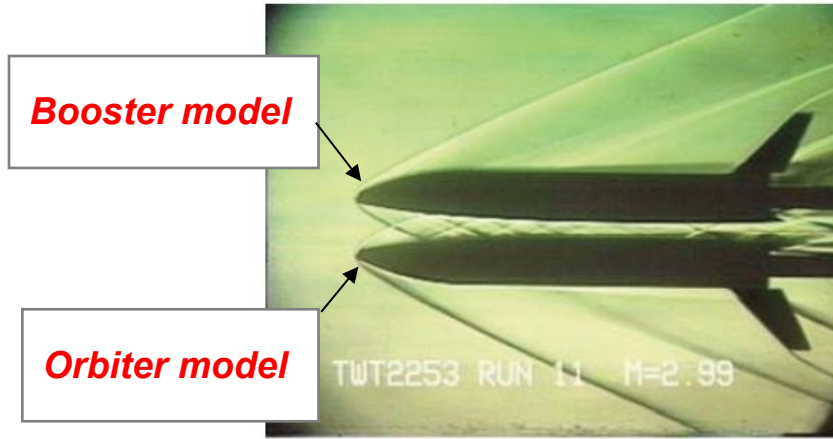
(d) Mach = 3.00, orbiter and booster in back-to-belly configuration; isolated booster rolled -90°

| Mach = 3.00, Booster in Back-to-Belly Configuration, $\Delta\alpha = 0^\circ$ |        |        |      |      |       |      |      |      |      |       |      |      |      |      |       |      |      |      |      |      |      |      |      |      |      |      |      | Run  |      |      |        |      |      |      |      |      |      |     |
|---|--------|--------|------|------|-------|------|------|------|------|-------|------|------|------|------|-------|------|------|------|------|------|------|------|------|------|------|------|------|------|------|------|--------|------|------|------|------|------|------|-----|
| Z setpoint  | 1.00   | 13.130 |      |      |       |      |      |      |      |       |      |      |      |      |       |      |      |      |      |      |      |      |      |      |      |      |      |      | 3781 | 3780 | 3779   | 3778 | 3777 | 169  |      |      |      |     |
|   | 0.90   | 11.810 |      |      |       |      |      |      |      |       |      |      |      |      |       |      |      |      |      | 3794 | 3793 | 3792 | 3791 | 3790 | 3789 | 3788 | 3787 | 3786 | 3785 | 3784 | 3783   | 3782 | 170  |      |      |      |      |     |
|   | 0.80   | 10.500 |      |      |       |      |      |      |      |       |      |      |      |      |       |      |      |      |      | 3807 | 3806 | 3805 | 3804 | 3803 | 3802 | 3801 | 3800 | 3799 | 3798 | 3797 | 3796   | 3795 | 171  |      |      |      |      |     |
|   | 0.70   | 9.188  |      |      |       |      |      |      |      |       |      |      |      |      | 3824  | 3823 | 3822 | 3821 | 3820 | 3819 | 3818 | 3817 | 3816 | 3815 | 3814 | 3813 | 3812 | 3811 | 3810 | 3809 | 3808   | 172  |      |      |      |      |      |     |
|   | 0.60   | 7.875  |      |      |       |      |      |      |      |       |      |      | 3843 | 3842 | 3841  | 3840 | 3839 | 3838 | 3837 | 3836 | 3835 | 3834 | 3833 | 3832 | 3831 | 3830 | 3829 | 3828 | 3827 | 3826 | 3825   | 173  |      |      |      |      |      |     |
|   | 0.50   | 6.563  |      |      |       |      |      |      |      |       |      |      |      |      |       |      | 3864 | 3863 | 3862 | 3861 | 3860 | 3859 | 3858 | 3857 | 3856 | 3855 | 3854 | 3853 | 3852 | 3851 | 3850   | 3849 | 3848 | 3847 | 3846 | 3845 | 3844 | 174 |
|   | 0.40   | 5.250  |      |      |       |      |      |      |      |       |      |      |      |      |       |      |      |      |      |      |      |      |      |      |      |      |      |      |      |      |        |      |      |      | 175  |      |      |     |
|   | 0.35   | 4.594  |      |      |       |      |      |      |      |       |      |      |      |      |       |      |      |      |      |      |      |      |      |      |      |      |      |      |      |      |        |      |      |      | 176  |      |      |     |
|   | 0.30   | 3.938  | 3951 | 3950 | 3949  | 3948 | 3947 | 3946 | 3945 | 3944  | 3943 | 3942 | 3941 | 3940 | 3939  | 3938 | 3937 | 3936 | 3935 | 3934 | 3933 | 3932 | 3931 | 3930 | 3929 | 3928 | 3927 | 3926 | 3925 | 3924 | 3923   |      |      | 177  |      |      |      |     |
|   | 0.25   | 3.281  | 3980 | 3979 | 3978  | 3977 | 3976 | 3975 | 3974 | 3973  | 3972 | 3971 | 3970 | 3969 | 3968  | 3967 | 3966 | 3965 | 3964 | 3963 | 3962 | 3961 | 3960 | 3959 | 3958 | 3957 | 3956 | 3955 | 3954 | 3953 | 3952   |      |      | 178  |      |      |      |     |
|   | 0.20   | 2.625  | 4009 | 4008 | 4007  | 4006 | 4005 | 4004 | 4003 | 4002  | 4001 | 4000 | 3999 | 3998 | 3997  | 3996 | 3995 | 3994 | 3993 | 3992 | 3991 | 3990 | 3989 | 3988 | 3987 | 3986 | 3985 | 3984 | 3983 | 3982 | 3981   |      |      | 179  |      |      |      |     |
|   | 0.15   | 1.969  | 4038 | 4037 | 4036  | 4035 | 4034 | 4033 | 4032 | 4031  | 4030 | 4029 | 4028 | 4027 | 4026  | 4025 | 4024 | 4023 | 4022 | 4021 | 4020 | 4019 | 4018 | 4017 | 4016 | 4015 | 4014 | 4013 | 4012 | 4011 | 4010   |      |      | 180  |      |      |      |     |
|   | 0.10   | 1.313  | 4067 | 4066 | 4065  | 4064 | 4063 | 4062 | 4061 | 4060  | 4059 | 4058 | 4057 | 4056 | 4055  | 4054 | 4053 | 4052 | 4051 | 4050 |      |      |      |      |      |      |      |      |      |      |        |      |      | 181  |      |      |      |     |
|   | 0.05   | 0.656  | 4085 | 4084 | 4083  | 4082 | 4081 | 4080 | 4079 | 4078  | 4077 | 4076 | 4075 | 4074 | 4073  | 4072 | 4071 |      |      |      |      |      |      |      |      |      |      |      |      |      |        |      |      | 182  |      |      |      |     |
|   | 0.00   | 0.000  | 4114 | 4113 | 4112  | 4111 | 4110 | 4109 | 4108 | 4107  | 4106 | 4105 | 4104 | 4103 | 4102  | 4101 | 4100 | 4099 | 4098 | 4097 | 4096 | 4095 | 4094 | 4093 | 4092 | 4091 | 4090 | 4089 | 4088 | 4087 | 4086   |      |      | 183  |      |      |      |     |
| Z/L   | inches | 0      | 1    | 2    | 2.625 | 4    | 5.25 | 6    | 7    | 7.875 | 9    | 10   | 10.5 | 12   | 13.13 | 14   | 15   | 16   | 17   | 18   | 19   | 20   | 21   | 22   | 23   | 24   | 25   | 26   | 27   | 28   | inches |      |      |      |      |      |      |     |
|   |        | 0.00   | 0.08 | 0.15 | 0.20  | 0.30 | 0.40 | 0.46 | 0.53 | 0.60  | 0.69 | 0.76 | 0.80 | 0.91 | 1.00  | 1.07 | 1.14 | 1.22 | 1.30 | 1.37 | 1.45 | 1.52 | 1.60 | 1.68 | 1.75 | 1.83 | 1.90 | 1.98 | 2.06 | 2.13 | X/L    |      |      |      |      |      |      |     |
| -----X setpoint-----  |        |        |      |      |       |      |      |      |      |       |      |      |      |      |       |      |      |      |      |      |      |      |      |      |      |      |      |      |      |      |        |      |      |      |      |      |      |     |
| Mach = 3.00, Isolated Booster Rolled -90 Degrees, $\alpha = 0^\circ$          |        |        |      |      |       |      |      |      |      |       |      |      |      |      |       |      |      |      |      |      |      |      |      |      |      |      |      | Run  |      |      |        |      |      |      |      |      |      |     |
| Z setpoint  | 1.00   | 13.130 |      |      |       |      |      |      |      |       |      |      |      |      |       |      |      |      |      |      |      |      |      |      |      |      |      |      |      |      |        |      | 206  |      |      |      |      |     |
|   | 0.90   | 11.810 |      |      |       |      |      |      |      |       |      |      |      |      |       |      |      |      |      |      |      |      |      |      |      |      |      |      |      |      |        |      | 207  |      |      |      |      |     |
|   | 0.80   | 10.500 |      |      |       |      |      |      |      |       |      |      |      |      |       |      |      |      |      |      |      |      |      |      |      |      |      |      |      |      |        |      | 208  |      |      |      |      |     |
|   | 0.70   | 9.188  |      |      |       |      |      |      |      |       |      |      |      |      |       |      |      |      |      |      |      |      |      |      |      |      |      |      |      |      |        |      | 209  |      |      |      |      |     |
|   | 0.60   | 7.875  |      |      |       |      |      |      |      |       |      |      |      |      |       |      |      |      |      |      |      |      |      |      |      |      |      |      |      |      |        |      | 210  |      |      |      |      |     |
|   | 0.50   | 6.563  |      |      |       |      |      |      |      |       |      |      |      |      |       |      |      |      |      |      |      |      |      |      |      |      |      |      |      |      |        |      | 211  |      |      |      |      |     |
|   | 0.40   | 5.250  |      |      |       |      |      |      |      |       |      |      |      |      |       |      |      |      |      |      |      |      |      |      |      |      |      |      |      |      |        |      | 212  |      |      |      |      |     |
|   | 0.35   | 4.594  |      |      |       |      |      |      |      |       |      |      |      |      |       |      |      |      |      |      |      |      |      |      |      |      |      |      |      |      |        |      | 213  |      |      |      |      |     |
|   | 0.30   | 3.938  | 4779 | 4778 | 4777  | 4776 | 4775 | 4774 | 4773 | 4772  | 4771 | 4770 | 4769 | 4768 | 4767  | 4766 | 4765 | 4764 | 4763 | 4762 | 4761 | 4760 | 4759 | 4758 | 4757 | 4756 | 4755 | 4754 | 4753 | 4752 | 4751   |      | 214  |      |      |      |      |     |
|   | 0.25   | 3.281  | 4808 | 4807 | 4806  | 4805 | 4804 | 4803 | 4802 | 4801  | 4800 | 4799 | 4798 | 4797 | 4796  | 4795 | 4794 | 4793 | 4792 | 4791 | 4790 | 4789 | 4788 | 4787 | 4786 | 4785 | 4784 | 4783 | 4782 | 4781 | 4780   |      | 215  |      |      |      |      |     |
|   | 0.20   | 2.625  | 4837 | 4836 | 4835  | 4834 | 4833 | 4832 | 4831 | 4830  | 4829 | 4828 | 4827 | 4826 | 4825  | 4824 | 4823 | 4822 | 4821 | 4820 | 4819 | 4818 | 4817 | 4816 | 4815 | 4814 | 4813 | 4812 | 4811 | 4810 | 4809   |      | 216  |      |      |      |      |     |
|   | 0.15   | 1.969  | 4866 | 4865 | 4864  | 4863 | 4862 | 4861 | 4860 | 4859  | 4858 | 4857 | 4856 | 4855 | 4854  | 4853 | 4852 | 4851 | 4850 | 4849 | 4848 | 4847 | 4846 | 4845 | 4844 | 4843 | 4842 | 4841 | 4840 | 4839 | 4838   |      | 217  |      |      |      |      |     |
|   | 0.10   | 1.313  | 4895 | 4894 | 4893  | 4892 | 4891 | 4890 | 4889 | 4888  | 4887 | 4886 | 4885 | 4884 | 4883  | 4882 | 4881 | 4880 | 4879 | 4878 | 4877 | 4876 | 4875 | 4874 | 4873 | 4872 | 4871 | 4870 | 4869 | 4868 | 4867   |      | 218  |      |      |      |      |     |
|   | 0.05   | 0.656  | 4913 | 4912 | 4911  | 4910 | 4909 | 4908 | 4907 | 4906  | 4905 | 4904 | 4903 | 4902 | 4901  | 4900 | 4899 |      |      |      |      |      |      |      |      |      |      |      |      |      |        |      | 219  |      |      |      |      |     |
|   | 0.00   | 0.000  | 4942 | 4941 | 4940  | 4939 | 4938 | 4937 | 4936 | 4935  | 4934 | 4933 | 4932 | 4931 | 4930  | 4929 | 4928 | 4927 | 4926 | 4925 | 4924 | 4923 | 4922 | 4921 | 4920 | 4919 | 4918 | 4917 | 4916 | 4915 | 4914   |      | 220  |      |      |      |      |     |
| Z/L   | inches | 0      | 1    | 2    | 2.625 | 4    | 5.25 | 6    | 7    | 7.875 | 9    | 10   | 10.5 | 12   | 13.13 | 14   | 15   | 16   | 17   | 18   | 19   | 20   | 21   | 22   | 23   | 24   | 25   | 26   | 27   | 28   | inches |      |      |      |      |      |      |     |
|   |        | 0.00   | 0.08 | 0.15 | 0.20  | 0.30 | 0.40 | 0.46 | 0.53 | 0.60  | 0.69 | 0.76 | 0.80 | 0.91 | 1.00  | 1.07 | 1.14 | 1.22 | 1.30 | 1.37 | 1.45 | 1.52 | 1.60 | 1.68 | 1.75 | 1.83 | 1.90 | 1.98 | 2.06 | 2.13 | X/L    |      |      |      |      |      |      |     |
| -----X setpoint-----  |        |        |      |      |       |      |      |      |      |       |      |      |      |      |       |      |      |      |      |      |      |      |      |      |      |      |      |      |      |      |        |      |      |      |      |      |      |     |





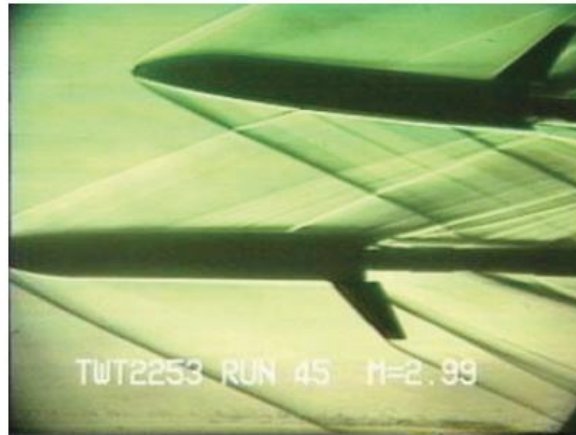
*Figure 1. Langley Glide-Back Booster (LGBB) concept in a belly-to-belly configuration.*



(a)  $x_{setpt}/L = z_{setpt}/L = 0.0$ ,  $\Delta\alpha = 0^\circ$



(b)  $x_{setpt}/L = 0.2$ ,  $z_{setpt}/L = 0.16$ ,  $\Delta\alpha = 5^\circ$

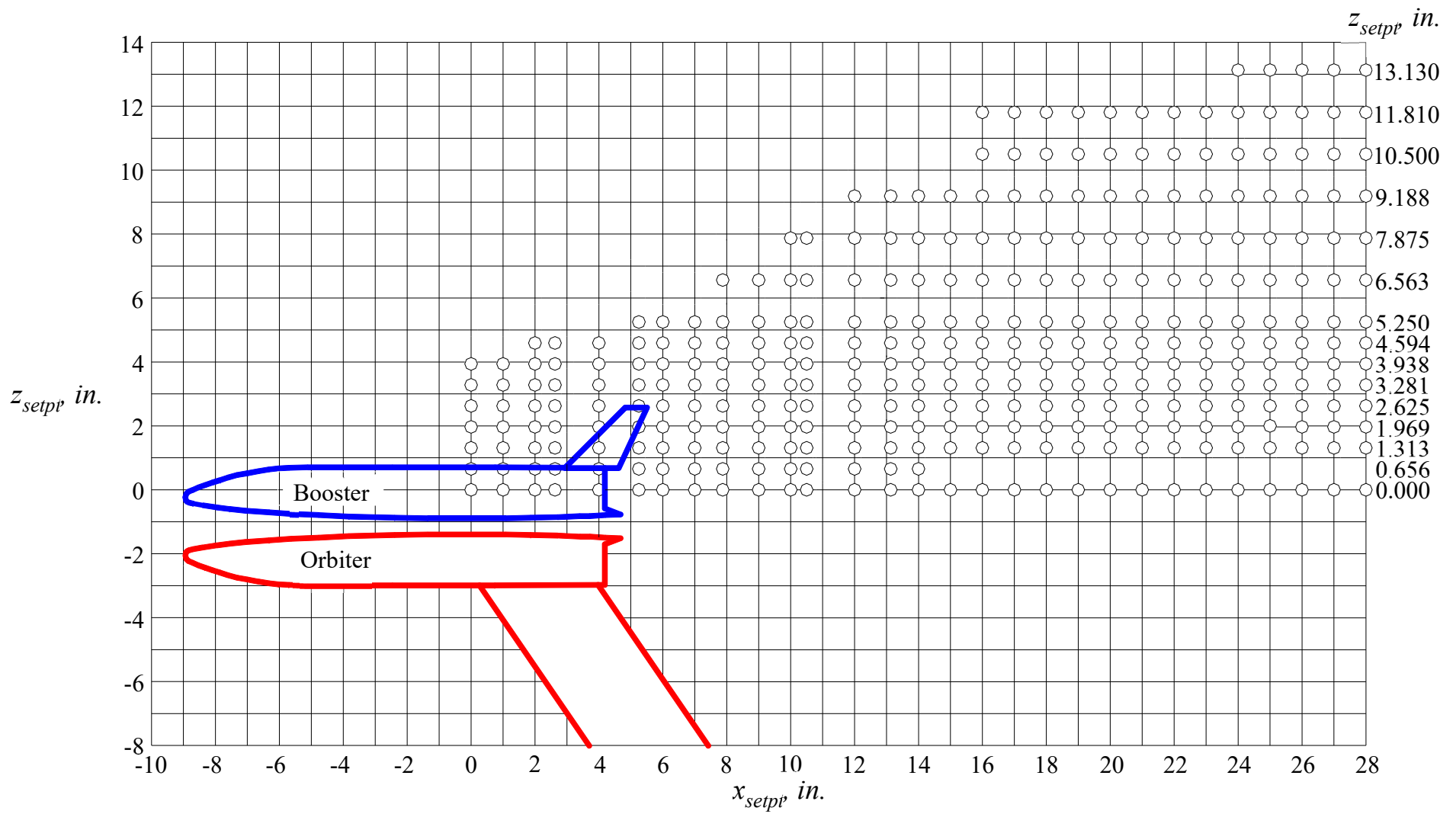


(c)  $x_{setpt}/L = 0.4$ ,  $z_{setpt}/L = 0.25$ ,  $\Delta\alpha = 5^\circ$



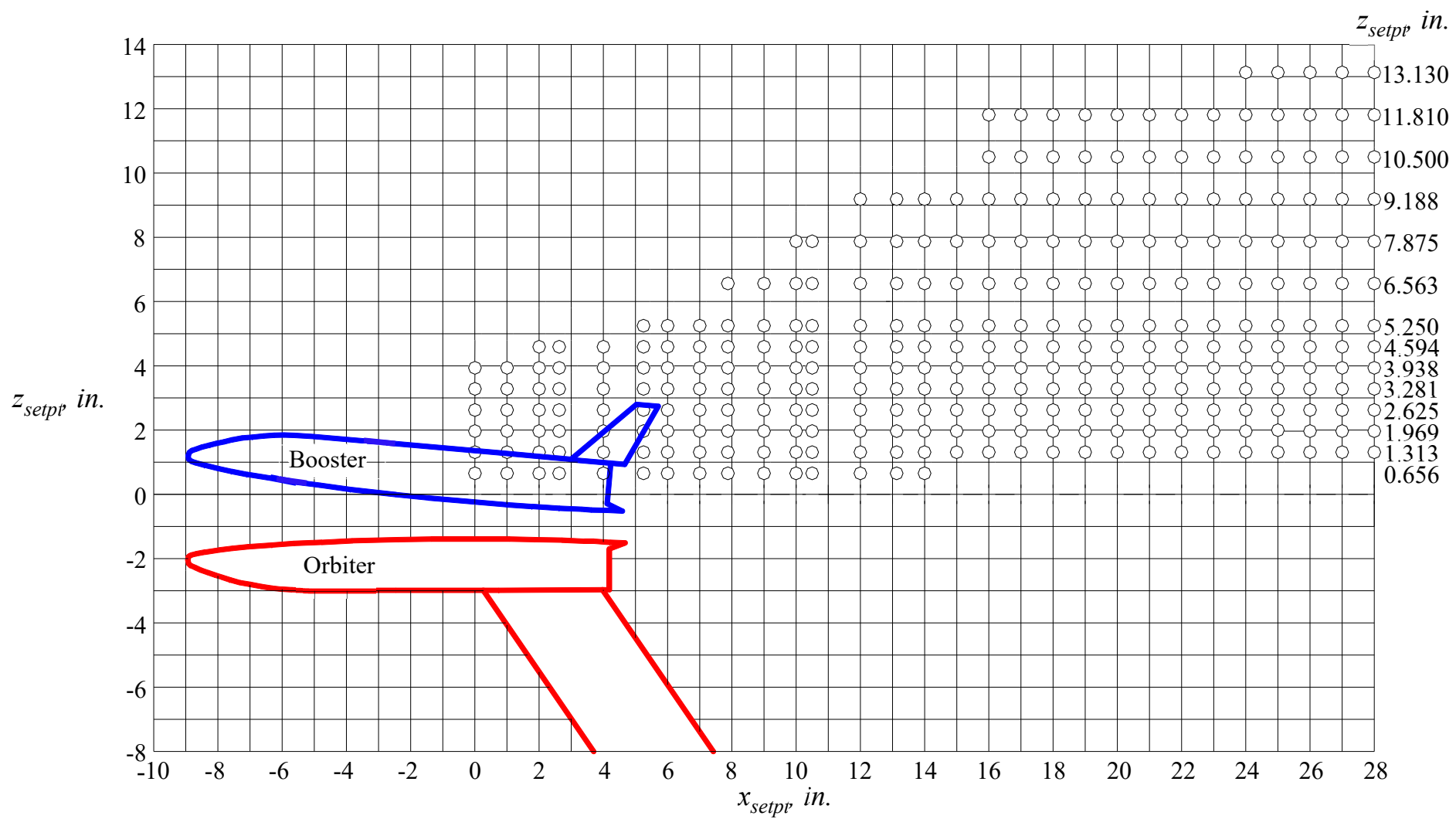
(d)  $x_{setpt}/L = 0.8$ ,  $z_{setpt}/L = 0.36$ ,  $\Delta\alpha = 10^\circ$

Figure 2. Schlieren images from NASA MSFC ARF TWT testing of 0.01-scale LGBB models at Mach = 2.99 [18].



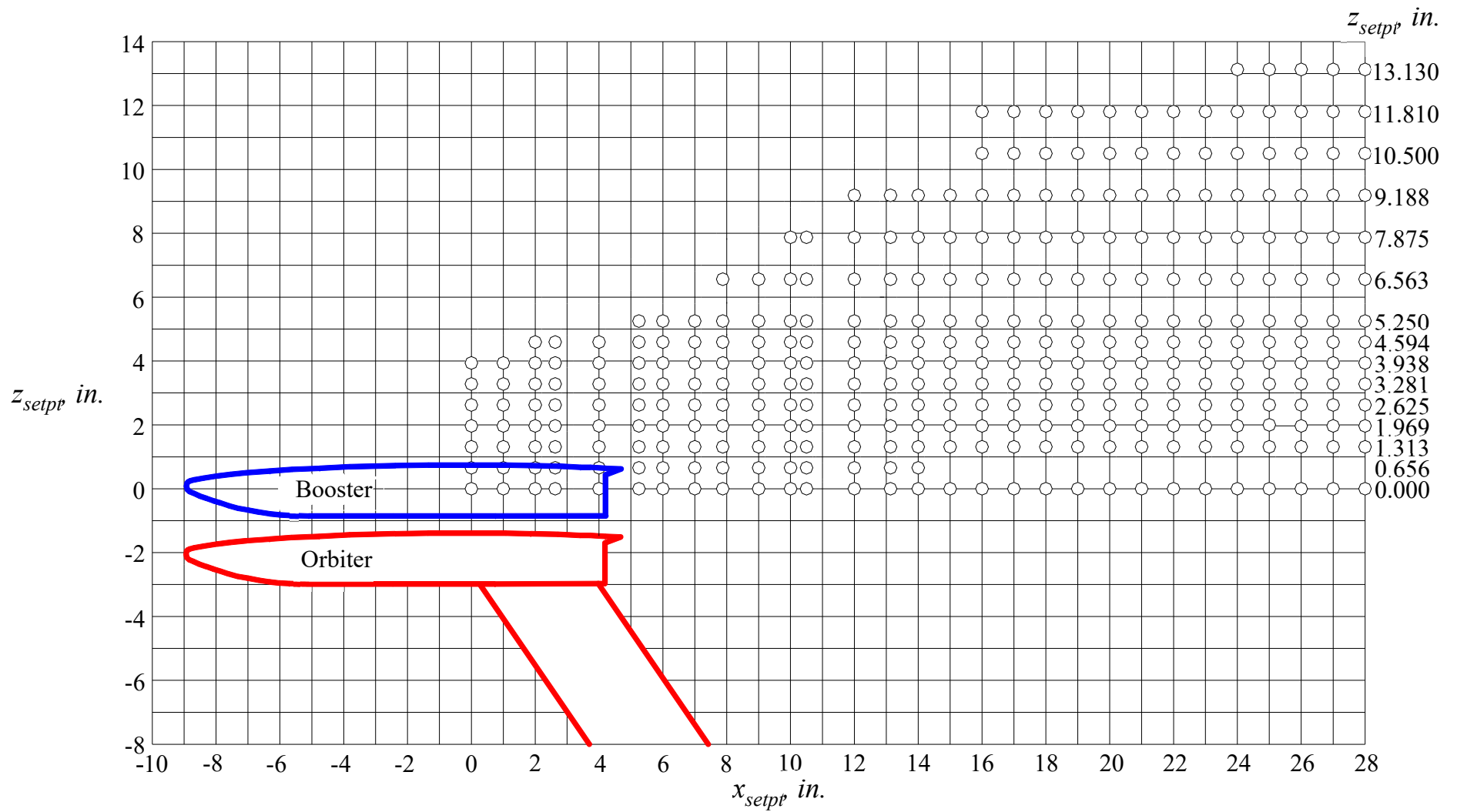
(a) Belly-to-belly configuration,  $\Delta\alpha = 0^\circ$

Figure 3. Test grid matrices for the LGBB orbiter and booster models in UPWT Tests 1741 and 1745.



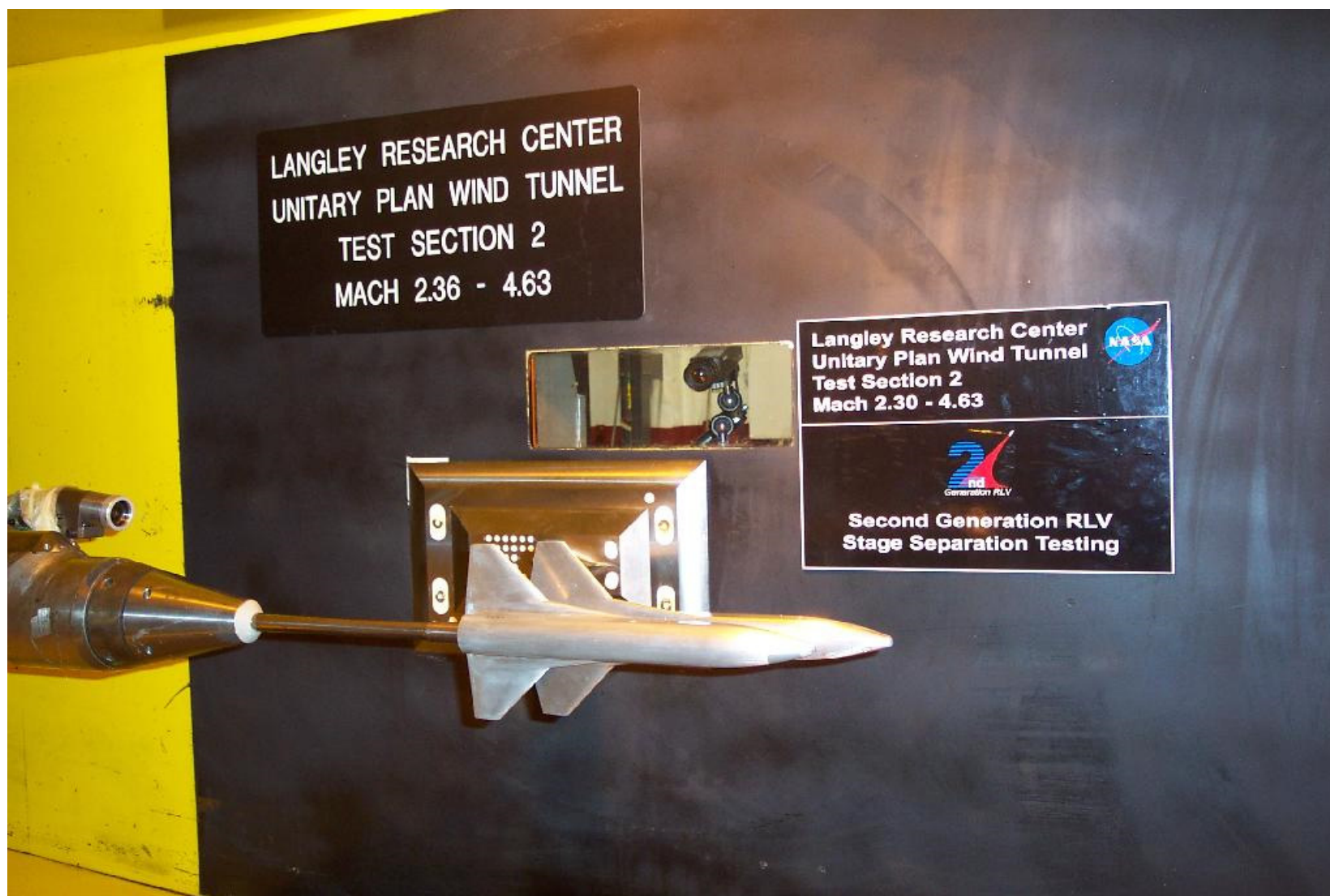
(b) Belly-to-belly configuration,  $\Delta\alpha = 5^\circ$

Figure 3. Continued.



(c) Back-to-belly configuration,  $\Delta\alpha = 0^\circ$

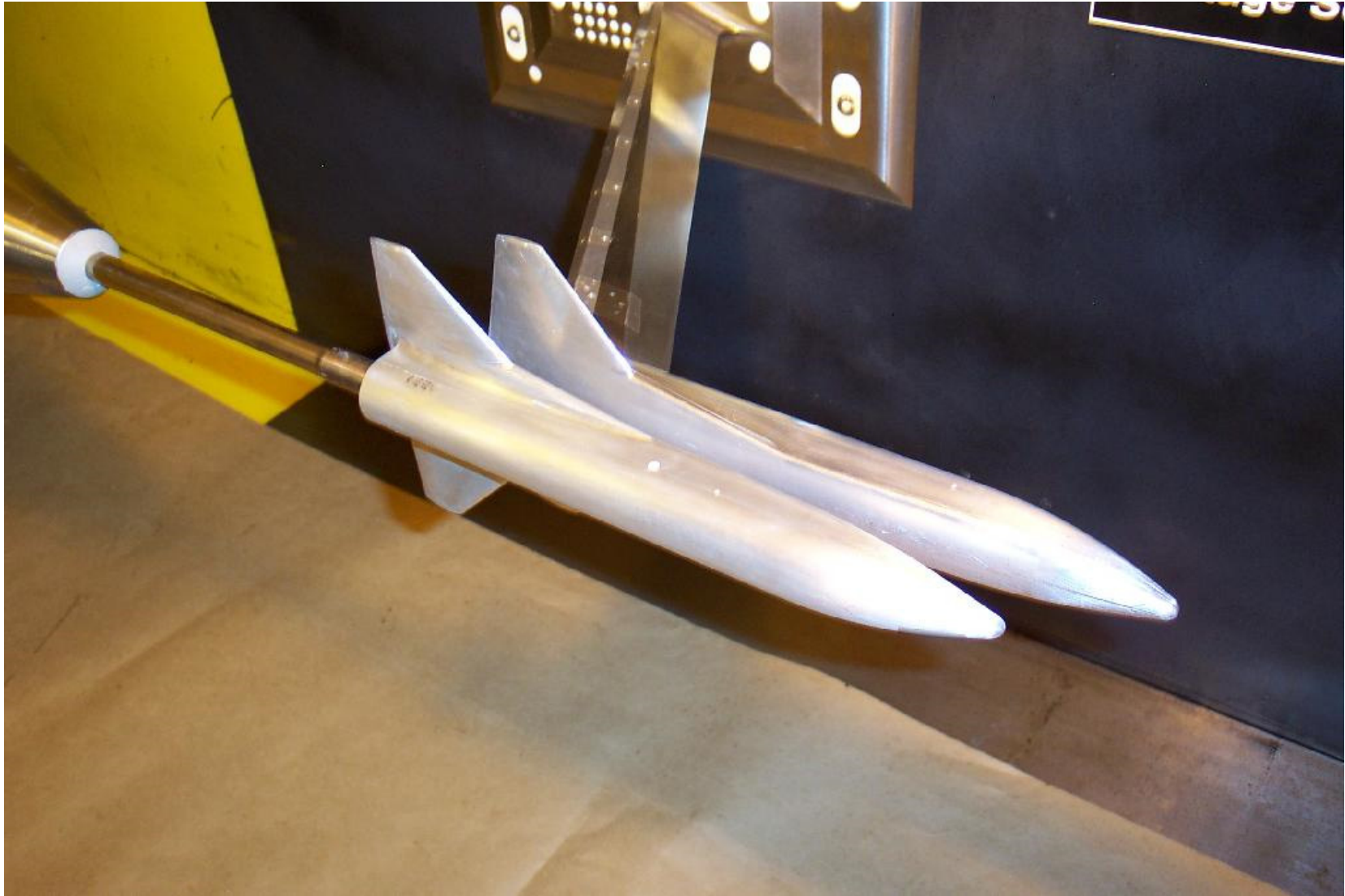
Figure 3. Concluded.



*(a) Overall view of orbiter and booster model installation*

*Figure 4. Uninstrumented 0.0175-scale LGBB orbiter and booster models installed in UPWT Test Section 2 during Test 1739.*





*(b) Close-up view of orbiter and booster models*

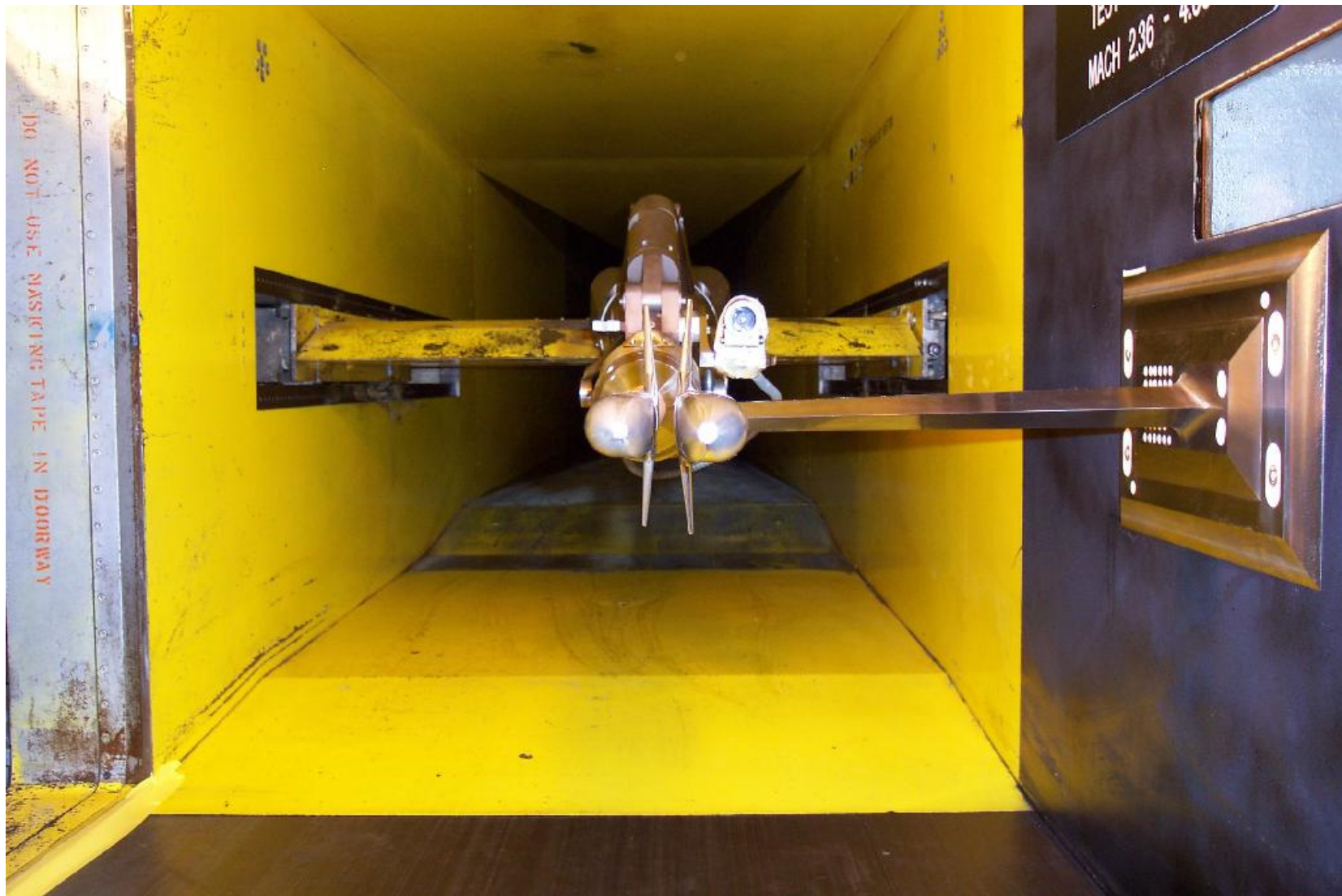
*Figure 4. Continued.*



*(c) Front view of orbiter and booster models*

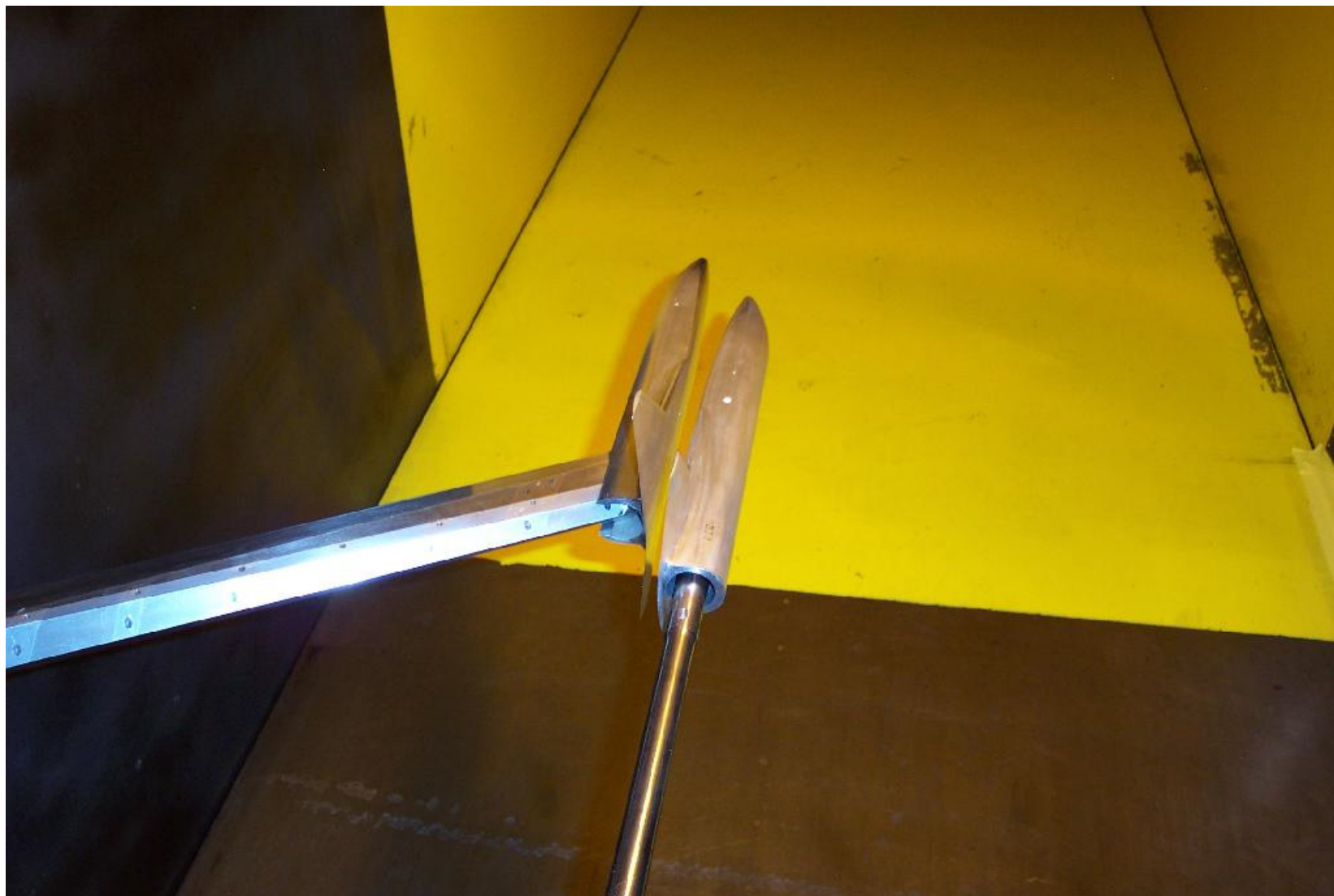
*Figure 4. Continued.*





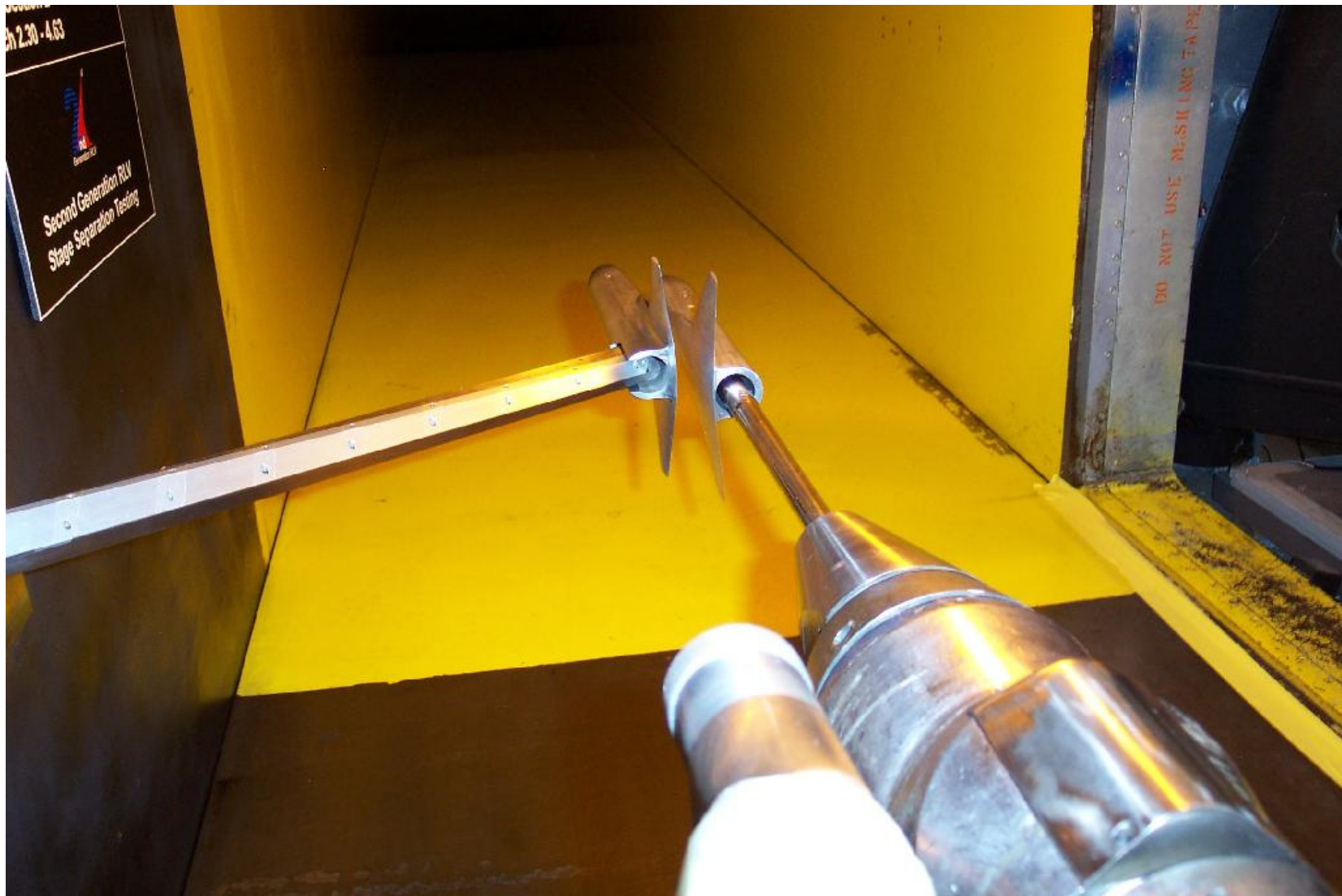
*(d) Head-on view of orbiter and booster models*

*Figure 4. Continued.*



*(e) Rear view of orbiter and booster models*

*Figure 4. Continued.*



*(f) Three-quarter rear view of orbiter and booster models*

*Figure 4. Concluded.*



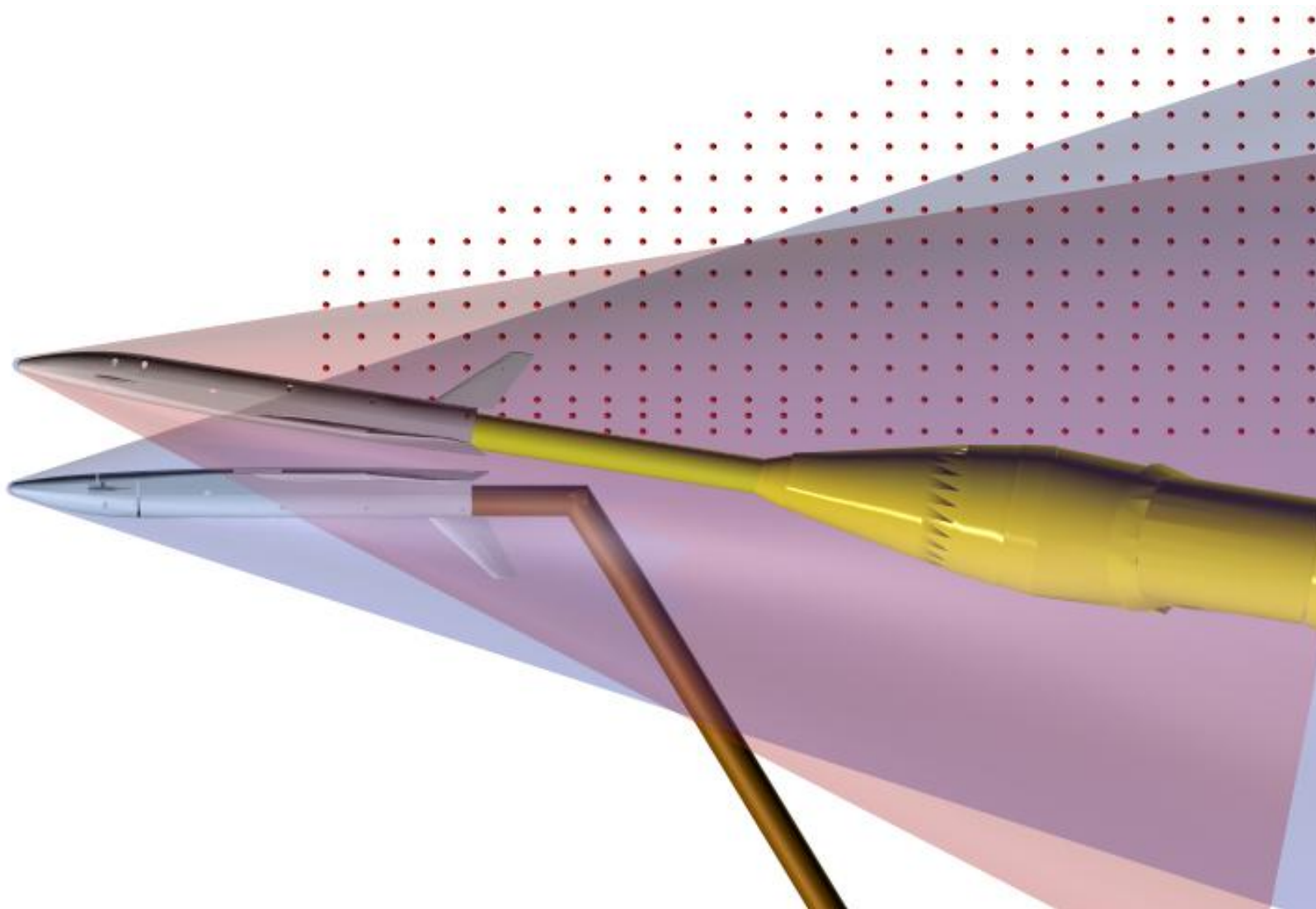


*Figure 5. Virtual diagnostics [23] rendering of orbiter and booster models at Mach = 3.0 (Test grid is shown in the background.).*

$S_w = 19.184 \text{ in}^2 (0.1332 \text{ ft}^2)$   
 $b_w = 6.525 \text{ in.}$   
 $L = 13.125 \text{ in.}$   
 $d = 1.441 \text{ in.}$

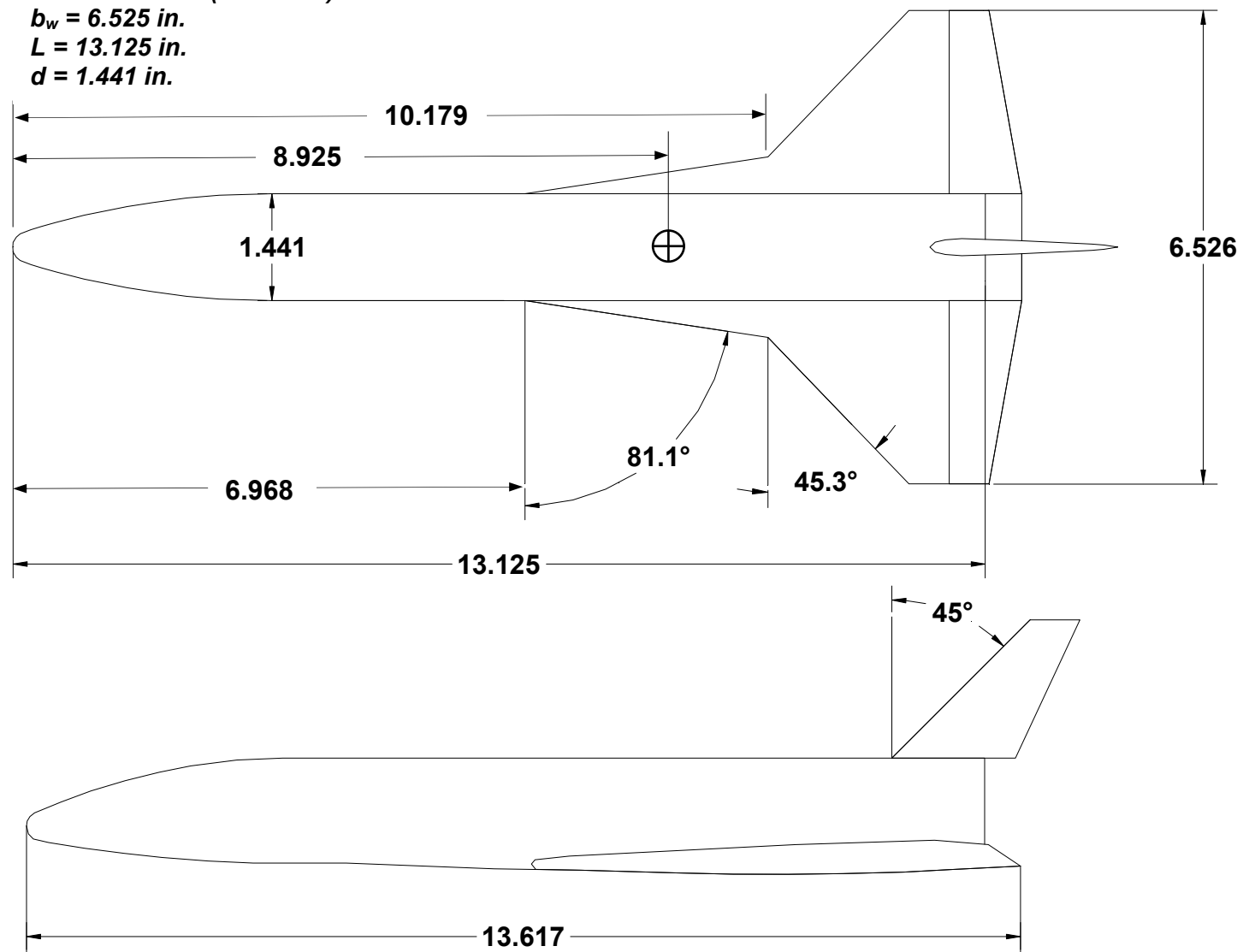
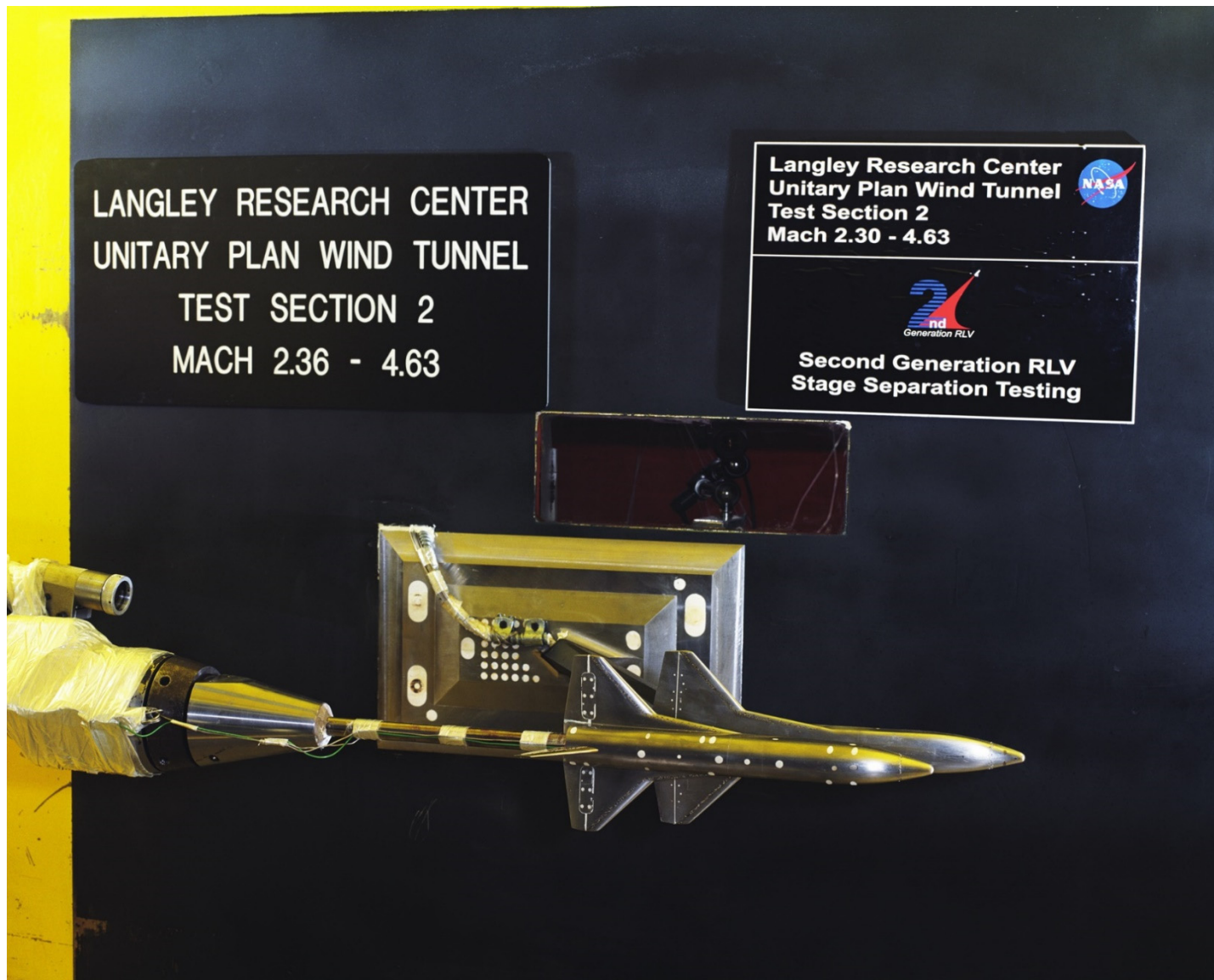
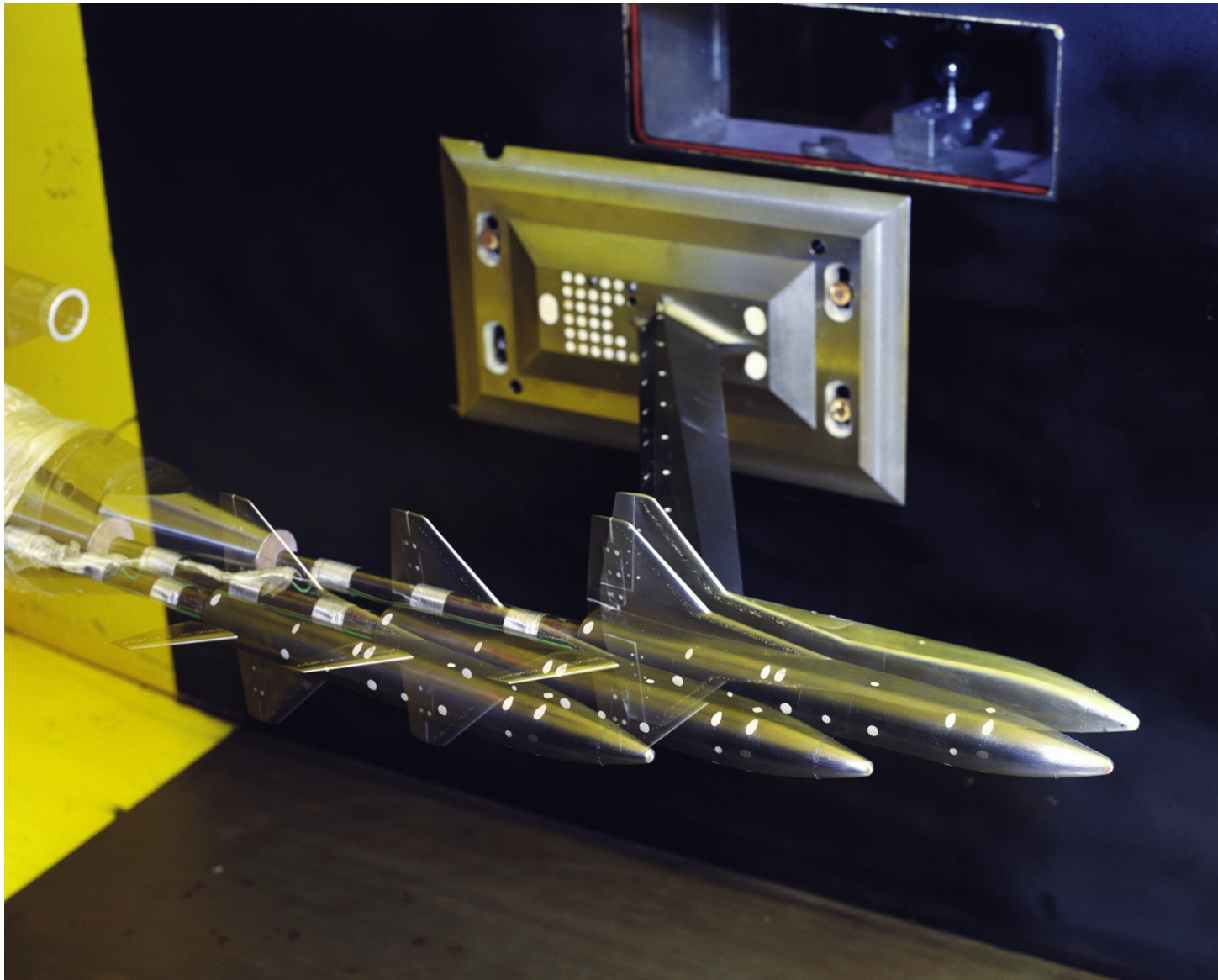


Figure 6. Sketch of LGBB model with reference dimensions (All dimensions in illustration are in inches.).



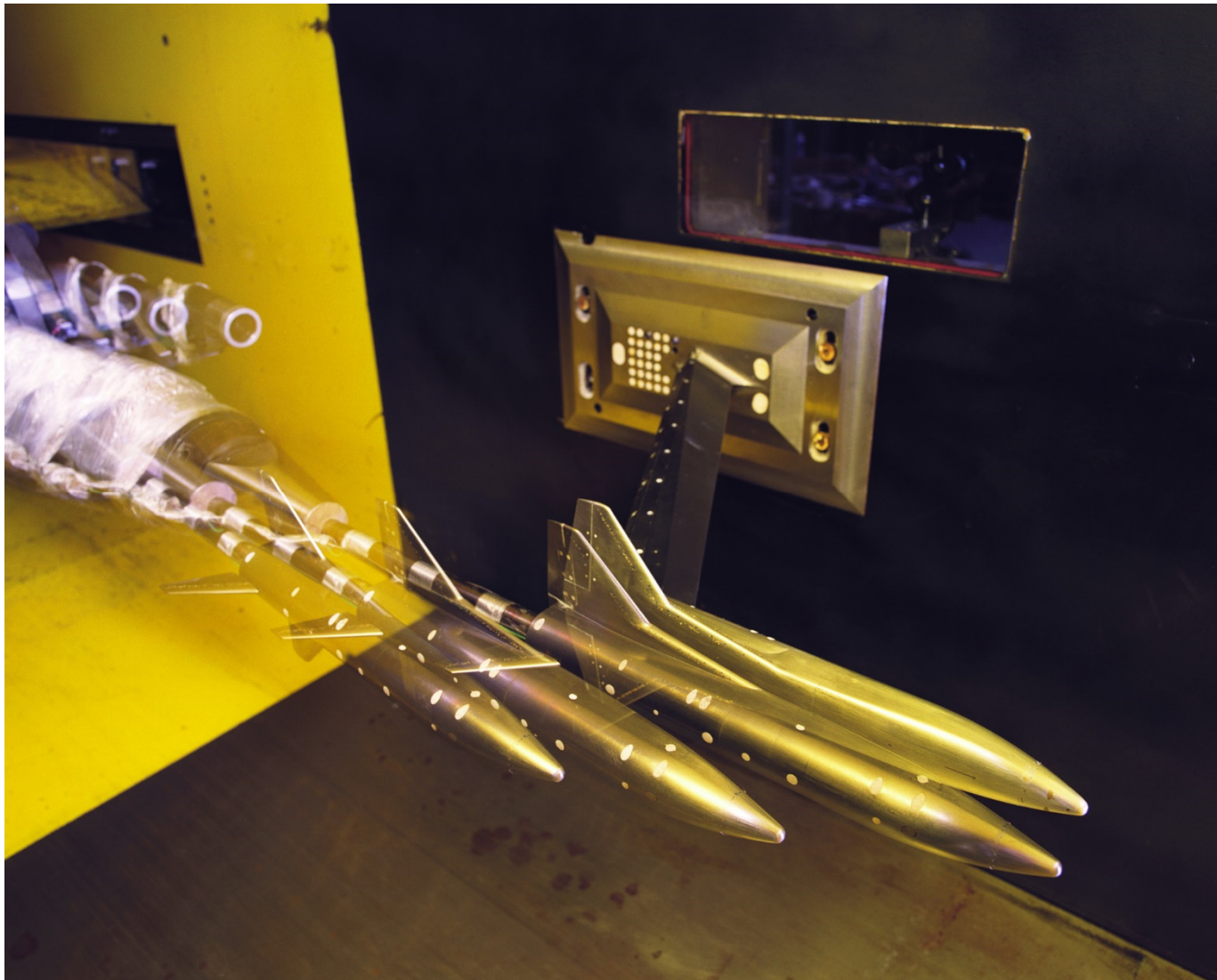
(a) Overall view of orbiter and booster model installation

Figure 7. Instrumented 0.0175-scale LGBB orbiter and booster models installed in UPWT Test Section 2 during Tests 1741 and 1745.



*(b) Multiple exposure photographs of booster model moving away from orbiter model*  
*Figure 7. Continued.*

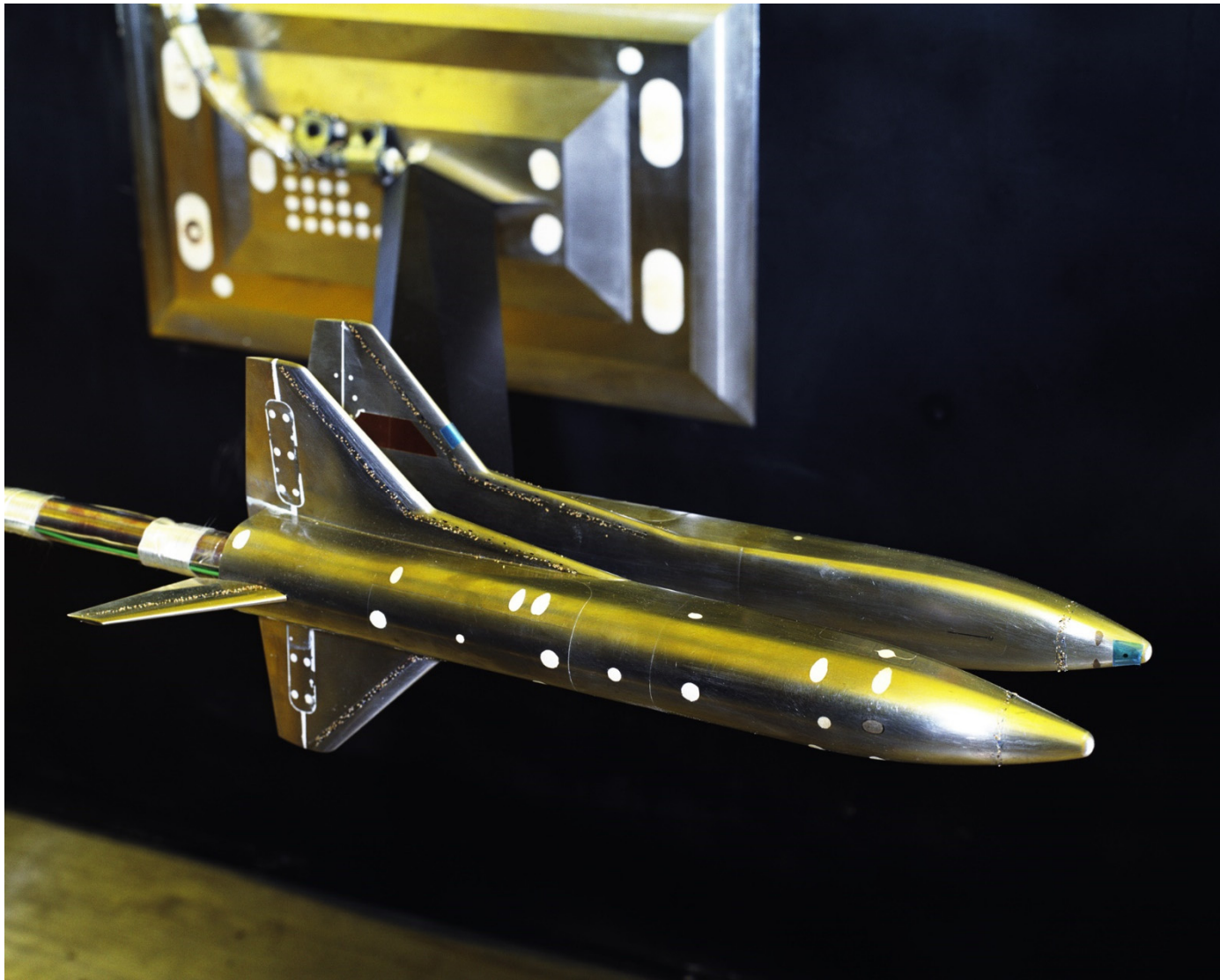




*(c) Multiple exposure photographs of booster model moving away from orbiter model (alternate view)*

*Figure 7. Continued.*





*(d) Close-up view of orbiter and booster models*

*Figure 7. Continued.*



*(e) Front view of orbiter and booster models*

*Figure 7. Continued.*





*(f) Front view of booster model moving away from orbiter model*

*Figure 7. Concluded.*

| <b>Orifice<br/>Number</b> | <b>MS<br/>(in.)</b> | <b>BL<br/>(in.)</b> |
|---------------------------|---------------------|---------------------|
| 101                       | 0.300               | 0.000               |
| 102                       | 2.157               | 0.000               |
| 103                       | 4.014               | 0.000               |
| 104                       | 5.871               | 0.000               |
| 105                       | 7.729               | 0.000               |
| 106                       | 9.586               | 0.000               |
| 107                       | 11.443              | 0.000               |
| 108                       | 13.300              | 0.000               |
| 201                       | 10.717              | 1.632               |
| 202                       | 11.293              | 1.632               |
| 203                       | 11.869              | 1.632               |
| 204                       | 12.444              | 1.632               |
| 301                       | 11.293              | -1.632              |

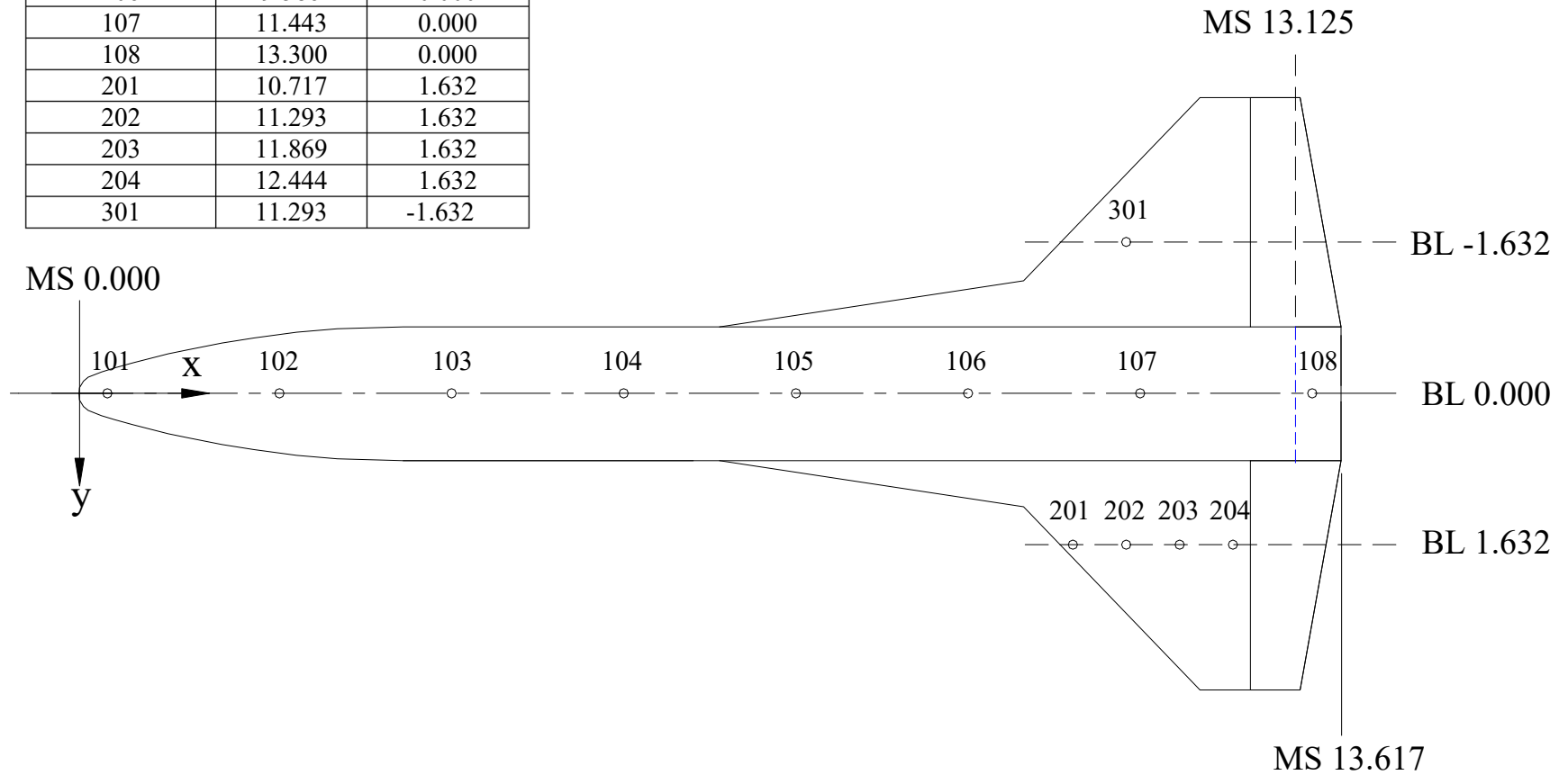


Figure 8. Sketch of 0.0175-scale LGBB orbiter model surface static pressure orifice locations; model shown in inverted position.  
(All dimensions are in inches.)

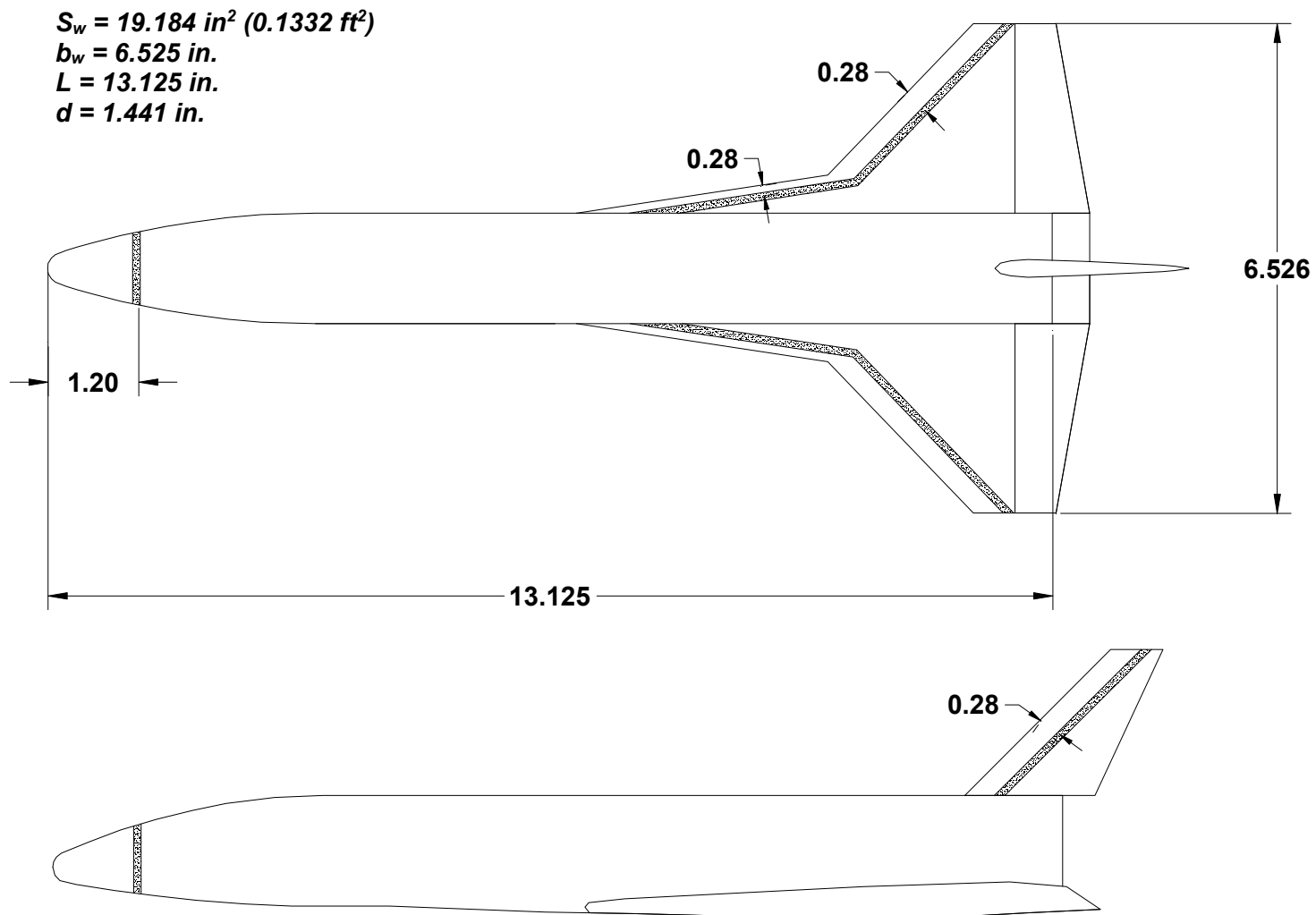
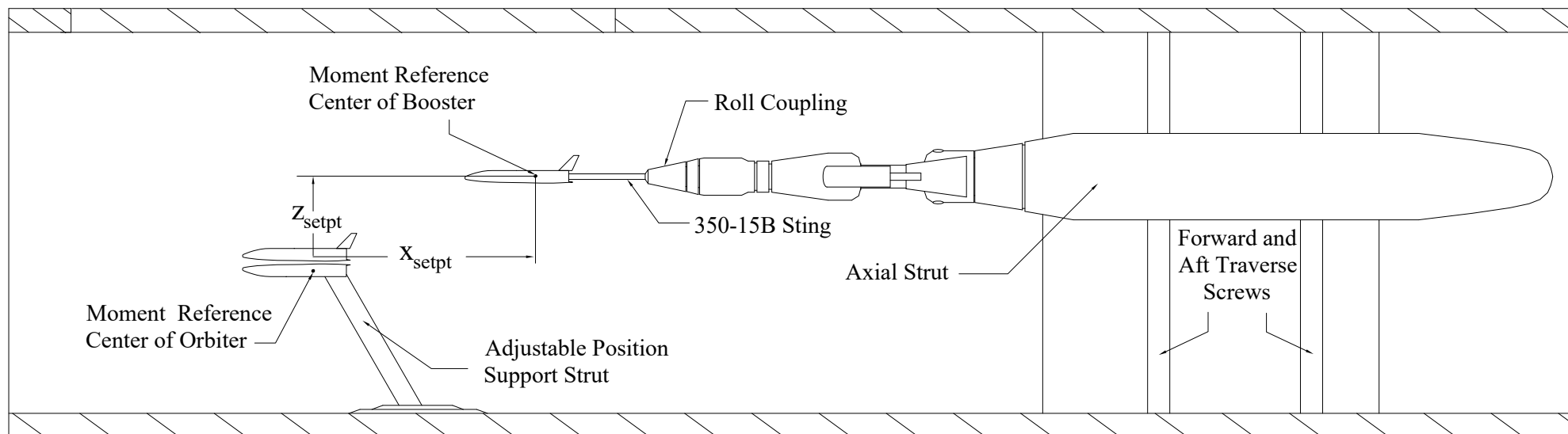


Figure 9. Boundary layer transition grit patterns on the 0.0175-scale LGBB models during UPWT Tests 1741 and 1745.  
 (Orbiter model does not include vertical tail.)



*Figure 10. Illustration of overall test setup showing major support system components in the NASA LaRC UPWT Test Section 2.*

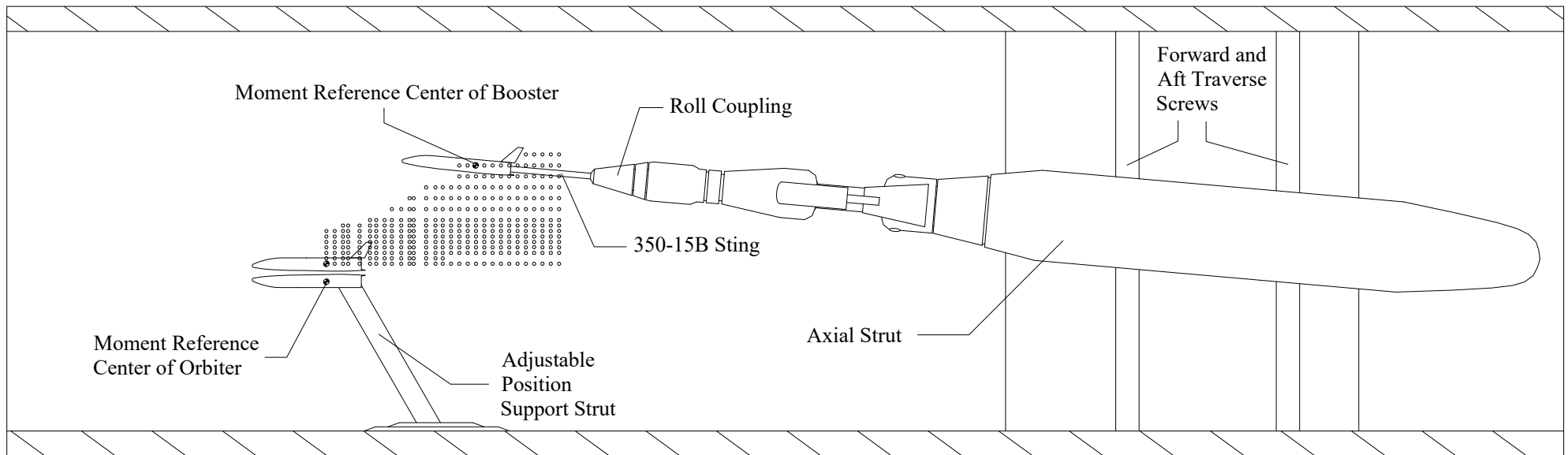


Figure 11. Test grid matrix superimposed on overall test setup for UPWT Test 1739, 1741, and 1745.

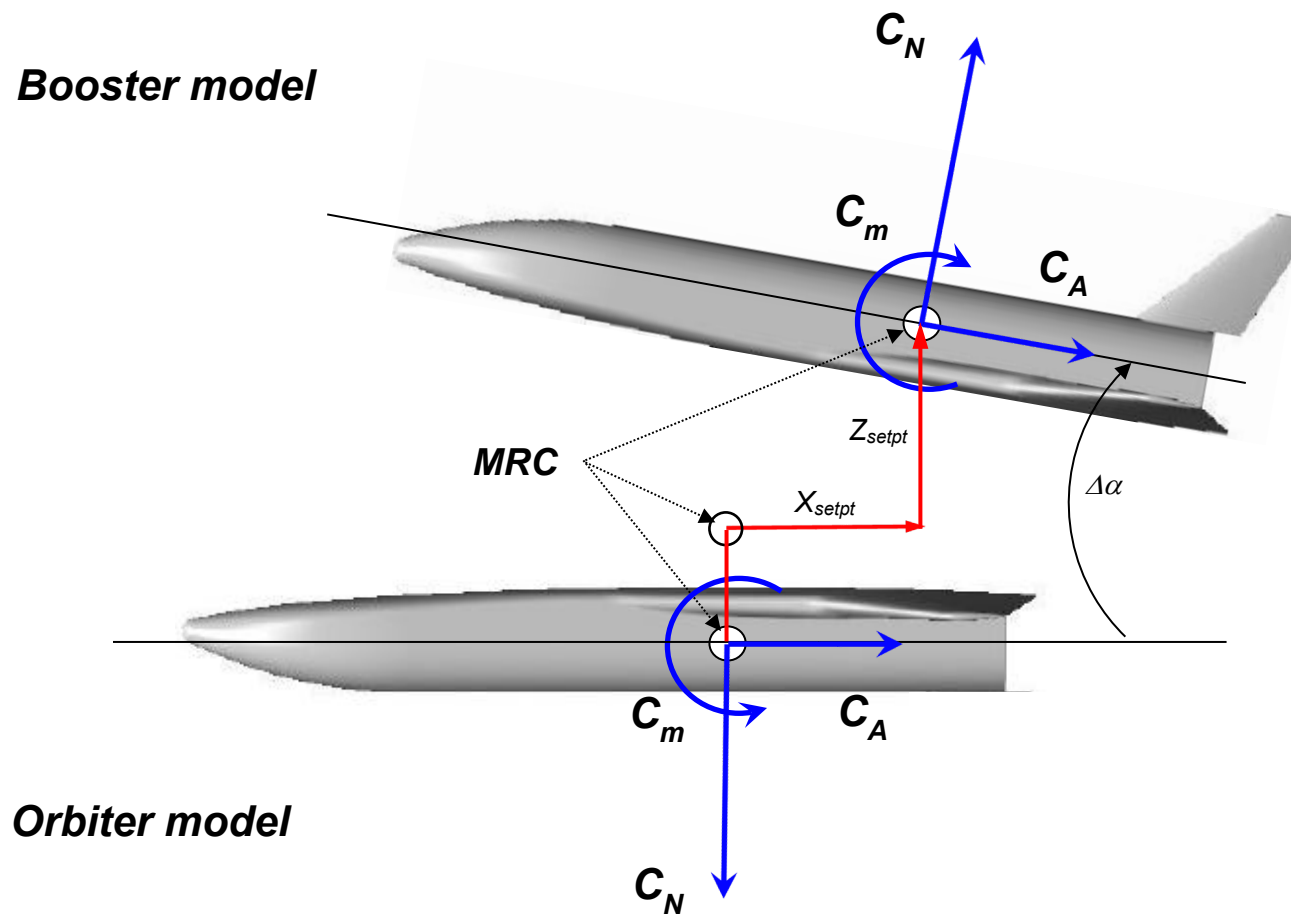


Figure 12. Definition of test parameters  $x_{setpt}$ ,  $z_{setpt}$ ,  $\Delta\alpha$  and orbiter and booster model aerodynamic coefficients.



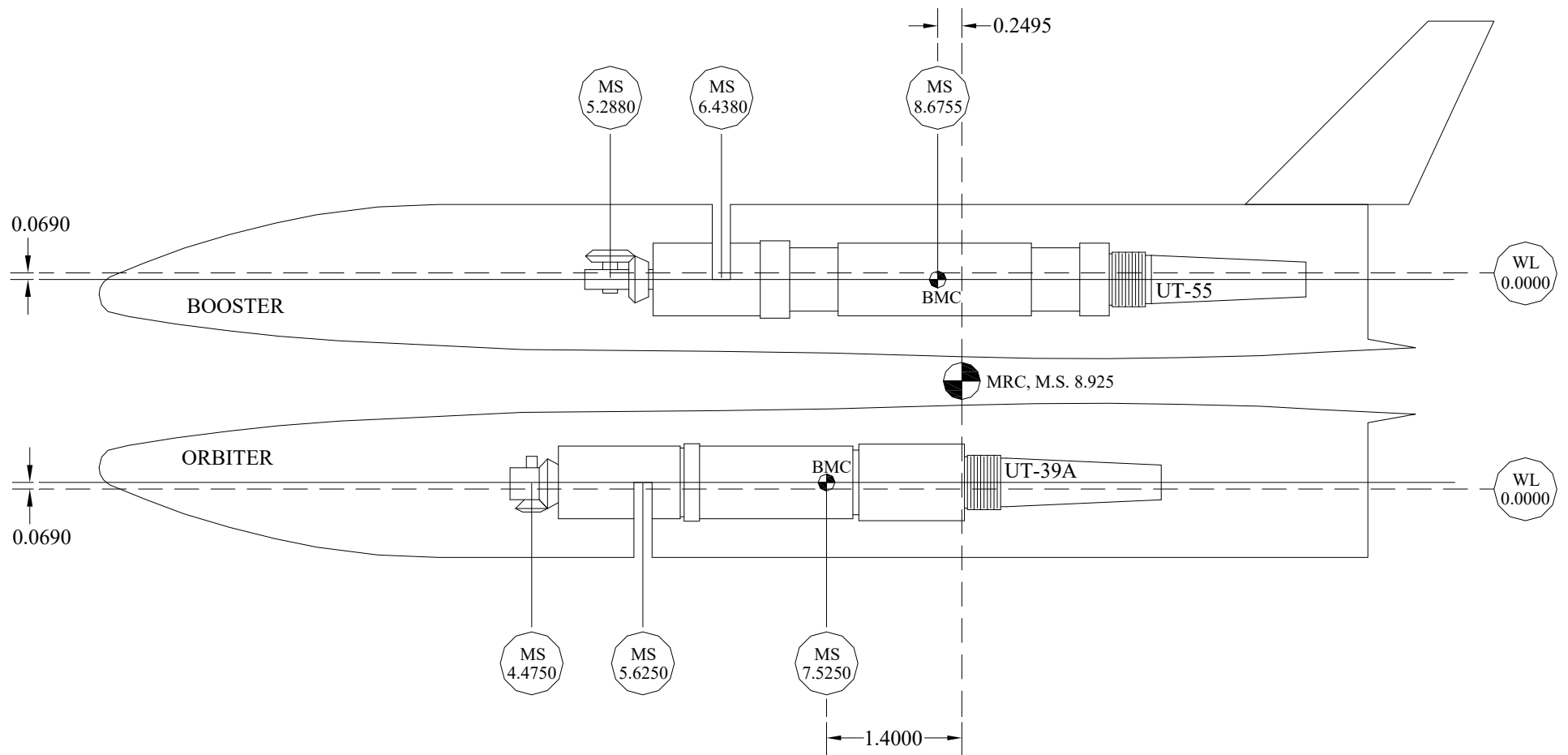


Figure 13. Installation of UT-39A and UT-55 balances in orbiter and booster models with balance moment center (BMC) and moment reference center (MRC) locations and transfer distances.

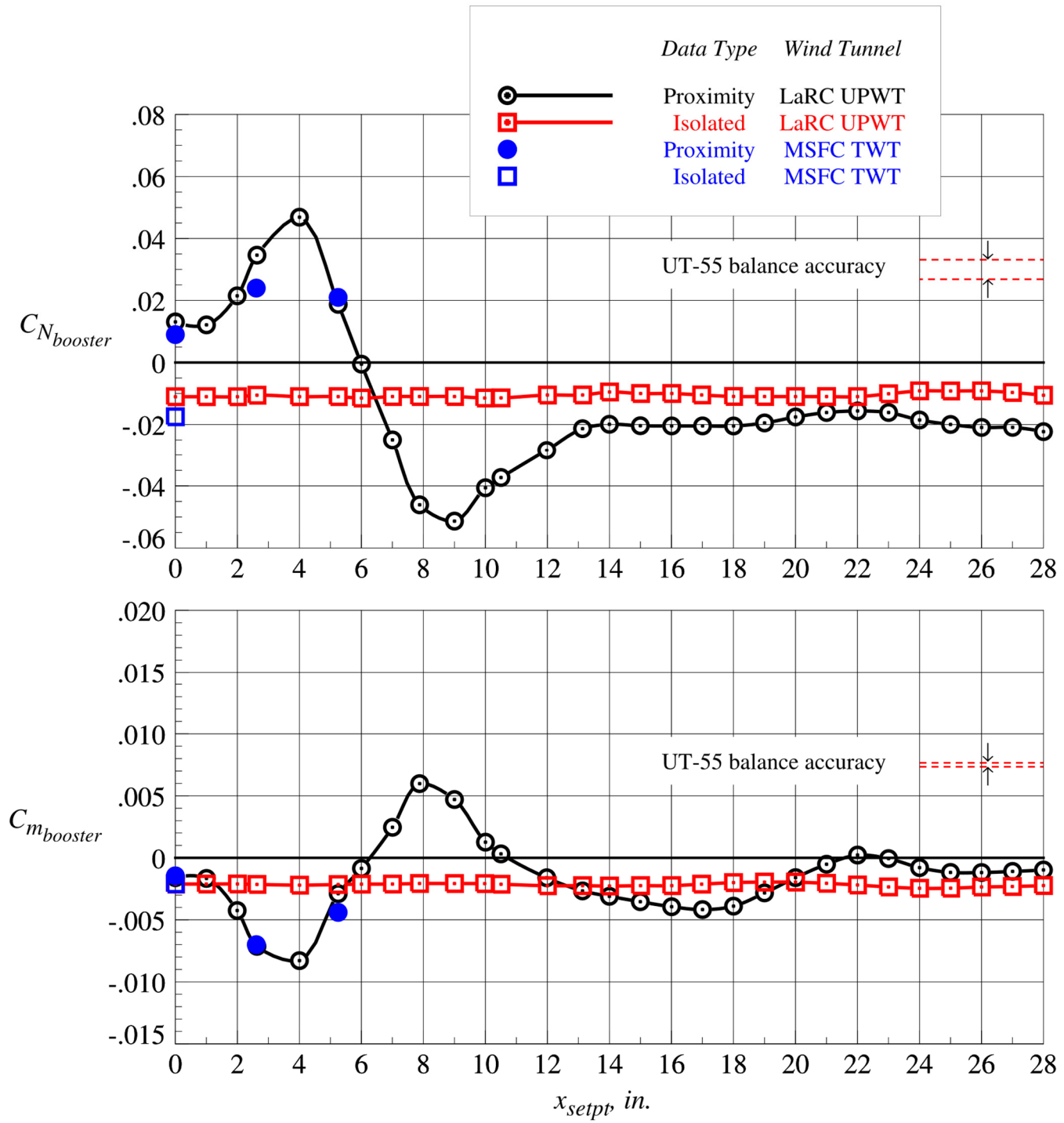
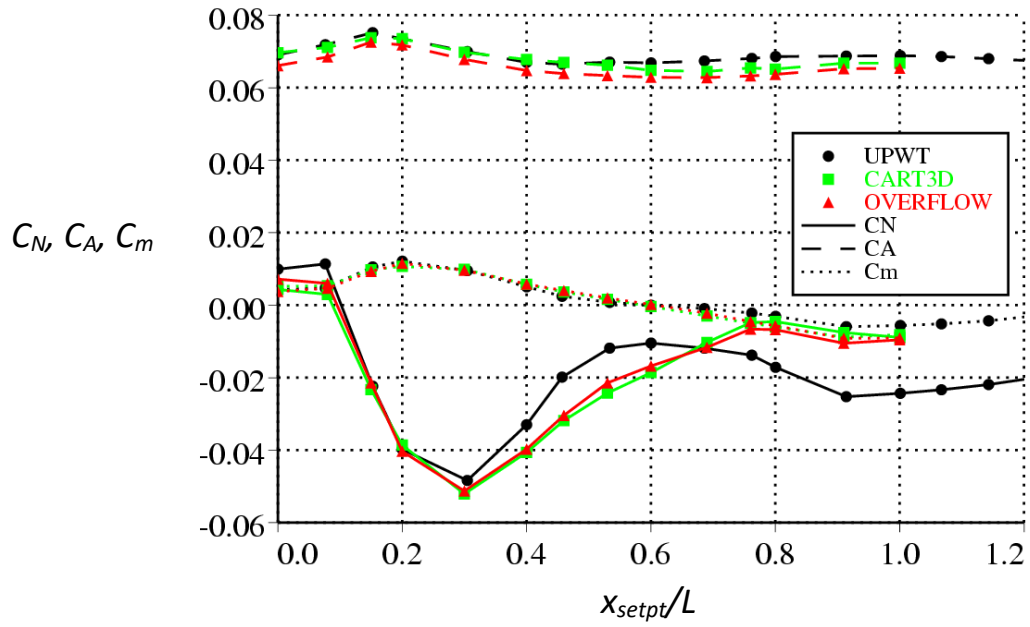
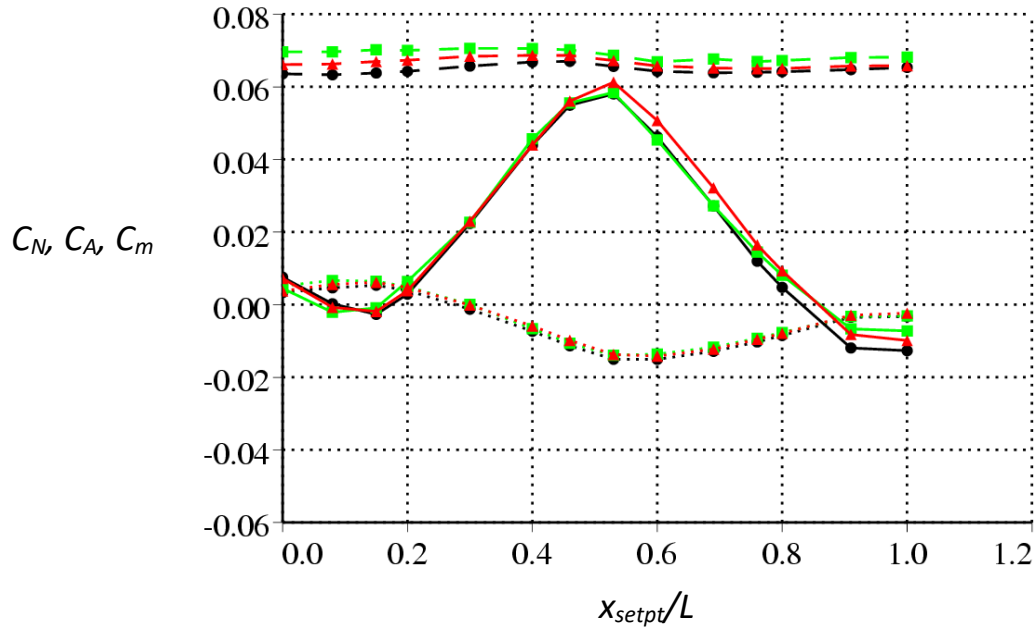


Figure 14. Comparison of LGBB booster longitudinal aerodynamic coefficients obtained in the NASA LaRC UPWT (Mach = 3.00) and NASA MSFC ARF TWT (Mach = 2.99).



(a) *Booster model*



(b) *Orbiter model*

Figure 15. Comparison of experimental and CFD proximity aerodynamic coefficients for the LGBB booster and orbiter models at Mach = 3.0 [20].

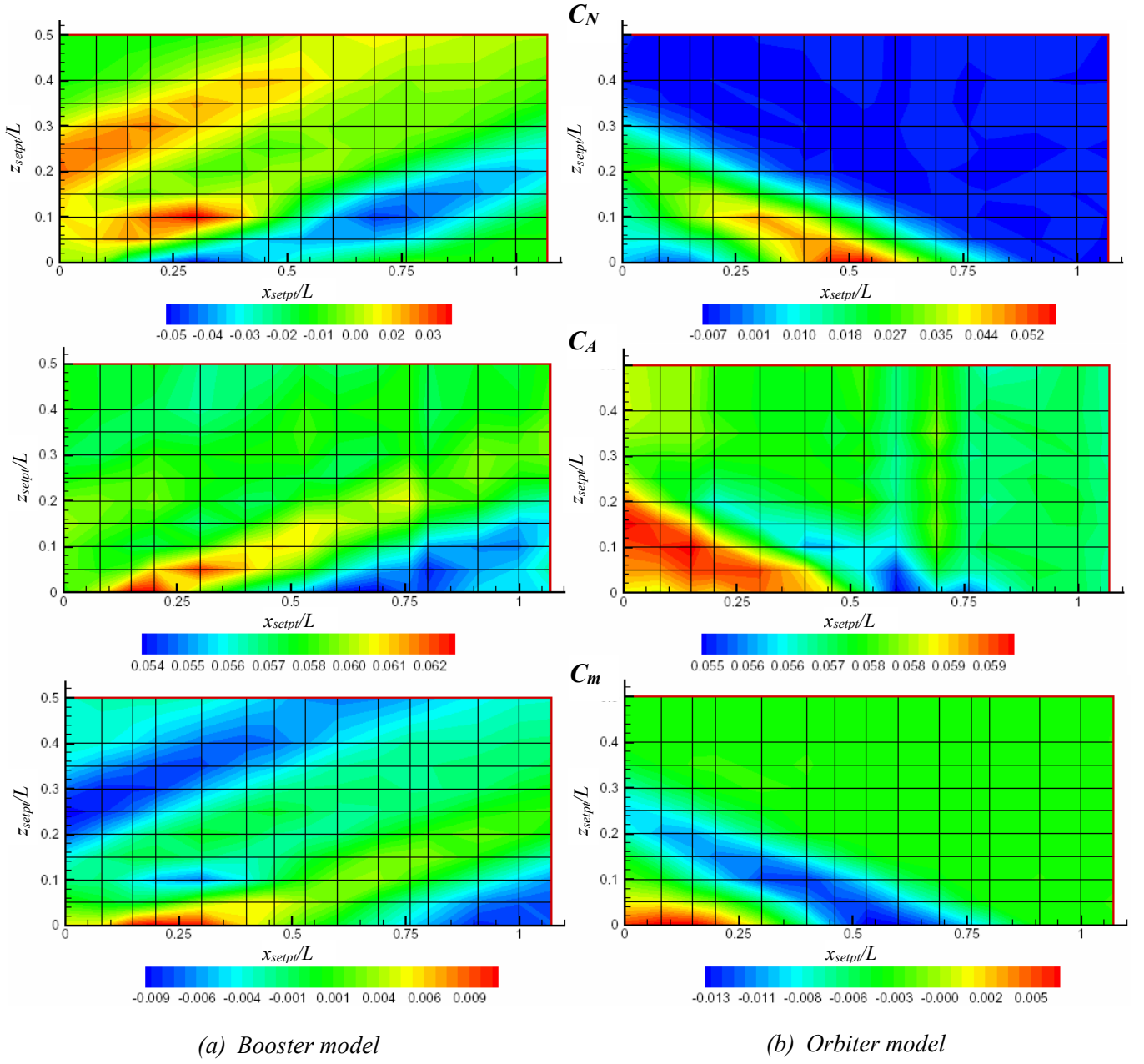
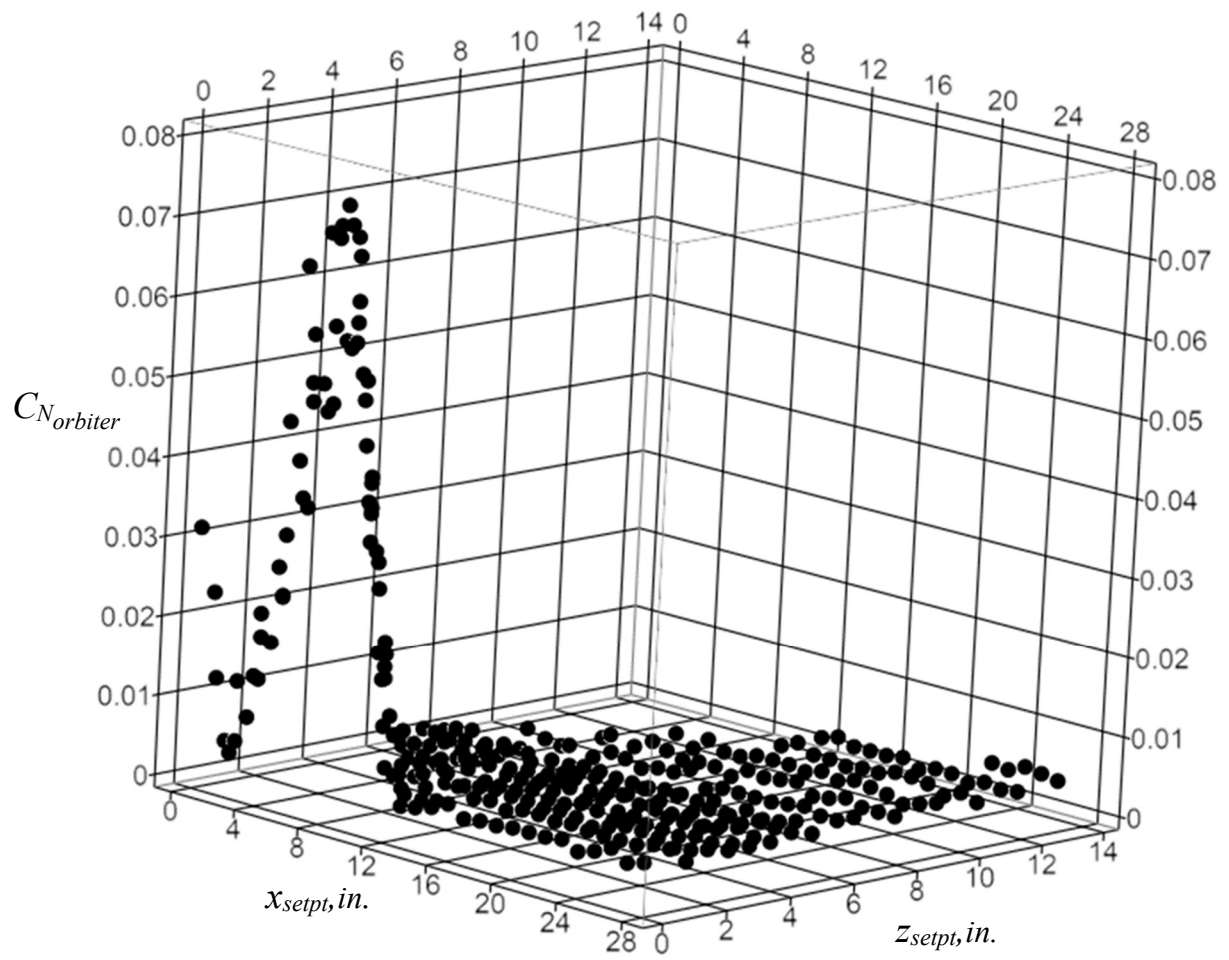
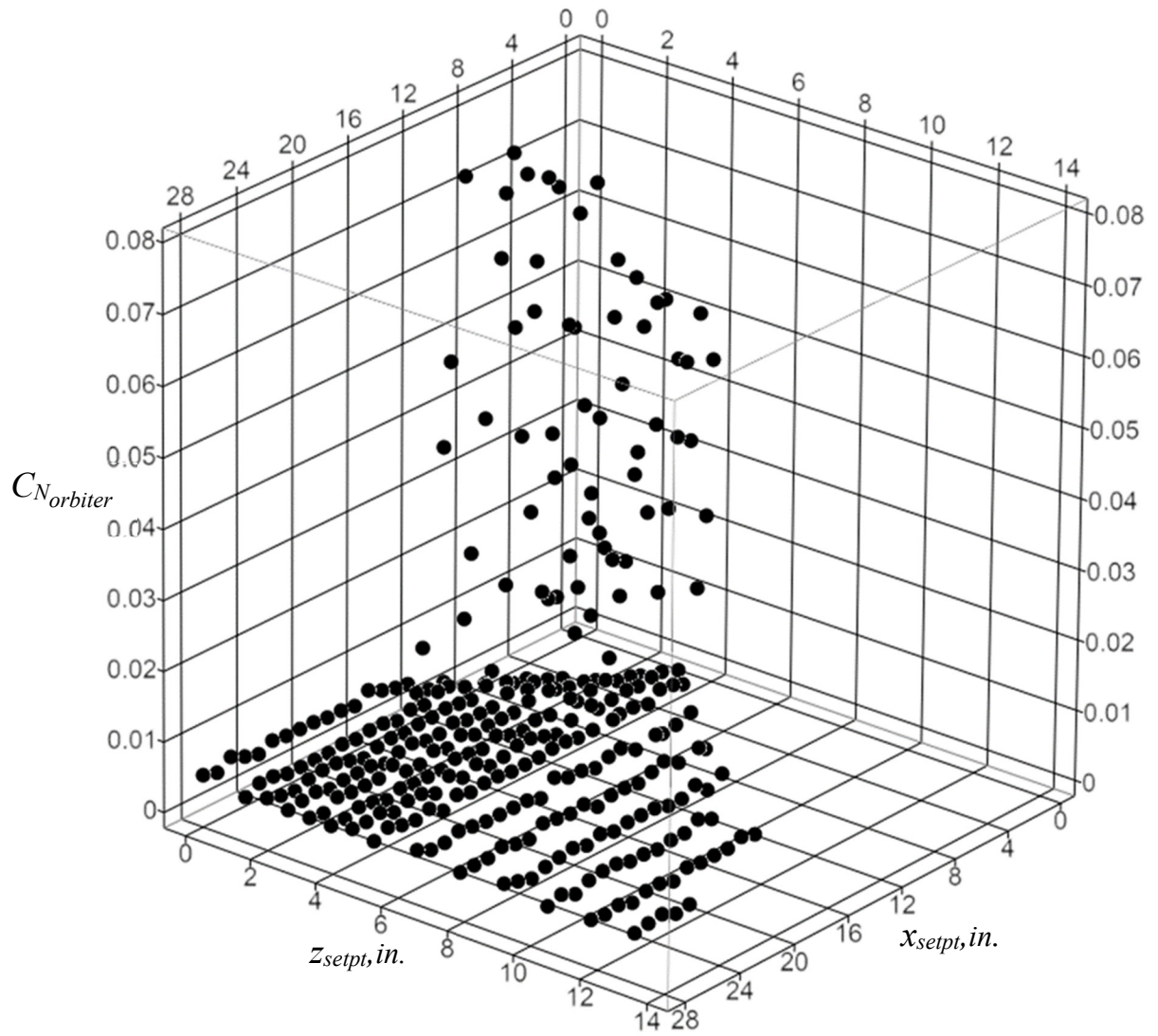


Figure 16. CFD color contour maps of LGBB booster and orbiter proximity aerodynamic coefficients at Mach = 3.0 [20].



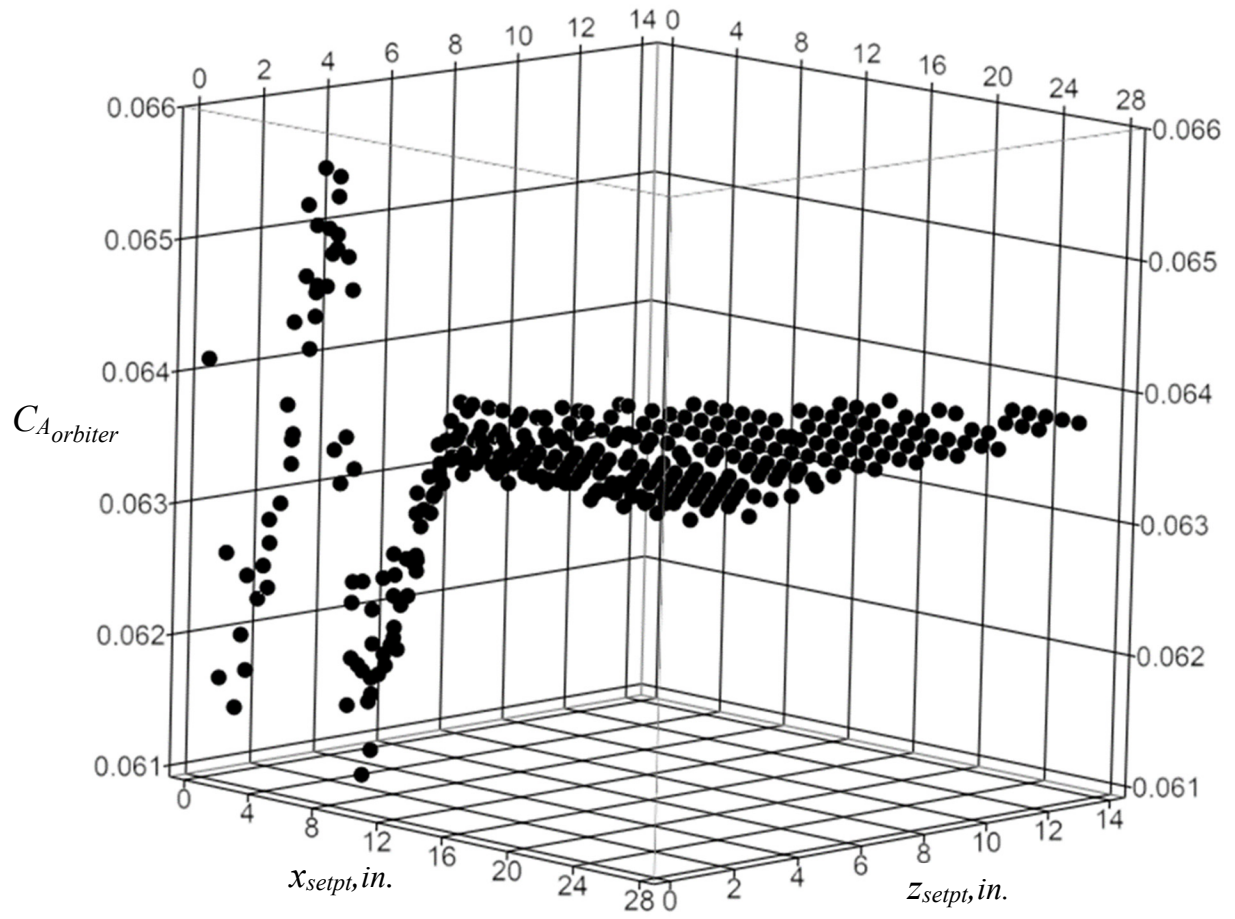
(a) Orbiter normal force coefficient (view from lower right quadrant of  $x_{setpt}$ - $z_{setpt}$  experimental space)

Figure 17. 3-D scatter plots of the orbiter proximity aerodynamic coefficients at  $Mach = 2.3$ ,  $\Delta\alpha = 0^\circ$ .



(b) Orbiter normal force coefficient (view from upper right quadrant of  $x_{setpt}-z_{setpt}$  experimental space).

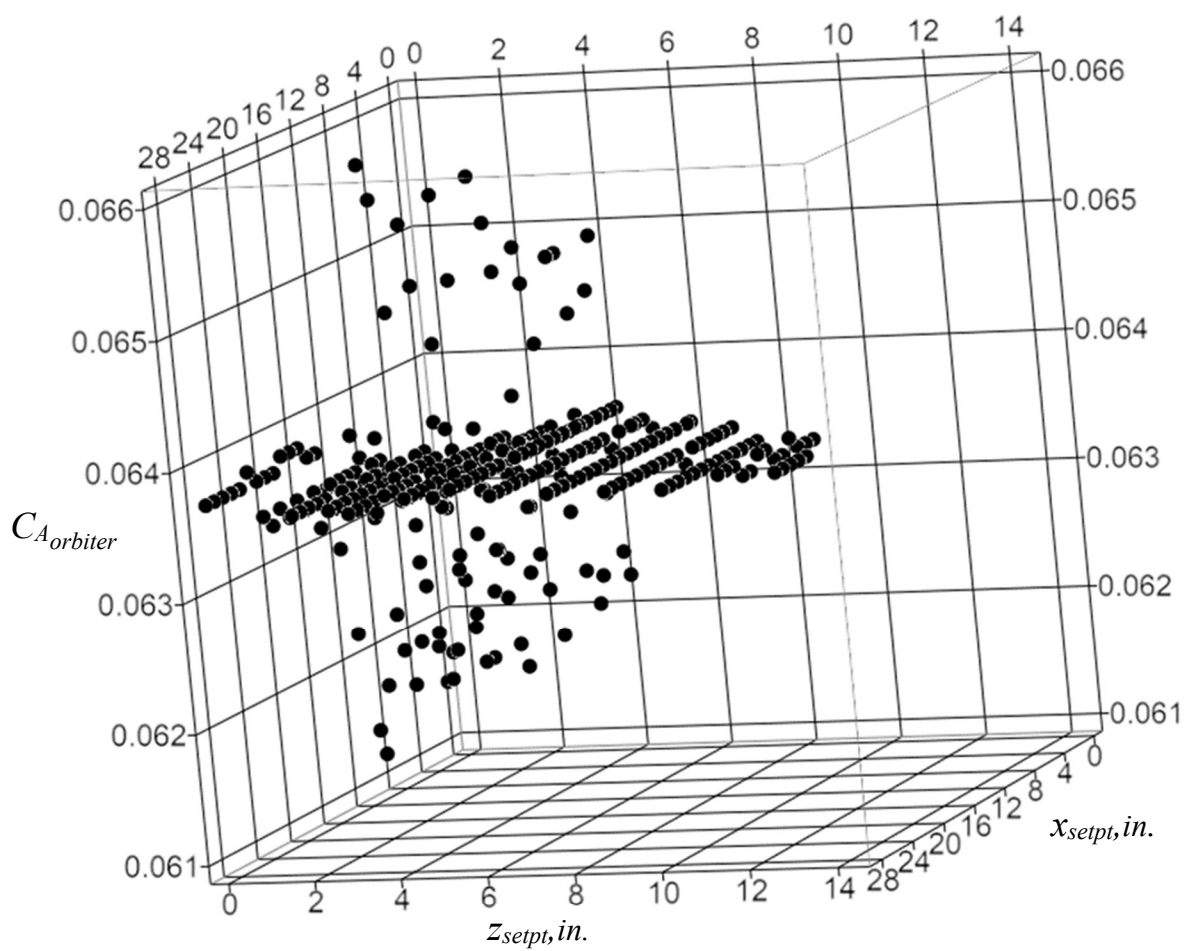
Figure 17. Continued.



(c) Orbiter axial force coefficient (view from lower right quadrant of  $x_{setpt}$ - $z_{setpt}$  experimental space)

Figure 17. Continued.

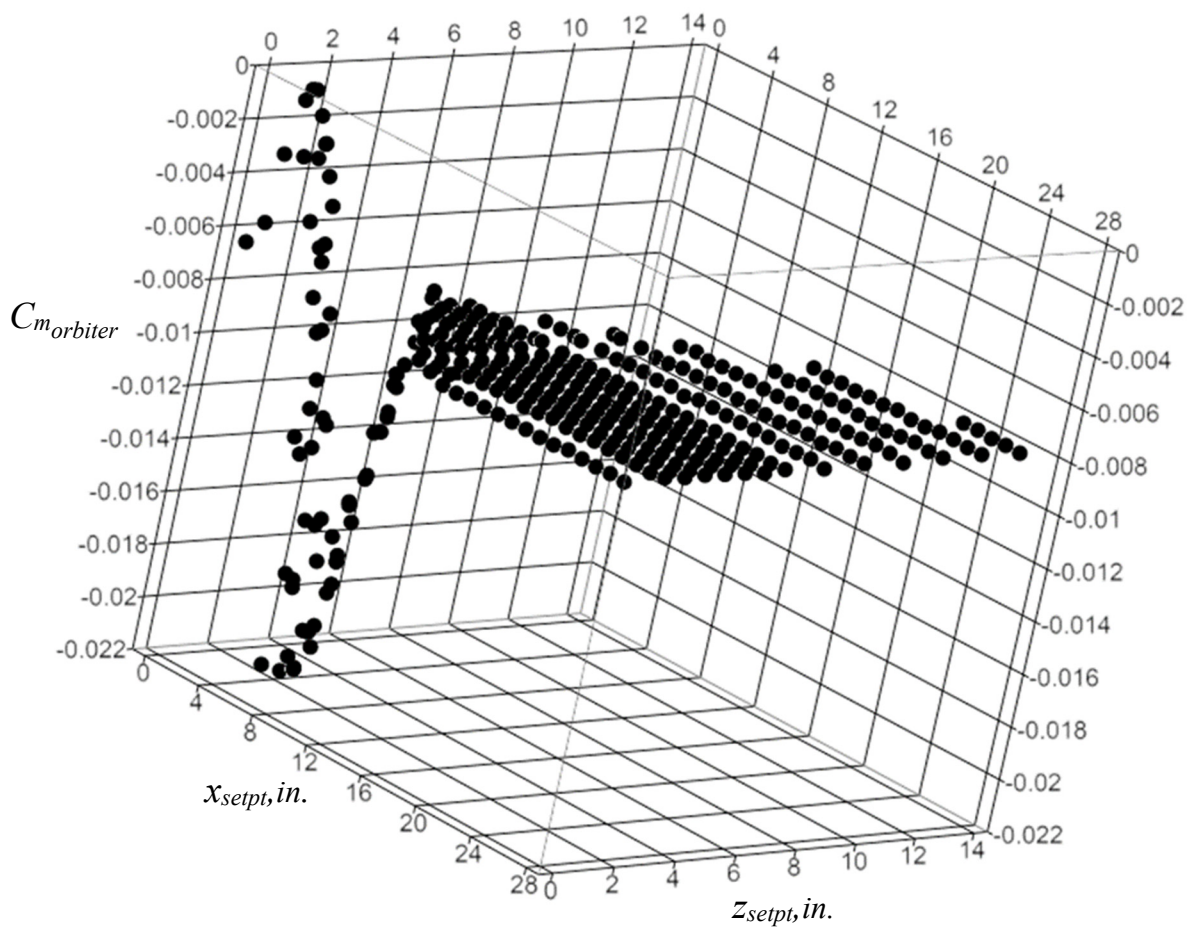




(d) Orbiter axial force coefficient (view from upper right quadrant of  $x_{setpt}$ - $z_{setpt}$  experimental space)

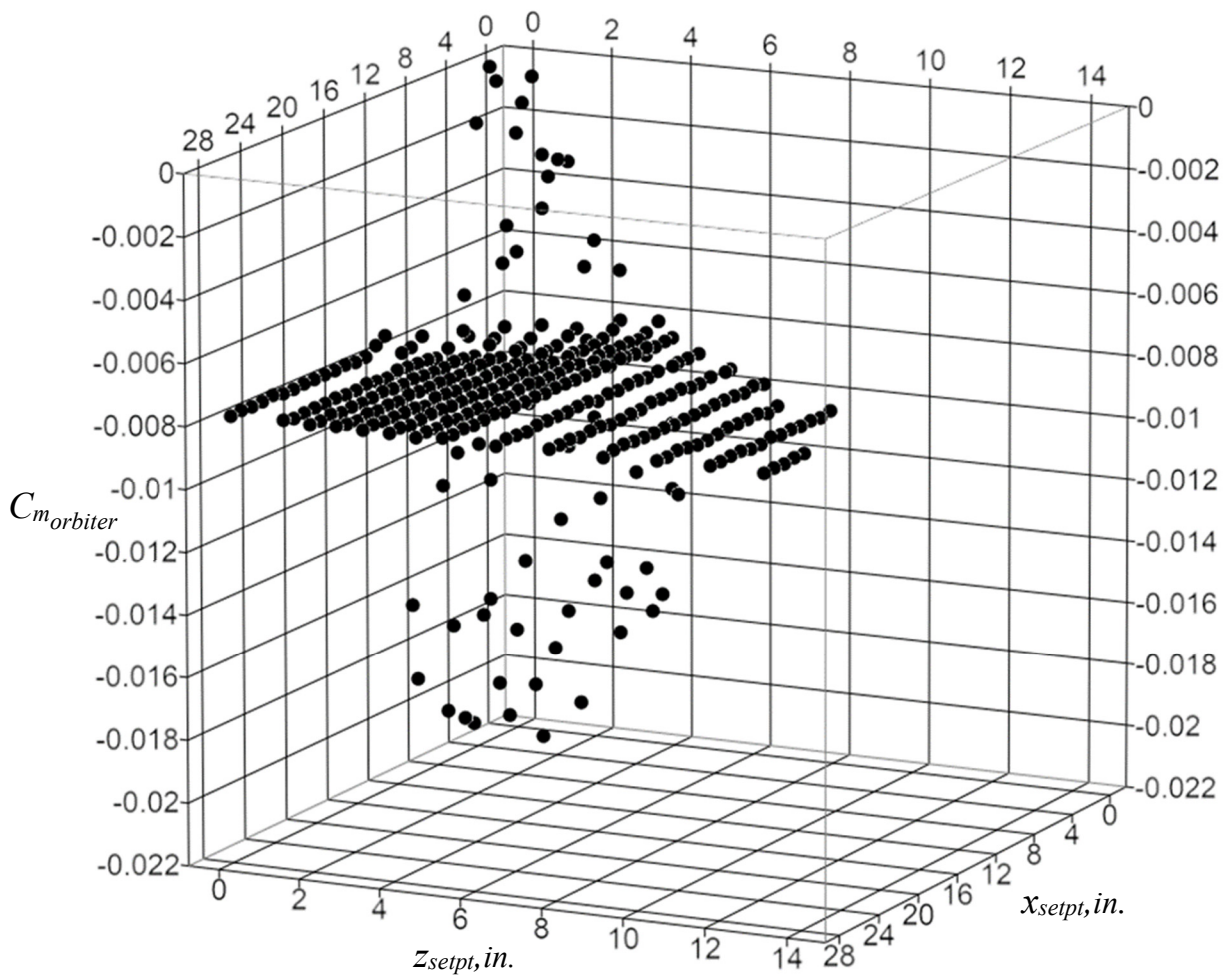
Figure 17. Continued.





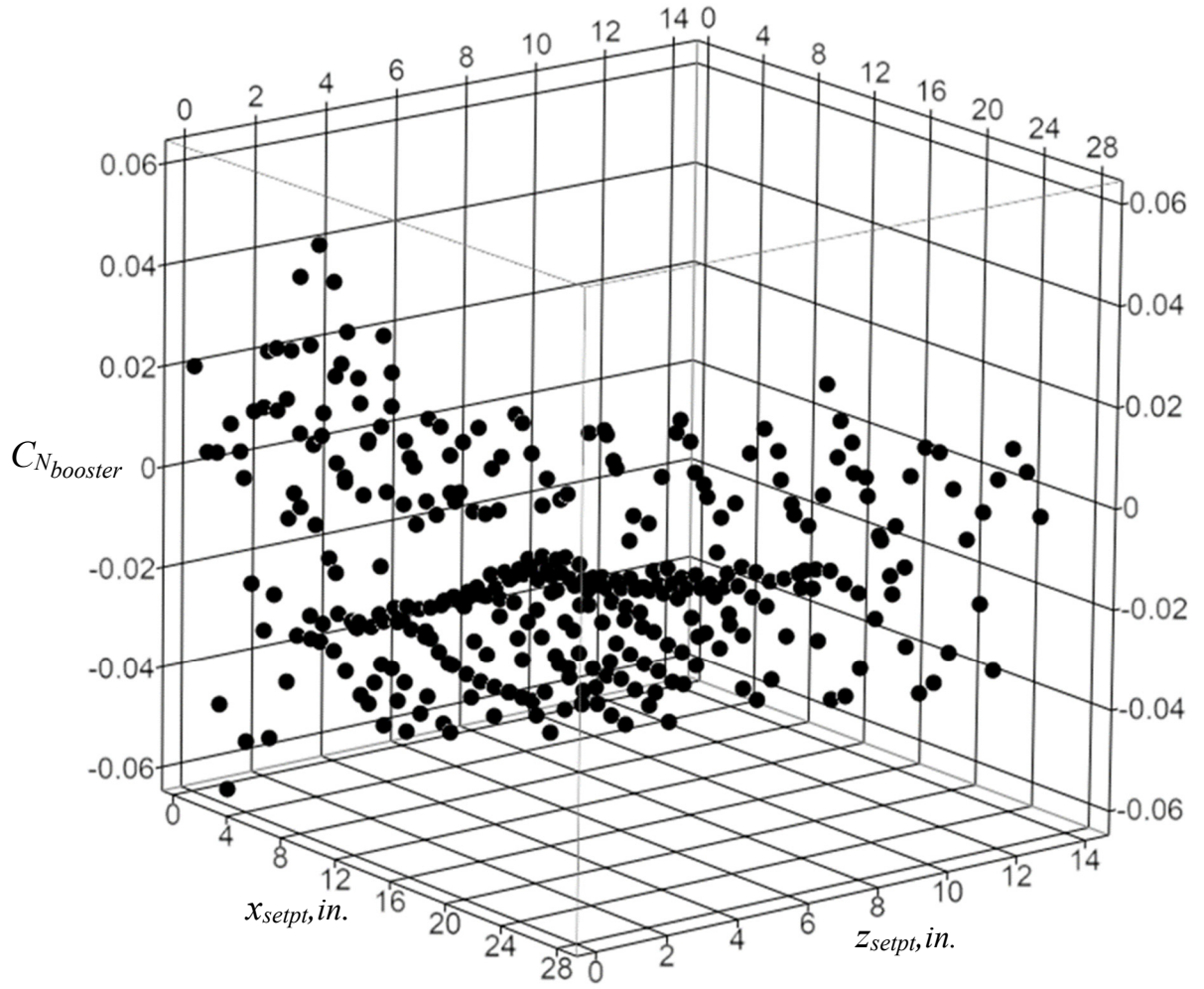
(e) Orbiter pitching moment coefficient (view from lower right quadrant of  $x_{setpt}$ - $z_{setpt}$  experimental space)

Figure 17. Continued.



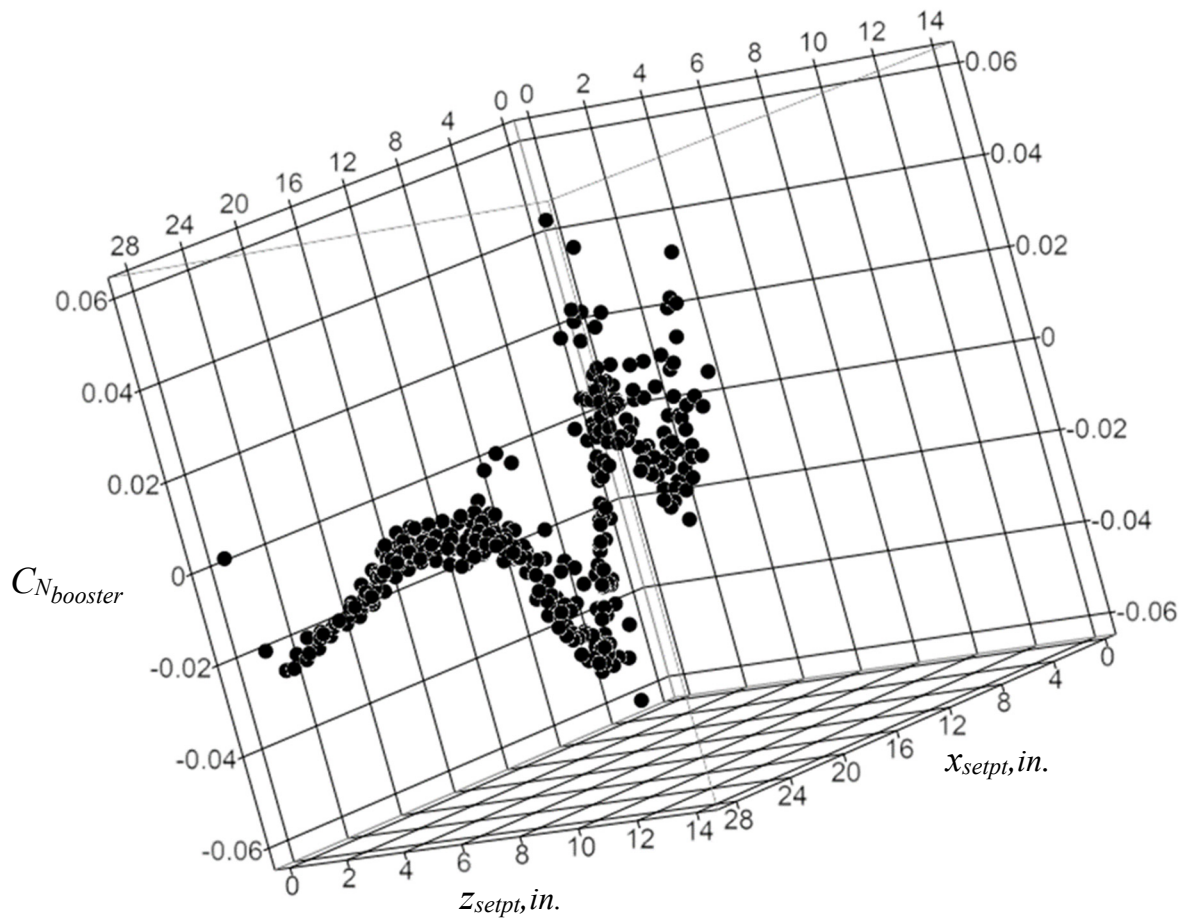
(f) Orbiter pitching moment coefficient (view from upper right quadrant of  $x_{setpt}$ - $z_{setpt}$  experimental space)

Figure 17. Concluded.



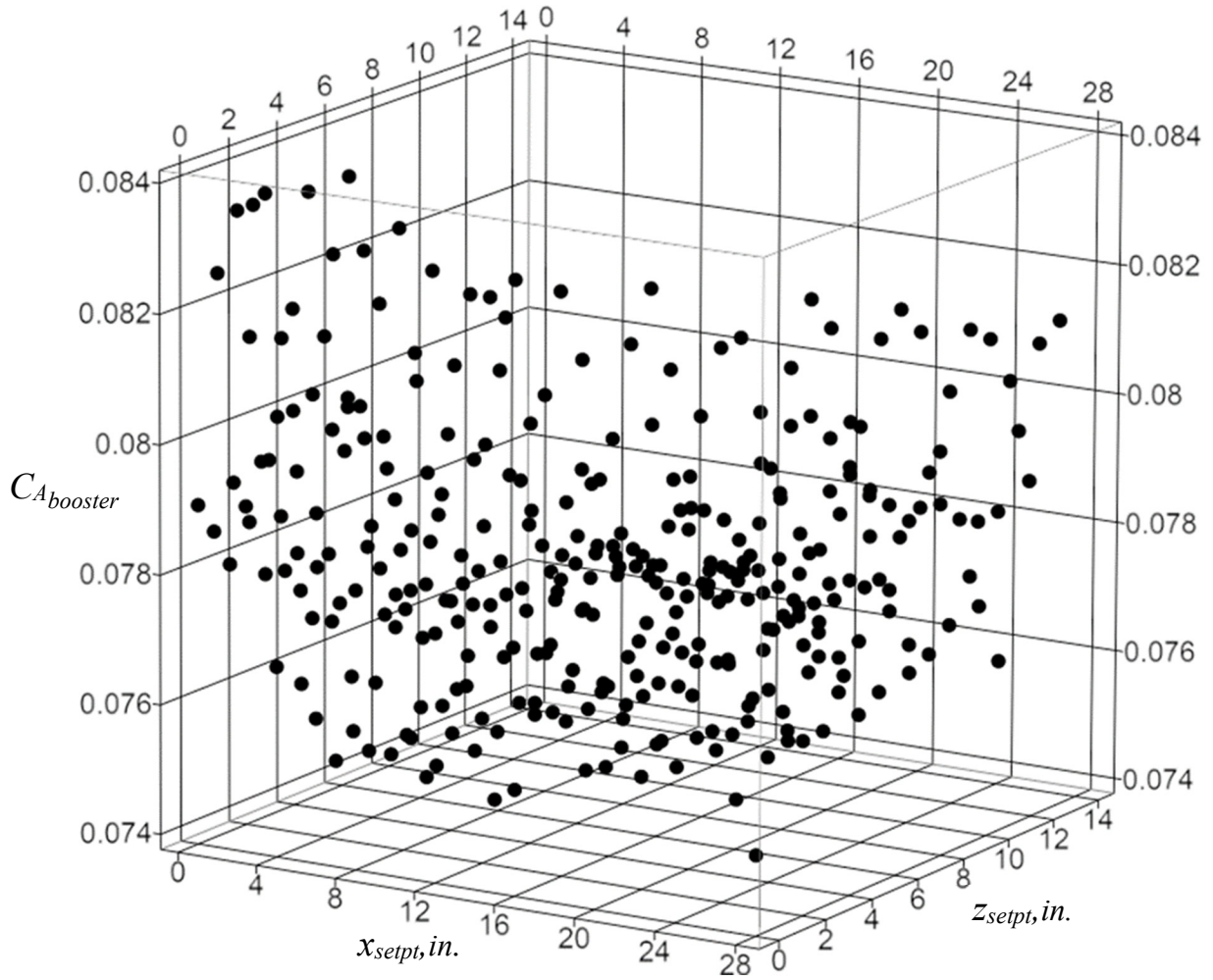
(a) Booster normal force coefficient (view from lower right quadrant of  $x_{setpt}$ - $z_{setpt}$  experimental space)

Figure 18. 3-D scatter plots of the booster proximity aerodynamic coefficients at  $Mach = 2.3$ ,  $\Delta\alpha = 0^\circ$ .



(b) Booster normal force coefficient (view from upper right quadrant of  $x_{setpt}$ - $z_{setpt}$  experimental space)

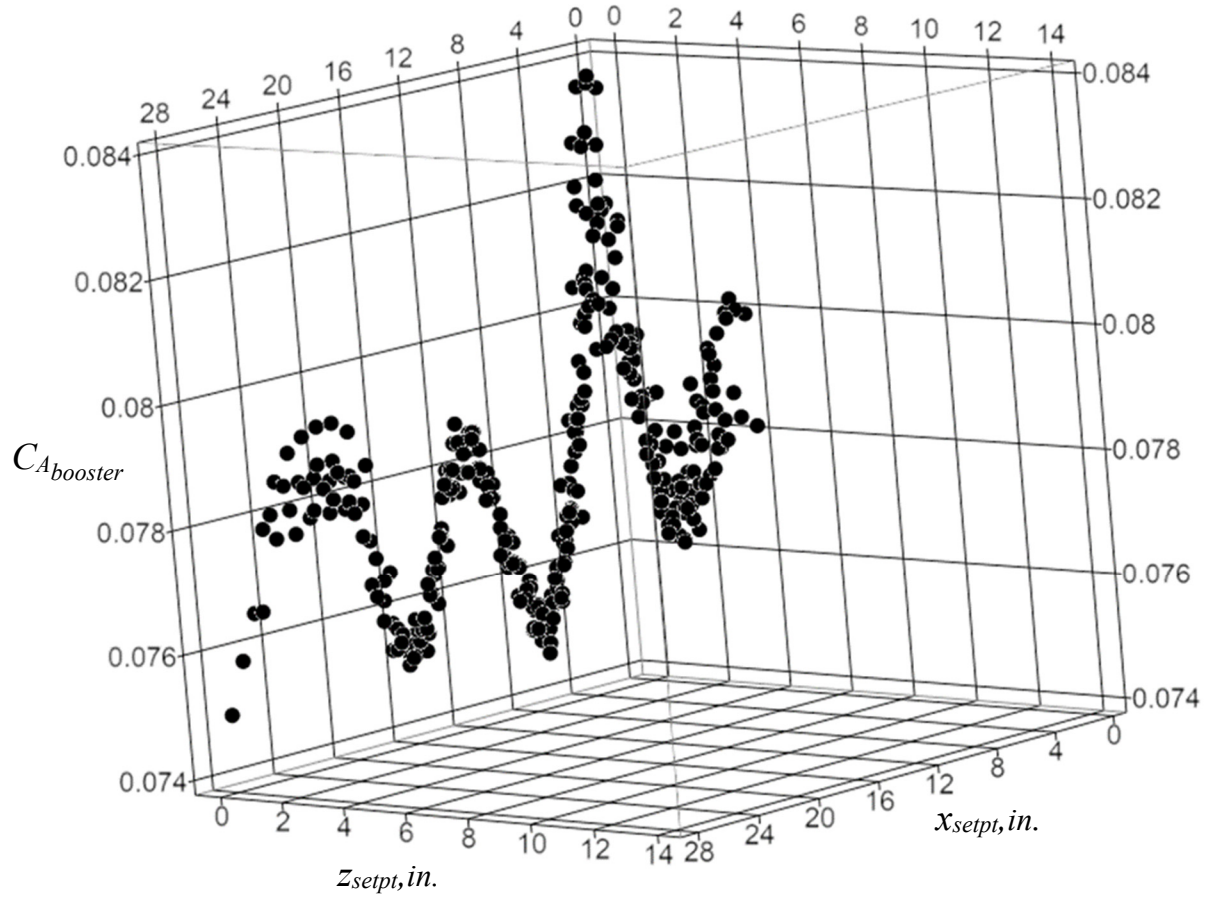
Figure 18. Continued.



(c) Booster axial force coefficient (view from lower right quadrant of  $x_{setpt}$ - $z_{setpt}$  experimental space)

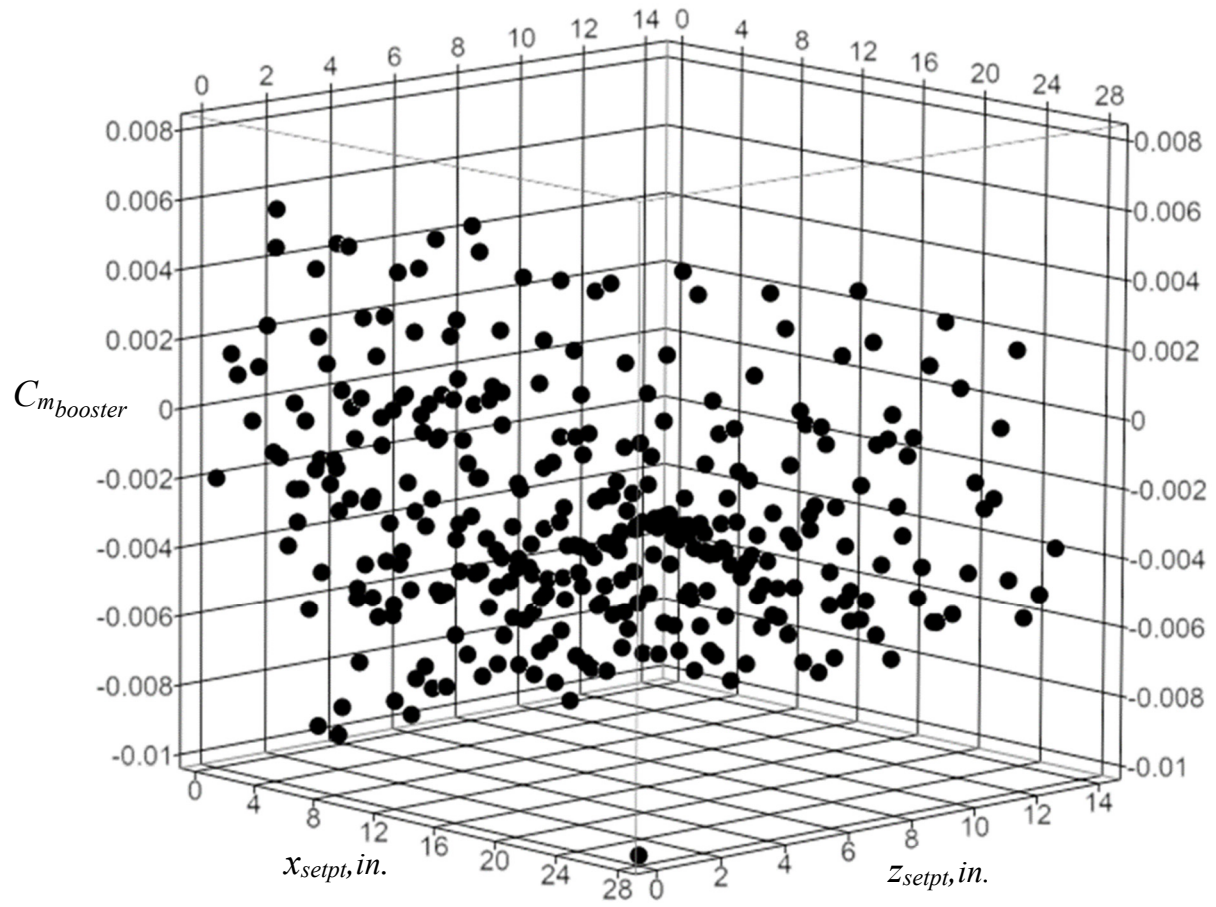
Figure 18. Continued.





(d) Booster axial force coefficient (view from upper right quadrant of  $x_{setpt}$ - $z_{setpt}$  experimental space)

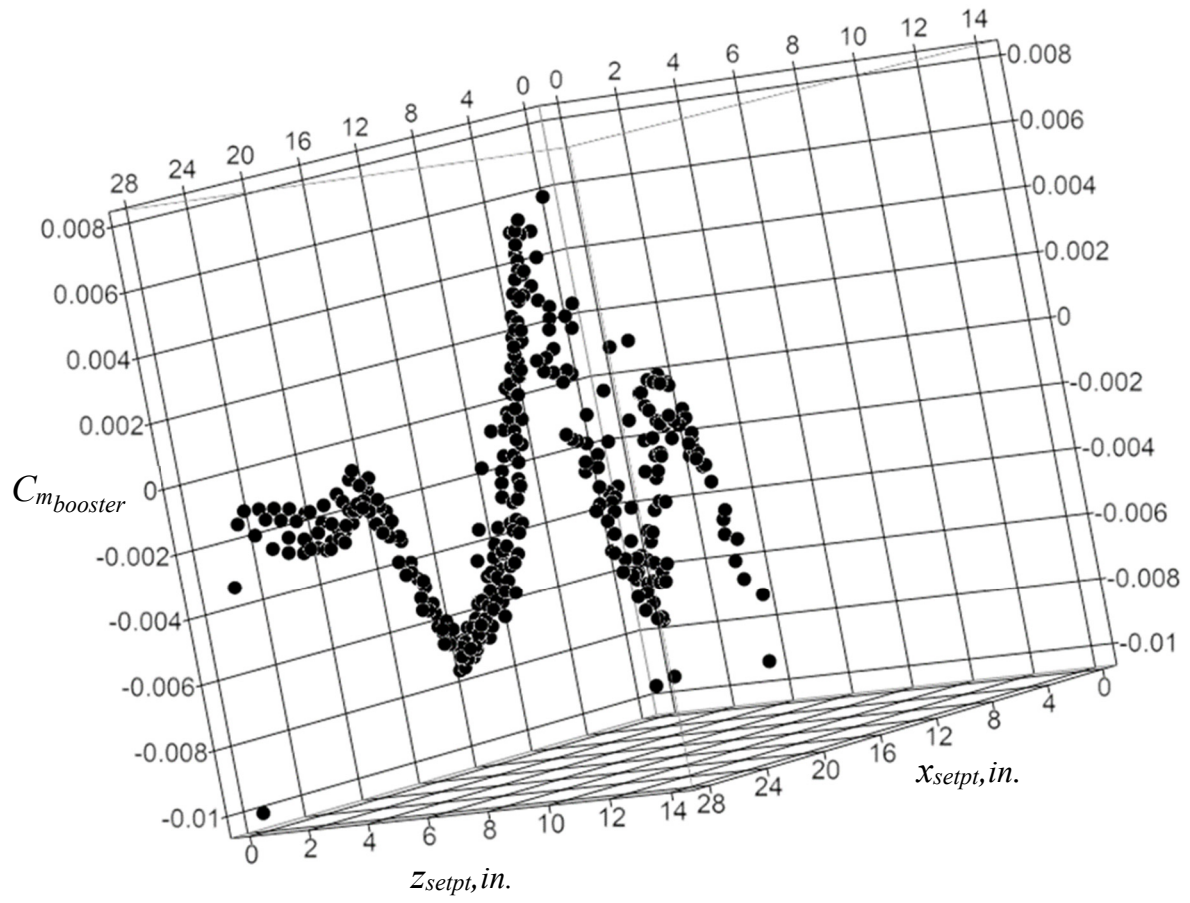
Figure 18. Continued.



(e) Booster pitching moment coefficient (view from lower right quadrant of  $x_{setpt}$ - $z_{setpt}$  experimental space)

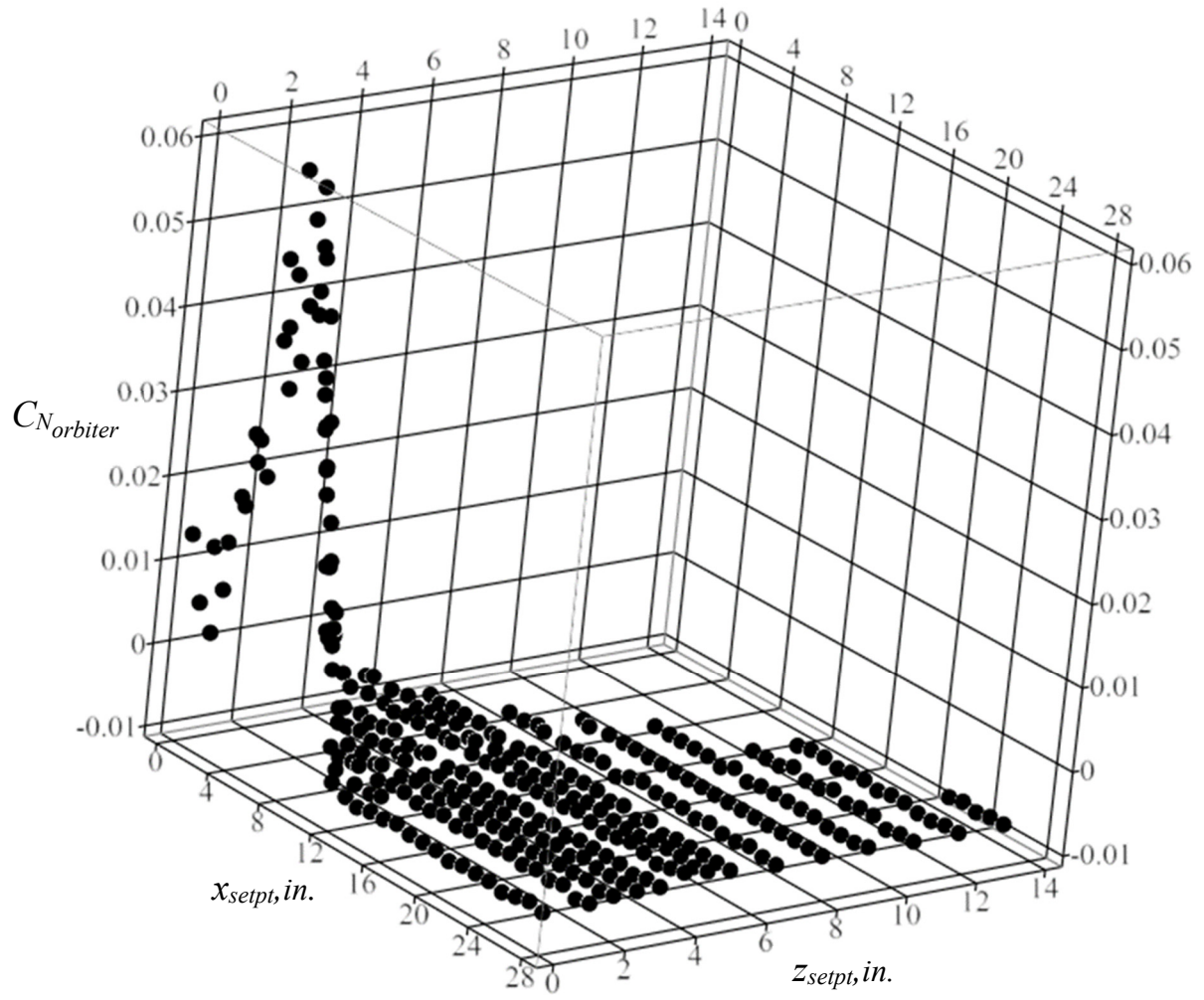
Figure 18. Continued.





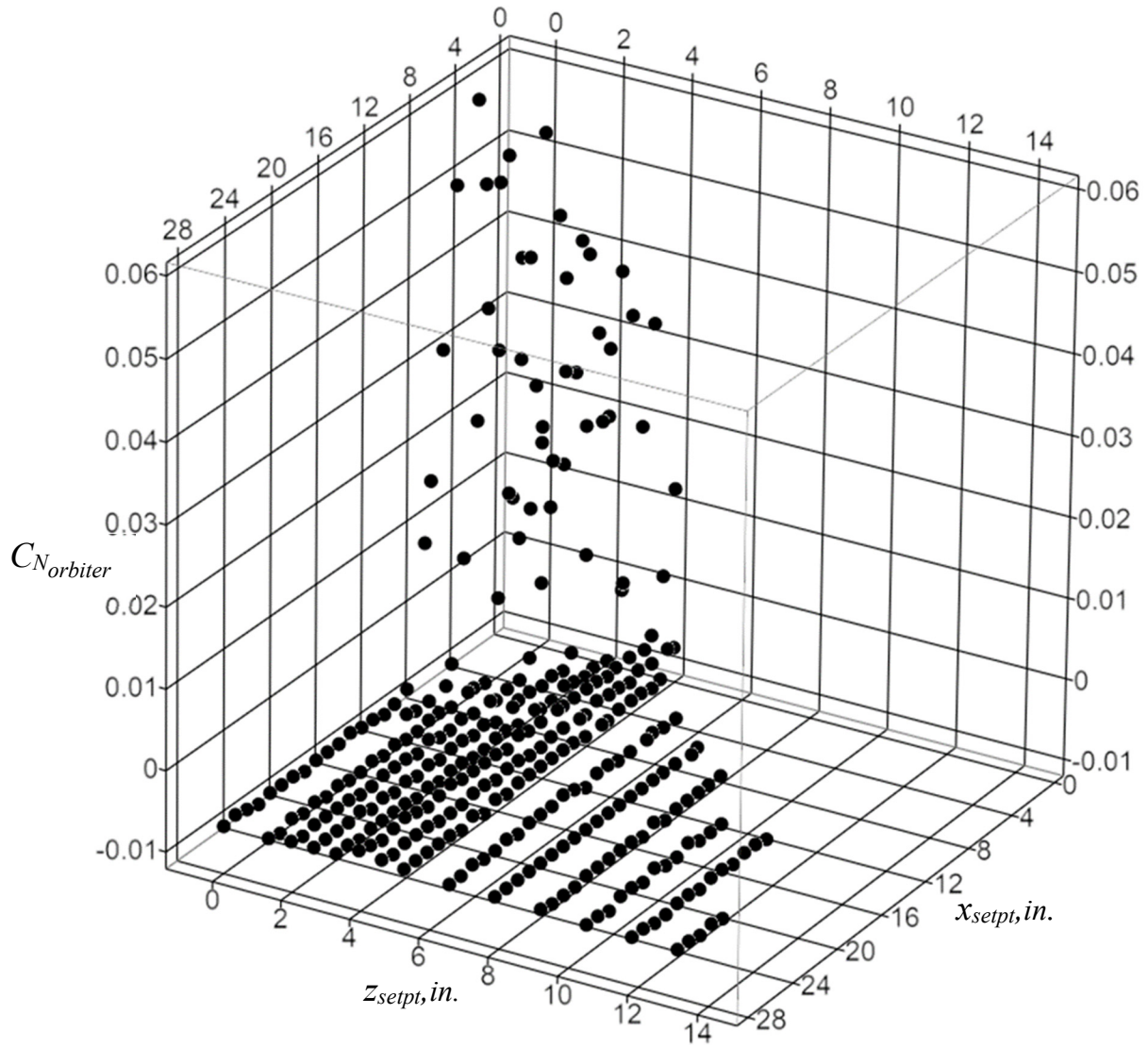
(f) Booster pitching moment coefficient (view from upper right quadrant of  $x_{setpt}$ - $z_{setpt}$  experimental space)

Figure 18. Concluded.



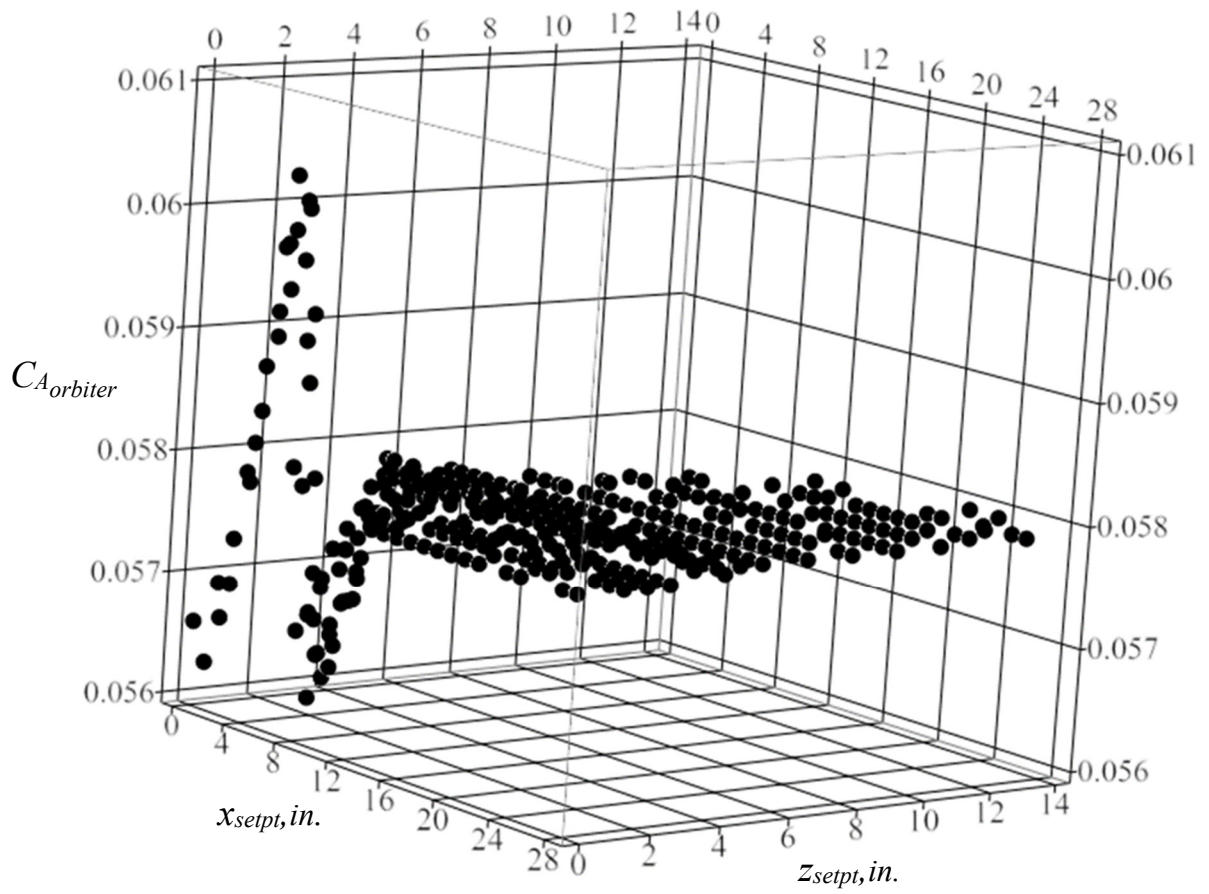
(a) Orbiter normal force coefficient (view from lower right quadrant of  $x_{setpt}$ - $z_{setpt}$  experimental space)

Figure 19. 3-D scatter plots of the orbiter proximity aerodynamic coefficients at  $Mach = 3.0$ ,  $\Delta\alpha = 0^\circ$ .



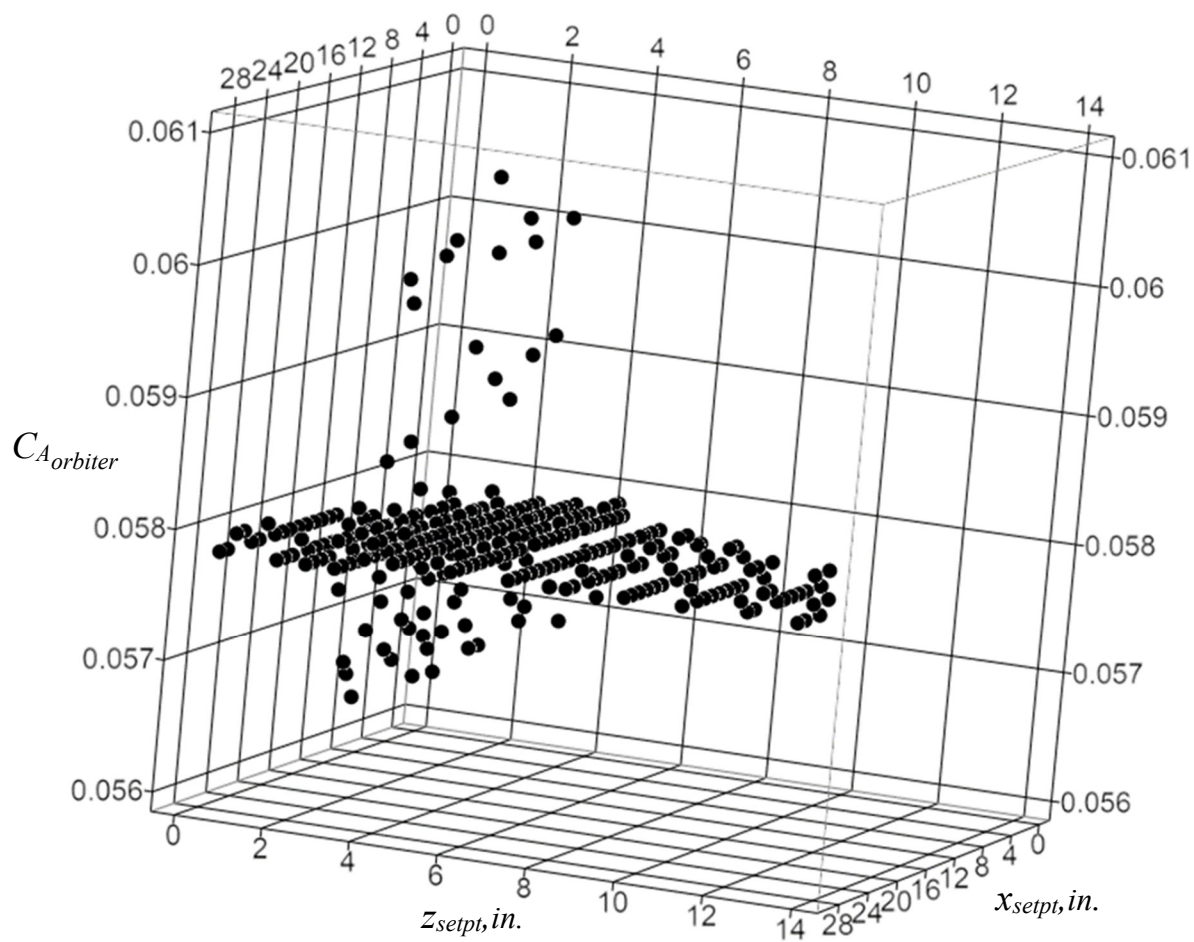
(b) Orbiter normal force coefficient (view from upper right quadrant of  $x_{setpt}$ - $z_{setpt}$  experimental space)

Figure 19. Continued.



(c) Orbiter axial force coefficient (view from lower right quadrant of  $x_{setpt}$ - $z_{setpt}$  experimental space)

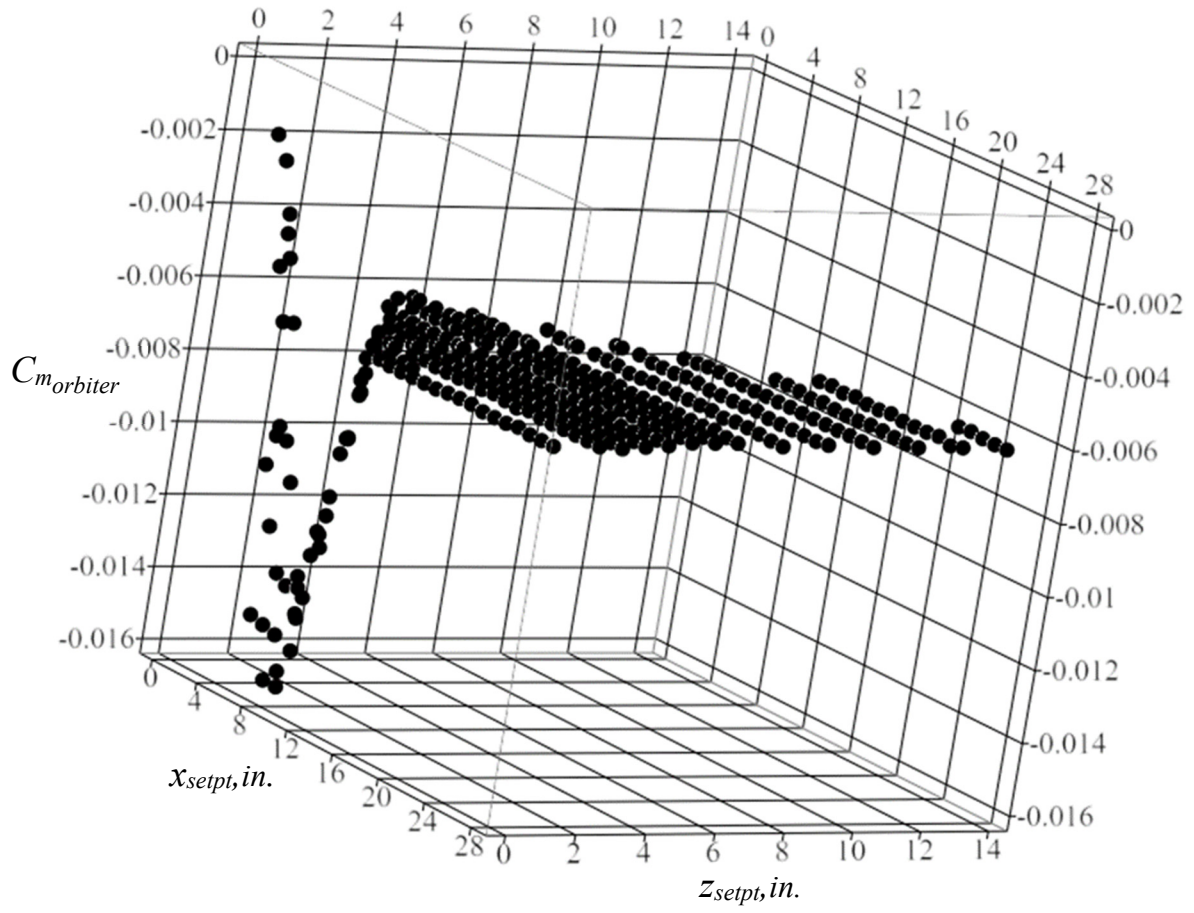
Figure 19. Continued.



(d) Orbiter axial force coefficient (view from upper right quadrant of  $x_{setpt}$ - $z_{setpt}$  experimental space)

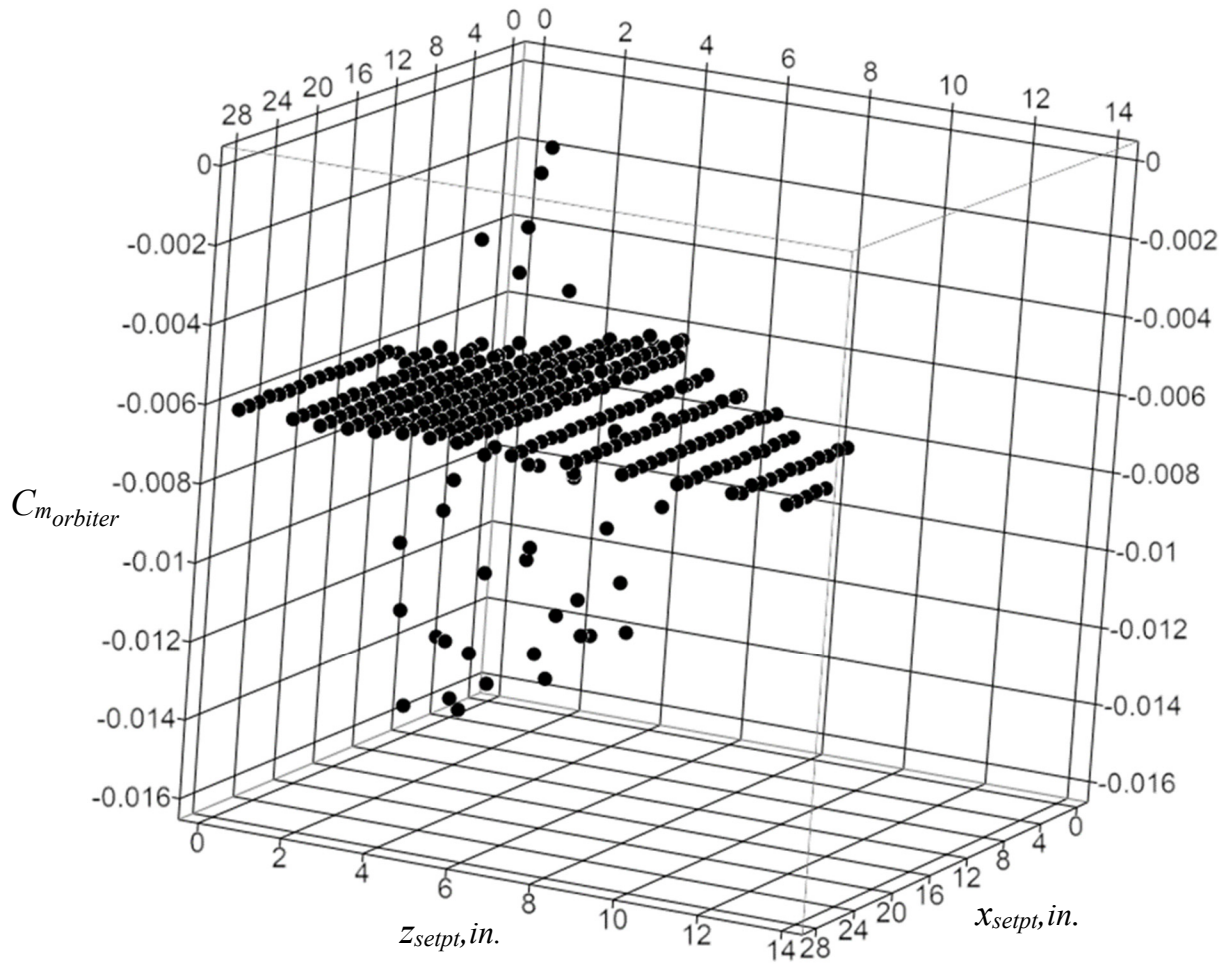
Figure 19. Continued.





(e) Orbiter pitching moment coefficient (view from lower right quadrant of  $x_{setpt}$ - $z_{setpt}$  experimental space)

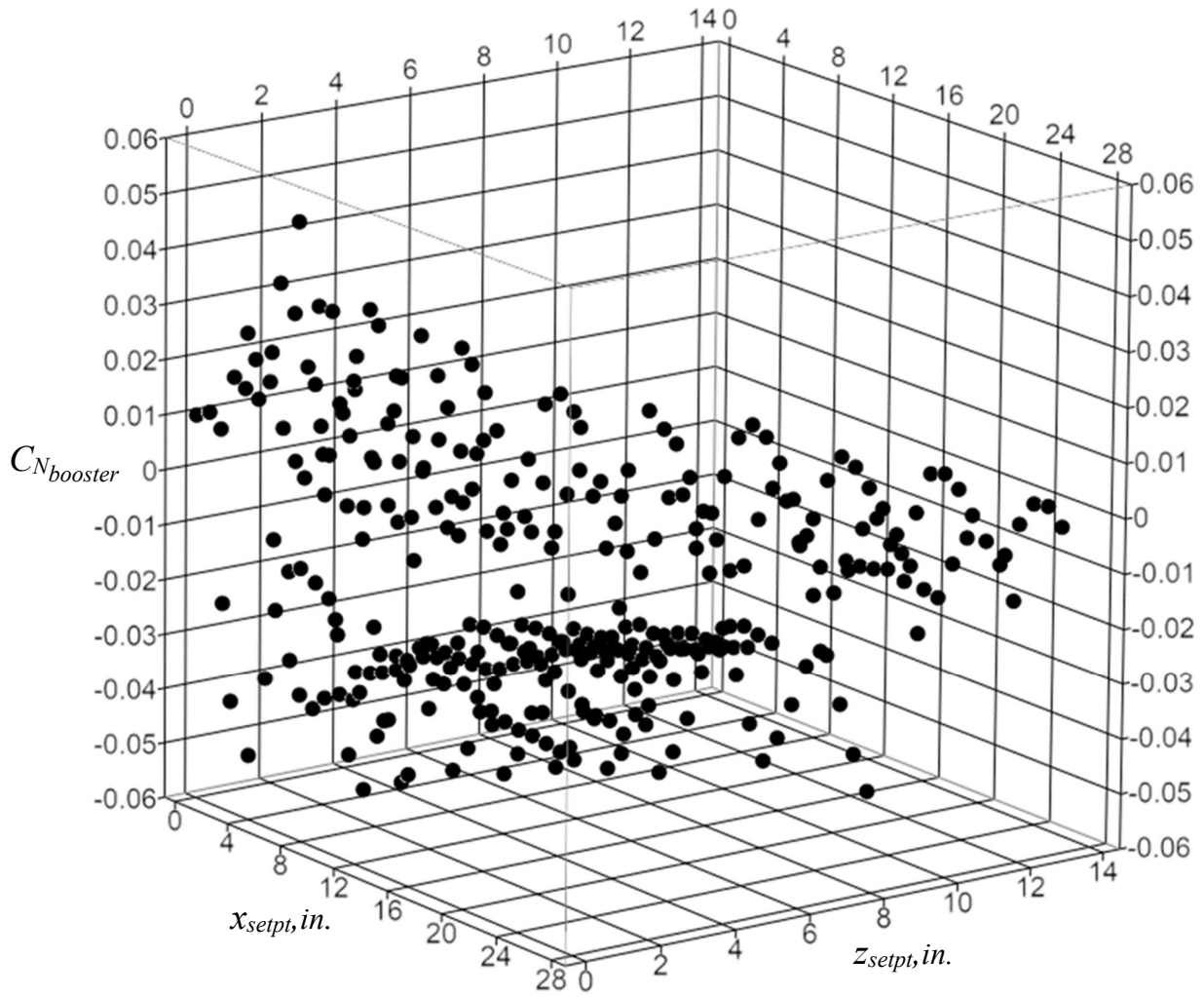
Figure 19. Continued.



(f) Orbiter pitching moment coefficient (view from upper right quadrant of  $x_{setpt}$ - $z_{setpt}$  experimental space)

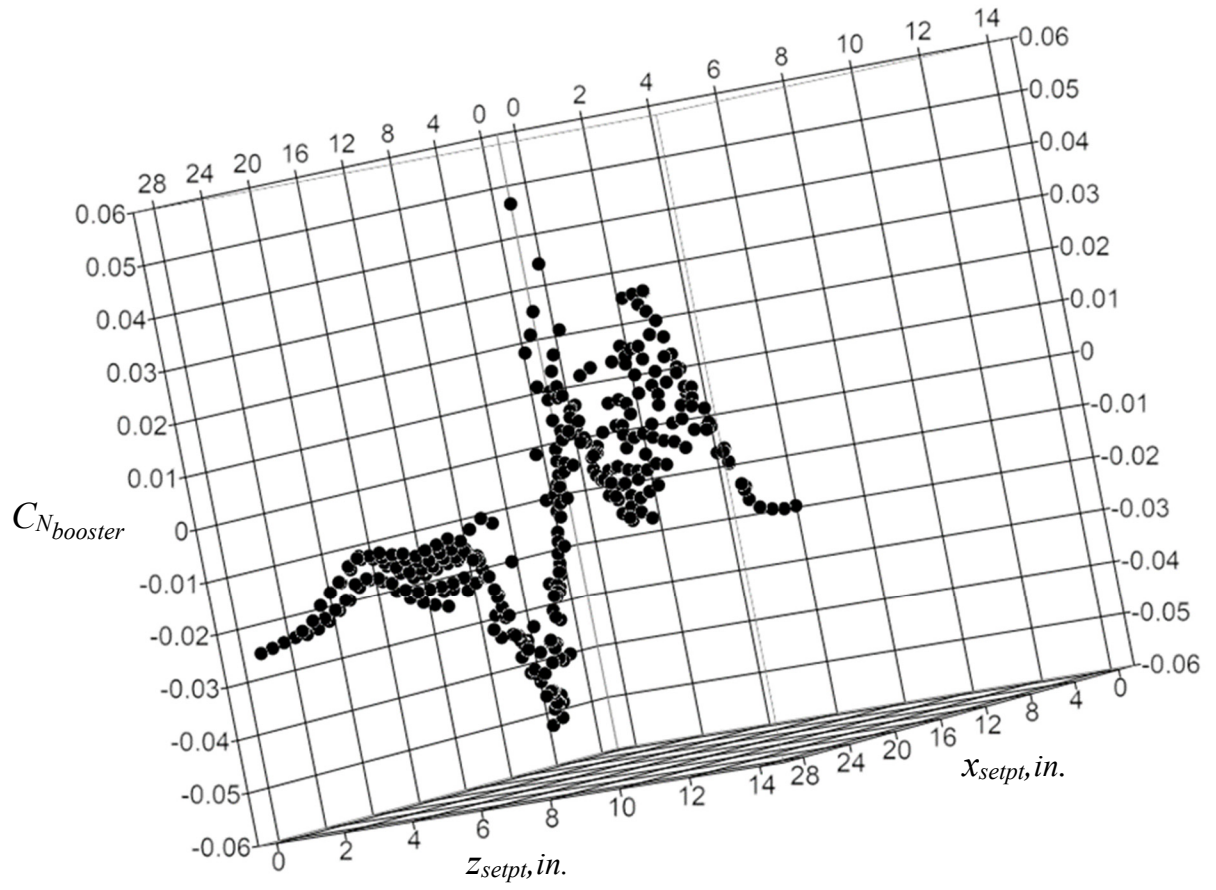
Figure 19. Concluded.





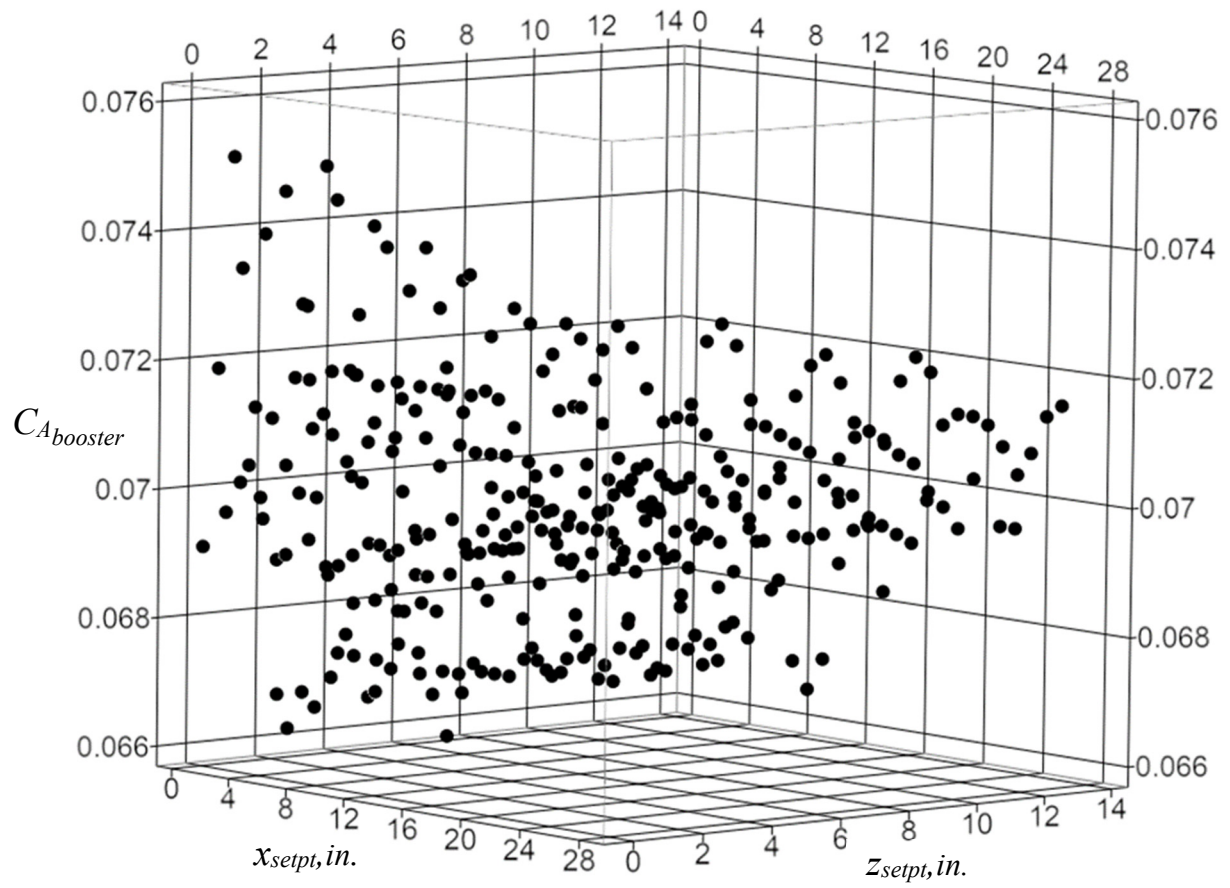
(a) Booster normal force coefficient (view from lower right quadrant of  $x_{setpt}$ - $z_{setpt}$  experimental space)

Figure 20. 3-D scatterplots of the booster proximity aerodynamic coefficients at Mach = 3.0,  $\Delta\alpha = 0^\circ$ .



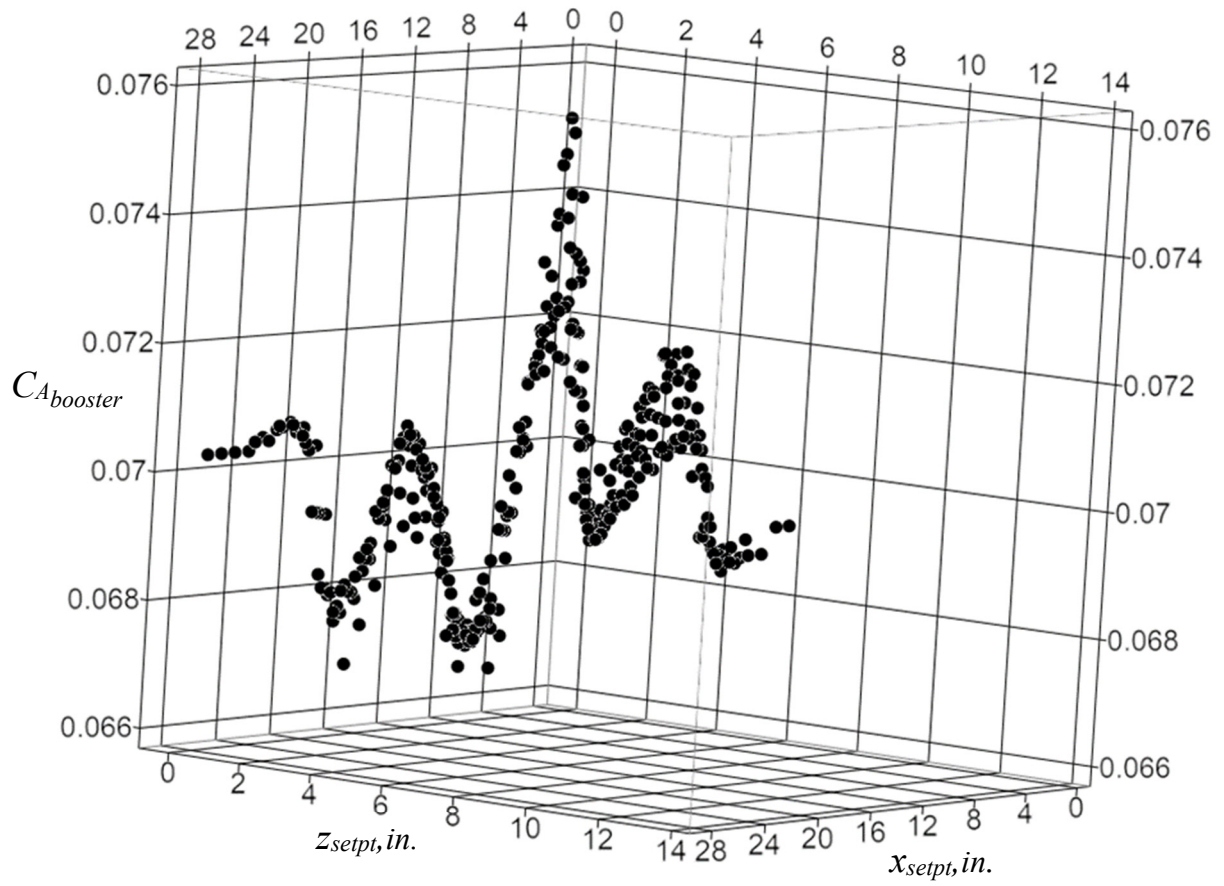
(b) Booster normal force coefficient (view from upper right quadrant of  $x_{setpt}$ - $z_{setpt}$  experimental space)

Figure 20. Continued.



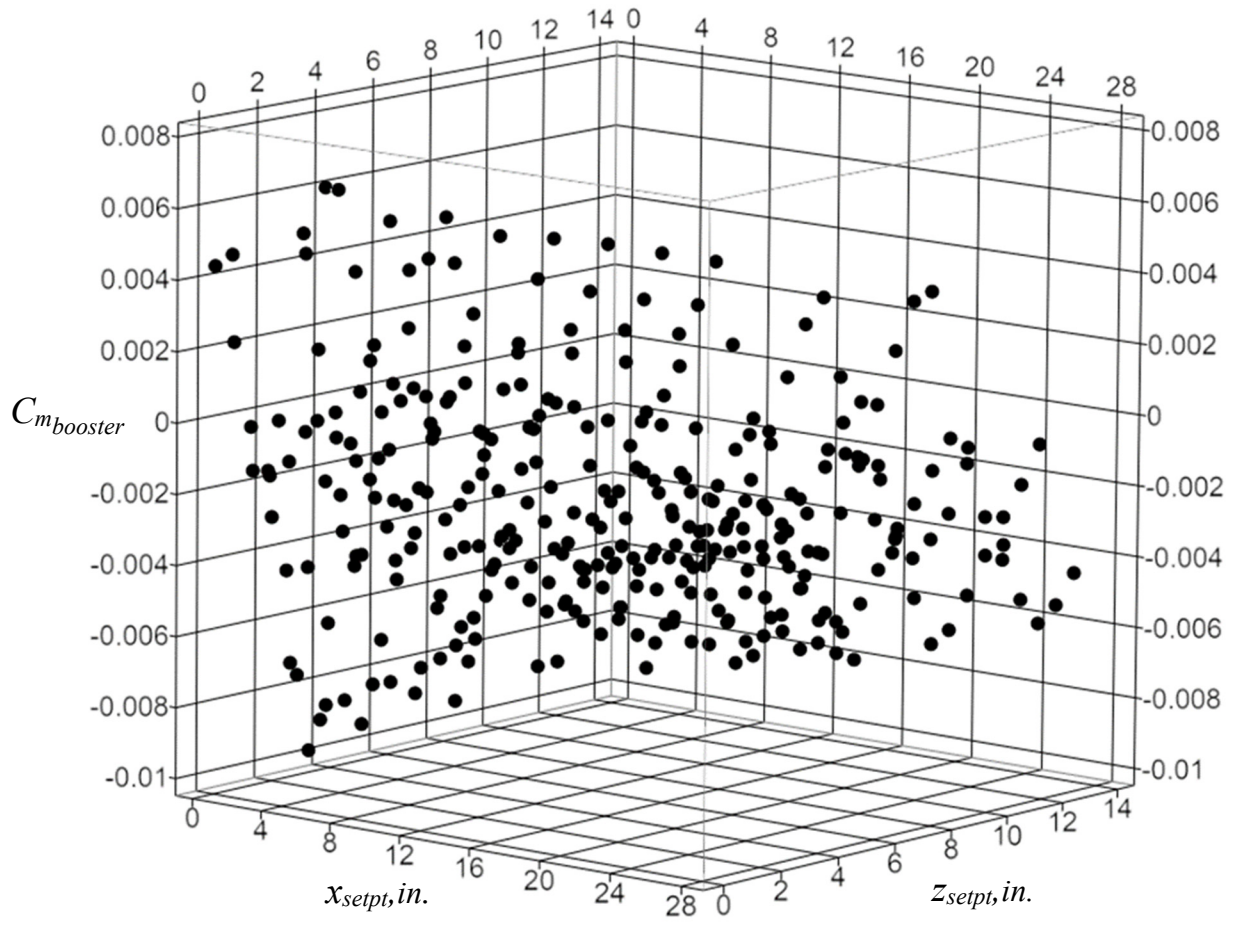
(c) Booster axial force coefficient (view from lower right quadrant of  $x_{setpt}$ - $z_{setpt}$  experimental space)

Figure 20. Continued.



(d) Booster axial force coefficient (view from upper right quadrant of  $x_{setpt}$ - $z_{setpt}$  experimental space)

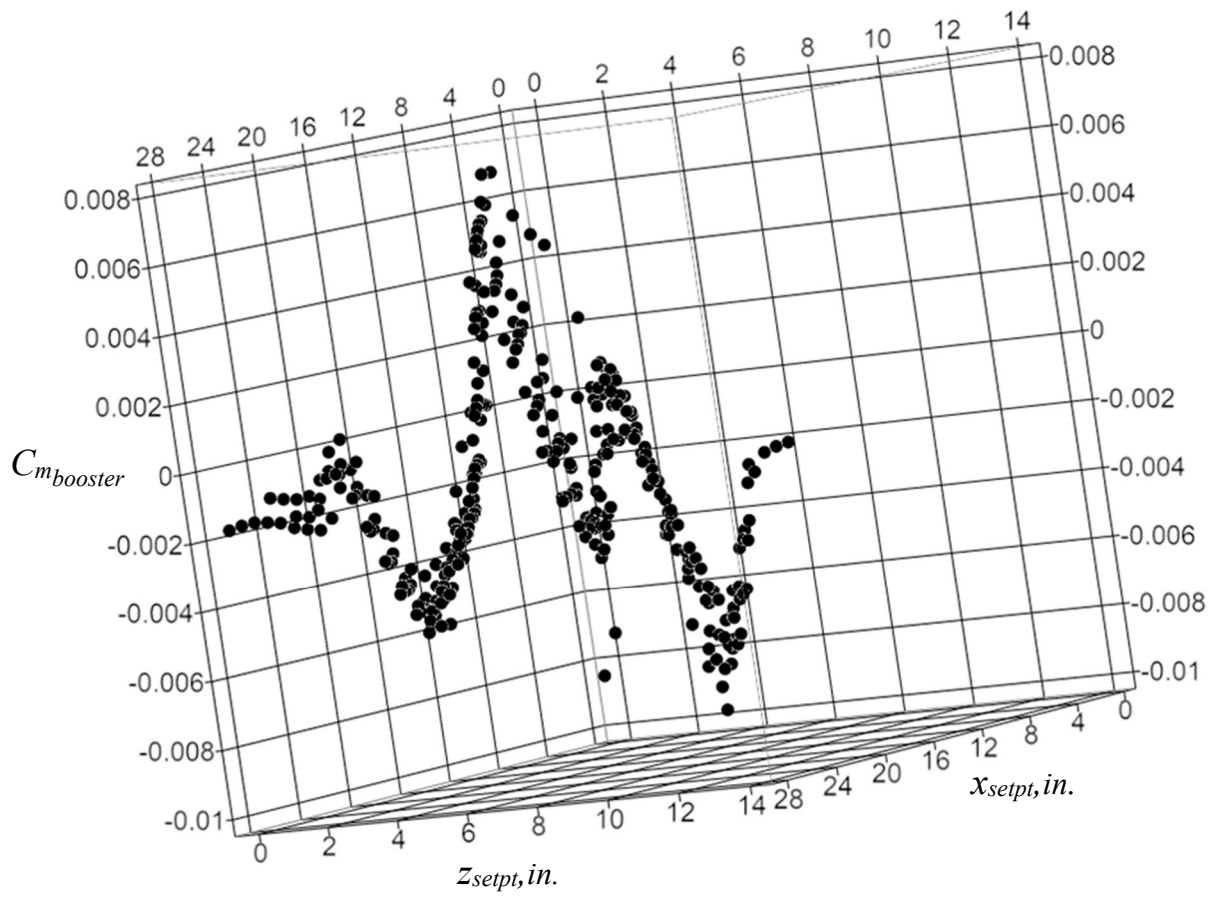
Figure 20. Continued.



(e) Booster pitching moment coefficient (view from lower right quadrant of  $x_{setpt}$ - $z_{setpt}$  experimental space)

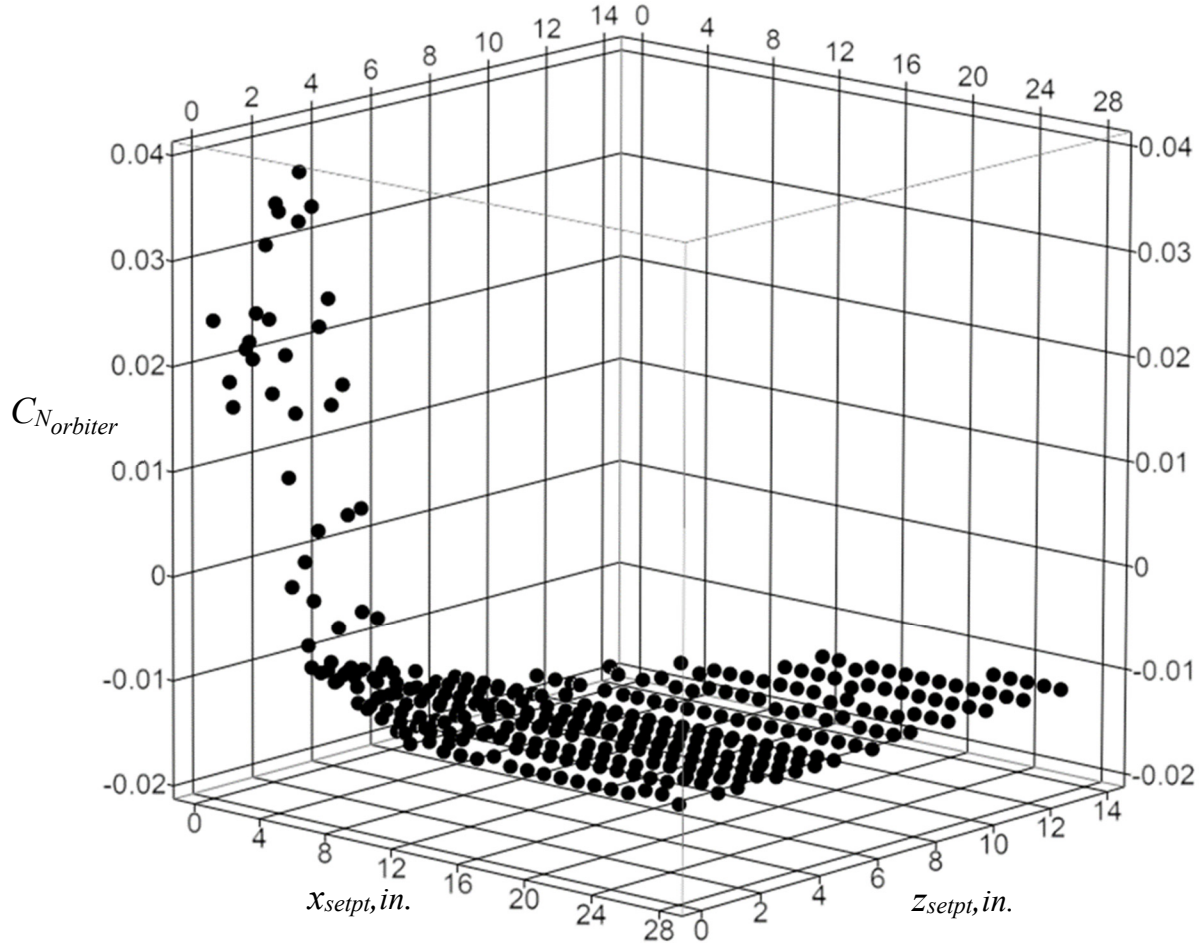
Figure 20. Continued.





(f) Booster pitching moment coefficient (view from upper right quadrant of  $x_{setpt}$ - $z_{setpt}$  experimental space)

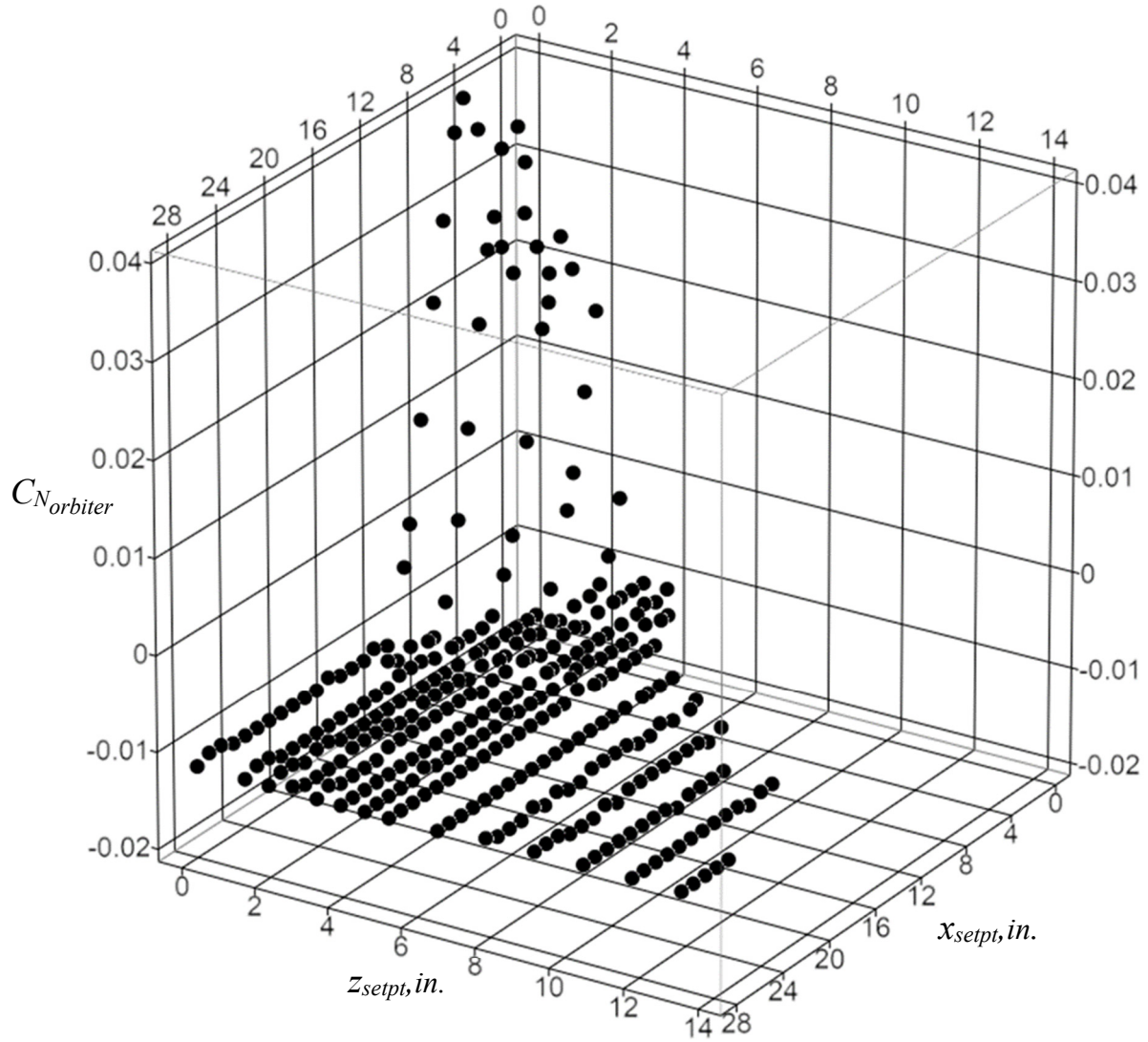
Figure 20. Concluded.



(a) Orbiter normal force coefficient (view from lower right quadrant of  $x_{setpt}$ - $z_{setpt}$  experimental space)

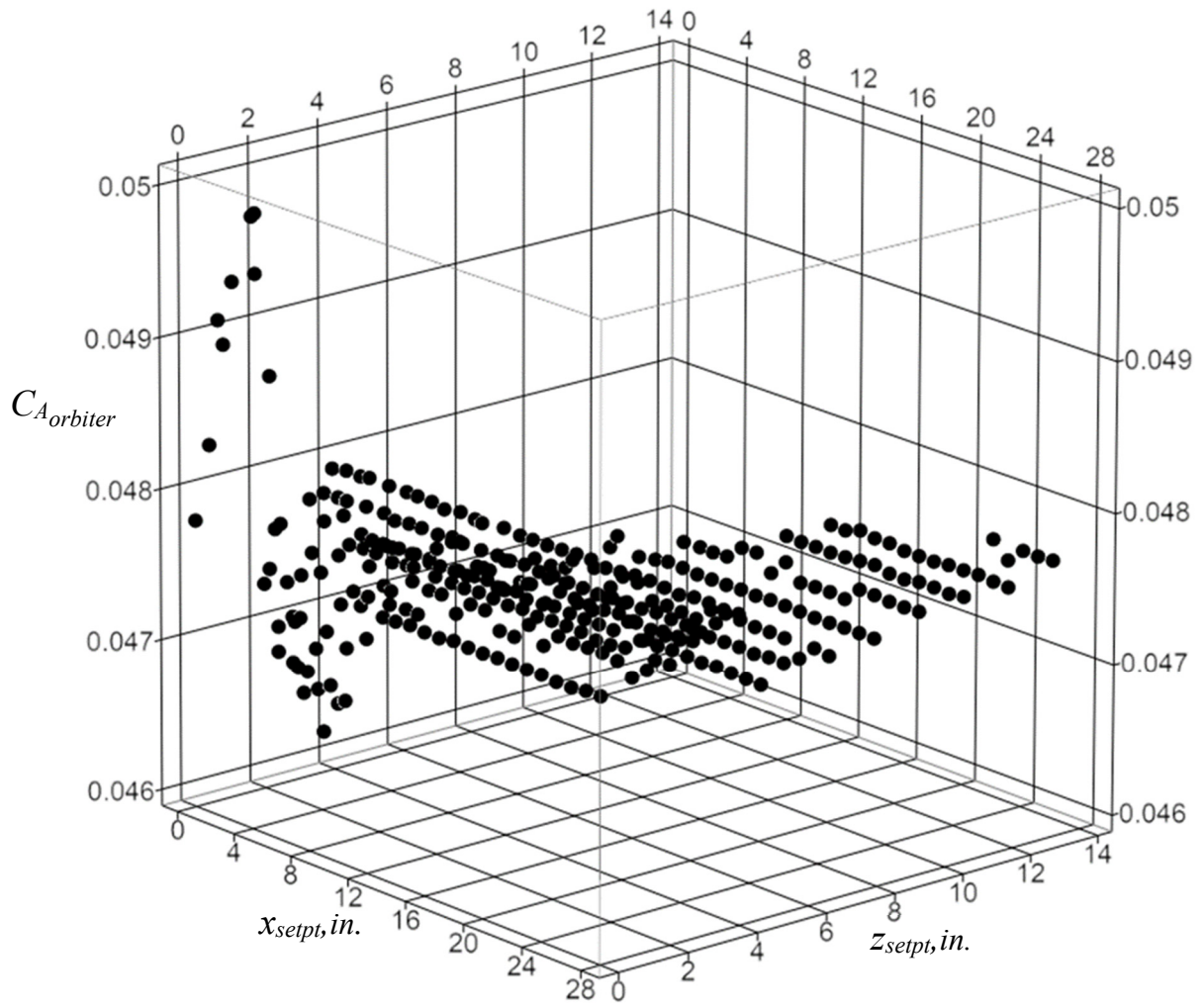
Figure 21. 3-D scatter plots of the orbiter proximity aerodynamic coefficients at  $Mach = 4.5$ ,  $\Delta\alpha = 0^\circ$ .





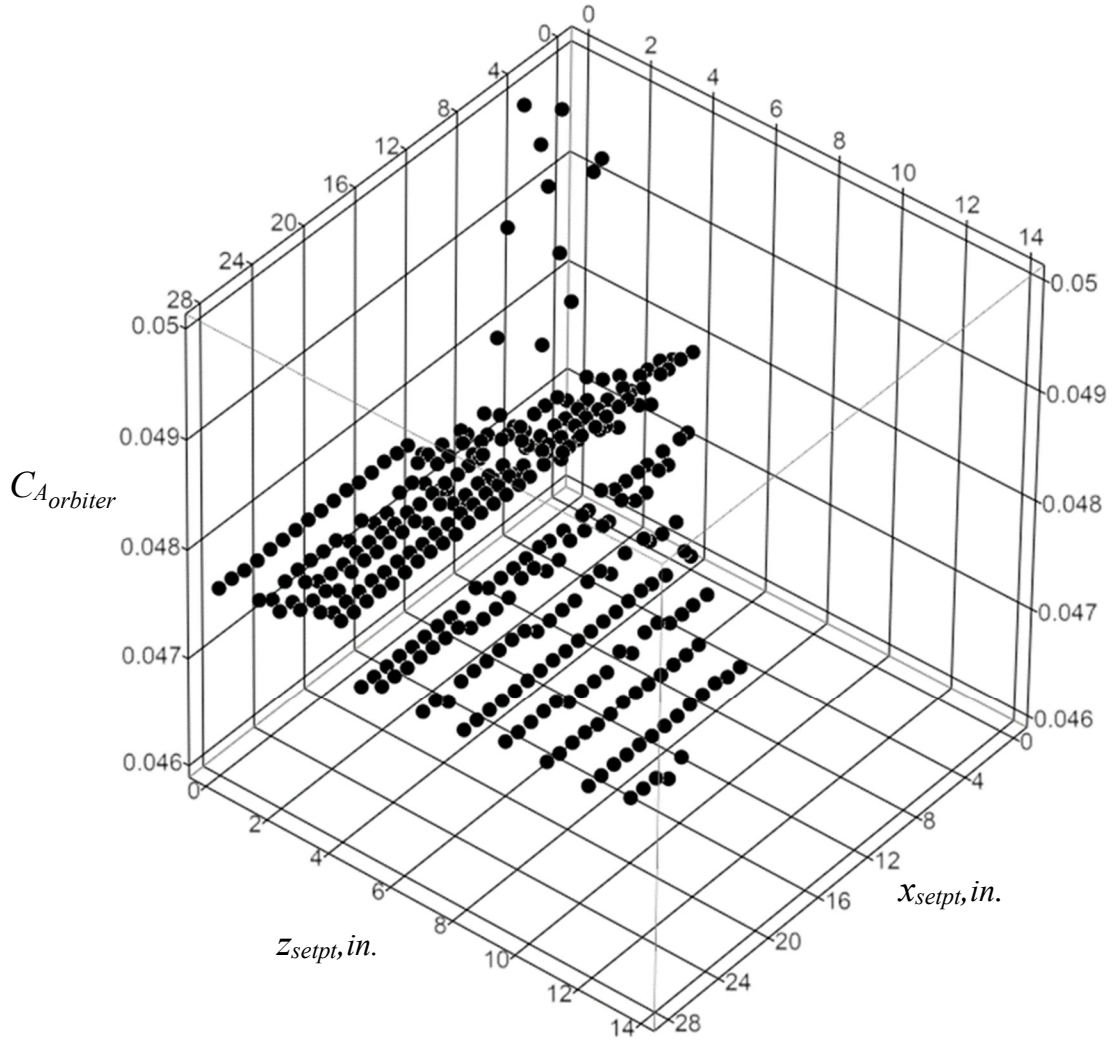
(b) Orbiter normal force coefficient (view from upper right quadrant of  $x_{setpt}$ - $z_{setpt}$  experimental space)

Figure 21. Continued.



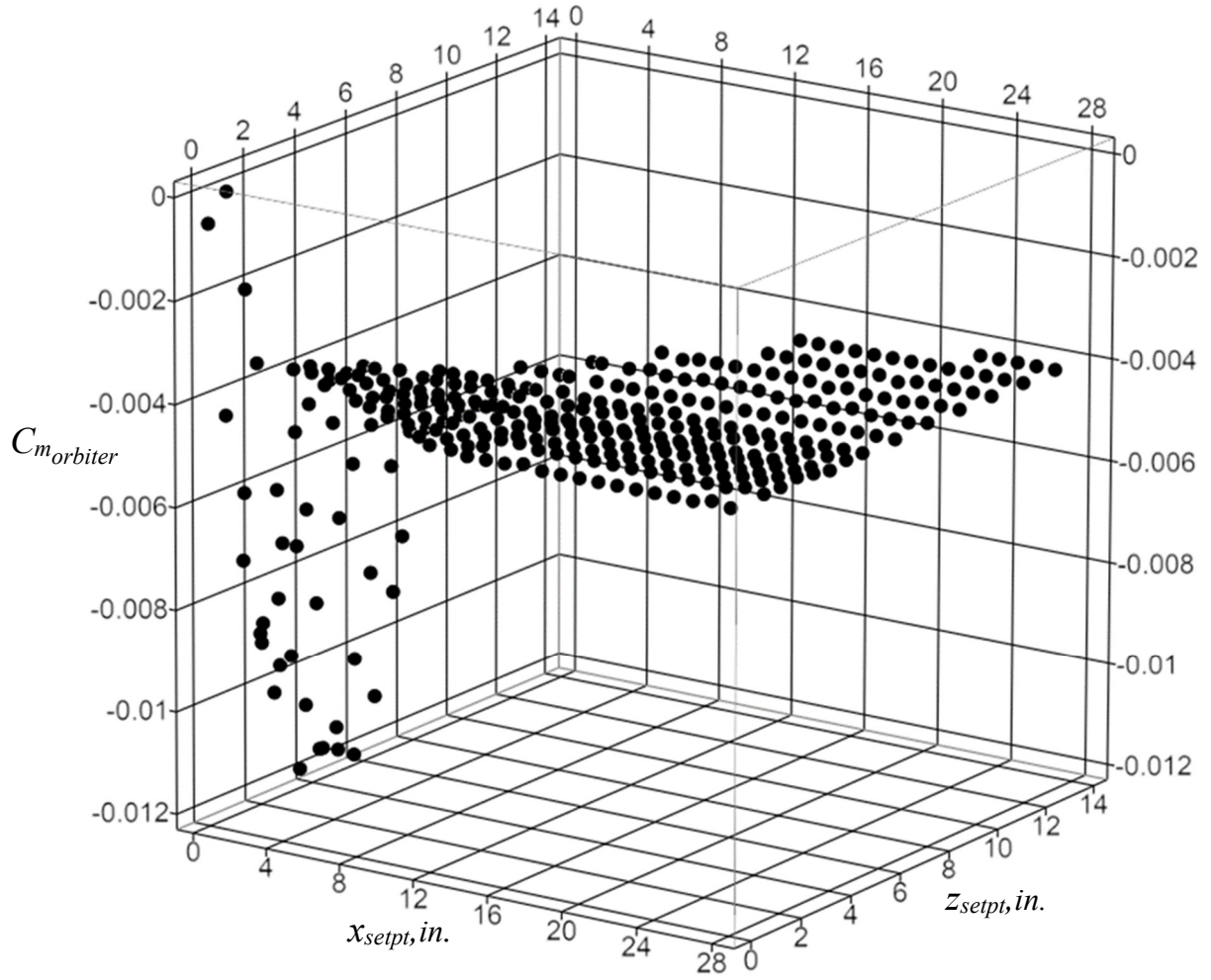
(c) Orbiter axial force coefficient (view from lower right quadrant of  $x_{setpt}$ - $z_{setpt}$  experimental space)

Figure 21. Continued.



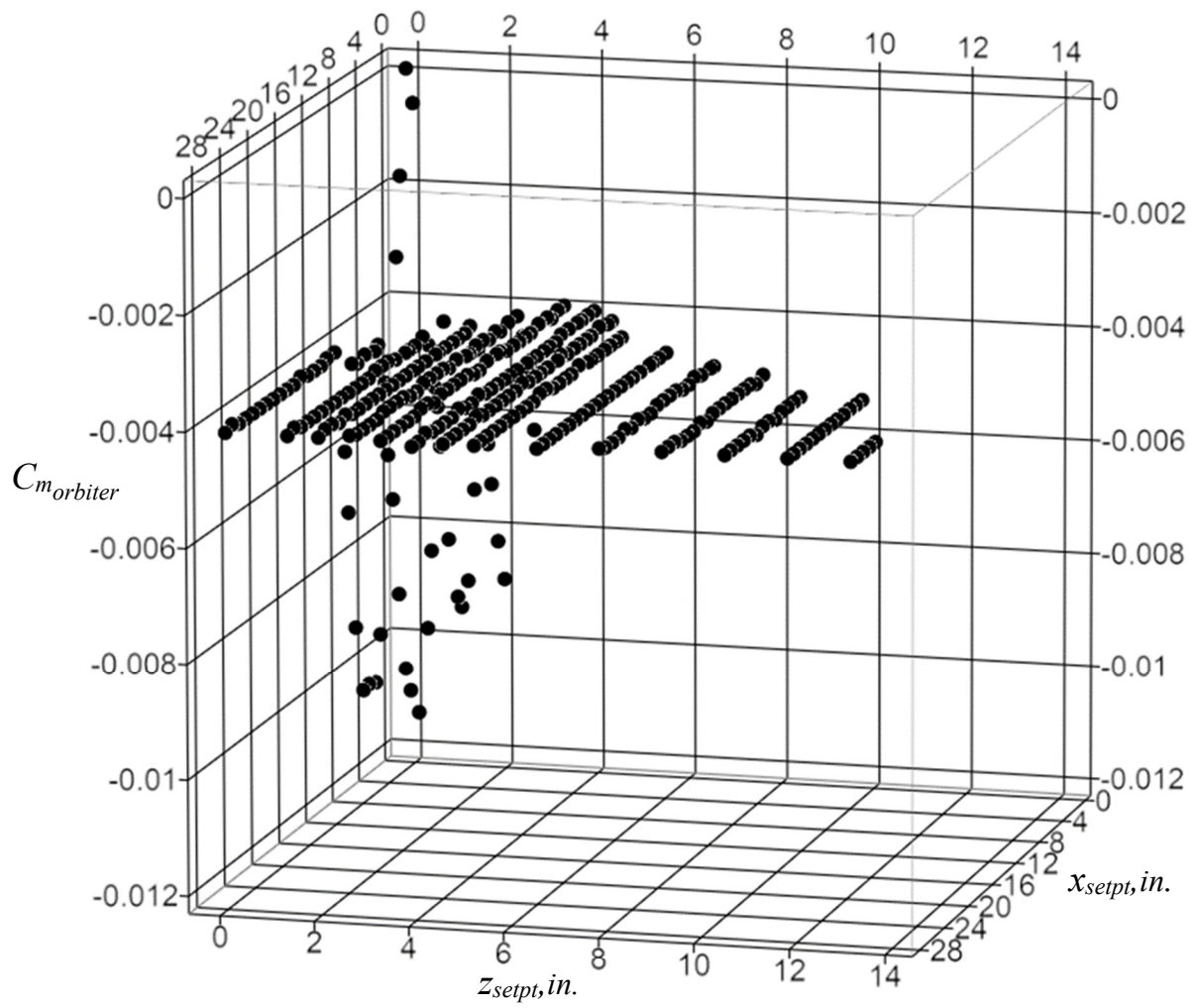
(d) Orbiter axial force coefficient (view from upper right quadrant of  $x_{setpt}$ - $z_{setpt}$  experimental space)

Figure 21. Continued.



(e) Orbiter pitching moment coefficient (view from lower right quadrant of  $x_{setpt}$ - $z_{setpt}$  experimental space)

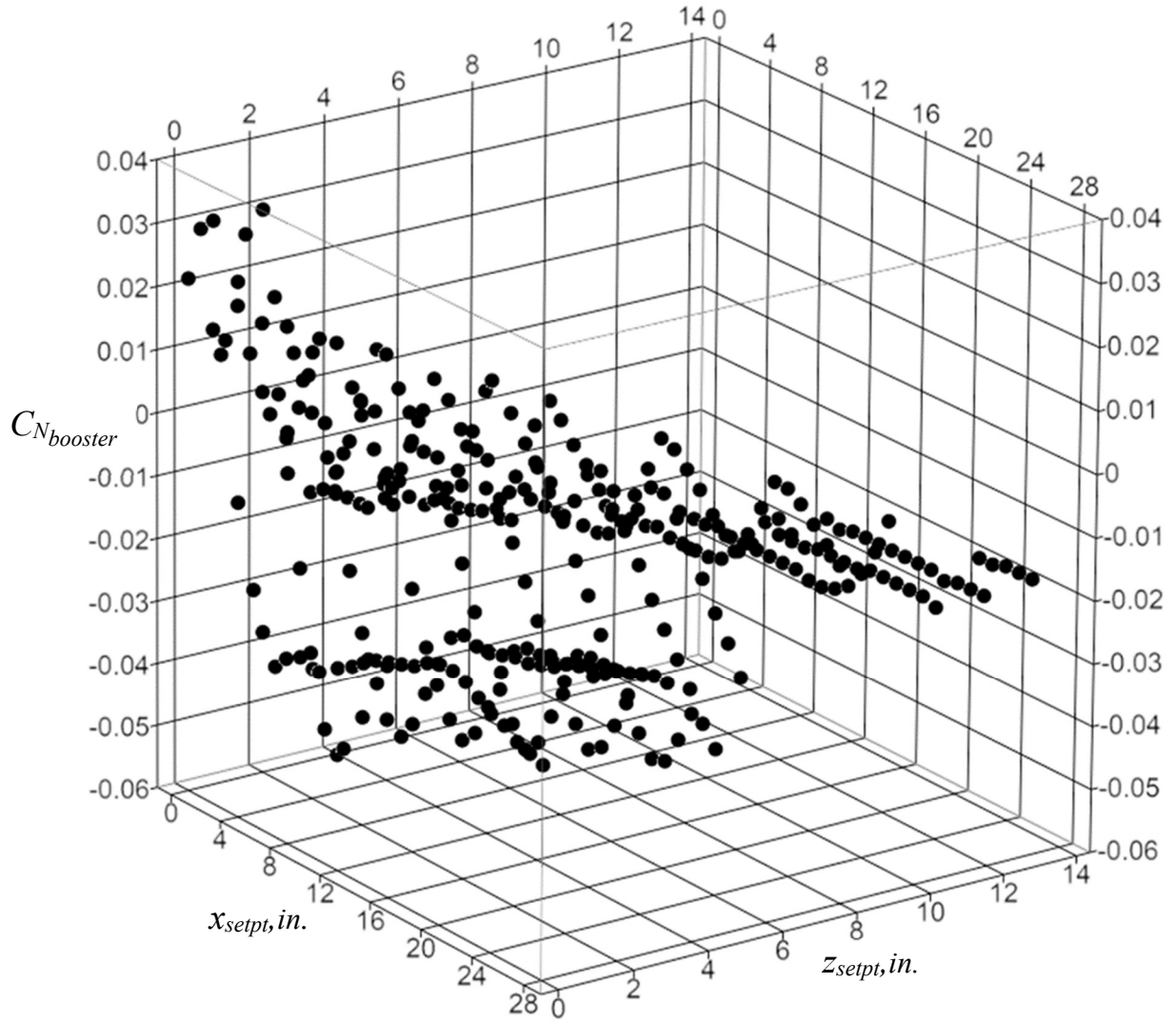
Figure 21. Continued.



(f) Orbiter pitching moment coefficient (view from upper right quadrant of  $x_{setpt}$ - $z_{setpt}$  experimental space)

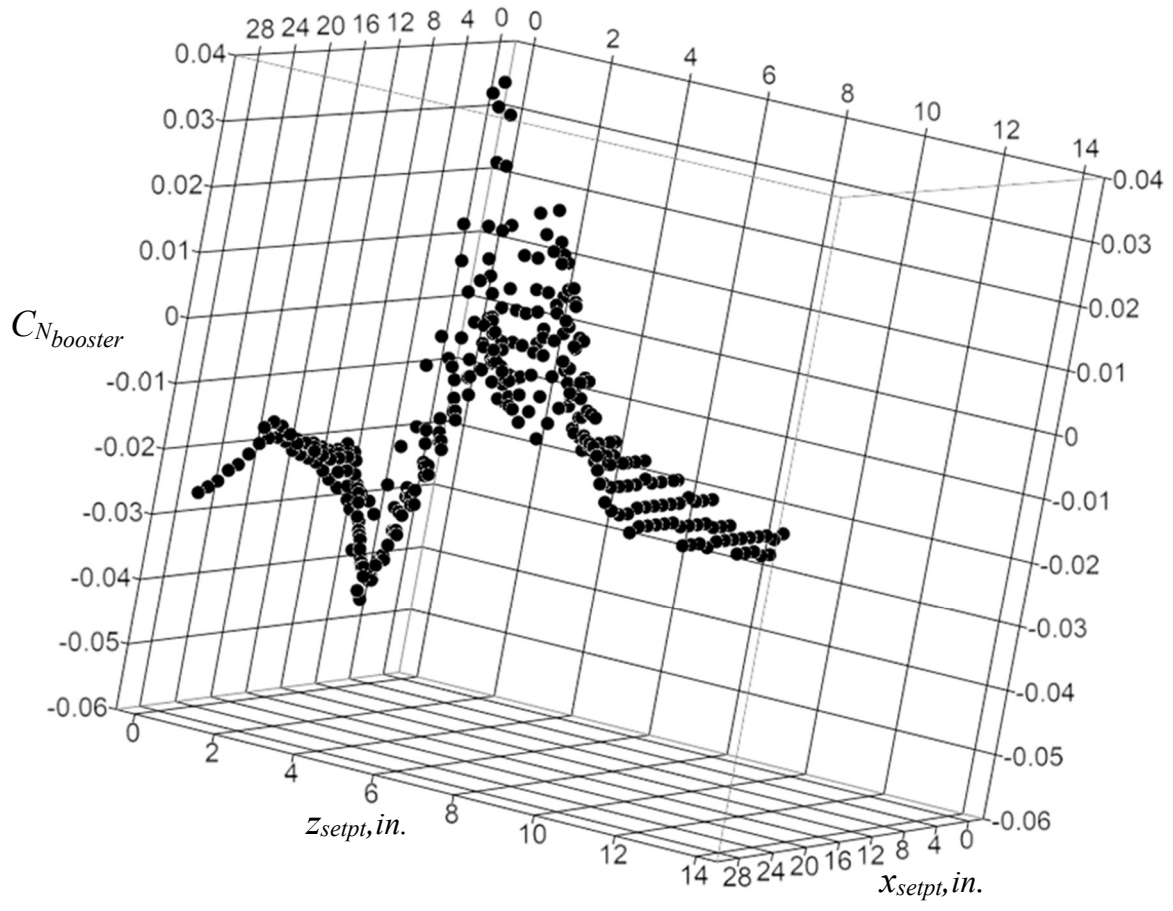
Figure 21. Concluded.





(a) Booster normal force coefficient (view from lower right quadrant of  $x_{setpt}$ - $z_{setpt}$  experimental space)

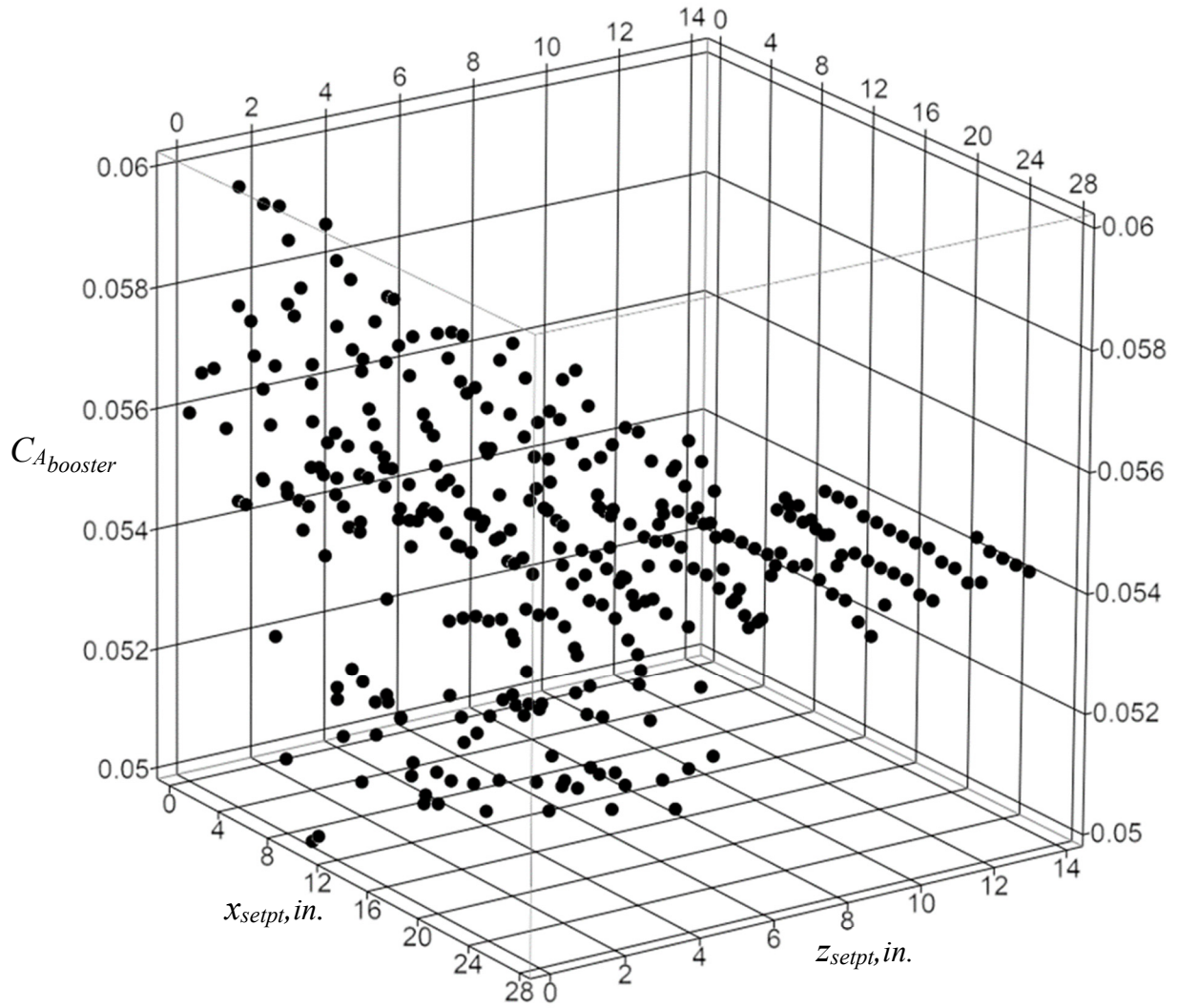
Figure 22. 3-D scatter plots of the booster proximity aerodynamic coefficients at  $Mach = 4.5$ ,  $\Delta\alpha = 0^\circ$ .



(b) Booster normal force coefficient (view from upper right quadrant of  $x_{setpt}$ - $z_{setpt}$  experimental space)

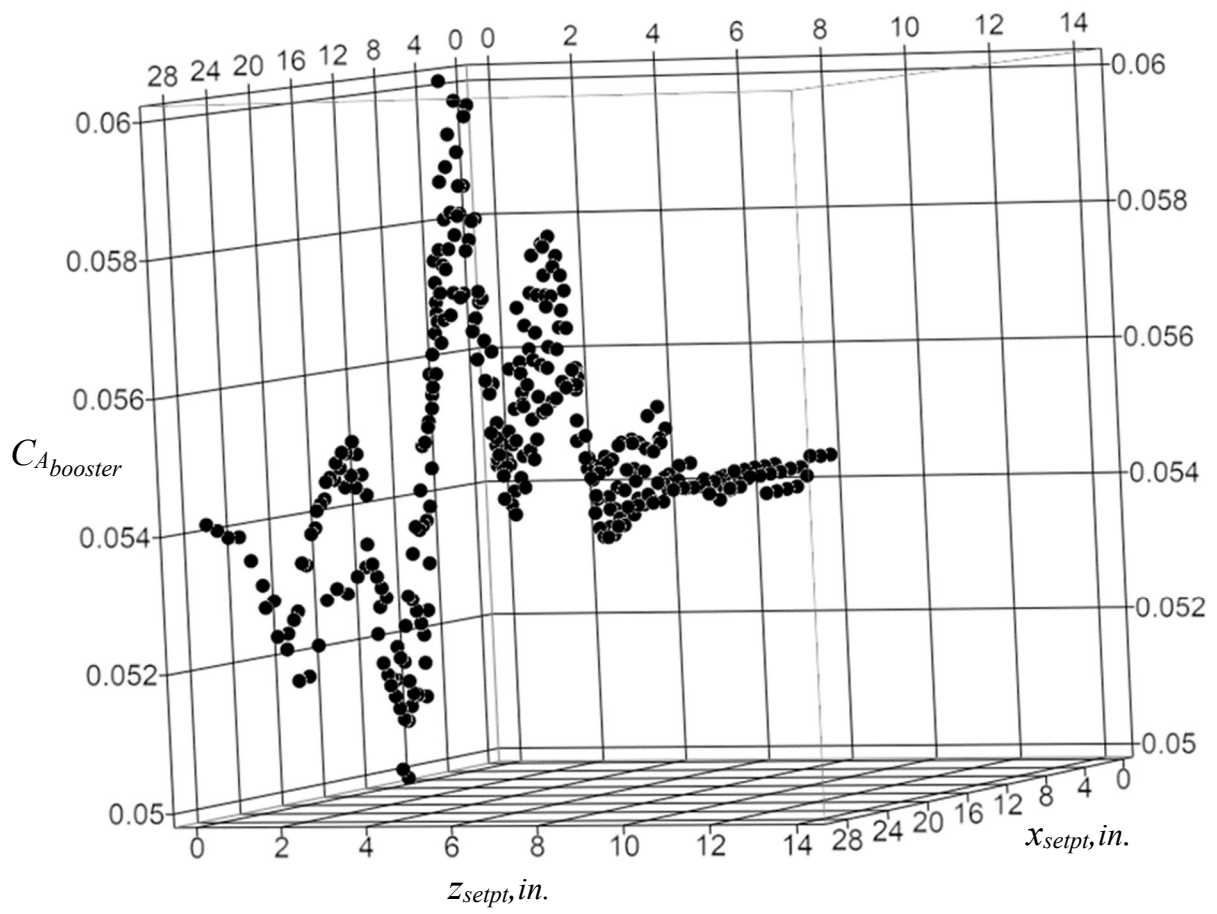
Figure 22. Continued.





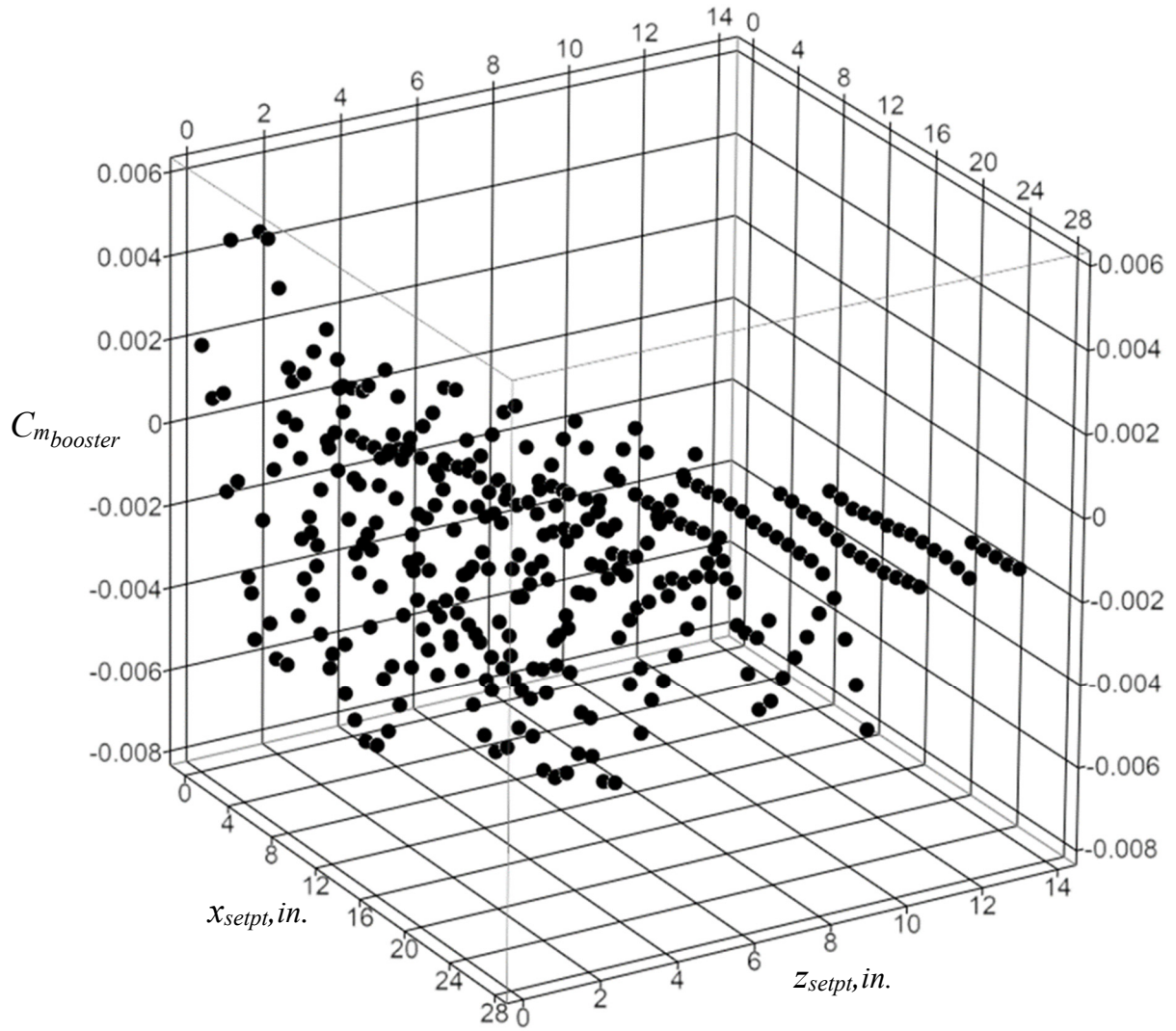
(c) Booster axial force coefficient (view from lower right quadrant of  $x_{setpt}$ - $z_{setpt}$  experimental space)

Figure 22. Continued.



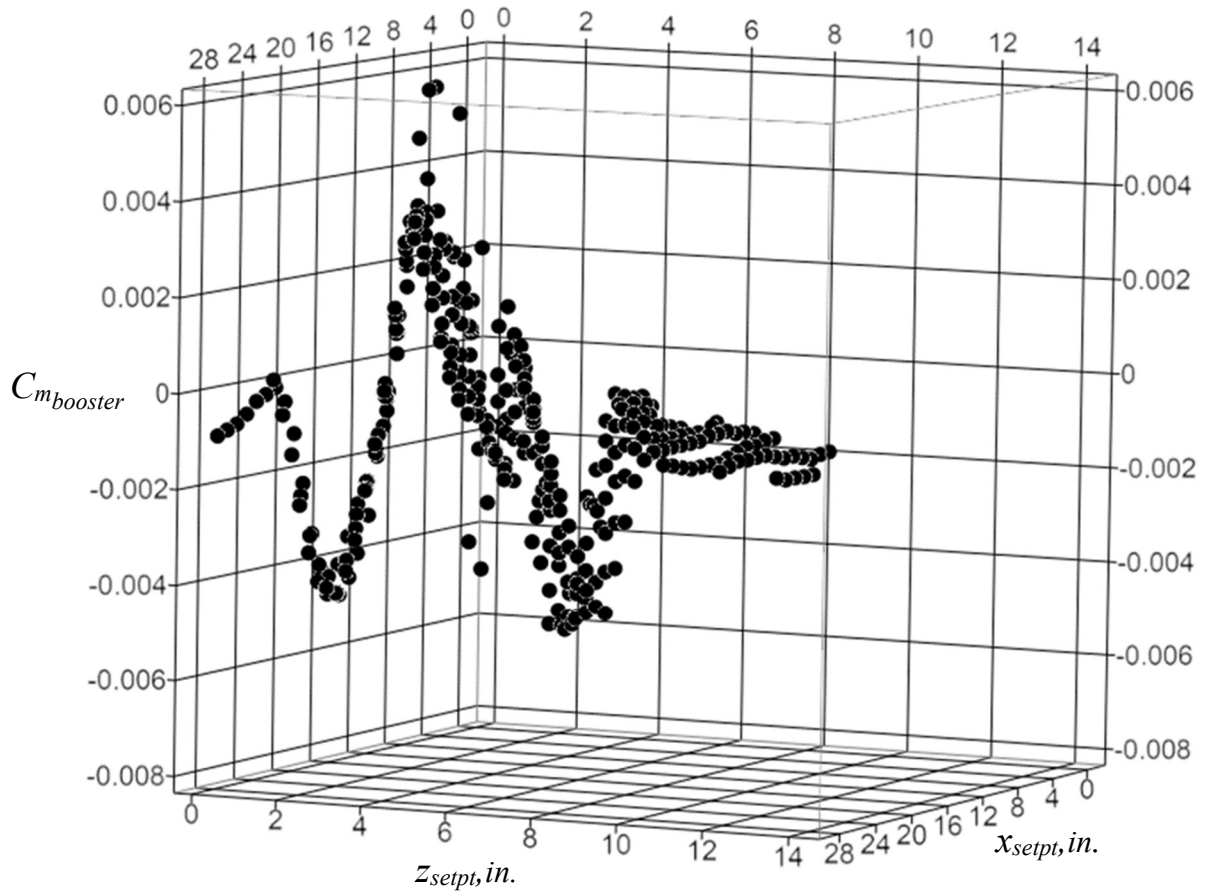
(d) Booster axial force coefficient (view from upper right quadrant of  $x_{setpt}$ - $z_{setpt}$  experimental space)

Figure 22. Continued.



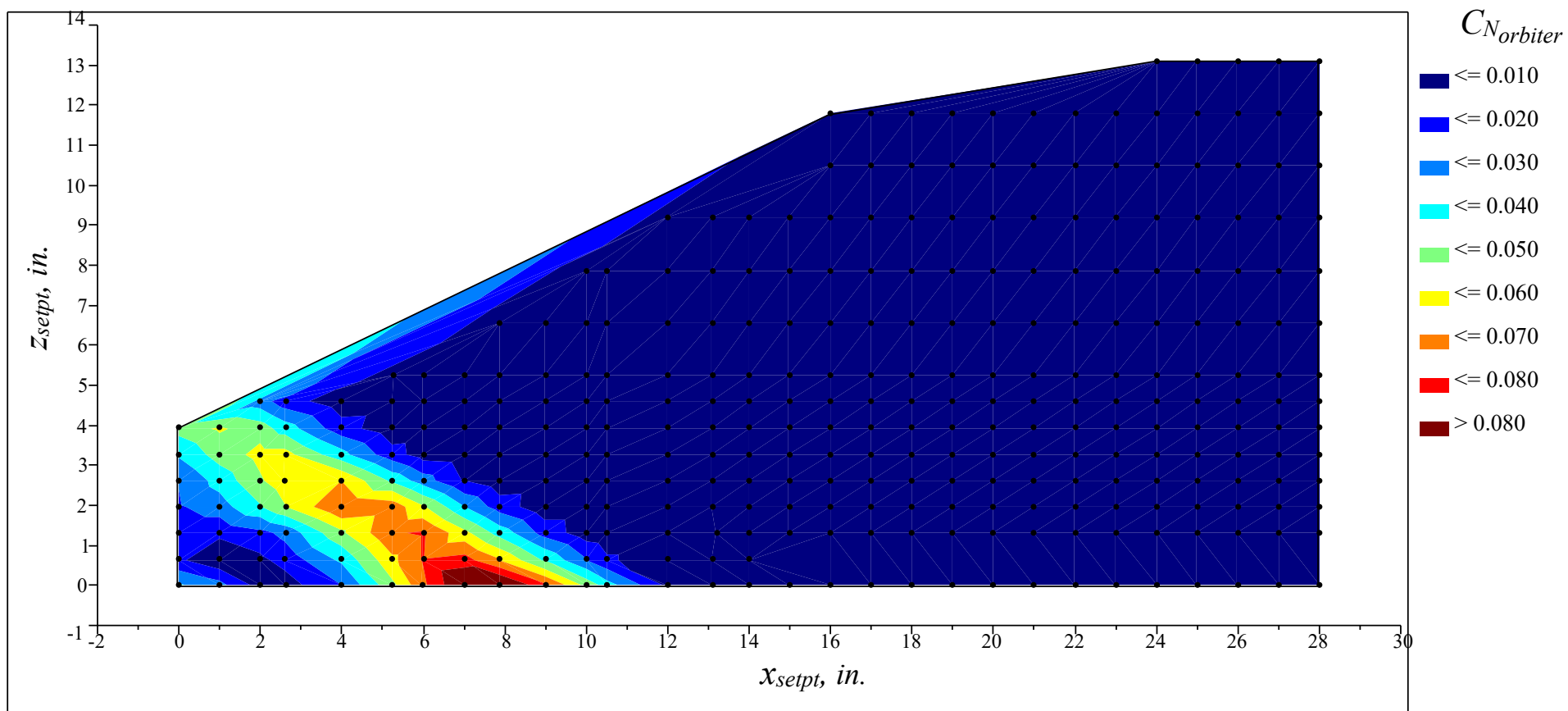
(e) Booster pitching moment coefficient (view from lower right quadrant of  $x_{setpt}$ - $z_{setpt}$  experimental space)

Figure 22. Continued.



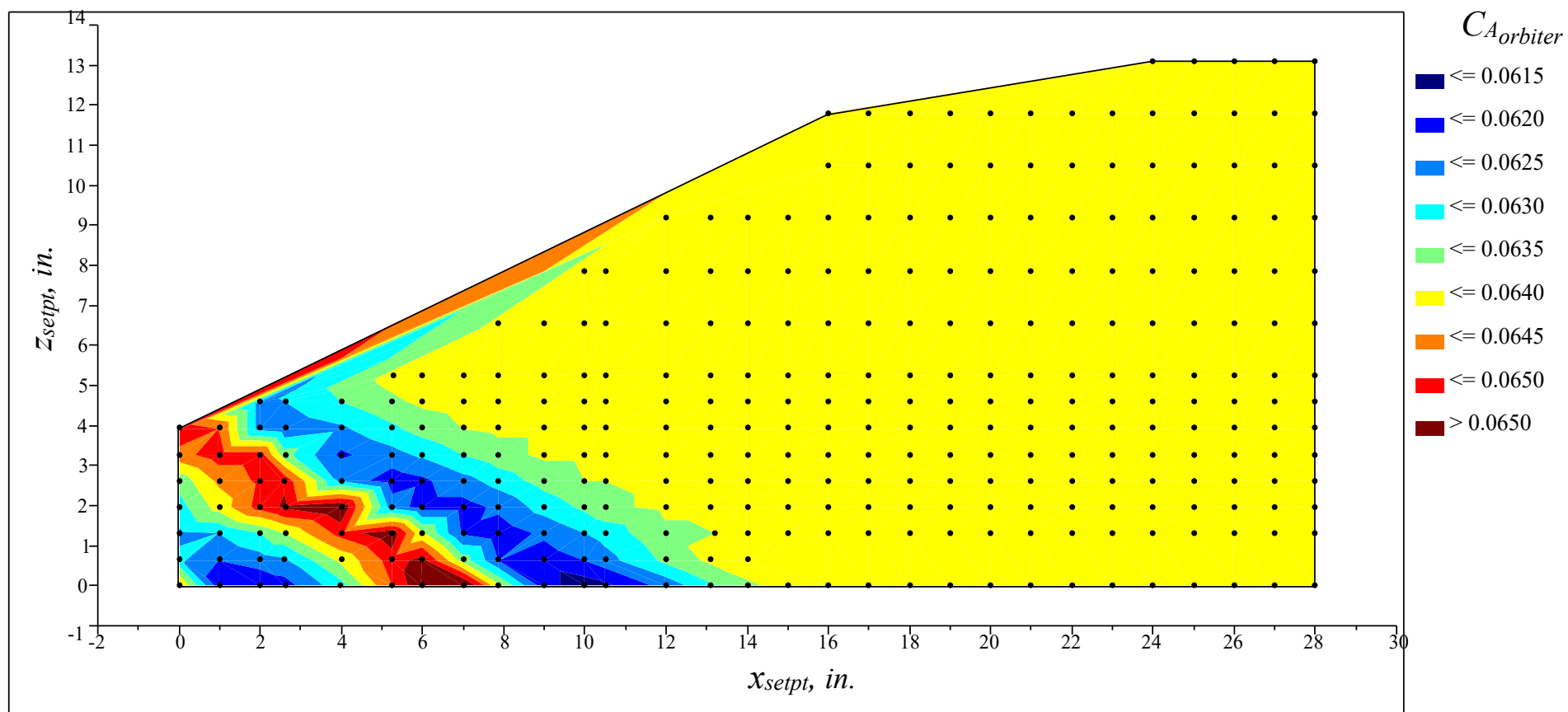
(f) Booster pitching moment coefficient (view from upper right quadrant of  $x_{setpt}$ - $z_{setpt}$  experimental space)

Figure 22. Concluded.



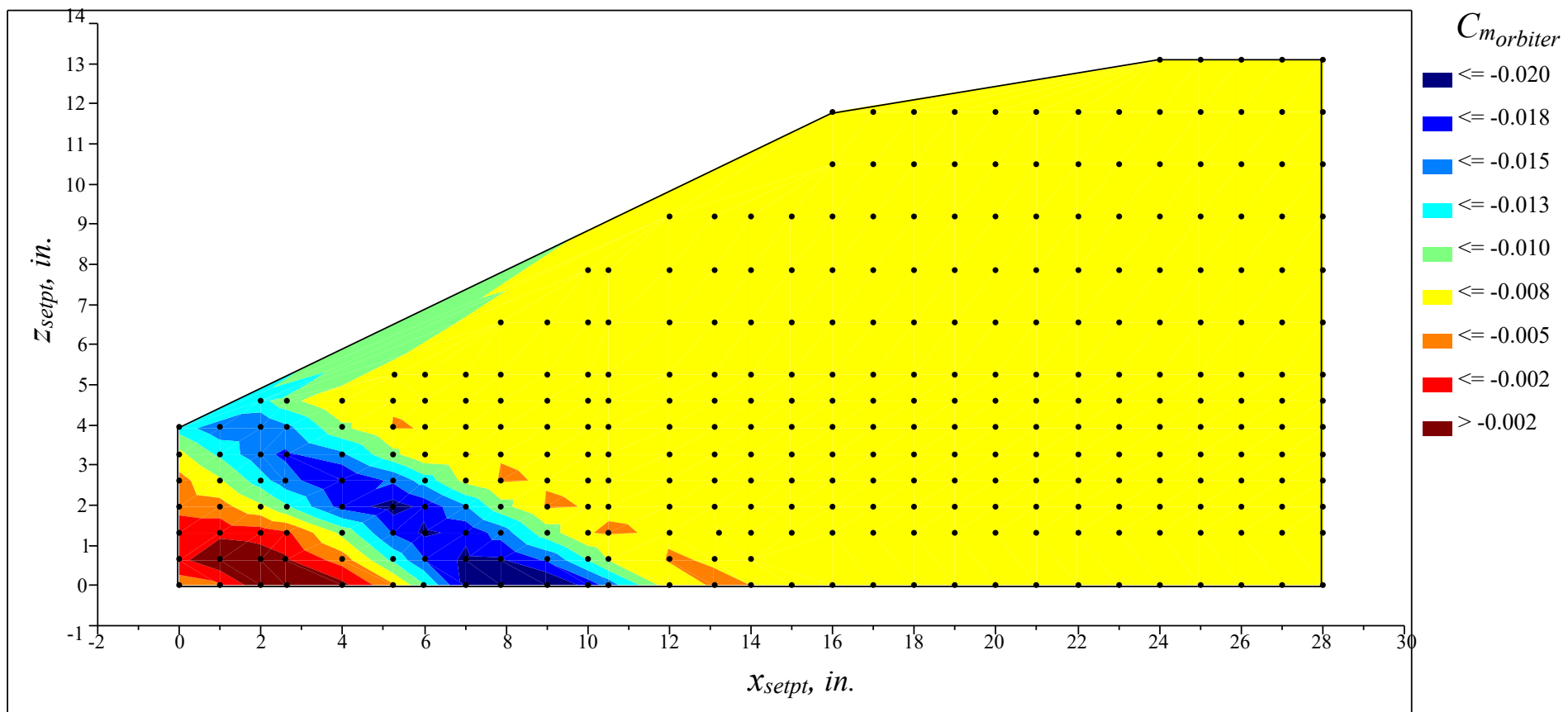
(a) Orbiter normal force coefficient

Figure 23. Contour plots of the orbiter proximity aerodynamic coefficients at  $Mach = 2.3$ ,  $\Delta\alpha = 0^\circ$ .



(b) Orbiter axial force coefficient

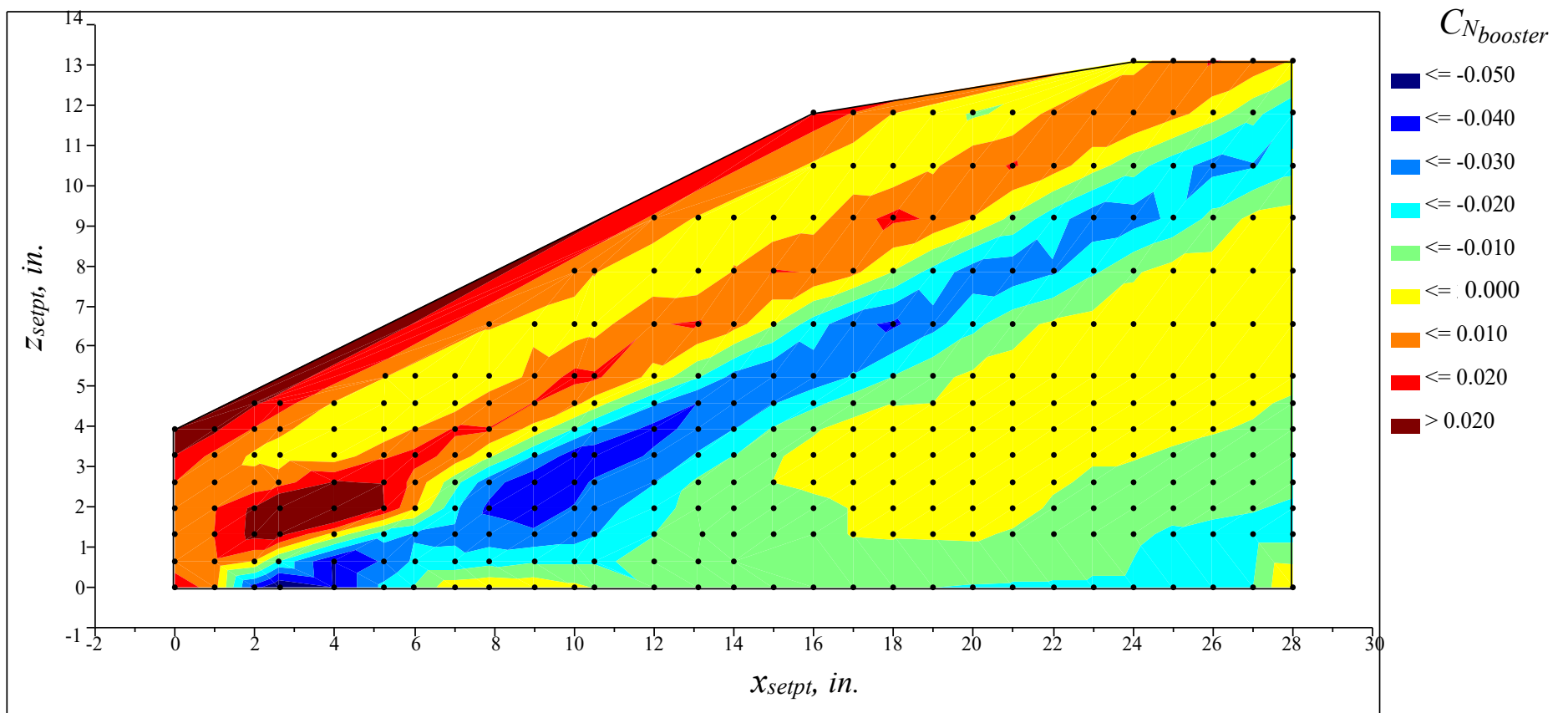
Figure 23. Continued.



(c) Orbiter pitching moment coefficient

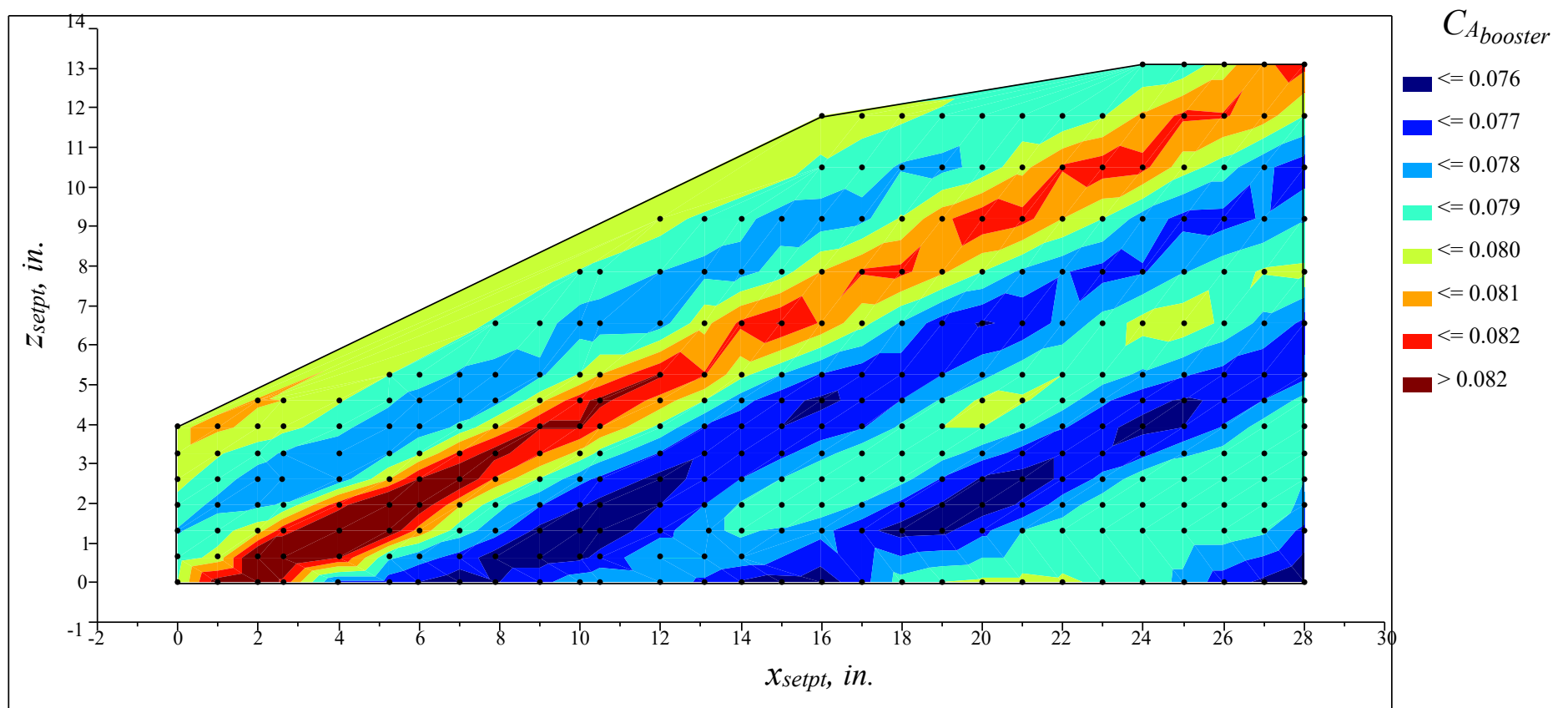
Figure 23. Concluded.





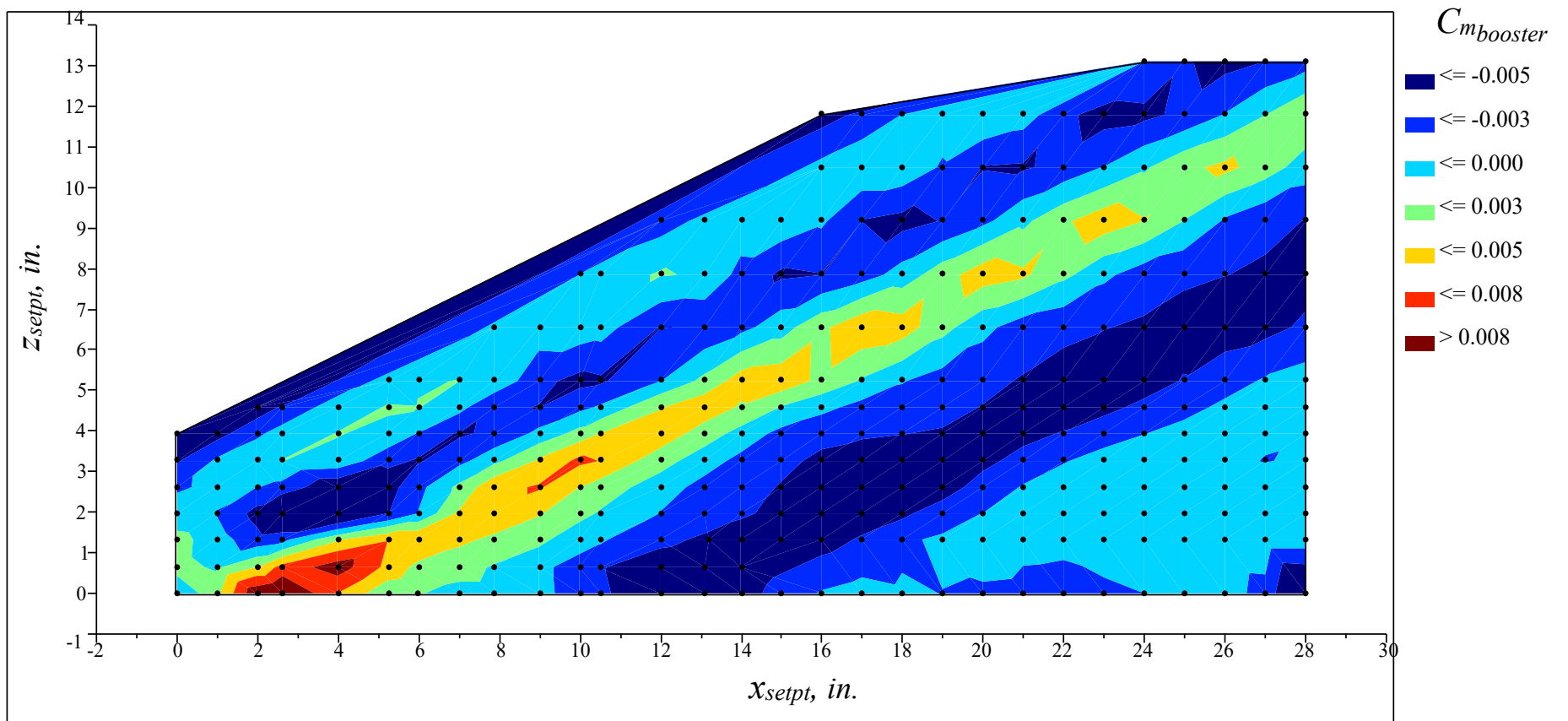
(a) Booster normal force coefficient

Figure 24. Contour plots of the booster proximity aerodynamic coefficients at  $Mach = 2.3$ ,  $\Delta\alpha = 0^\circ$ .



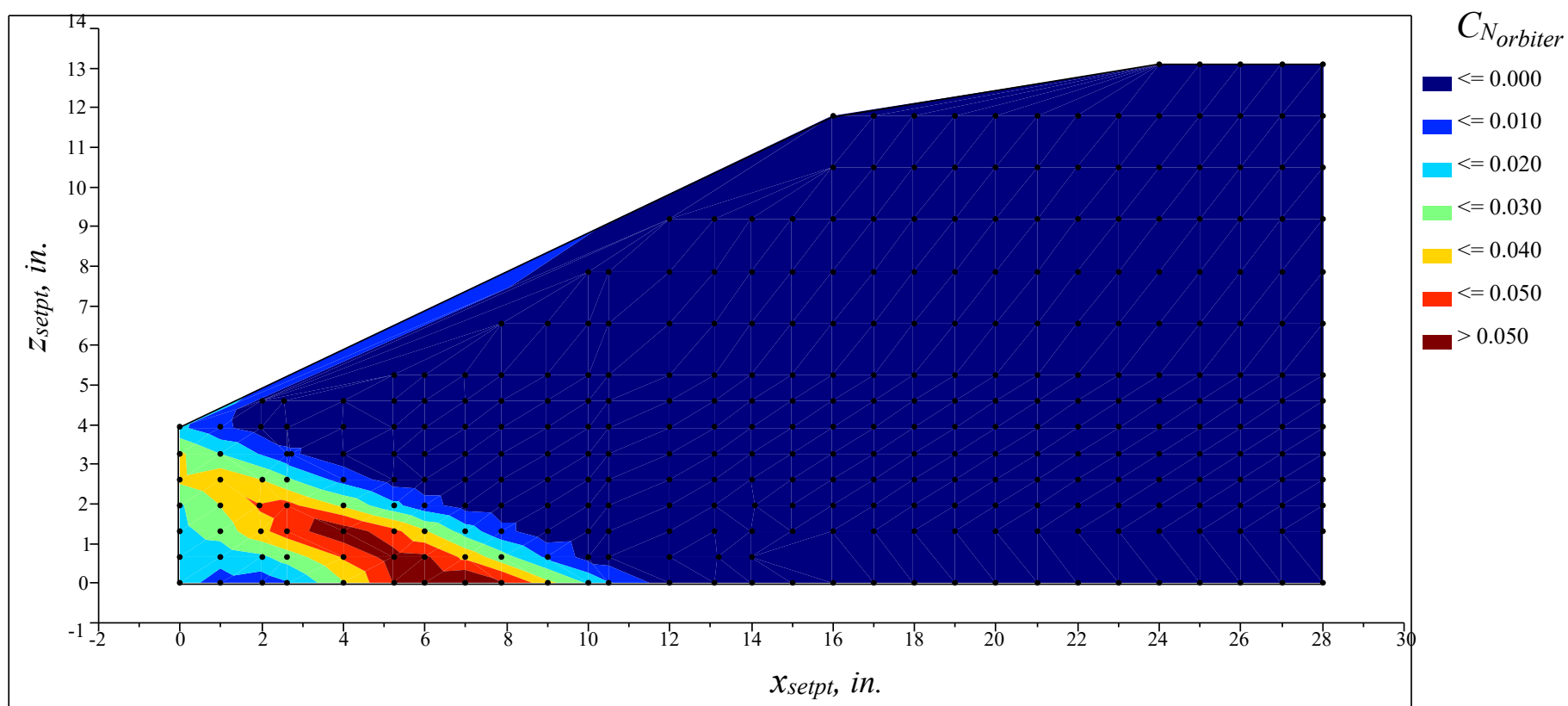
(b) Booster axial force coefficient

Figure 24. Continued.



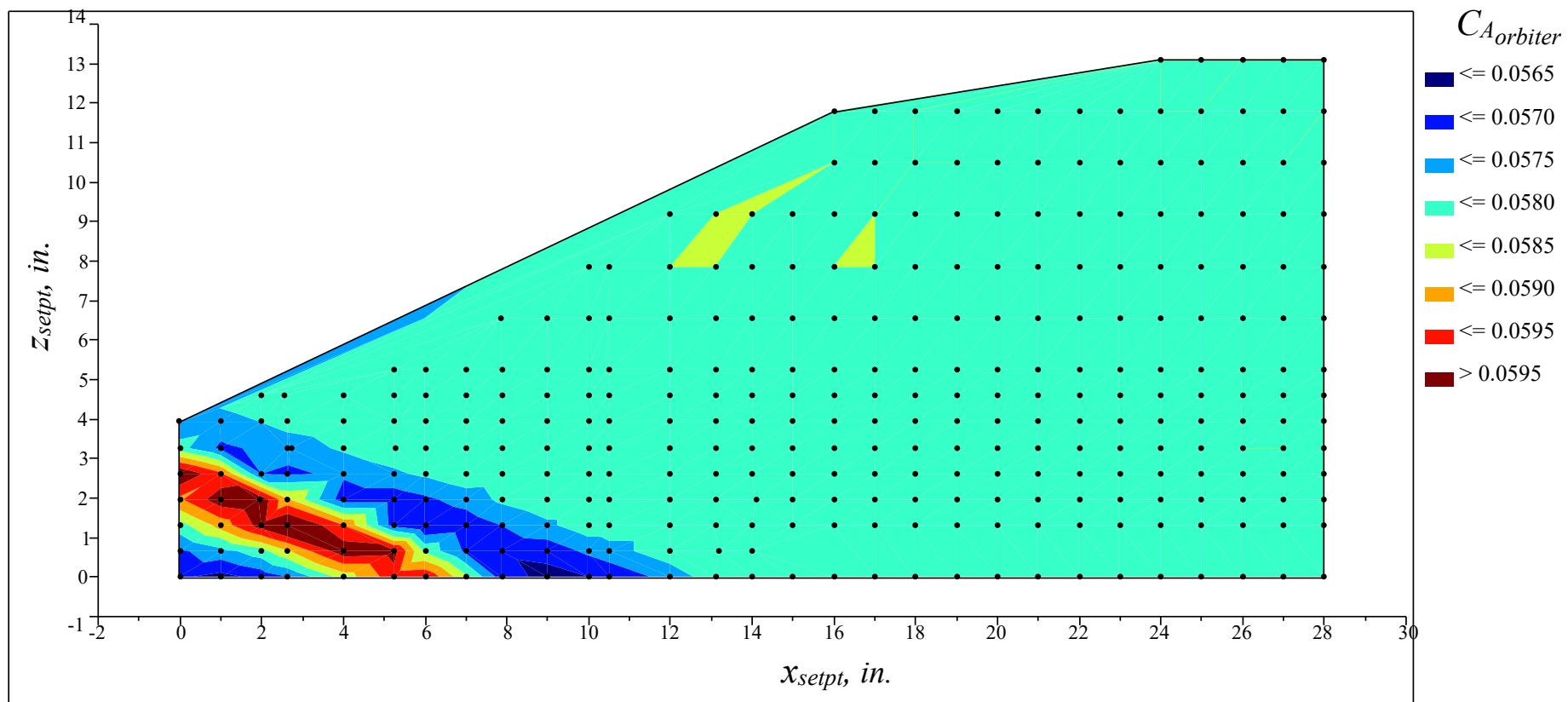
(c) Booster pitching moment coefficient

Figure 24. Concluded.



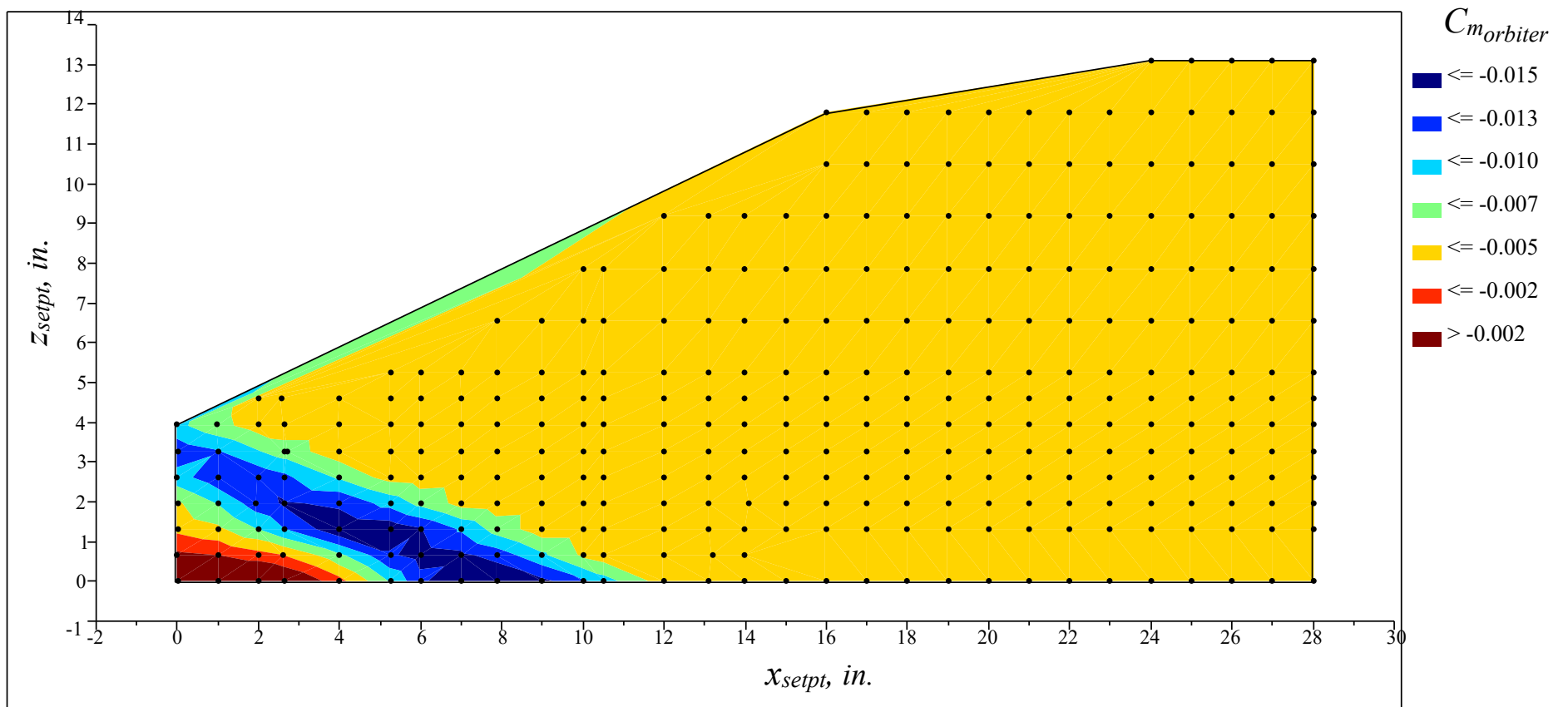
(a) Orbiter normal force coefficient

Figure 25. Contour plots of the orbiter proximity aerodynamic coefficients at  $Mach = 3.0$ ,  $\Delta\alpha = 0^\circ$ .



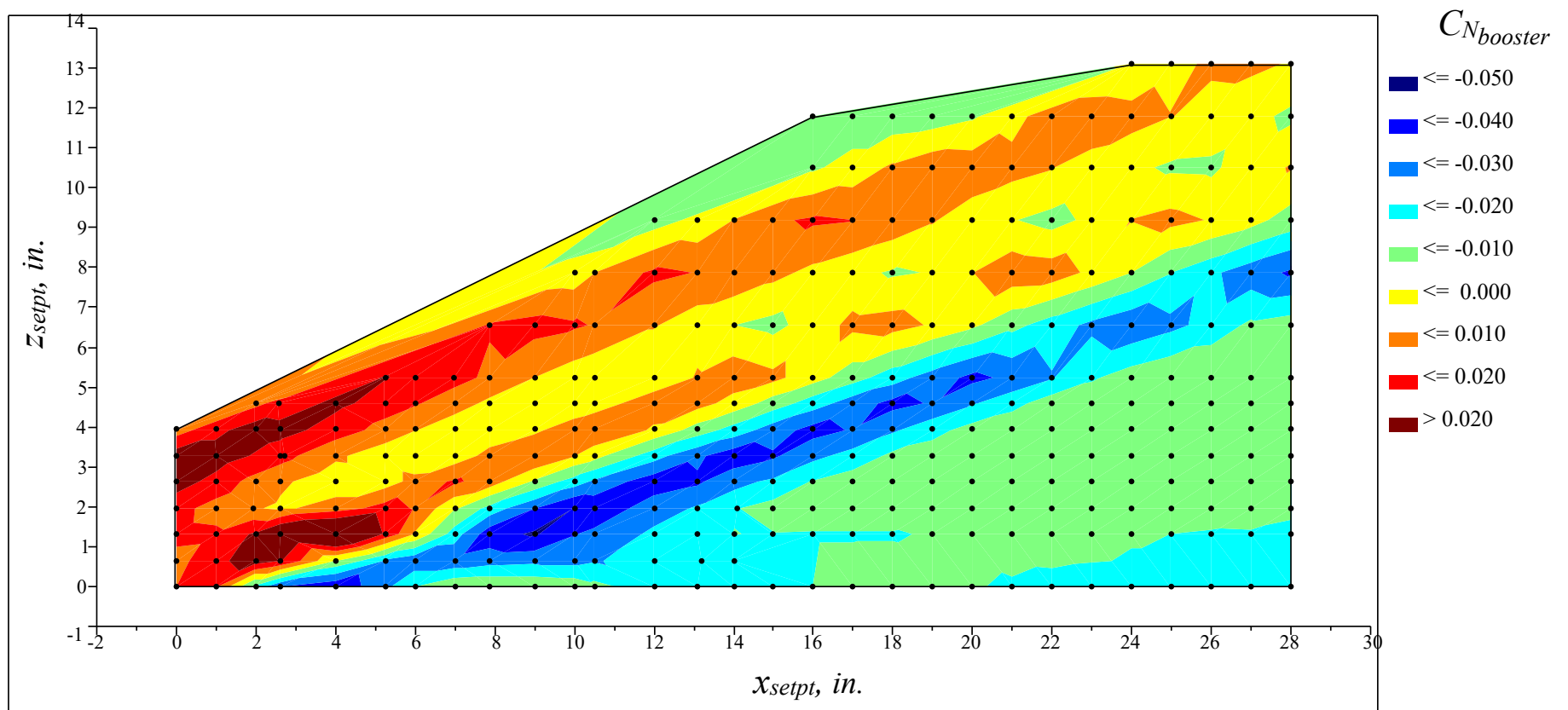
(b) Orbiter axial force coefficient

Figure 25. Continued.



(c) Orbiter pitching moment coefficient

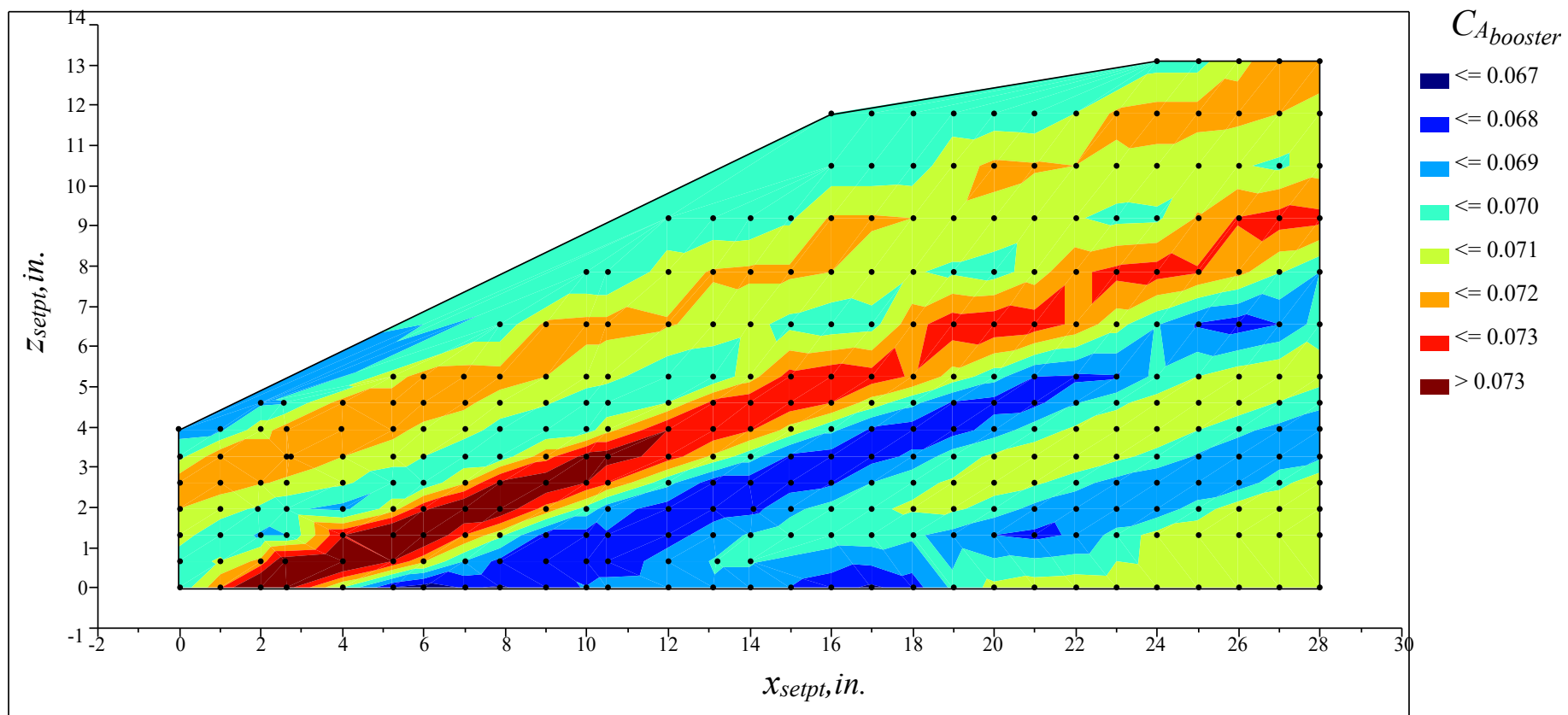
Figure 25. Concluded.



(a) Booster normal force coefficient

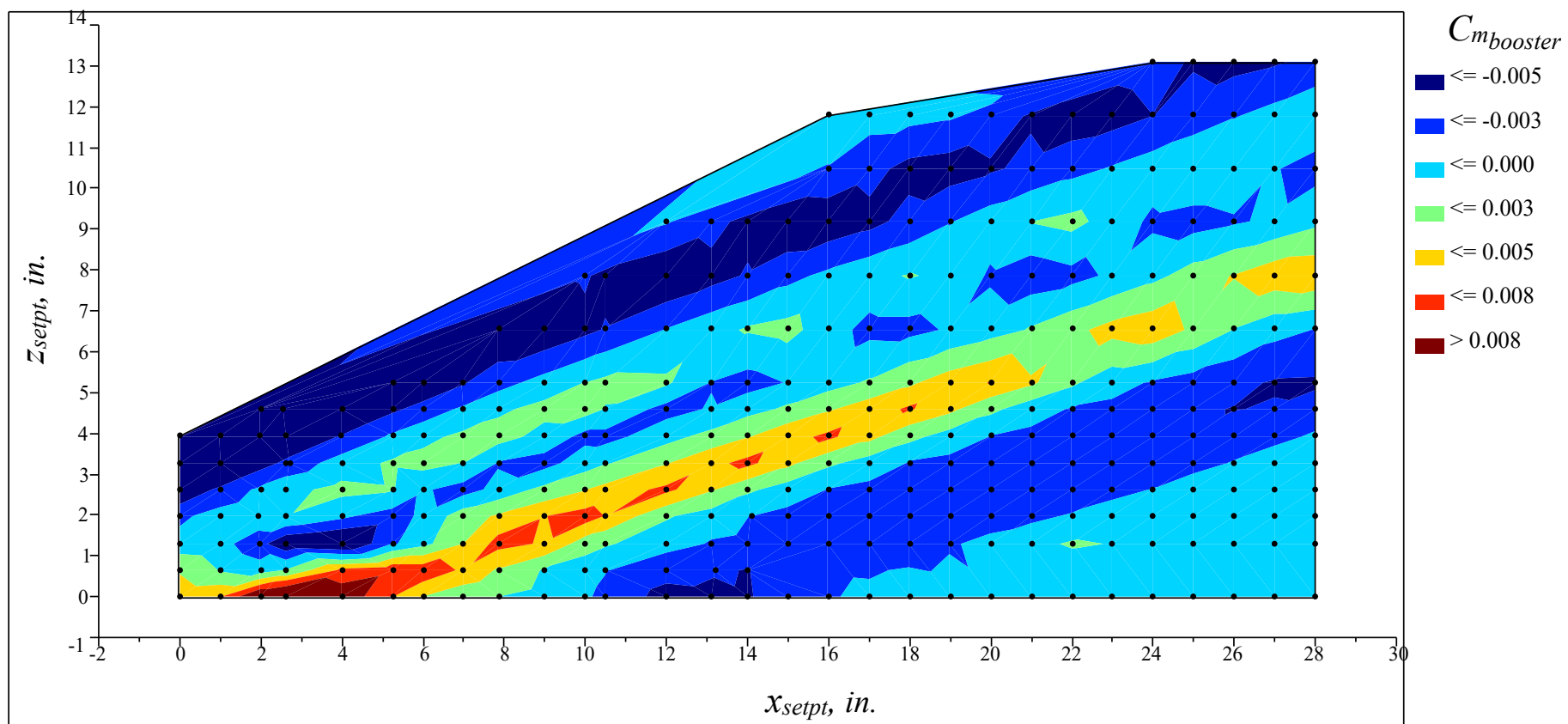
Figure 26. Contour plots of the booster proximity aerodynamic coefficients at  $Mach = 3.0$ ,  $\Delta\alpha = 0^\circ$ .





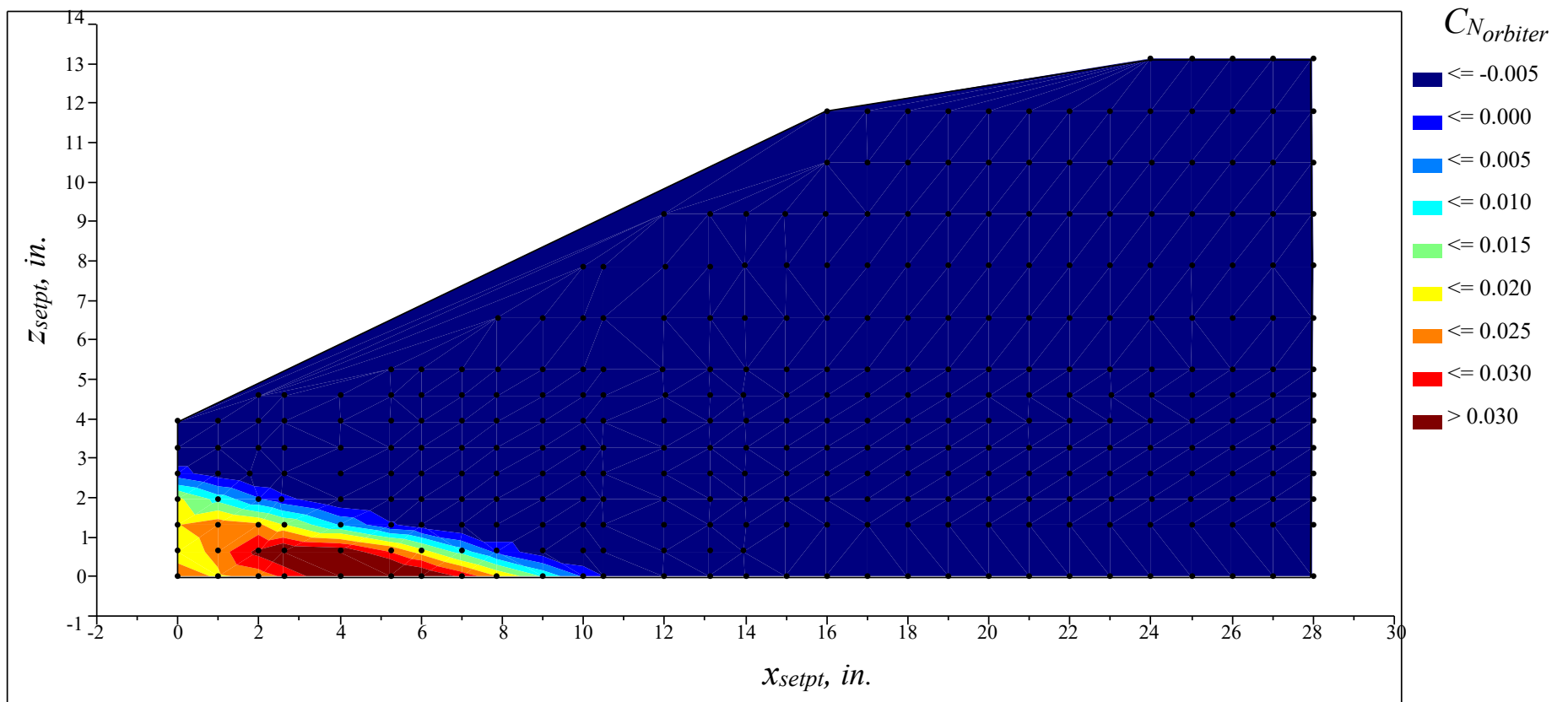
(b) Booster axial force coefficient

Figure 26. Continued.



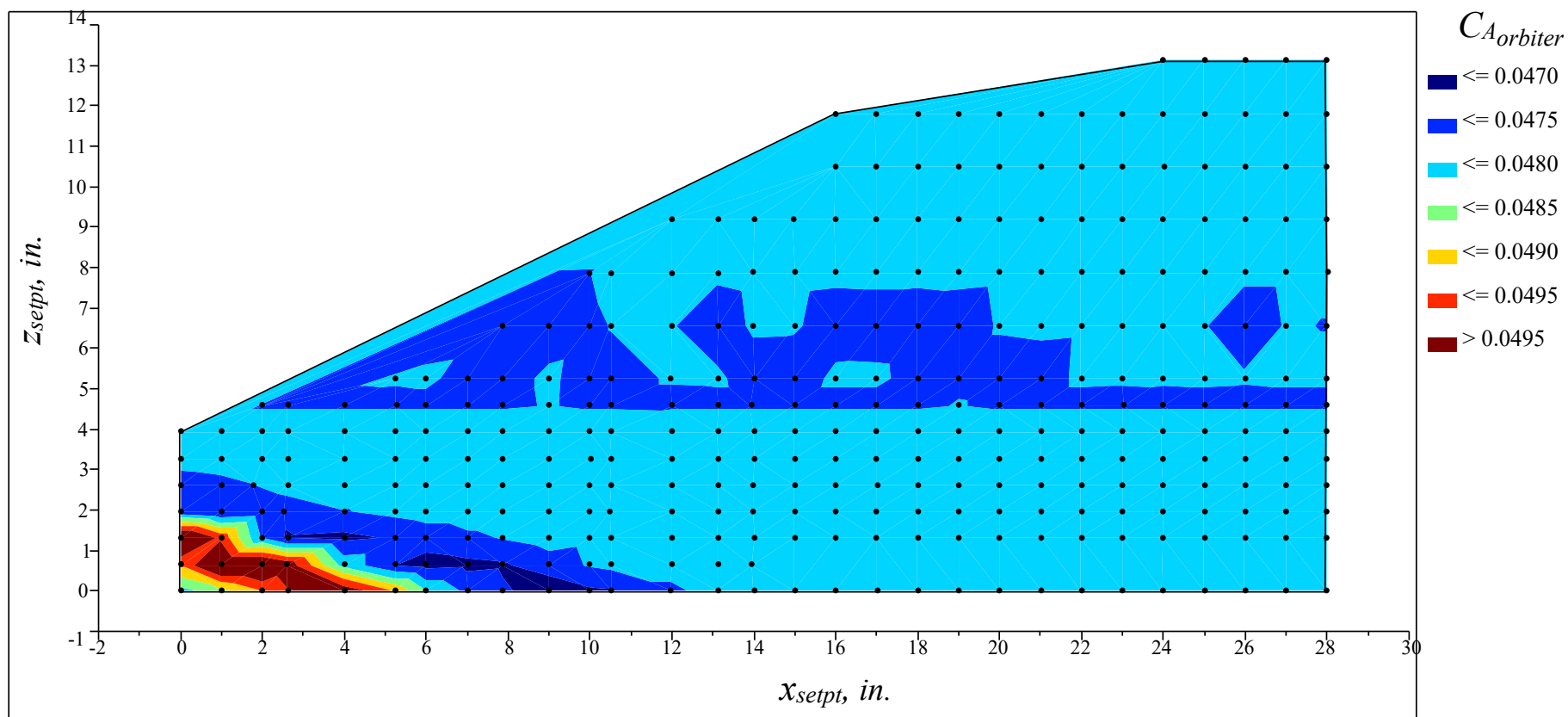
(c) Booster pitching moment coefficient

Figure 26. Concluded.



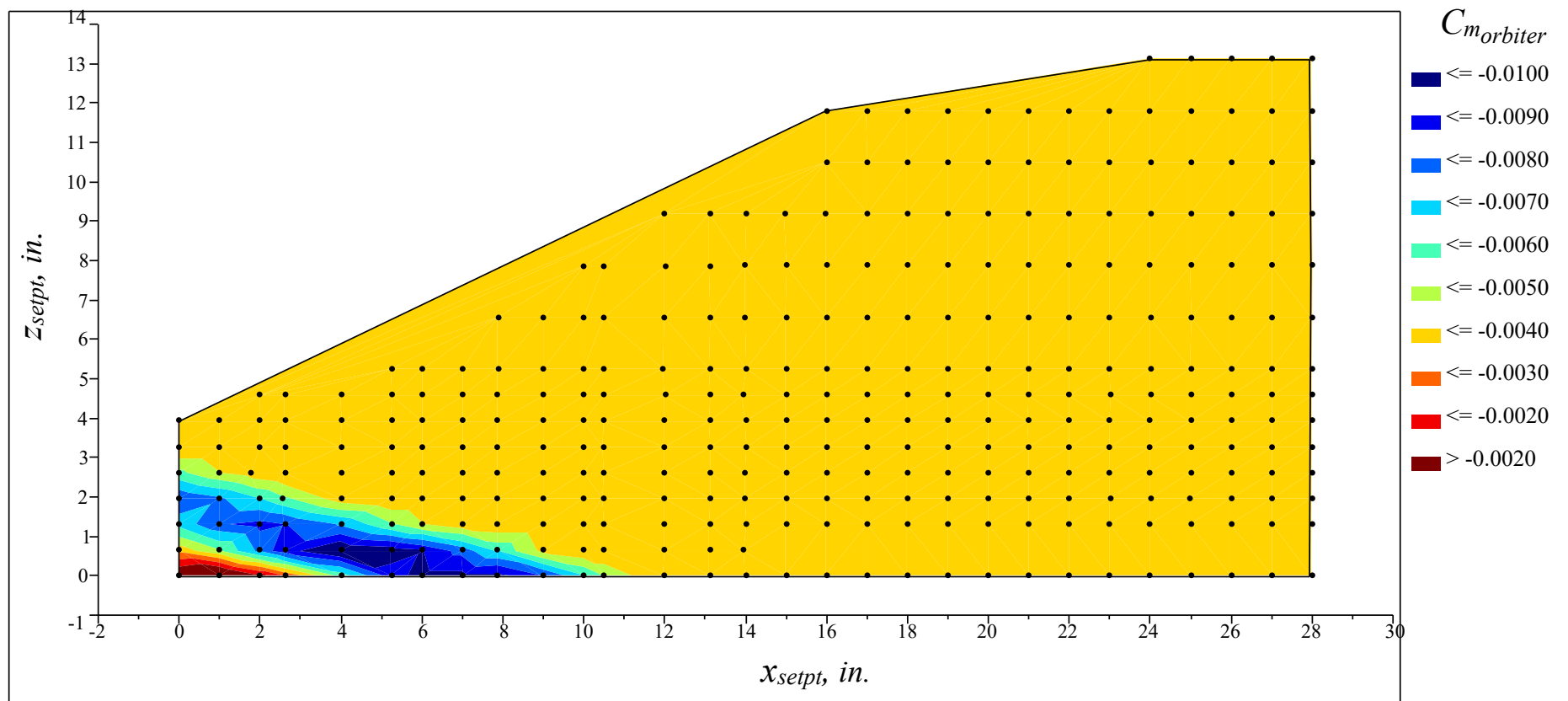
(a) Orbiter normal force coefficient

Figure 27. Contour plots of the orbiter proximity aerodynamic coefficients at  $Mach = 4.5$ ,  $\Delta\alpha = 0^\circ$ .



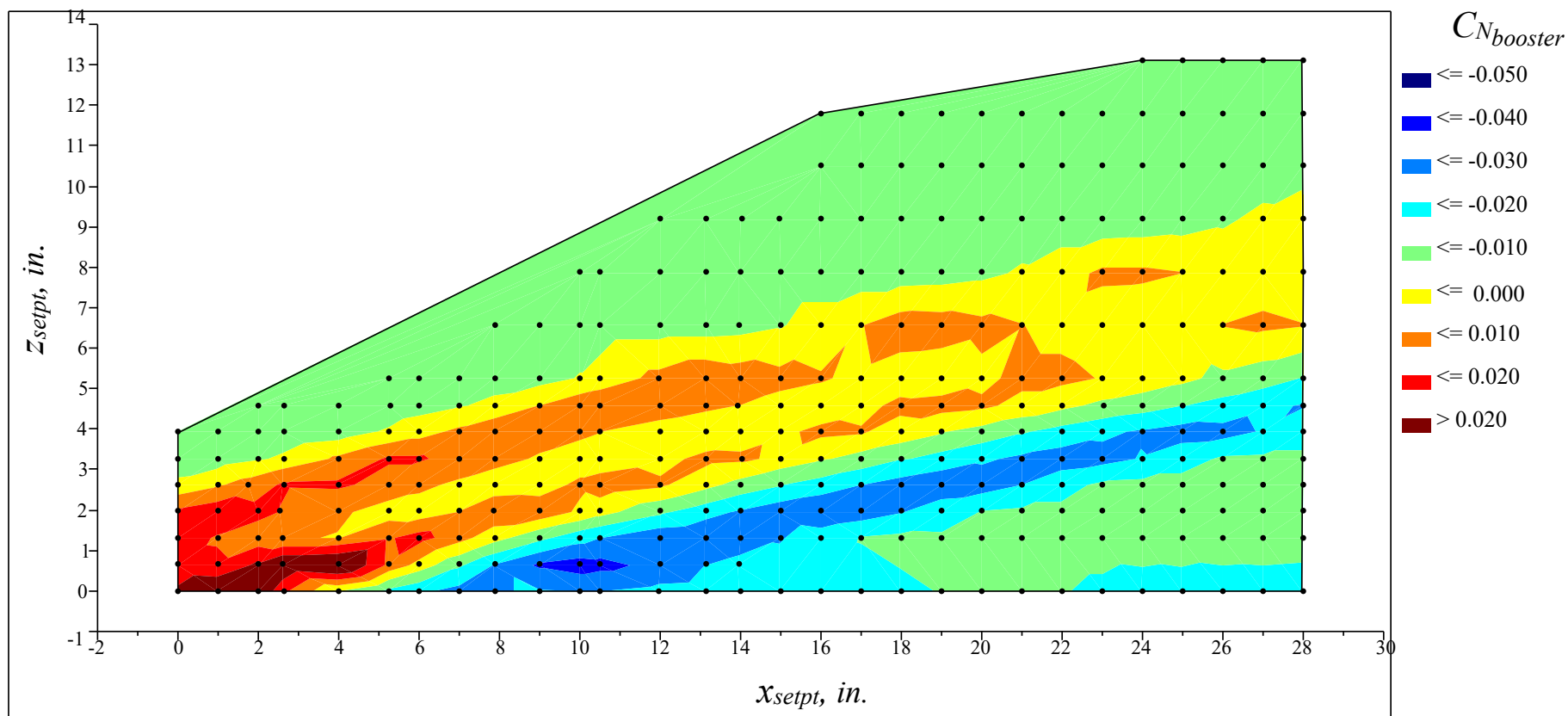
(b) Orbiter axial force coefficient

Figure 27. Continued.



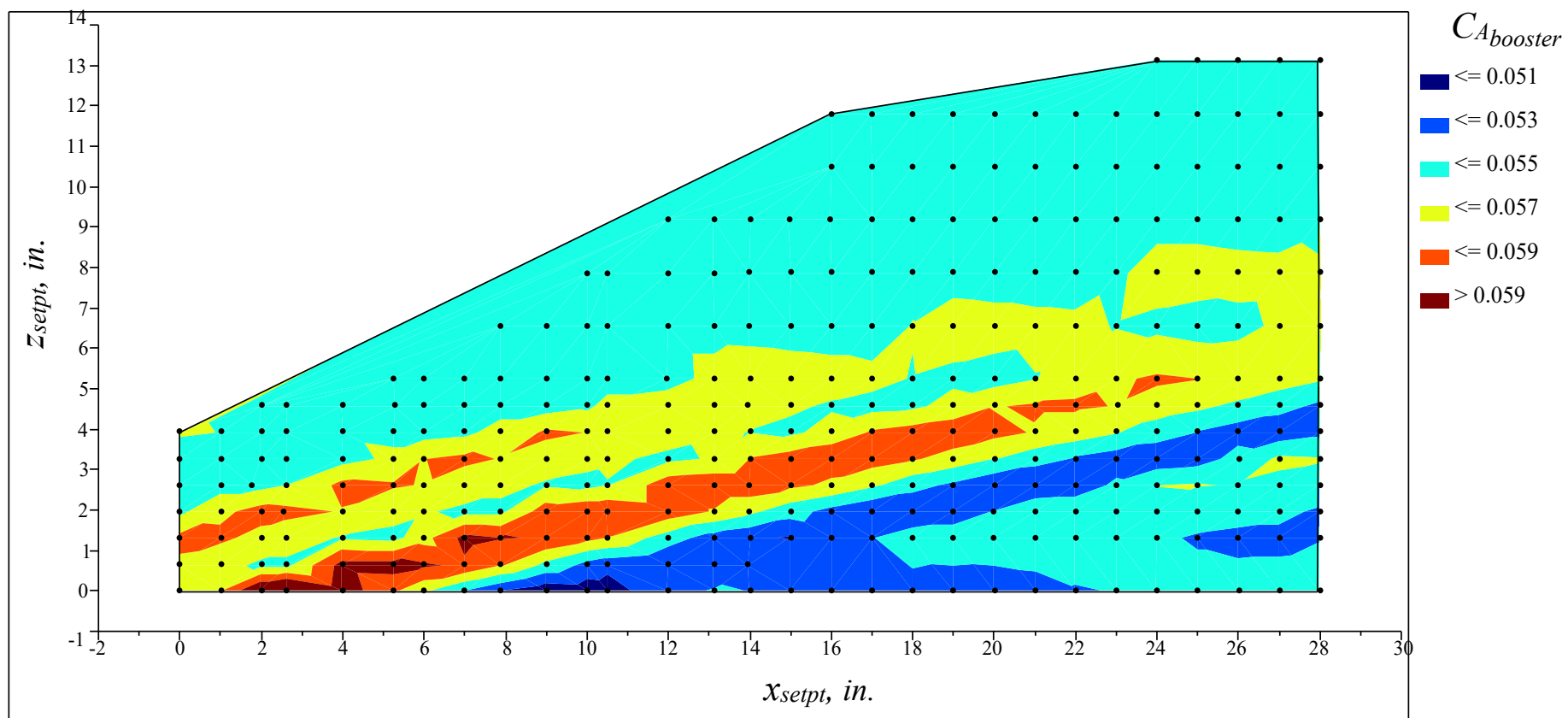
(c) Orbiter pitching moment coefficient

Figure 27. Concluded.



(a) Booster normal force coefficient

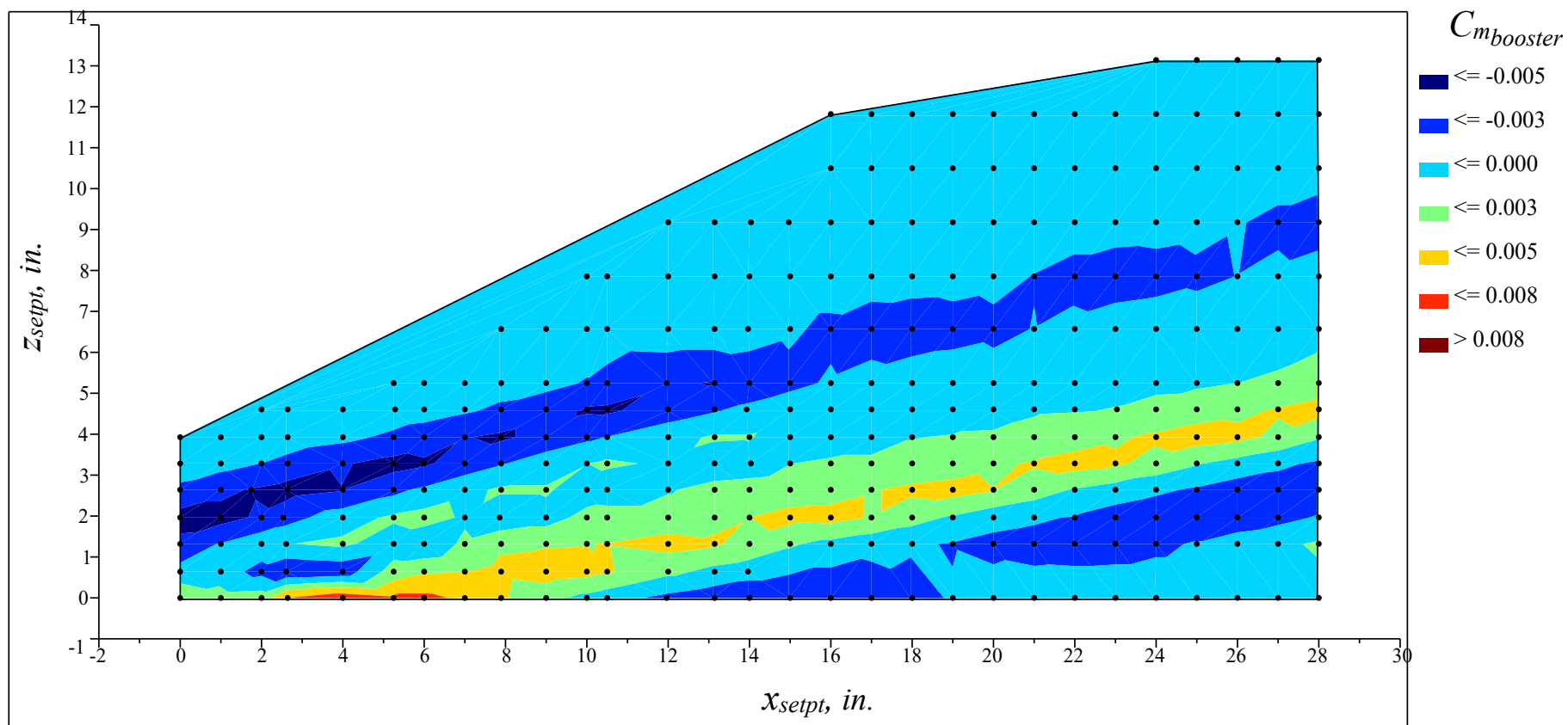
Figure 28. Contour plots of the booster proximity aerodynamic coefficients at  $Mach = 4.5$ ,  $\Delta\alpha = 0^\circ$ .



(b) Booster axial force coefficient

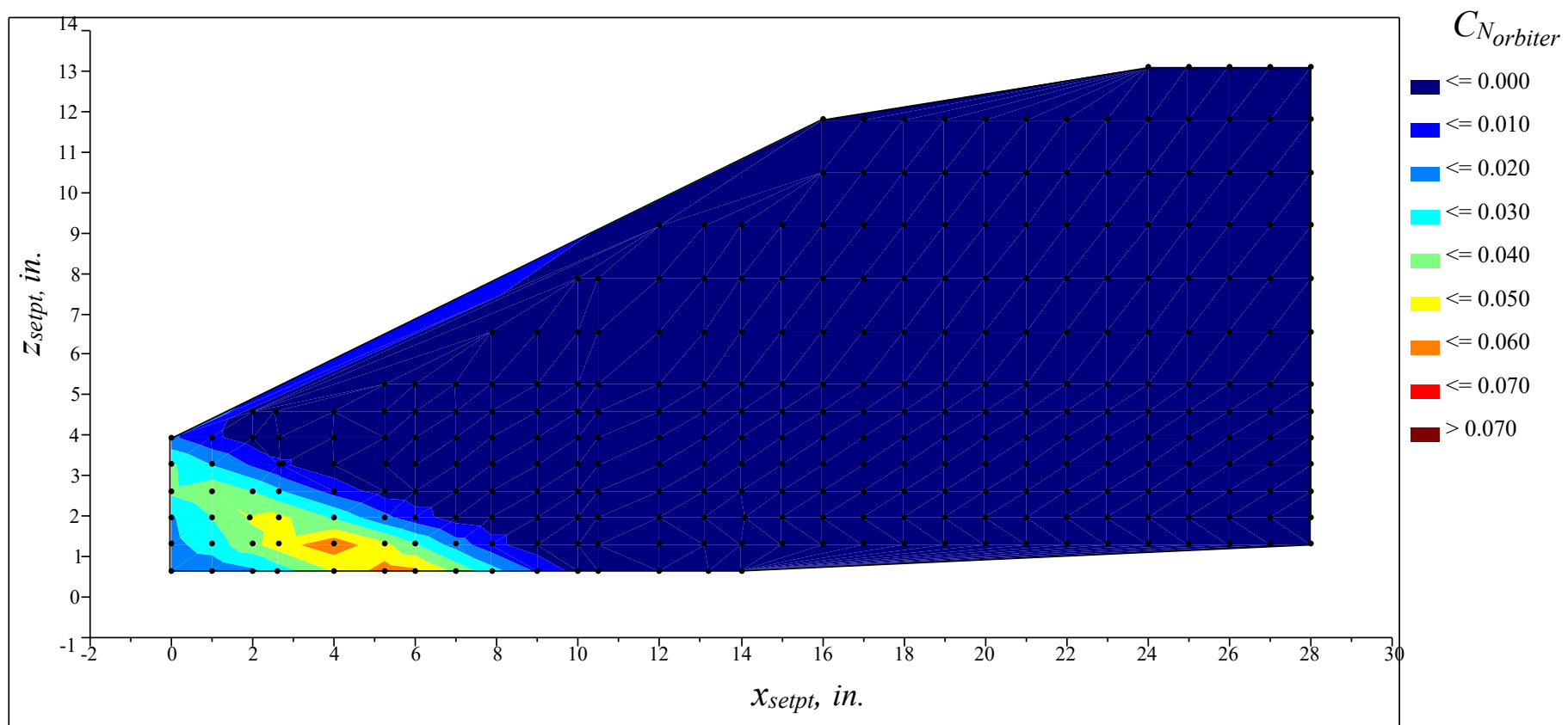
Figure 28. Continued.





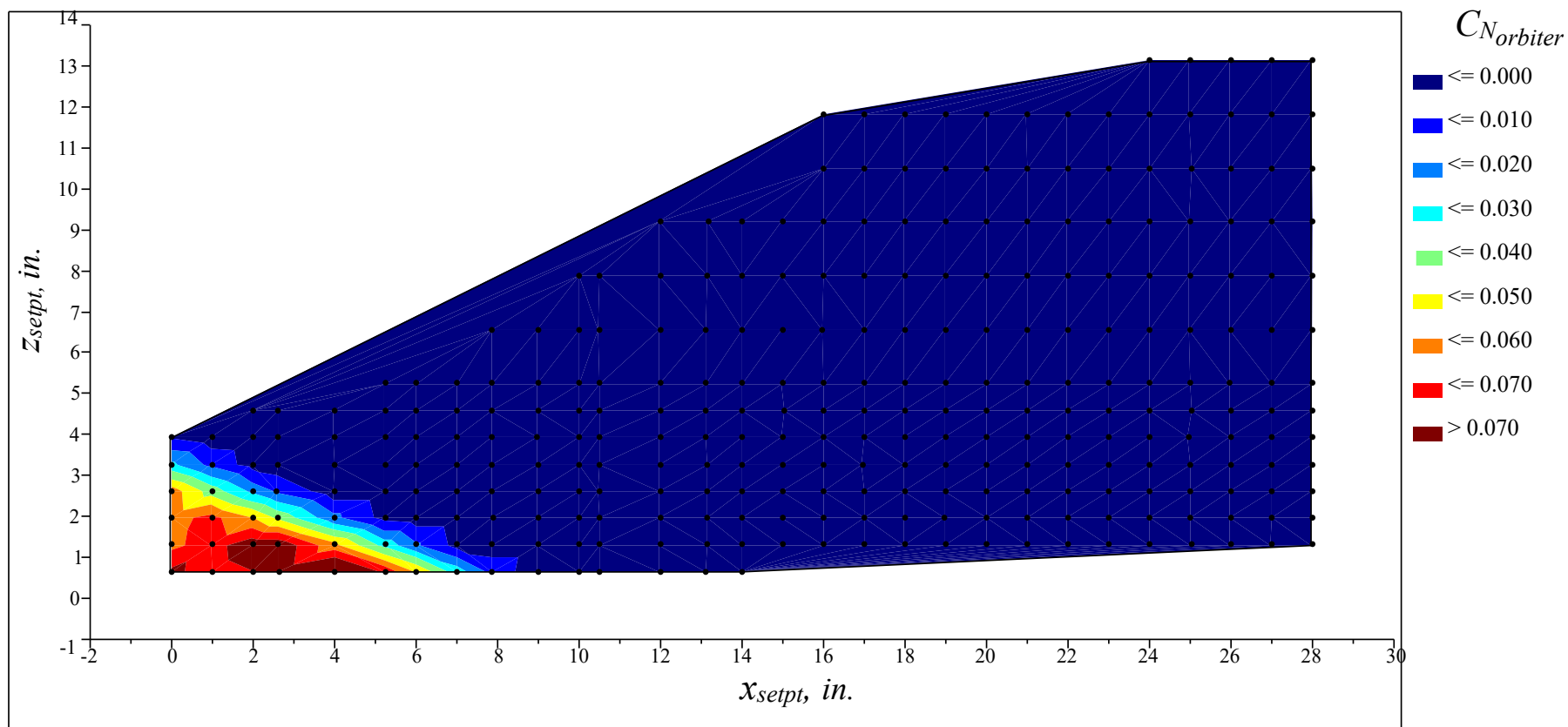
(c) Booster pitching moment coefficient

Figure 28. Concluded.



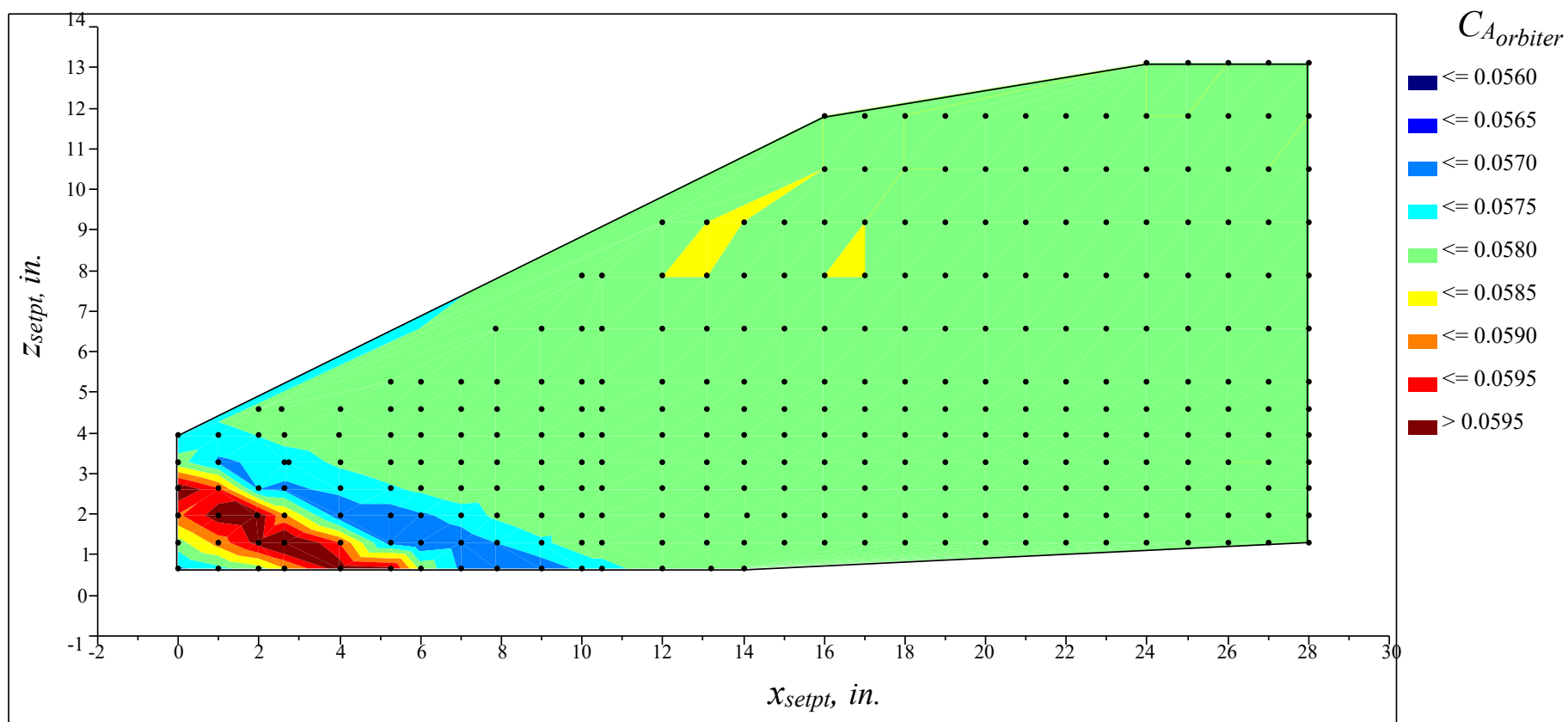
(a) Orbiter normal force coefficient,  $\Delta\alpha = 0^\circ$

Figure 29. Contour plots of the orbiter proximity aerodynamic coefficients at  $Mach = 3.0$ ,  $\Delta\alpha = 0^\circ$  and  $5^\circ$ .



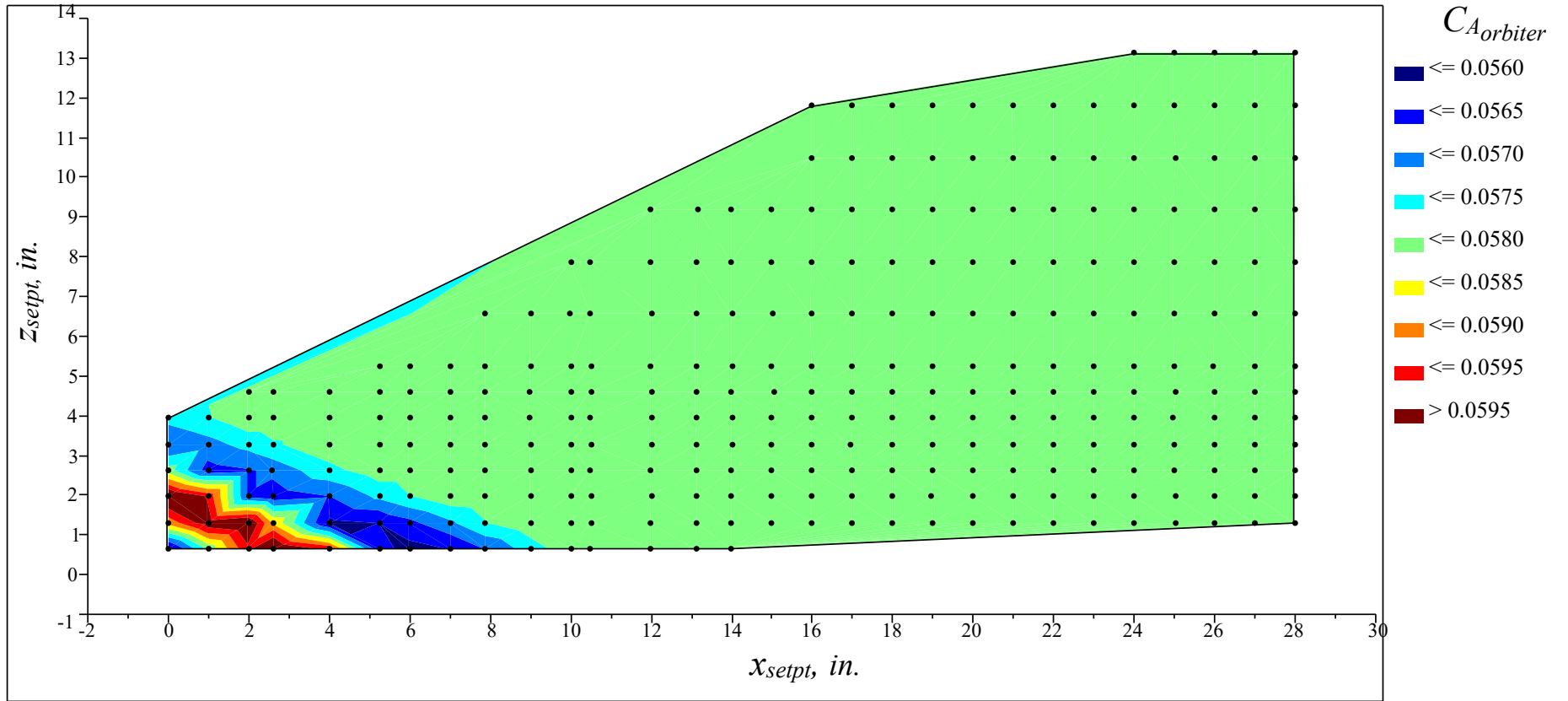
(b) Orbiter normal force coefficient,  $\Delta\alpha = 5^\circ$

Figure 29. Continued.



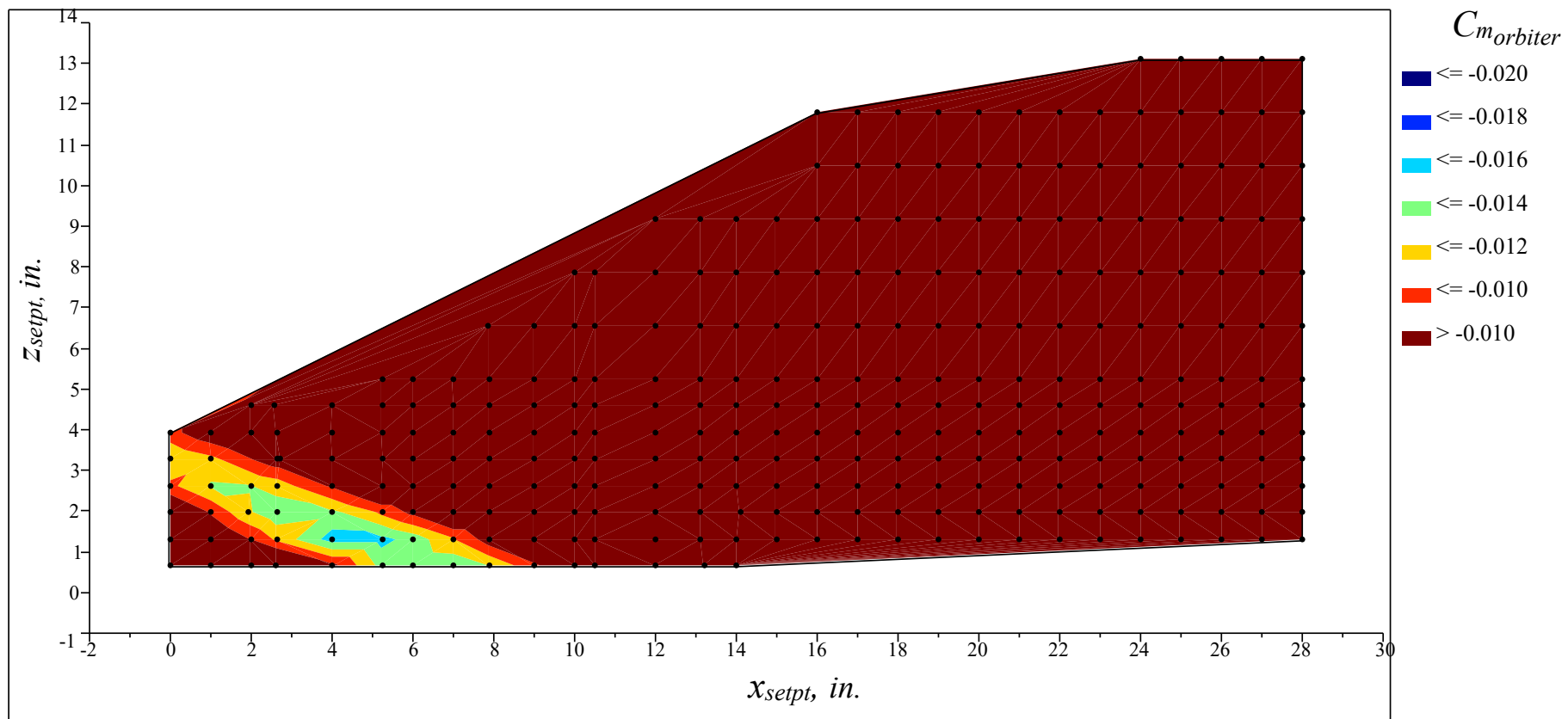
(c) Orbiter axial force coefficient,  $\Delta\alpha = 0^\circ$

Figure 29. Continued.



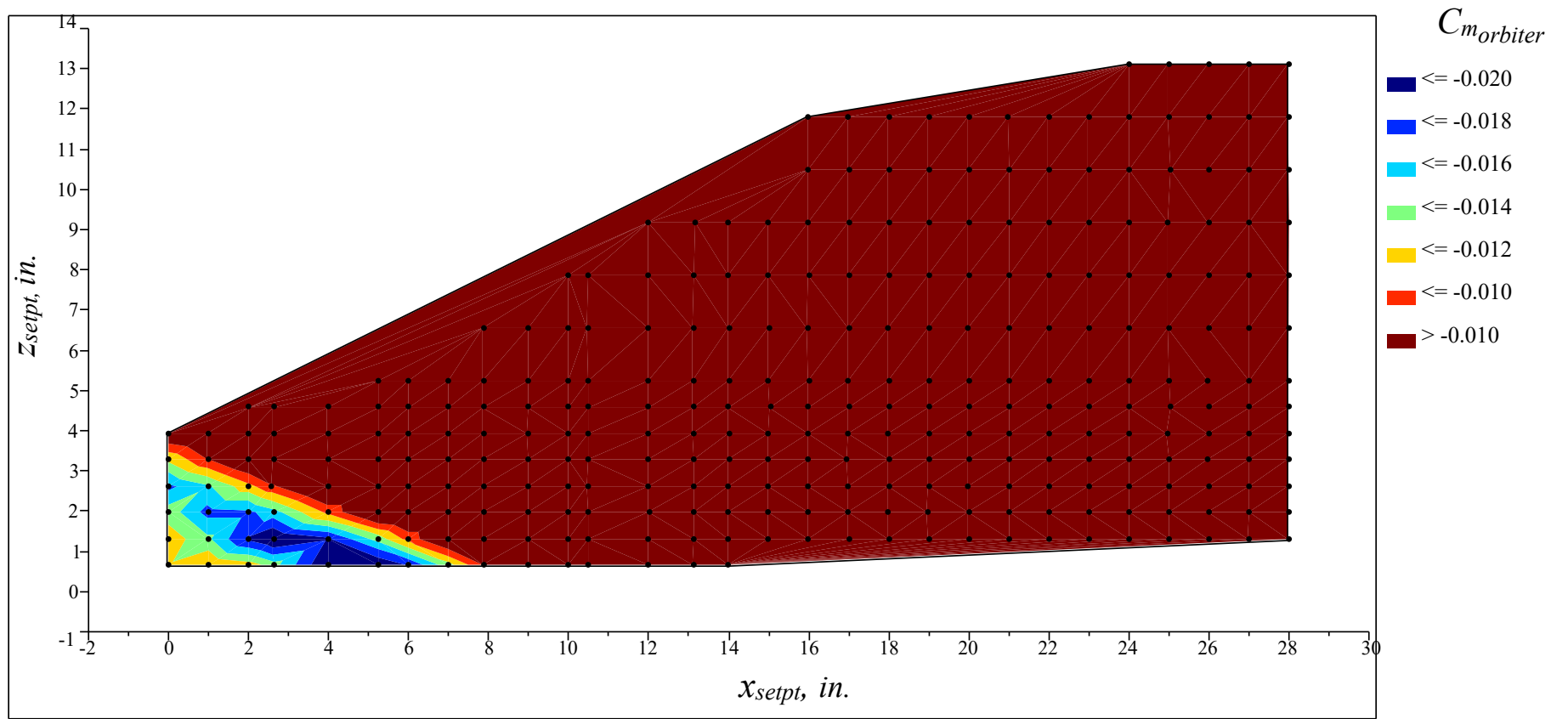
(d) Orbiter axial force coefficient,  $\Delta\alpha = 5^\circ$

Figure 29. Continued.



(e) Orbiter pitching moment coefficient,  $\Delta\alpha = 0^\circ$

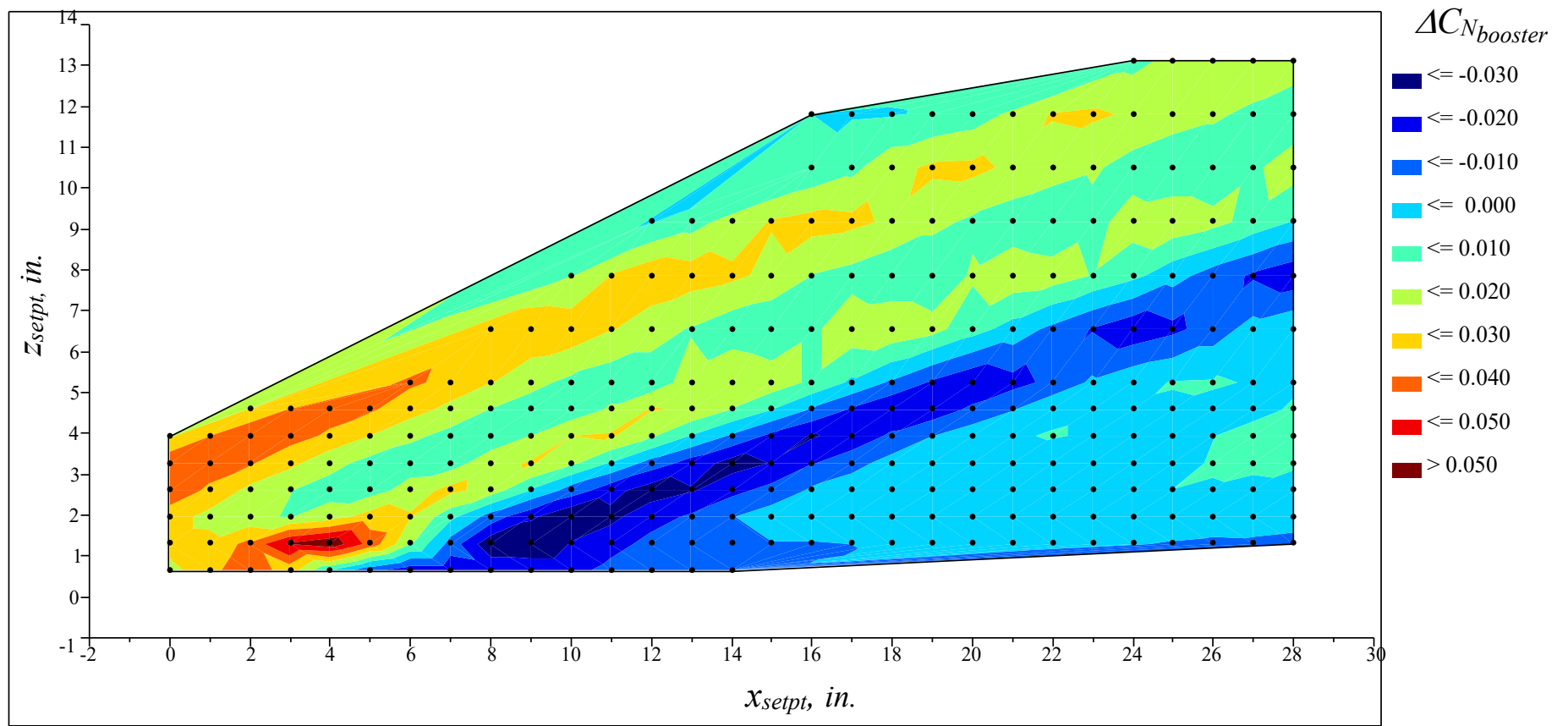
Figure 29. Continued.



(f) Orbiter pitching moment coefficient,  $\Delta\alpha = 5^\circ$

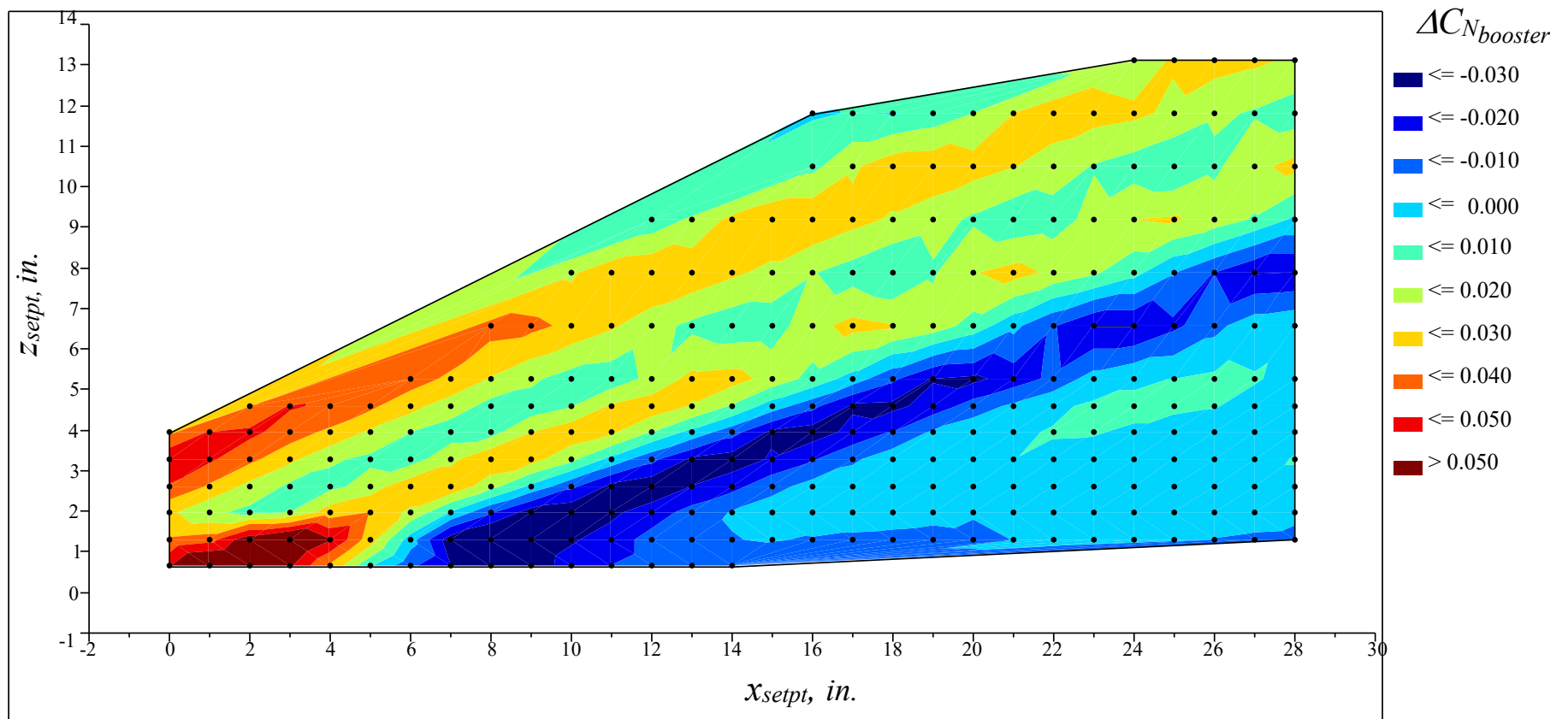
Figure 29. Concluded.





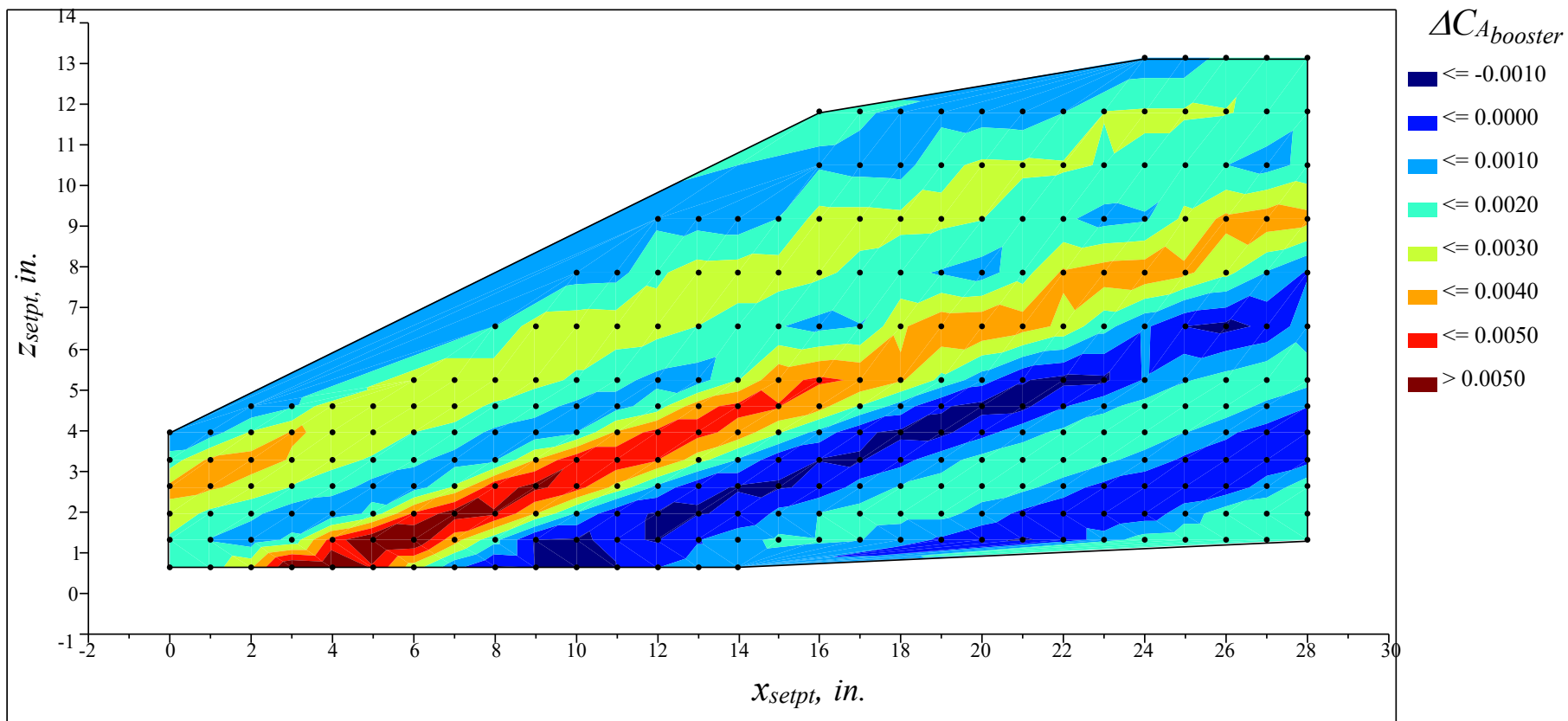
(a) Booster incremental normal force coefficient,  $\Delta\alpha = 0^\circ$

Figure 30. Contour plots of the booster aerodynamic interference increments at Mach = 3.0,  $\Delta\alpha = 0^\circ$  and  $5^\circ$ .



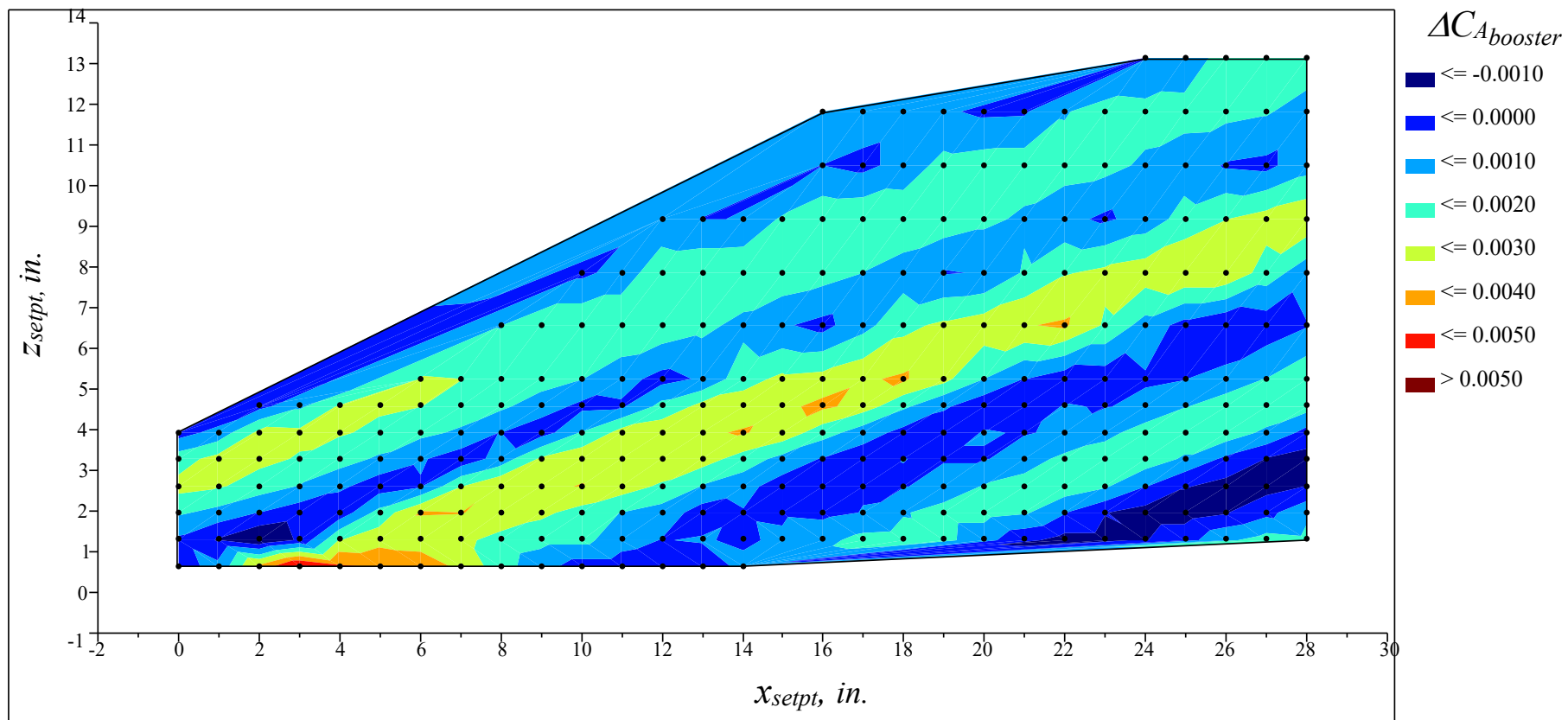
(b) Booster incremental normal force coefficient,  $\Delta\alpha = 5^\circ$

Figure 30. Continued.



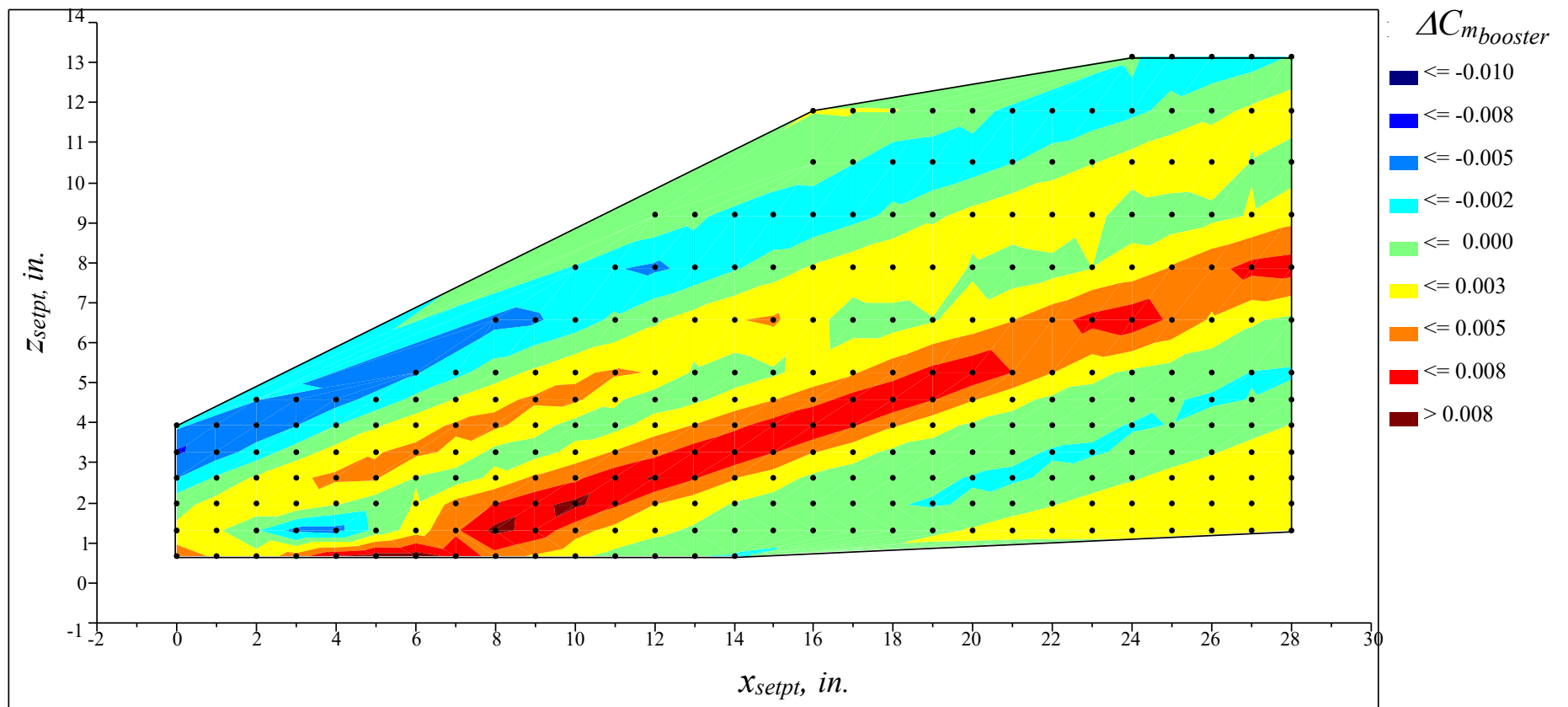
(c) Booster incremental axial force coefficient,  $\Delta\alpha = 0^\circ$

Figure 30. Continued.



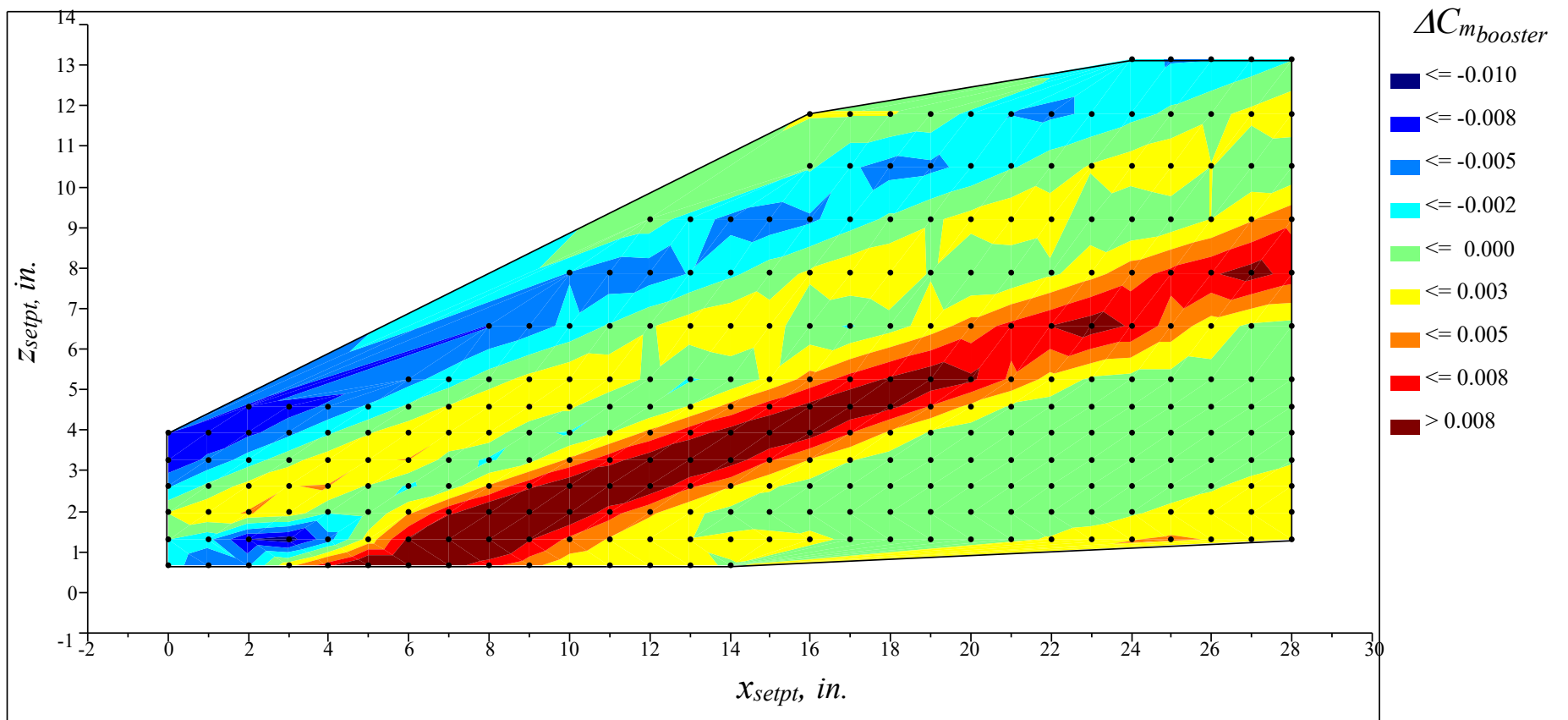
(d) Booster incremental axial force coefficient,  $\Delta\alpha = 5^\circ$

Figure 30. Continued.



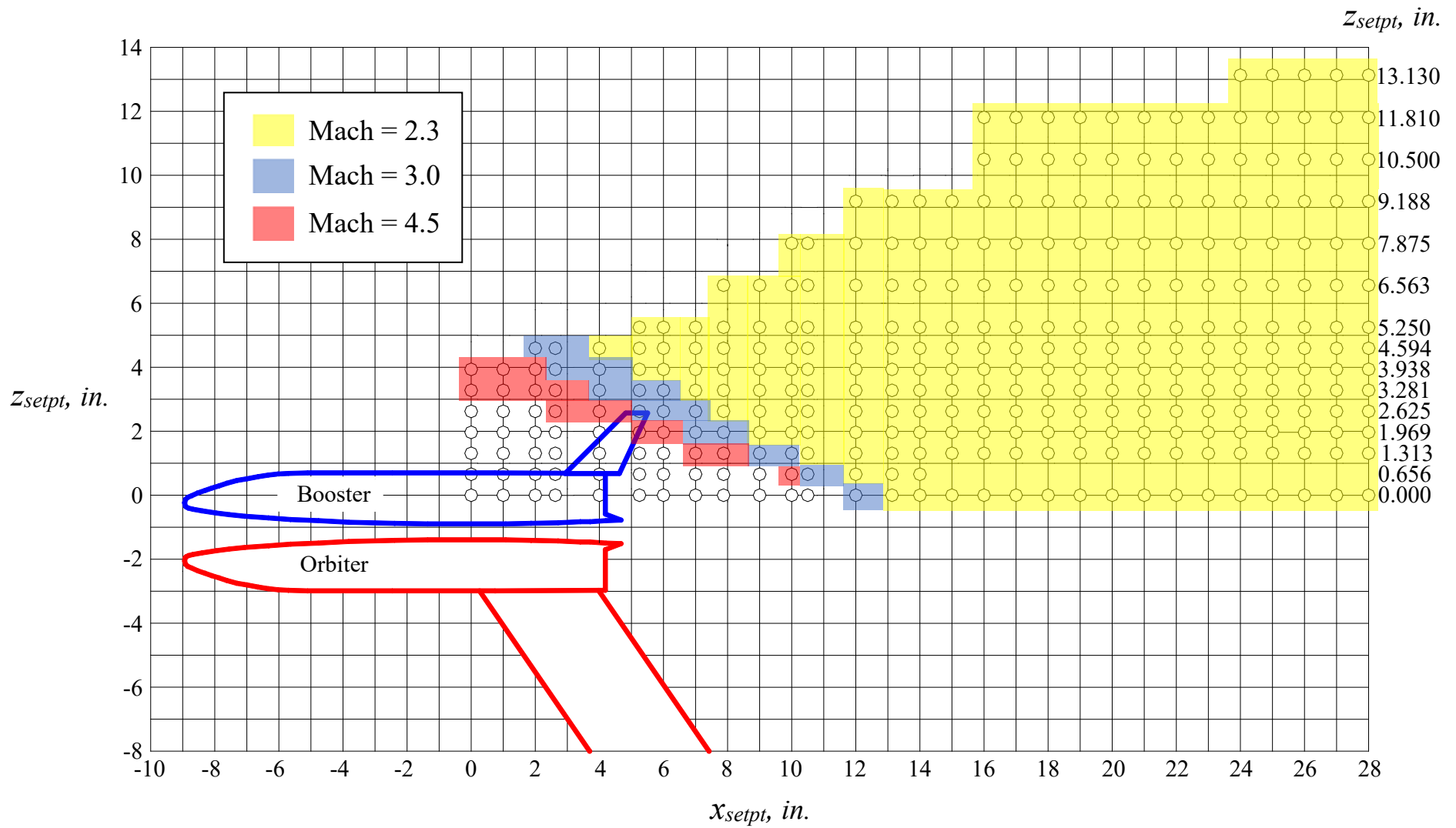
(e) Booster incremental pitching moment coefficient,  $\Delta\alpha = 0^\circ$

Figure 30. Continued.



(f) Booster incremental pitching moment coefficient,  $\Delta \alpha = 5^\circ$

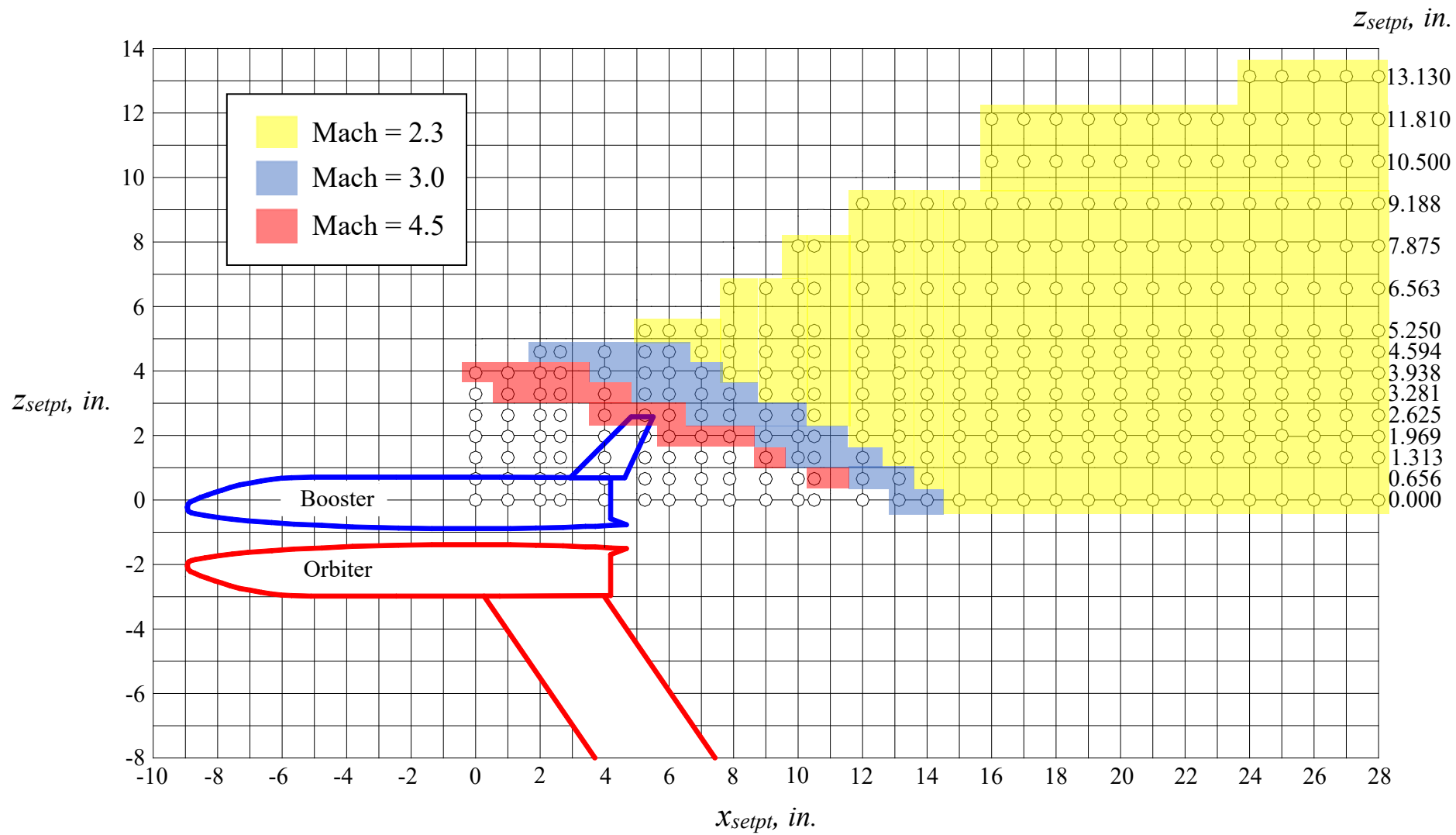
Figure 30. Concluded.



(a) Orbiter normal force coefficient,  $C_{N_{orbiter}}$

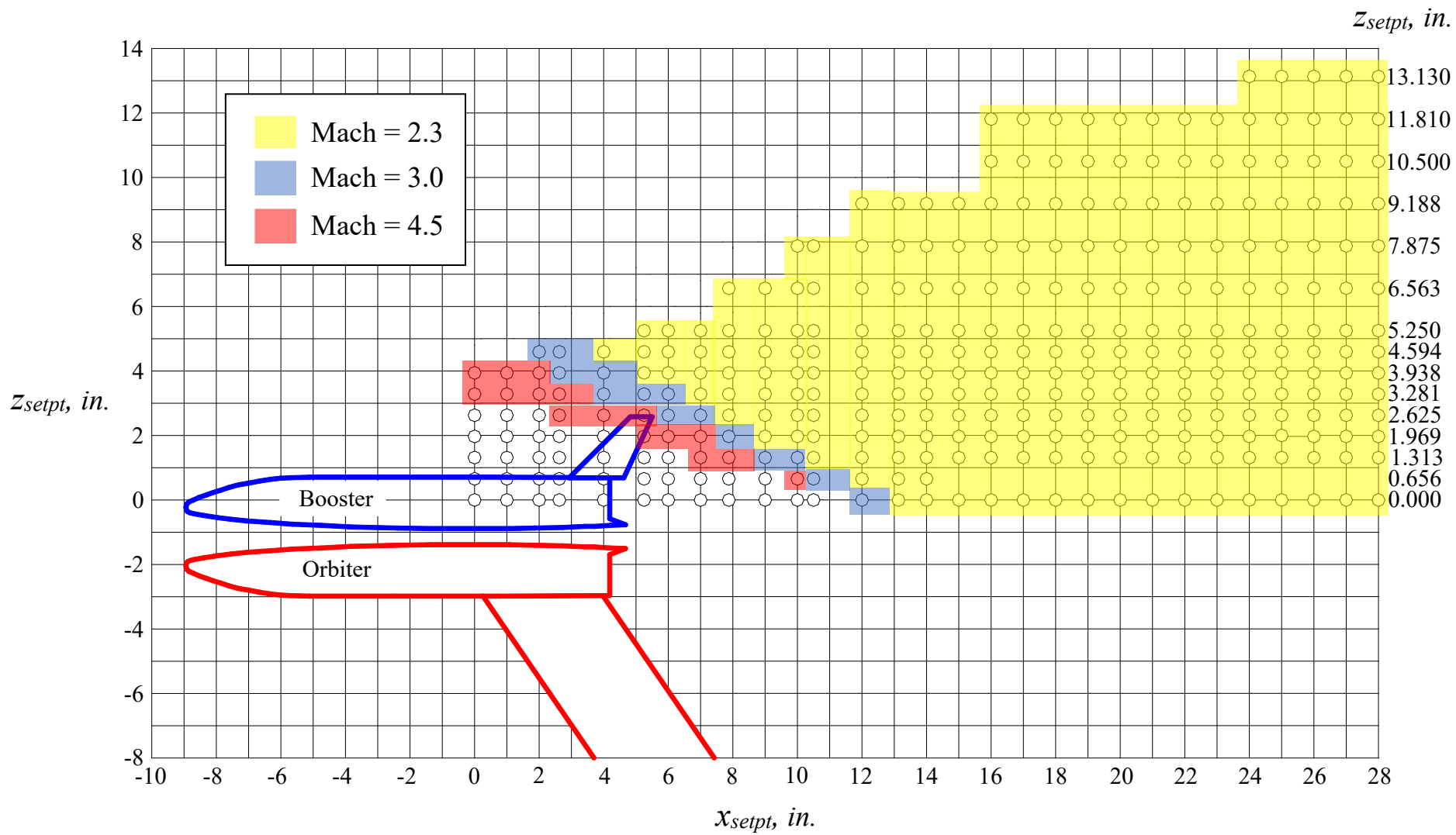
Figure 31. Influence of the booster on the orbiter aerodynamic characteristics at Mach = 2.3, 3.0, and 4.5;  $\Delta\alpha = 0^\circ$ .  
(Shaded regions denote the areas in which the orbiter aerodynamic coefficients are not affected by the booster.)





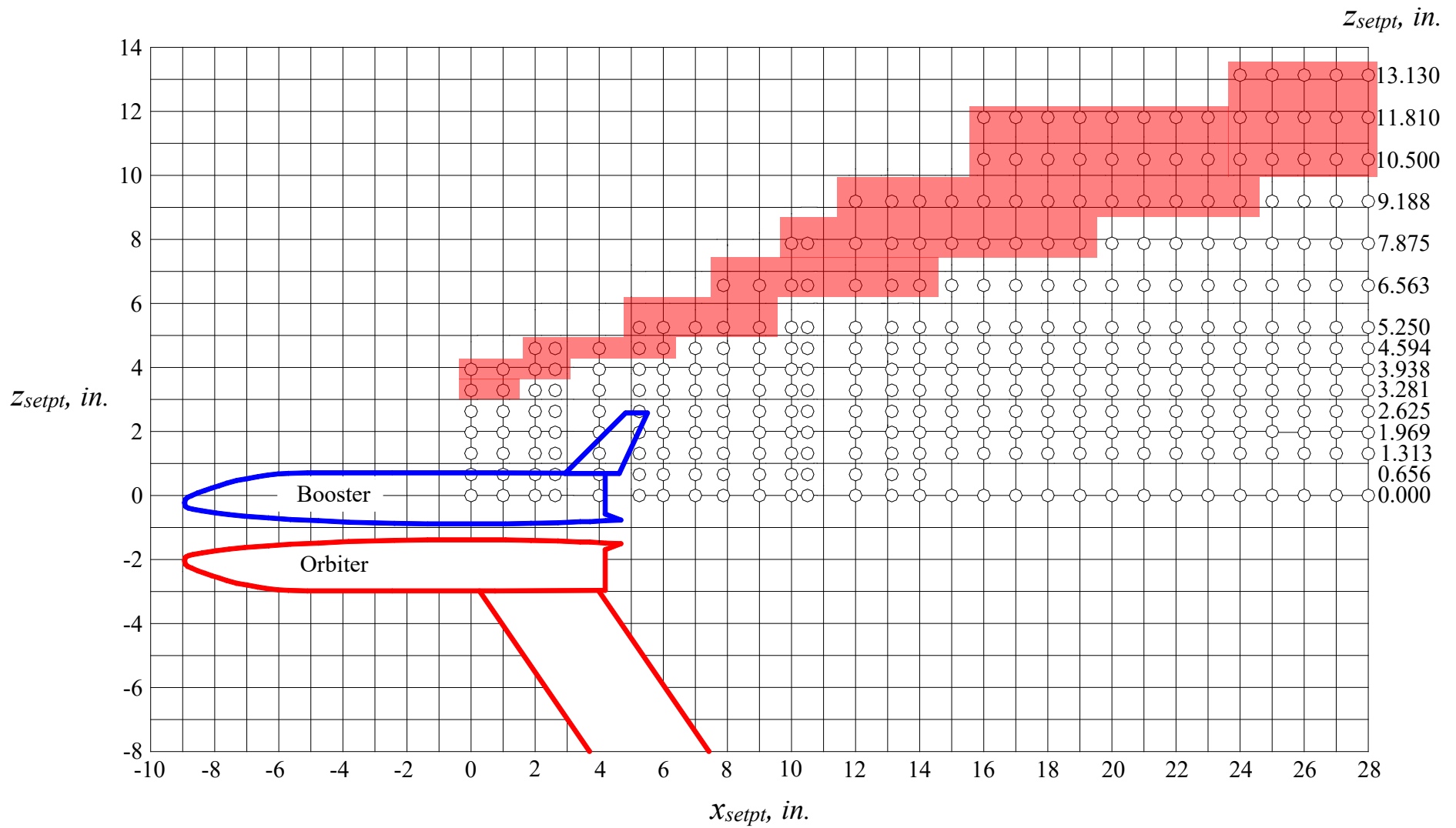
(b) Orbiter axial force coefficient,  $C_{A_{orbiter}}$

Figure 31. Continued.



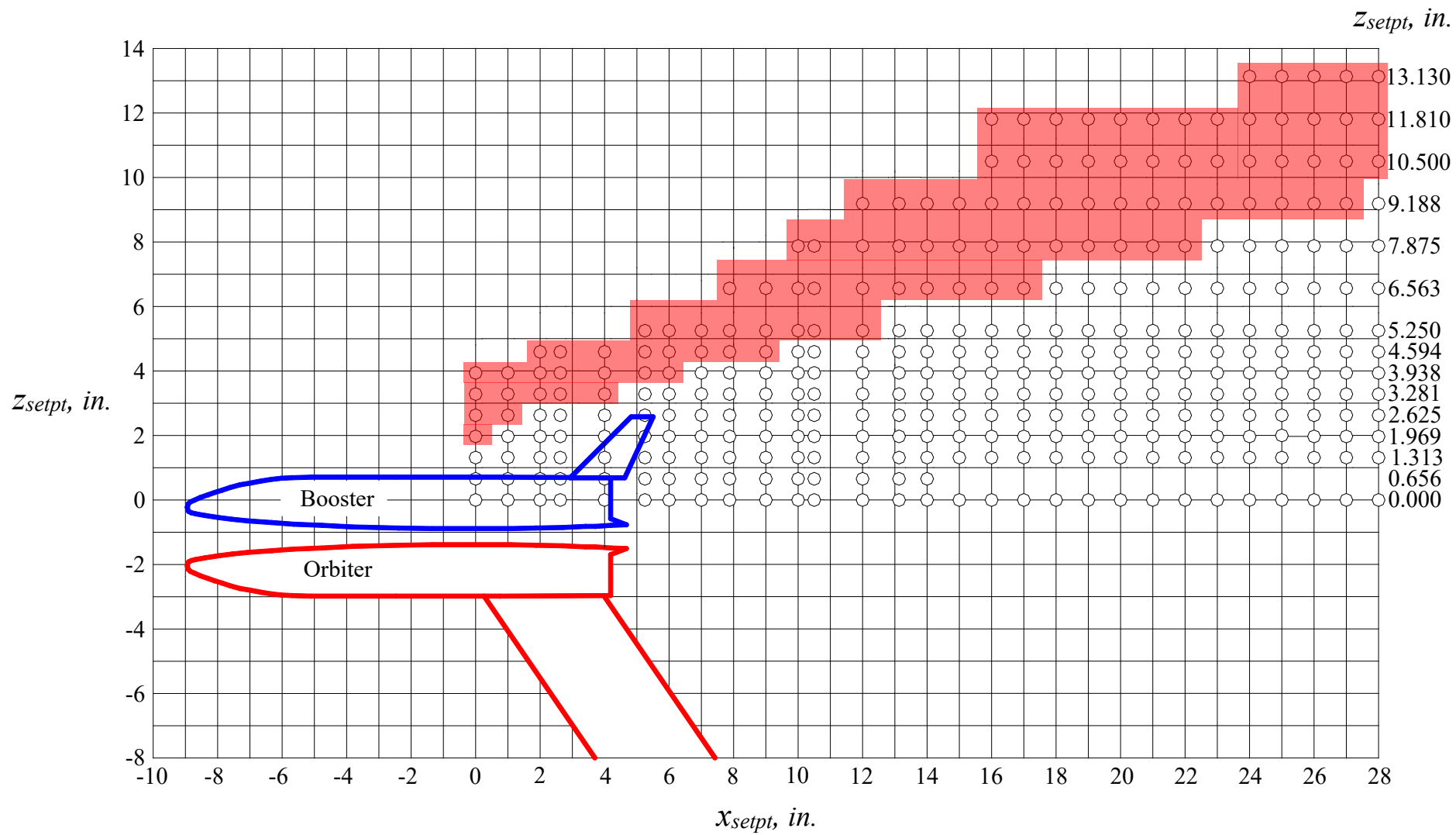
(c) Orbiter pitching moment coefficient,  $C_{m_{orbiter}}$

Figure 31. Concluded.



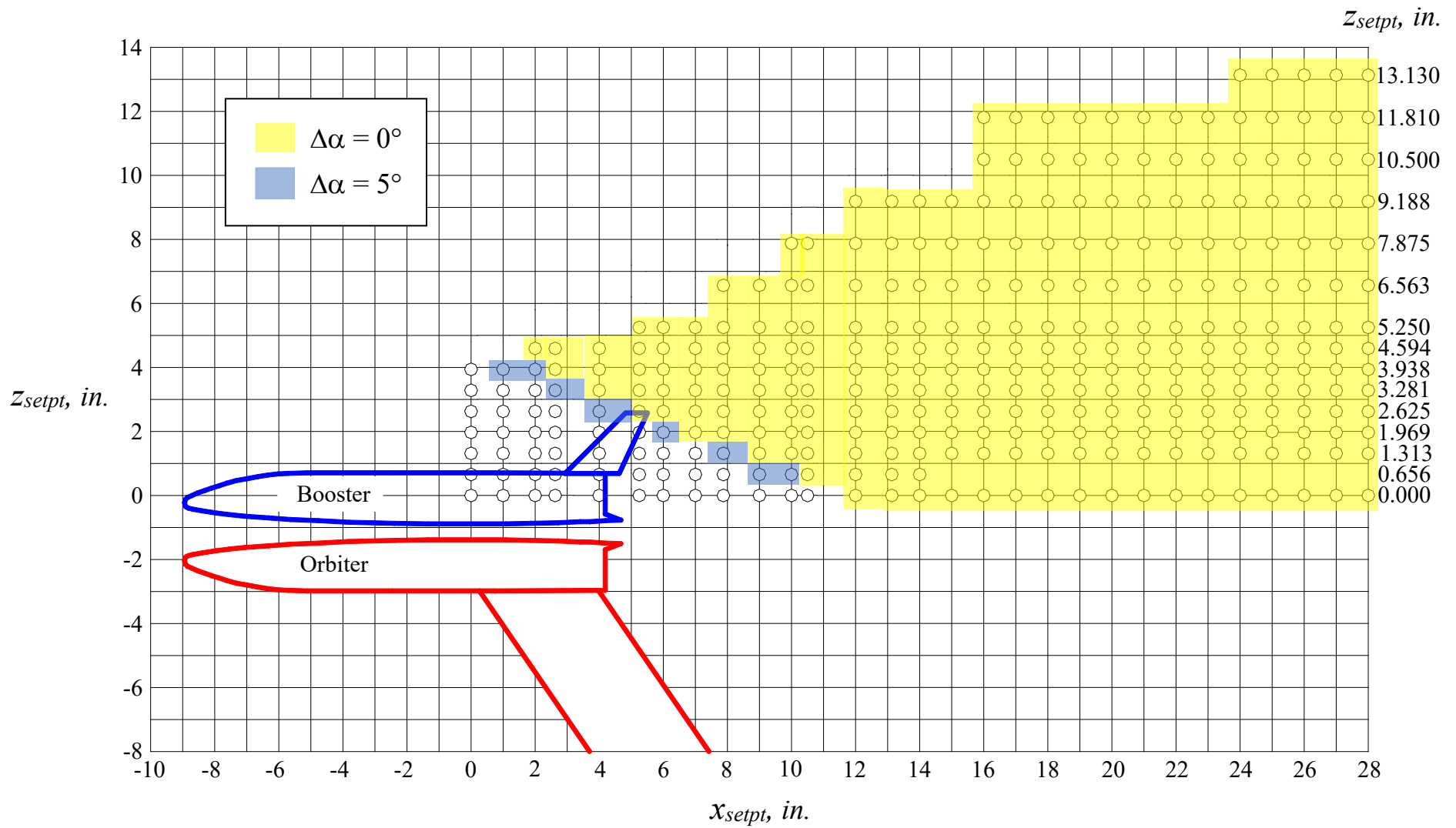
(a) Booster normal force and pitching moment coefficients,  $C_{N_{booster}}$  and  $C_{m_{booster}}$

Figure 32. Influence of the orbiter on the booster aerodynamic characteristics at  $Mach = 4.5$ ;  $\Delta\alpha = 0^\circ$ .  
(Shaded regions denote the areas in which the booster aerodynamic coefficients are not affected by the orbiter.)



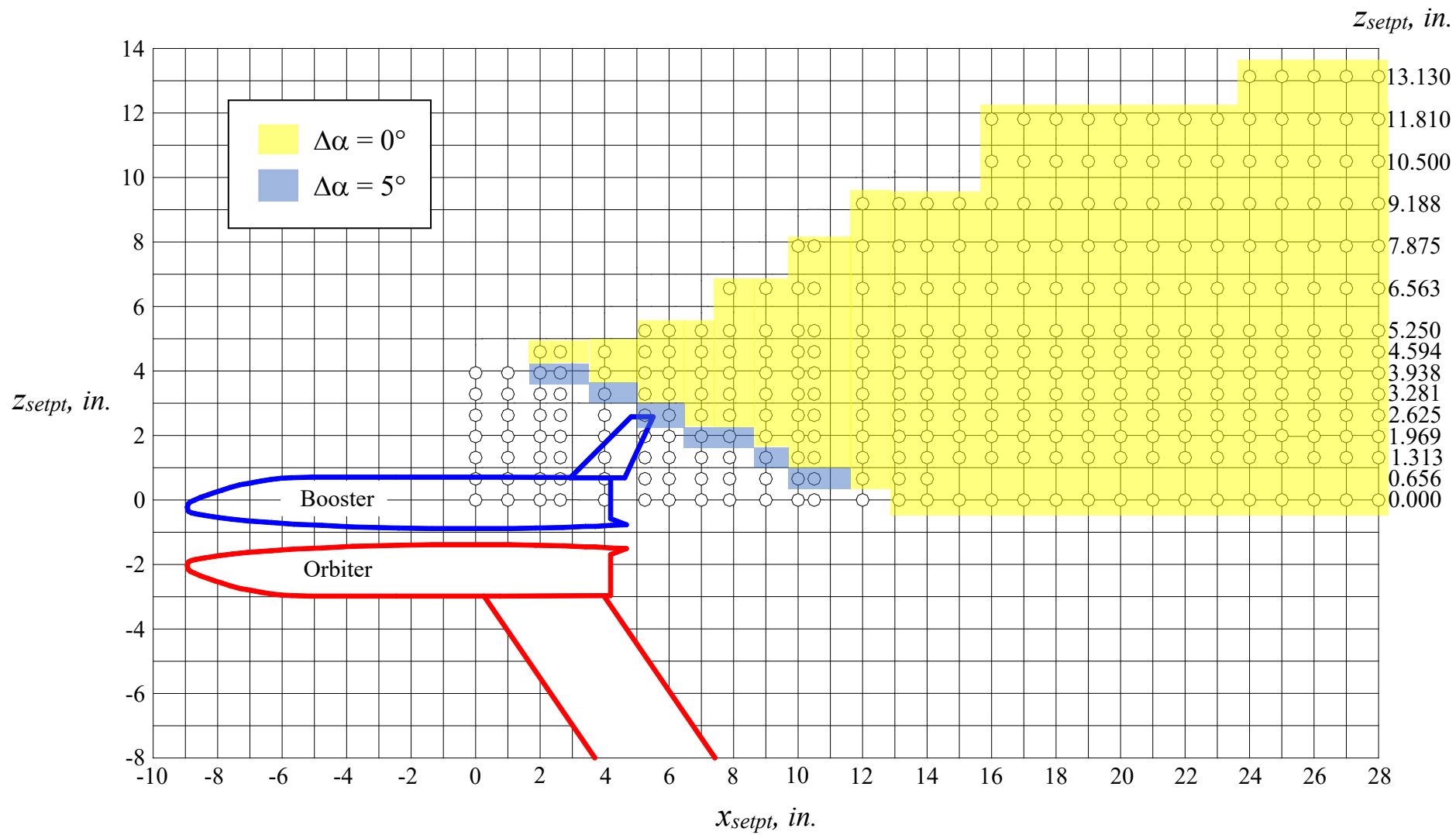
(b) Booster axial force coefficient,  $C_{A_{booster}}$

Figure 32. Concluded.



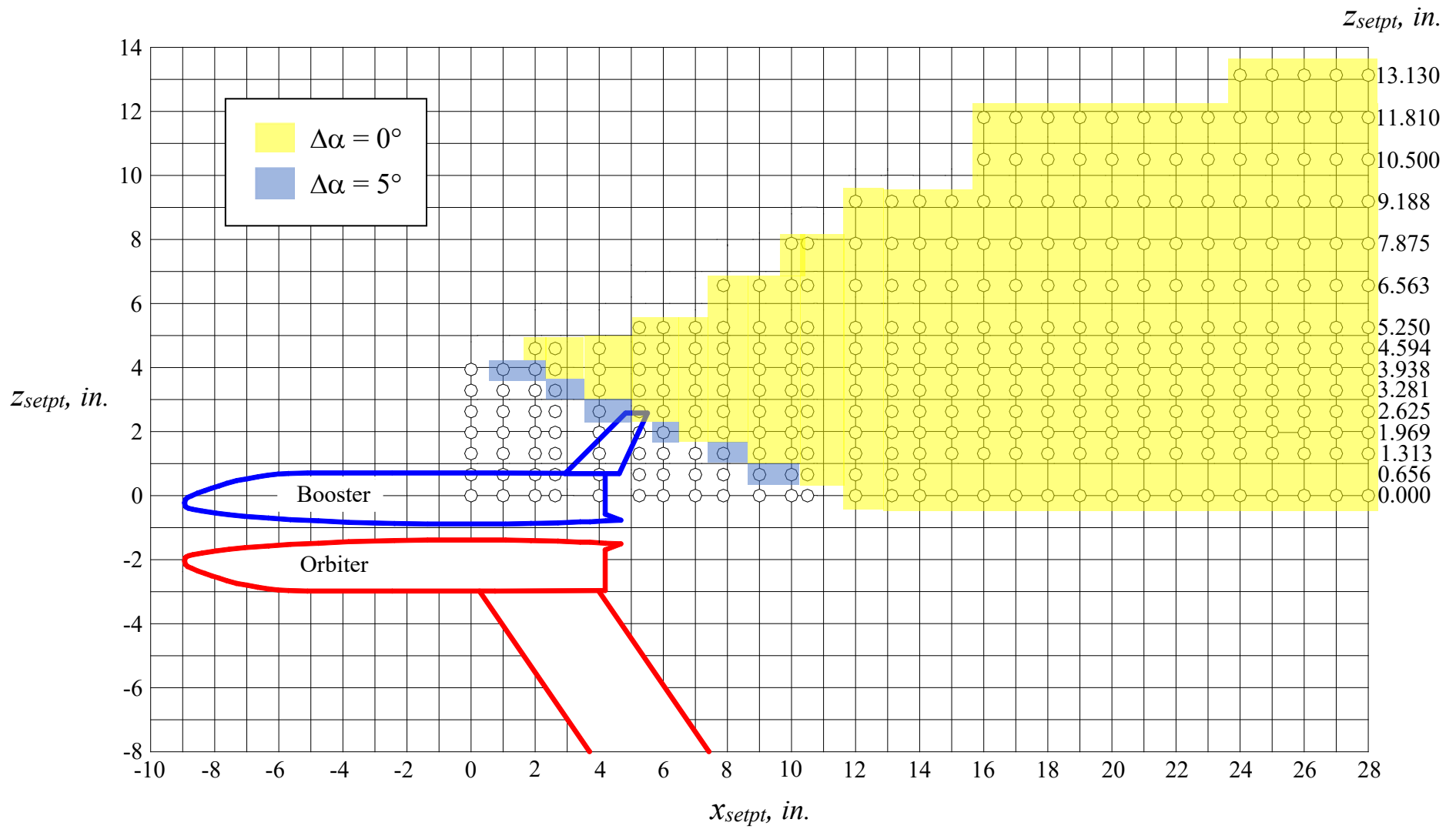
(a) Orbiter normal force coefficient,  $C_{N_{orbiter}}$

Figure 33. Influence of the booster on the orbiter aerodynamic characteristics at Mach = 3.0 and  $\Delta\alpha = 0^\circ$  and  $5^\circ$ .  
(Shaded regions denote the areas in which the orbiter aerodynamic coefficients are not affected by the booster.)



(b) Orbiter axial force coefficient,  $C_{A_{orbiter}}$

Figure 33. Continued.



(c) Orbiter pitching moment coefficient,  $C_{m_{orbiter}}$

Figure 33. Concluded.



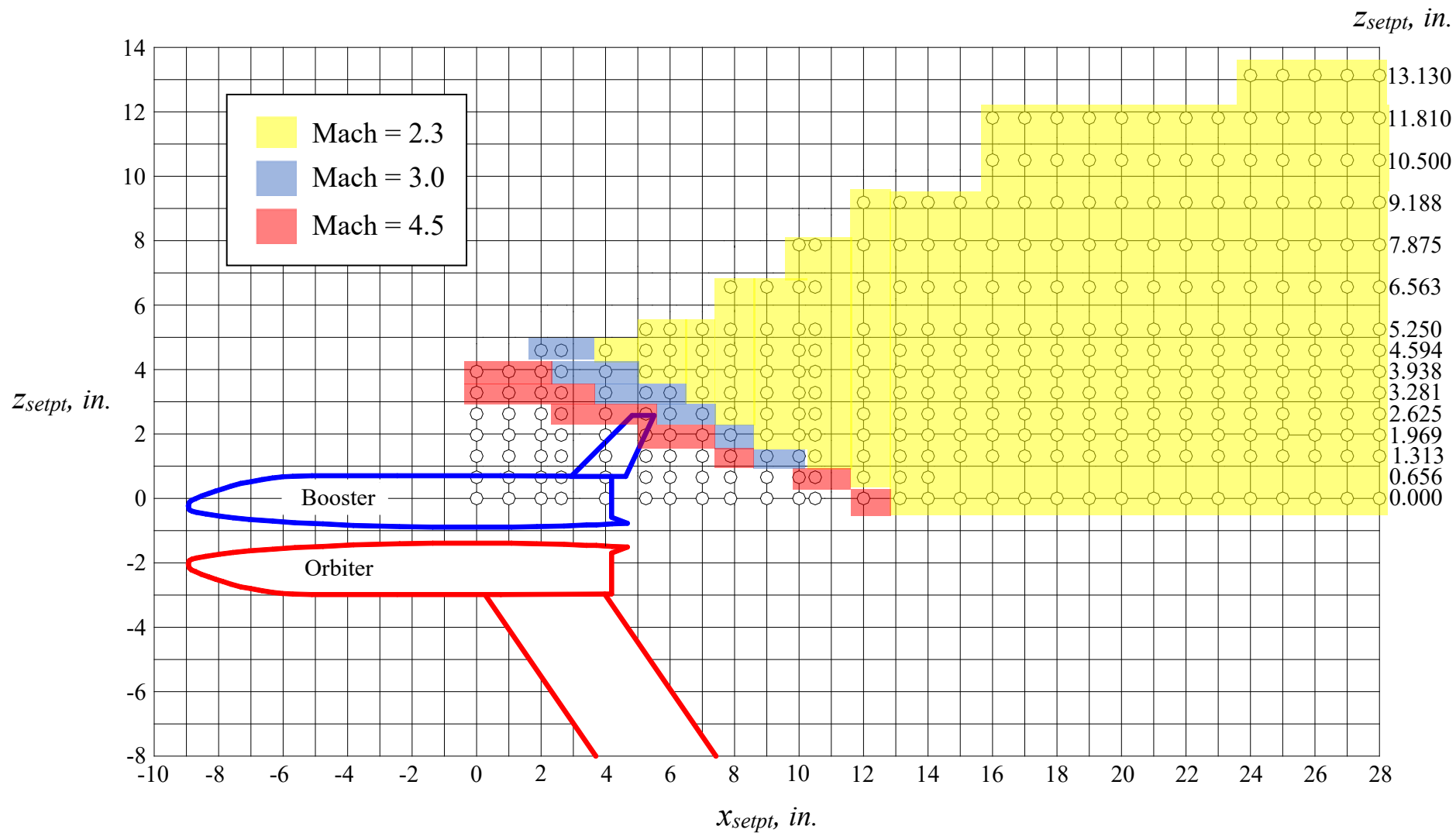


Figure 34. Influence of the booster on the orbiter surface static pressure coefficients at Mach = 2.3, 3.0, and 4.5;  $\Delta\alpha = 0^\circ$ . (Shaded regions denote the areas in which the orbiter pressure coefficients are not affected by the booster.)

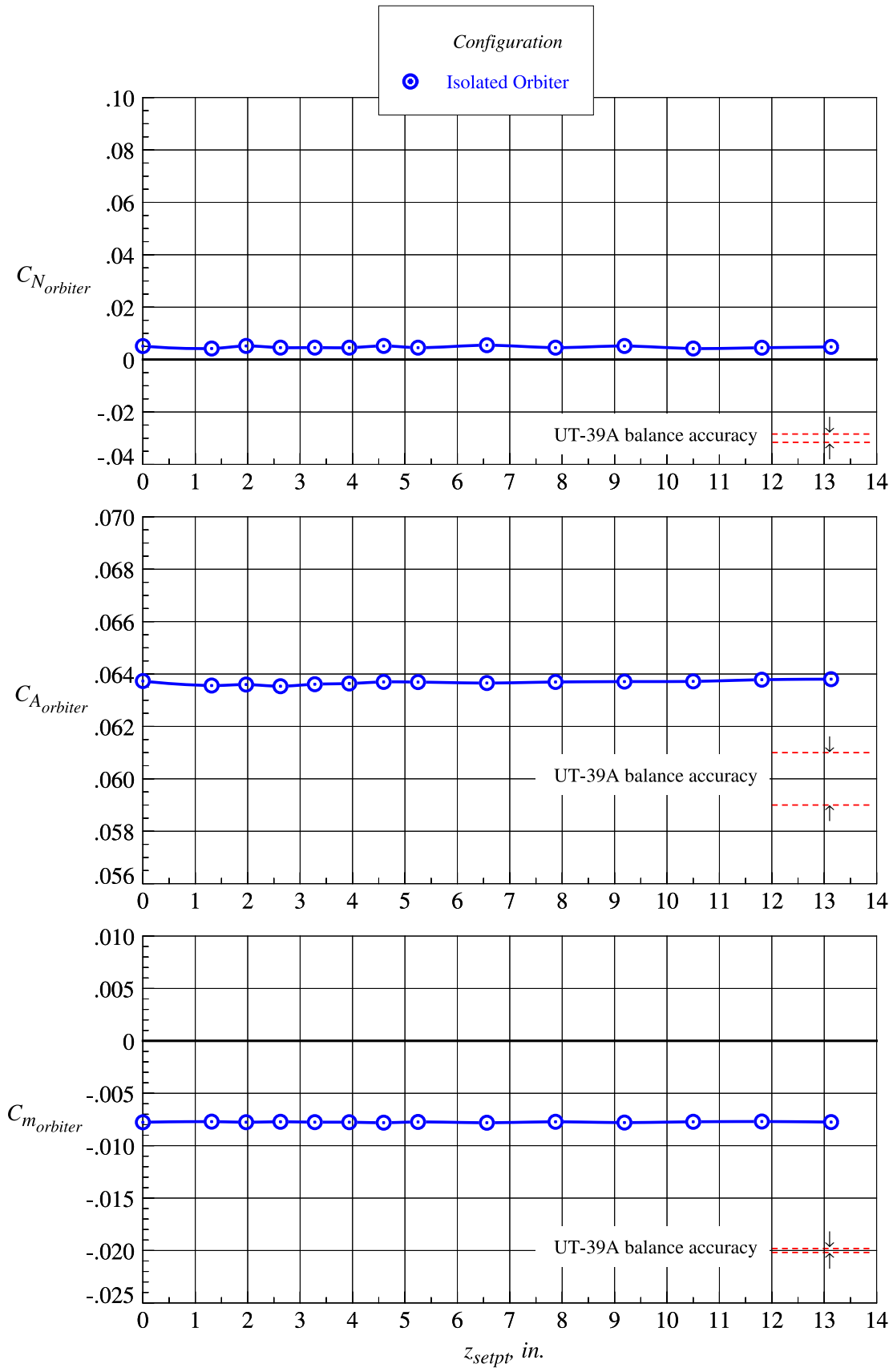


Figure 35. Data repeatability of the isolated orbiter at Mach = 2.3; booster at  $x_{setpt} = 28$  inches.

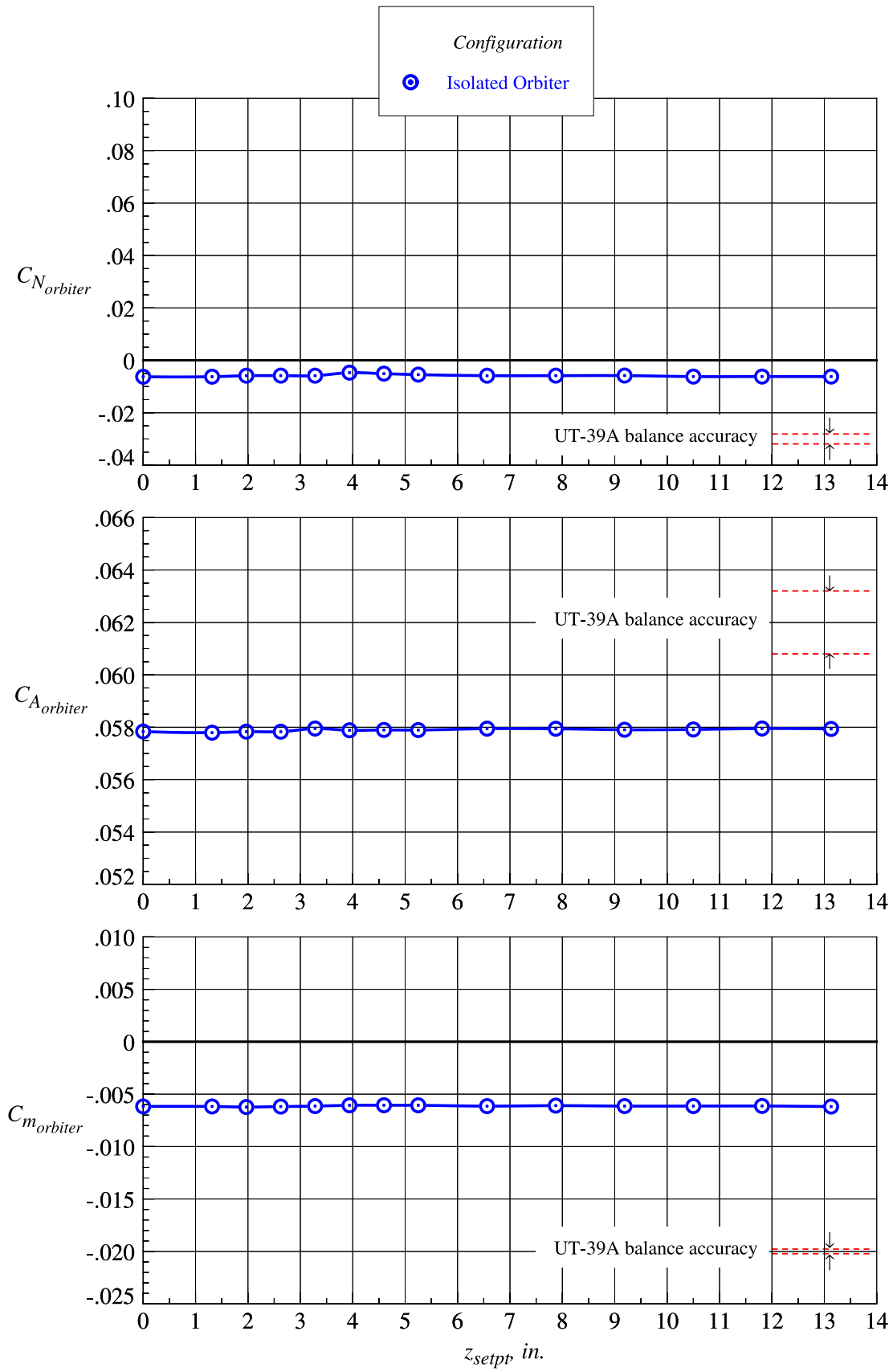


Figure 36. Data repeatability of the isolated orbiter at Mach = 3.0; booster at  $x_{setpb} = 28$  inches.

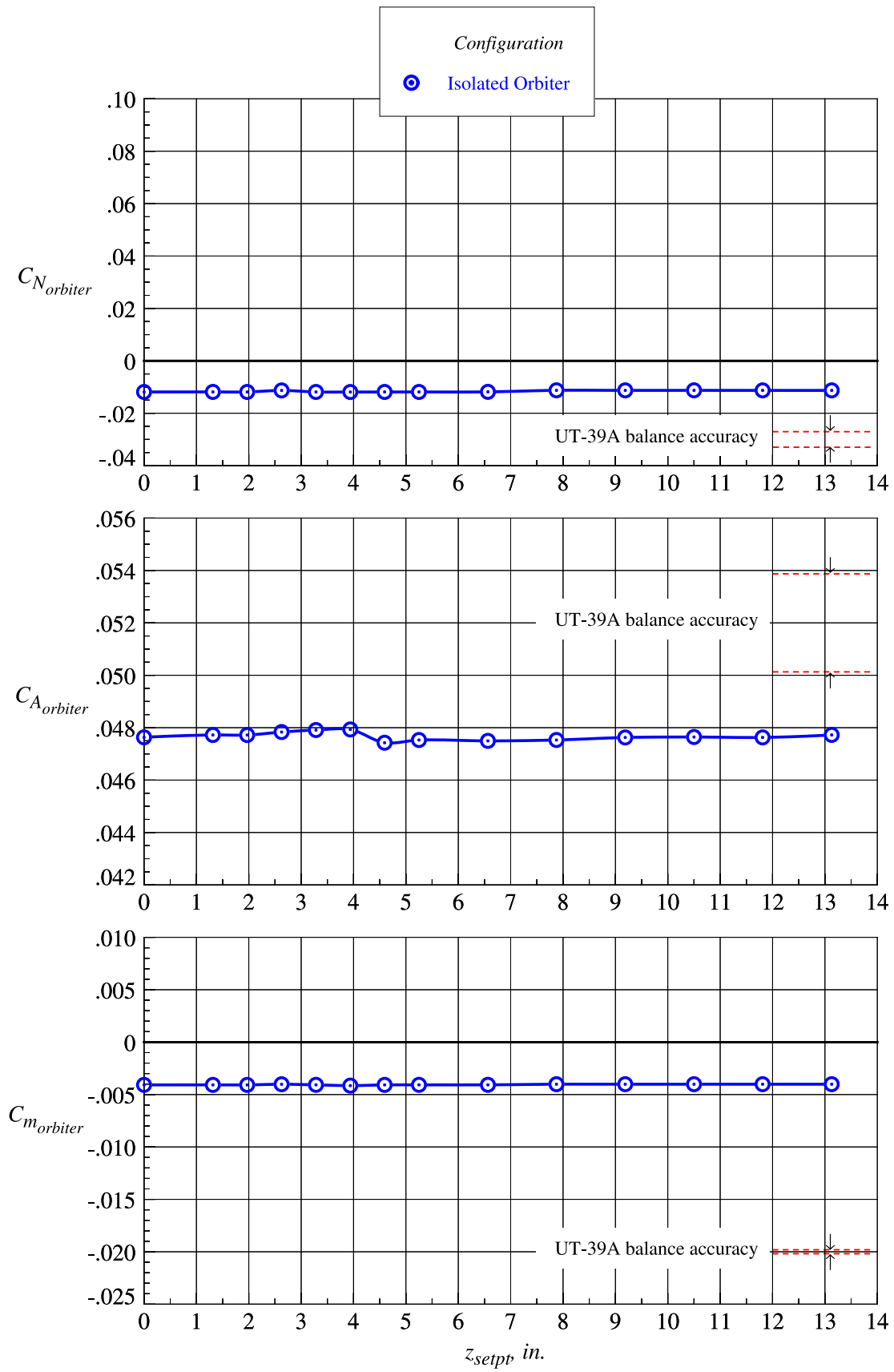
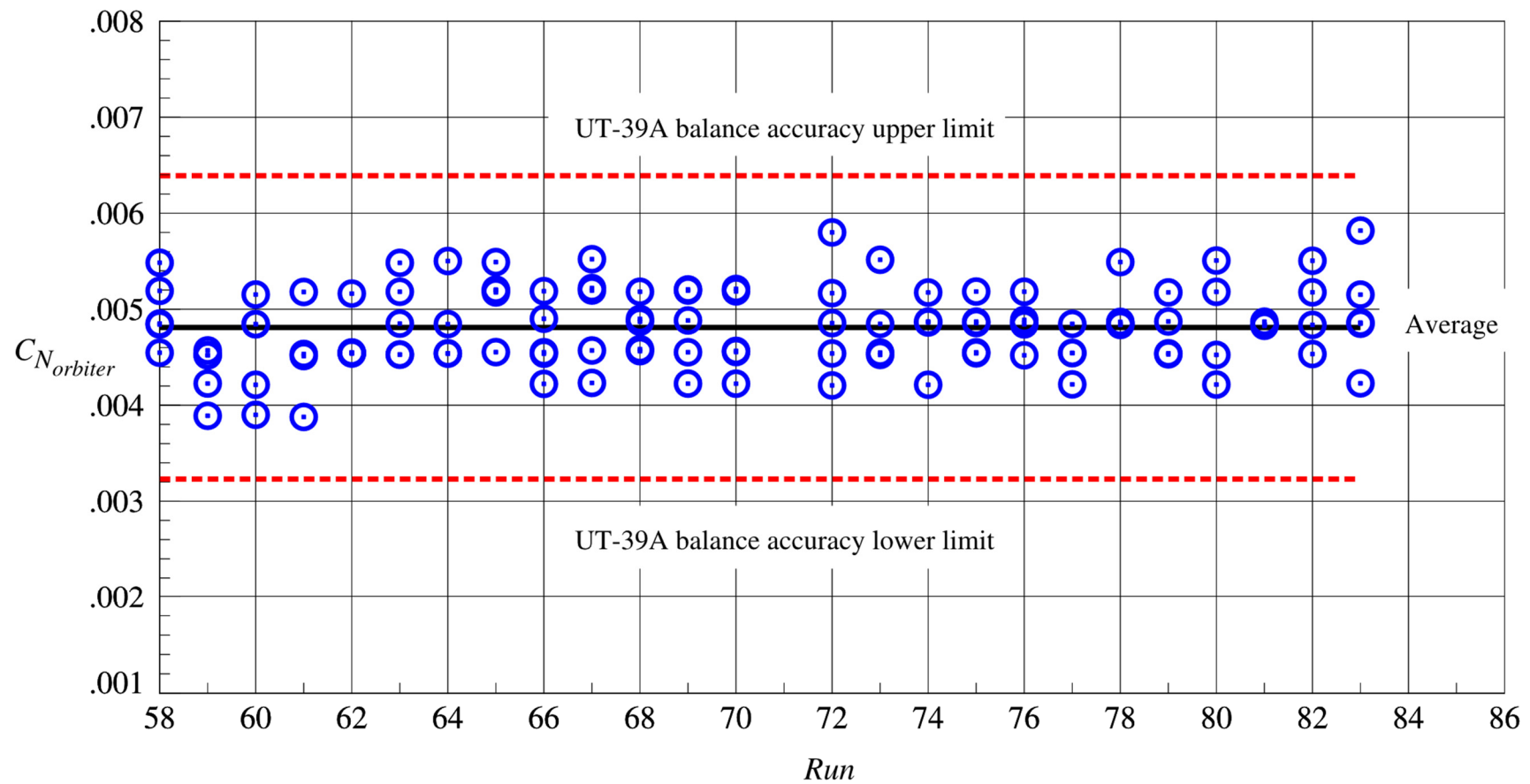
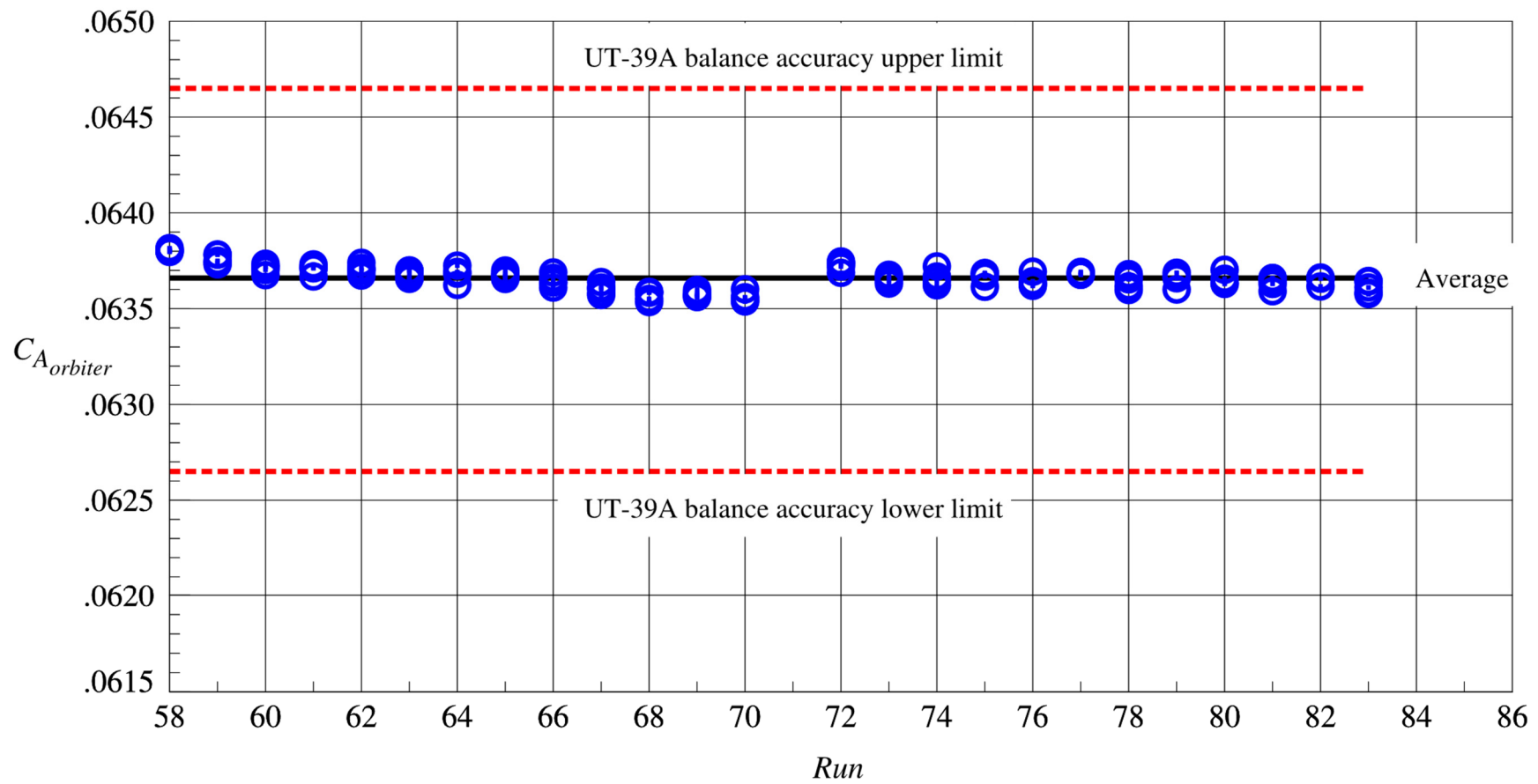


Figure 37. Data repeatability of the isolated orbiter at Mach = 4.5; booster at  $x_{setpp} = 28$  inches.



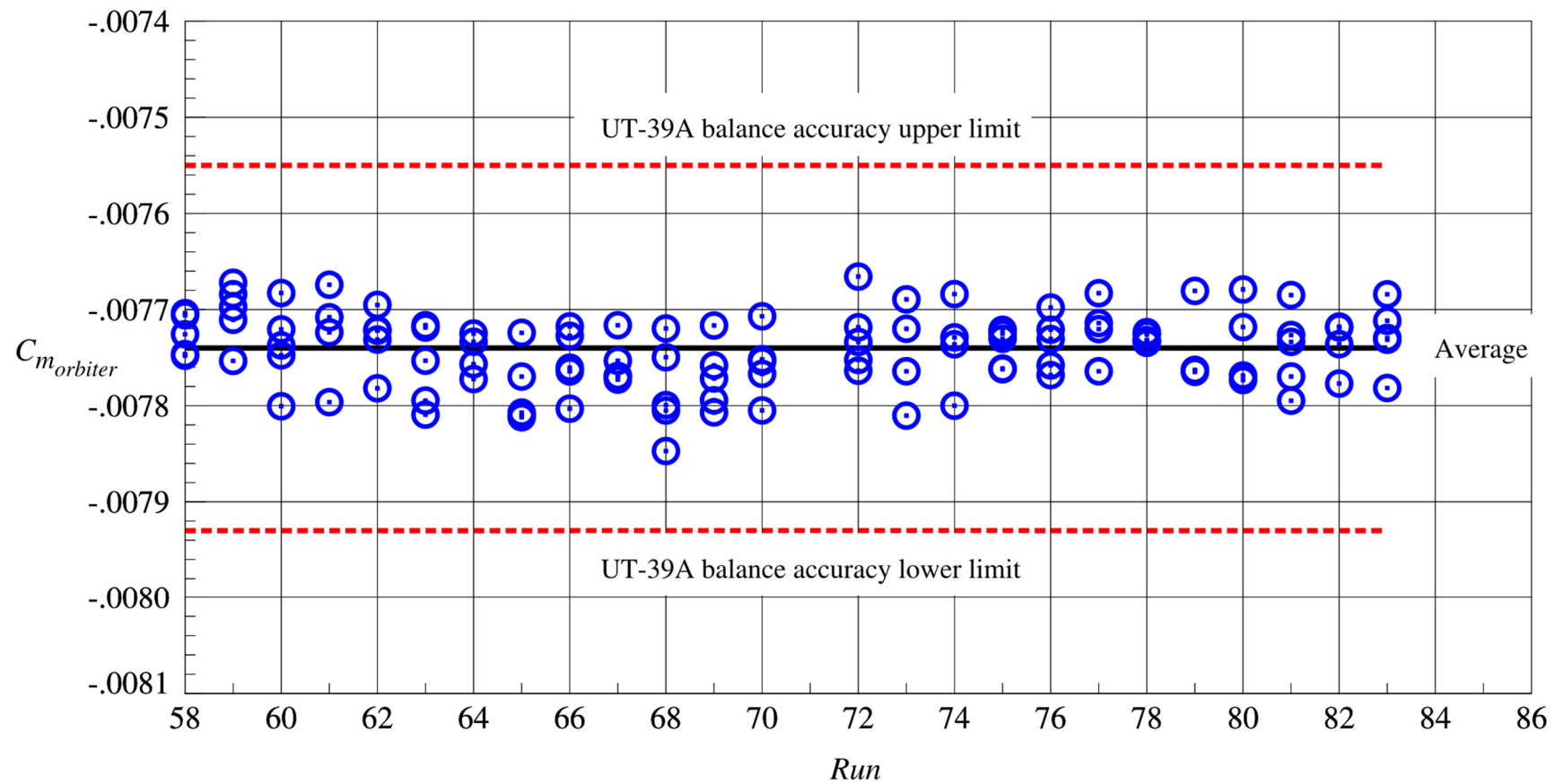
(a) Orbiter normal force coefficient

Figure 38. Data repeatability of the isolated orbiter at Mach = 2.3; booster at  $x_{sept} = 24$  to 28 inches.



(b) Orbiter axial force coefficient

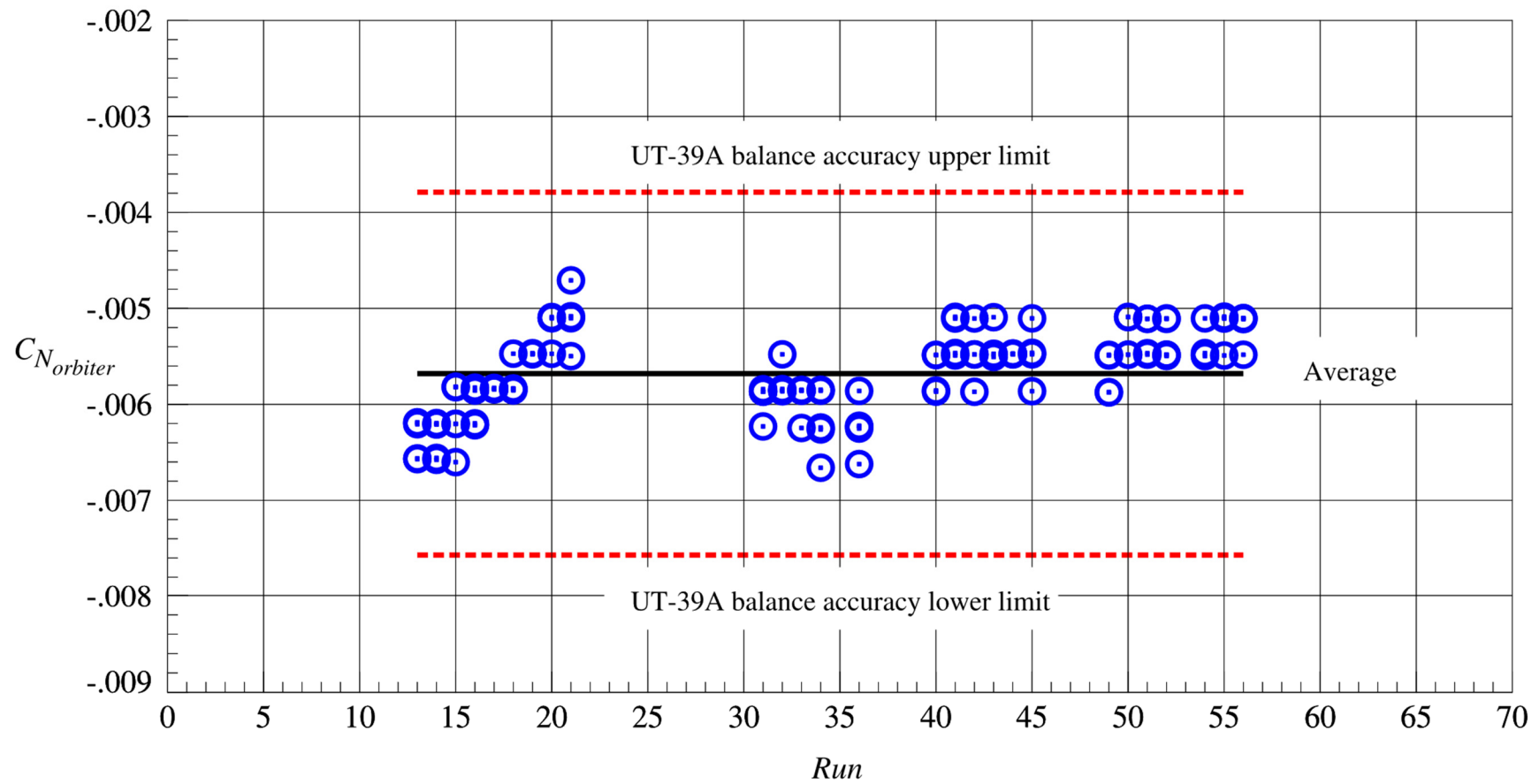
Figure 38. Continued.



(c) Orbiter pitching moment coefficient

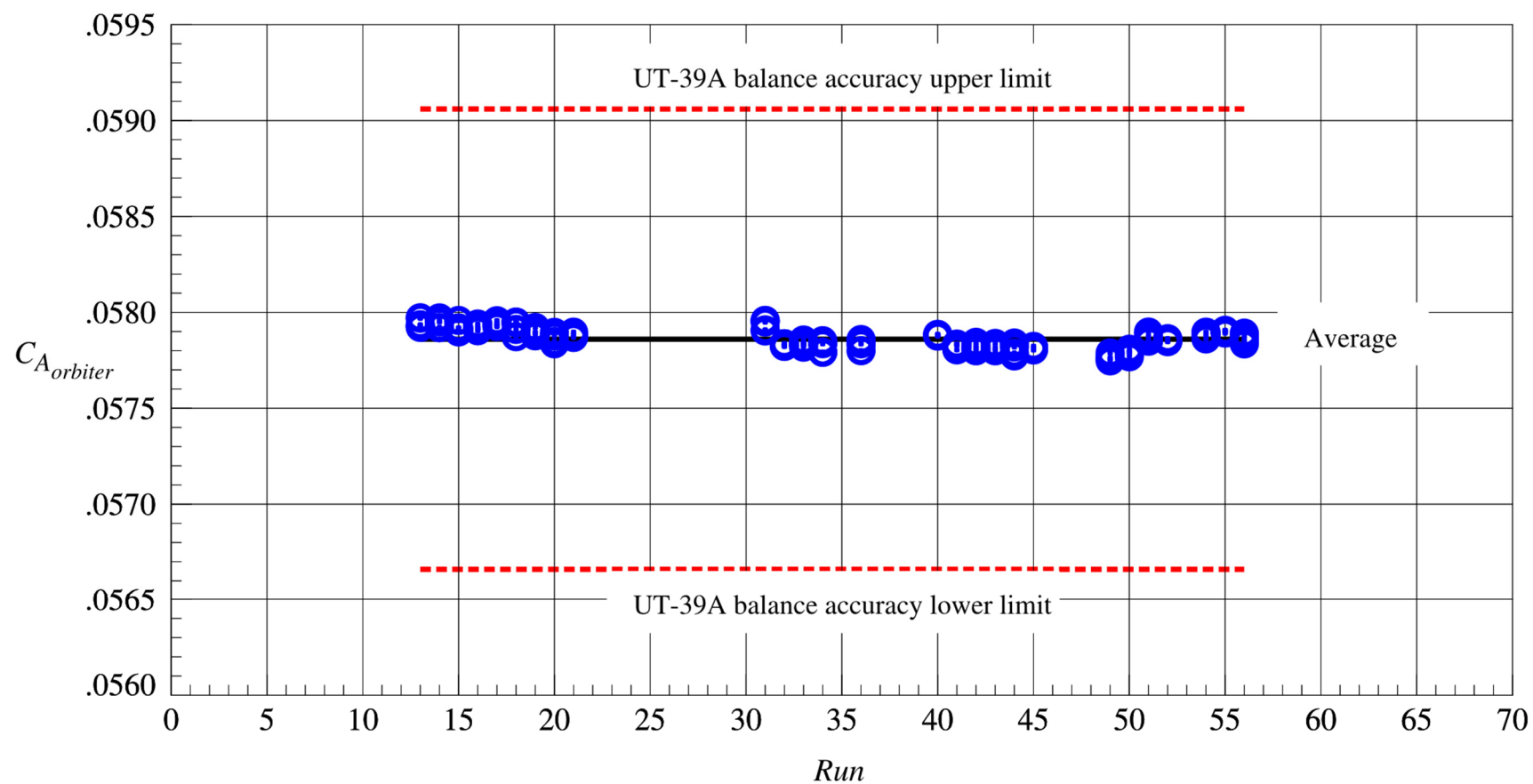
Figure 38. Concluded.





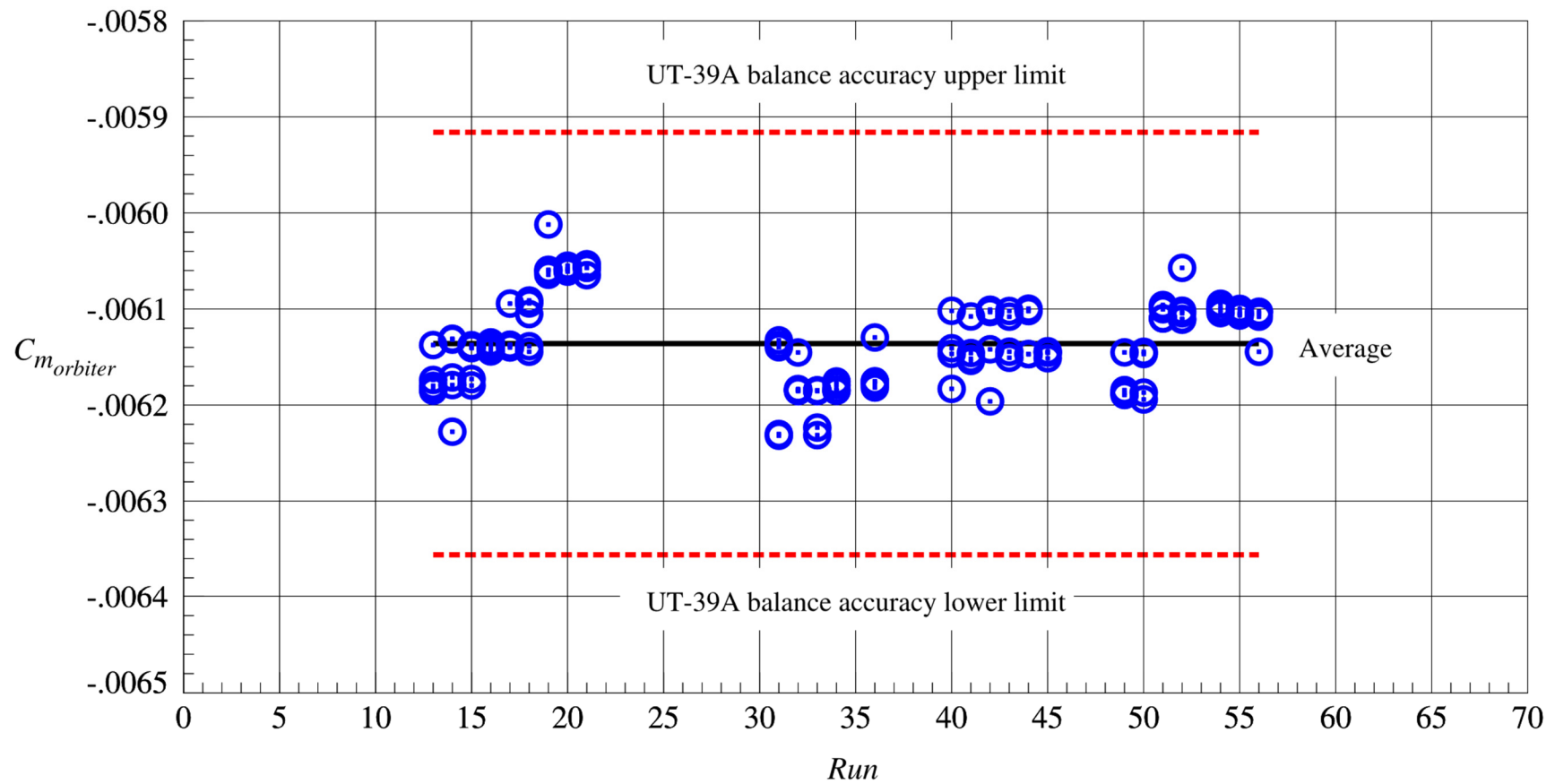
(a) Orbiter normal force coefficient

Figure 39. Data repeatability of the isolated orbiter at Mach = 3.0; booster at  $x_{sept} = 24$  to 28 inches.



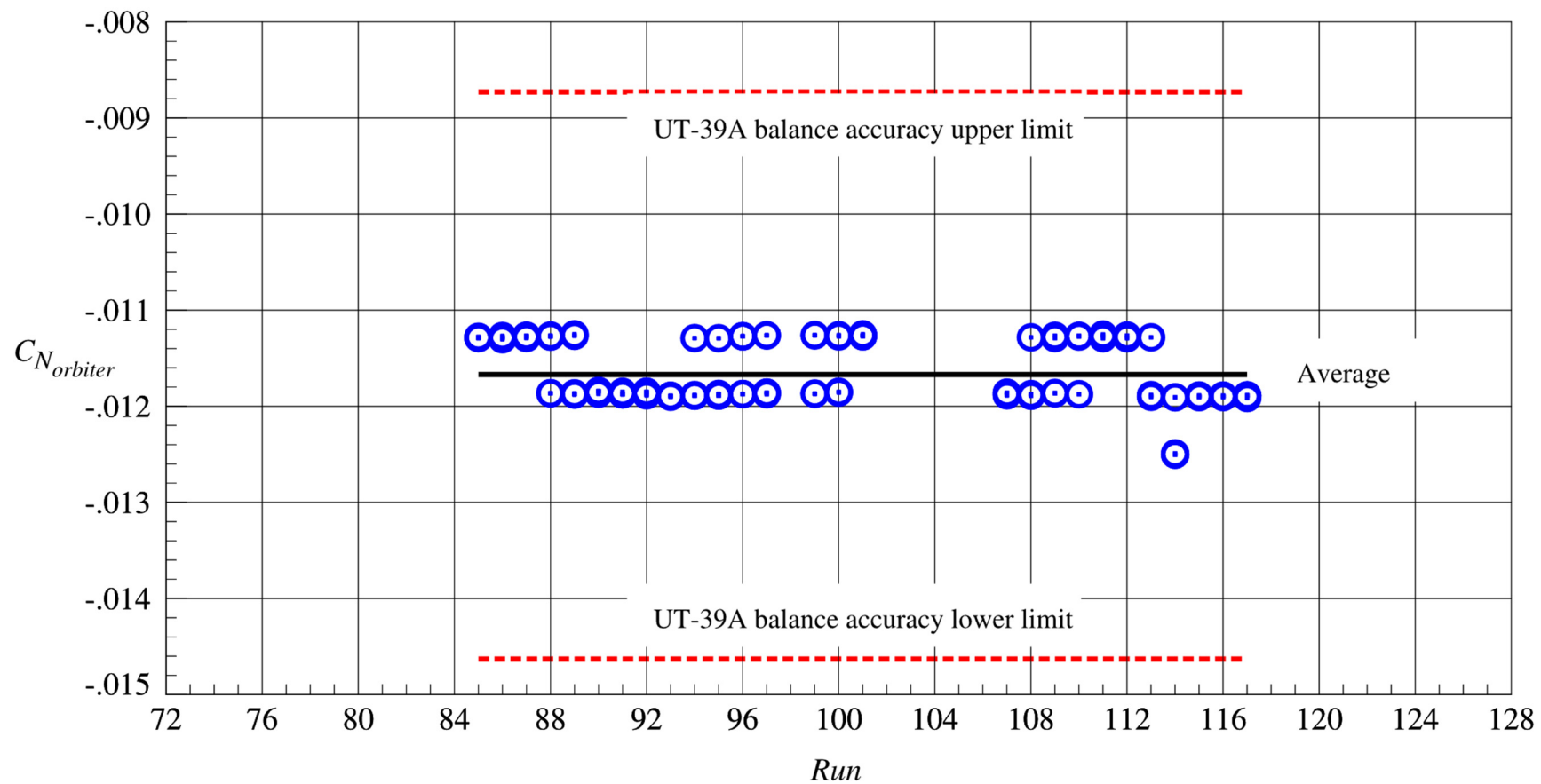
(b) Orbiter axial force coefficient

Figure 39. Continued.



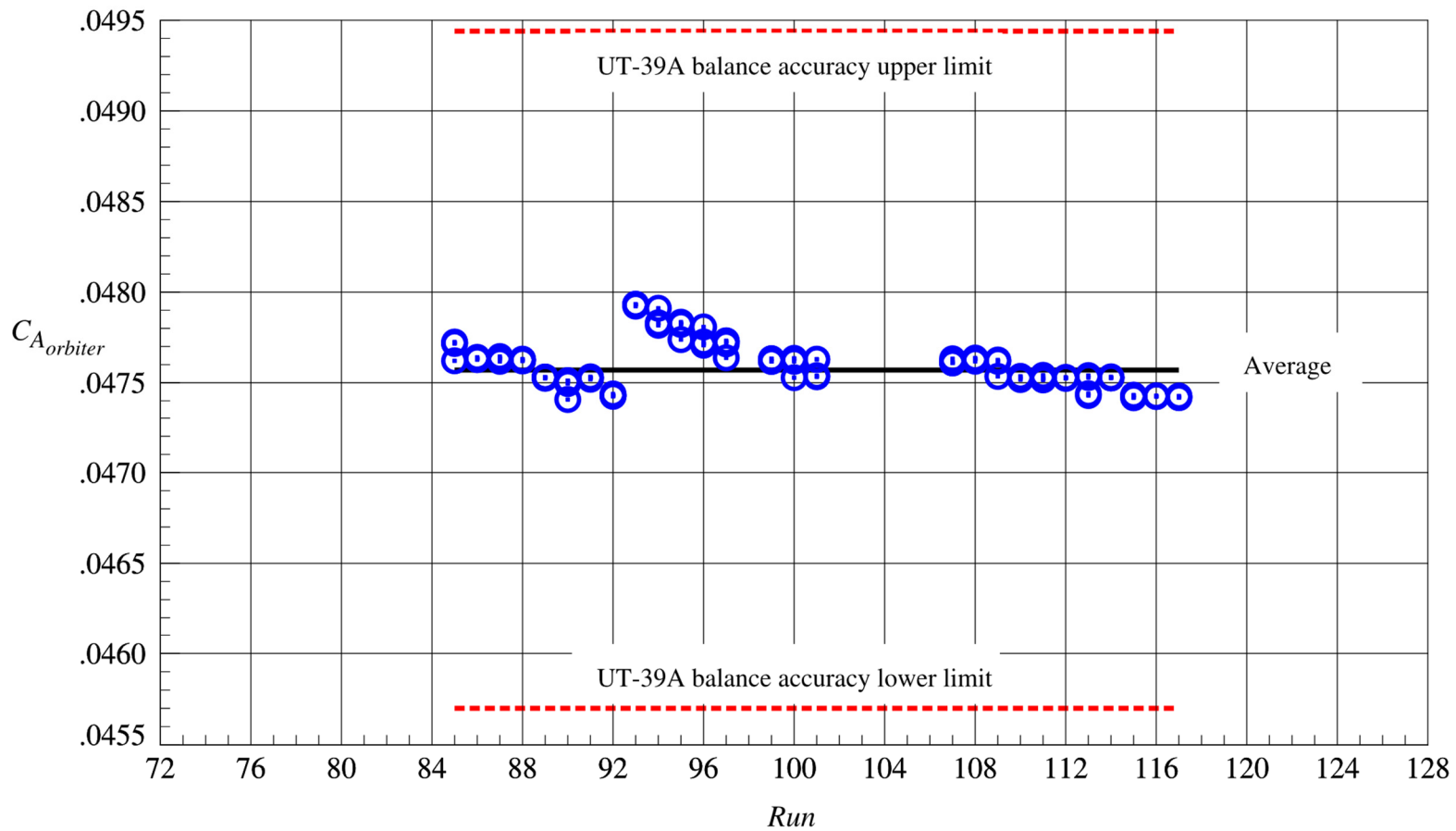
(c) Orbiter pitching moment coefficient

Figure 39. Concluded.



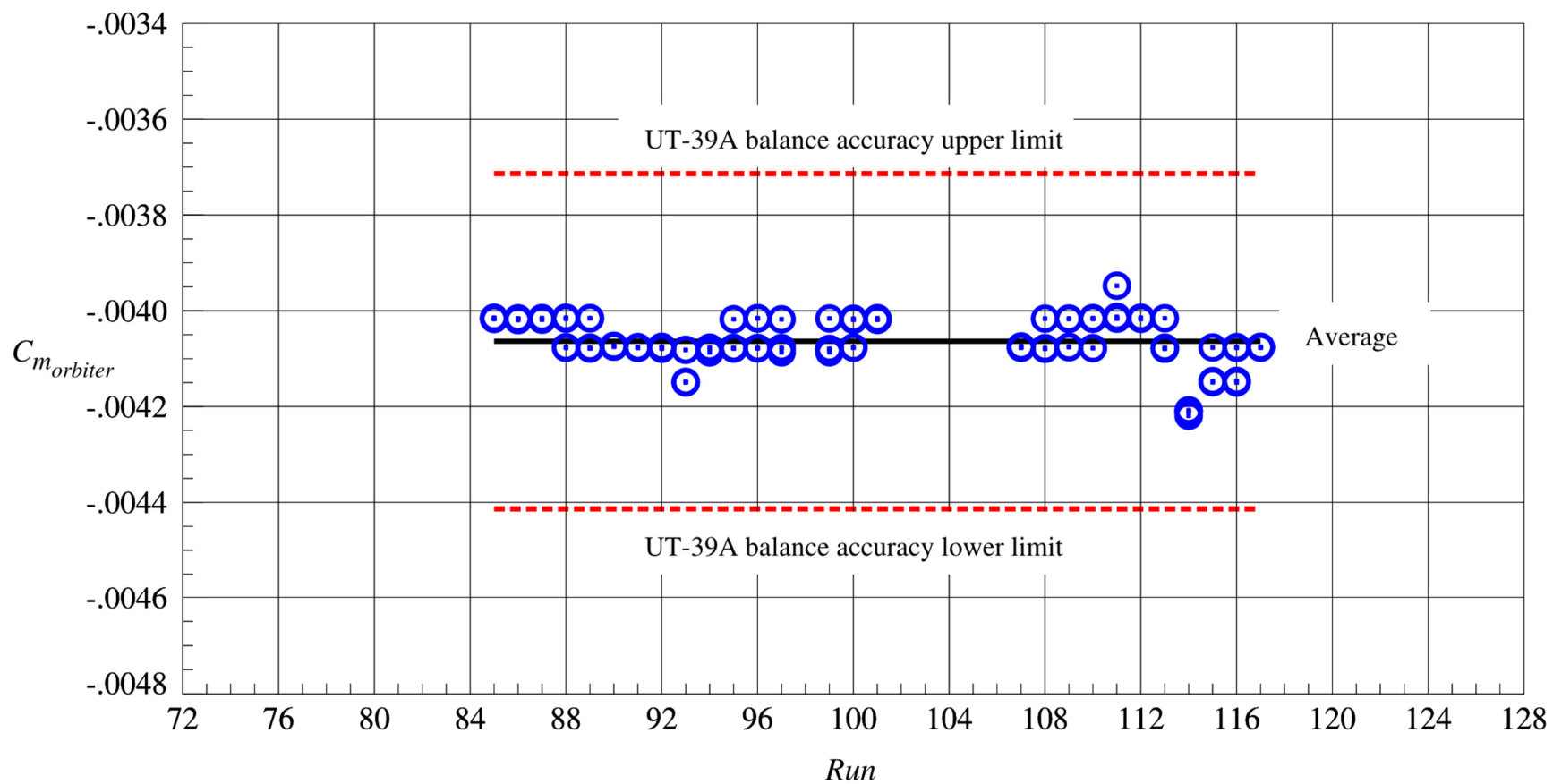
(a) Orbiter normal force coefficient

Figure 40. Data repeatability of the isolated orbiter at Mach = 4.5; booster at  $x_{sept} = 24$  to 28 inches.



(b) Orbiter axial force coefficient

Figure 40. Continued.



(c) Orbiter pitching moment coefficient

Figure 40. Concluded.

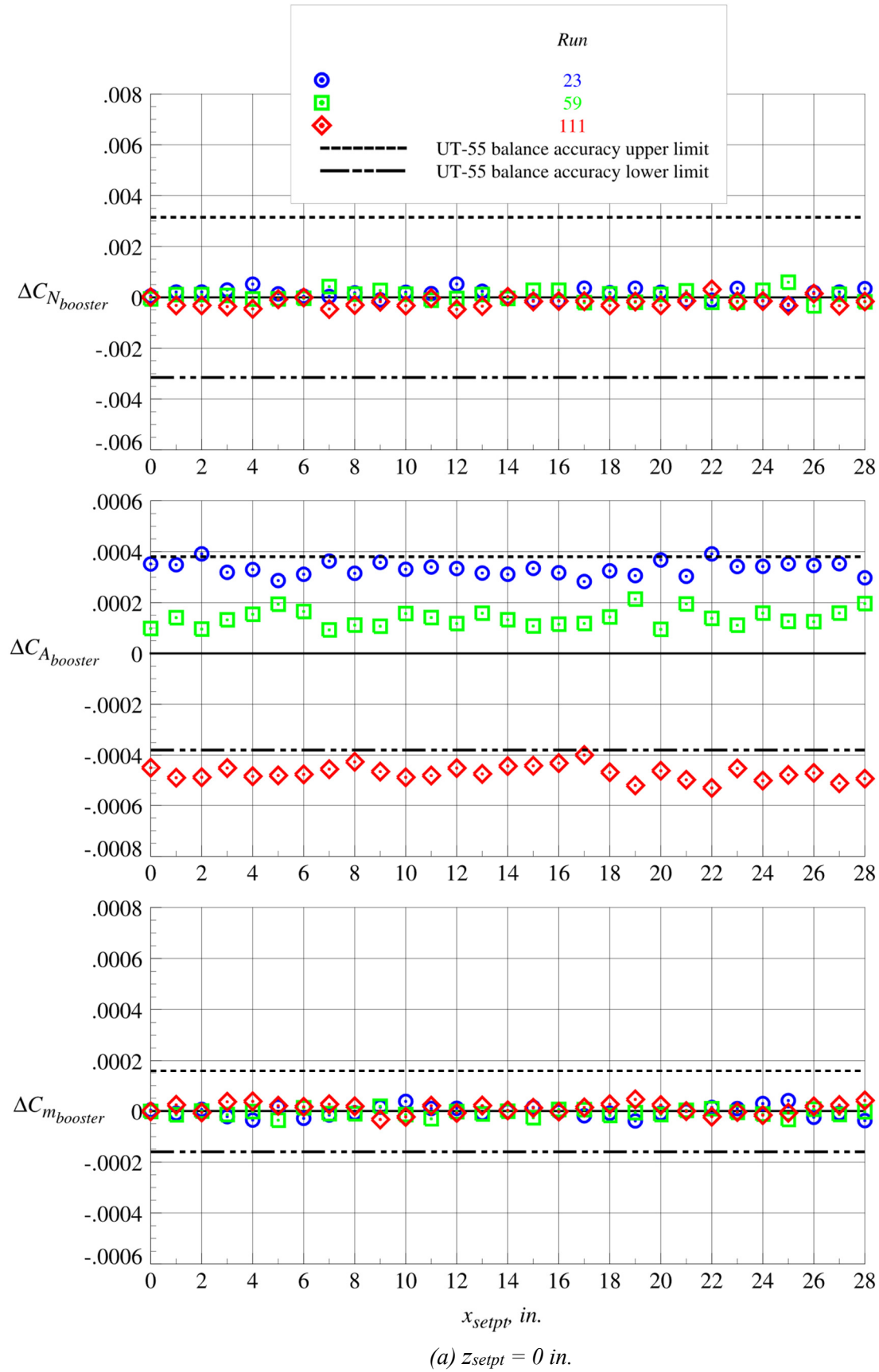
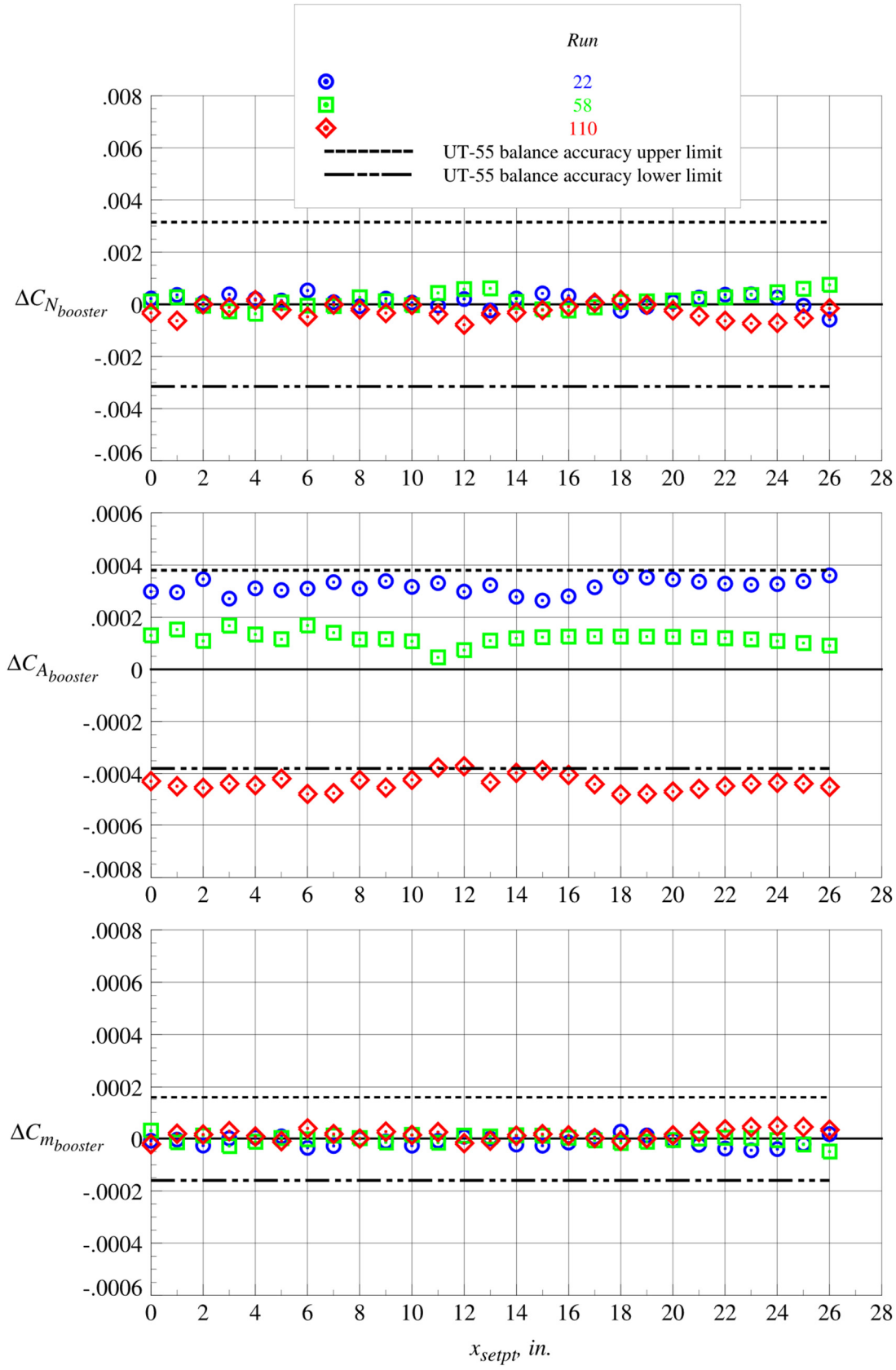


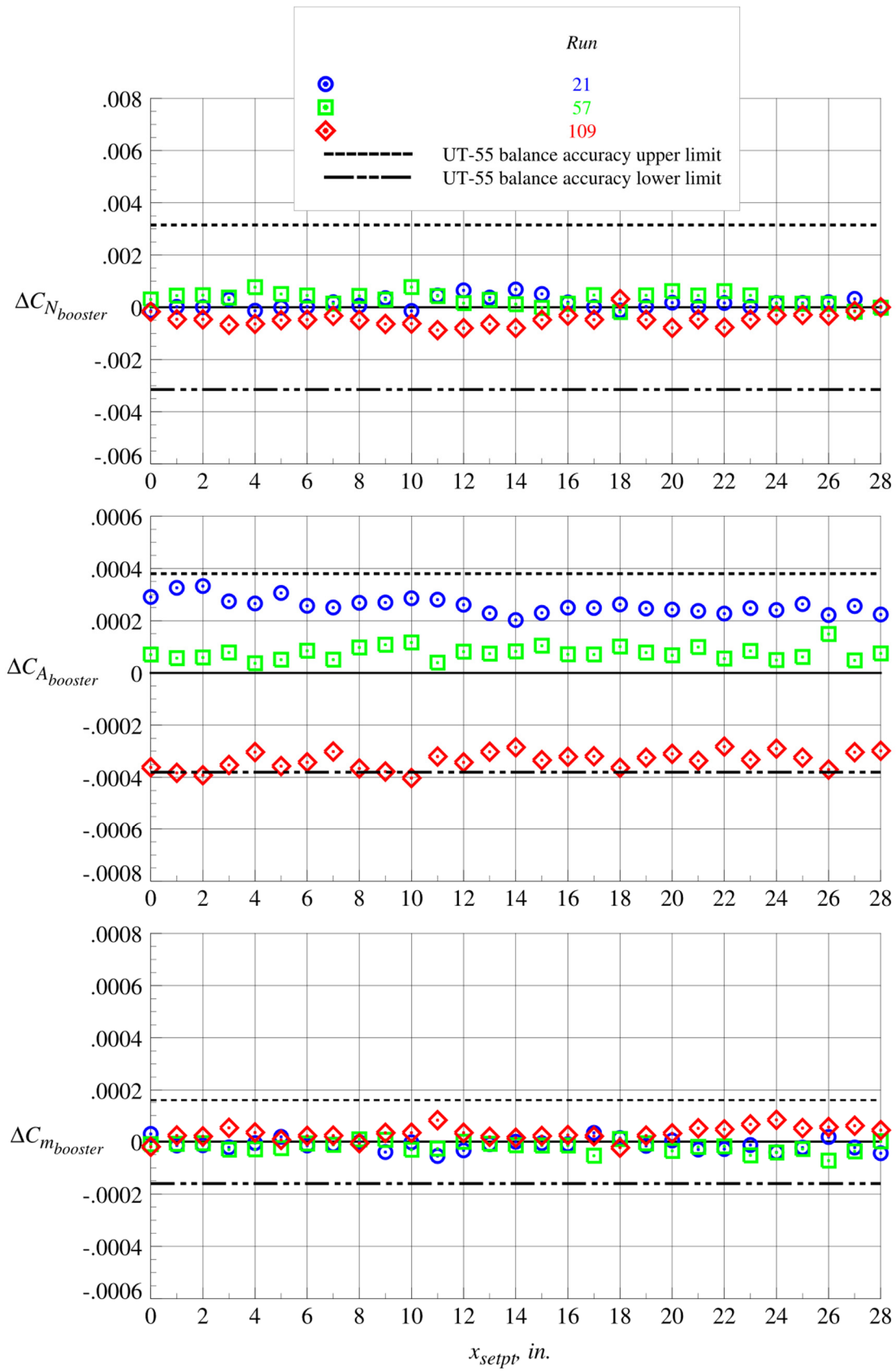
Figure 41. Data repeatability of the isolated booster at Mach = 3.0; repeat runs at fixed  $z_{setpt}$ .





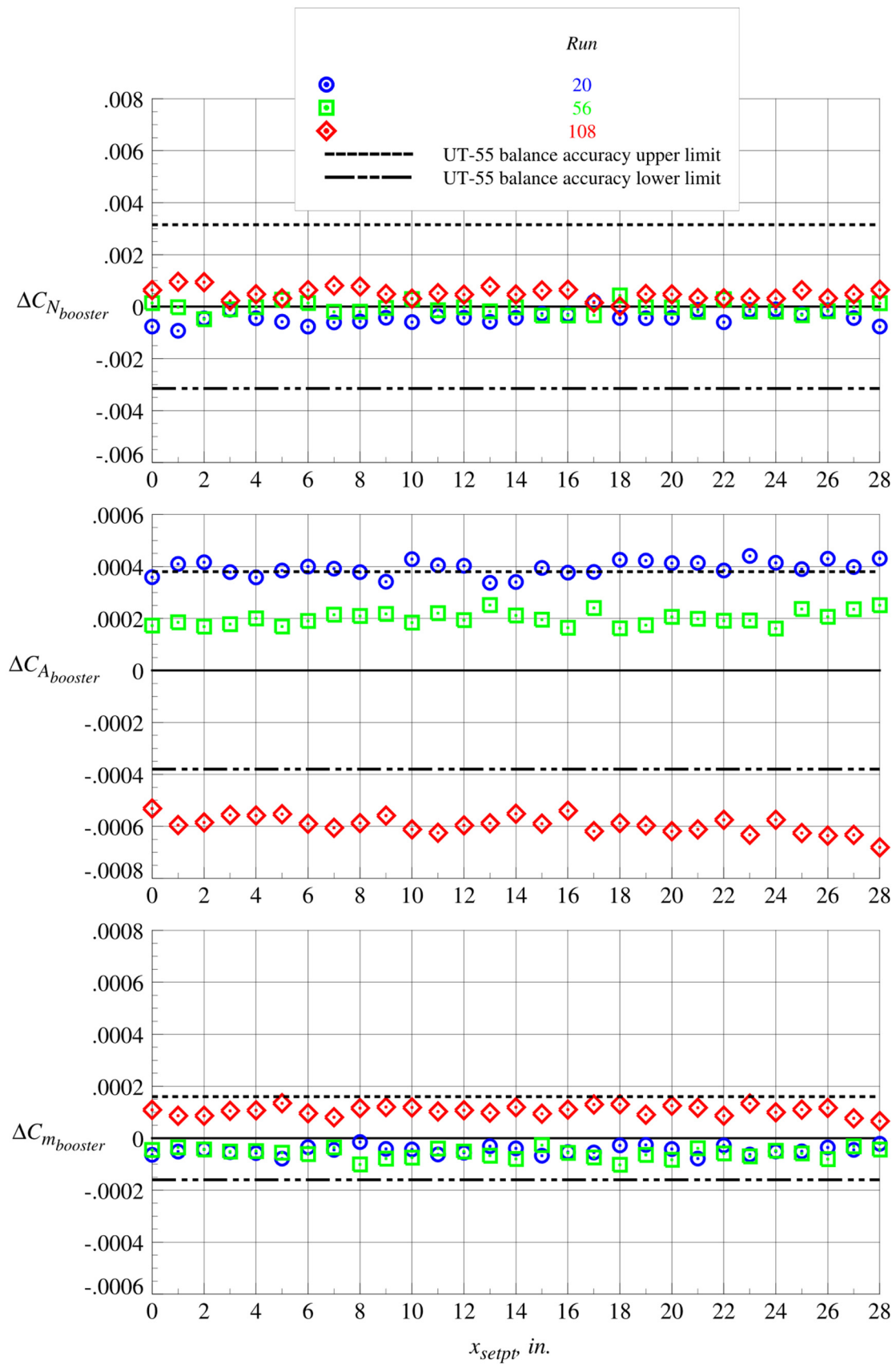
(b)  $z_{setpt} = 0.656$  in.

Figure 41. Continued.



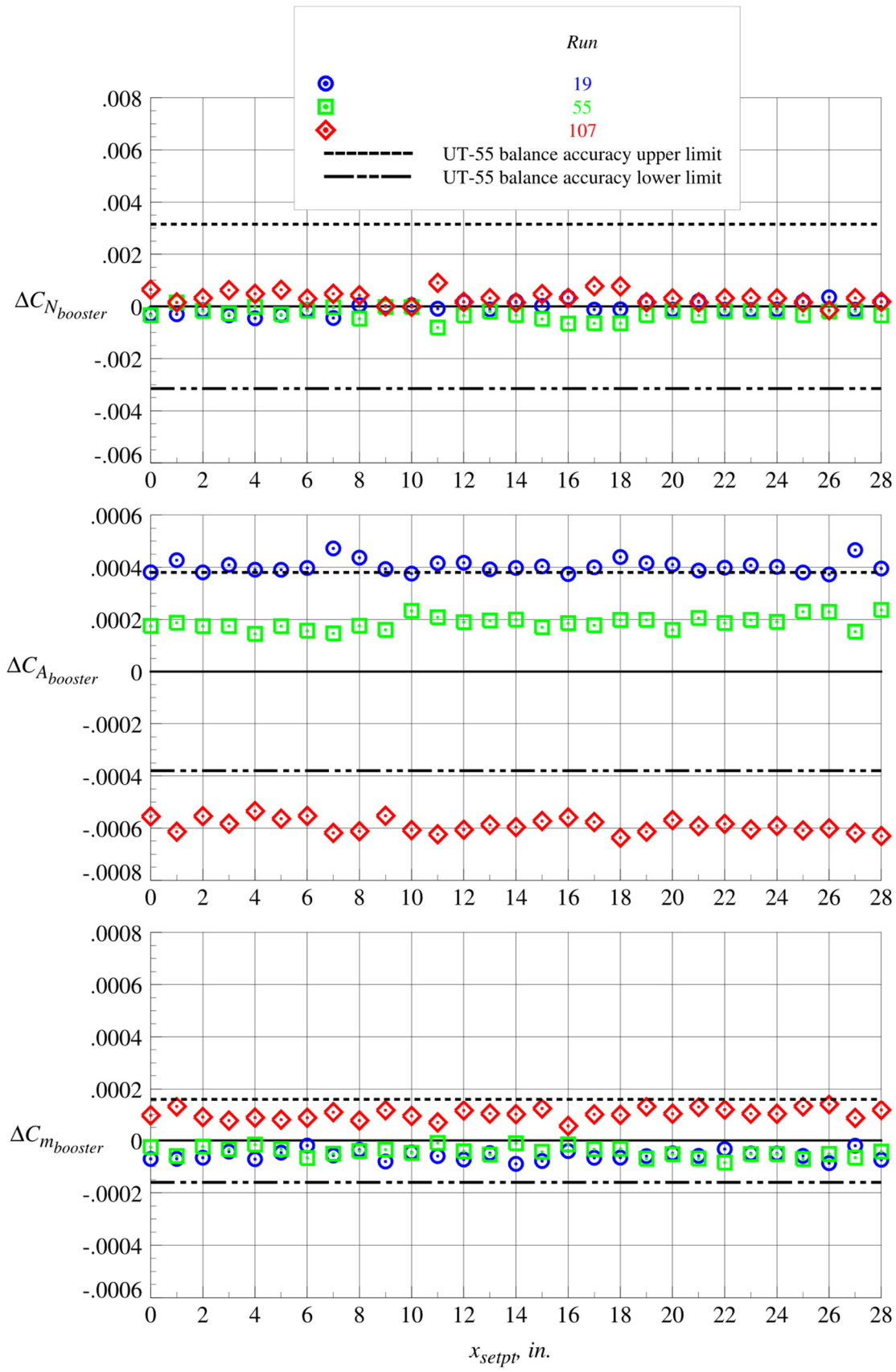
(c)  $z_{setpt} = 1.313$  in.

Figure 41. Continued.



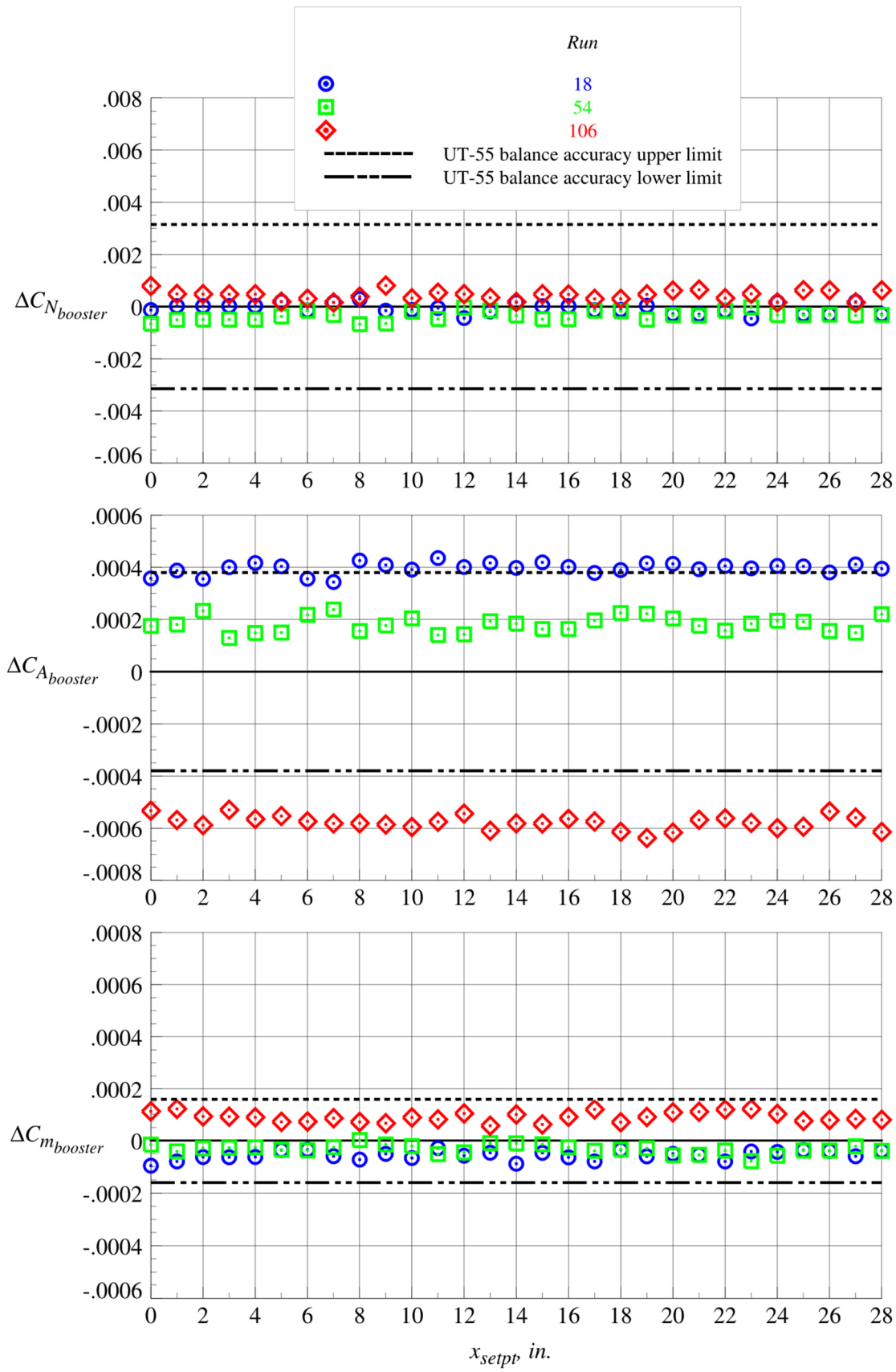
(d)  $z_{setpt} = 1.969$  in.

Figure 41. Continued.



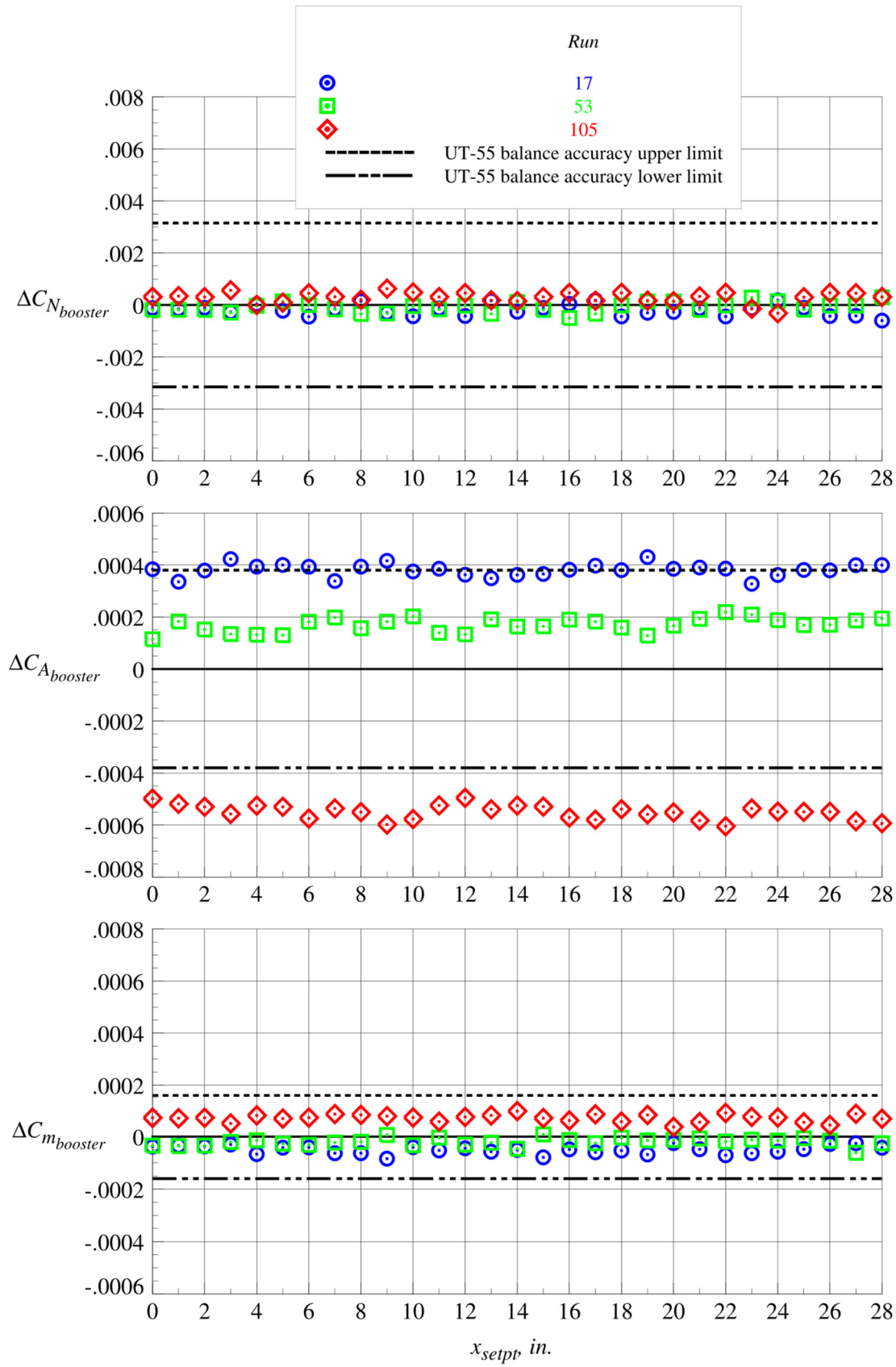
(e)  $z_{setpt} = 2.625$  in.

Figure 41. Continued.



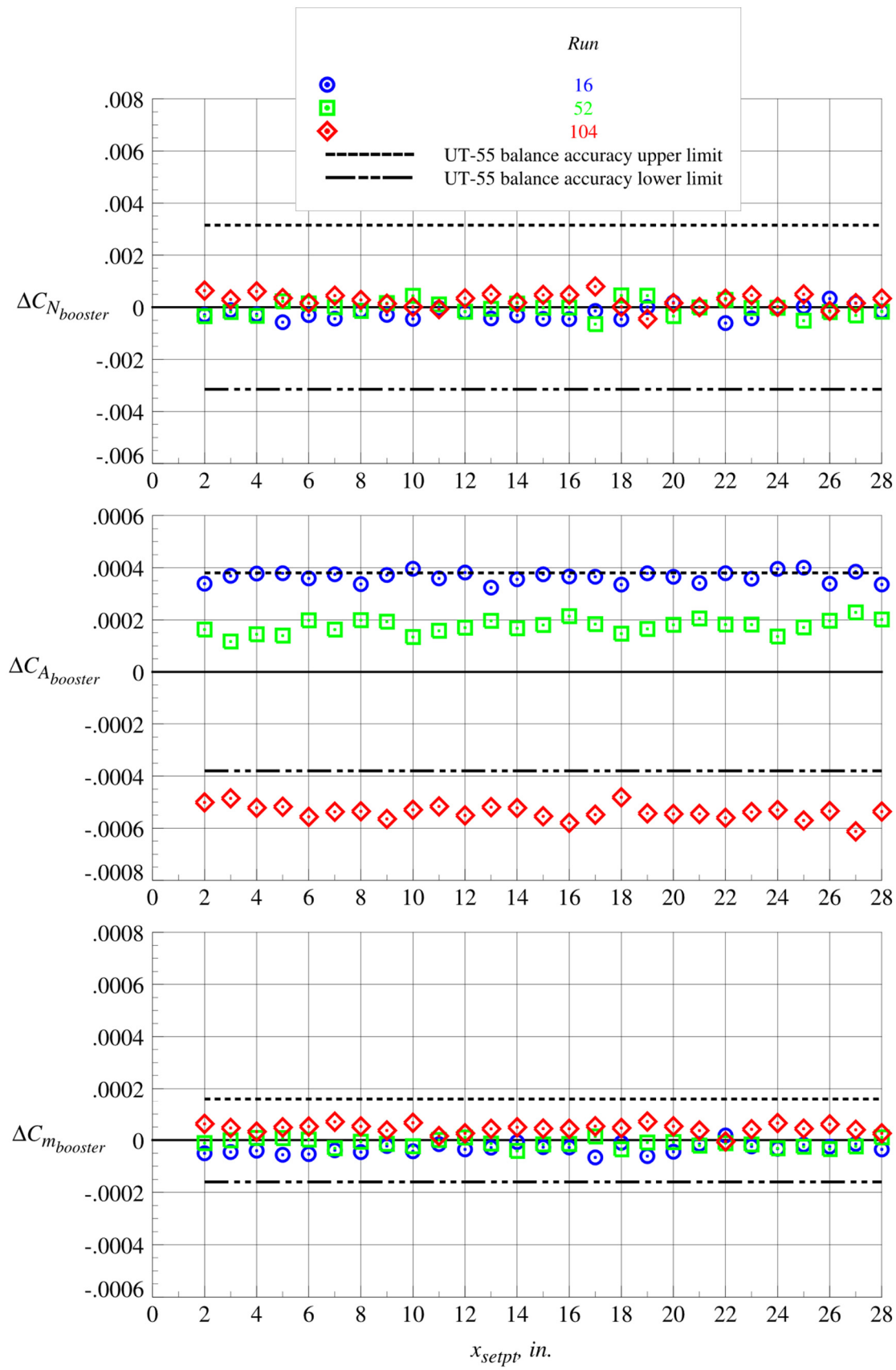
(f)  $z_{setpt} = 3.281$  in.

Figure 41. Continued.



(g)  $z_{setpt} = 3.938$  in.

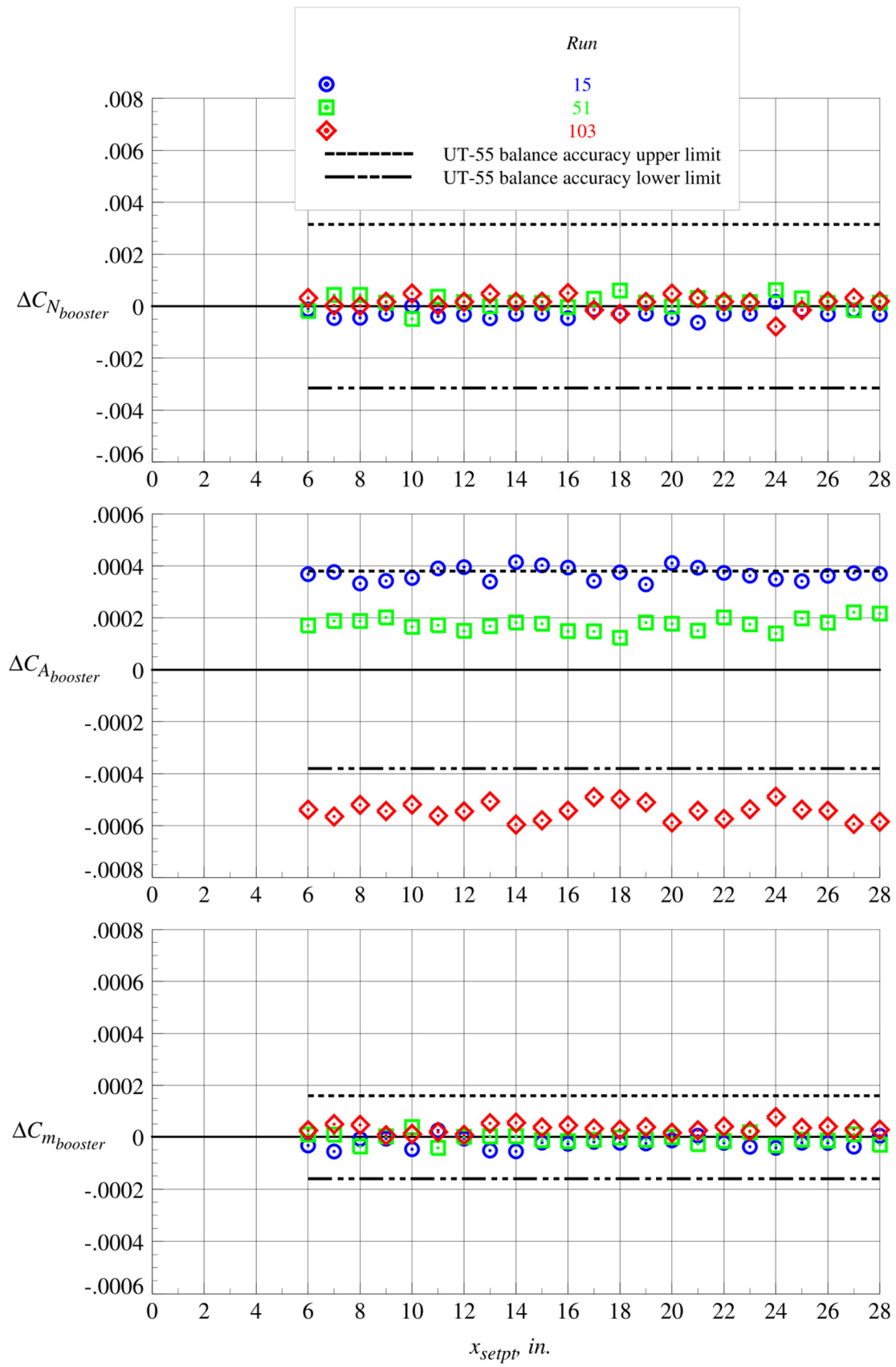
Figure 41. Continued.



(h)  $z_{setpt} = 4.594$  in.

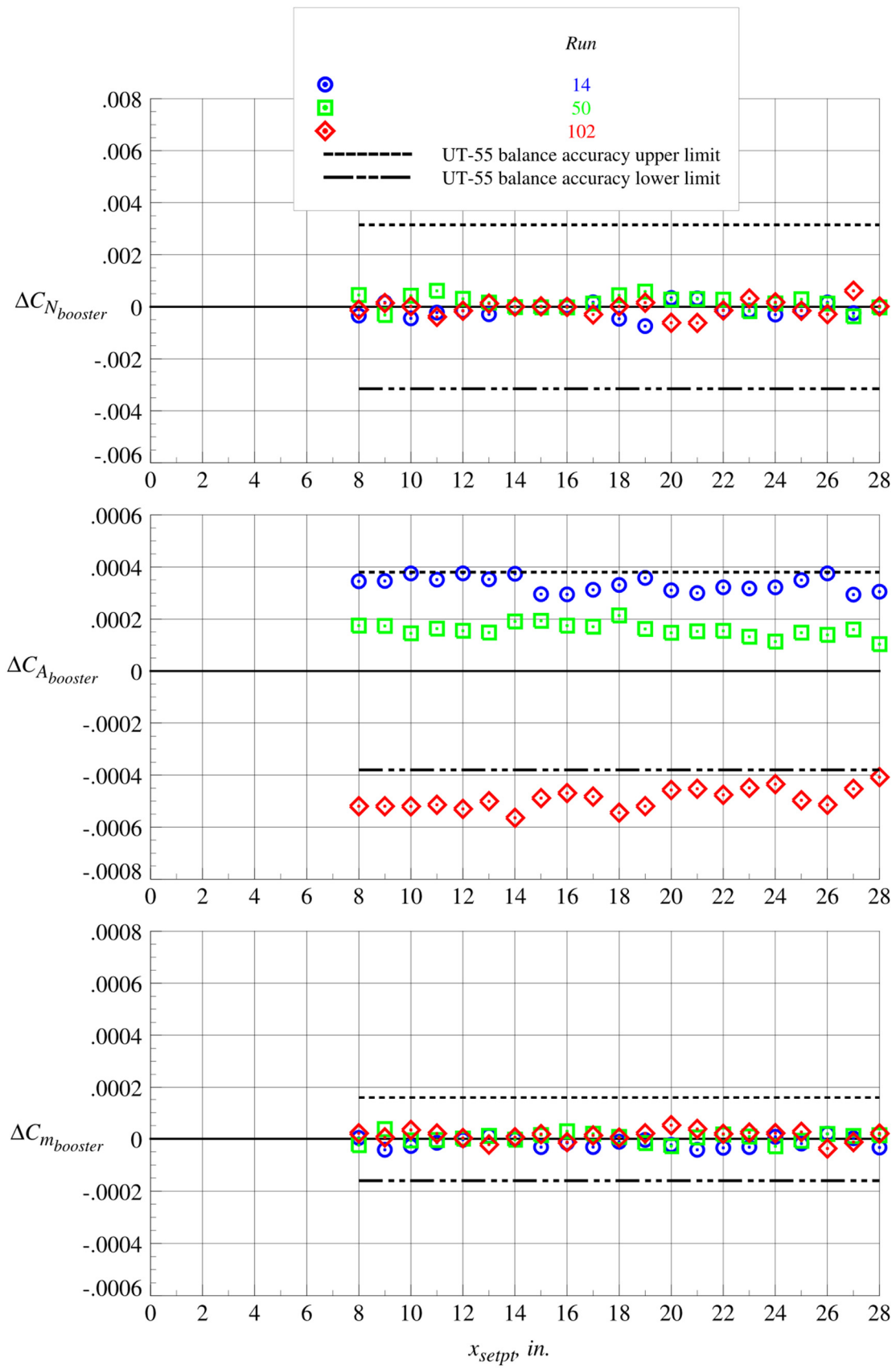
Figure 41. Continued.





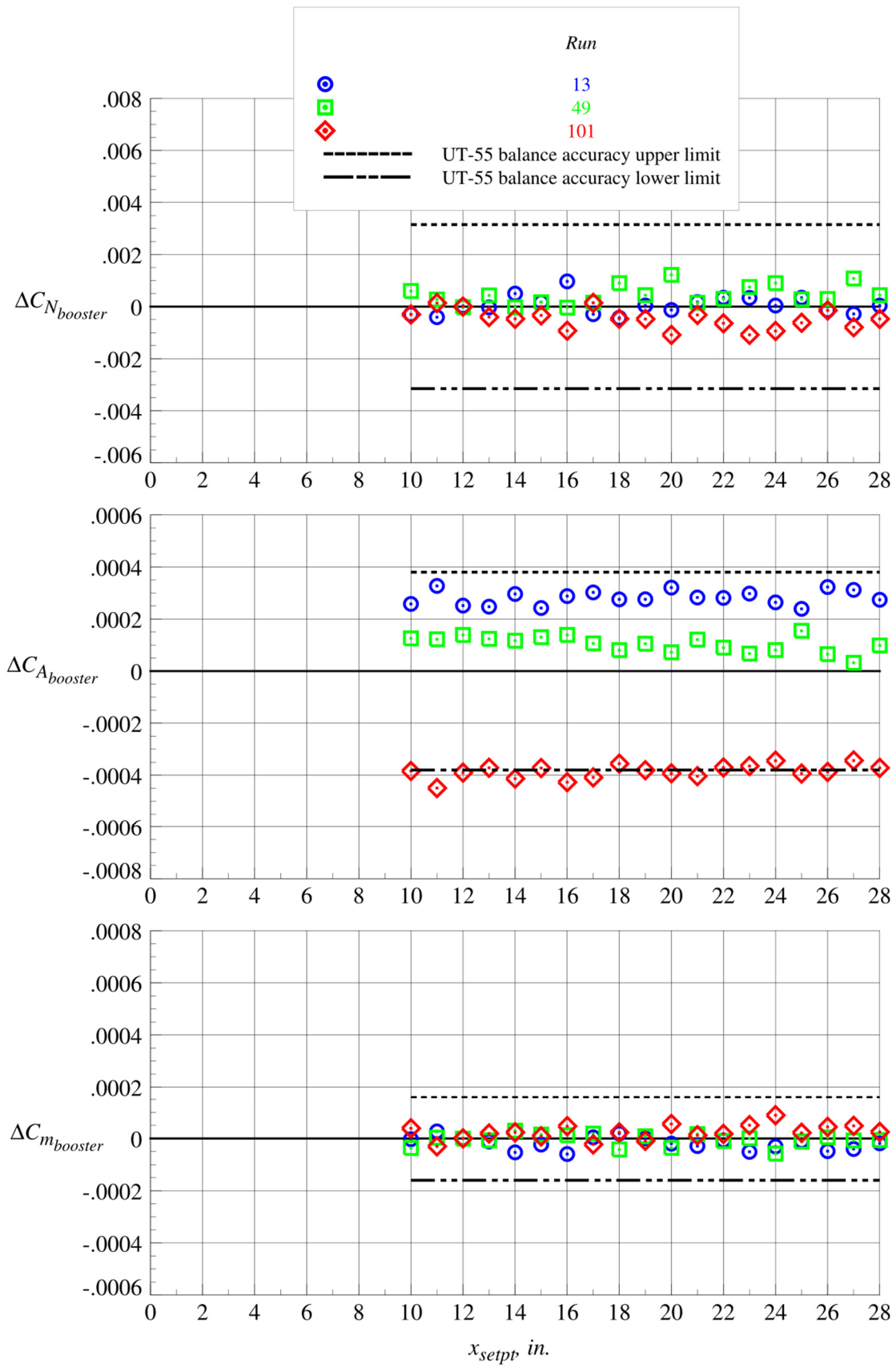
(i)  $z_{setpt} = 5.250$  in.

Figure 41. Continued.



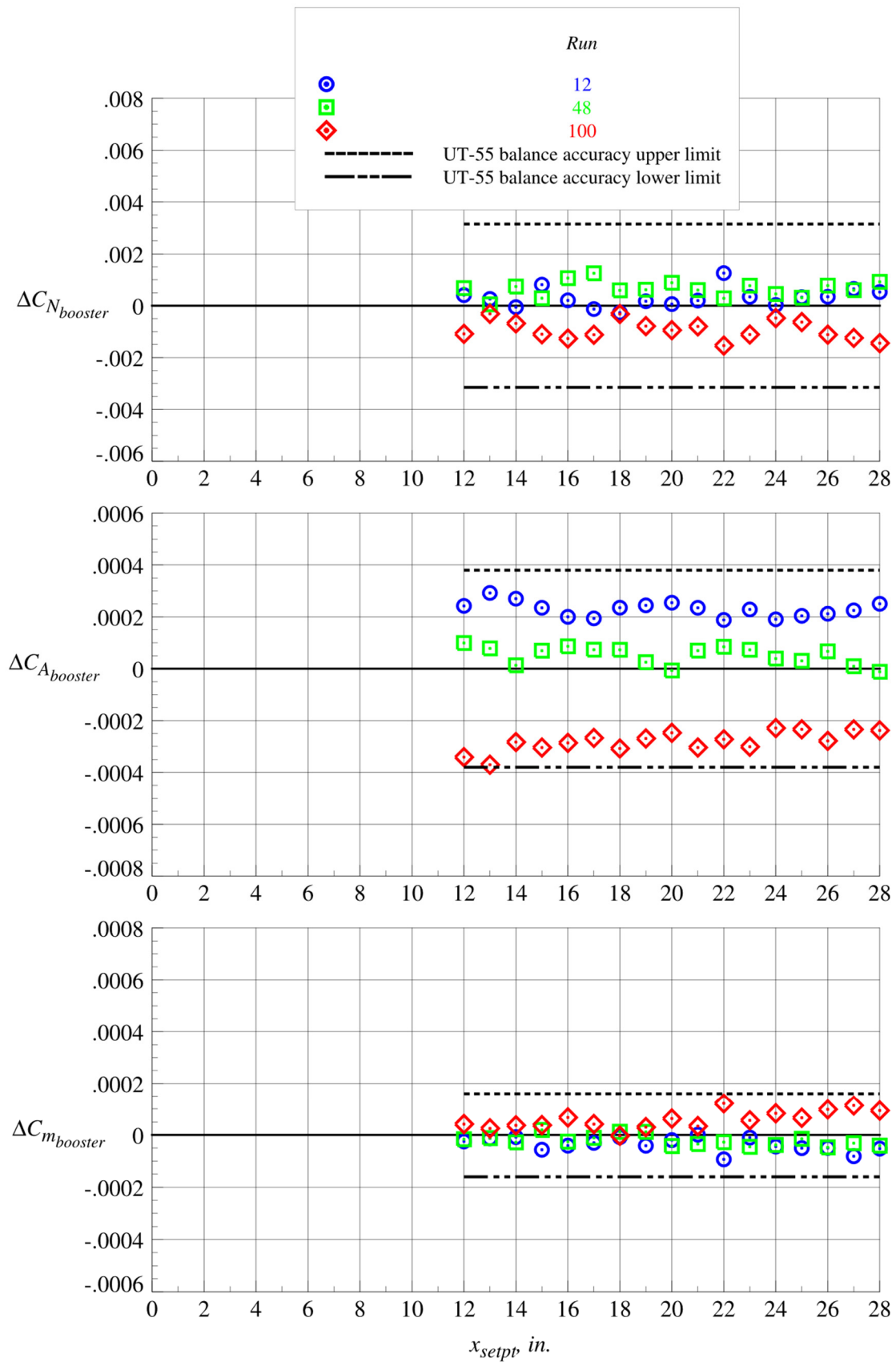
(j)  $z_{setpt} = 6.563$  in.

Figure 41. Continued.



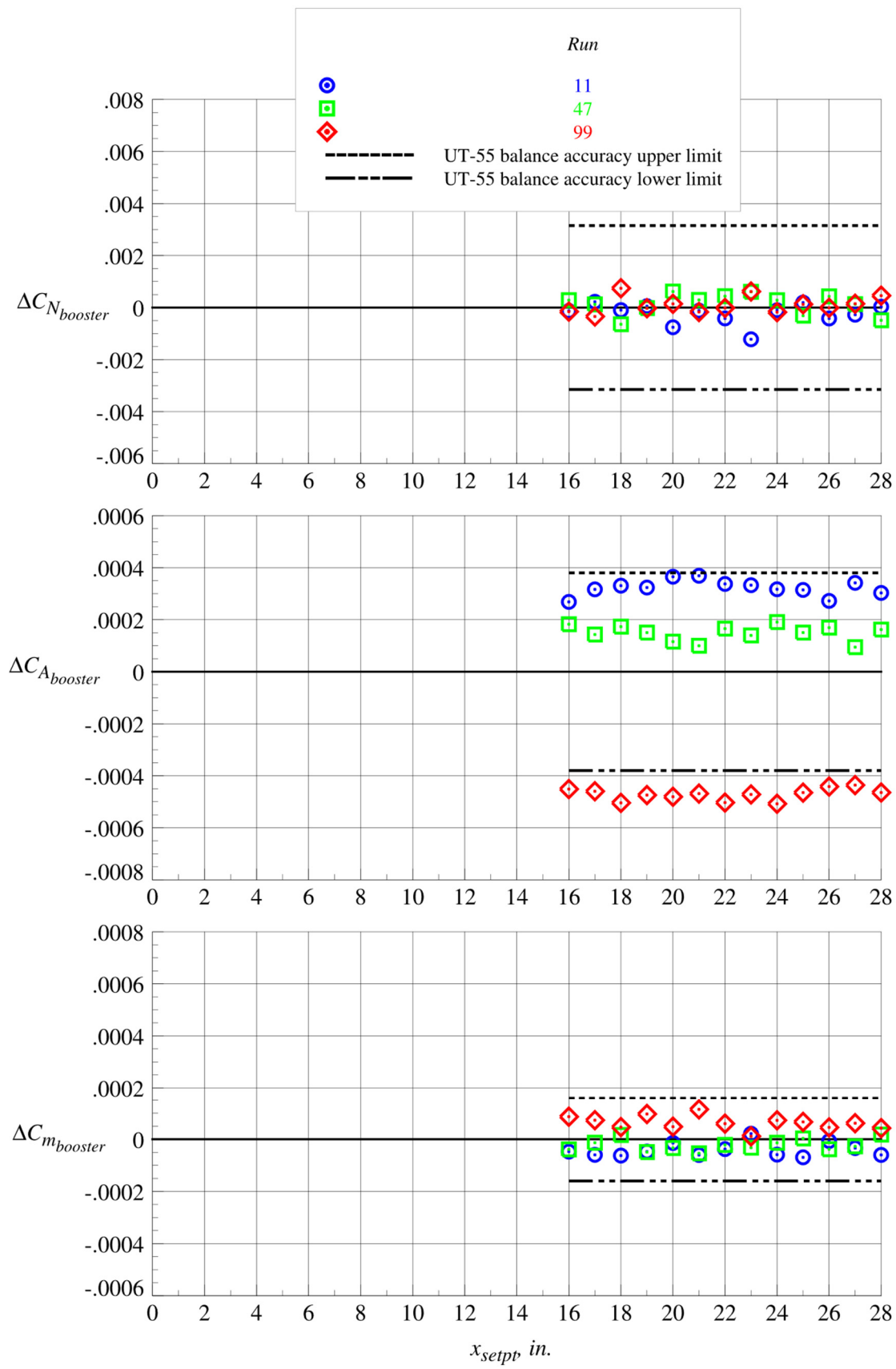
(k)  $z_{setpt} = 7.875$  in.

Figure 41. Continued.



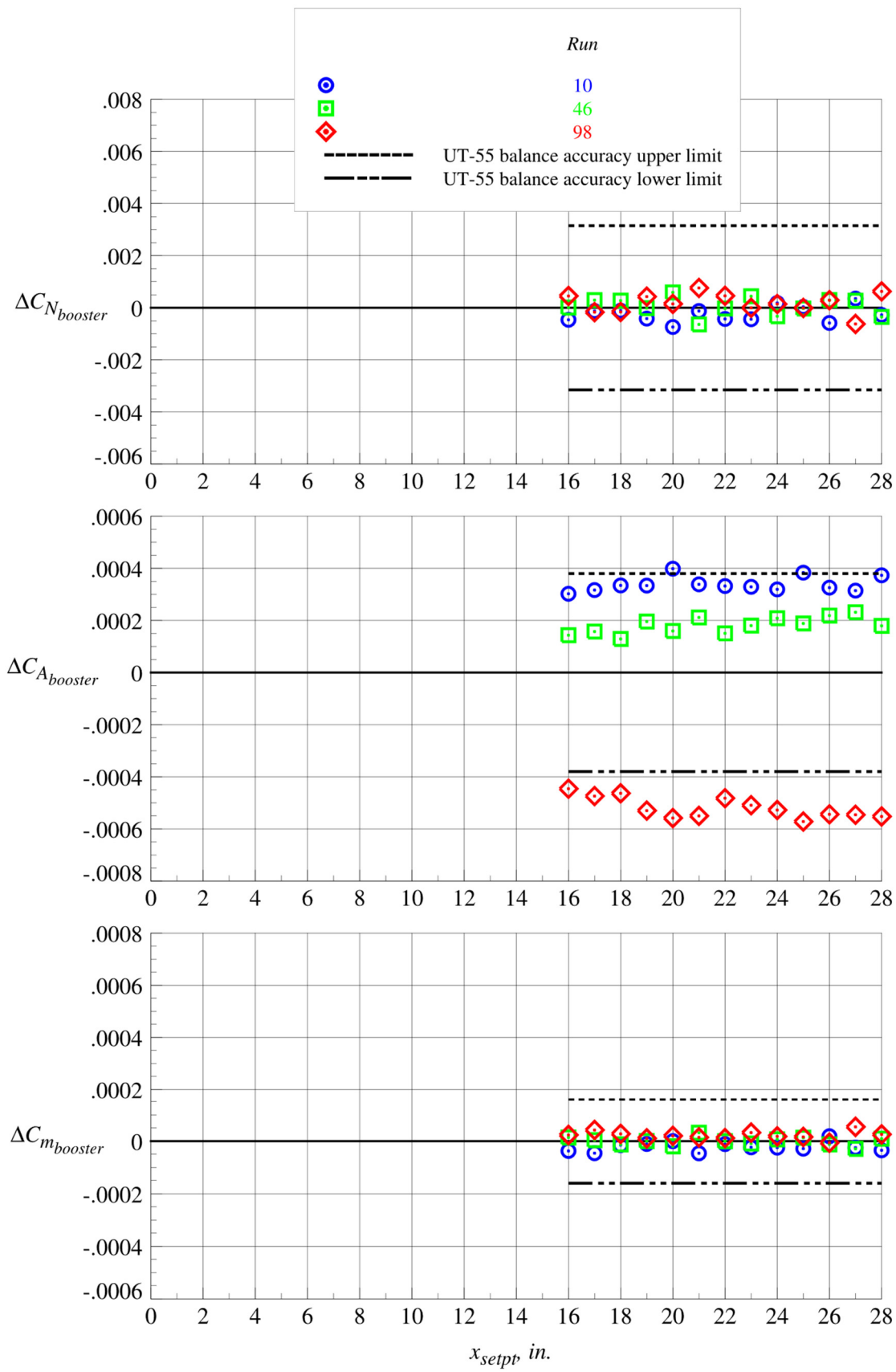
(l)  $z_{setpt} = 9.188$  in.

Figure 41. Continued.



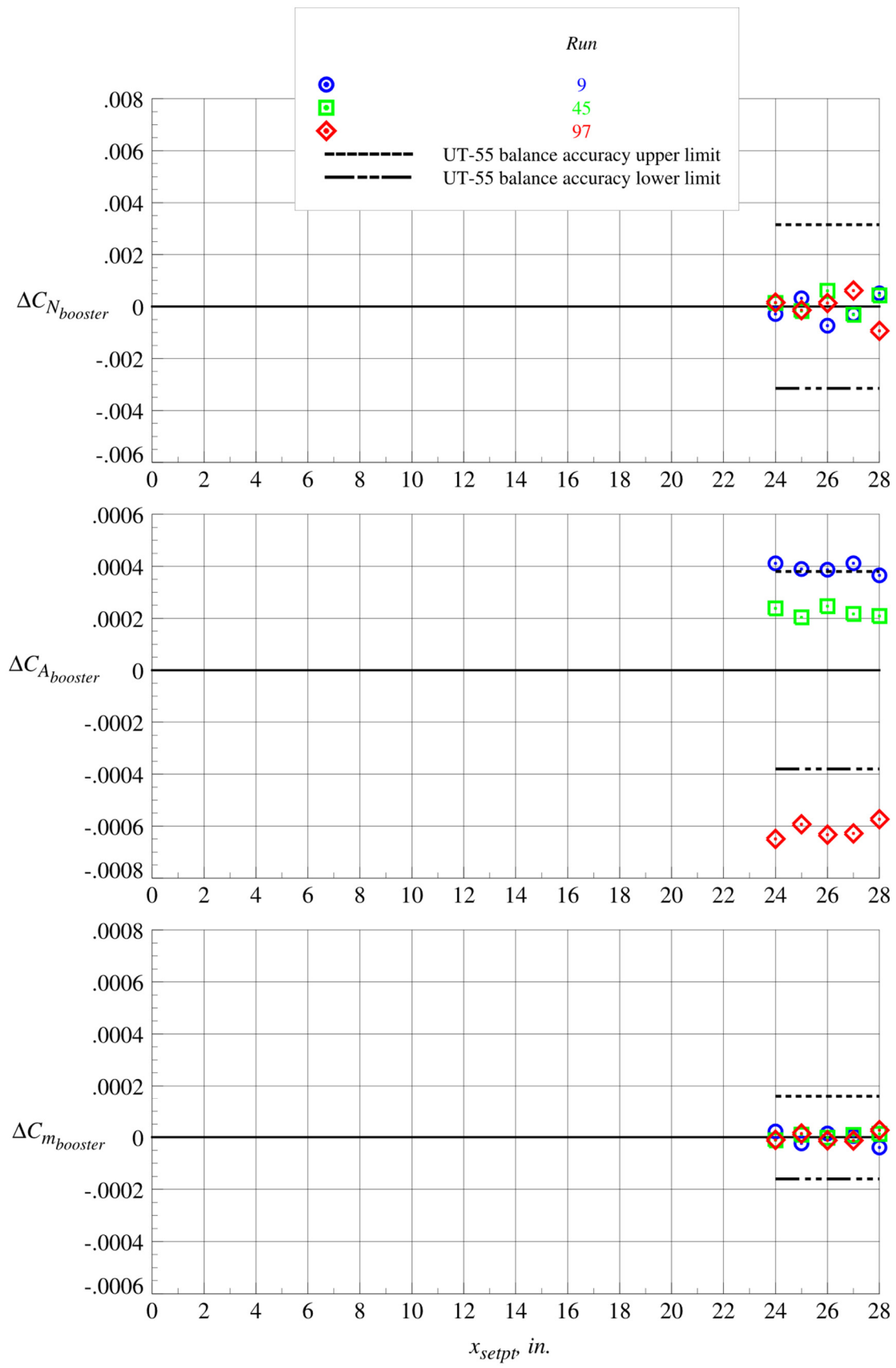
(m)  $z_{setpt} = 10.500$  in.

Figure 41. Continued.



(n)  $z_{setpt} = 11.810$  in.

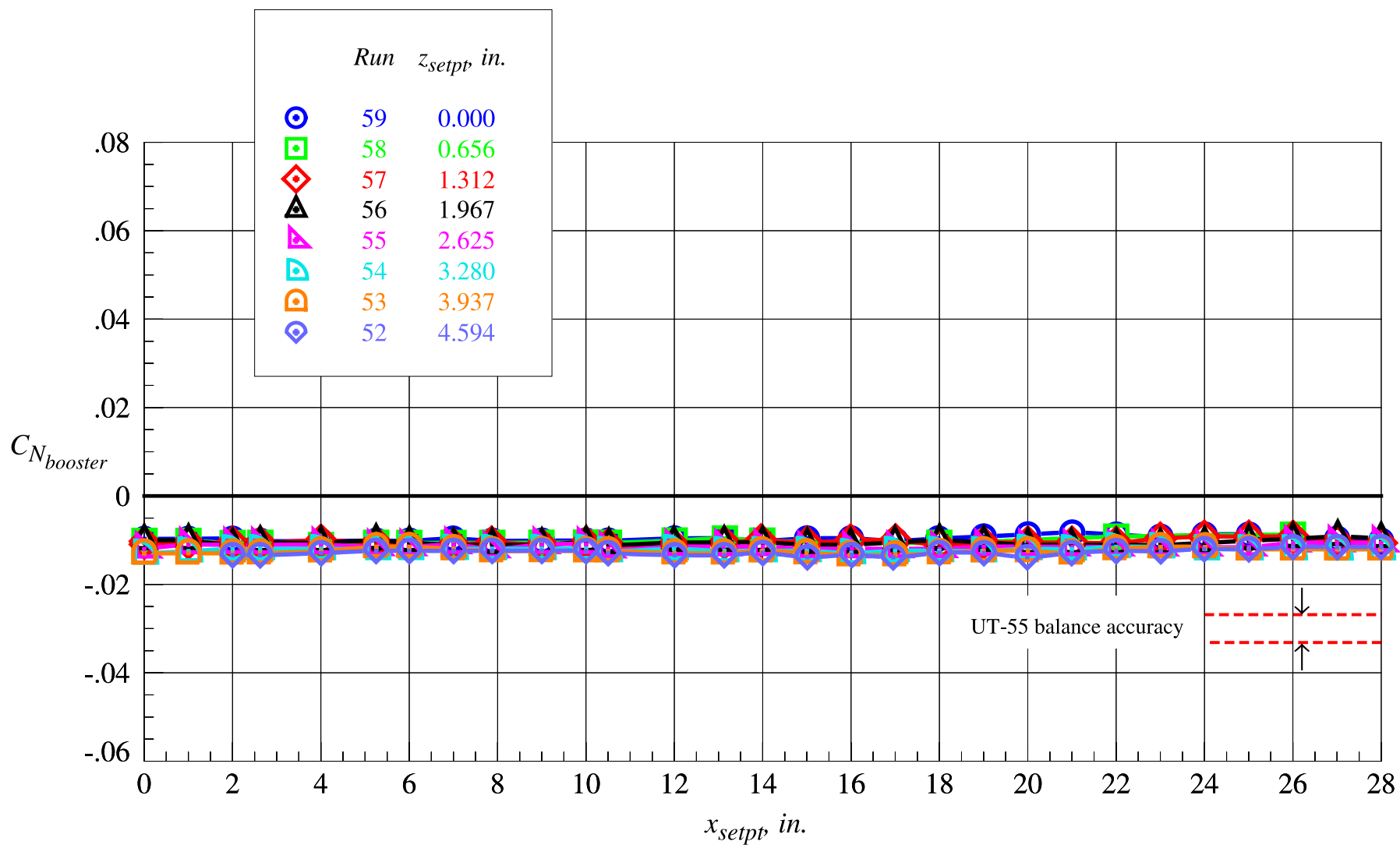
Figure 41. Continued.



(o)  $z_{setpt} = 13.130$  in.

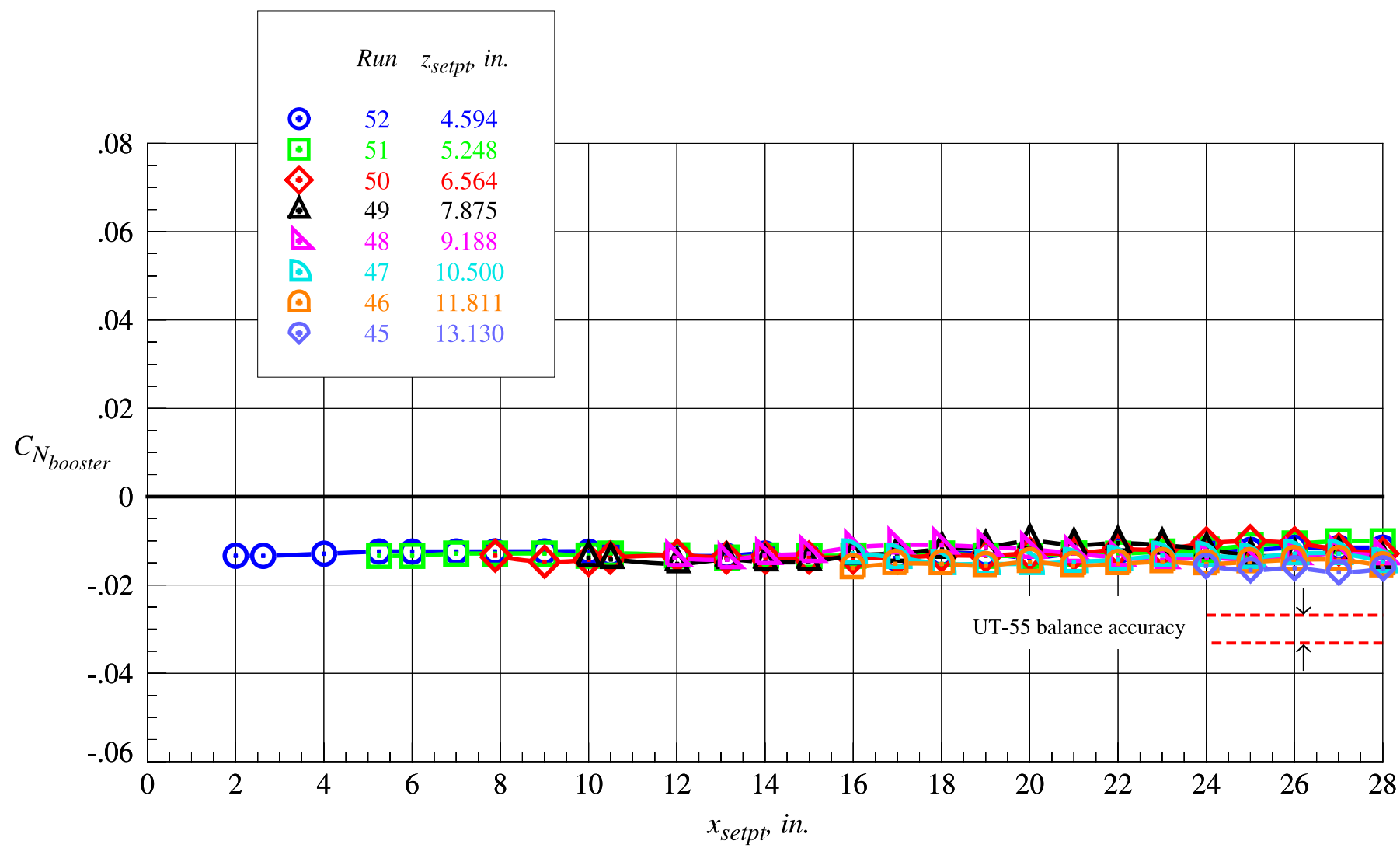
Figure 41. Concluded.





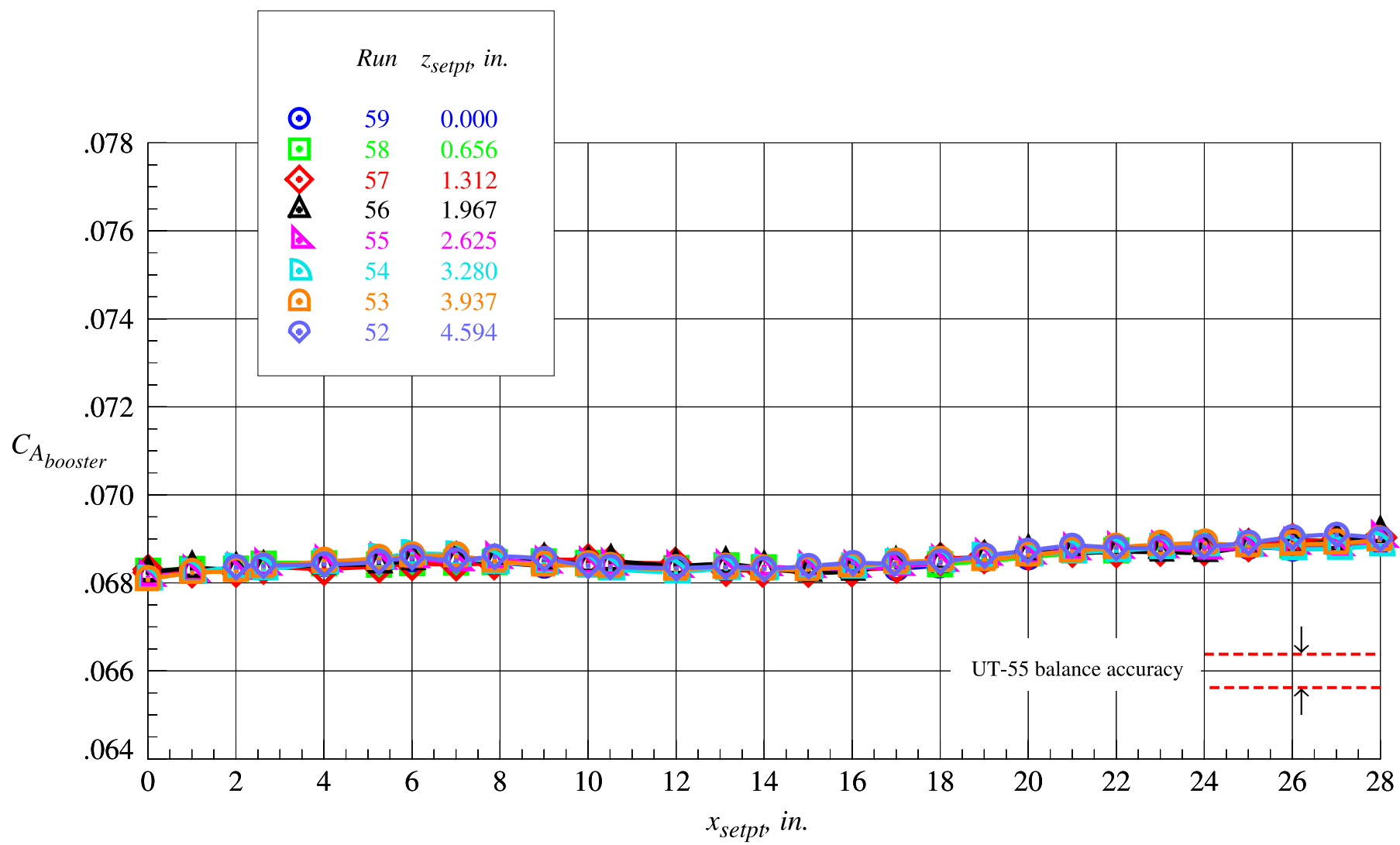
(a) Booster normal force coefficient, part 1

Figure 42. Data repeatability of the isolated booster at Mach = 3.0 across the range of  $z_{setpt}$ .



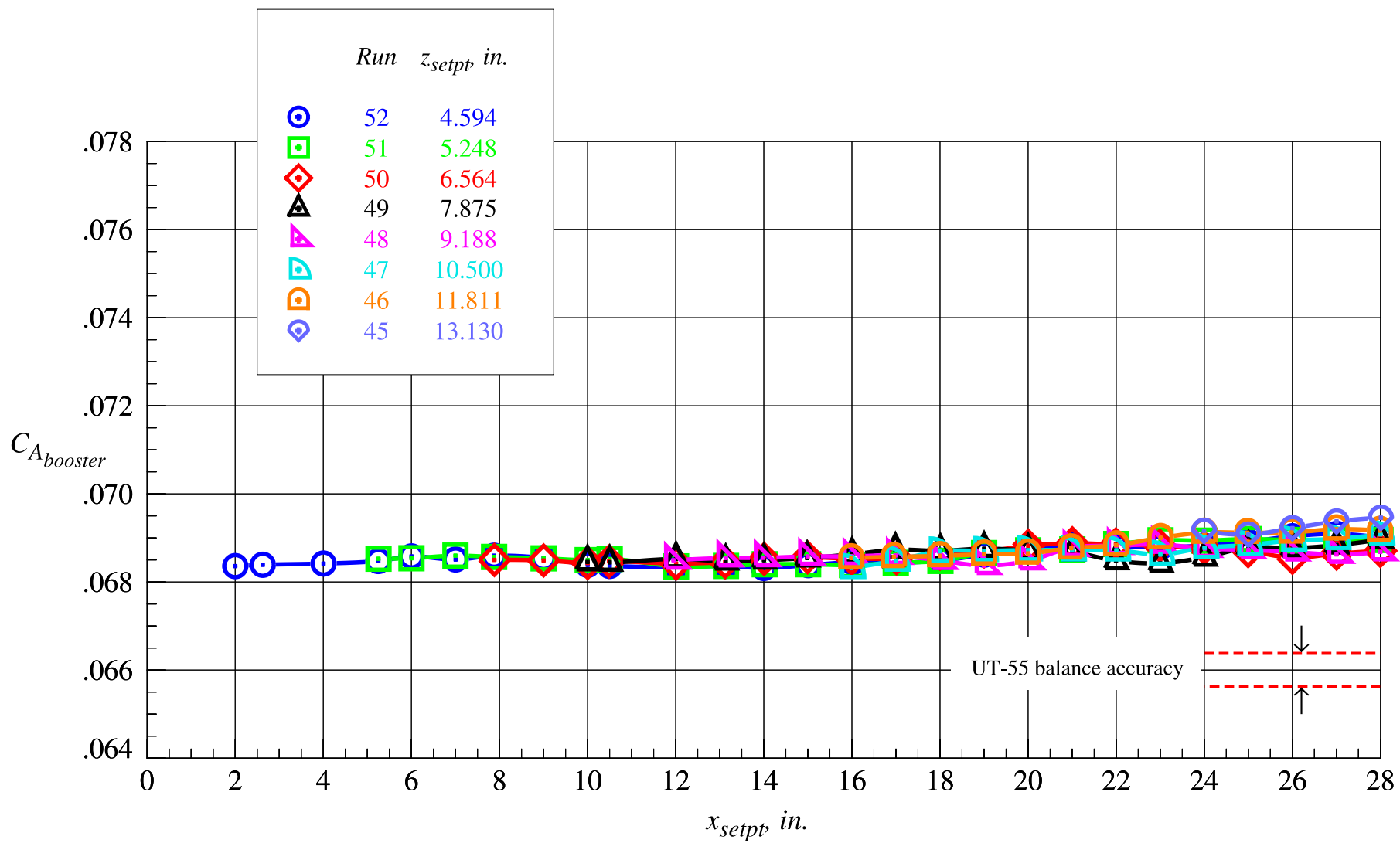
(b) Booster normal force coefficient, part 2

Figure 42. Continued.



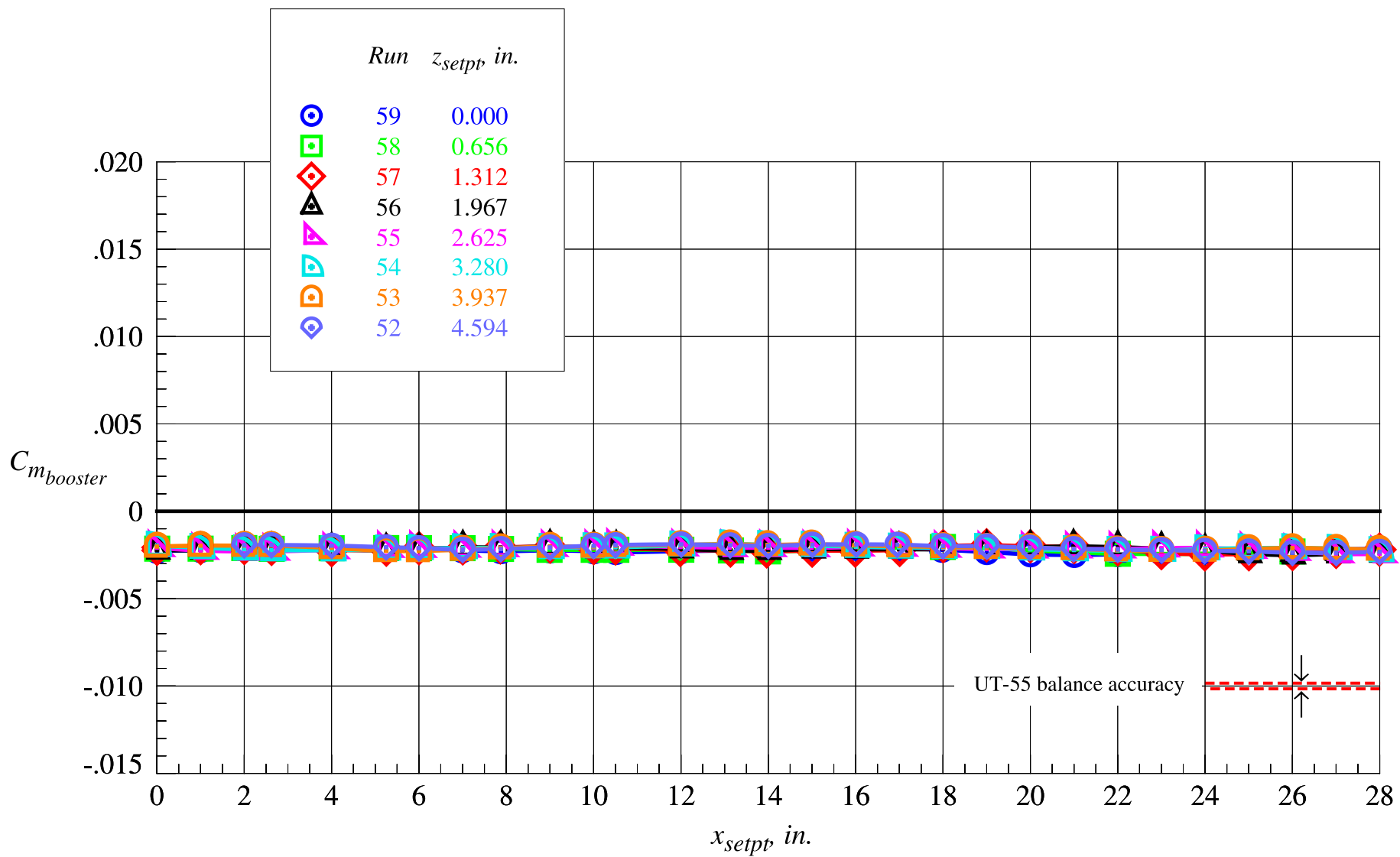
(c) Booster axial force coefficient, part 1

Figure 42. Continued.



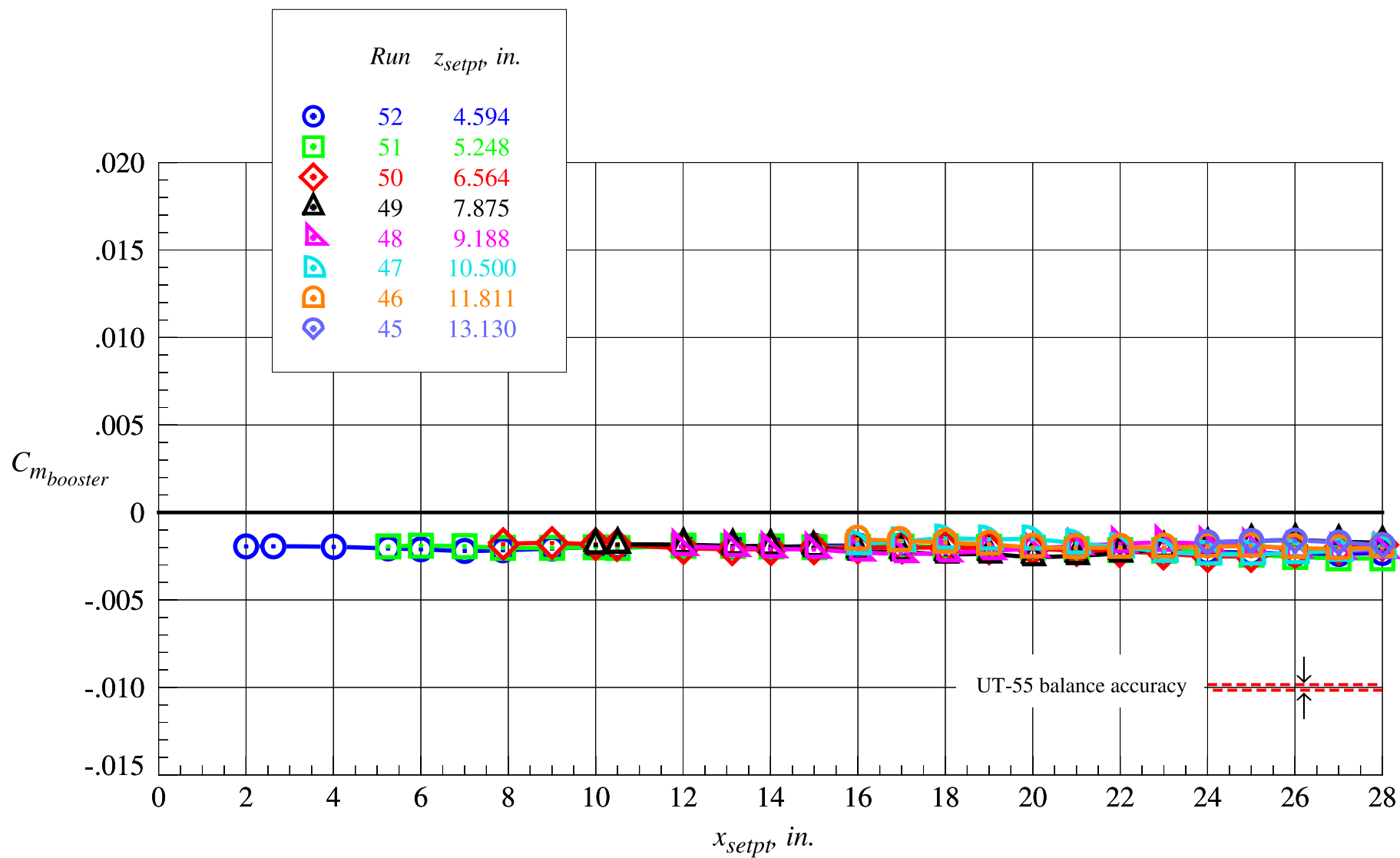
(d) Booster axial force coefficient, part 2

Figure 42. Continued.



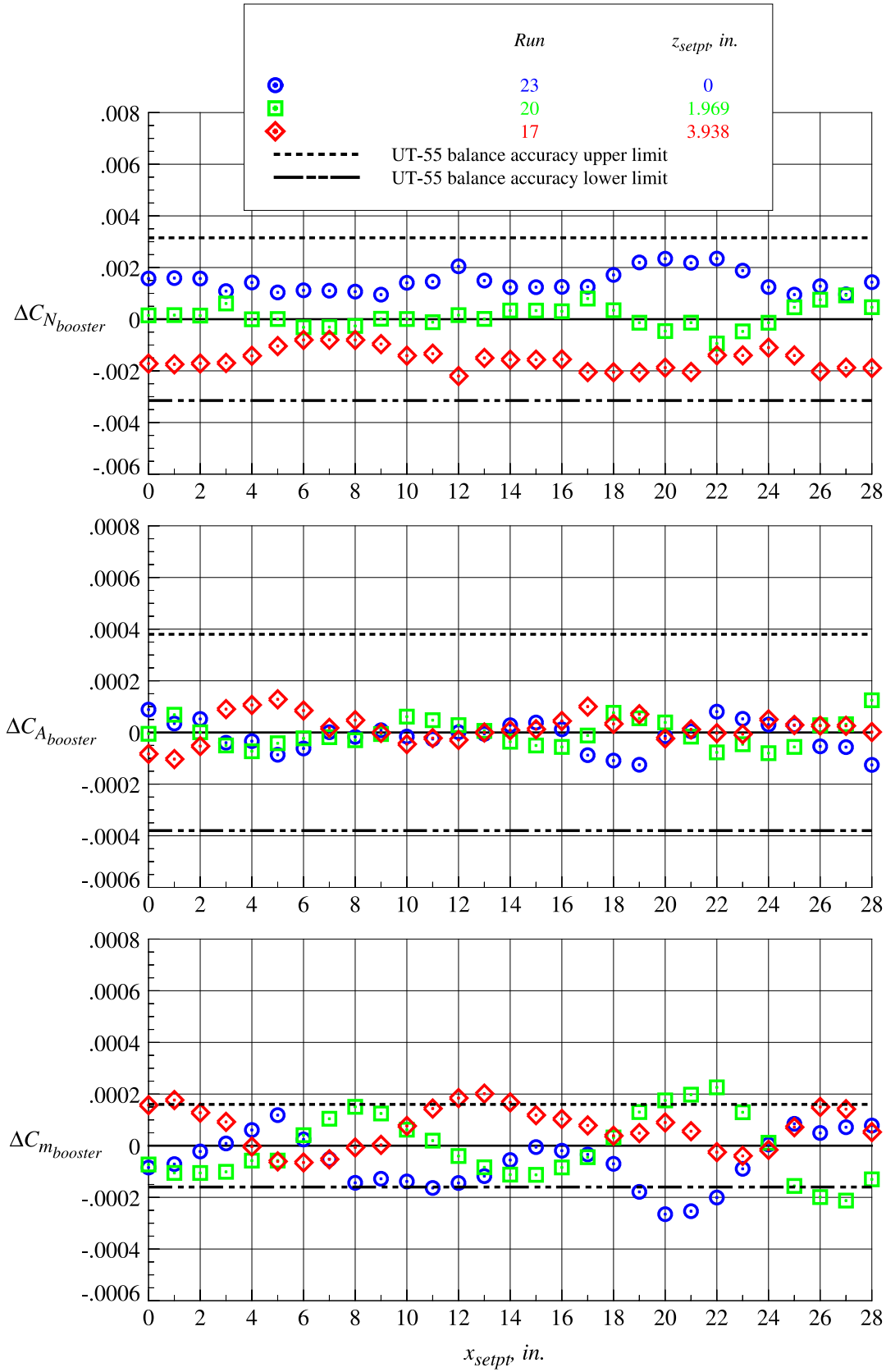
(e) Booster pitching moment coefficient, part 1

Figure 42. Continued.



(f) Booster pitching moment coefficient, part 2

Figure 42. Concluded.



(a)  $z_{setpt} = 0, 1.969, \text{ and } 3.938$  in.

Figure 43. Data repeatability of the isolated booster at Mach = 3.0 and selected  $z_{setpt}$  locations.



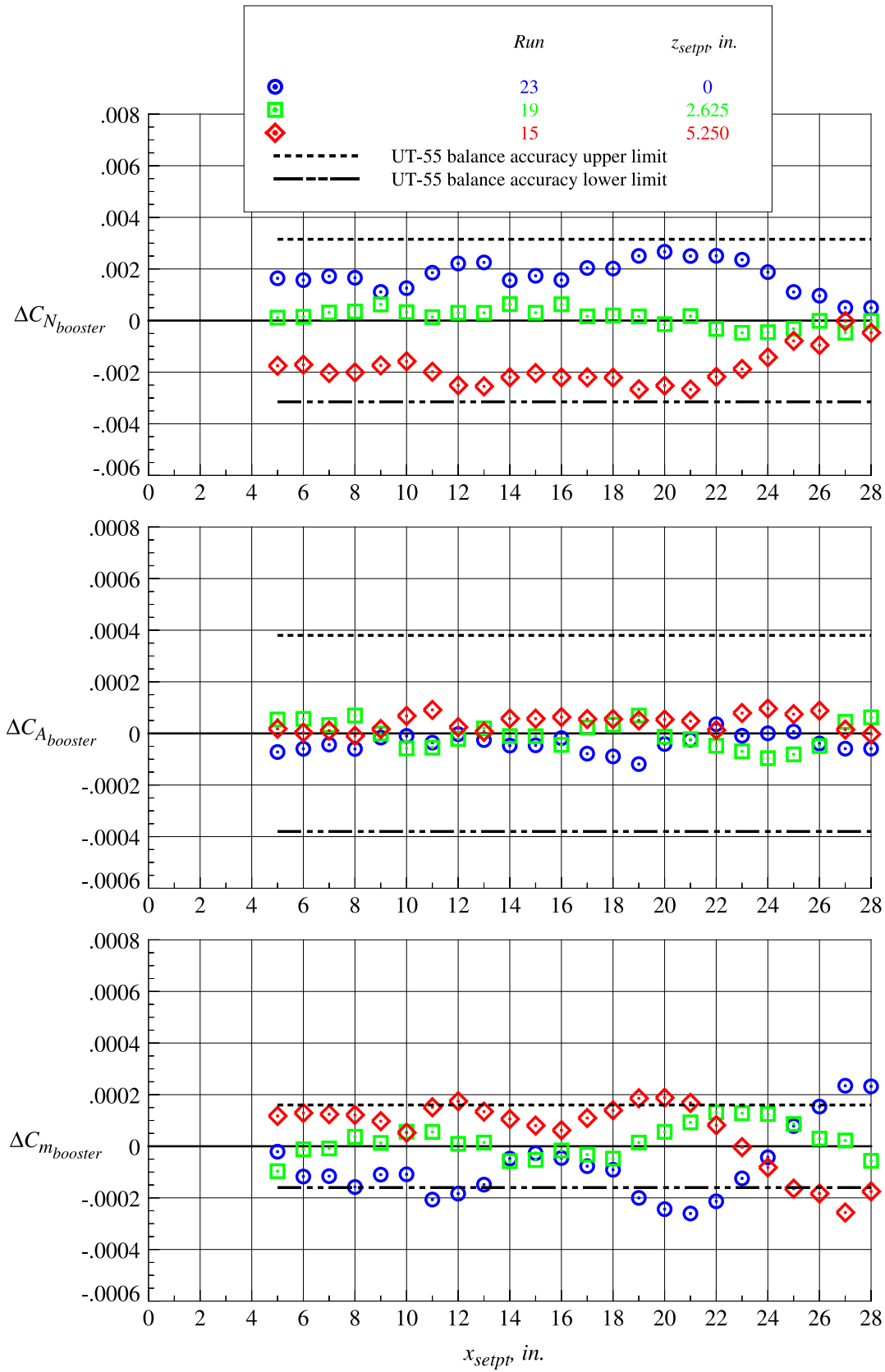
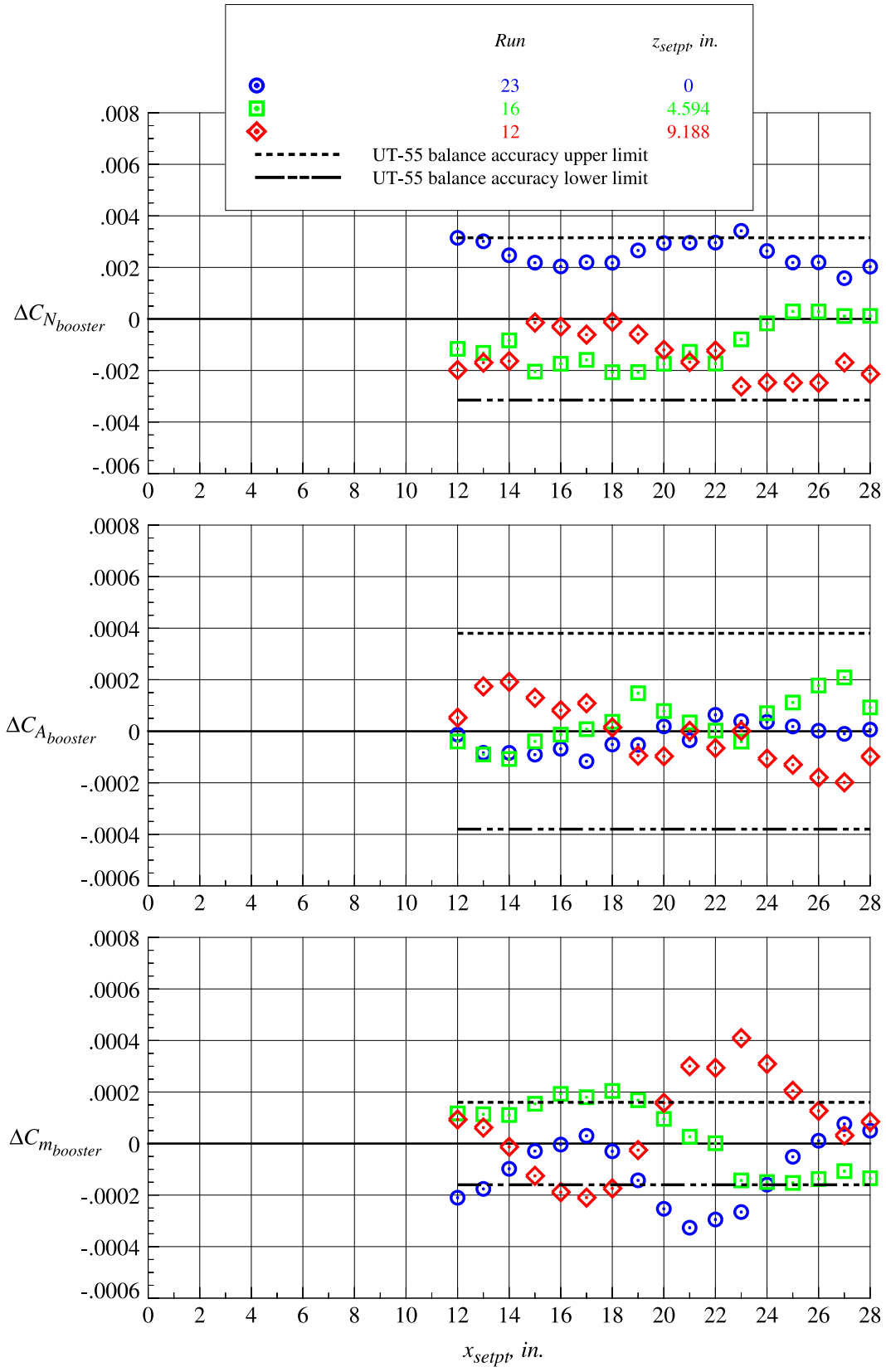
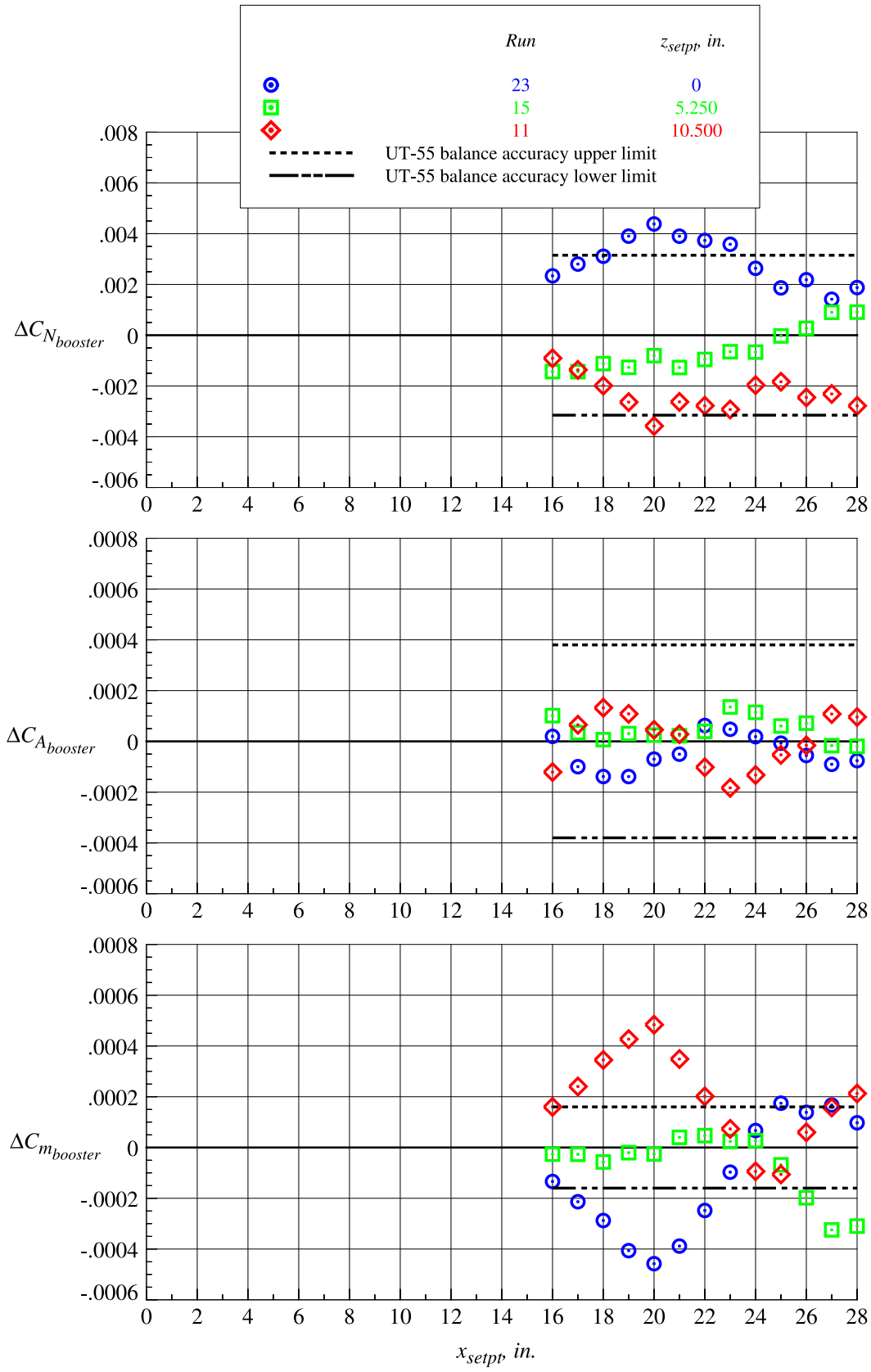


Figure 43. Continued.



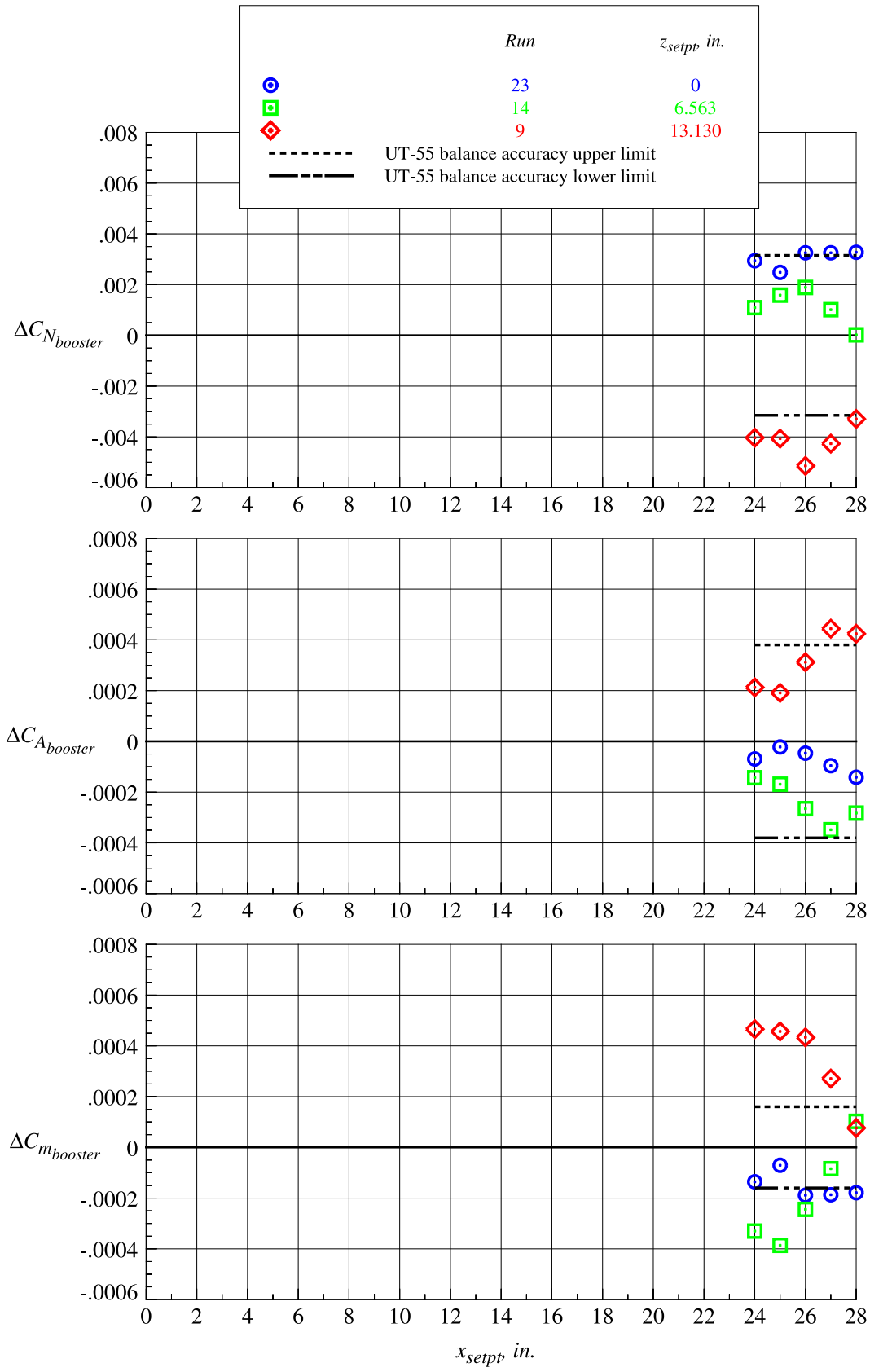
(c)  $z_{setpt} = 0, 4.594, \text{ and } 9.188 \text{ in.}$

Figure 43. Continued.



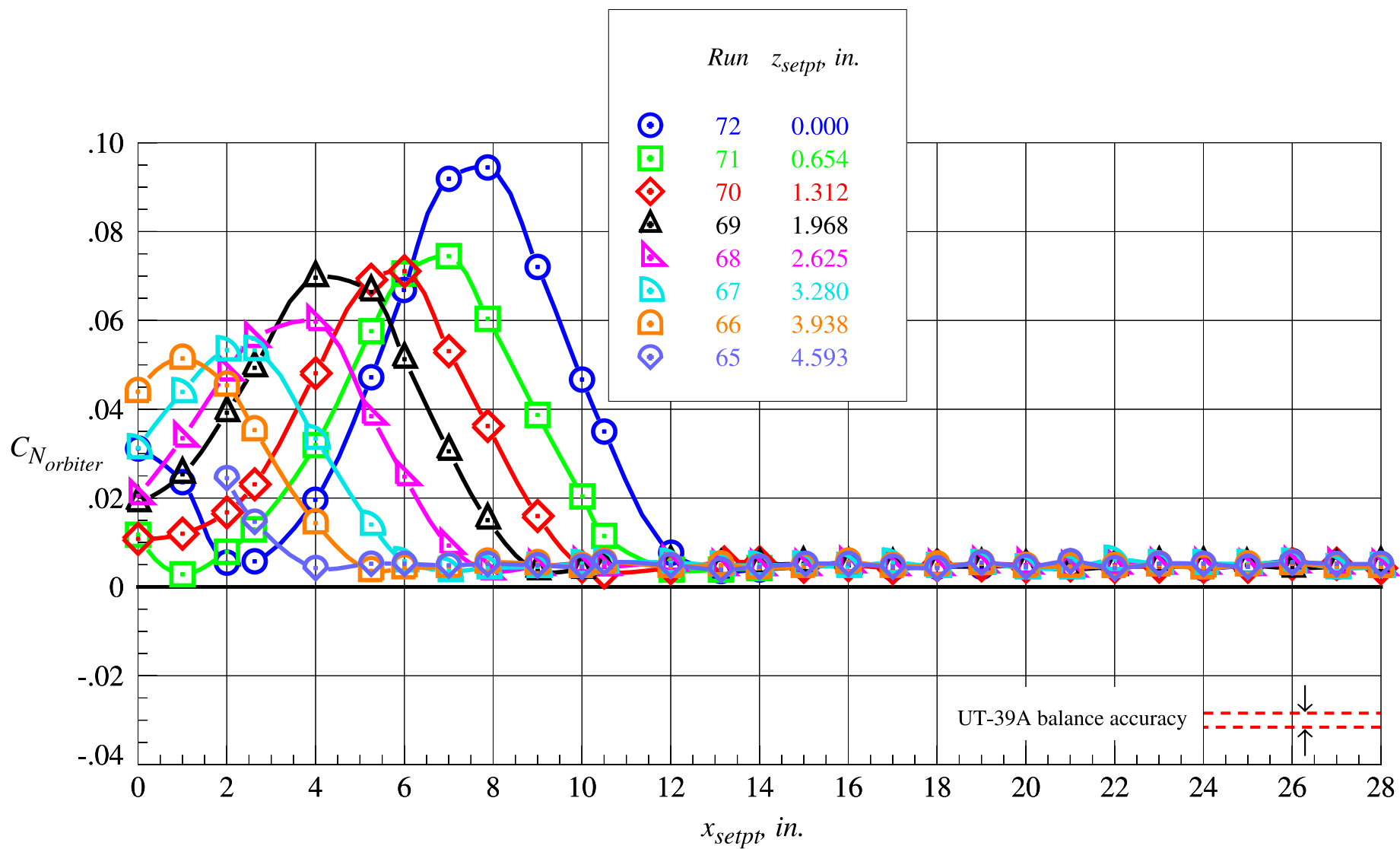
(d)  $z_{setpt} = 0, 5.250, \text{ and } 10.500 \text{ in.}$

Figure 43. Continued.



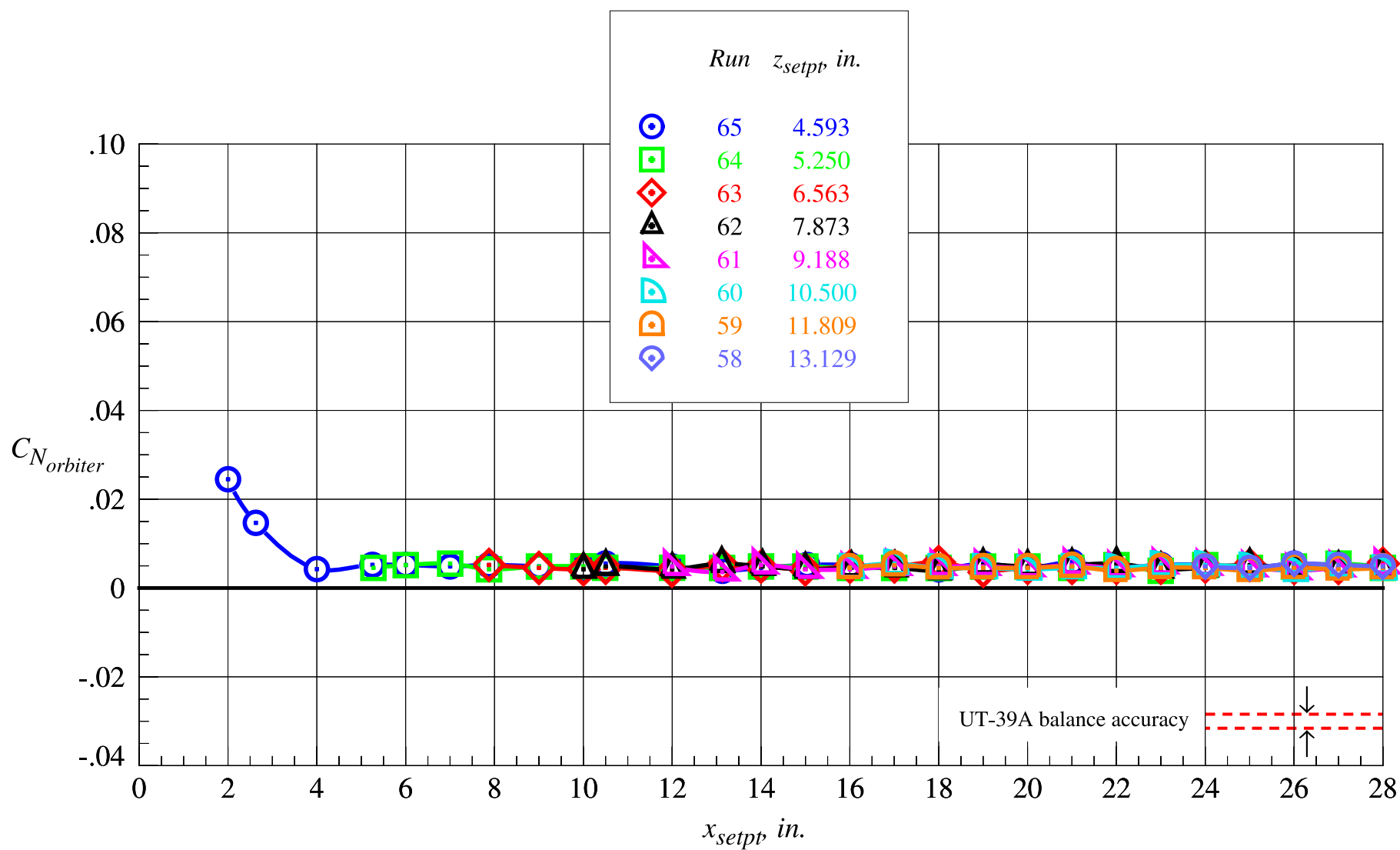
(e)  $z_{setpt} = 0, 6.564, \text{ and } 13.130$  in.

Figure 43. Concluded.



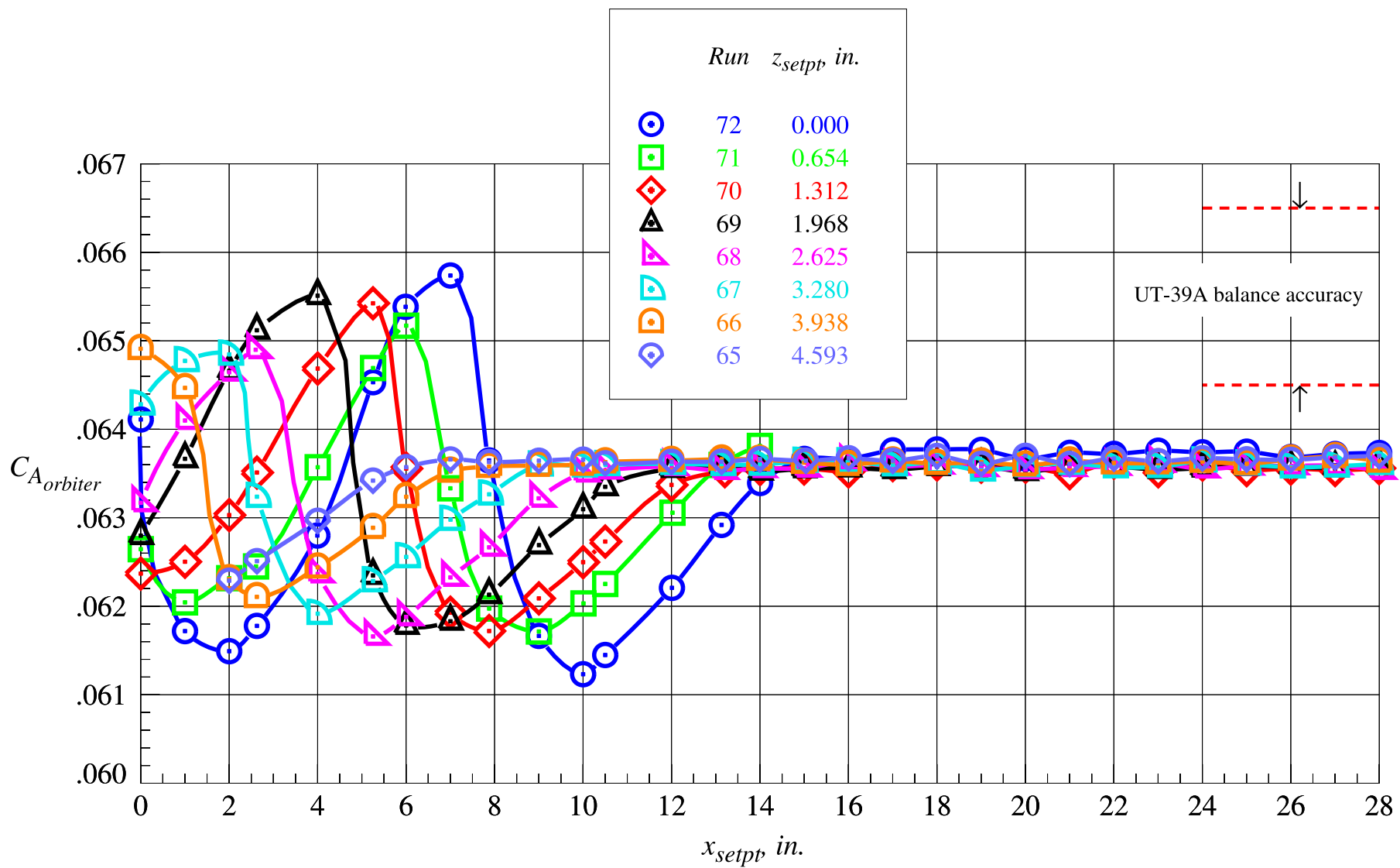
(a) Orbiter normal force coefficient, part 1

Figure 44. Orbiter proximity aerodynamic characteristics at Mach = 2.3 and  $\Delta\alpha = 0^\circ$ .



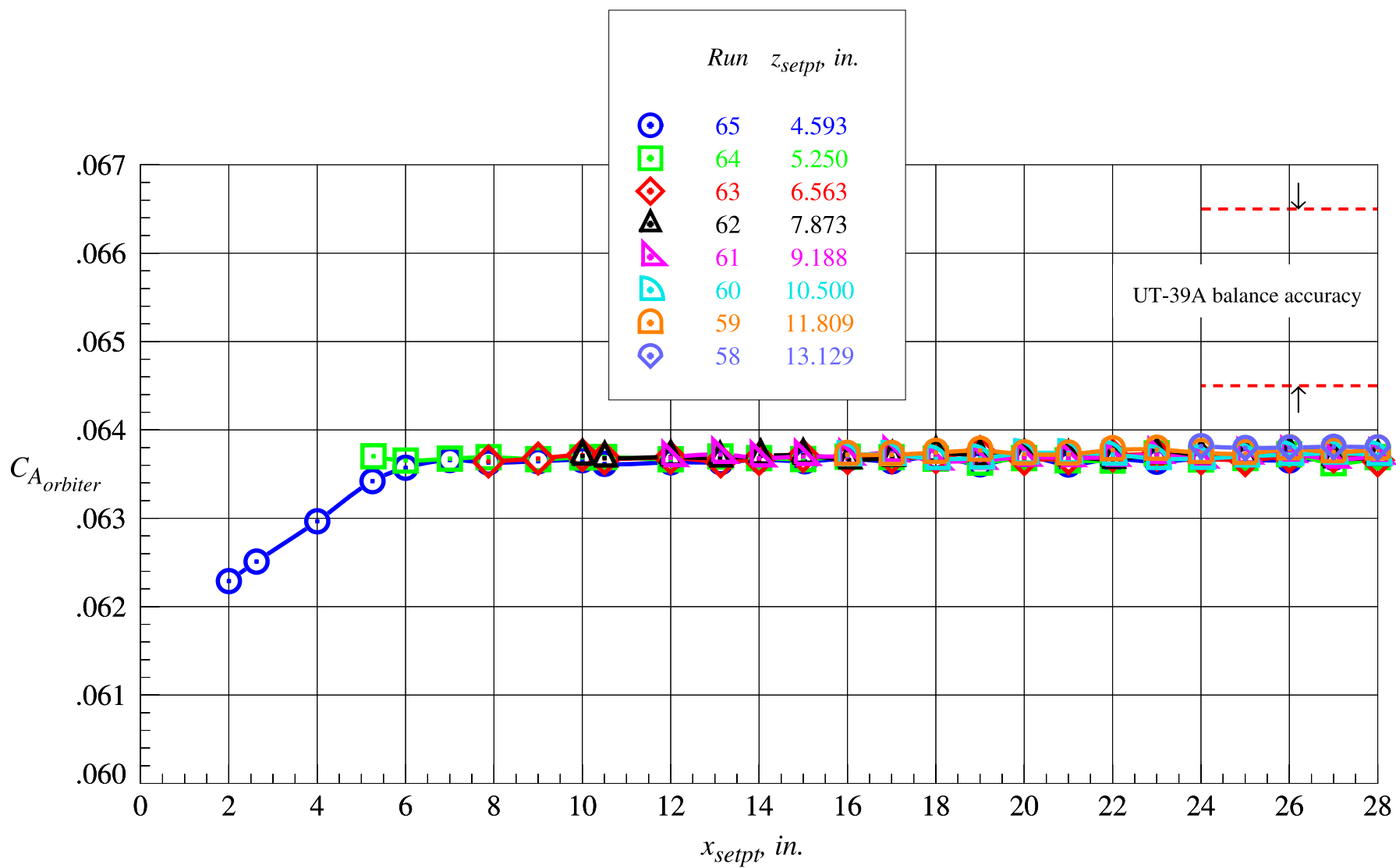
(b) Orbiter normal force coefficient, part 2

Figure 44. Continued.



(c) Orbiter axial force coefficient, part 1

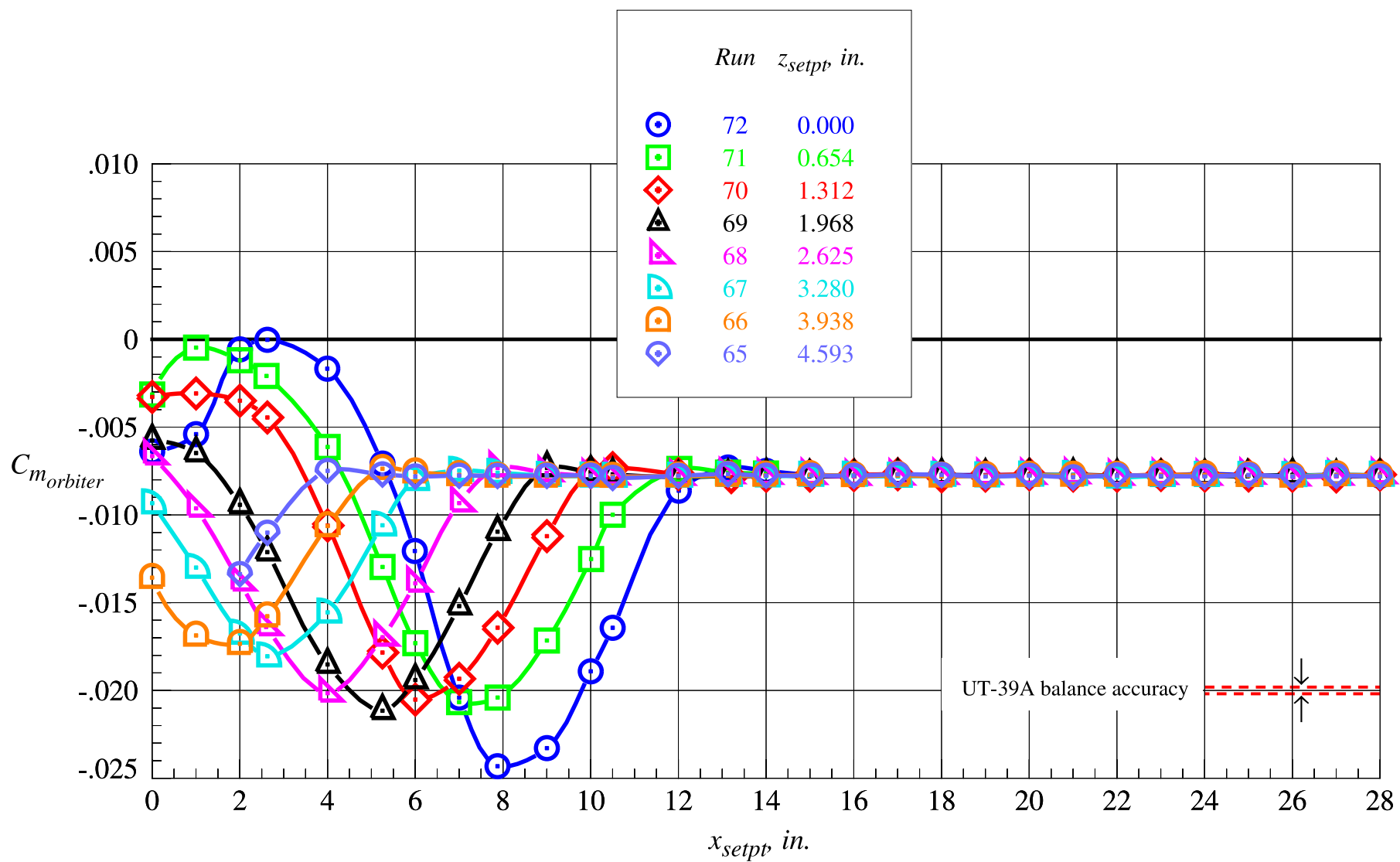
Figure 44. Continued.



(d) Orbiter axial force coefficient, part 2

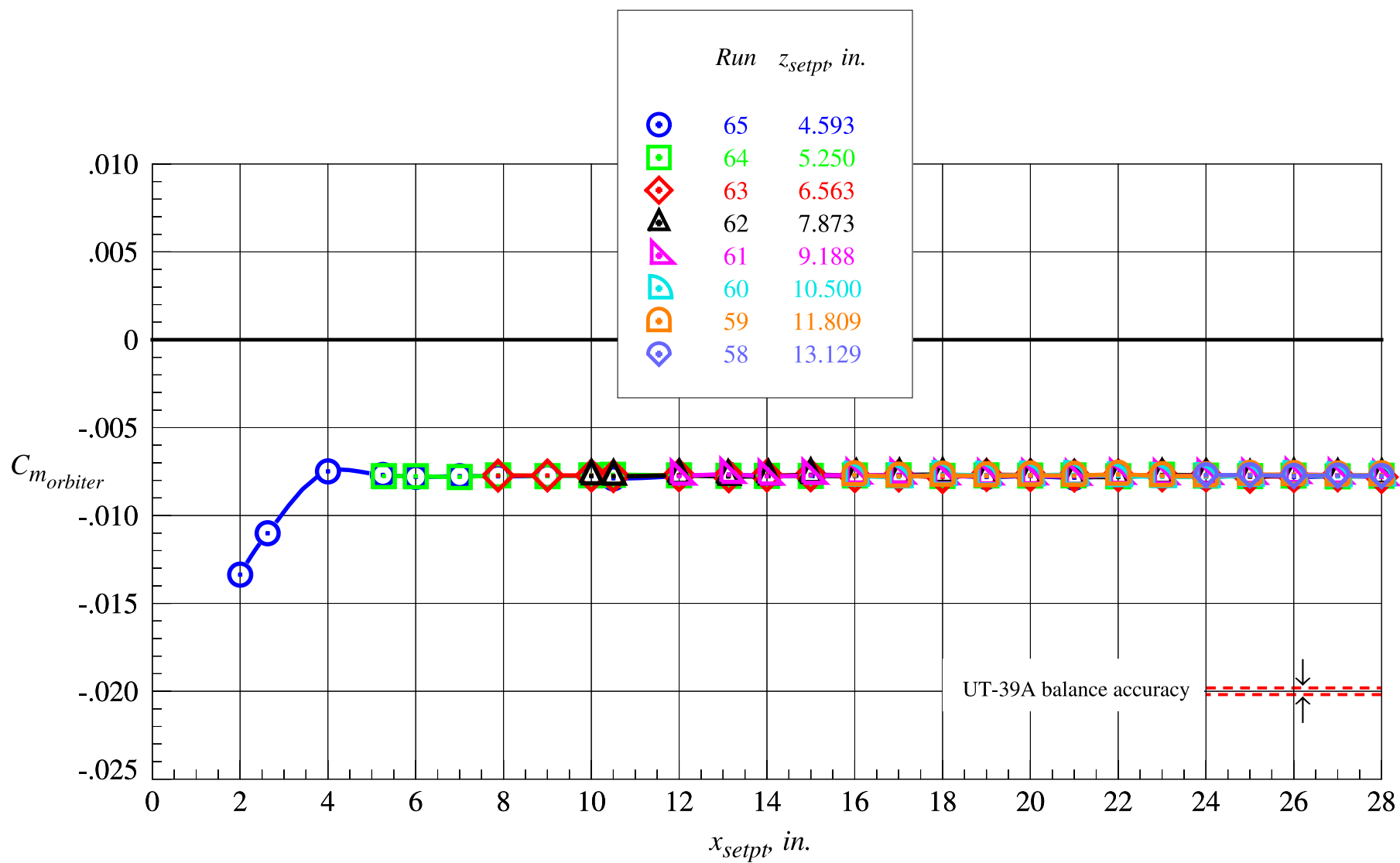
Figure 44. Continued.





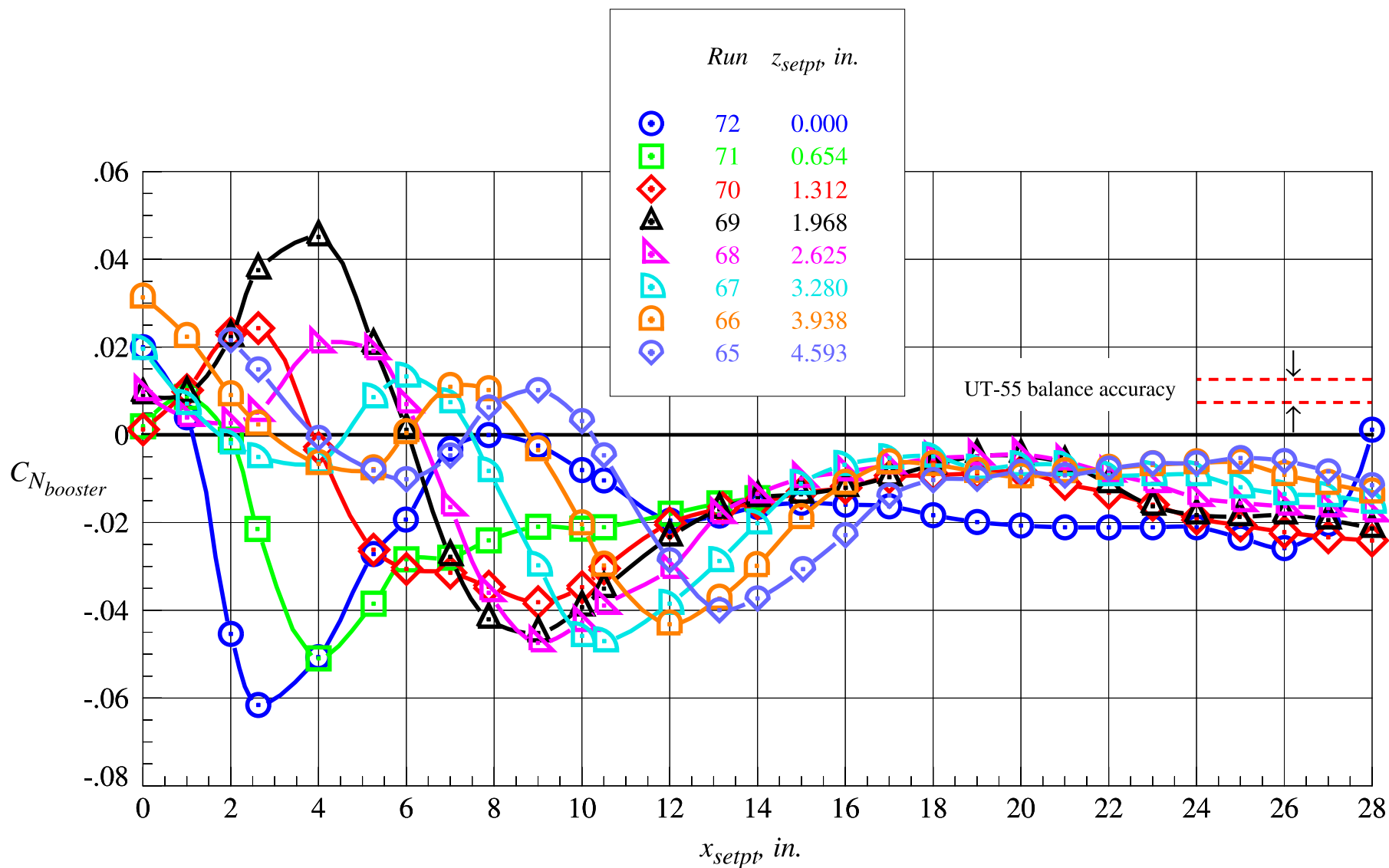
(e) Orbiter pitching moment coefficient, part 1

Figure 44. Continued.



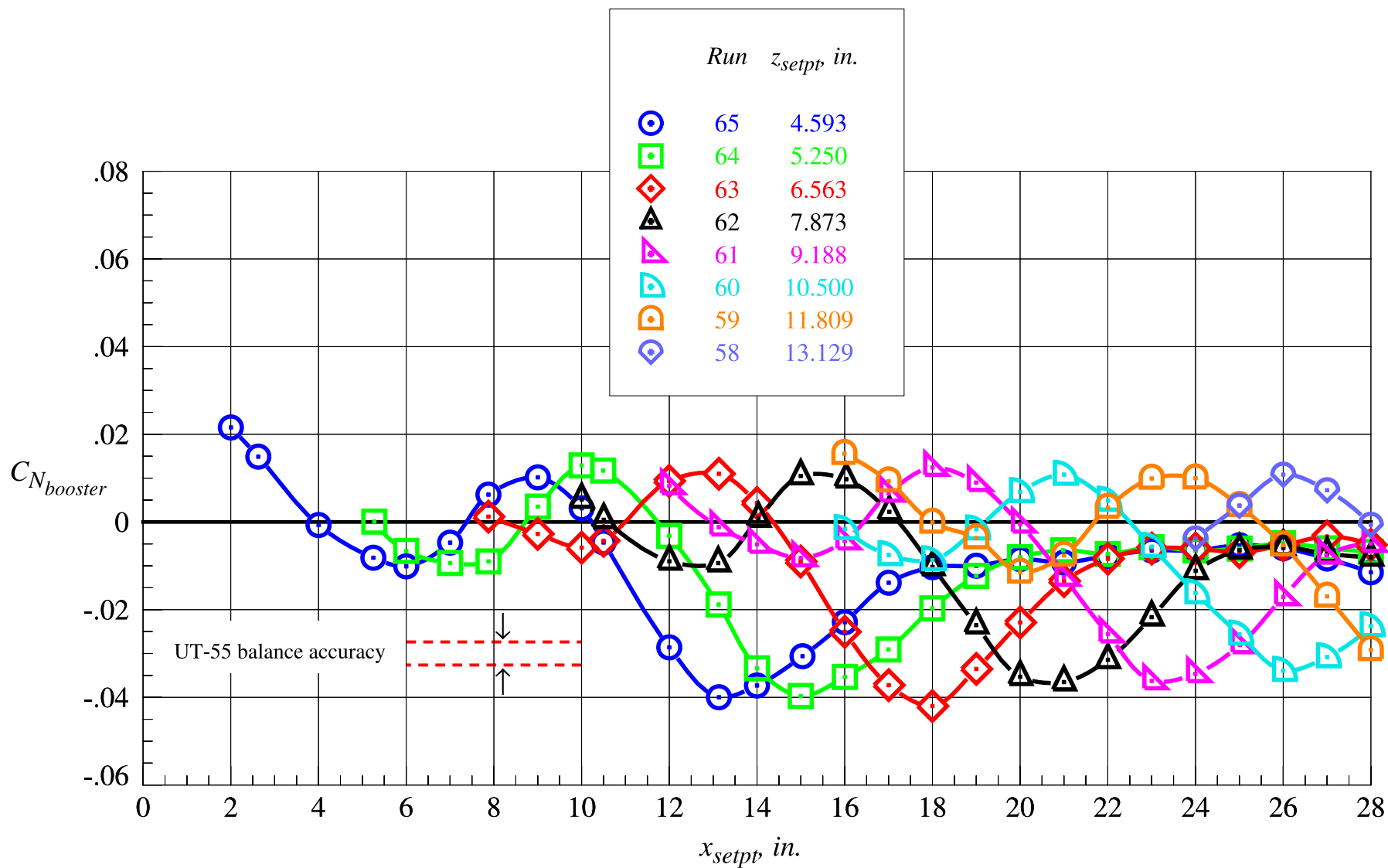
(f) Orbiter pitching moment coefficient, part 2

Figure 44. Concluded.



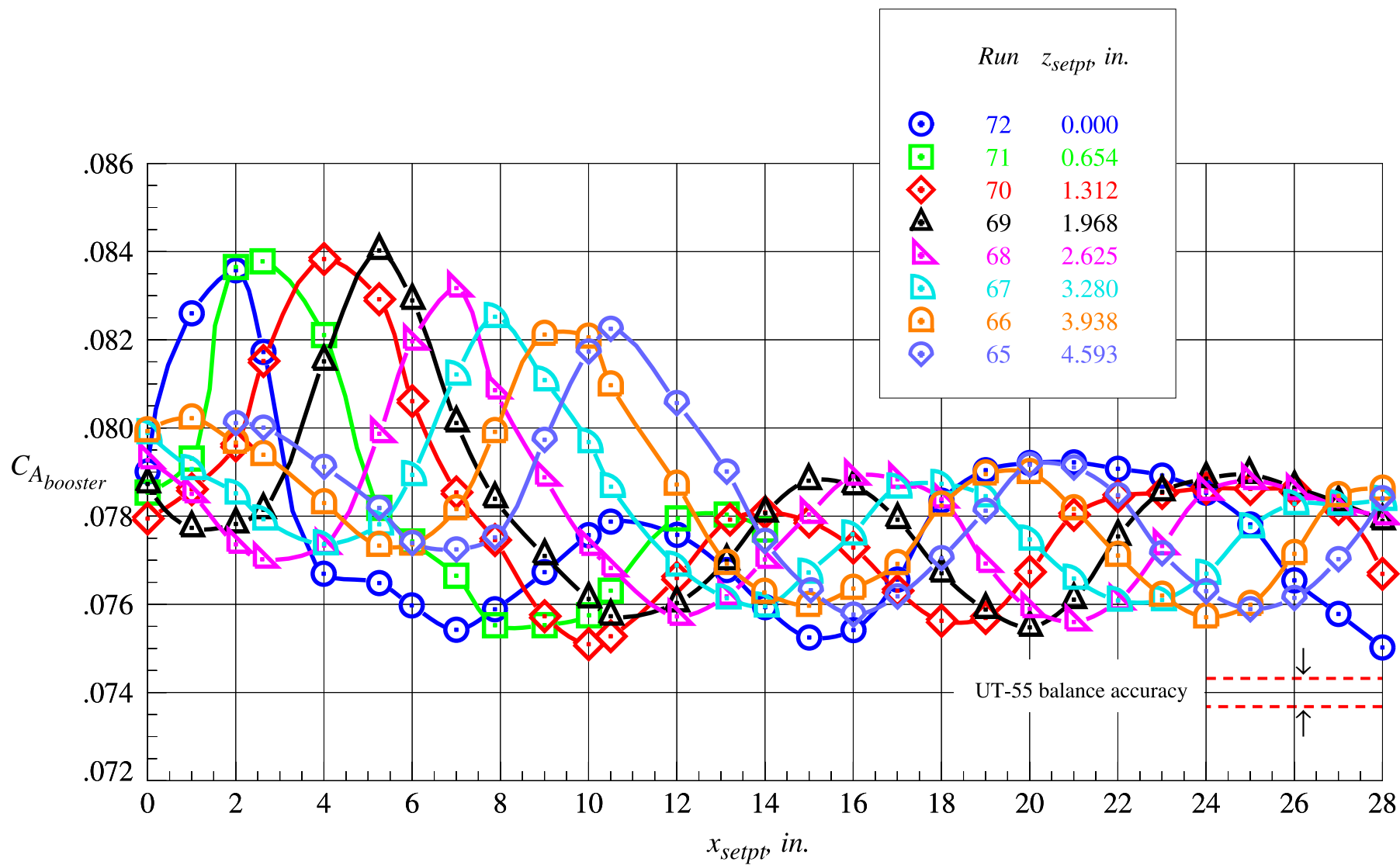
(a) Booster normal force coefficient, part 1

Figure 45. Booster proximity aerodynamic characteristics at Mach = 2.3 and  $\Delta\alpha = 0^\circ$ .



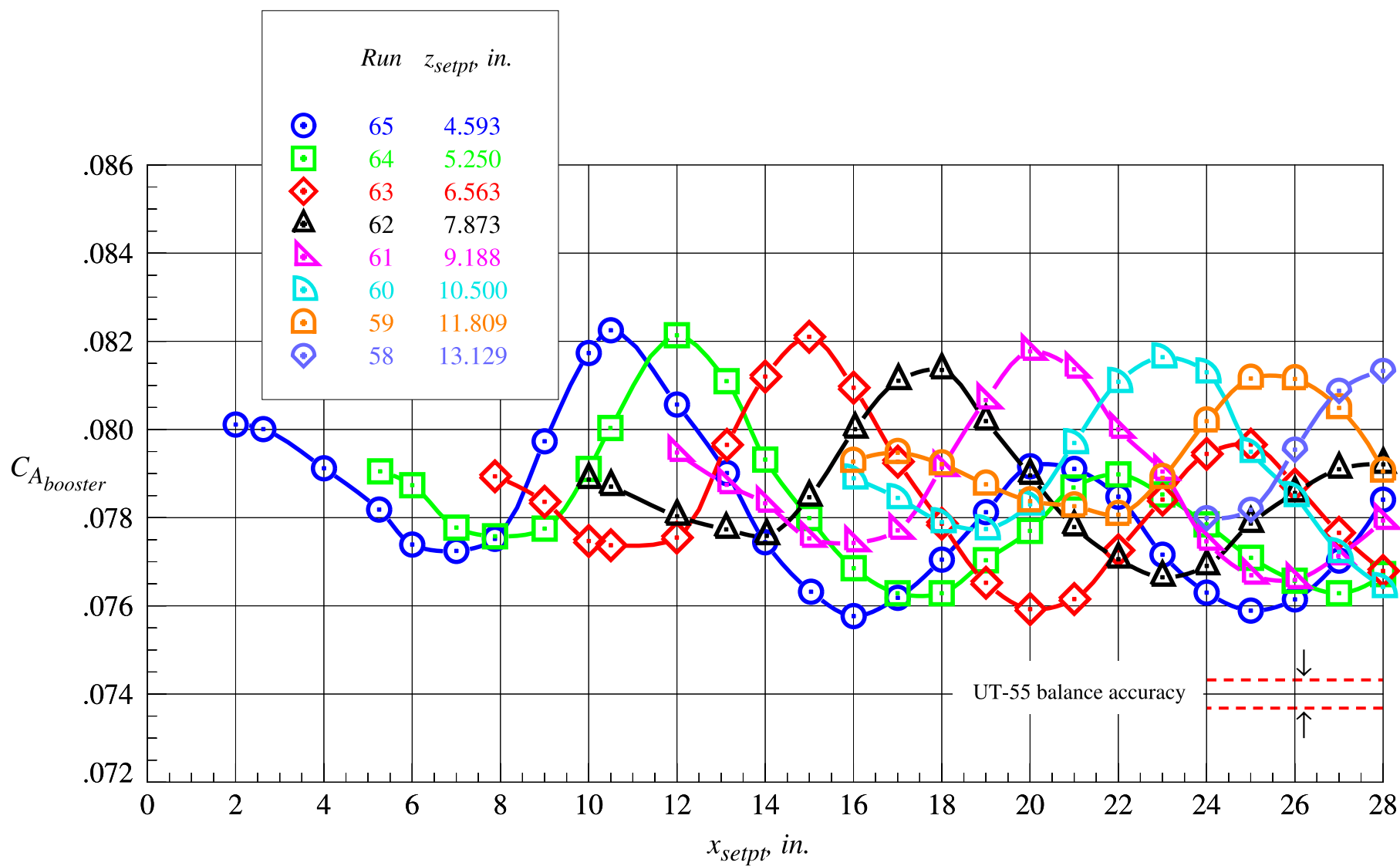
(b) Booster normal force coefficient, part 2

Figure 45. Continued.



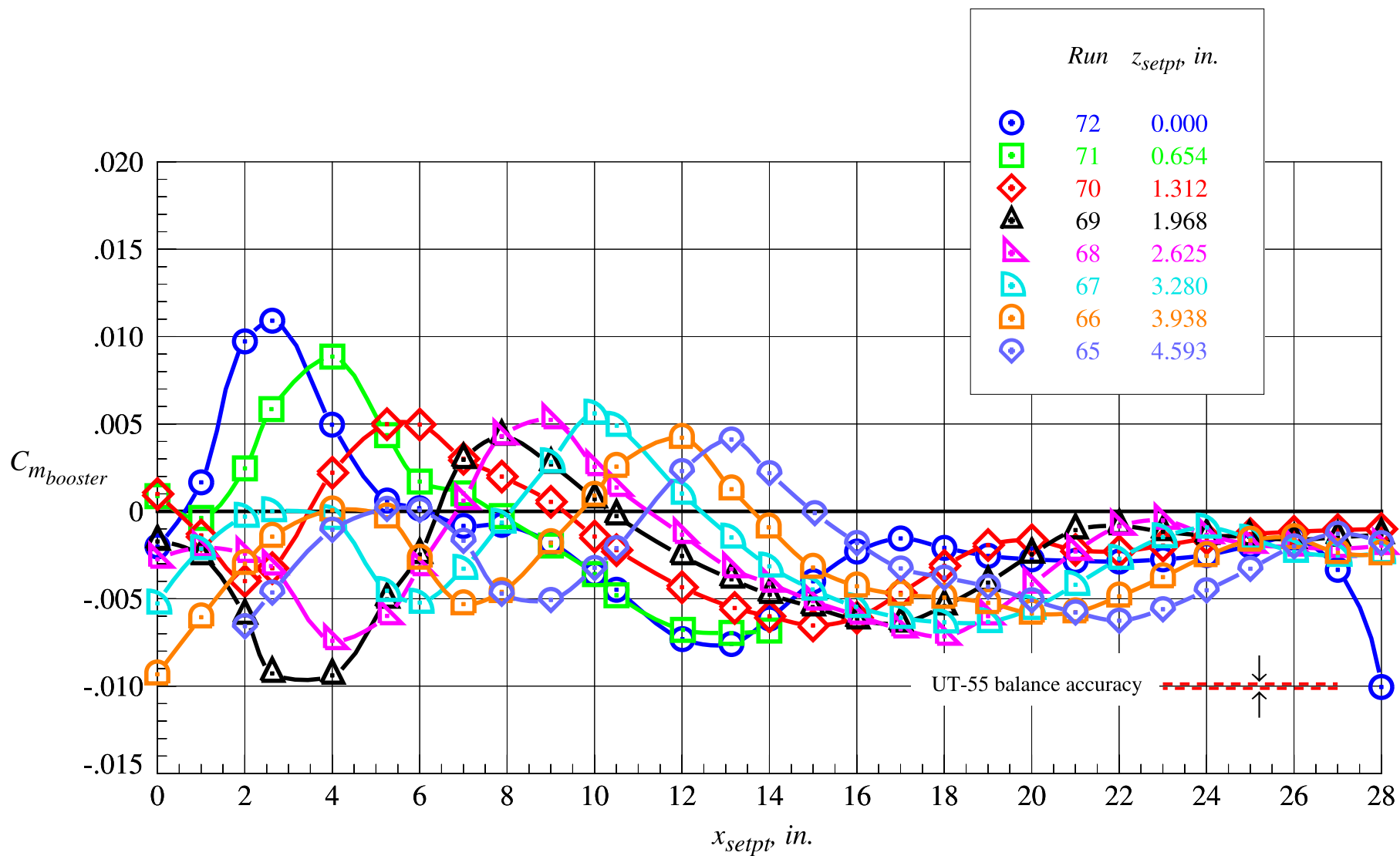
(c) Booster axial force coefficient, part 1

Figure 45. Continued.



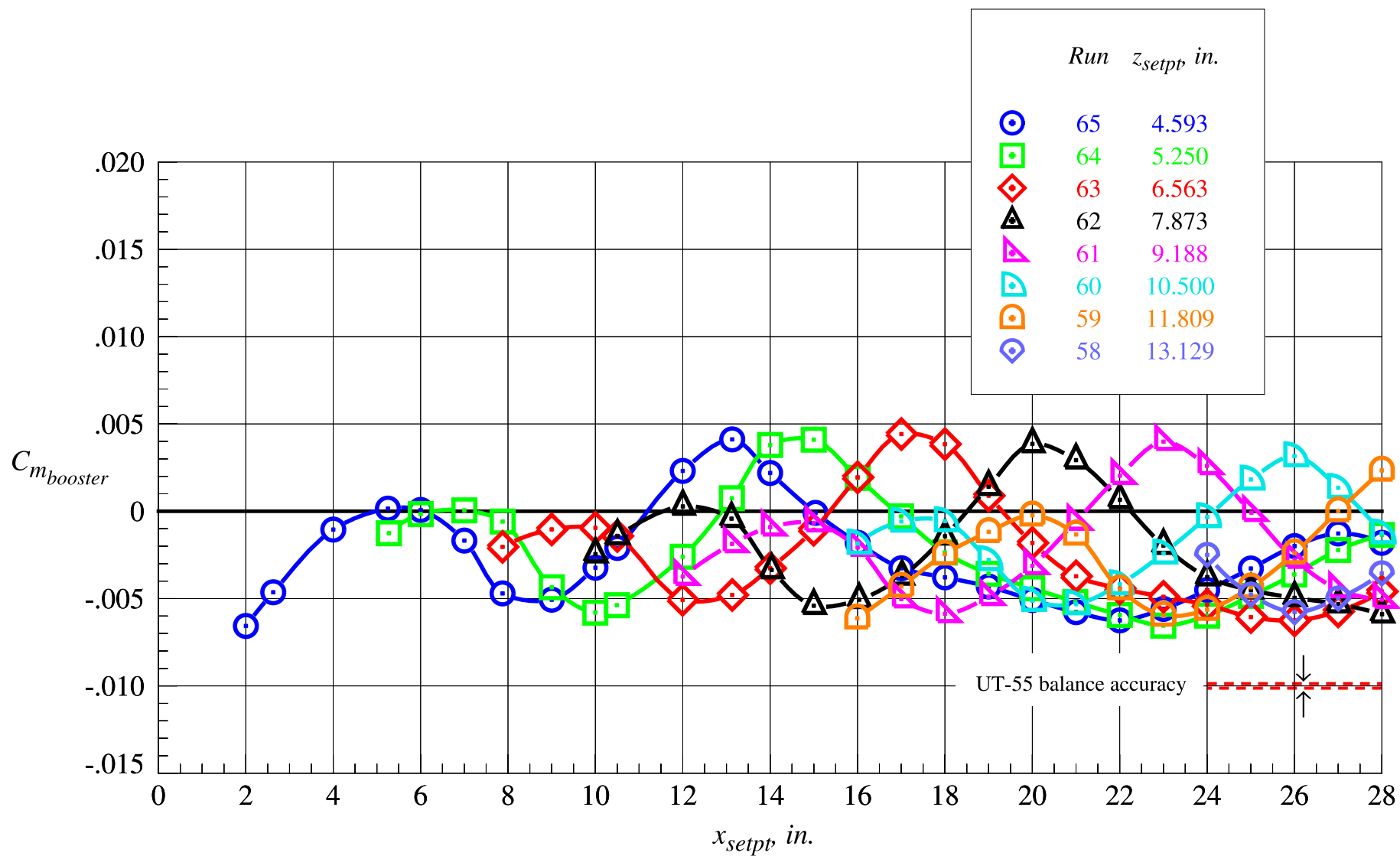
(d) Booster axial force coefficient, part 2

Figure 45. Continued.



(e) Booster pitching moment coefficient, part 1

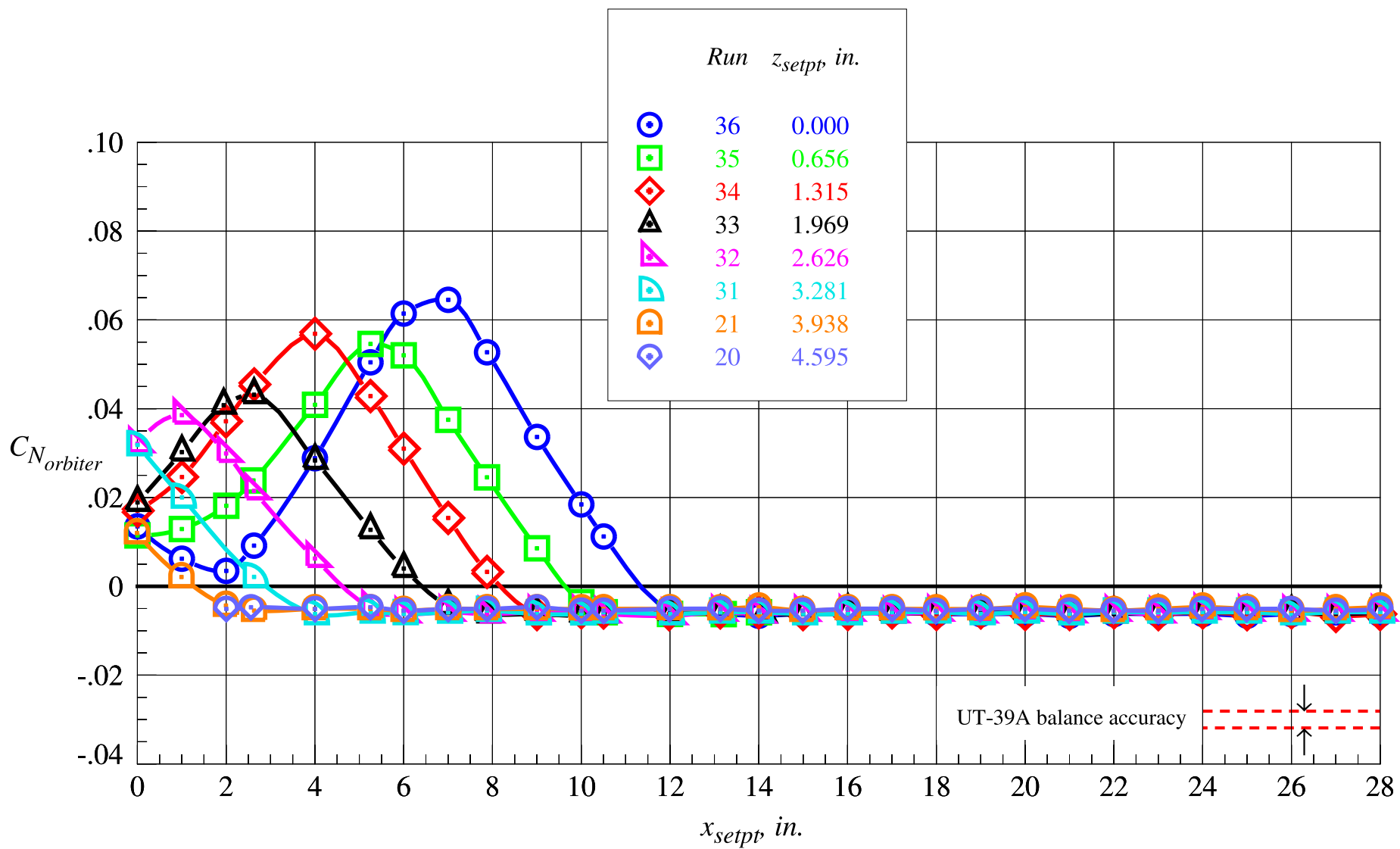
Figure 45. Continued.



(f) Booster pitching moment coefficient, part 2

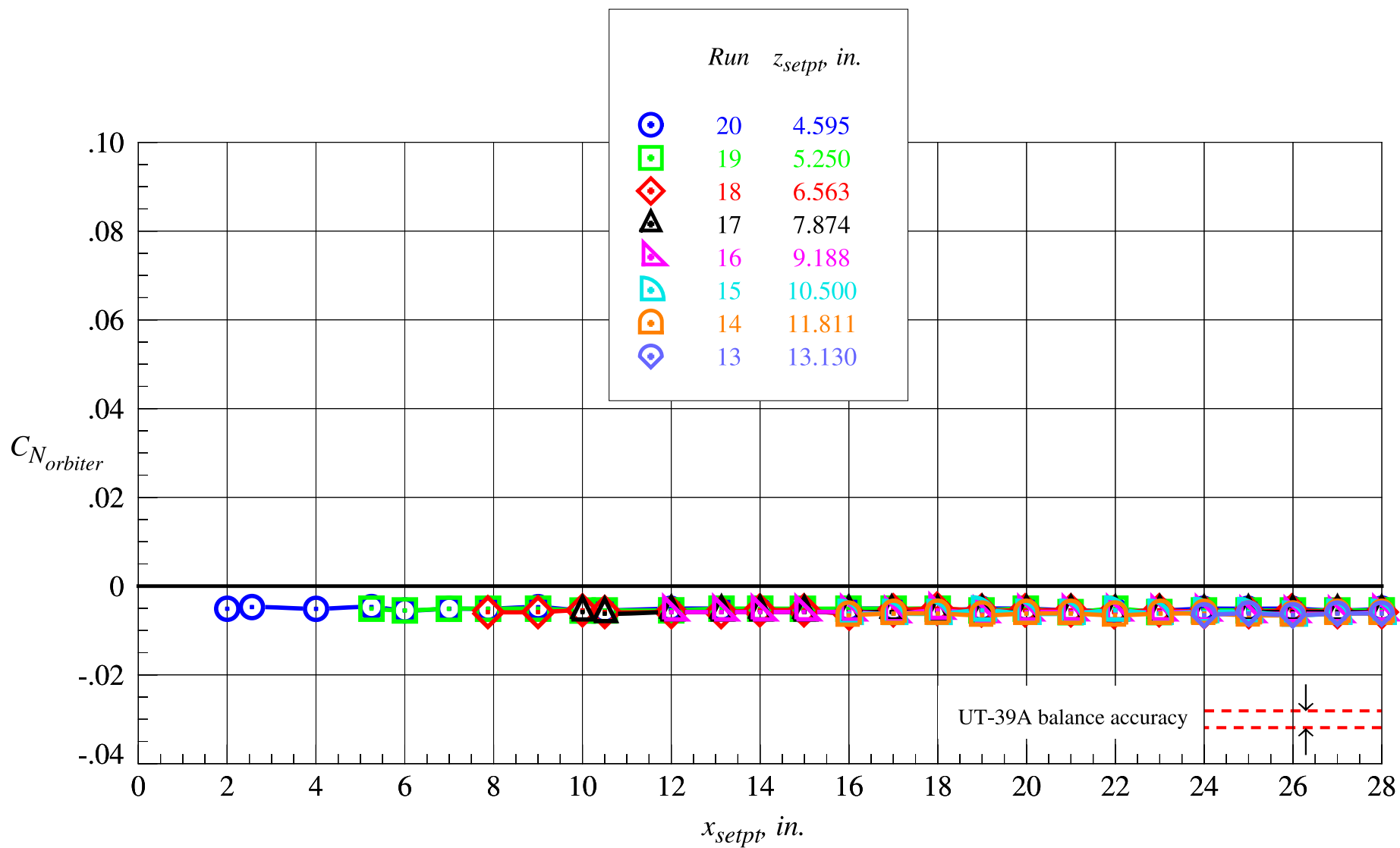
Figure 45. Concluded.





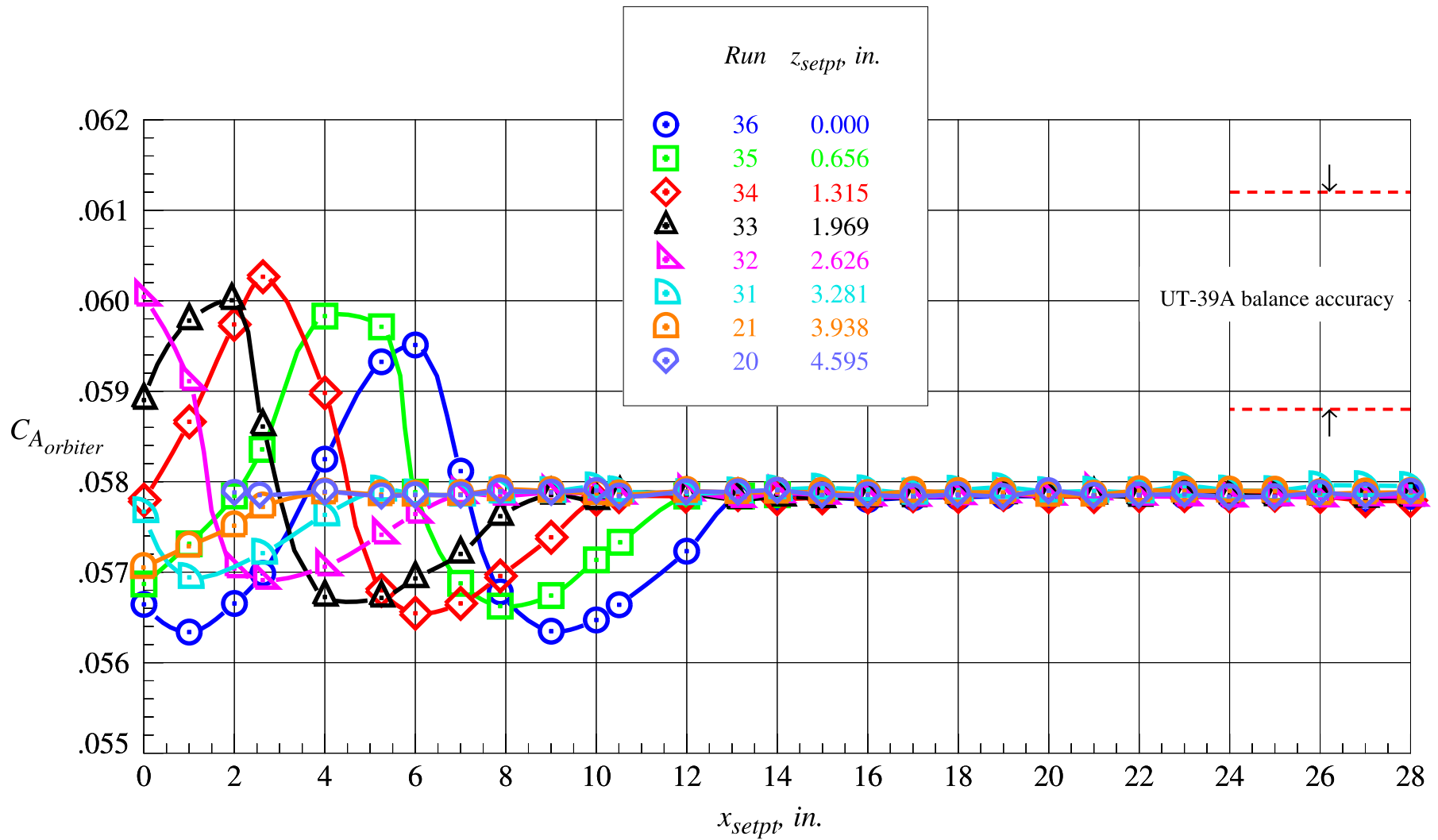
(a) Orbiter normal force coefficient, part 1

Figure 46. Orbiter proximity aerodynamic characteristics at  $Mach = 3.0$  and  $\Delta\alpha = 0^\circ$ .



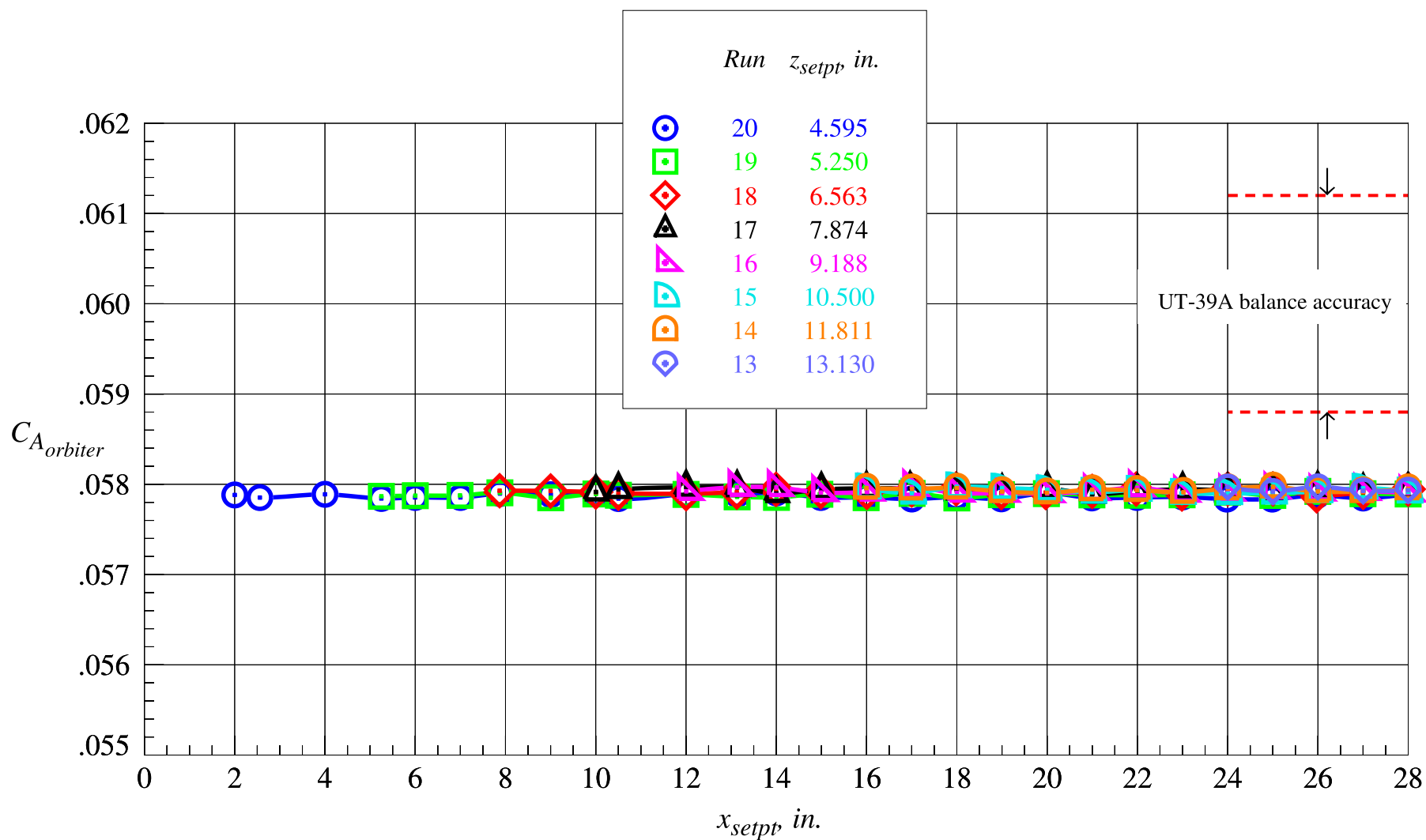
(b) Orbiter normal force coefficient, part 2

Figure 46. Continued.



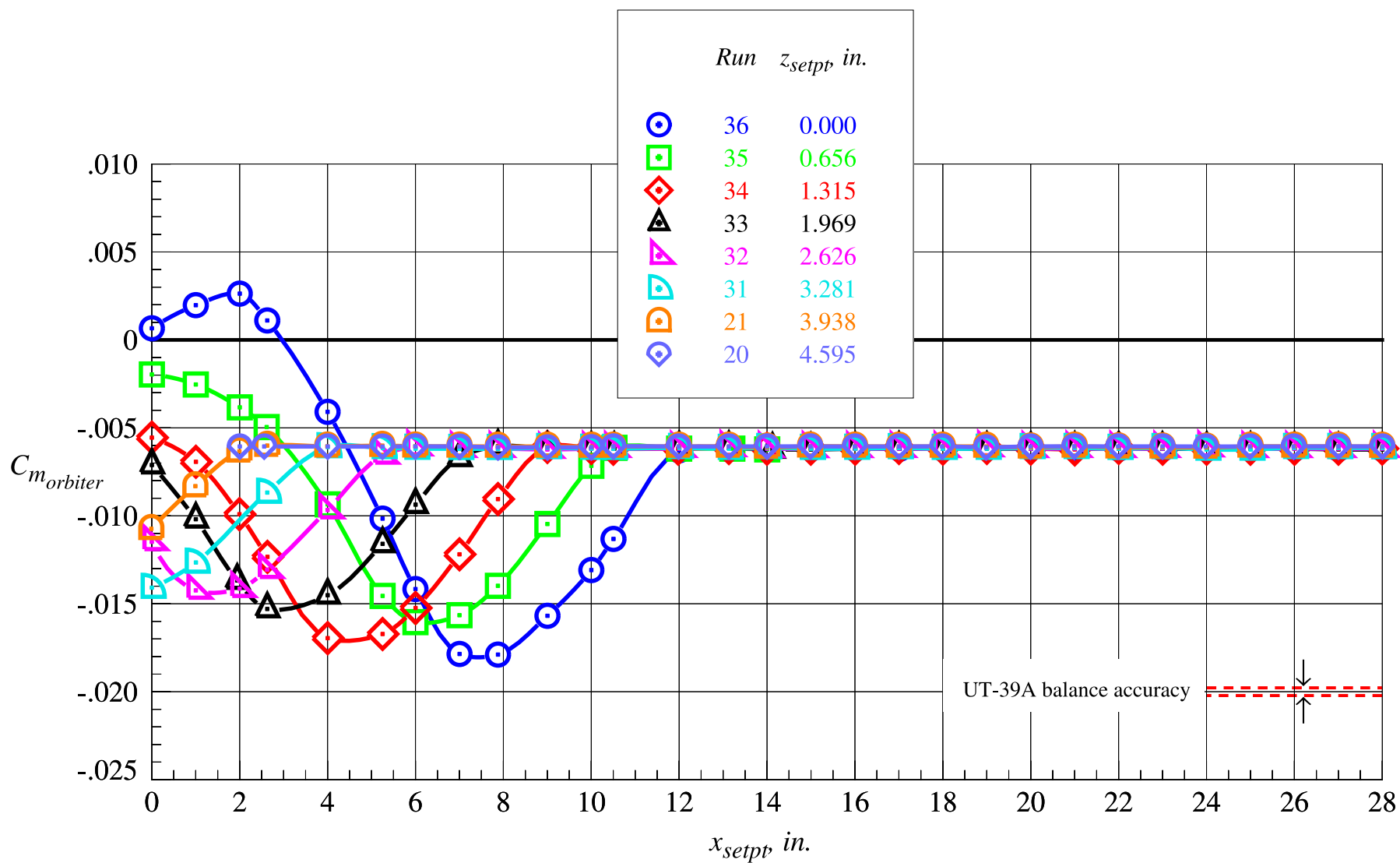
(c) Orbiter axial force coefficient, part 1

Figure 46. Continued.



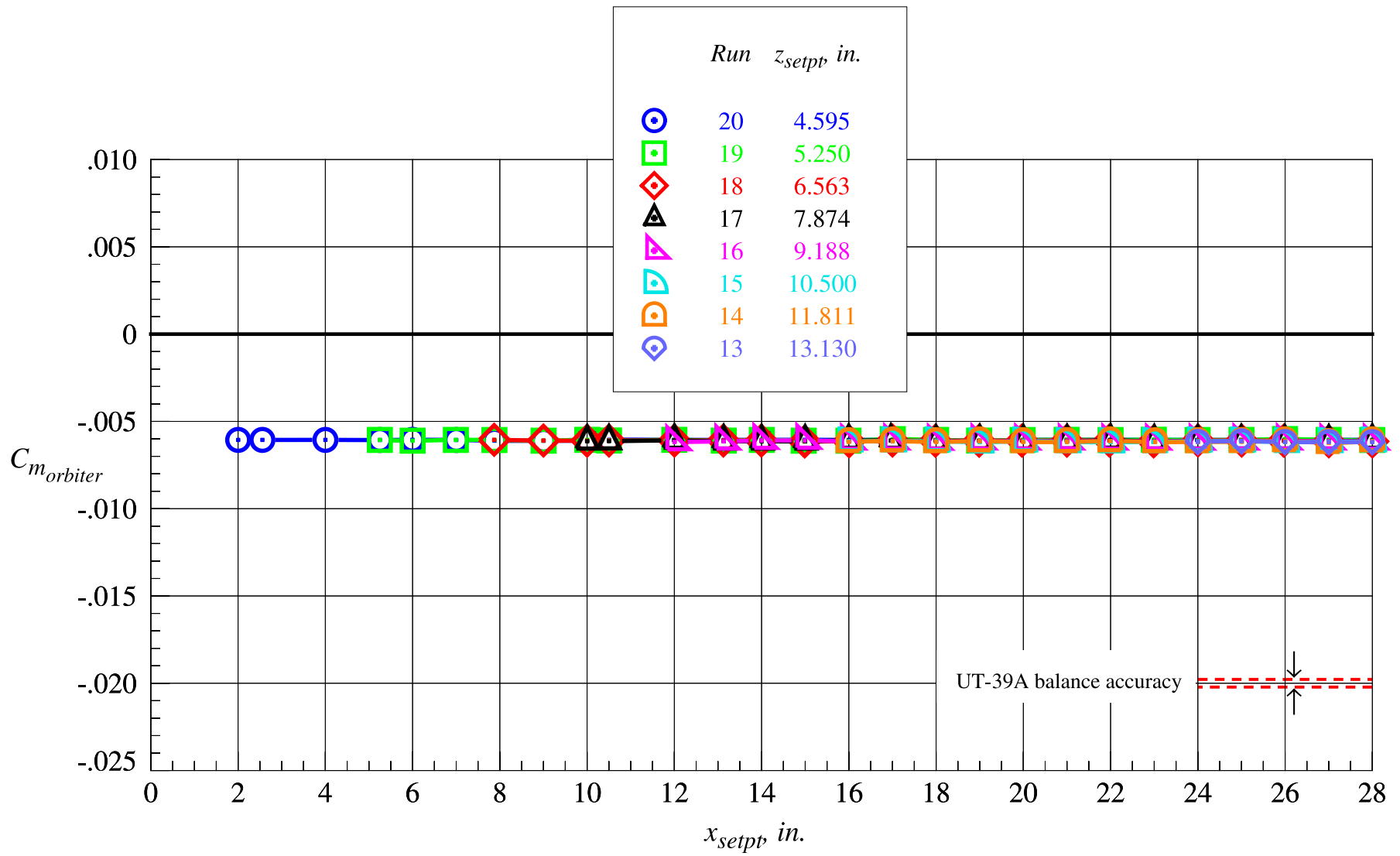
(d) Orbiter axial force coefficient, part 2

Figure 46. Continued.



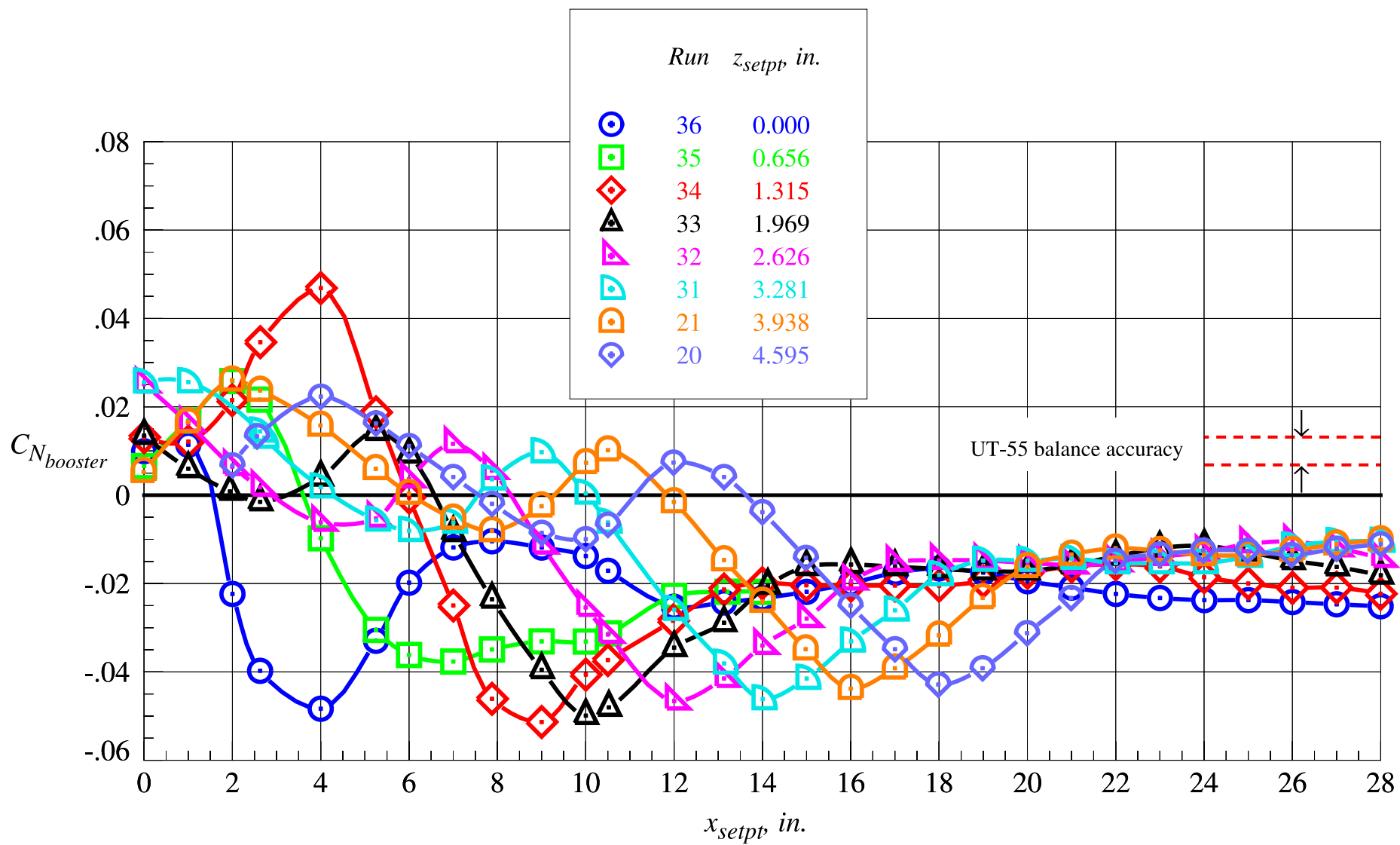
(e) Orbiter pitching moment coefficient, part 1

Figure 46. Continued.



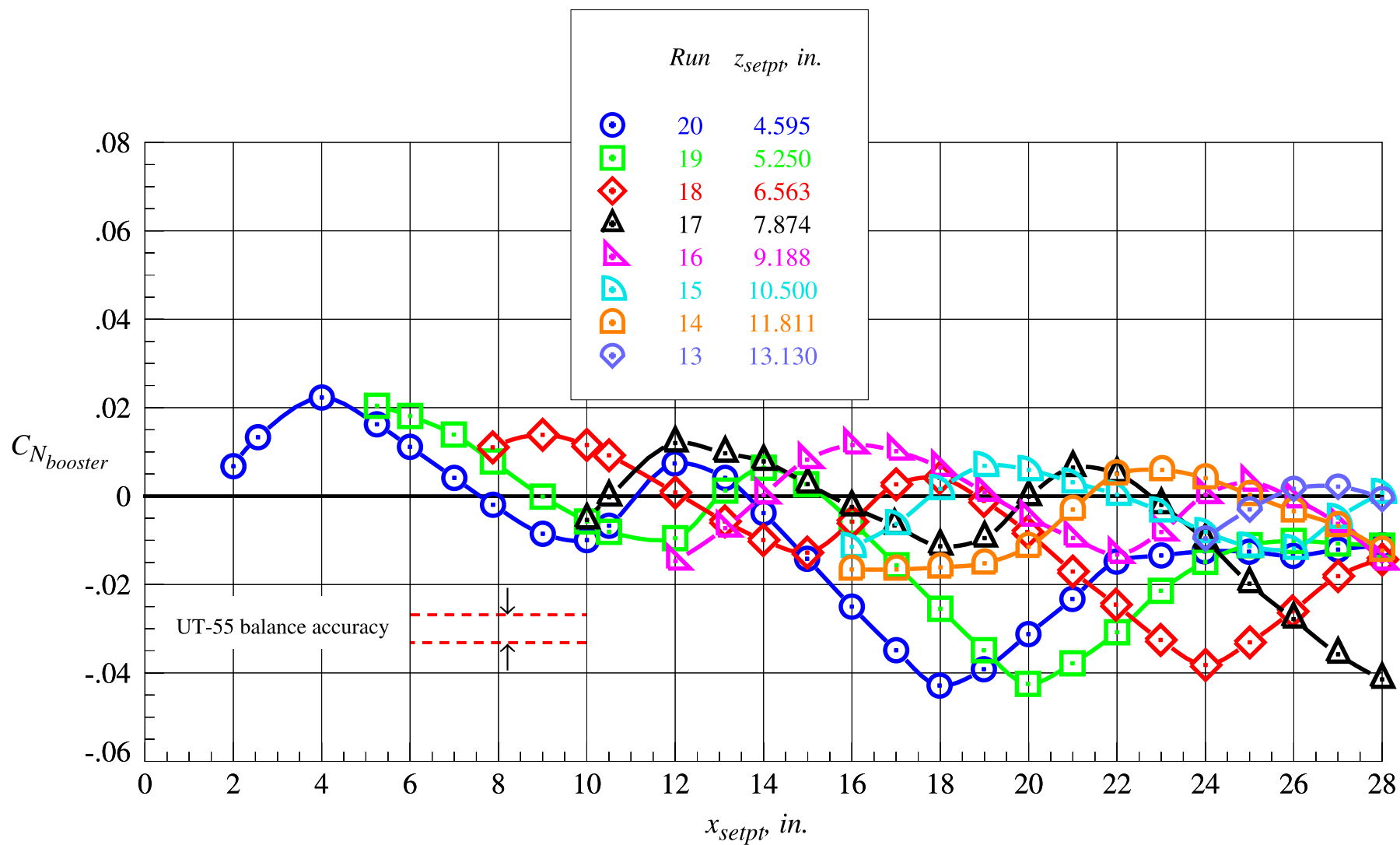
(f) Orbiter pitching moment coefficient, part 2

Figure 46. Concluded.



(a) Booster normal force coefficient, part 1

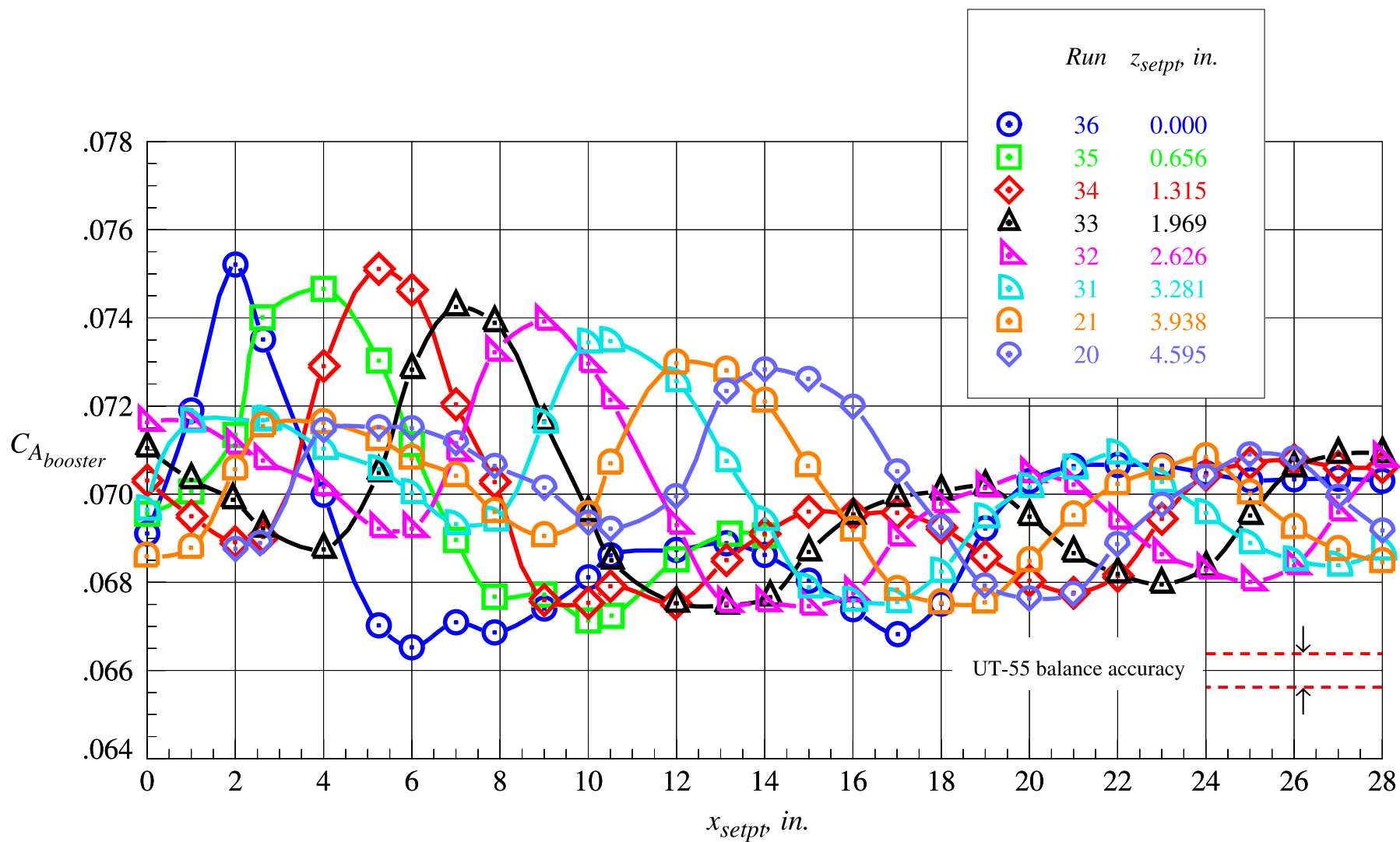
Figure 47. Booster proximity aerodynamic characteristics at Mach = 3.0 and  $\Delta\alpha = 0^\circ$ .



(b) Booster normal force coefficient, part 2

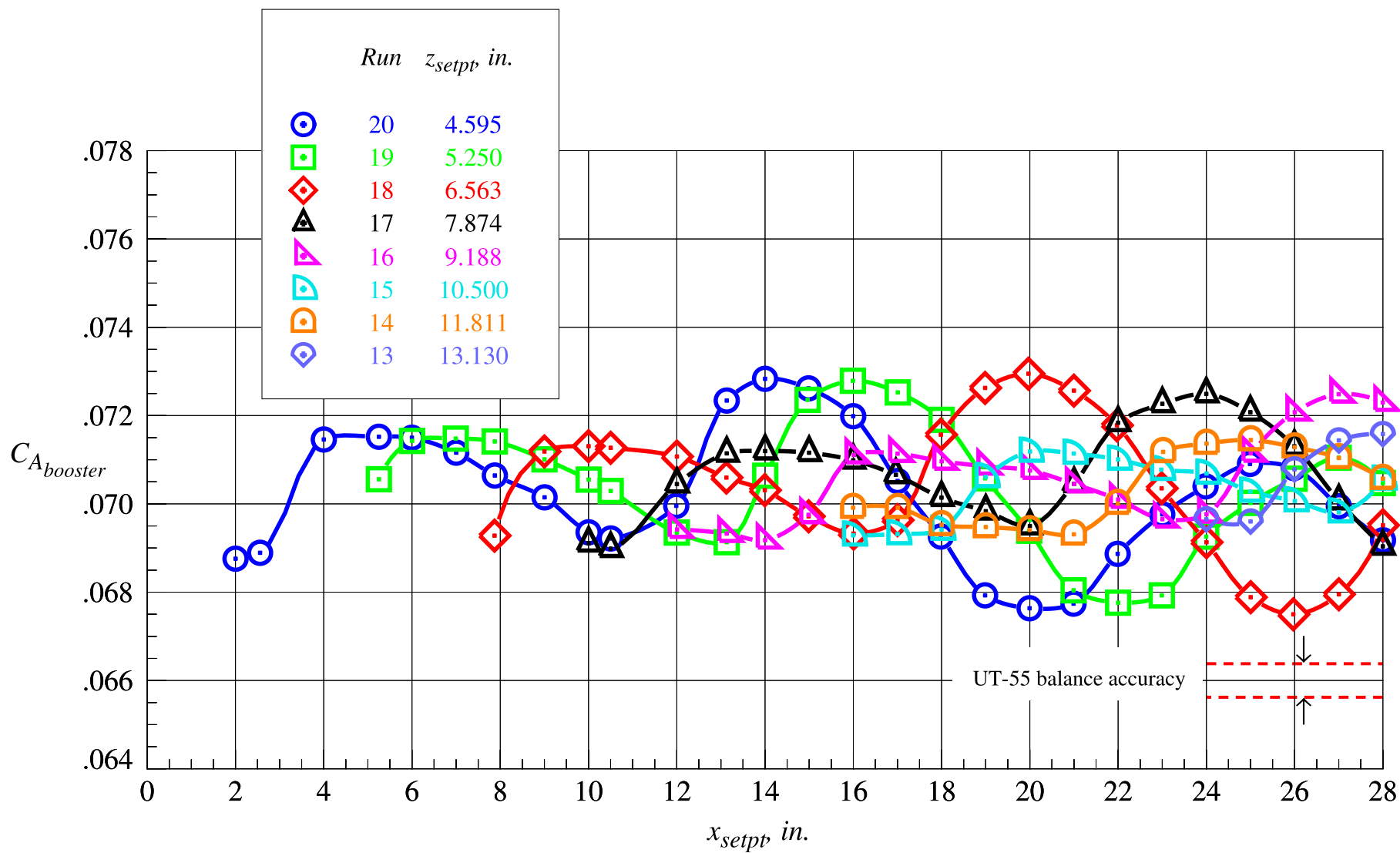
Figure 47. Continued.





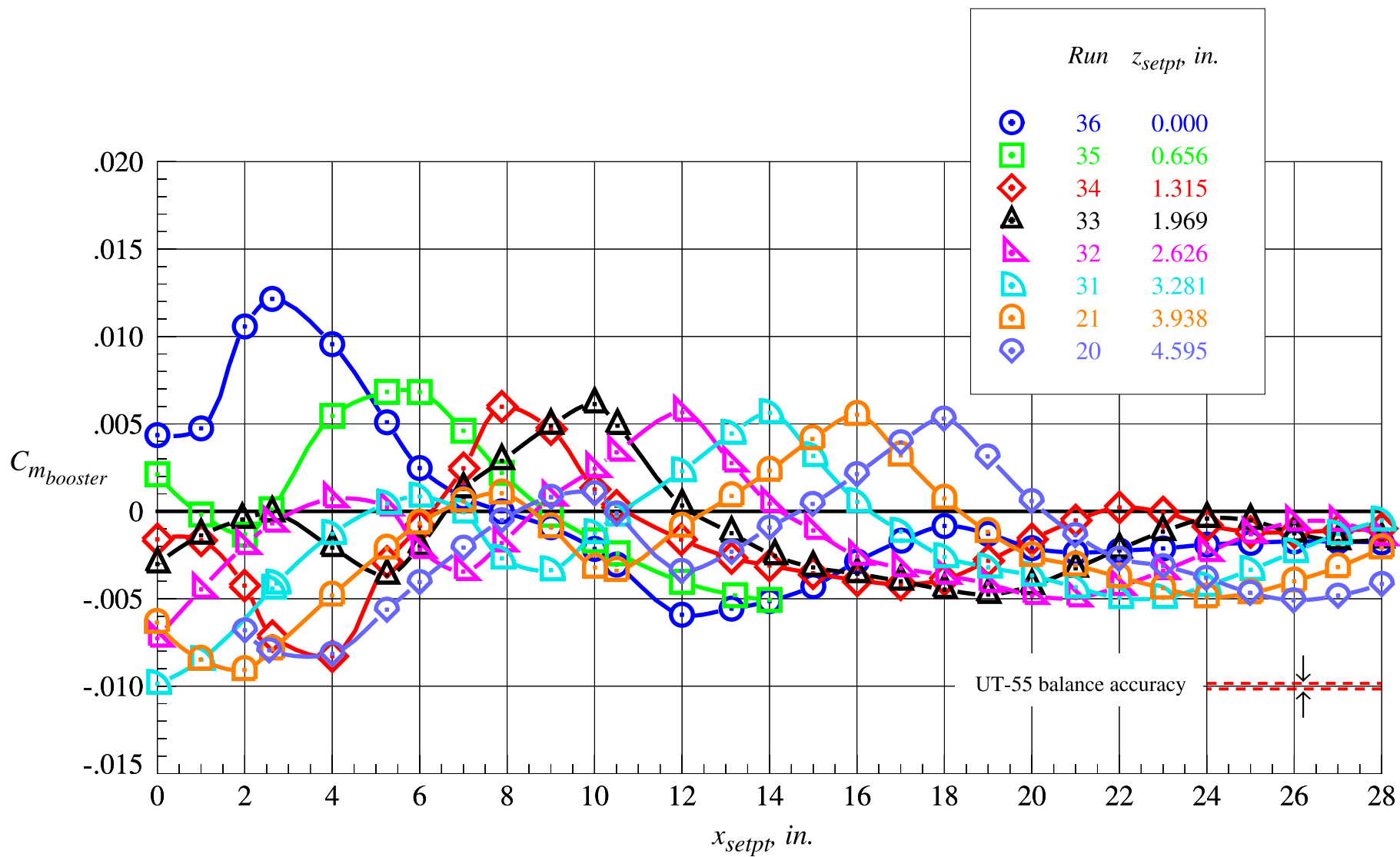
(c) Booster axial force coefficient, part 1

Figure 47. Continued.



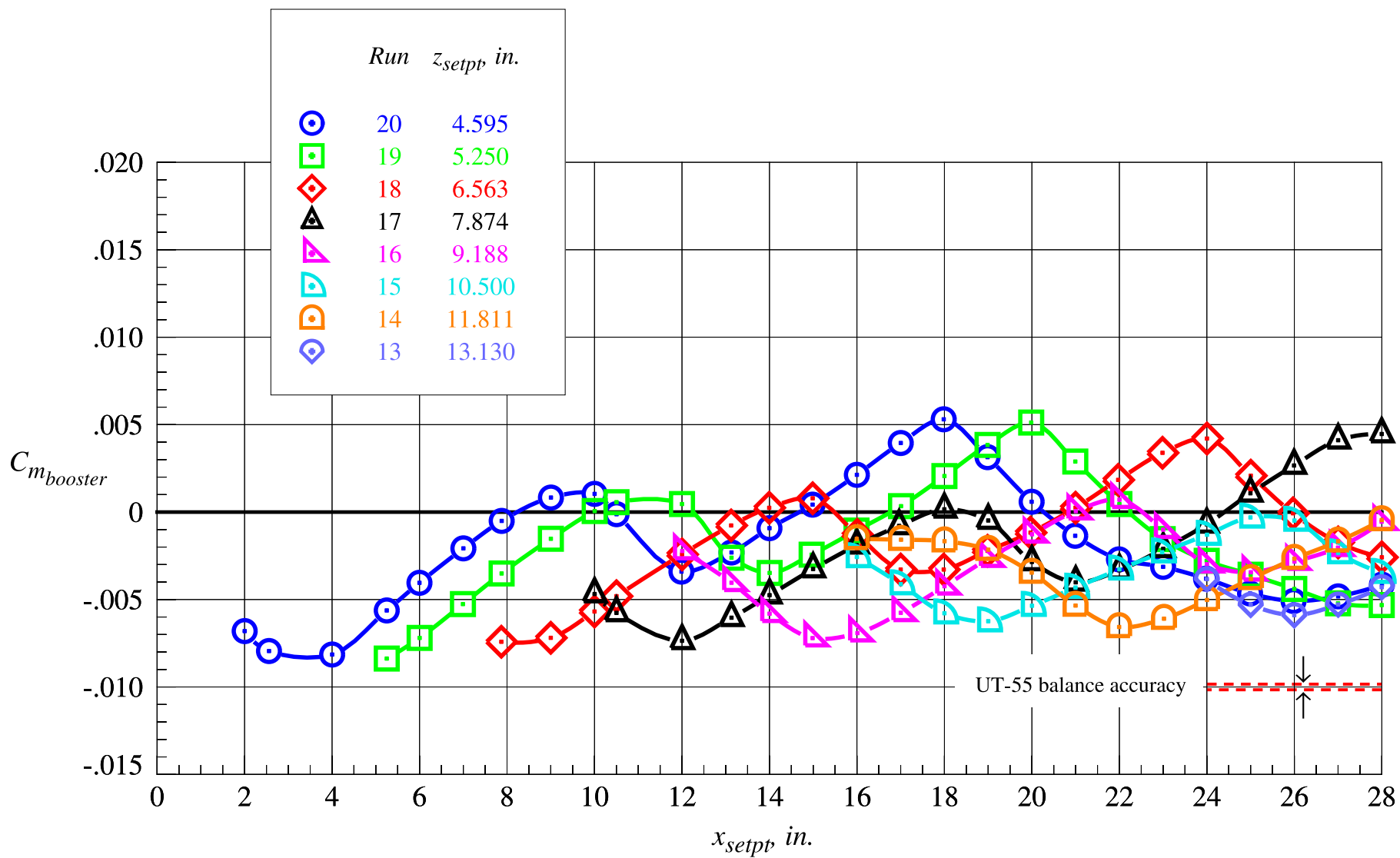
(d) Booster axial force coefficient, part 2

Figure 47. Continued.



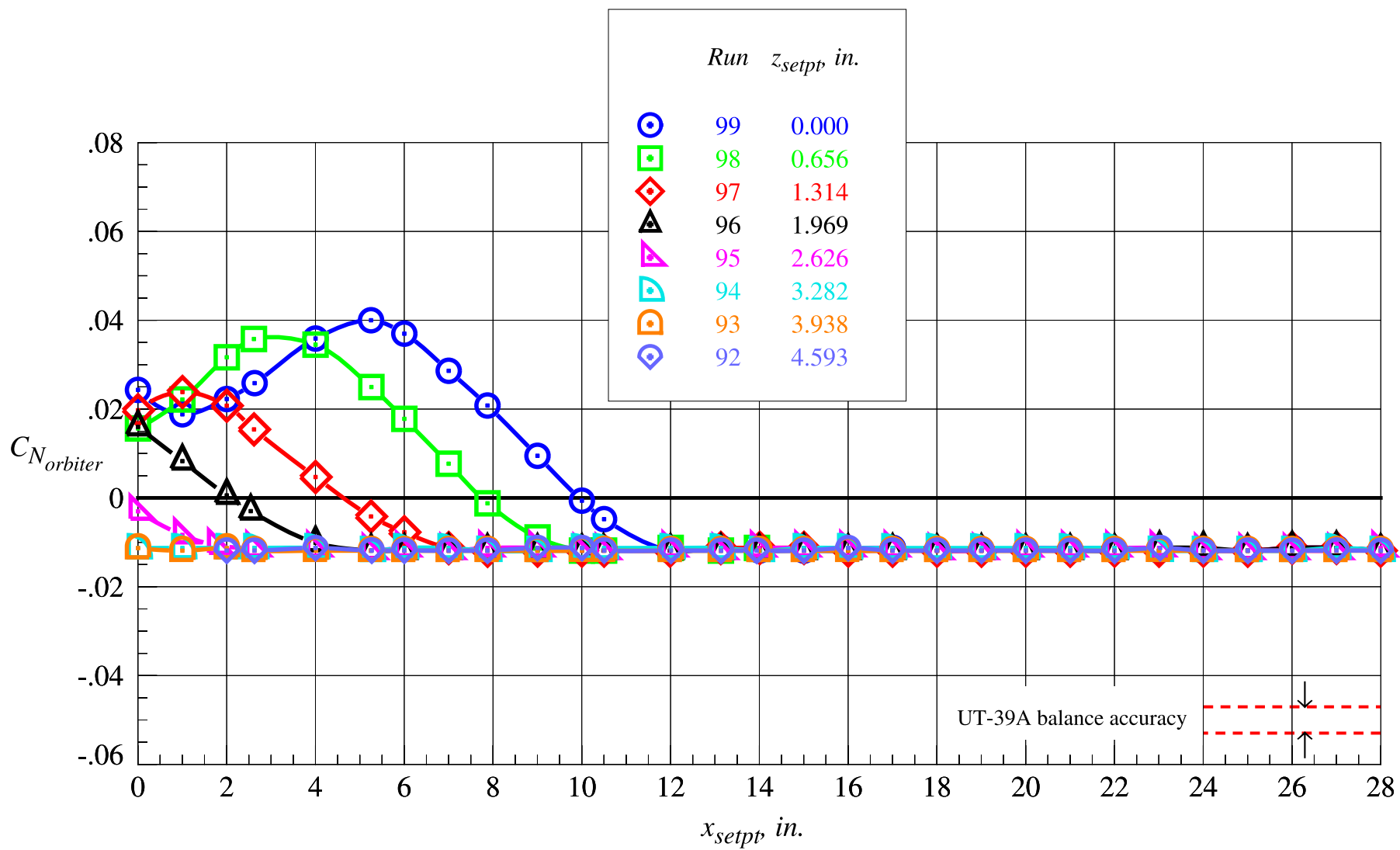
(e) Booster pitching moment coefficient, part 1

Figure 47. Continued.



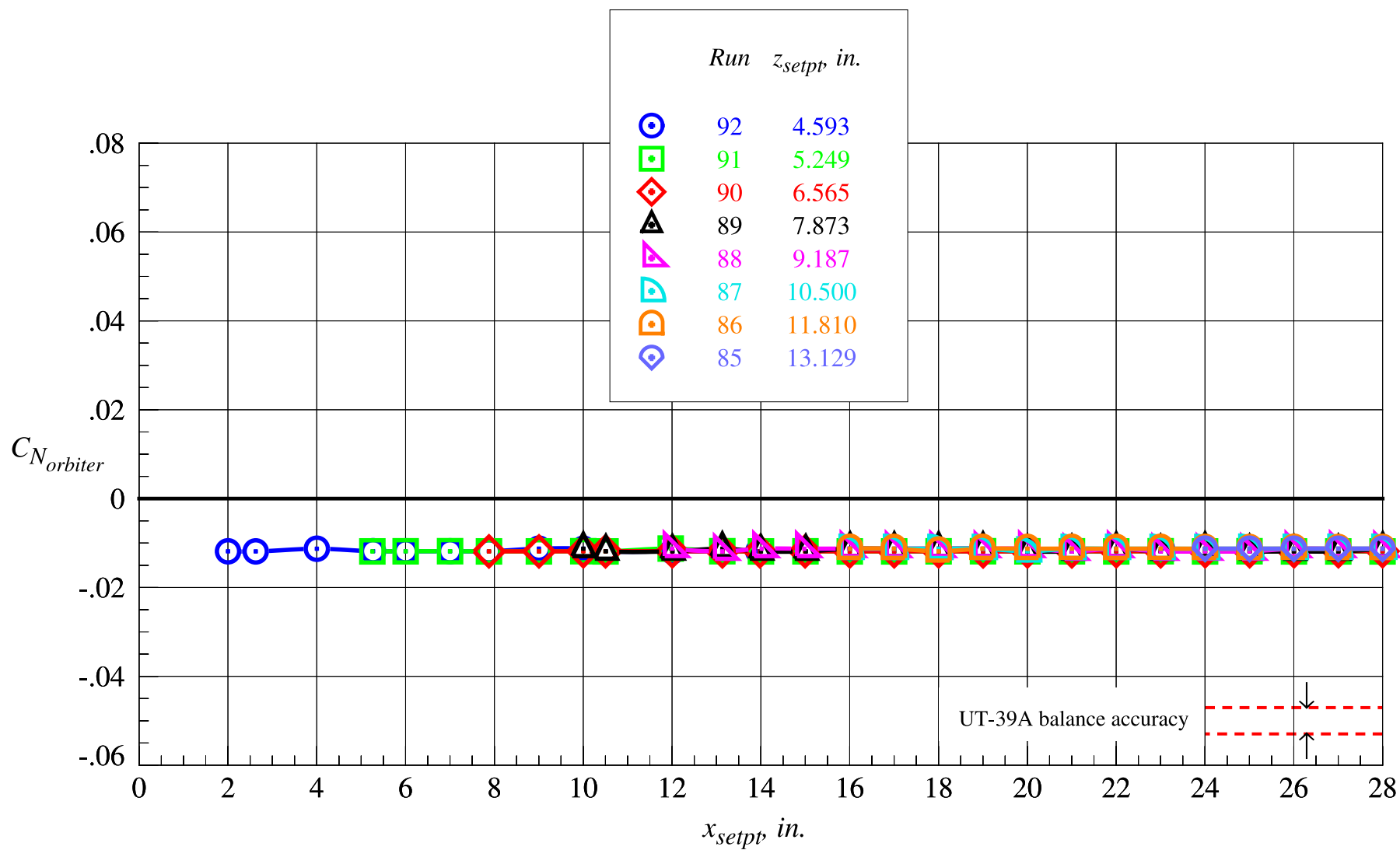
(f) Booster pitching moment coefficient, part 2

Figure 47. Concluded.



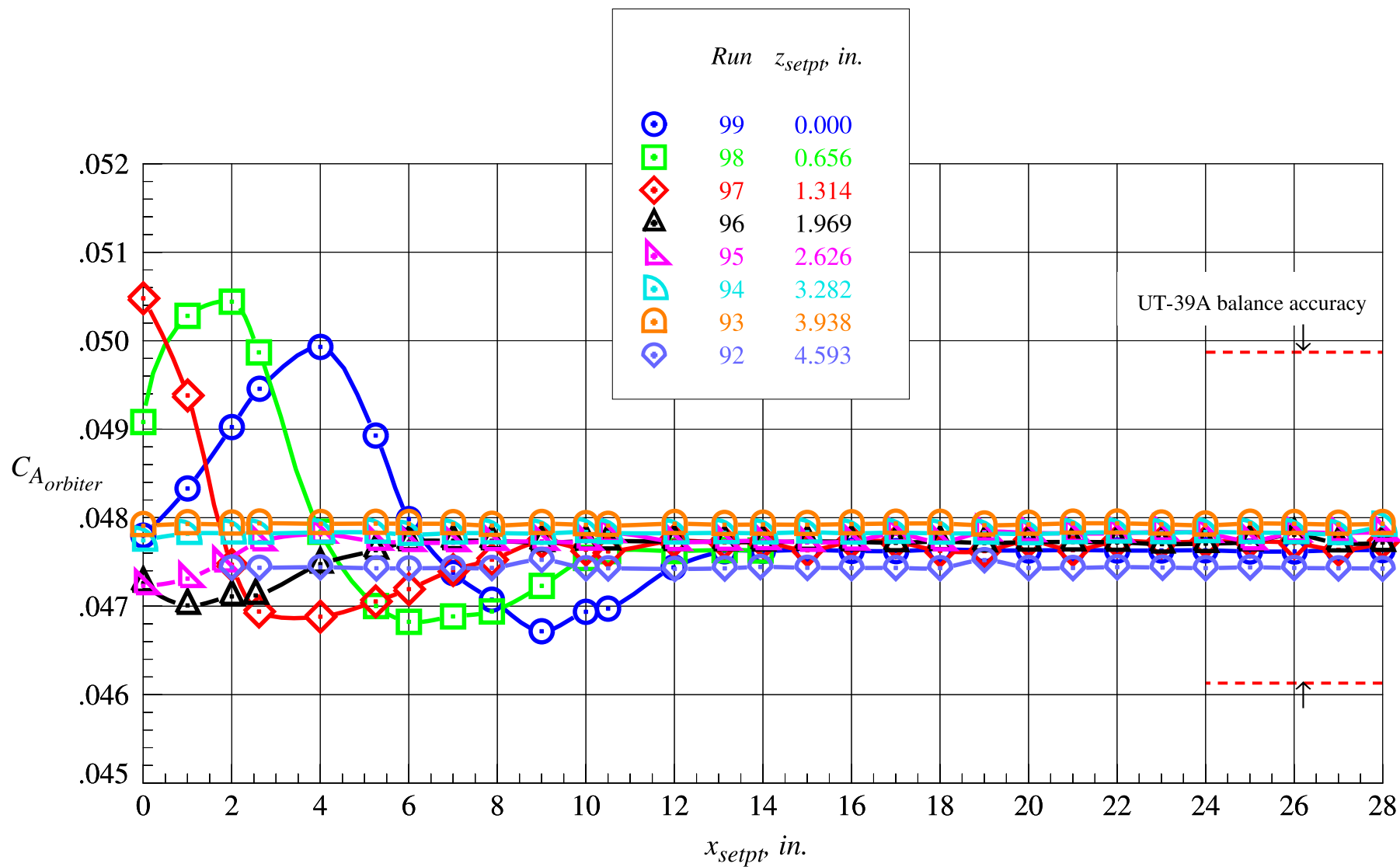
(a) Orbiter normal force coefficient, part 1

Figure 48. Orbiter proximity aerodynamic characteristics at Mach = 4.5 and  $\Delta\alpha = 0^\circ$ .



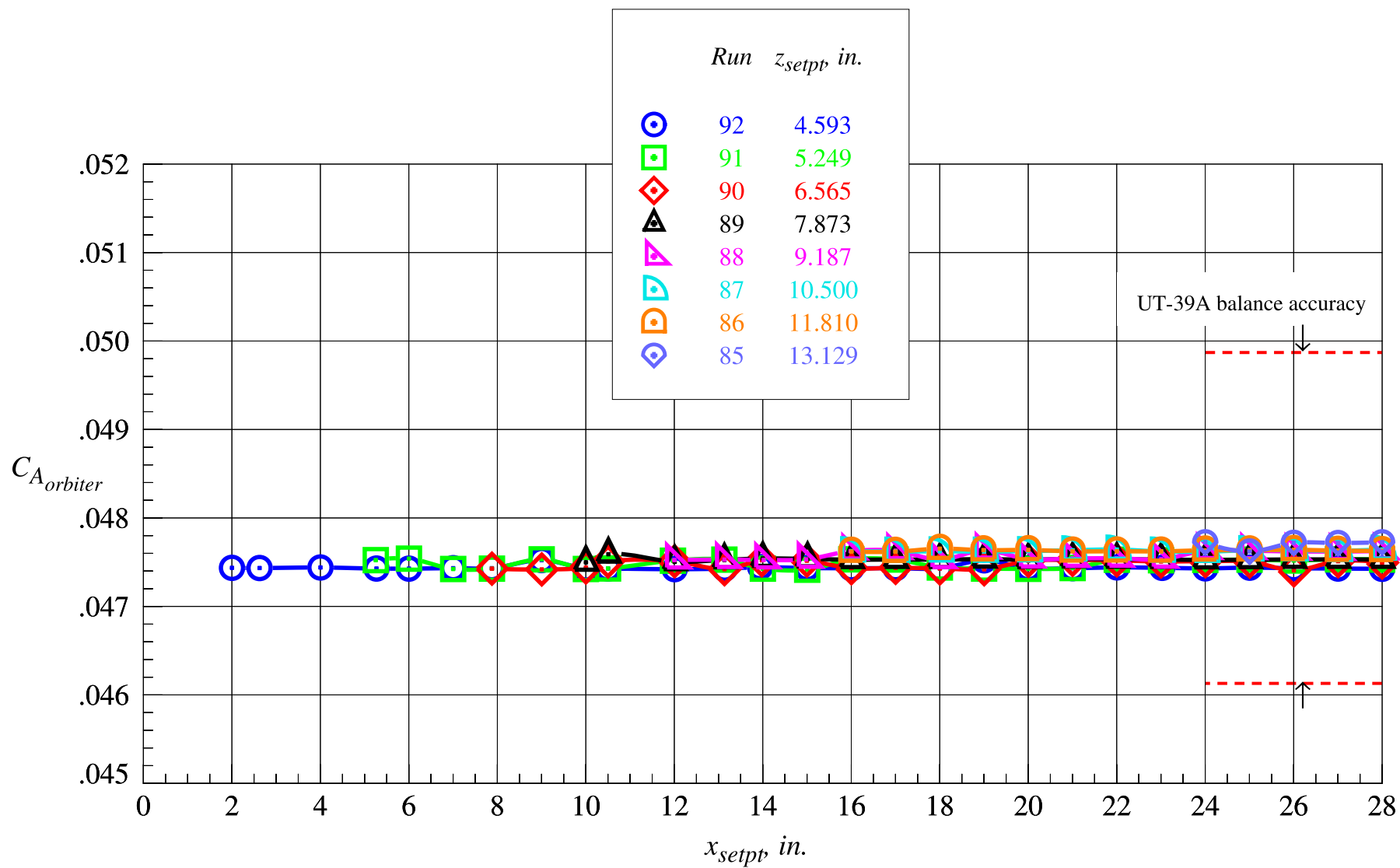
(b) Orbiter normal force coefficient, part 2

Figure 48. Continued.



(c) Orbiter axial force coefficient, part 1

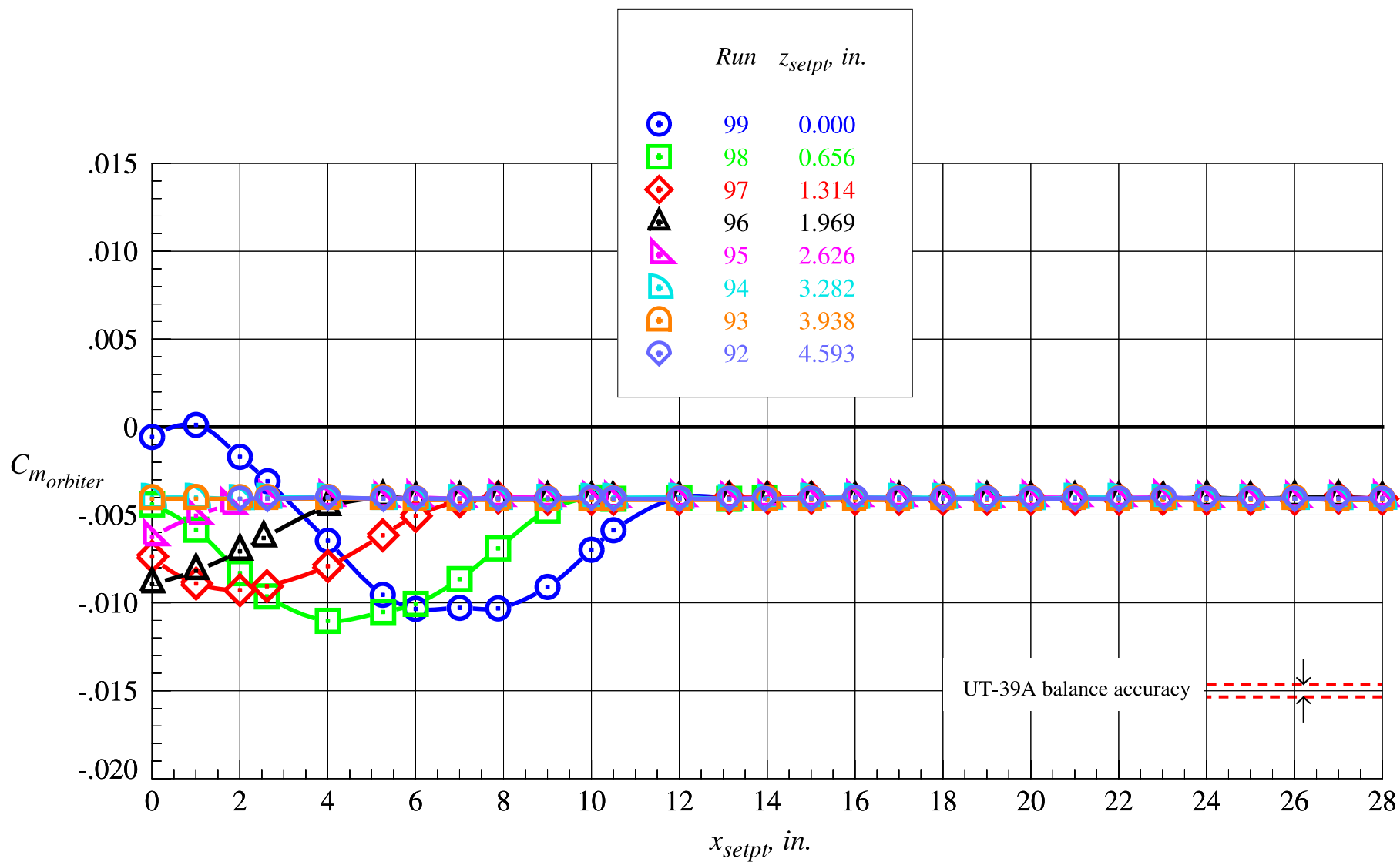
Figure 48. Continued.



(d) Orbiter axial force coefficient, part 2

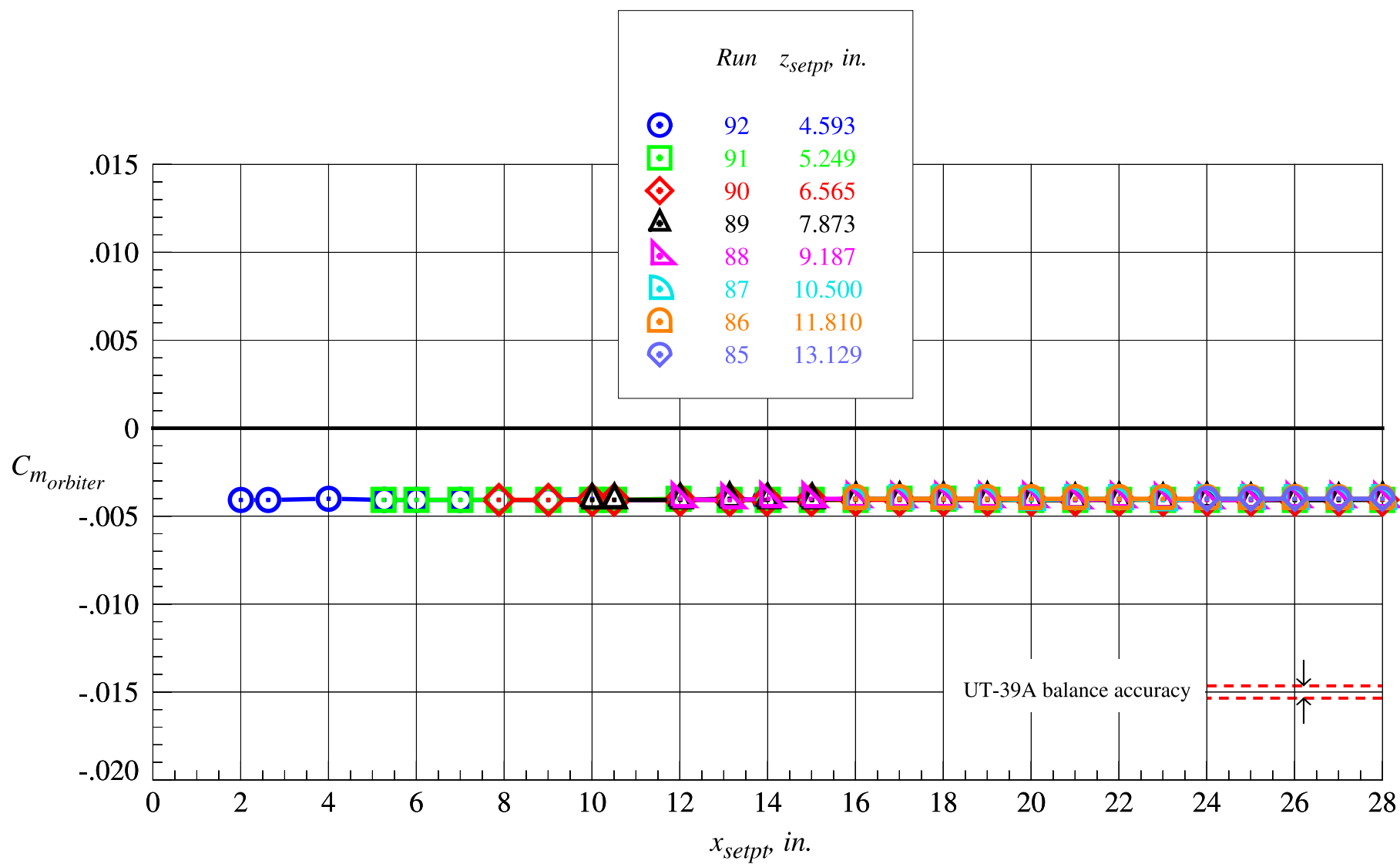
Figure 48. Continued.





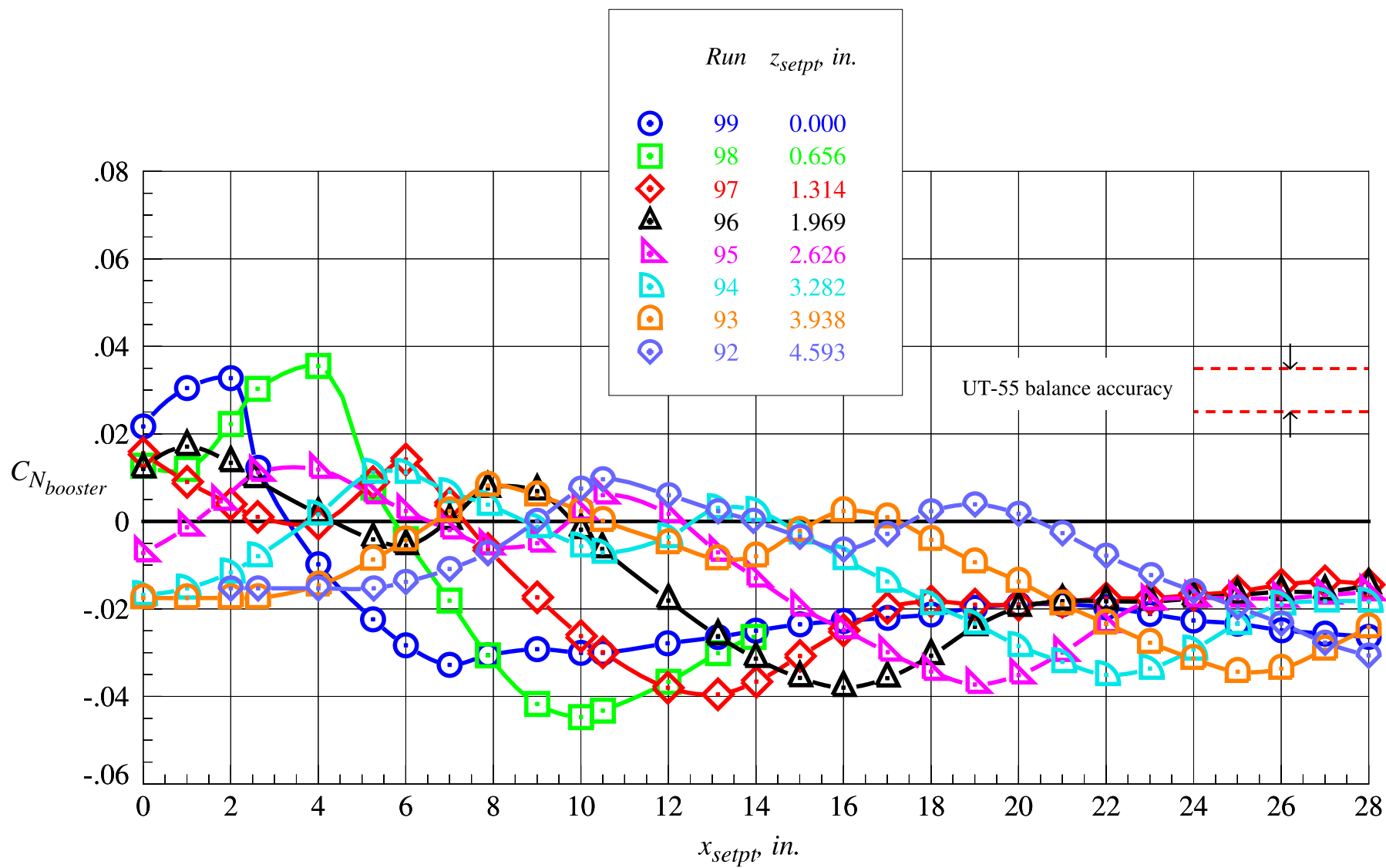
(e) Orbiter pitching moment coefficient, part 1

Figure 48. Continued.



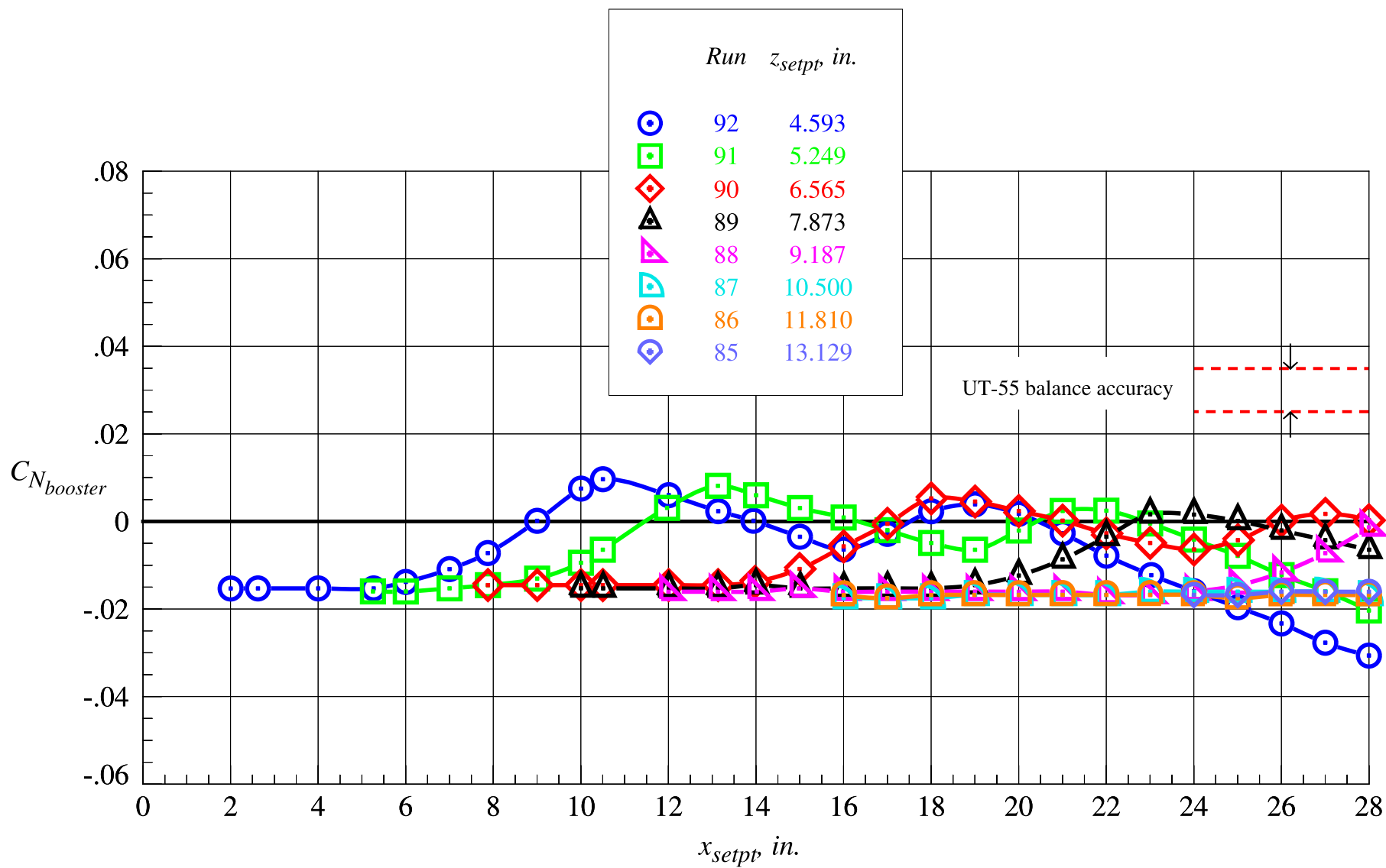
(f) Orbiter pitching moment coefficient, part 2

Figure 48. Concluded.



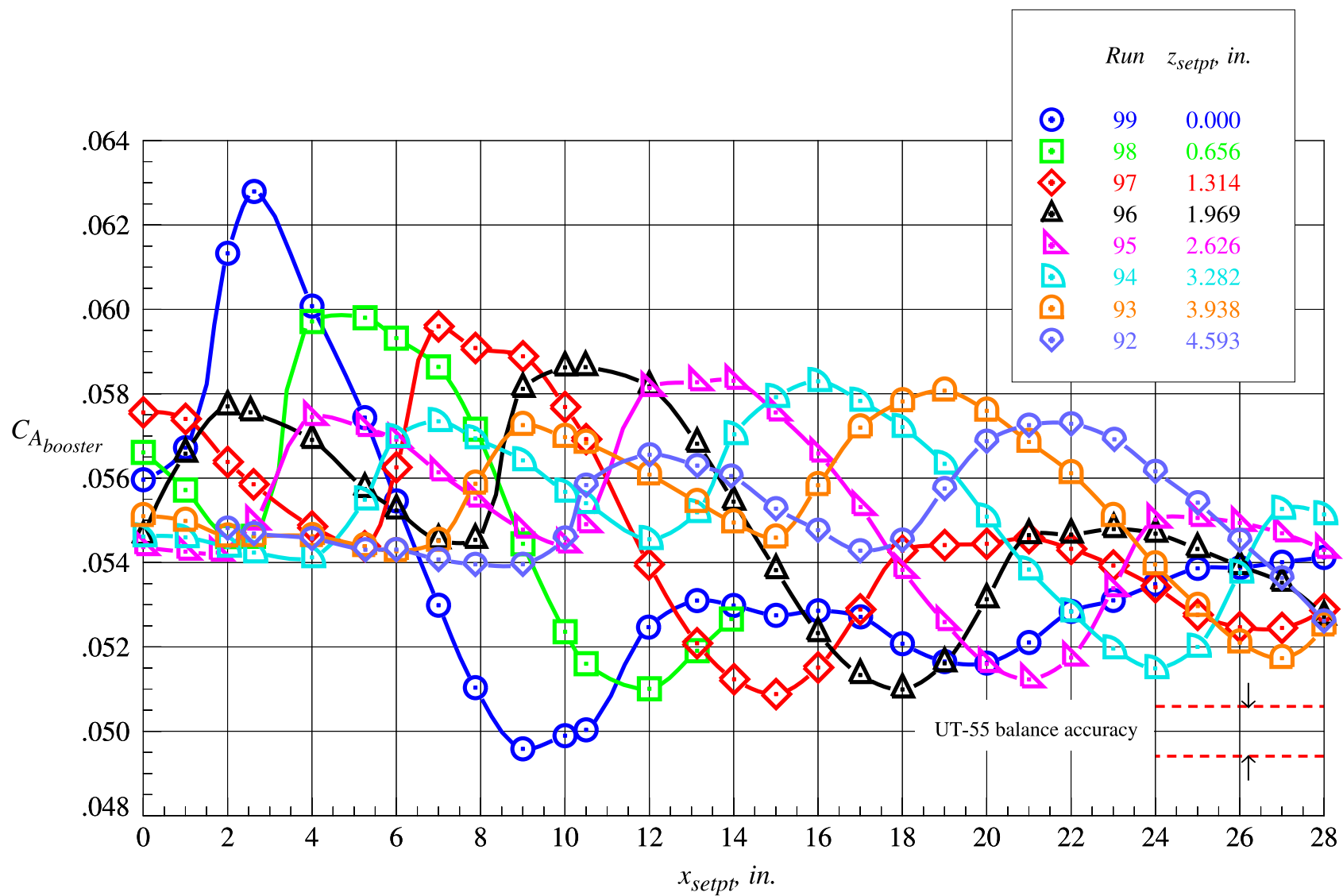
(a) Booster normal force coefficient, part 1

Figure 49. Booster proximity aerodynamic characteristics at Mach = 4.5 and  $\Delta\alpha = 0^\circ$ .



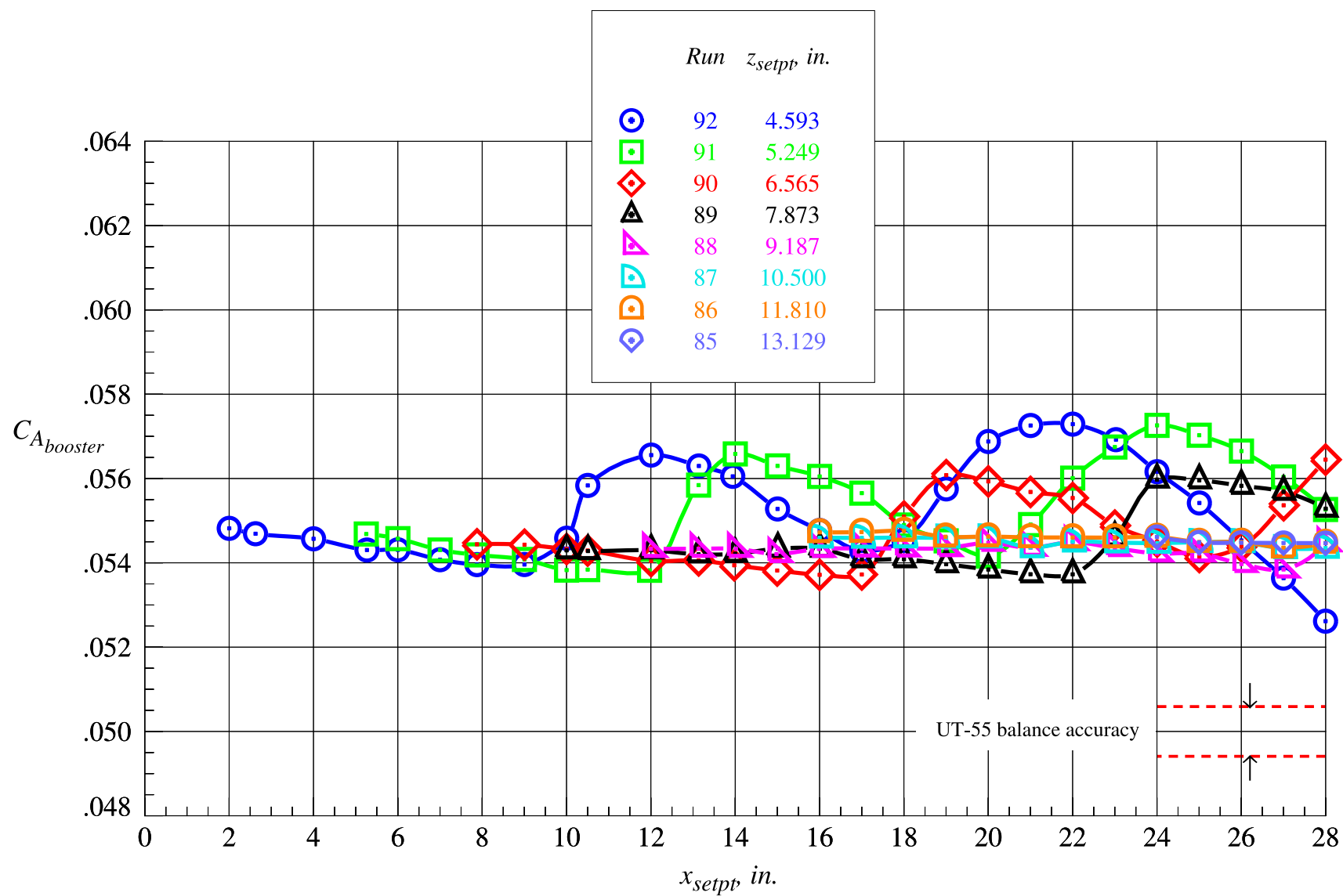
(b) Booster normal force coefficient, part 2

Figure 49. Continued.



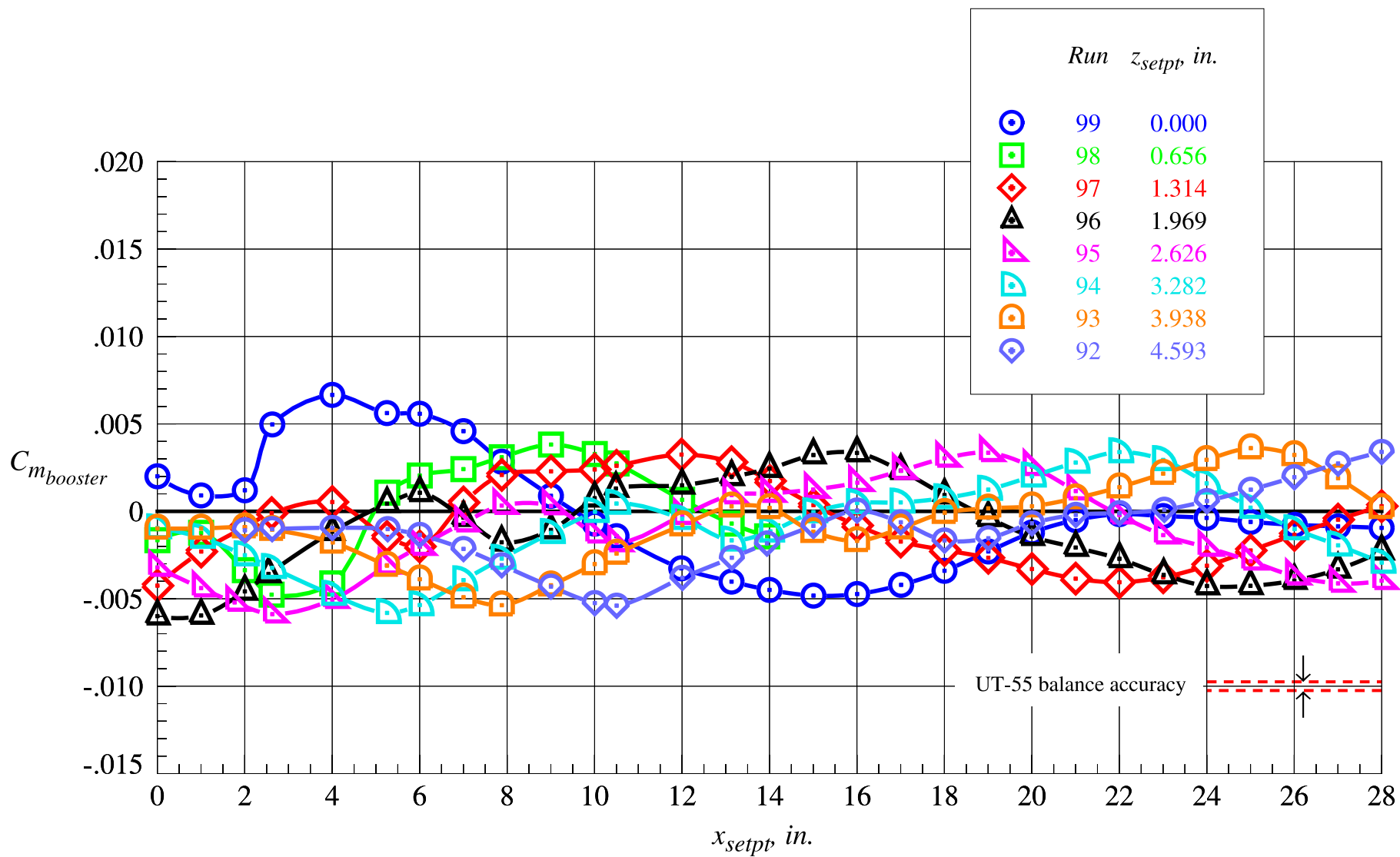
(c) Booster axial force coefficient, part 1

Figure 49. Continued.



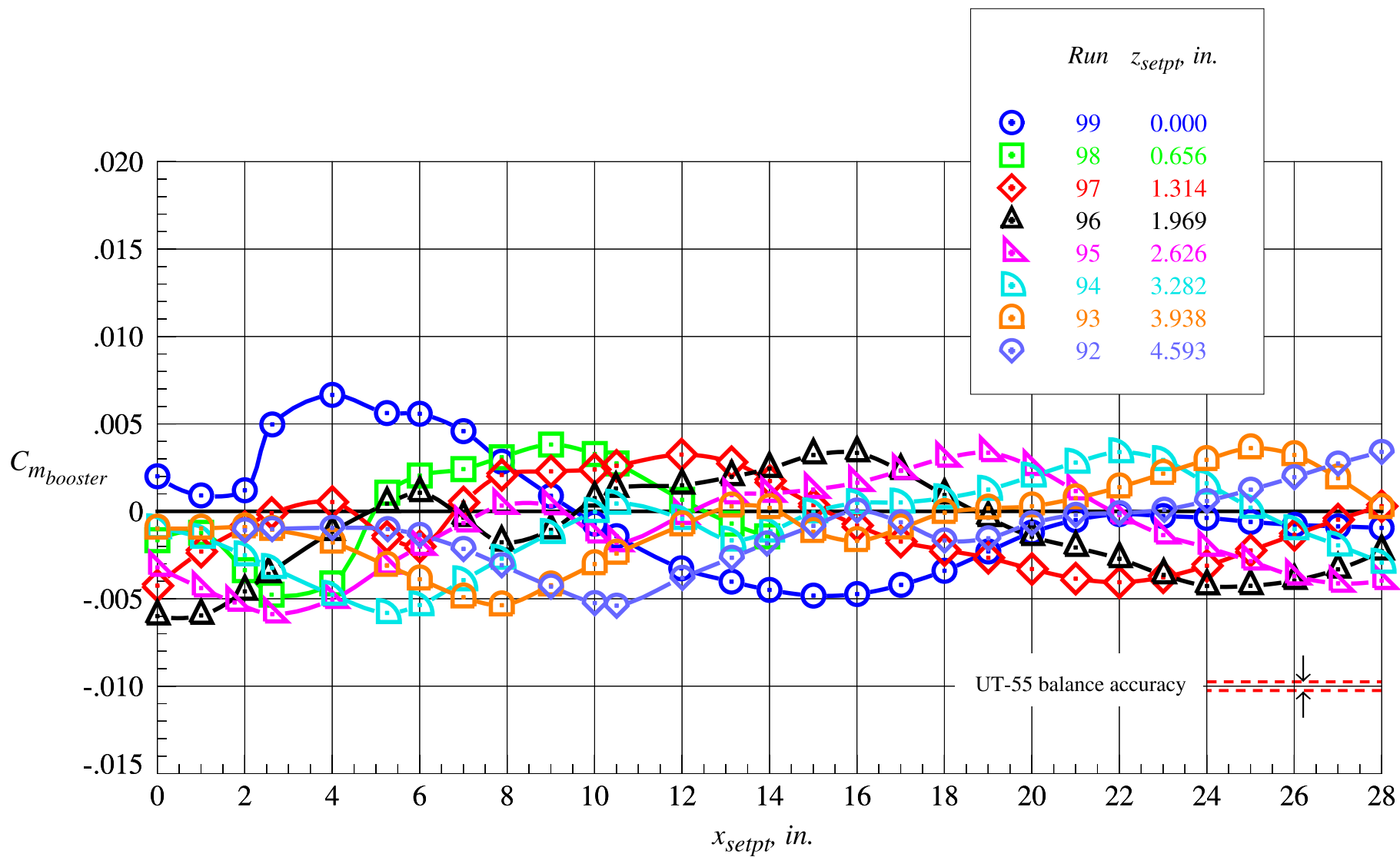
(d) Booster axial force coefficient, part 2

Figure 49. Continued.



(e) Booster pitching moment coefficient, part 1

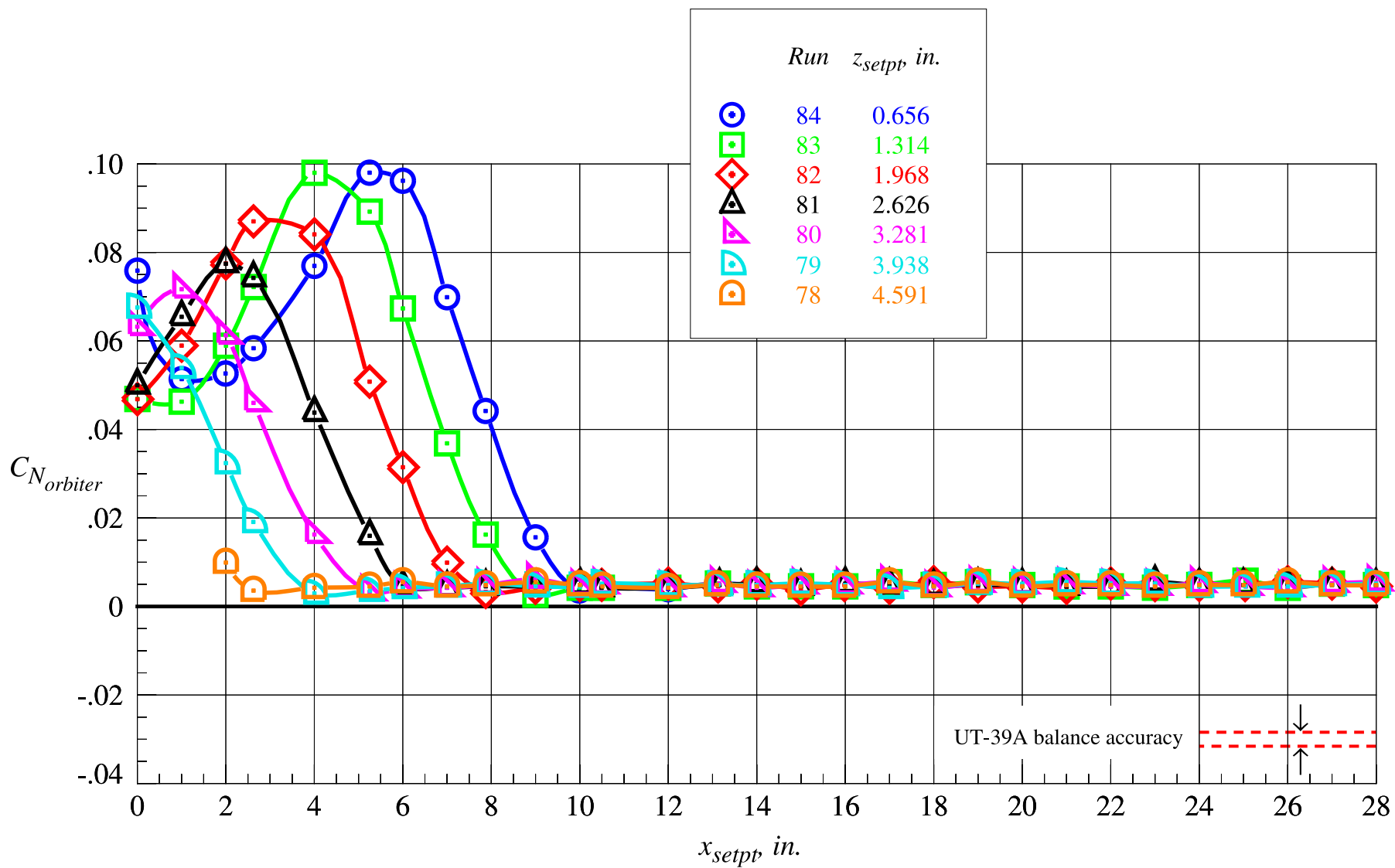
Figure 49. Continued.



(f) Booster pitching moment coefficient, part 2

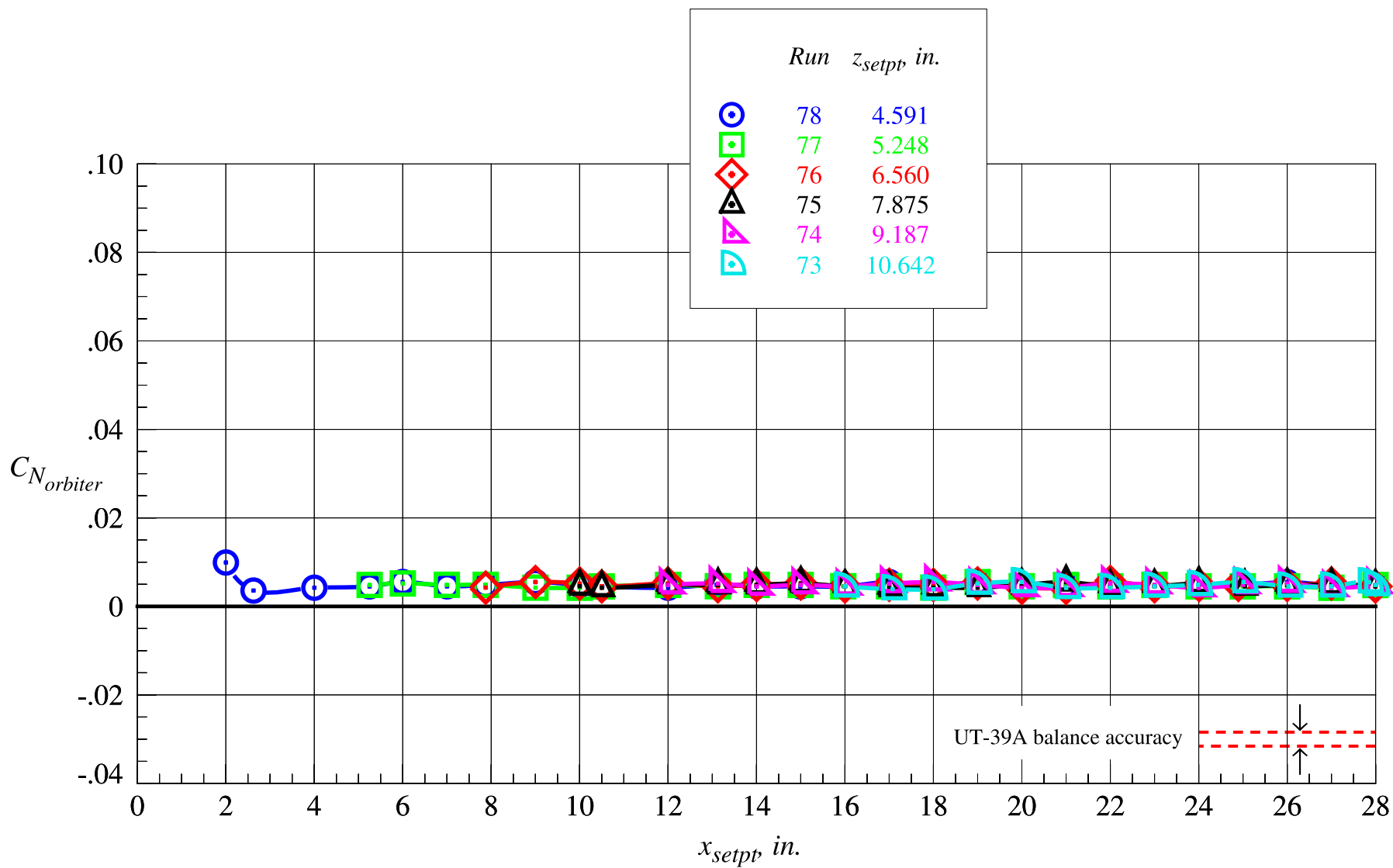
Figure 49. Concluded.





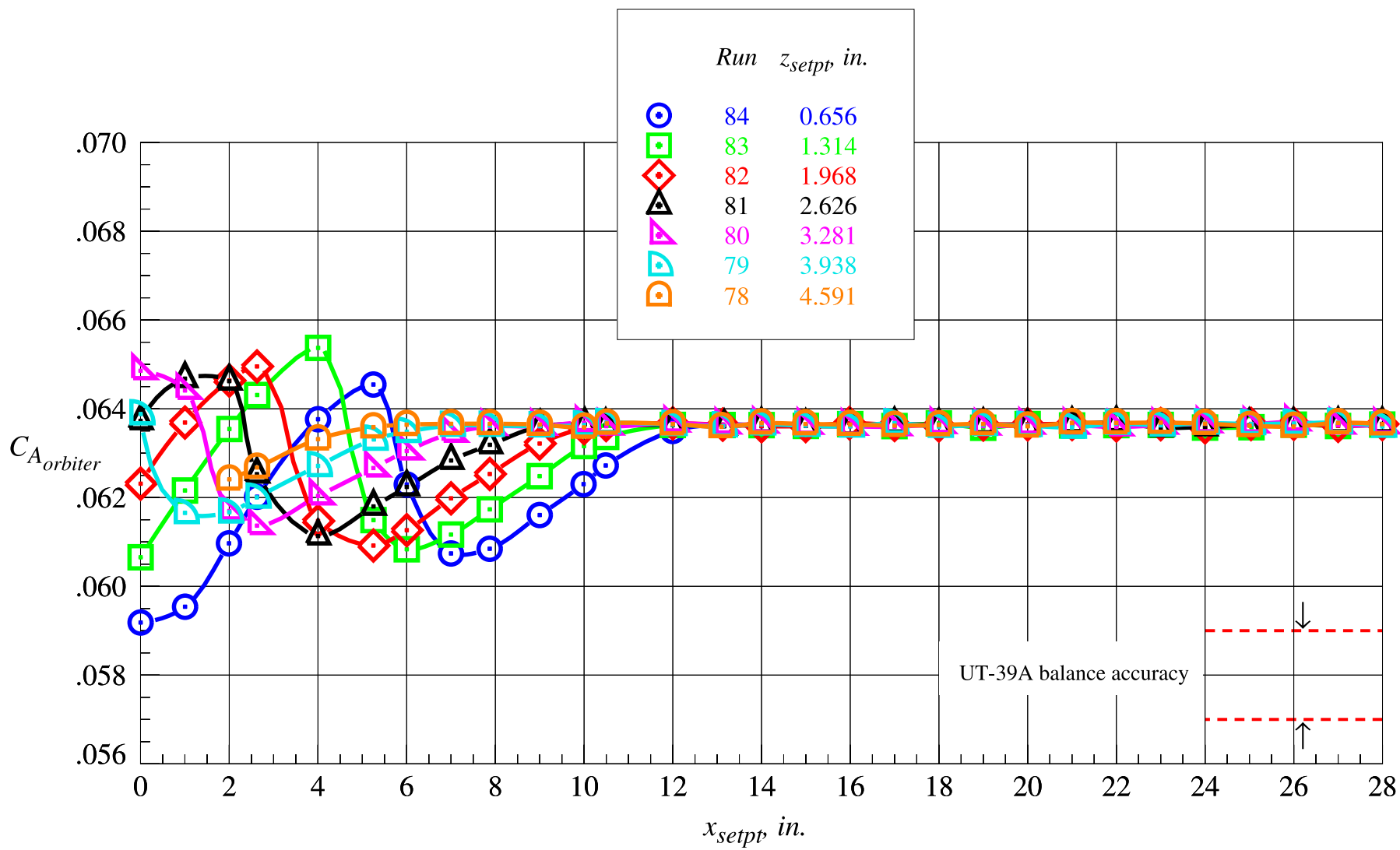
(a) Orbiter normal force coefficient, part 1

Figure 50. Orbiter proximity aerodynamic characteristics at Mach = 2.3 and  $\Delta\alpha = 5^\circ$ .



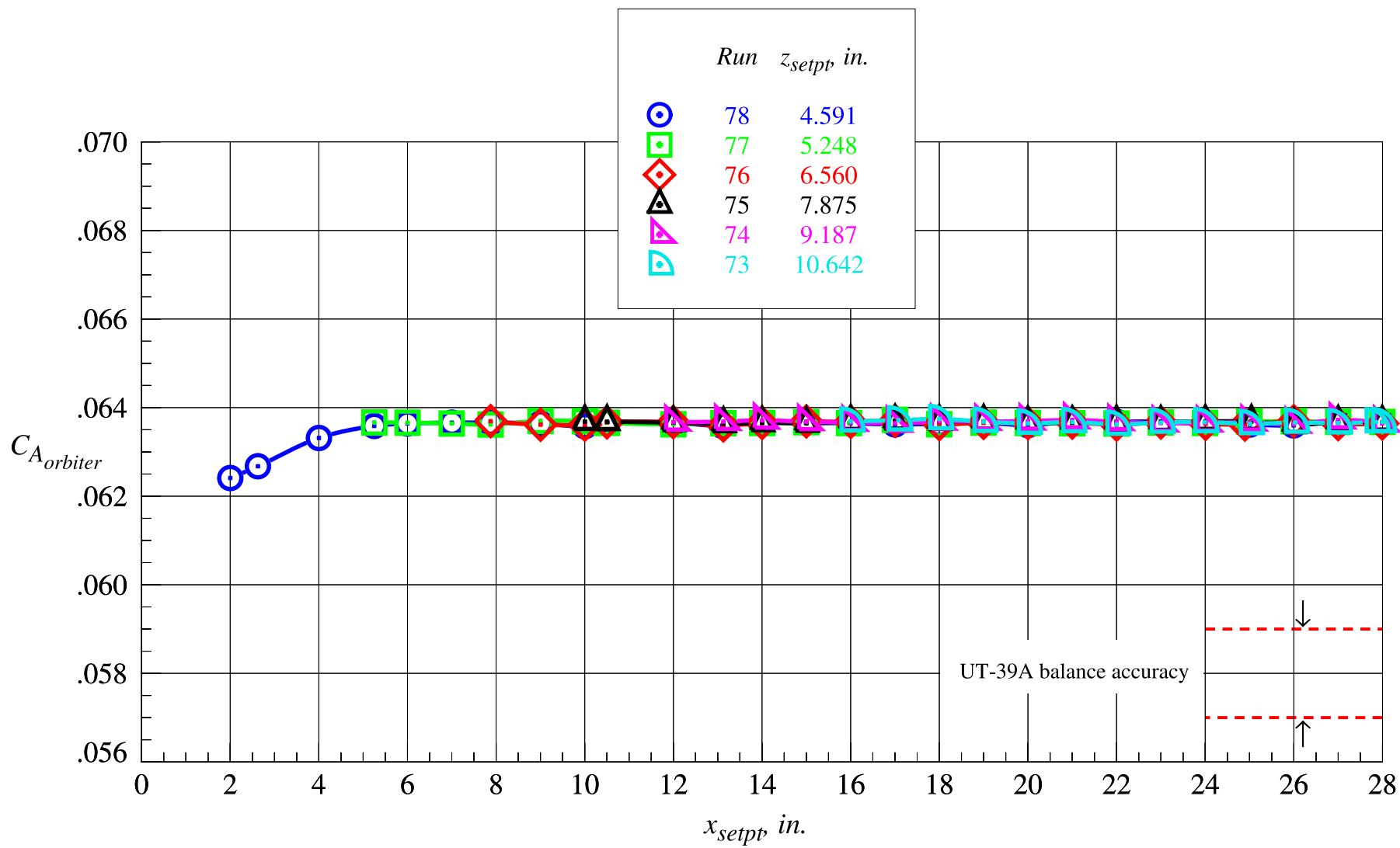
(b) Orbiter normal force coefficient, part 2

Figure 50. Continued.



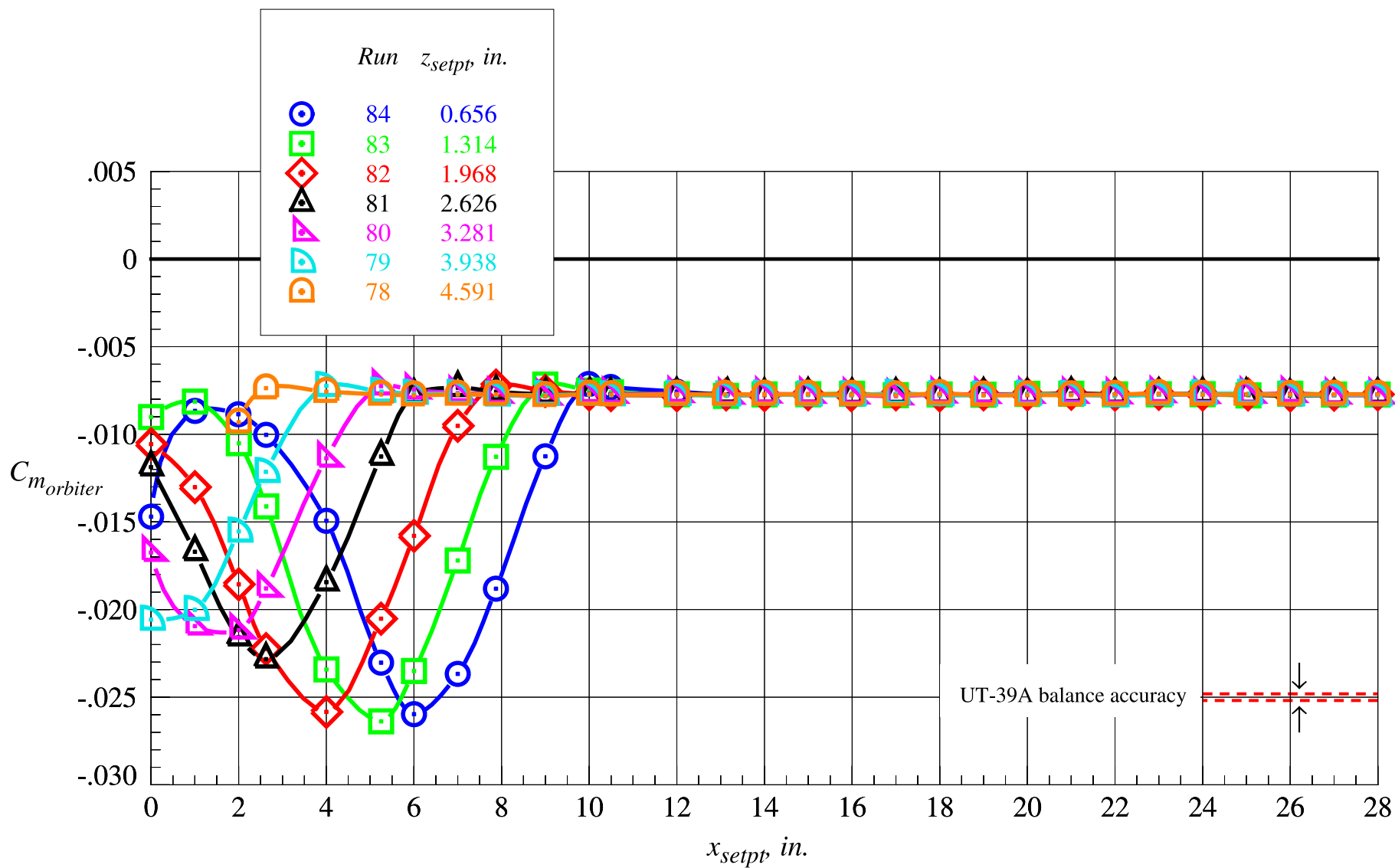
(c) Orbiter axial force coefficient, part 1

Figure 50. Continued.



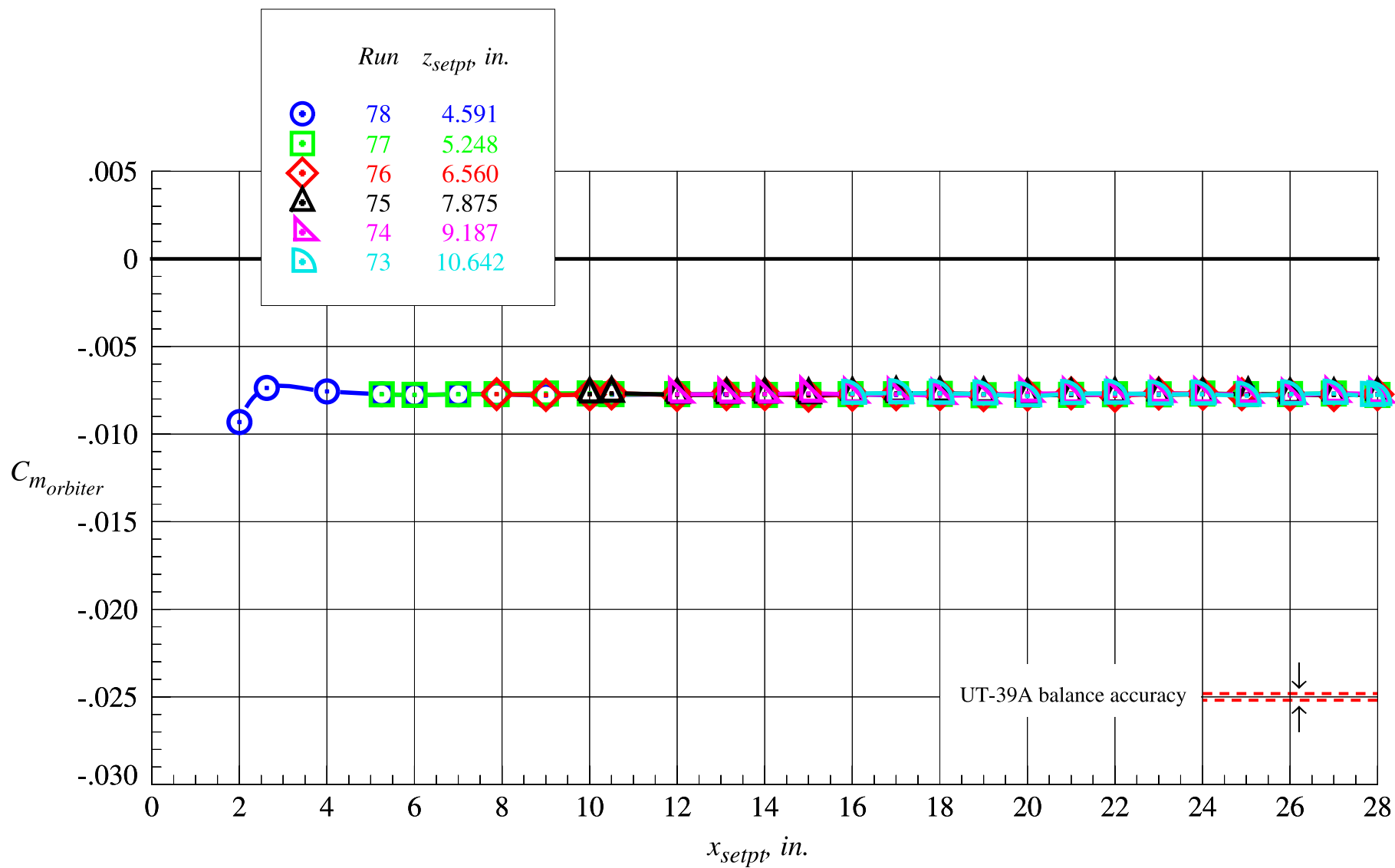
(d) Orbiter axial force coefficient, part 2

Figure 50. Continued.



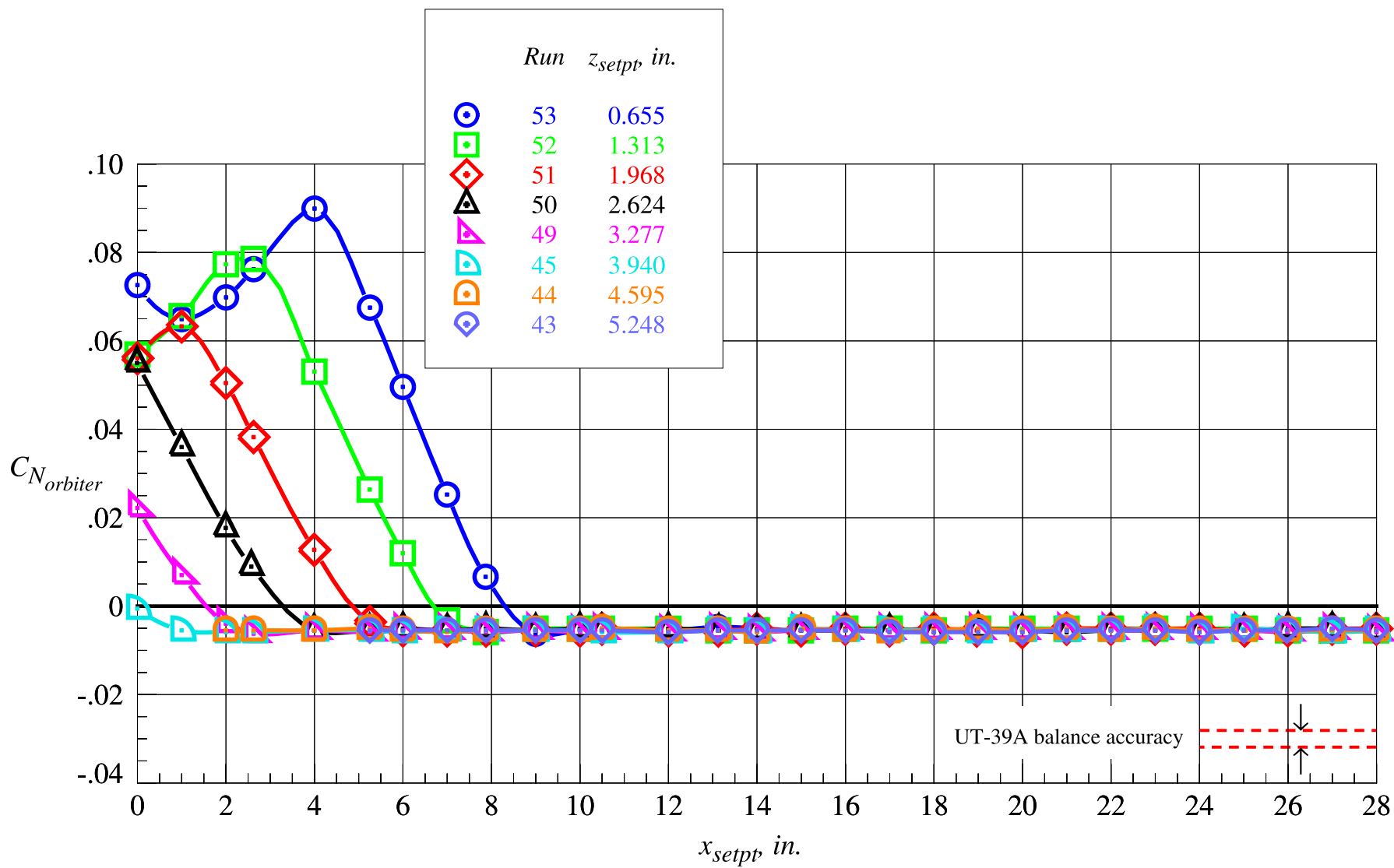
(e) Orbiter pitching moment coefficient, part 1

Figure 50. Continued.



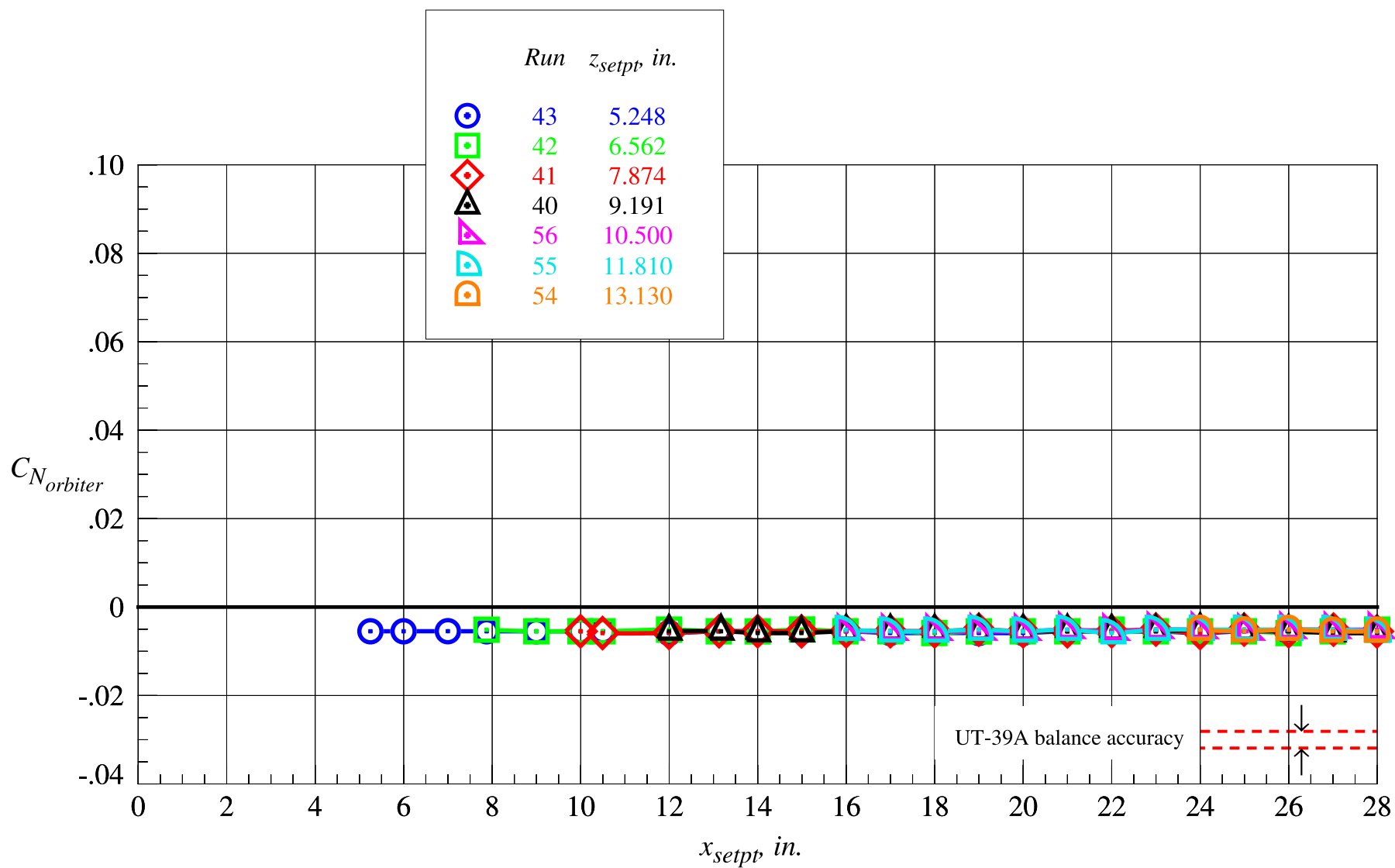
(f) Orbiter pitching moment coefficient, part 2

Figure 50. Concluded.



(a) Orbiter normal force coefficient, part 1

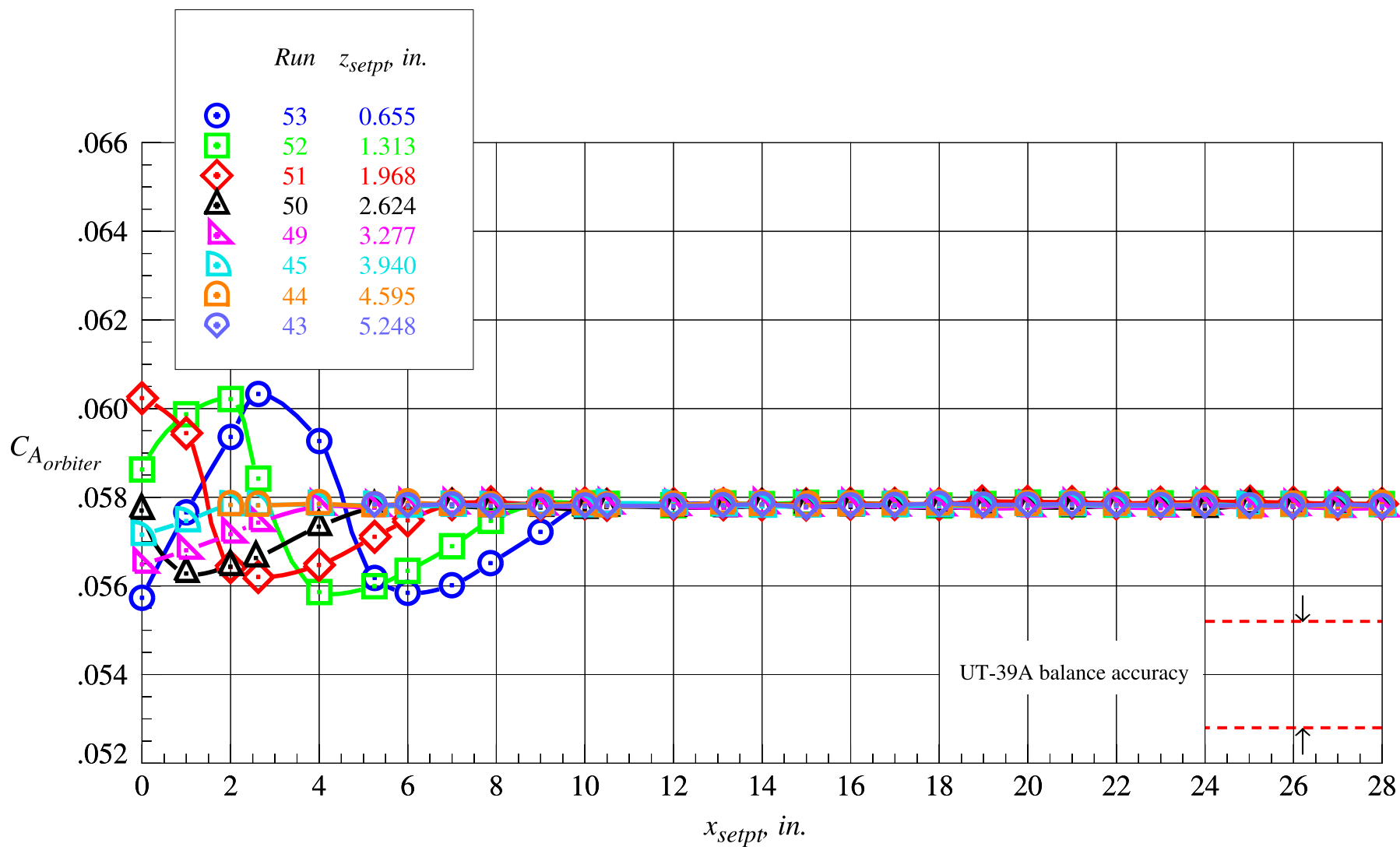
Figure 51. Orbiter proximity aerodynamic characteristics at  $Mach = 3.0$  and  $\Delta\alpha = 5^\circ$ .



(b) Orbiter normal force coefficient, part 2

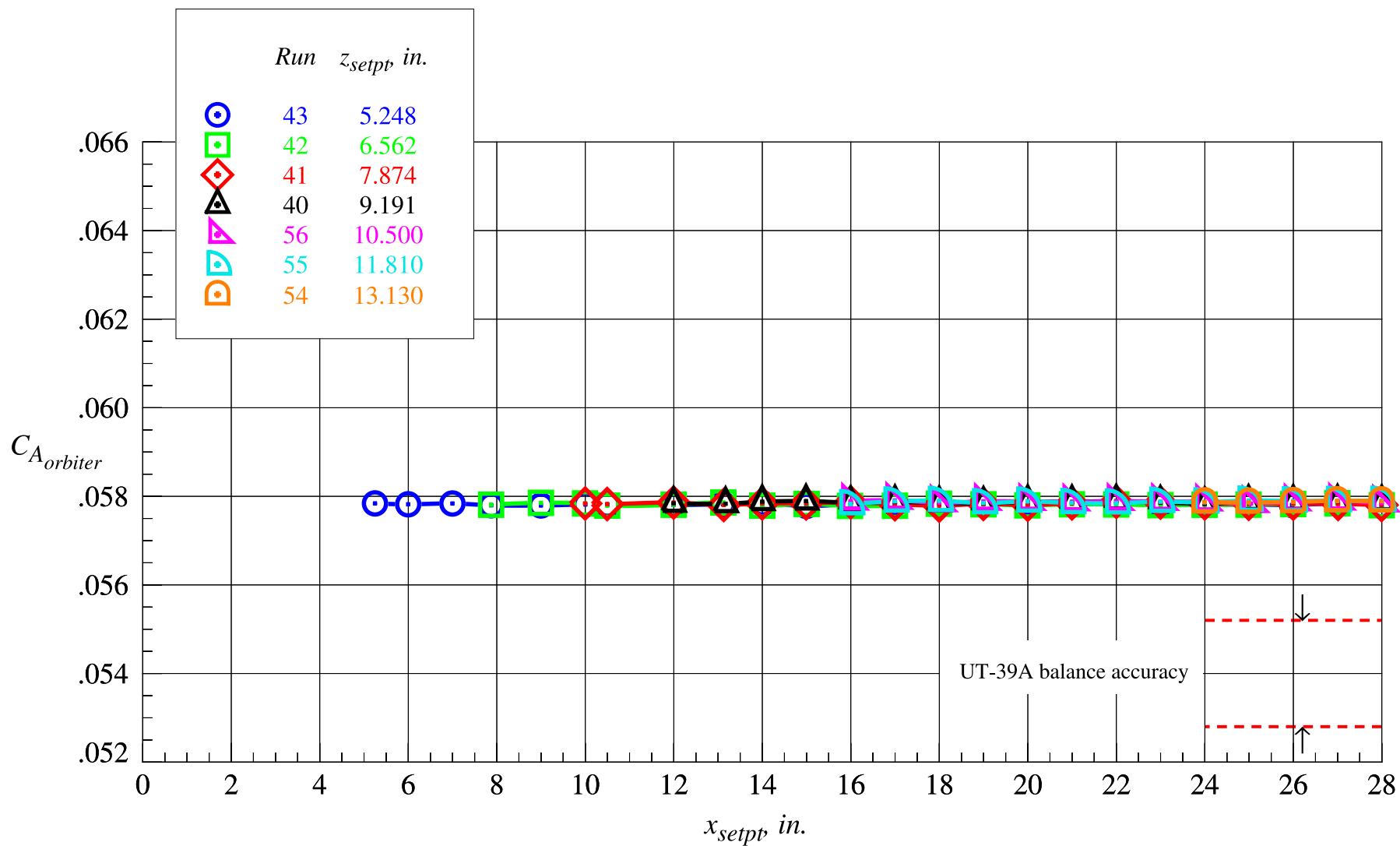
Figure 51. Continued.





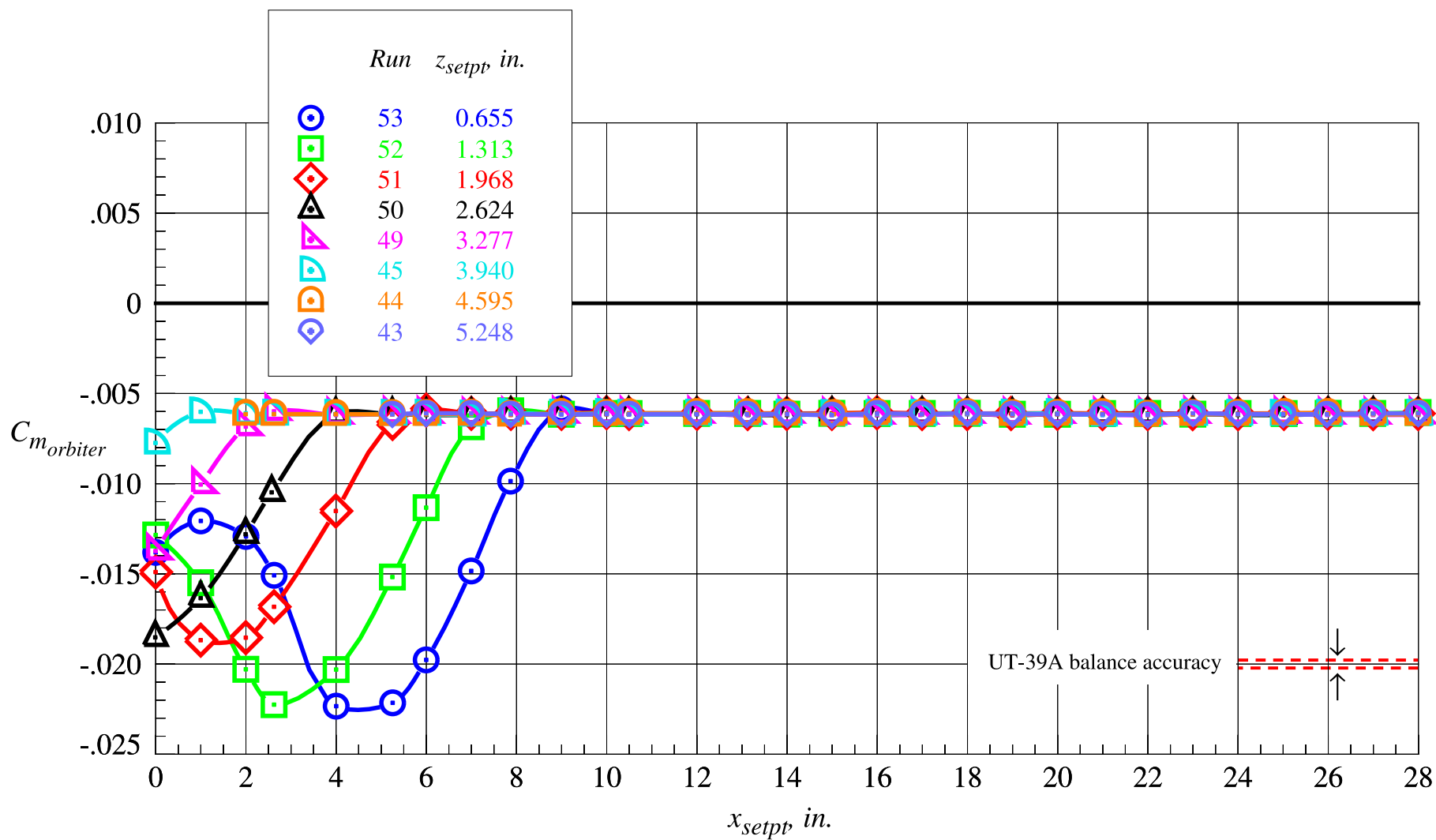
(c) Orbiter axial force coefficient, part 1

Figure 51. Continued.



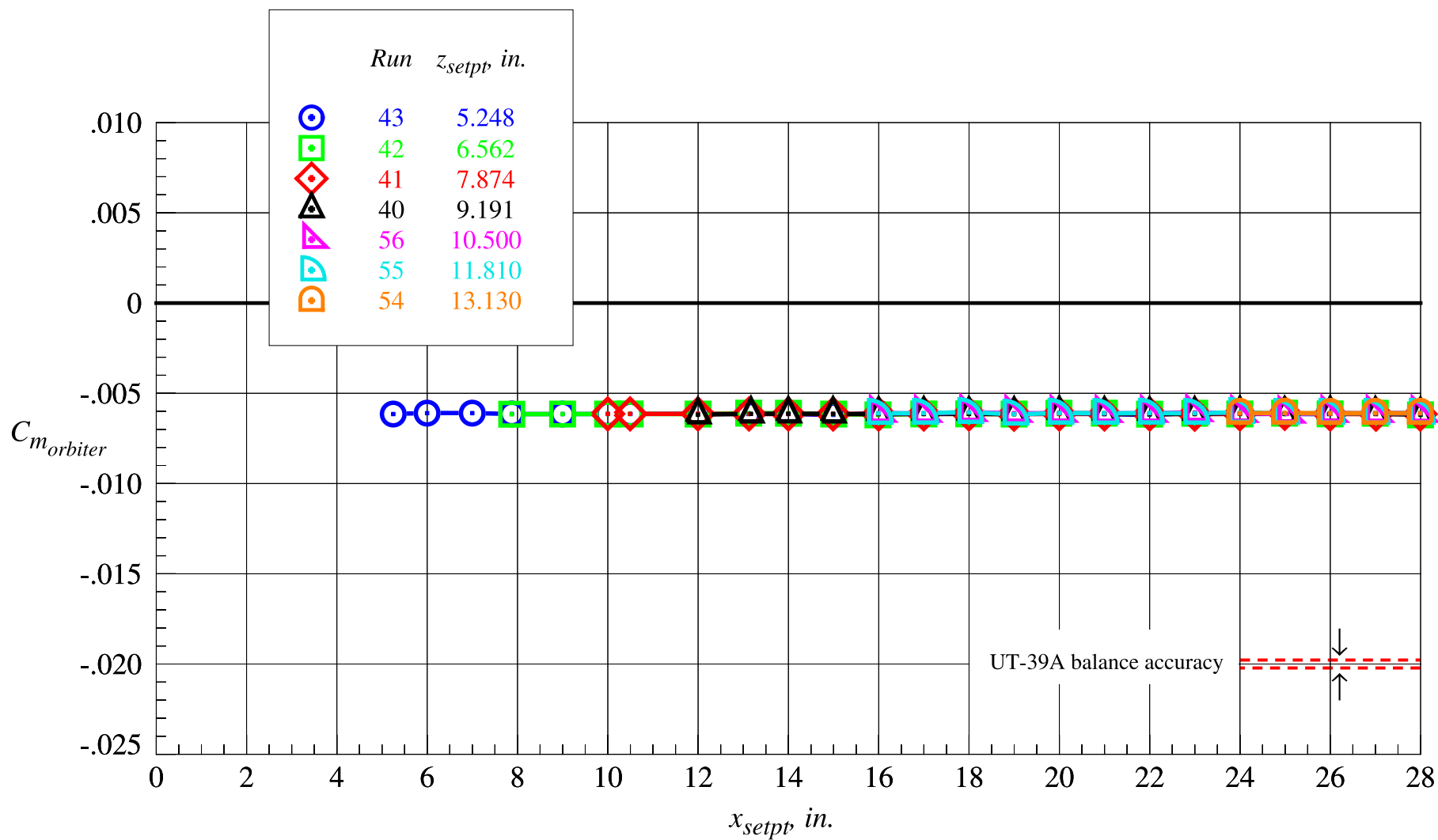
(d) Orbiter axial force coefficient, part 2

Figure 51. Continued.



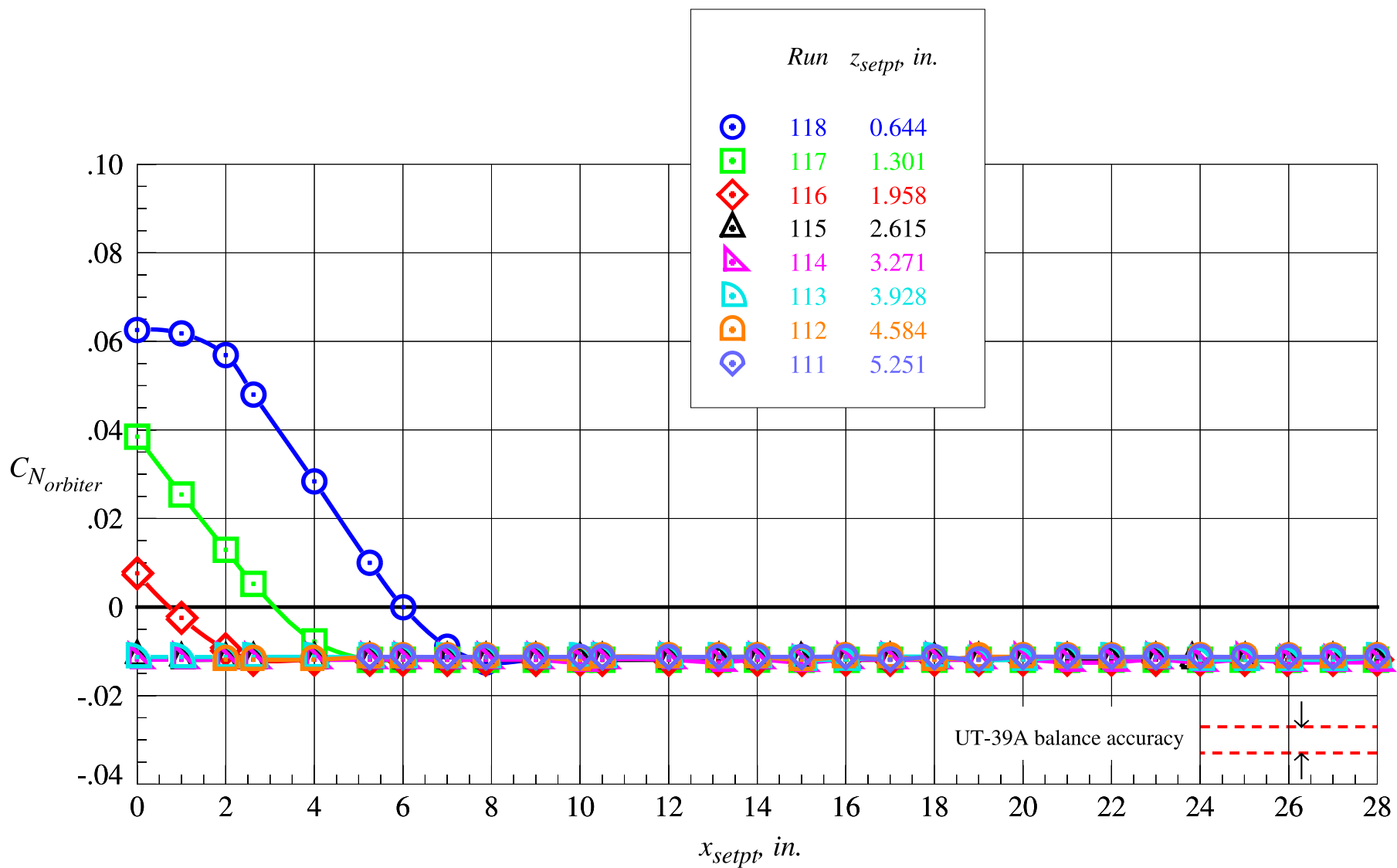
(e) Orbiter pitching moment coefficient, part 1

Figure 51. Continued.



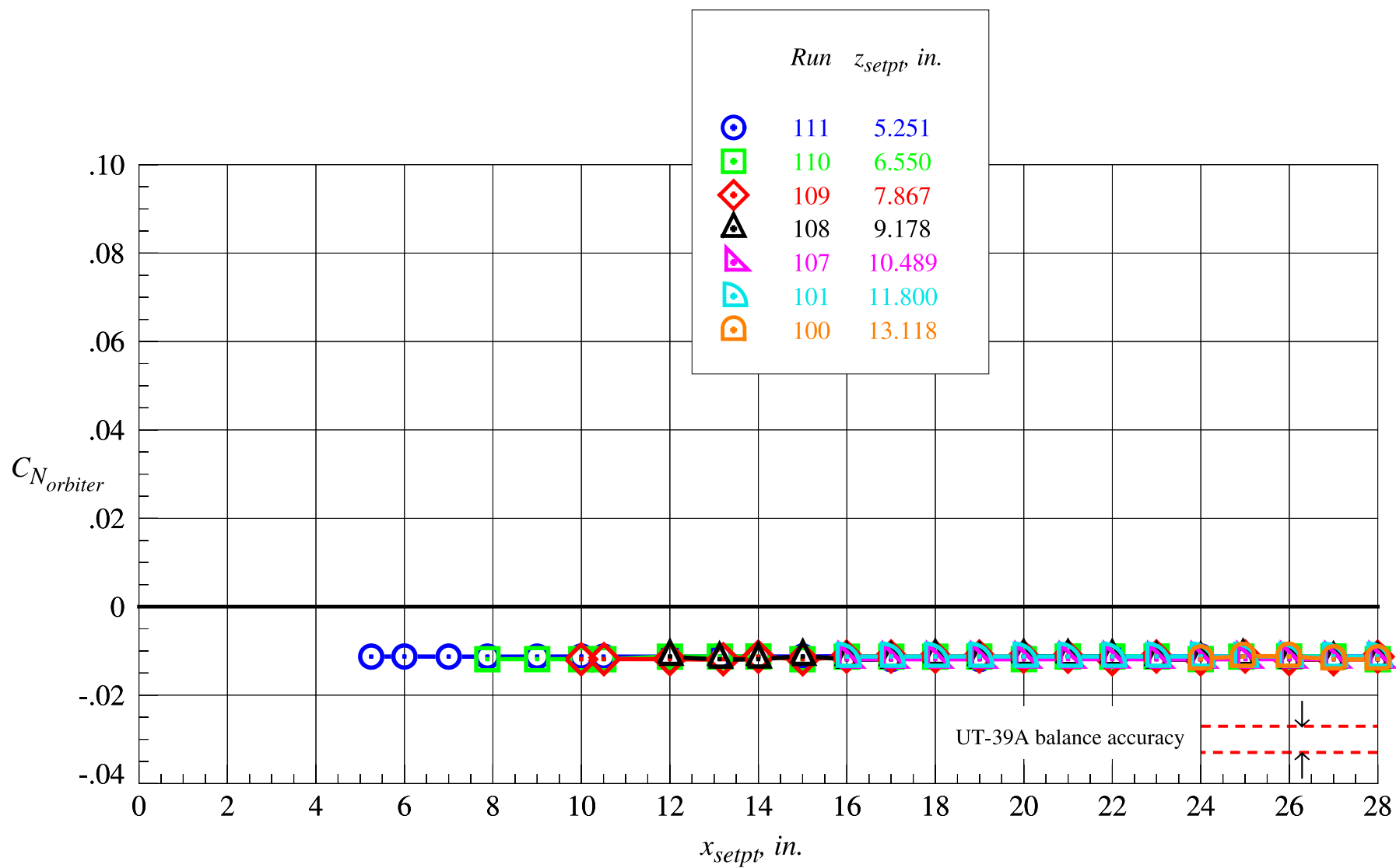
(f) Orbiter pitching moment coefficient, part 2

Figure 51. Concluded.



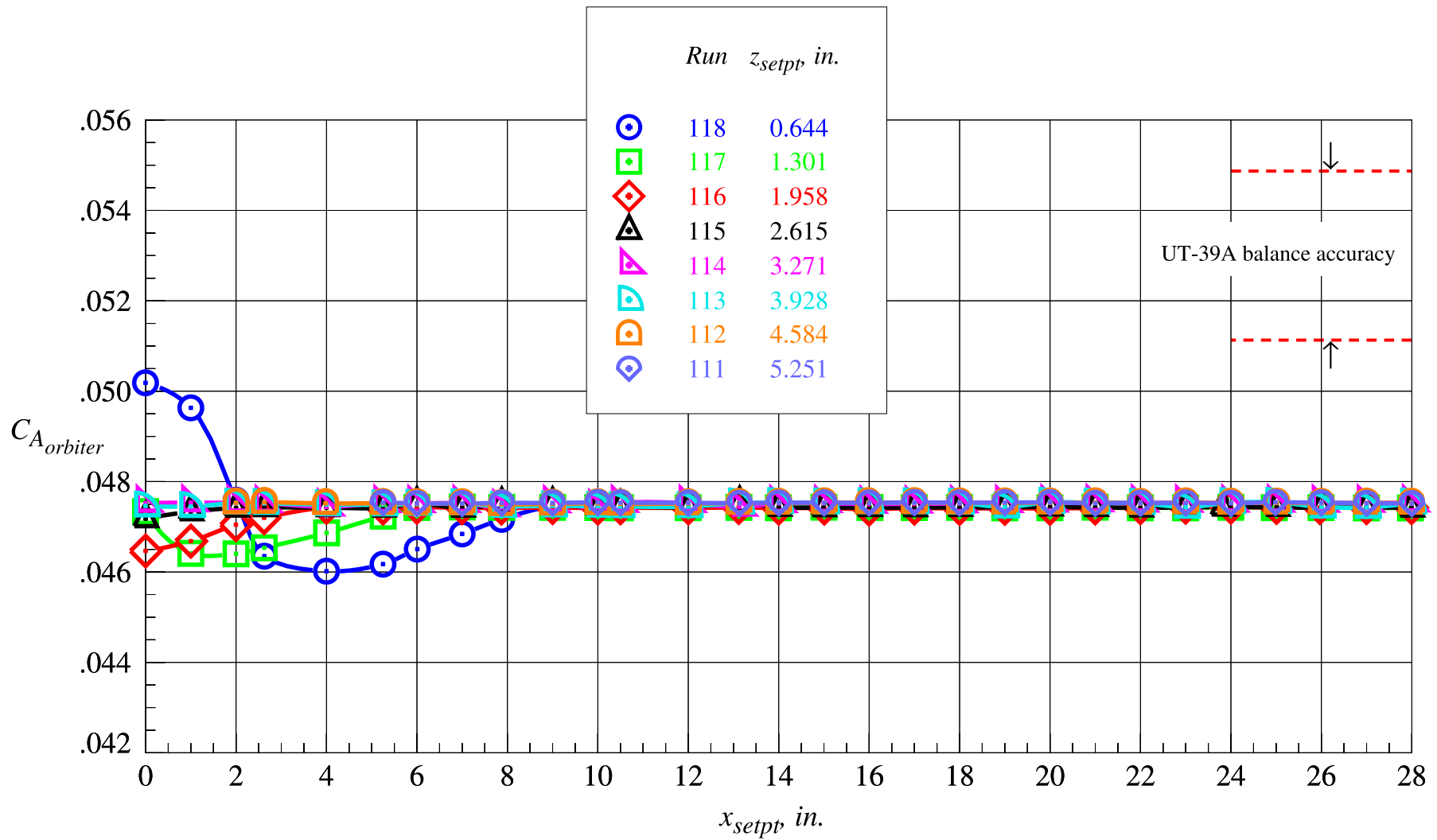
(a) Orbiter normal force coefficient, part 1

Figure 52. Orbiter proximity aerodynamic characteristics at  $Mach = 4.5$  and  $\Delta\alpha = 5^\circ$ .



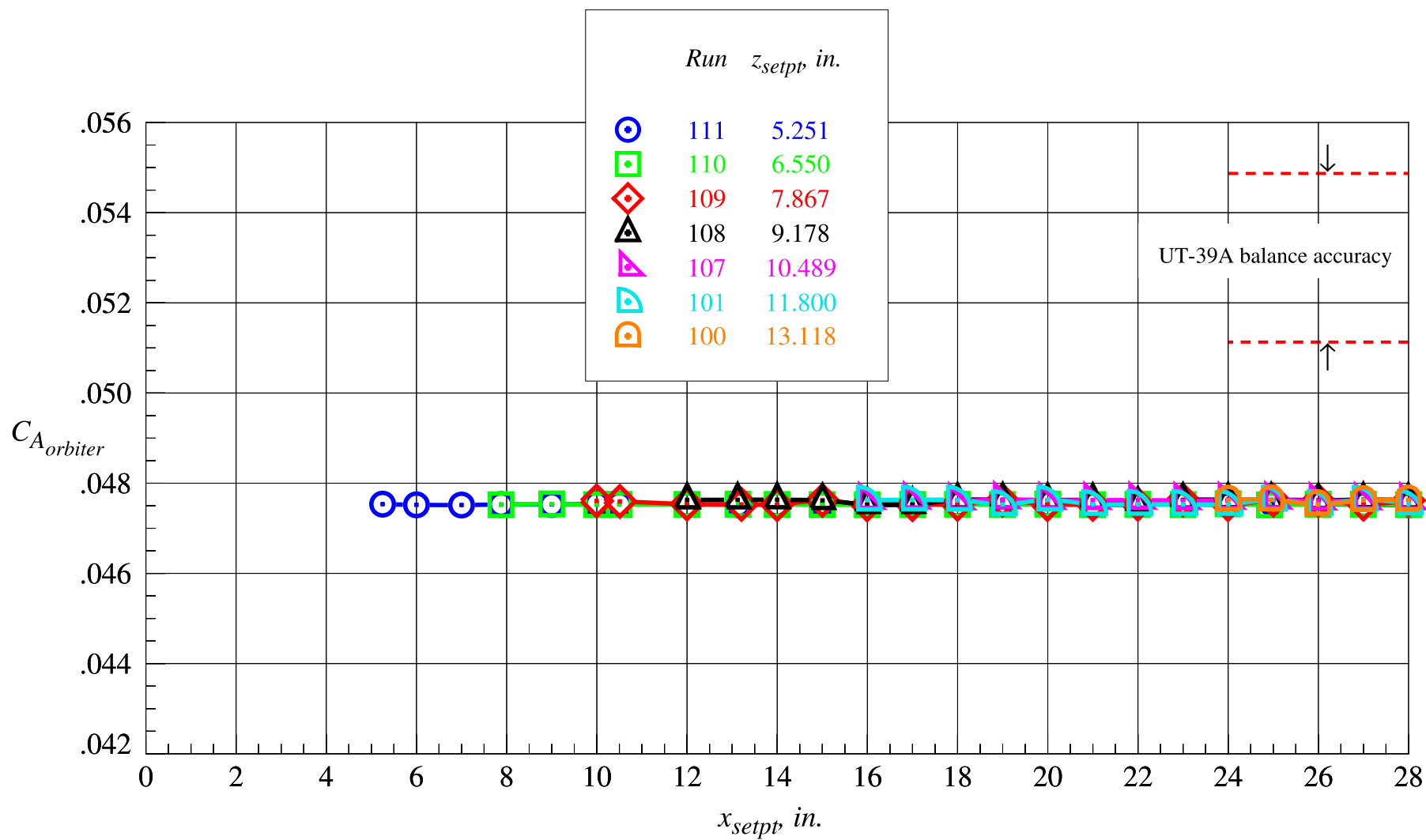
(b) Orbiter normal force coefficient, part 2

Figure 52. Continued.



(c) Orbiter axial force coefficient, part 1

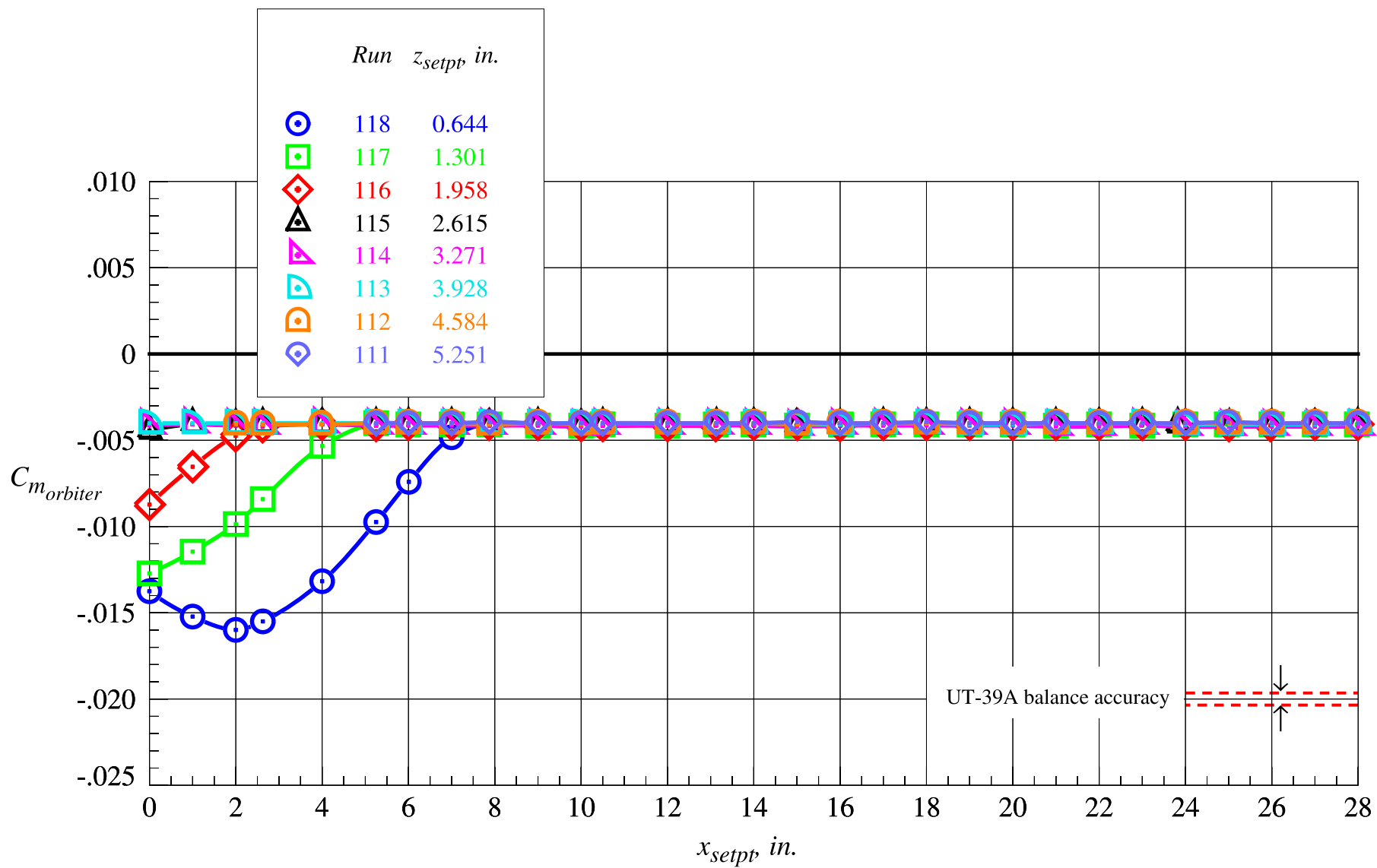
Figure 52. Continued.



(d) Orbiter axial force coefficient, part 2

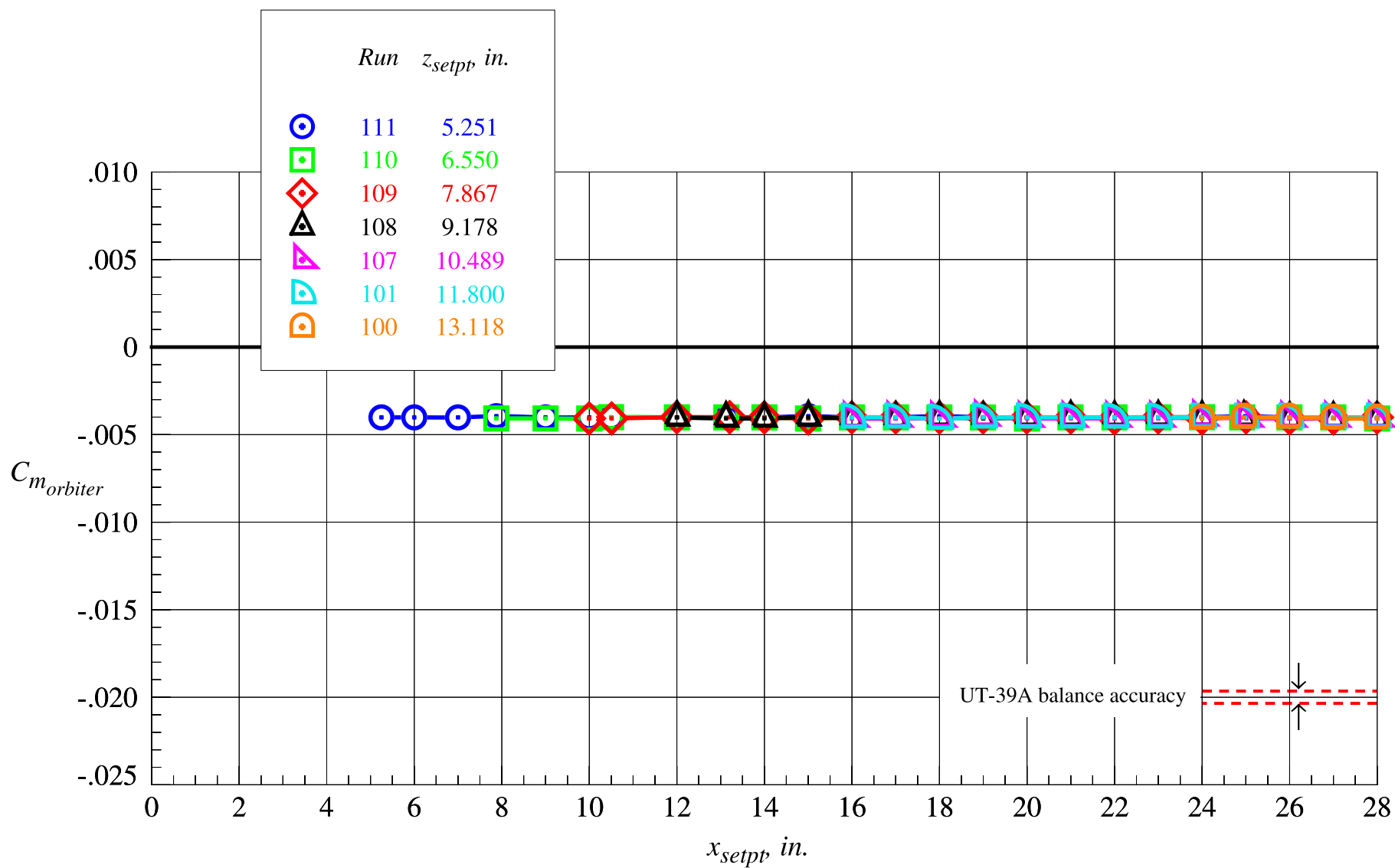
Figure 52. Continued.





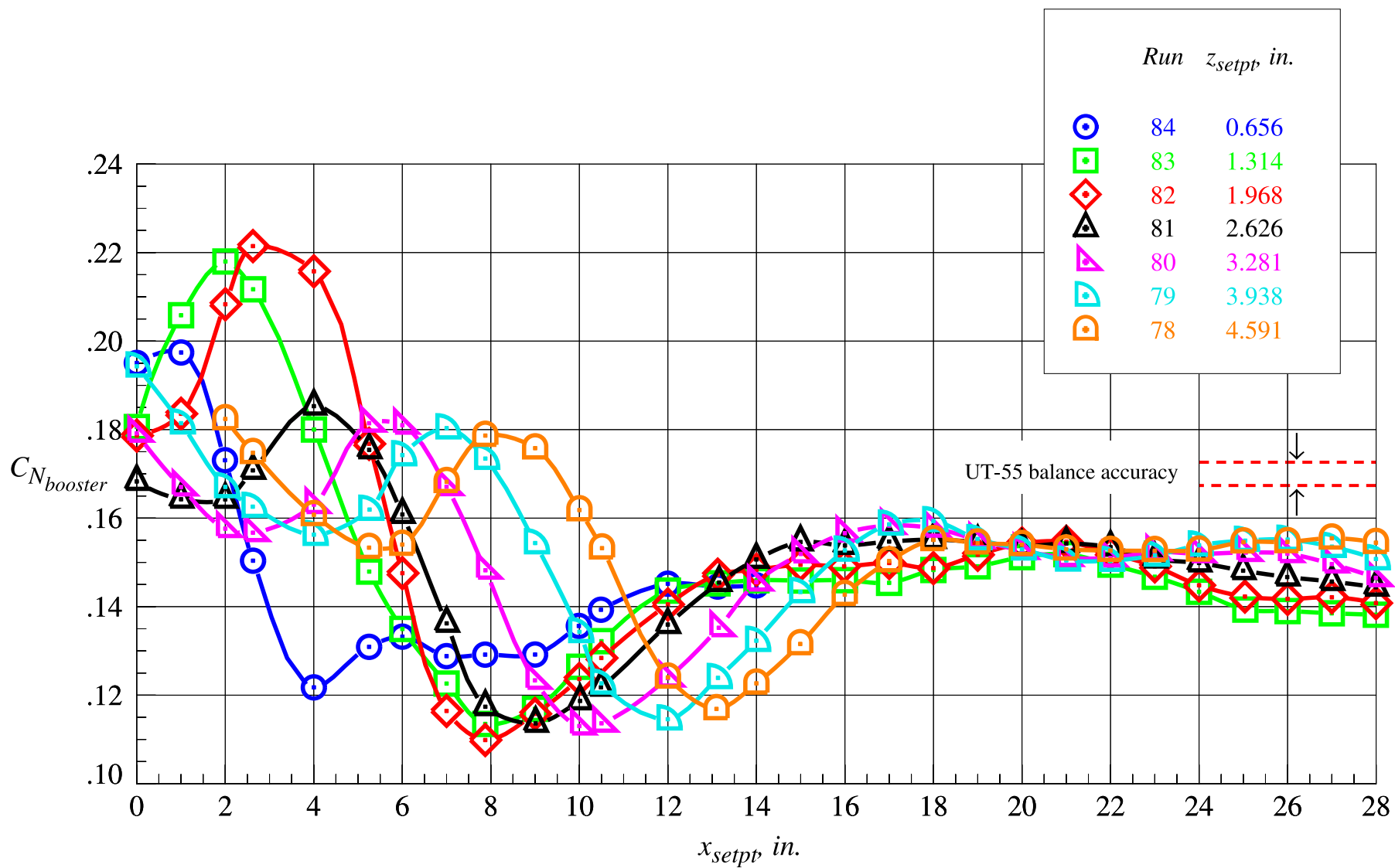
(e) Orbiter pitching moment coefficient, part 1

Figure 52. Continued.



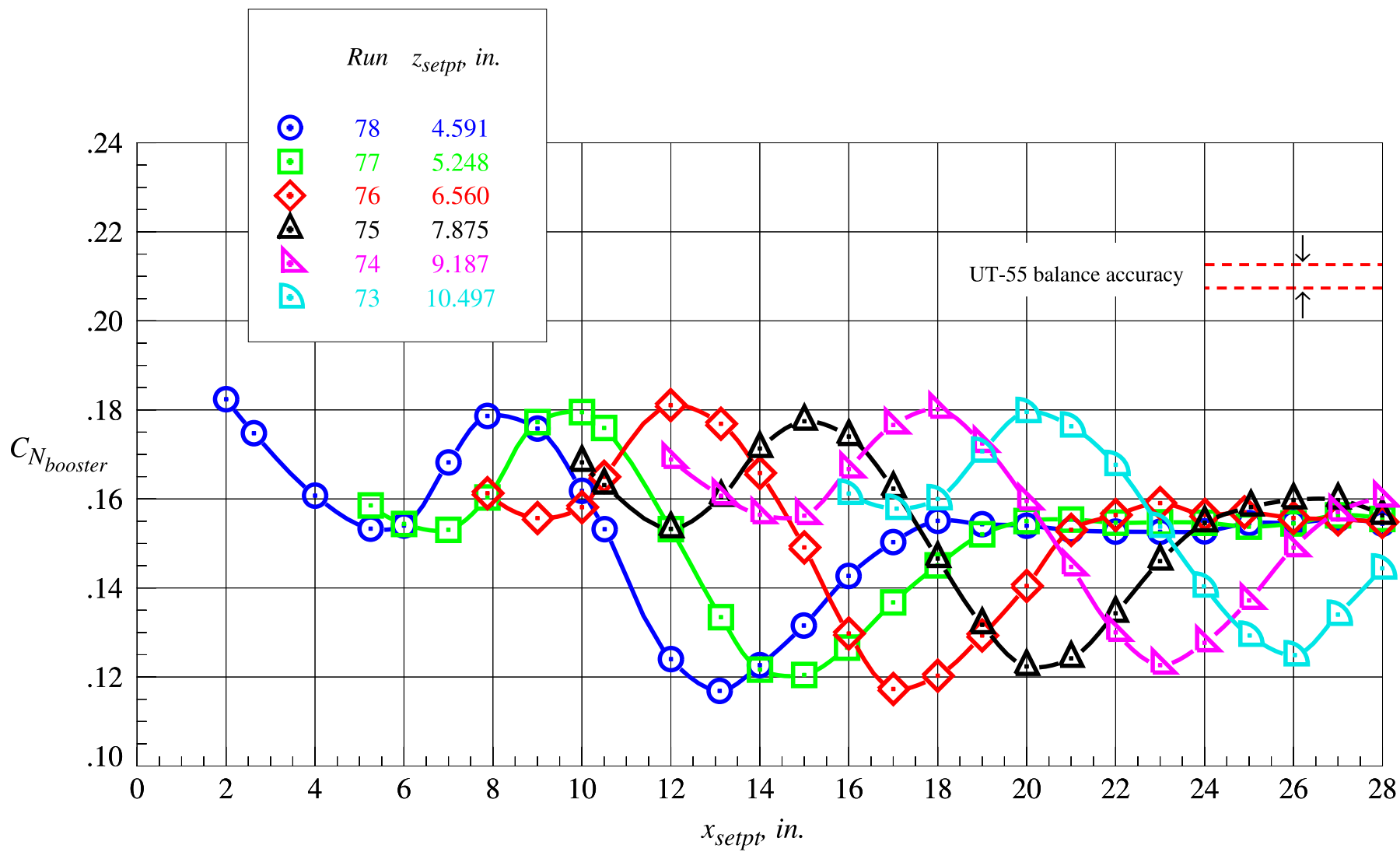
(f) Orbiter pitching moment coefficient, part 2

Figure 52. Concluded.



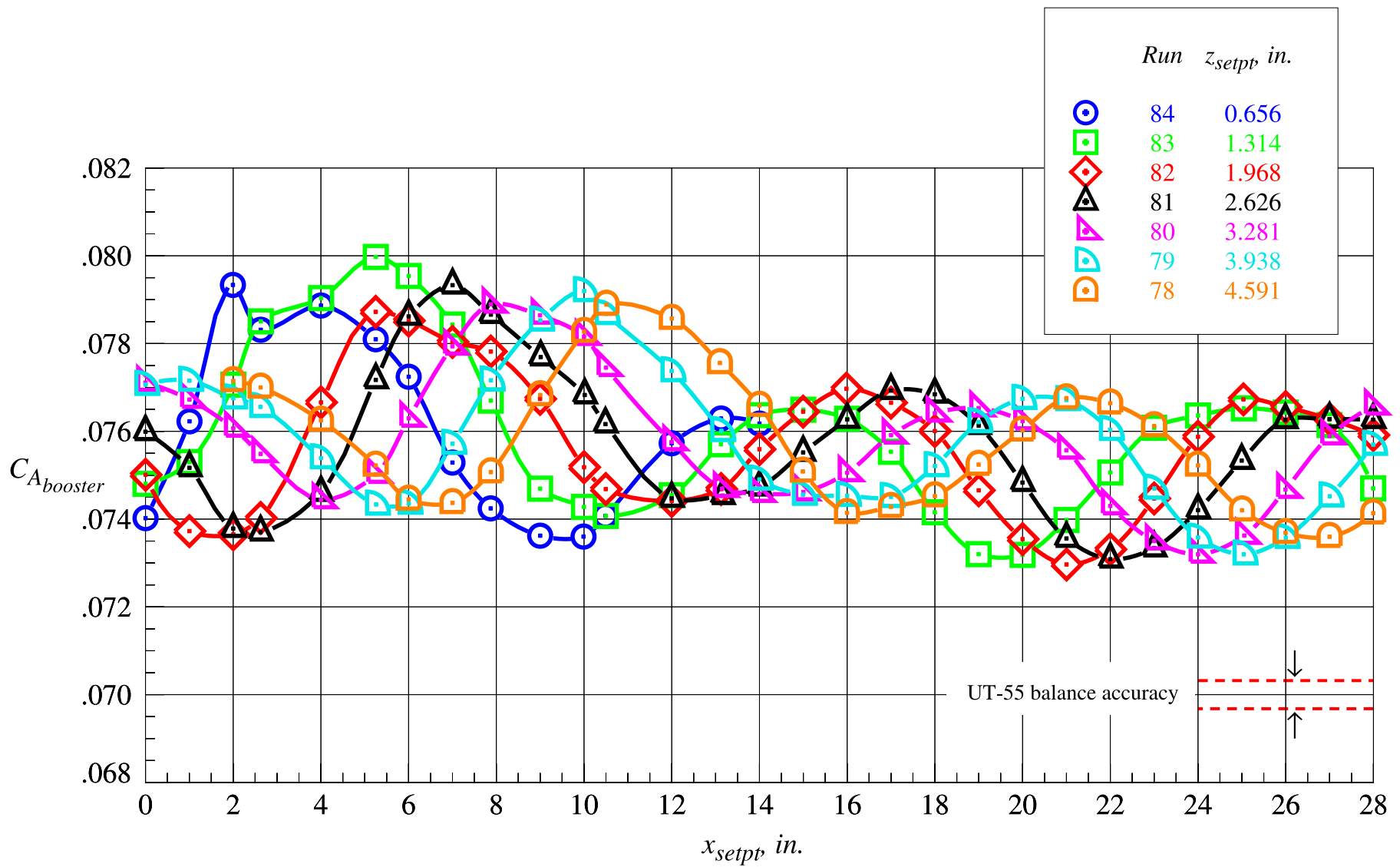
(a) Booster normal force coefficient, part 1

Figure 53. Booster proximity aerodynamic characteristics at Mach = 2.3 and  $\Delta\alpha = 5^\circ$ .



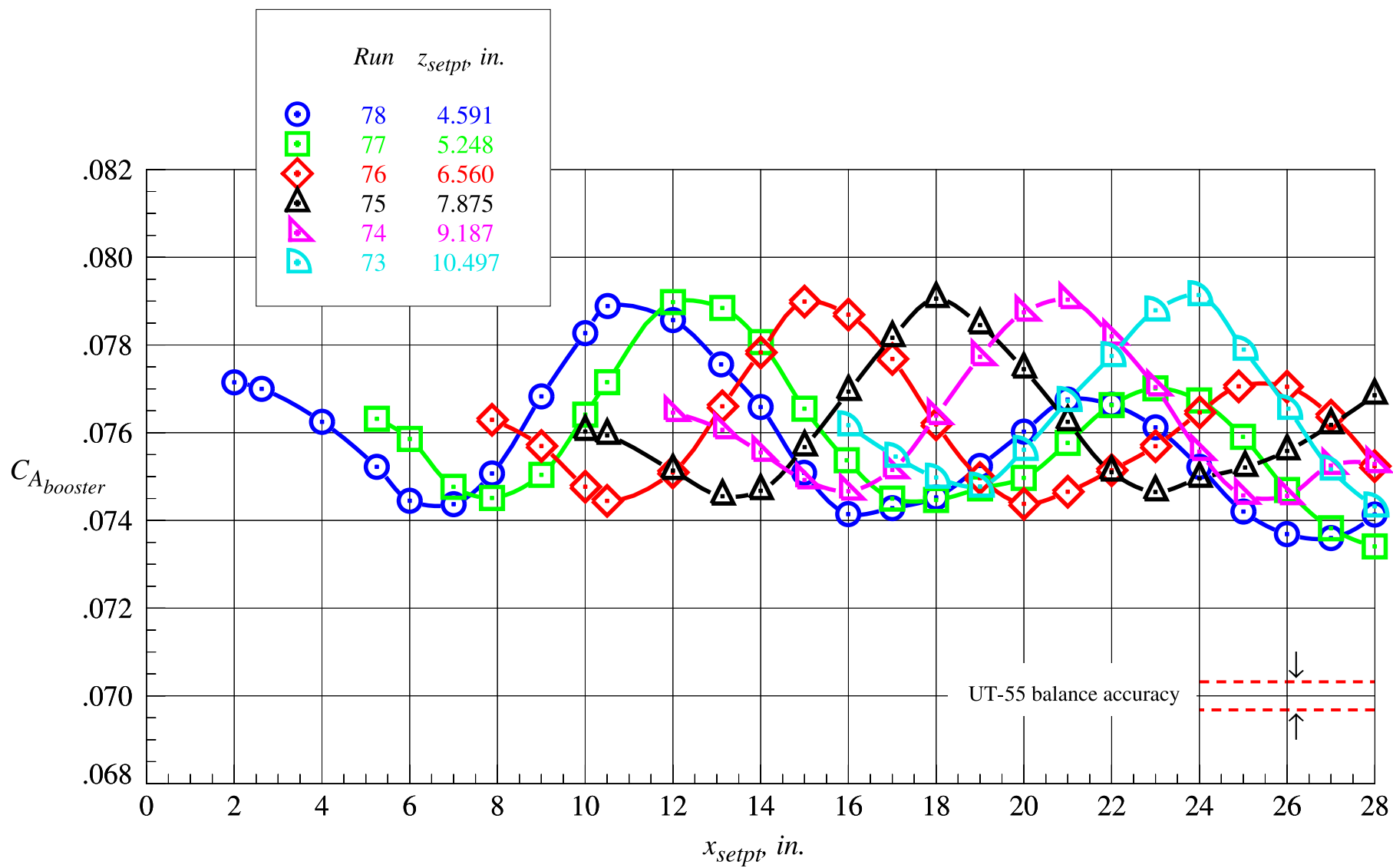
(b) Booster normal force coefficient, part 2

Figure 53. Continued.



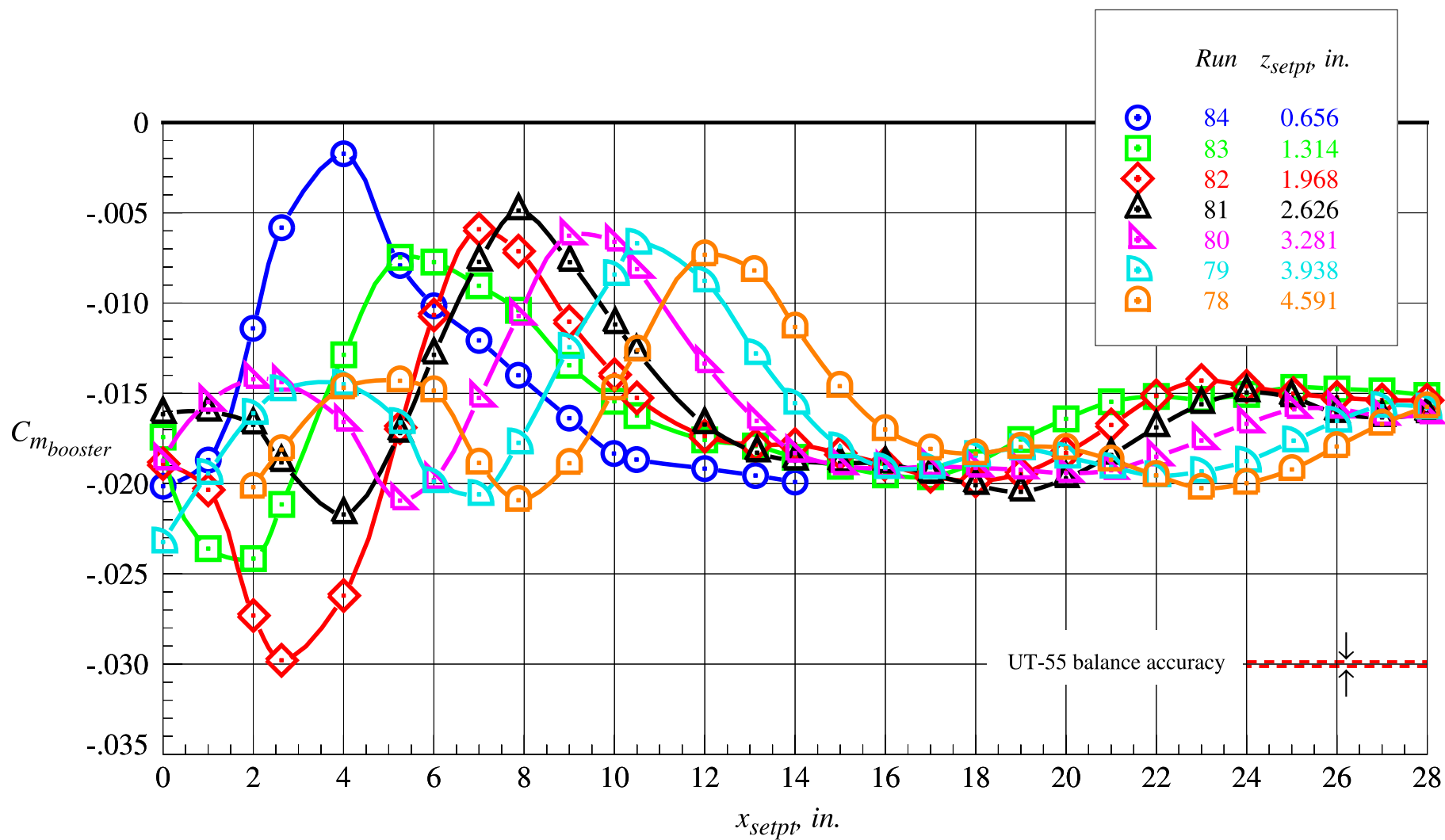
(c) Booster axial force coefficient, part 1

Figure 53. Continued.



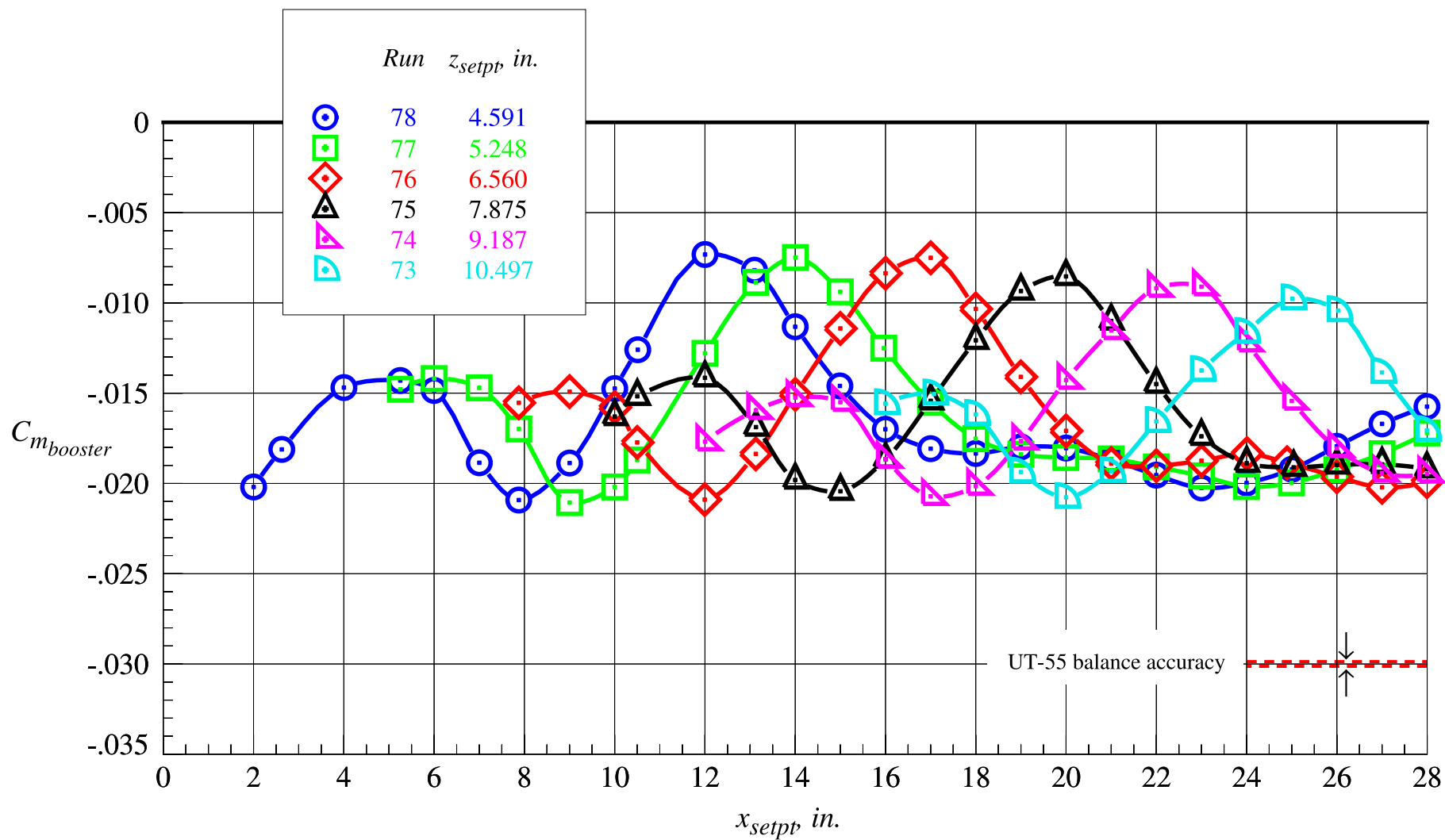
(d) Booster axial force coefficient, part 2

Figure 53. Continued.



(e) Booster pitching moment coefficient, part 1

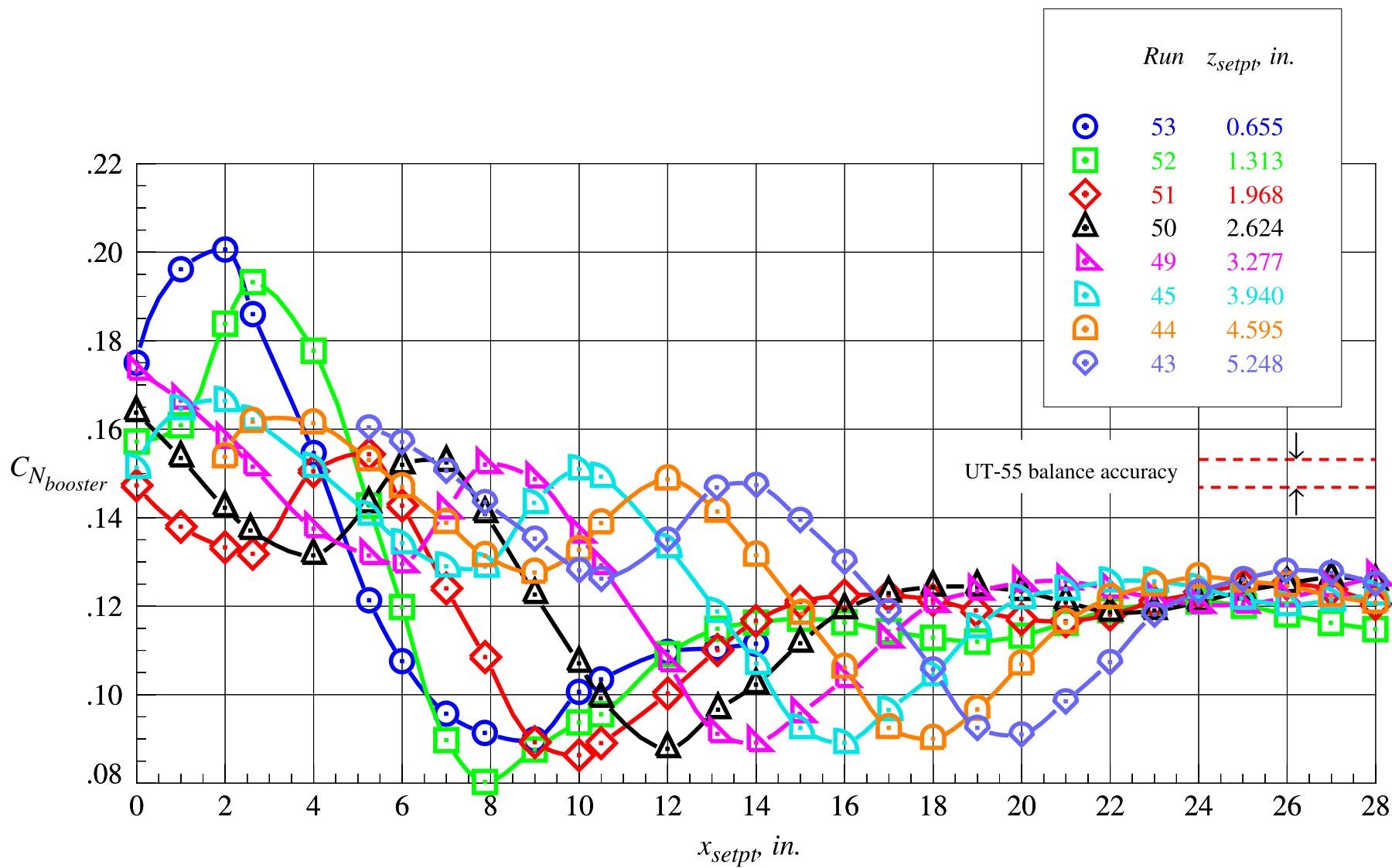
Figure 53. Continued.



(f) Booster pitching moment coefficient, part 2

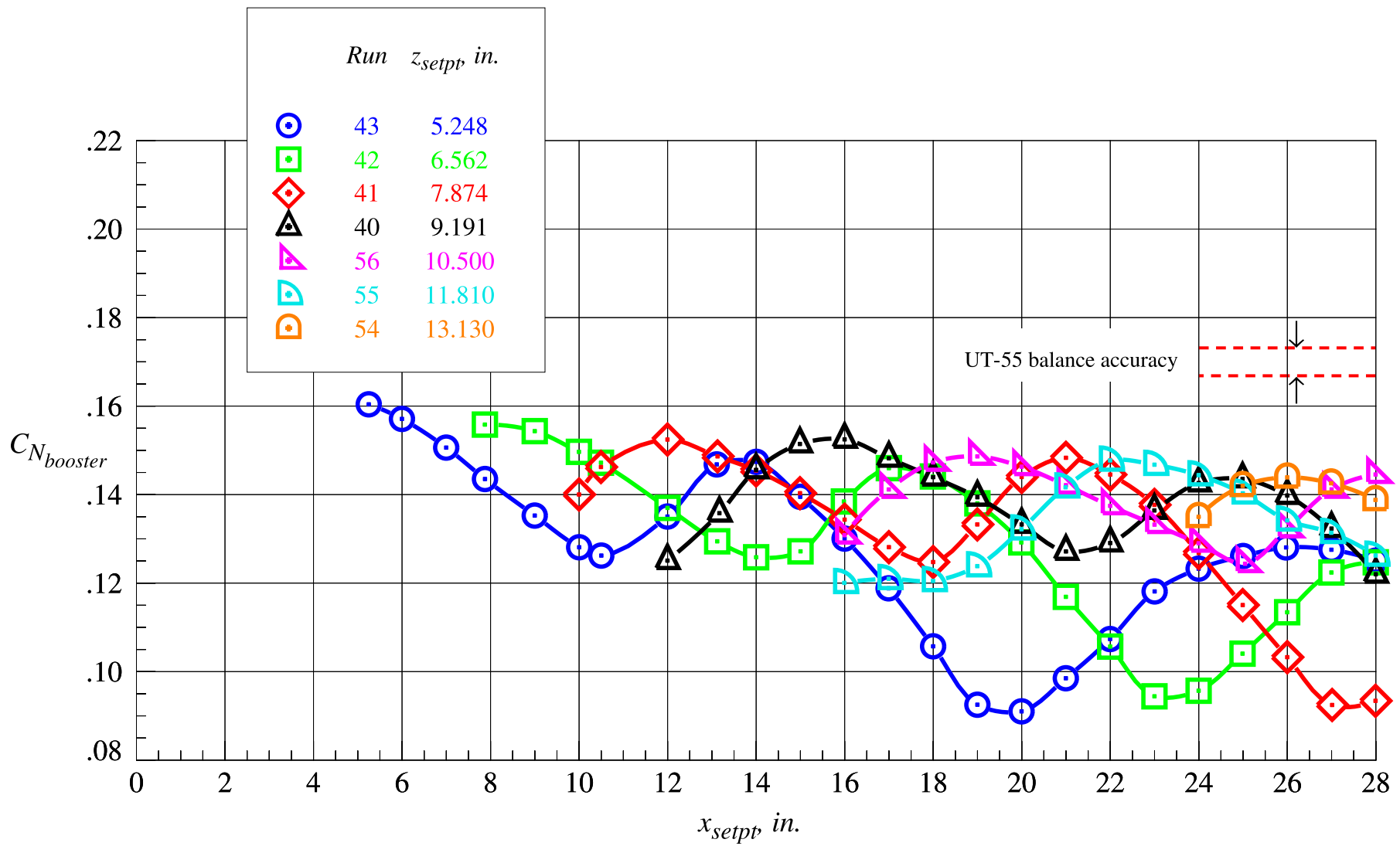
Figure 53. Concluded.





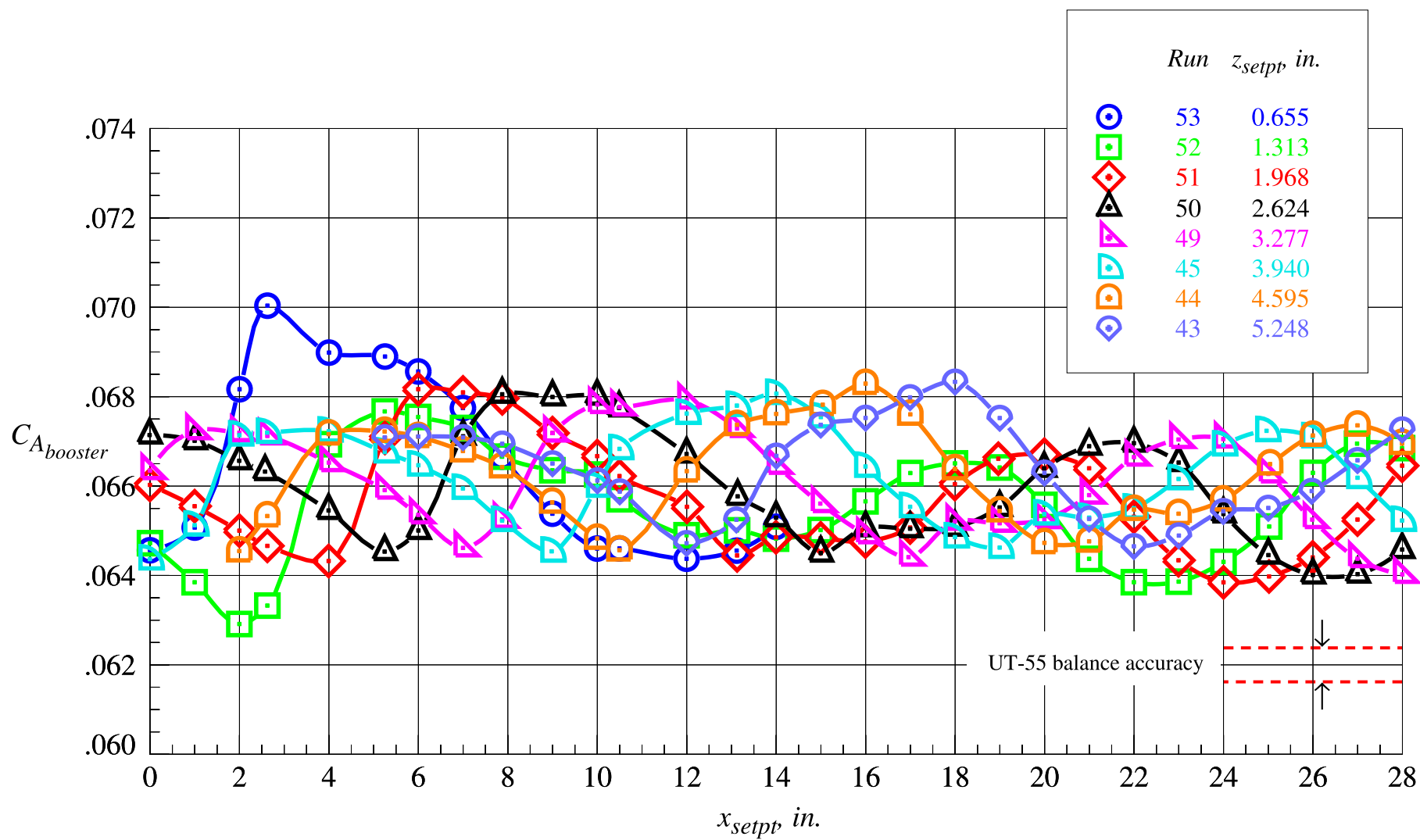
(a) Booster normal force coefficient, part 1

Figure 54. Booster proximity aerodynamic characteristics at Mach = 3.0 and  $\Delta\alpha = 5^\circ$ .



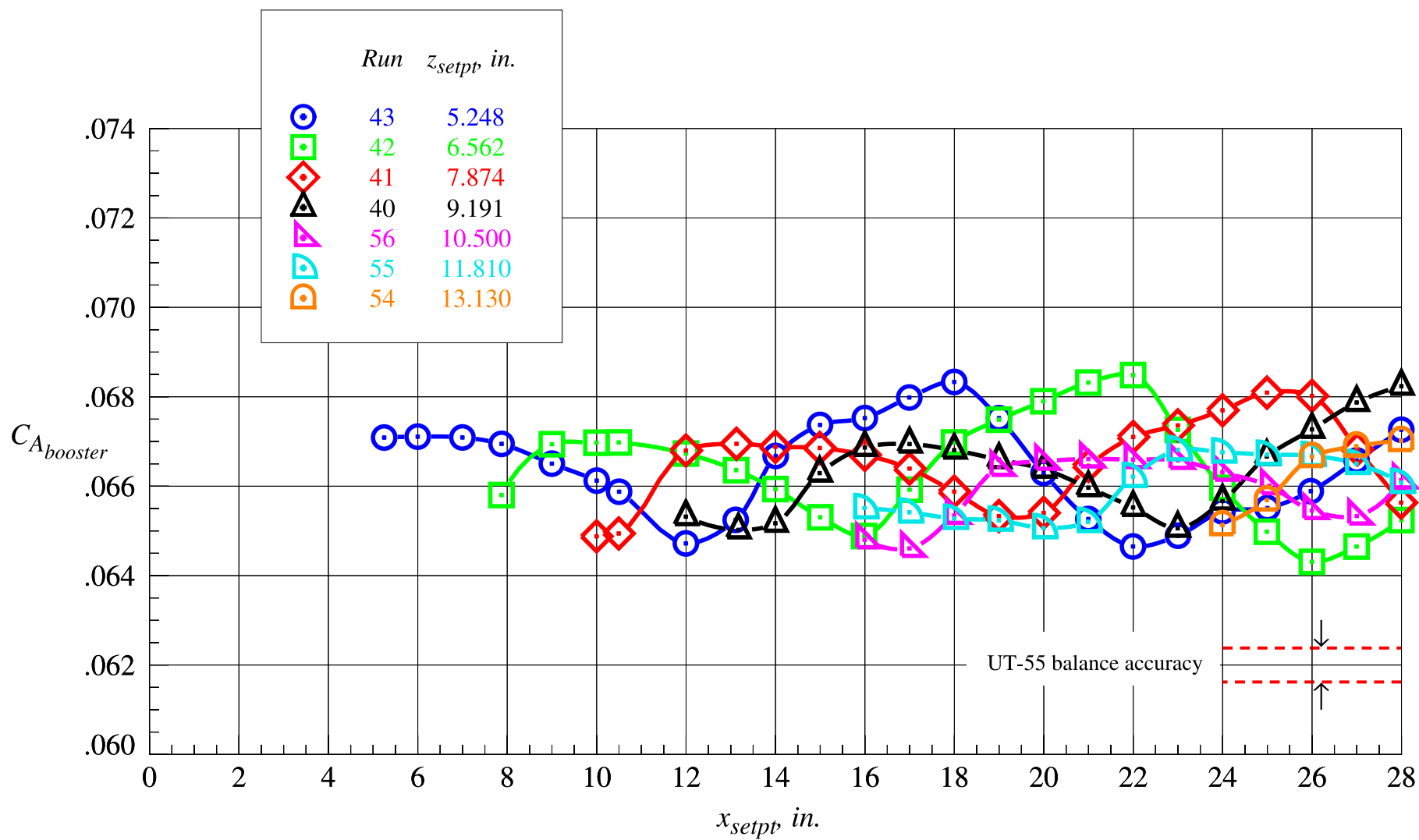
(b) Booster normal force coefficient, part 2

Figure 54. Continued.



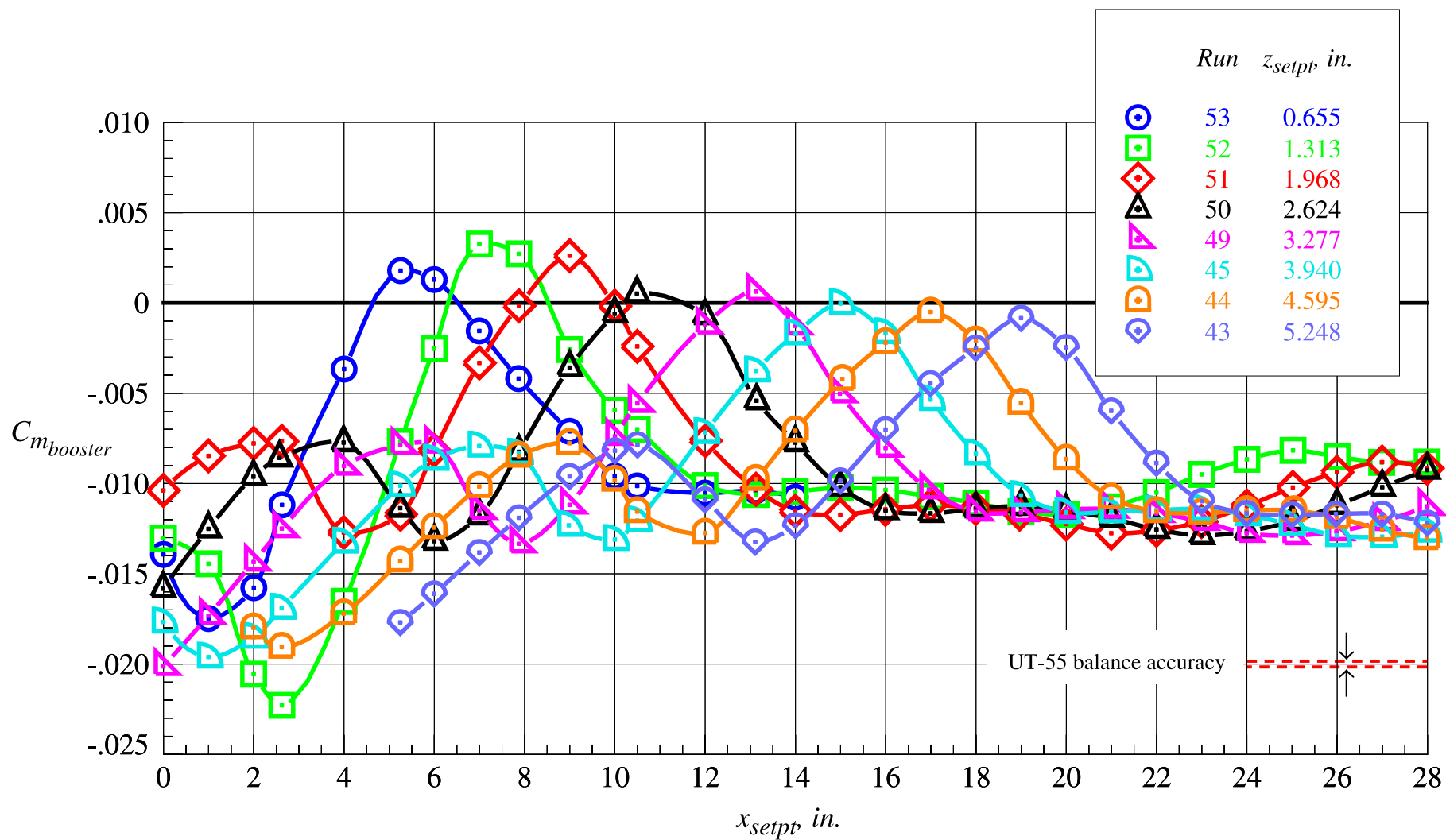
(c) Booster axial force coefficient, part 1

Figure 54. Continued.



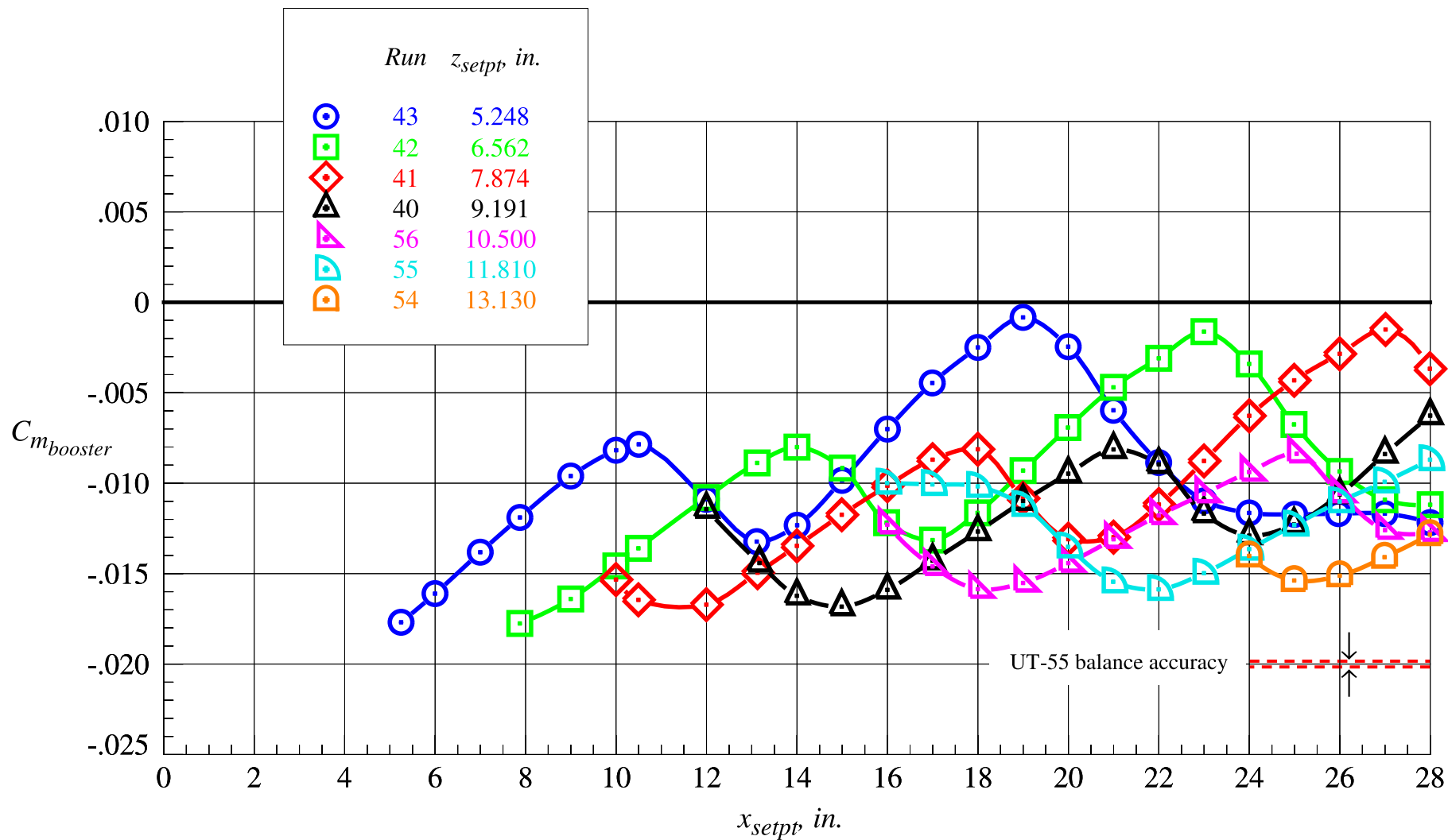
(d) Booster axial force coefficient, part 2

Figure 54. Continued.



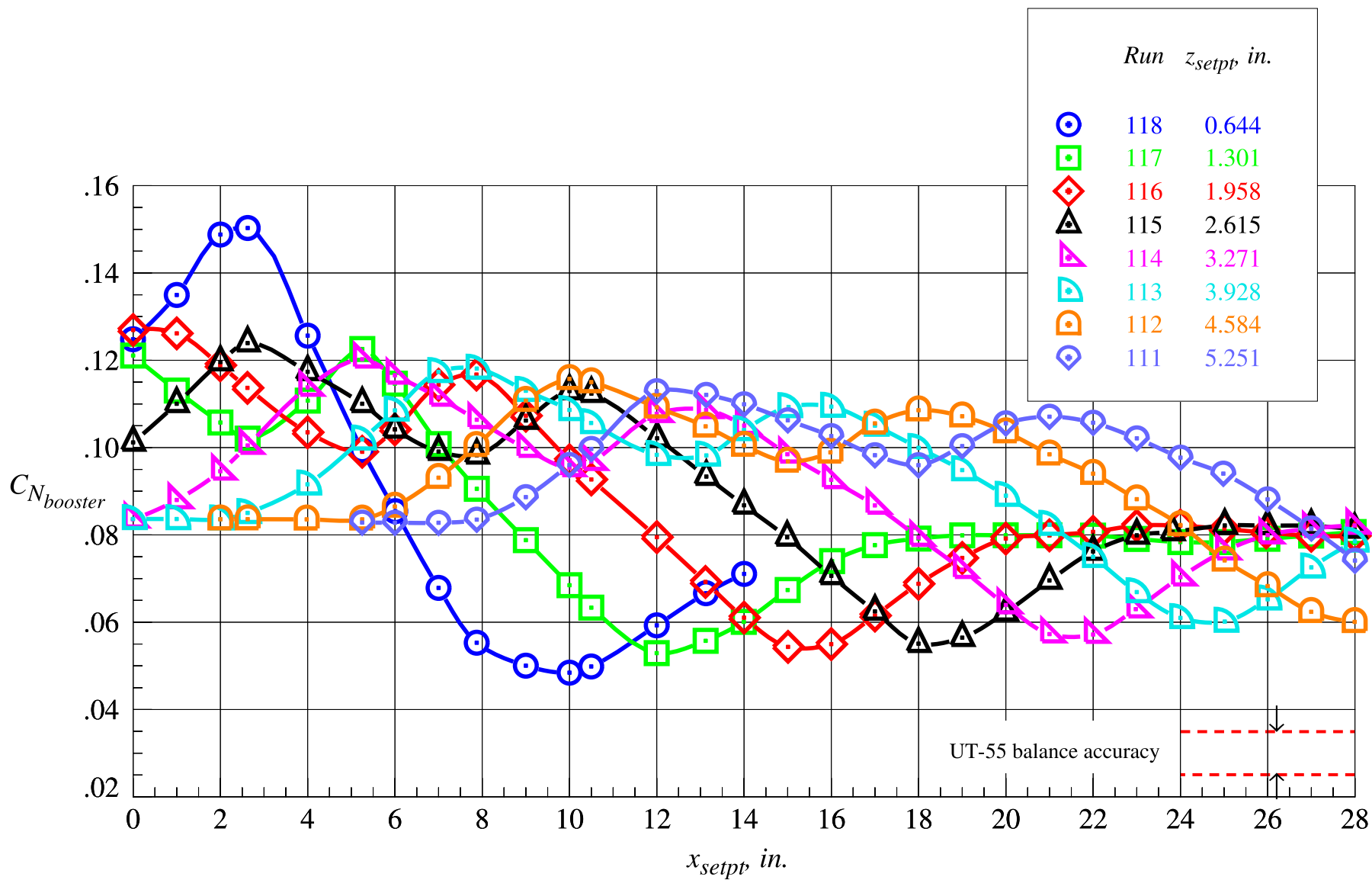
(e) Booster pitching moment coefficient, part 1

Figure 54. Continued.



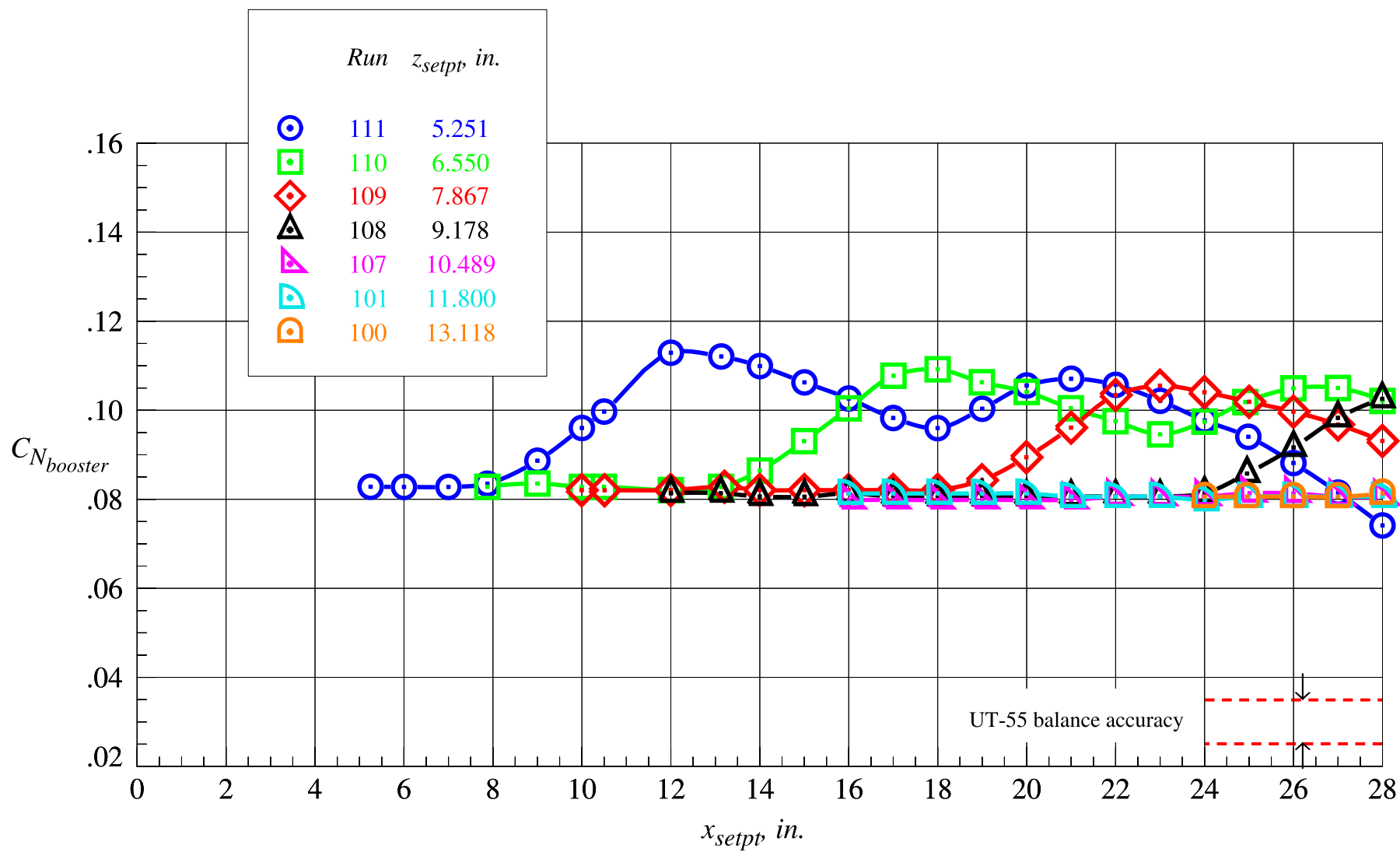
(f) Booster pitching moment coefficient, part 2

Figure 54. Concluded.



(a) Booster normal force coefficient, part 1

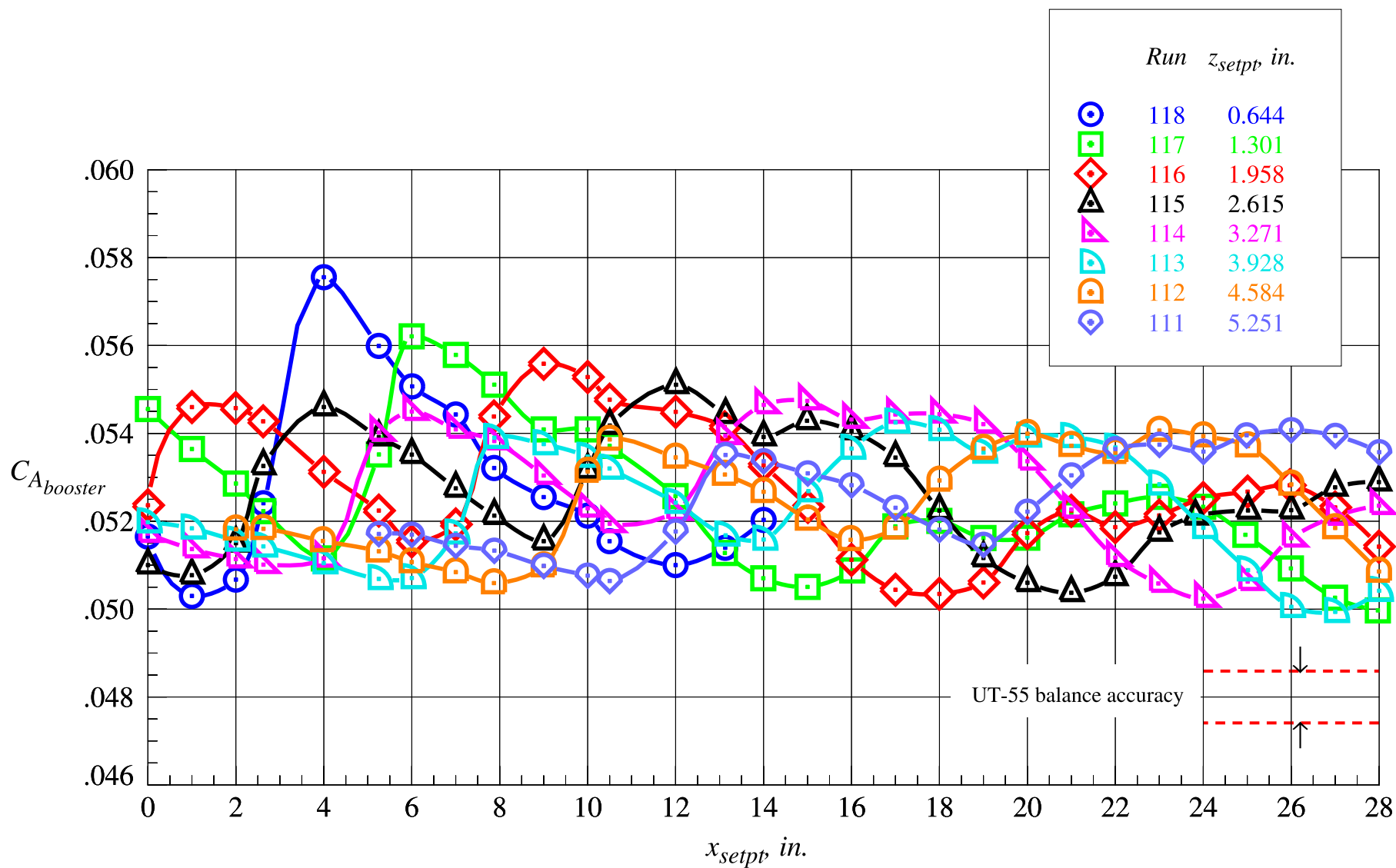
Figure 55. Booster proximity aerodynamic characteristics at Mach = 4.5 and  $\Delta\alpha = 5^\circ$ .



(b) Booster normal force coefficient, part 2

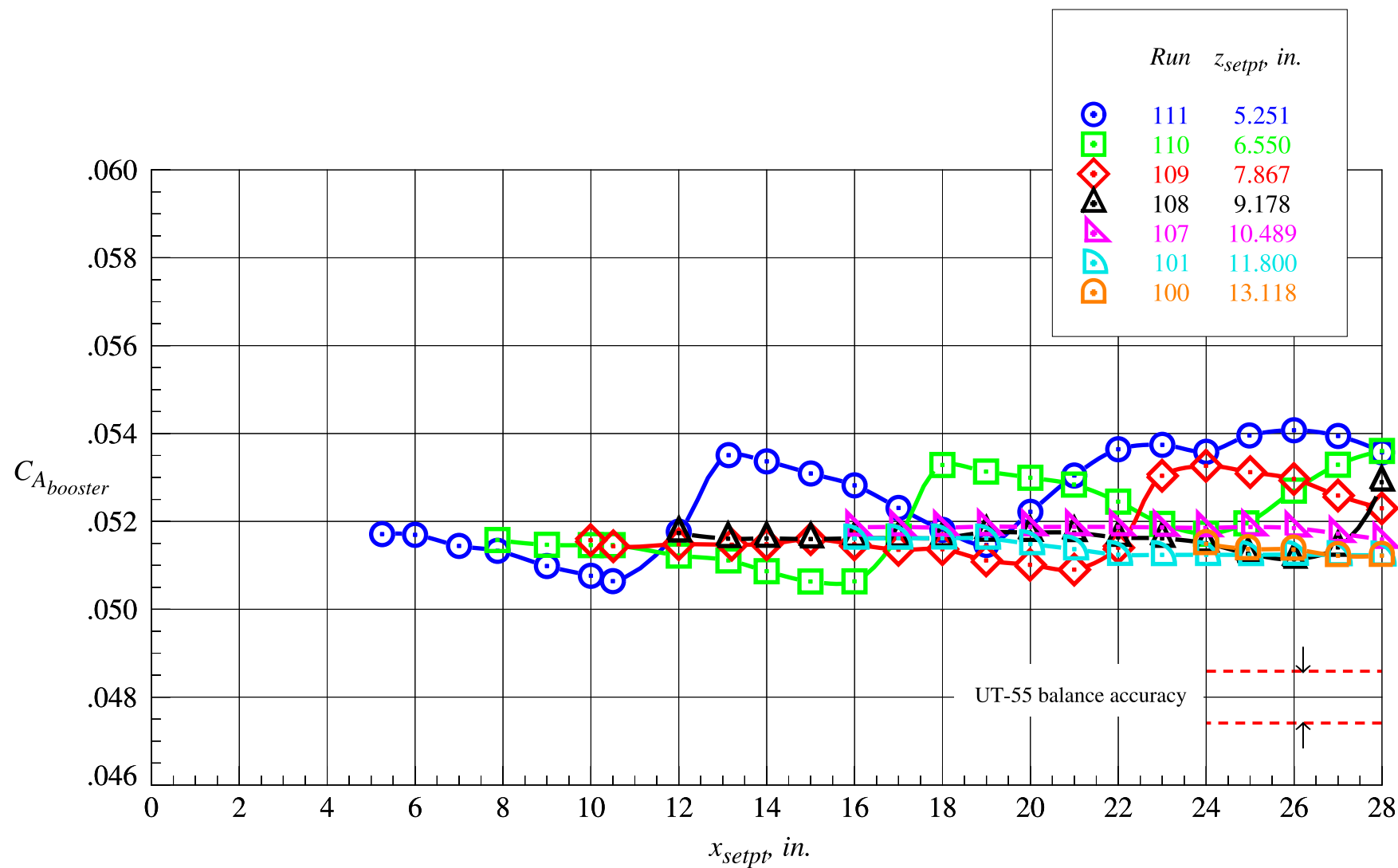
Figure 55. Continued.





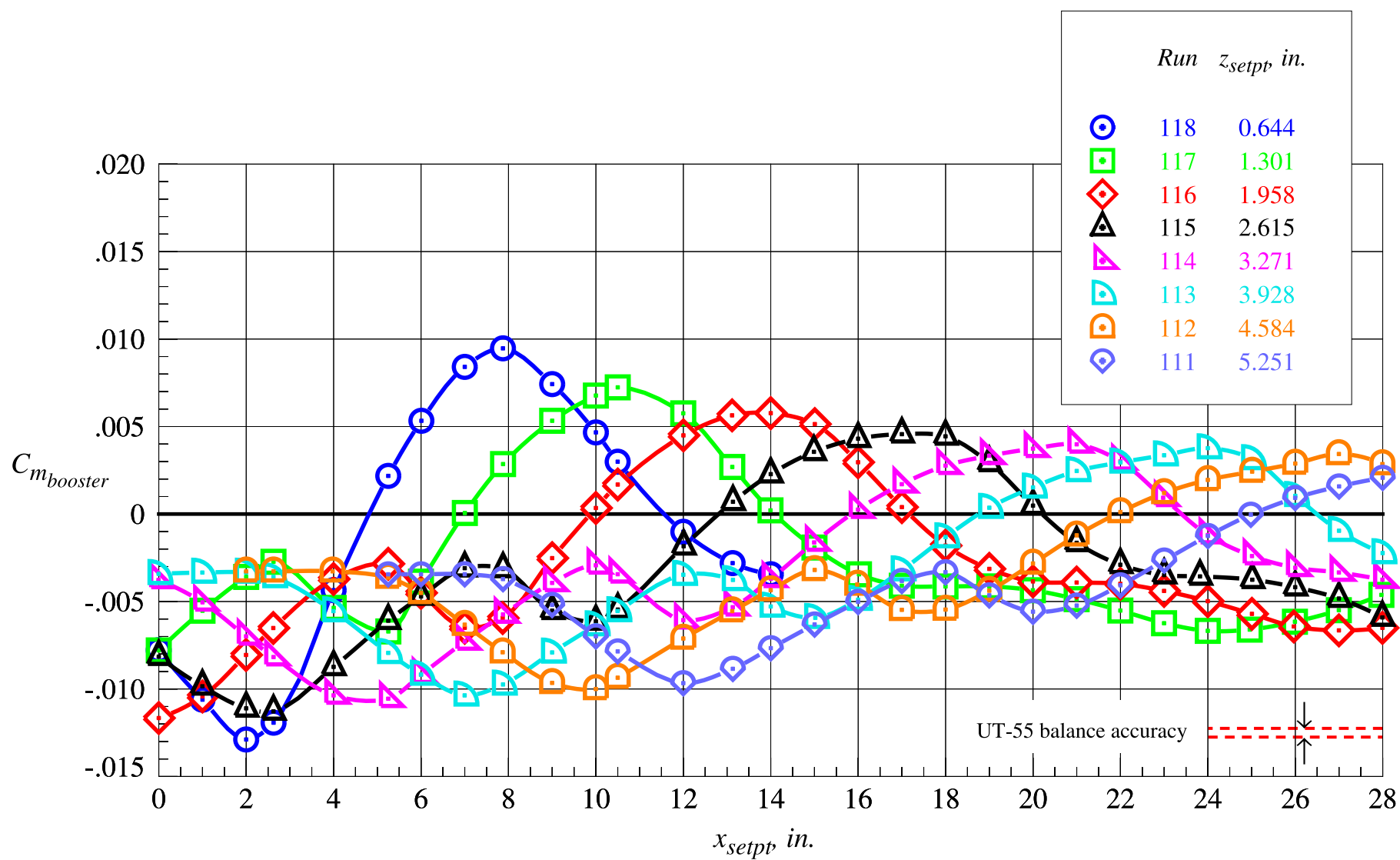
(c) Booster axial force coefficient, part 1

Figure 55. Continued.



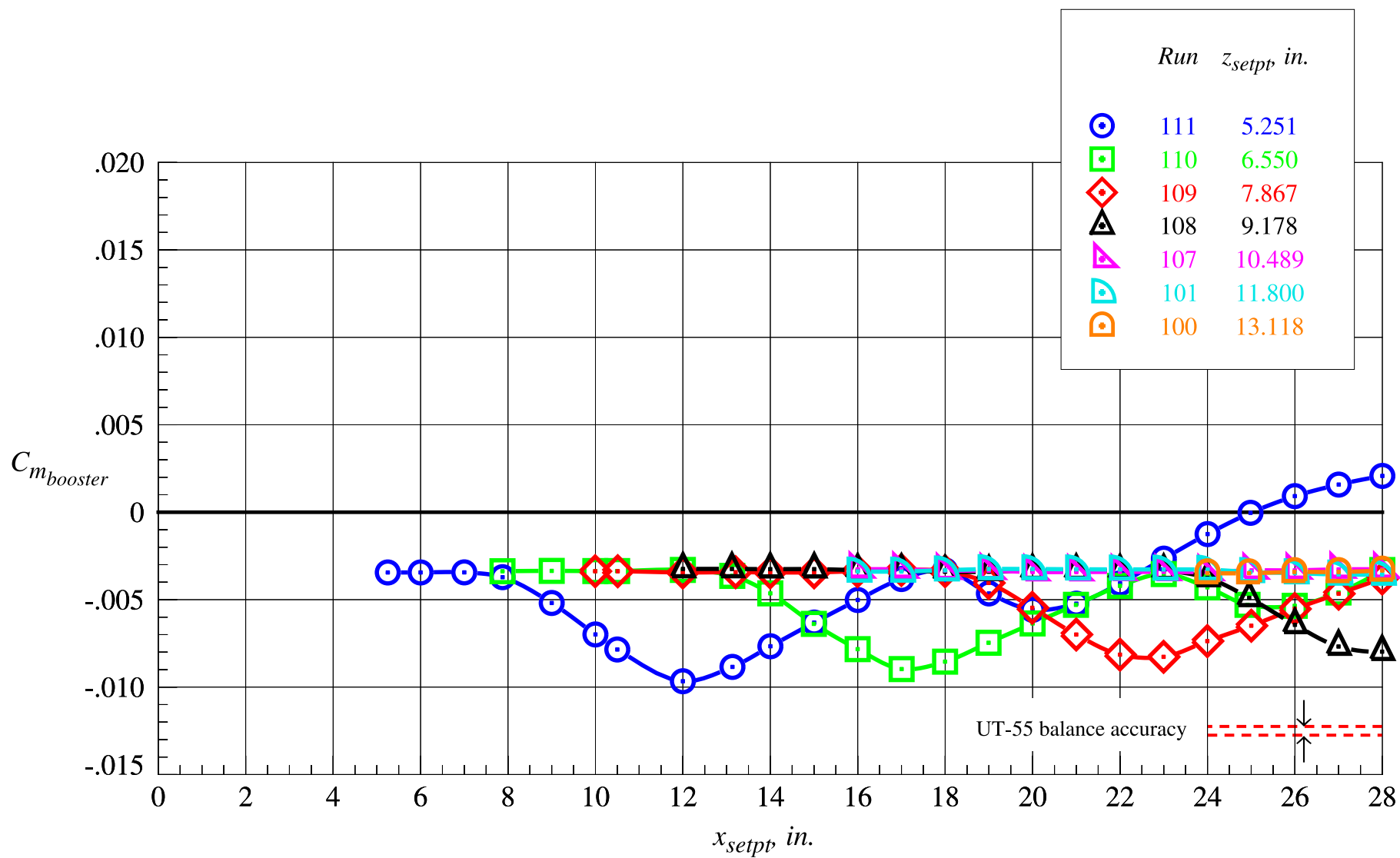
(d) Booster axial force coefficient, part 2

Figure 55. Continued.



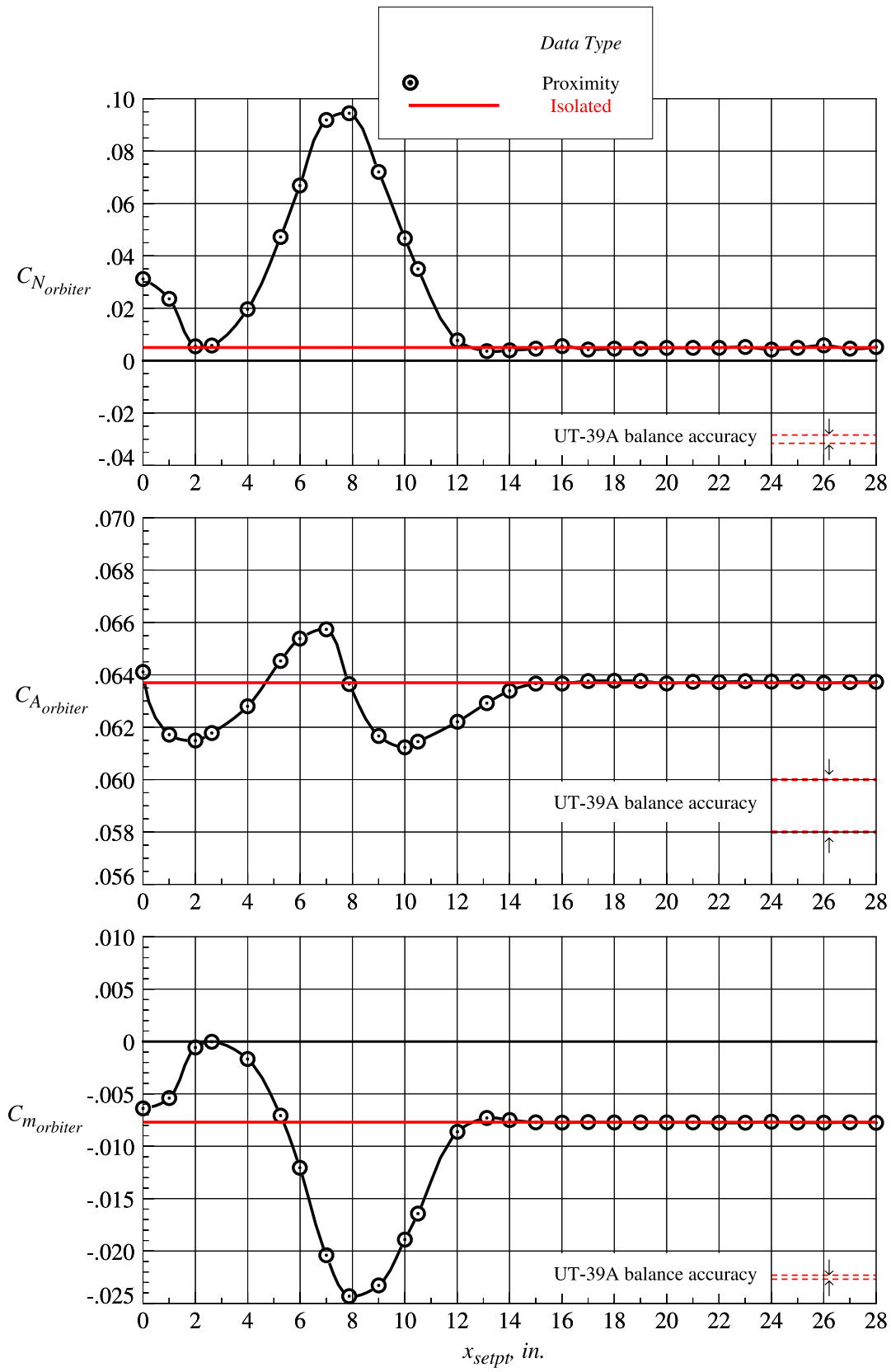
(e) Booster pitching moment coefficient, part 1

Figure 55. Continued.



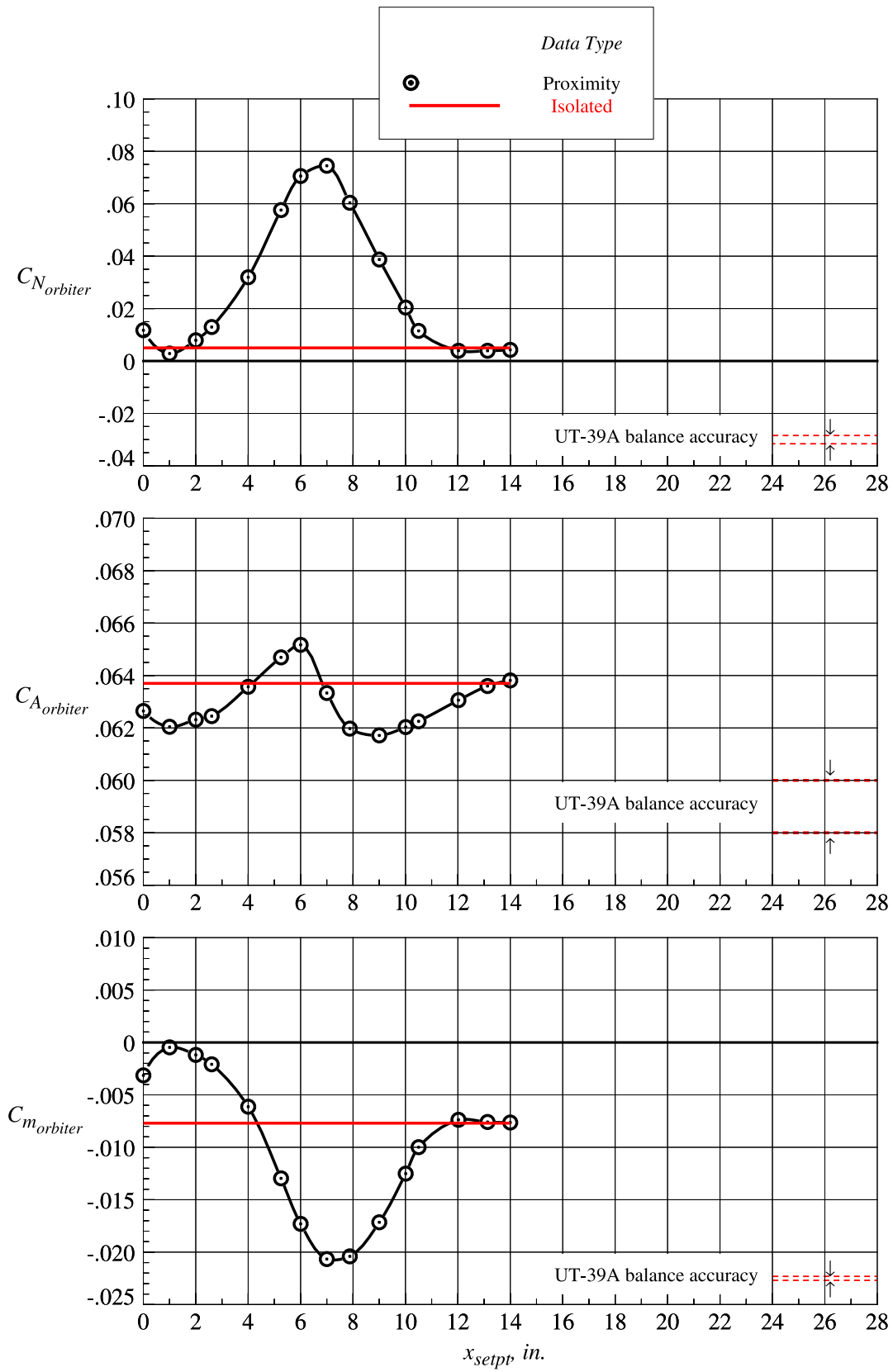
(f) Booster pitching moment coefficient, part 2

Figure 55. Concluded.



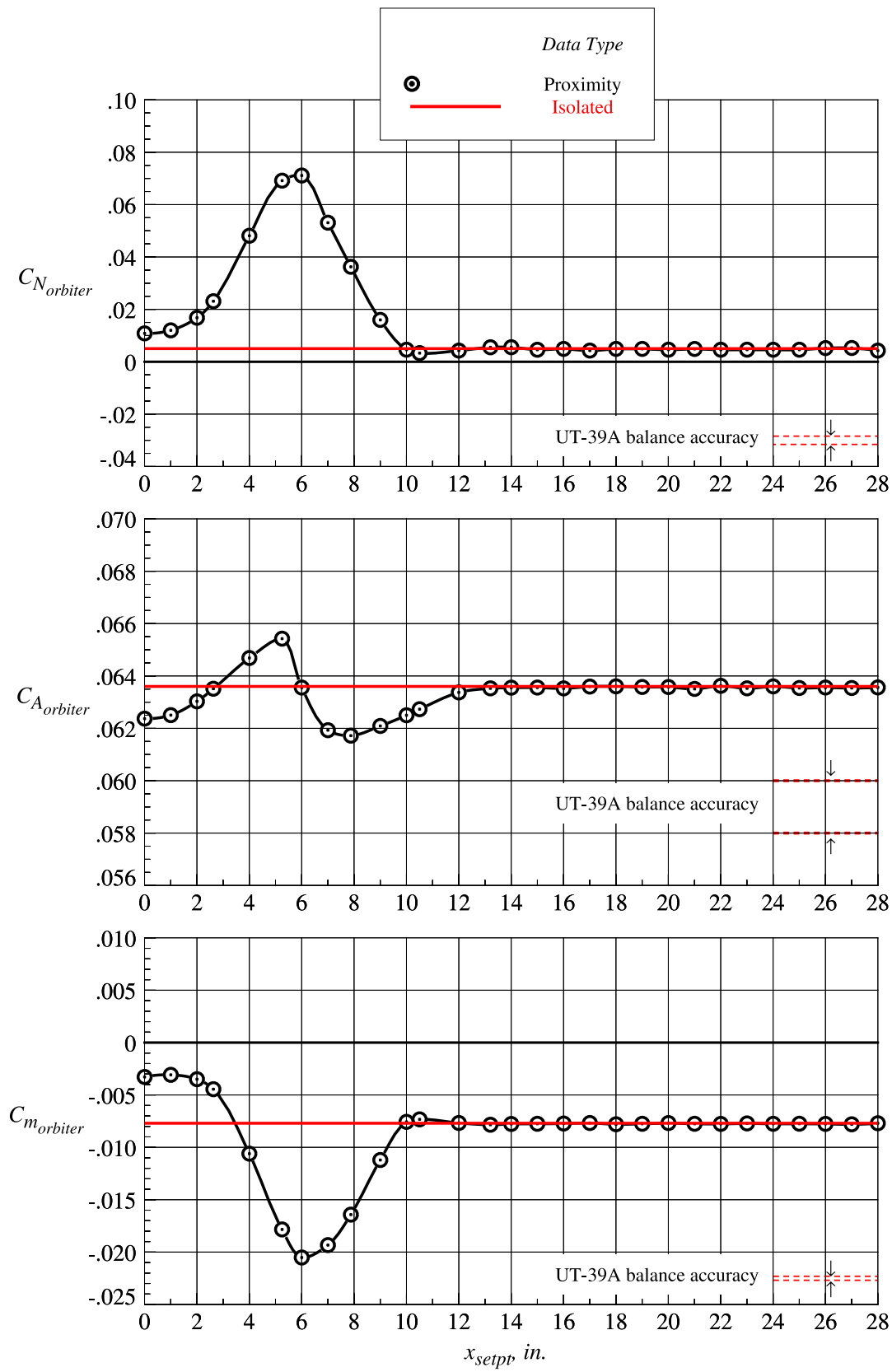
(a)  $z_{sept} = 0$  in.

Figure 56. Orbiter proximity and isolated aerodynamic characteristics at Mach = 2.3 and  $\Delta\alpha = 0^\circ$ .



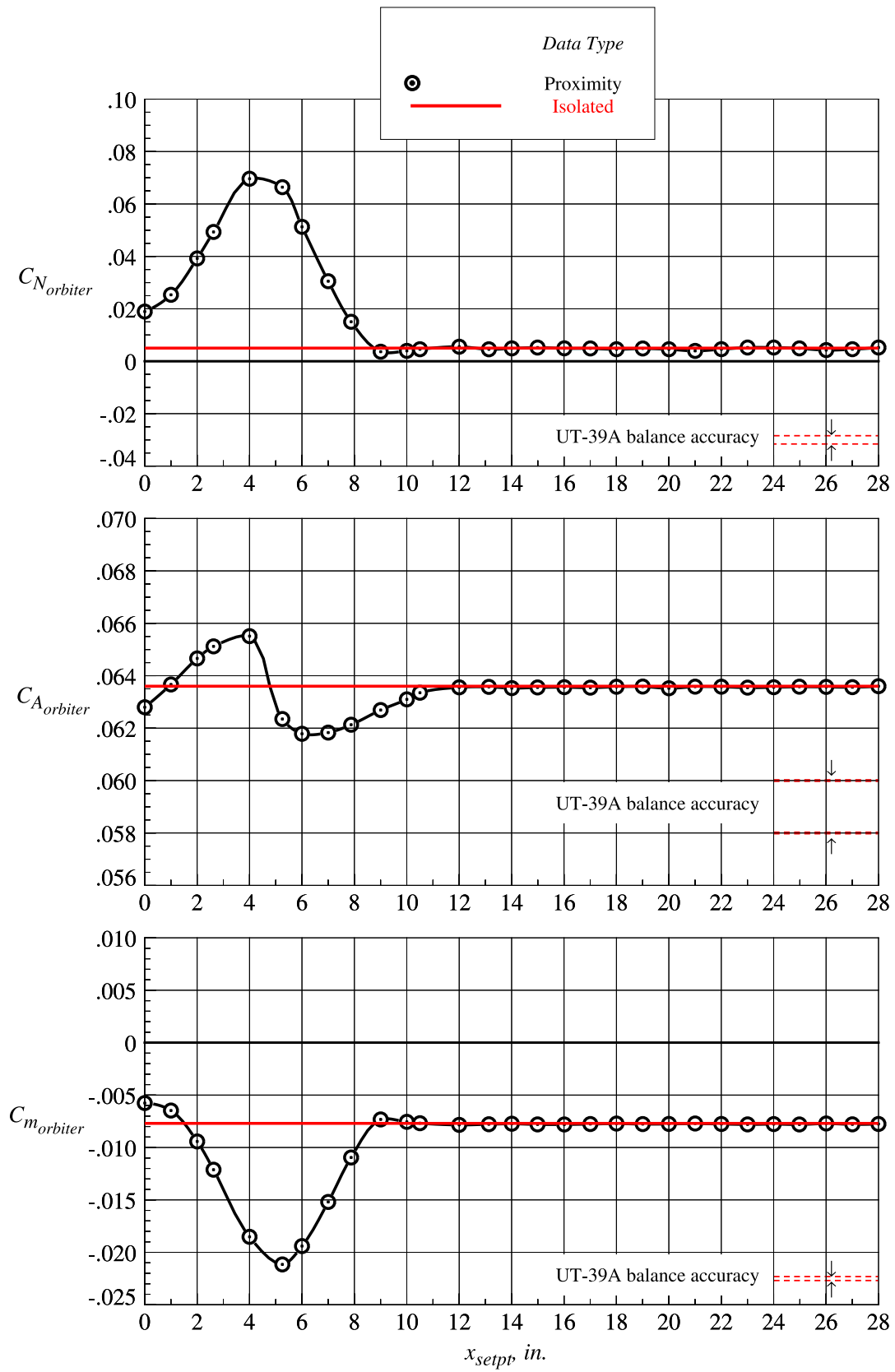
(b)  $z_{setpt} = 0.656$  in.

Figure 56. Continued.



(c)  $z_{setpt} = 1.313$  in.

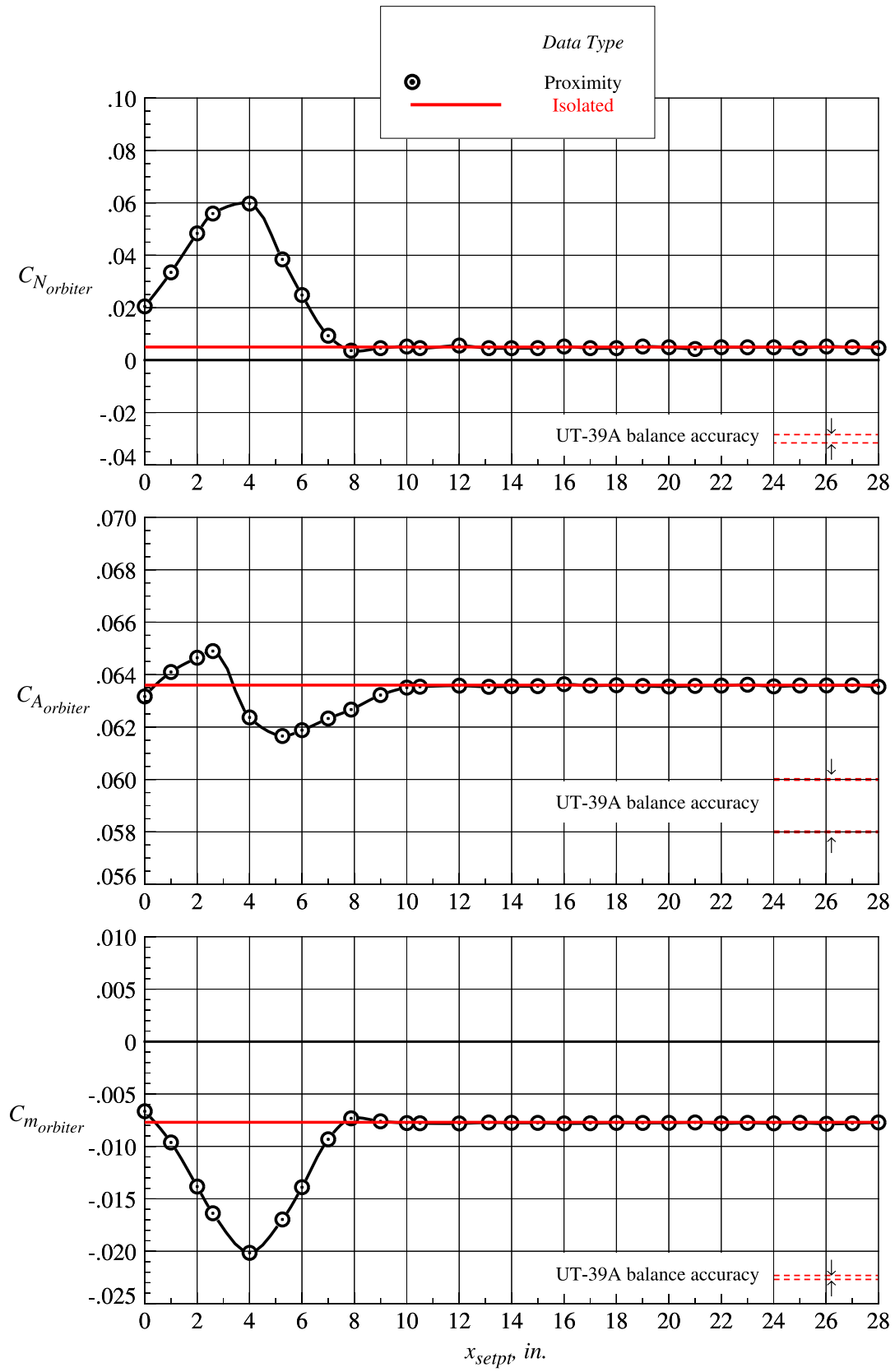
Figure 56. Continued.



(d)  $z_{setpt} = 1.969$  in.

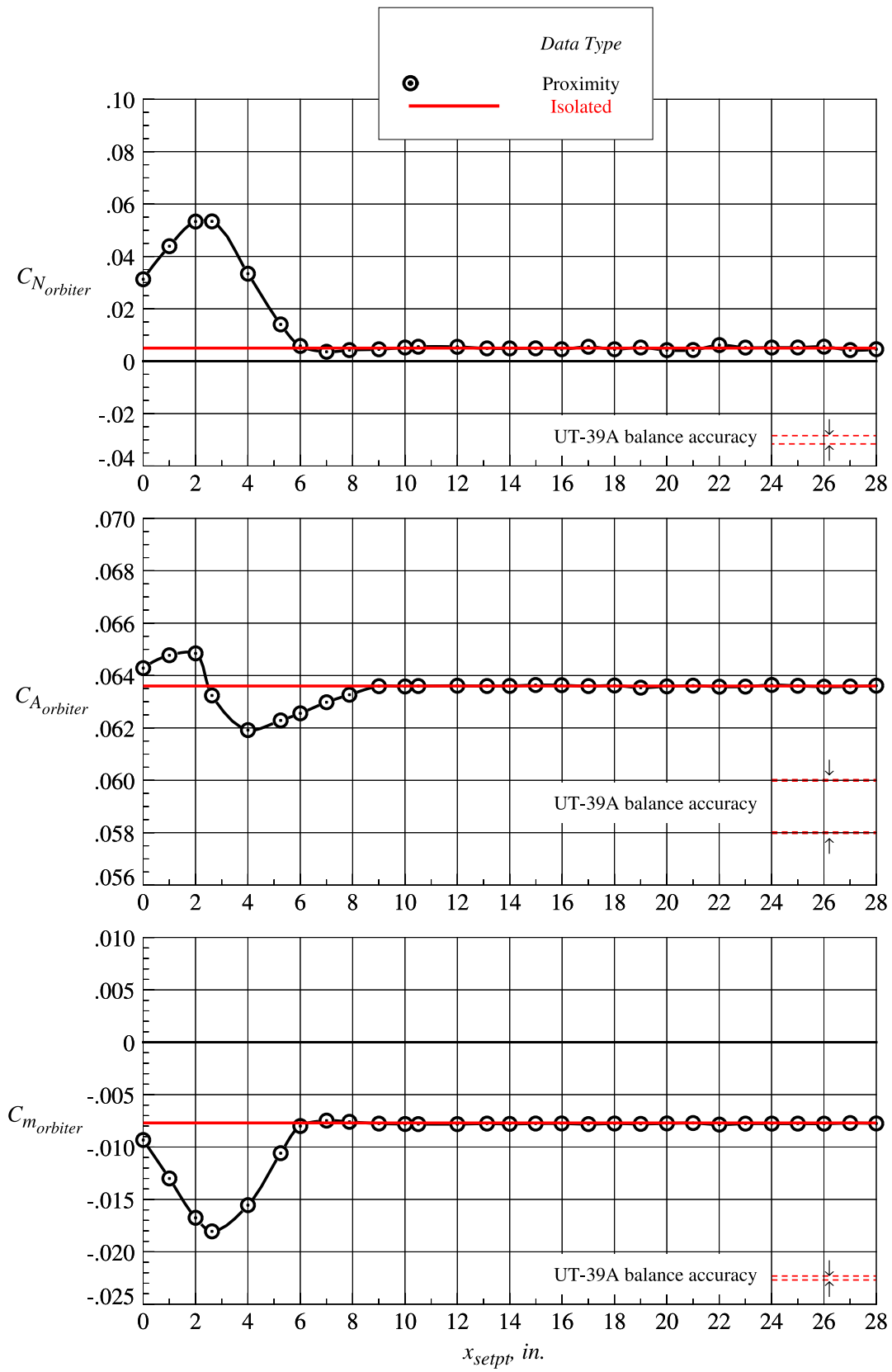
Figure 56. Continued.





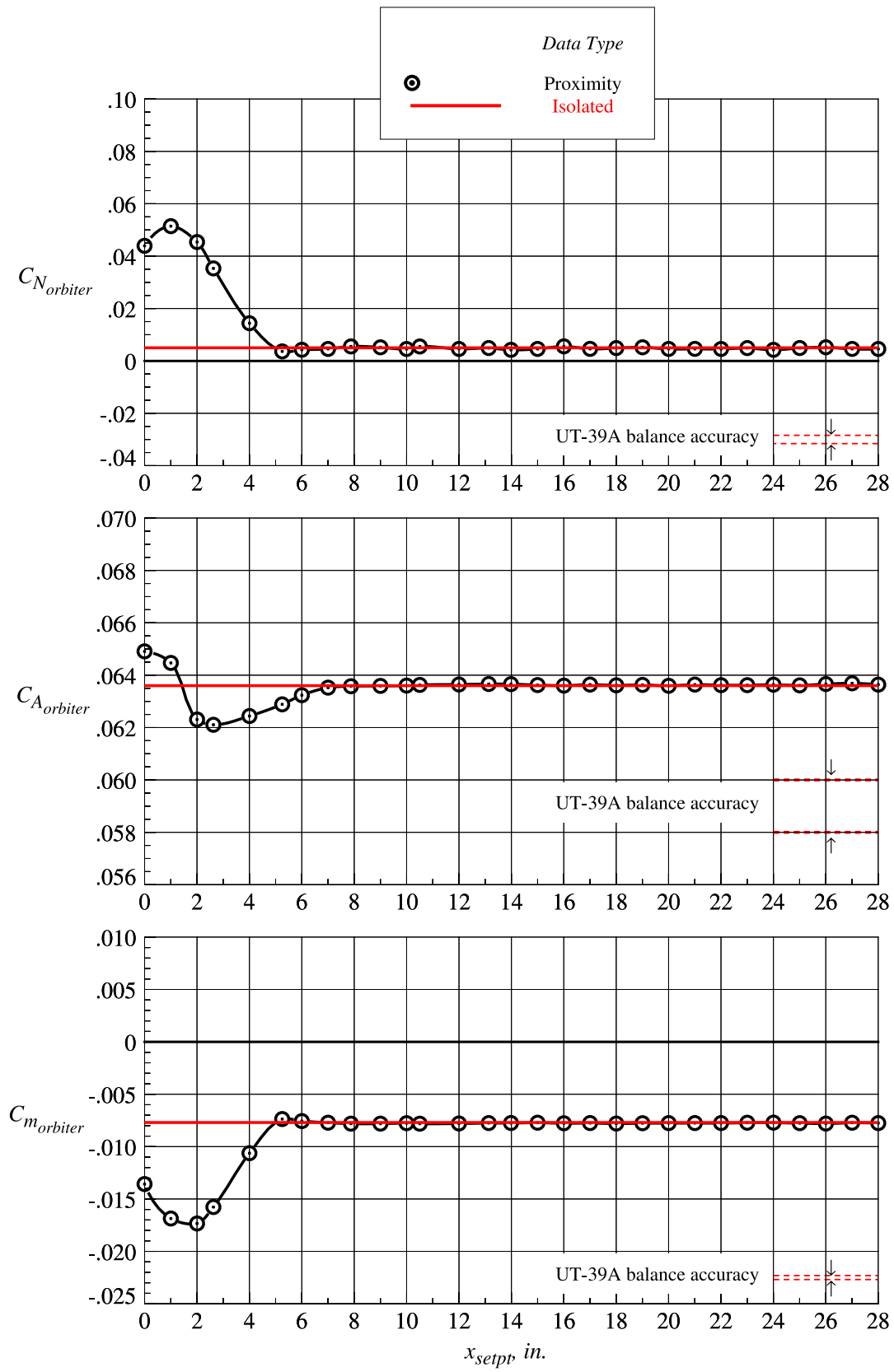
(e)  $z_{setpt} = 2.625$  in.

Figure 56. Continued.



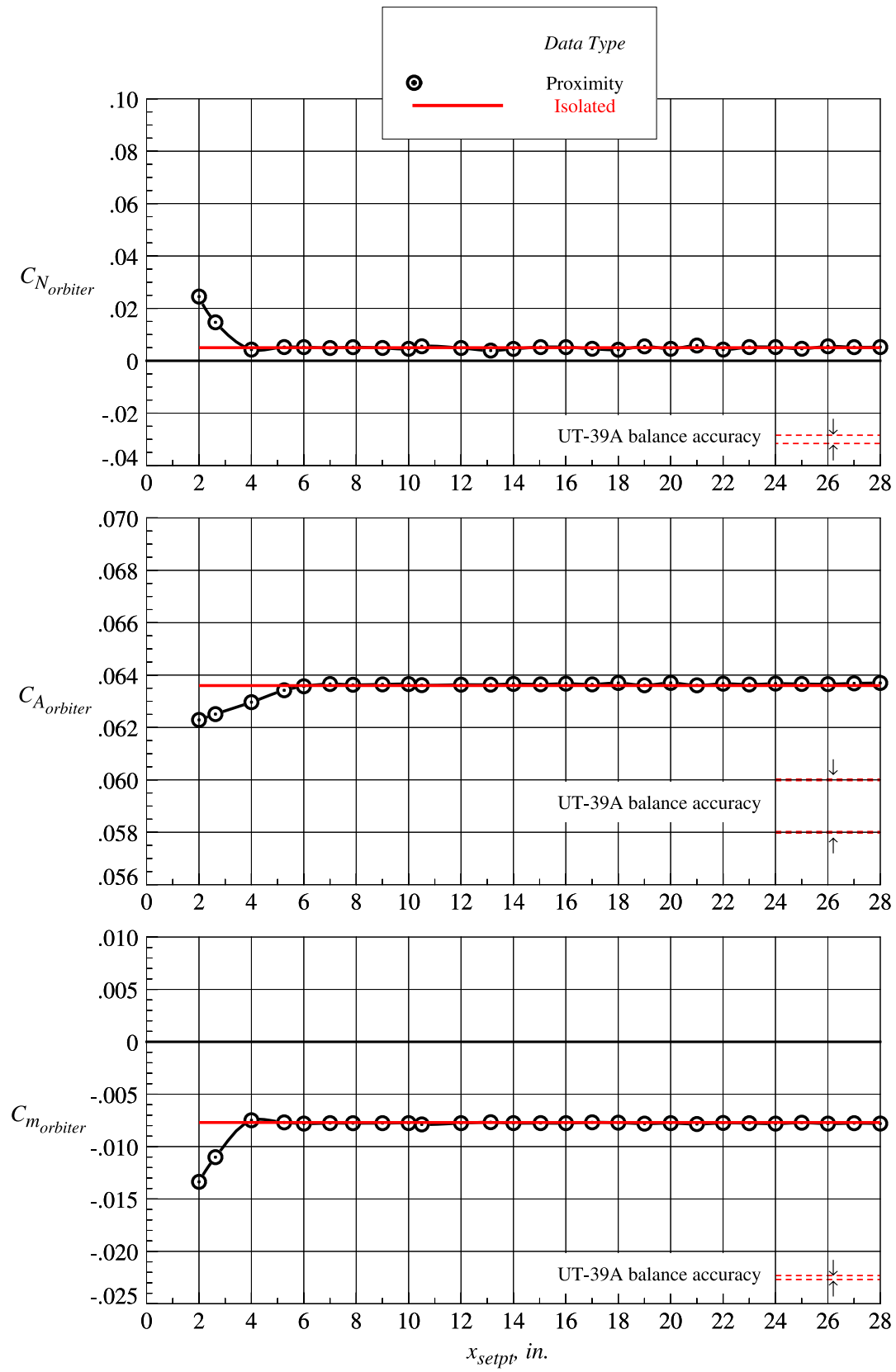
(f)  $z_{setpt} = 3.281 \text{ in.}$

Figure 56. Continued.



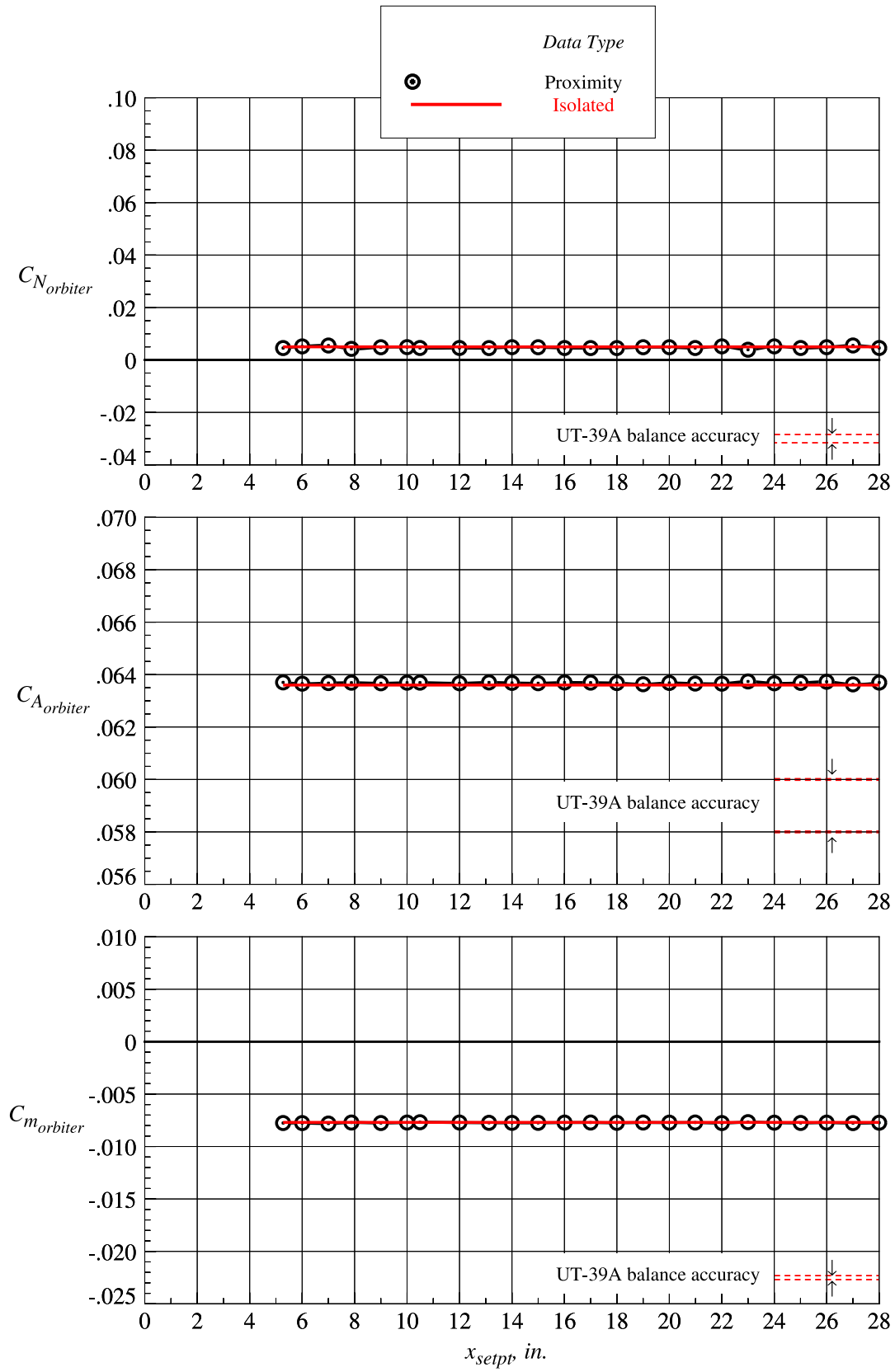
(g)  $z_{setpt} = 3.938$  in.

Figure 56. Continued.



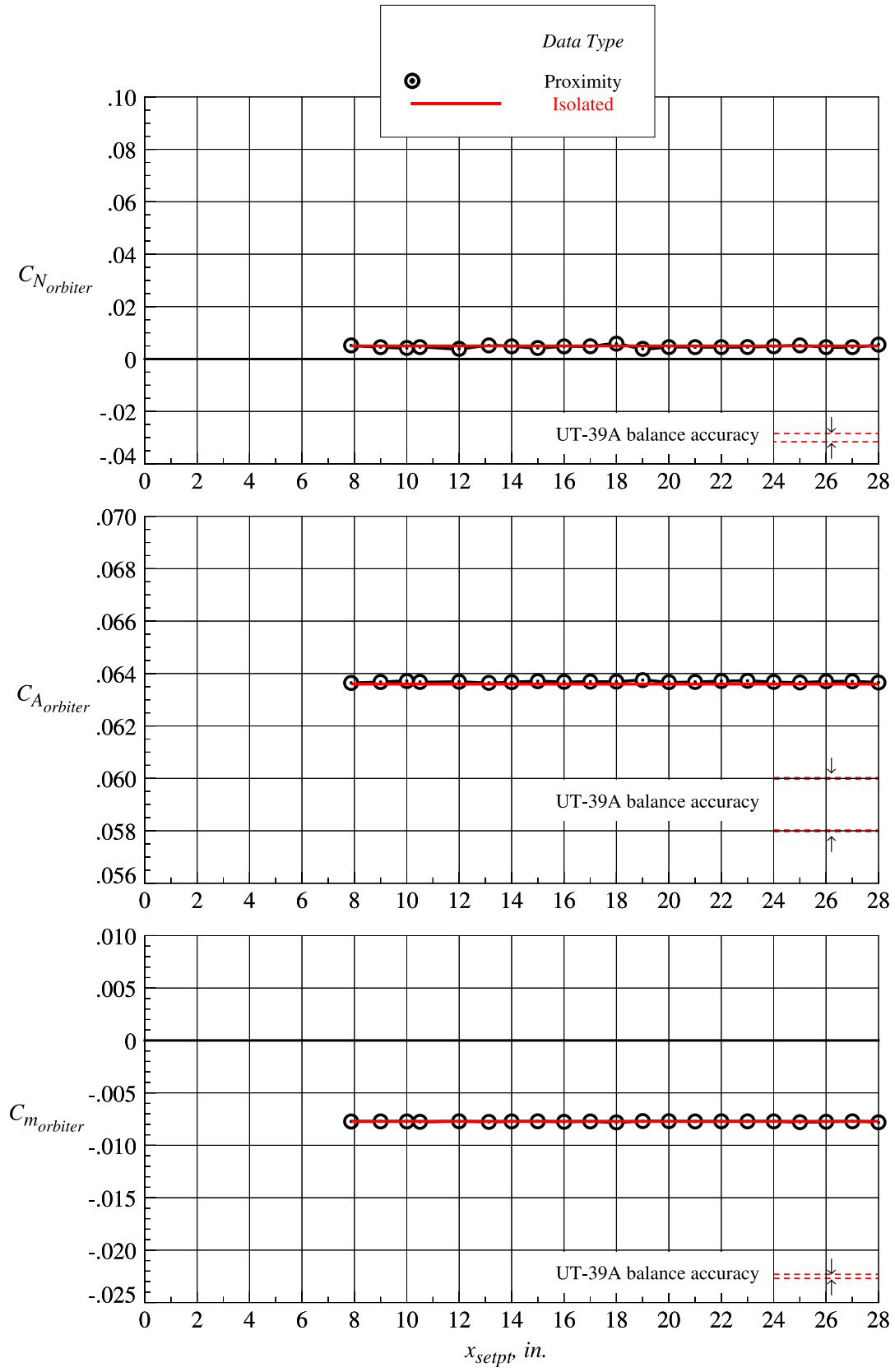
(h)  $z_{setpt} = 4.594$  in.

Figure 56. Continued.



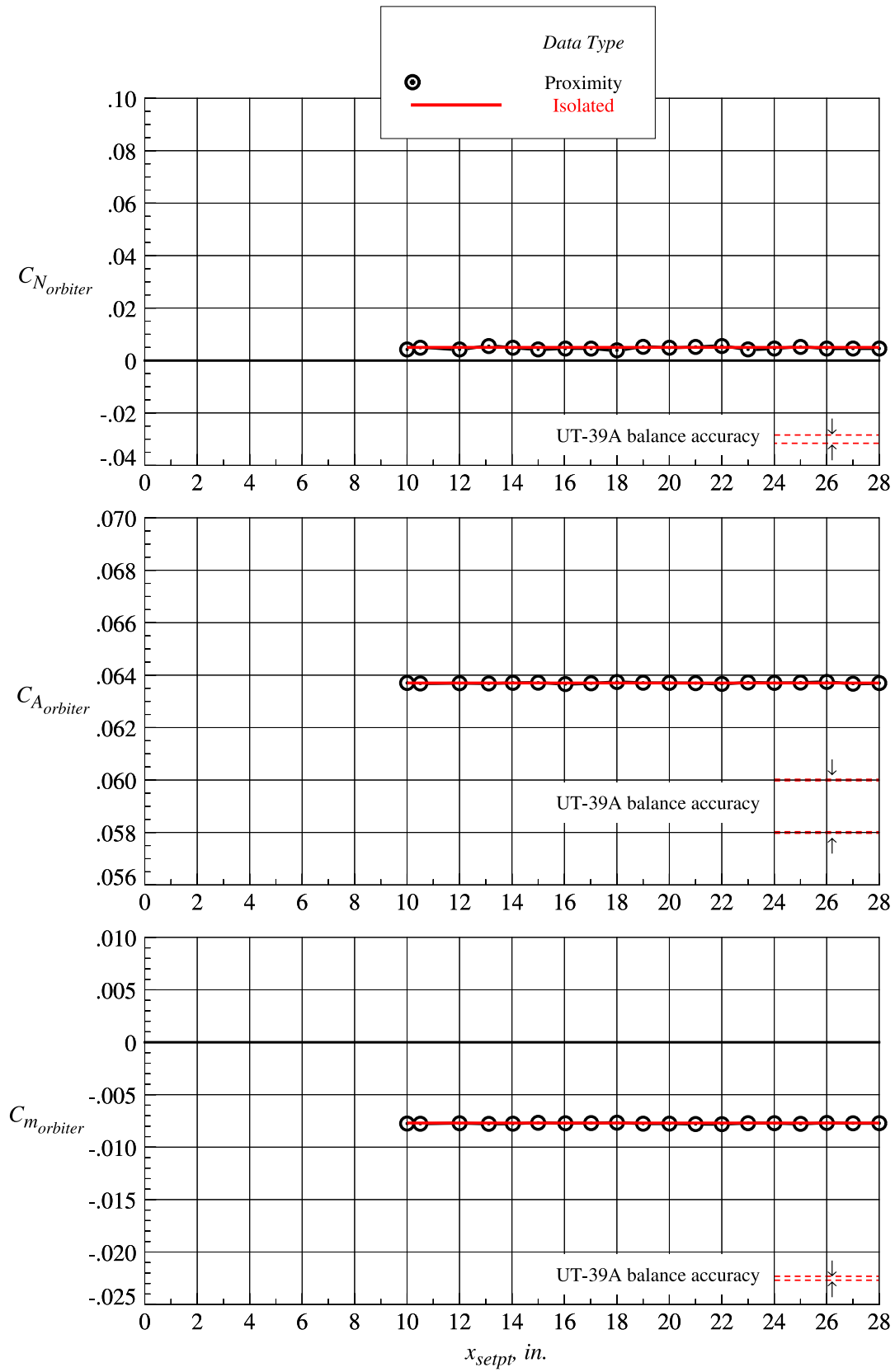
(i)  $z_{setpt} = 5.250$  in.

Figure 56. Continued.



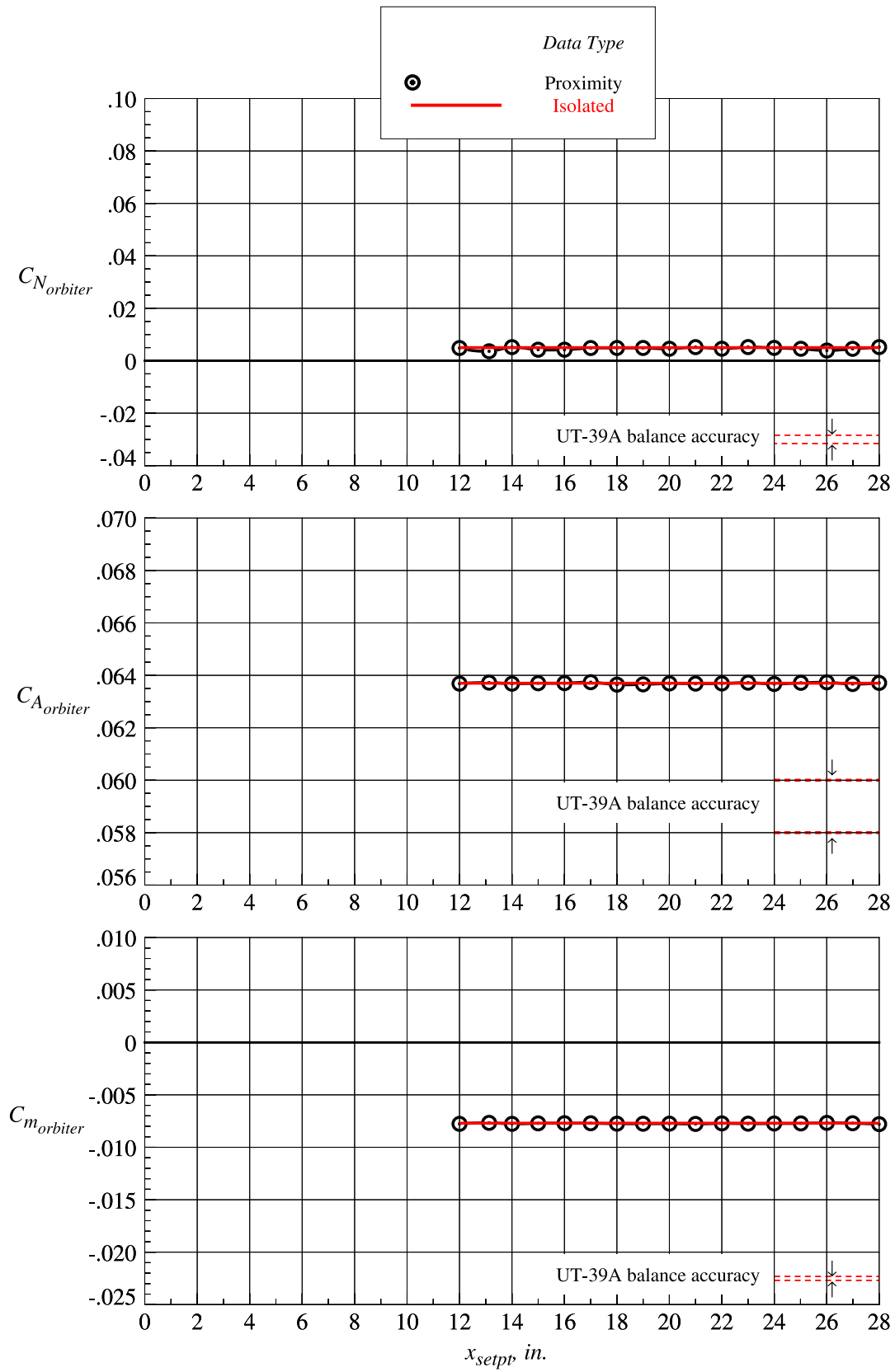
(j)  $z_{setpt} = 6.583$  in.

Figure 56. Continued.



(k)  $z_{setpt} = 7.875$  in.

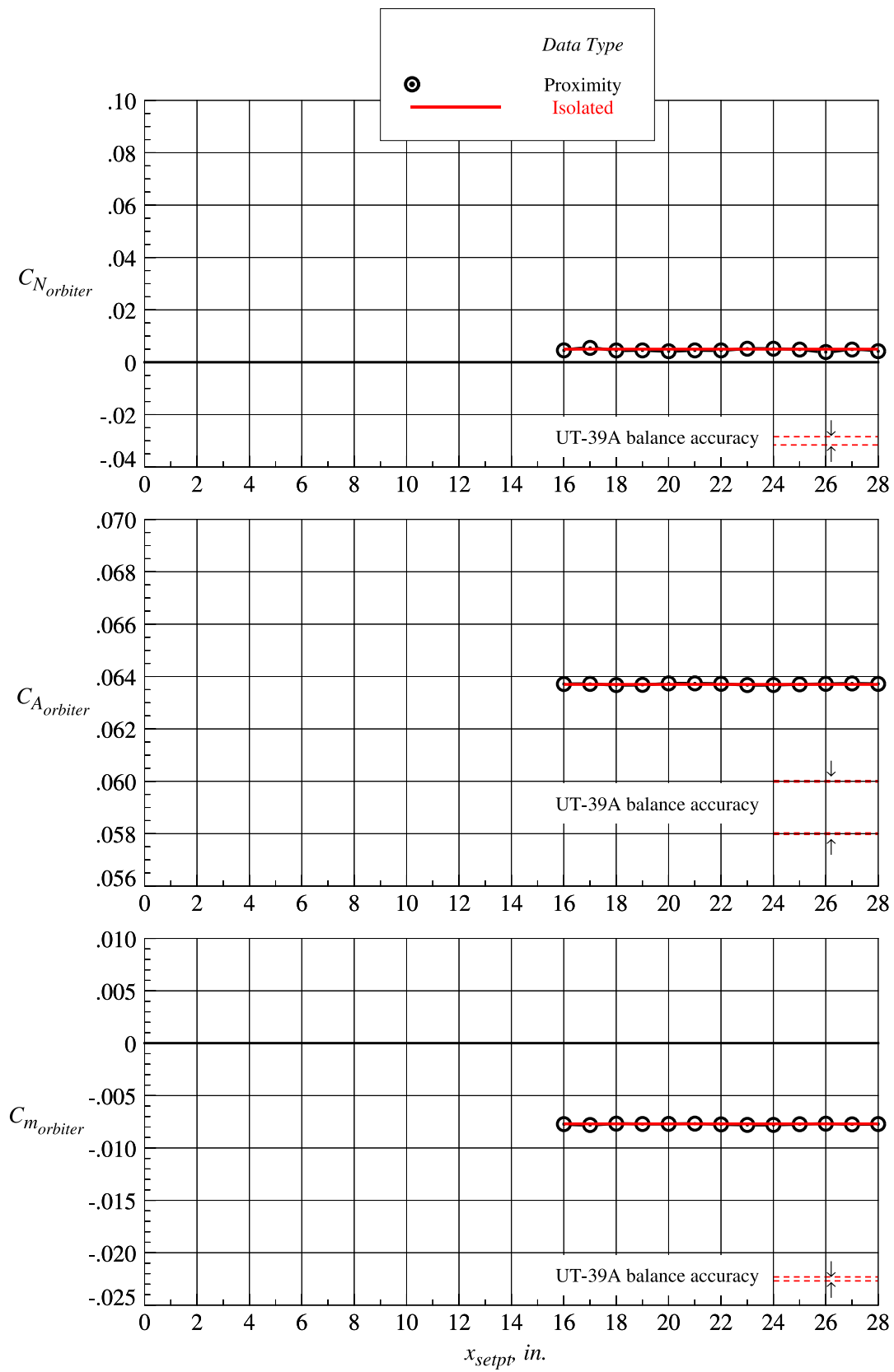
Figure 56. Continued.



(l)  $z_{setpt} = 9.188$  in.

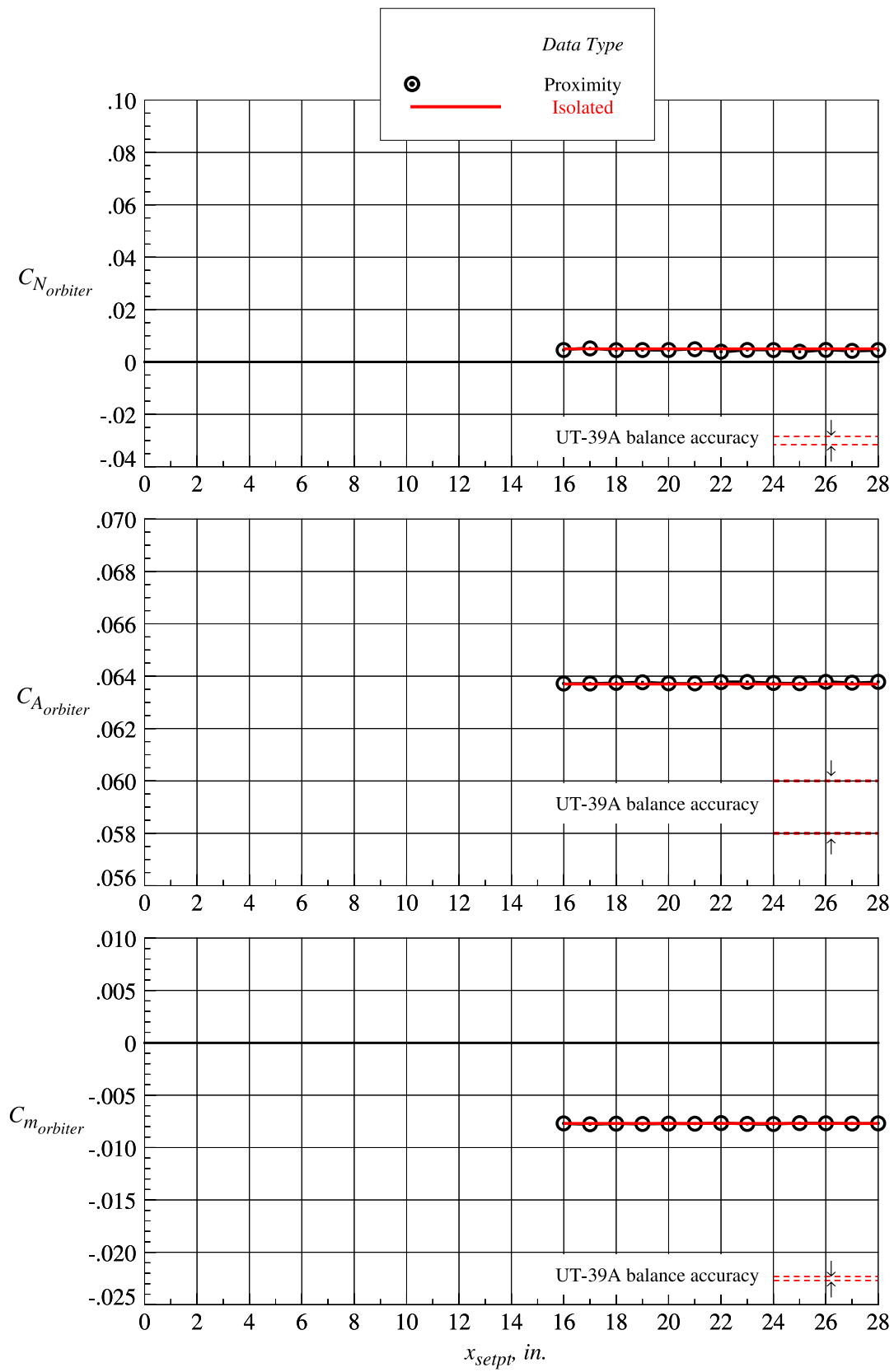
Figure 56. Continued.





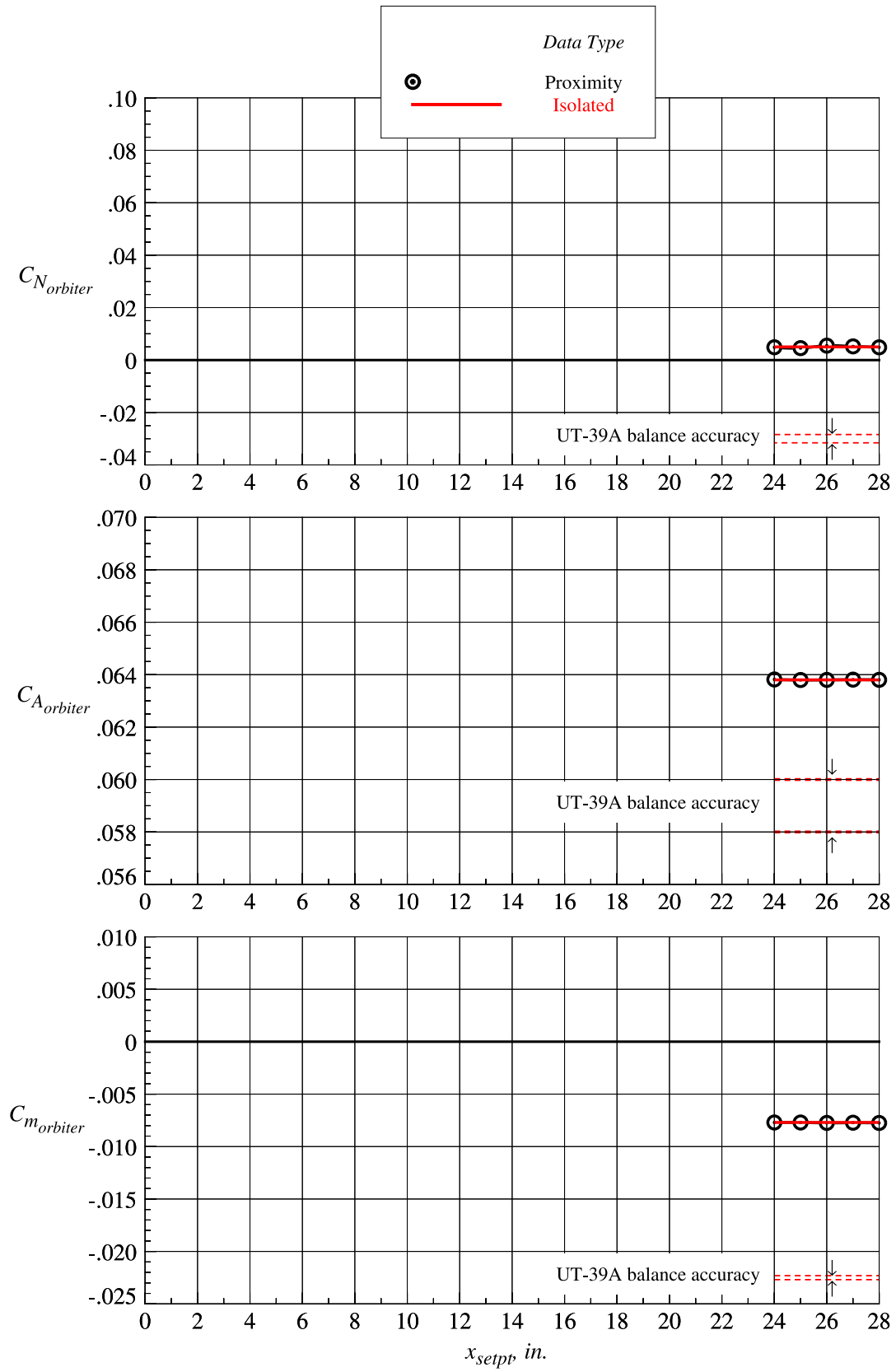
(m)  $z_{setpt} = 10.500$  in.

Figure 56. Continued.



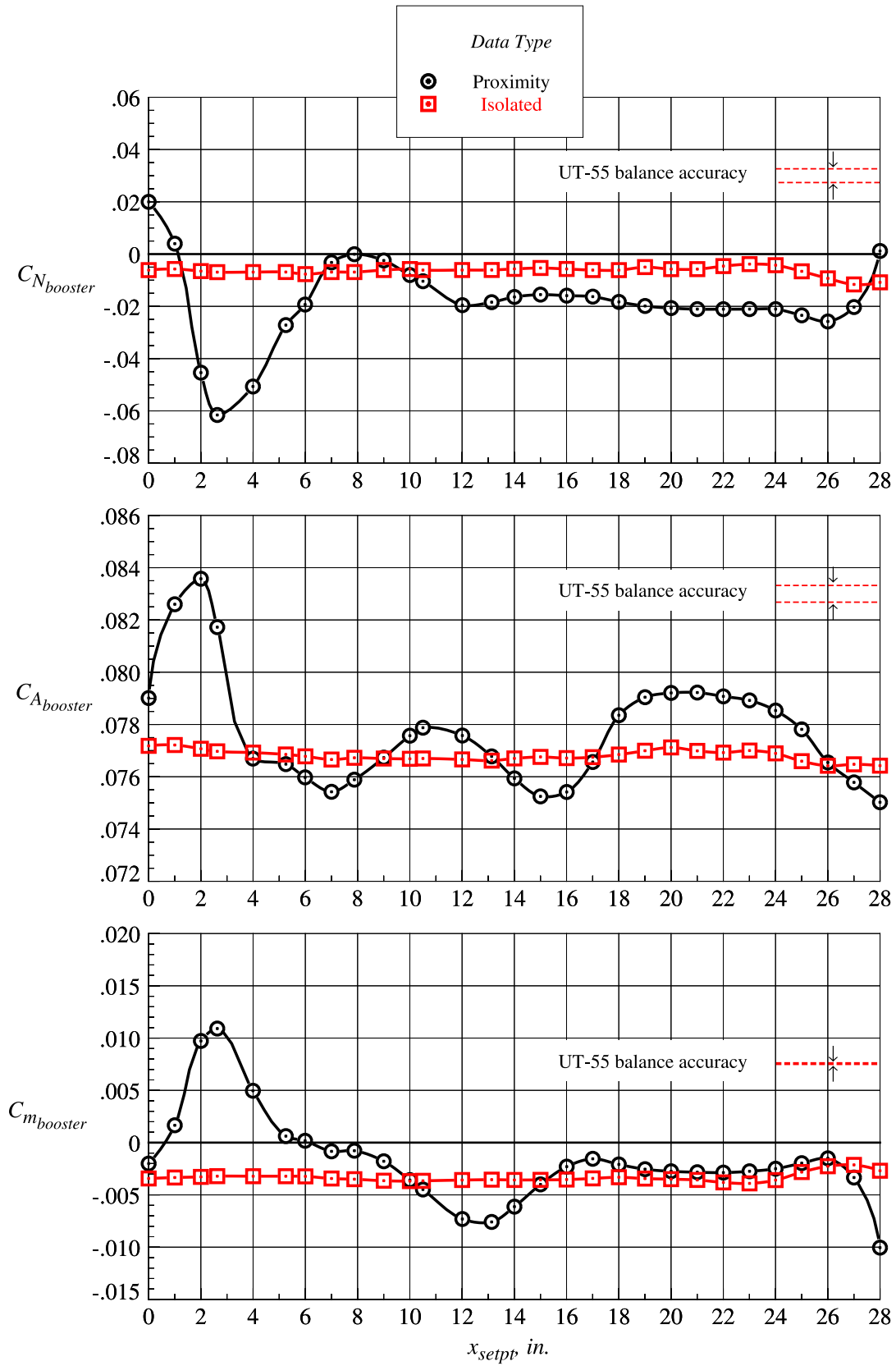
(n)  $z_{setpt} = 11.810$  in.

Figure 56. Continued.



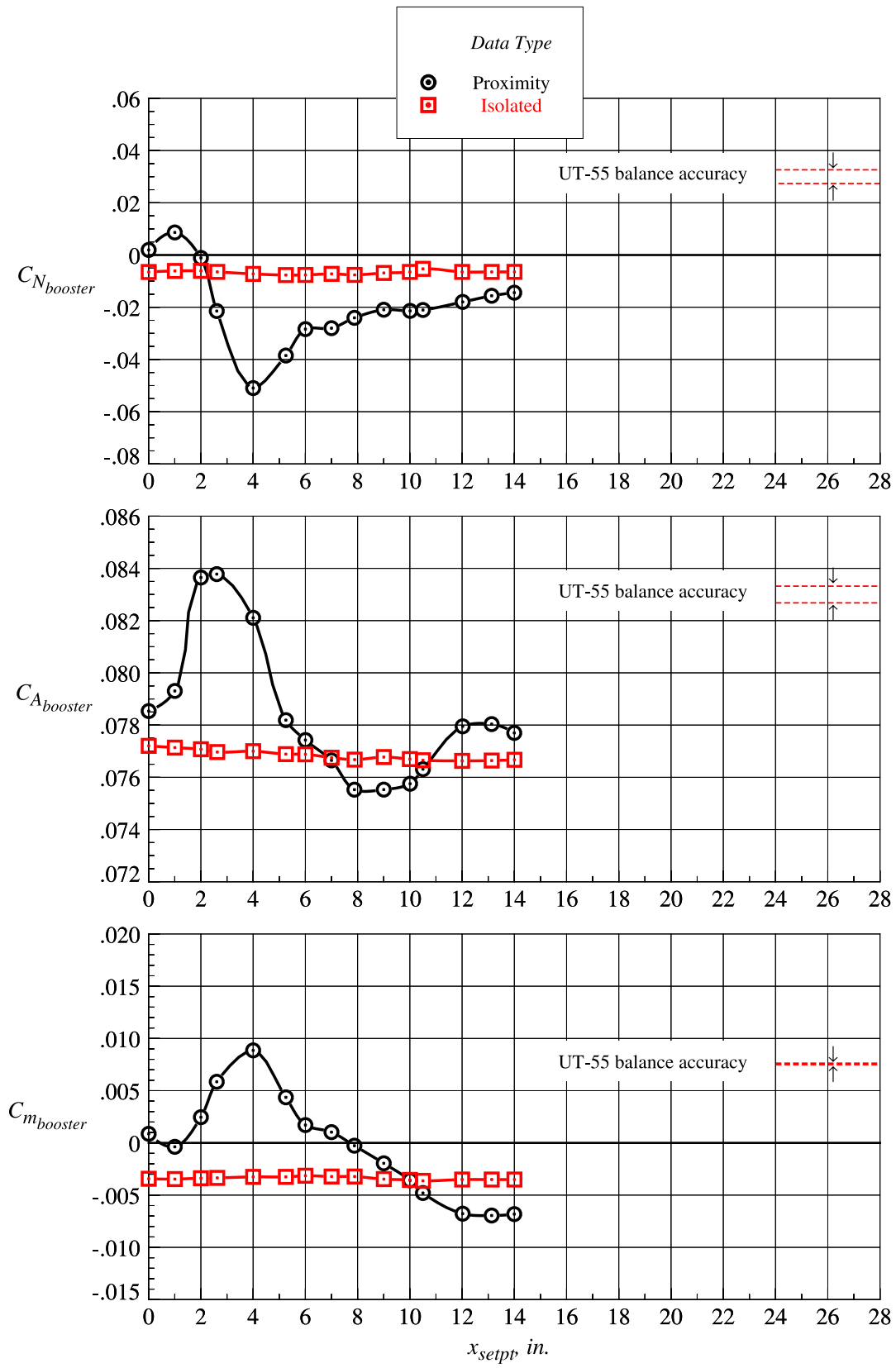
(o)  $z_{setpt} = 13.130$  in.

Figure 56. Concluded.



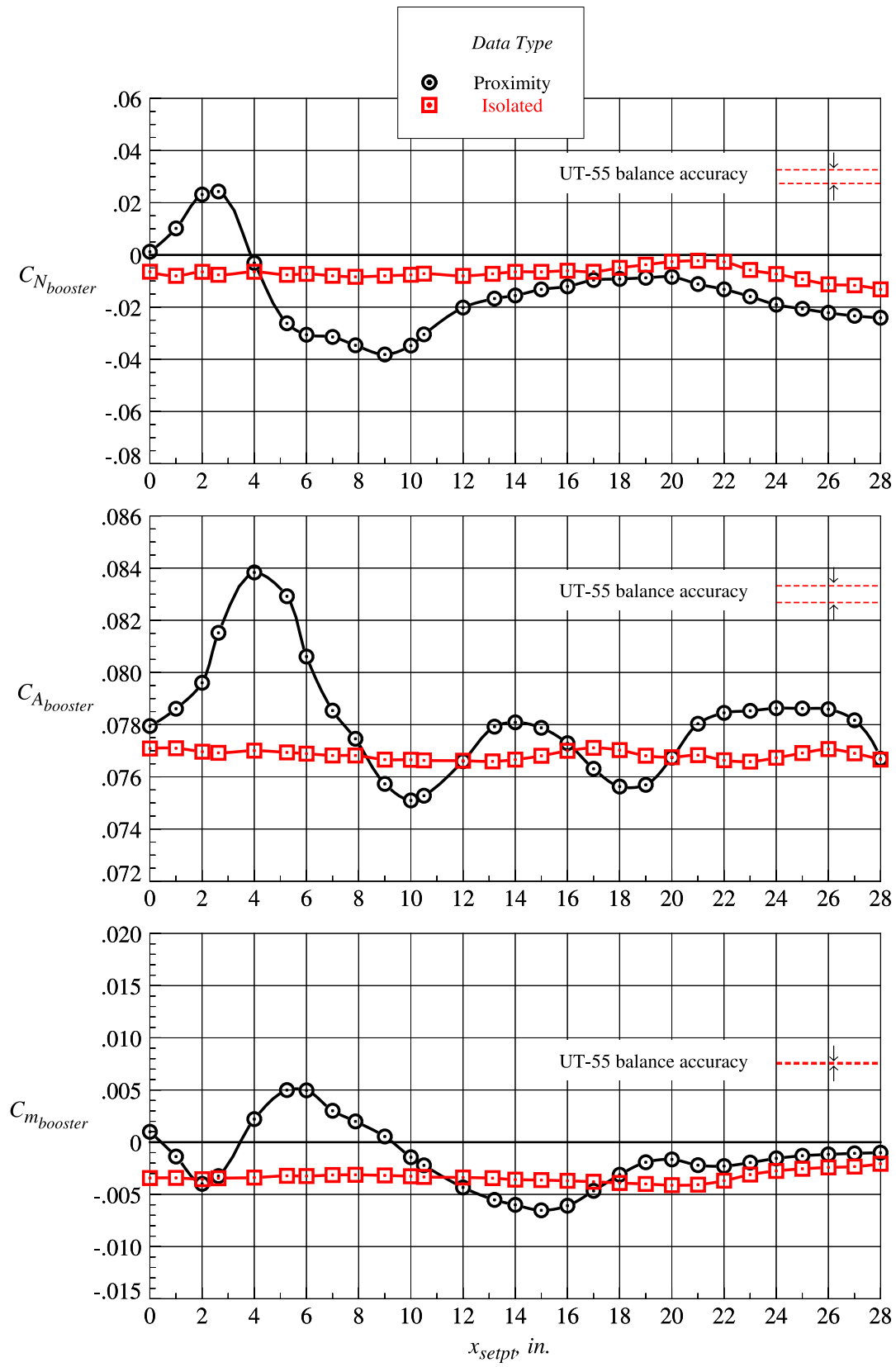
(a)  $z_{setpt} = 0$  in.

Figure 57. Booster proximity and isolated aerodynamic characteristics at Mach = 2.3 and  $\Delta\alpha = 0^\circ$ .



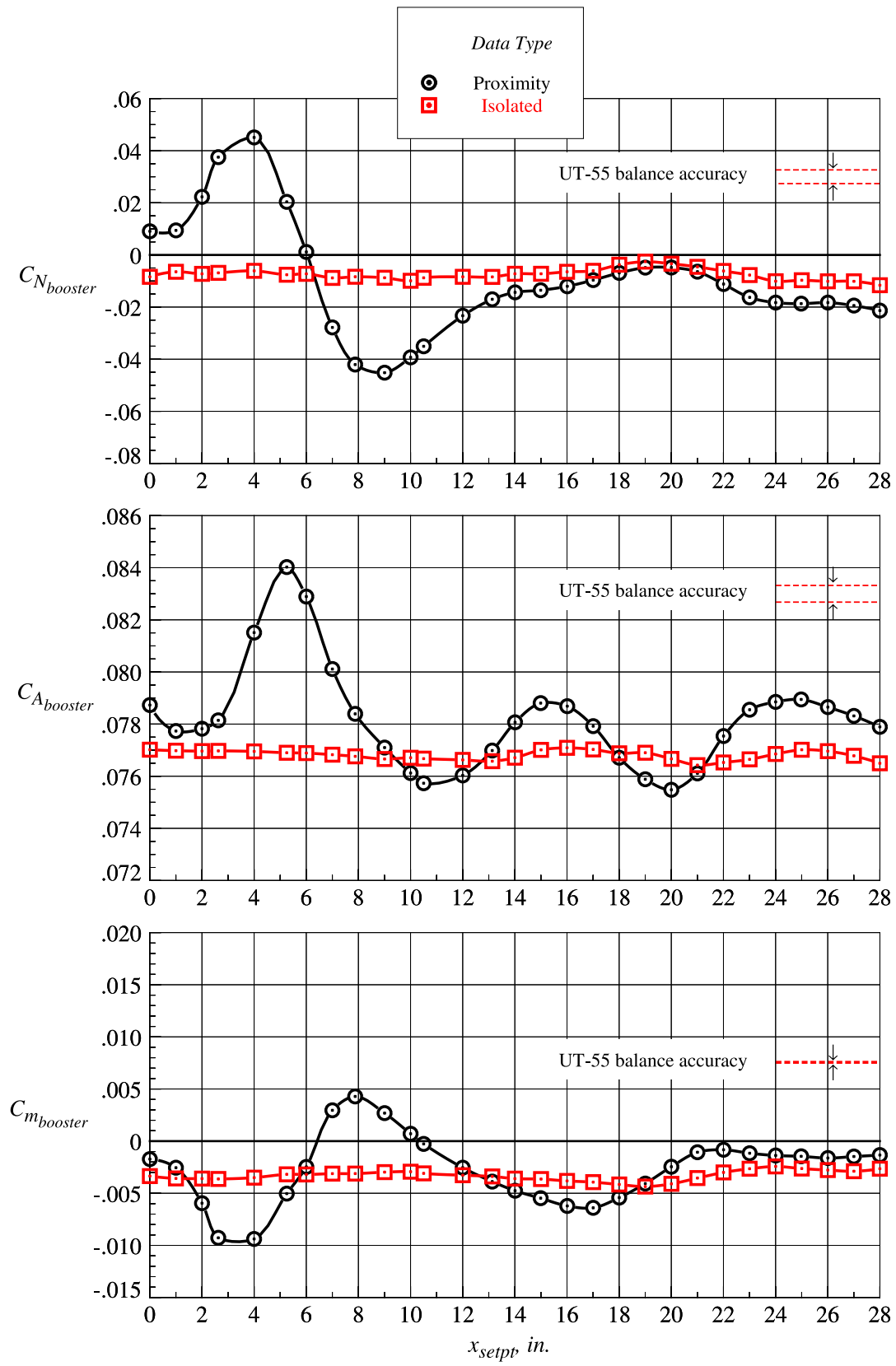
(b)  $z_{setpt} = 0.656$  in.

Figure 57. Continued.



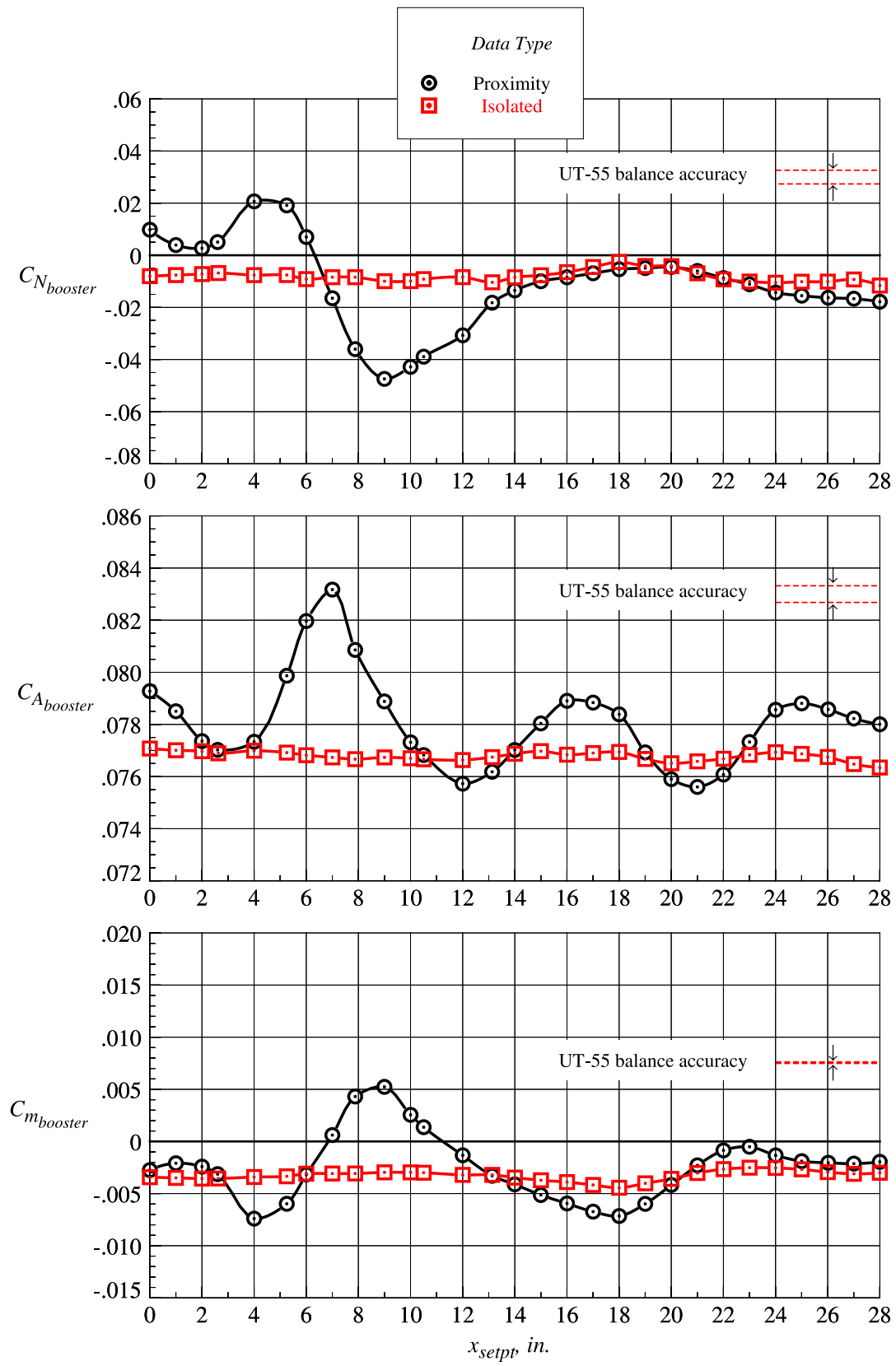
(c)  $z_{setpt} = 1.313$  in.

Figure 57. Continued.



(d)  $z_{setpt} = 1.969$  in.

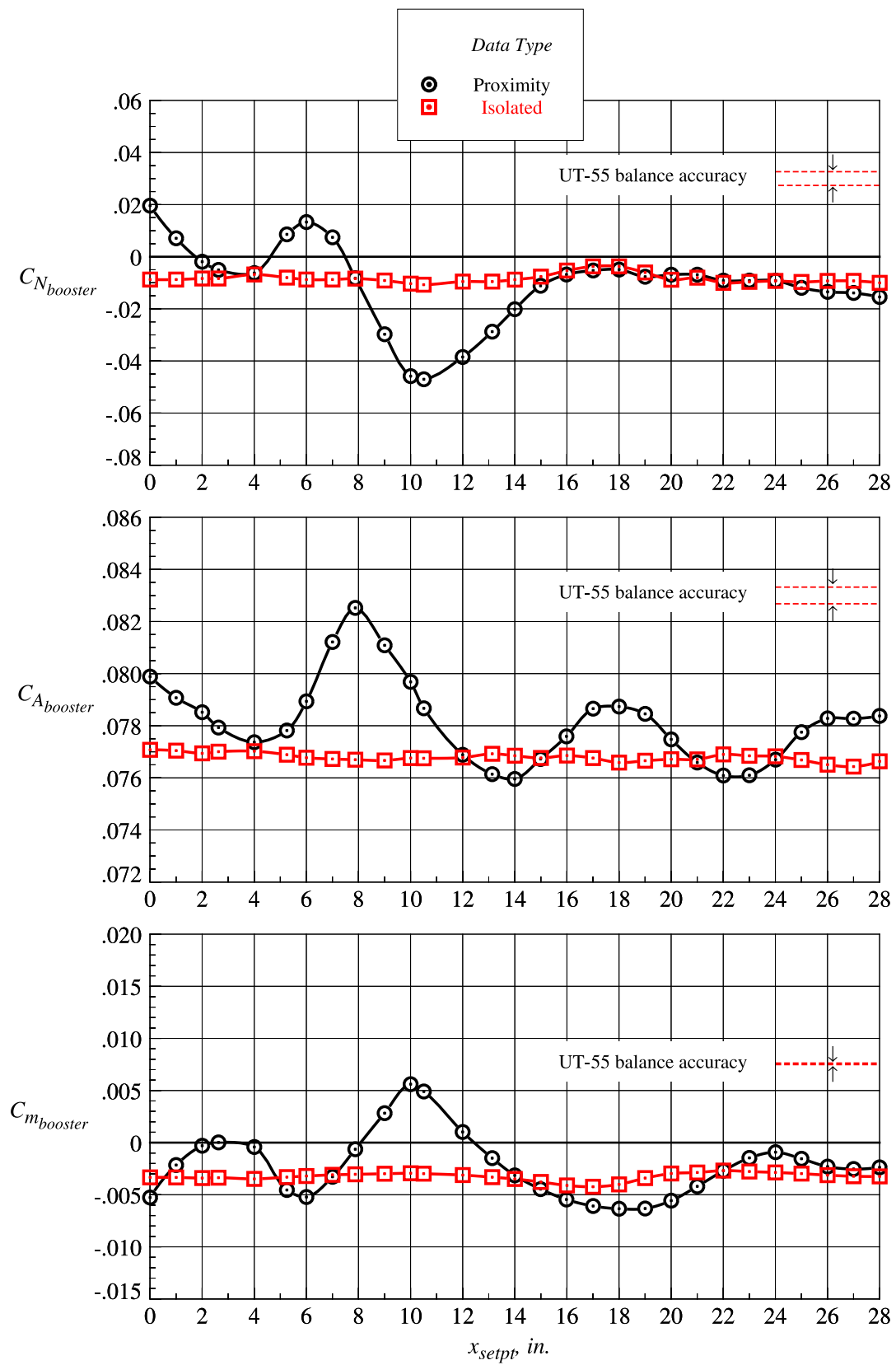
Figure 57. Continued.



(e)  $z_{setpt} = 2.625$  in.

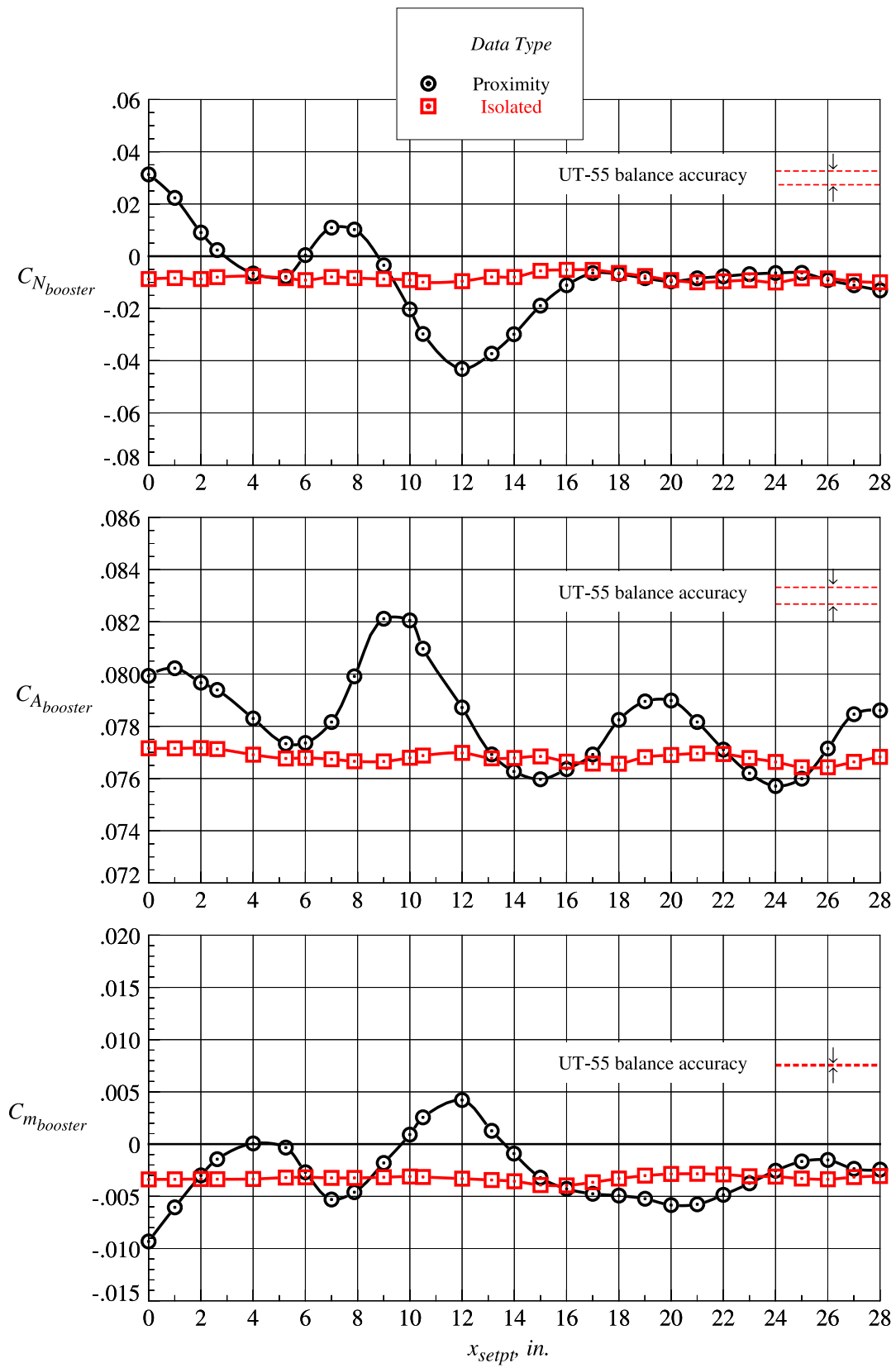
Figure 57. Continued.





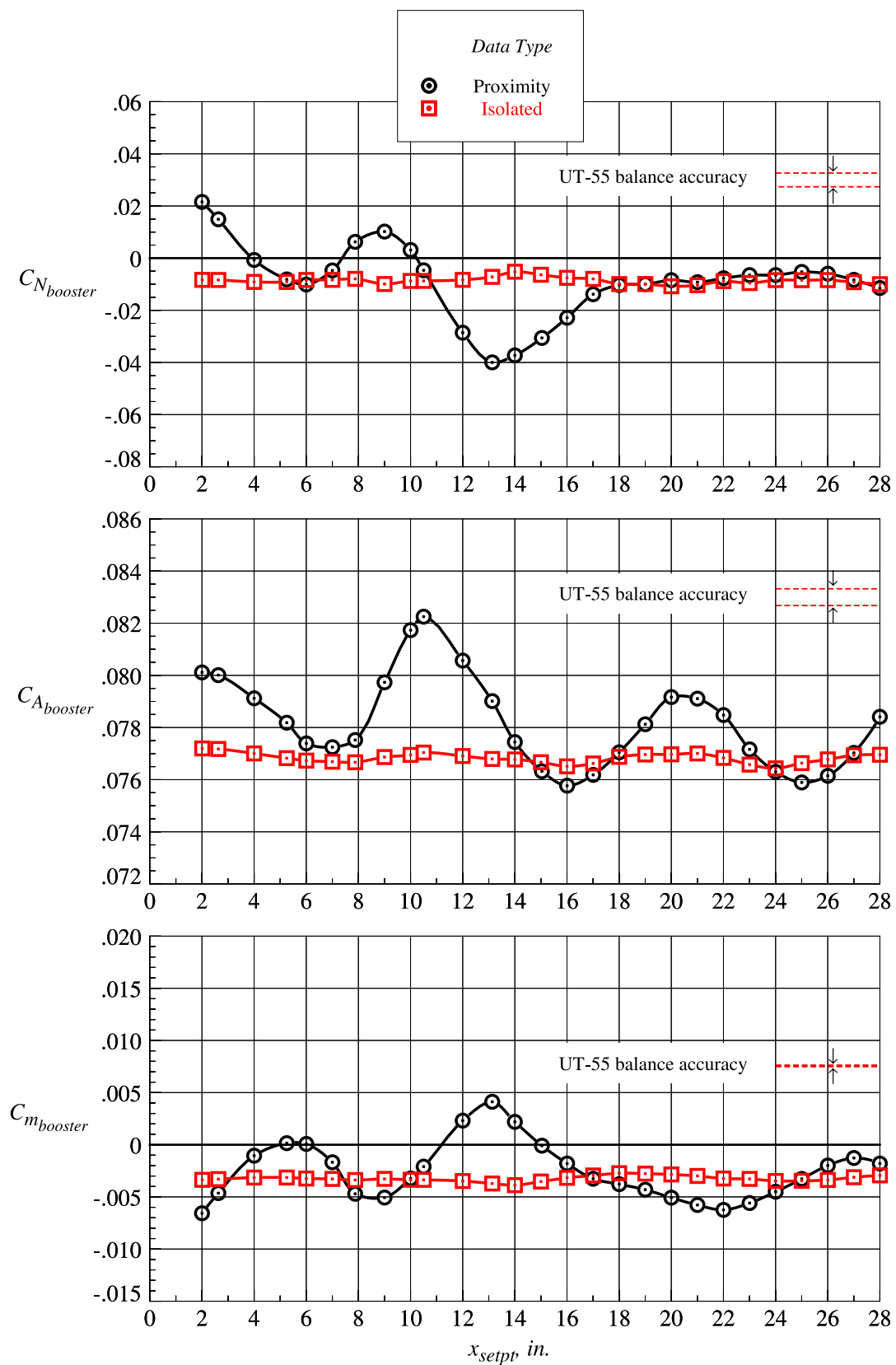
(f)  $z_{setpt} = 3.281$  in.

Figure 57. Continued.



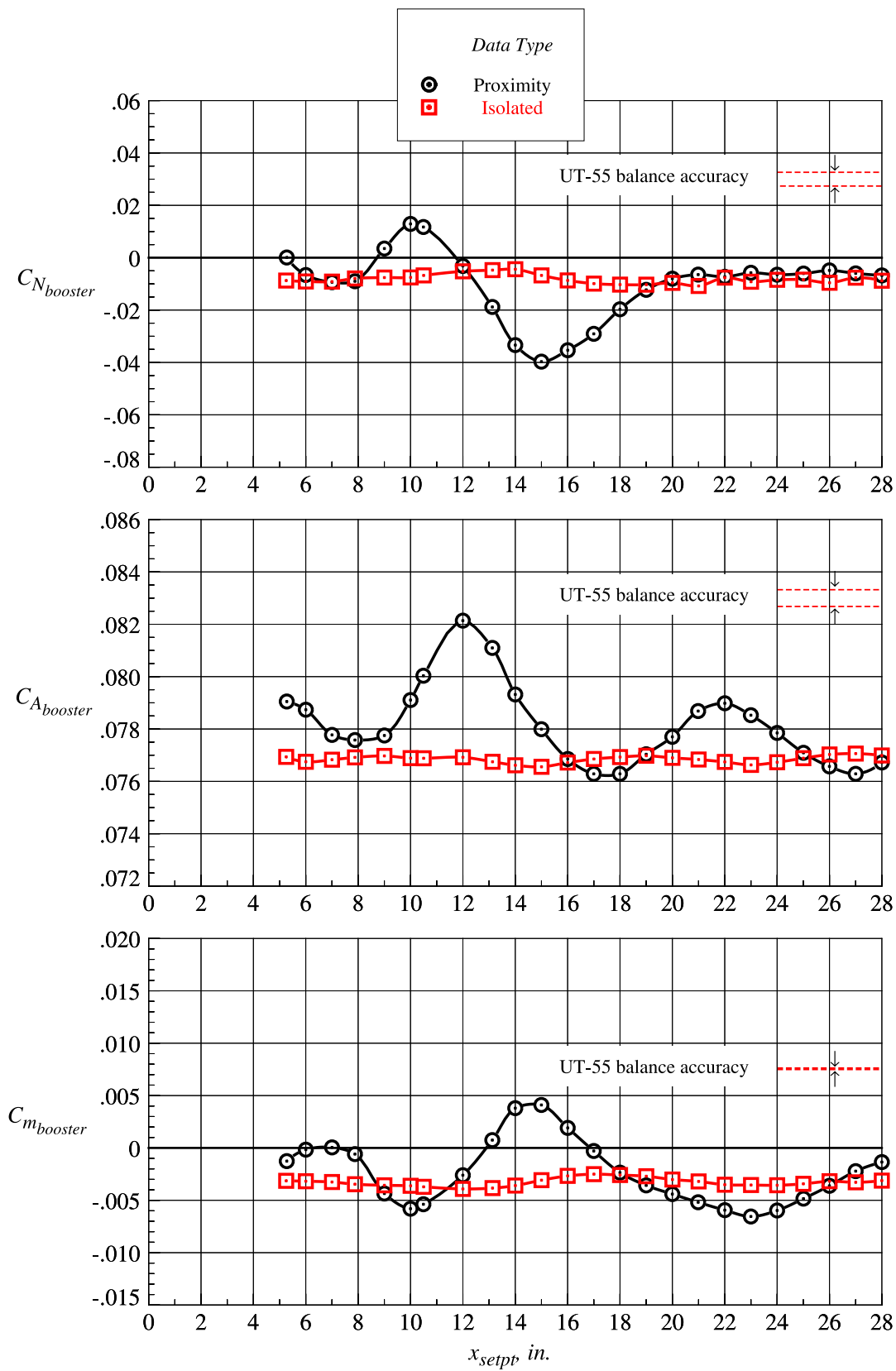
(g)  $z_{setpt} = 3.938$  in.

Figure 57. Continued.



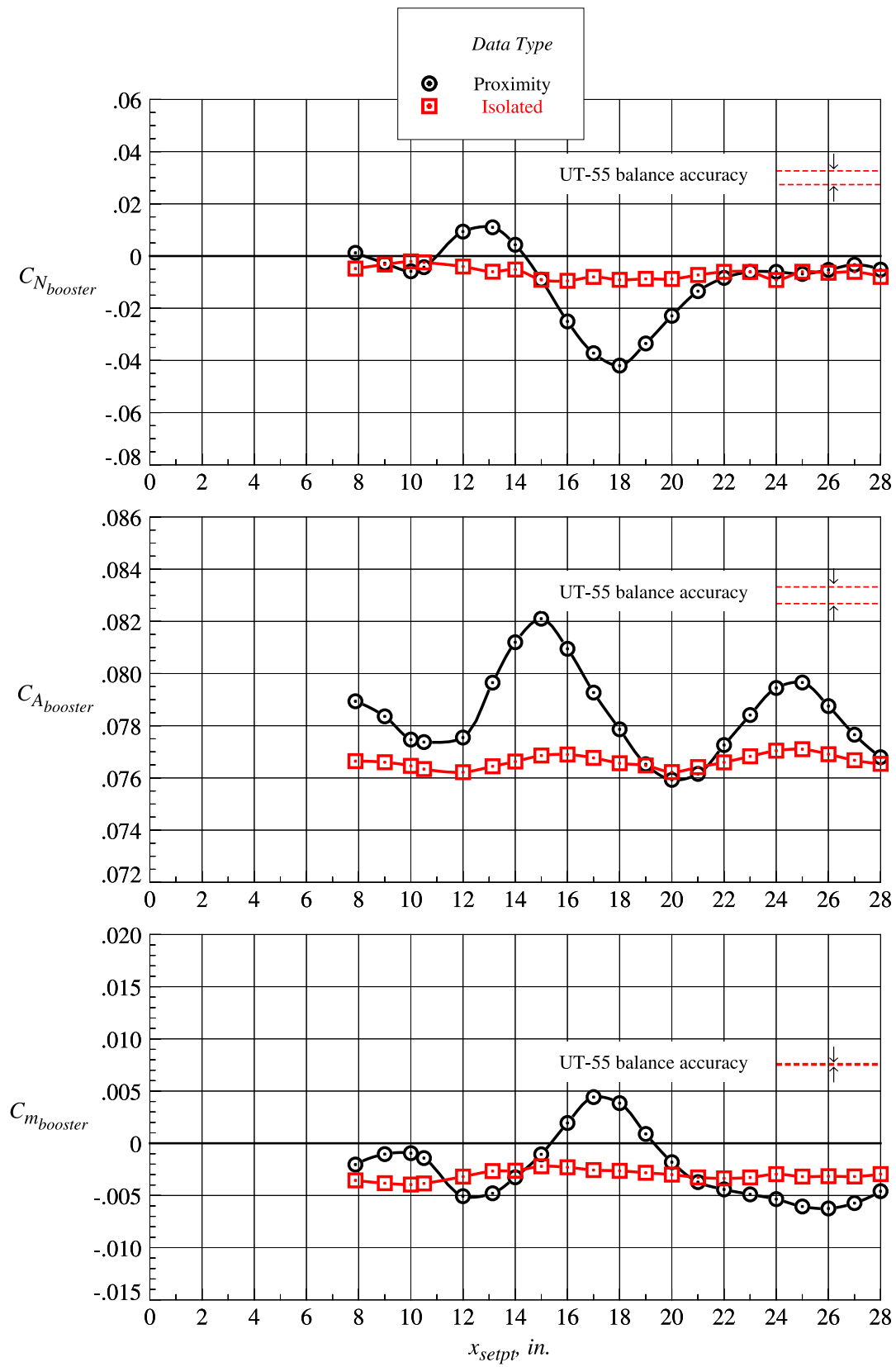
(h)  $z_{setpt} = 4.594$  in.

Figure 57. Continued.



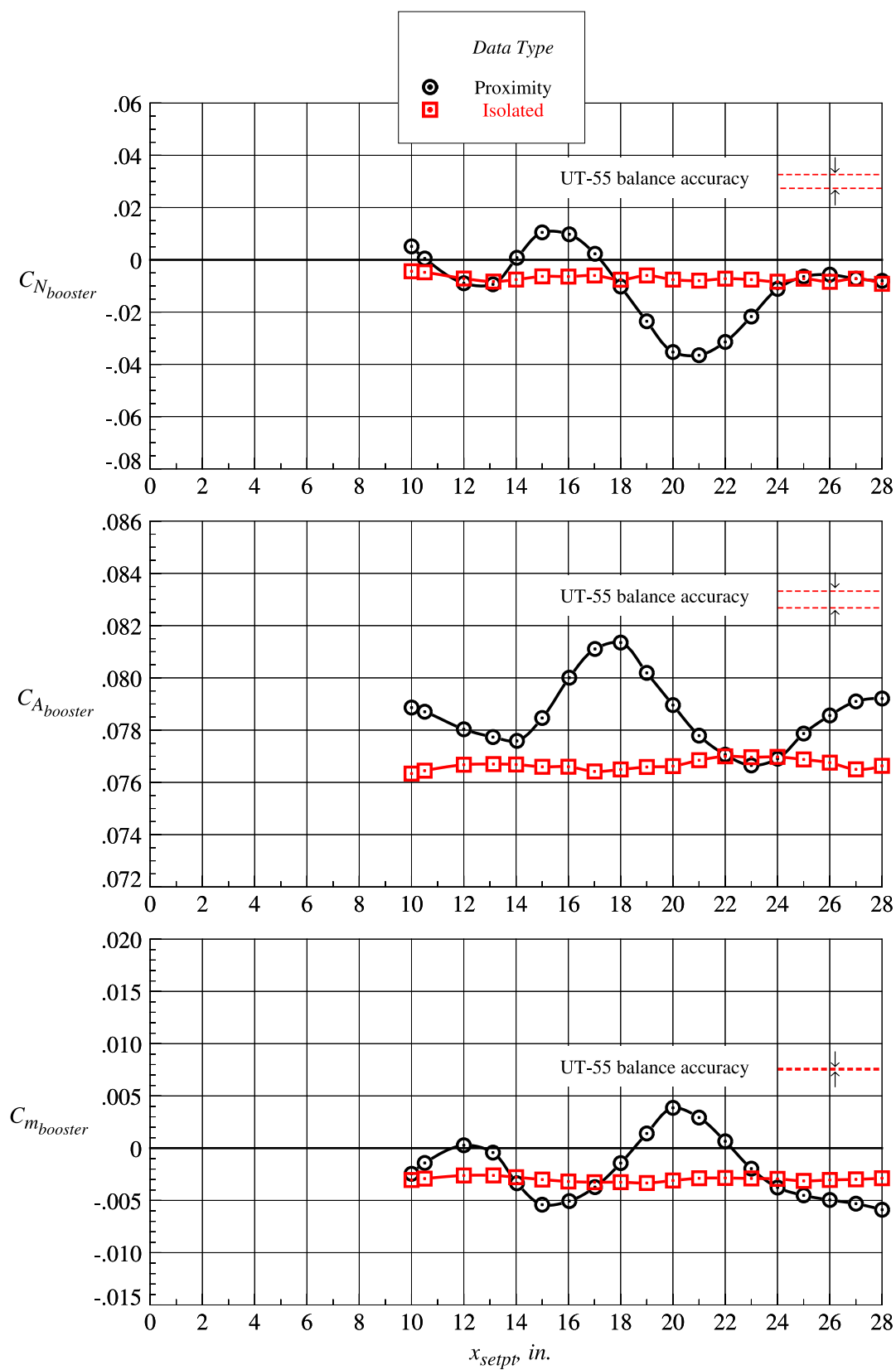
(i)  $z_{setpt} = 5.250$  in.

Figure 57. Continued.



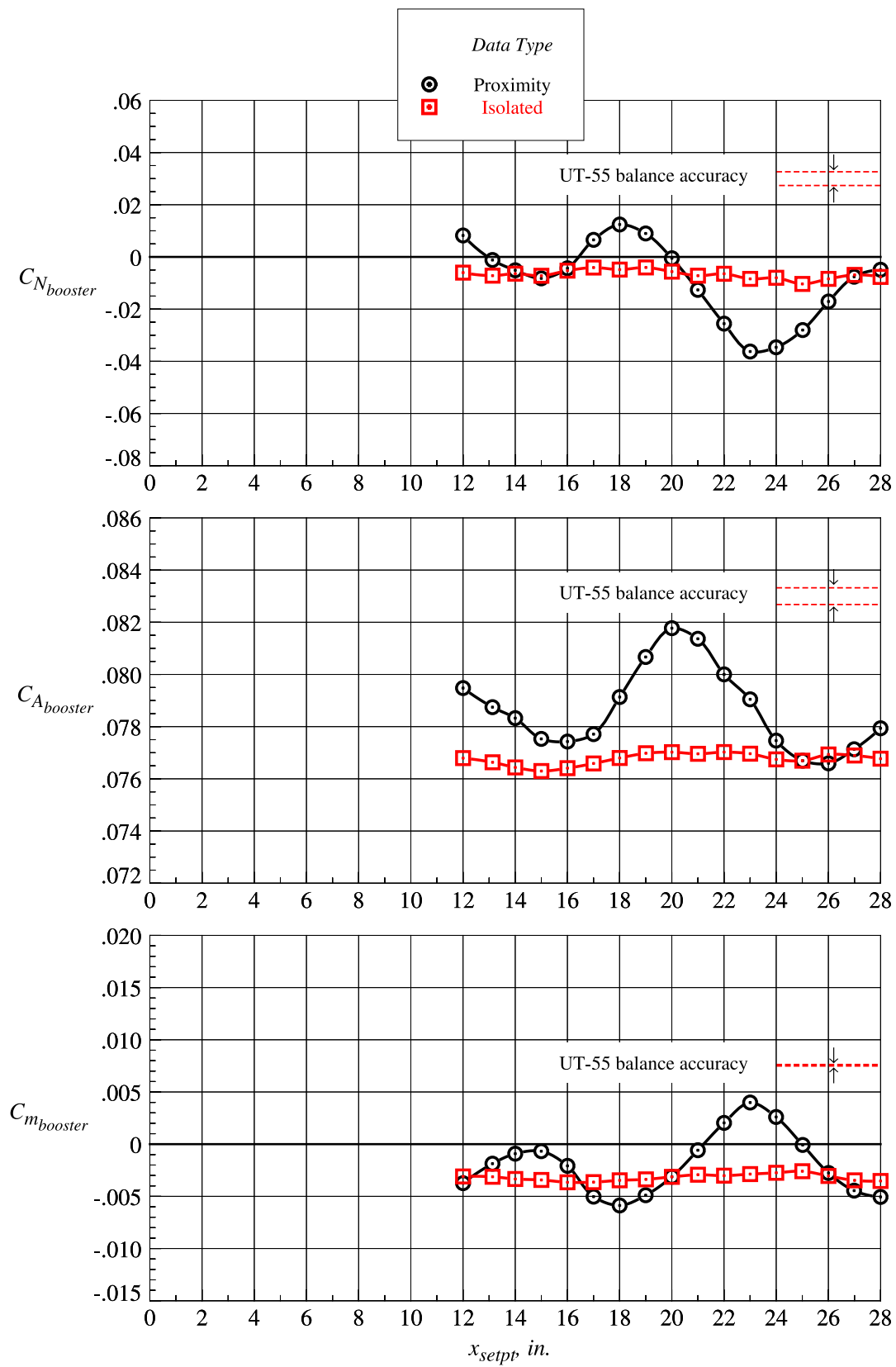
(j)  $z_{setpt} = 6.583$  in.

Figure 57. Continued.



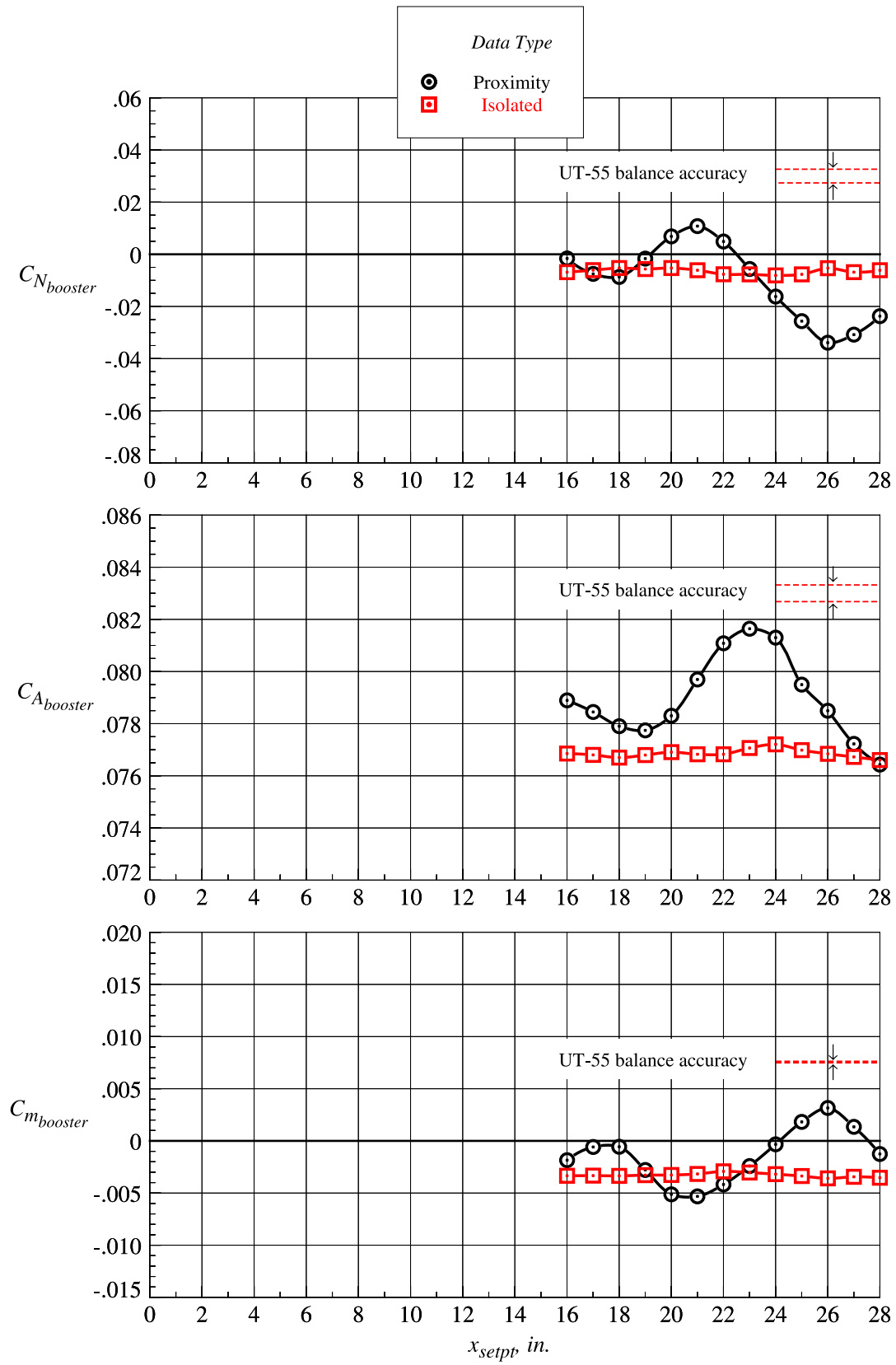
(k)  $z_{setpt} = 7.875$  in.

Figure 57. Continued.



(l)  $z_{setpt} = 9.188$  in.

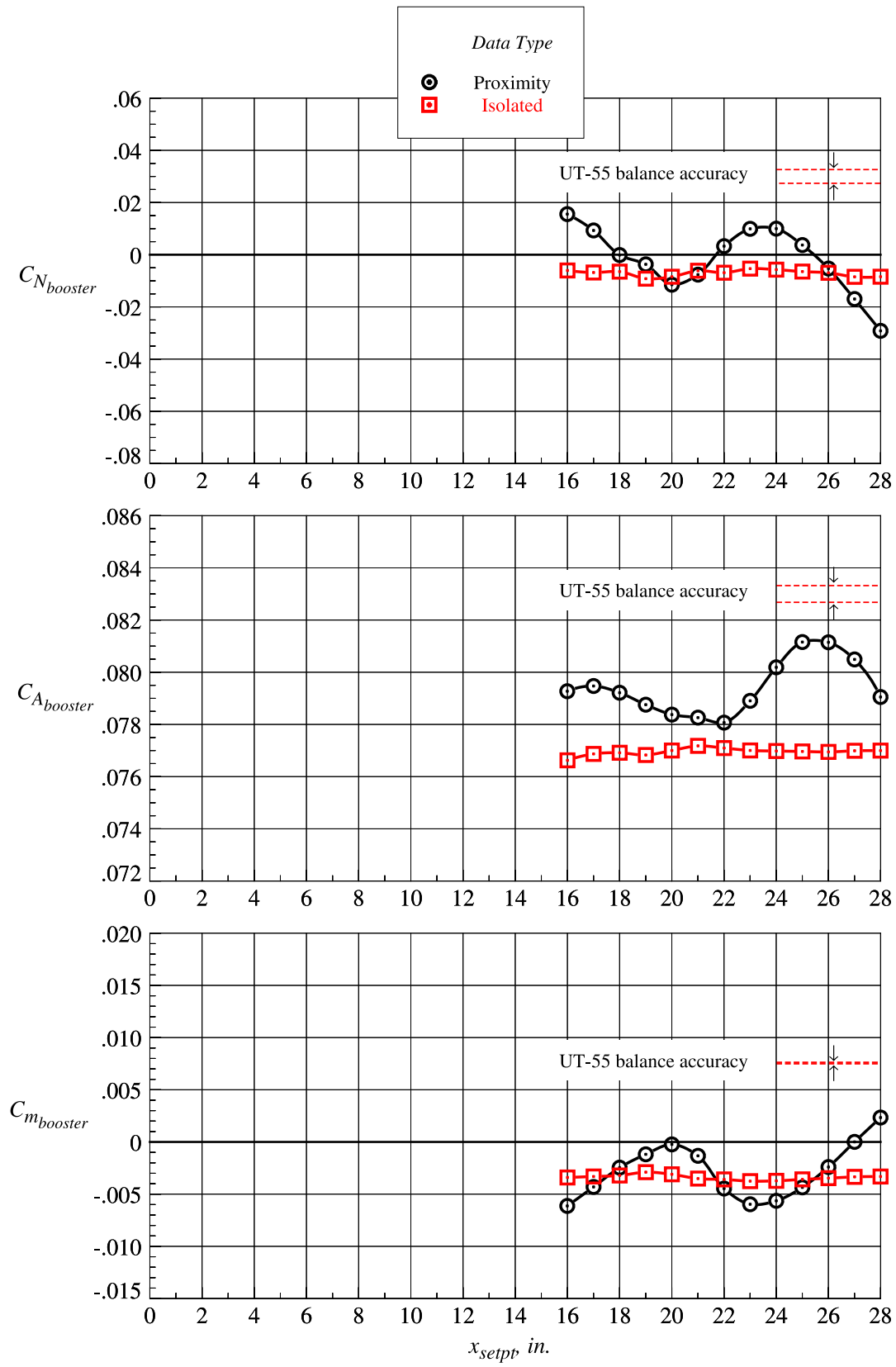
Figure 57. Continued.



(m)  $z_{setpt} = 10.500$  in.

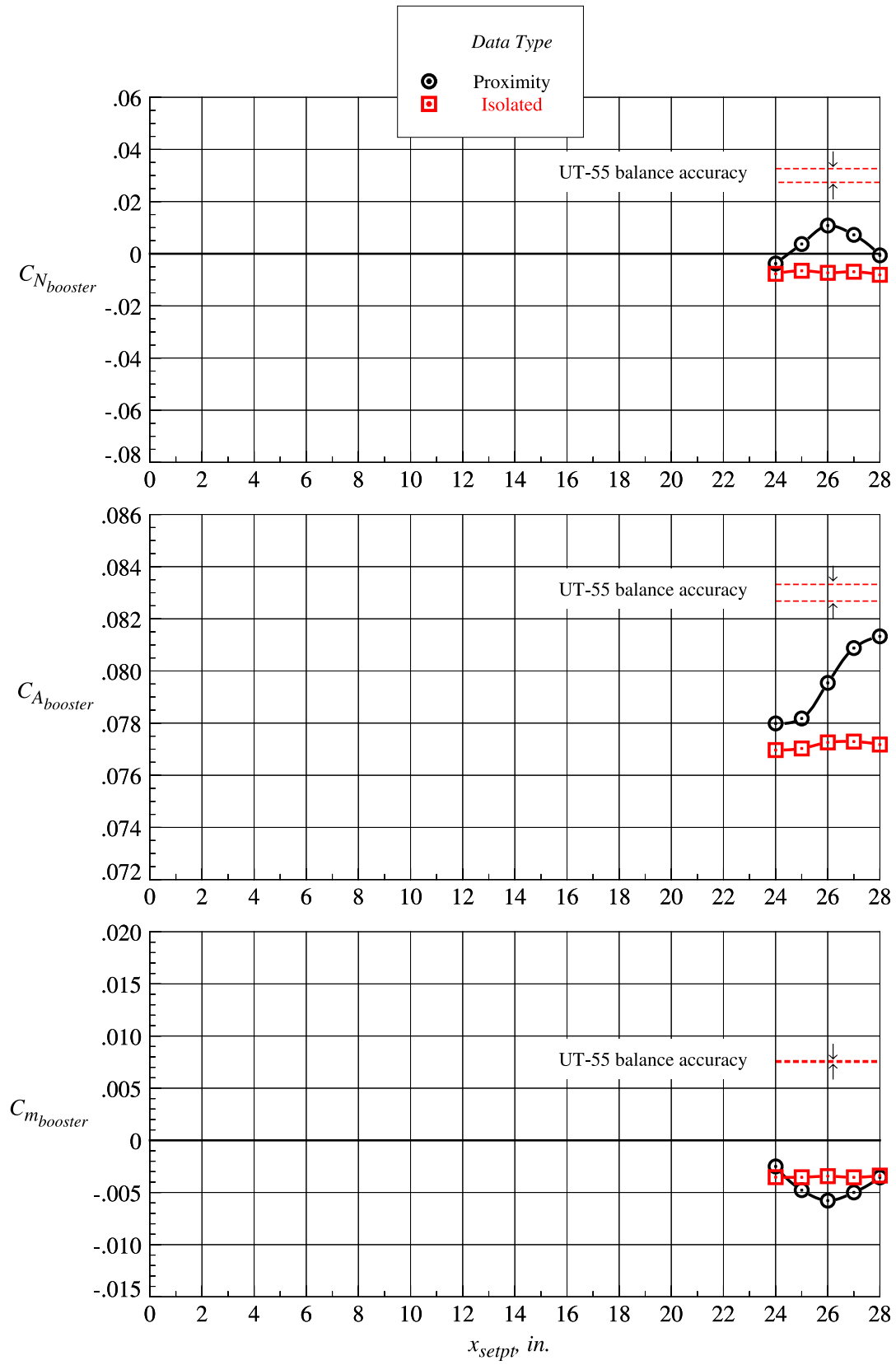
Figure 57. Continued.





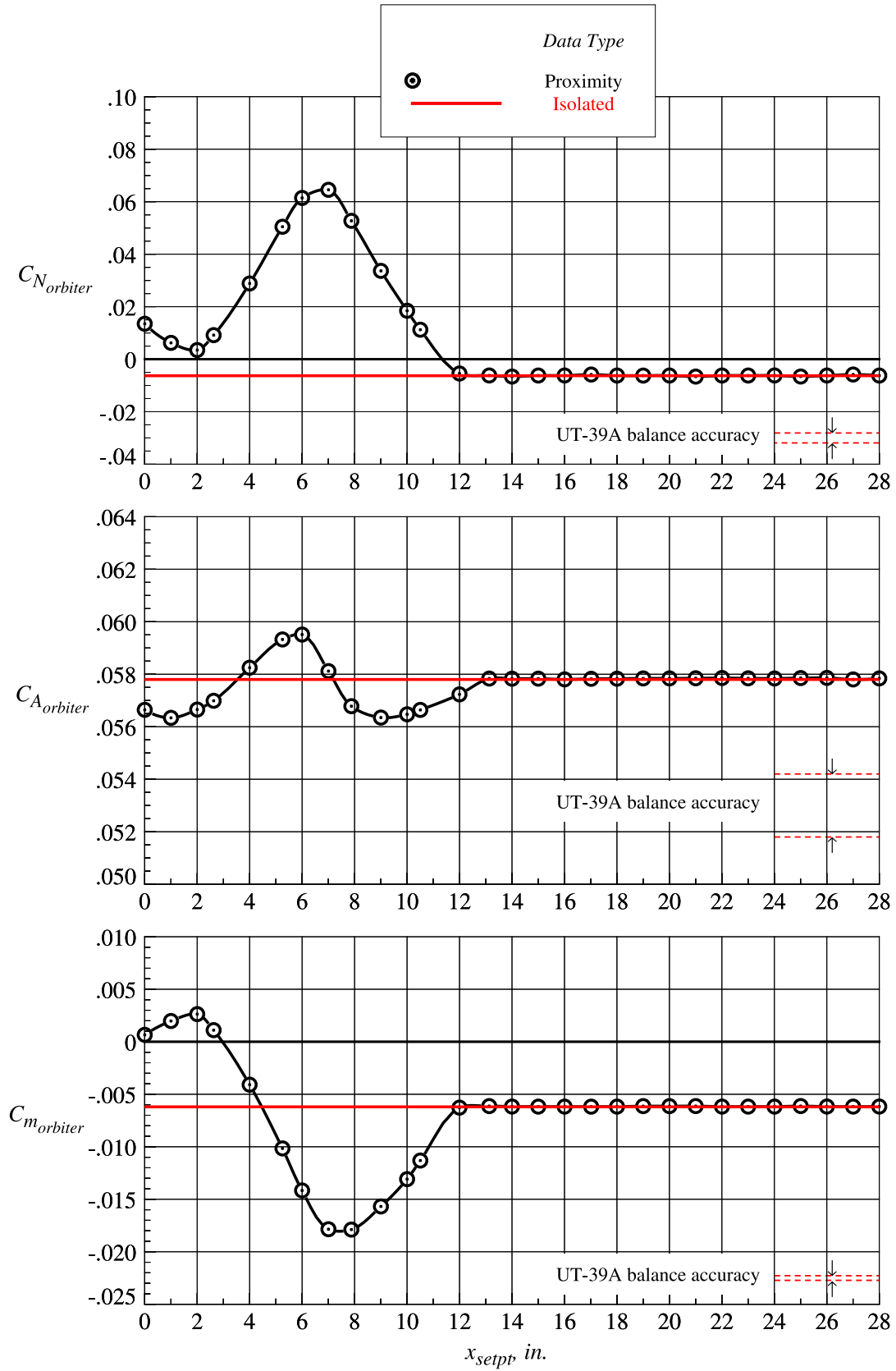
(n)  $z_{setpt} = 11.810$  in.

Figure 57. Continued.



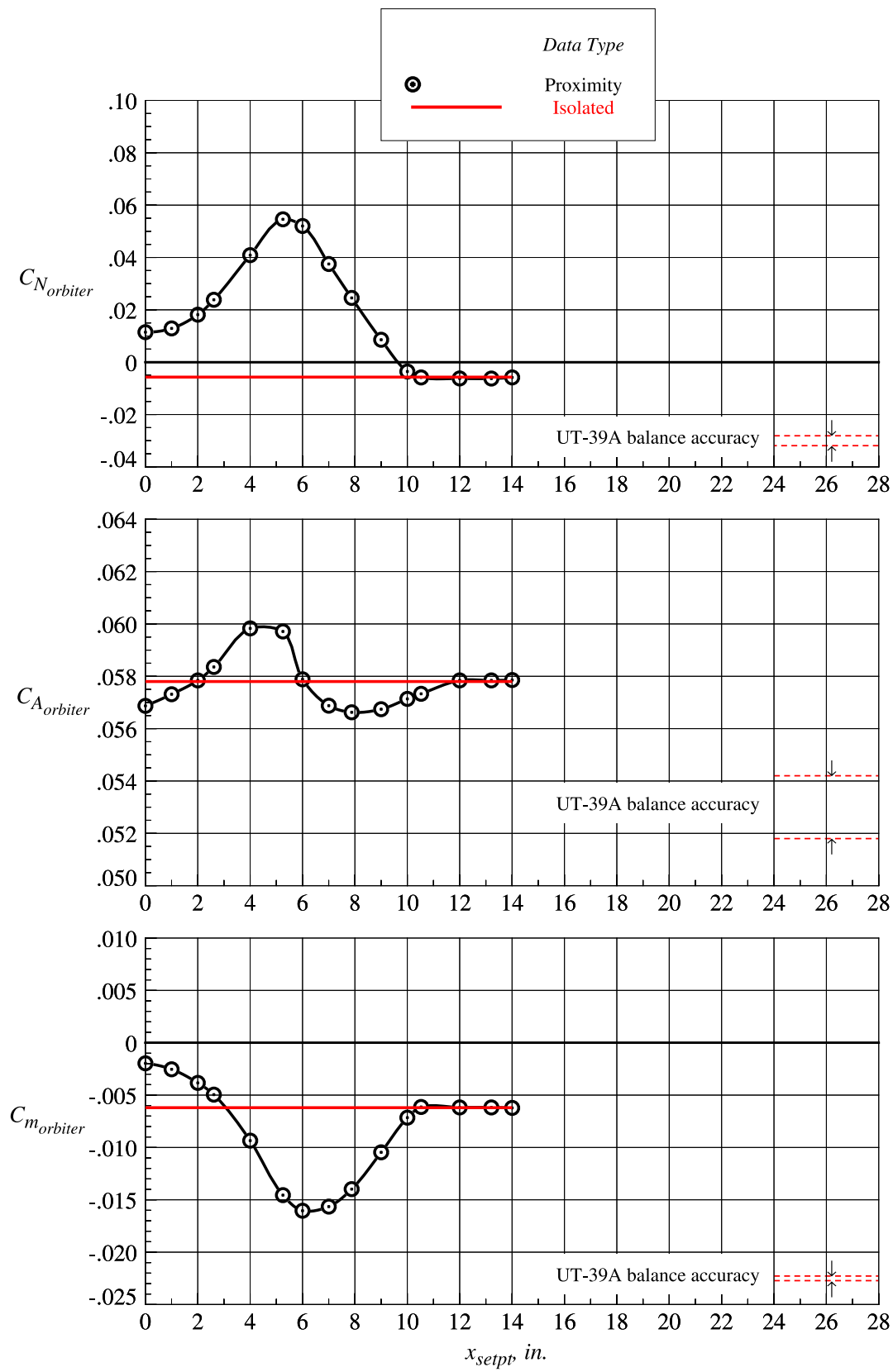
(o)  $z_{setpt} = 13.130$  in.

Figure 57. Concluded.



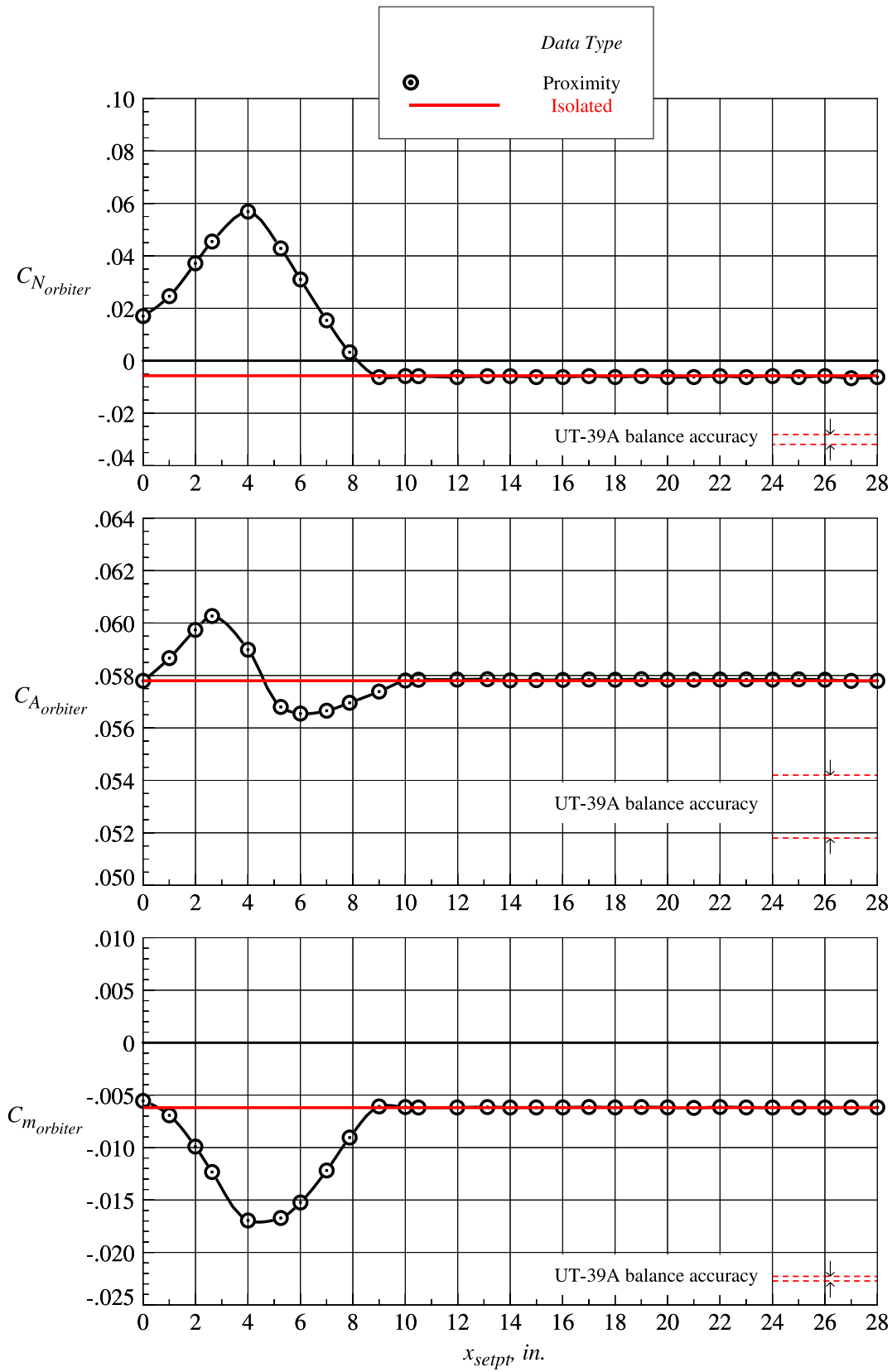
(a)  $z_{setpt} = 0$  in.

Figure 58. Orbiter proximity and isolated aerodynamic characteristics at Mach = 3.0 and  $\Delta\alpha = 0^\circ$ .



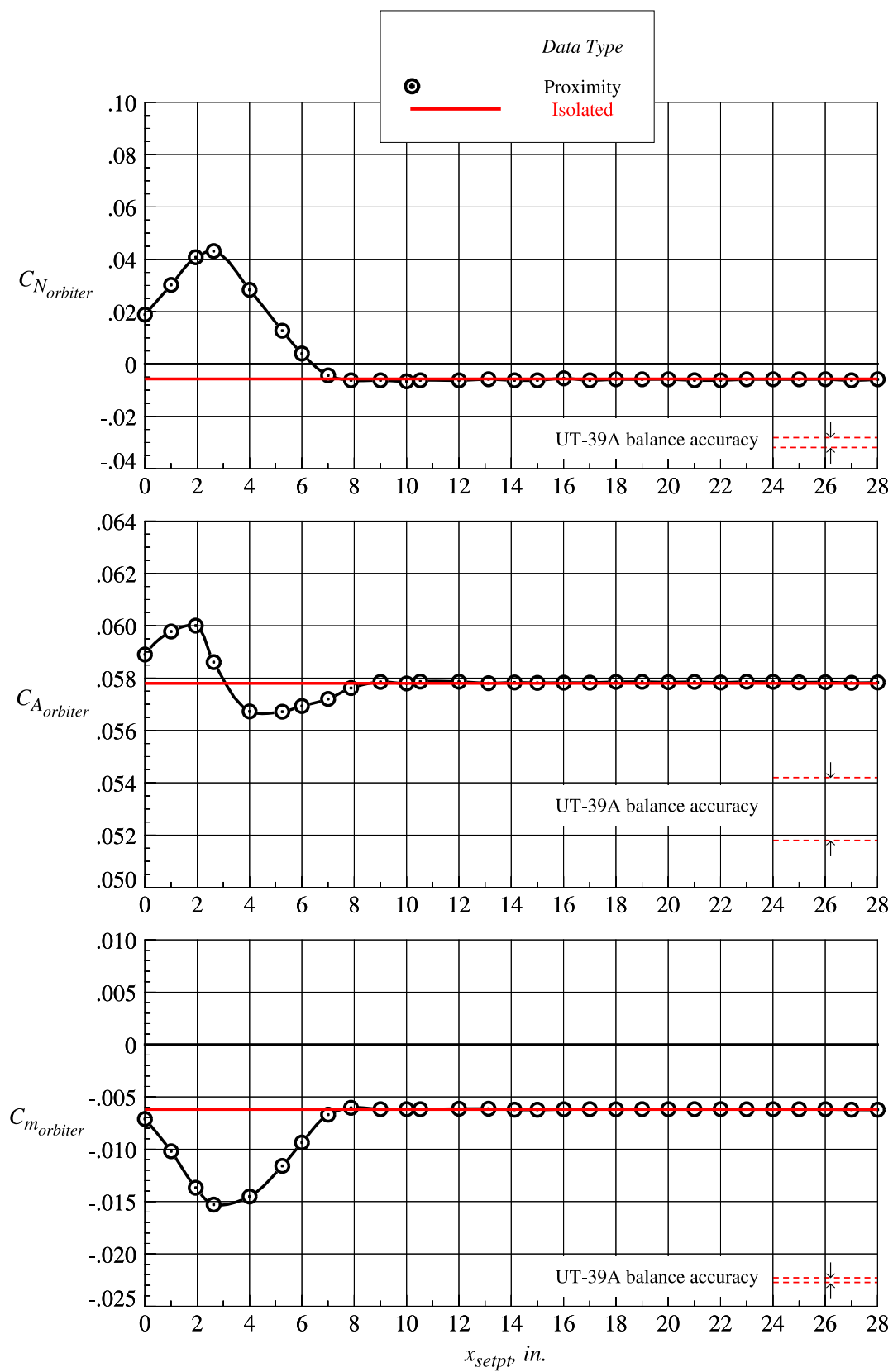
(b)  $z_{setpt} = 0.656$  in.

Figure 58. Continued.



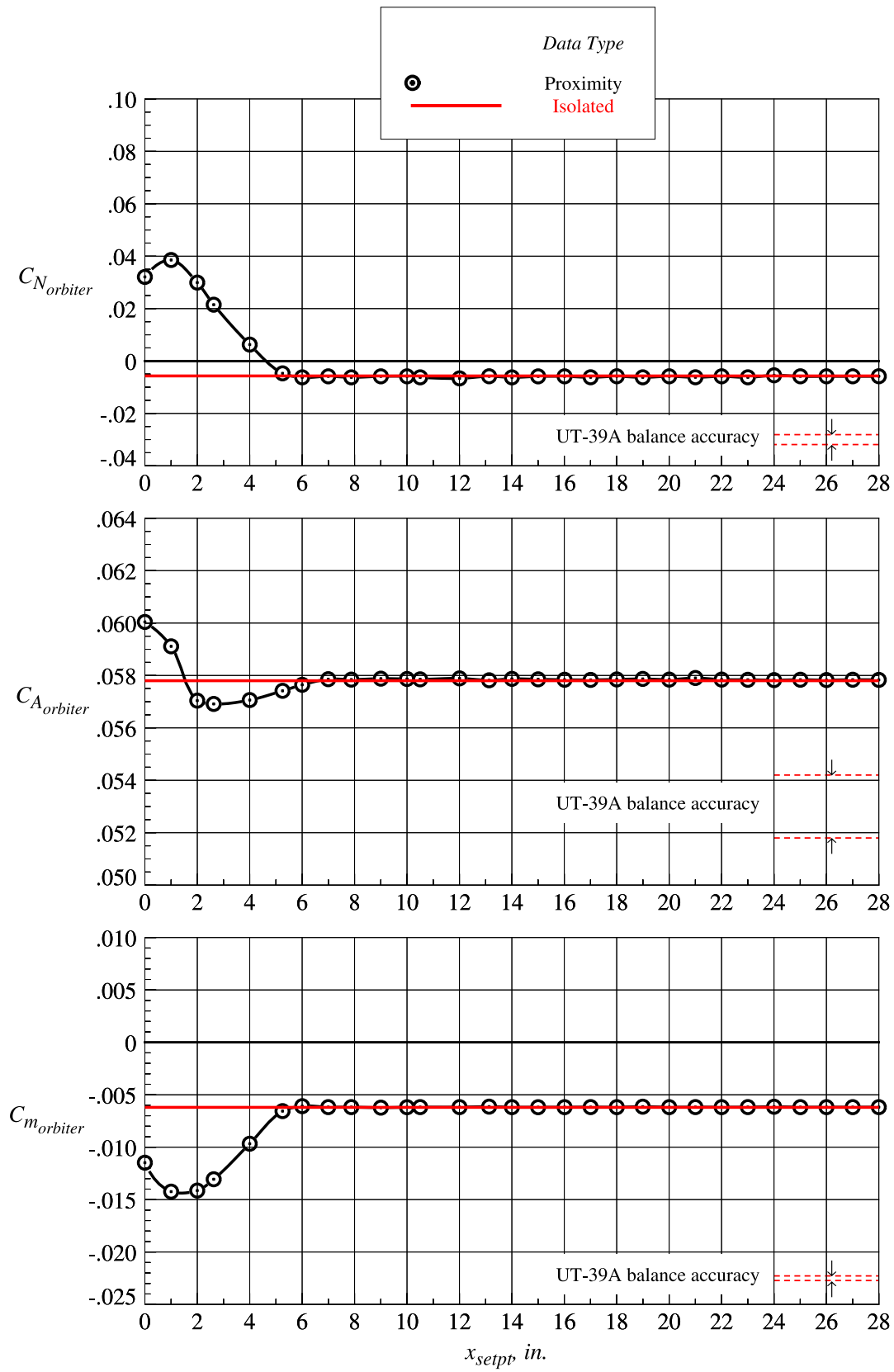
(c)  $z_{setpt} = 1.313$  in.

Figure 58. Continued.



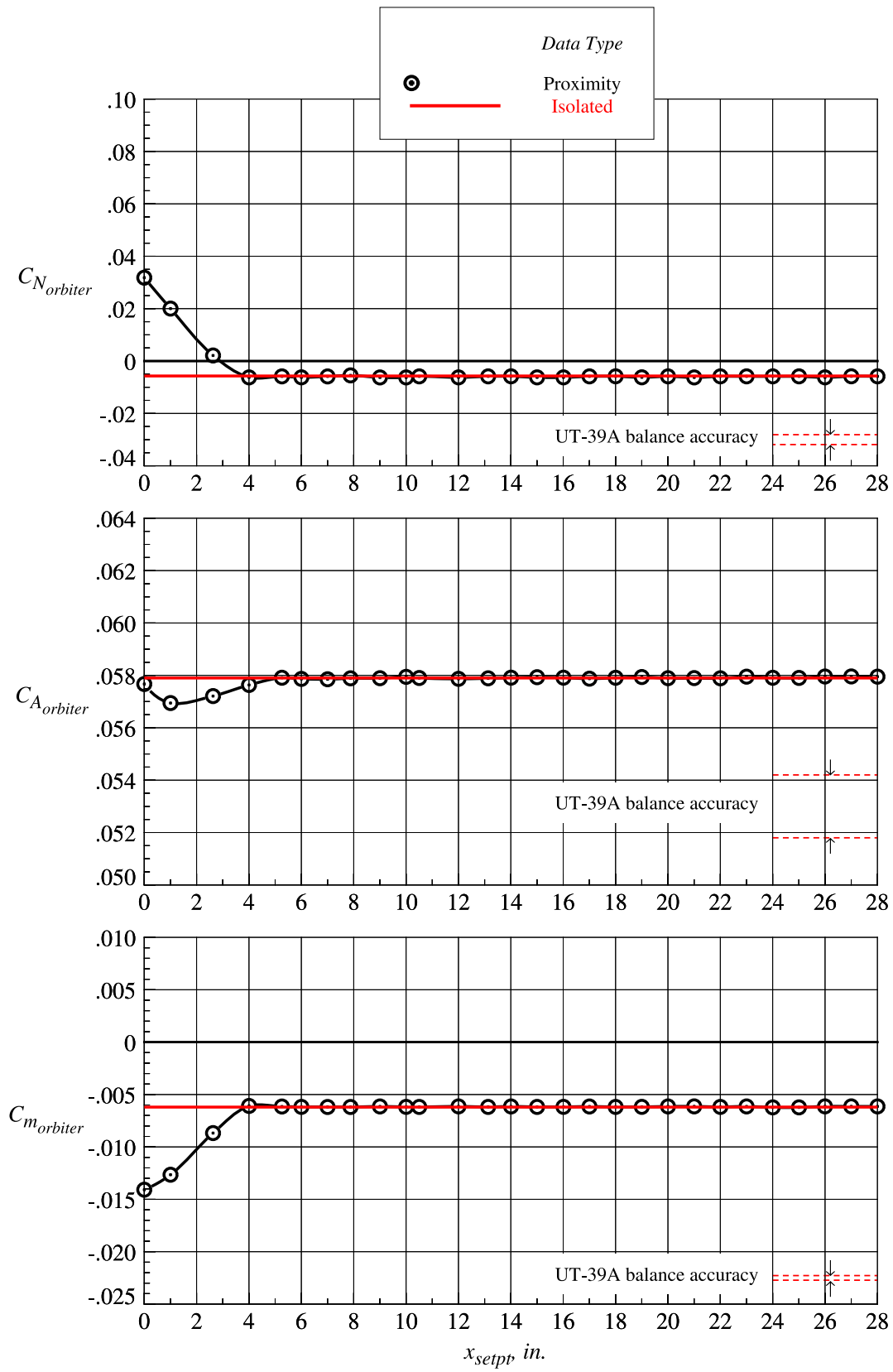
(d)  $z_{setpt} = 1.969$  in.

Figure 58. Continued.



(e)  $z_{setpt} = 2.625$  in.

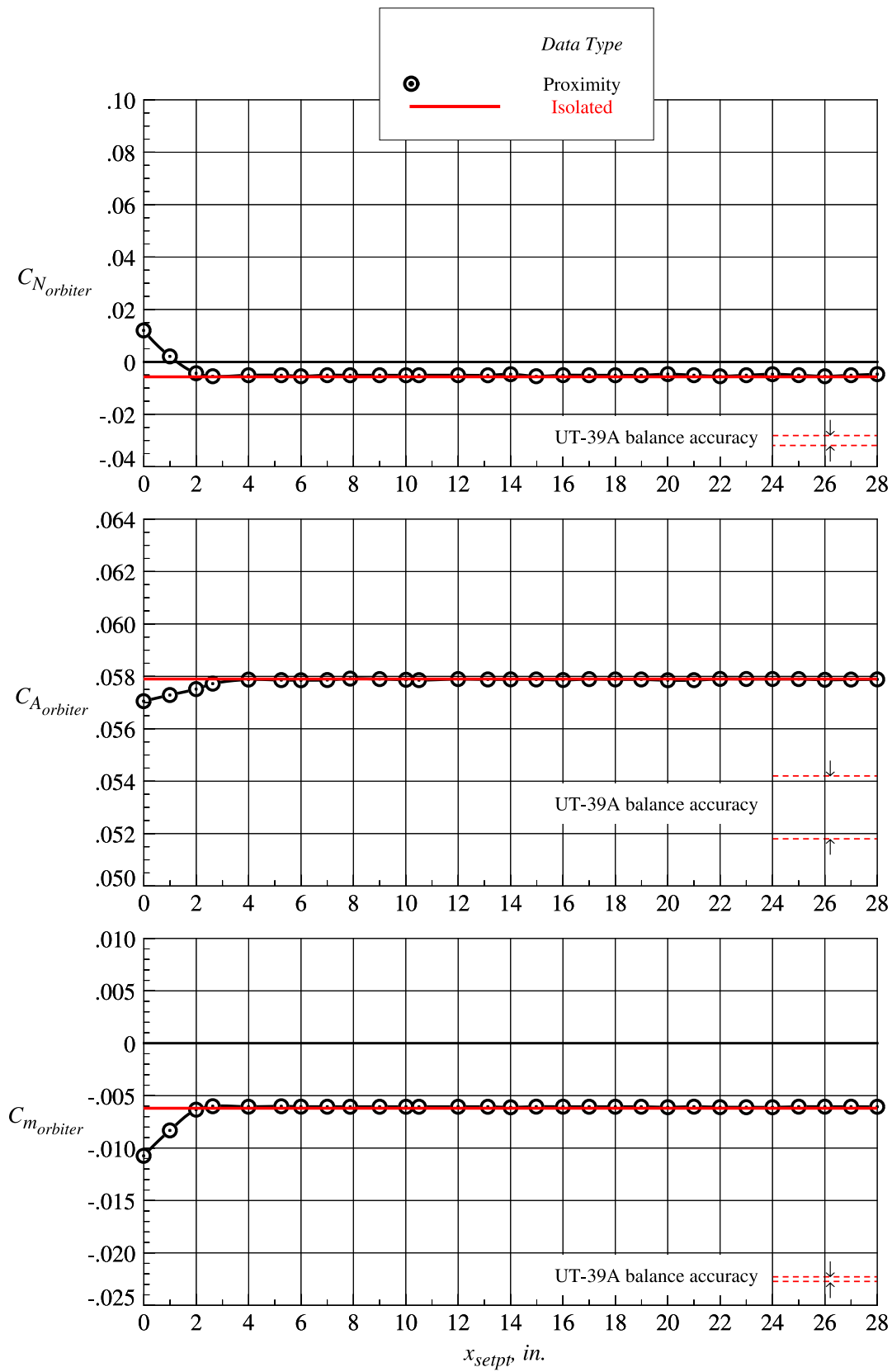
Figure 58. Continued.



(f)  $z_{setpt} = 3.281$  in.

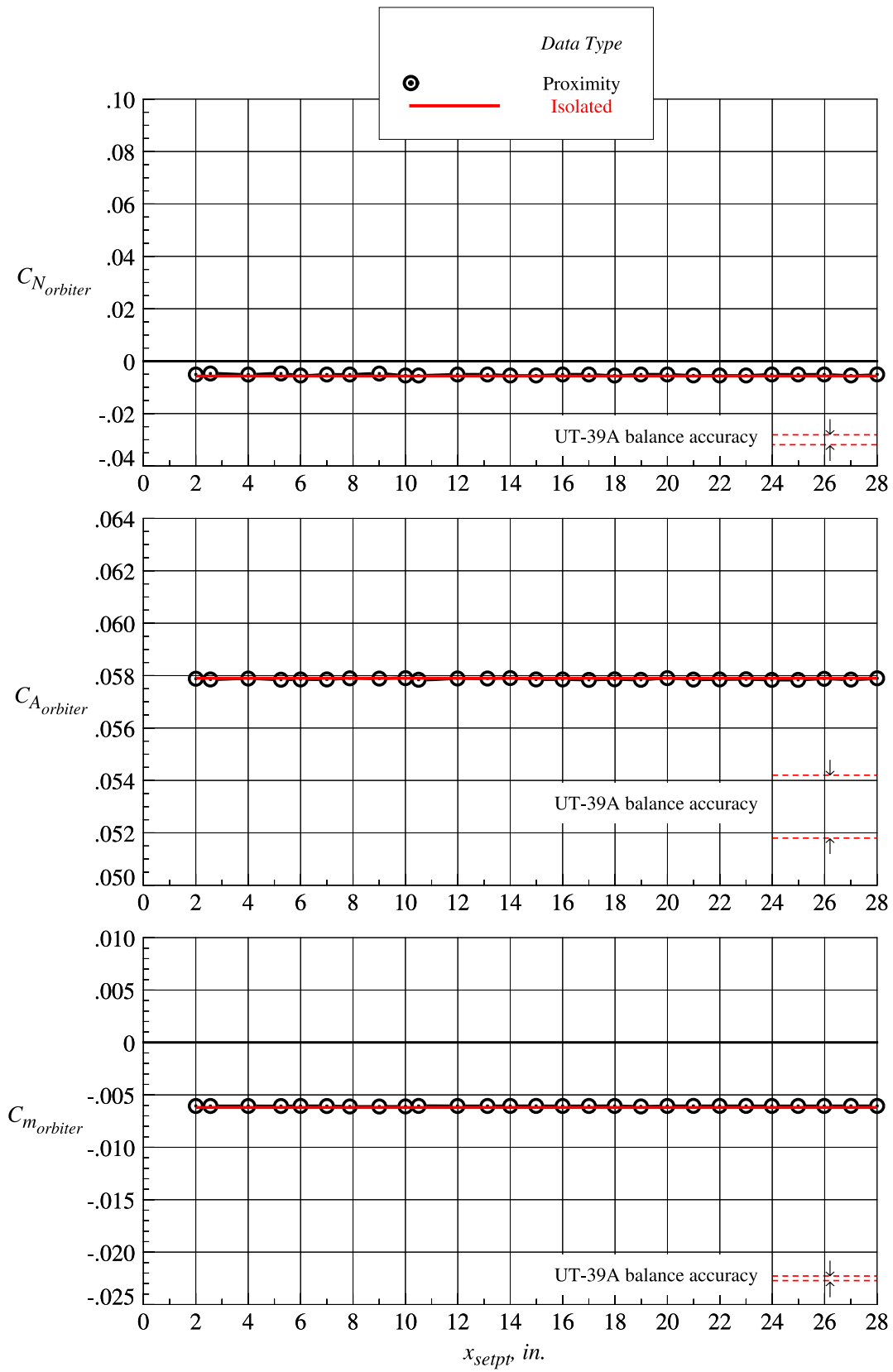
Figure 58. Continued.





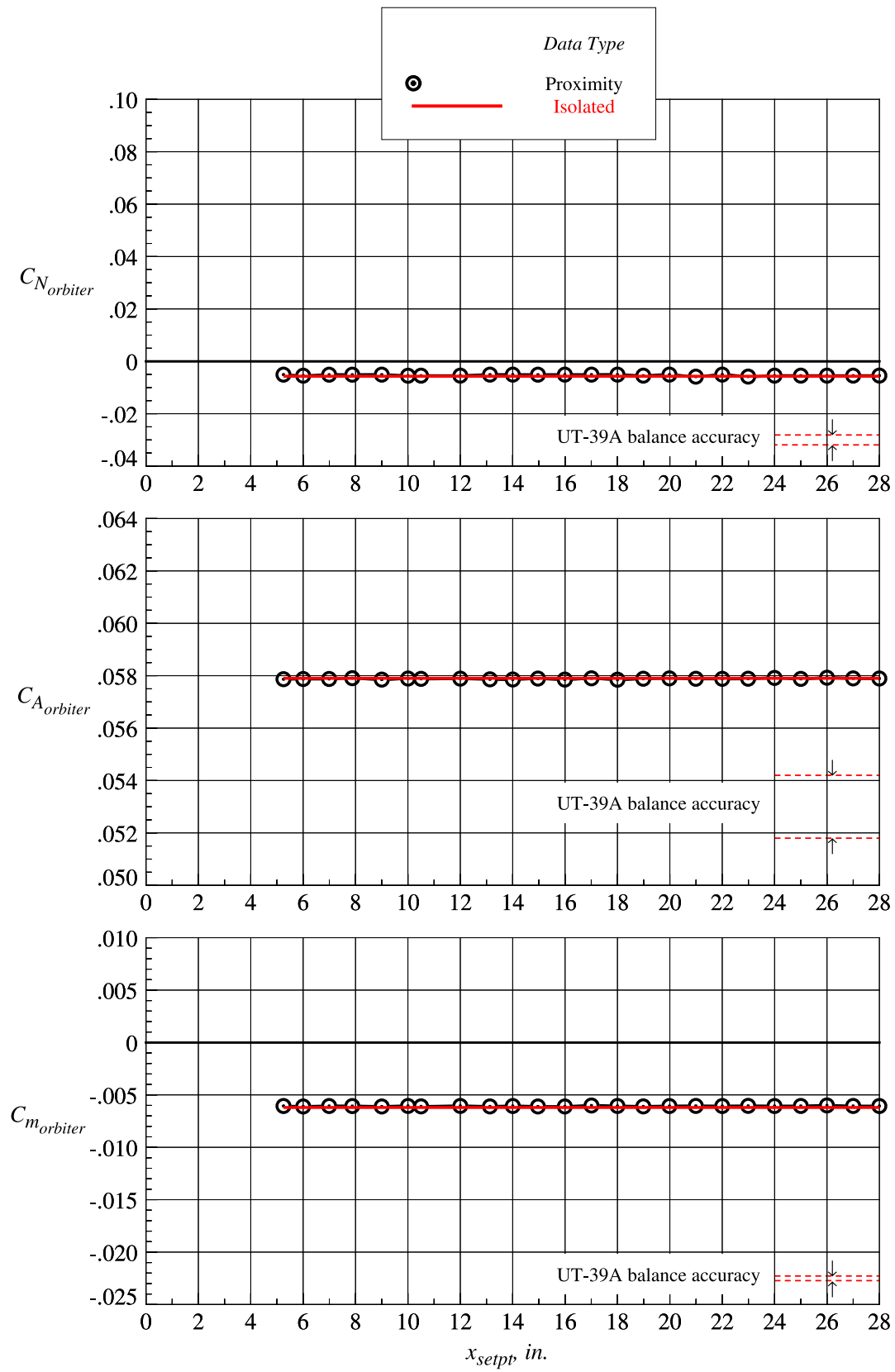
(g)  $z_{setpt} = 3.938$  in.

Figure 58. Continued.



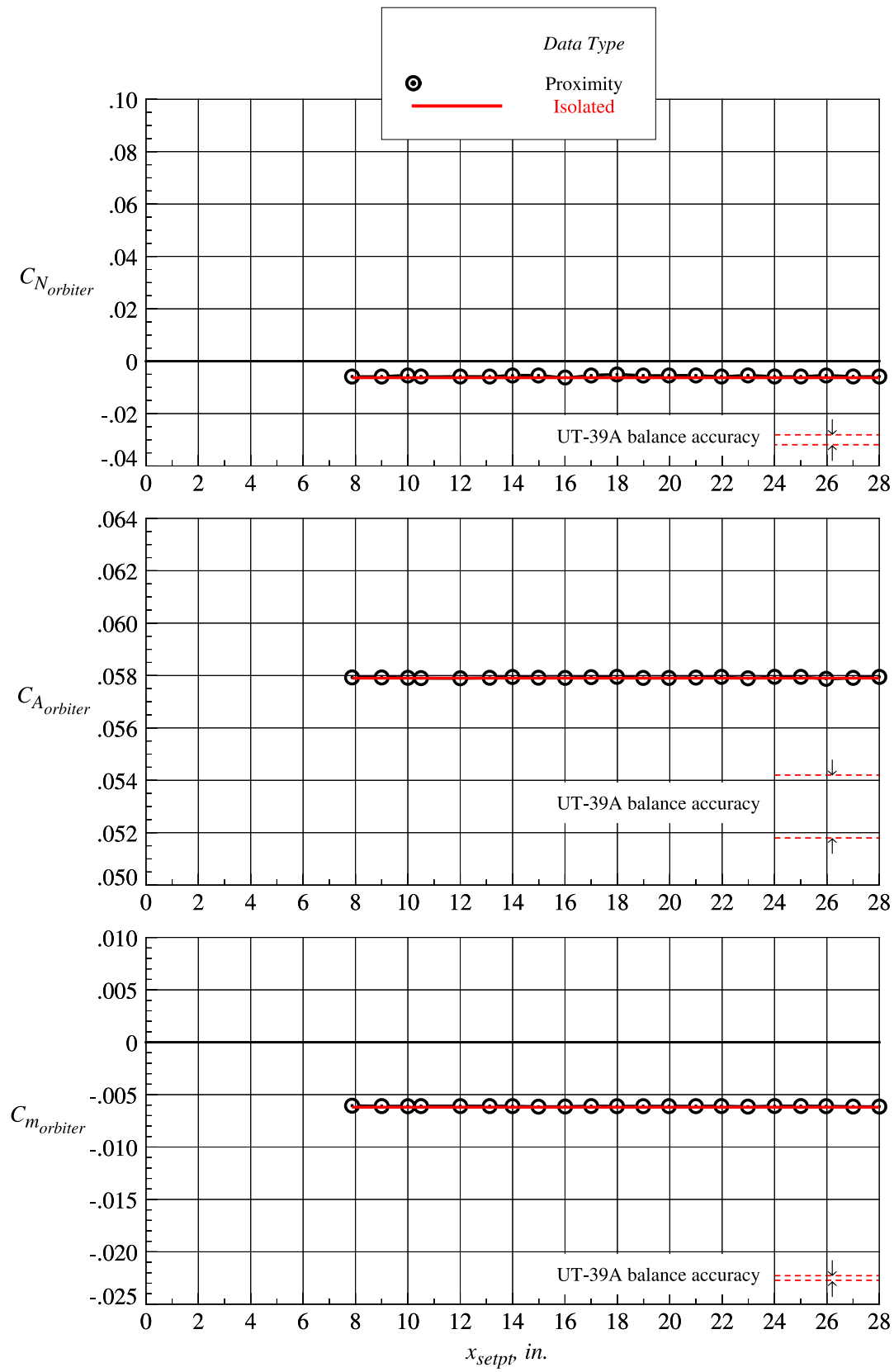
(h)  $z_{setpt} = 4.594$  in.

Figure 58. Continued.



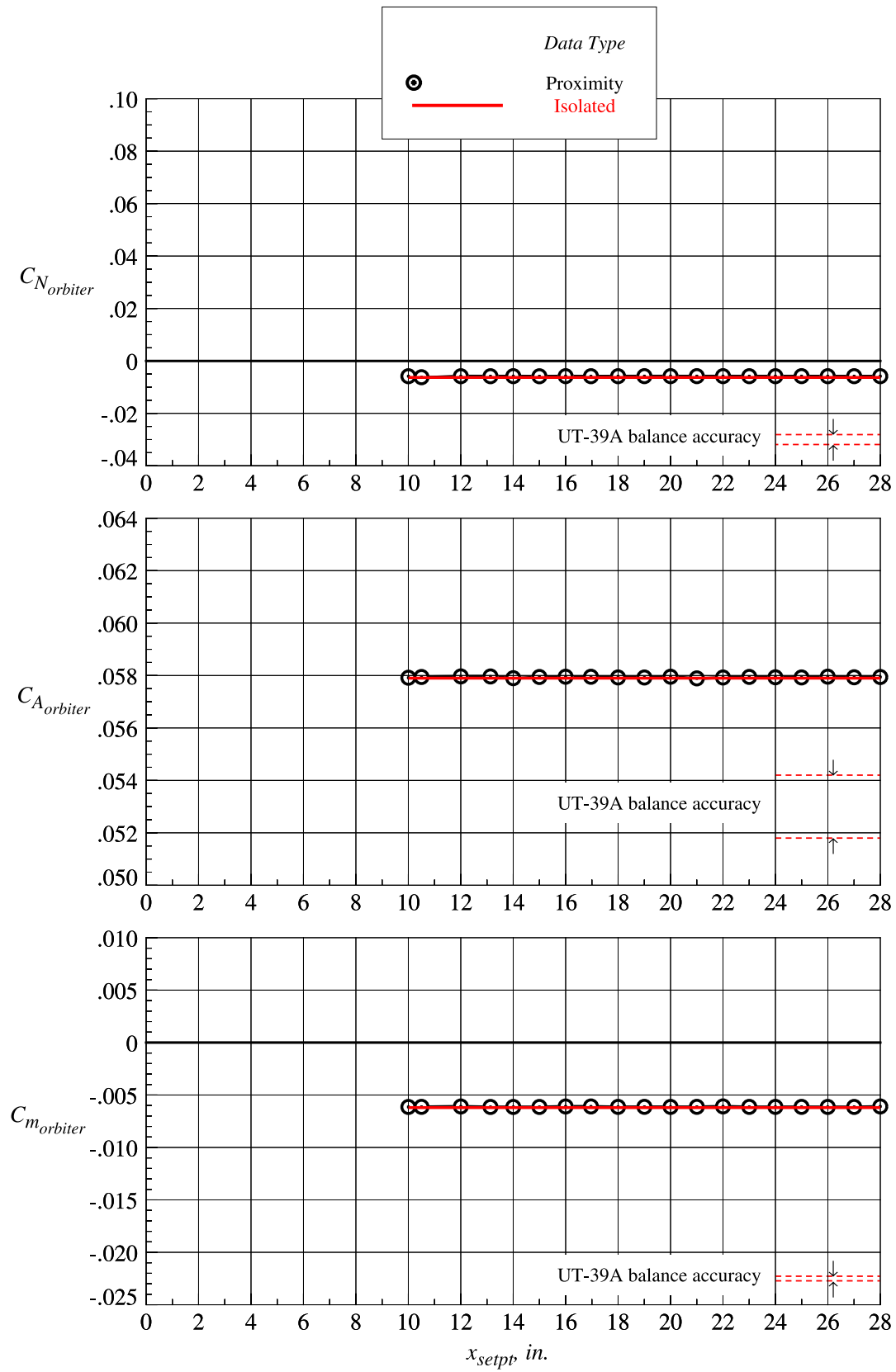
(i)  $z_{setpt} = 5.250$  in.

Figure 58. Continued.



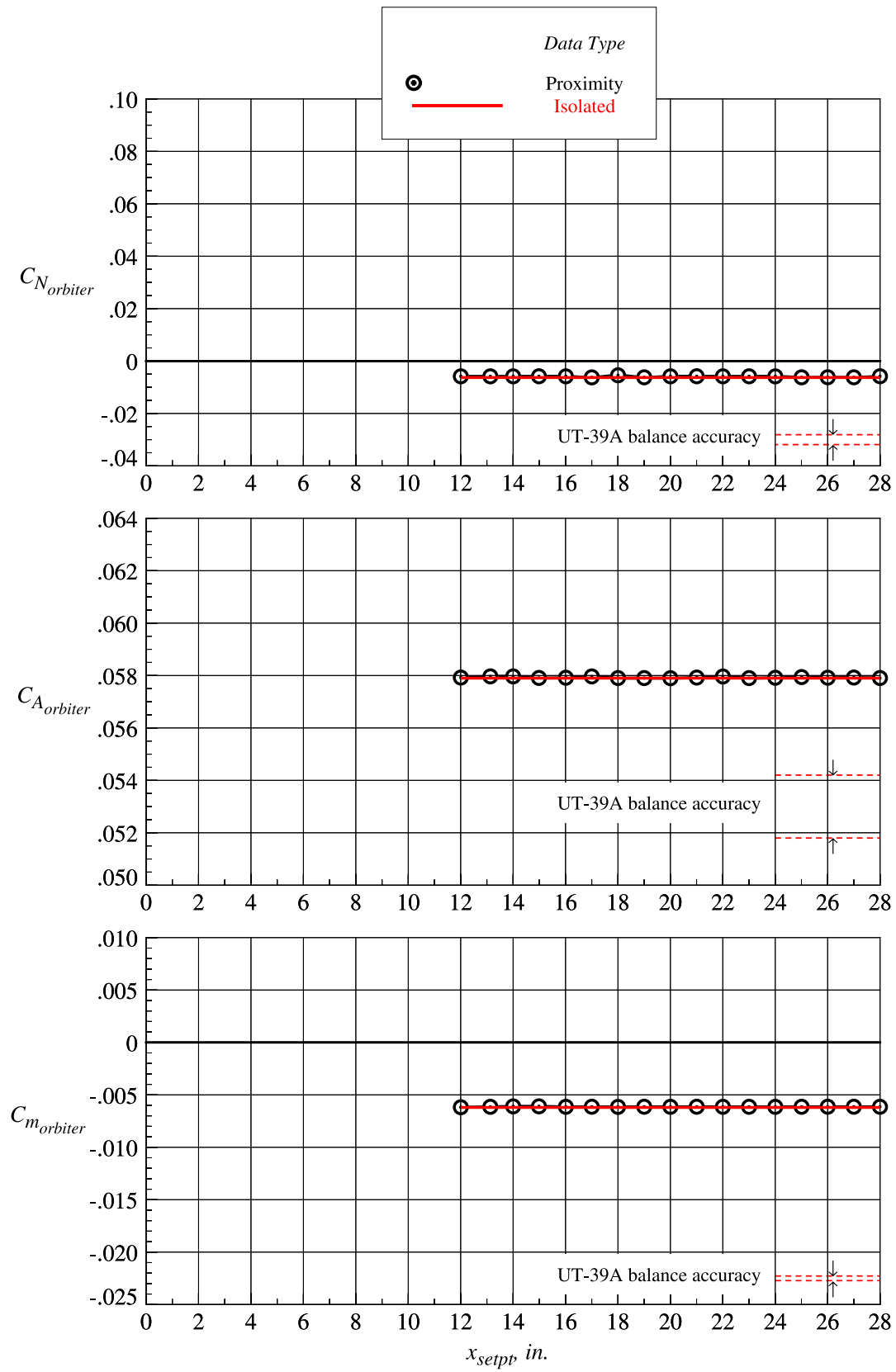
(j)  $z_{setpt} = 6.583$  in.

Figure 58. Continued.



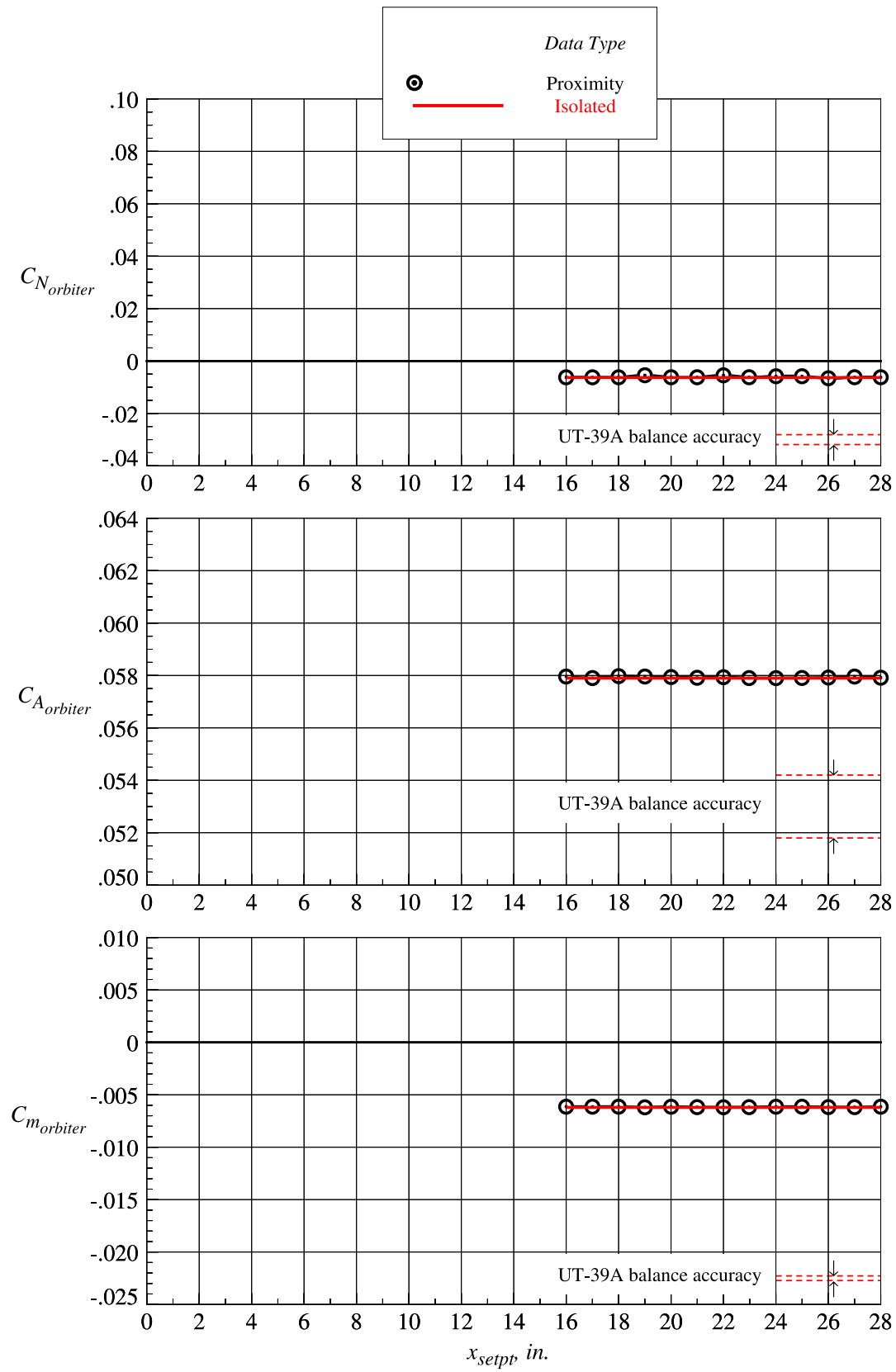
(k)  $z_{setpt} = 7.875$  in.

Figure 58. Continued.



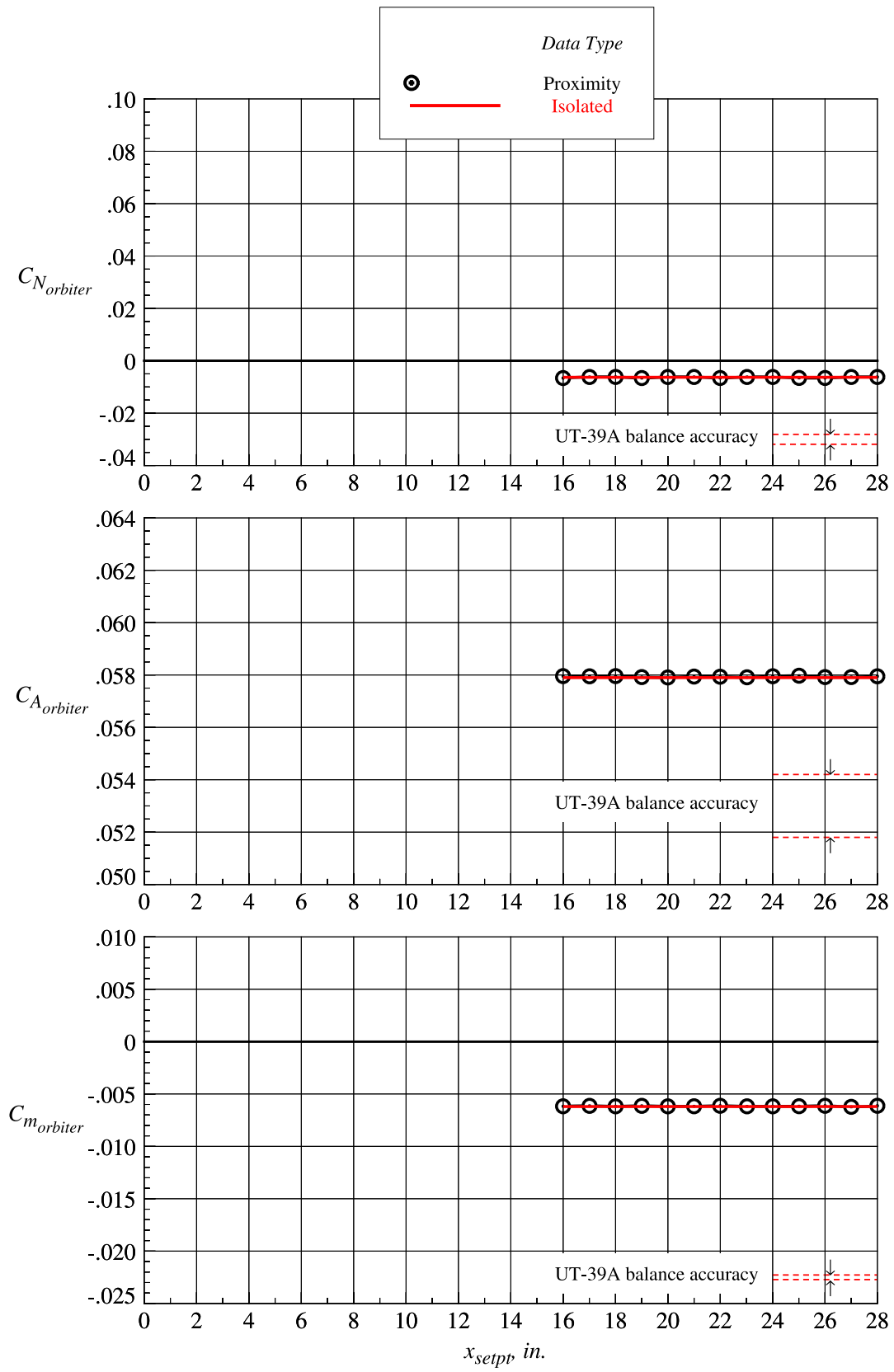
(l)  $z_{setpt} = 9.188$  in.

Figure 58. Continued.



(m)  $z_{setpt} = 10.500$  in.

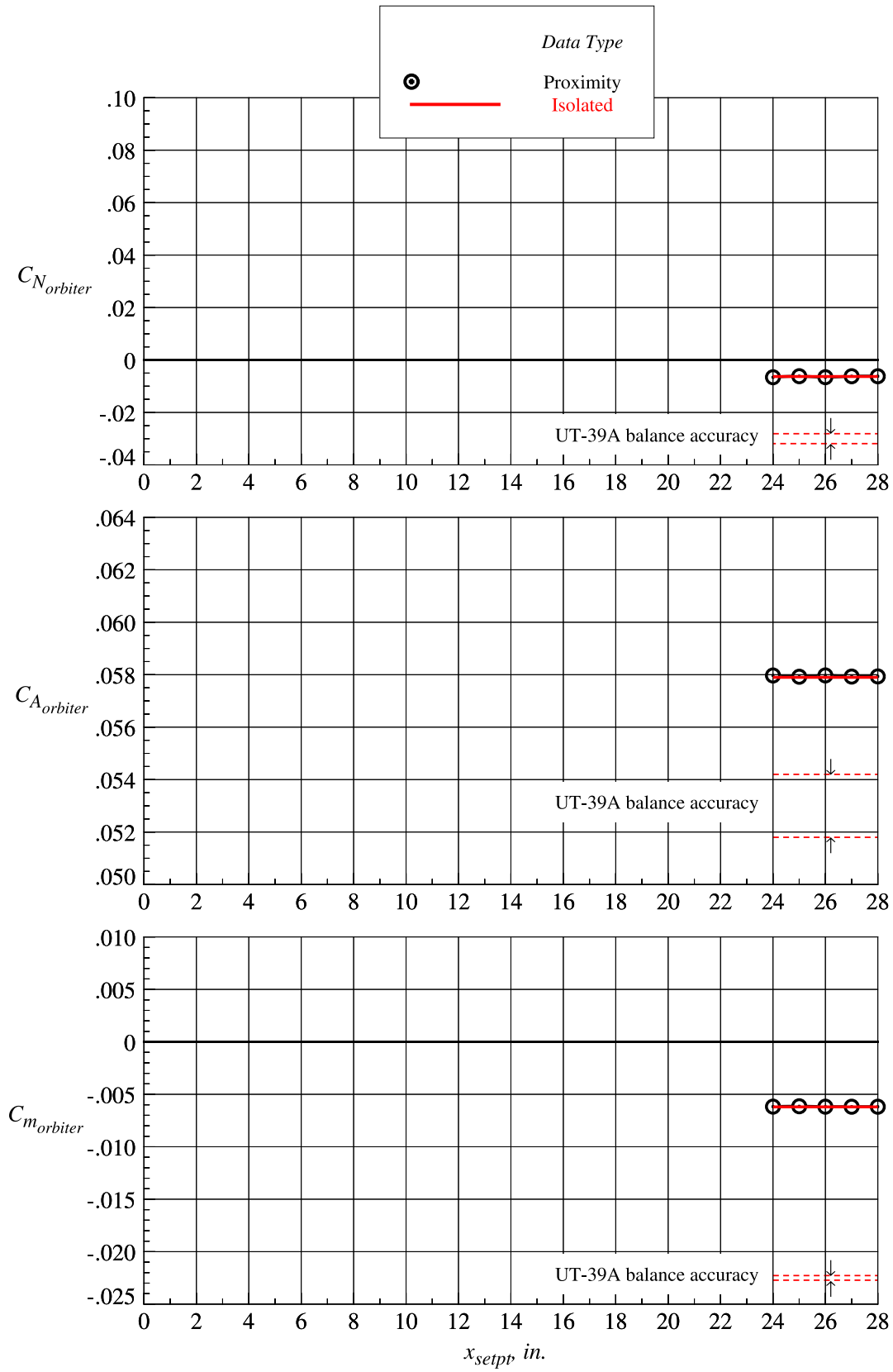
Figure 58. Continued.



(n)  $z_{setpt} = 11.810$  in.

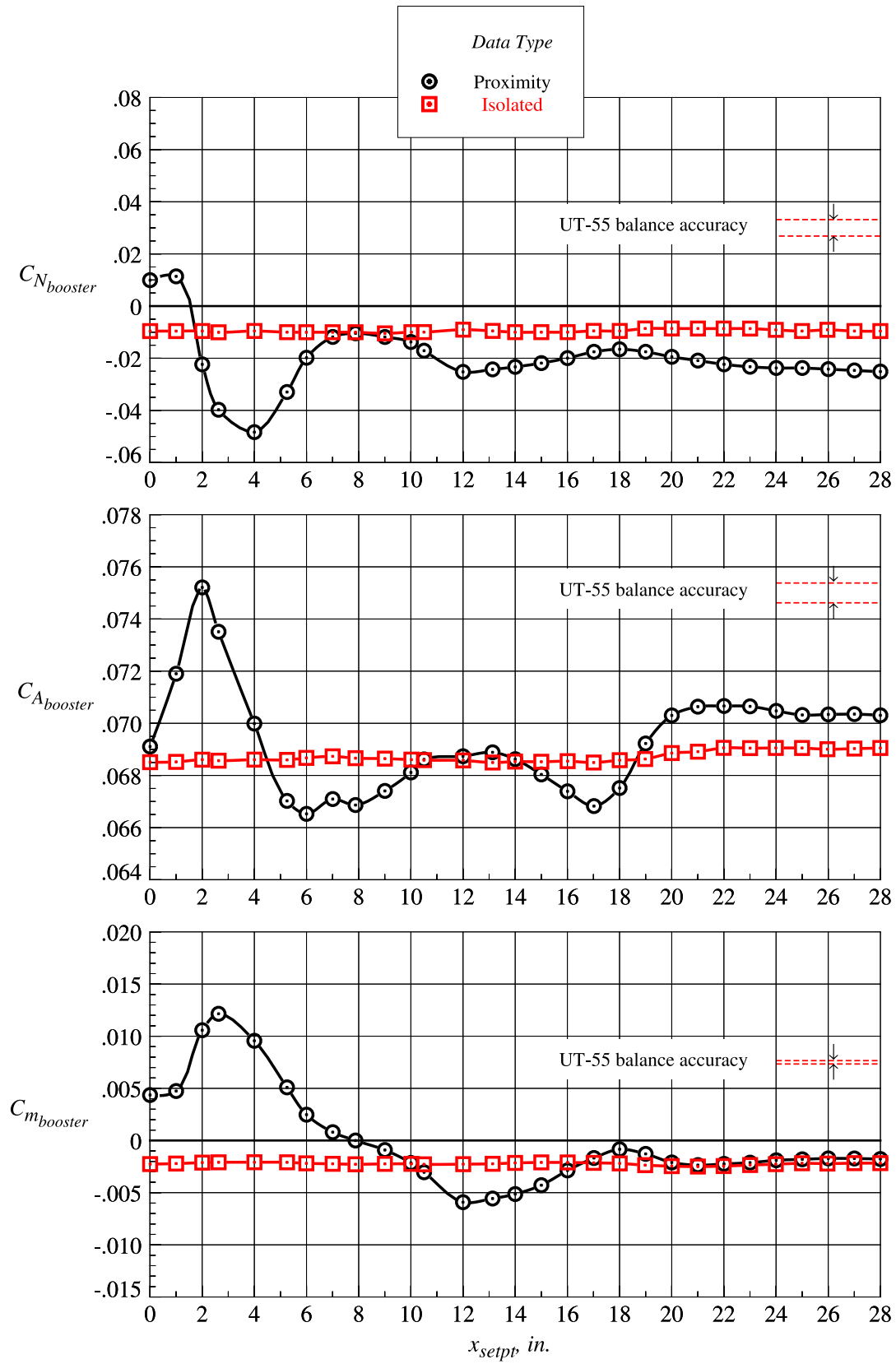
Figure 58. Continued.





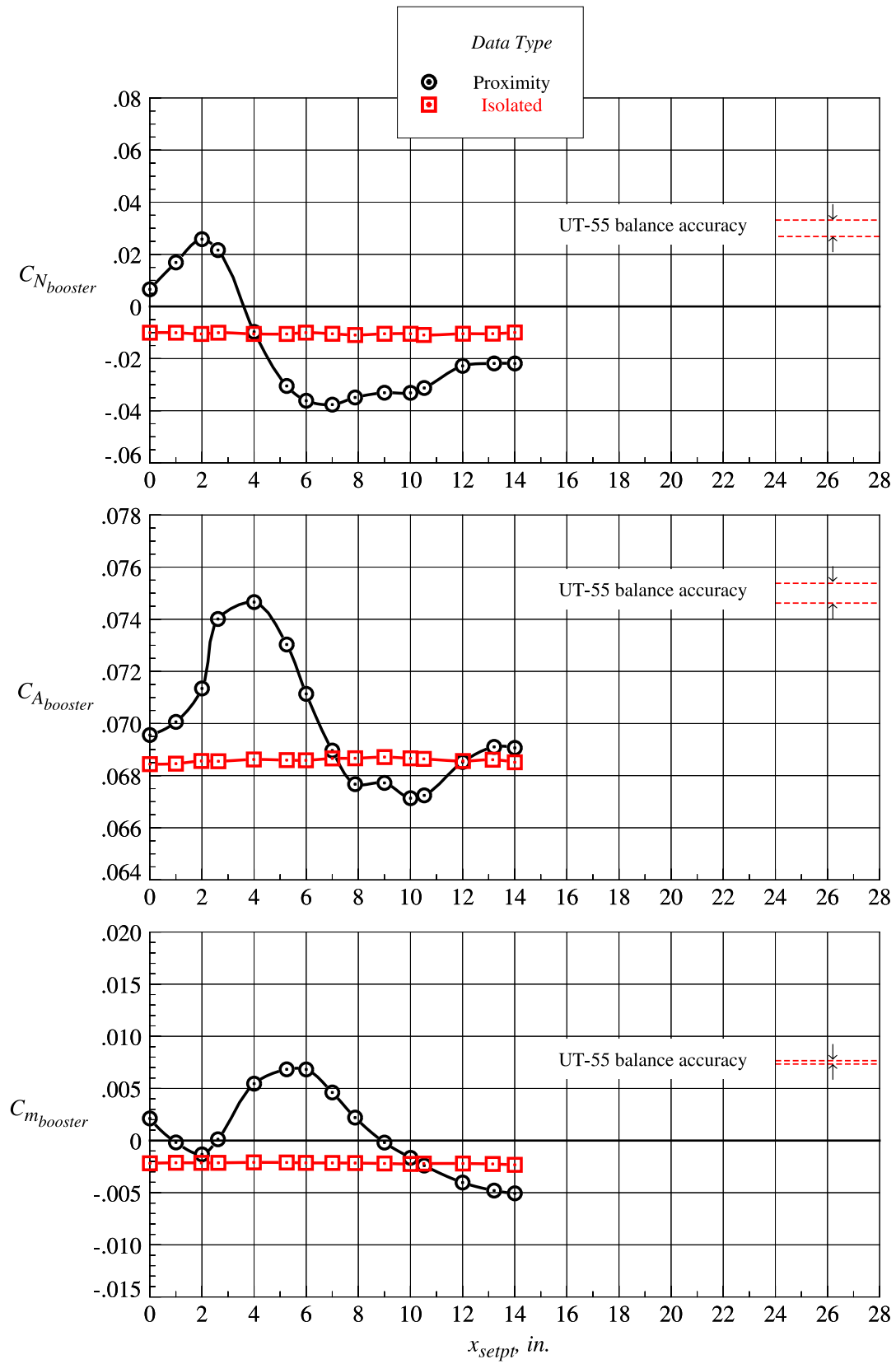
(o)  $z_{setpt} = 13.130$  in.

Figure 58. Concluded.



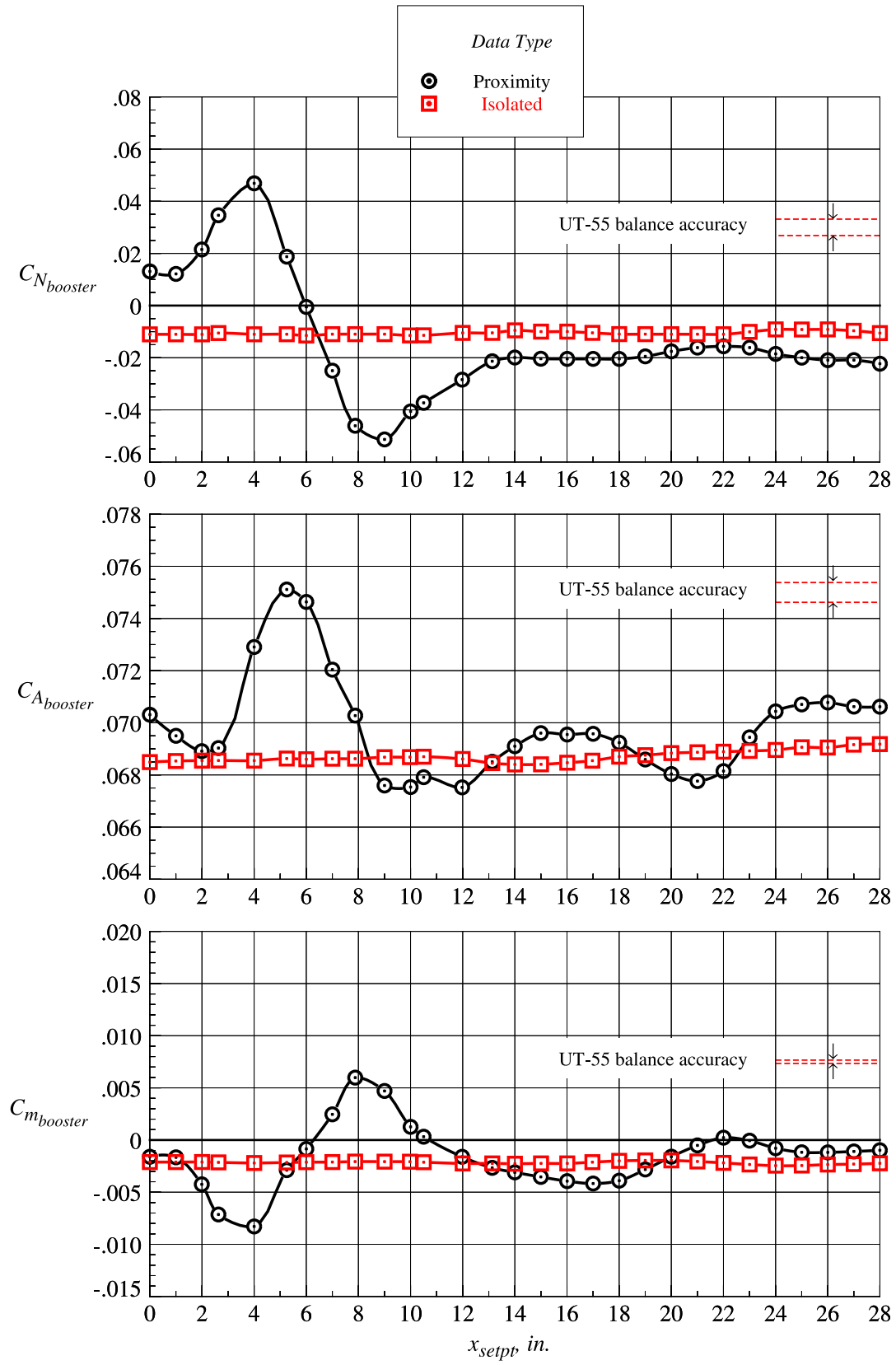
(a)  $z_{sept} = 0 \text{ in.}$

Figure 59. Booster proximity and isolated aerodynamic characteristics at Mach = 3.0 and  $\Delta\alpha = 0^\circ$ .



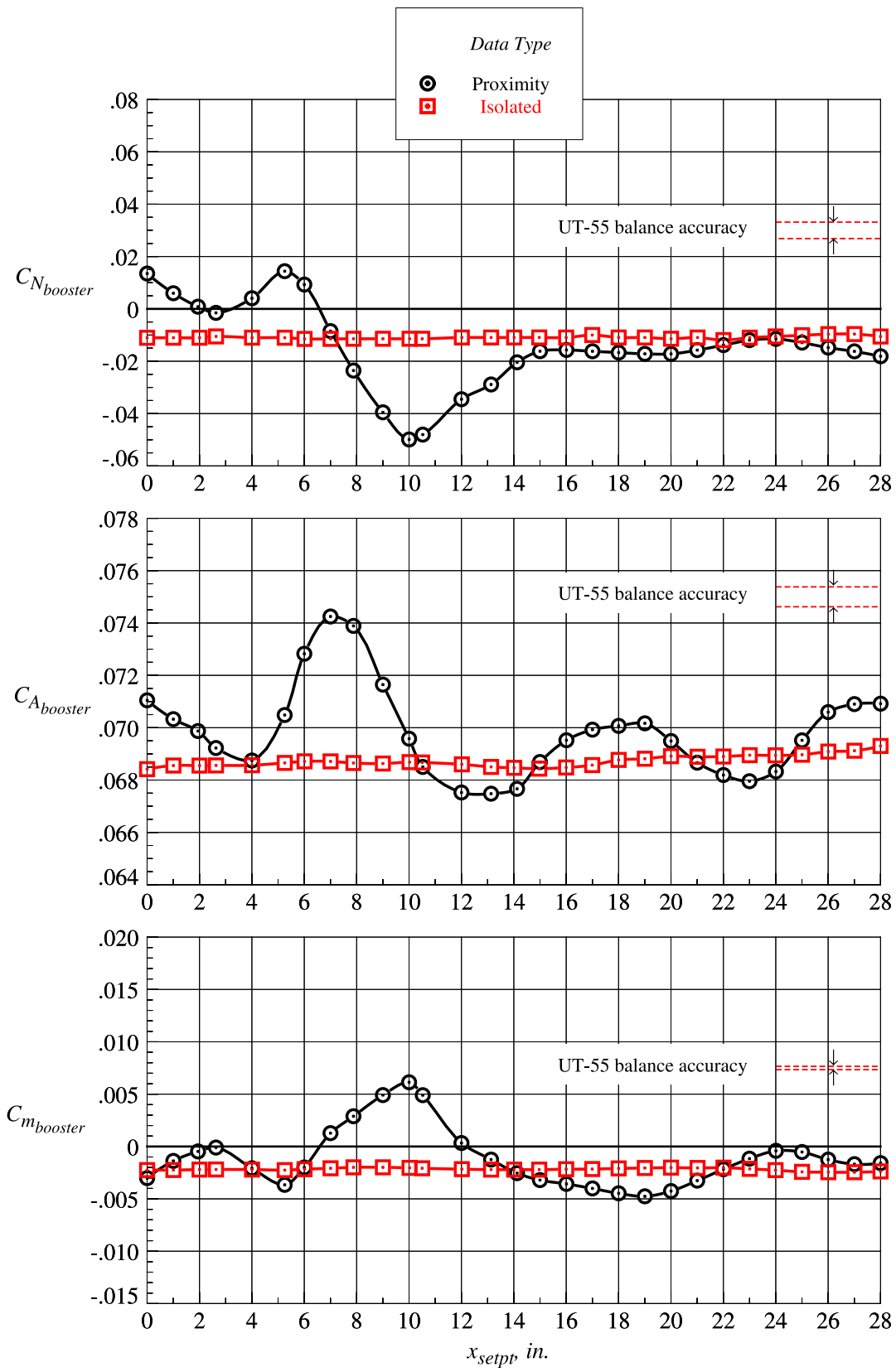
(b)  $z_{setpt} = 0.656$  in.

Figure 59. Continued.



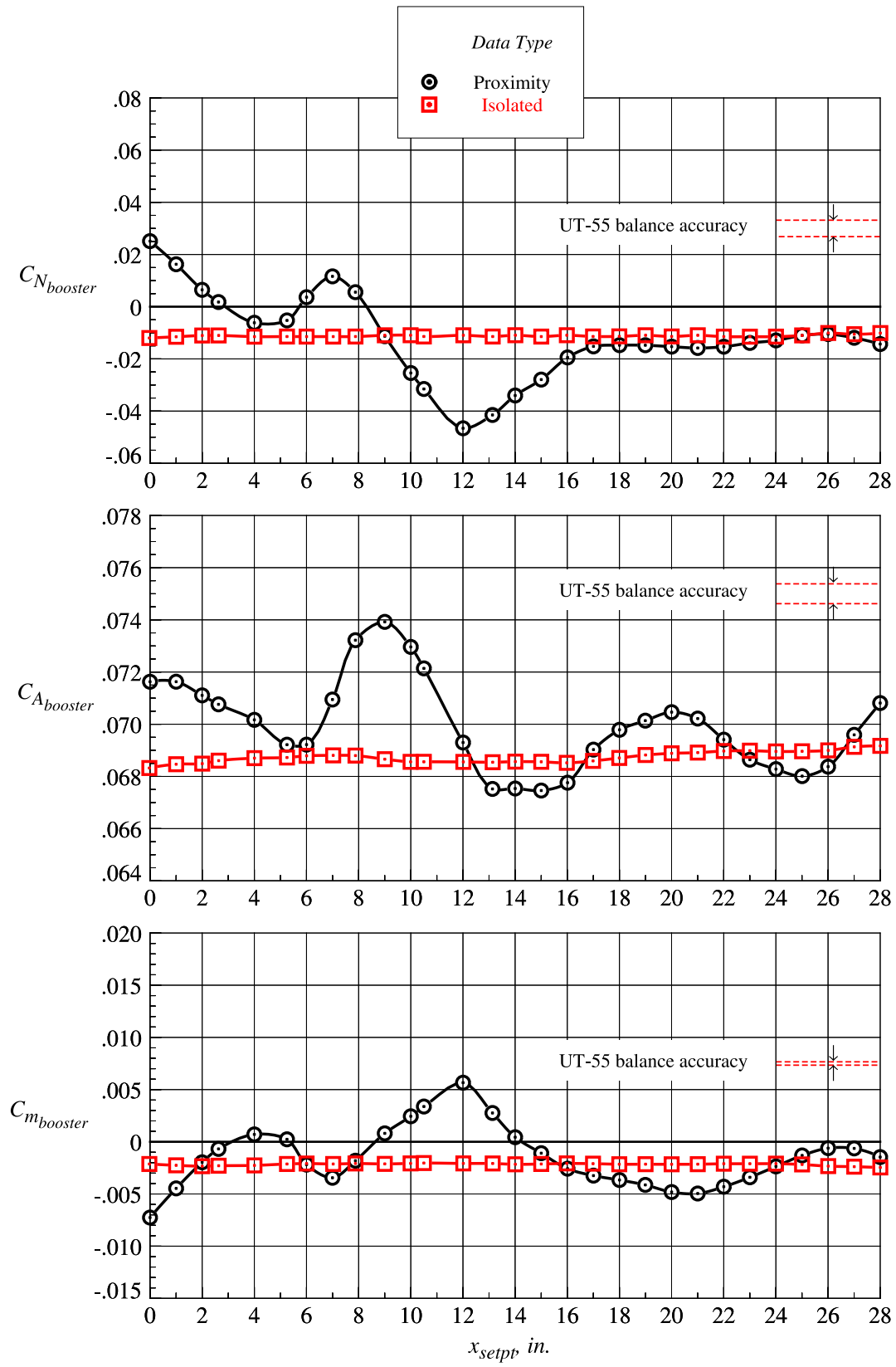
(c)  $z_{setpt} = 1.313$  in.

Figure 59. Continued.



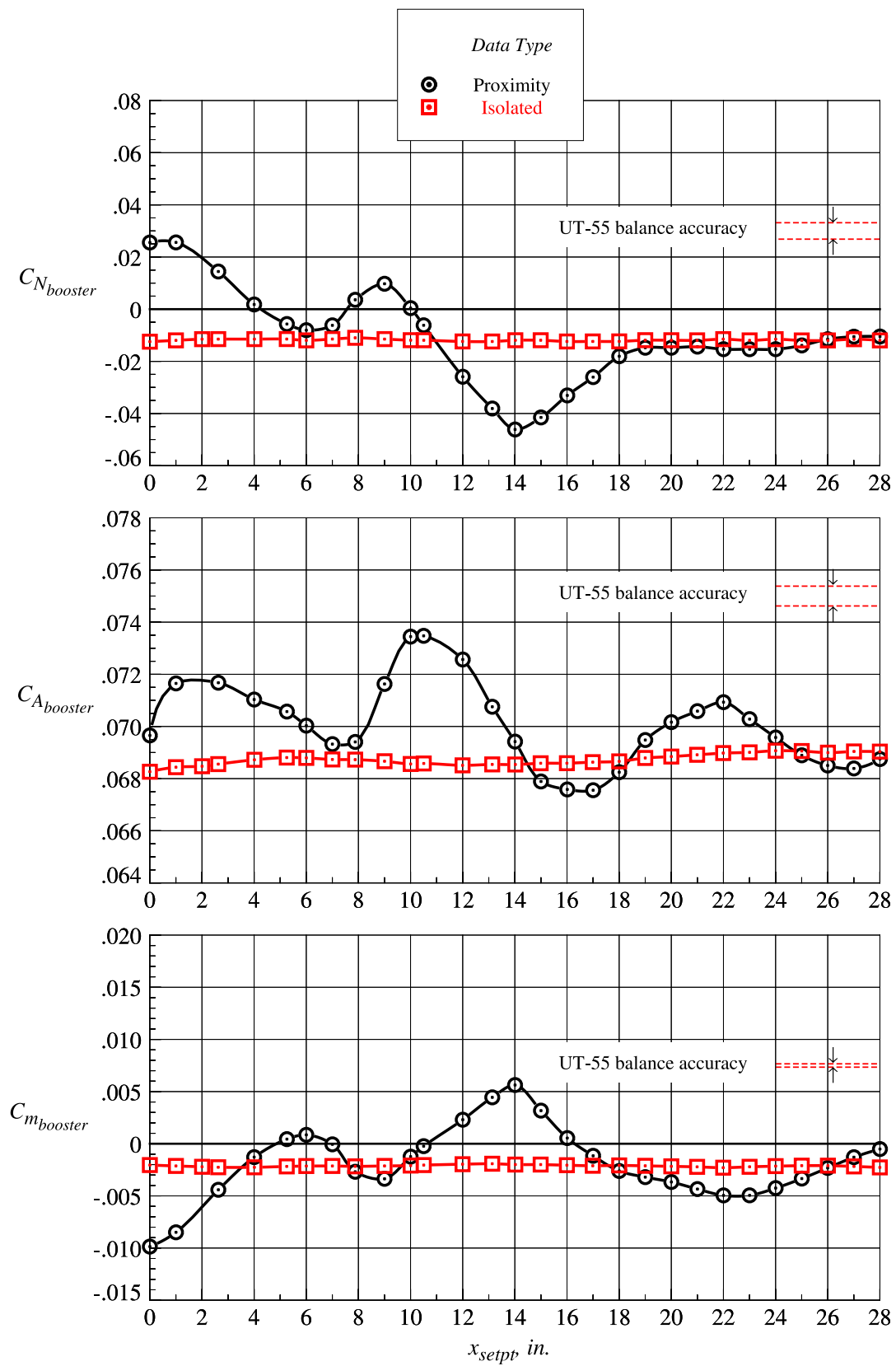
(d)  $z_{setpt} = 1.969$  in.

Figure 59. Continued.



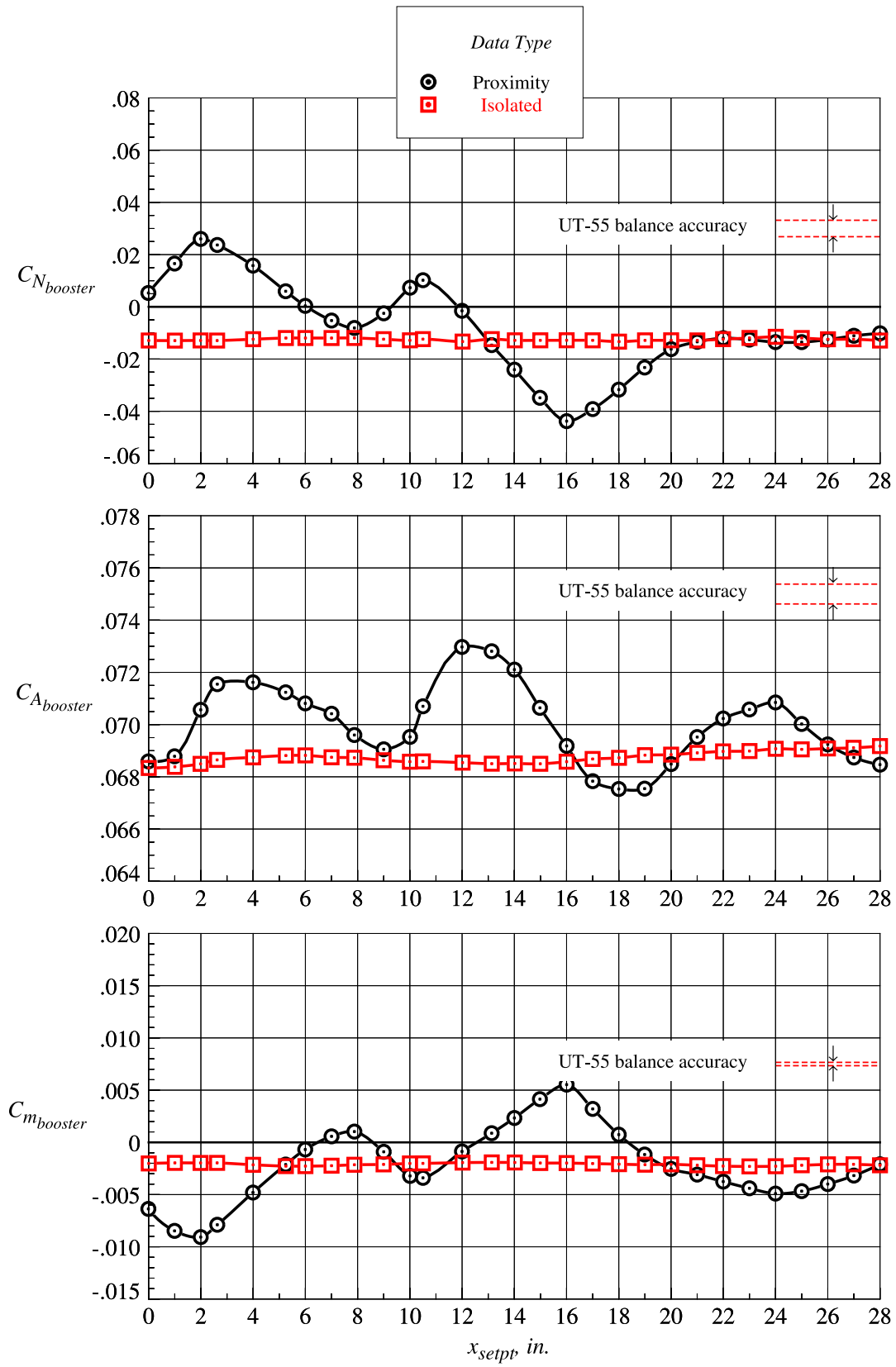
(e)  $z_{setpt} = 2.625$  in.

Figure 59. Continued.



(f)  $z_{setpt} = 3.281$  in.

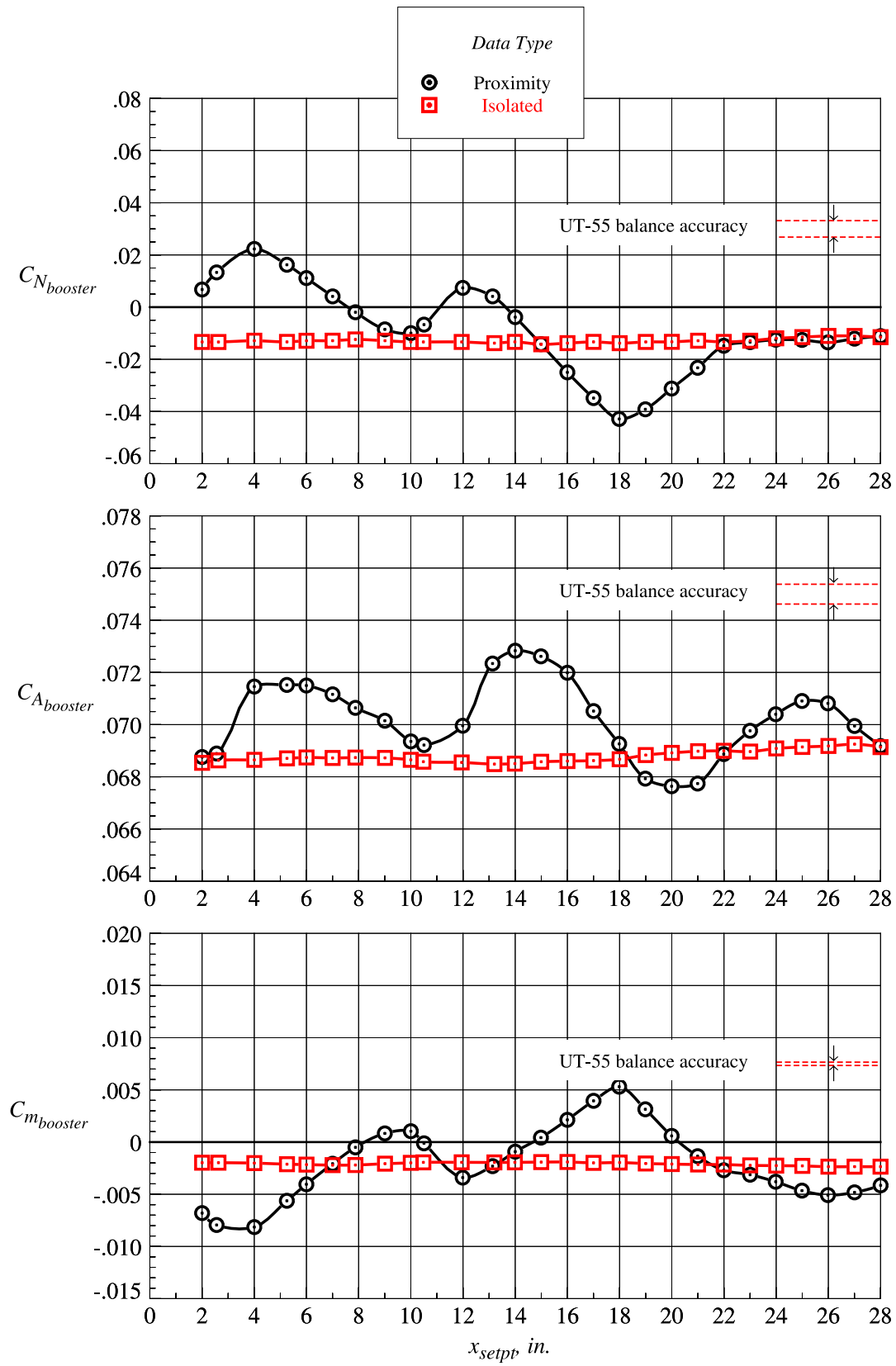
Figure 59. Continued.



(g)  $z_{setpt} = 3.938$  in.

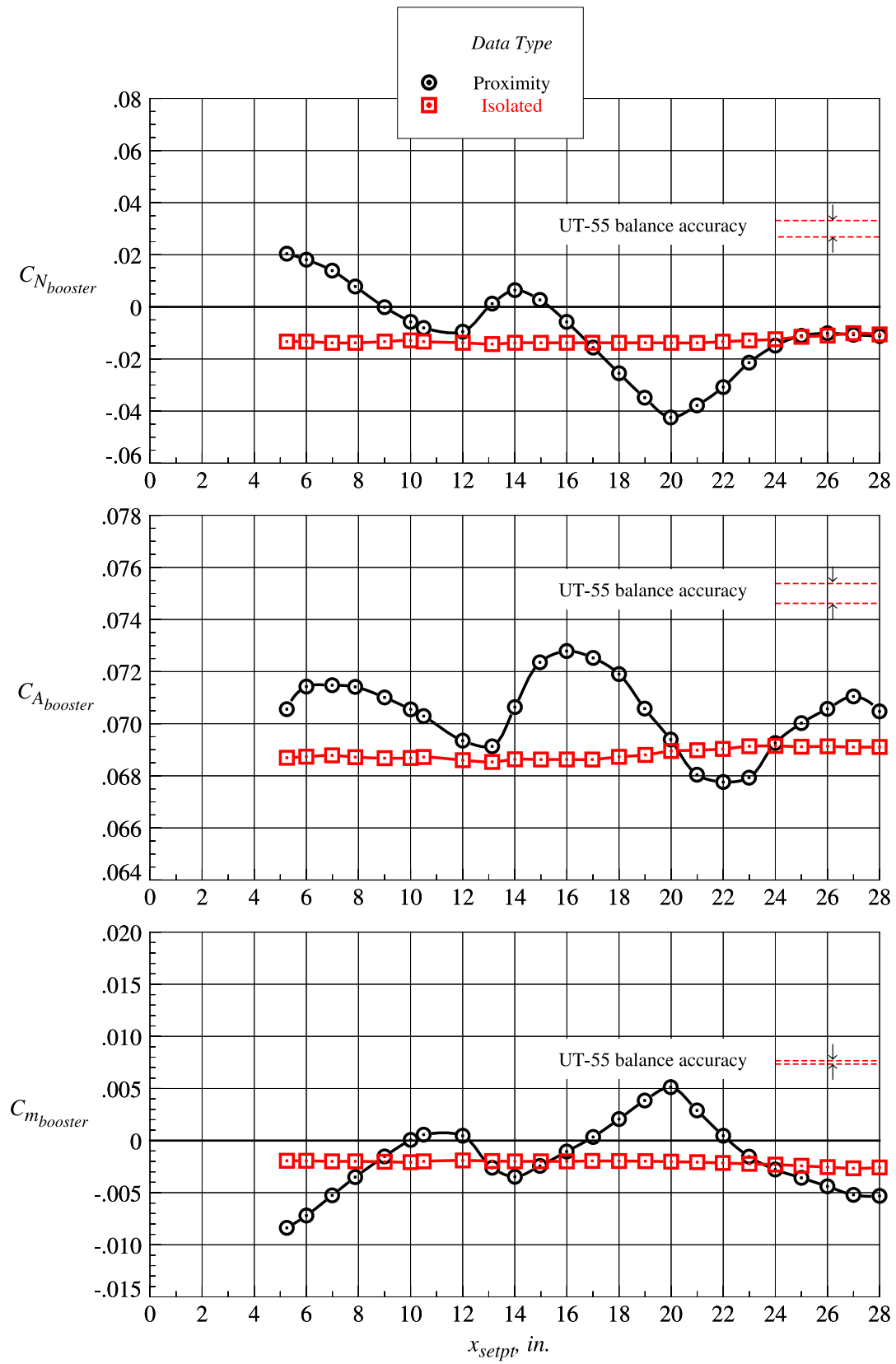
Figure 59. Continued.





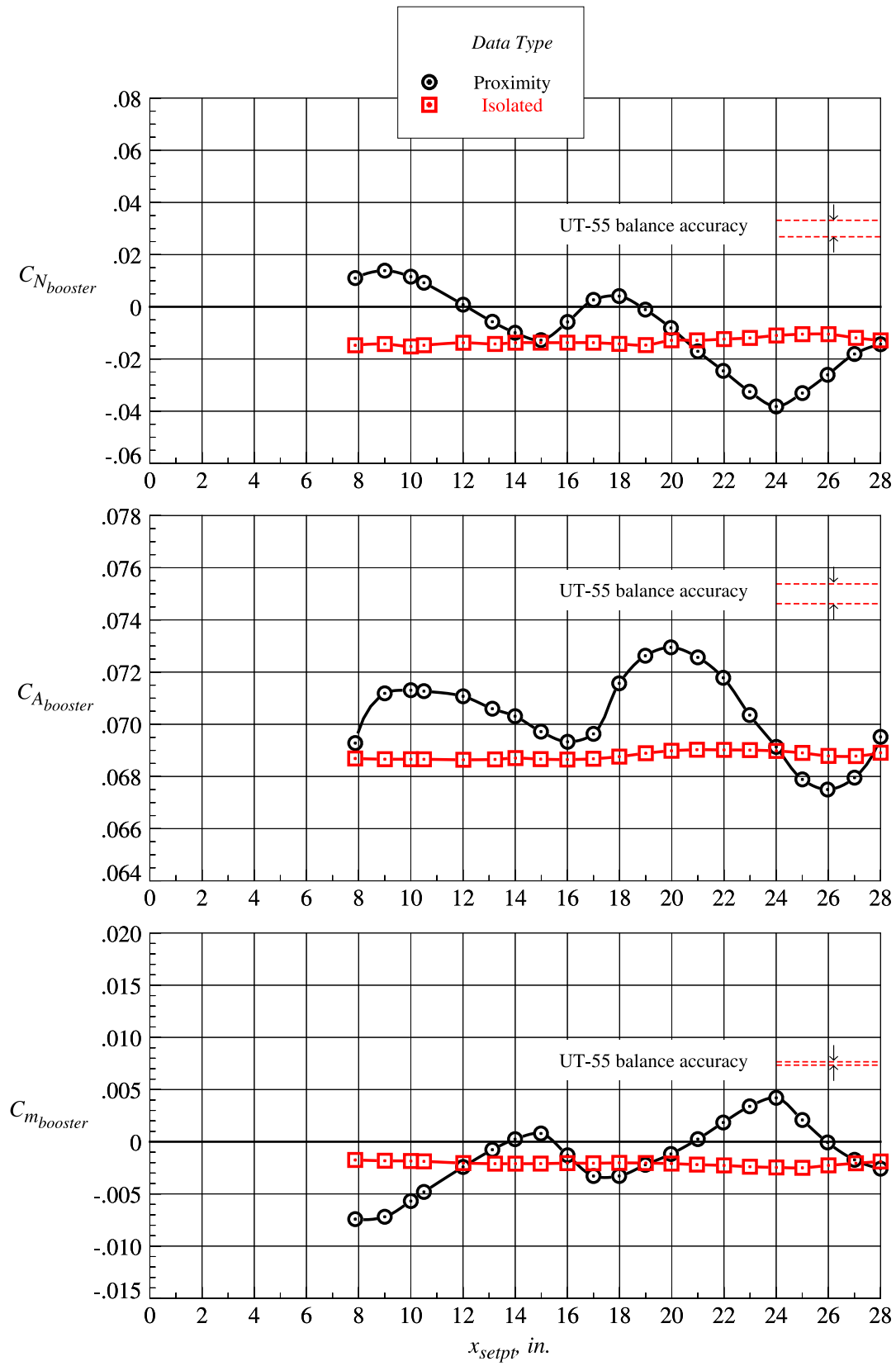
(h)  $z_{setpt} = 4.594$  in.

Figure 59. Continued.



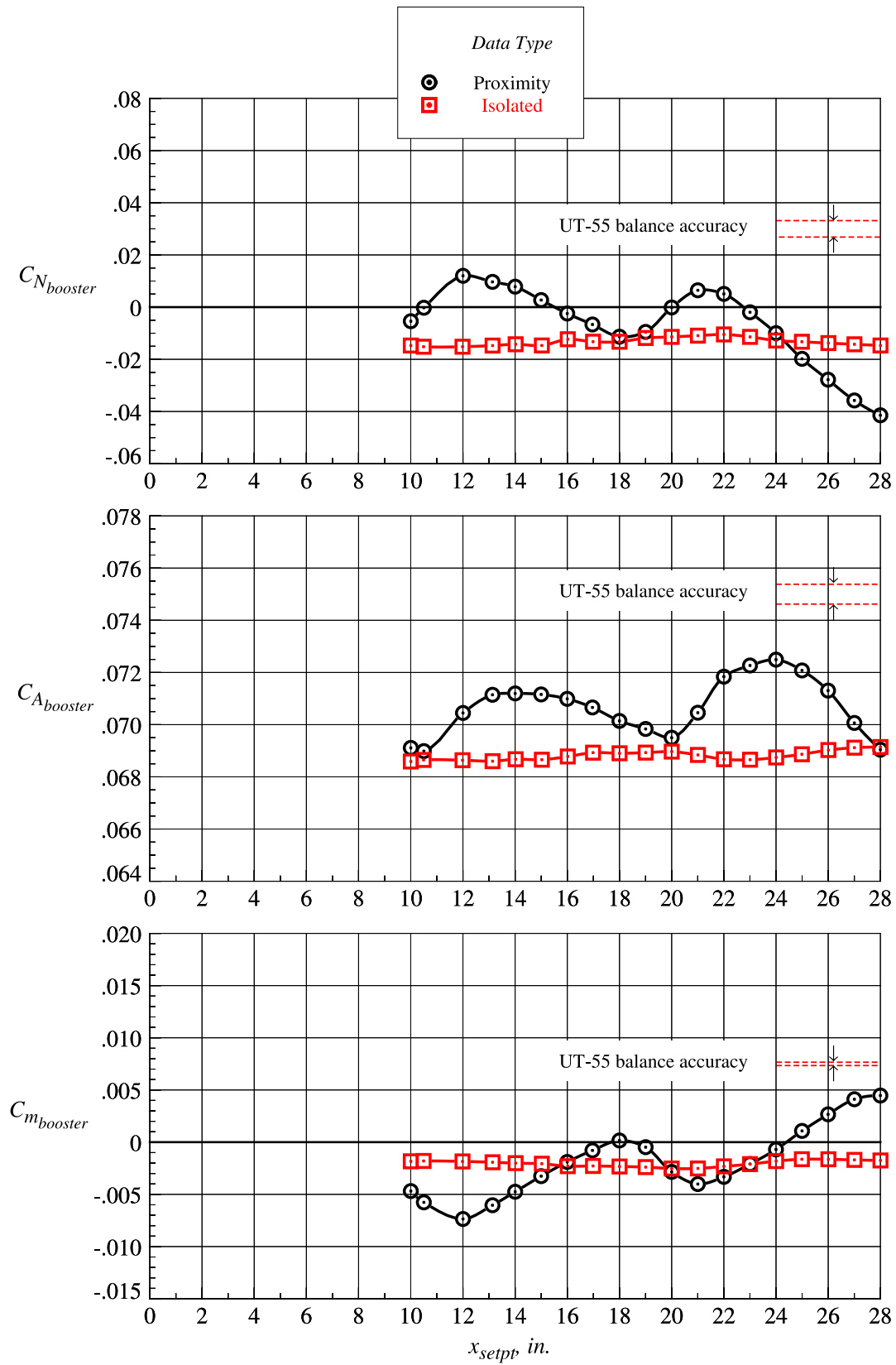
(i)  $z_{setpt} = 5.250$  in.

Figure 59. Continued.



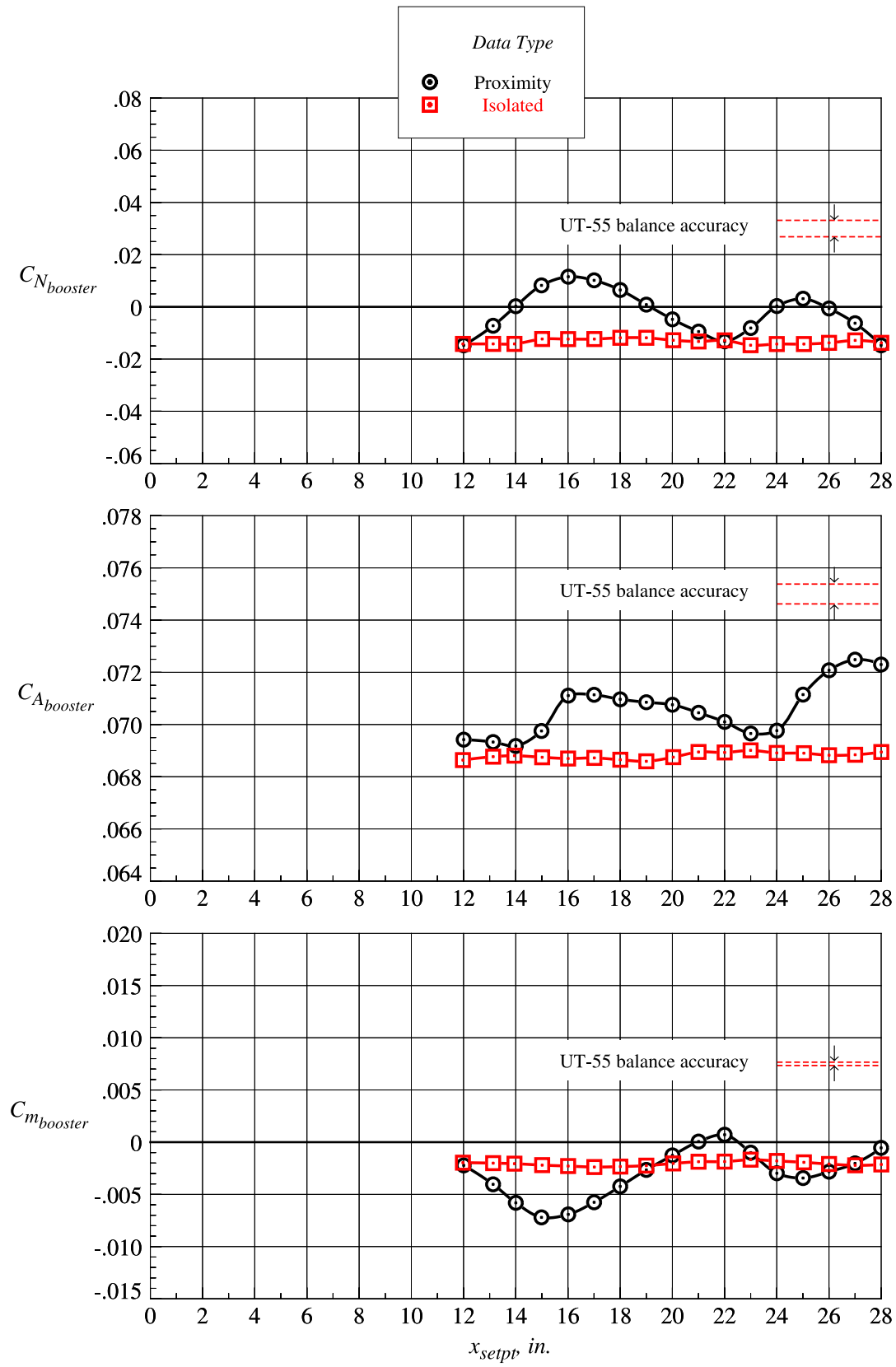
(j)  $z_{setpt} = 6.583$  in.

Figure 59. Continued.



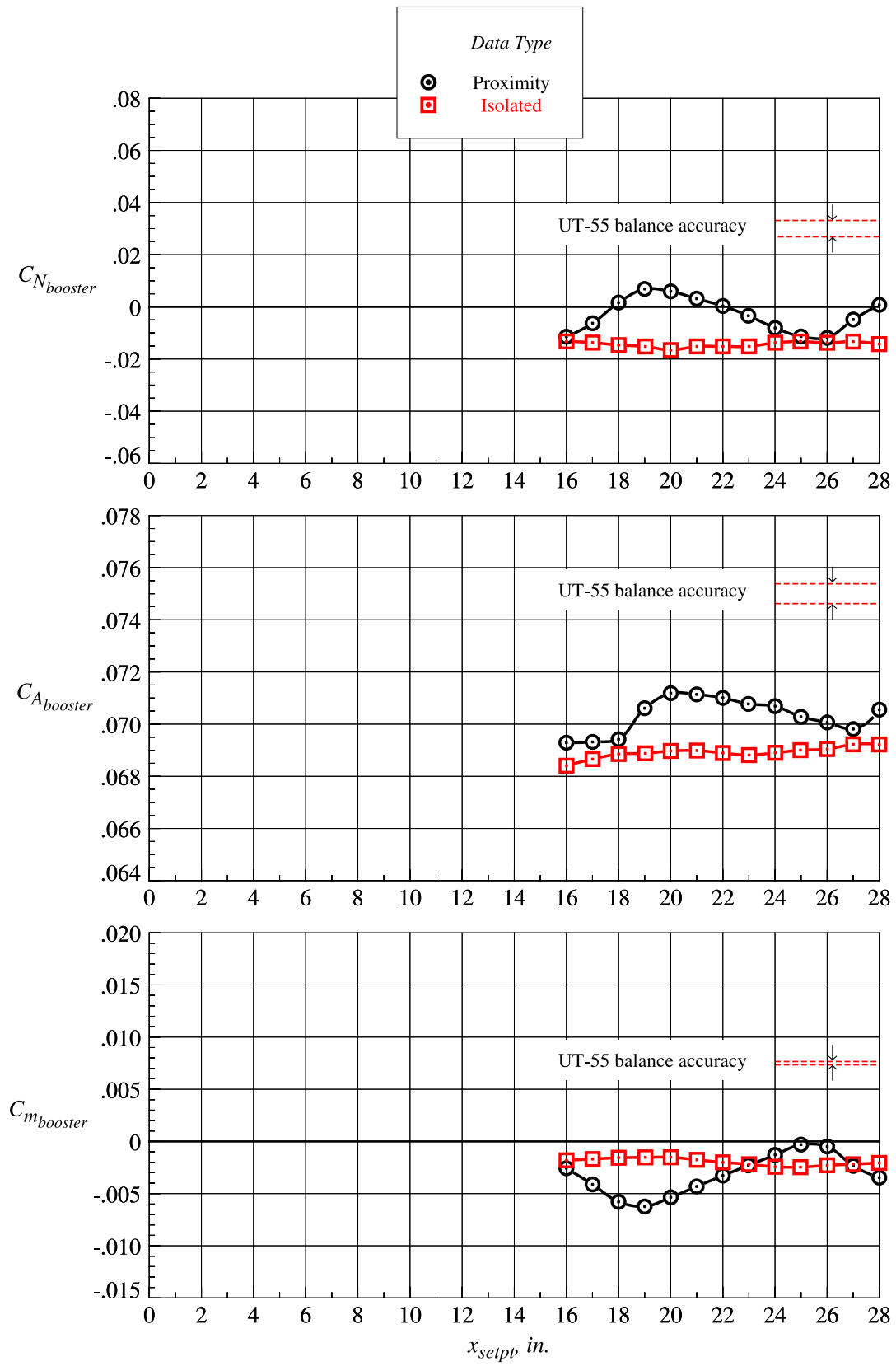
(k)  $z_{setpt} = 7.875$  in.

Figure 59. Continued.



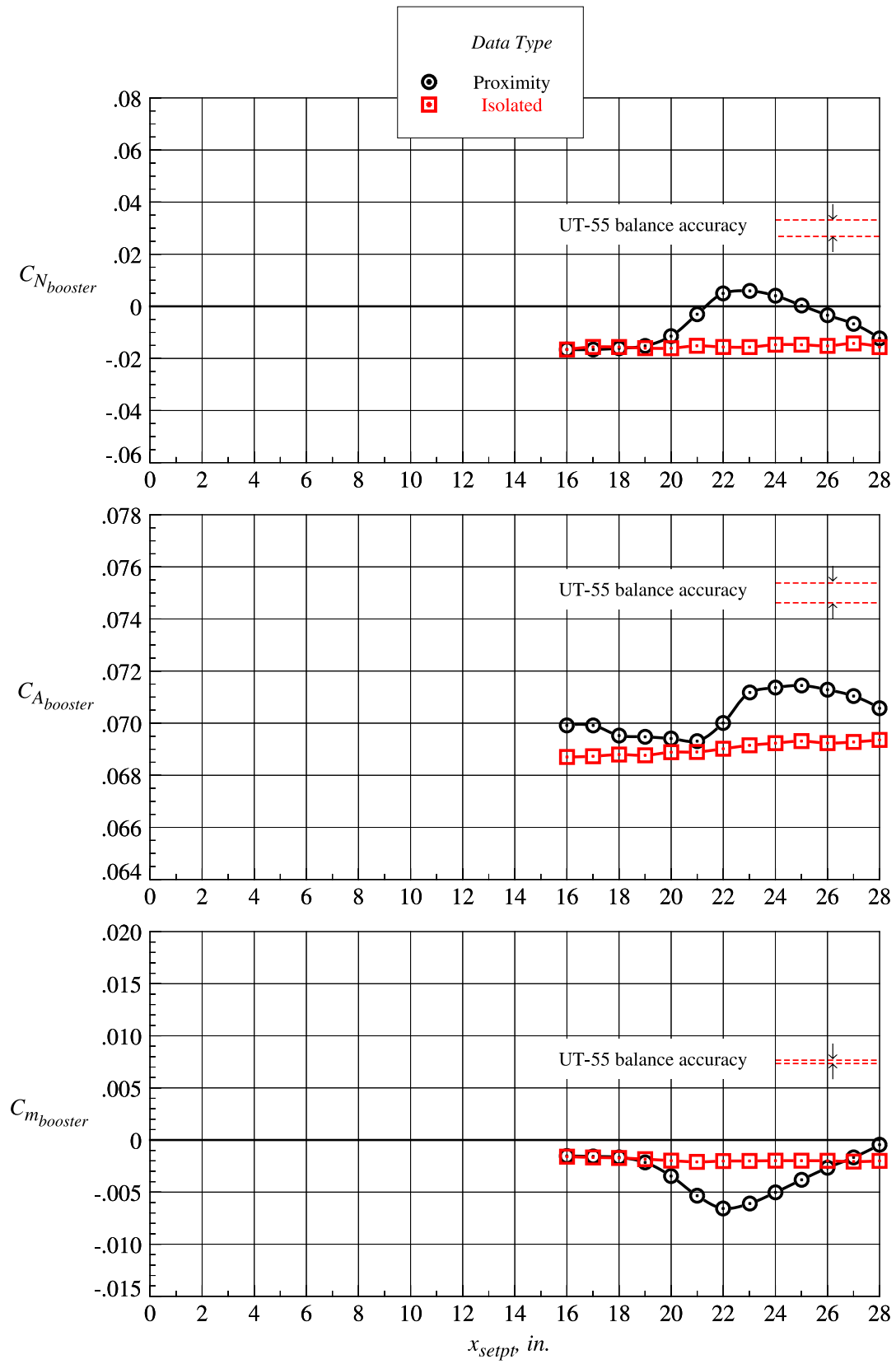
(l)  $z_{setpt} = 9.188$  in.

Figure 59. Continued.



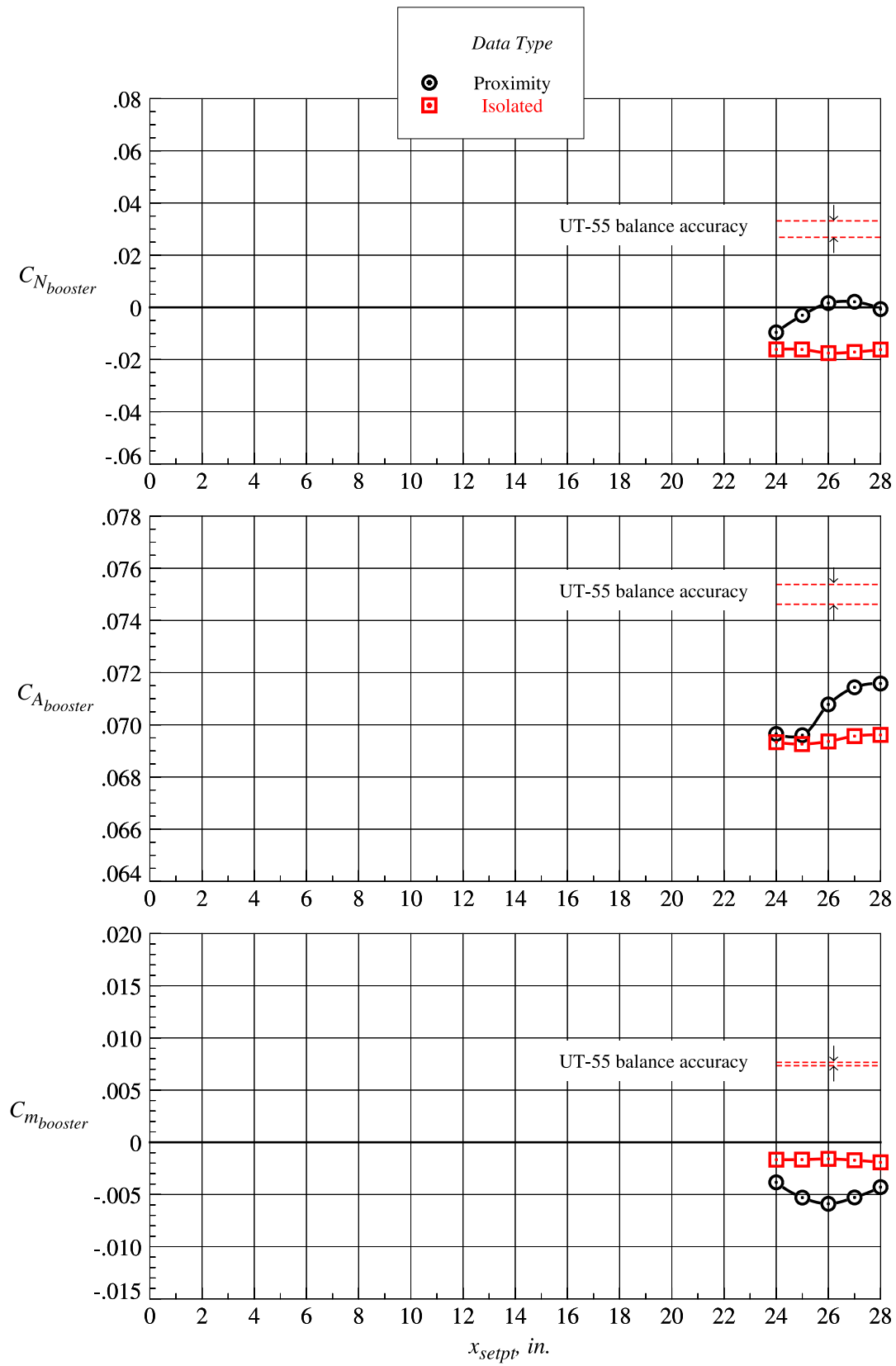
(m)  $z_{setpt} = 10.500$  in.

Figure 59. Continued.



(n)  $z_{setpt} = 11.810$  in.

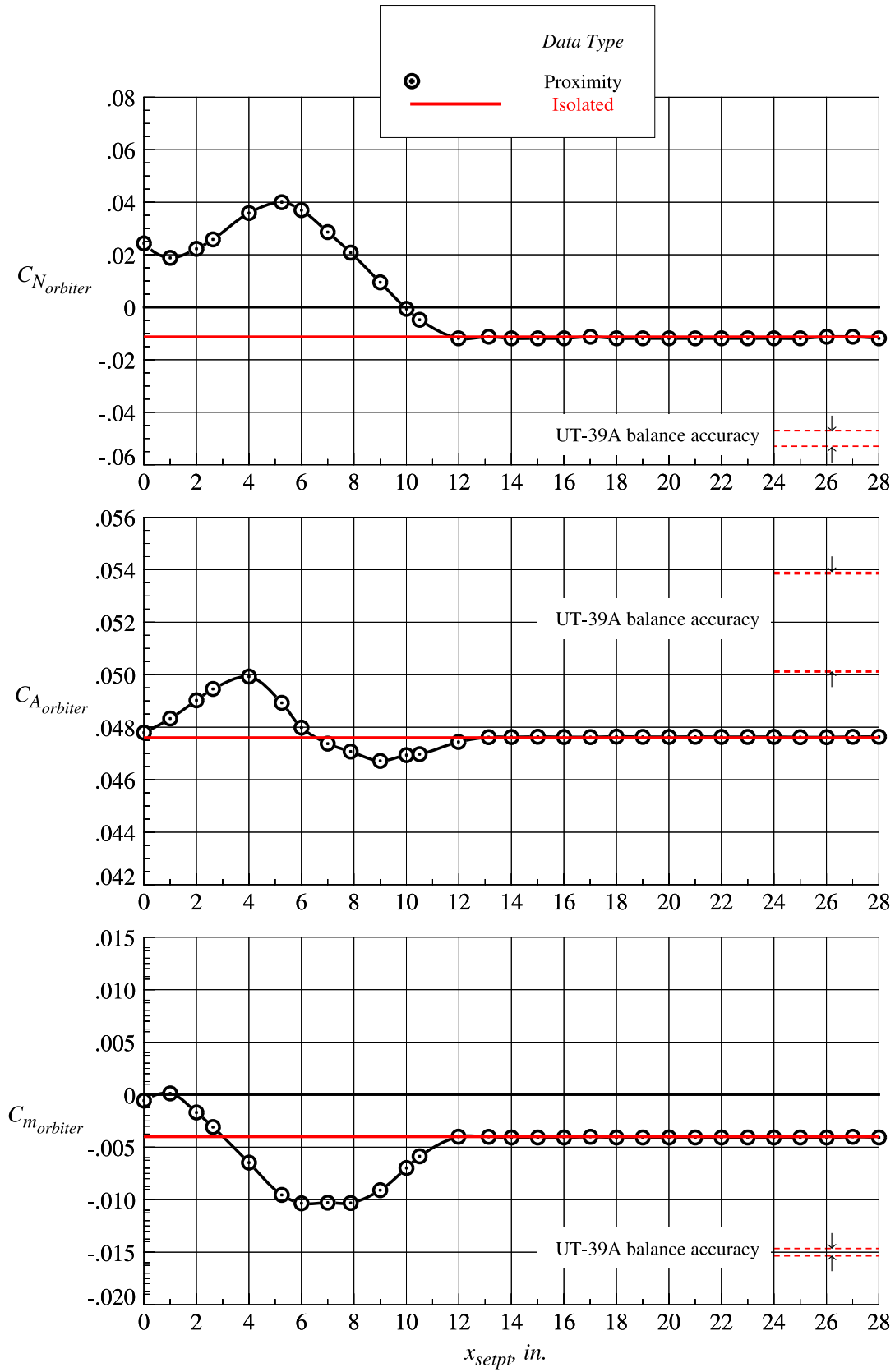
Figure 59. Continued.



(o)  $z_{setpt} = 13.130$  in.

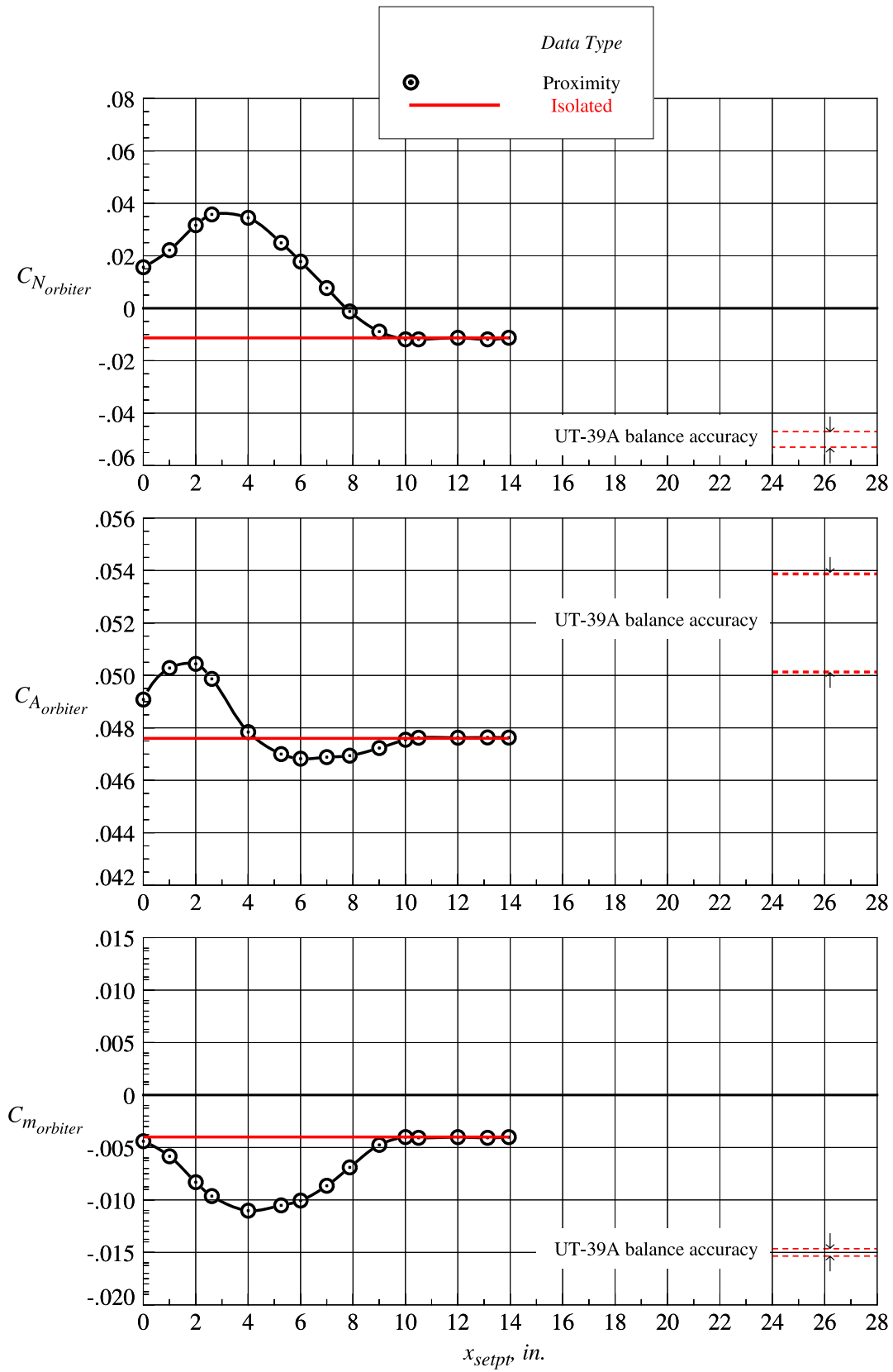
Figure 59. Concluded.





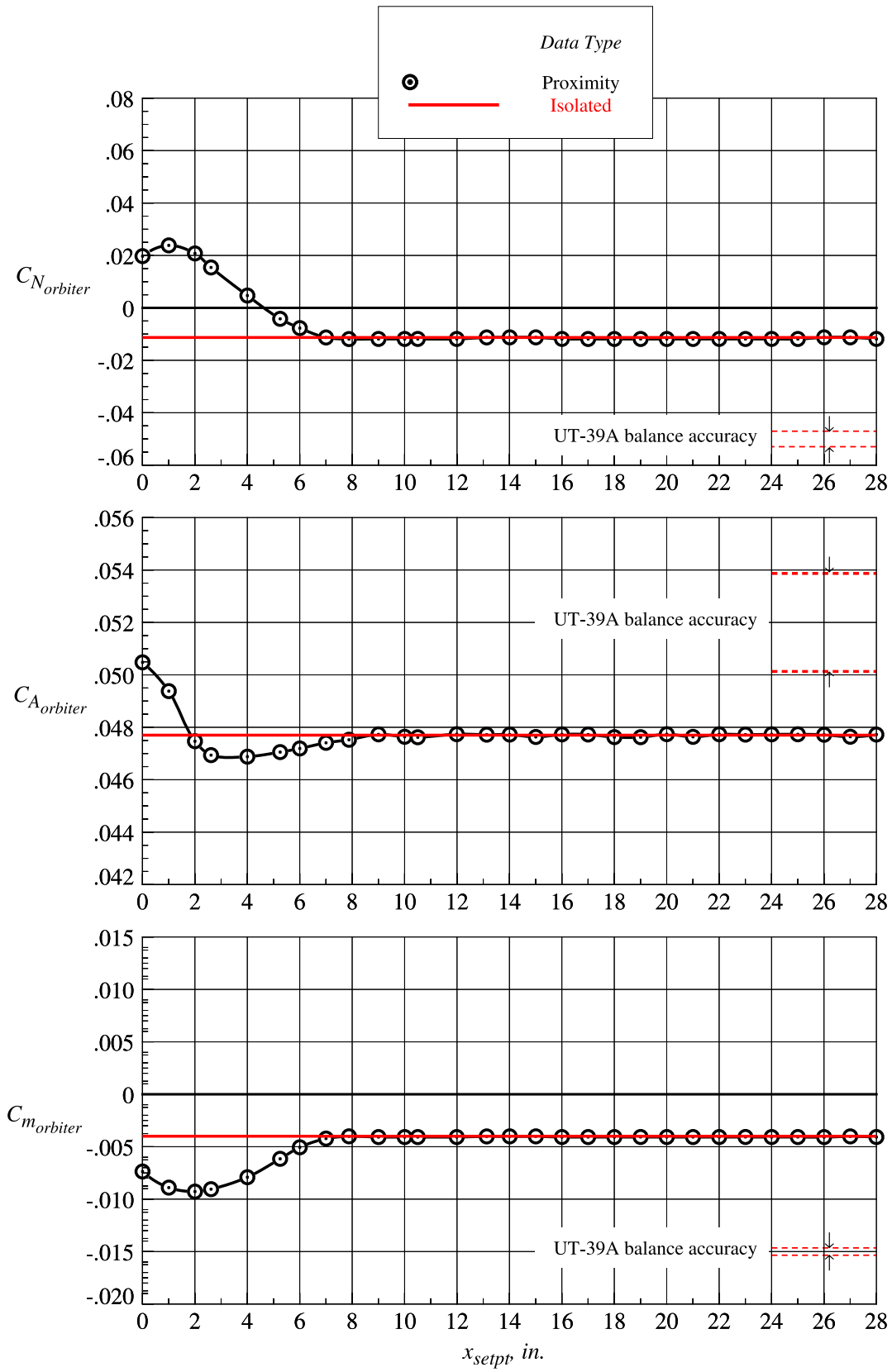
(a)  $z_{setpt} = 0$  in.

Figure 60. Orbiter proximity and isolated aerodynamic characteristics at Mach = 4.5 and  $\Delta\alpha = 0^\circ$ .



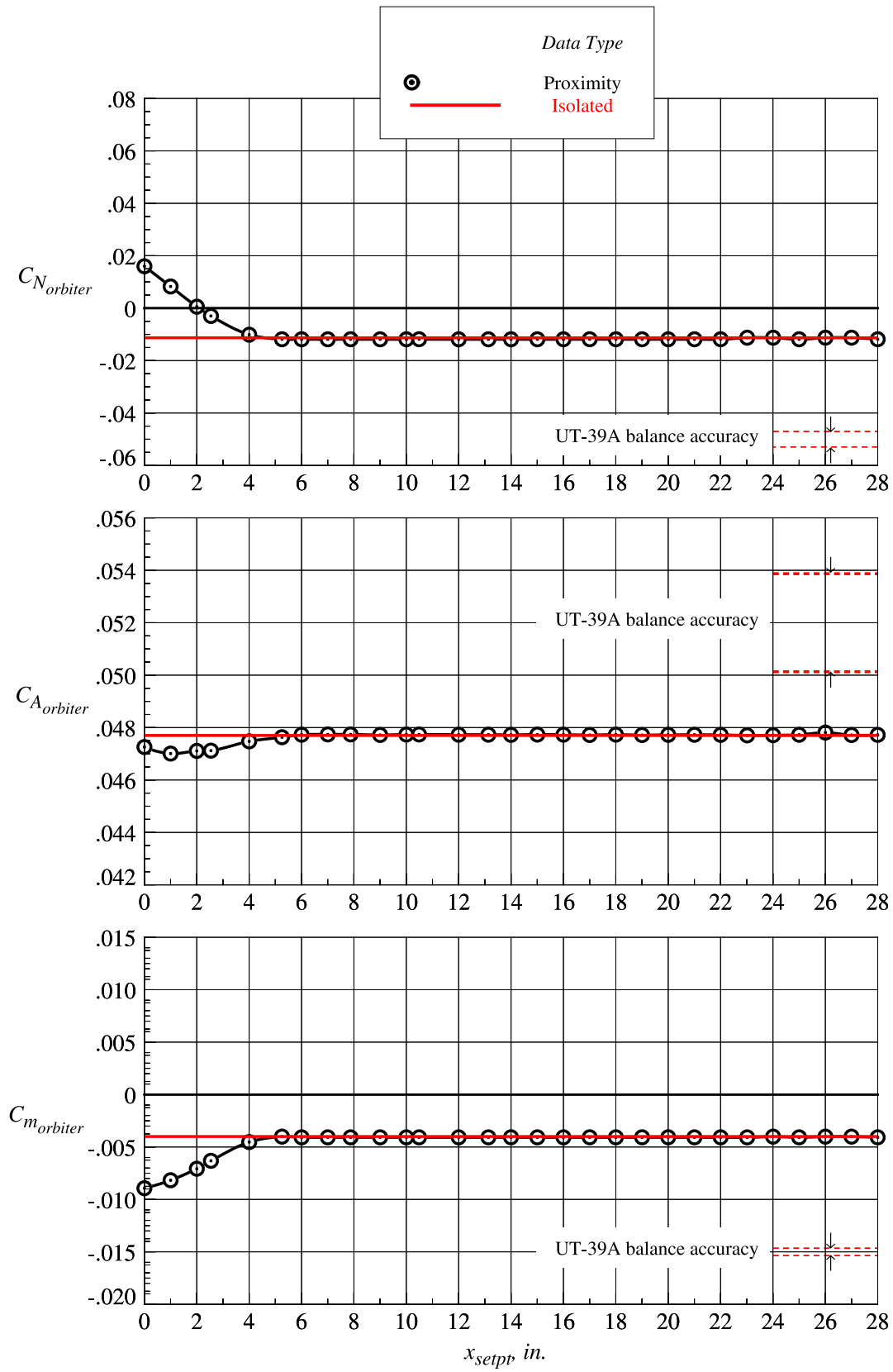
(b)  $z_{setpt} = 0.656$  in.

Figure 60. Continued.



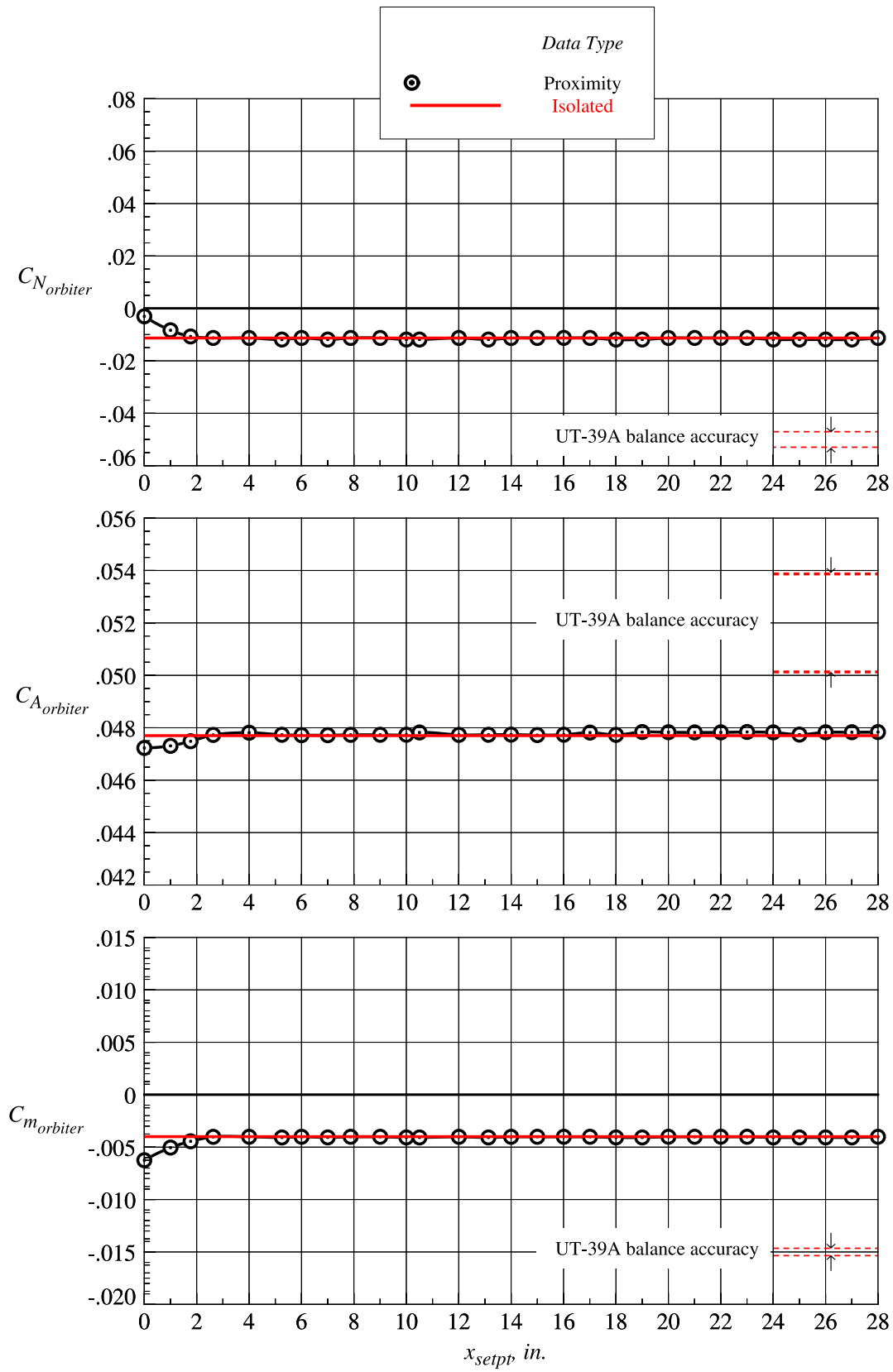
(c)  $z_{setpt} = 1.313$  in.

Figure 60. Continued.



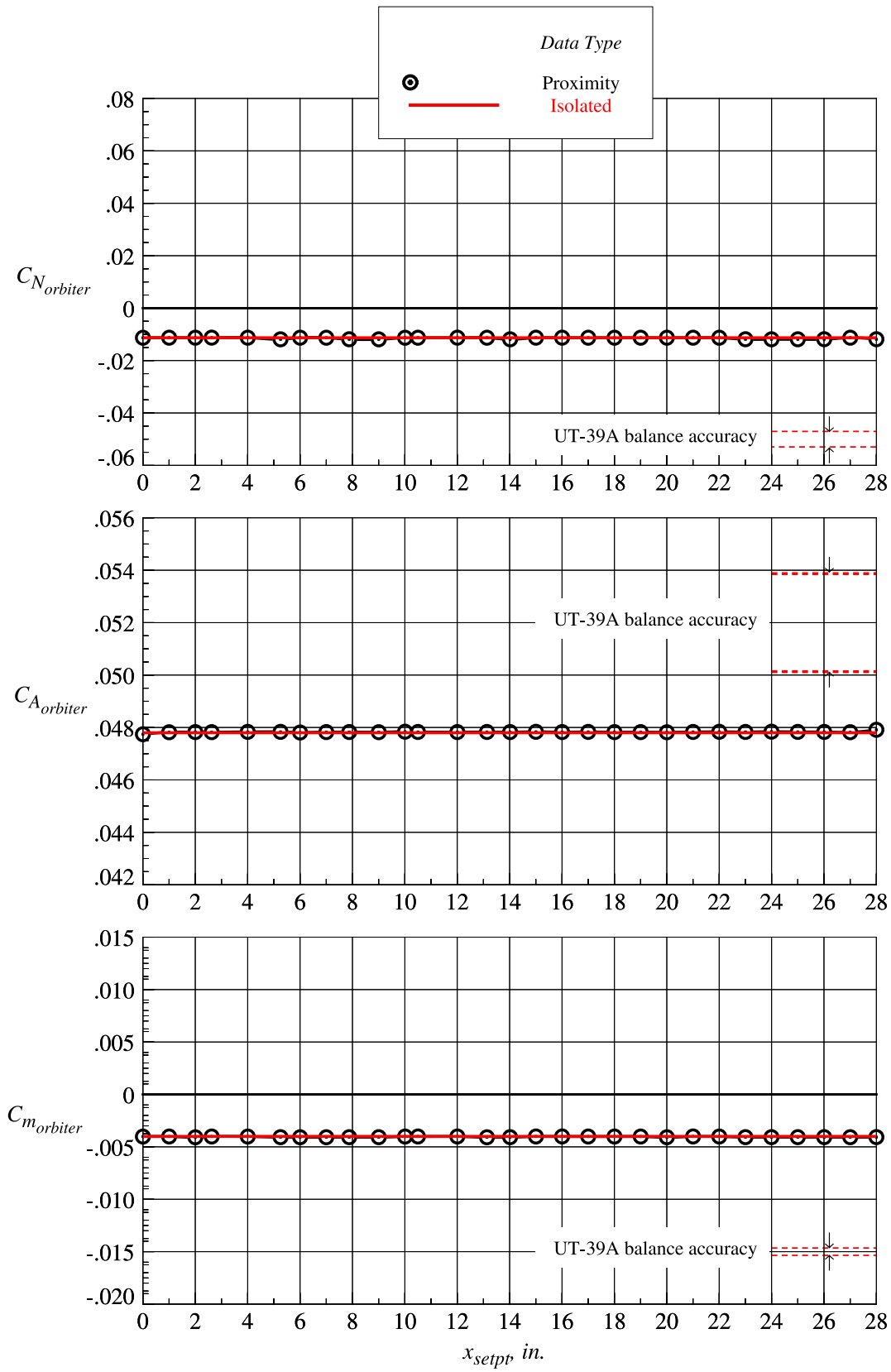
(d)  $z_{setpt} = 1.969$  in.

Figure 60. Continued.



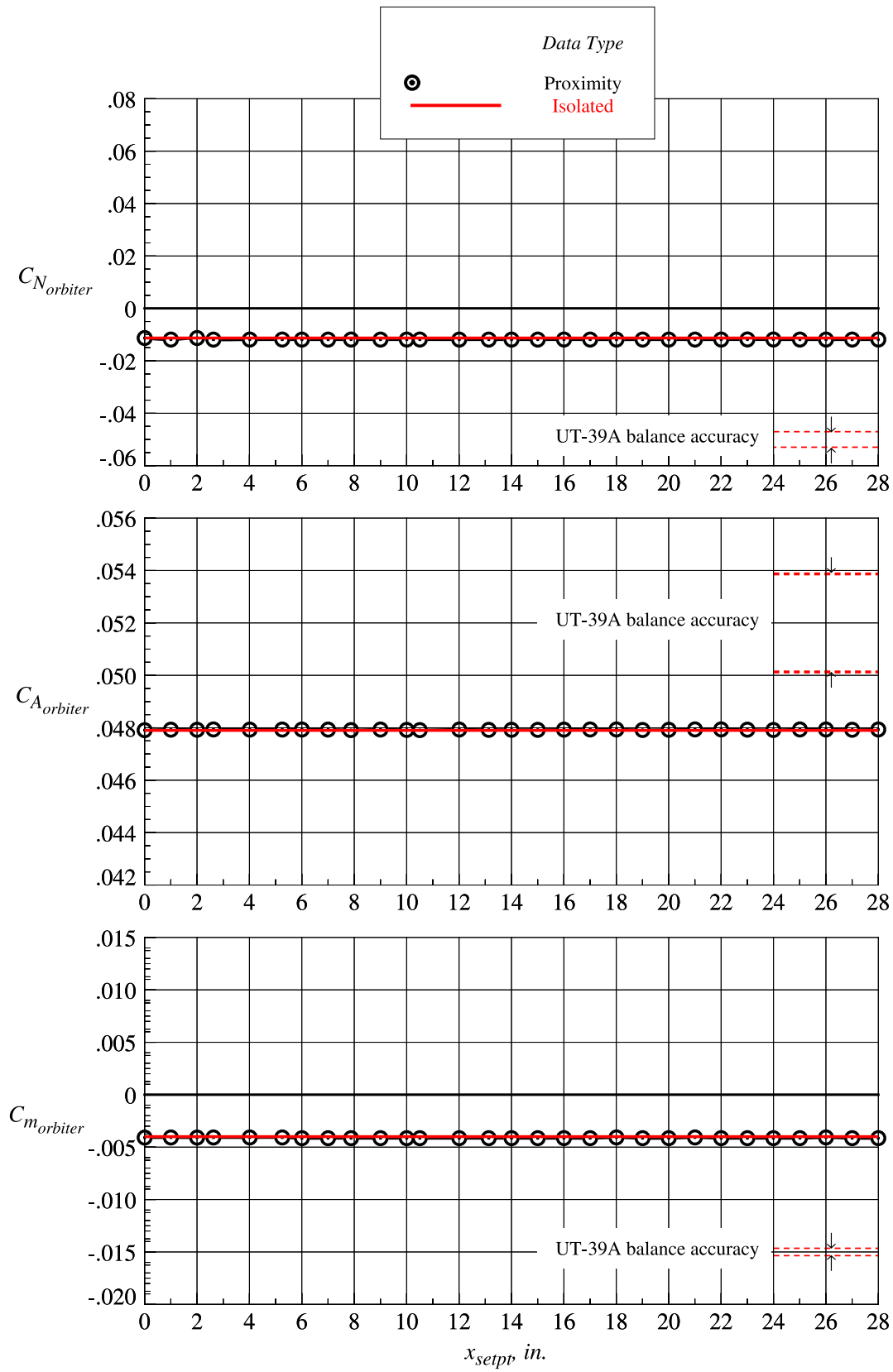
(e)  $z_{setpt} = 2.625$  in.

Figure 60. Continued.



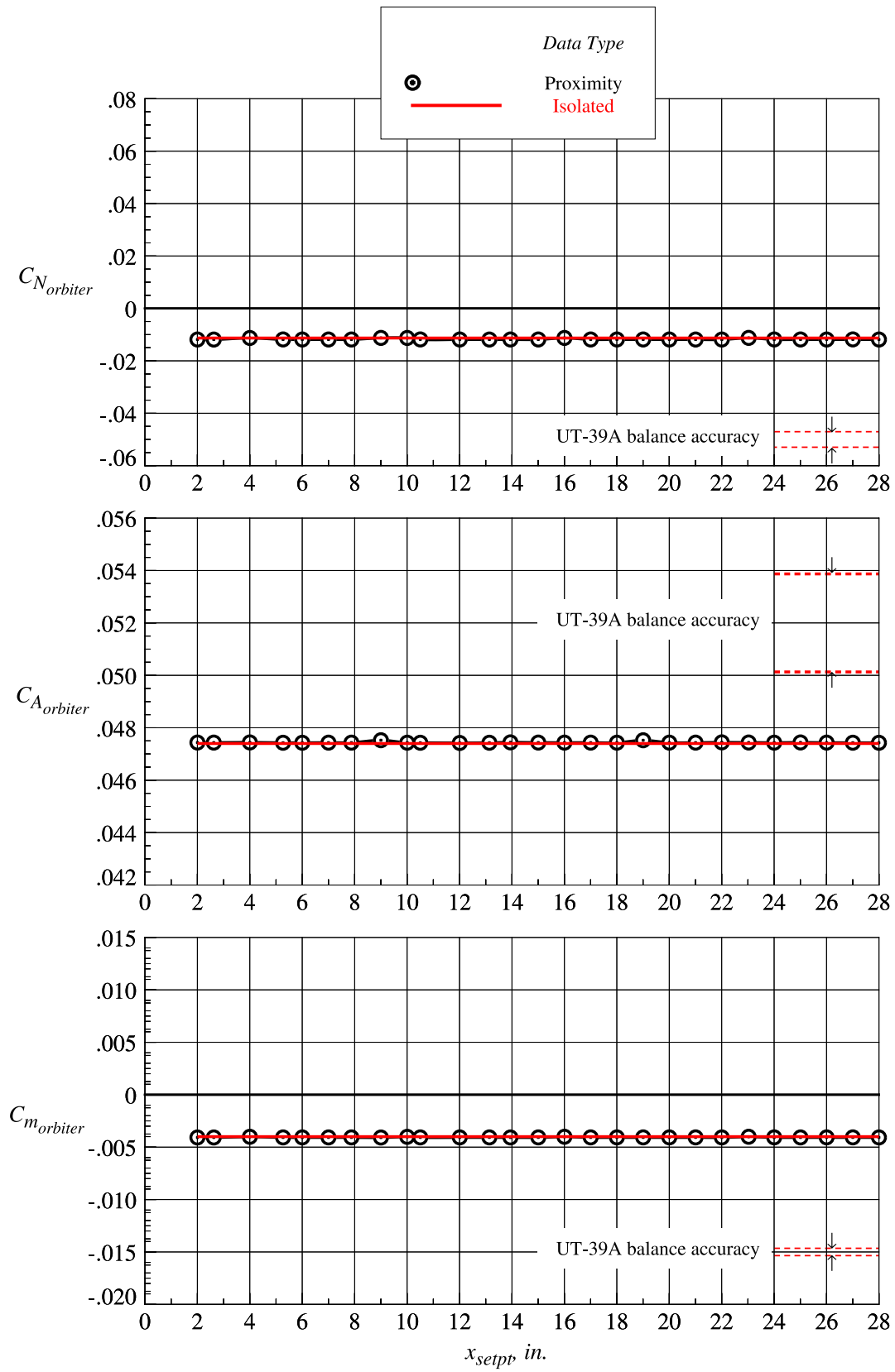
(f)  $z_{setpt} = 3.281$  in.

Figure 60. Continued.



(g)  $z_{setpt} = 3.938$  in.

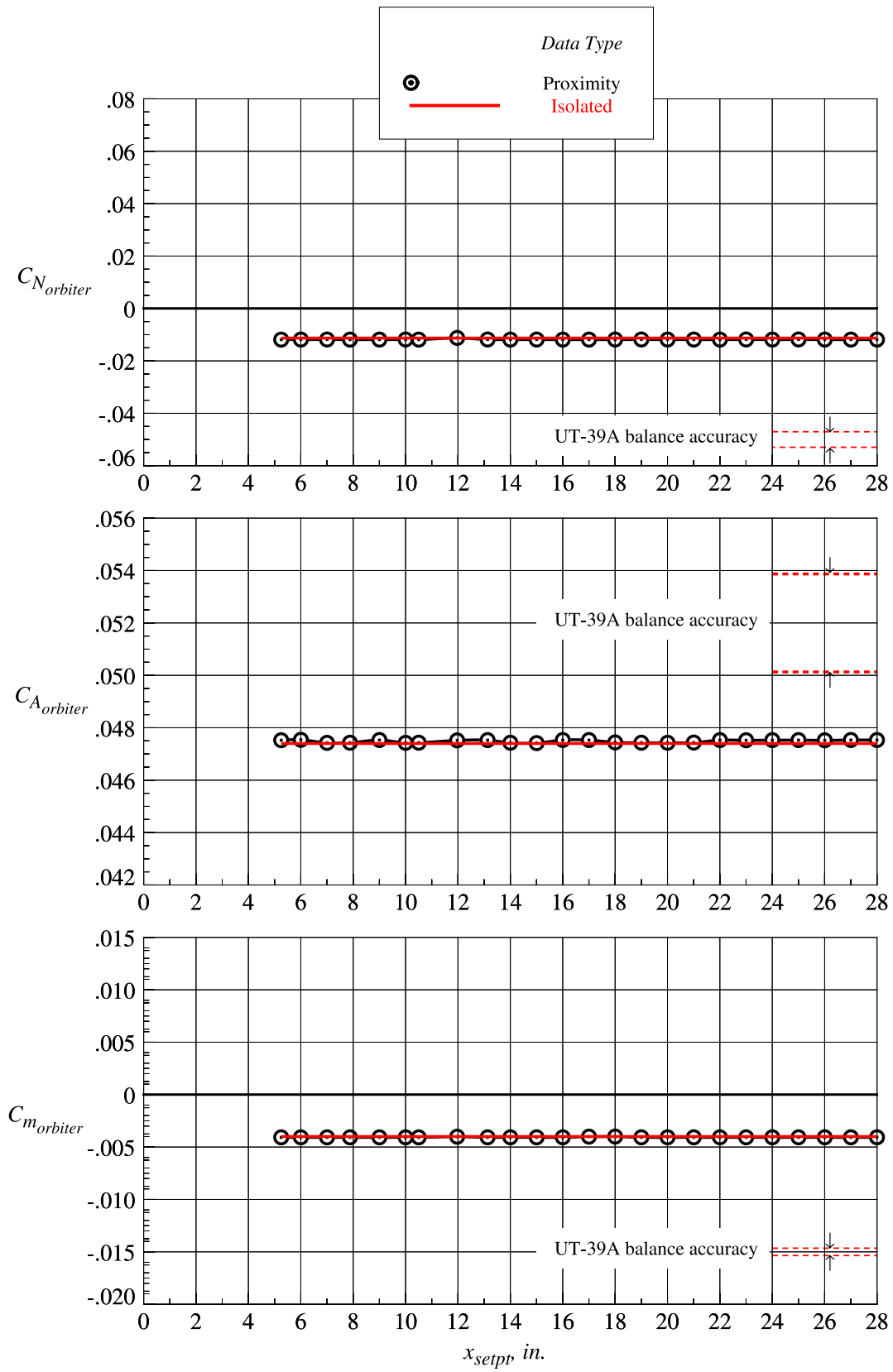
Figure 60. Continued.



(h)  $z_{setpt} = 4.594$  in.

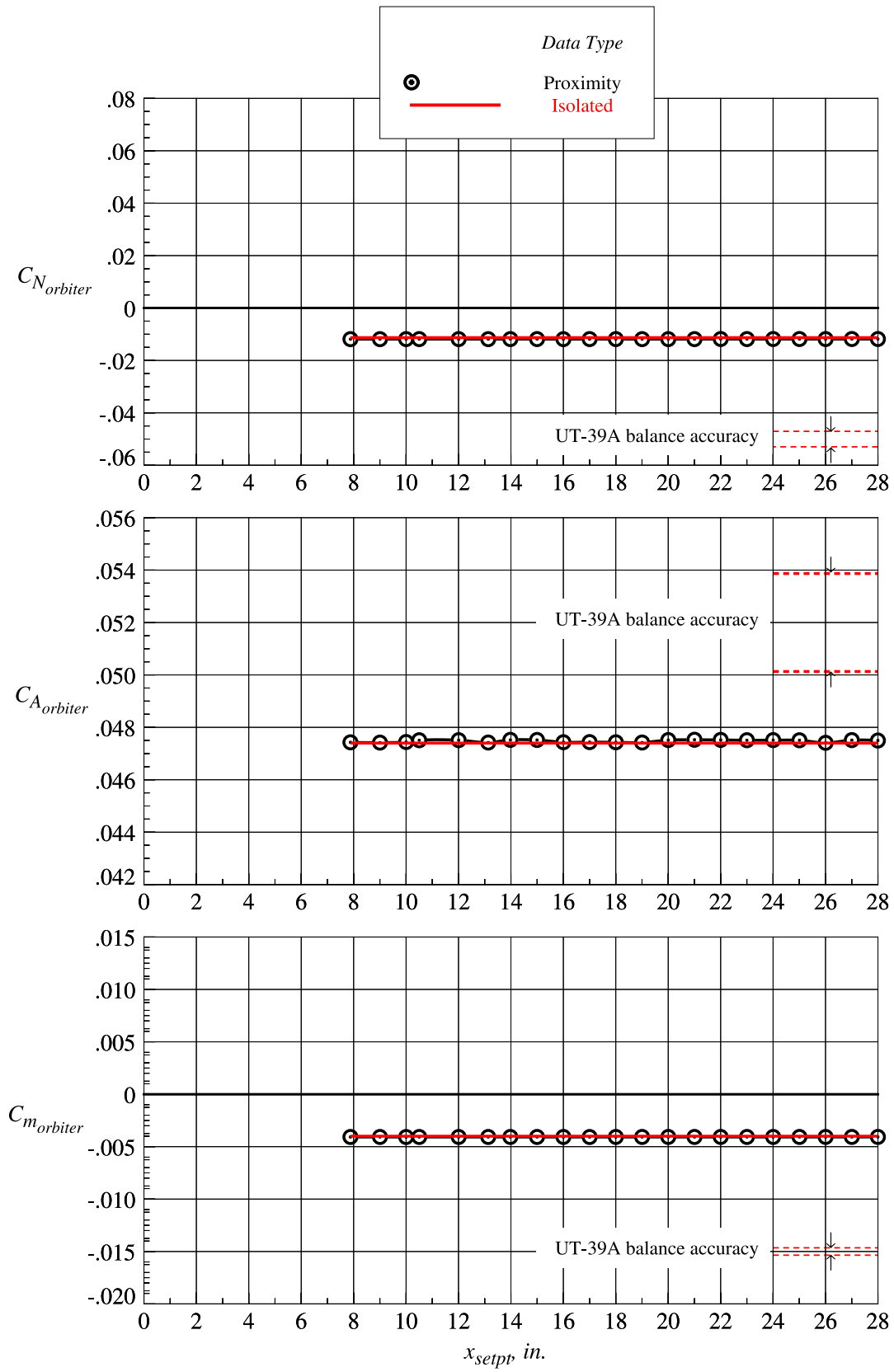
Figure 60. Continued.





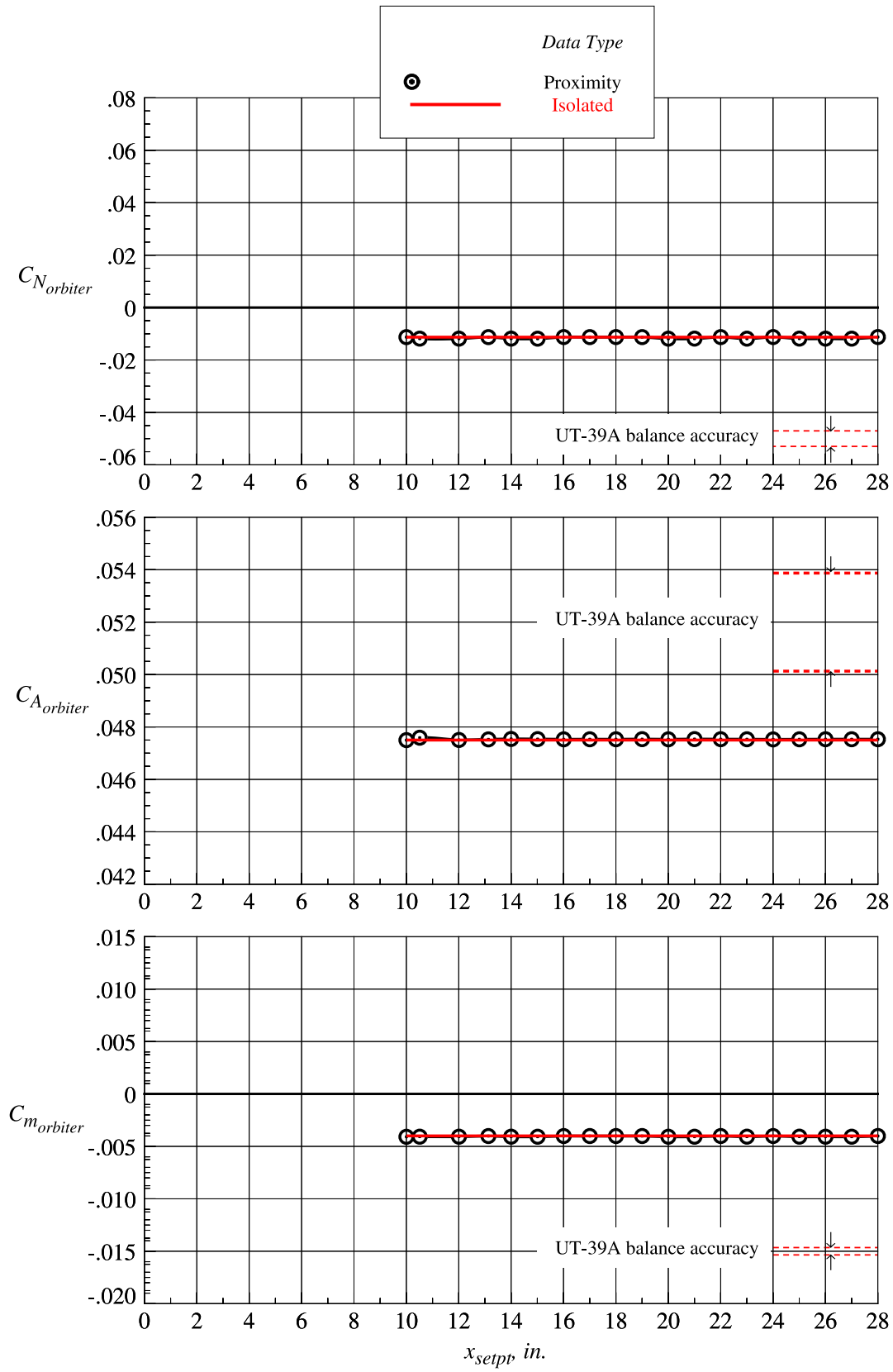
(i)  $z_{setpt} = 5.250$  in.

Figure 60. Continued.



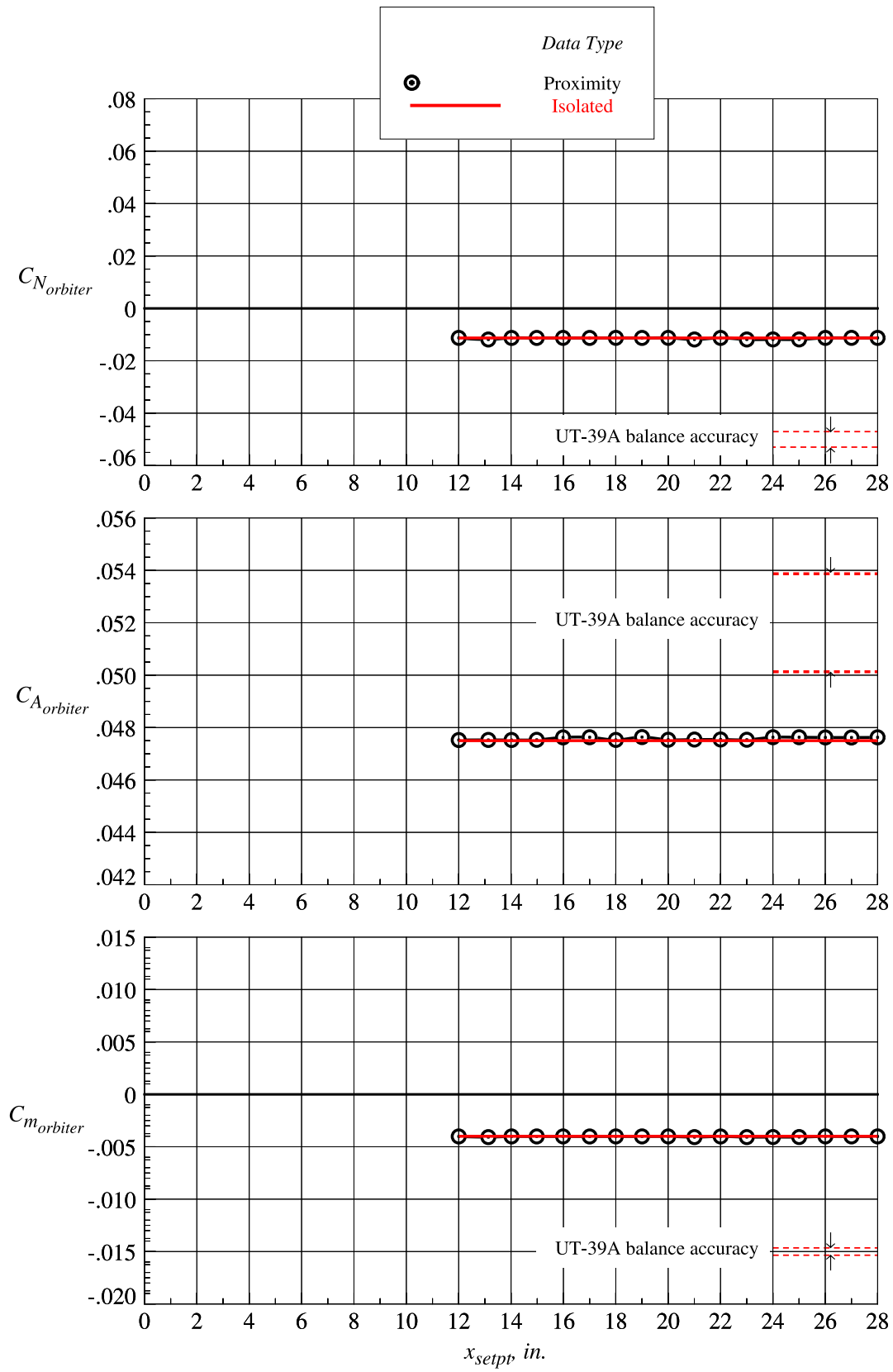
(j)  $z_{setpt} = 6.583$  in.

Figure 60. Continued.



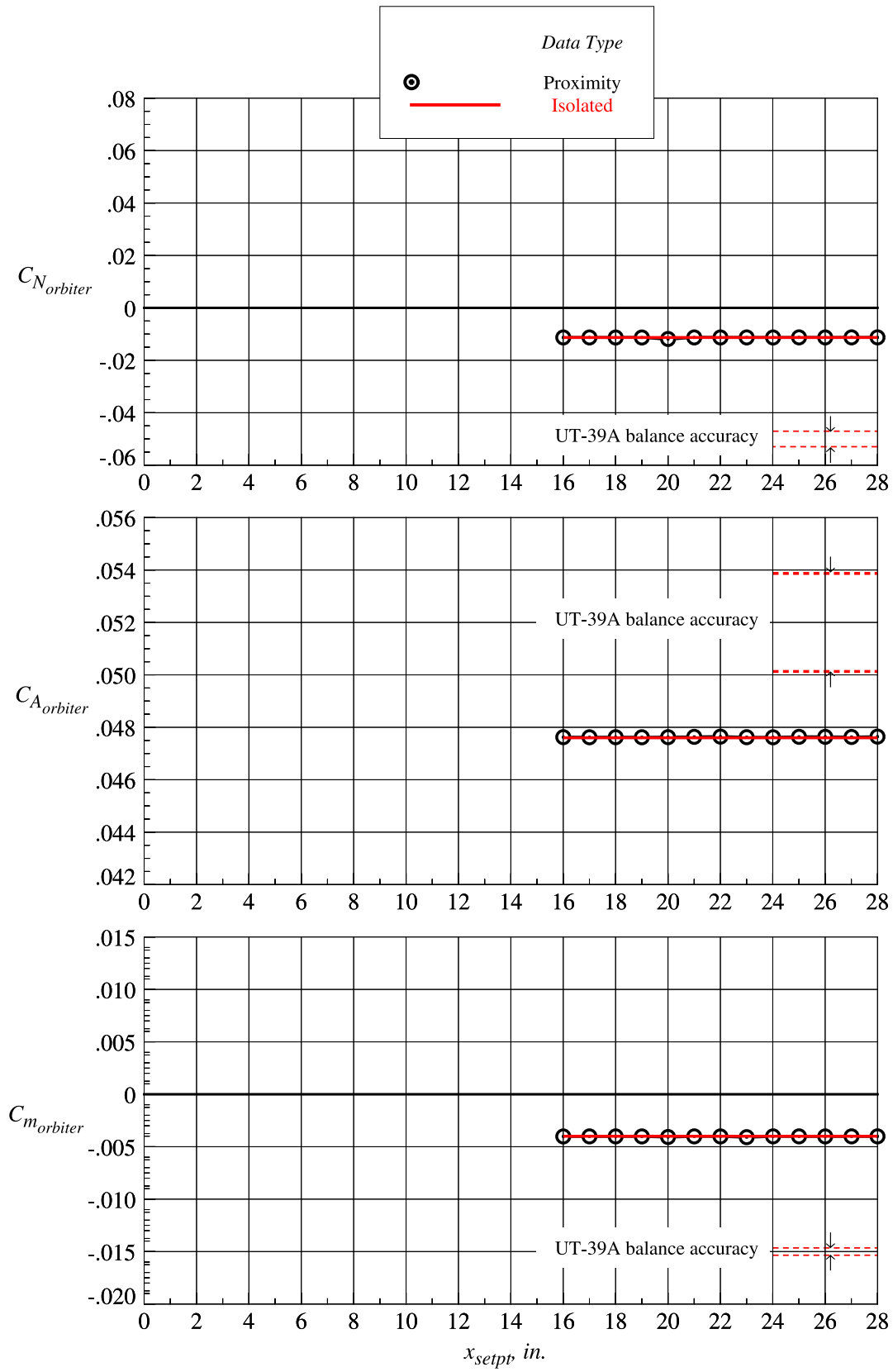
(k)  $z_{setpt} = 7.875$  in.

Figure 60. Continued.



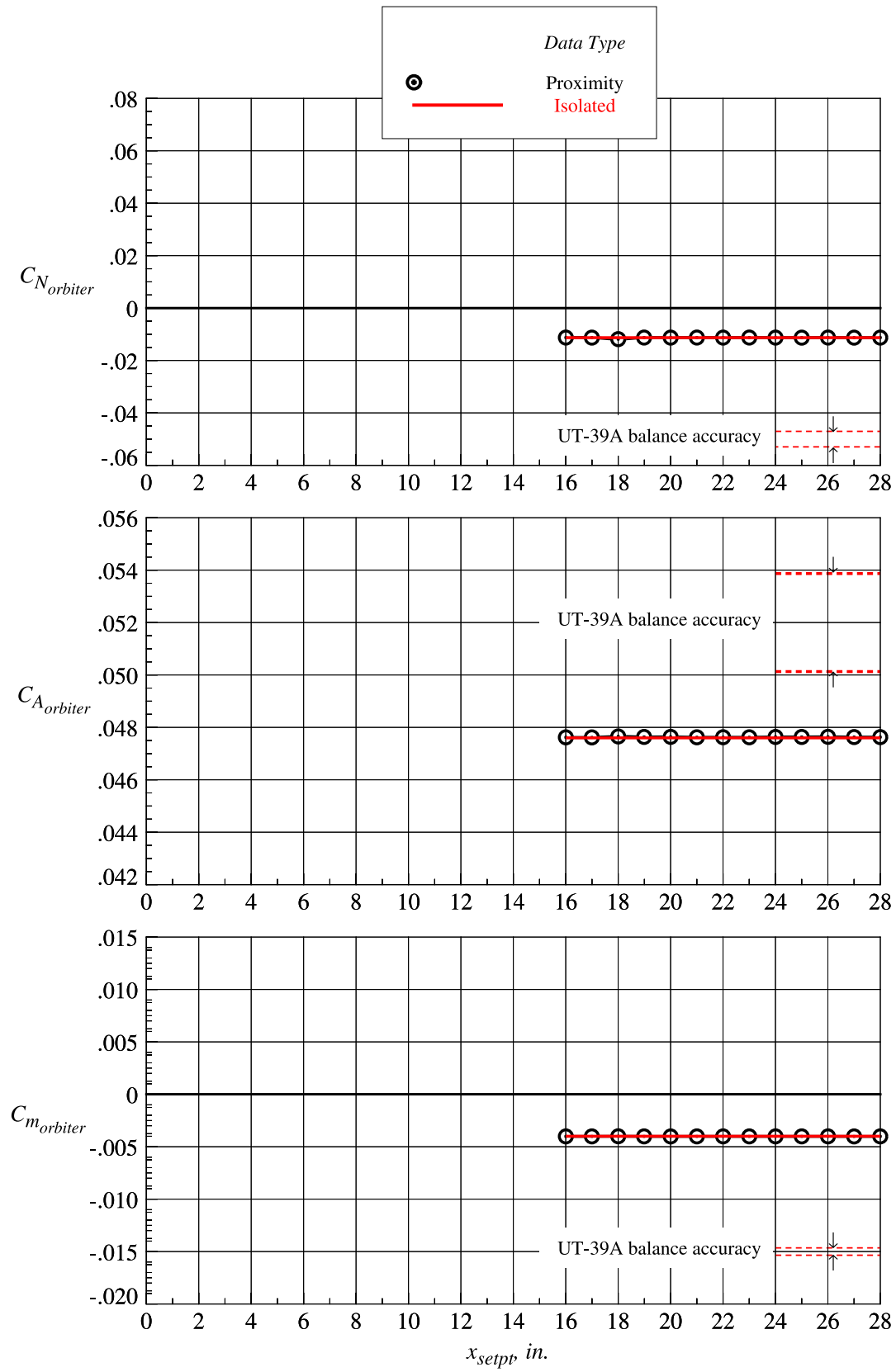
(l)  $z_{setpt} = 9.188$  in.

Figure 60. Continued.



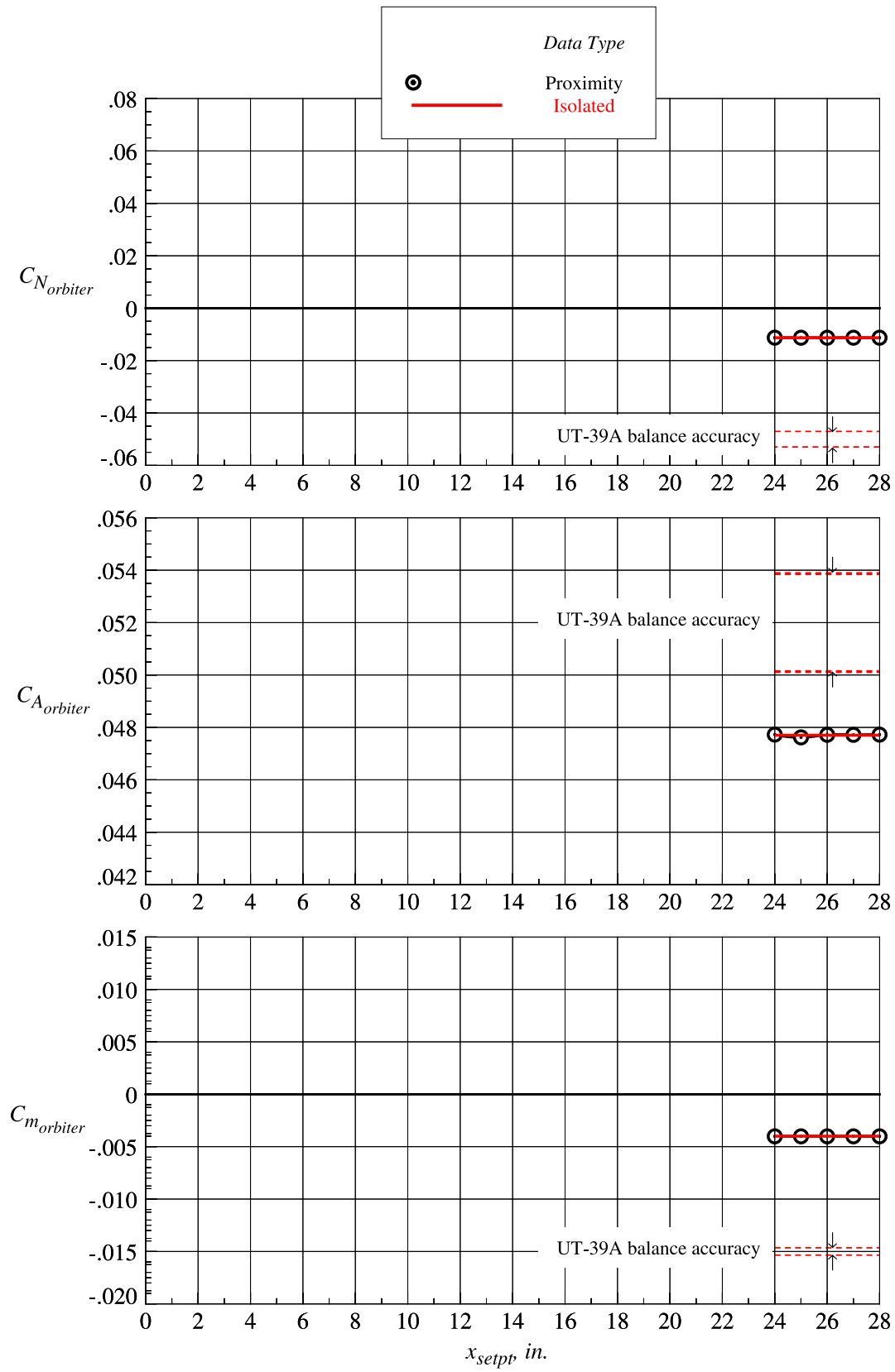
(m)  $z_{setpt} = 10.500$  in.

Figure 60. Continued.



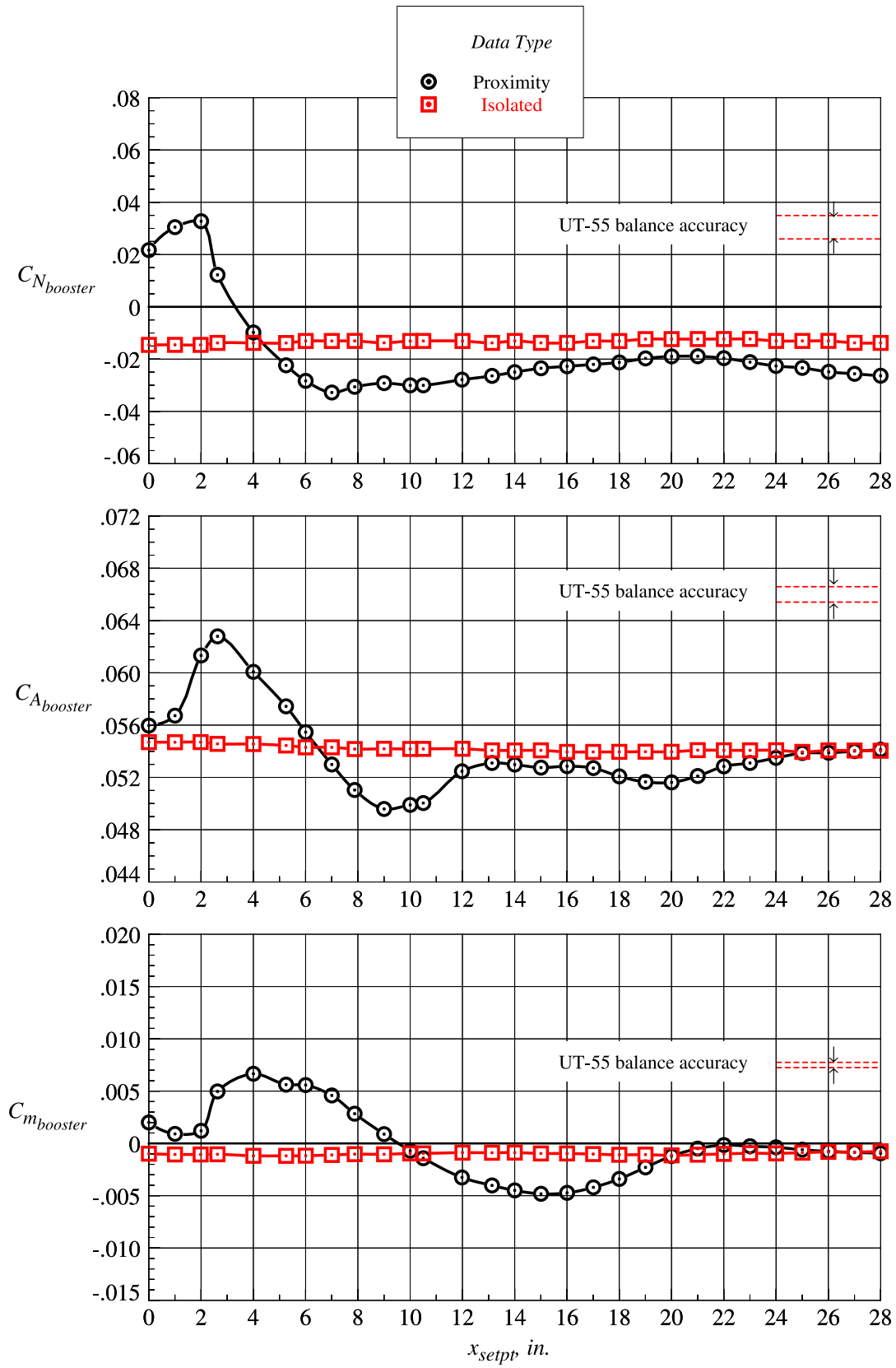
(n)  $z_{setpt} = 11.810$  in.

Figure 60. Continued.



(o)  $z_{setpt} = 13.130$  in.

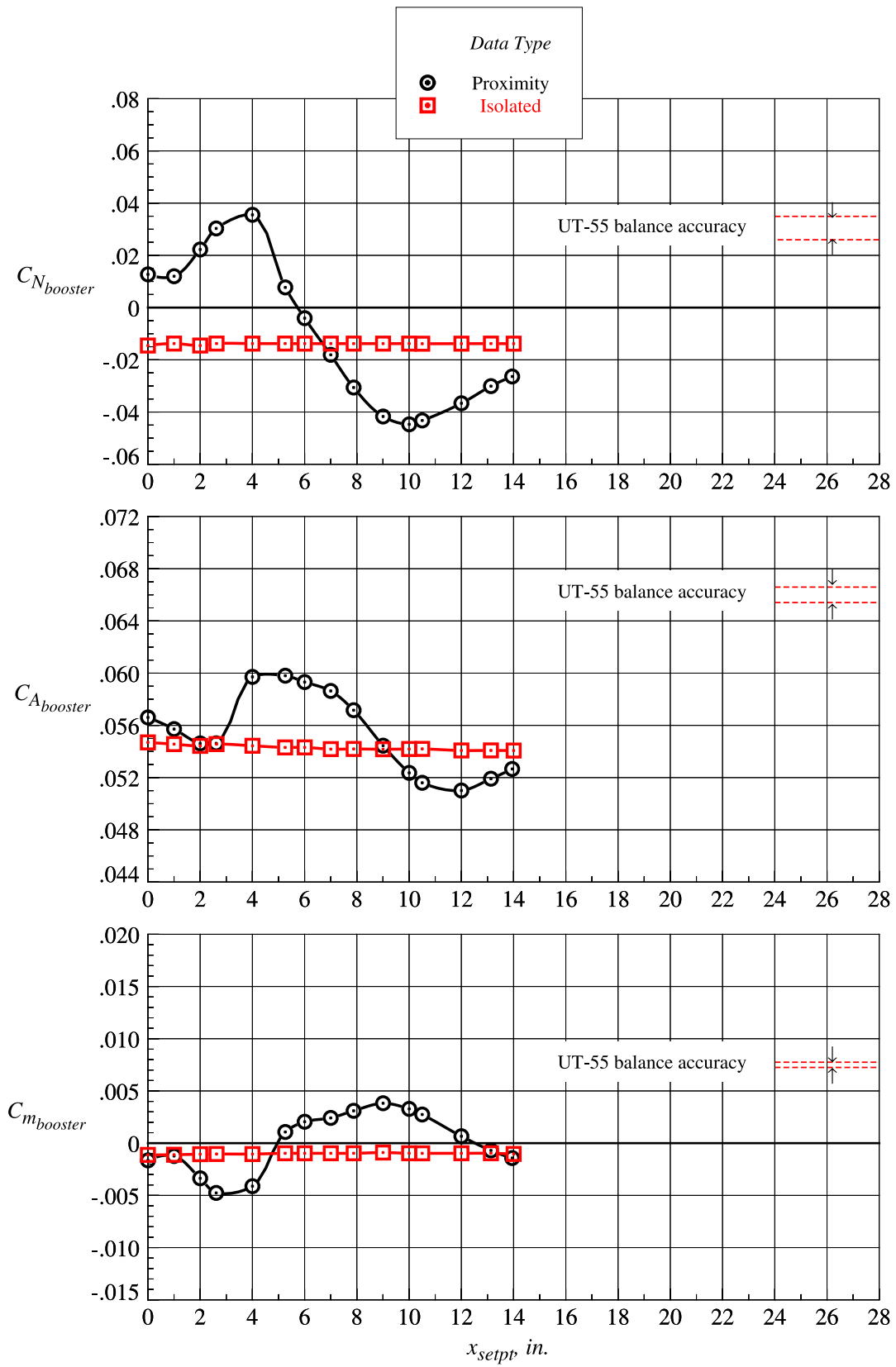
Figure 60. Concluded.



(a)  $z_{setp} = 0$  in.

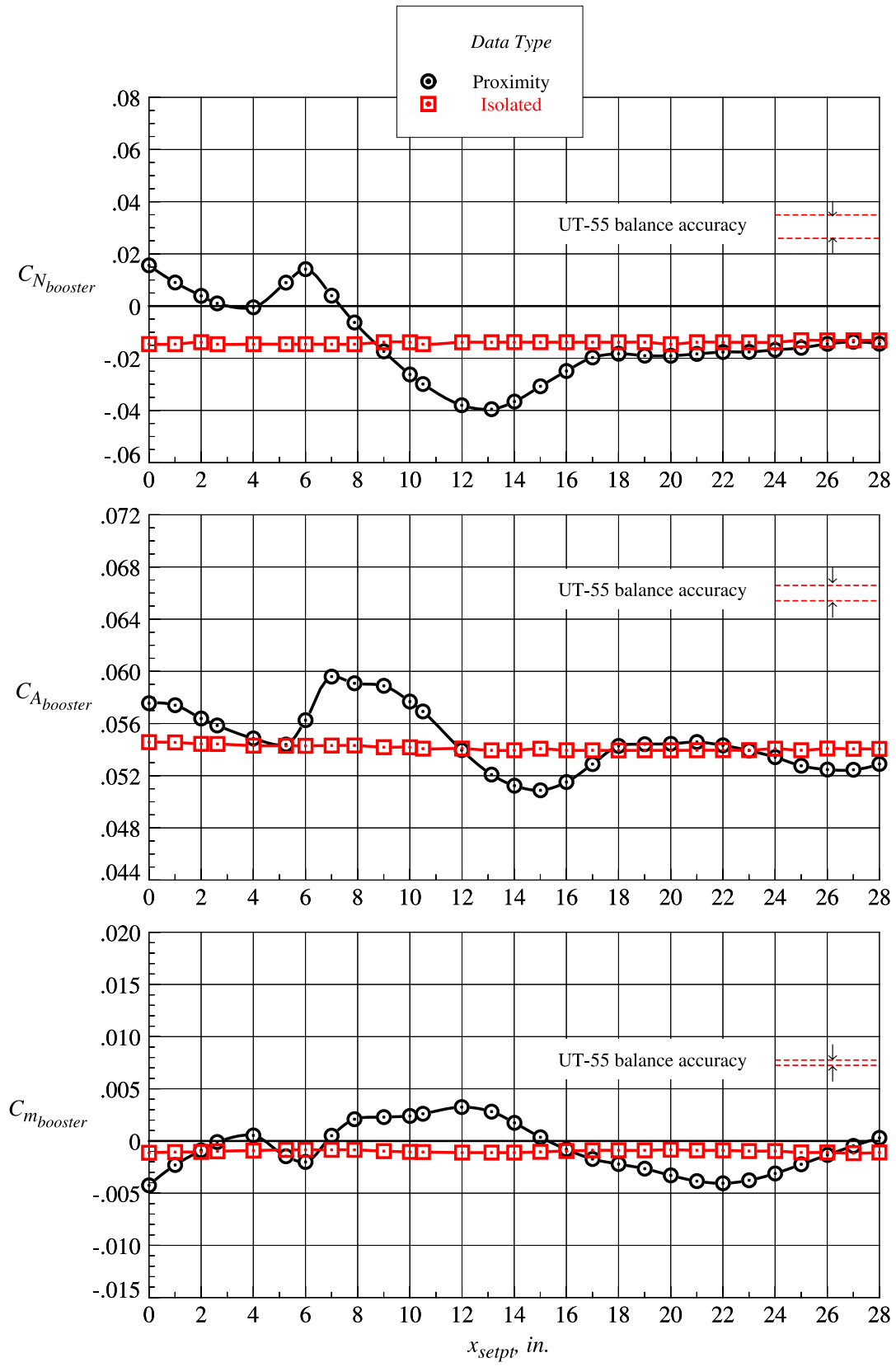
Figure 61. Booster proximity and isolated aerodynamic characteristics at Mach = 4.5 and  $\Delta\alpha = 0^\circ$ .





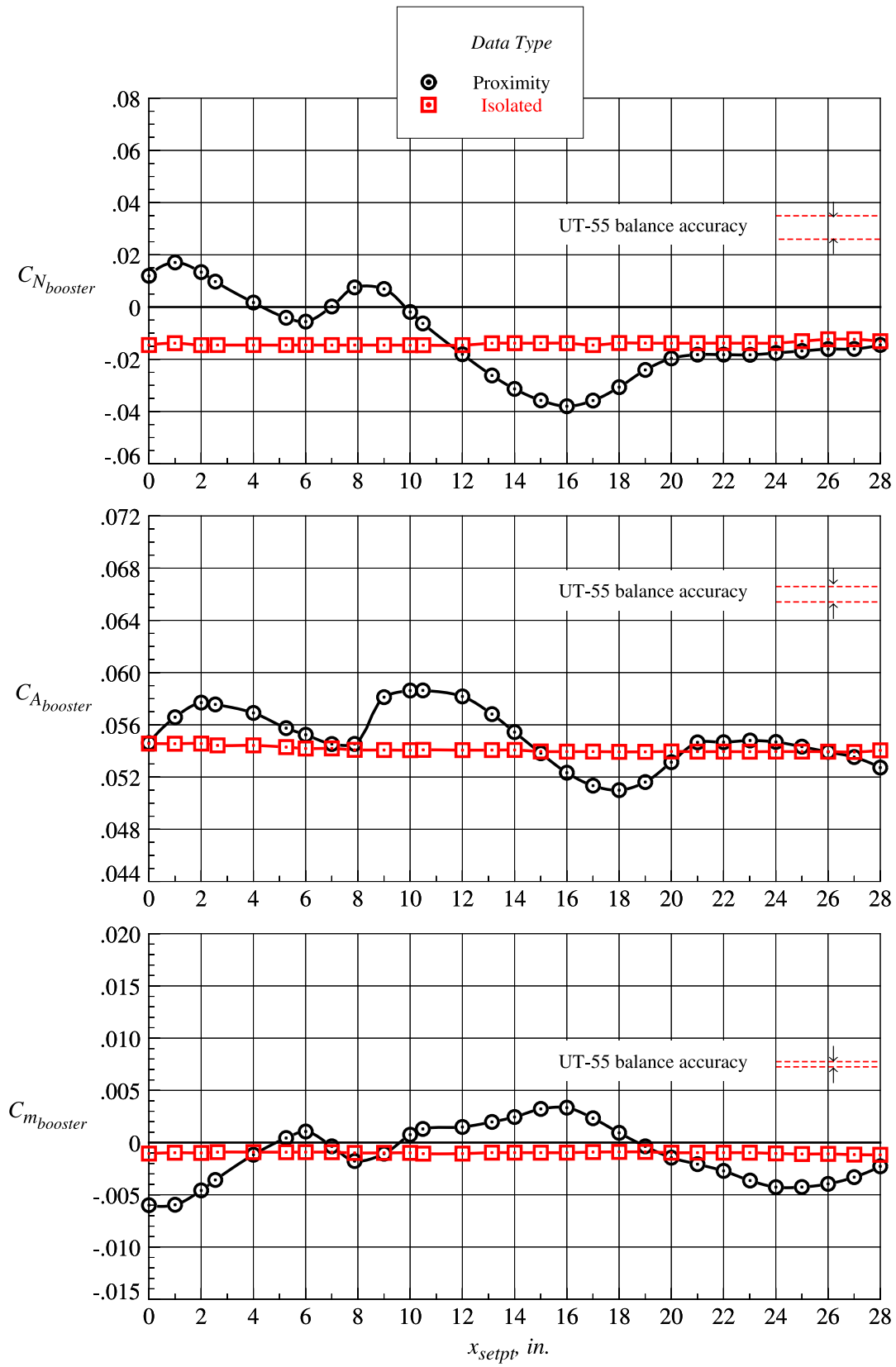
(b)  $z_{setpt} = 0.656$  in.

Figure 61. Continued.



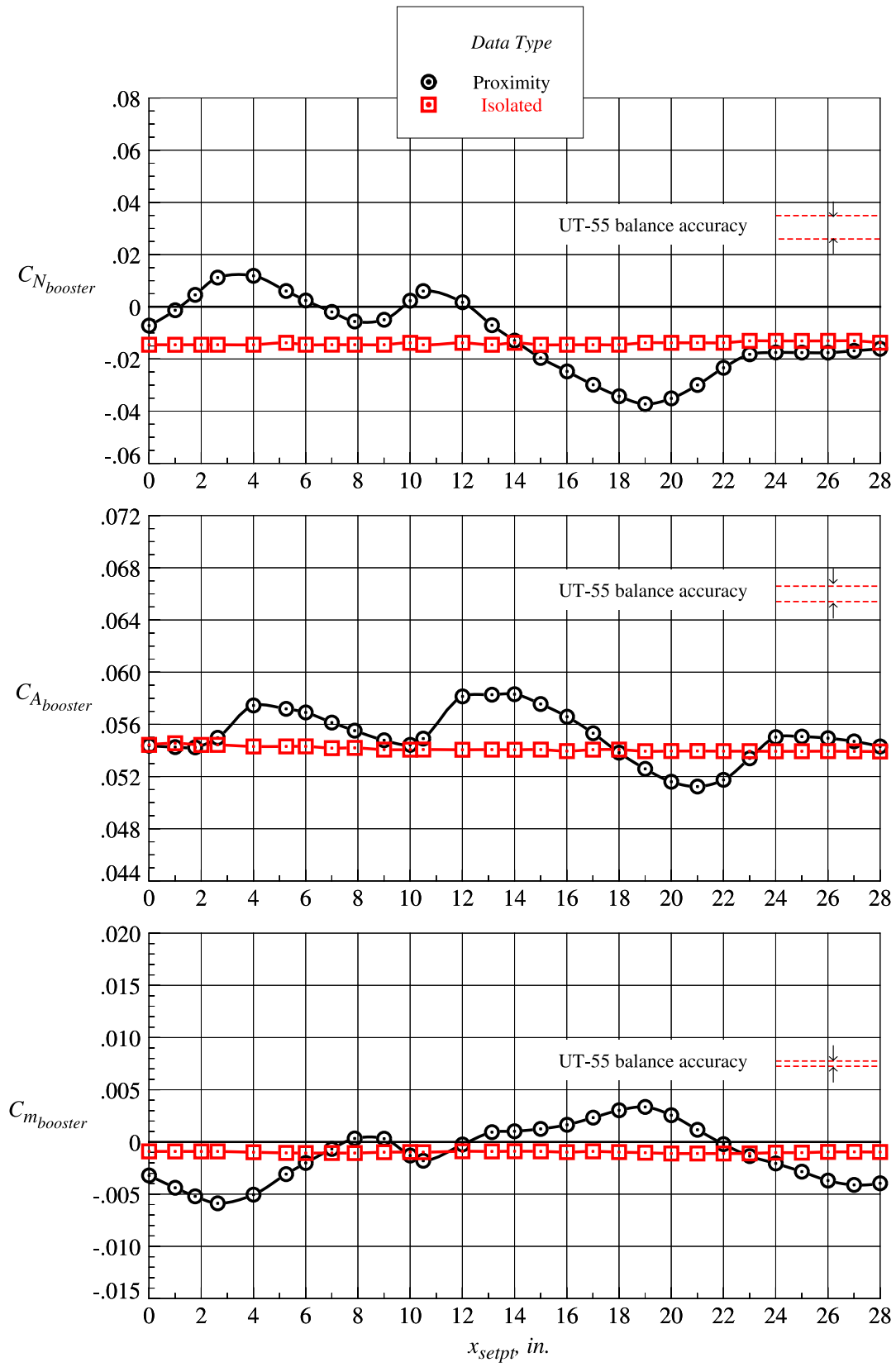
(c)  $z_{setpt} = 1.313$  in.

Figure 61. Continued.



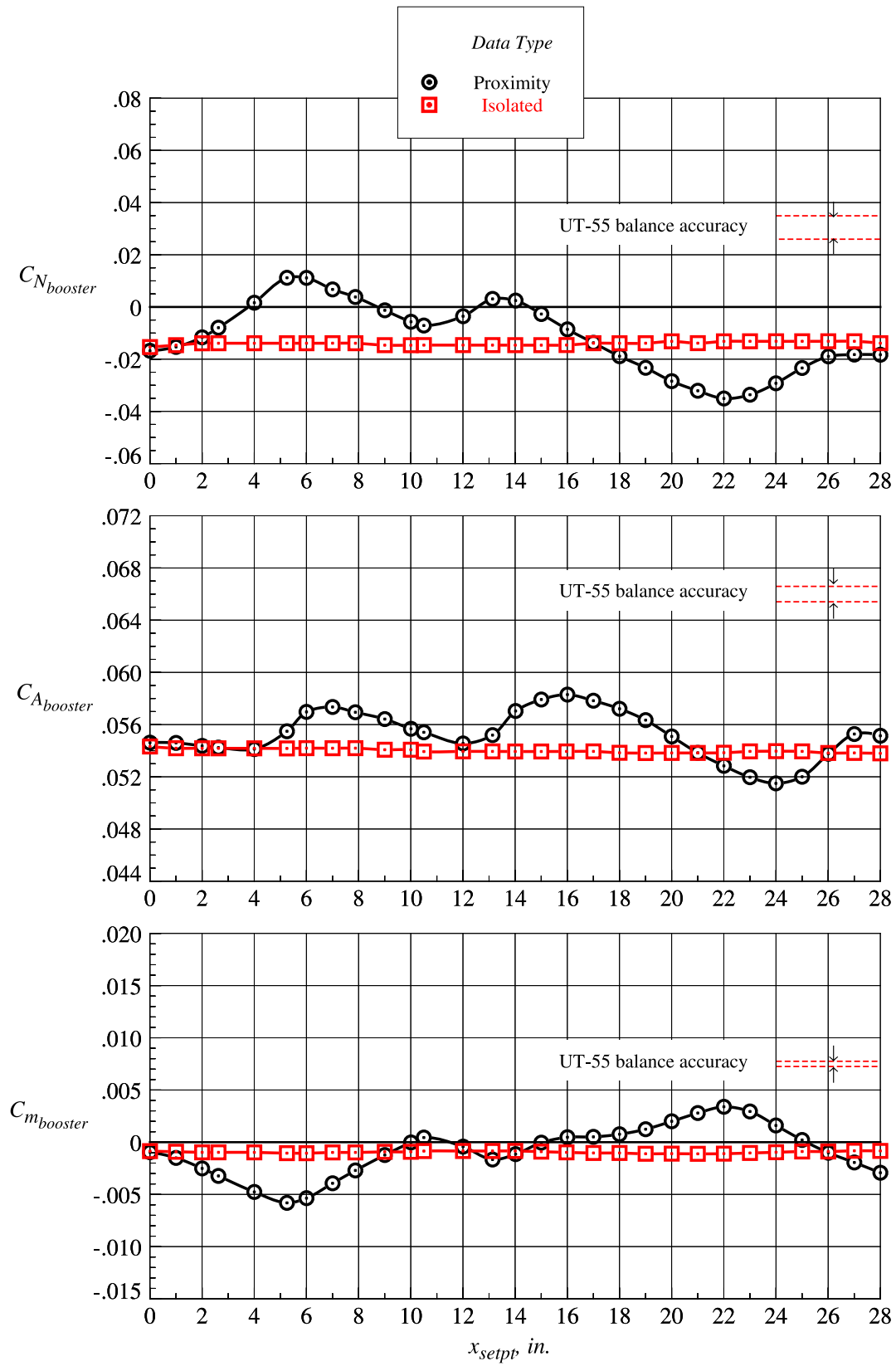
(d)  $z_{setpt} = 1.969$  in.

Figure 61. Continued.



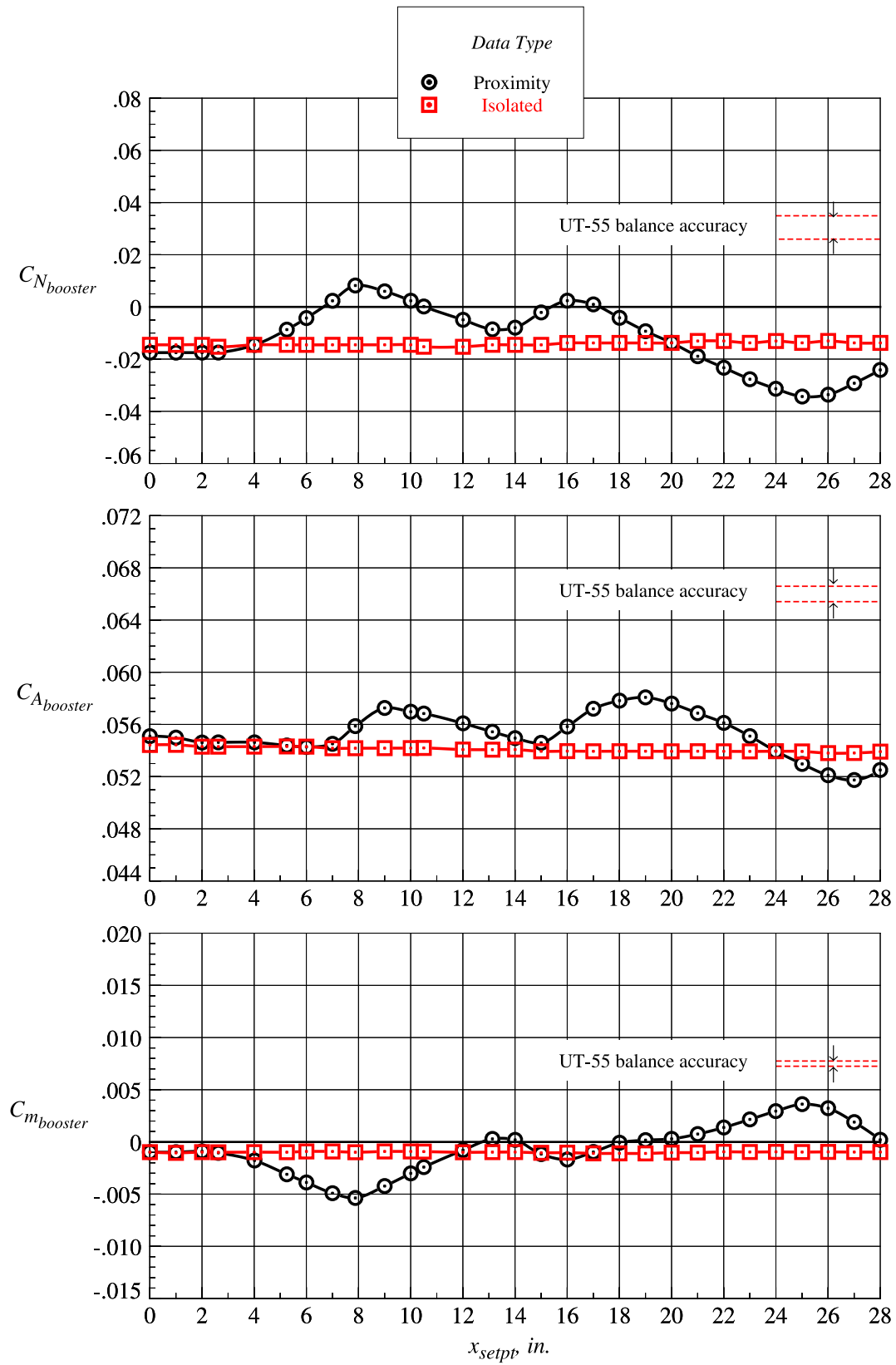
(e)  $z_{setpt} = 2.625 \text{ in.}$

Figure 61. Continued.



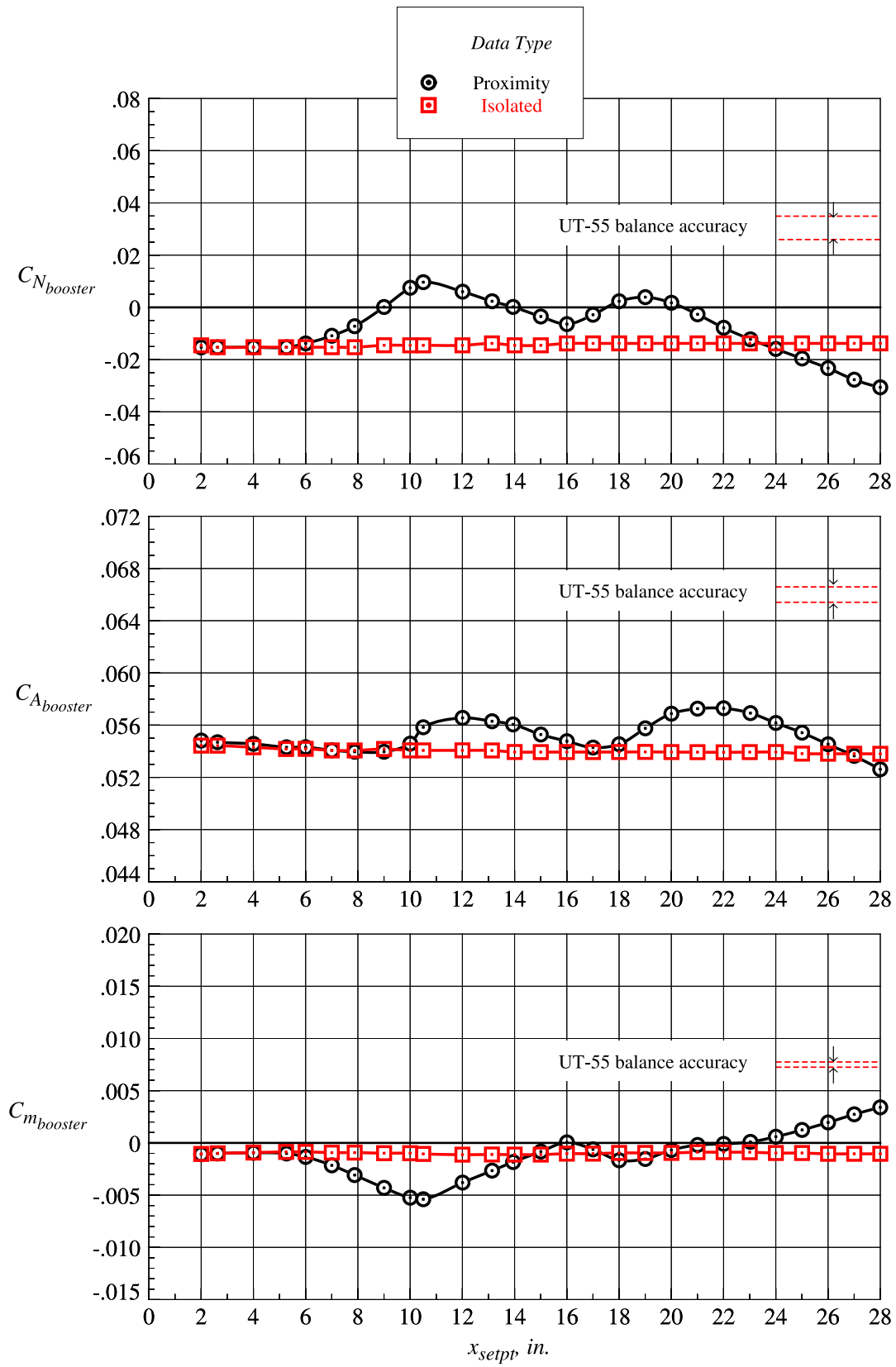
(f)  $z_{setpt} = 3.281$  in.

Figure 61. Continued.



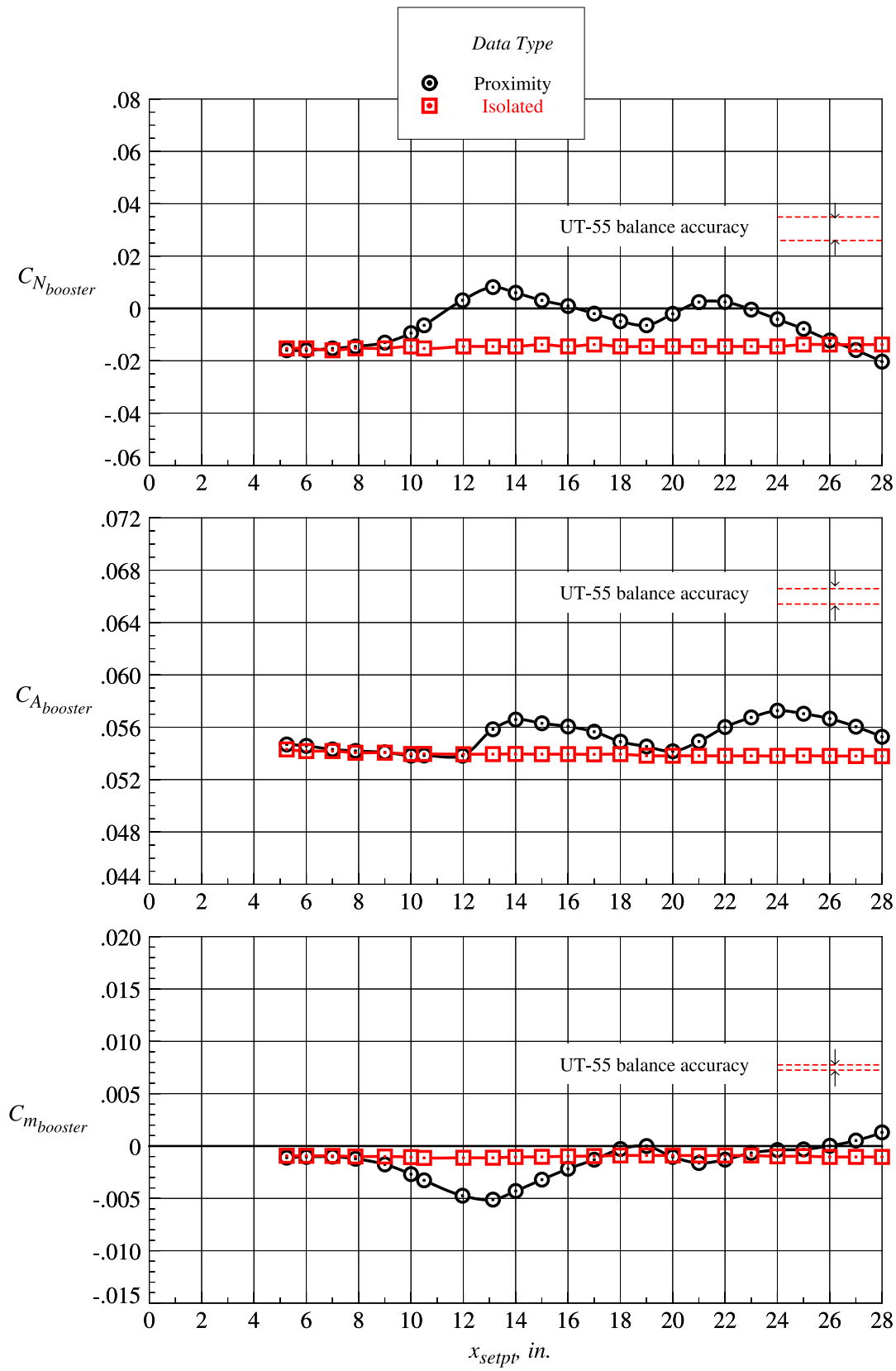
(g)  $z_{setpt} = 3.938$  in.

Figure 61. Continued.



(h)  $z_{setpt} = 4.594$  in.

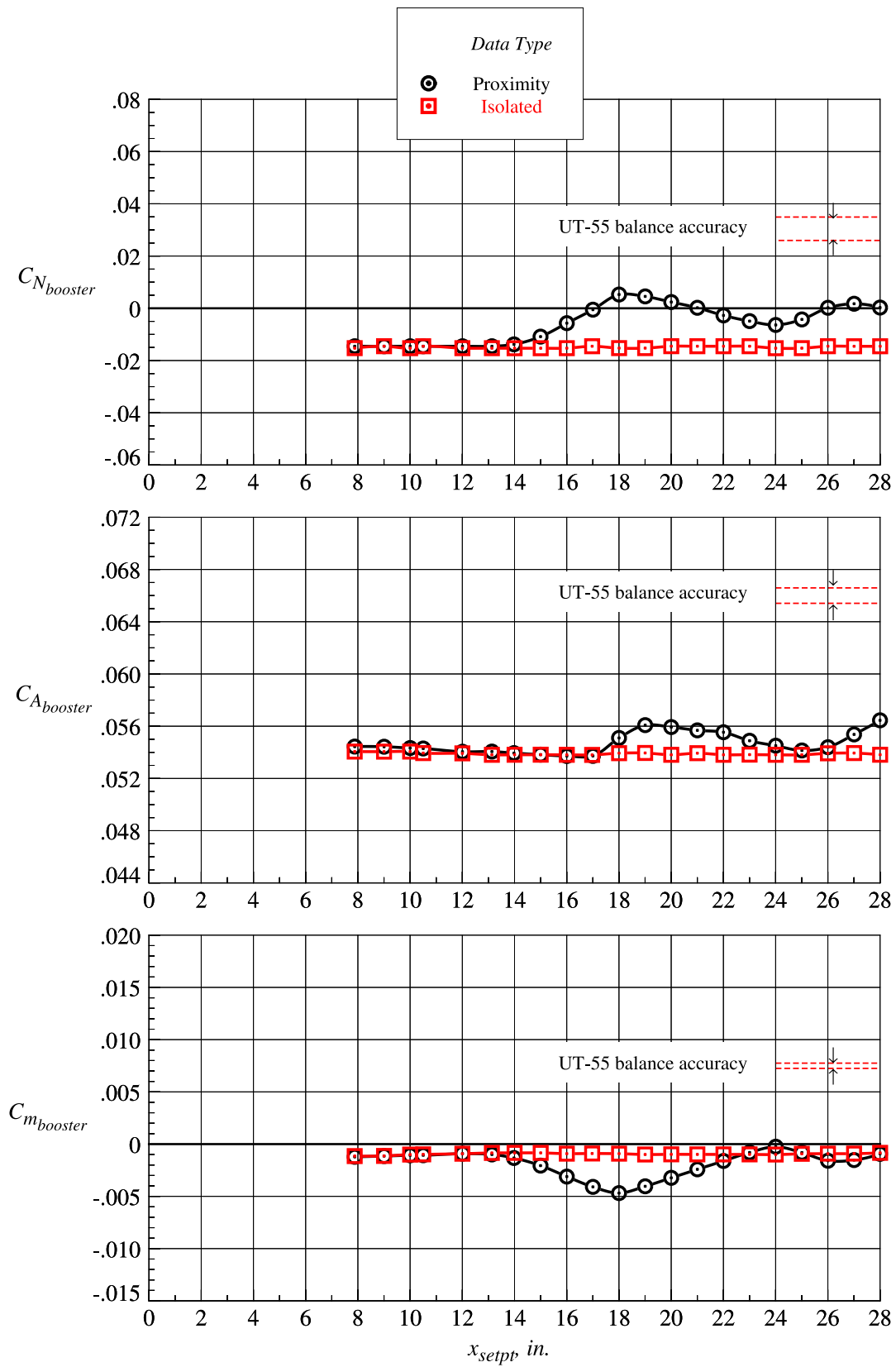
Figure 61. Continued.



(i)  $z_{setpt} = 5.250$  in.

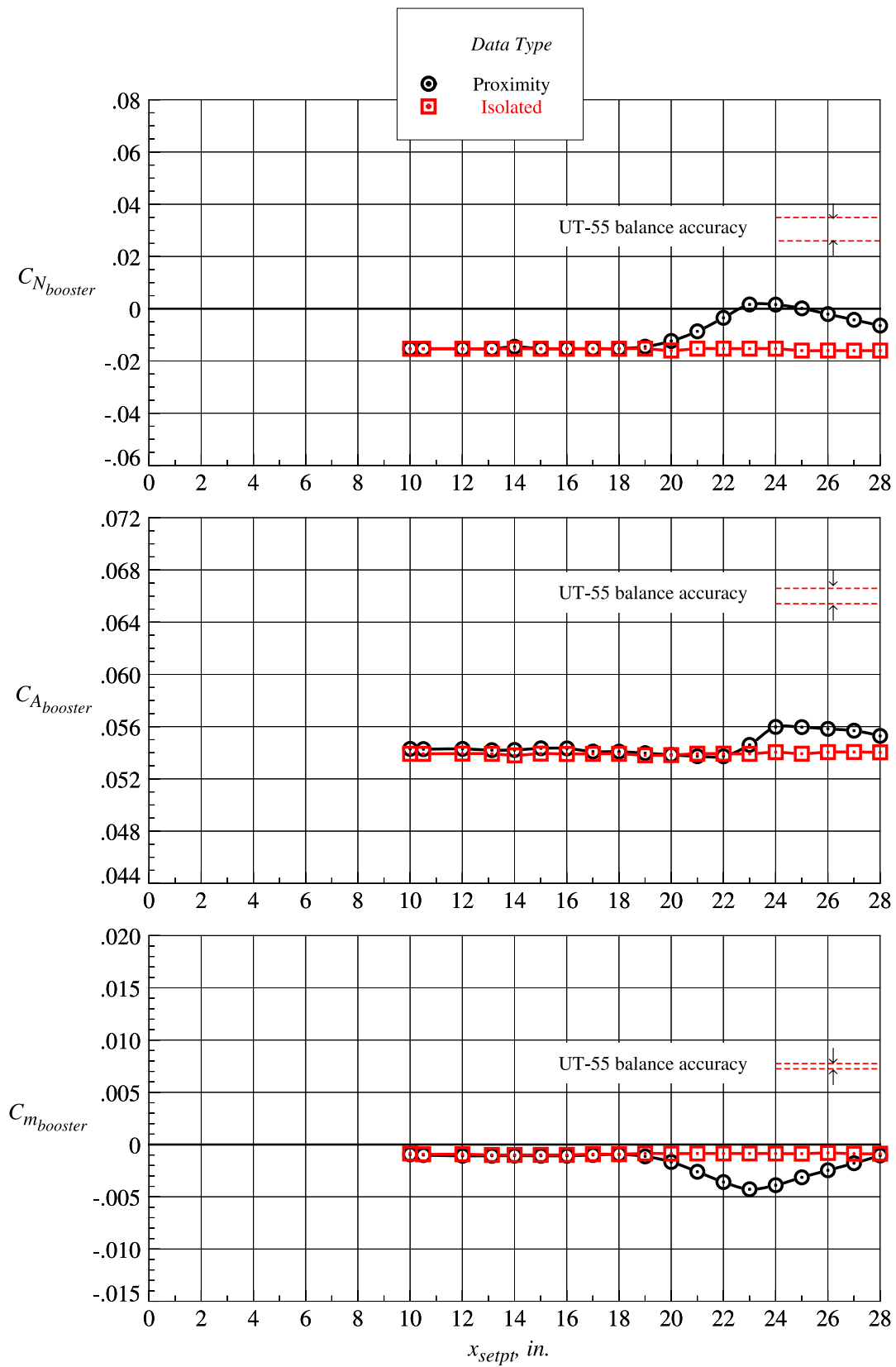
Figure 61. Continued.





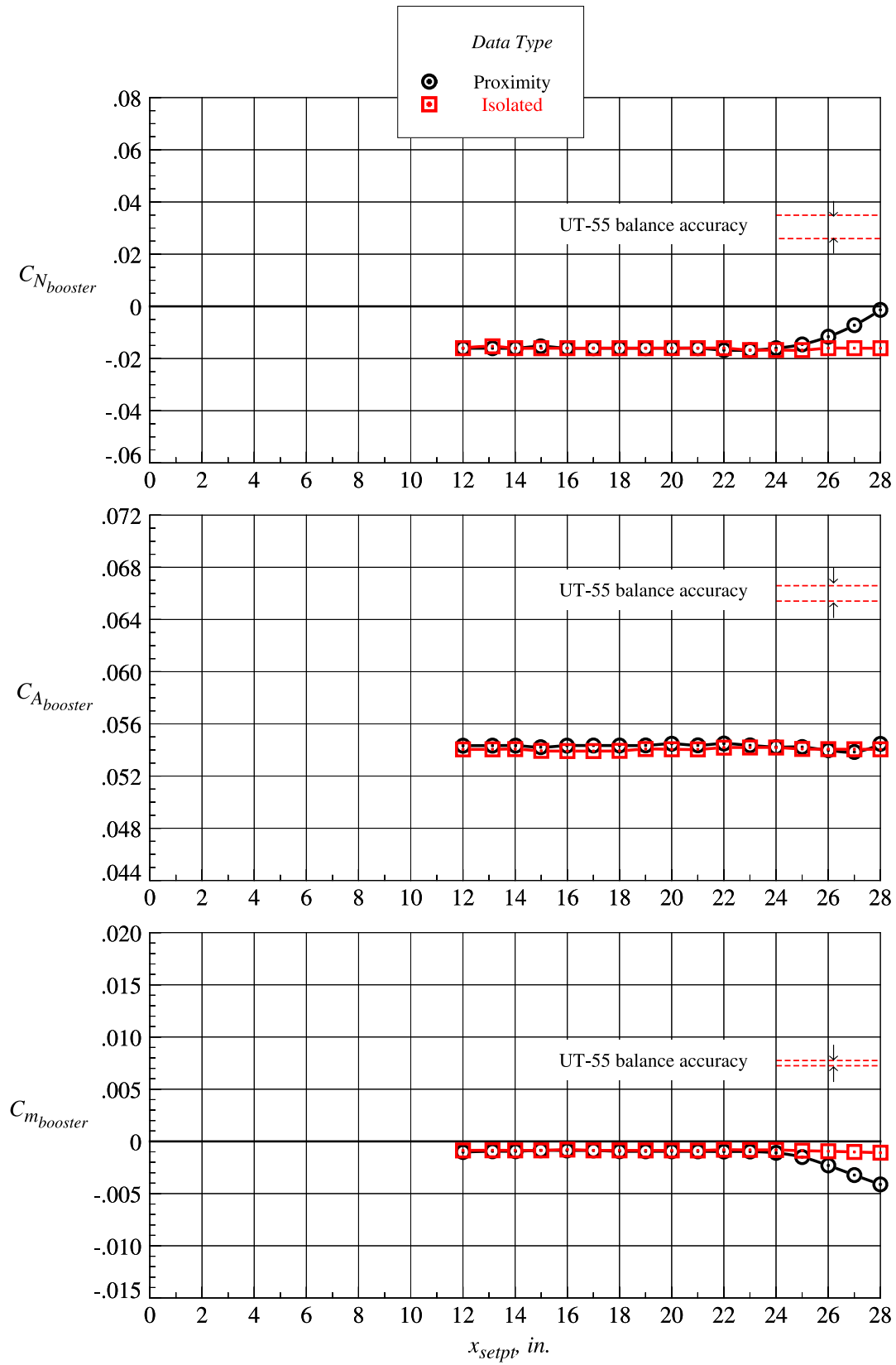
(j)  $z_{setpt} = 6.583$  in.

Figure 61. Continued.



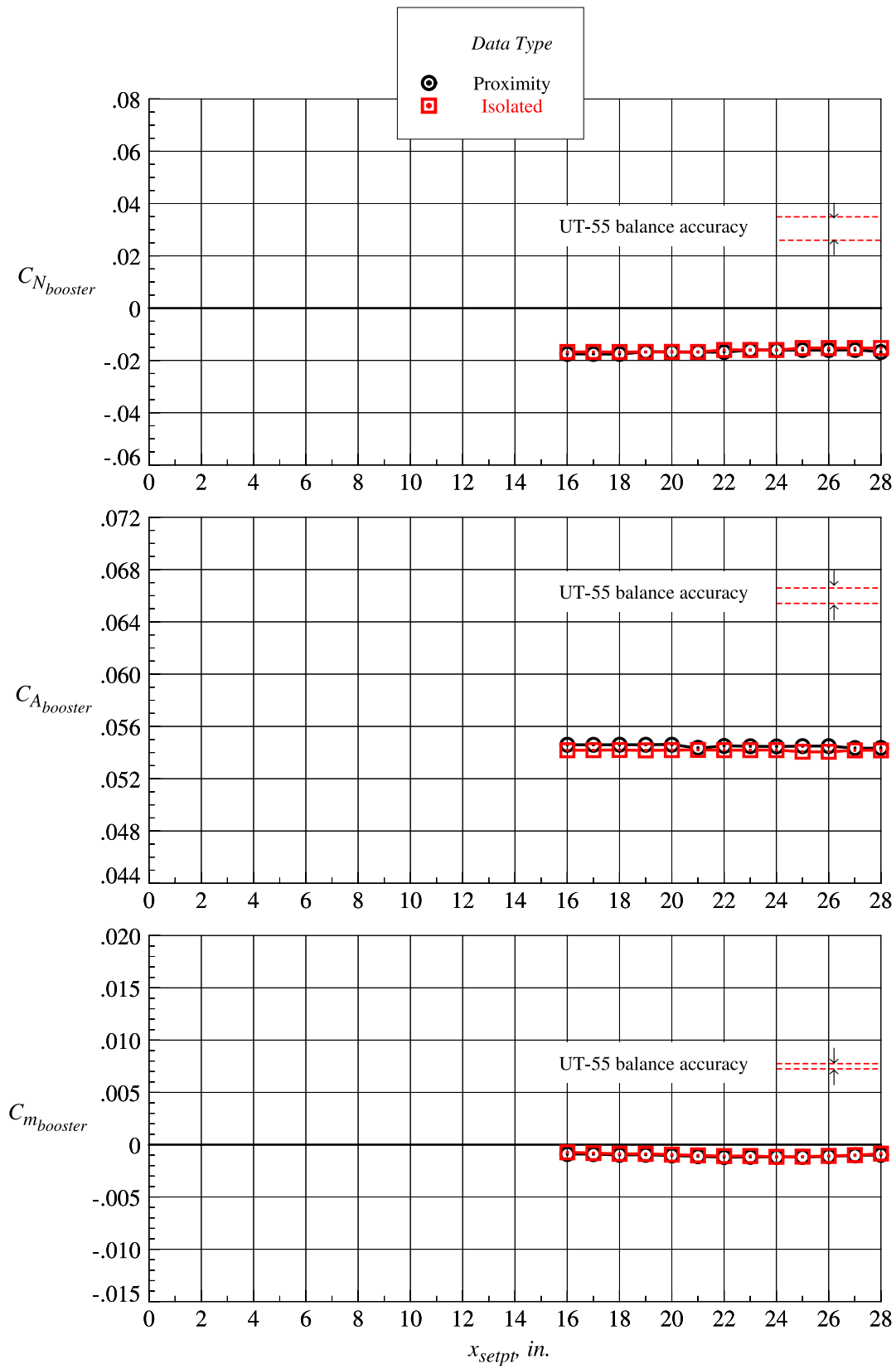
(k)  $z_{setpt} = 7.875$  in.

Figure 61. Continued.



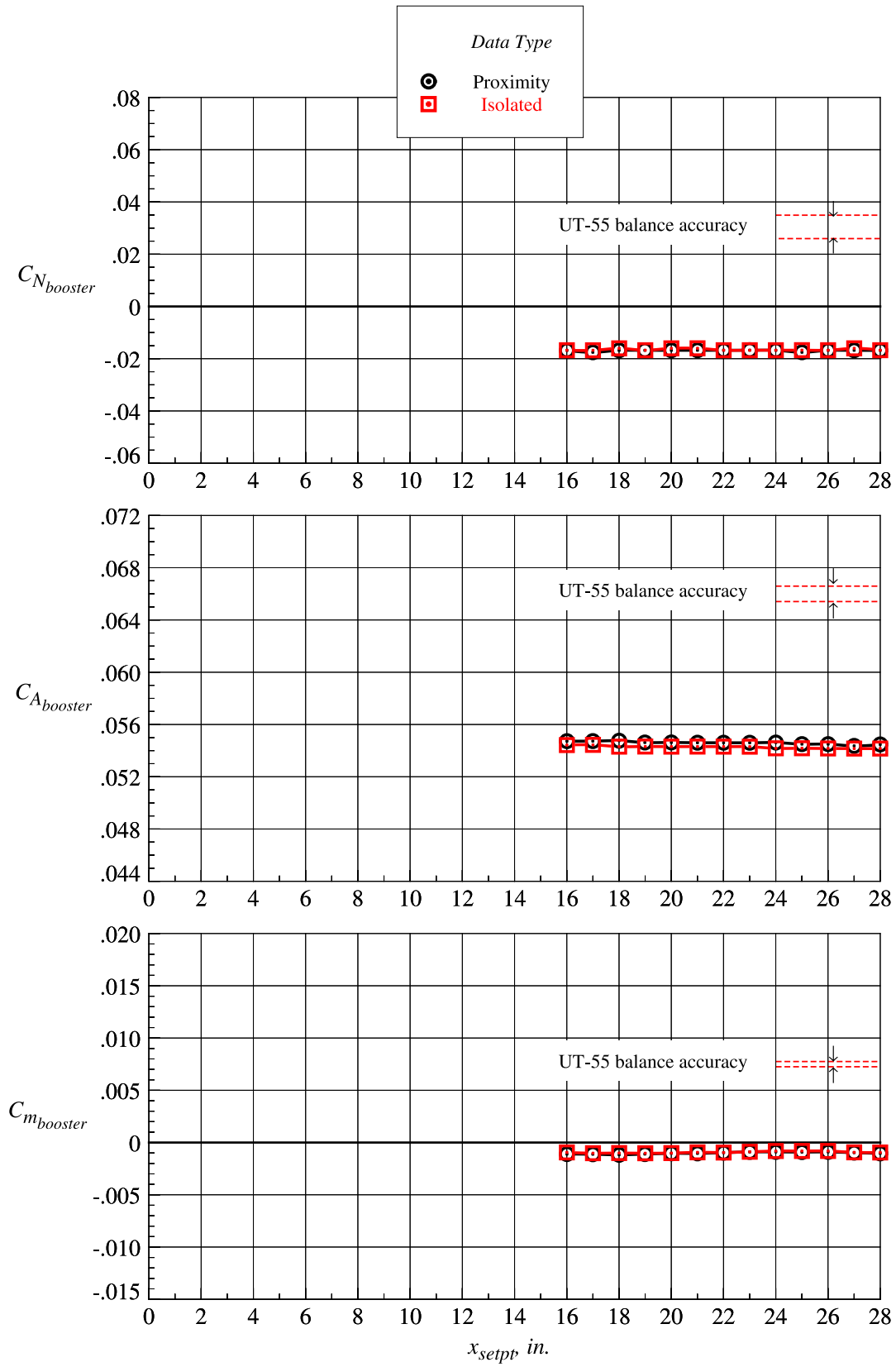
(l)  $z_{setpt} = 9.188$  in.

Figure 61. Continued.



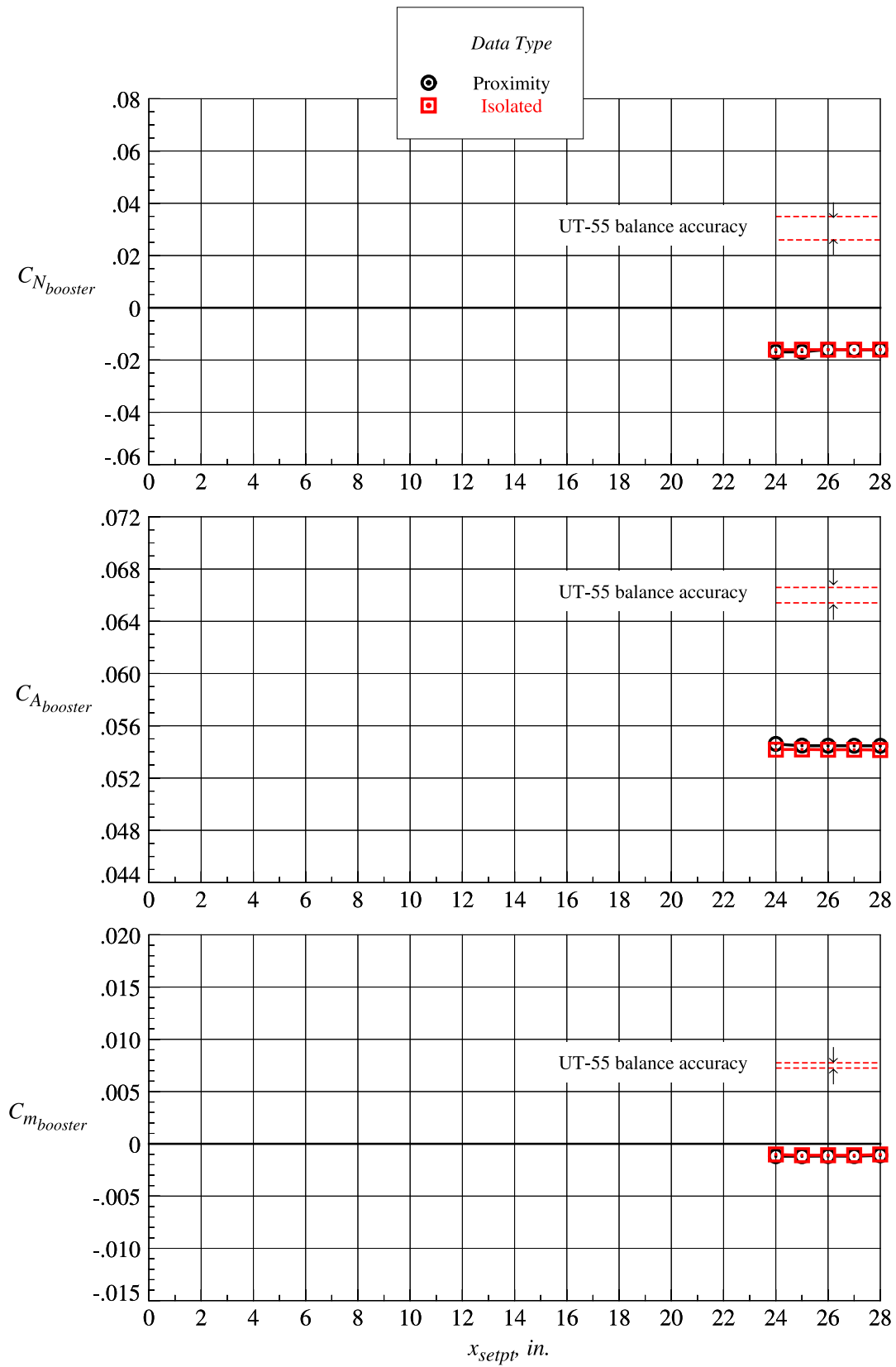
(m)  $z_{setpt} = 10.500$  in.

Figure 61. Continued.



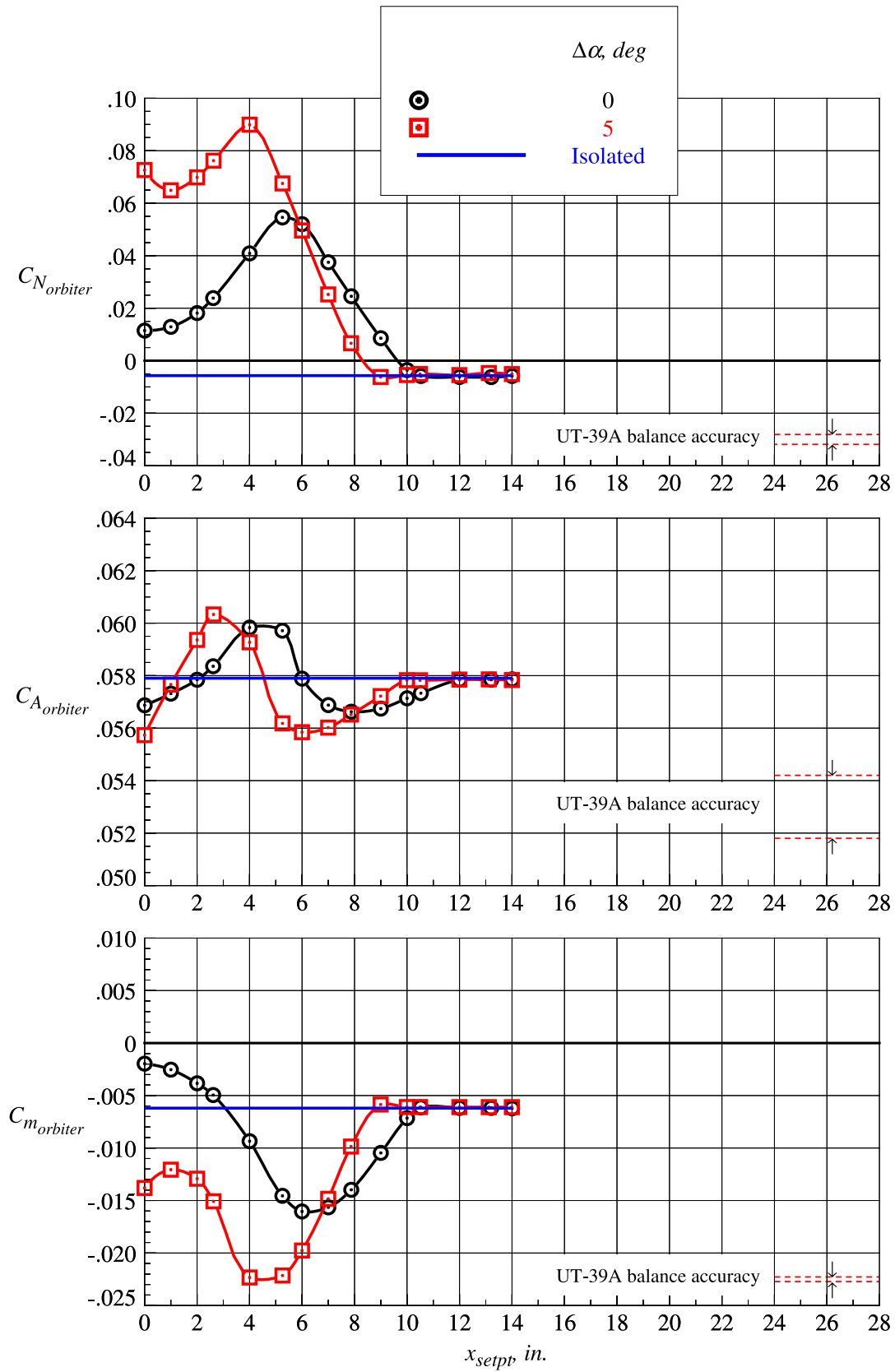
(n)  $z_{setpt} = 11.810$  in.

Figure 61. Continued.



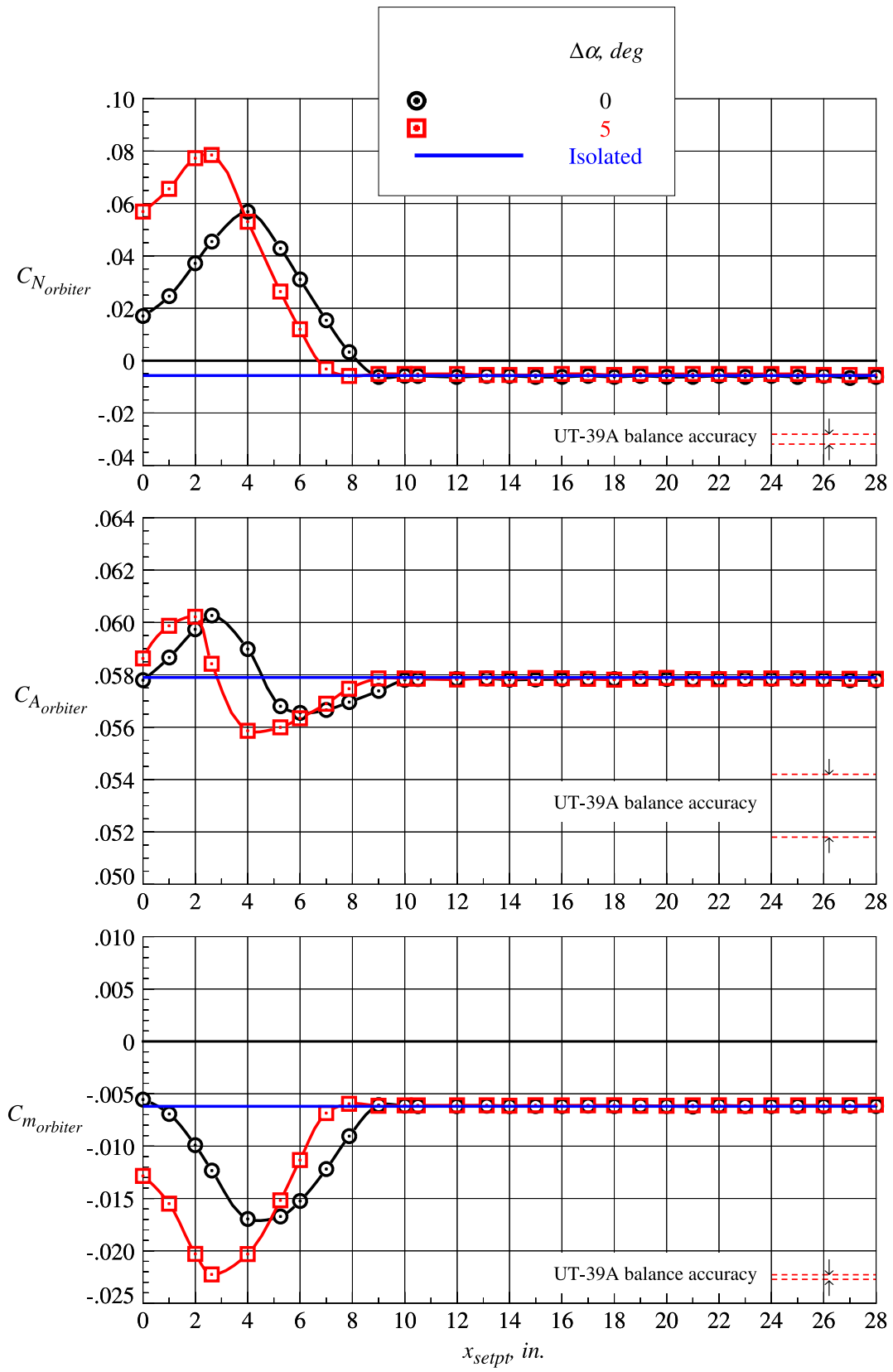
(o)  $z_{setpt} = 13.130$  in.

Figure 61. Concluded.



(a)  $z_{\text{setpt}} = 0.656 \text{ in.}$

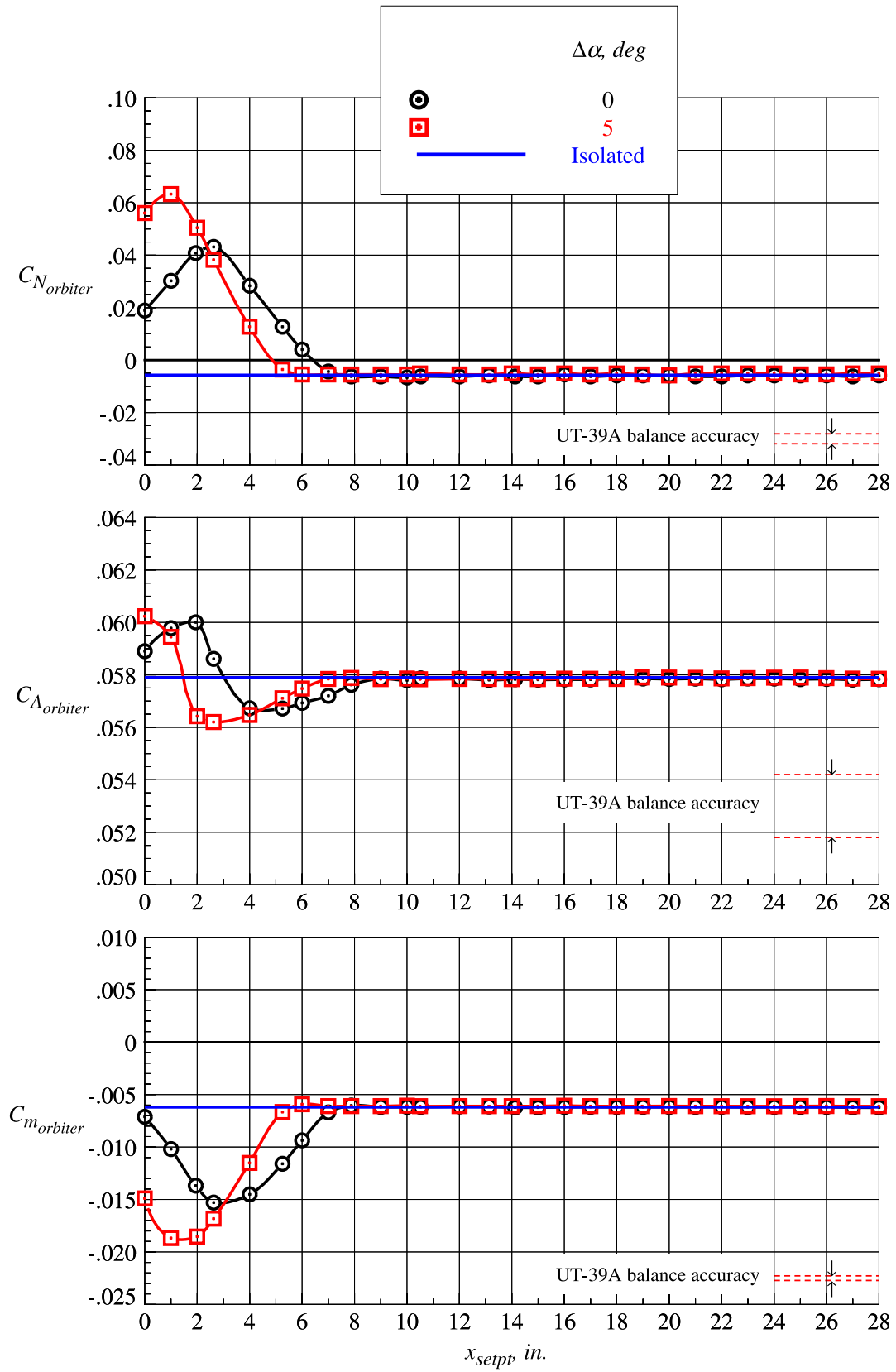
Figure 62. Orbiter proximity aerodynamic characteristics at  $\Delta\alpha = 0^\circ$  and  $5^\circ$ ;  $Mach = 3.0$ .



(b)  $z_{setpt} = 1.313$  in.

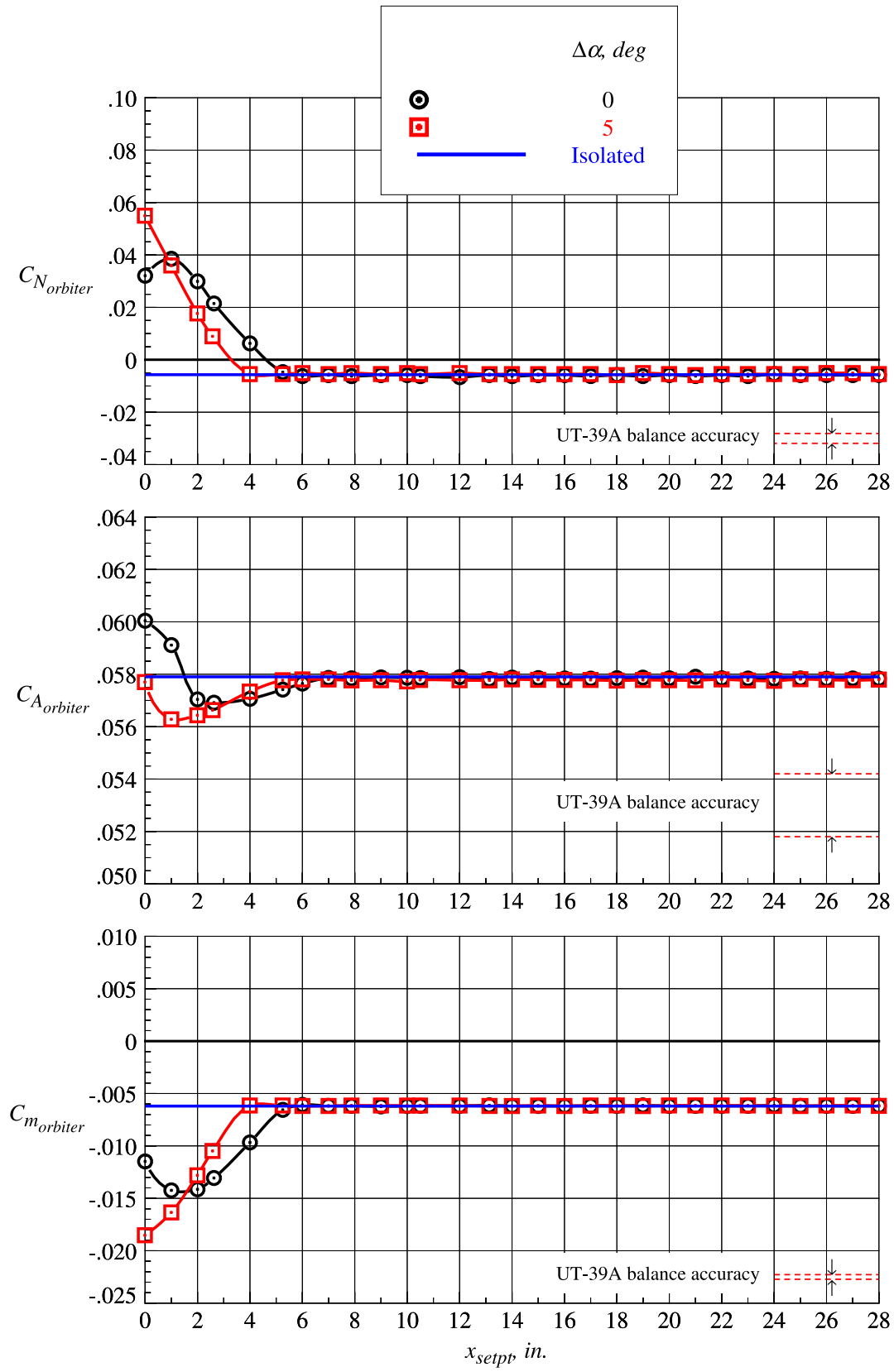
Figure 62. Continued.





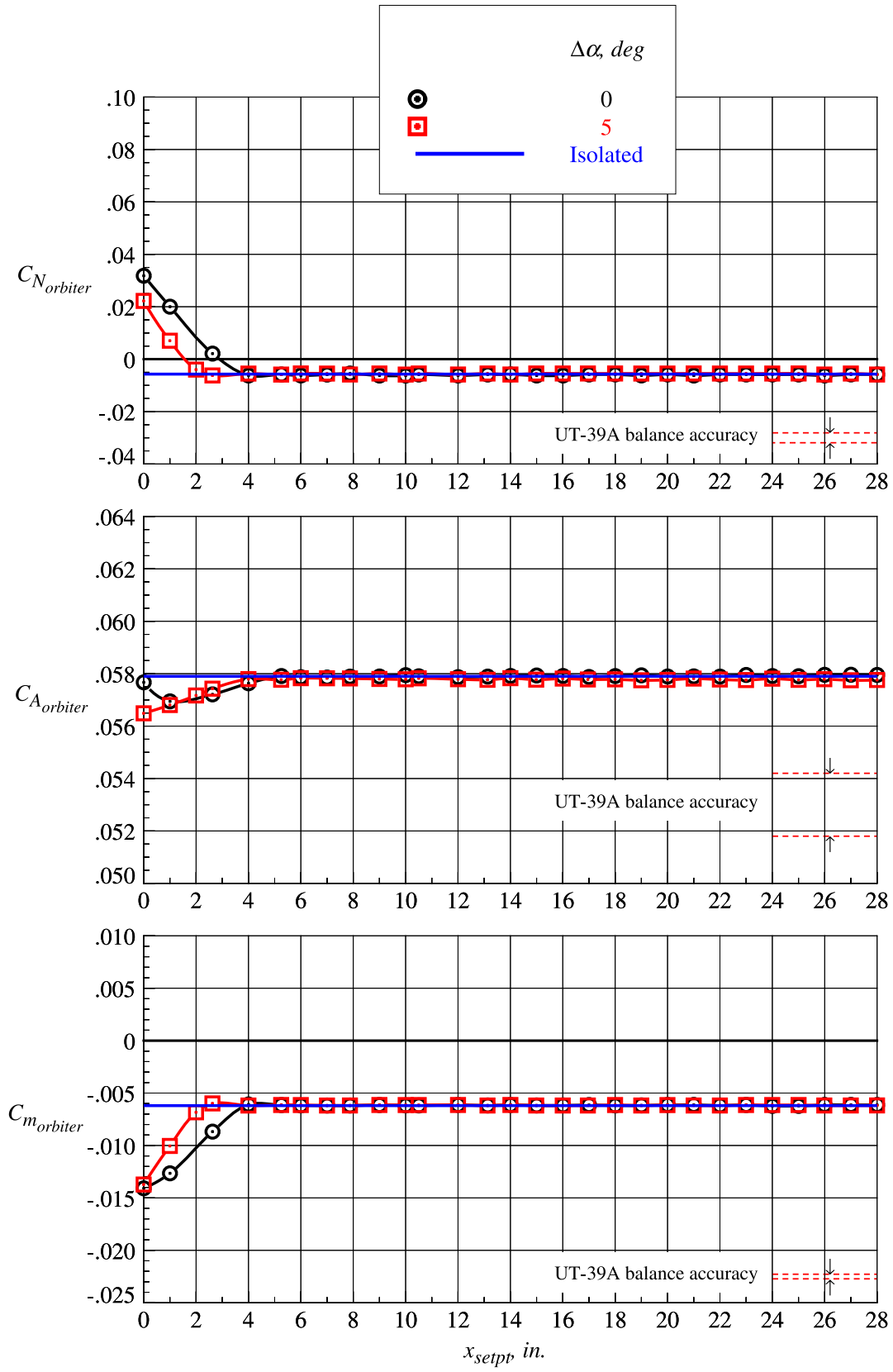
(c)  $z_{setpt} = 1.969$  in.

Figure 62. Continued.



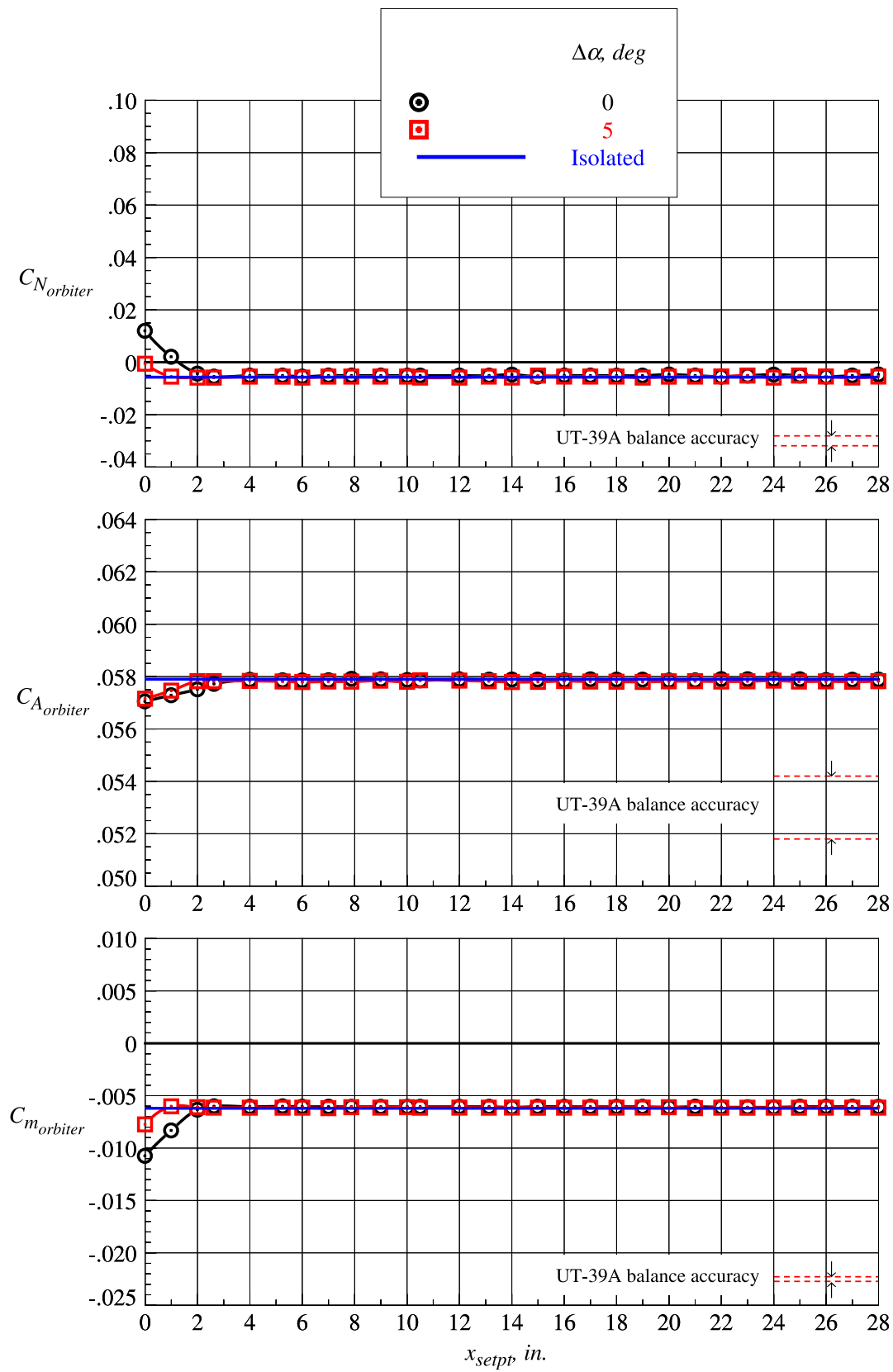
(d)  $z_{setpt} = 2.625 \text{ in.}$

Figure 62. Continued.



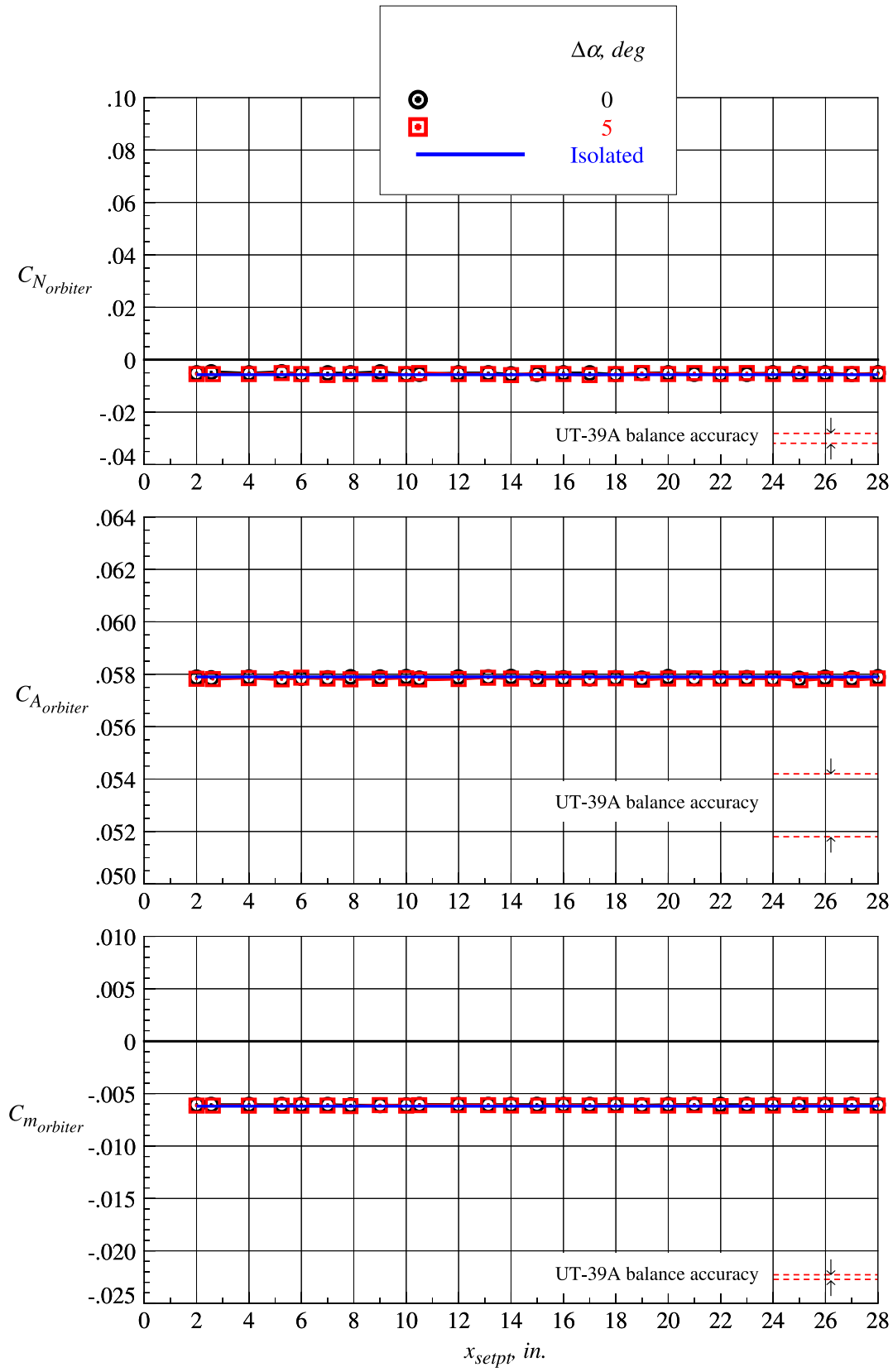
(e)  $z_{setpt} = 3.281$  in.

Figure 62. Continued.



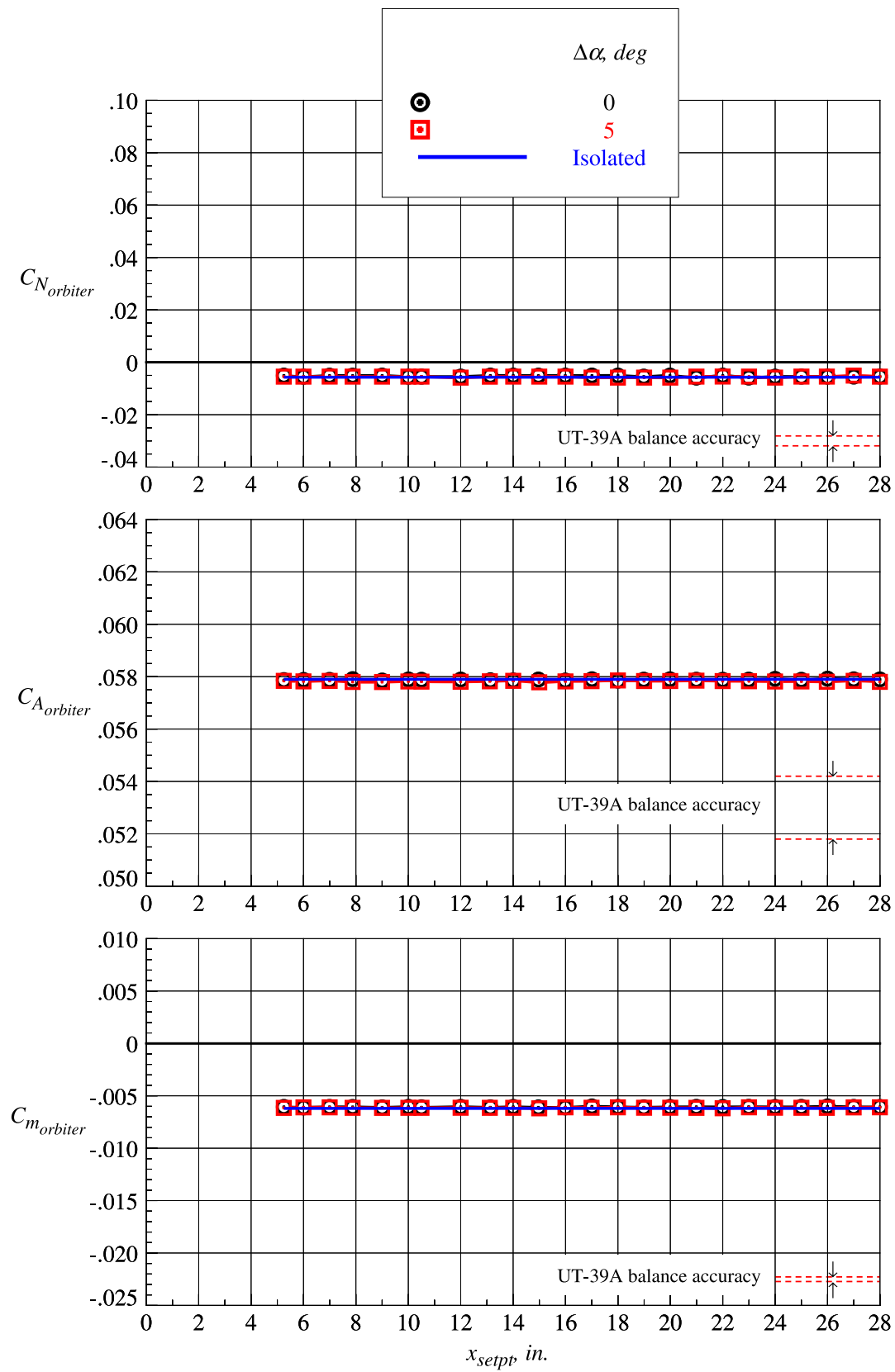
(f)  $z_{setpt} = 3.938$  in.

Figure 62. Continued.



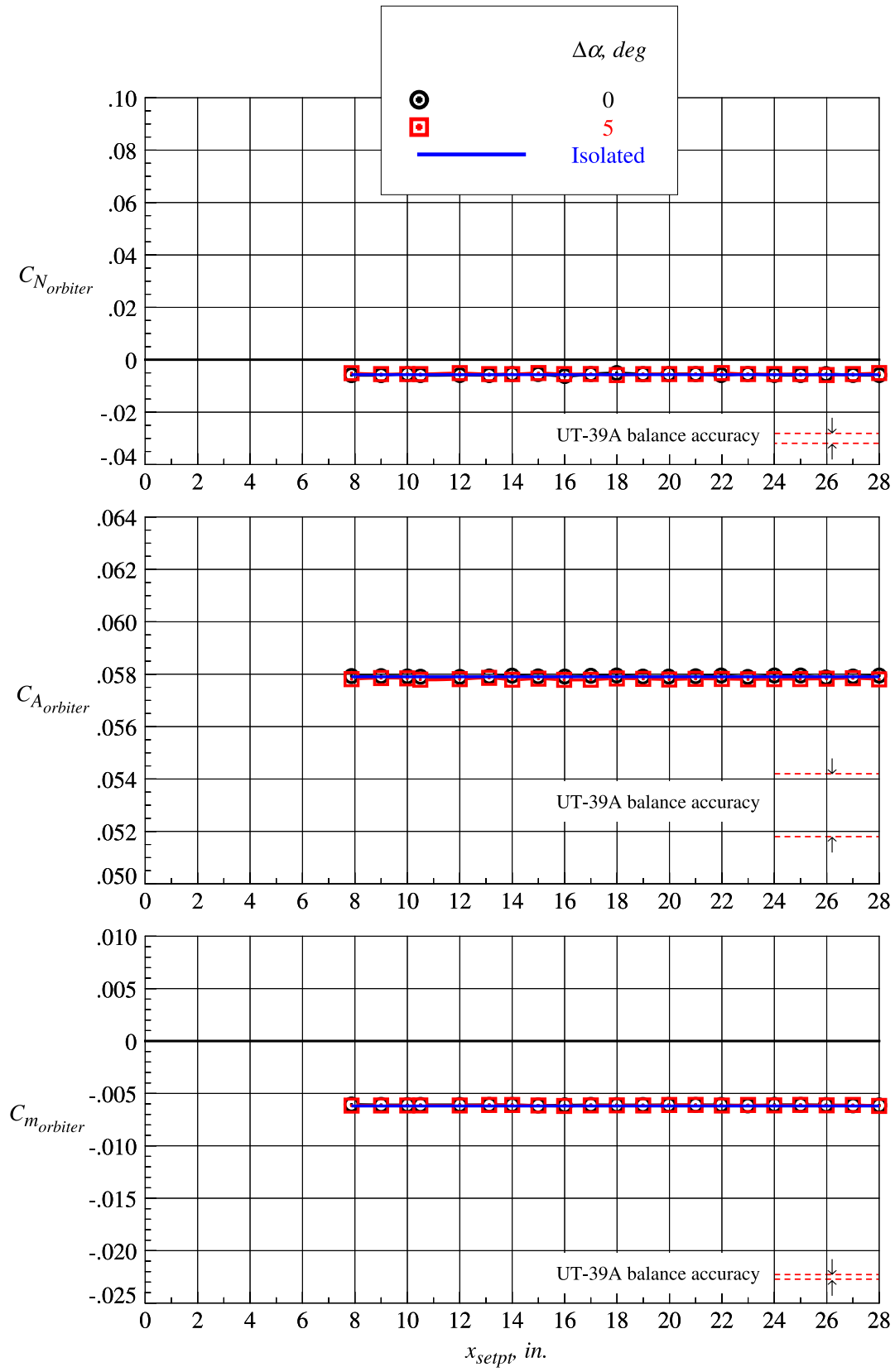
(g)  $z_{setpt} = 4.594$  in.

Figure 62. Continued.



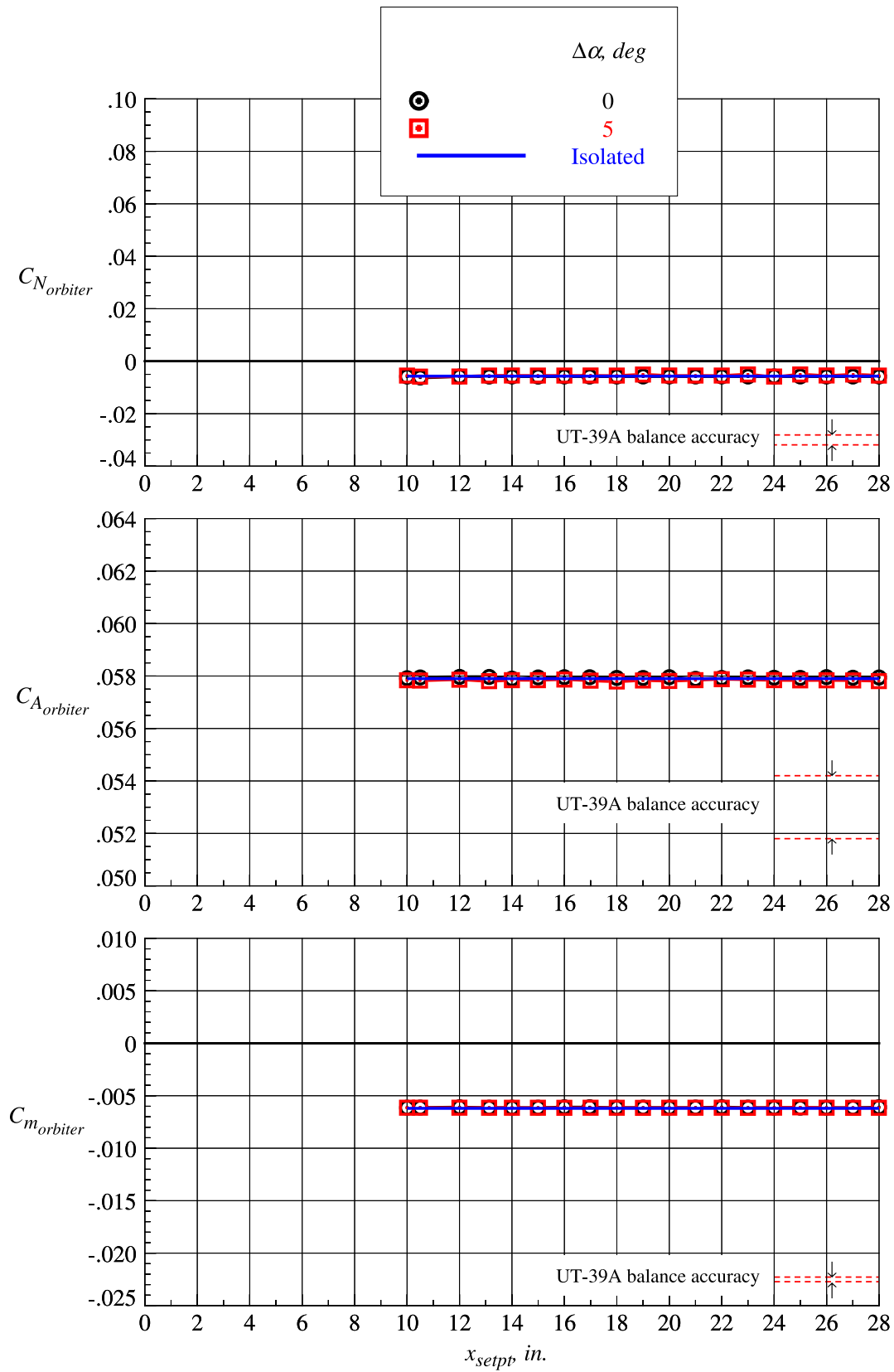
(h)  $z_{setpt} = 5.250 \text{ in.}$

Figure 62. Continued.



(i)  $z_{setpt} = 6.583 \text{ in.}$

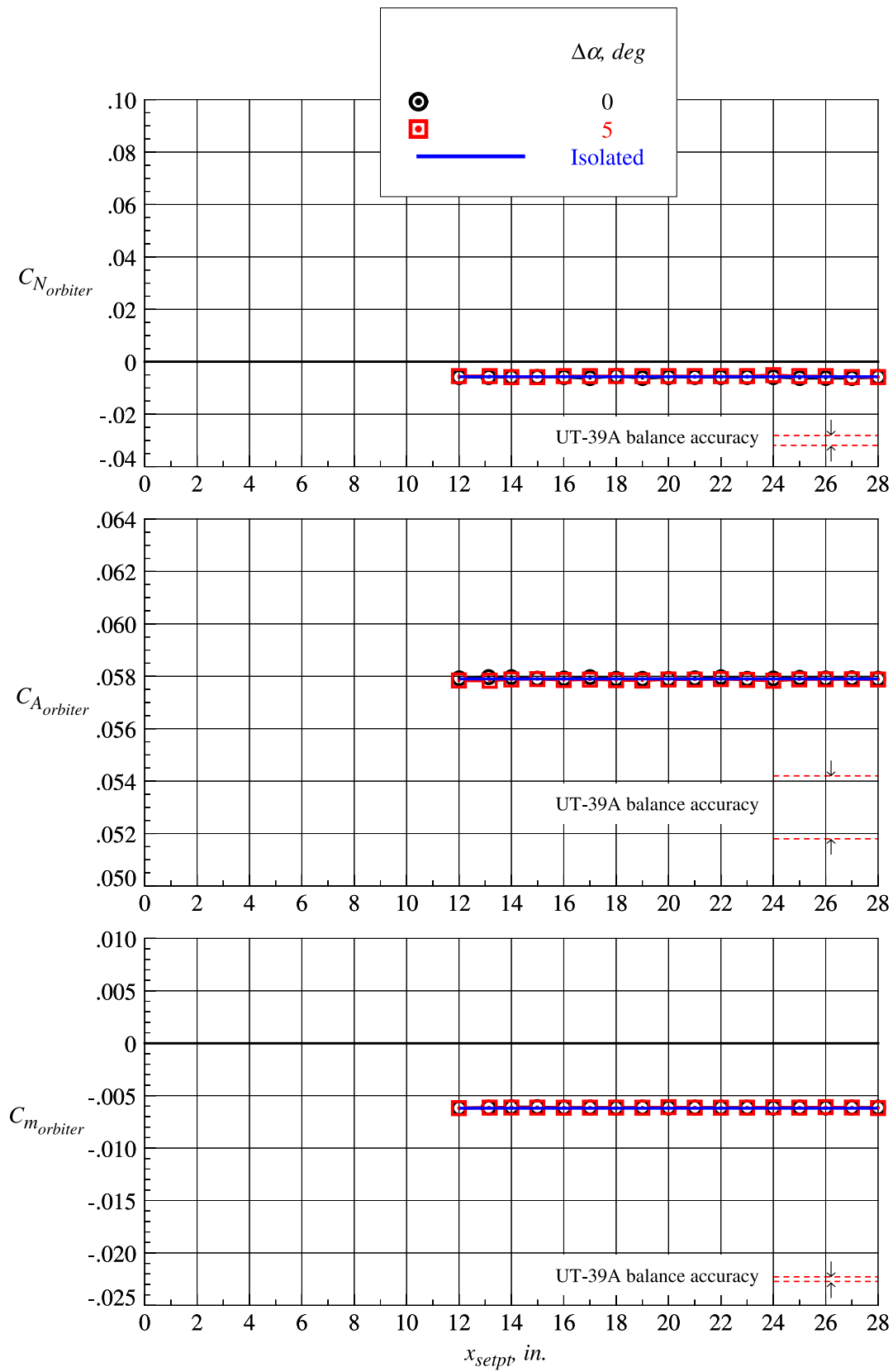
Figure 62. Continued.



(j)  $z_{setpt} = 7.875 \text{ in.}$

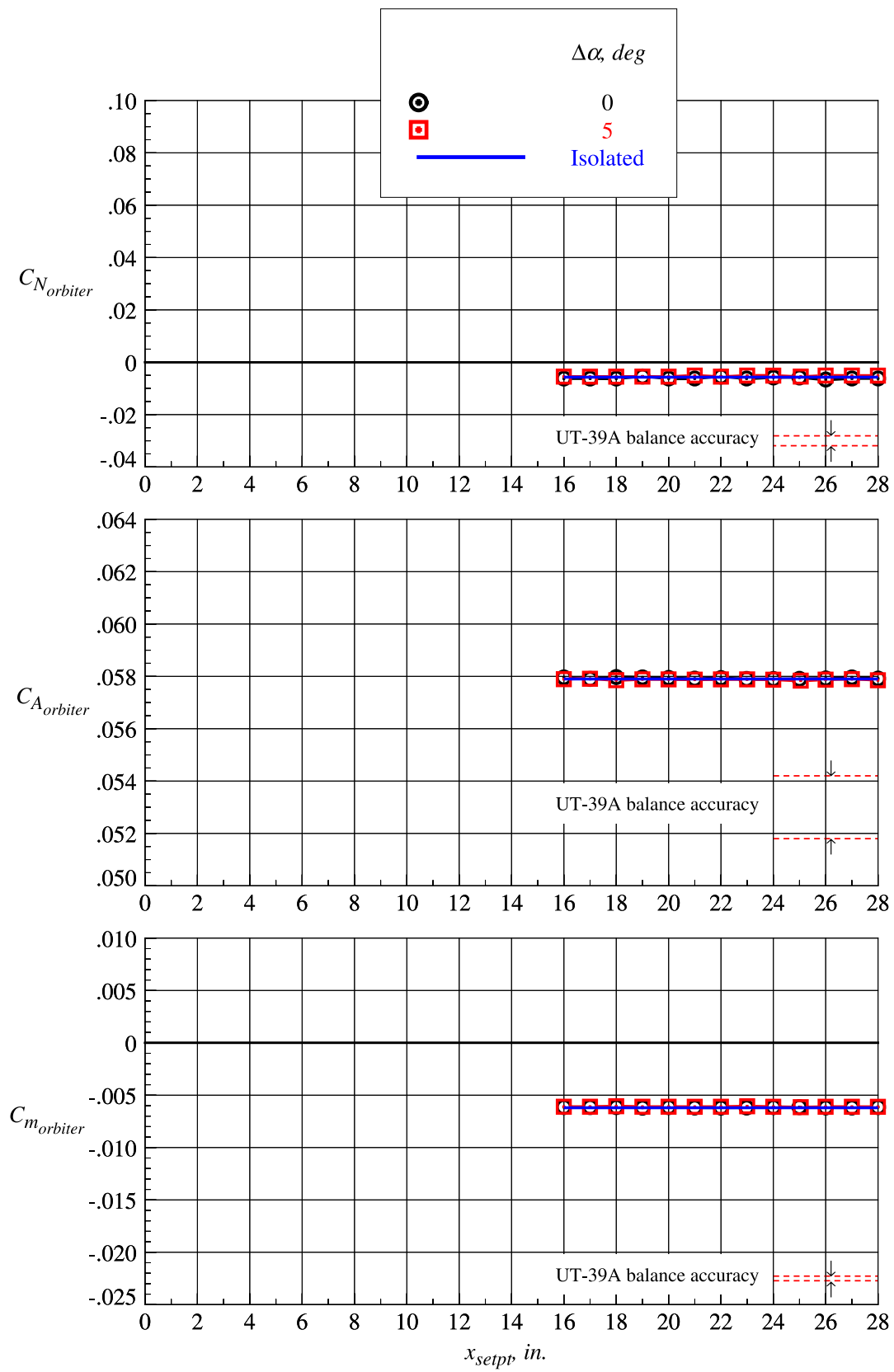
Figure 62. Continued.





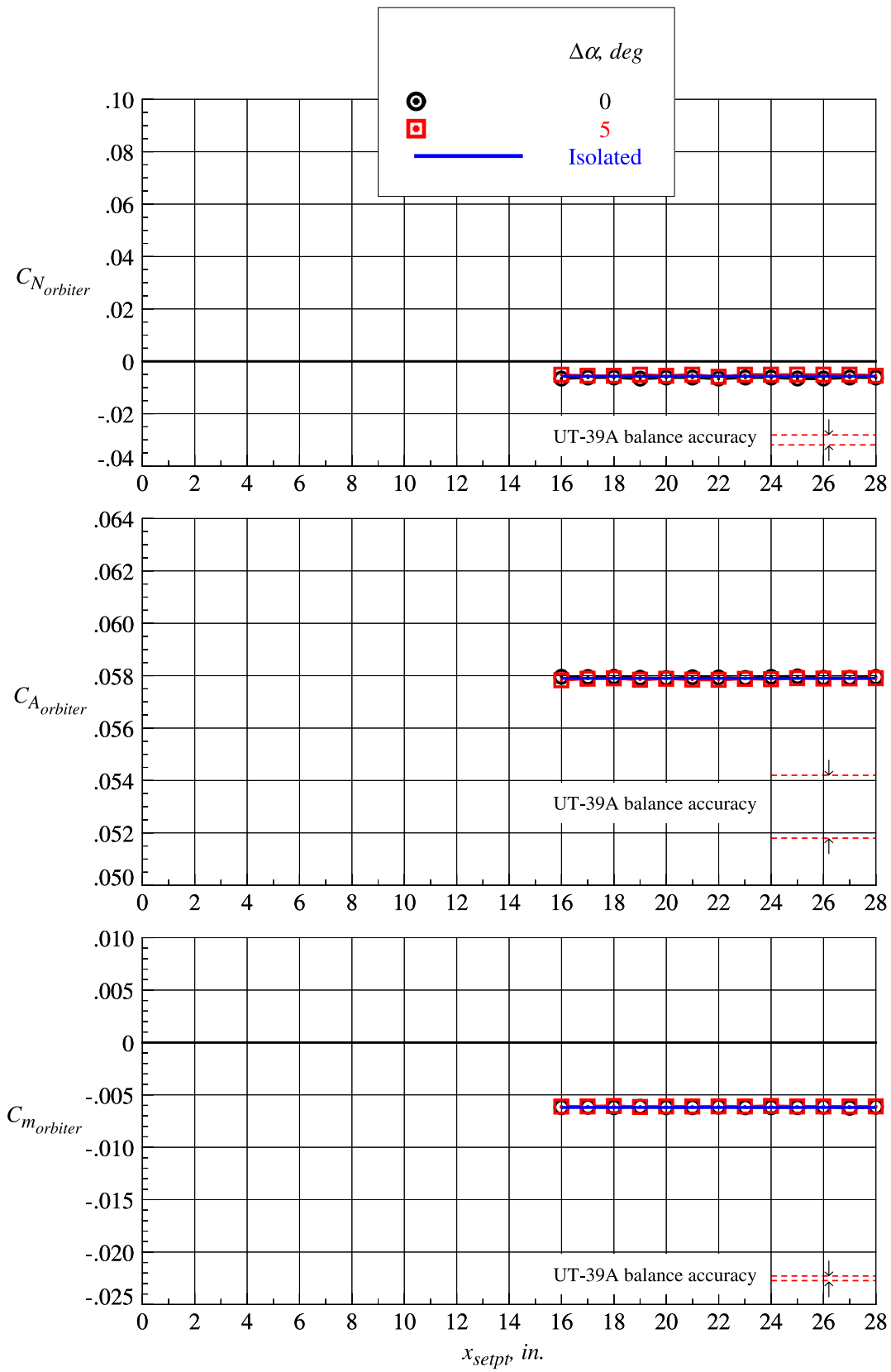
(k)  $z_{setpt} = 9.188 \text{ in.}$

Figure 62. Continued.



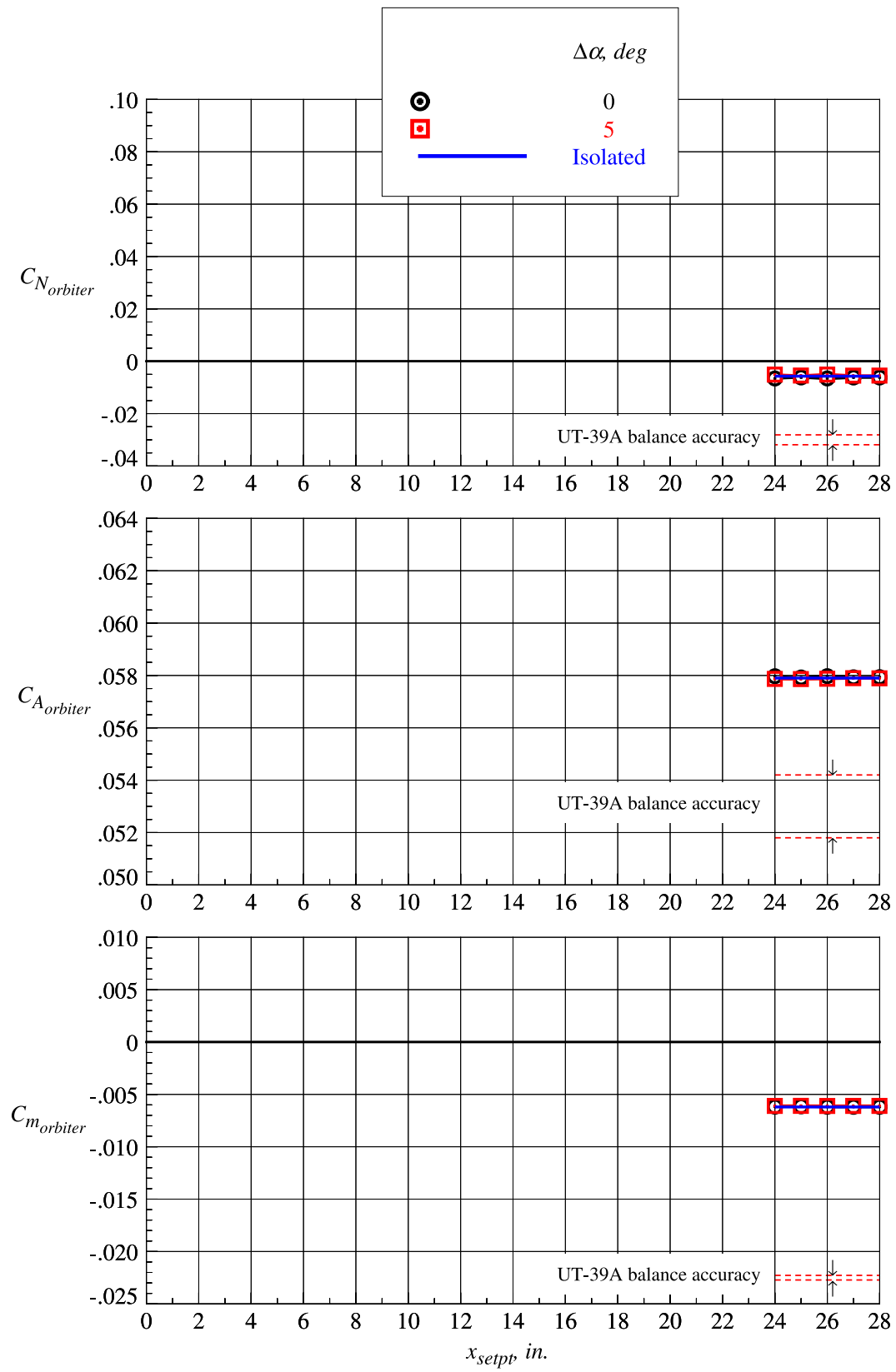
(l)  $z_{setpt} = 10.500$  in.

Figure 62. Continued.



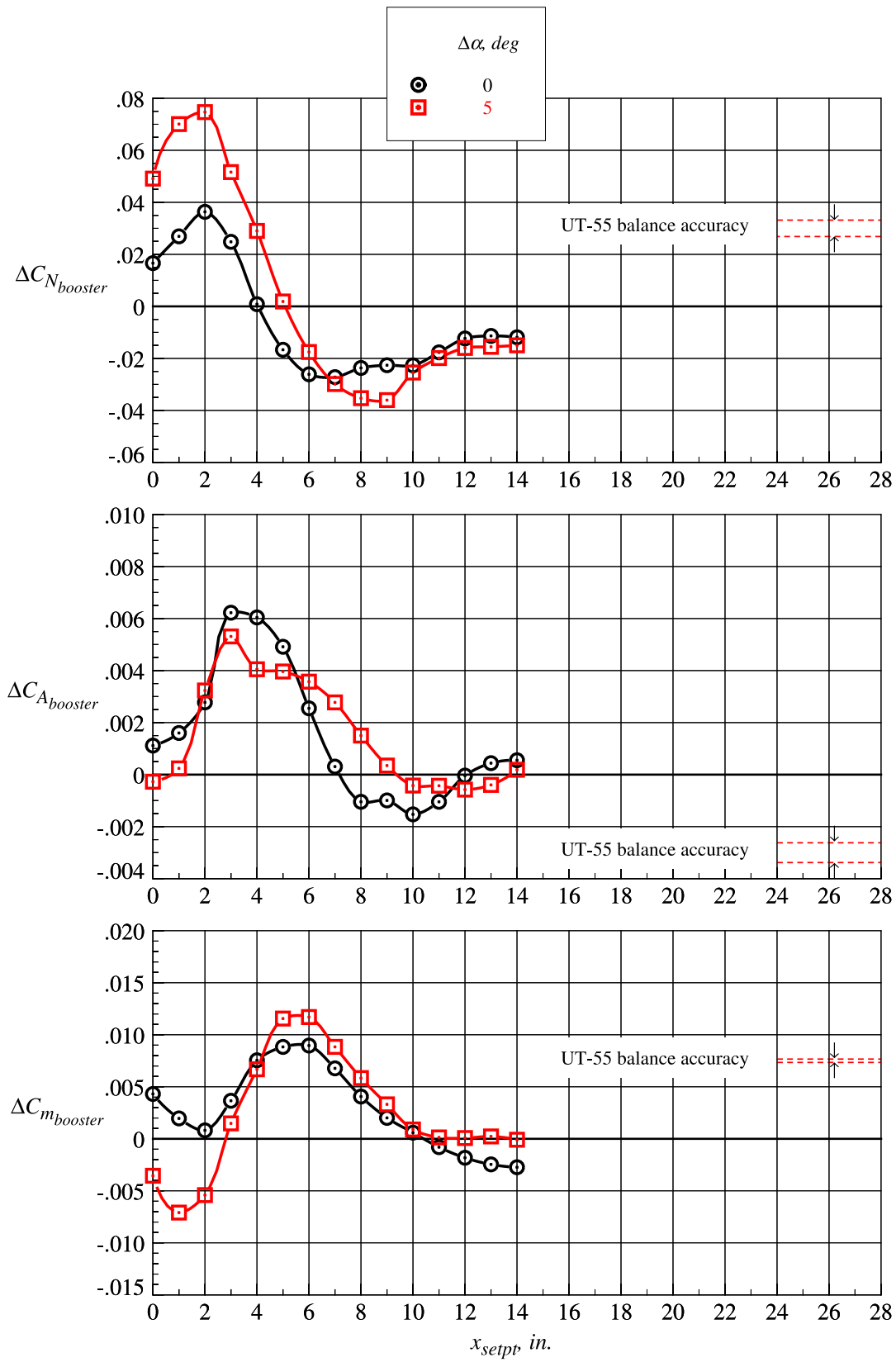
(m)  $z_{setpt} = 11.810 \text{ in.}$

Figure 62. Continued.



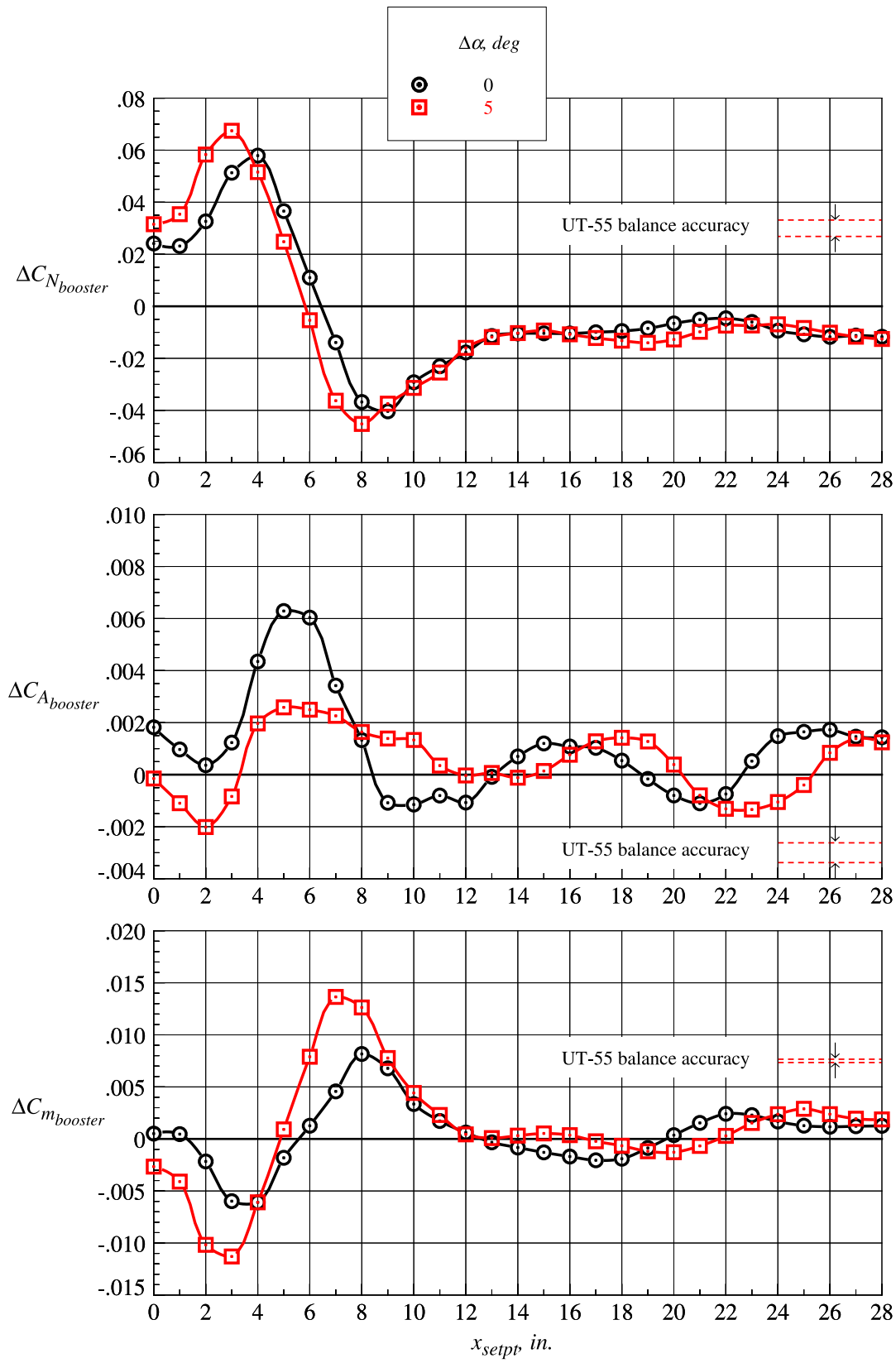
(n)  $z_{setpt} = 13.130 \text{ in.}$

Figure 62. Concluded.



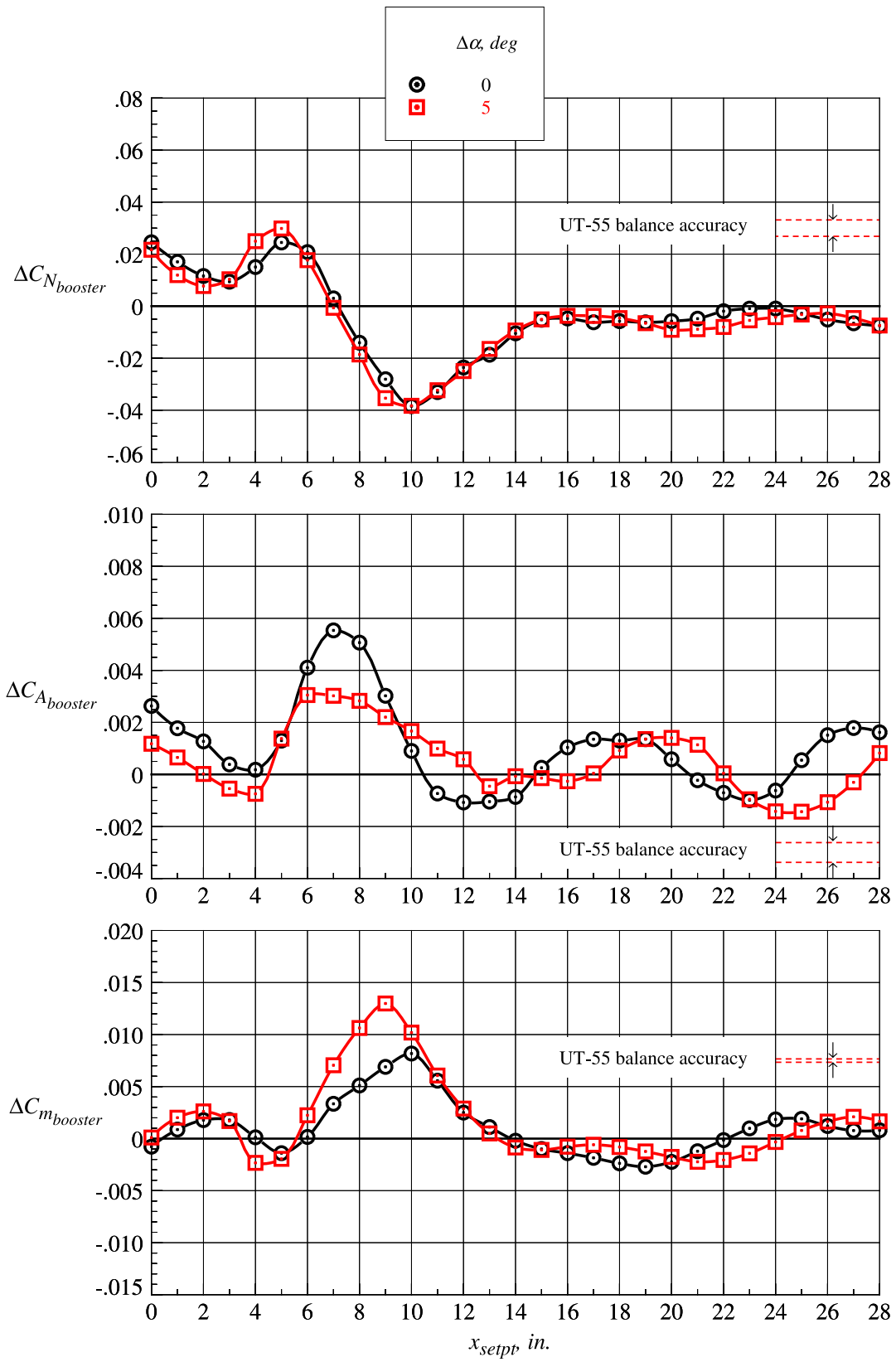
(a)  $z_{setpb} = 0.656$  in.

Figure 63. Booster interference aerodynamic characteristics at  $\Delta\alpha = 0^\circ$  and  $5^\circ$ ;  $Mach = 3.0$ .



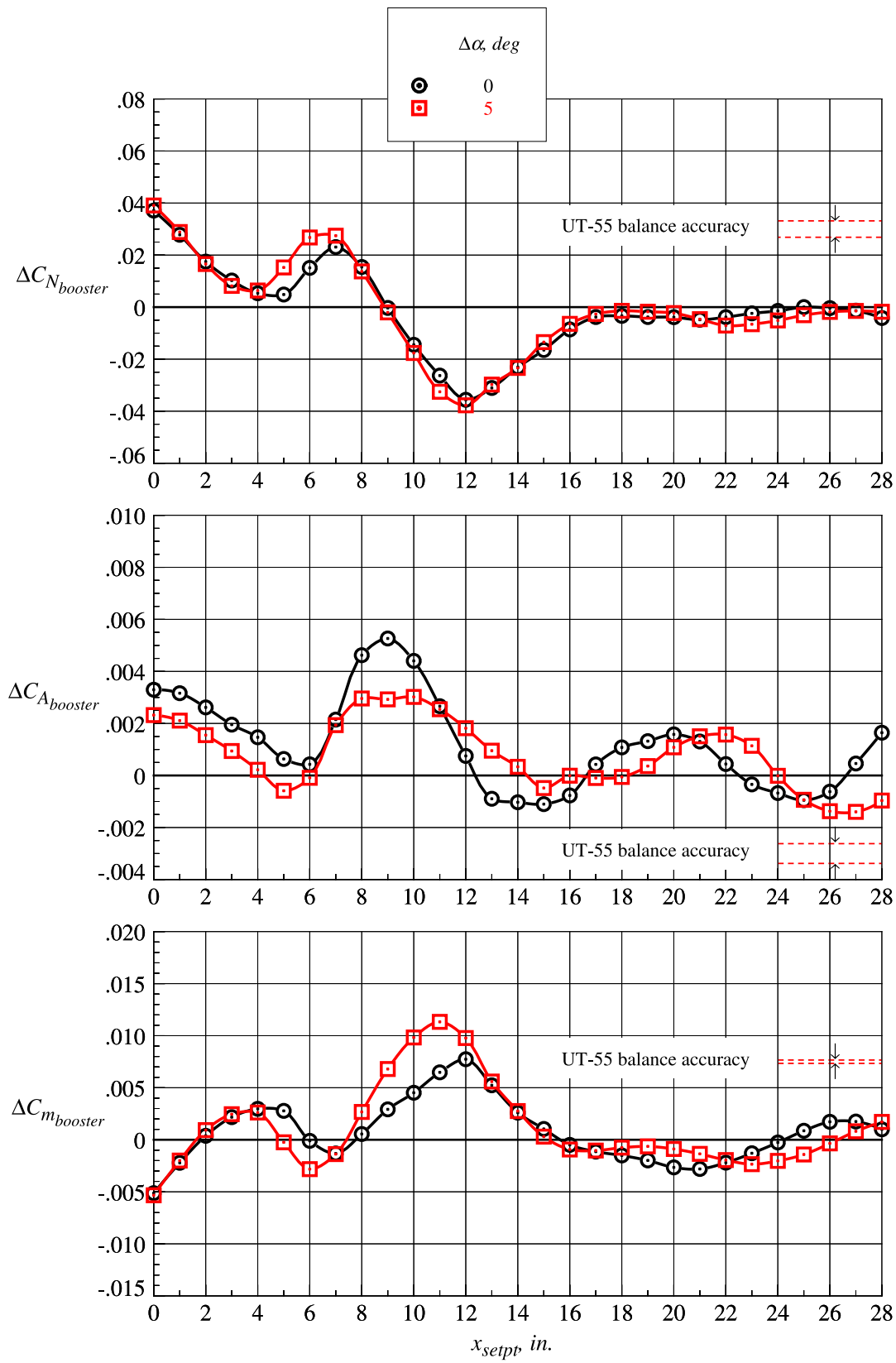
(b)  $z_{setpt} = 1.313$  in.

Figure 63. Continued.



(c)  $z_{setpt} = 1.969 \text{ in.}$

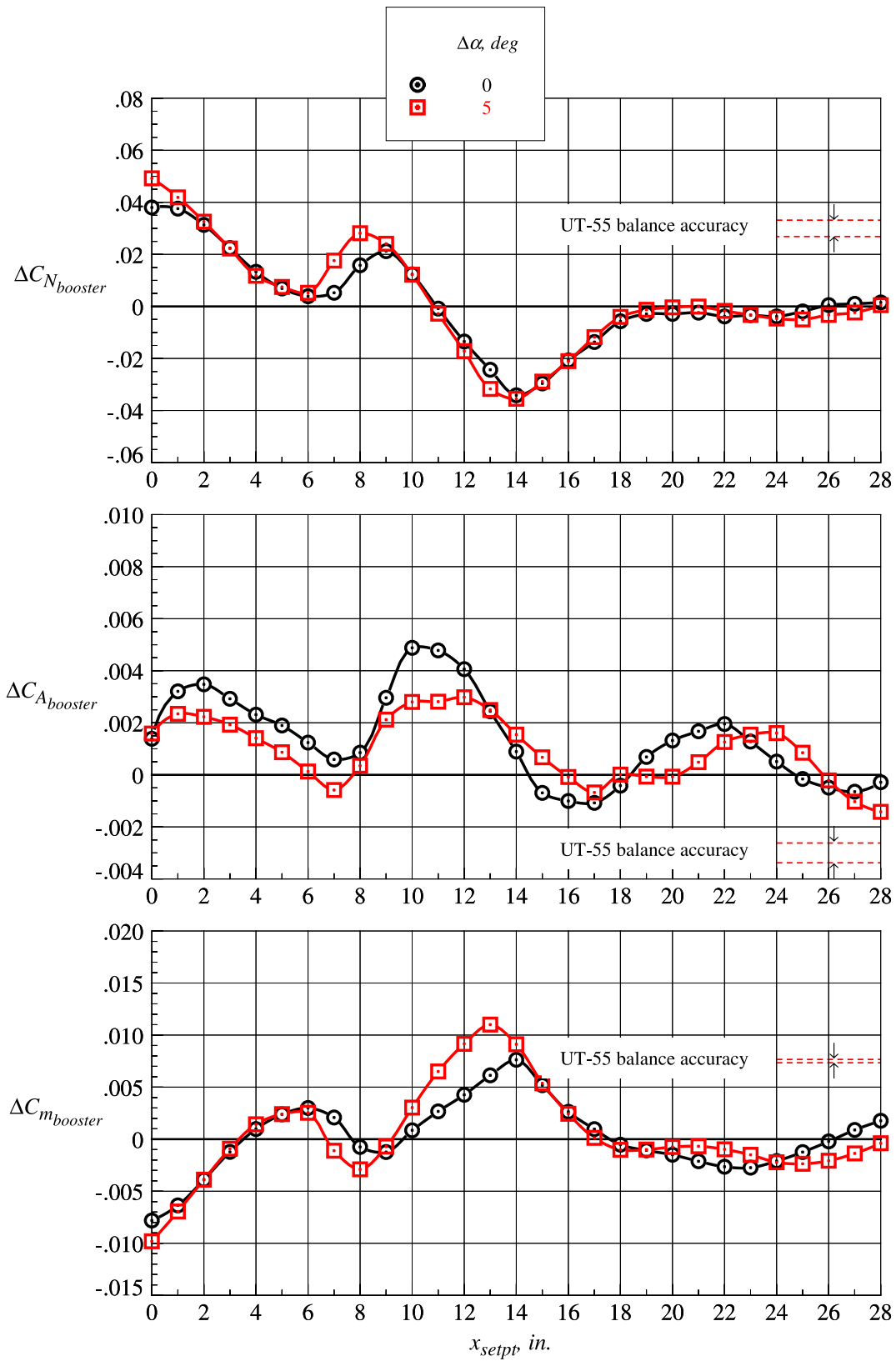
Figure 63. Continued.



(d)  $z_{setpt} = 2.625$  in.

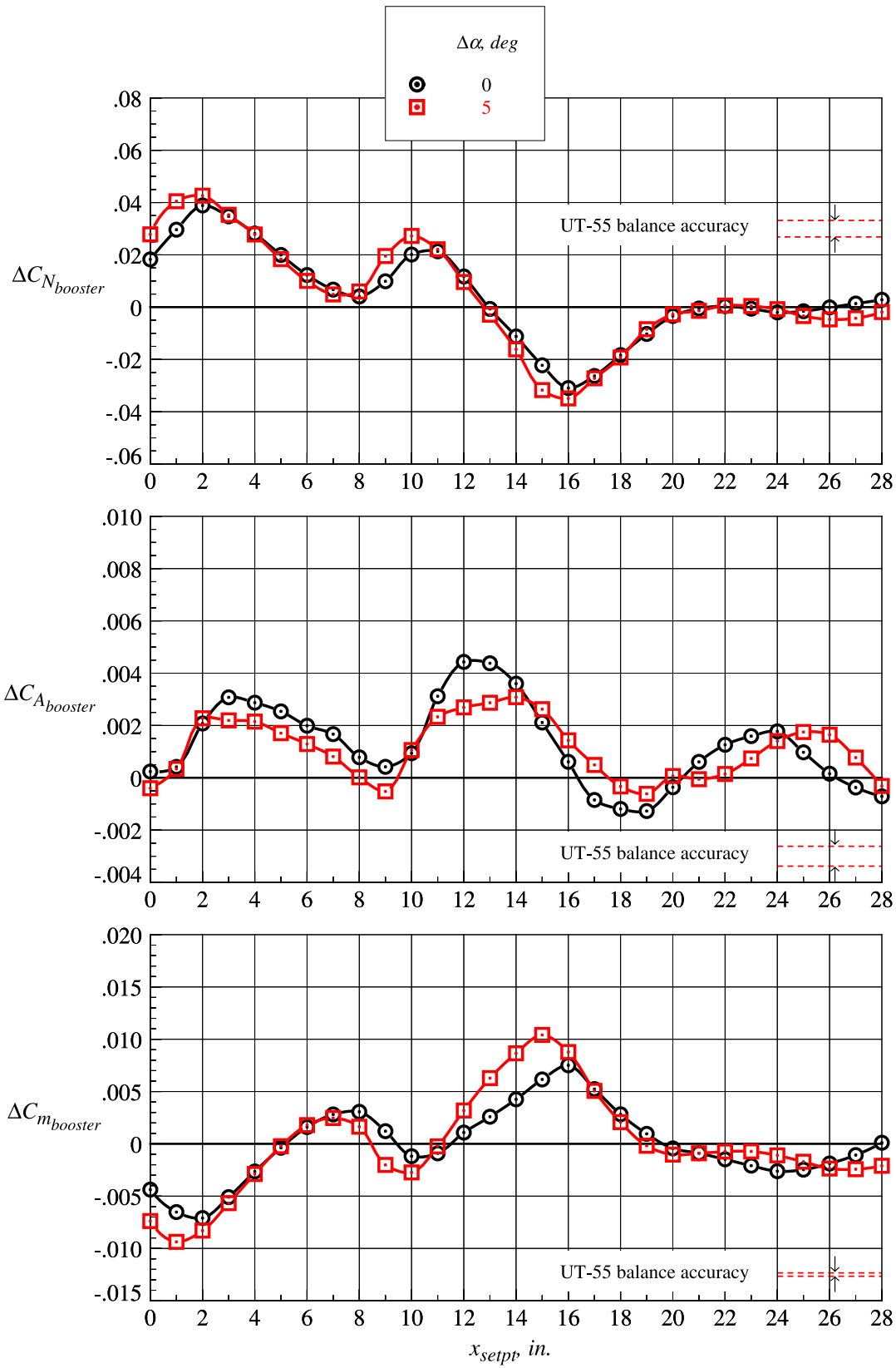
Figure 63. Continued.





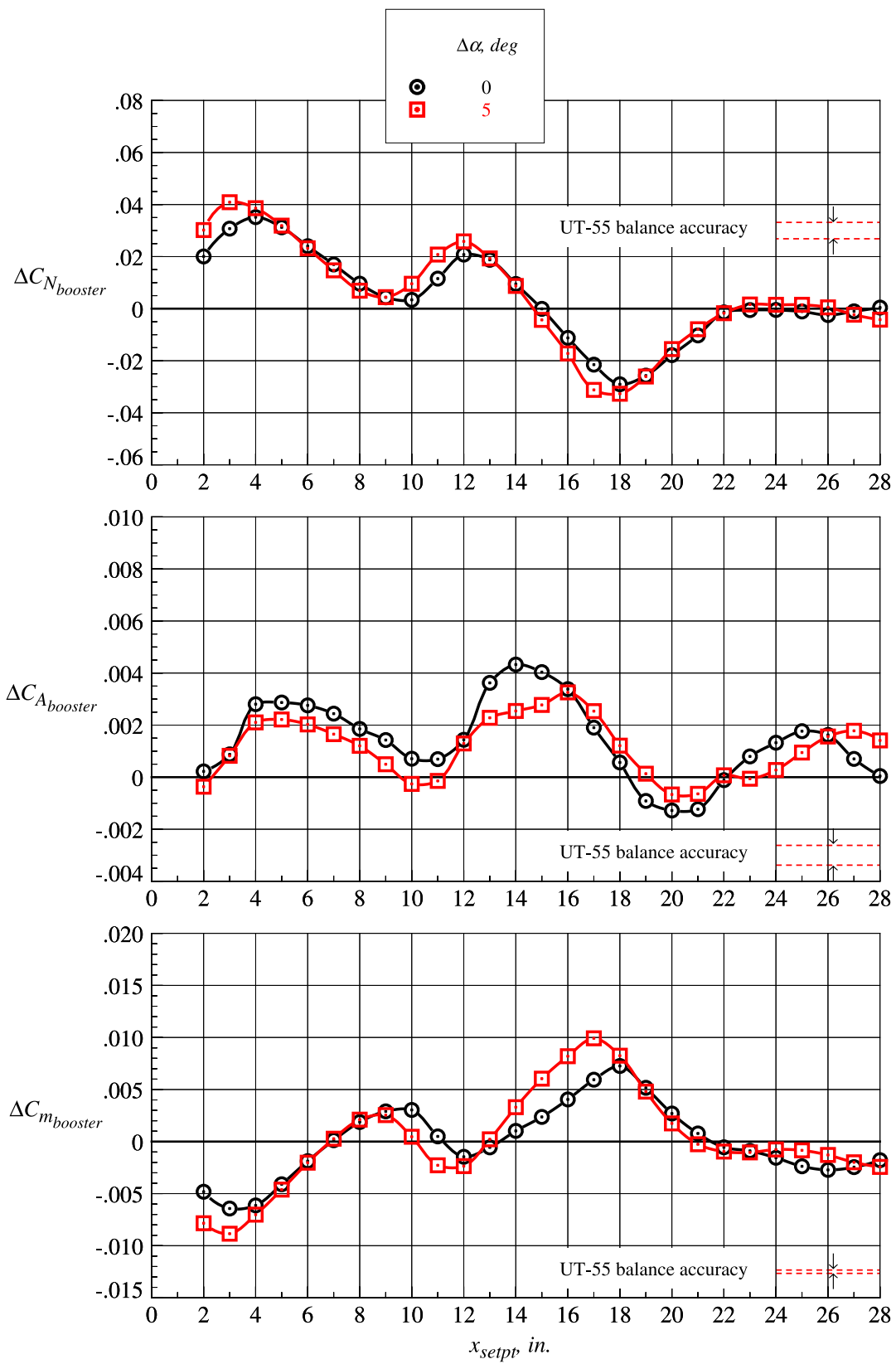
(e)  $z_{setpt} = 3.281$  in.

Figure 63. Continued.



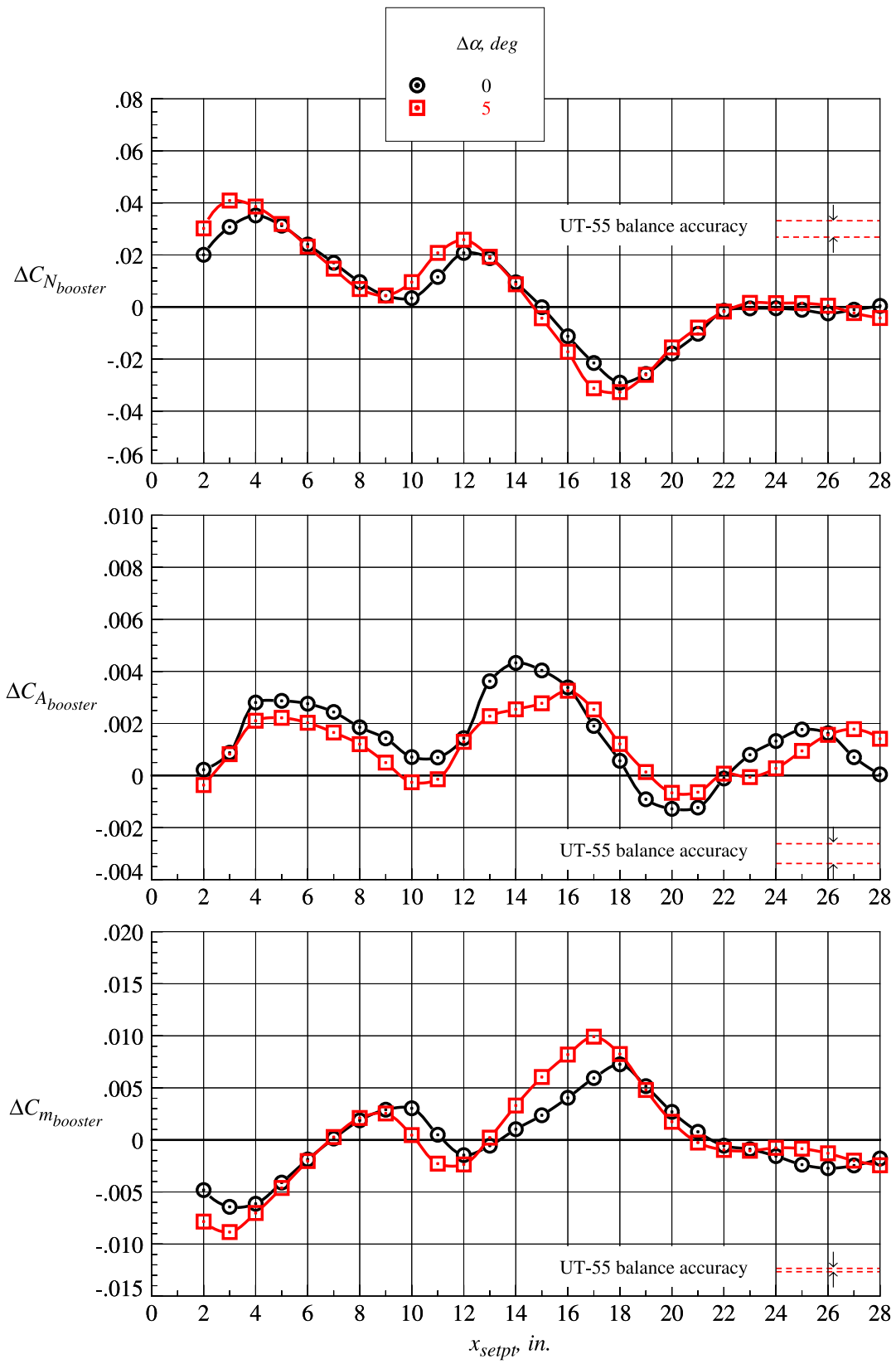
(f)  $z_{setpt} = 3.938 \text{ in.}$

Figure 63. Continued.



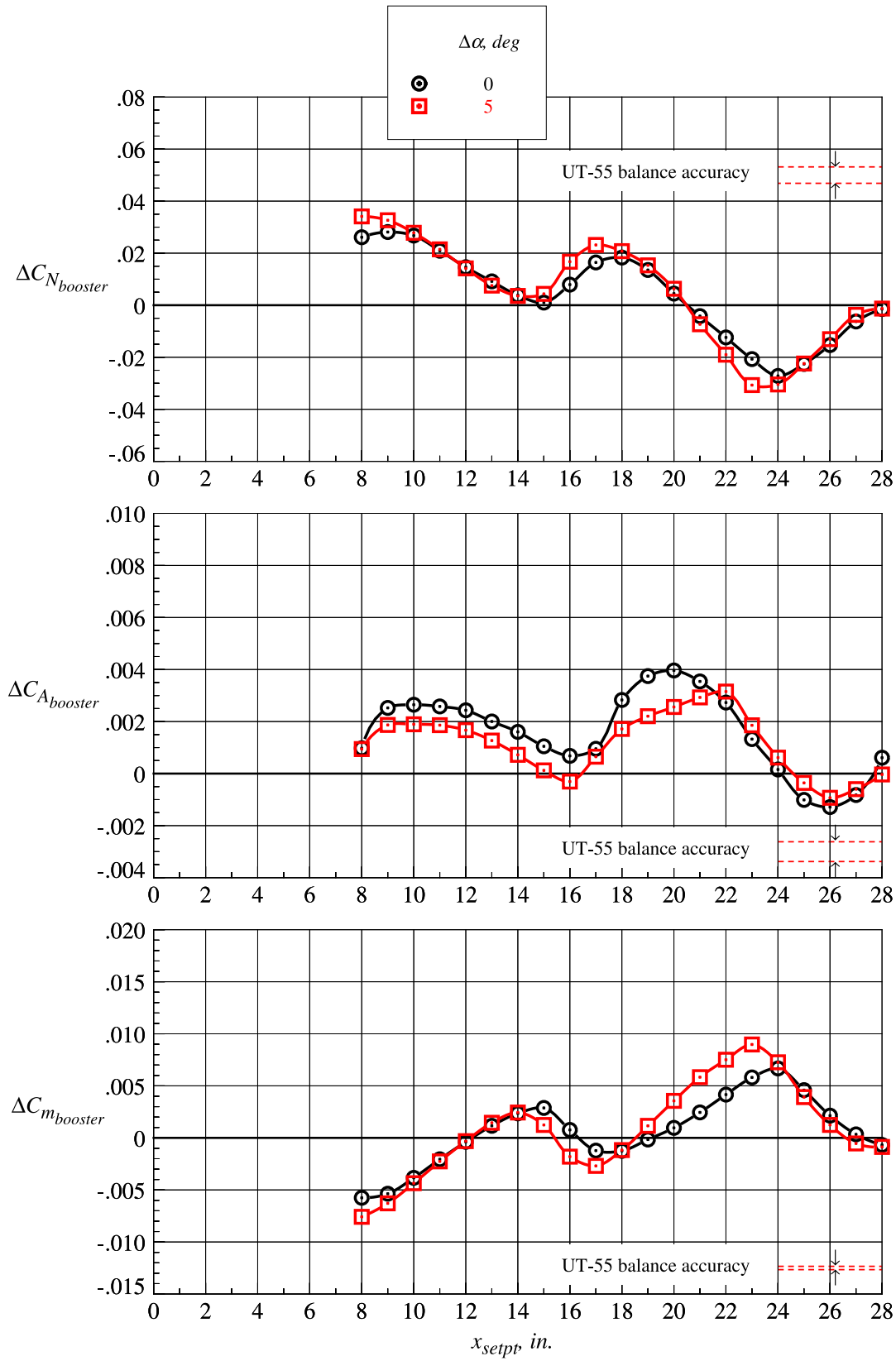
(g)  $z_{setpt} = 4.594 \text{ in.}$

Figure 63. Continued.



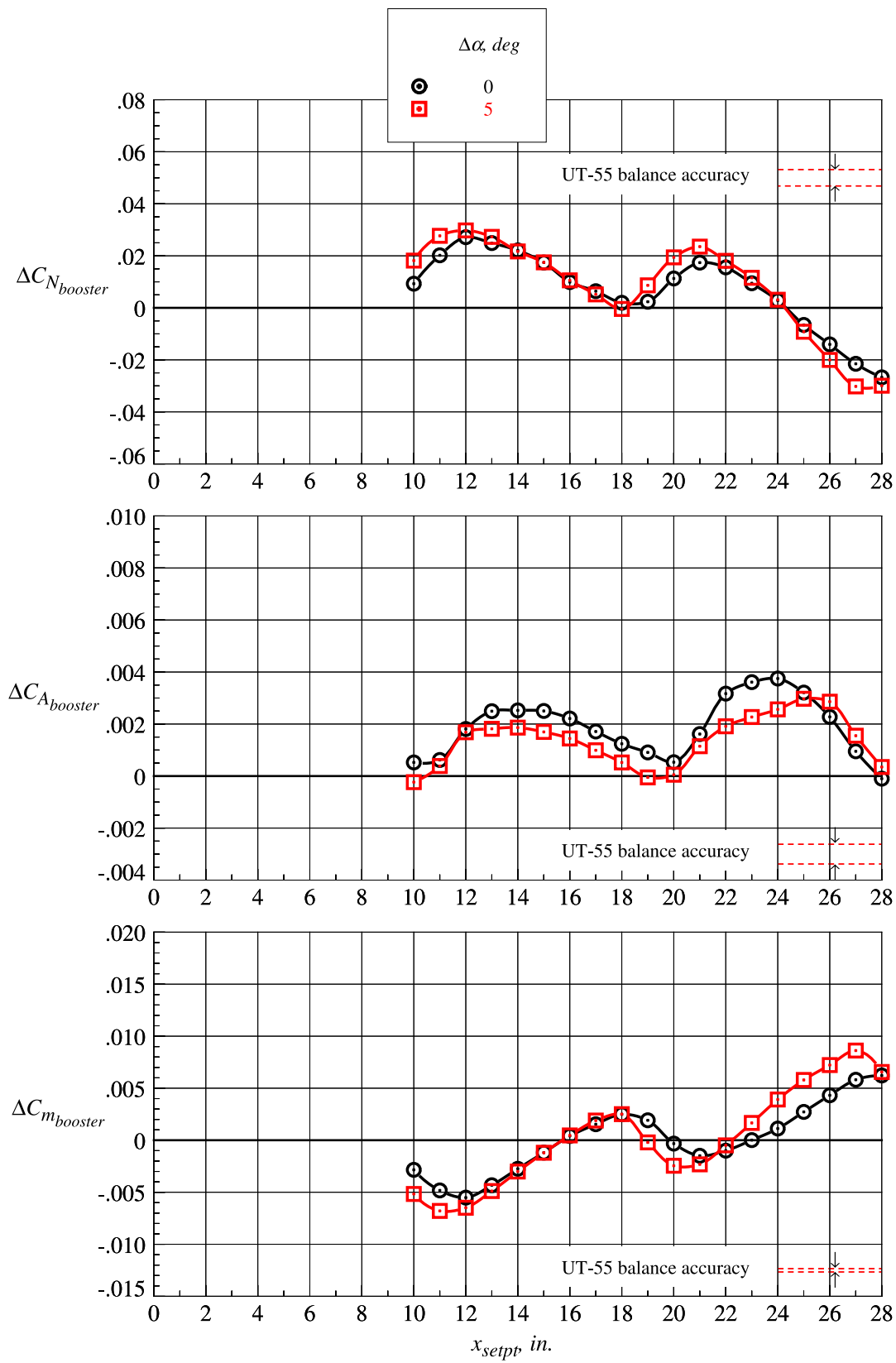
(h)  $z_{setpt} = 5.250 \text{ in.}$

Figure 63. Continued.



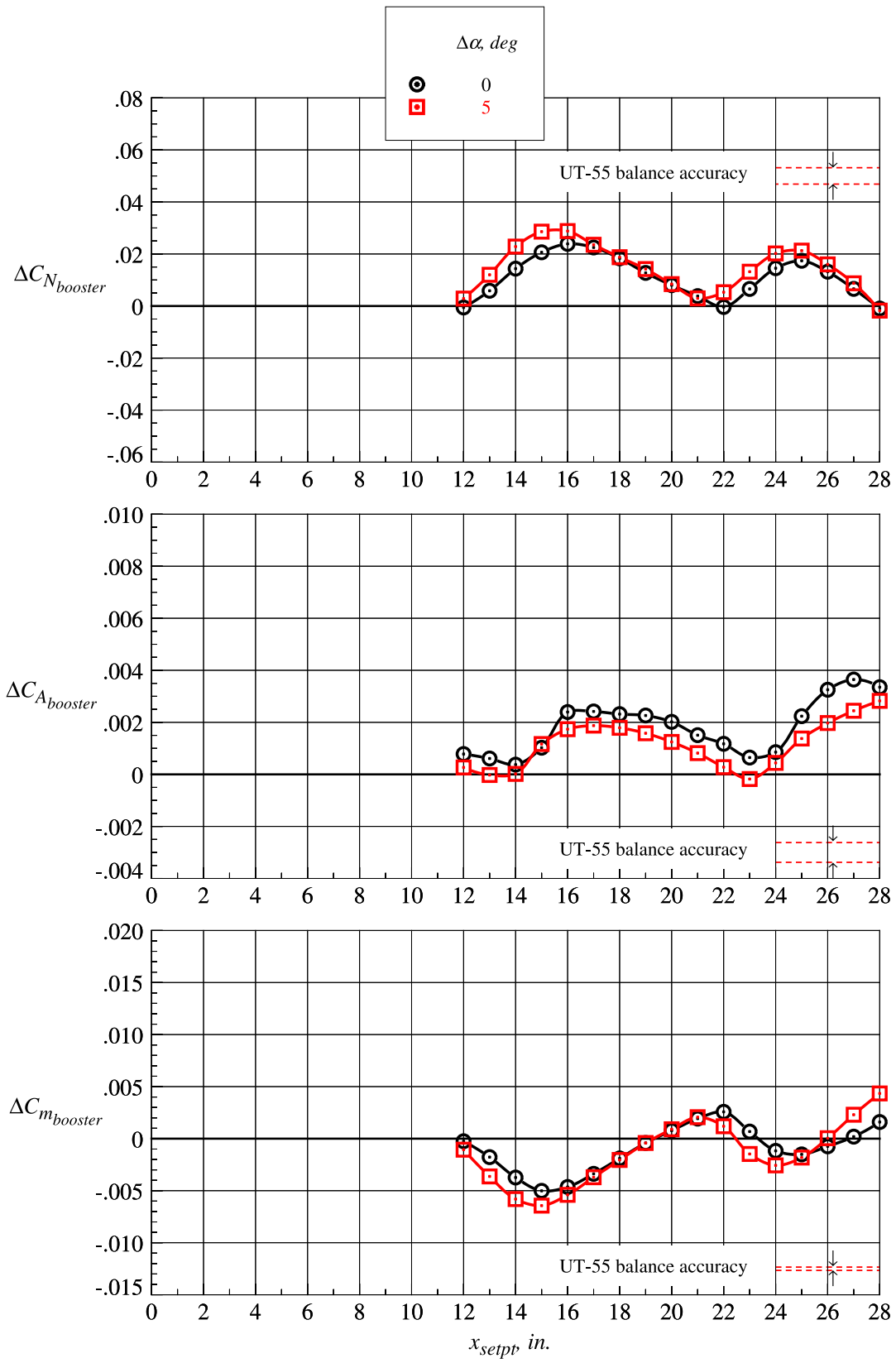
(i)  $z_{setpt} = 6.583 \text{ in.}$

Figure 63. Continued.



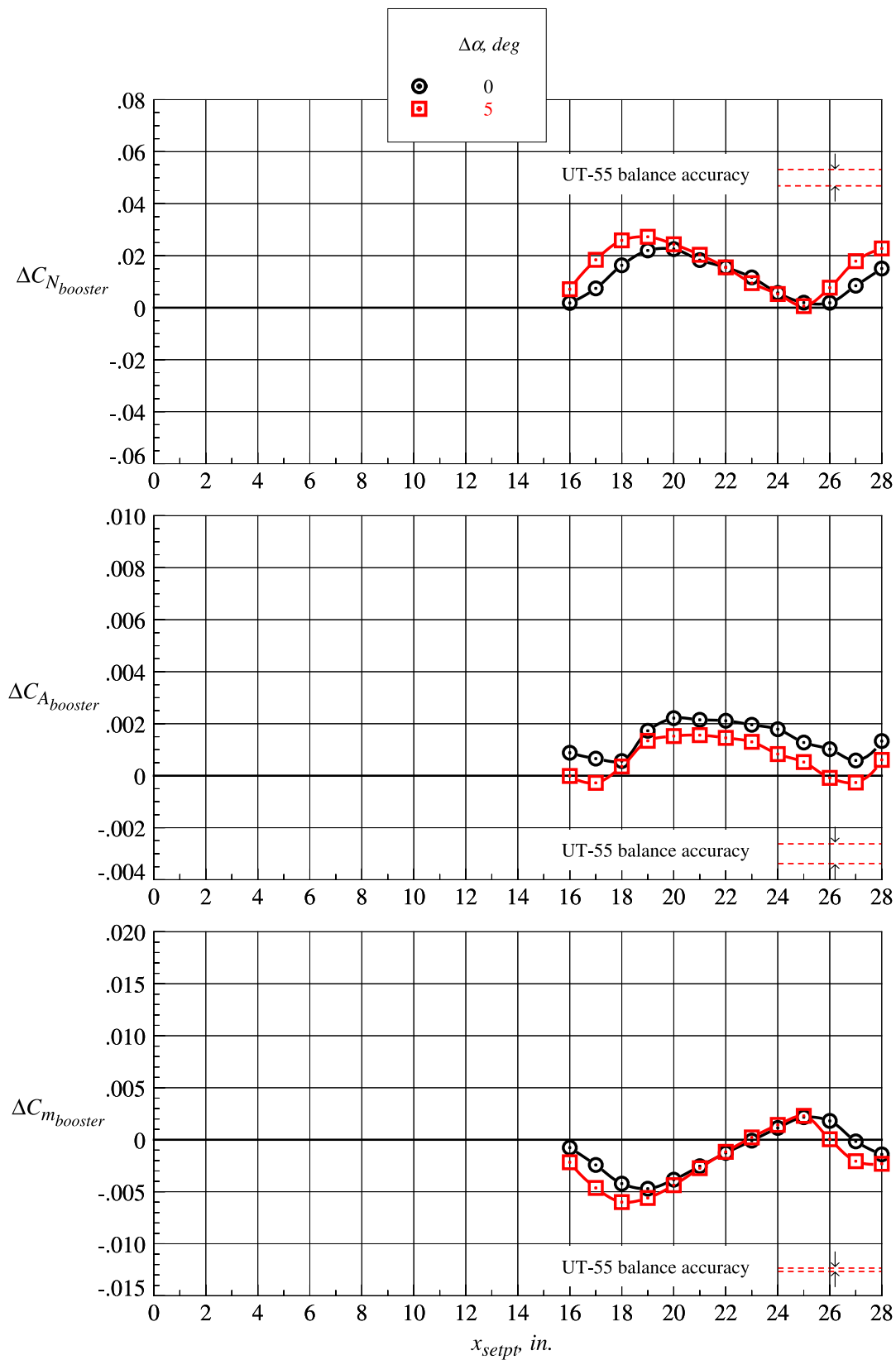
(j)  $z_{setpt} = 7.875$  in.

Figure 63. Continued.



(k)  $z_{setpt} = 9.188$  in.

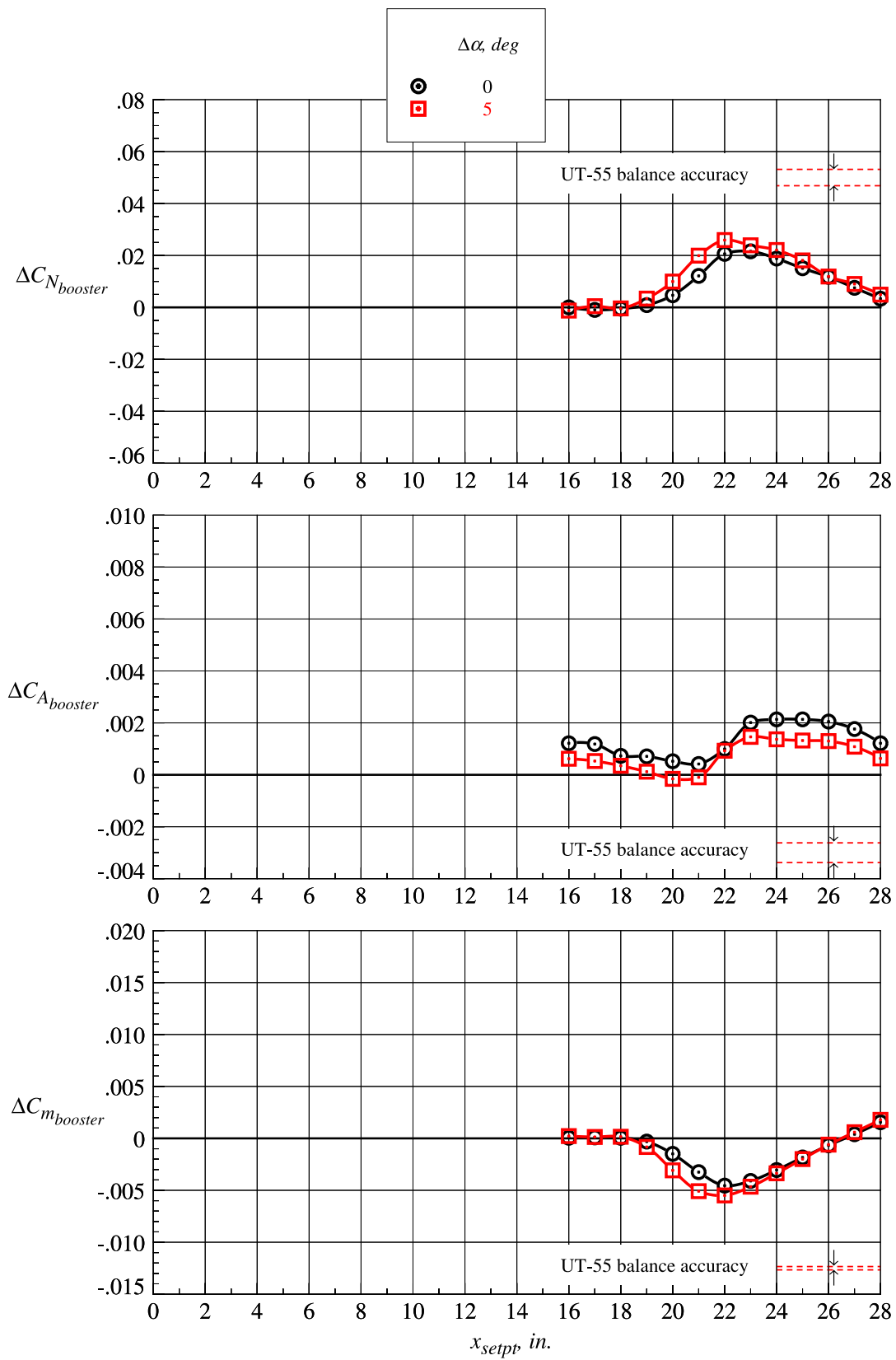
Figure 63. Continued.



(l)  $z_{setpt} = 10.500$  in.

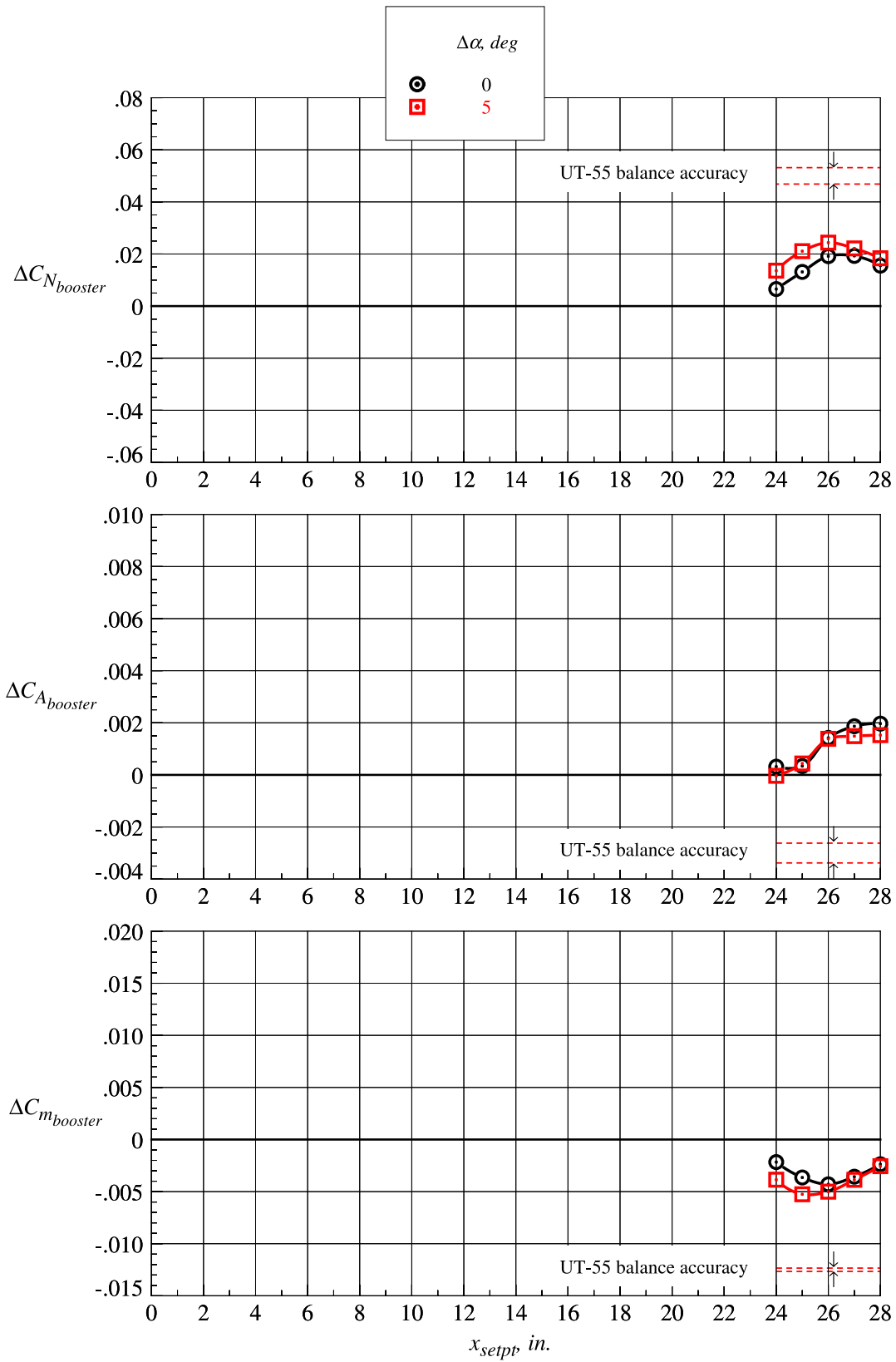
Figure 63. Continued.





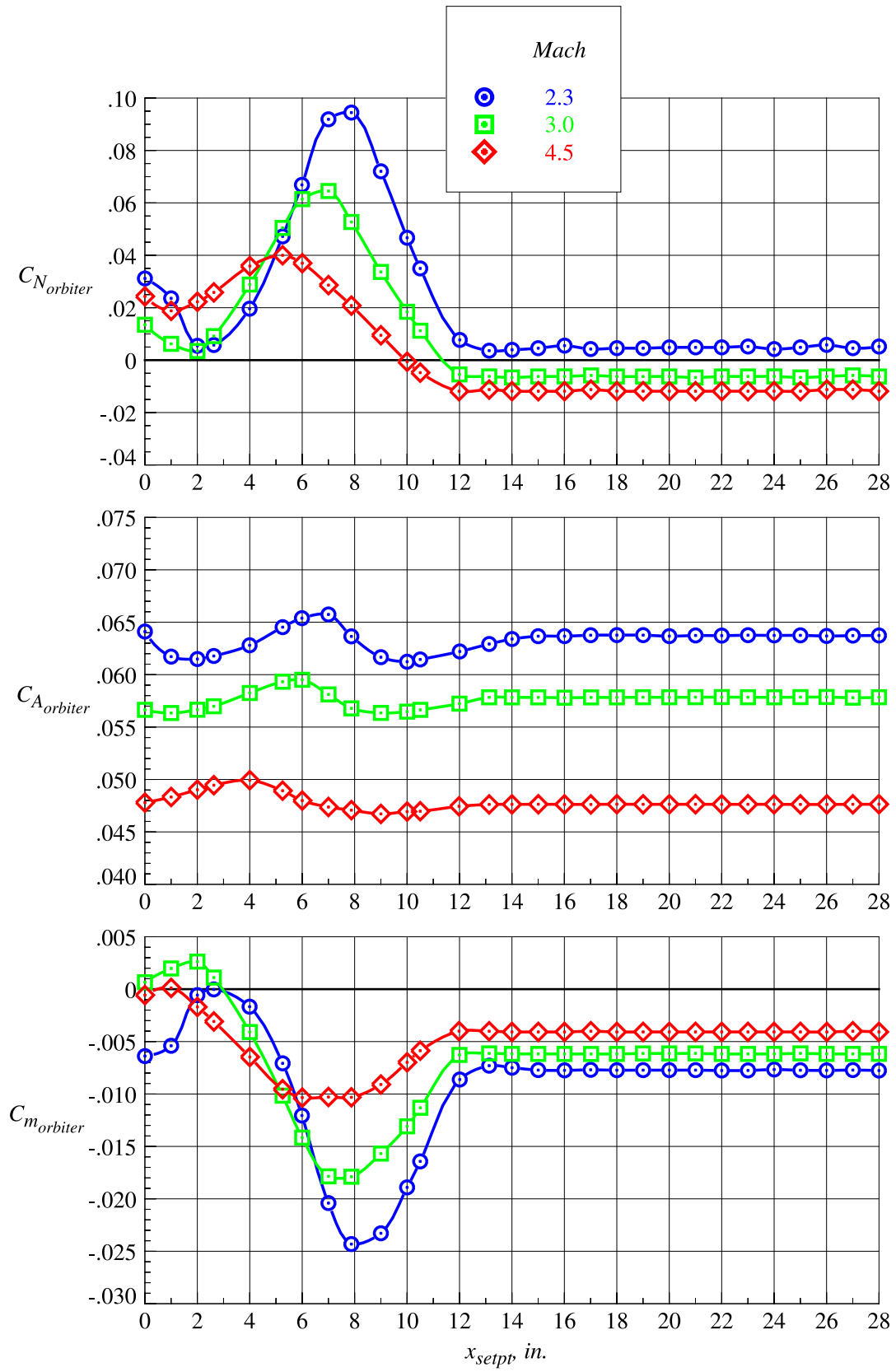
(m)  $z_{setpt} = 11.810$  in.

Figure 63. Continued.



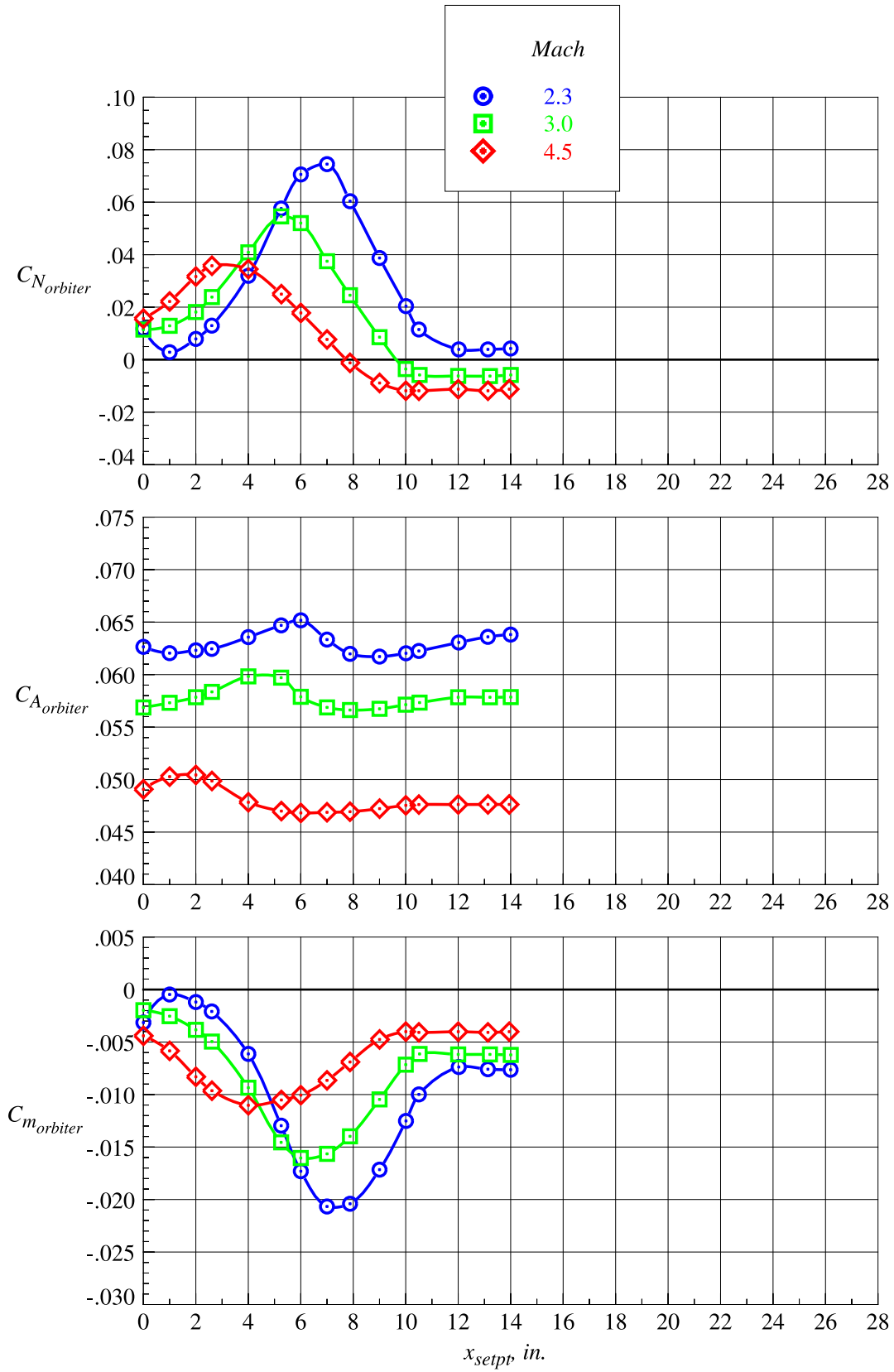
(n)  $z_{setpt} = 13.130 \text{ in.}$

Figure 63. Concluded.



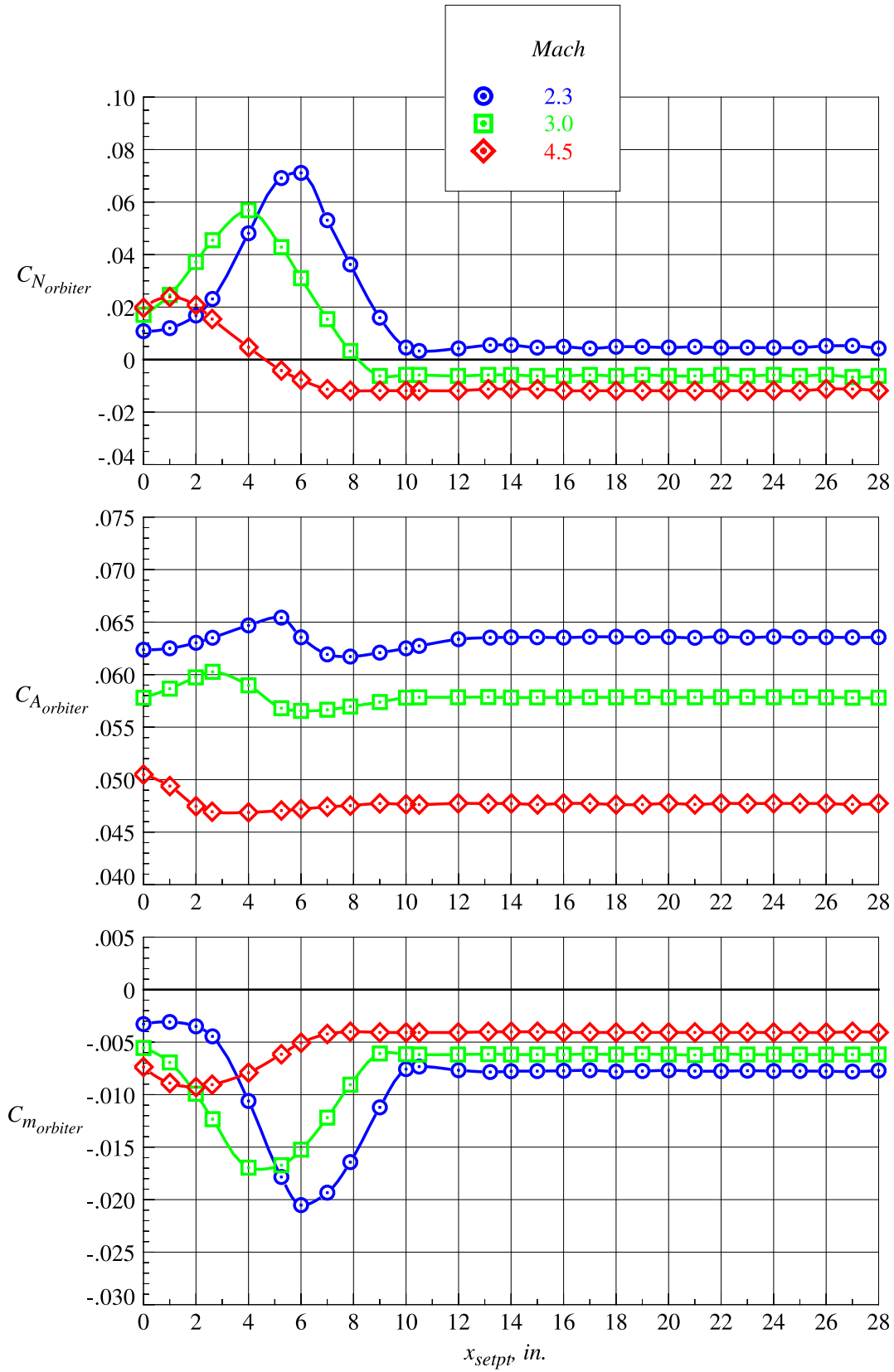
(a)  $z_{setpt} = 0 \text{ in.}$

Figure 64. Orbiter proximity aerodynamic characteristics at Mach = 2.3, 3.0, and 4.5;  $\Delta\alpha = 0^\circ$ .



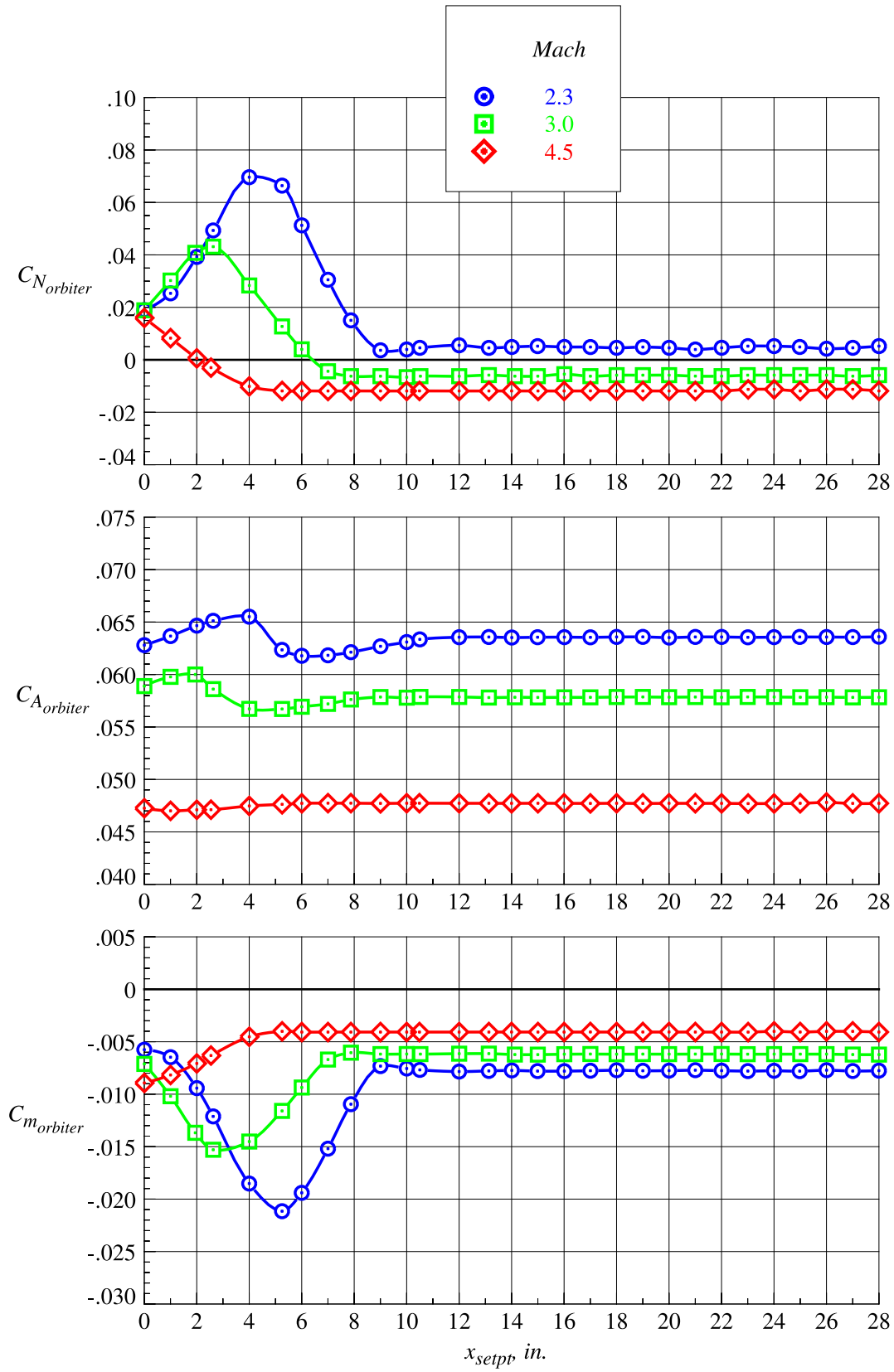
(b)  $z_{setpt} = 0.656$  in.

Figure 64. Continued.



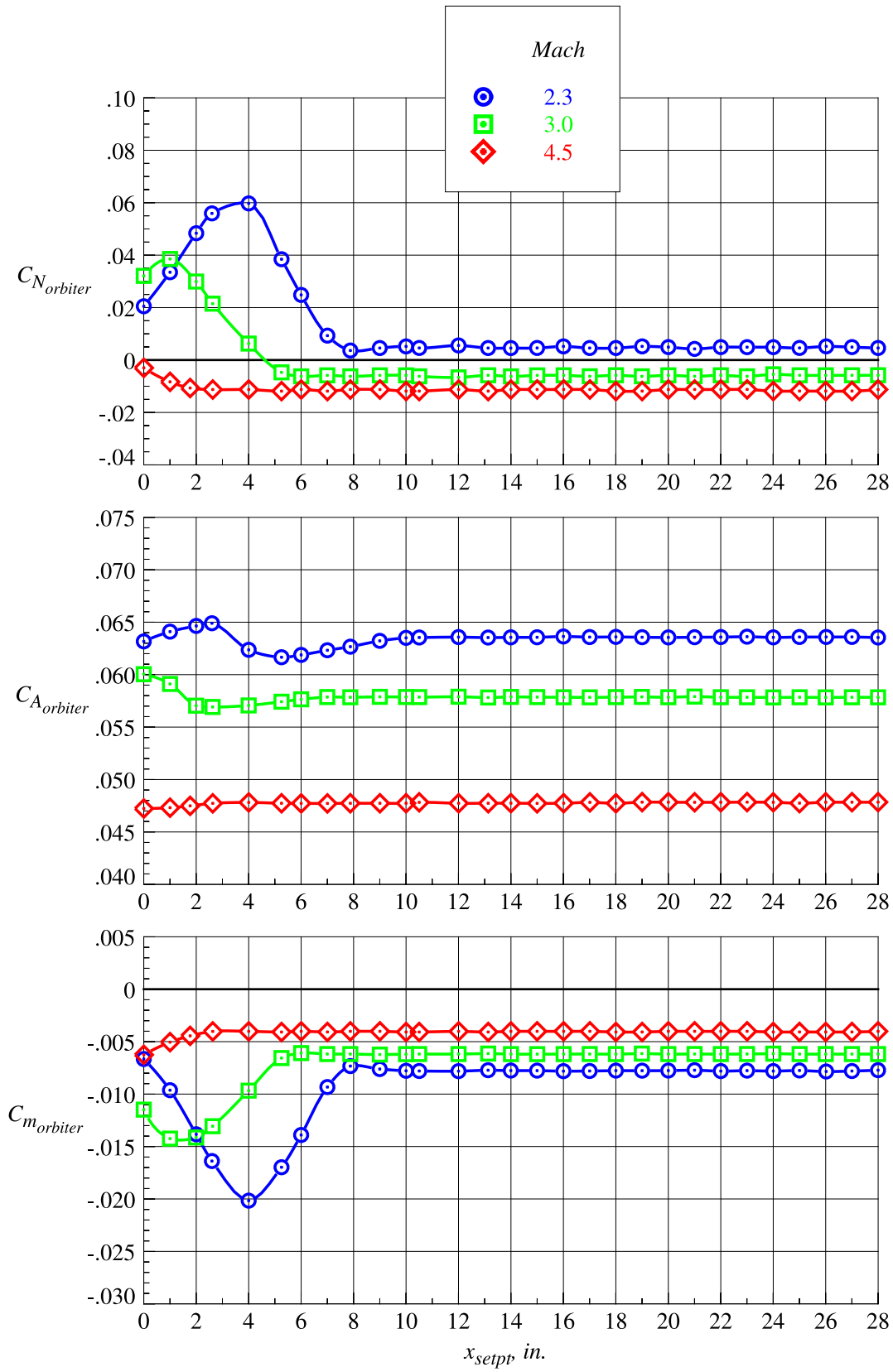
(c)  $z_{setpt} = 1.313$  in.

Figure 64. Continued.



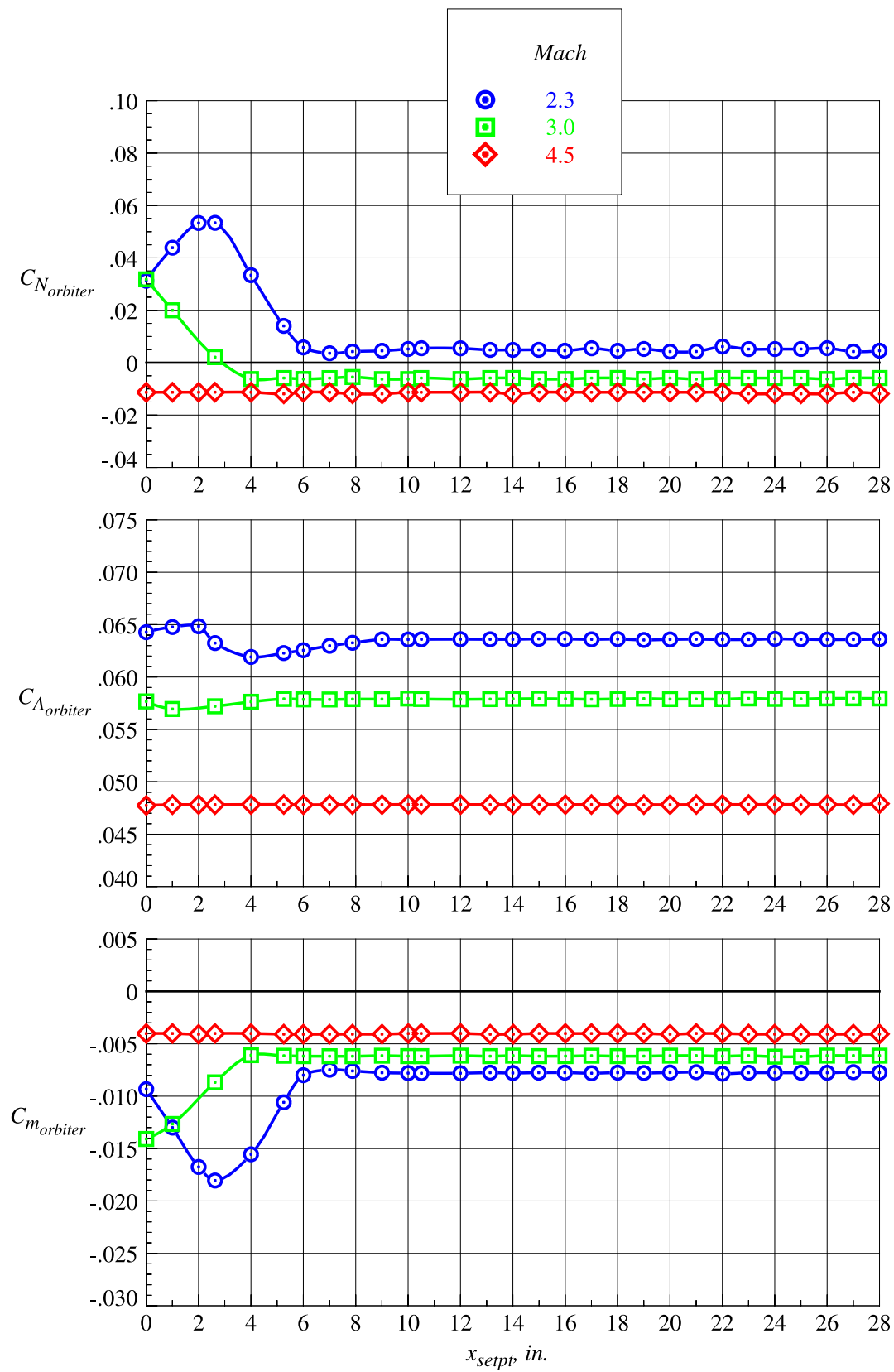
(d)  $z_{setpt} = 1.969$  in.

Figure 64. Continued.



(e)  $z_{setpt} = 2.625$  in.

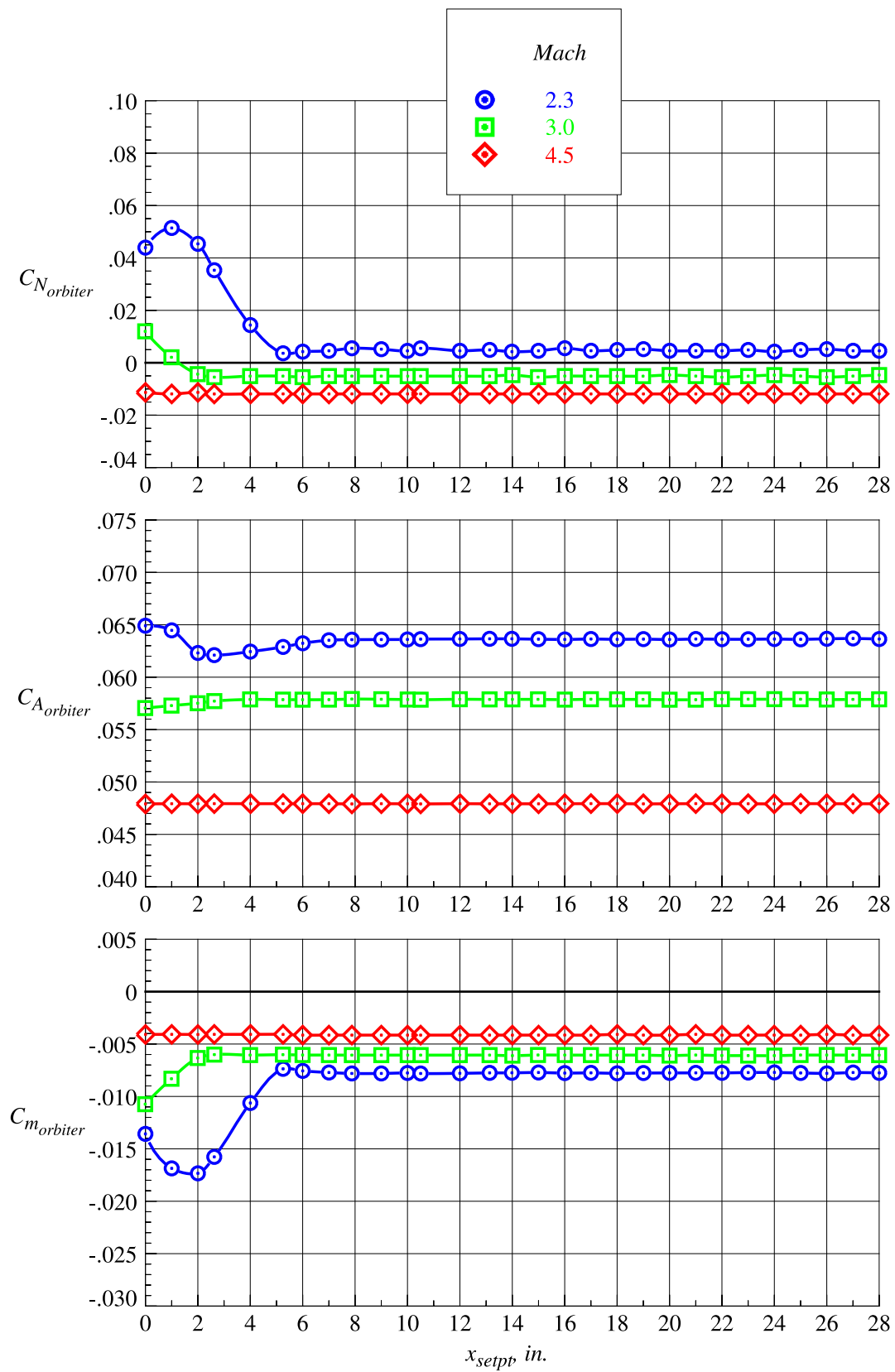
Figure 64. Continued.



(f)  $z_{setpt} = 3.281$  in.

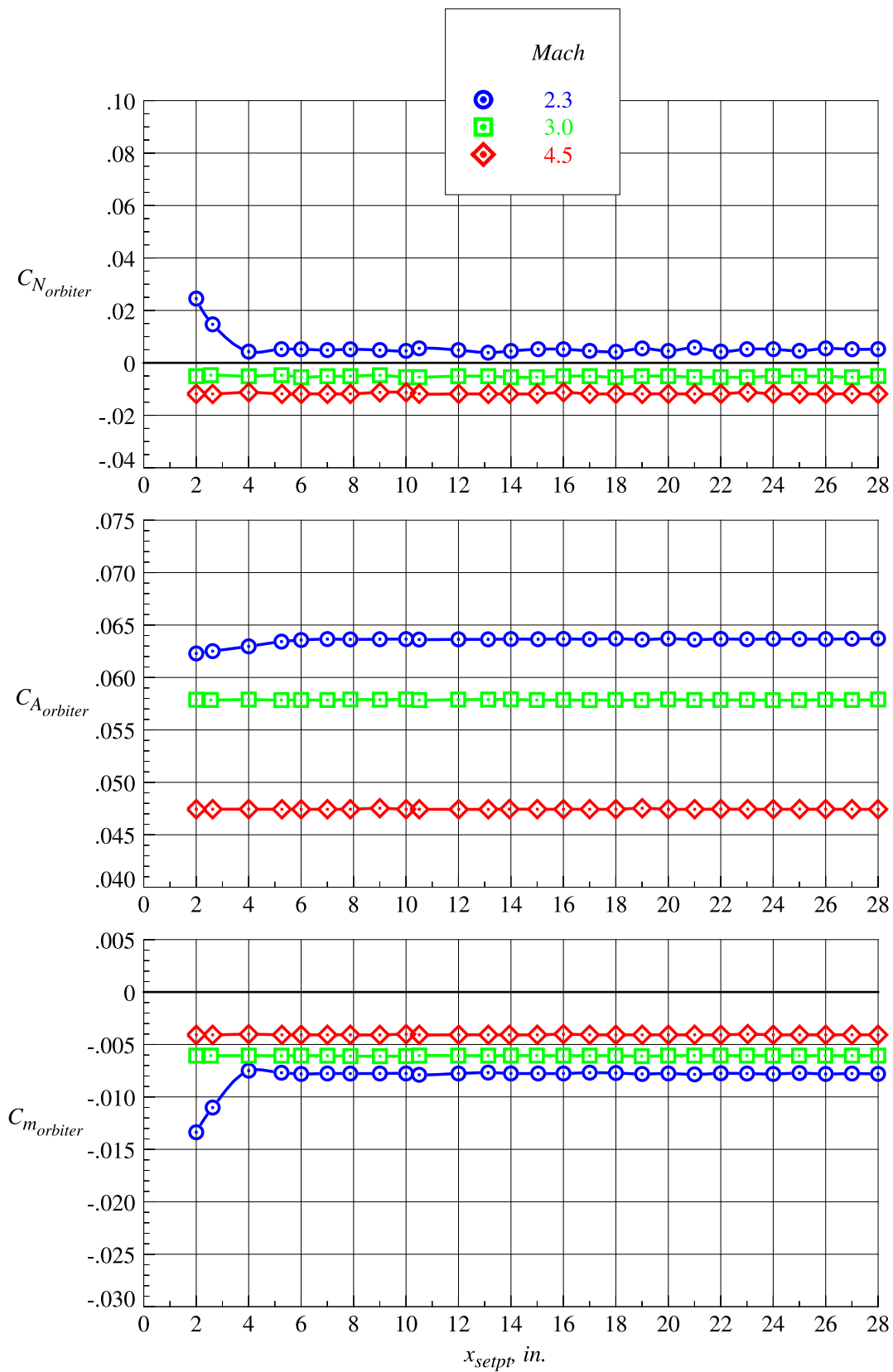
Figure 64. Continued.





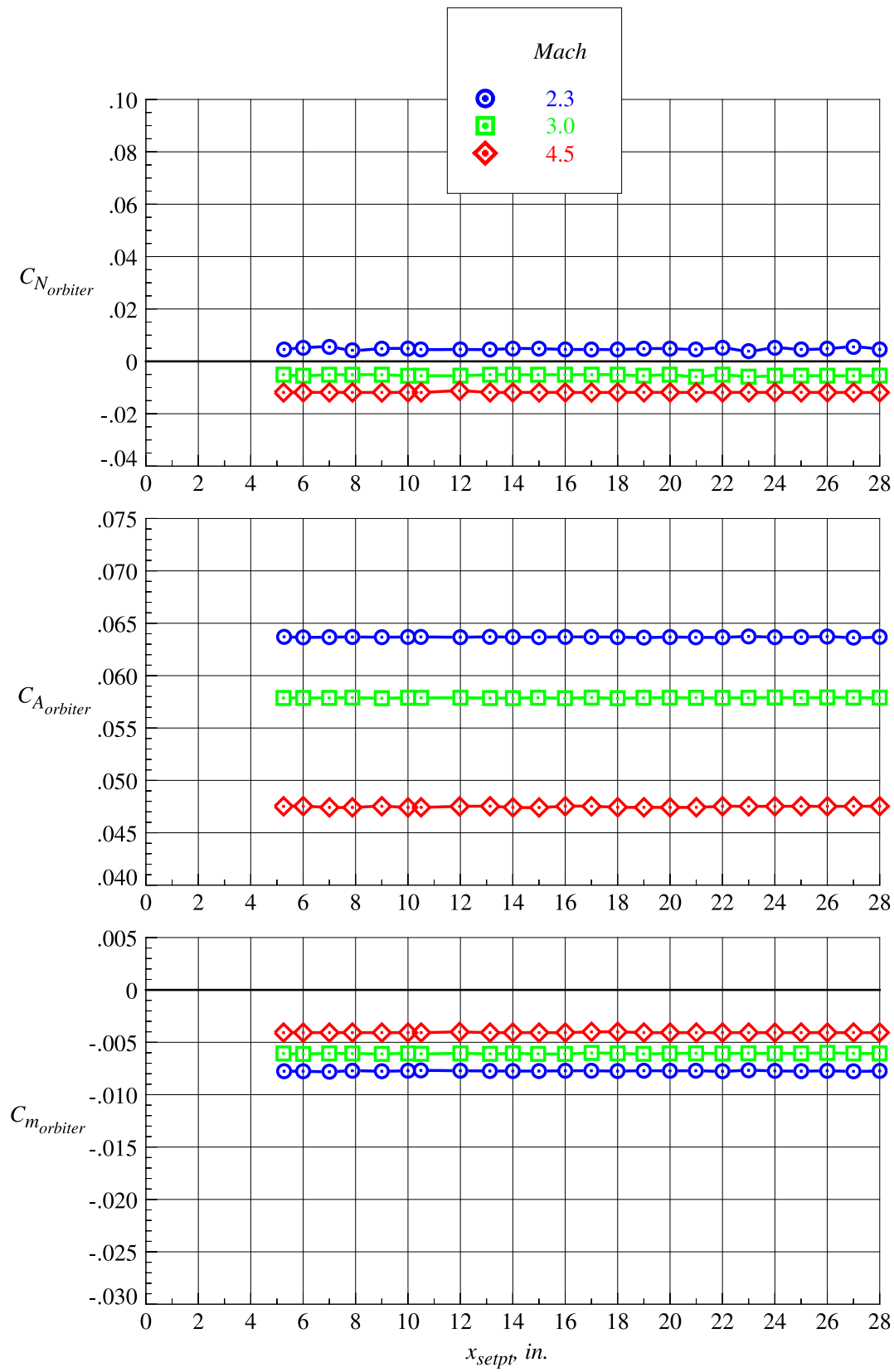
(g)  $z_{setpt} = 3.938$  in.

Figure 64. Continued.



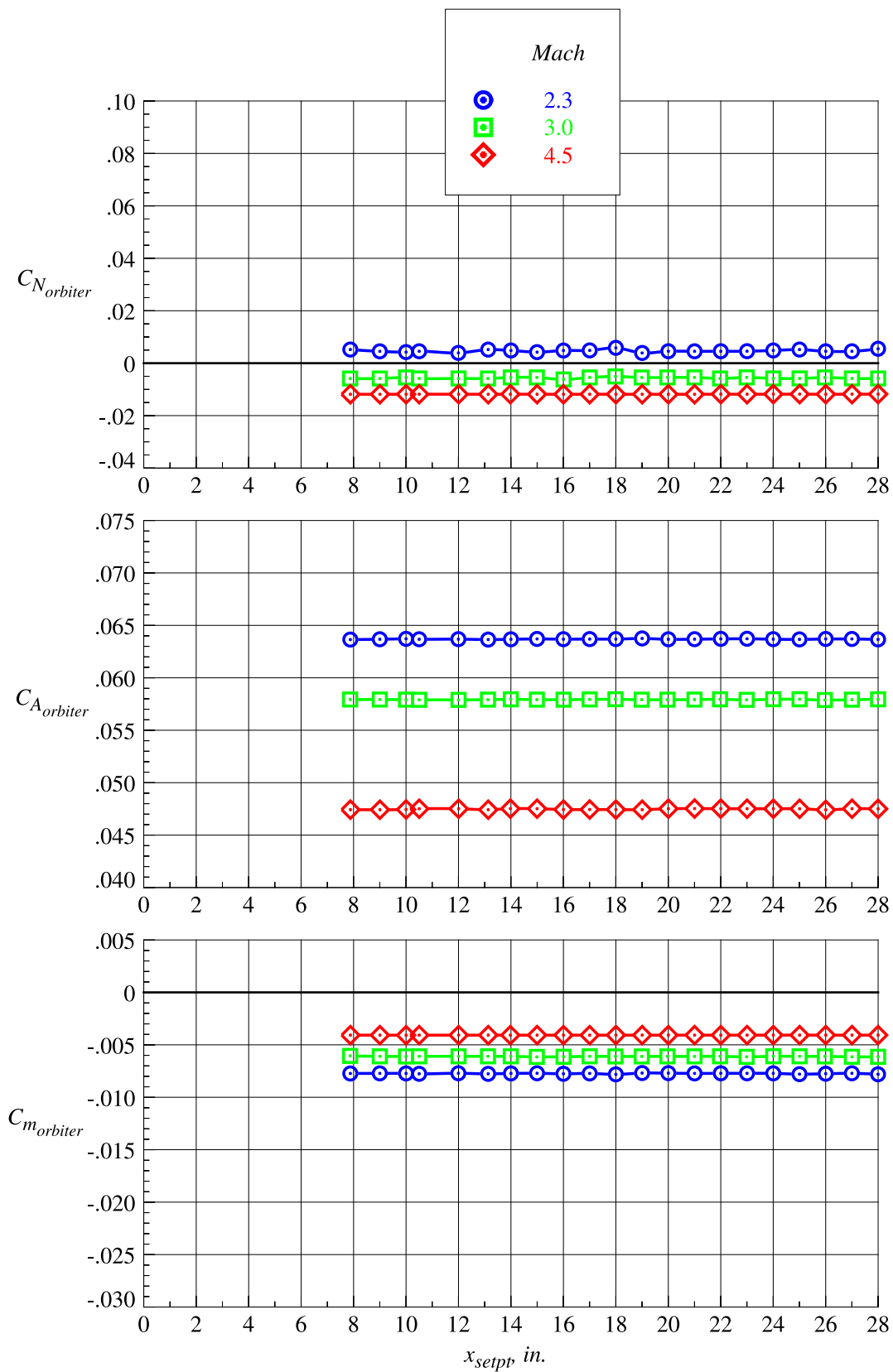
(h)  $z_{setpt} = 4.594$  in.

Figure 64. Continued.



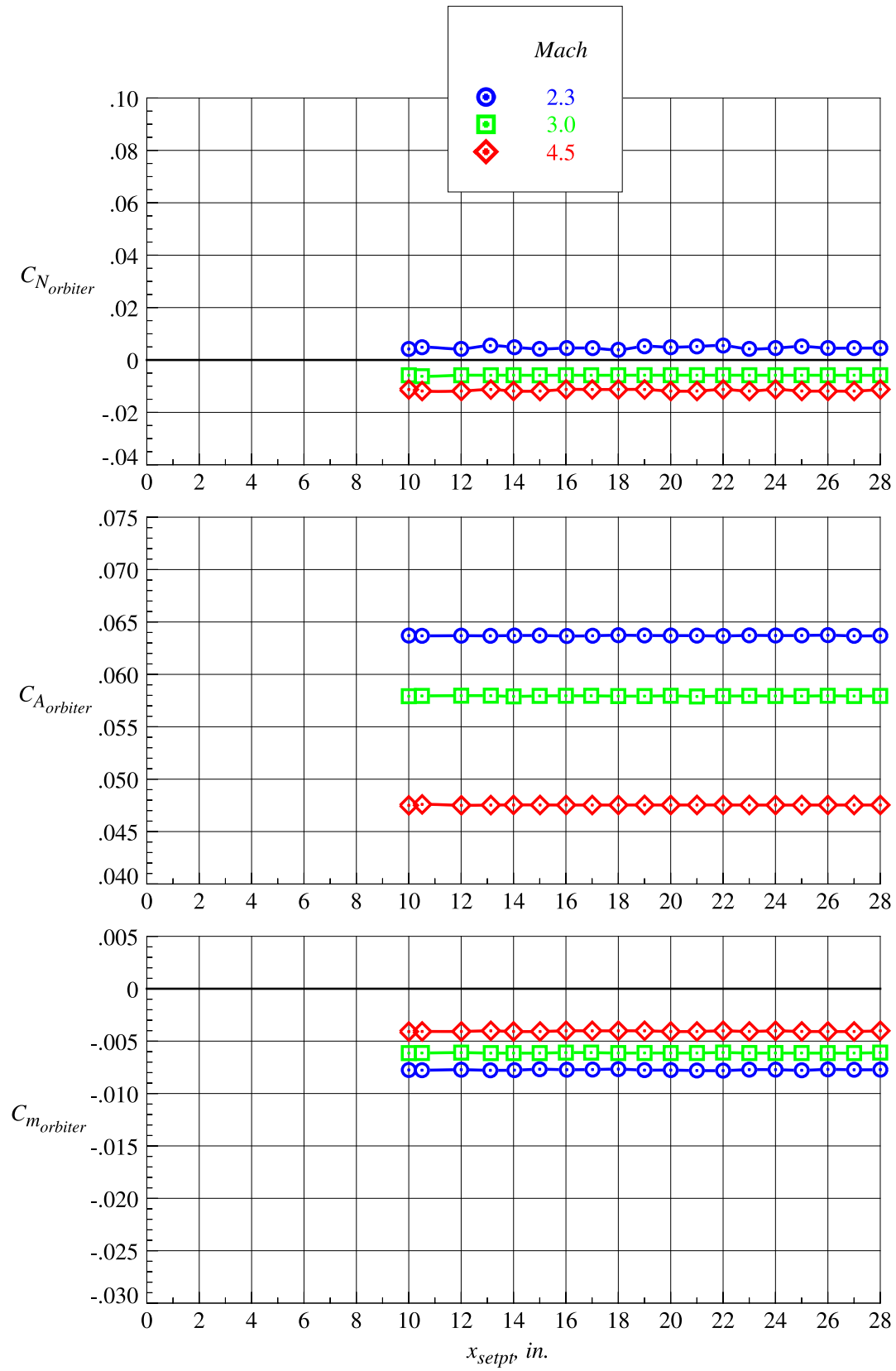
(i)  $z_{setpt} = 5.250 \text{ in.}$

Figure 64. Continued.



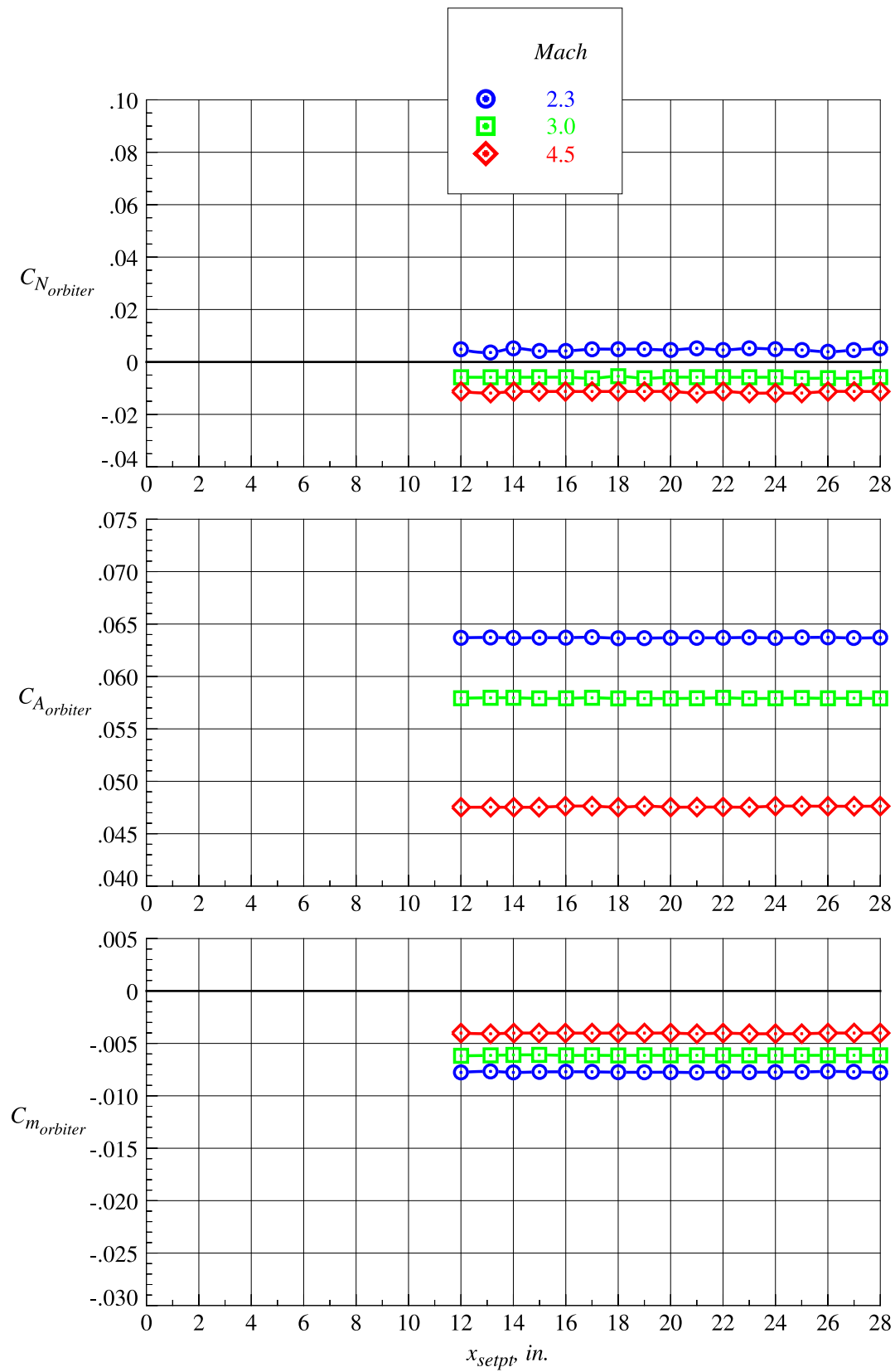
(j)  $z_{setpt} = 6.563$  in.

Figure 64. Continued.



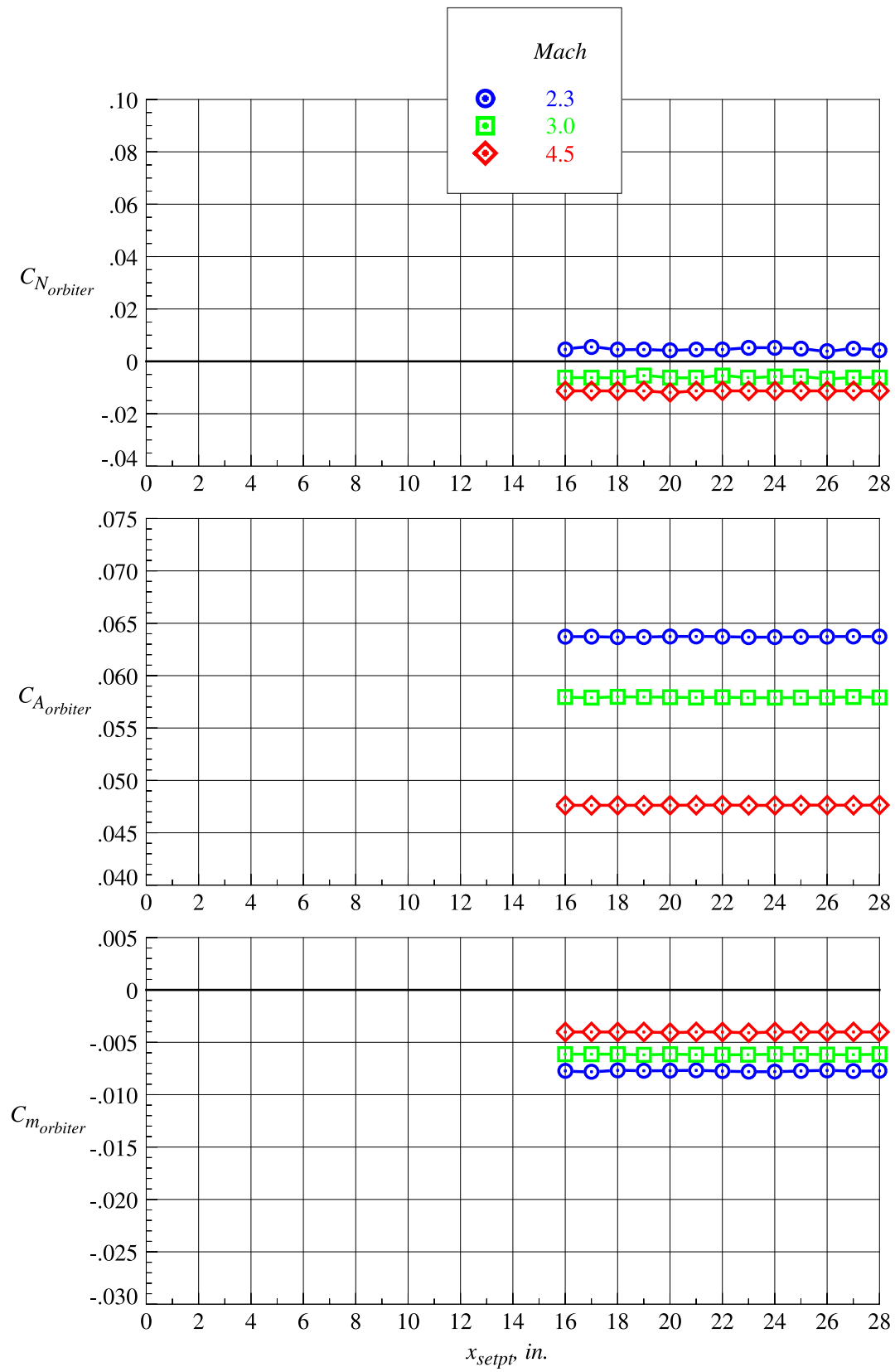
(k)  $z_{setpt} = 7.875$  in.

Figure 64. Continued.



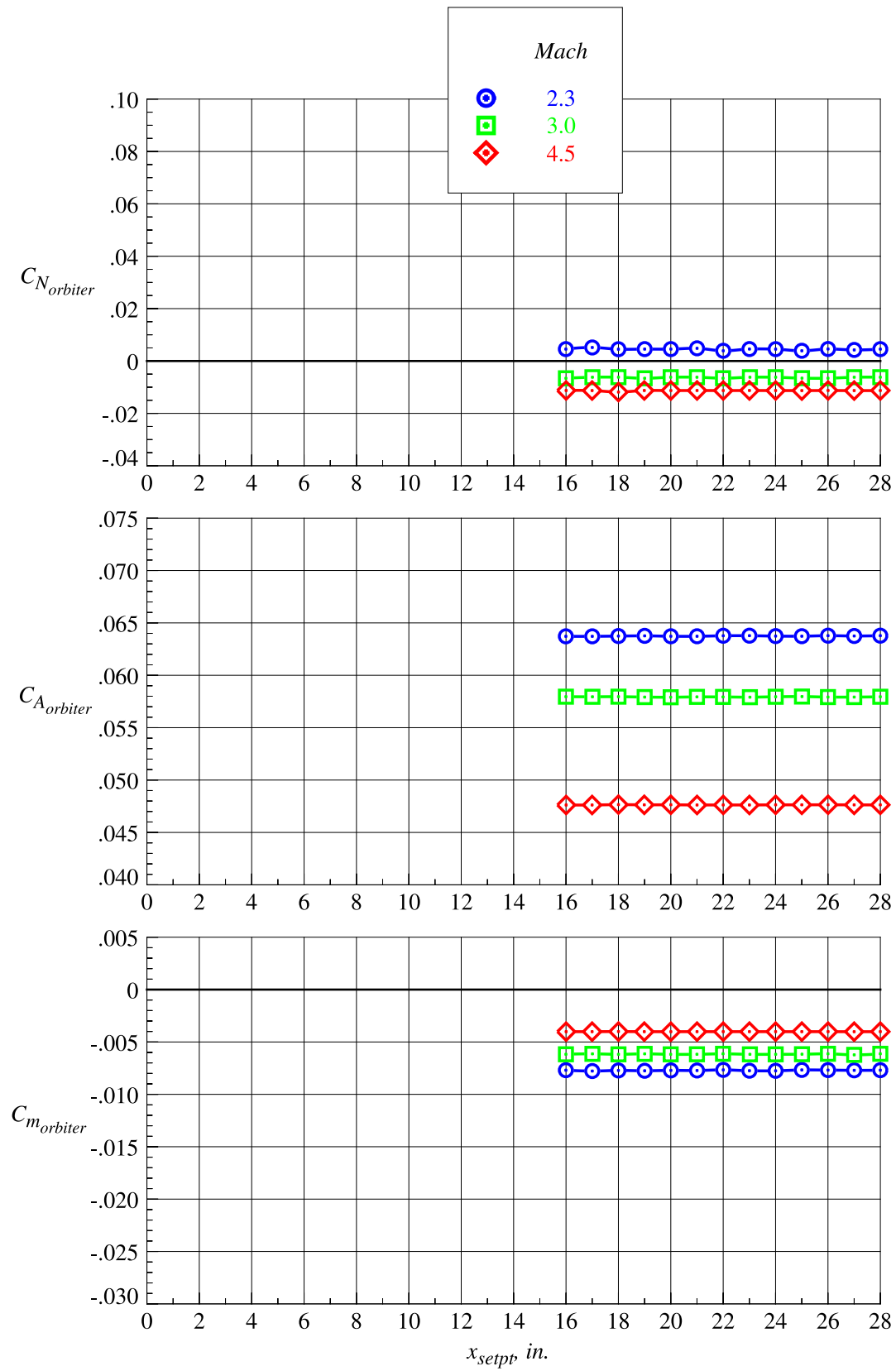
(l)  $z_{setpt} = 9.188 \text{ in.}$

Figure 64. Continued.



(m)  $z_{setpt} = 10.500$  in.

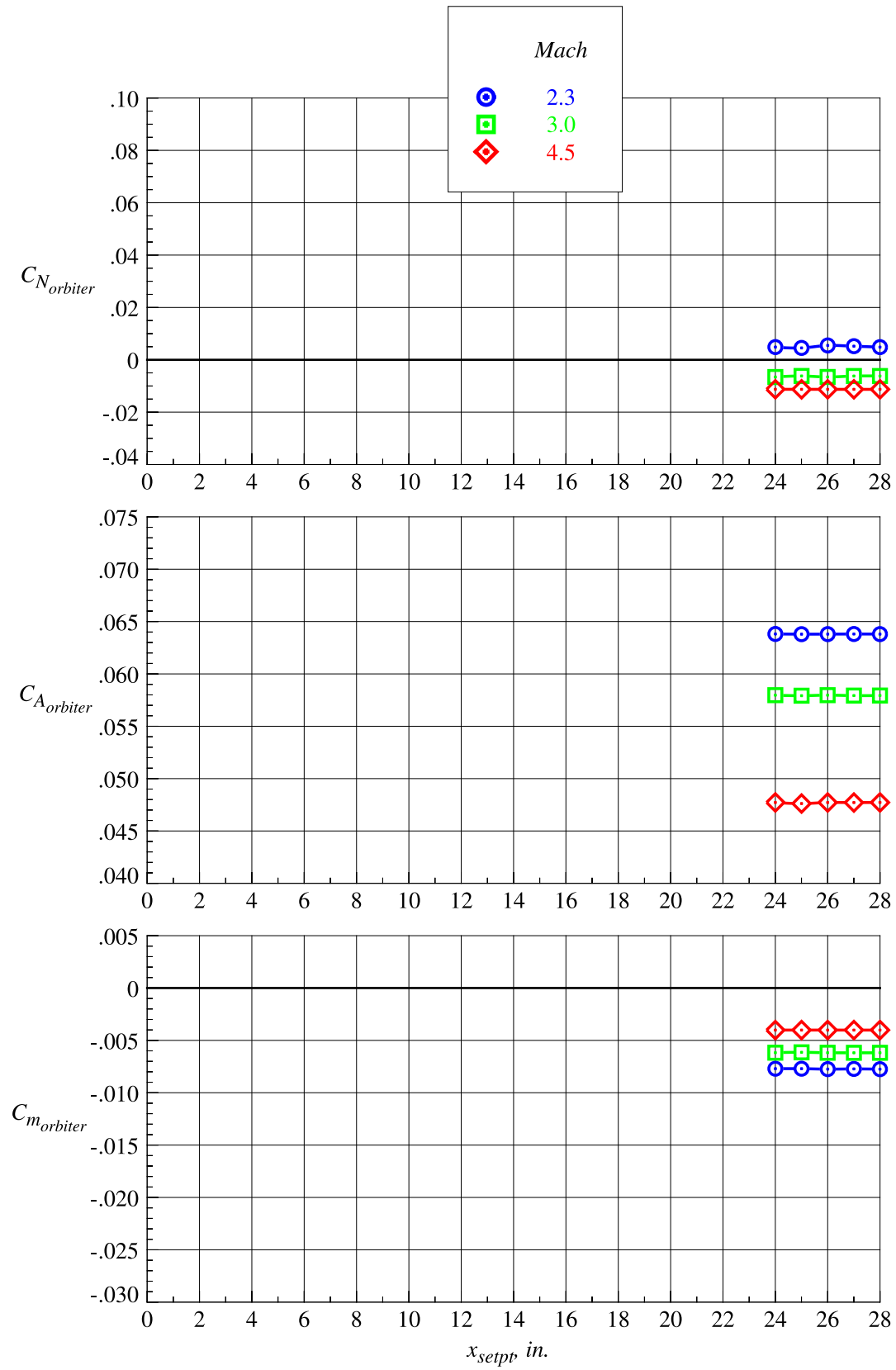
Figure 64. Continued.



(n)  $z_{setpt} = 11.810$  in.

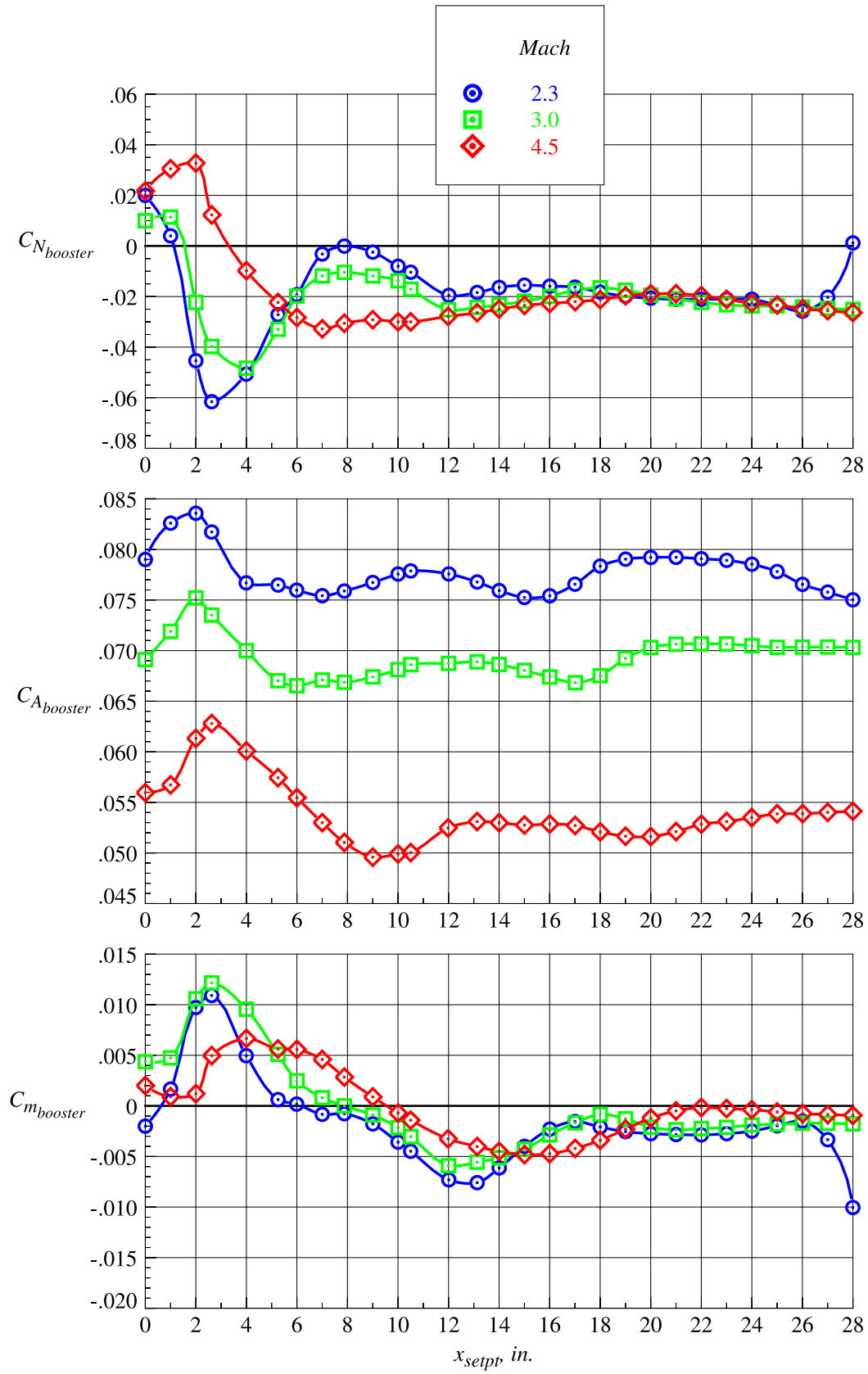
Figure 64. Continued.





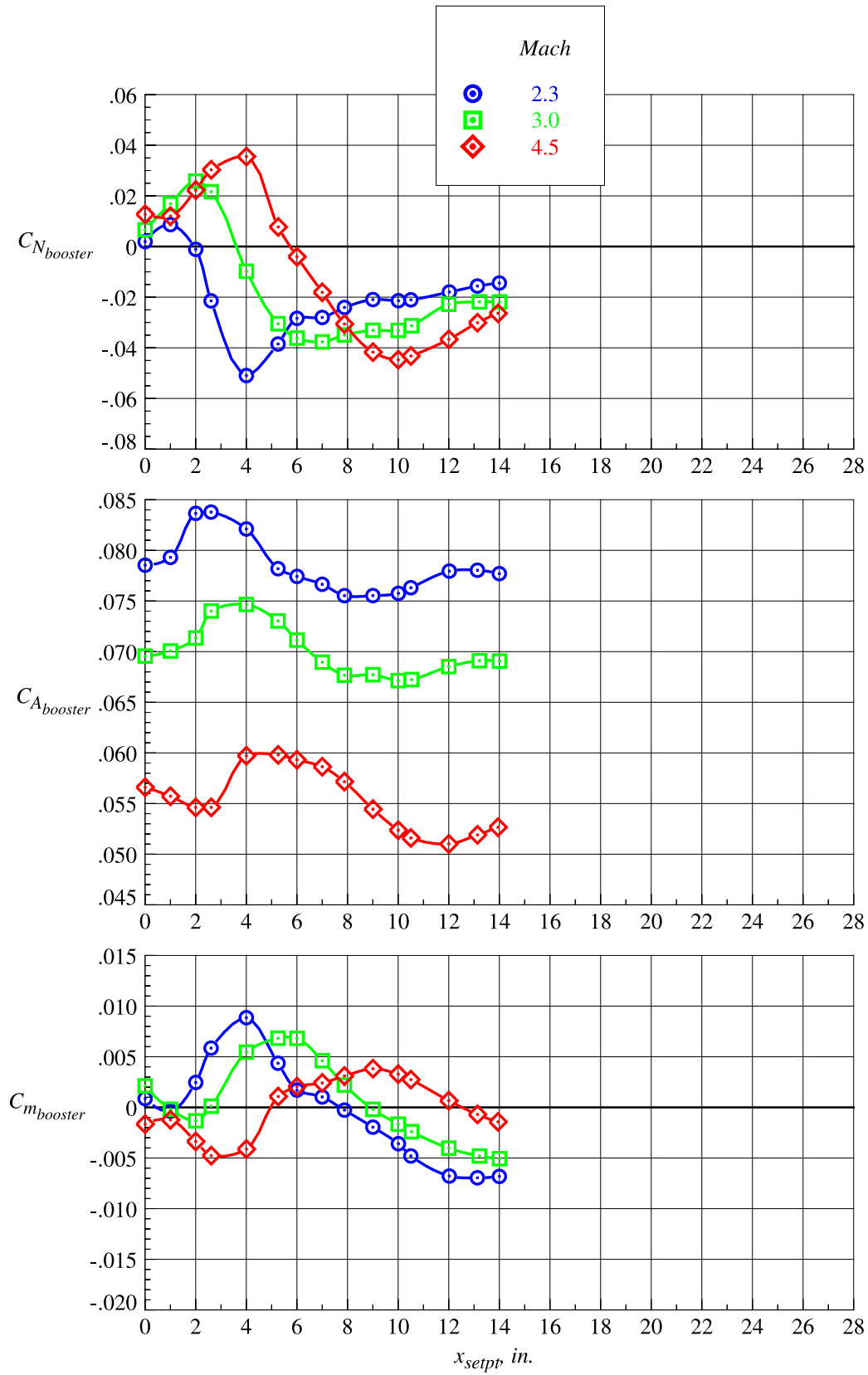
(o)  $z_{setpt} = 13.130$  in.

Figure 64. Concluded.



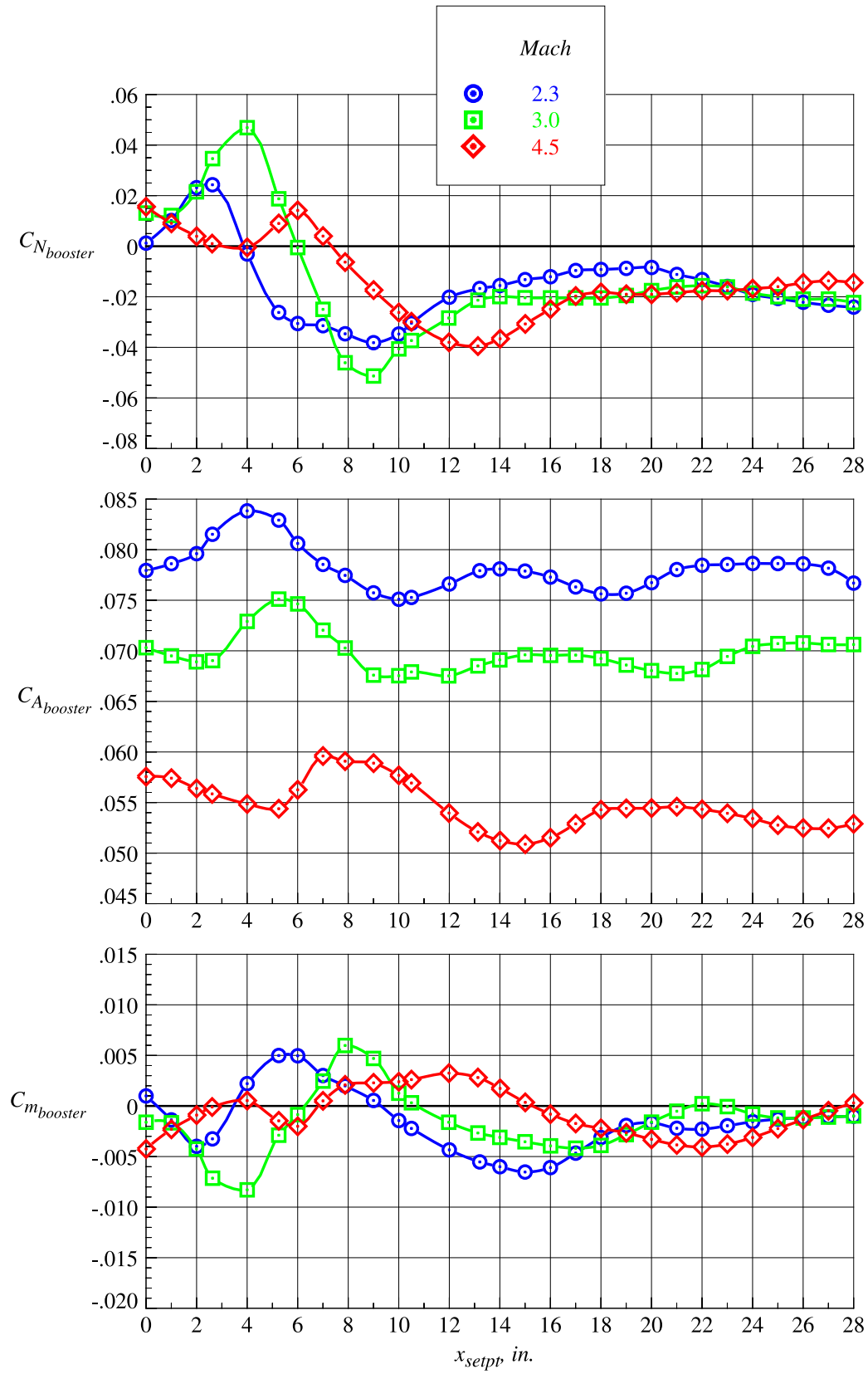
(a)  $z_{sept} = 0$  in.

Figure 65. Booster proximity aerodynamic characteristics at Mach = 2.3, 3.0, and 4.5;  $\Delta\alpha = 0^\circ$ .



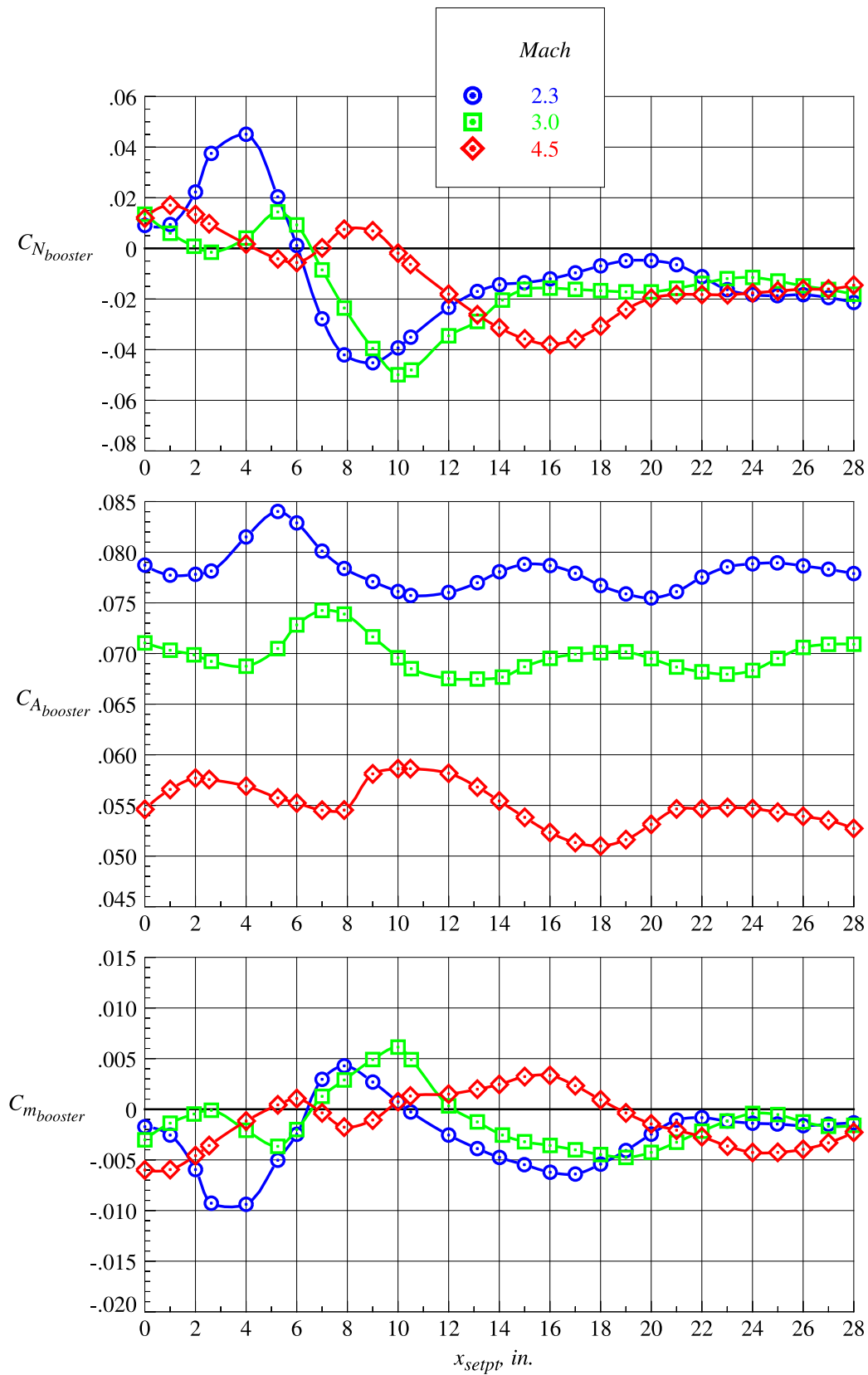
(b)  $z_{setpt} = 0.656 \text{ in.}$

Figure 65. Continued.



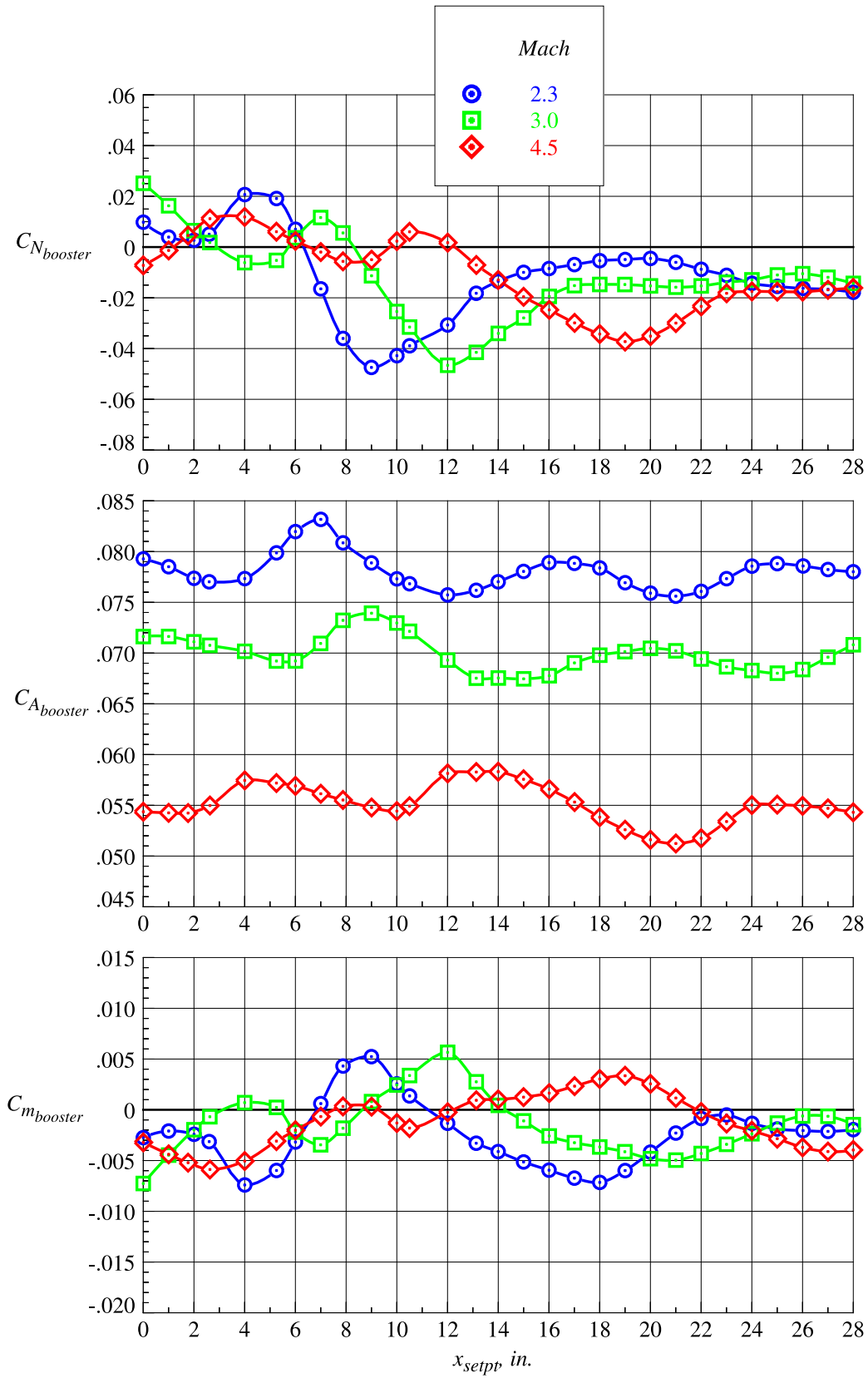
(c)  $z_{setpt} = 1.313$  in.

Figure 65. Continued.



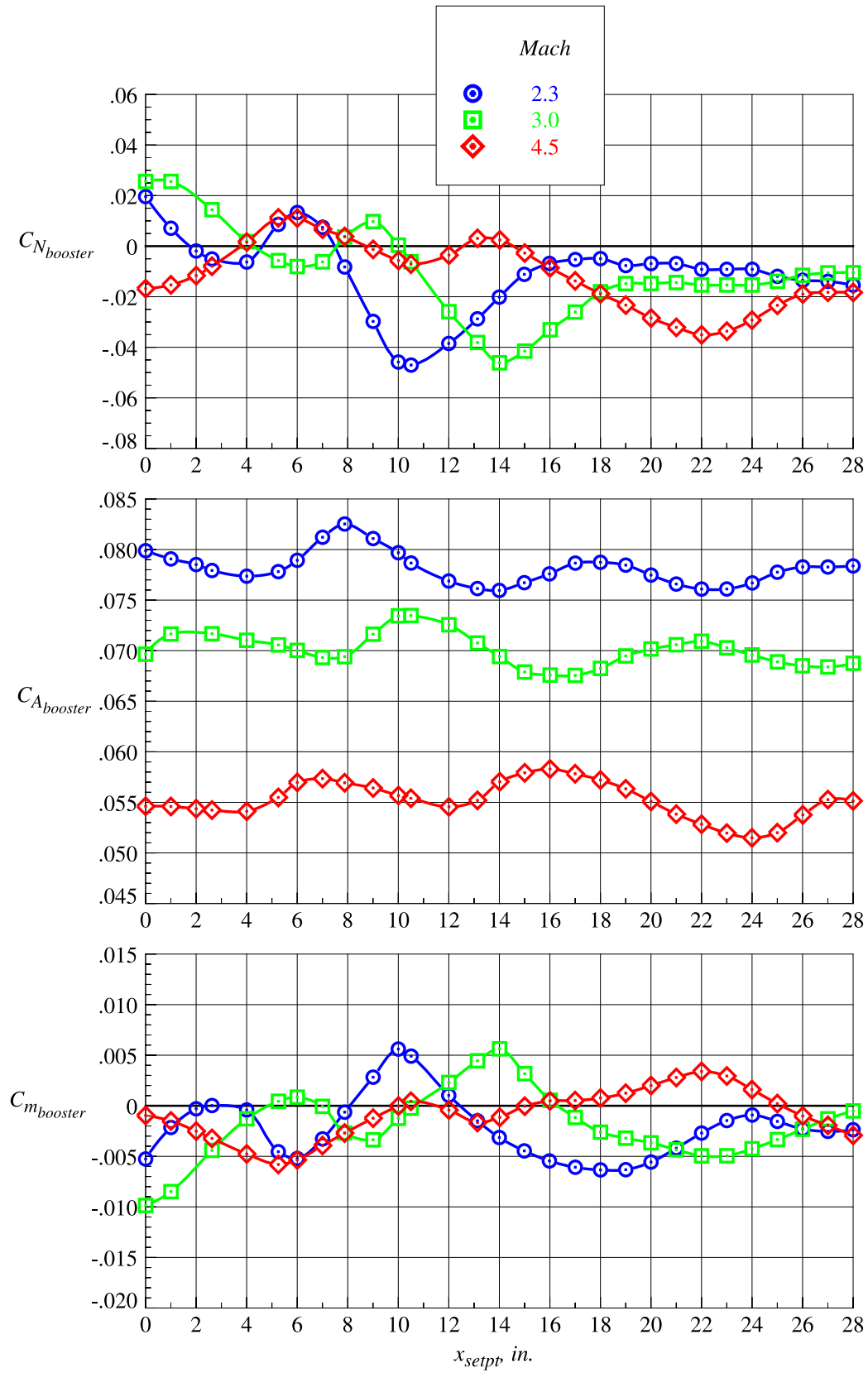
(d)  $z_{setpt} = 1.969$  in.

Figure 65. Continued.



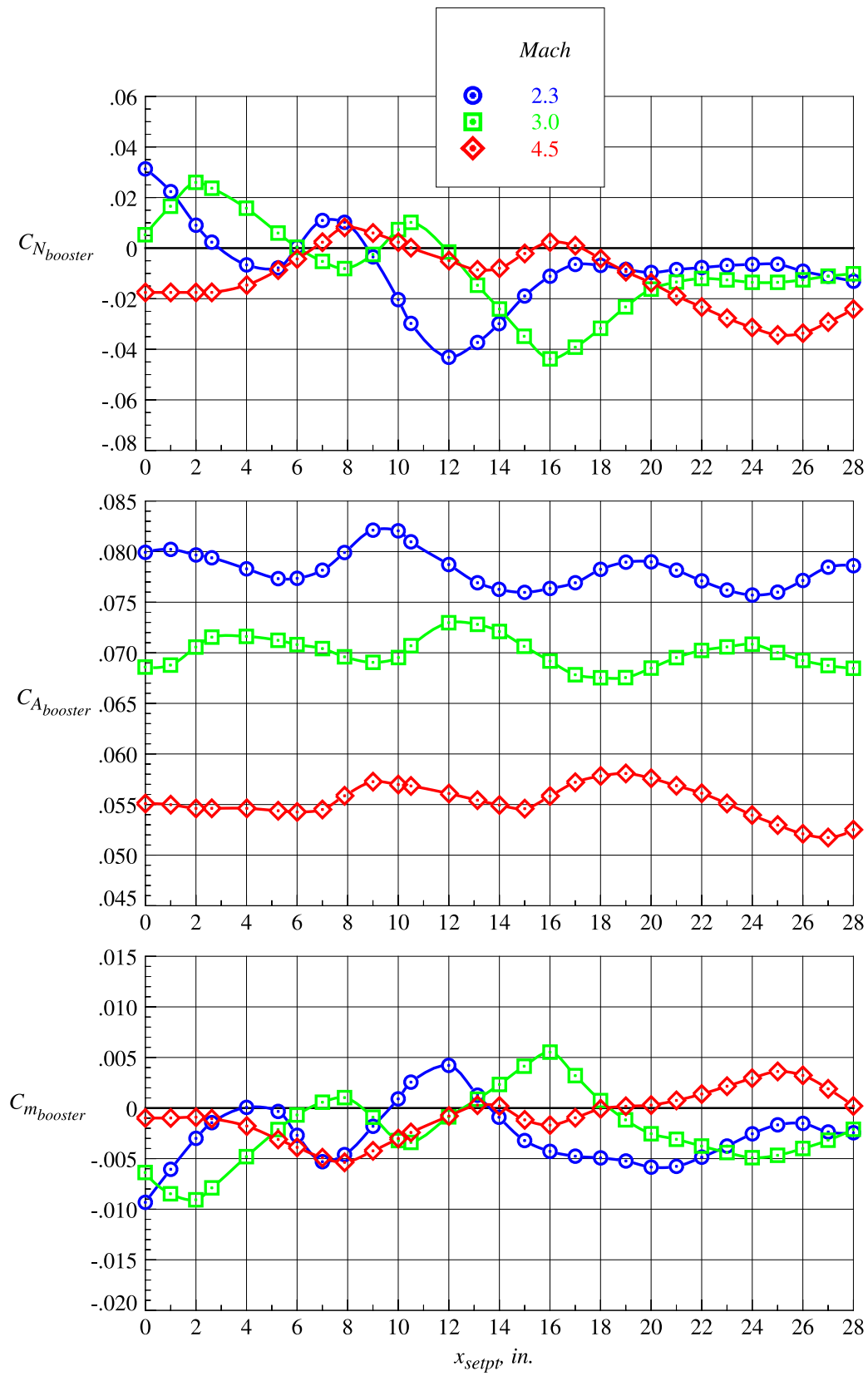
(e)  $z_{setpt} = 2.625$  in.

Figure 65. Continued.



(f)  $z_{setpt} = 3.281$  in.

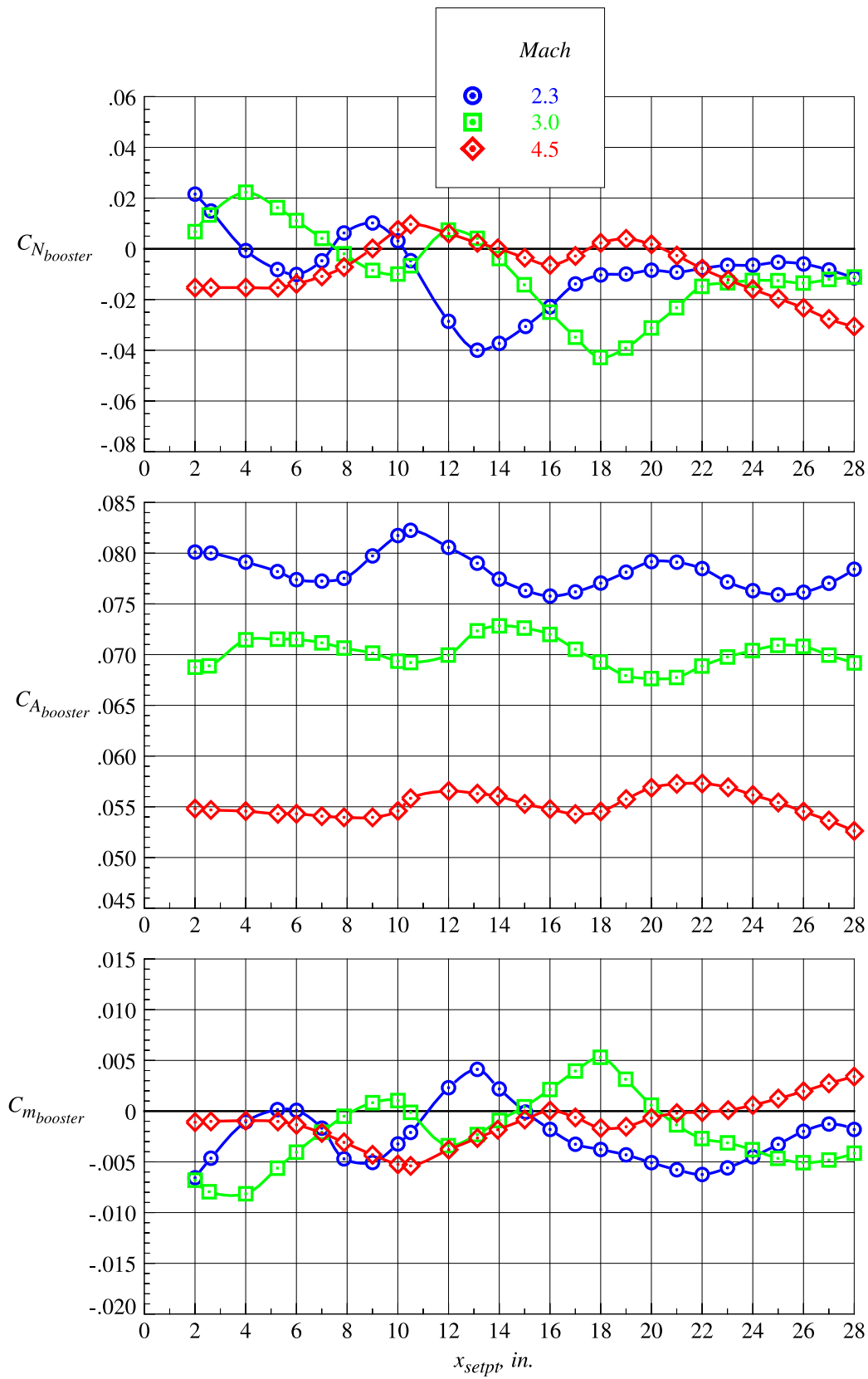
Figure 65. Continued.



(g)  $z_{setpt} = 3.938$  in.

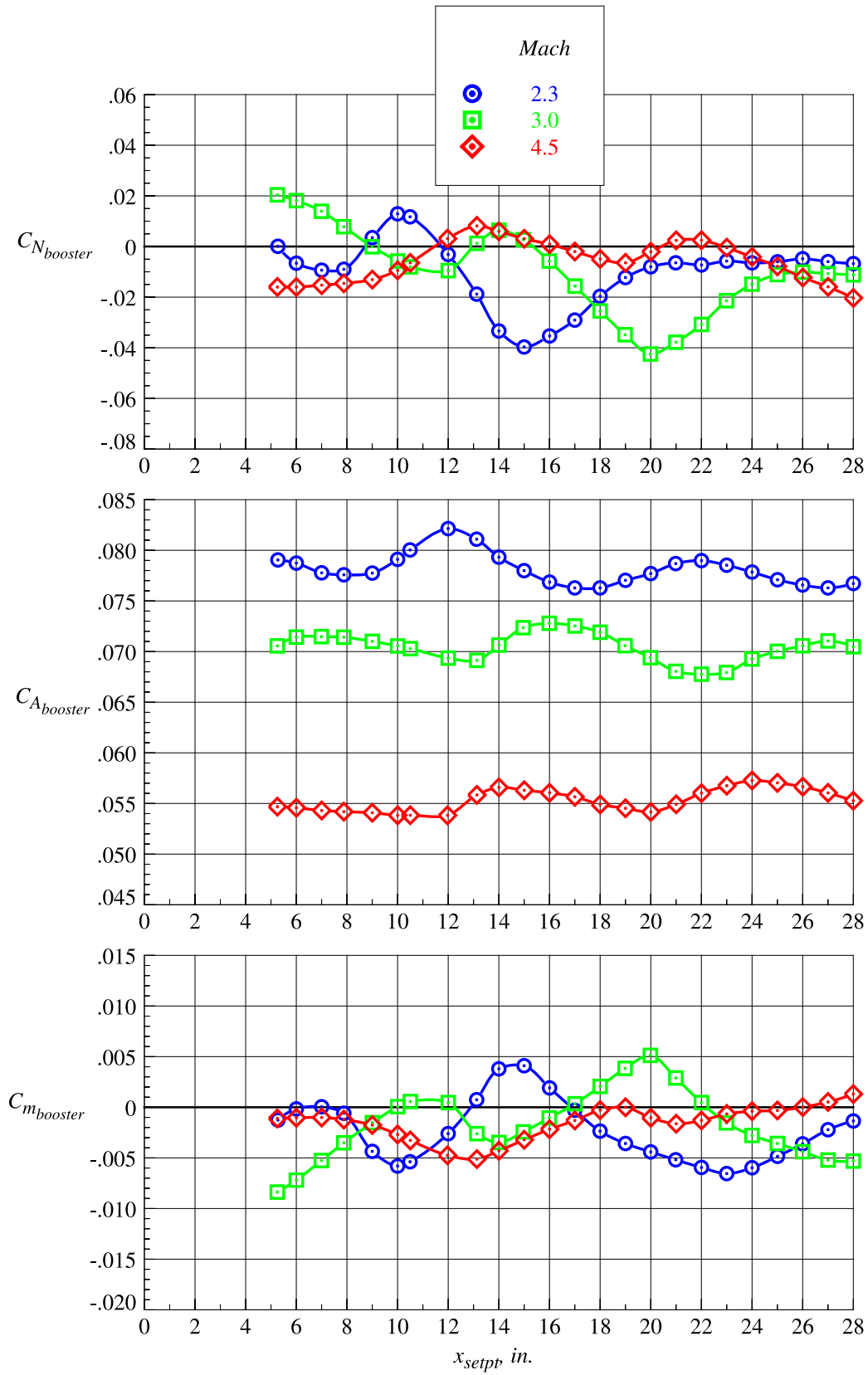
Figure 65. Continued.





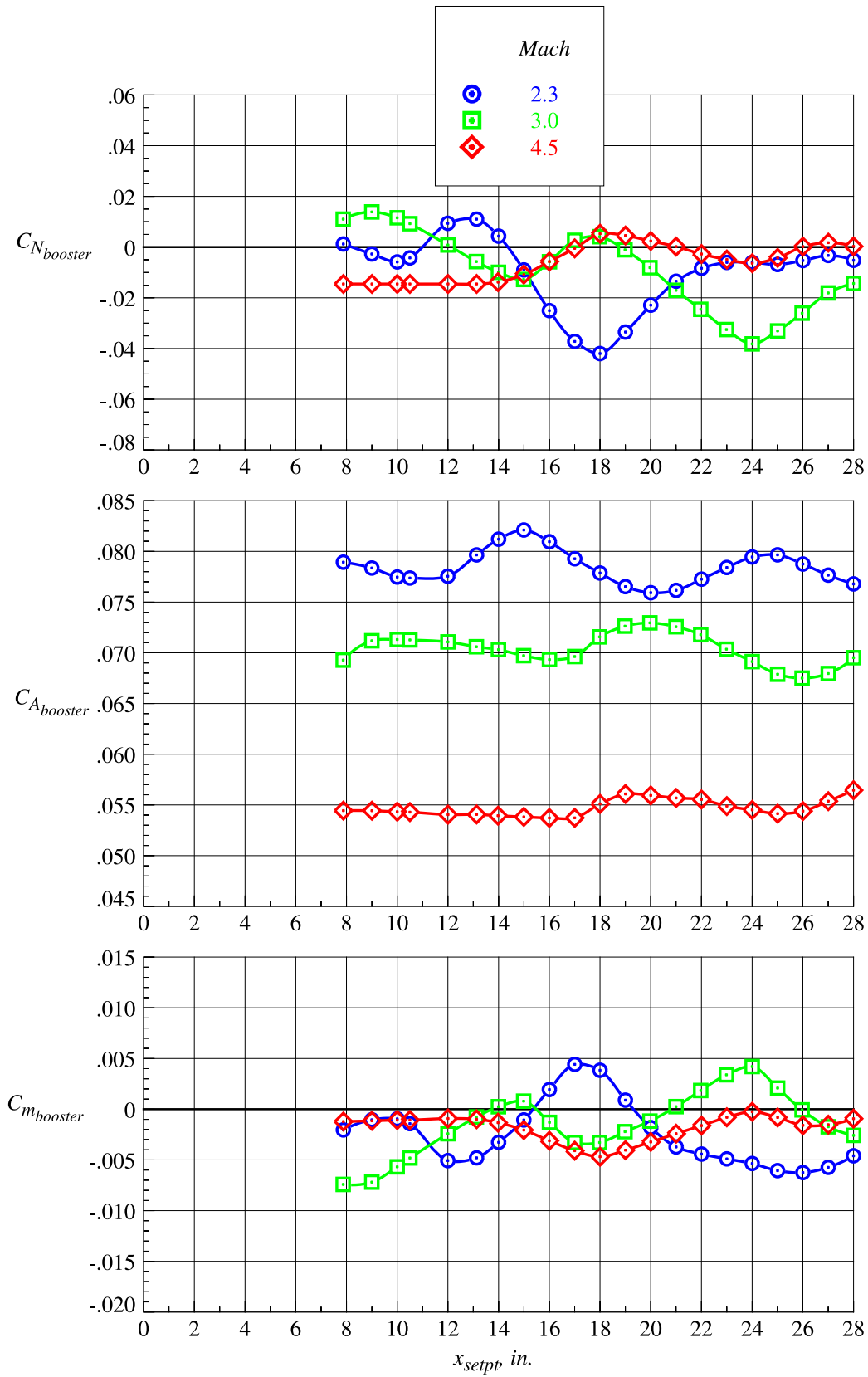
(h)  $z_{setpt} = 4.594$  in.

Figure 65. Continued.



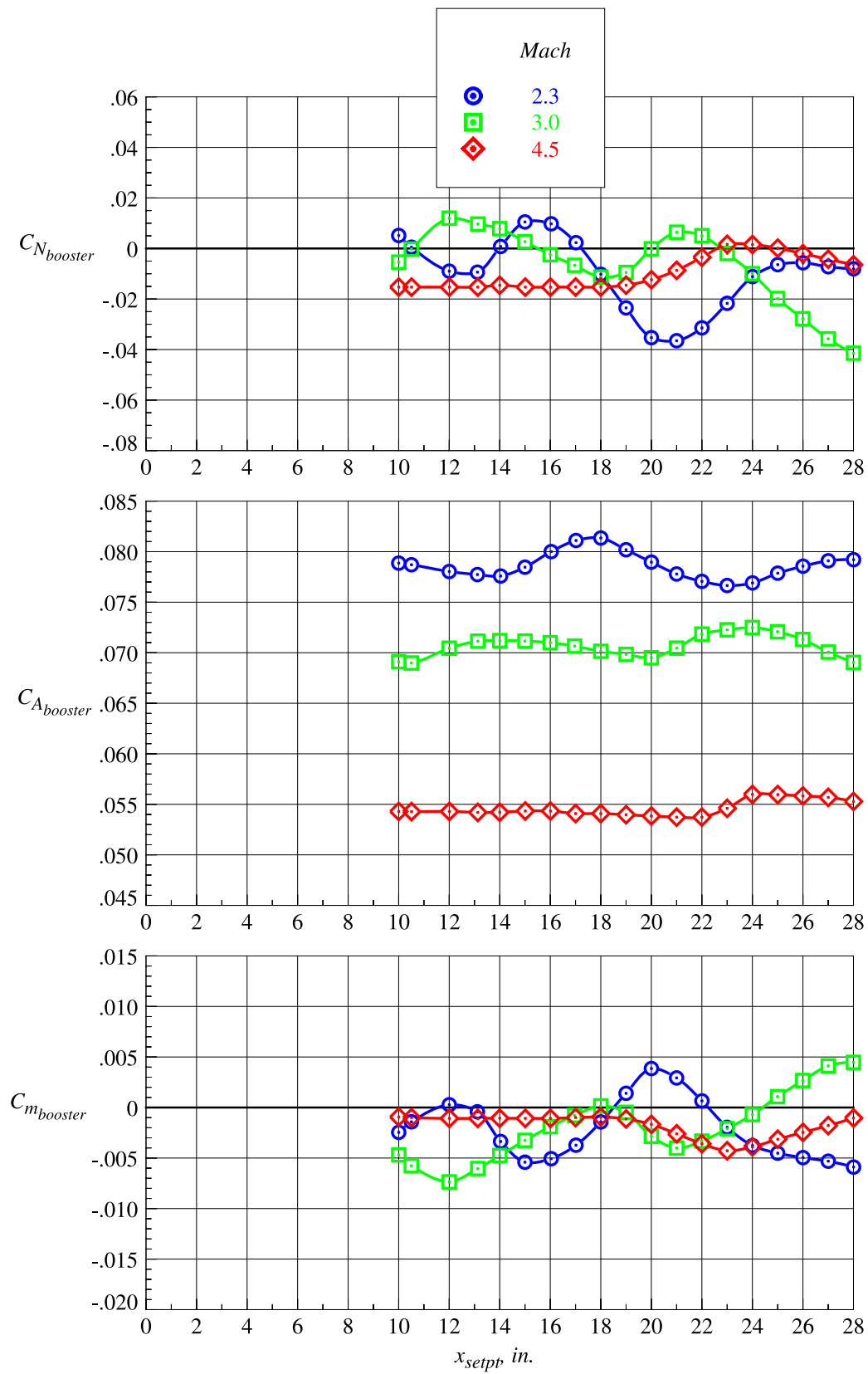
(i)  $z_{setpt} = 5.250$  in.

Figure 65. Continued.



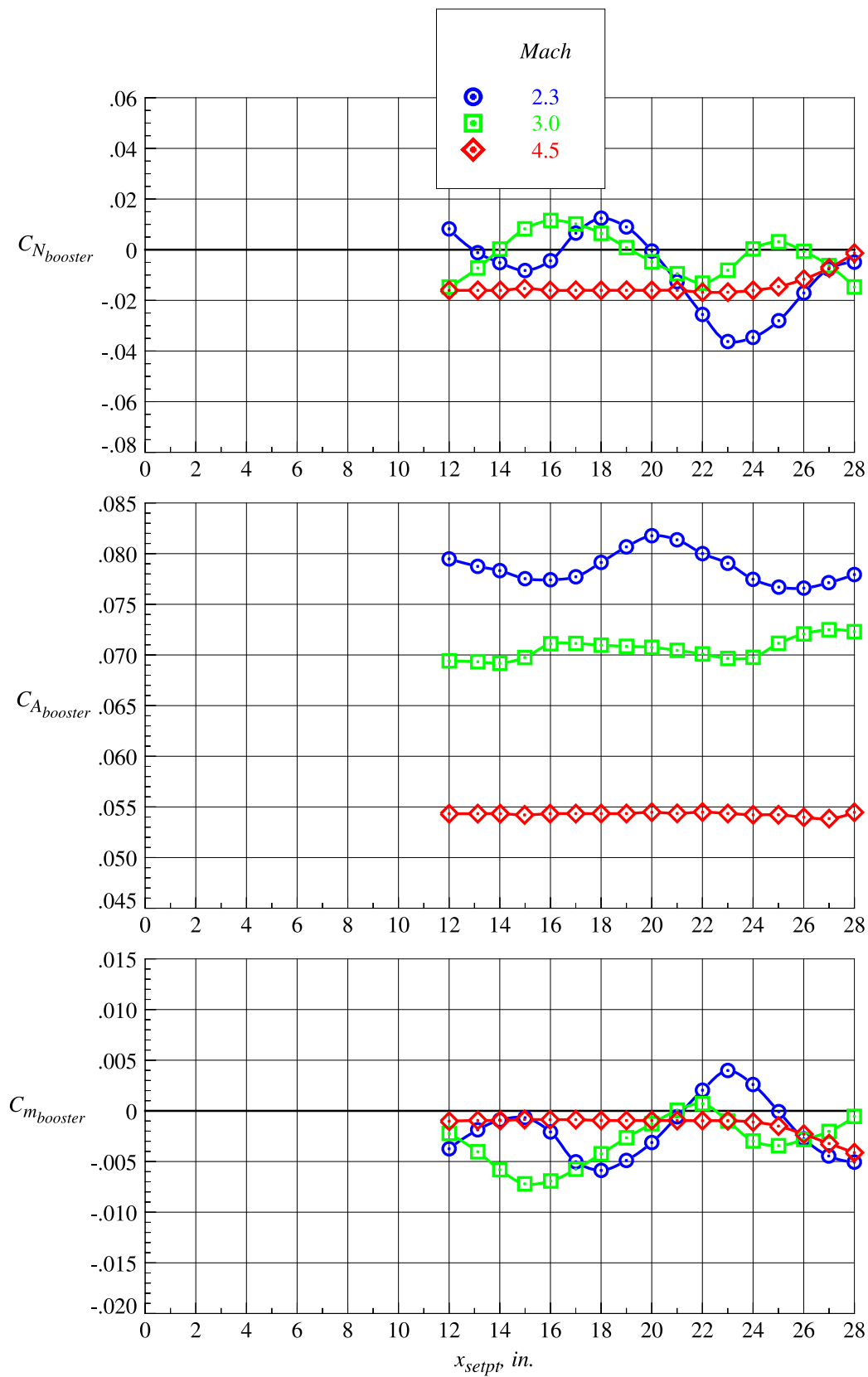
(j)  $z_{setpt} = 6.563$  in.

Figure 65. Continued.



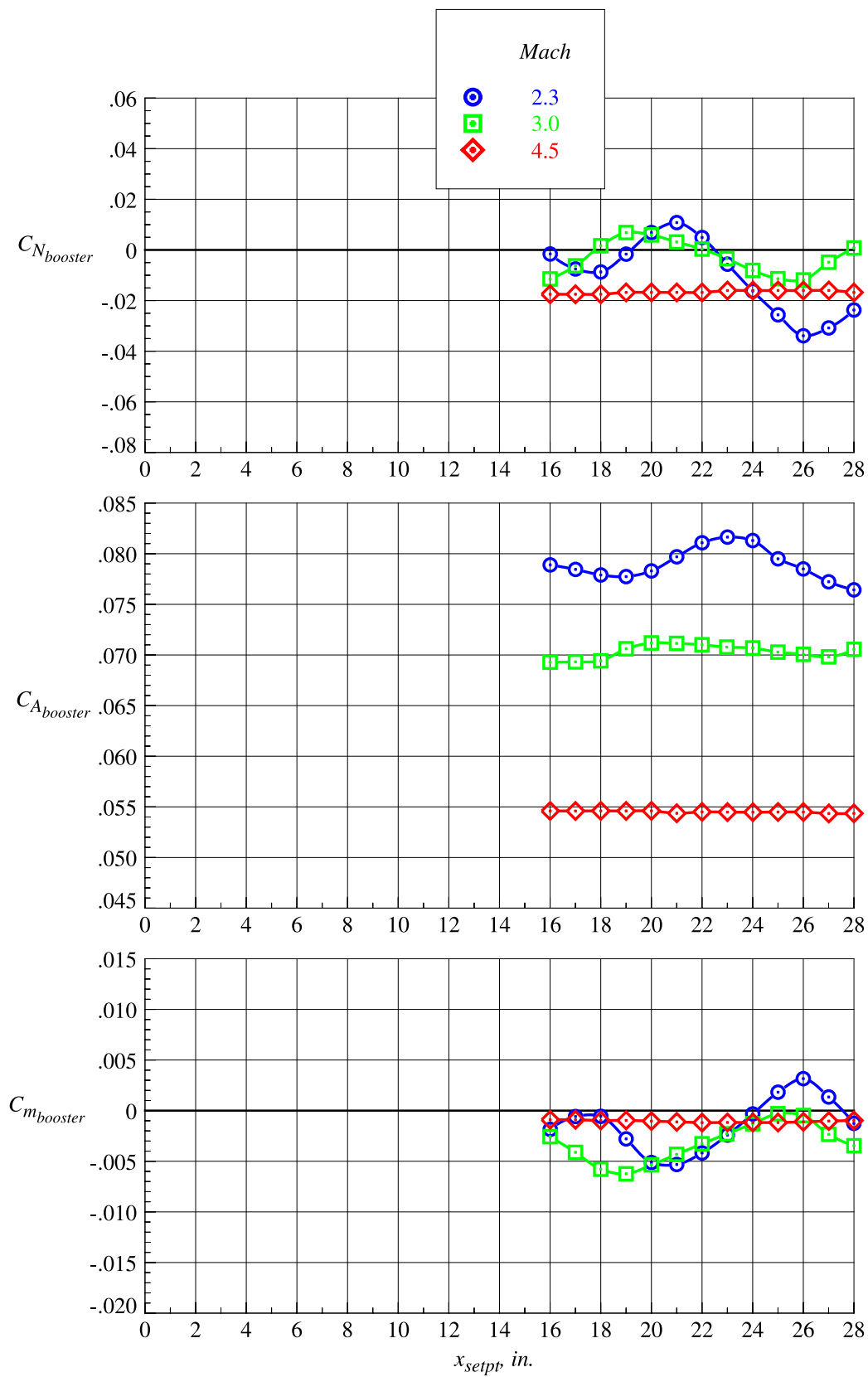
(k)  $z_{setpt} = 7.875$  in.

Figure 65. Continued.



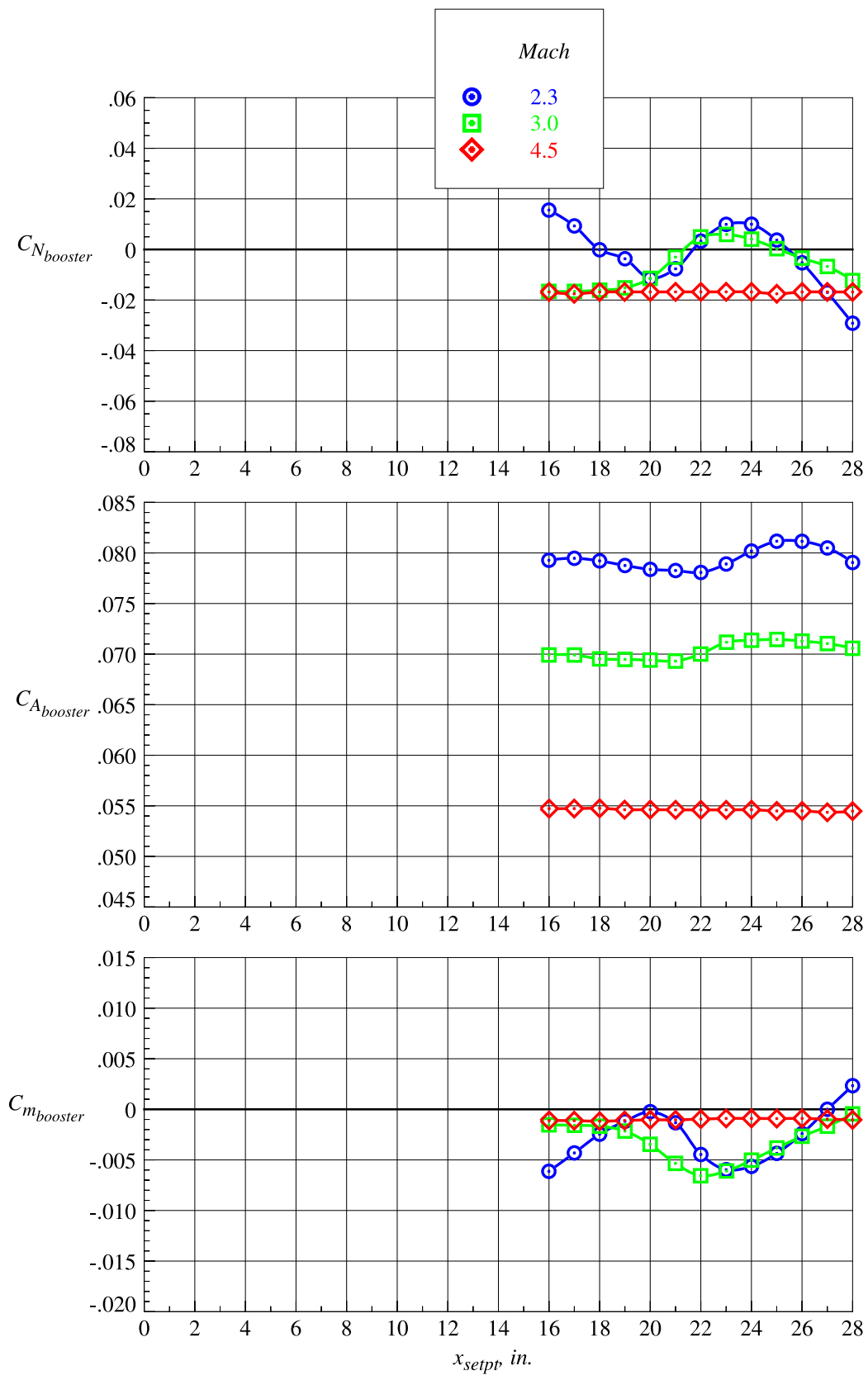
(l)  $z_{setpt} = 9.188$  in.

Figure 65. Continued.



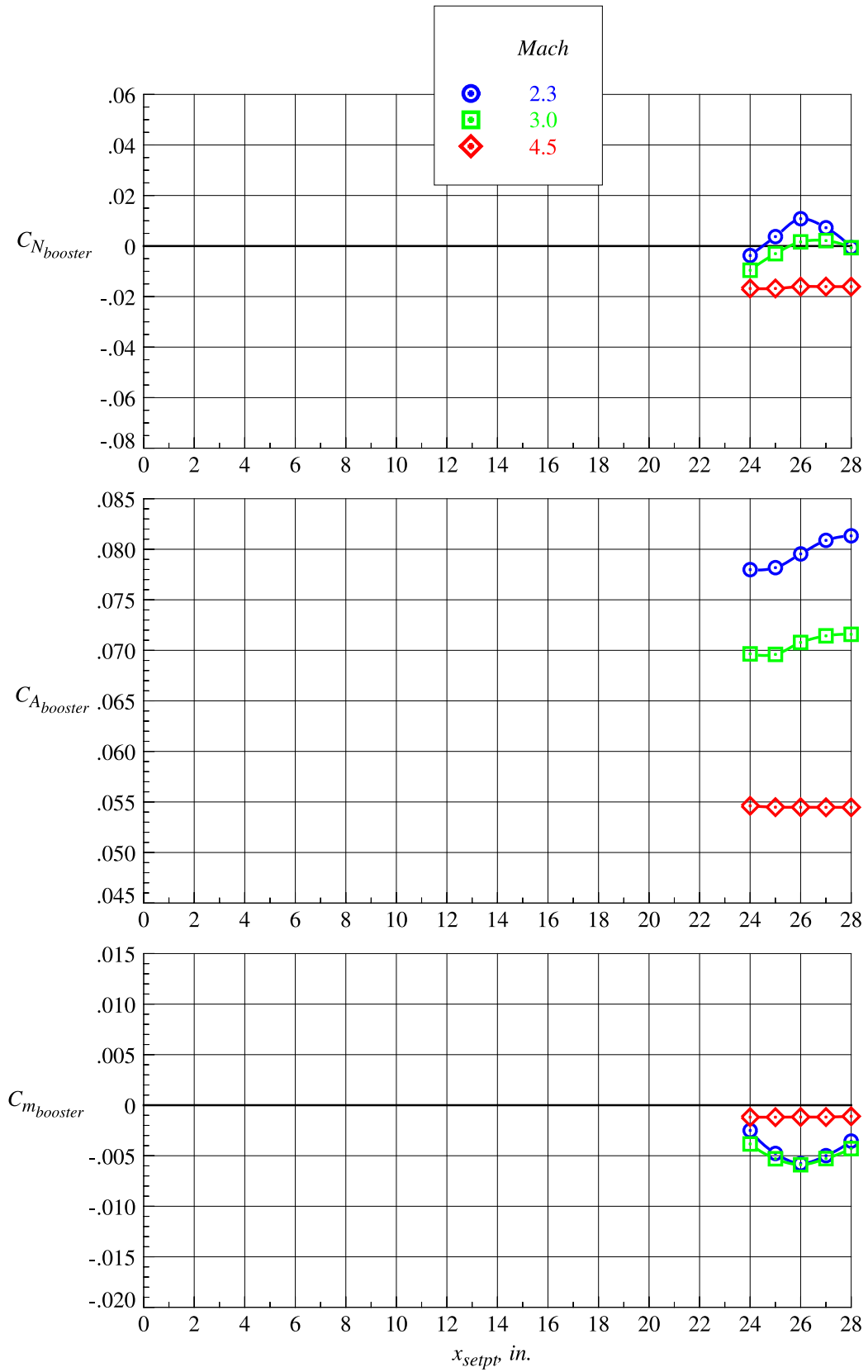
(m)  $z_{setpt} = 10.500$  in.

Figure 65. Continued.



(n)  $z_{setpt} = 11.810$  in.

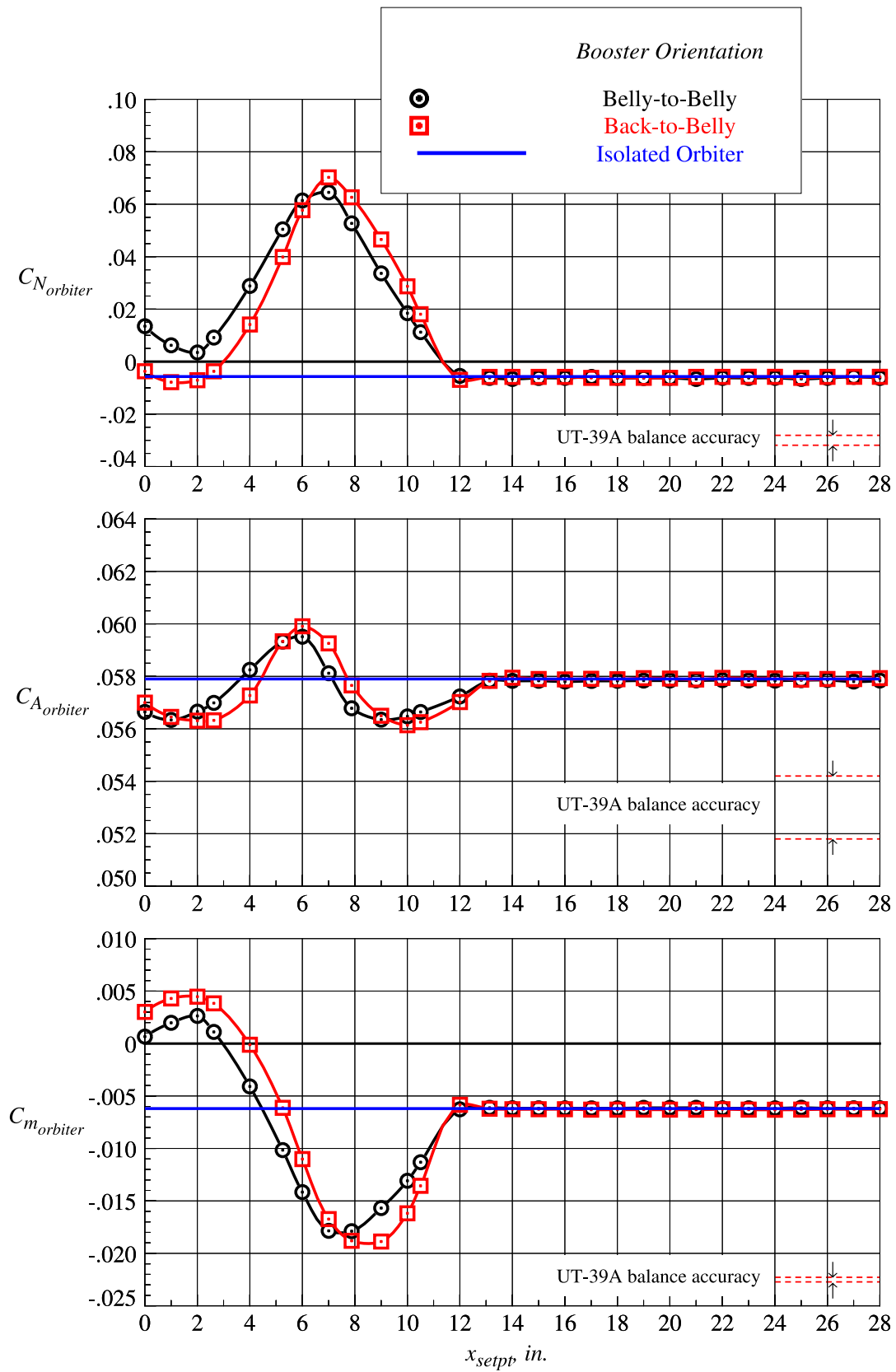
Figure 65. Continued.



(o)  $z_{setpt} = 13.130$  in.

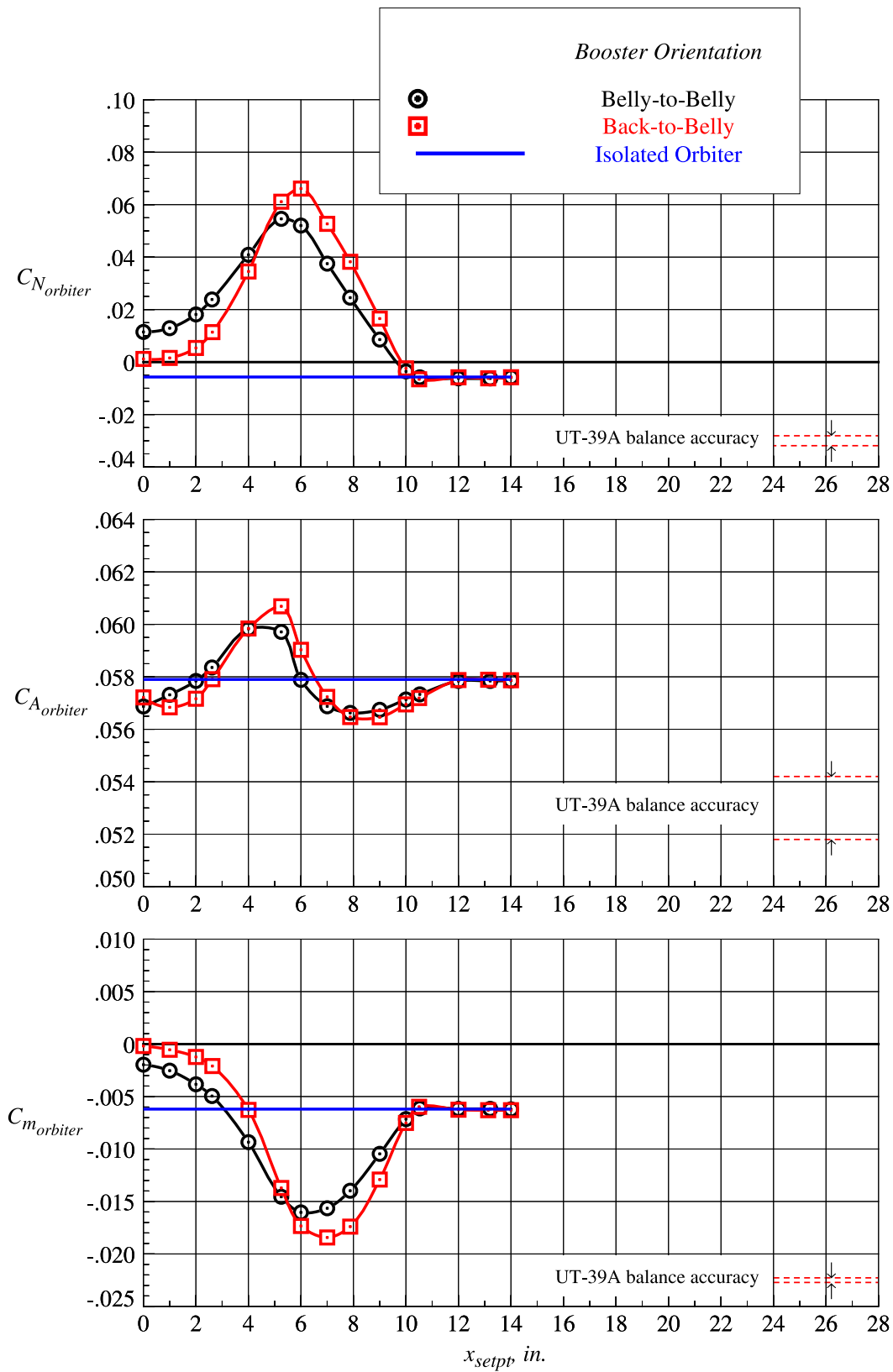
Figure 65. Concluded.





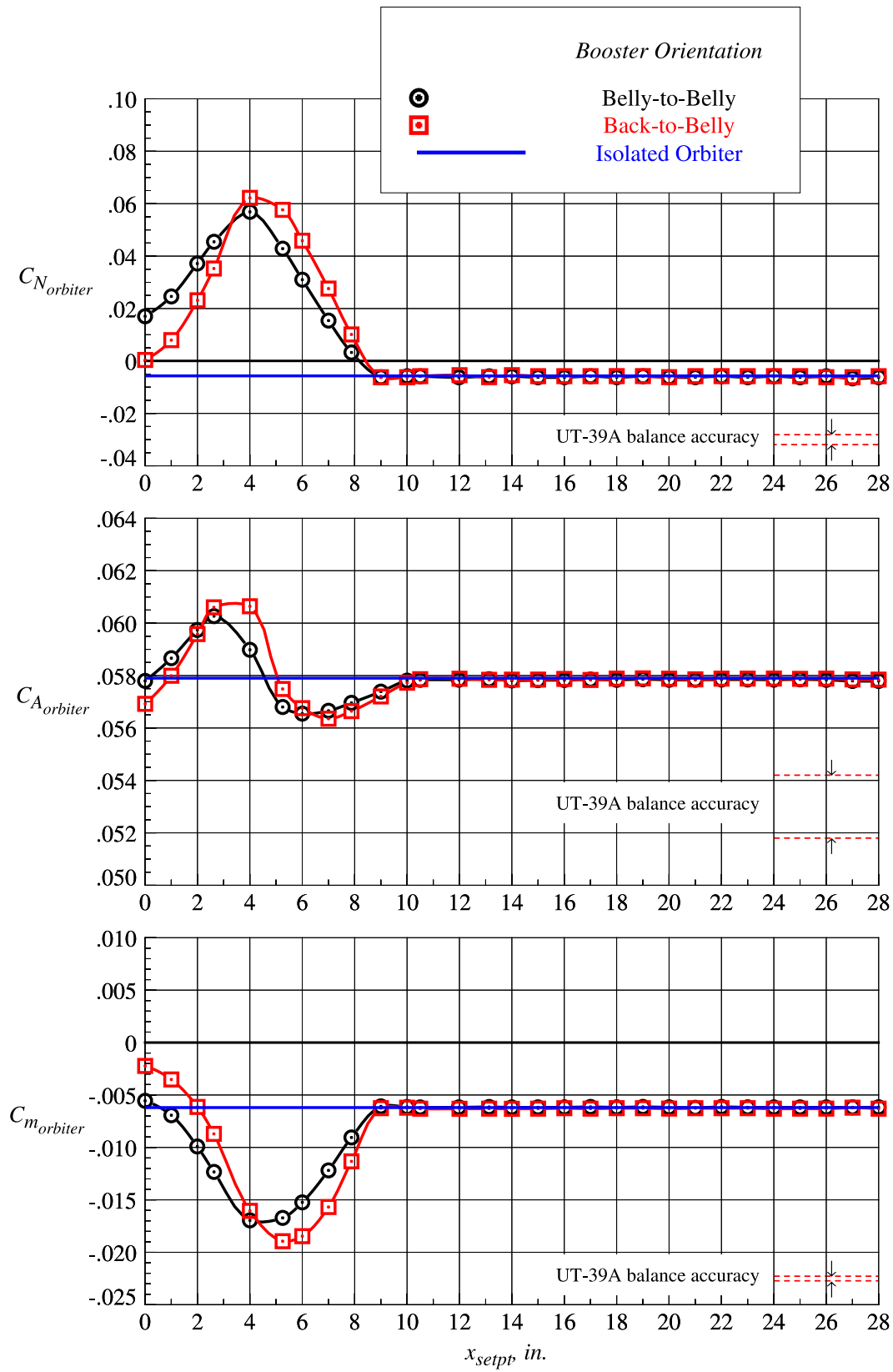
(a)  $z_{sept} = 0$  in.

Figure 66. Orbiter proximity aerodynamic characteristics in belly-to-belly and back-to-belly configurations at  $Mach = 3.0$  and  $\Delta\alpha = 0^\circ$ .



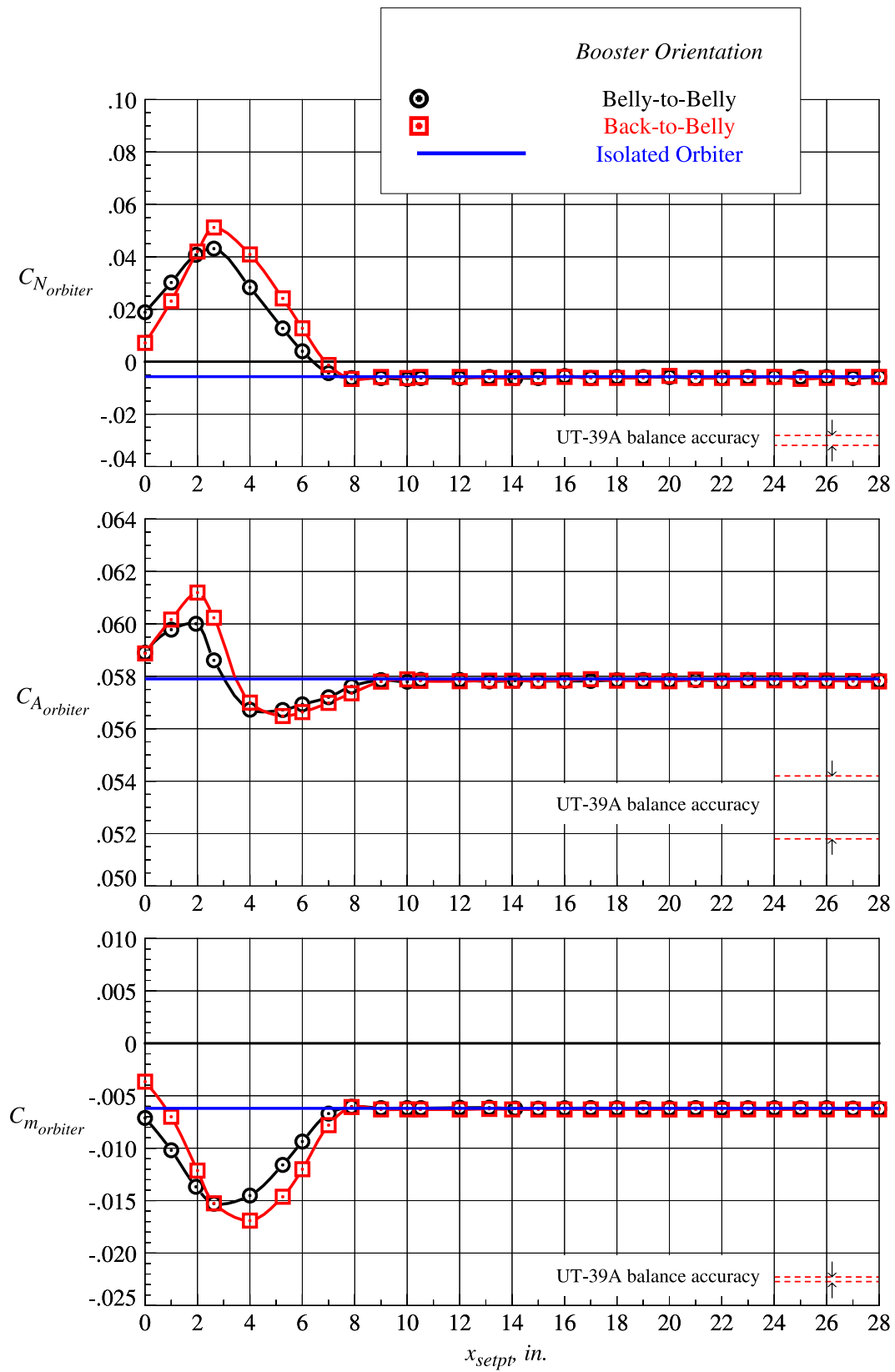
(b)  $z_{setpt} = 0.656 \text{ in.}$

Figure 66. Continued.



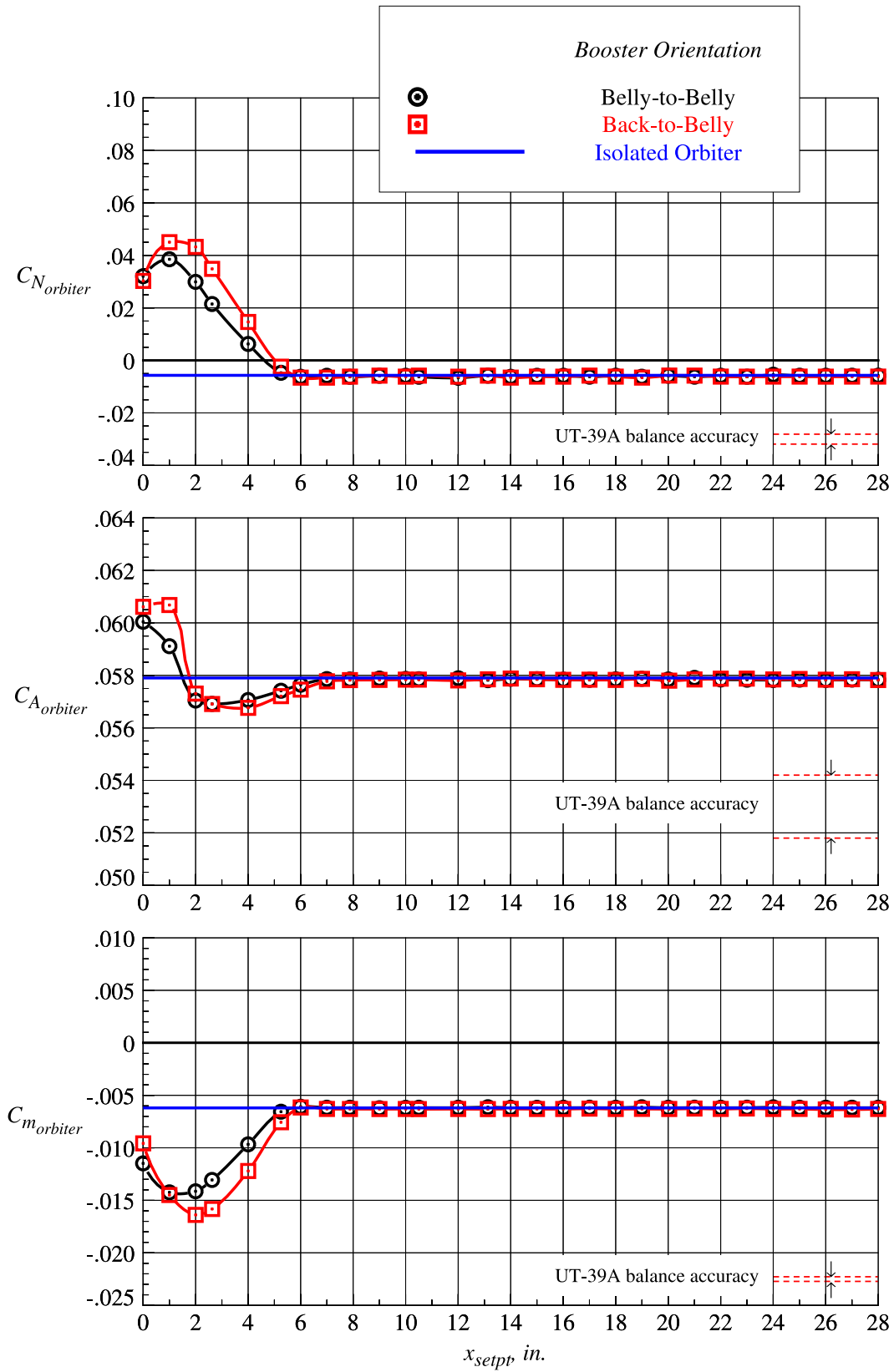
(c)  $z_{setpt} = 1.313$  in.

Figure 66. Continued.



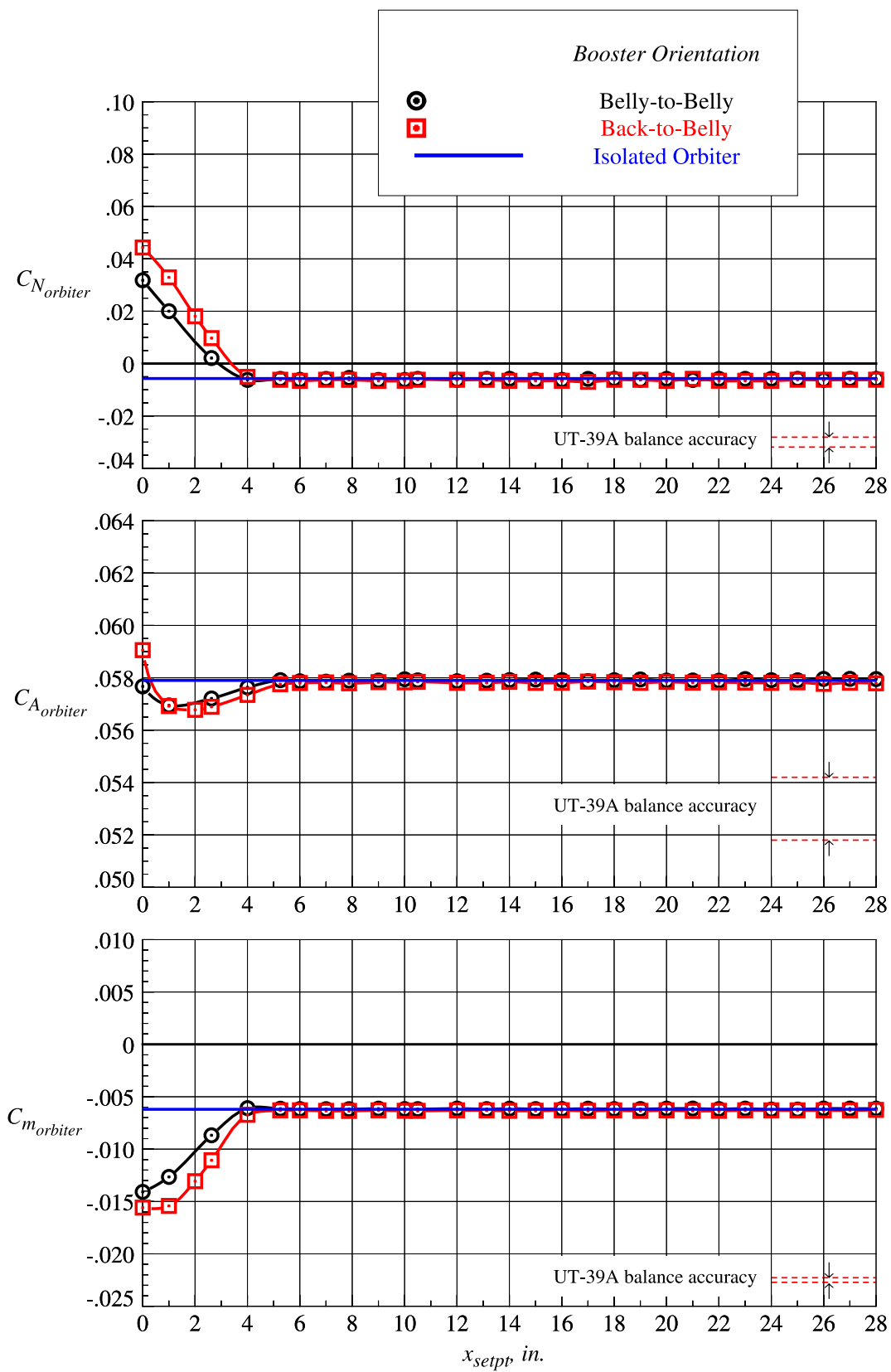
(d)  $z_{setpt} = 1.969$  in.

Figure 66. Continued.



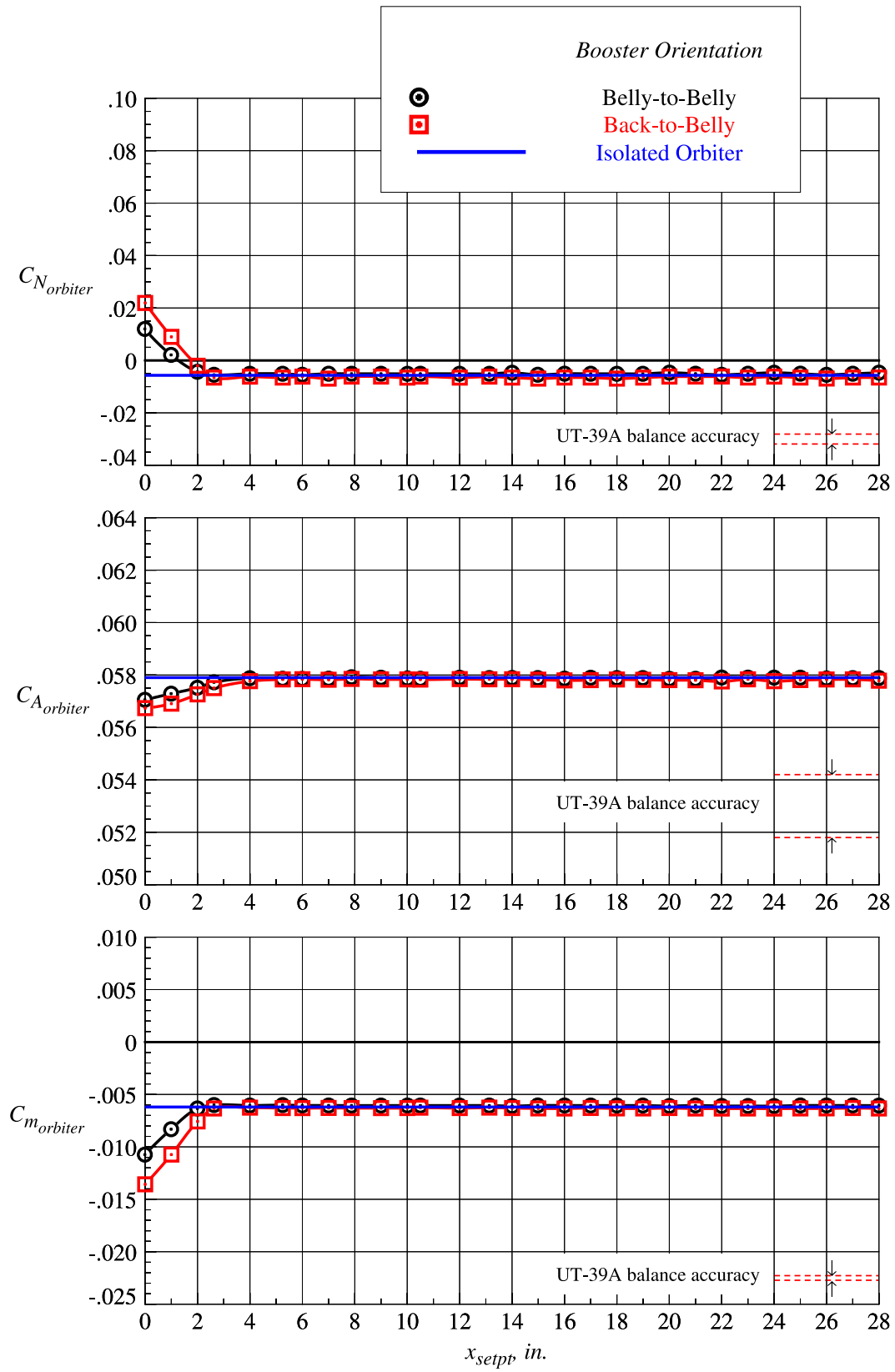
(e)  $z_{setpt} = 2.625$  in.

Figure 66. Continued.



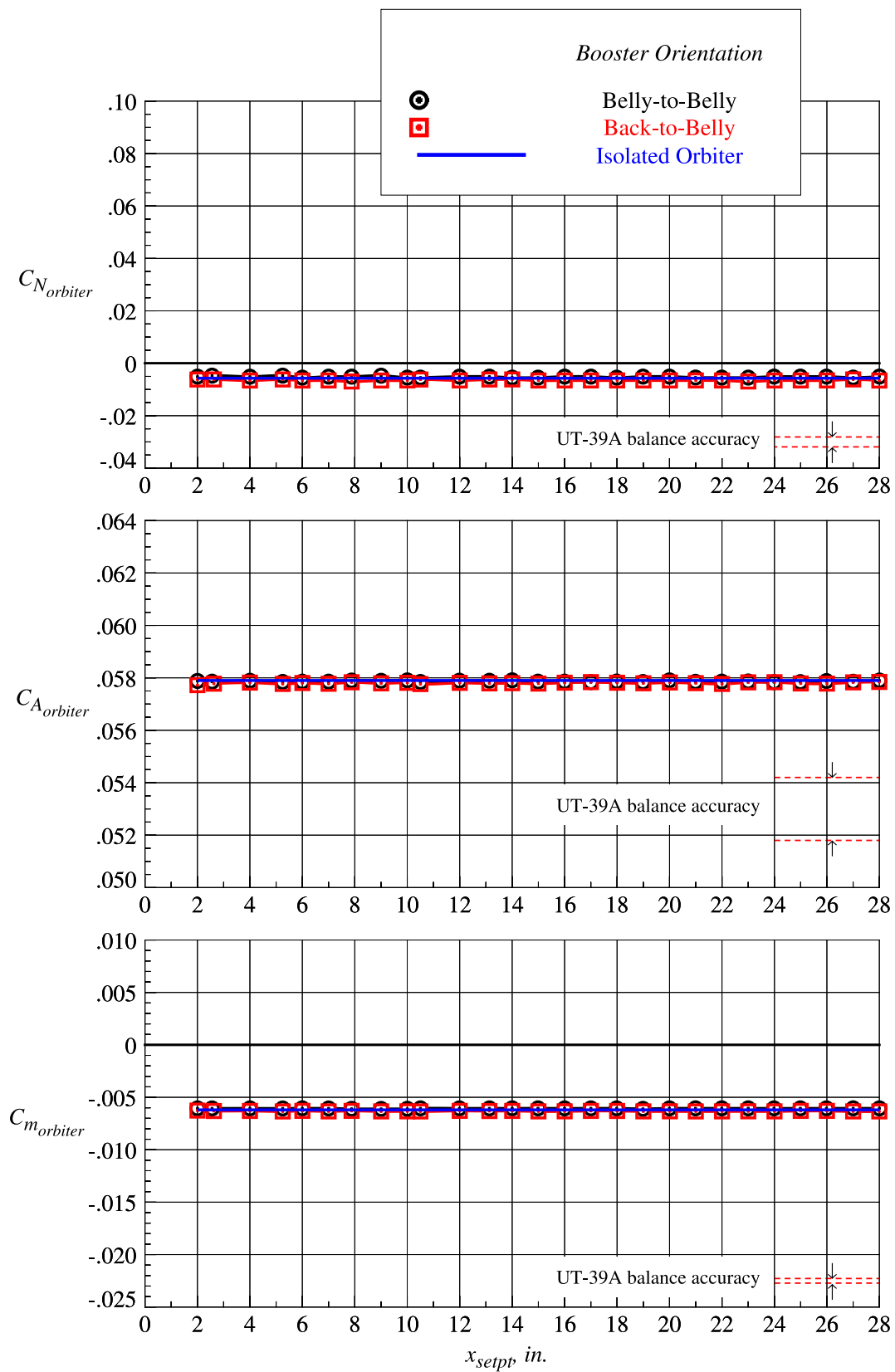
(f)  $z_{setpt} = 3.281$  in.

Figure 66. Continued.



(g)  $z_{setpt} = 3.938$  in.

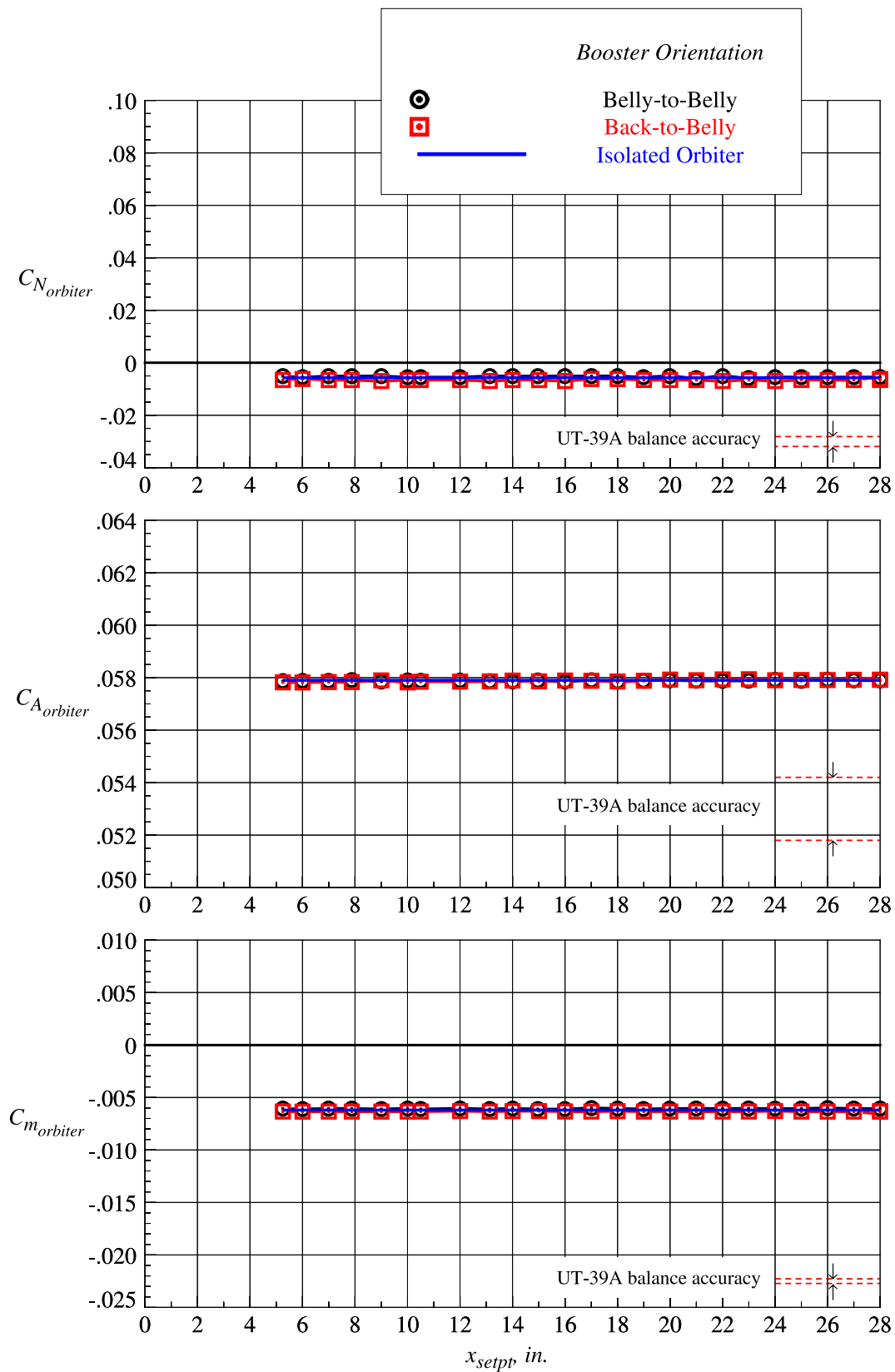
Figure 66. Continued.



(h)  $z_{setpt} = 4.594$  in.

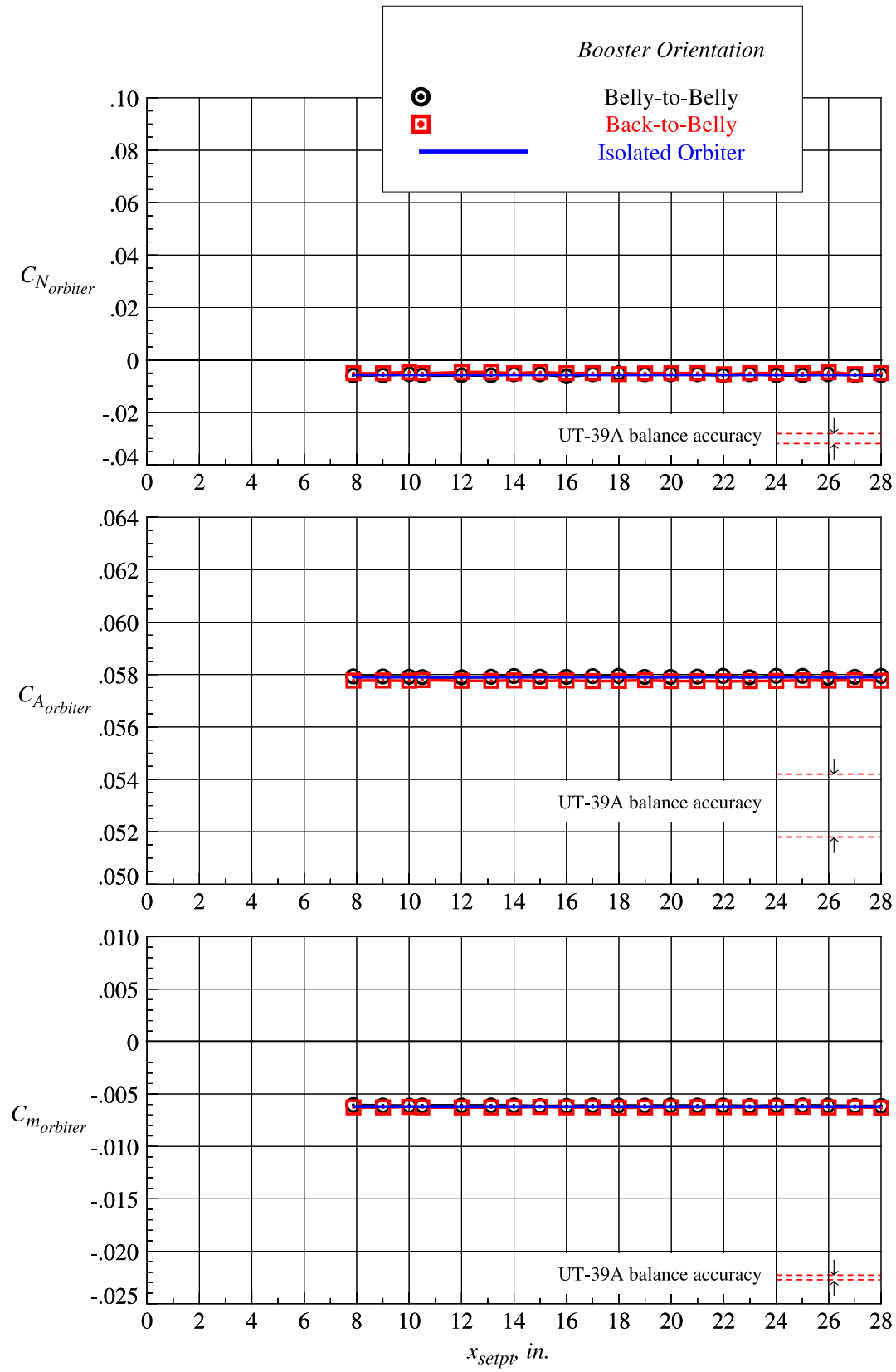
Figure 66. Continued.





(i)  $z_{setpt} = 5.250$  in.

Figure 66. Continued.



(j)  $z_{setpt} = 6.563$  in.

Figure 66. Concluded.

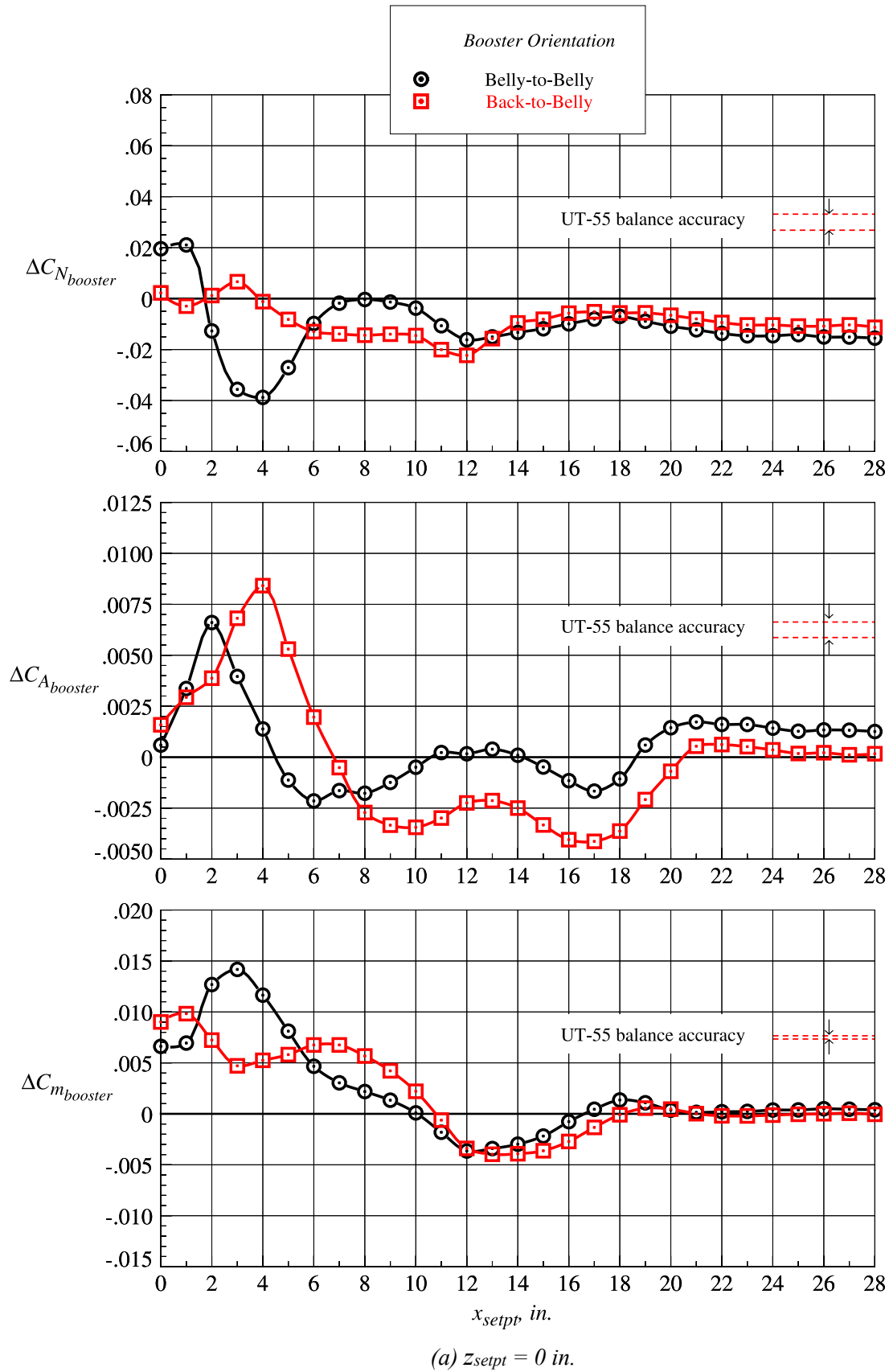
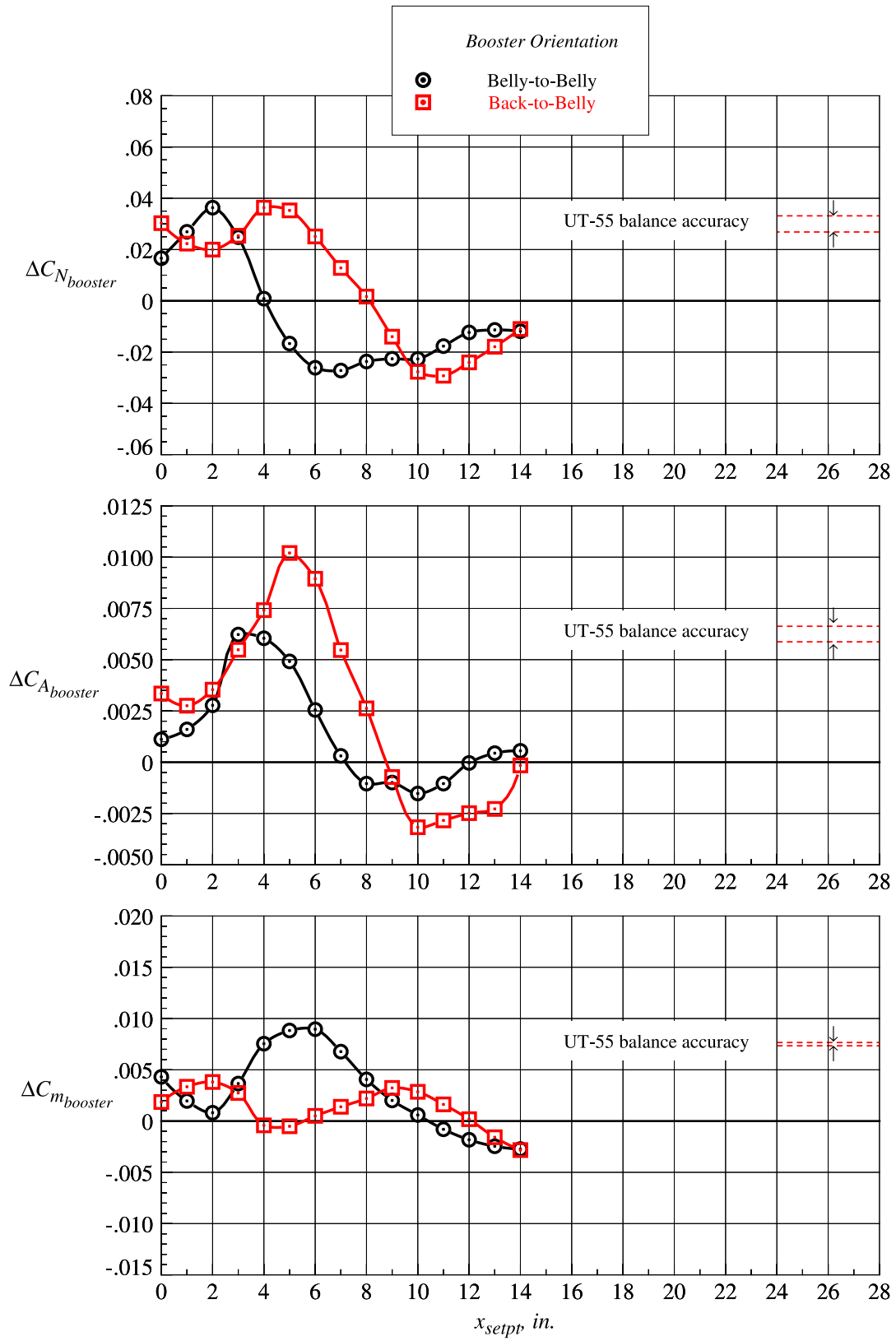
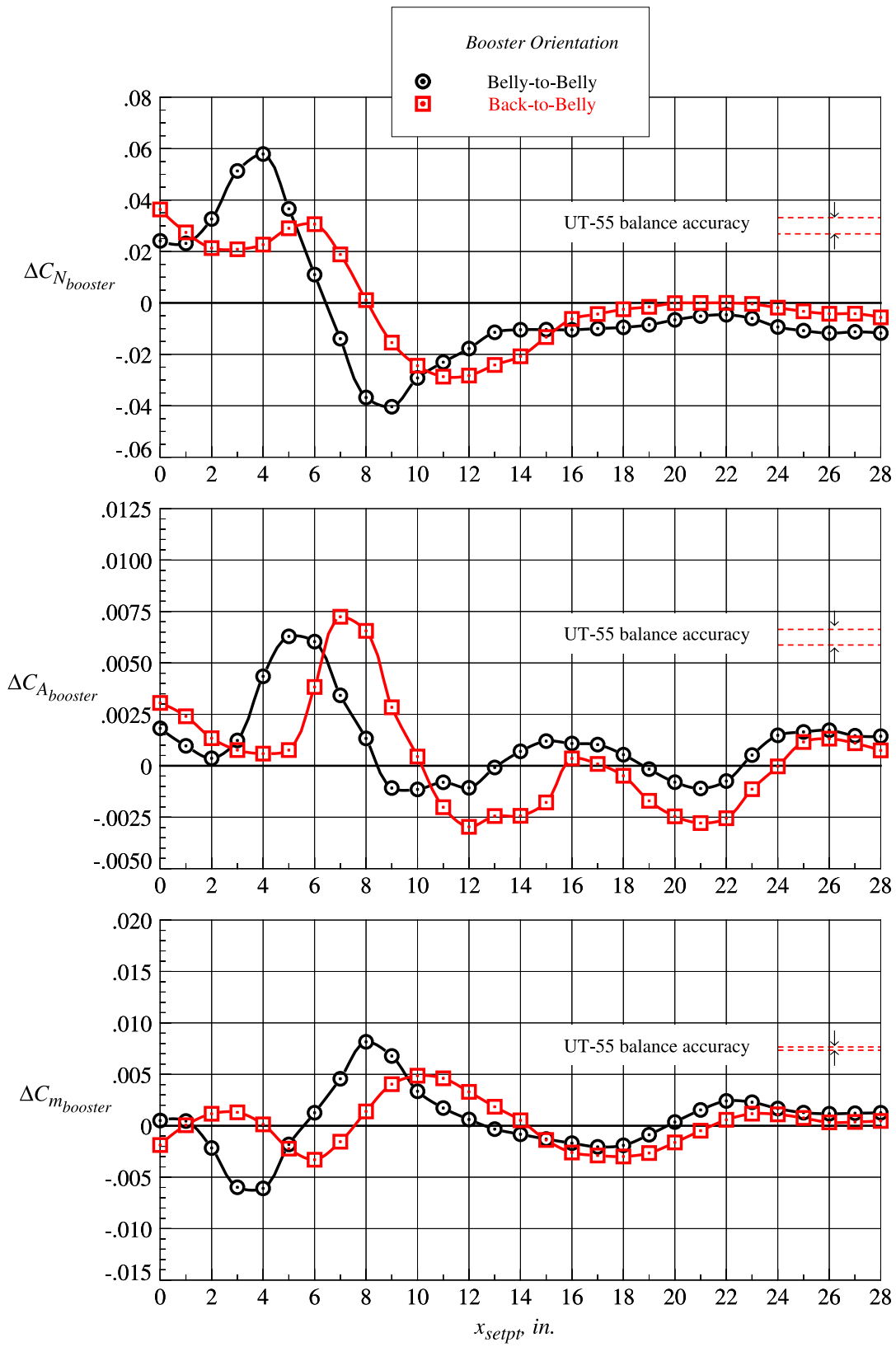


Figure 67. Booster proximity aerodynamic characteristics in belly-to-belly and back-to-belly configurations at Mach = 3.0 and  $\Delta\alpha = 0^\circ$ .



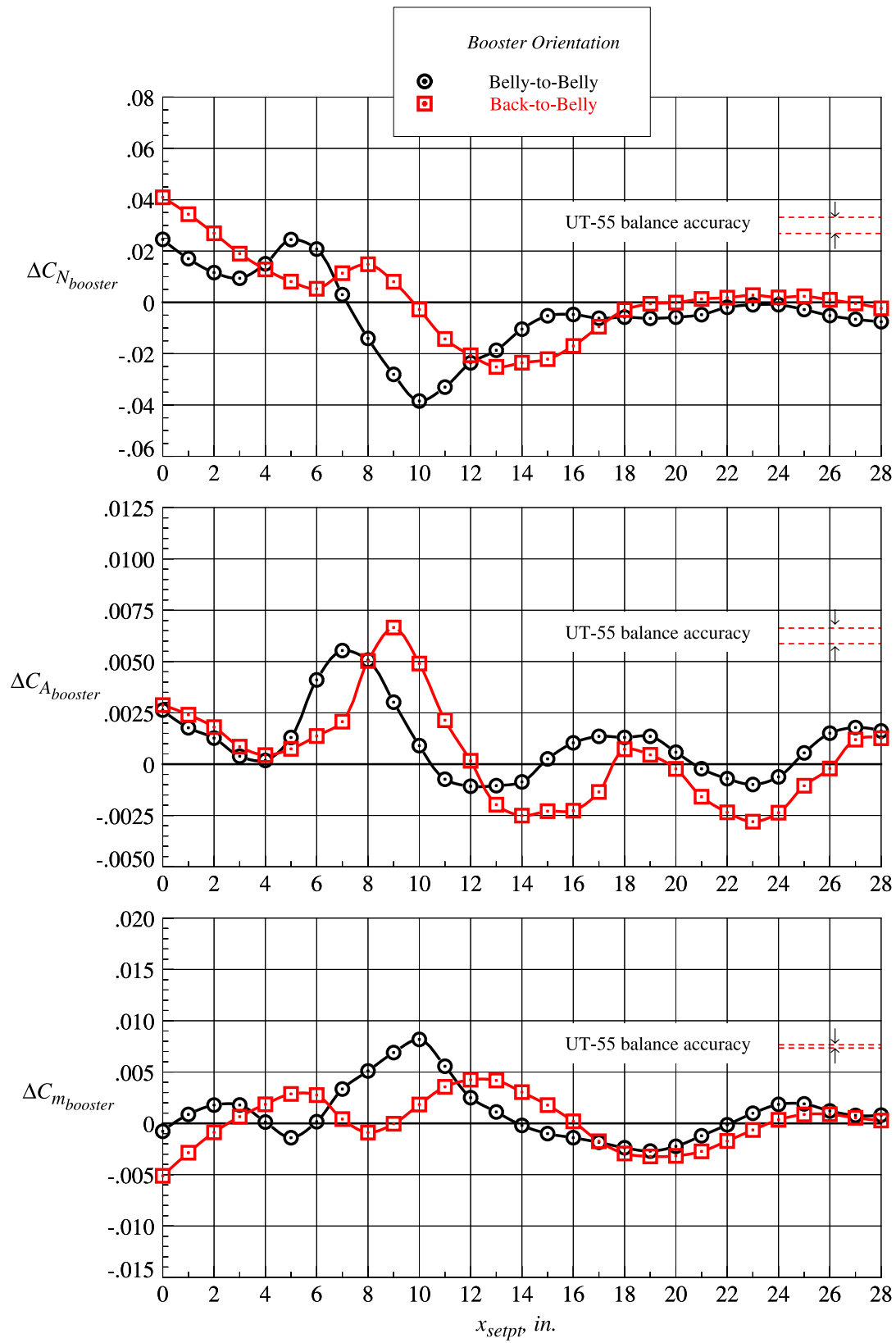
(b)  $z_{setpt} = 0.656$  in.

Figure 67. Continued.



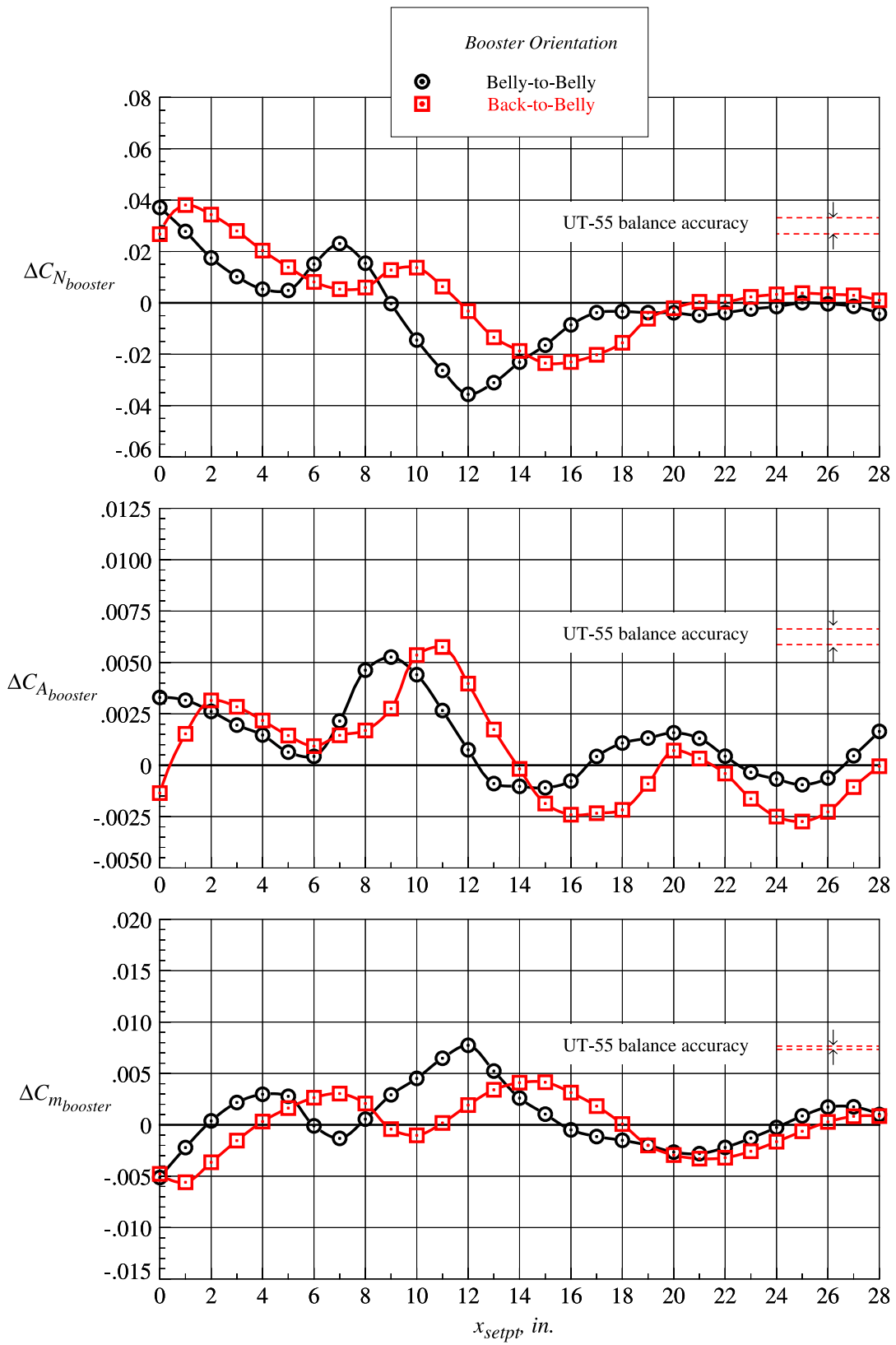
(c)  $z_{setpt} = 1.313$  in.

Figure 67. Continued.



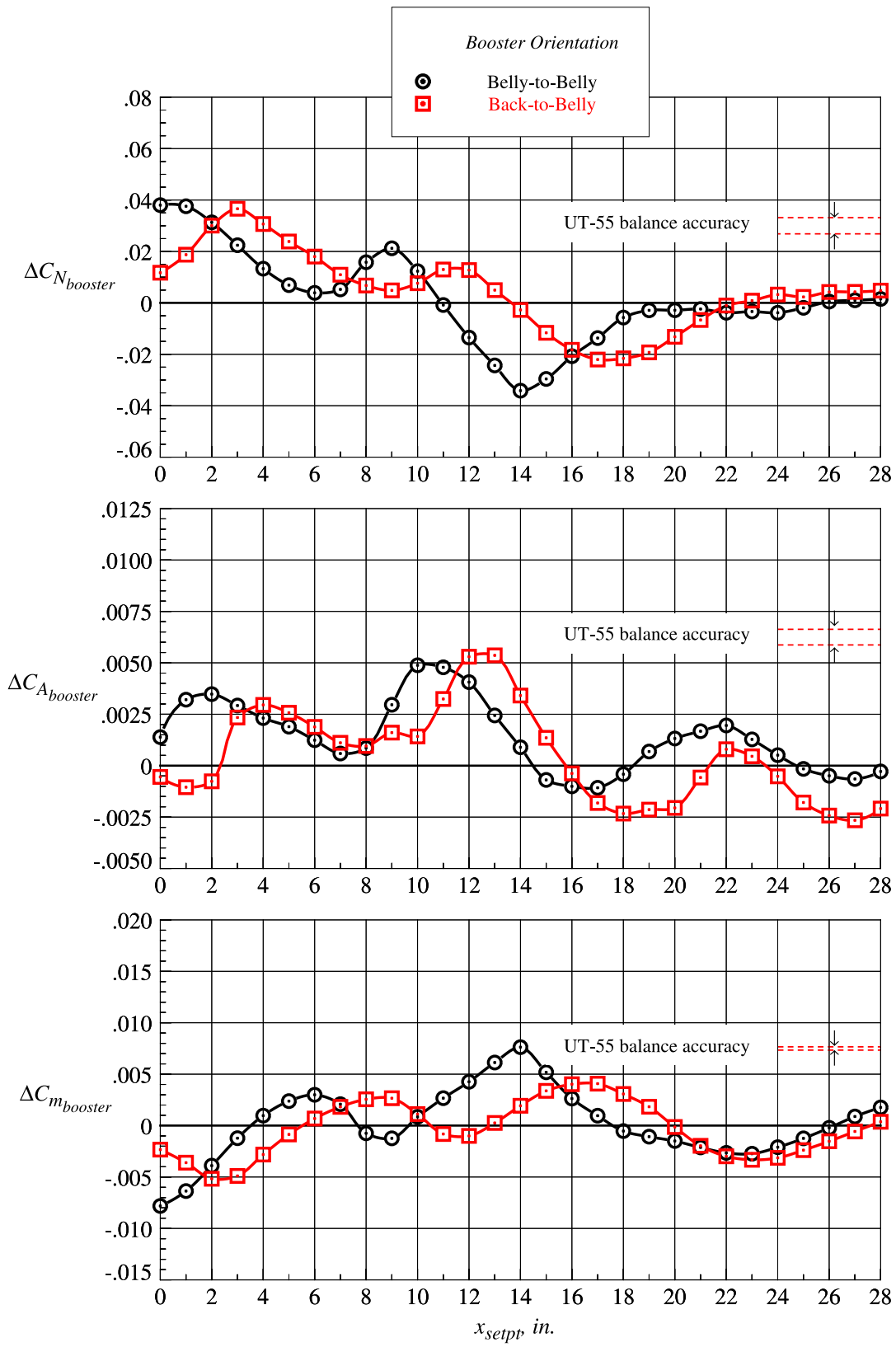
(d)  $z_{setpt} = 1.969 \text{ in.}$

Figure 67. Continued.



(e)  $z_{setpt} = 2.625 \text{ in.}$

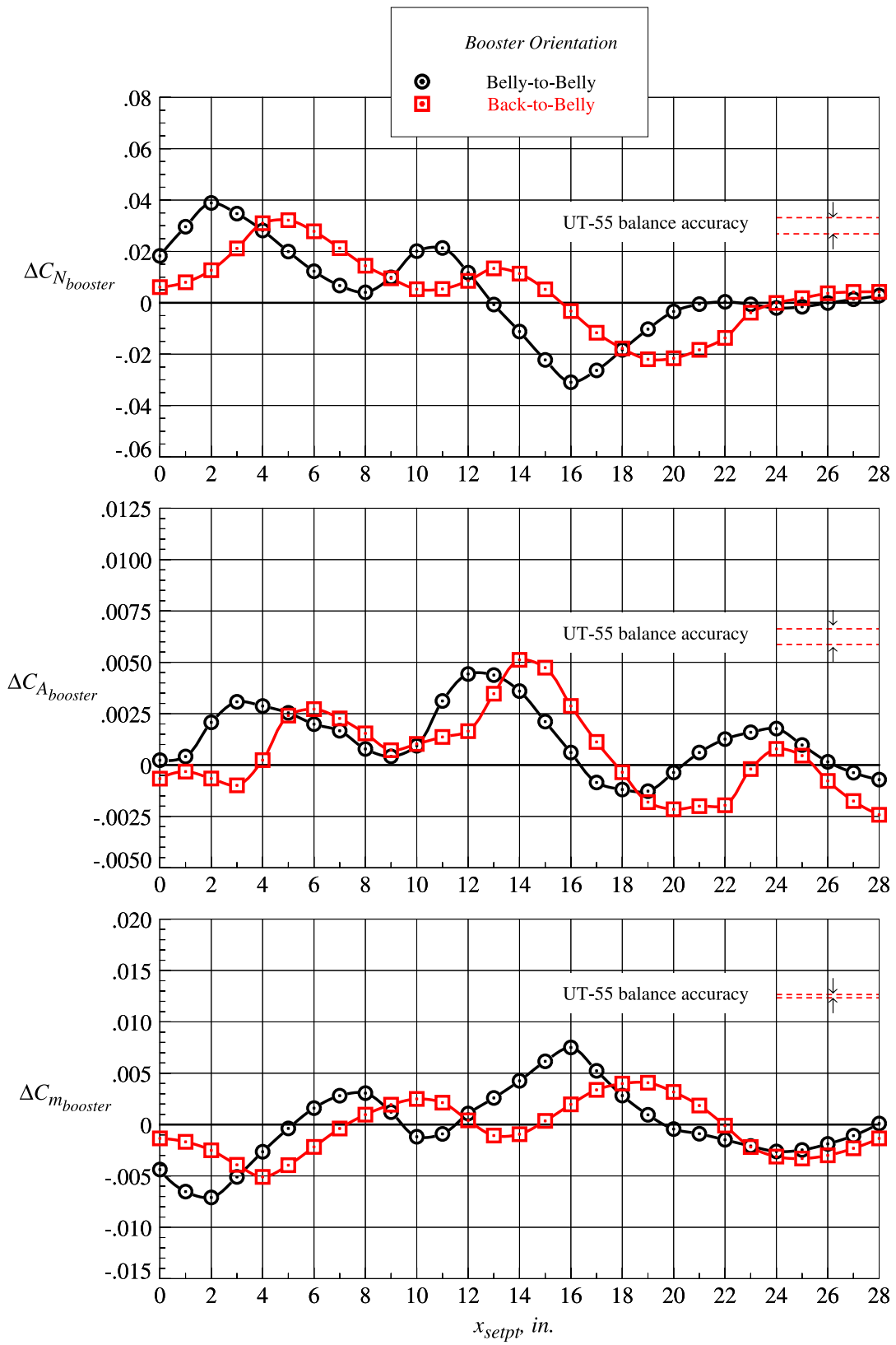
Figure 67. Continued.



(f)  $z_{setpt} = 3.281$  in.

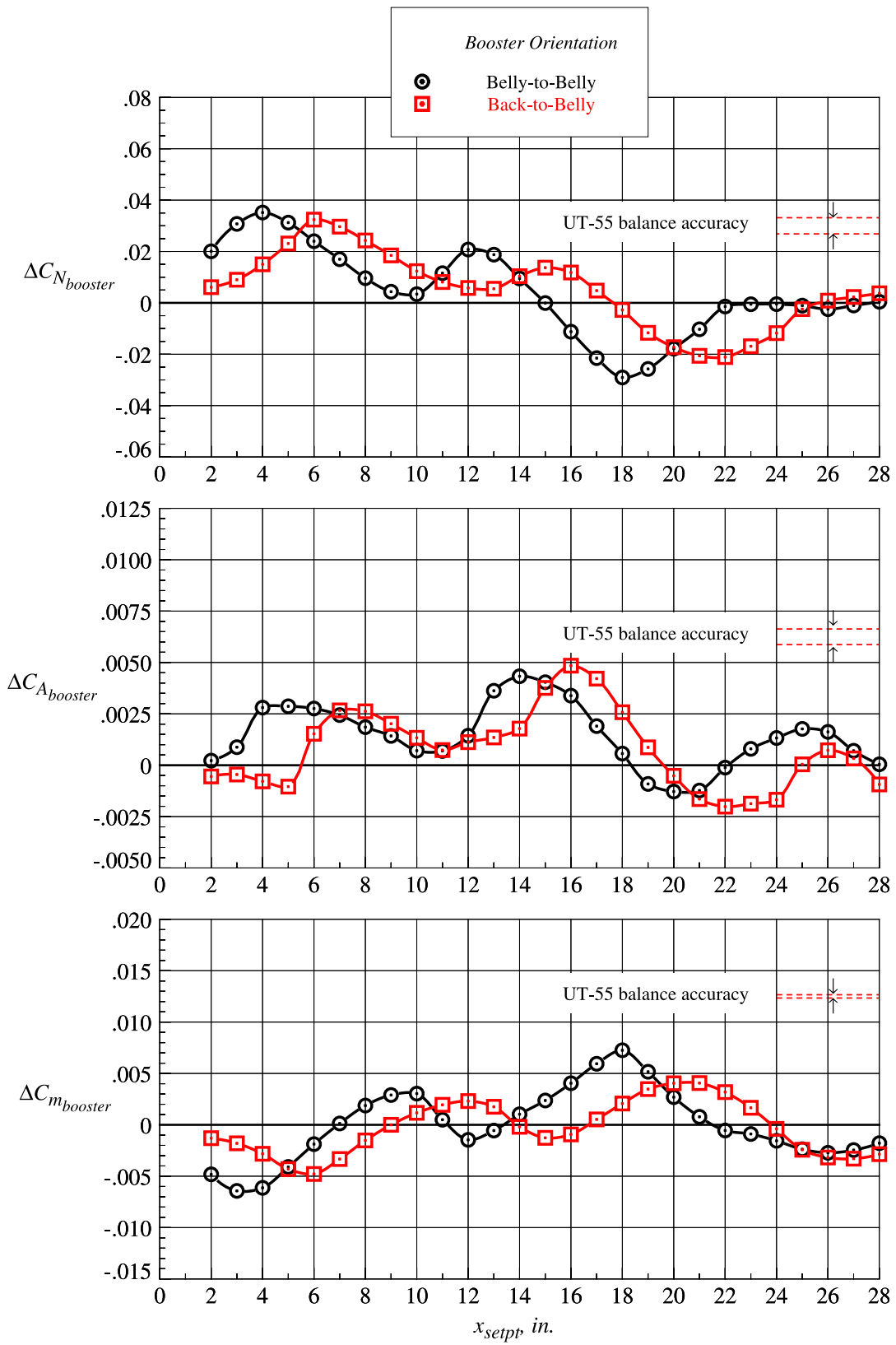
Figure 67. Continued.





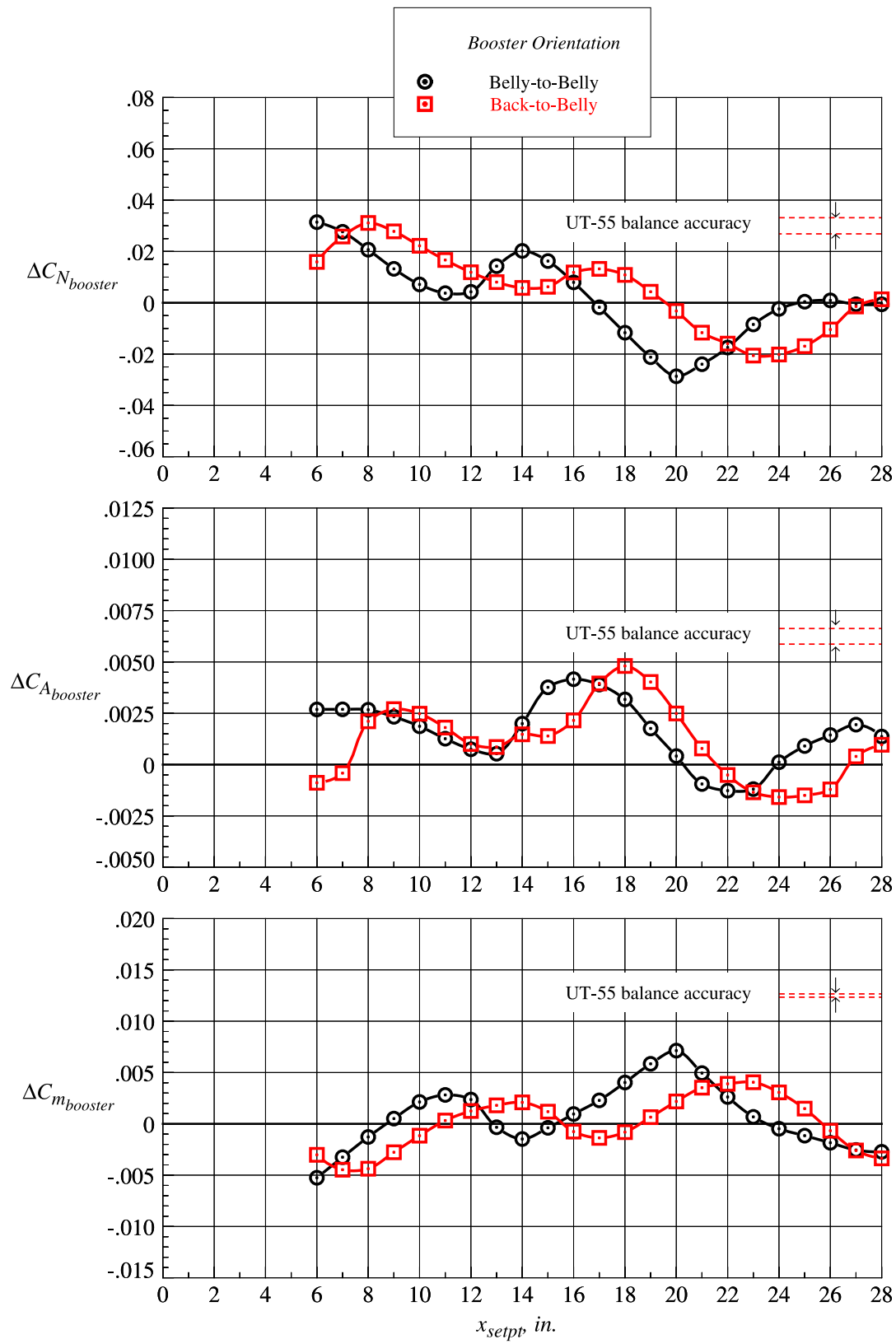
(g)  $z_{setpt} = 3.938$  in.

Figure 67. Continued.



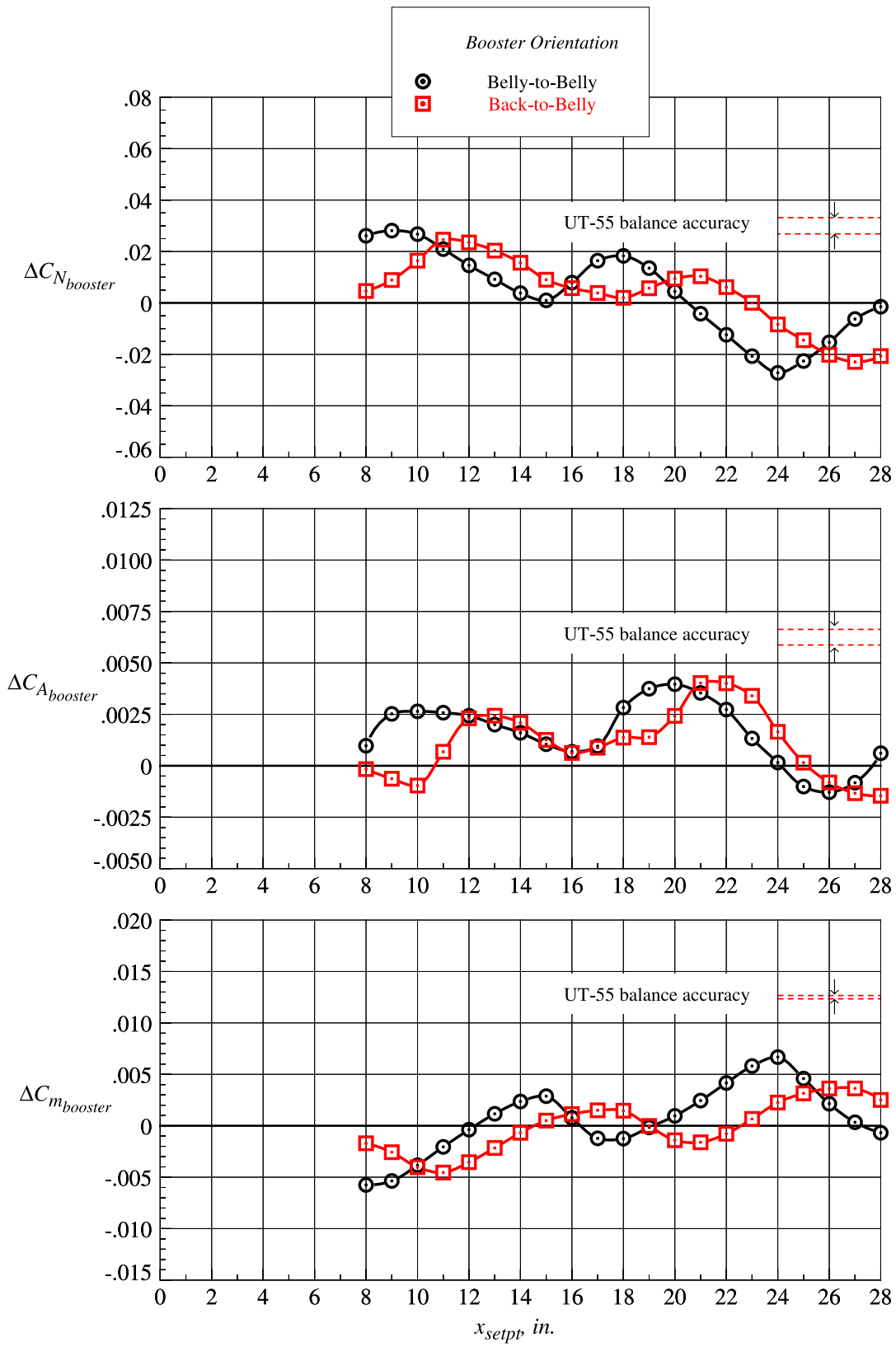
(h)  $z_{setpt} = 4.594 \text{ in.}$

Figure 67. Continued.



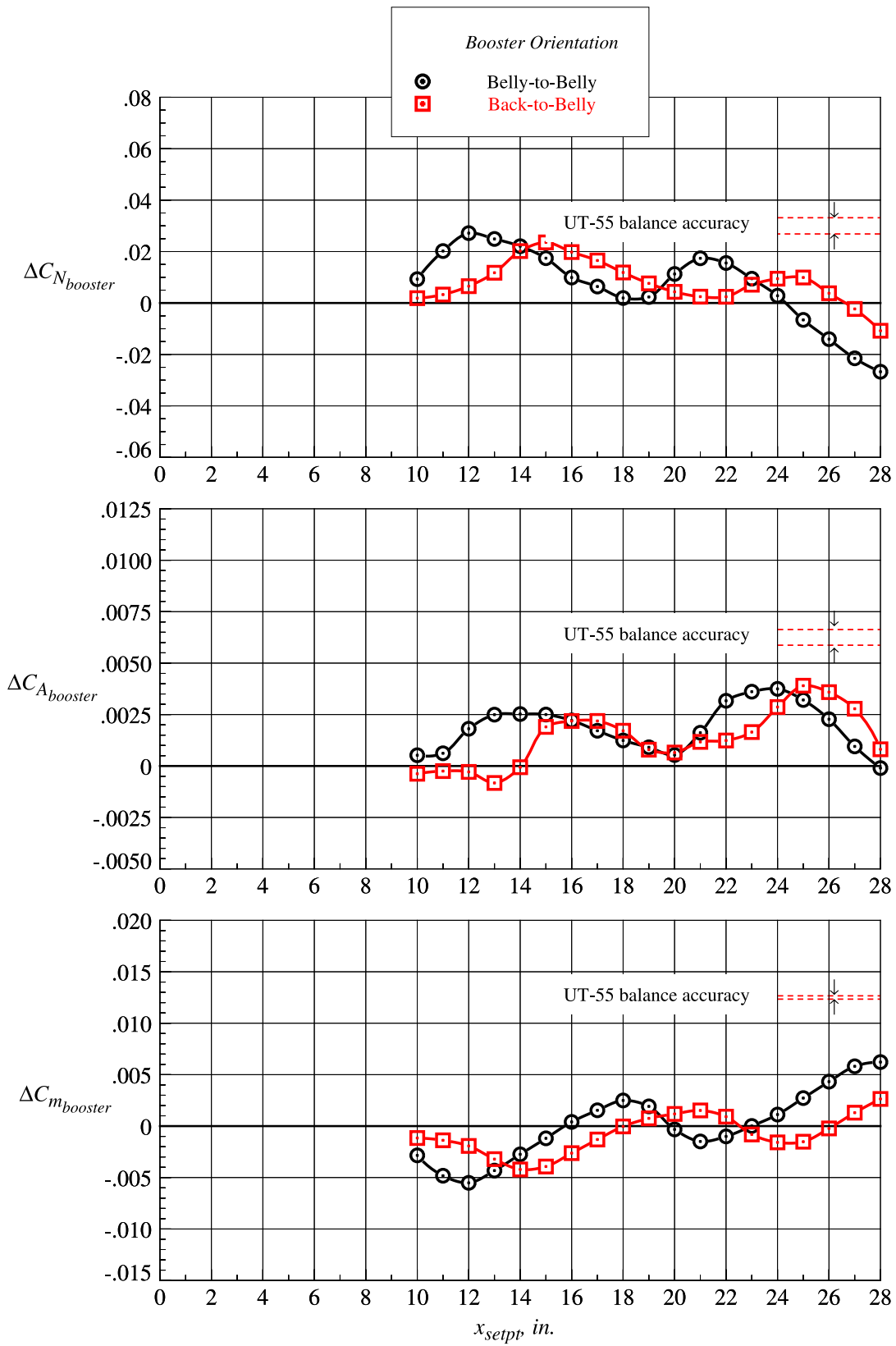
(i)  $z_{setpt} = 5.250$  in.

Figure 67. Continued.



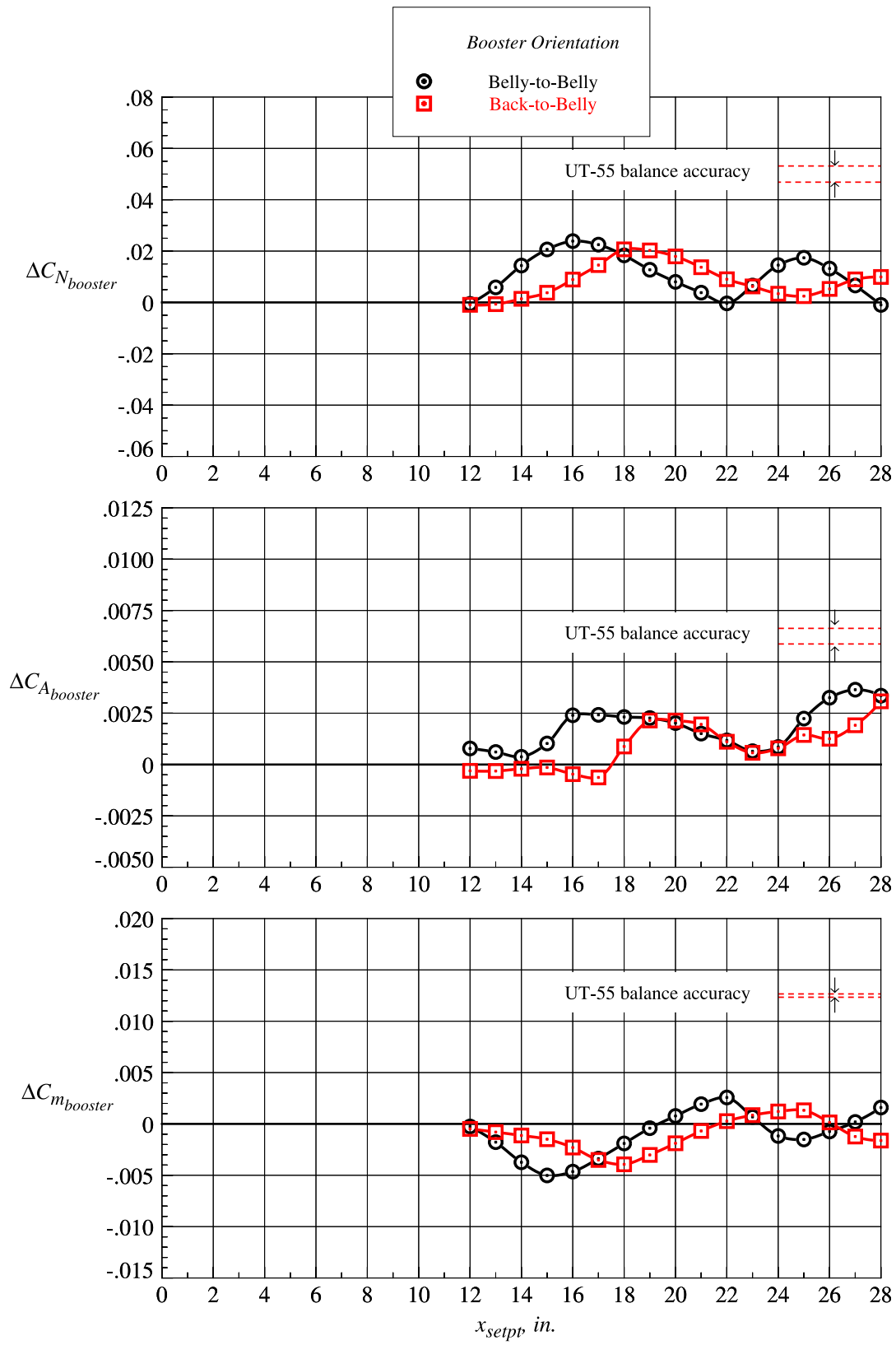
(j)  $z_{setpt} = 6.563 \text{ in.}$

Figure 67. Continued.



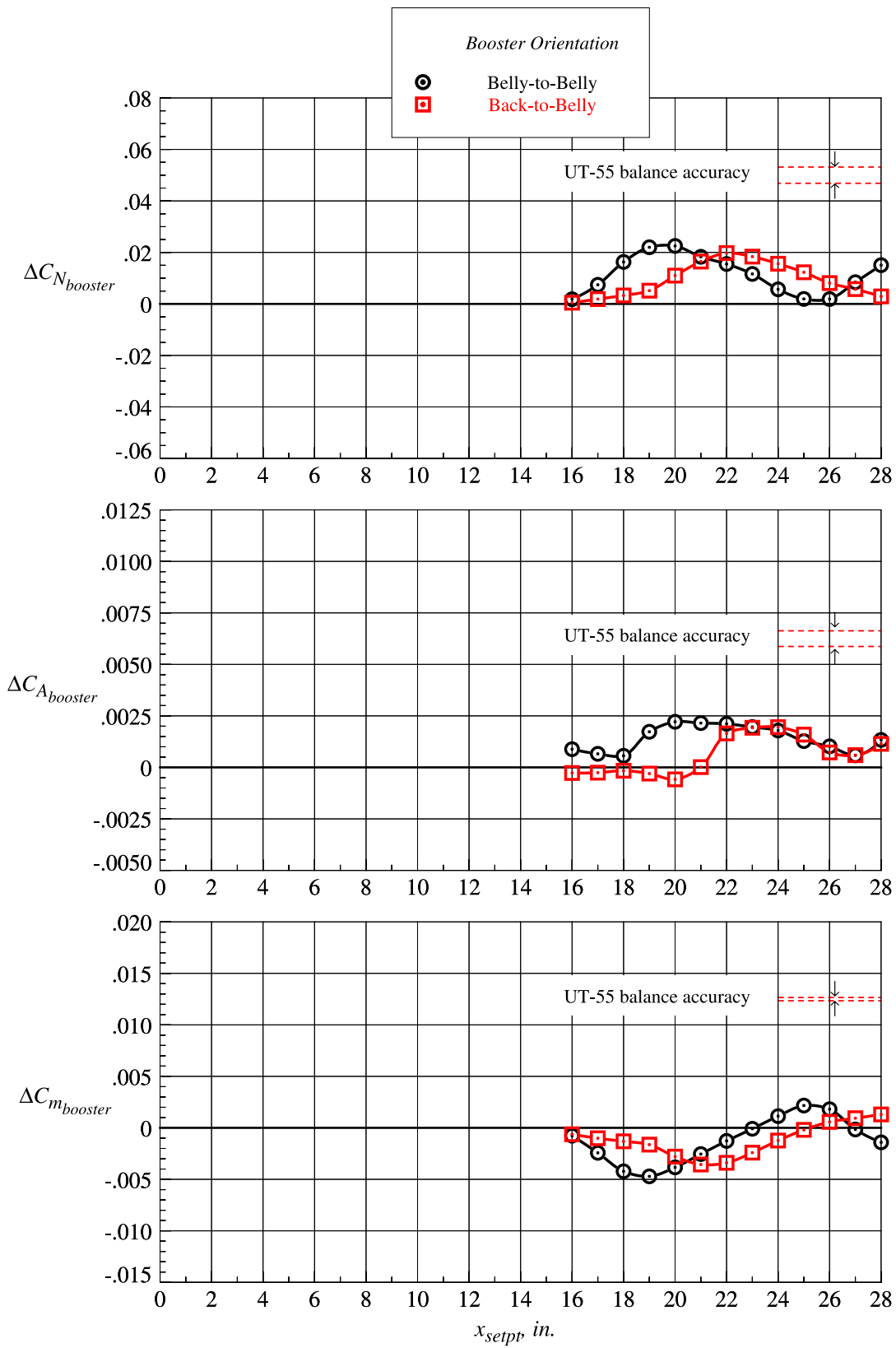
(k)  $z_{setpt} = 7.875$  in.

Figure 67. Continued.



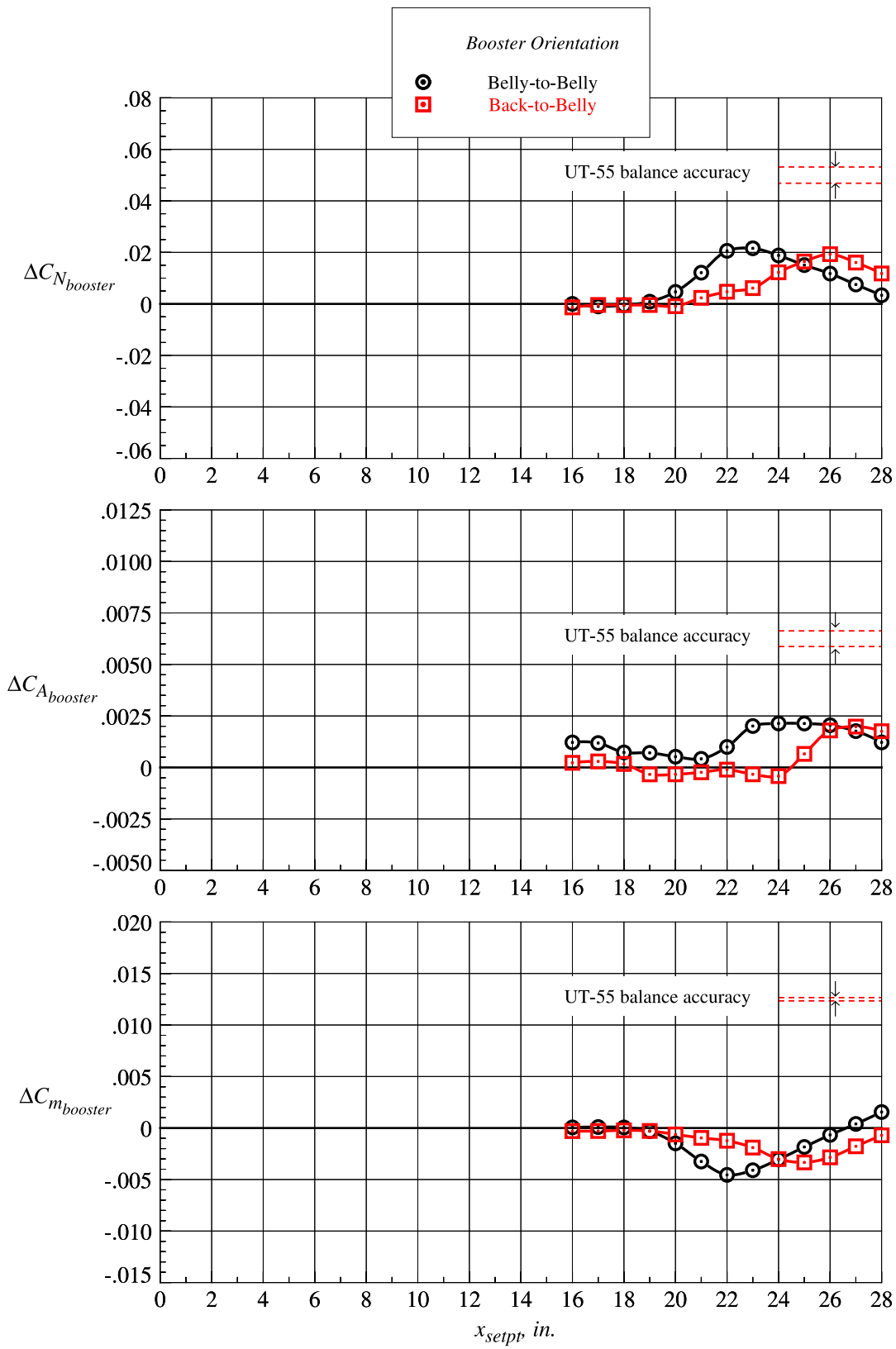
(l)  $z_{setpt} = 9.188$  in.

Figure 67. Continued.



(m)  $z_{setpt} = 10.500$  in.

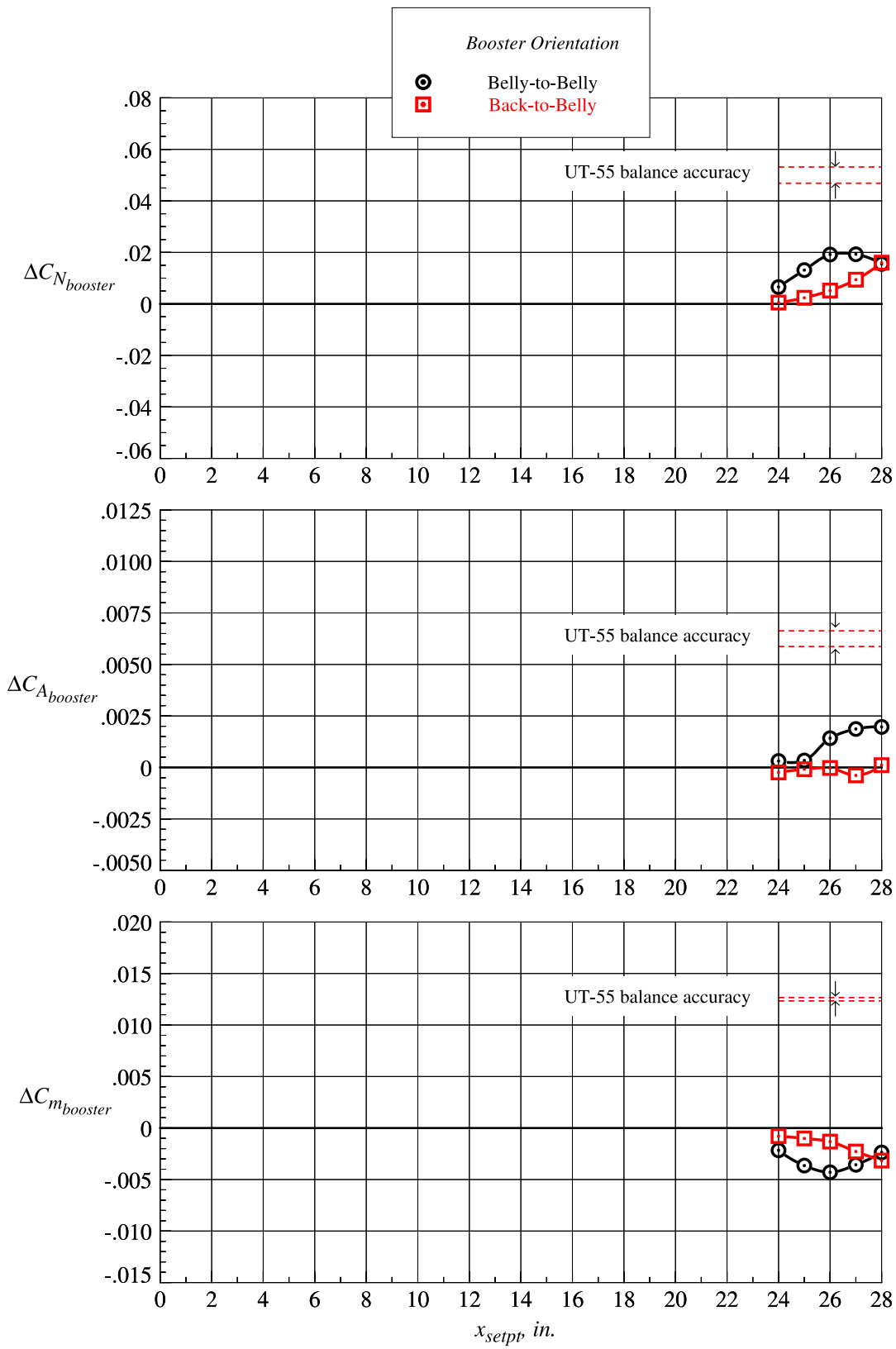
Figure 67. Continued.



(n)  $z_{setpt} = 11.810$  in.

Figure 67. Continued.





(o)  $z_{setpt} = 13.130$  in.

Figure 67. Concluded.

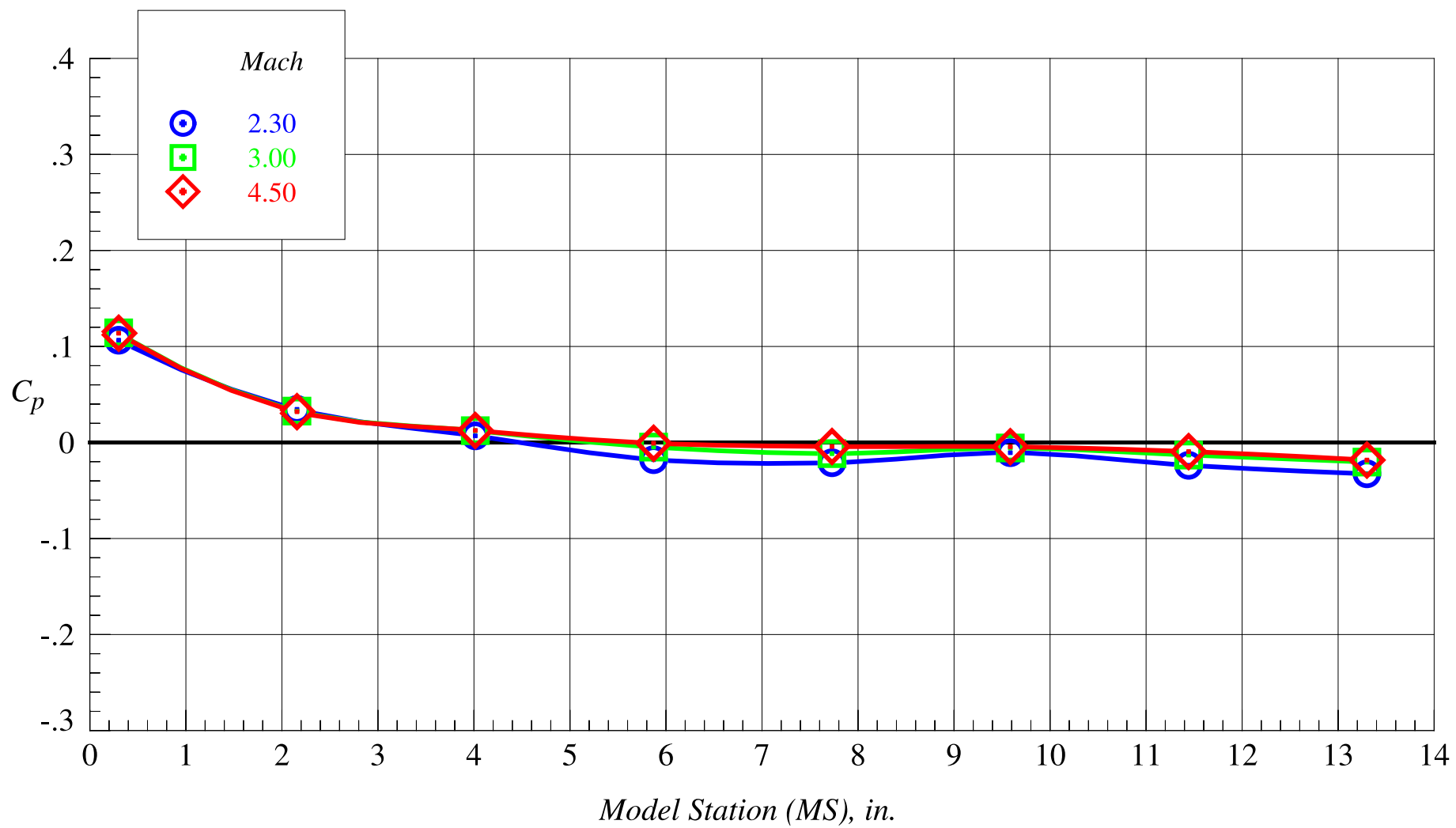
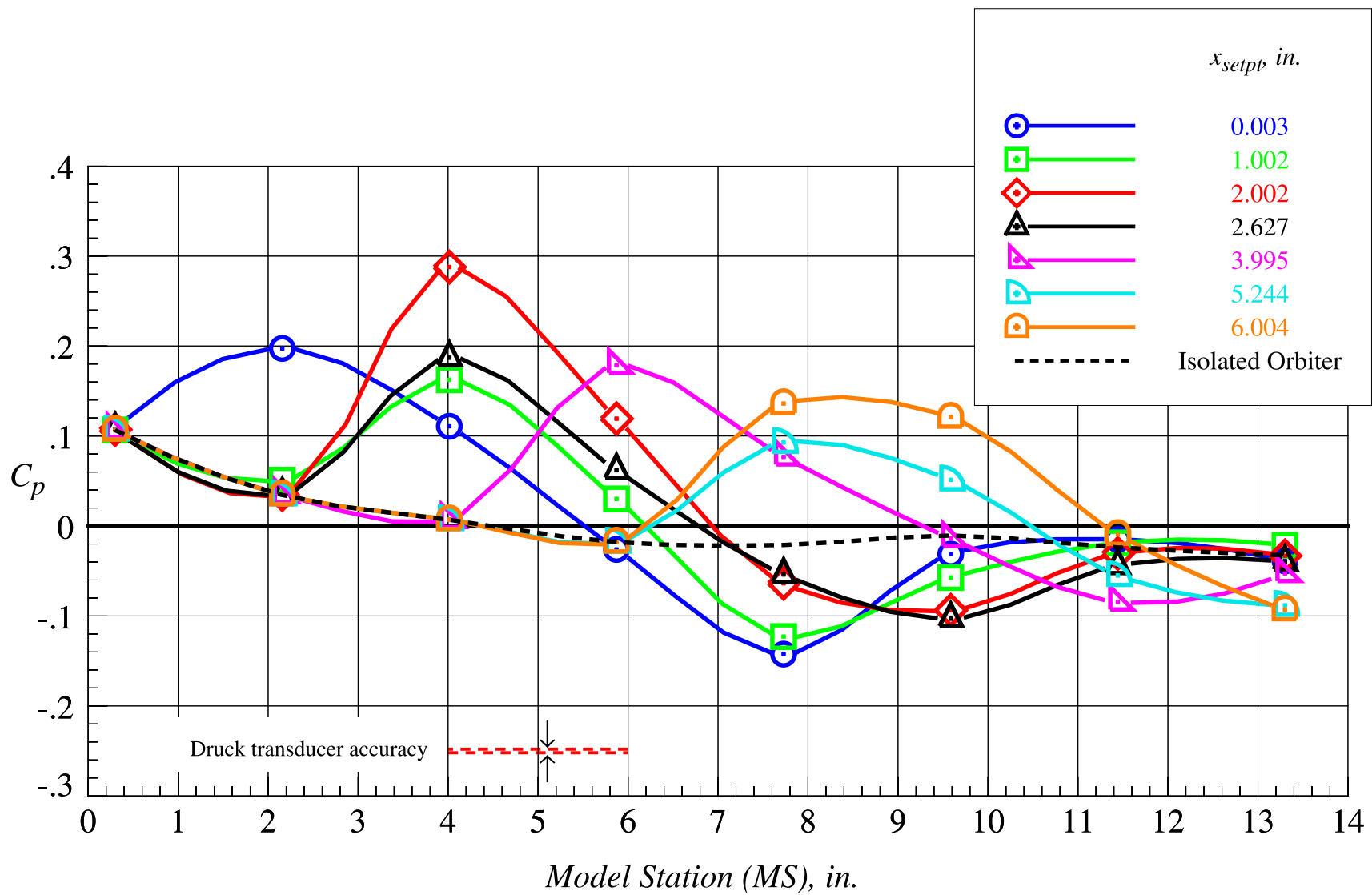
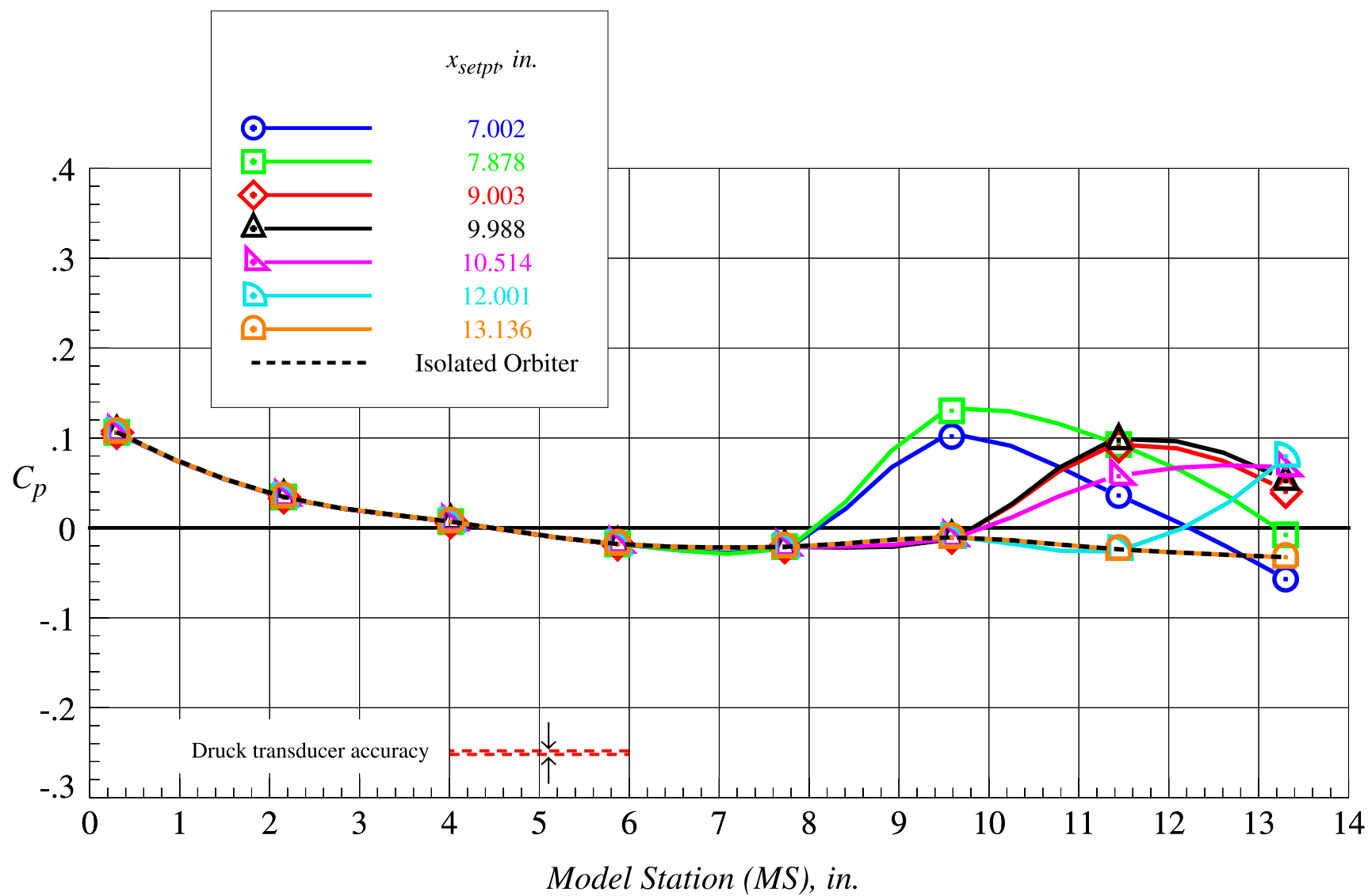


Figure 68. Isolated orbiter fuselage centerline lower surface static pressure distributions at Mach = 2.3, 3.0, and 4.5.



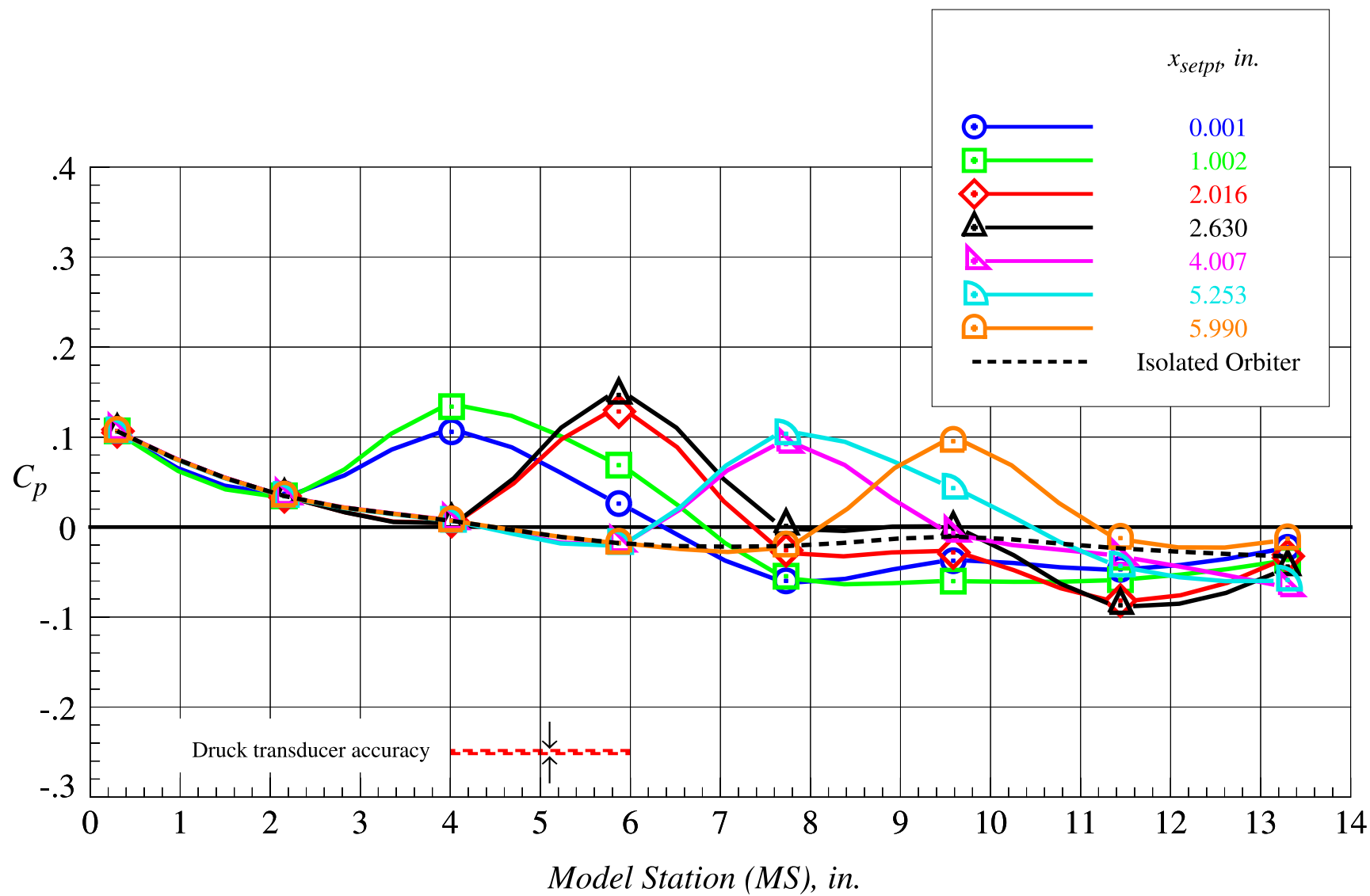
(a)  $z_{setpt} = 0$  in., part 1

Figure 69. Orbiter proximity surface static pressure distributions on fuselage centerline lower surface at Mach = 2.3 and  $\Delta\alpha = 0^\circ$ .



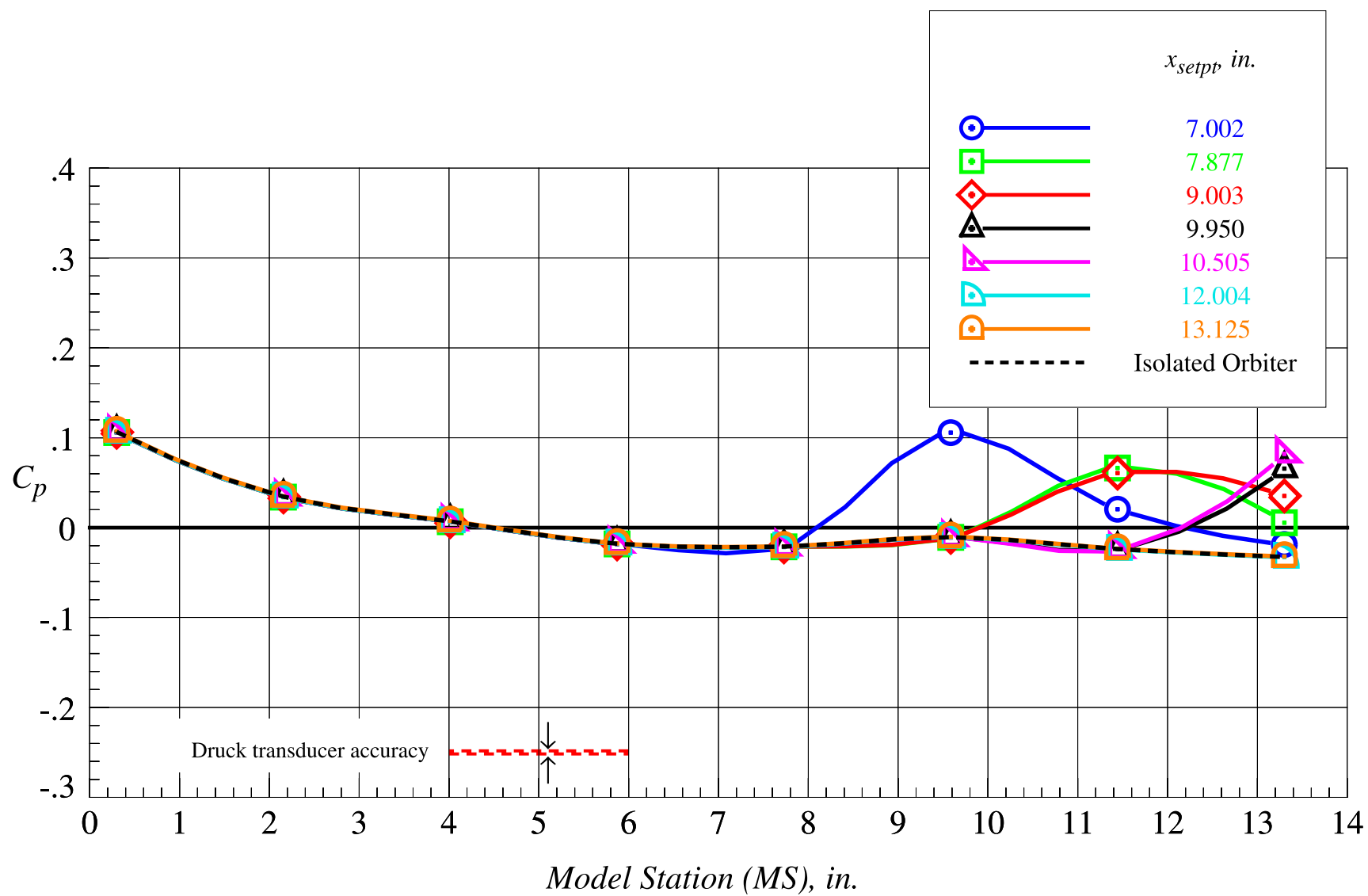
(b)  $z_{setpt} = 0$  in., part 2

Figure 69. Continued.



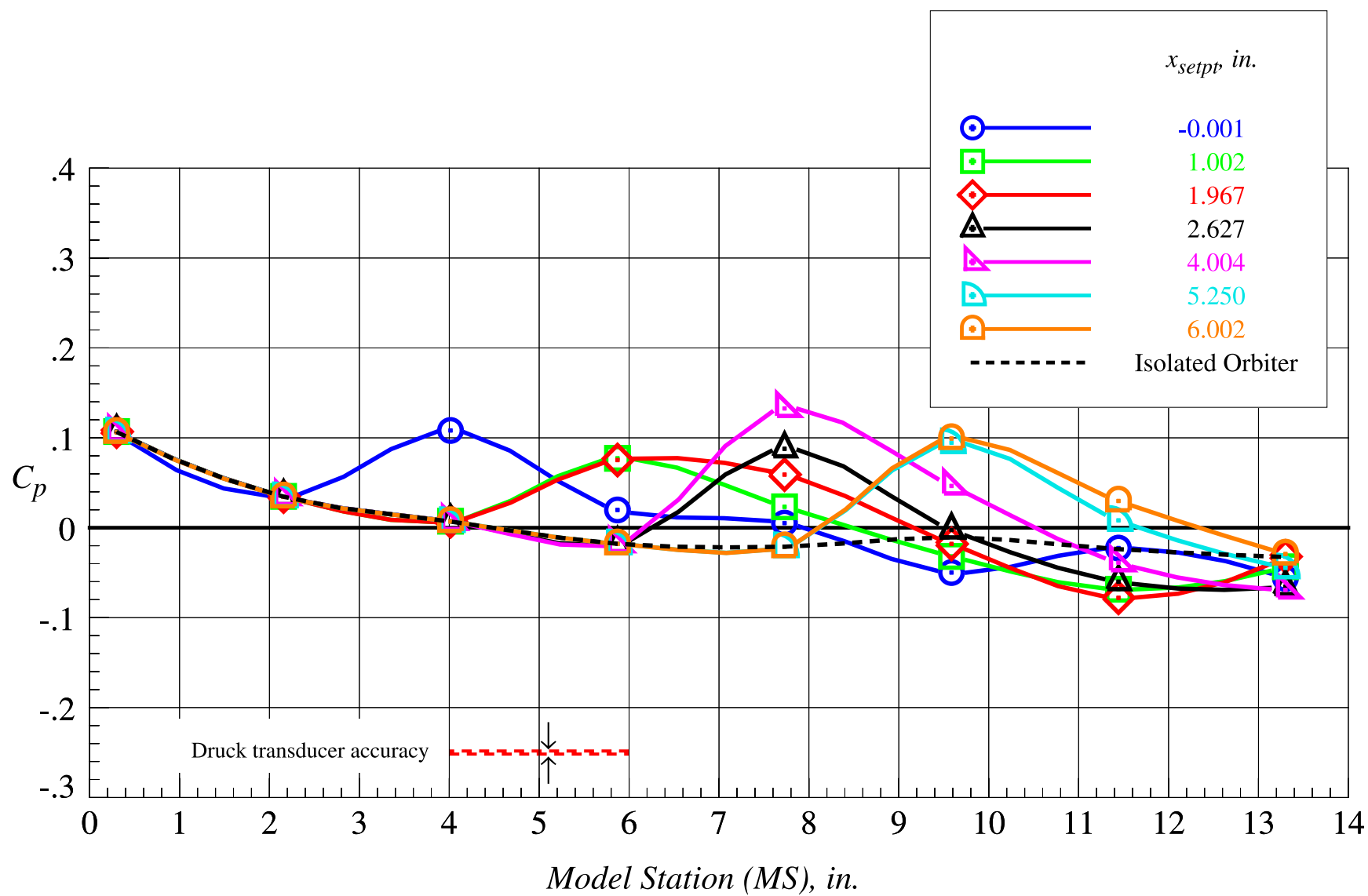
(c)  $z_{setpt} = 0.656$  in., part 1

Figure 69. Continued.



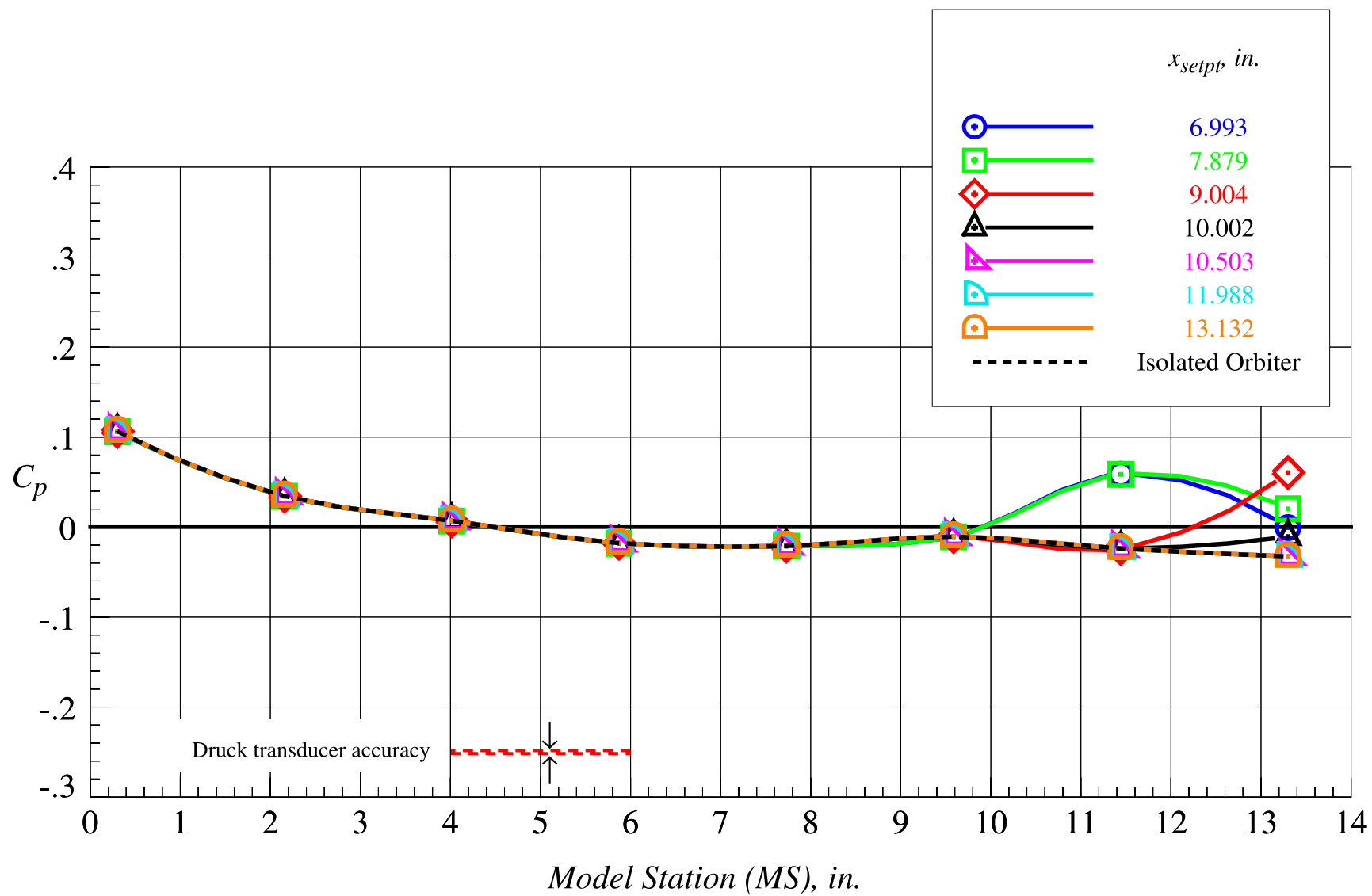
(d)  $z_{setpt} = 0.656$  in., part 2

Figure 69. Continued.



(e)  $z_{setpt} = 1.313$  in., part 1

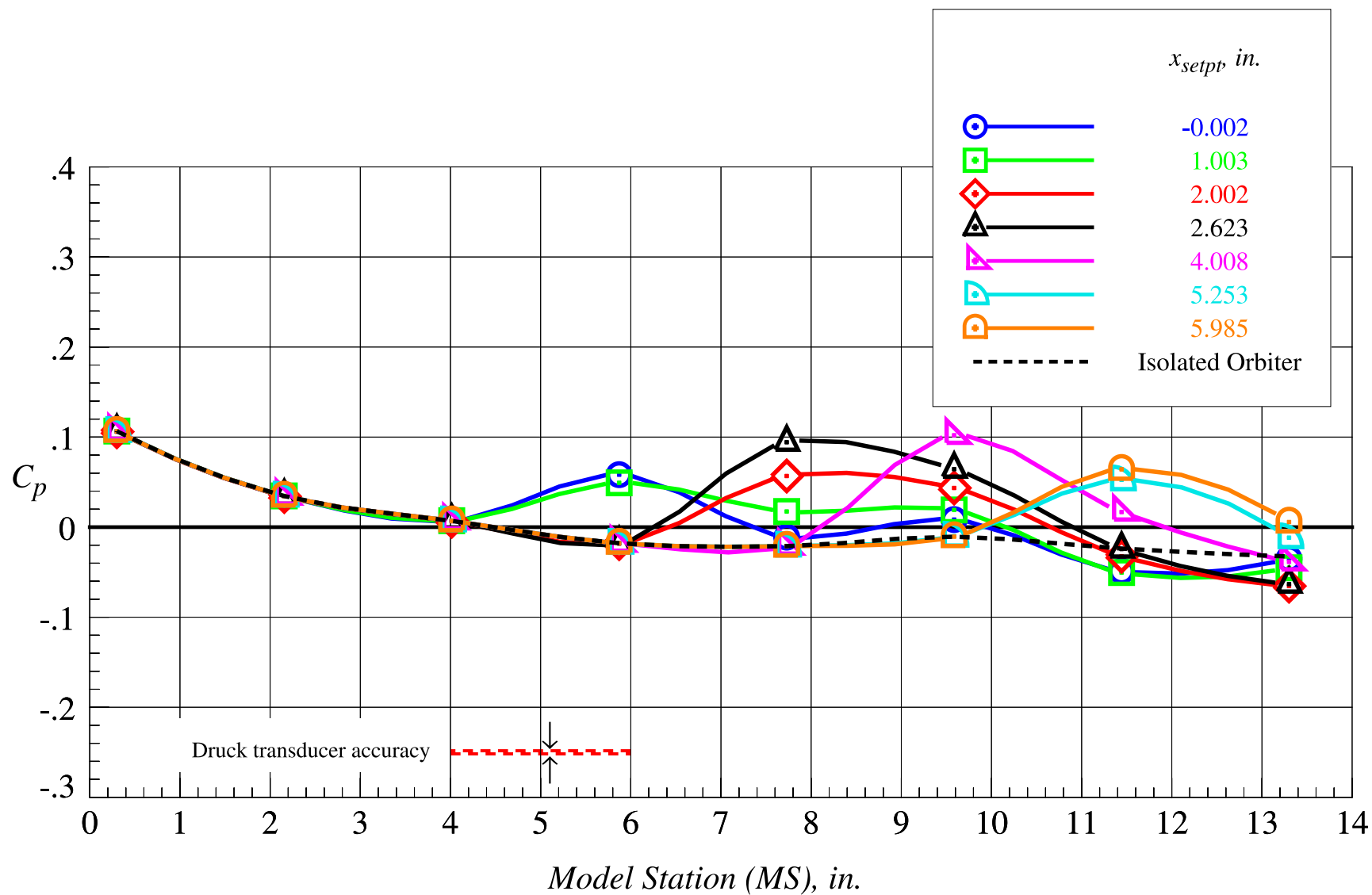
Figure 69. Continued.



(f)  $z_{setpt} = 1.313$  in., part 2

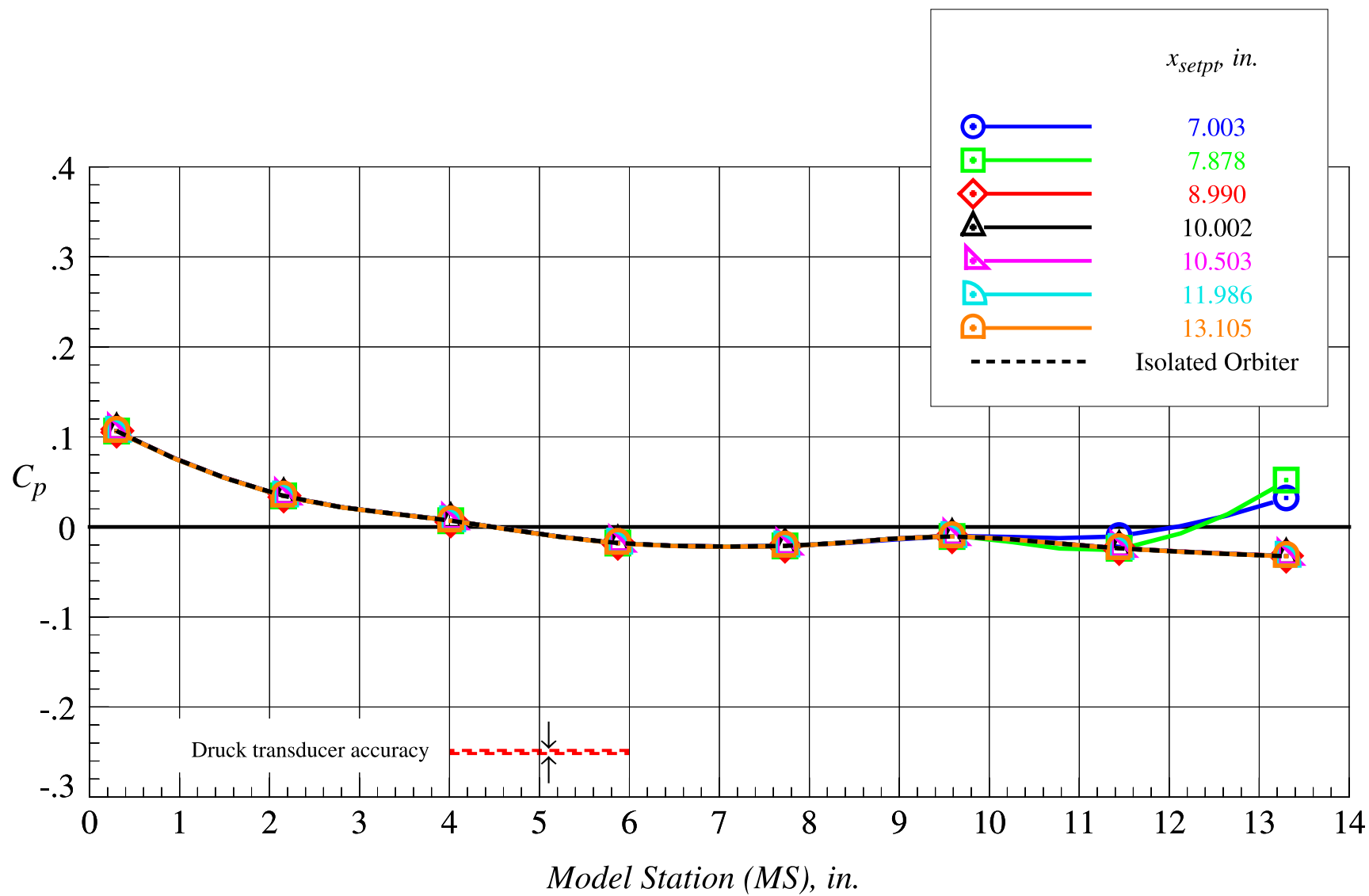
Figure 69. Continued.





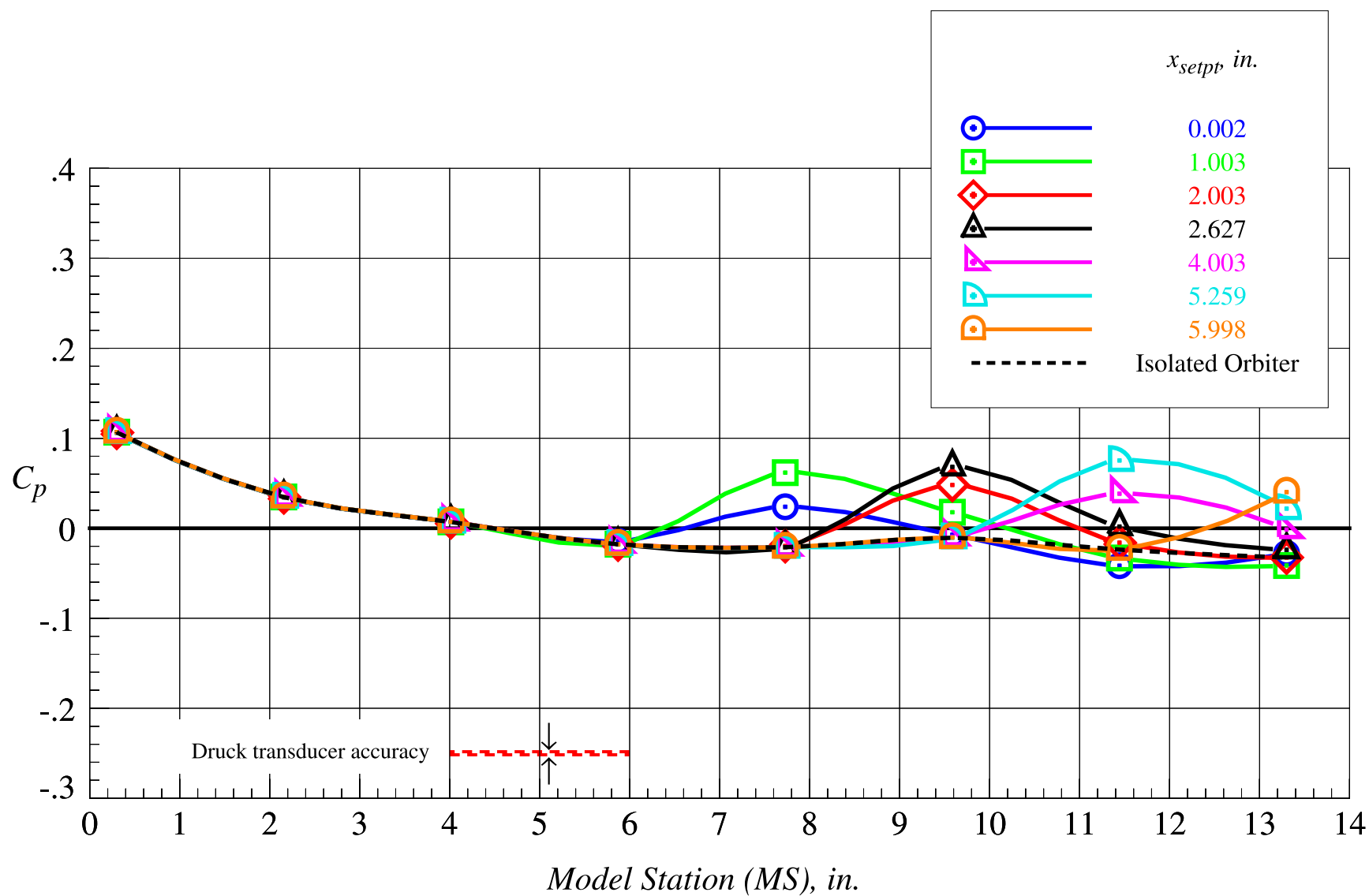
(g)  $z_{setpt} = 1.969$  in., part 1

Figure 69. Continued.



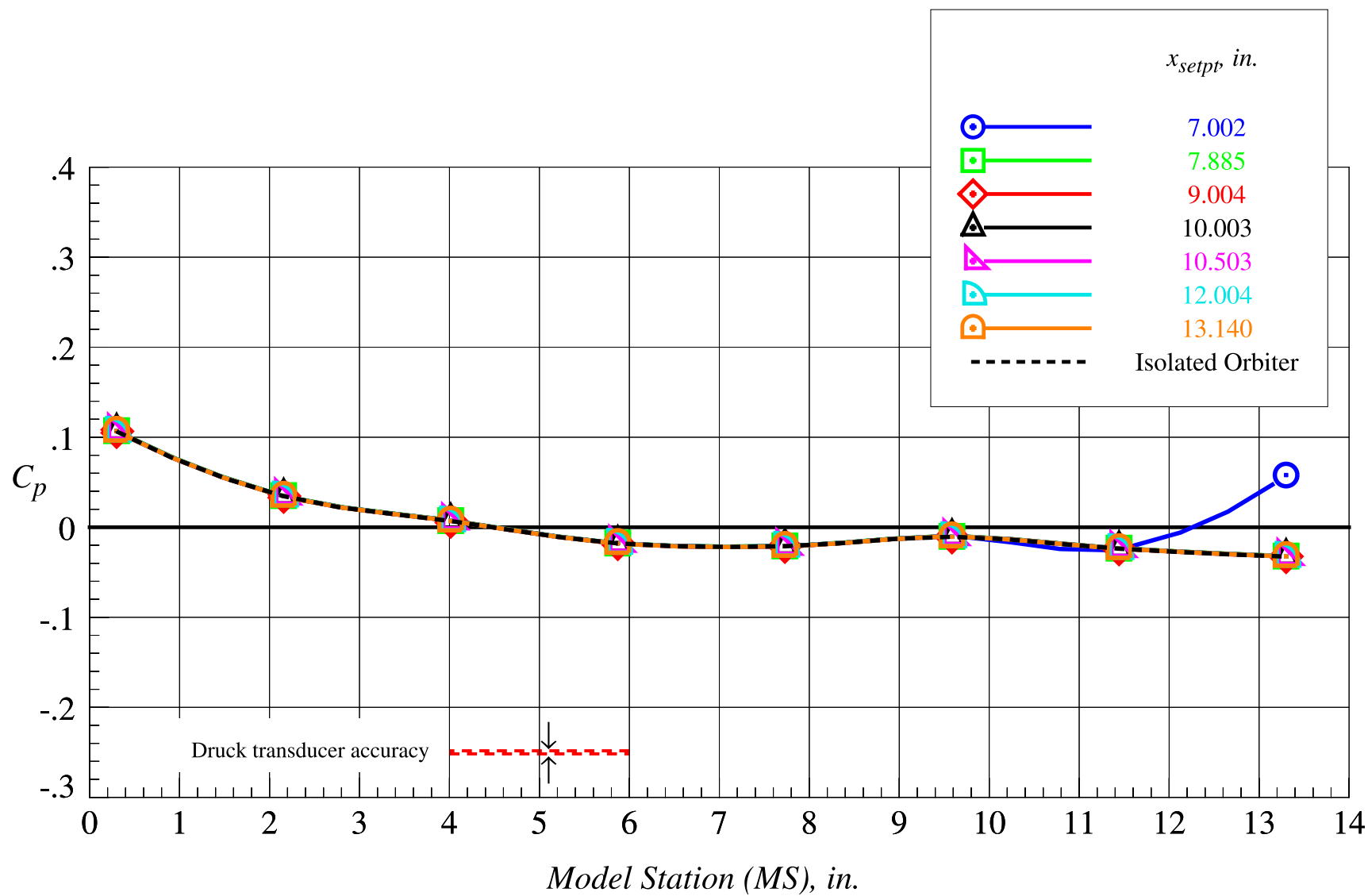
(h)  $z_{setpt} = 1.969$  in., part 2

Figure 69. Continued.



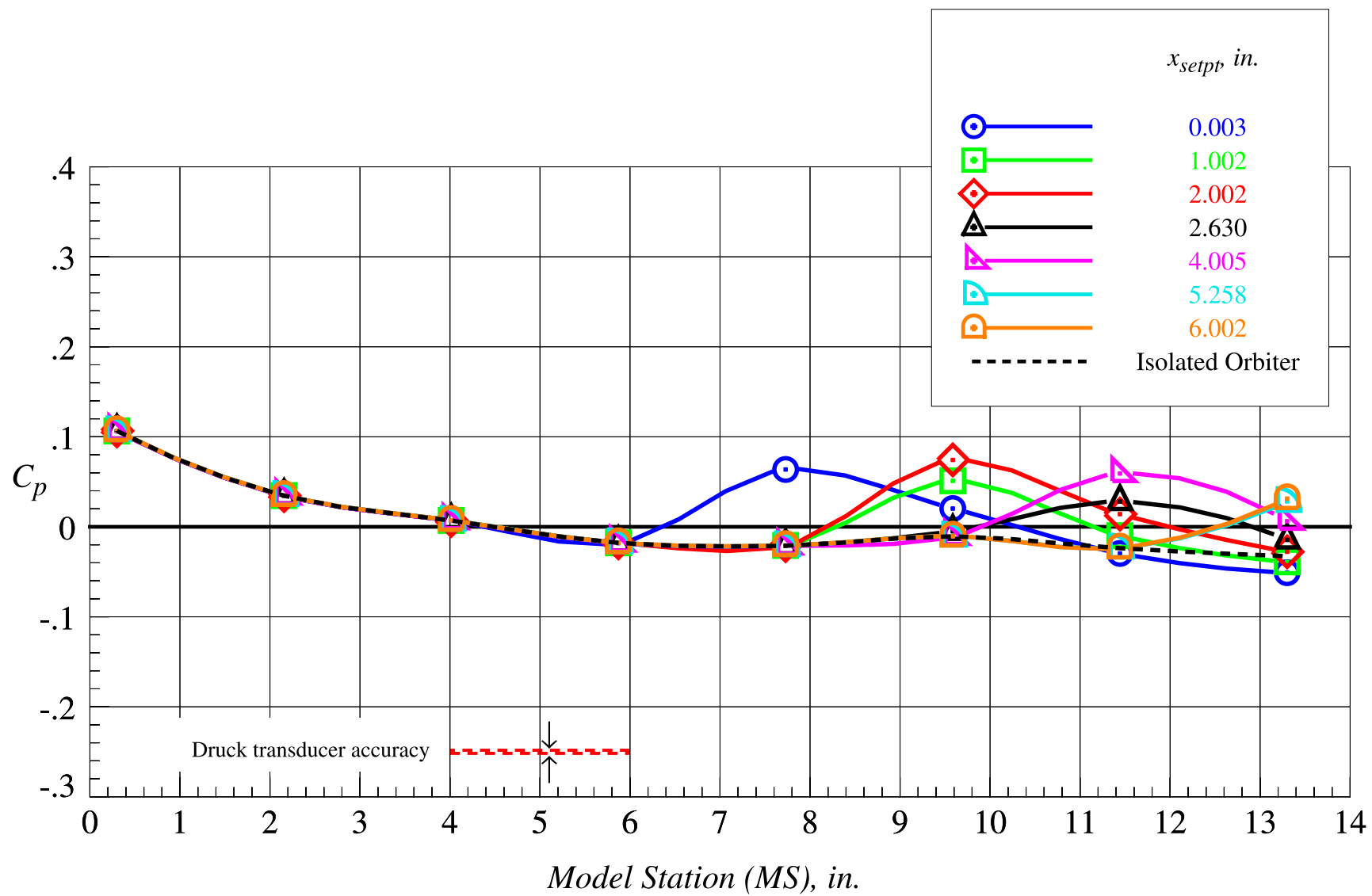
(i)  $z_{setpt} = 2.625$  in., part 1

Figure 69. Continued.



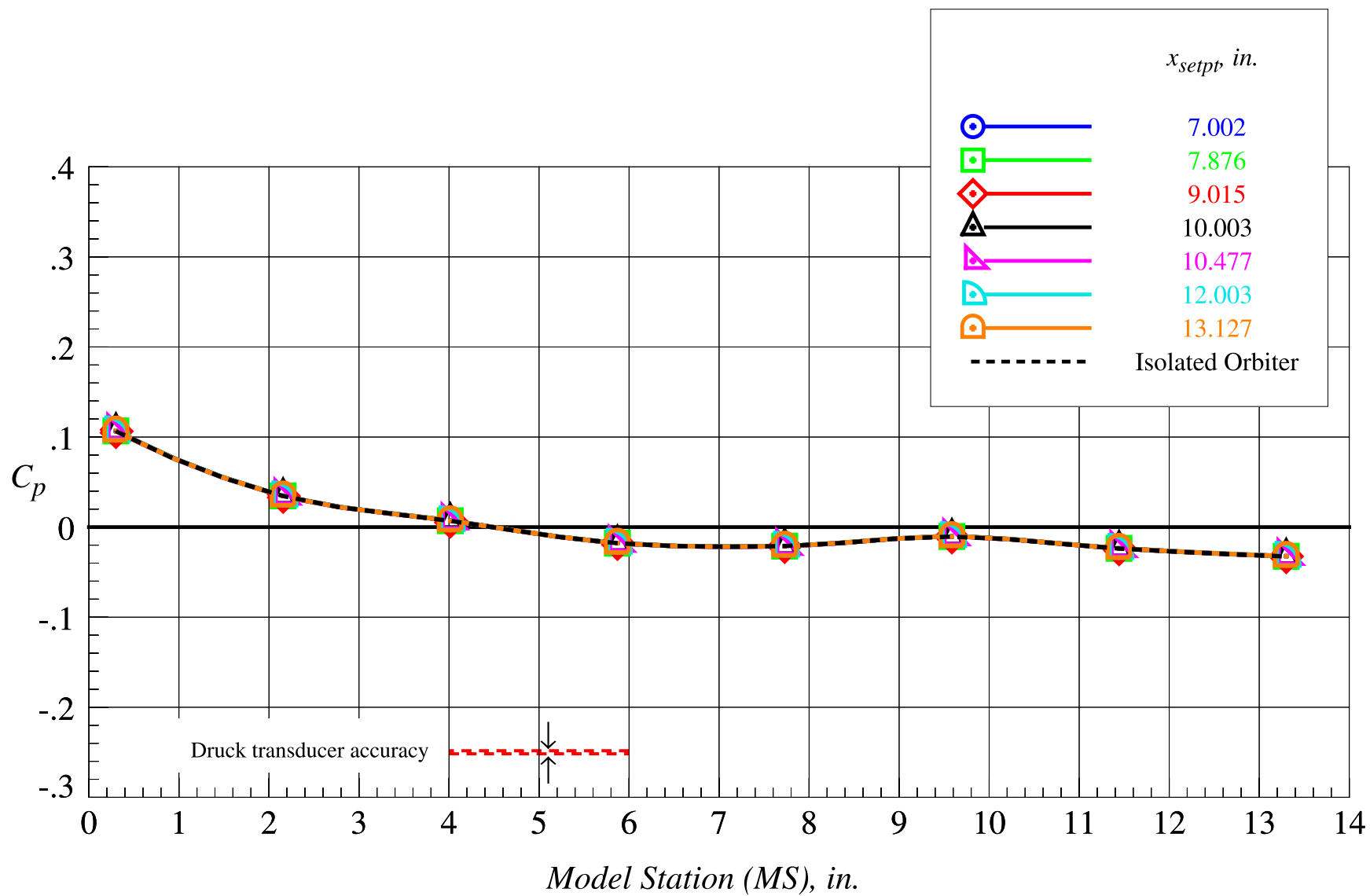
(j)  $z_{setpt} = 2.625$  in., part 2

Figure 69. Continued.



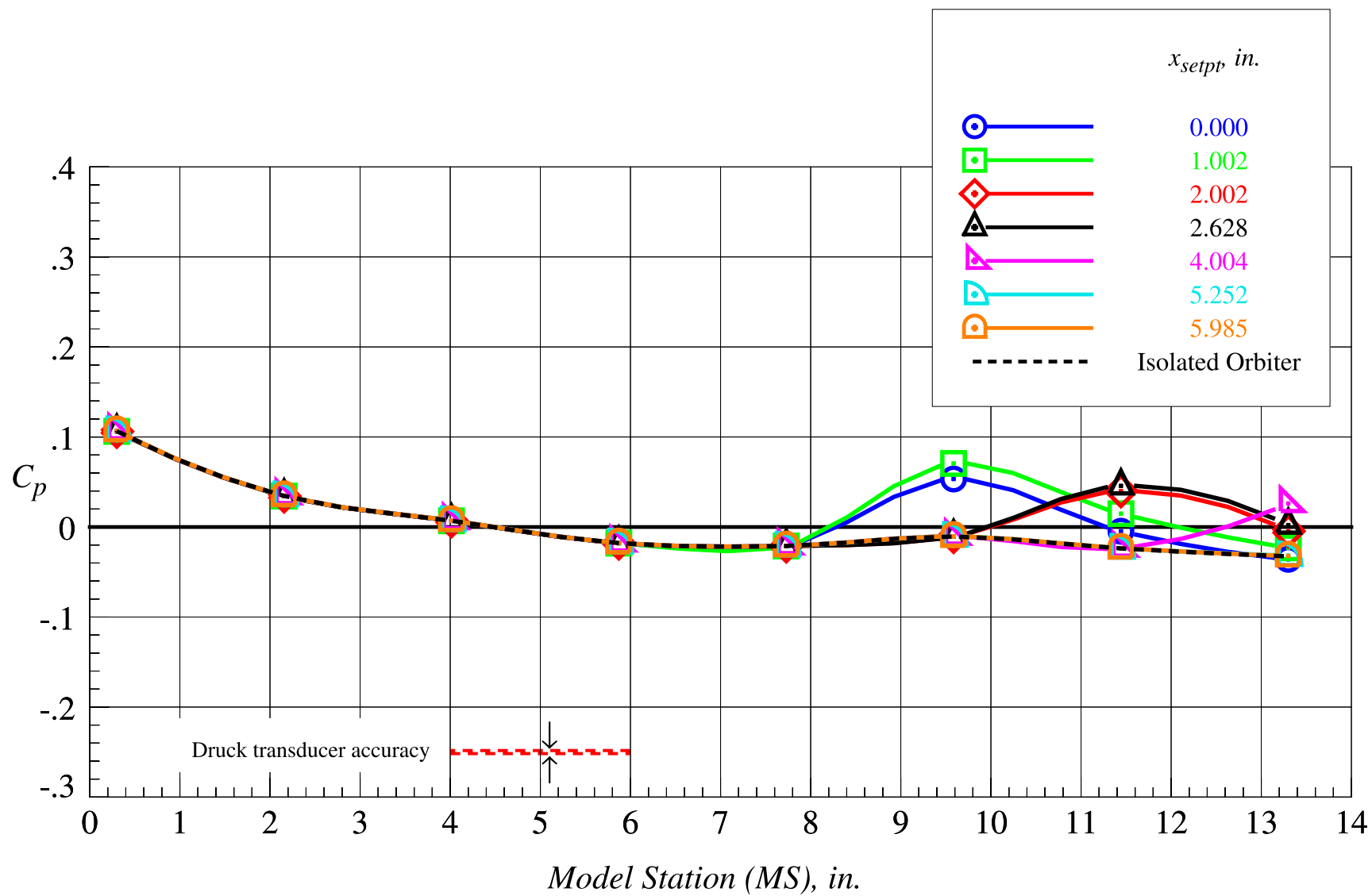
(k)  $z_{setpt} = 3.281$  in., part 1

Figure 69. Continued.



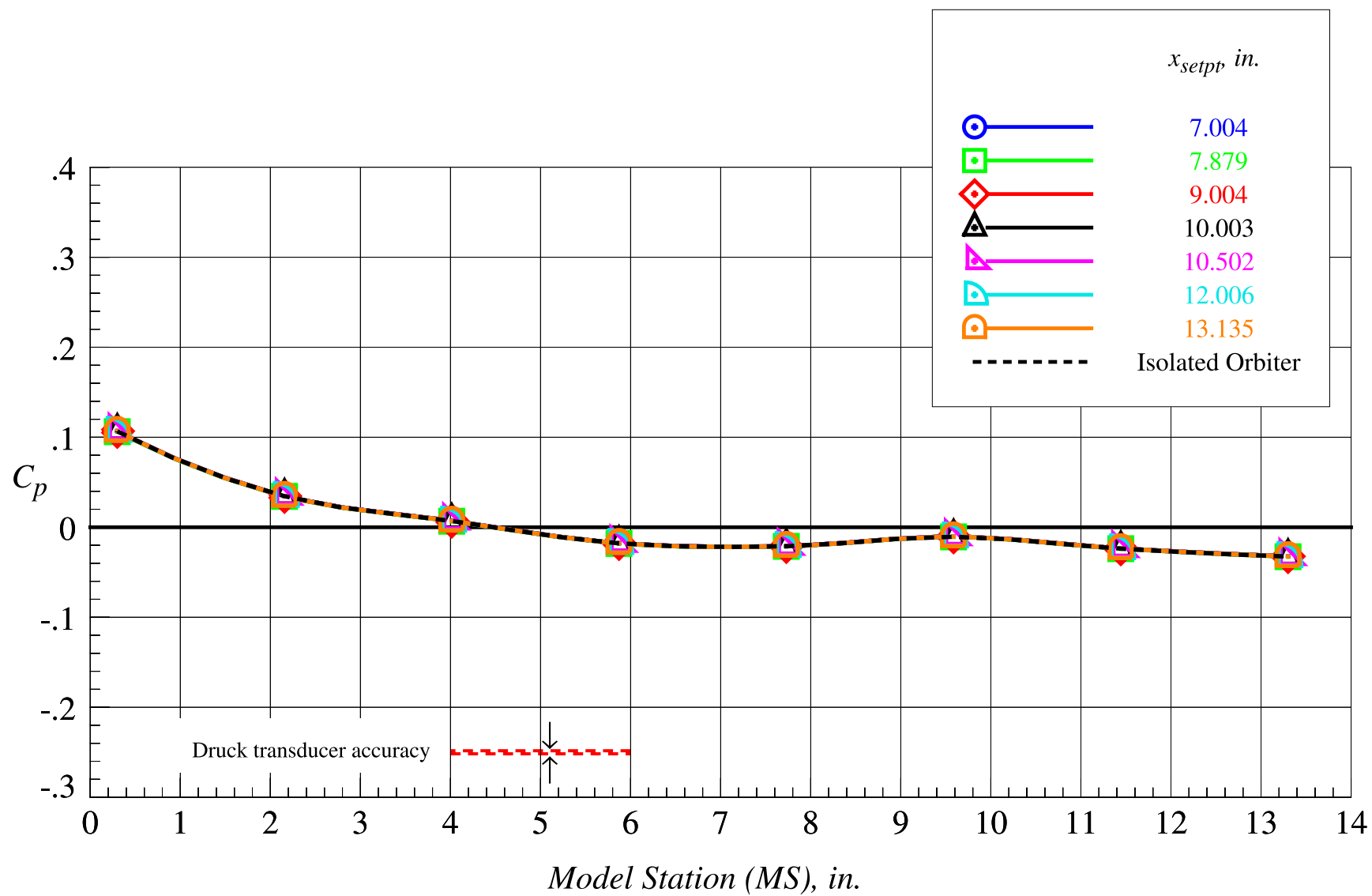
(l)  $z_{setpt} = 3.281$  in., part 2

Figure 69. Continued.



(m)  $z_{sept} = 3.938$  in., part 1

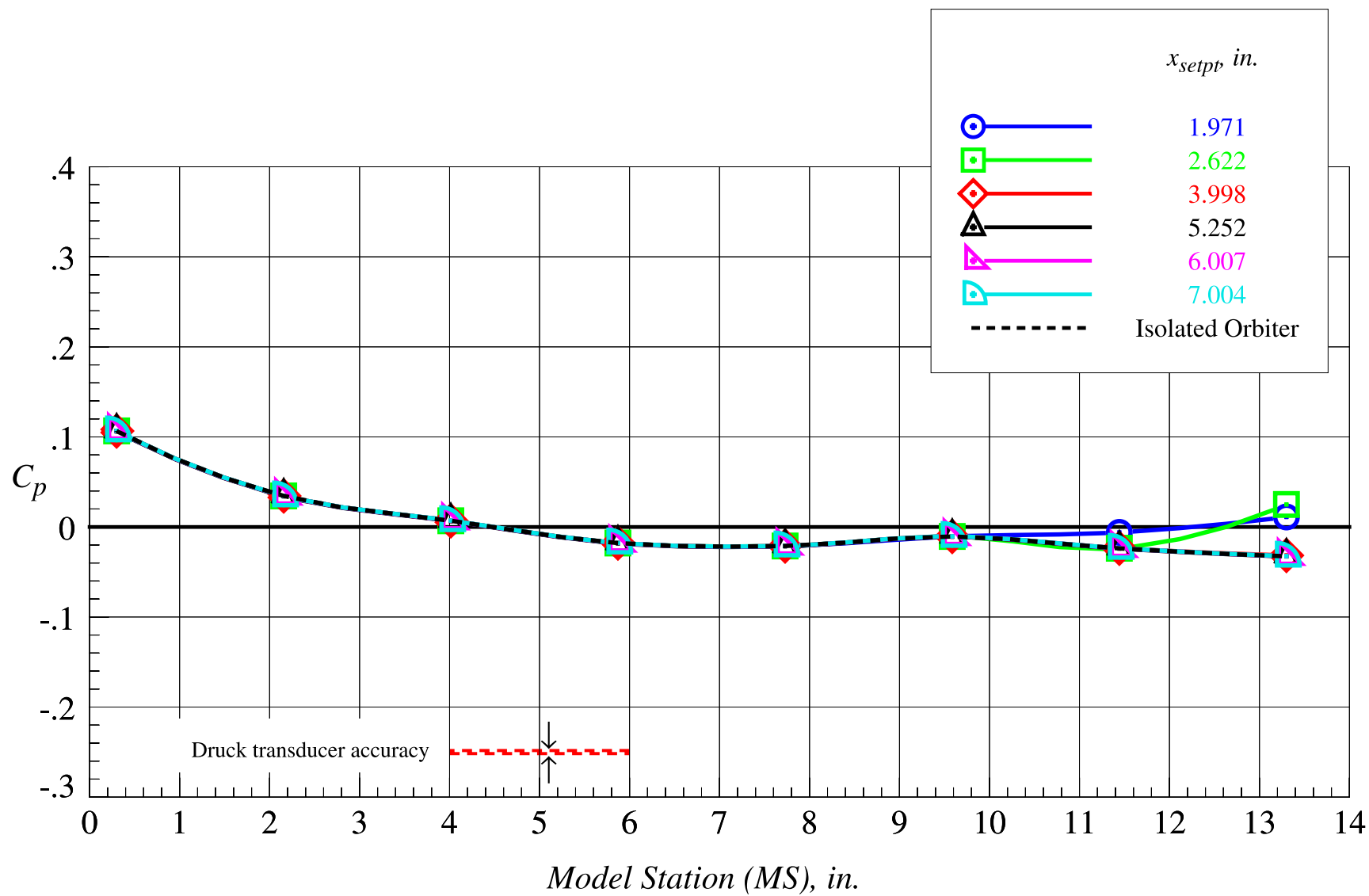
Figure 69. Continued.



(n)  $z_{setpt} = 3.938$  in., part 2

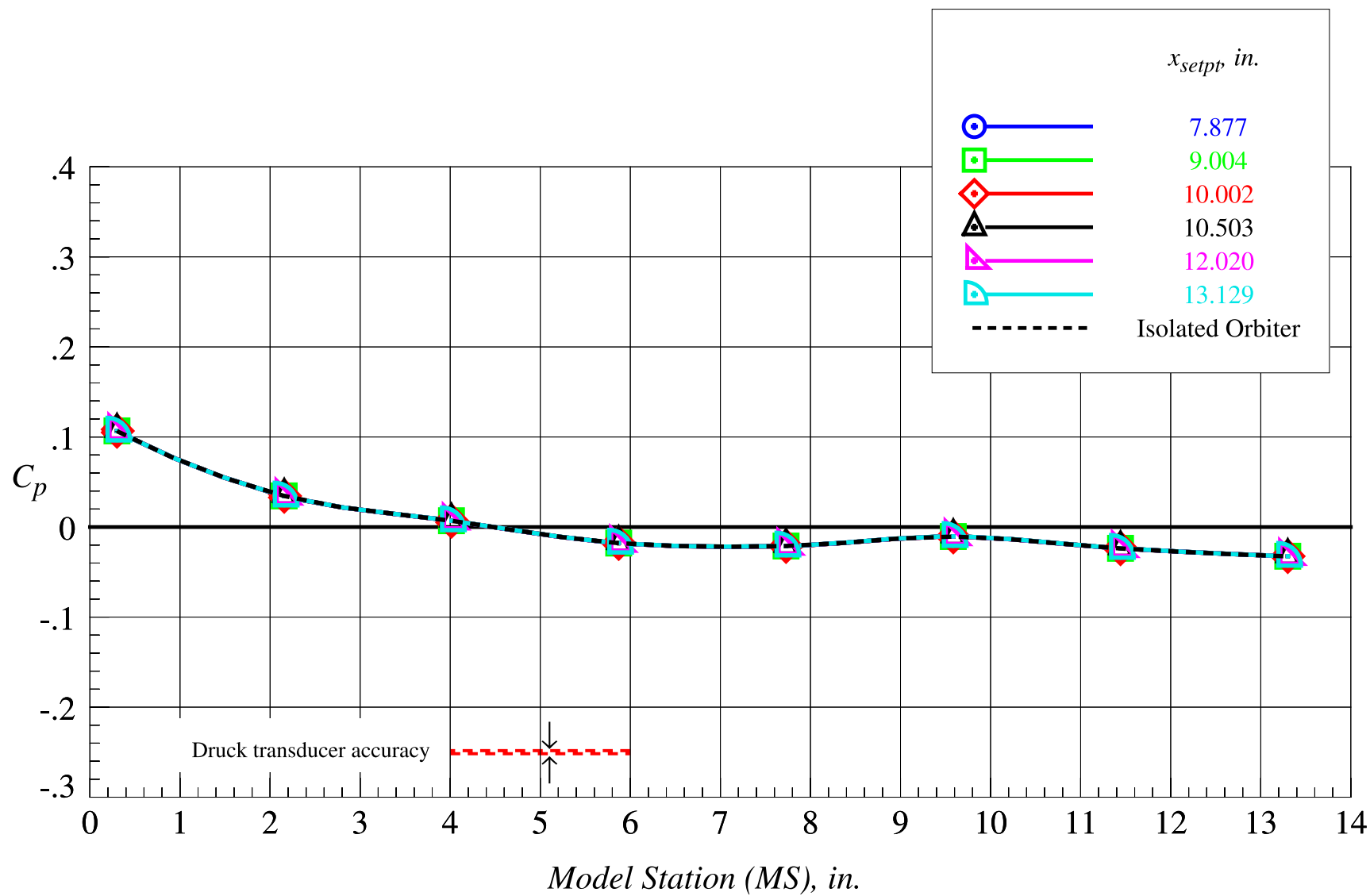
Figure 69. Continued.





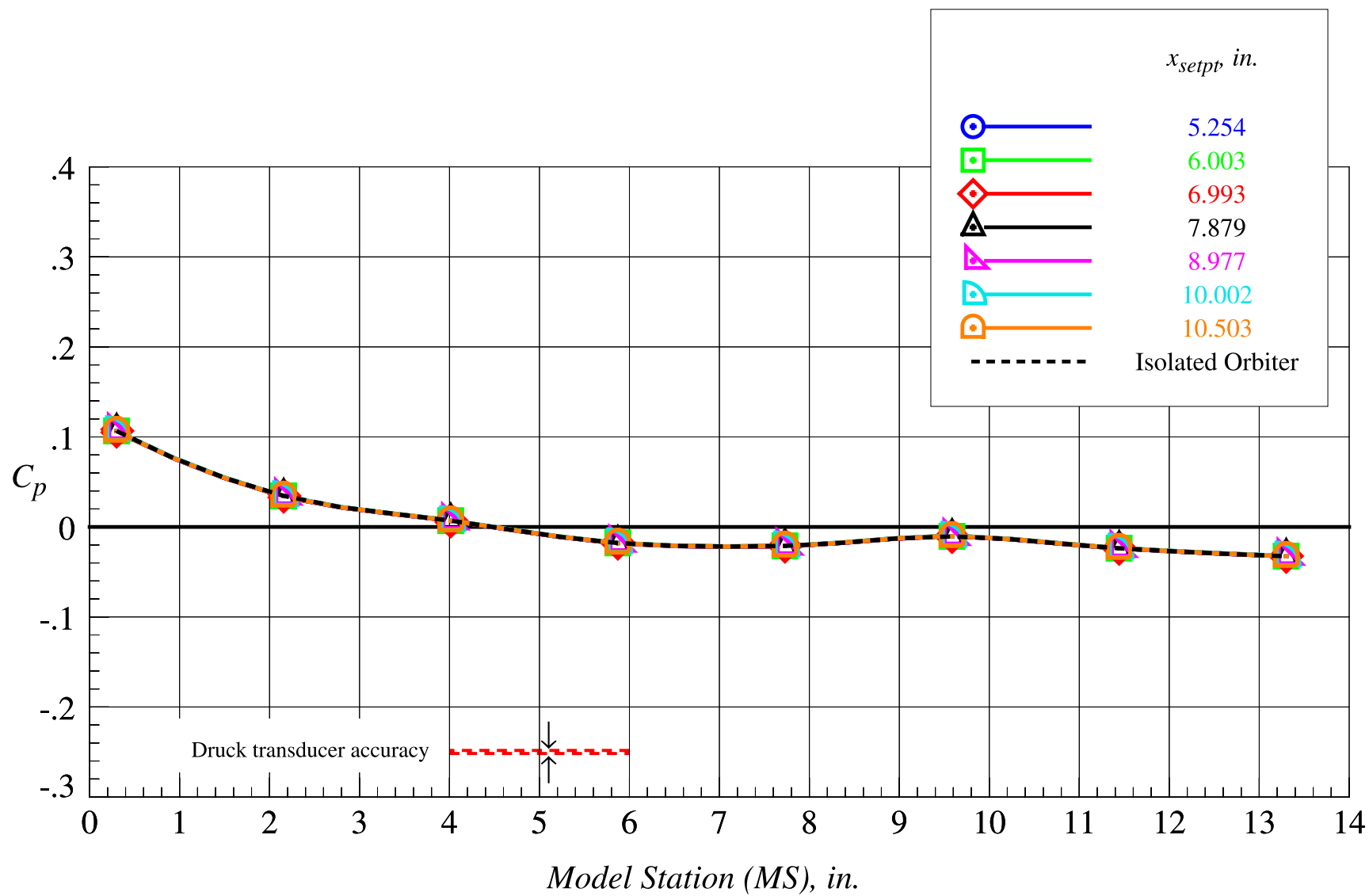
(o)  $z_{setpt} = 4.594$  in., part 1

Figure 69. Continued.



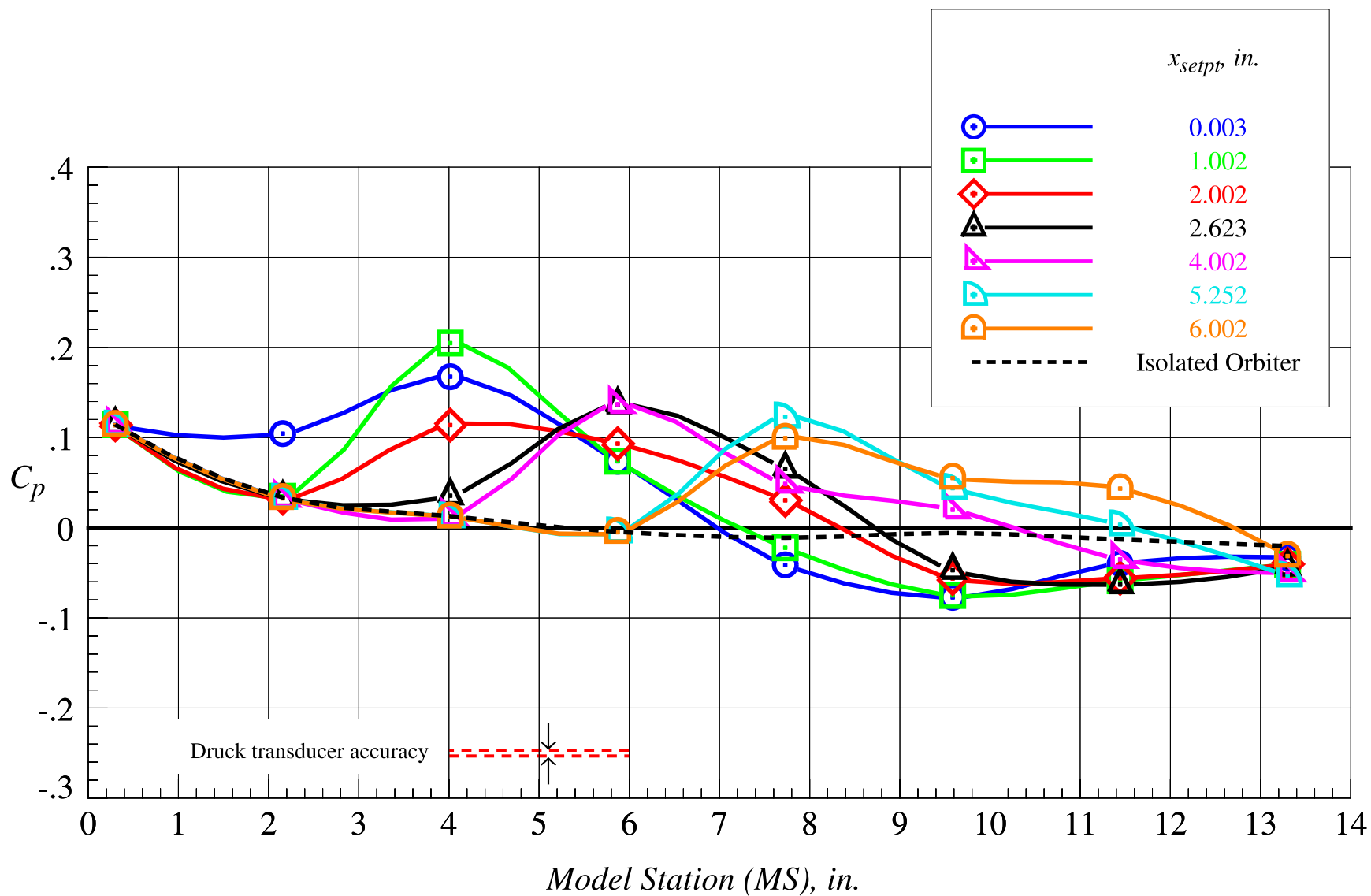
(p)  $z_{setpt} = 4.594$  in., part 2

Figure 69. Continued.



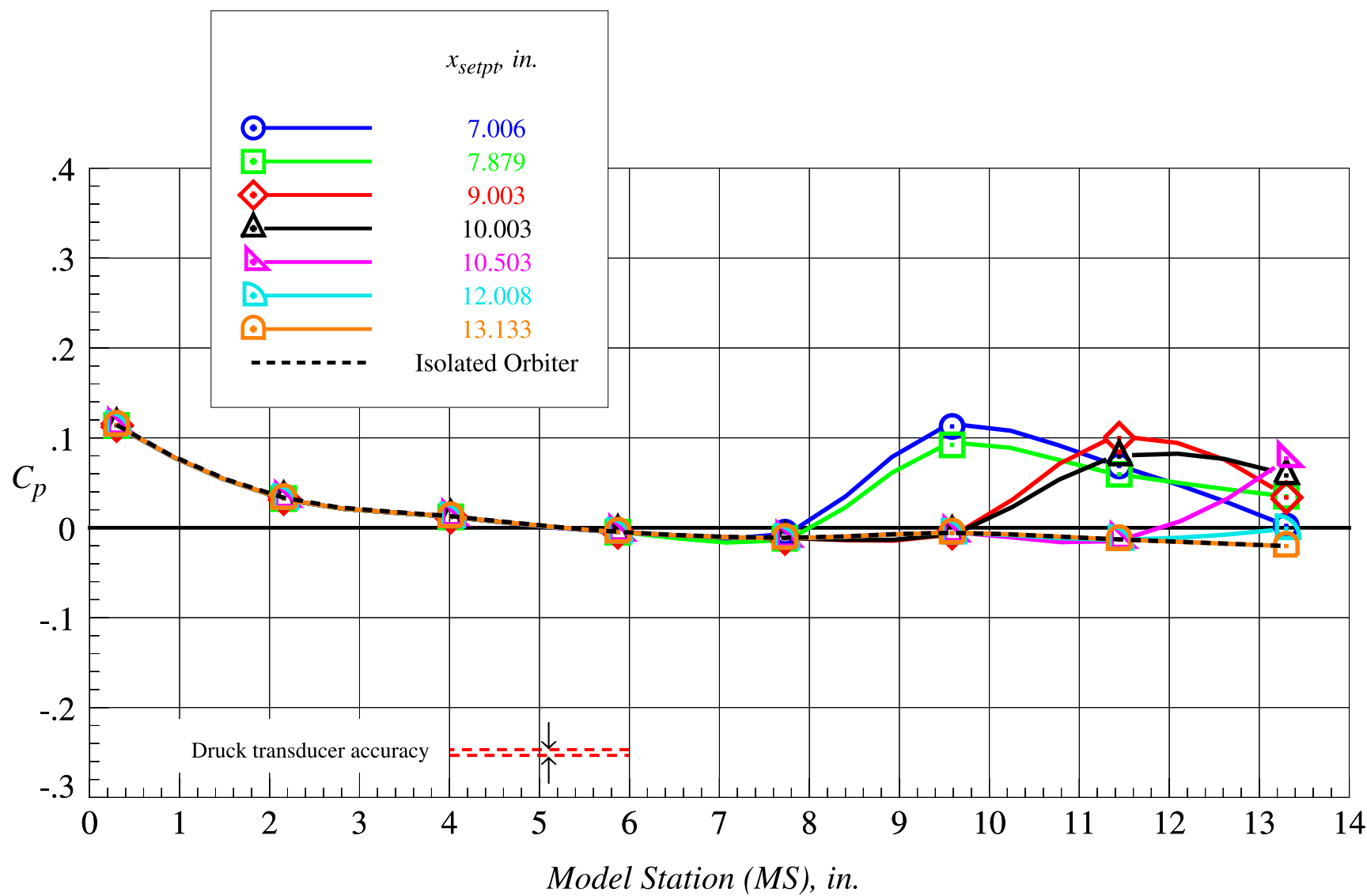
(q)  $z_{setpt} = 5.250$  in.

Figure 69. Concluded.



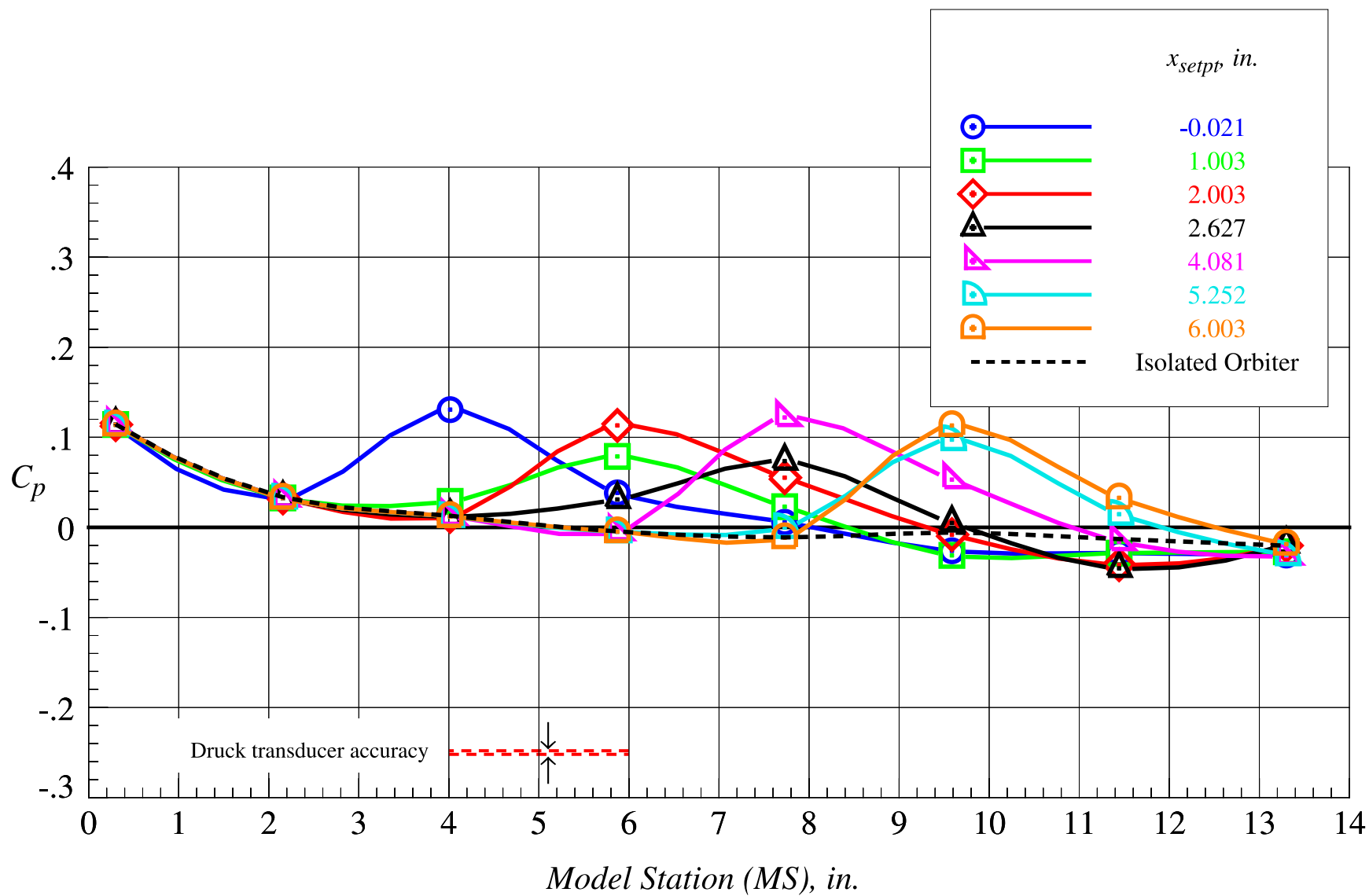
(a)  $z_{setpt} = 0$  in., part 1

Figure 70. Orbiter proximity surface static pressure distributions on fuselage centerline lower surface at Mach = 3.0 and  $\Delta\alpha = 0^\circ$ .



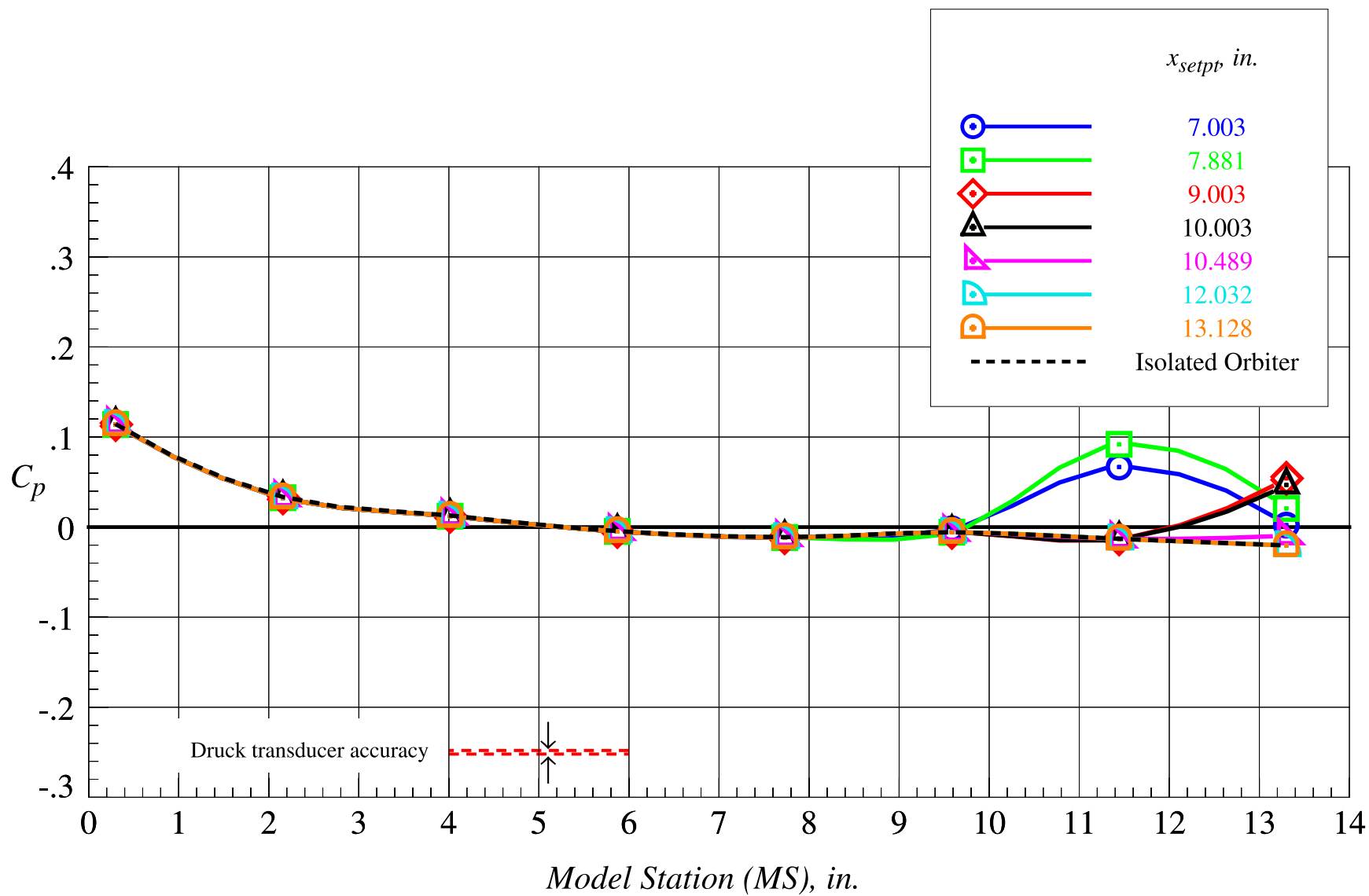
(b)  $z_{setpt} = 0$  in., part 2

Figure 70. Continued.



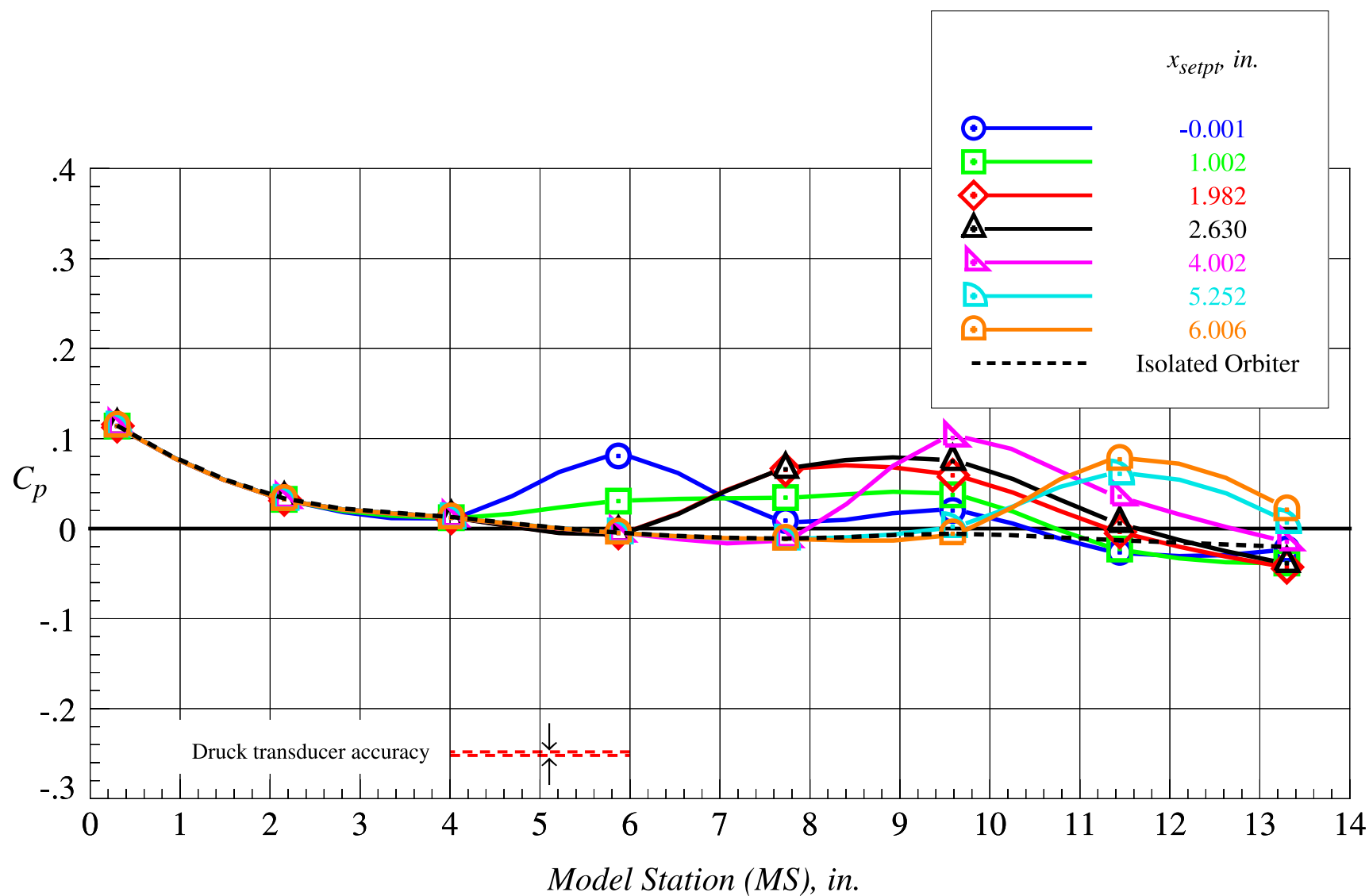
(c)  $z_{setpt} = 0.656$  in., part 1

Figure 70. Continued.



(d)  $z_{setpt} = 0.656$  in., part 2

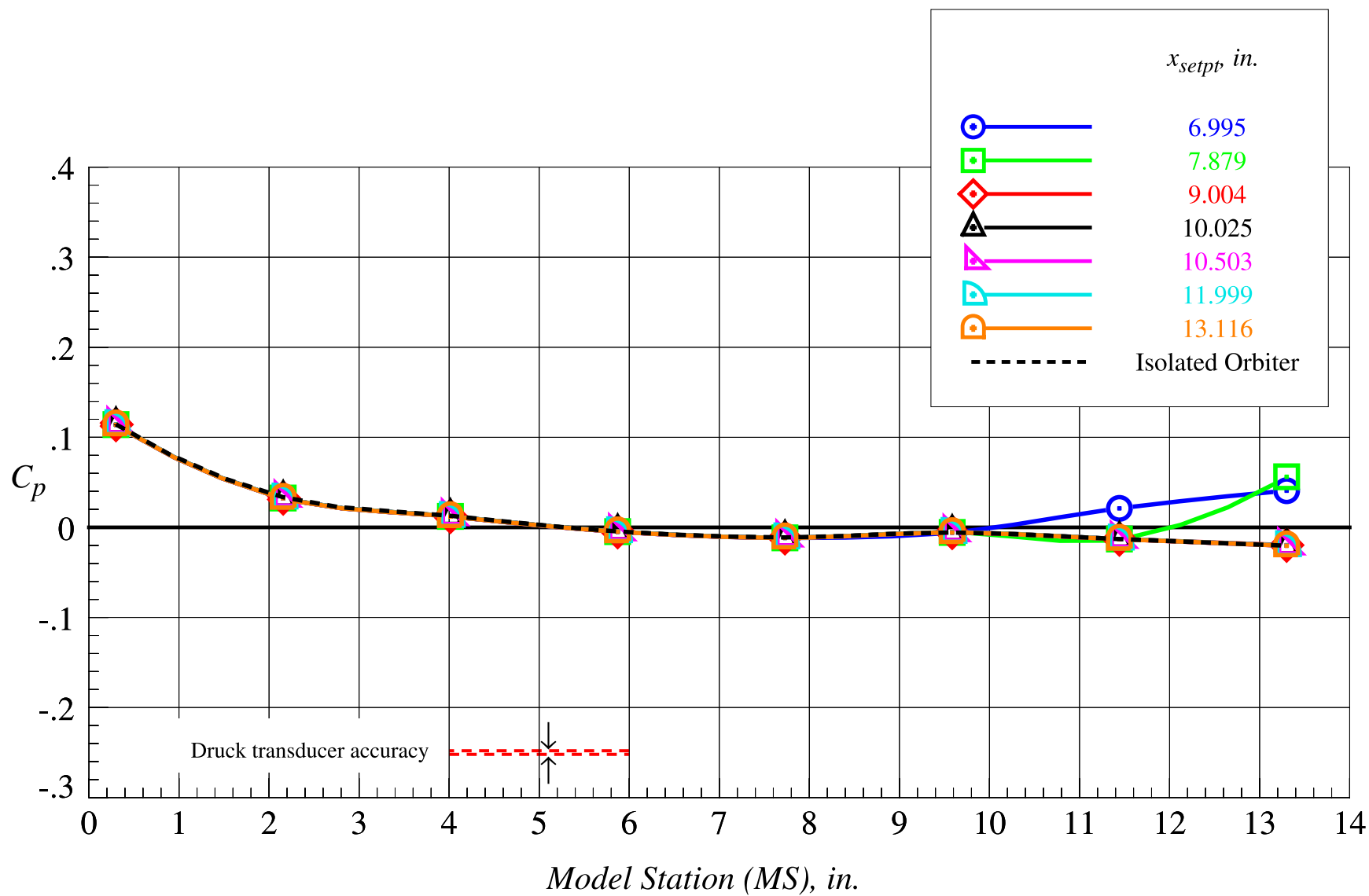
Figure 70. Continued.



(e)  $z_{setpt} = 1.313$  in., part 1

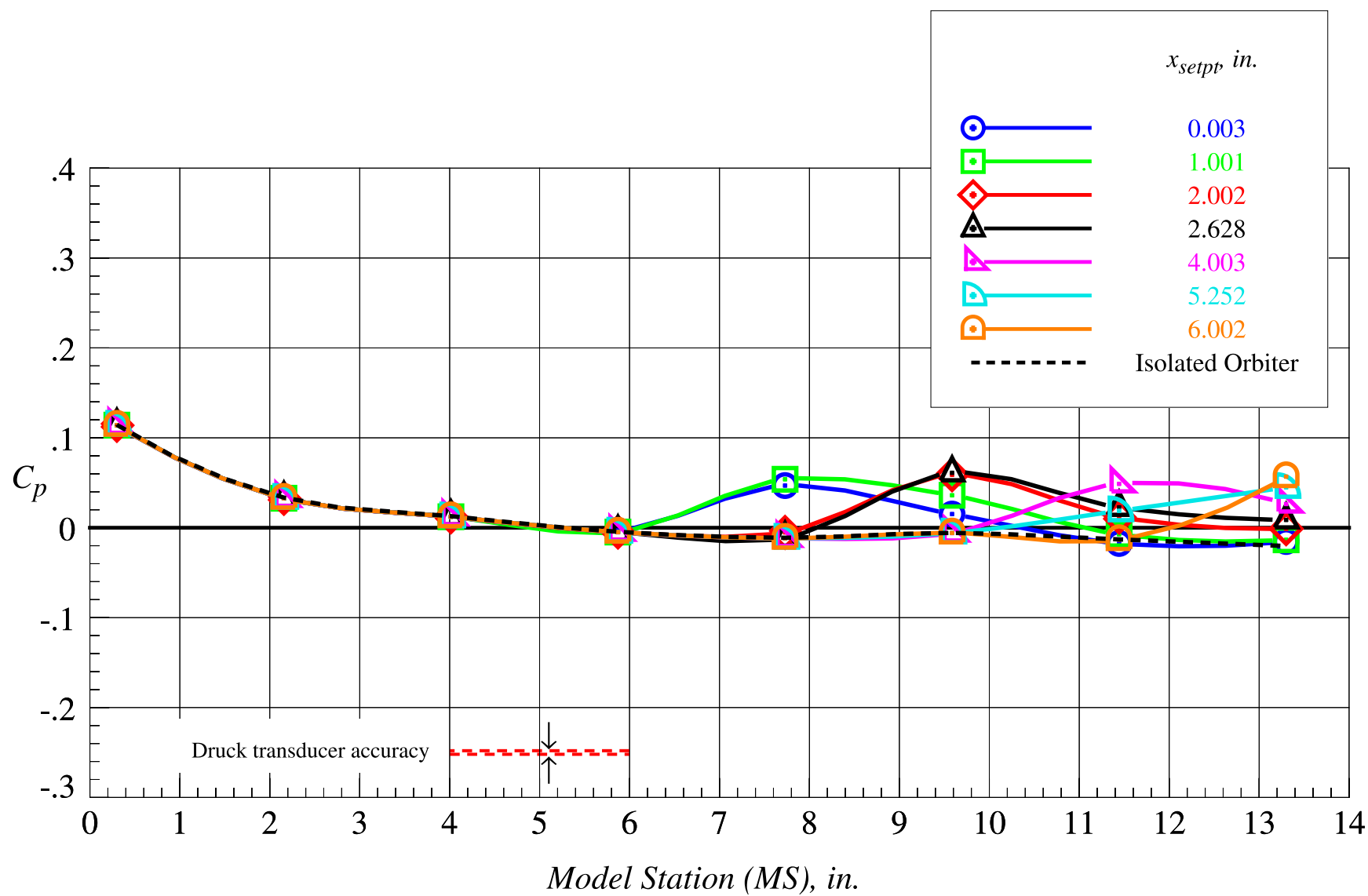
Figure 70. Continued.





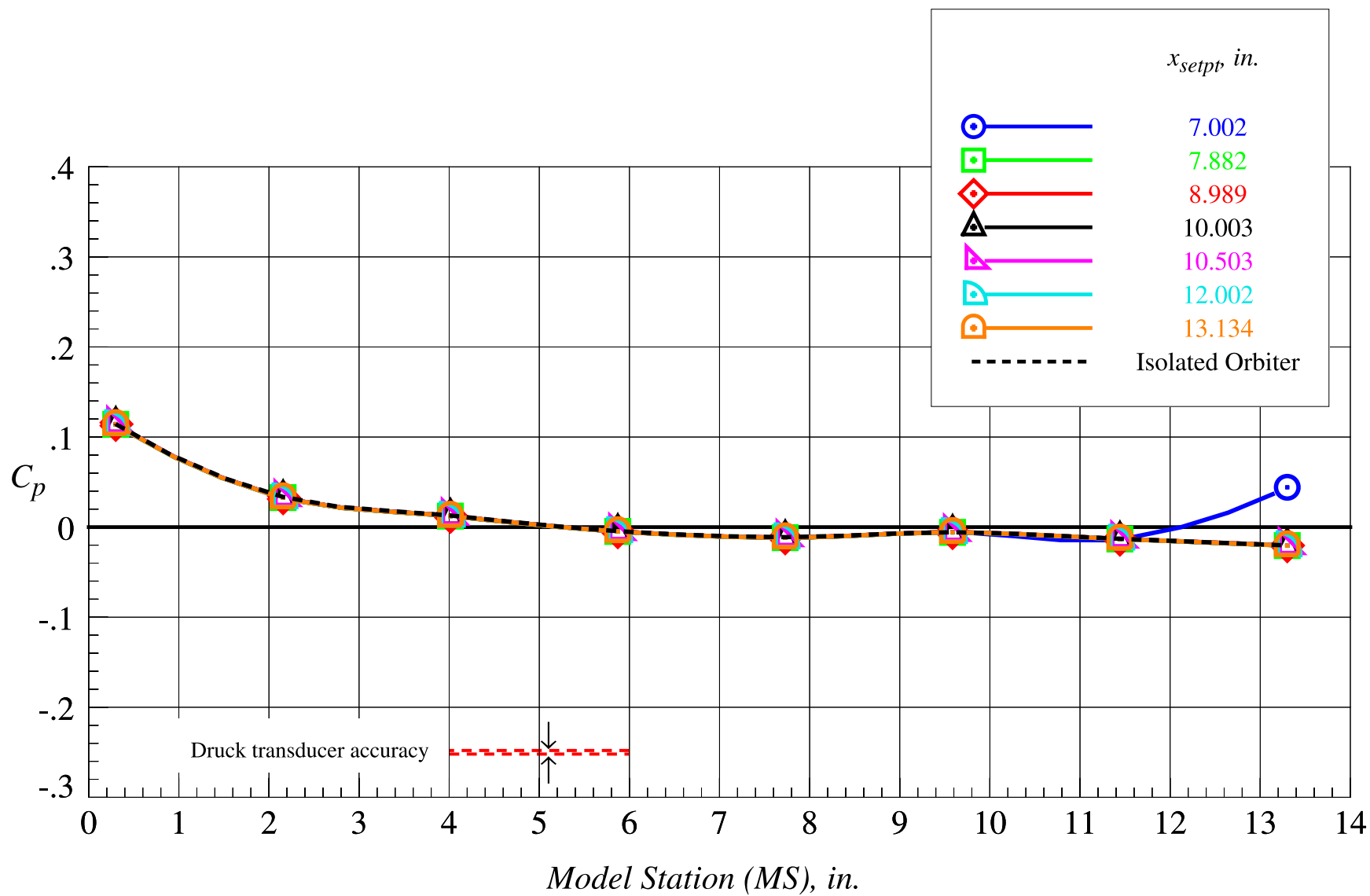
(f)  $z_{setpt} = 1.313$  in., part 2

Figure 70. Continued.



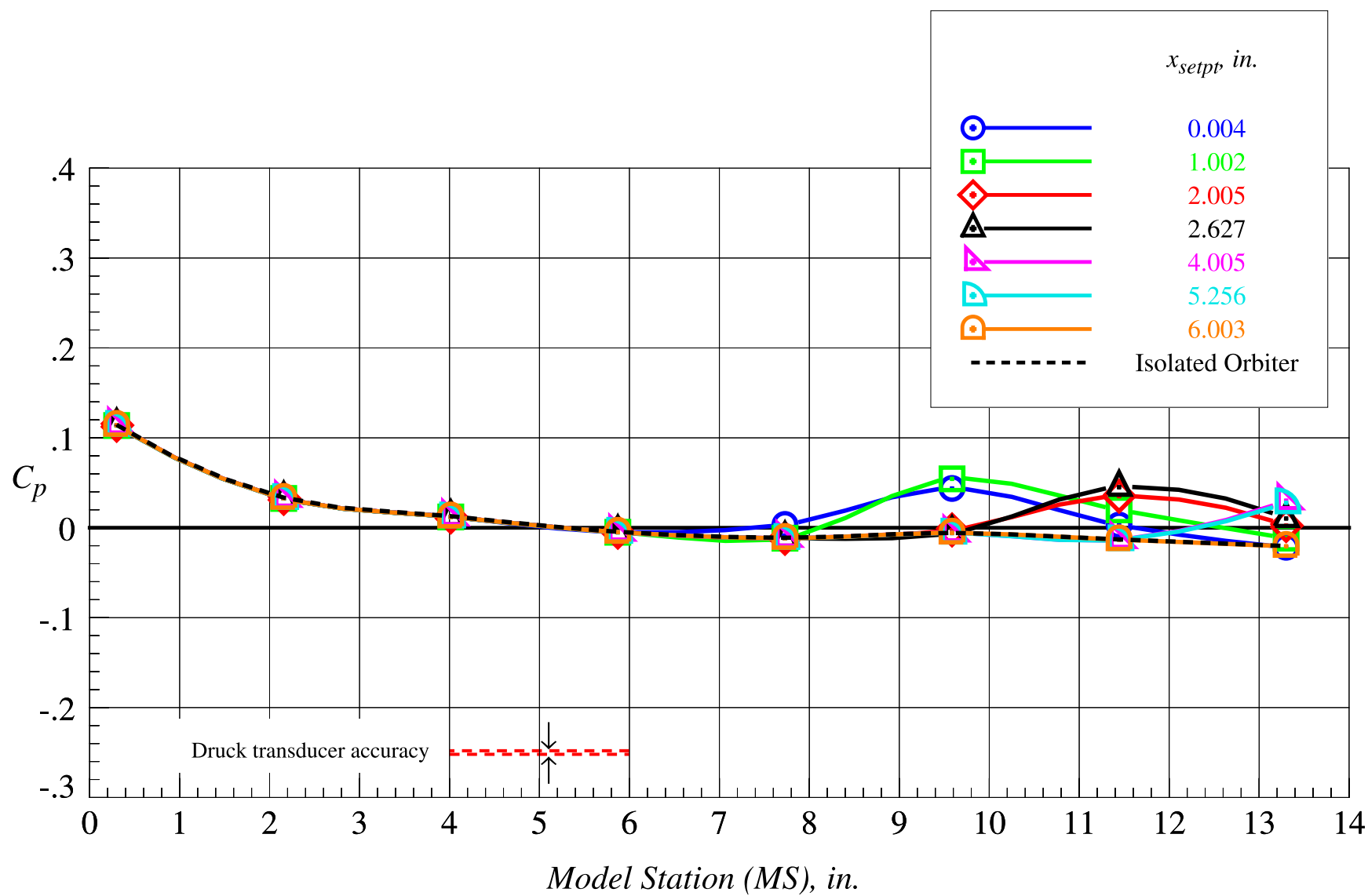
(g)  $z_{setpt} = 1.969$  in., part 1

Figure 70. Continued.



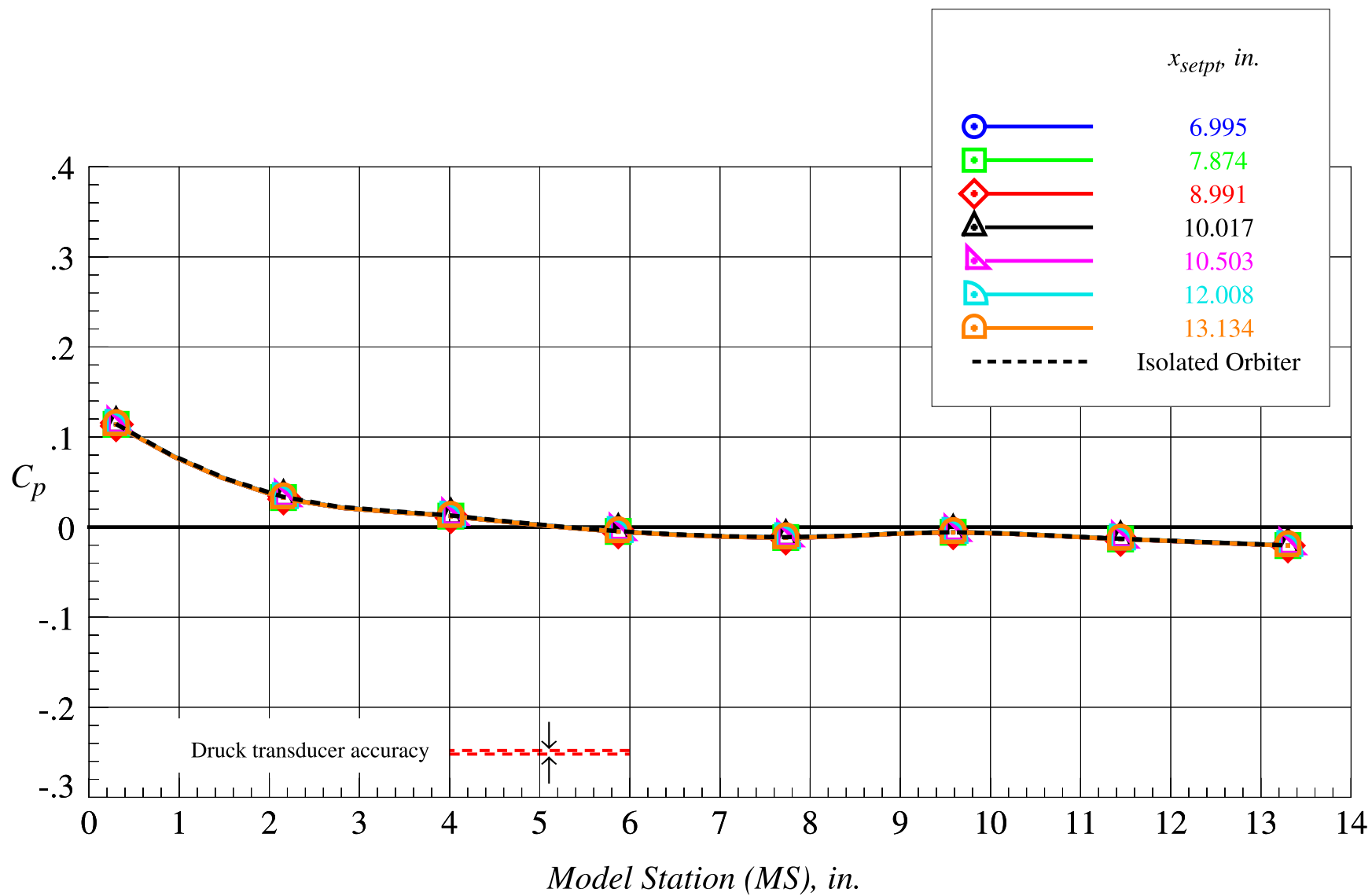
(h)  $z_{setpt} = 1.969$  in., part 2

Figure 70. Continued.



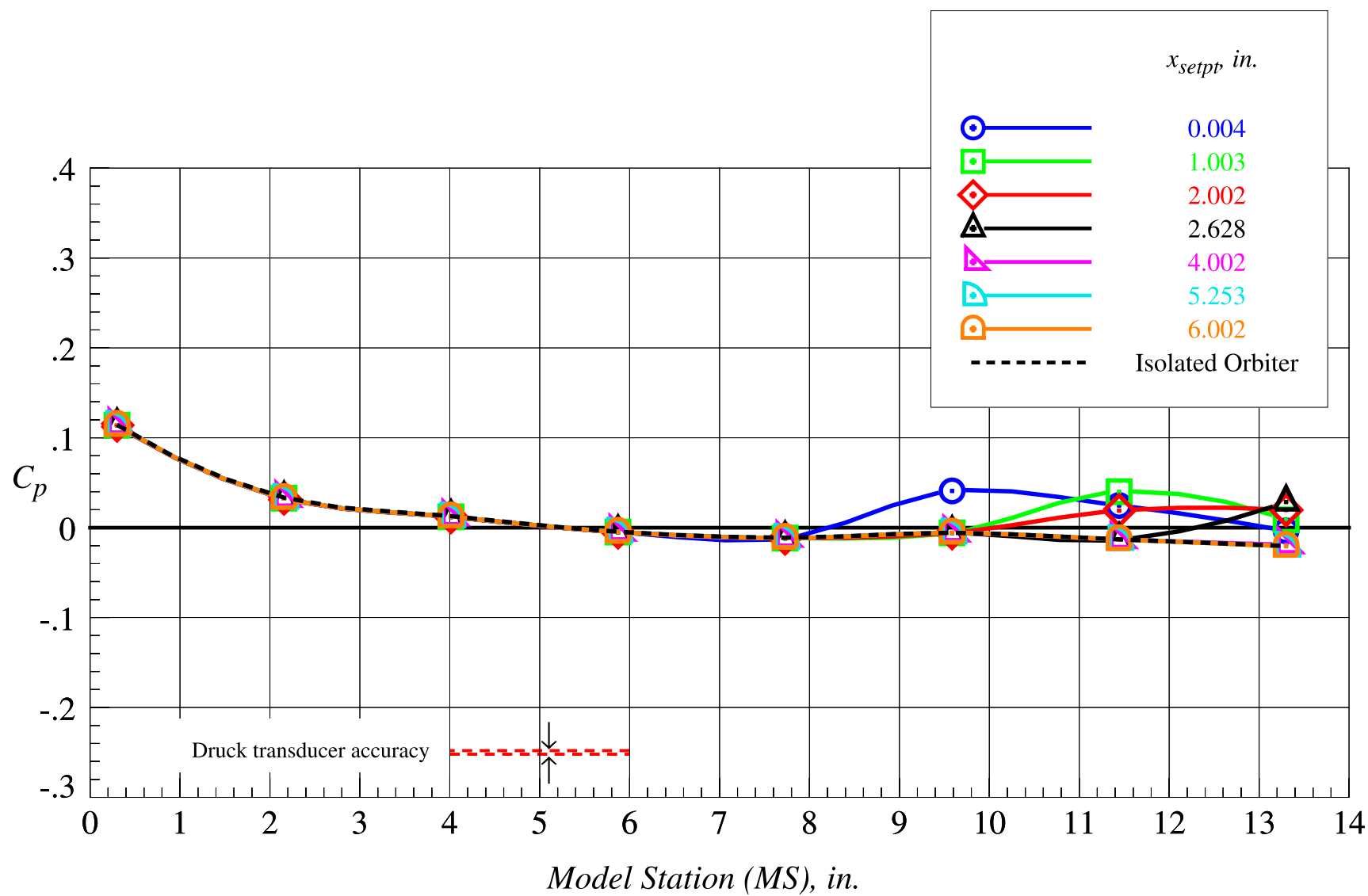
(i)  $z_{setpt} = 2.625$  in., part 1

Figure 70. Continued.



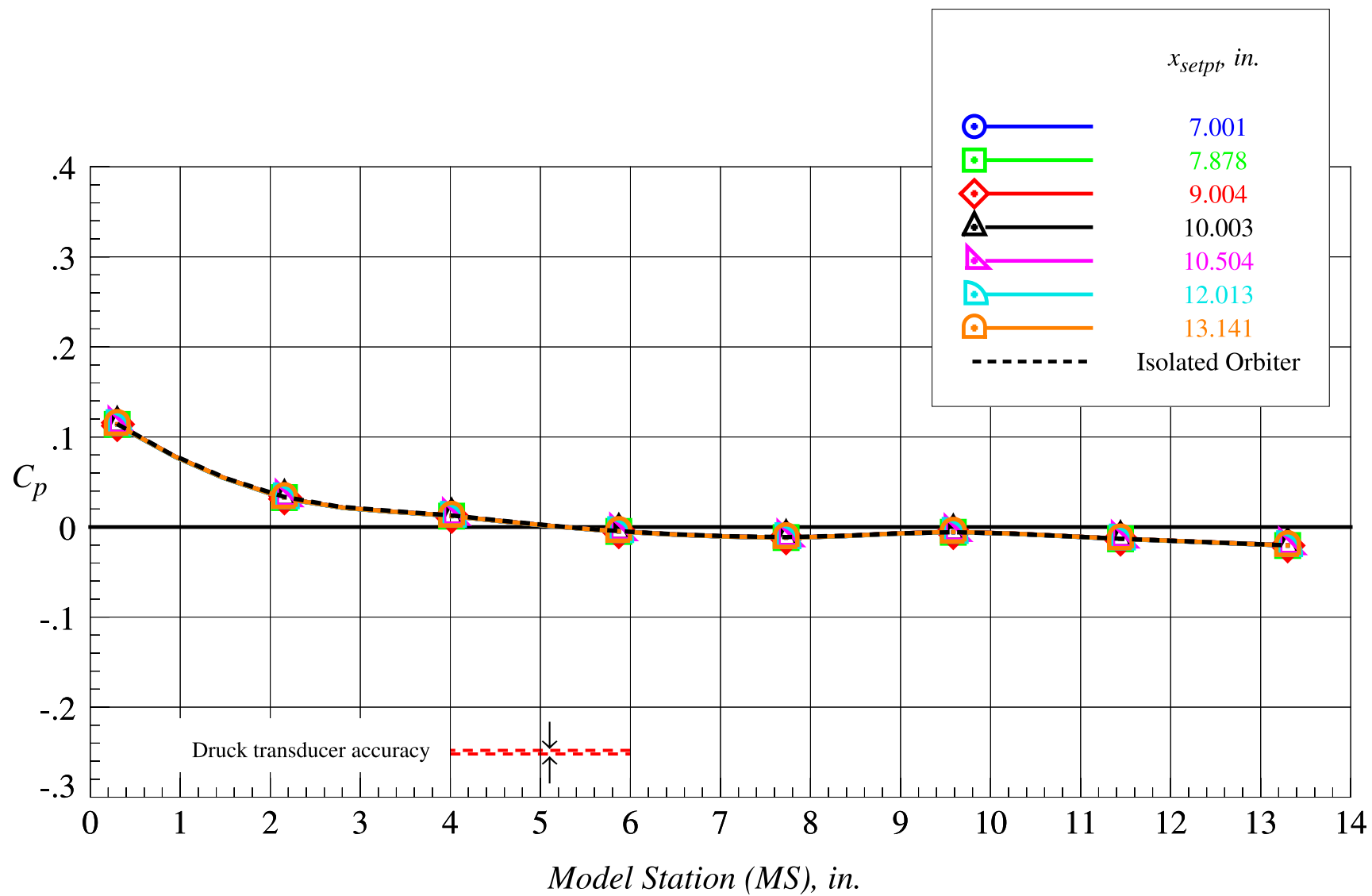
(j)  $z_{setpt} = 2.625$  in., part 2

Figure 70. Continued.



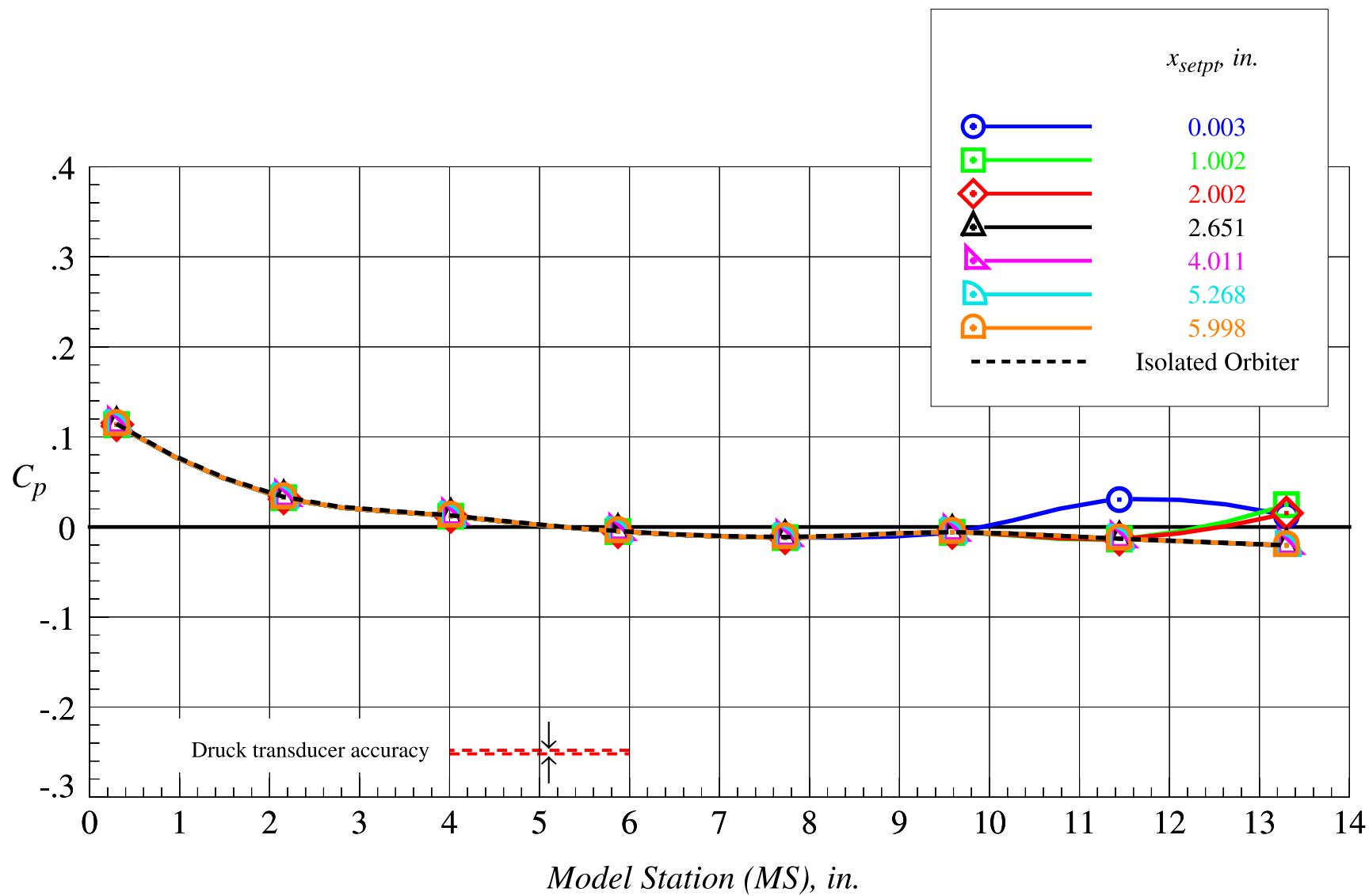
(k)  $z_{setpt} = 3.281$  in., part 1

Figure 70. Continued.



(l)  $z_{setpt} = 3.281$  in., part 2

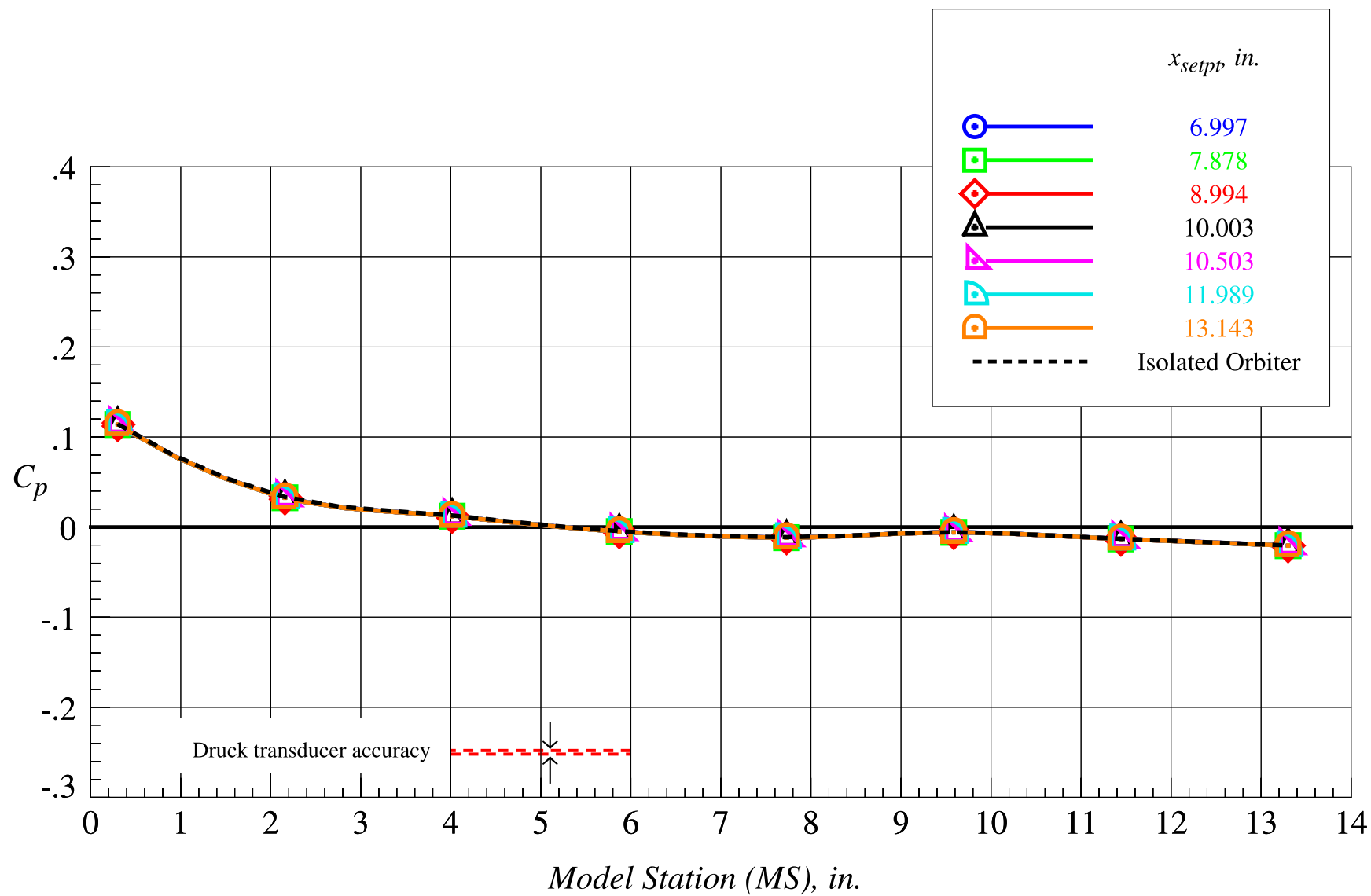
Figure 70. Continued.



(m)  $z_{setpt} = 3.938$  in., part 1

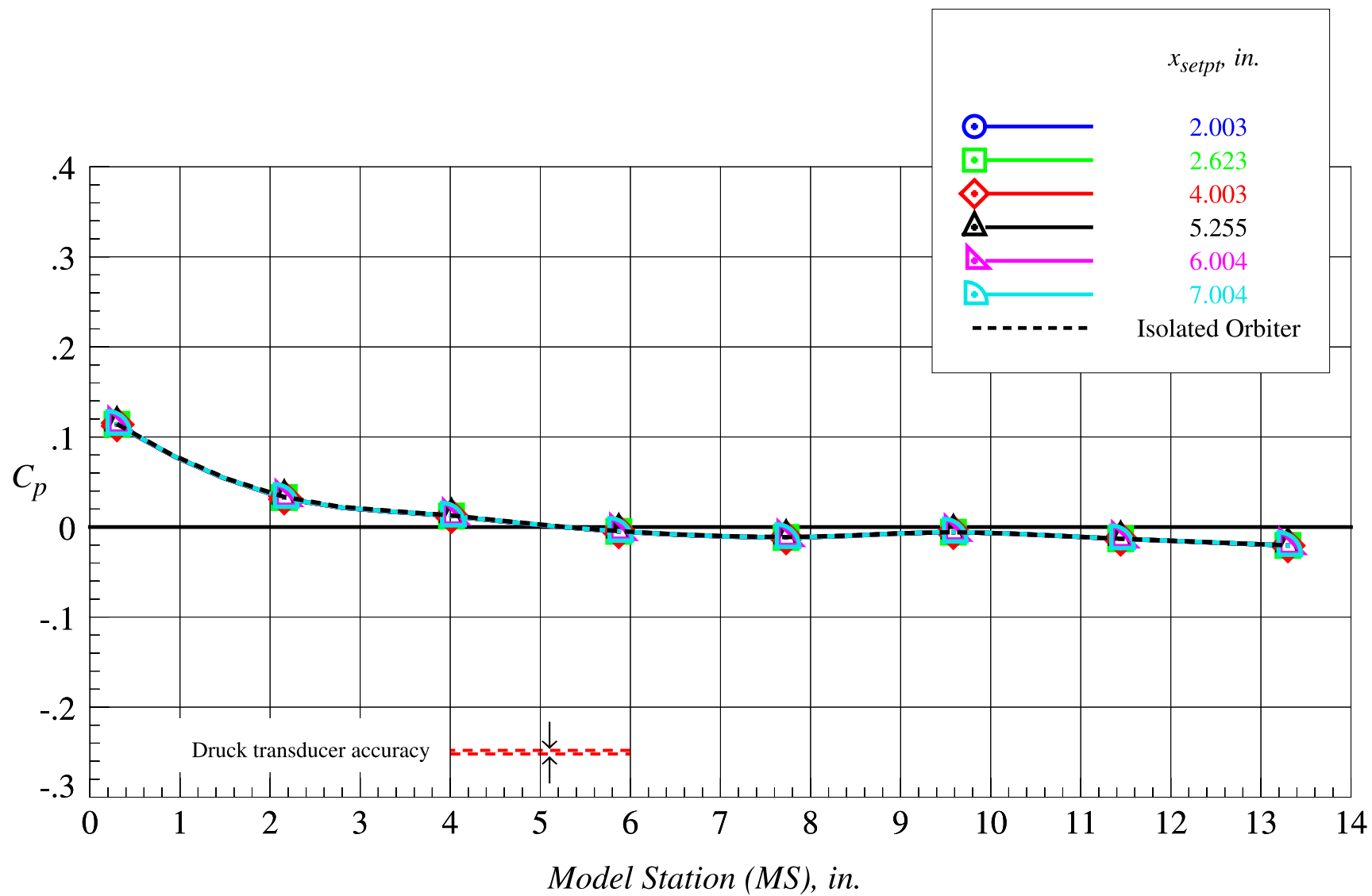
Figure 70. Continued.





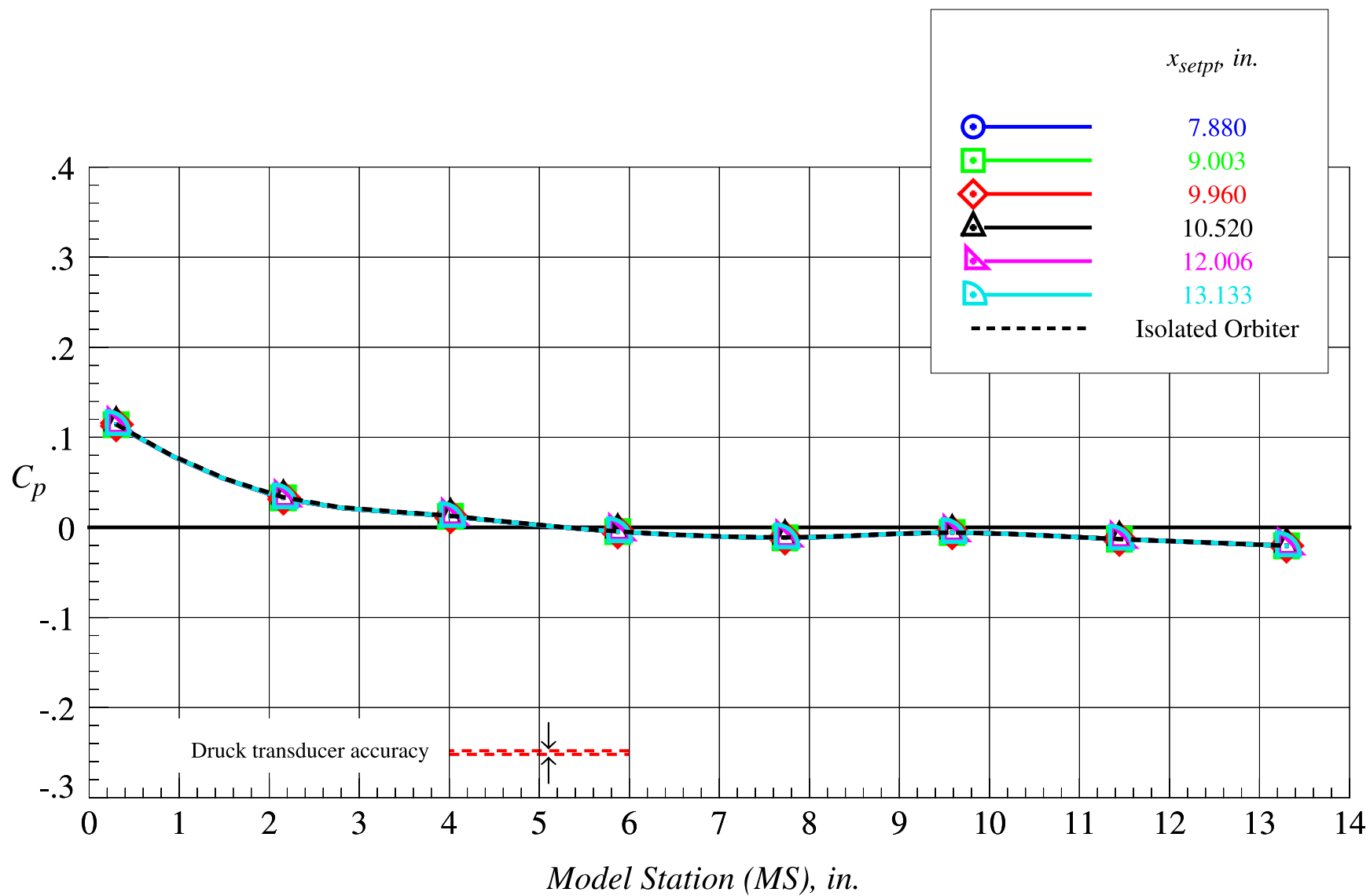
(n)  $z_{setpt} = 3.938$  in., part 2

Figure 70. Continued.



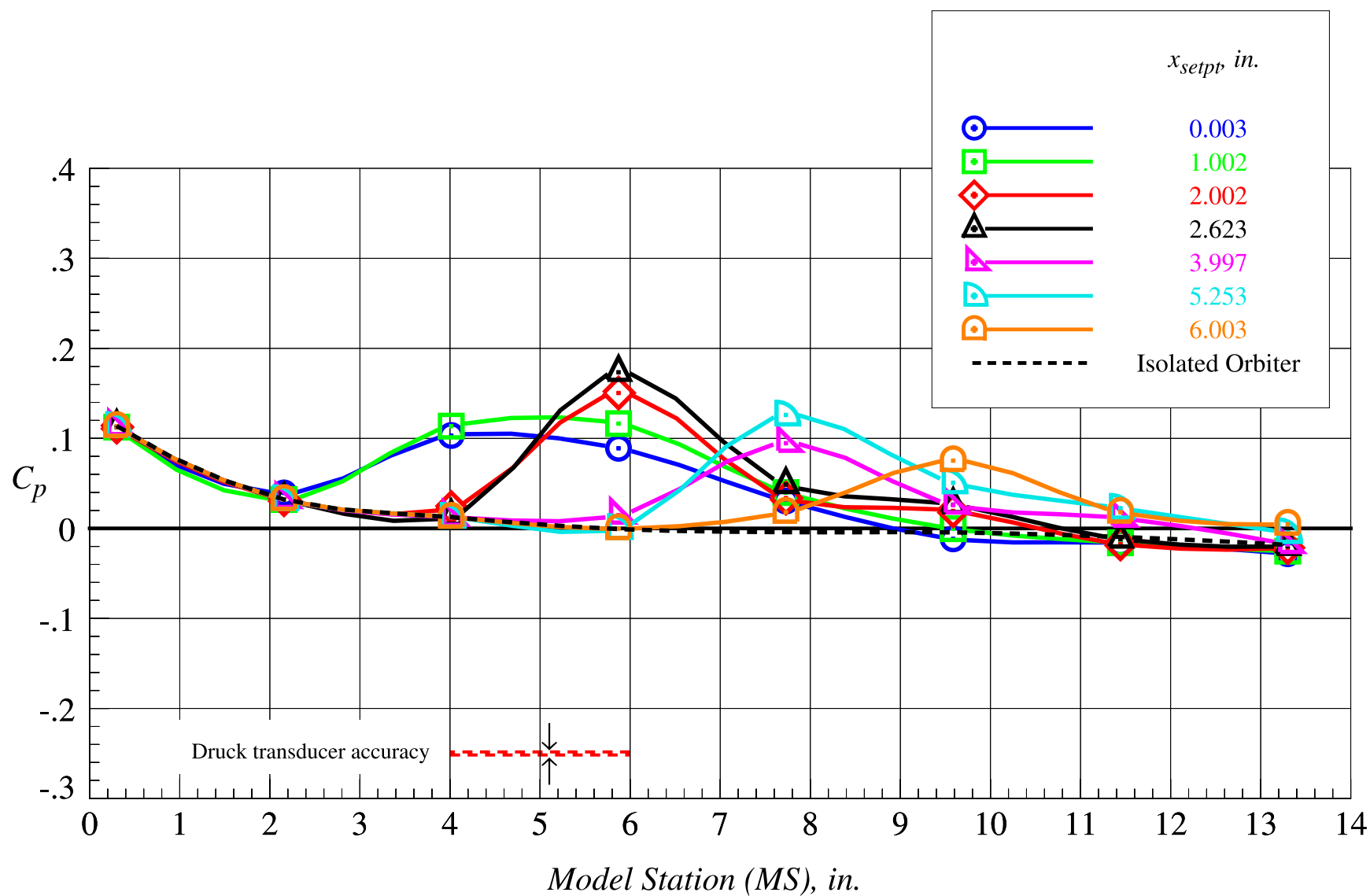
(o)  $z_{setpt} = 4.594$  in., part 1

Figure 70. Continued.



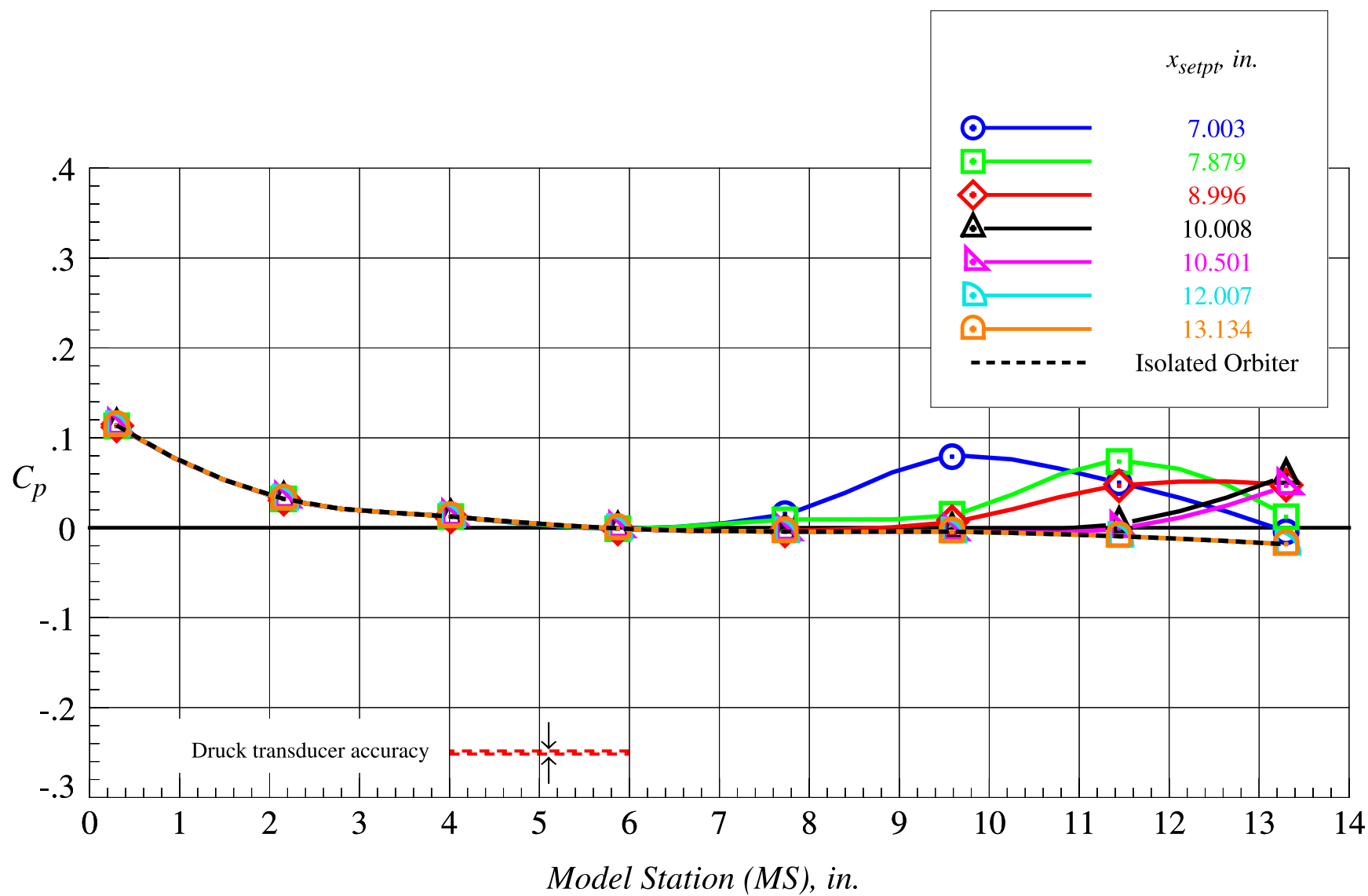
(p)  $z_{setpt} = 4.594$  in., part 2

Figure 70. Concluded.



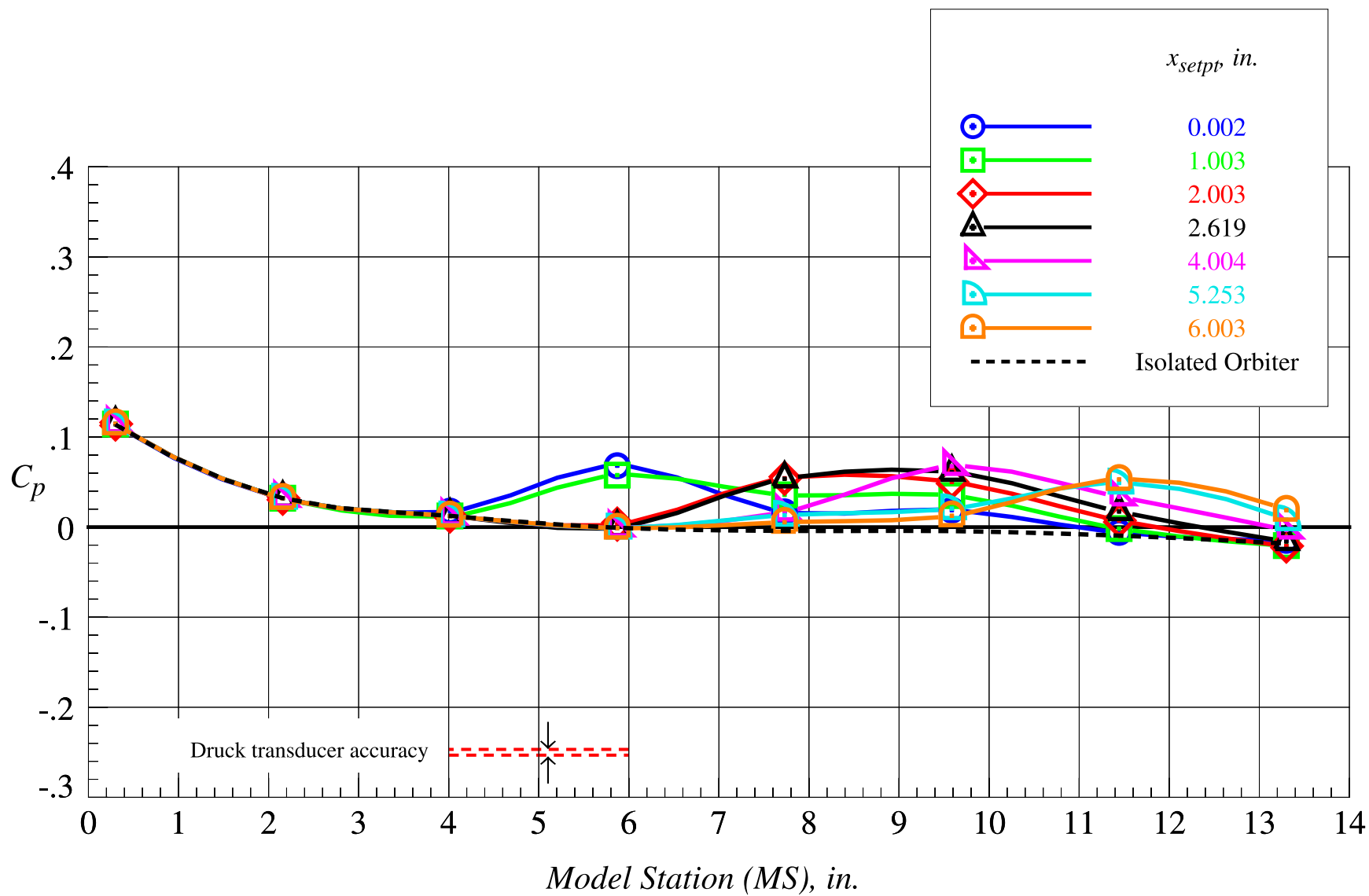
(a)  $z_{setpt} = 0$  in., part 1

Figure 71. Orbiter proximity surface static pressure distributions on fuselage centerline lower surface at Mach = 4.5 and  $\Delta\alpha = 0^\circ$ .



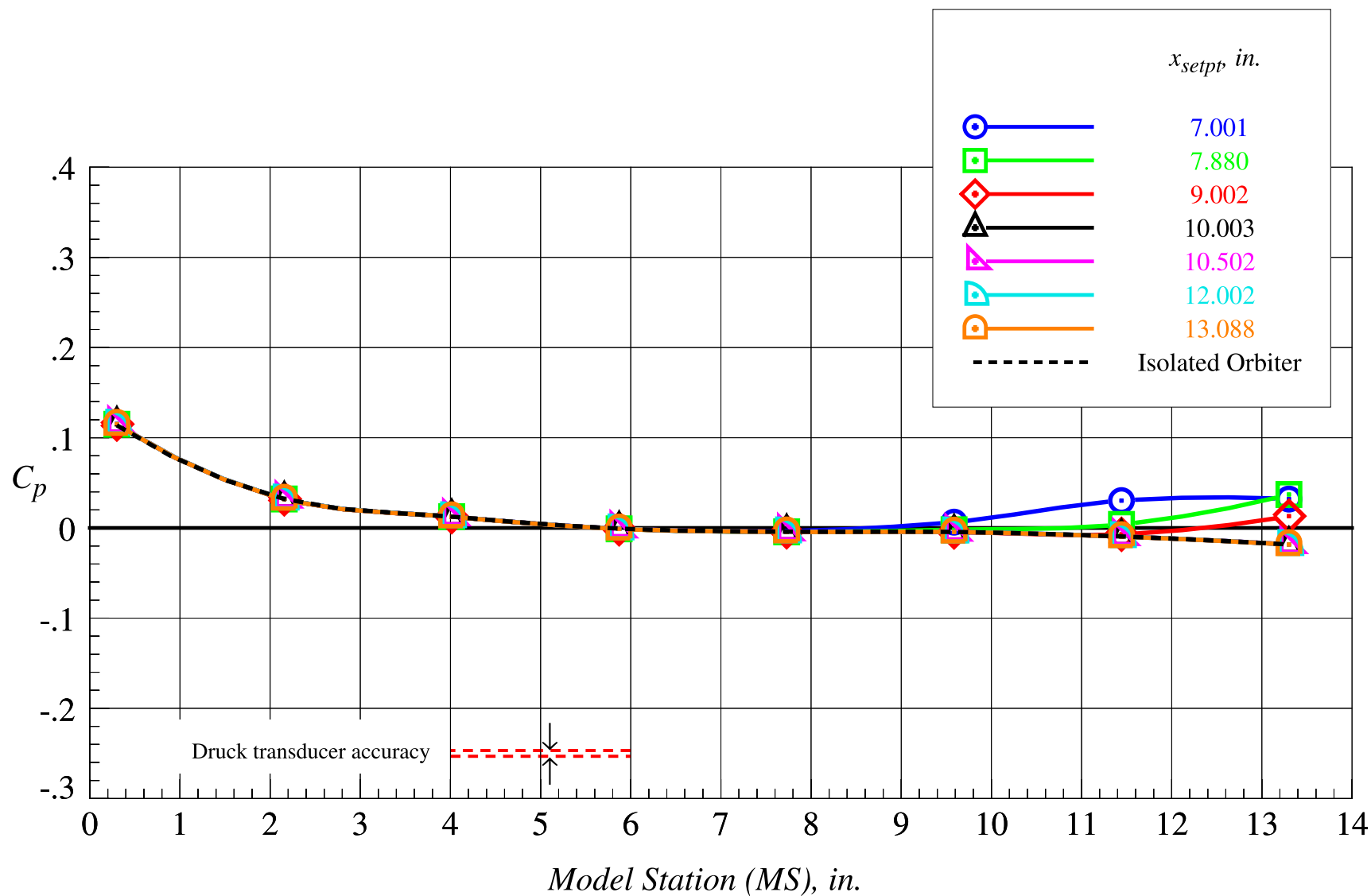
(b)  $z_{setpt} = 0$  in., part 2

Figure 71. Continued.



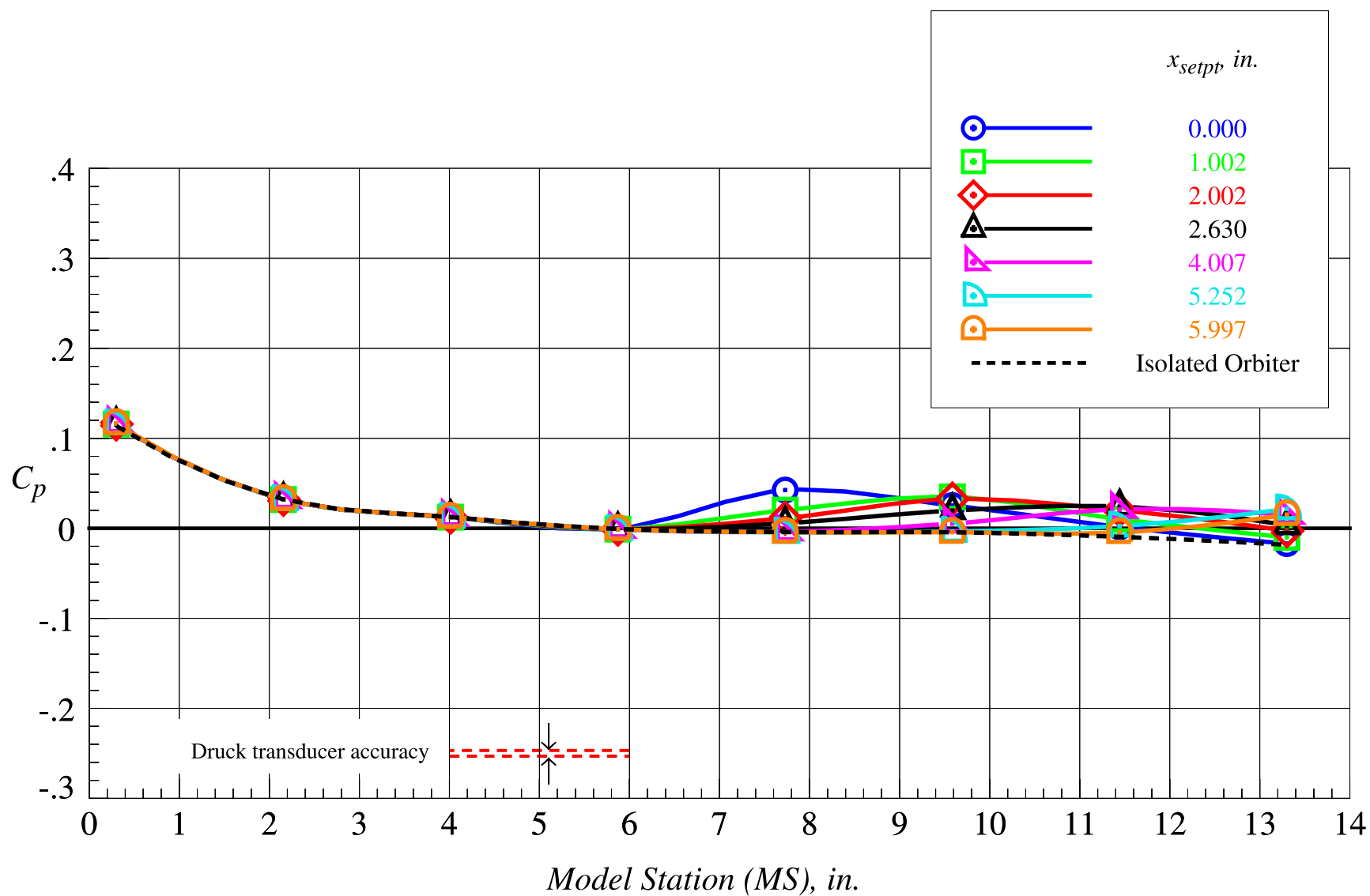
(c)  $z_{setpt} = 0.656$  in., part 1

Figure 71. Continued.



(d)  $z_{setpt} = 0.656$  in., part 2

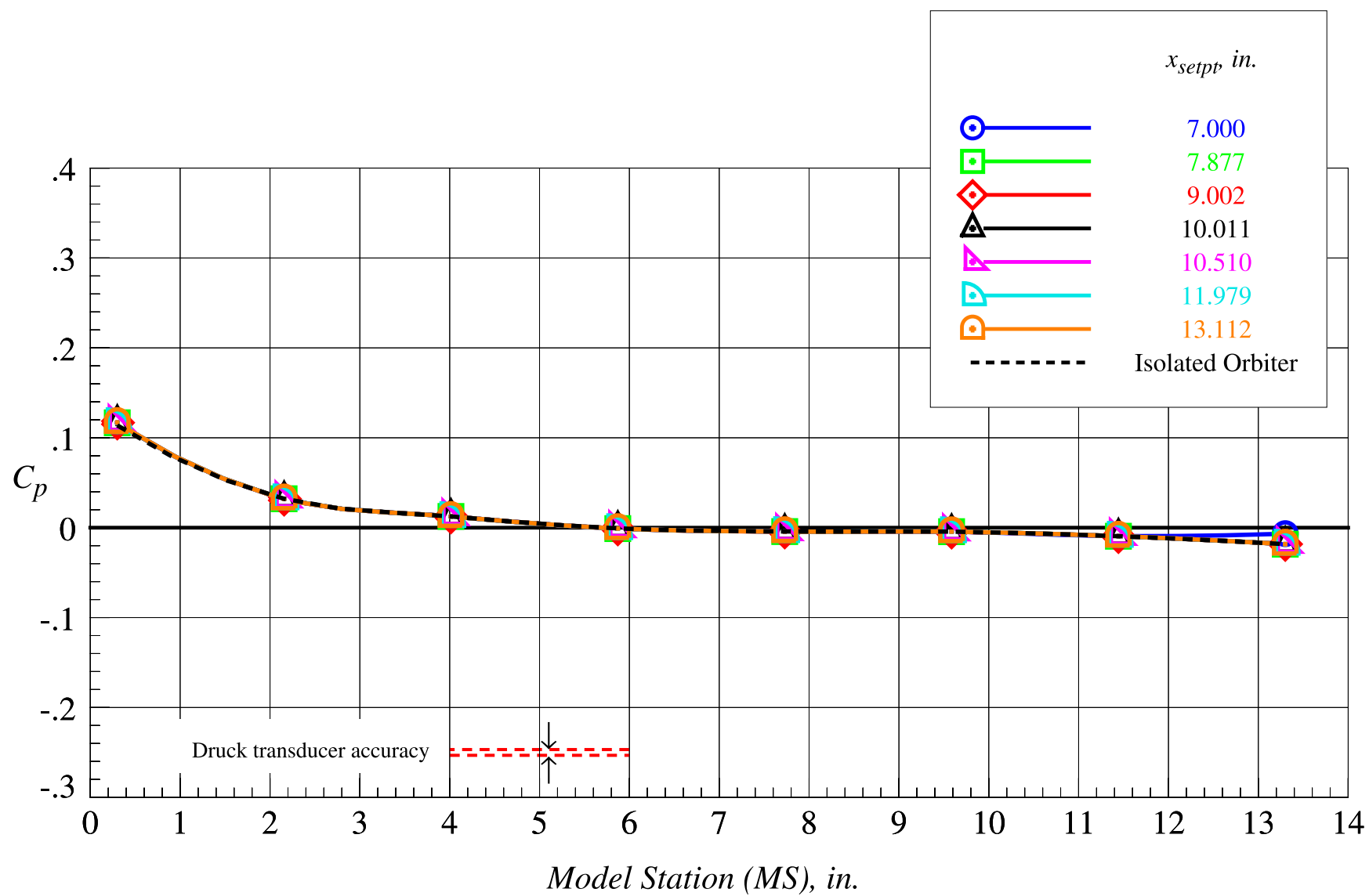
Figure 71. Continued.



(e)  $z_{setpt} = 1.313$  in., part 1

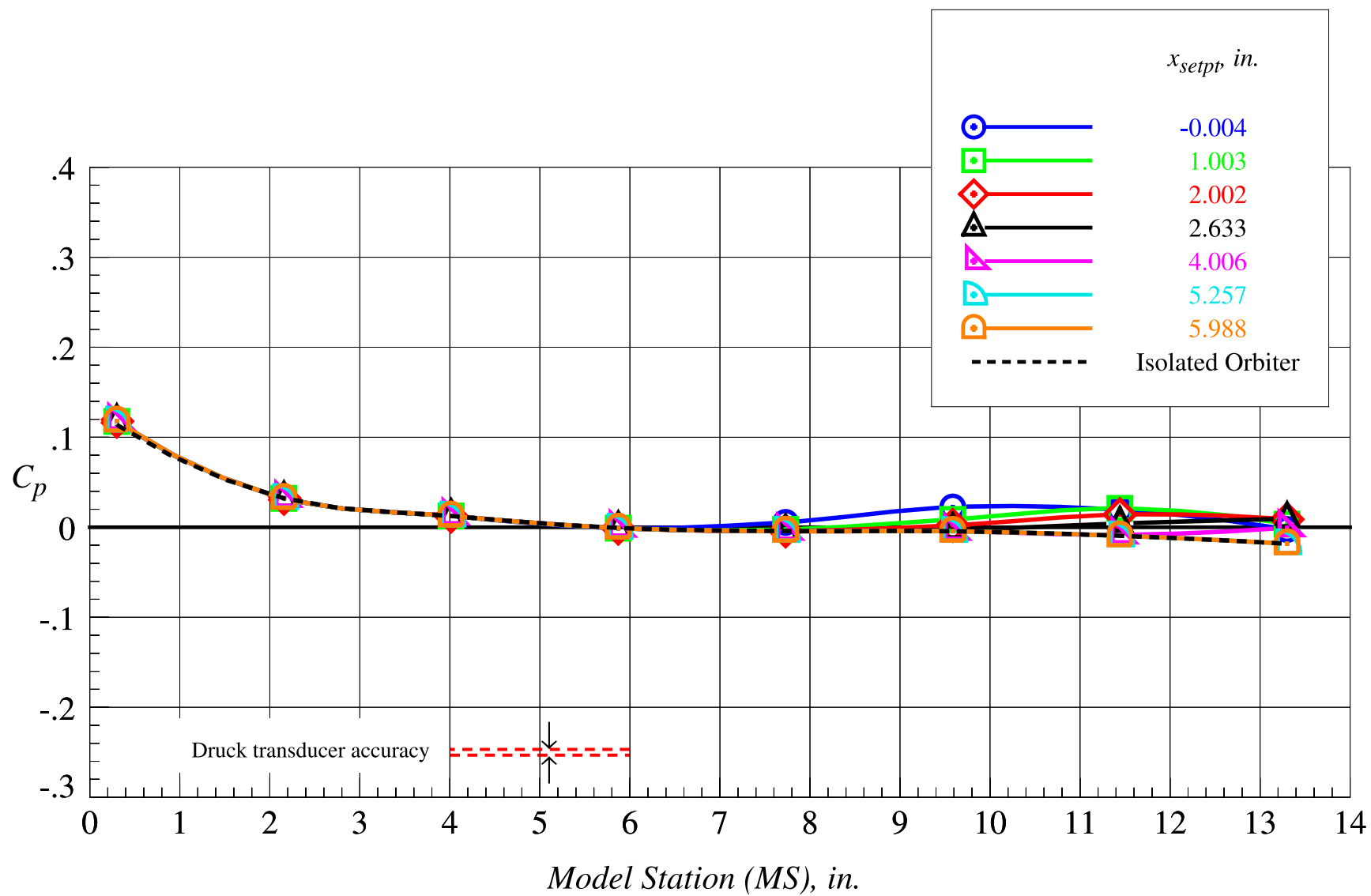
Figure 71. Continued.





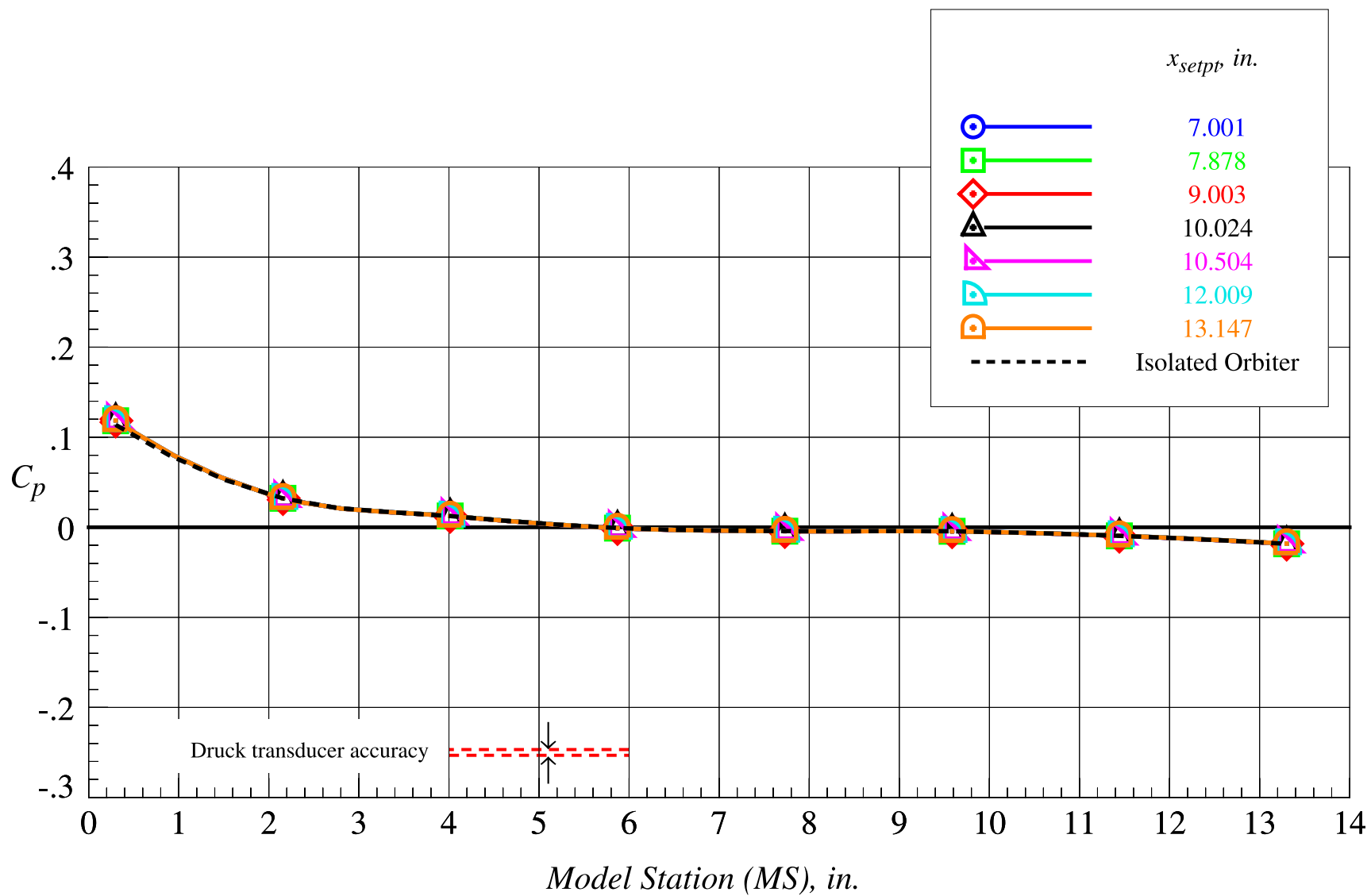
(f)  $z_{setpt} = 1.313$  in., part 2

Figure 71. Continued.



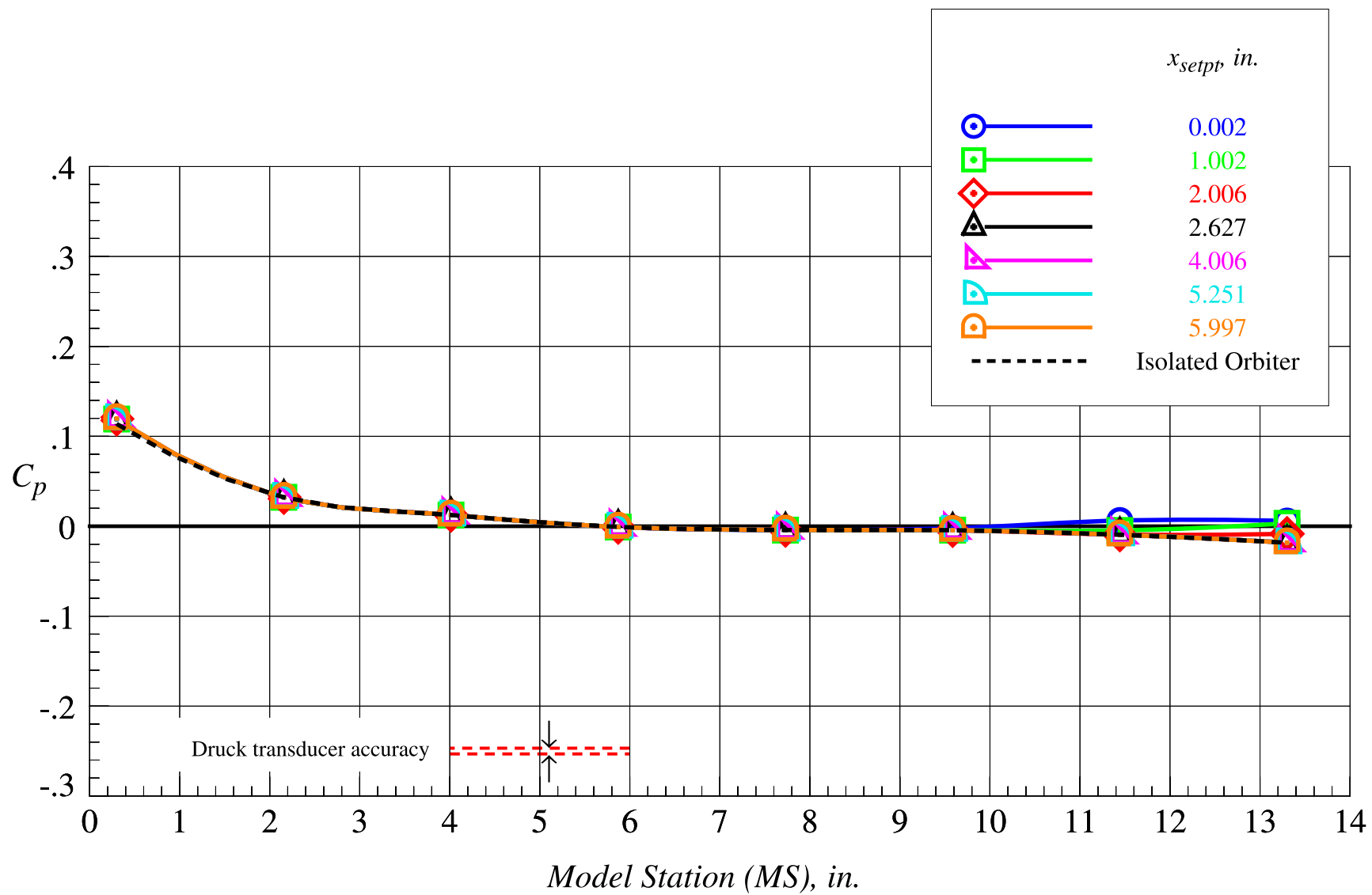
(g)  $z_{setpt} = 1.969$  in., part 1

Figure 71. Continued.



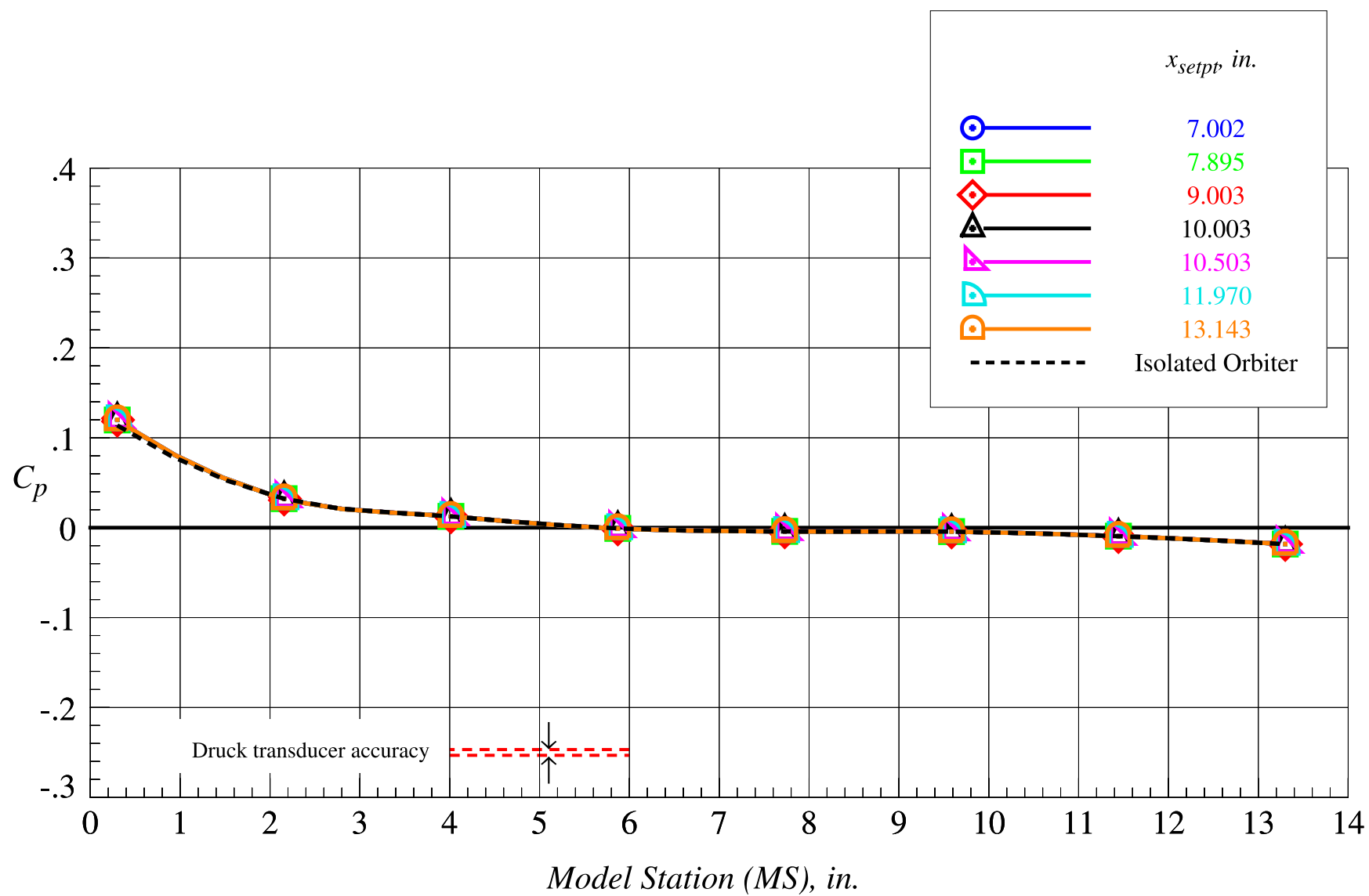
(h)  $z_{setpt} = 1.969$  in., part 2

Figure 71. Continued.



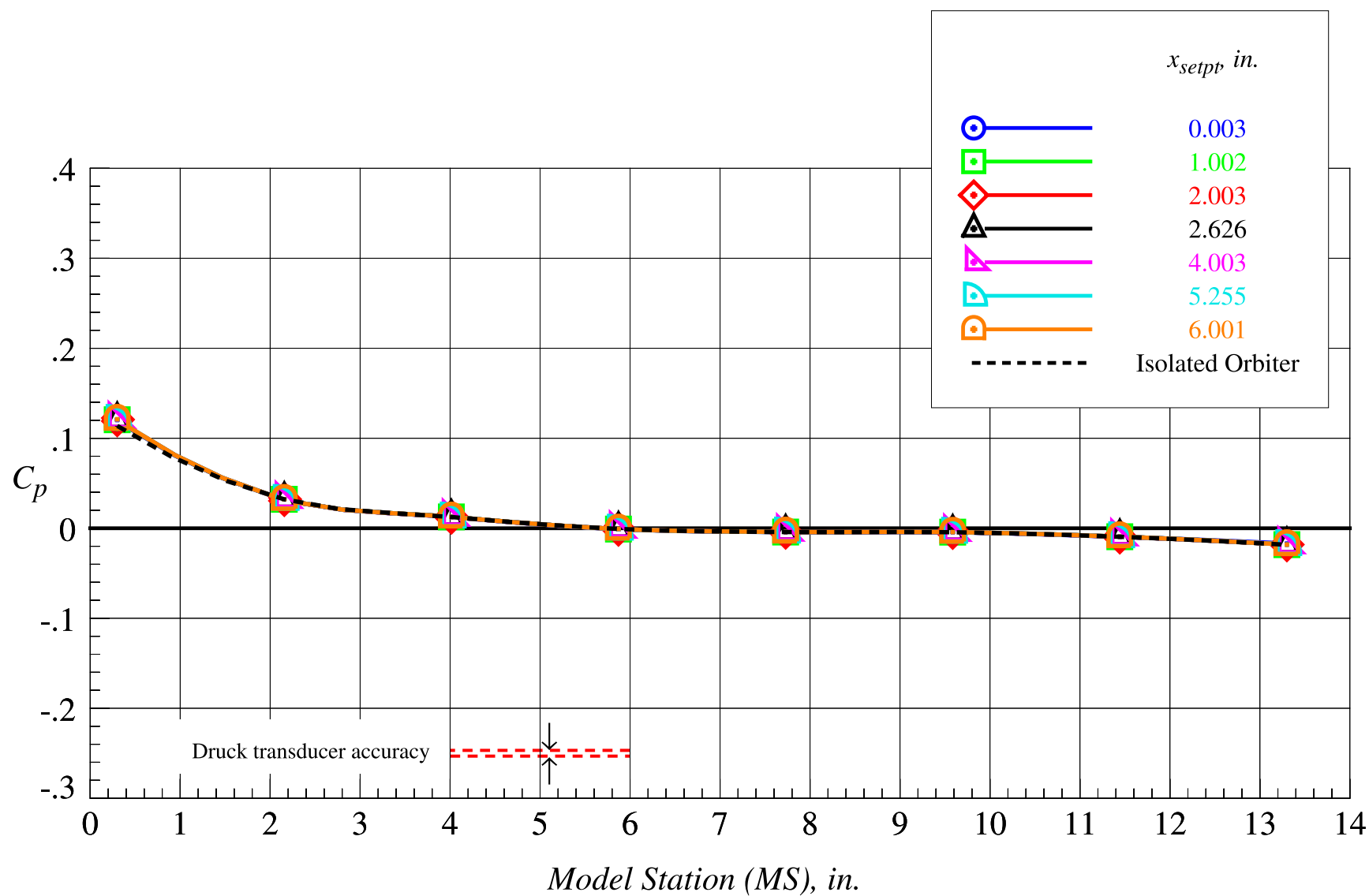
(i)  $z_{setpt} = 2.625$  in., part 1

Figure 71. Continued.



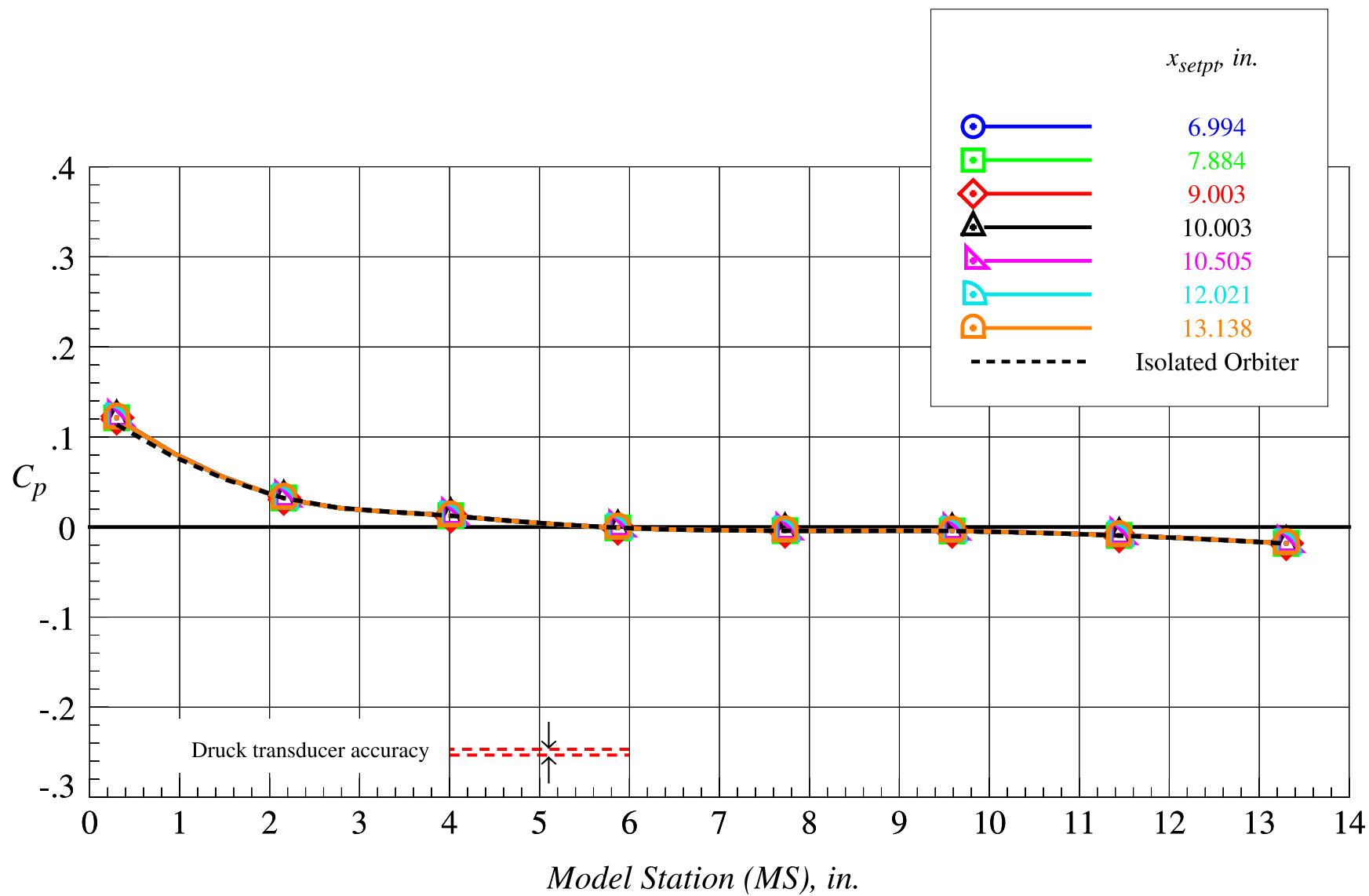
(j)  $z_{setpt} = 2.625$  in., part 2

Figure 71. Continued.



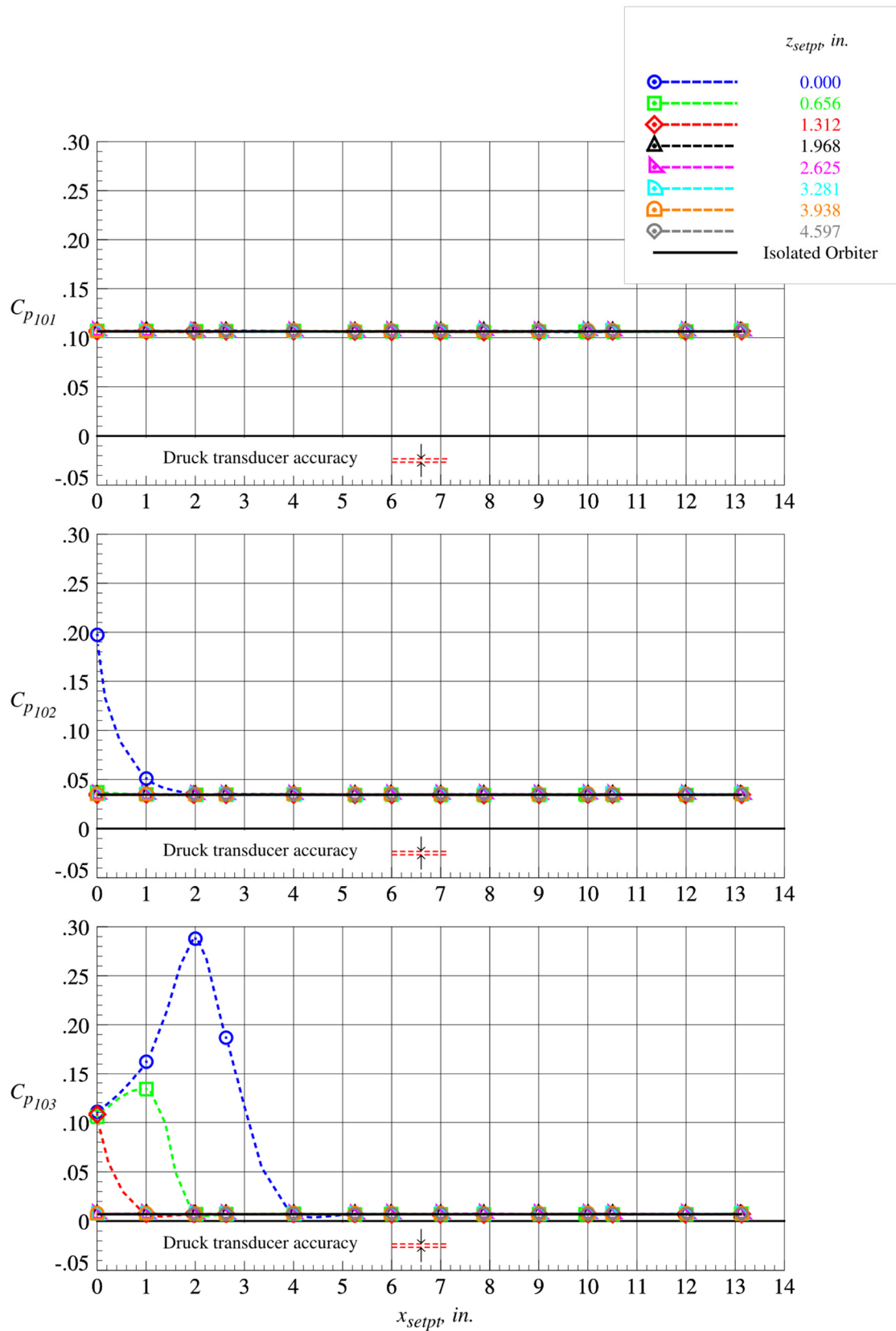
(k)  $z_{setpt} = 3.281$  in., part 1

Figure 71. Continued.



(l)  $z_{setpt} = 3.281$  in., part 2

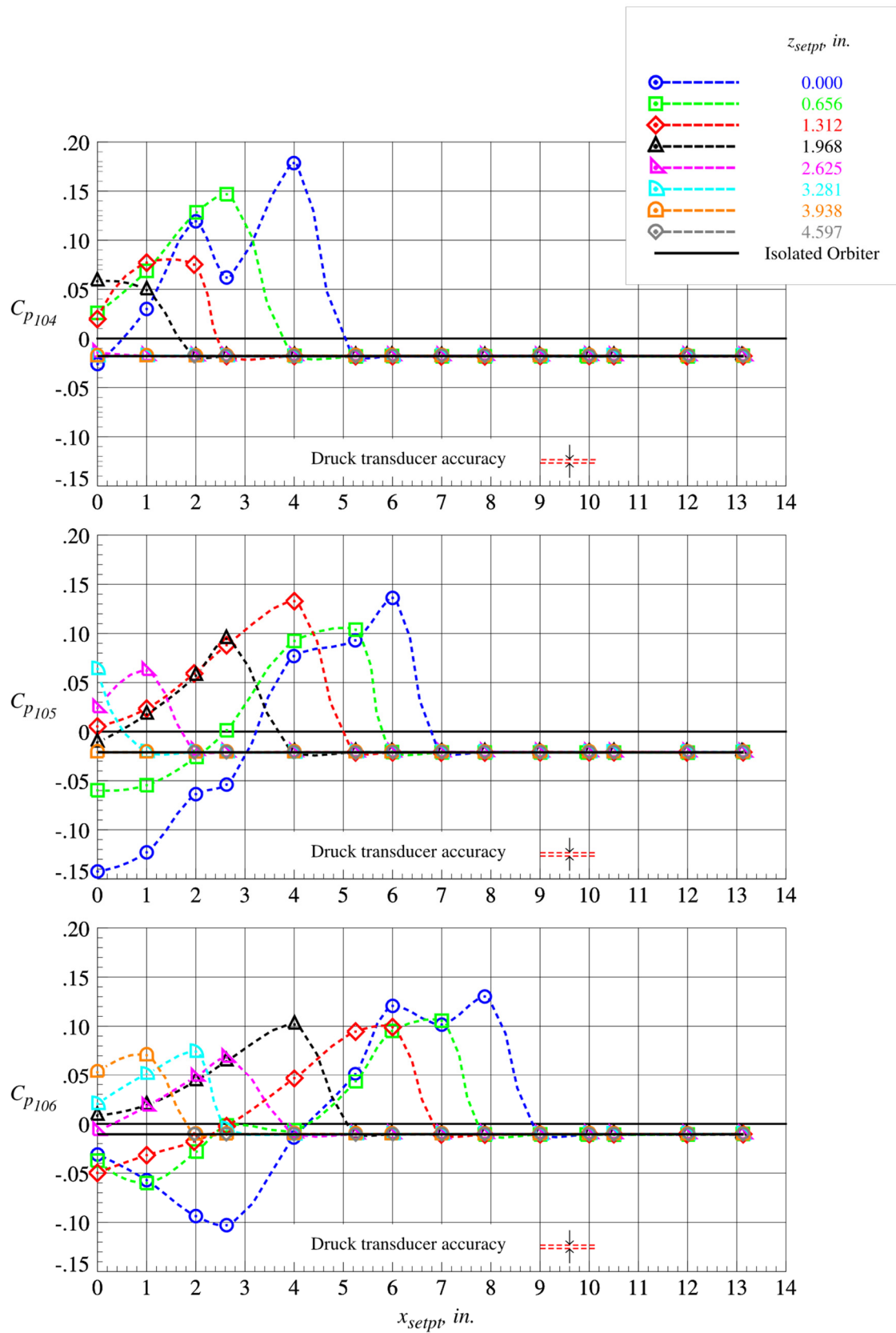
Figure 71. Concluded.



(a) fuselage centerline orifices 101, 102, and 103

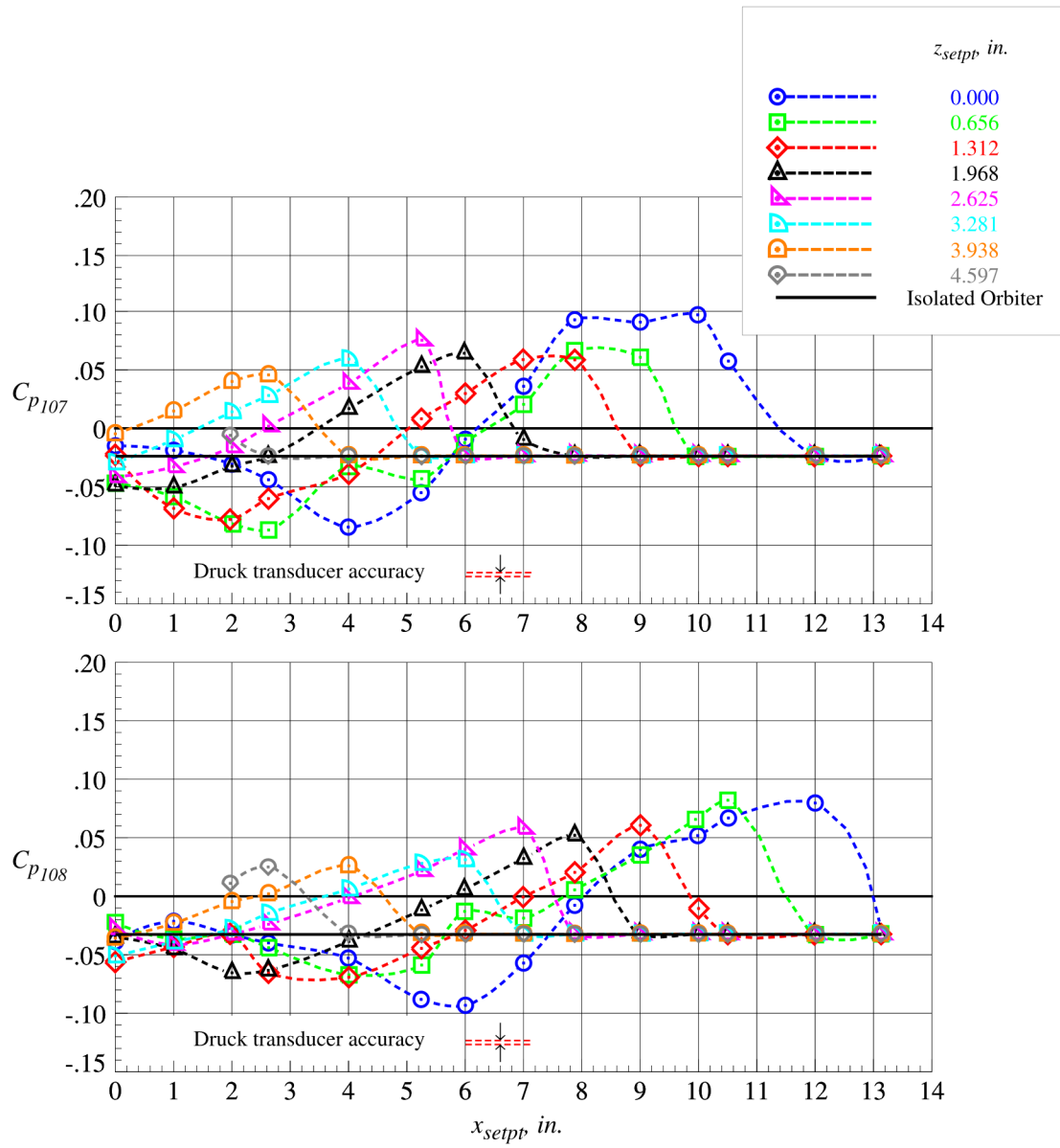
Figure 72. Orbiter individual surface static pressure coefficients on fuselage lower surface centerline at Mach = 2.3 and  $\Delta\alpha = 0^\circ$ .





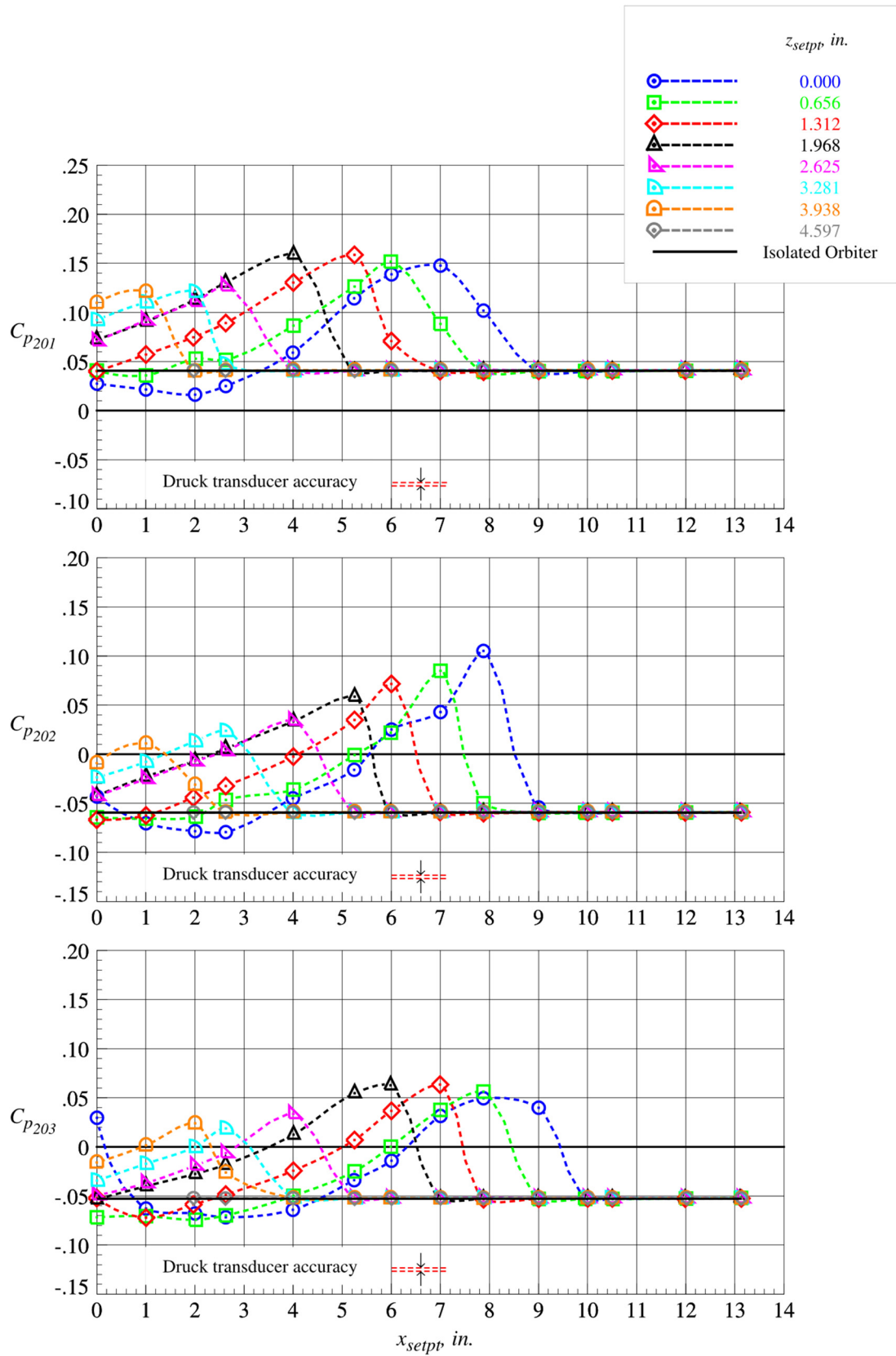
(b) fuselage centerline orifices 104, 105, and 106

Figure 72. Continued.



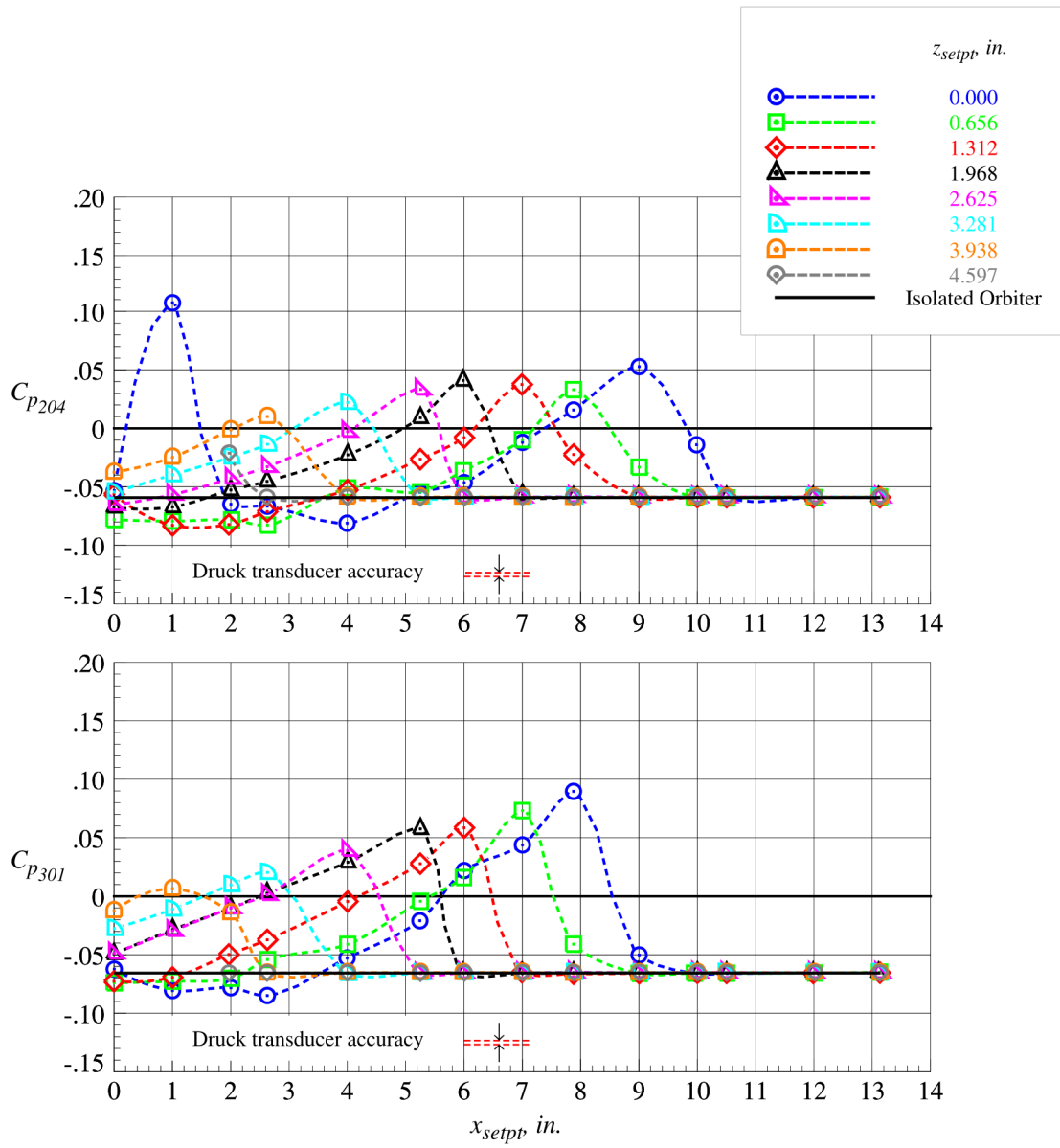
(c) fuselage centerline orifices 107 and 108

Figure 72. Concluded.



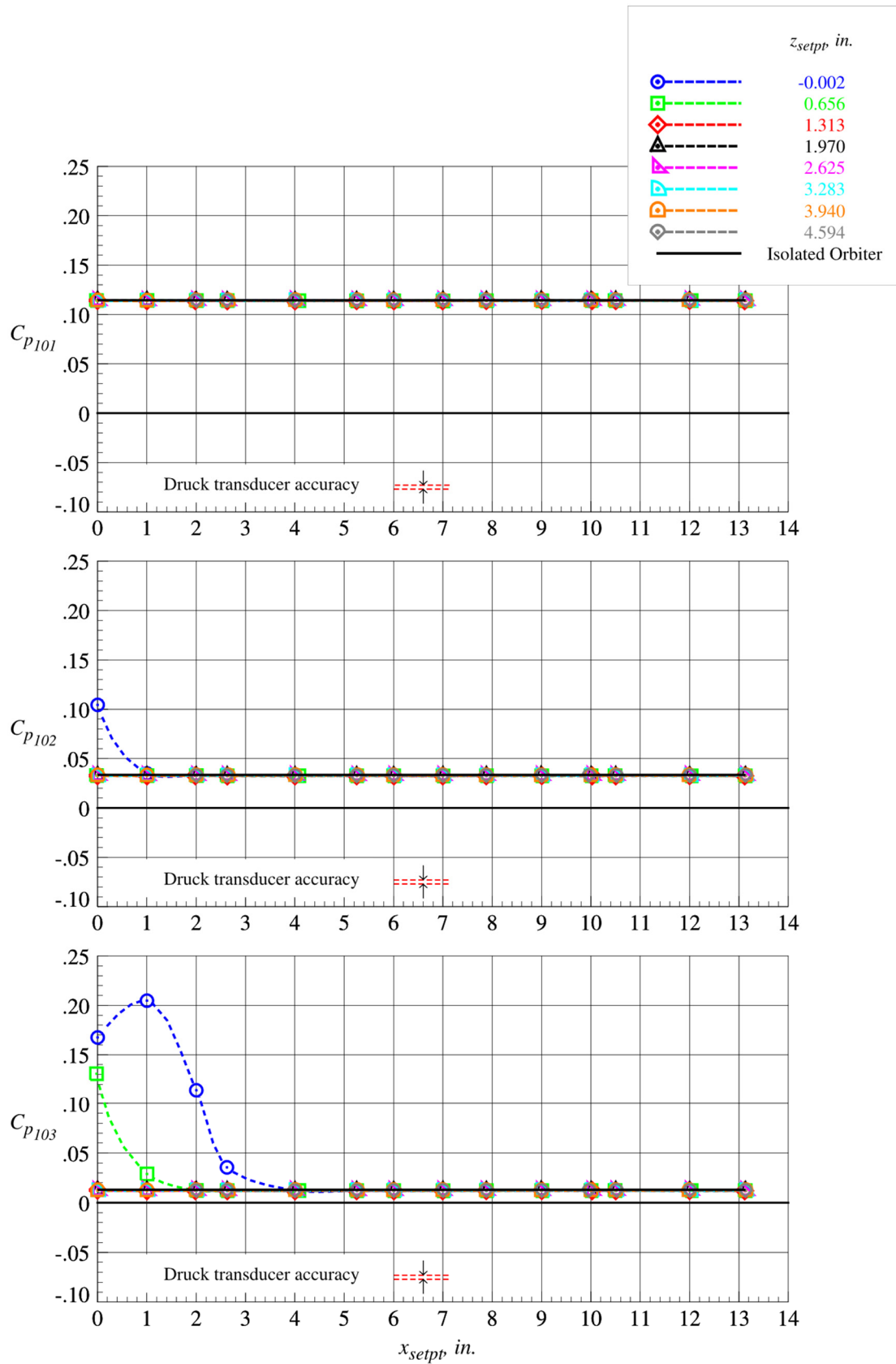
(a) right wing orifices 201, 202, and 203

Figure 73. Orbiter individual surface static pressure coefficients on wing lower surfaces at  $Mach = 2.3$  and  $\Delta\alpha = 0^\circ$ .



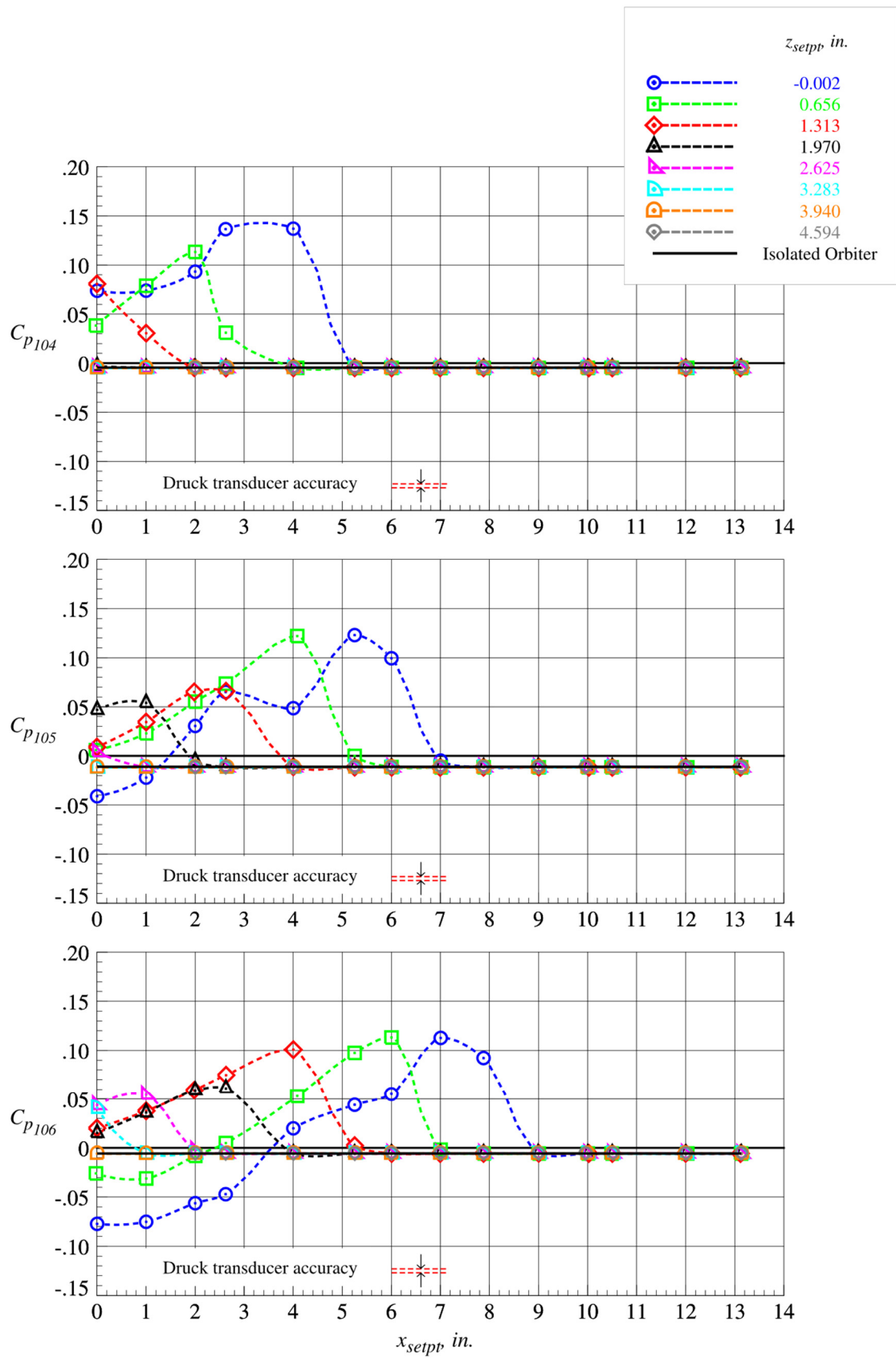
(b) left wing orifice 204 and right wing orifice 301

Figure 73. Concluded.



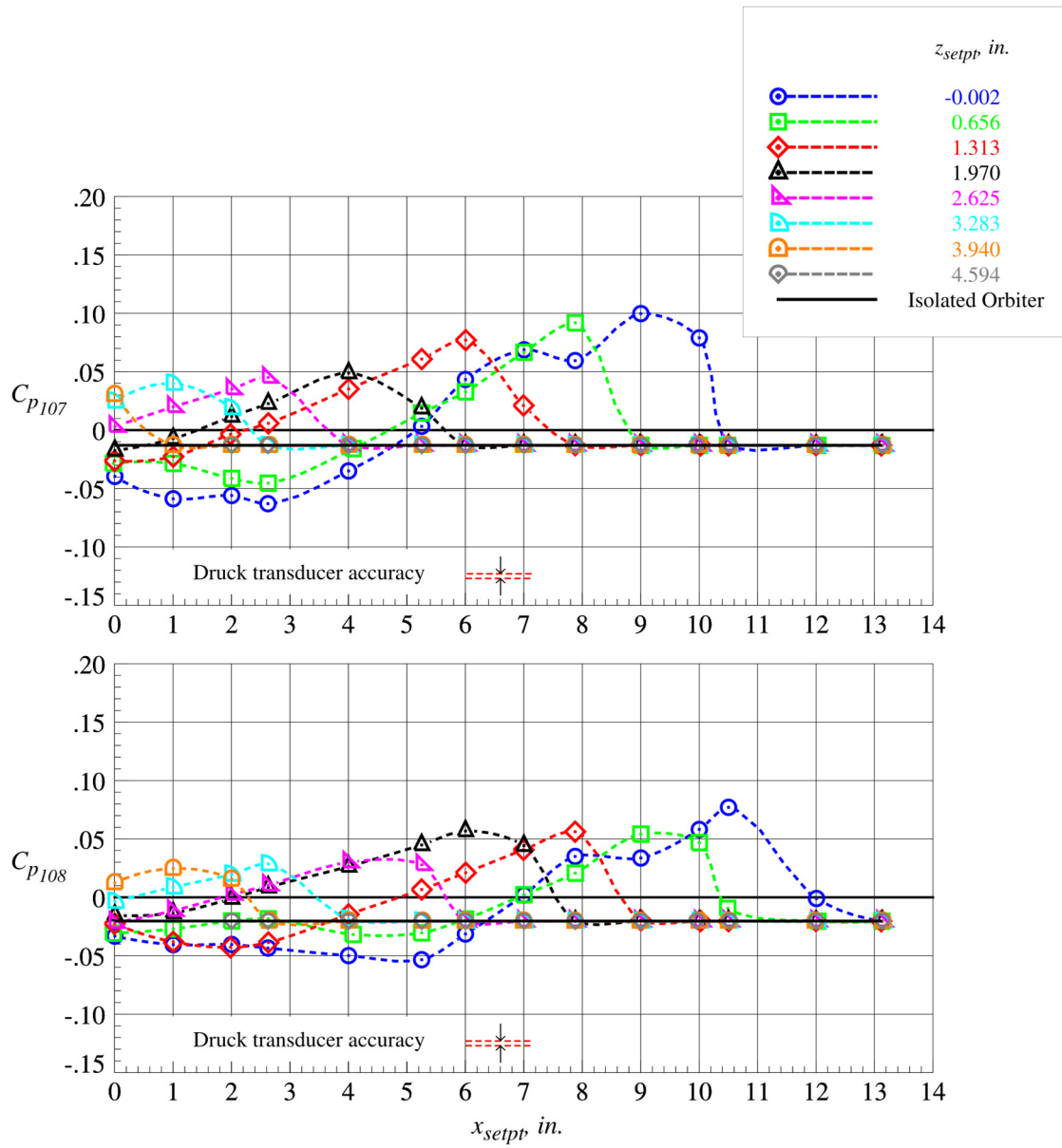
(a) fuselage centerline orifices 101, 102, and 103

Figure 74. Orbiter individual surface static pressure coefficients on fuselage lower surface centerline at Mach = 3.0 and  $\Delta\alpha = 0^\circ$ .



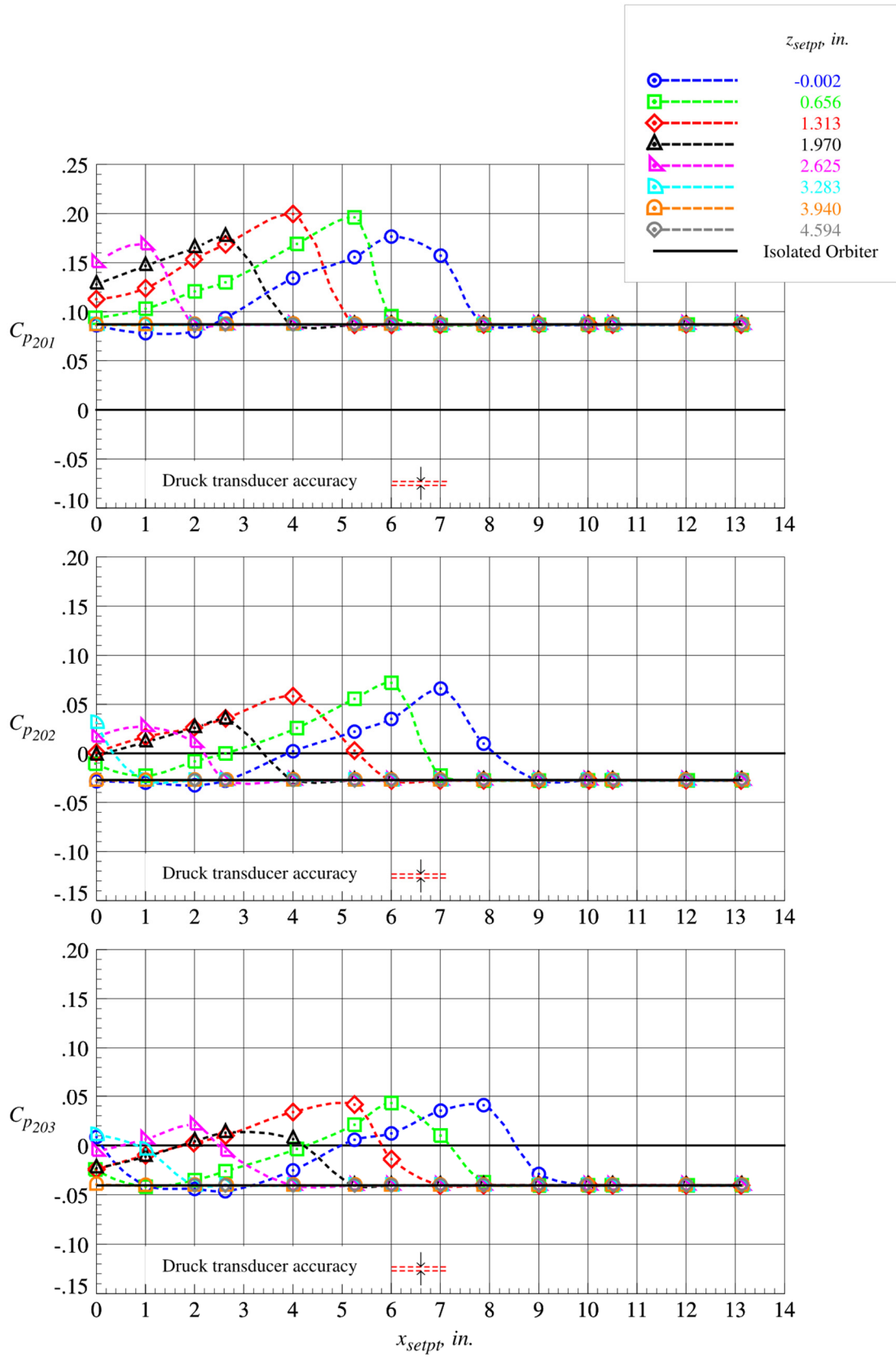
(b) fuselage centerline orifices 104, 105, and 106

Figure 74. Continued.



(c) fuselage centerline orifices 107 and 108

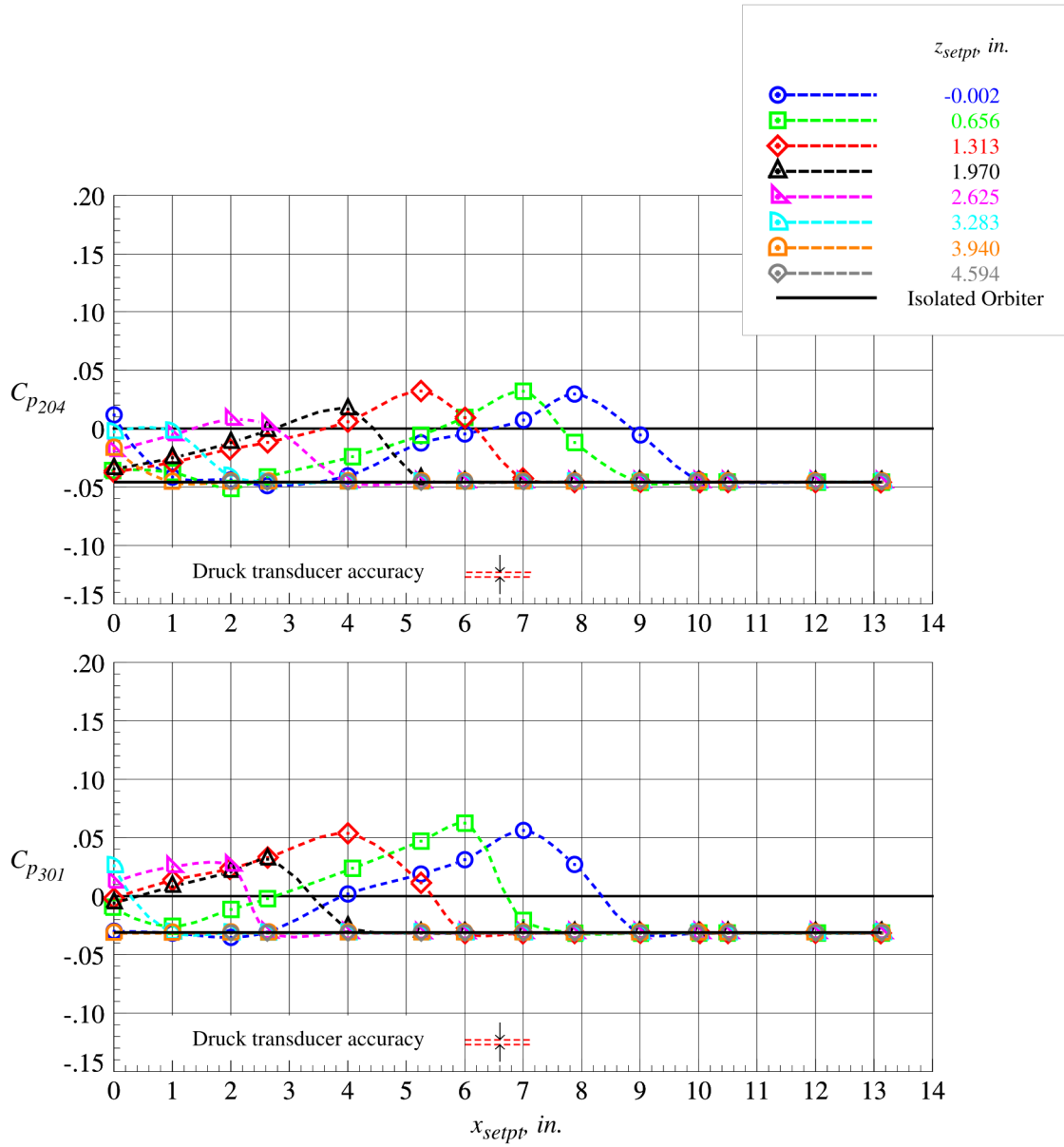
Figure 74. Concluded.



(a) right wing orifices 201, 202, and 203

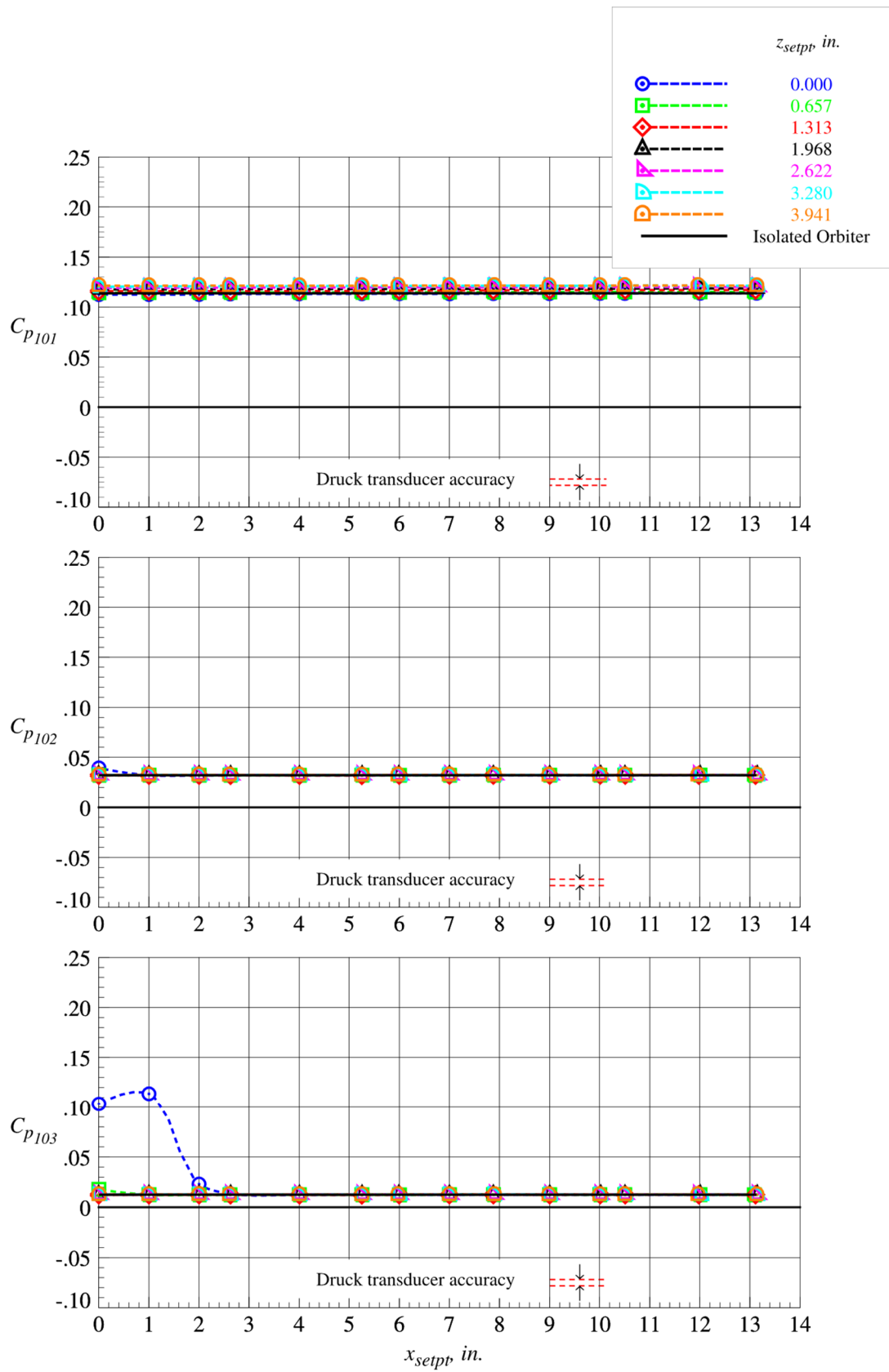
Figure 75. Orbiter individual surface static pressure coefficients on wing lower surfaces at Mach = 3.0 and  $\Delta\alpha = 0^\circ$ .





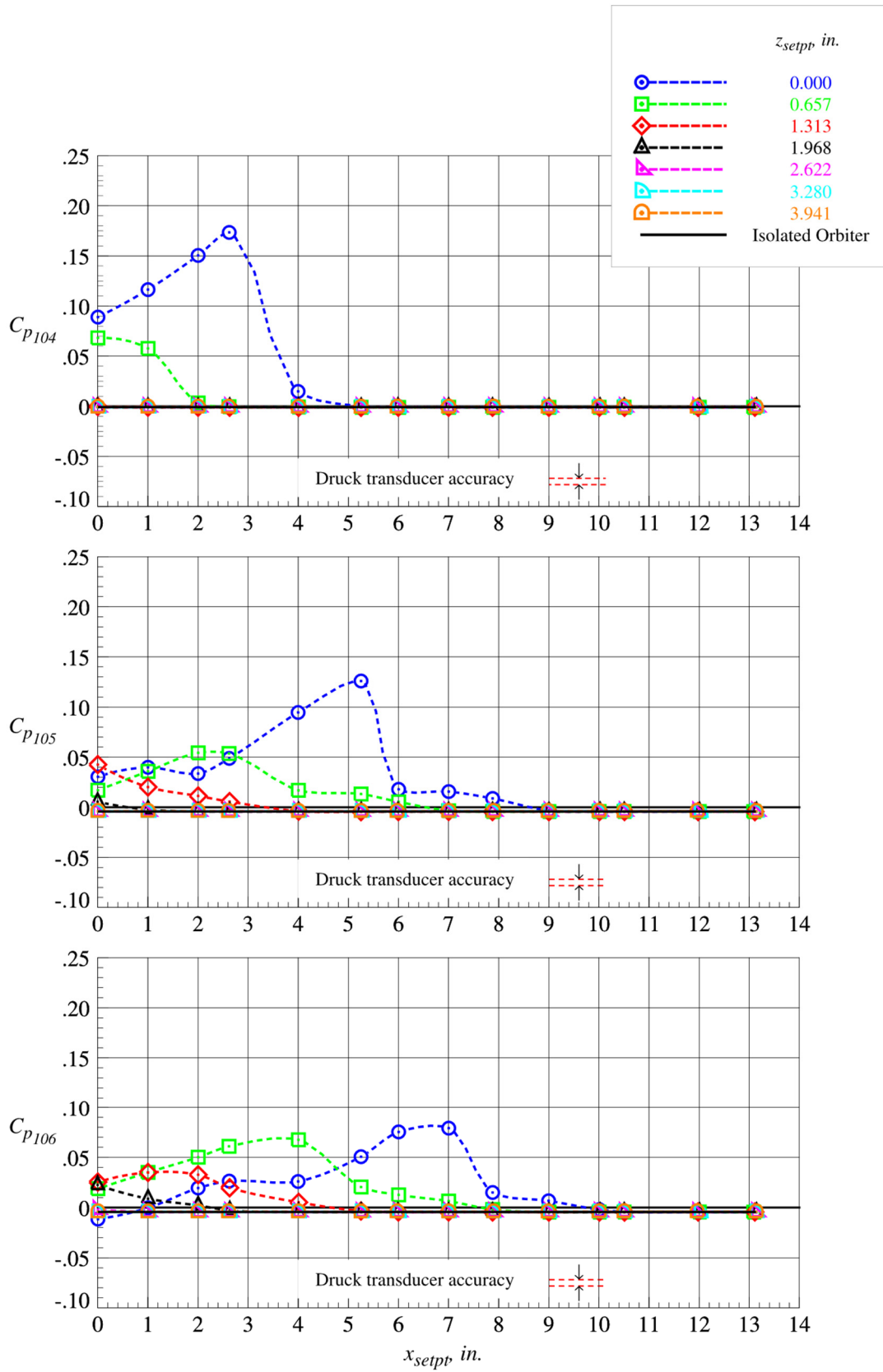
(b) left wing orifice 204 and right wing orifice 301

Figure 75. Concluded.



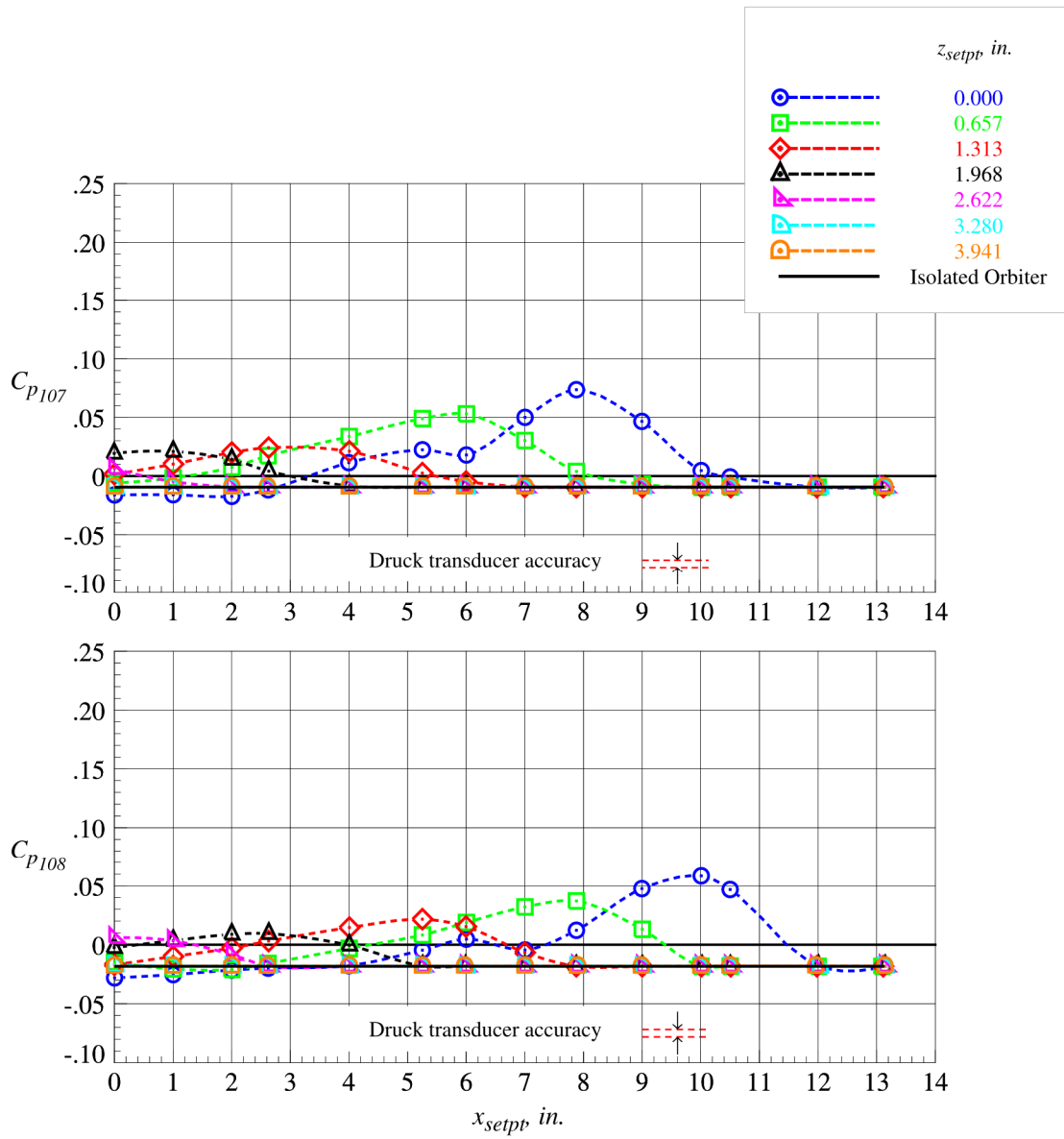
(a) fuselage centerline orifices 101, 102, and 103

Figure 76. Orbiter individual surface static pressure coefficients on fuselage lower surface centerline at Mach = 4.5 and  $\Delta\alpha = 0^\circ$ .



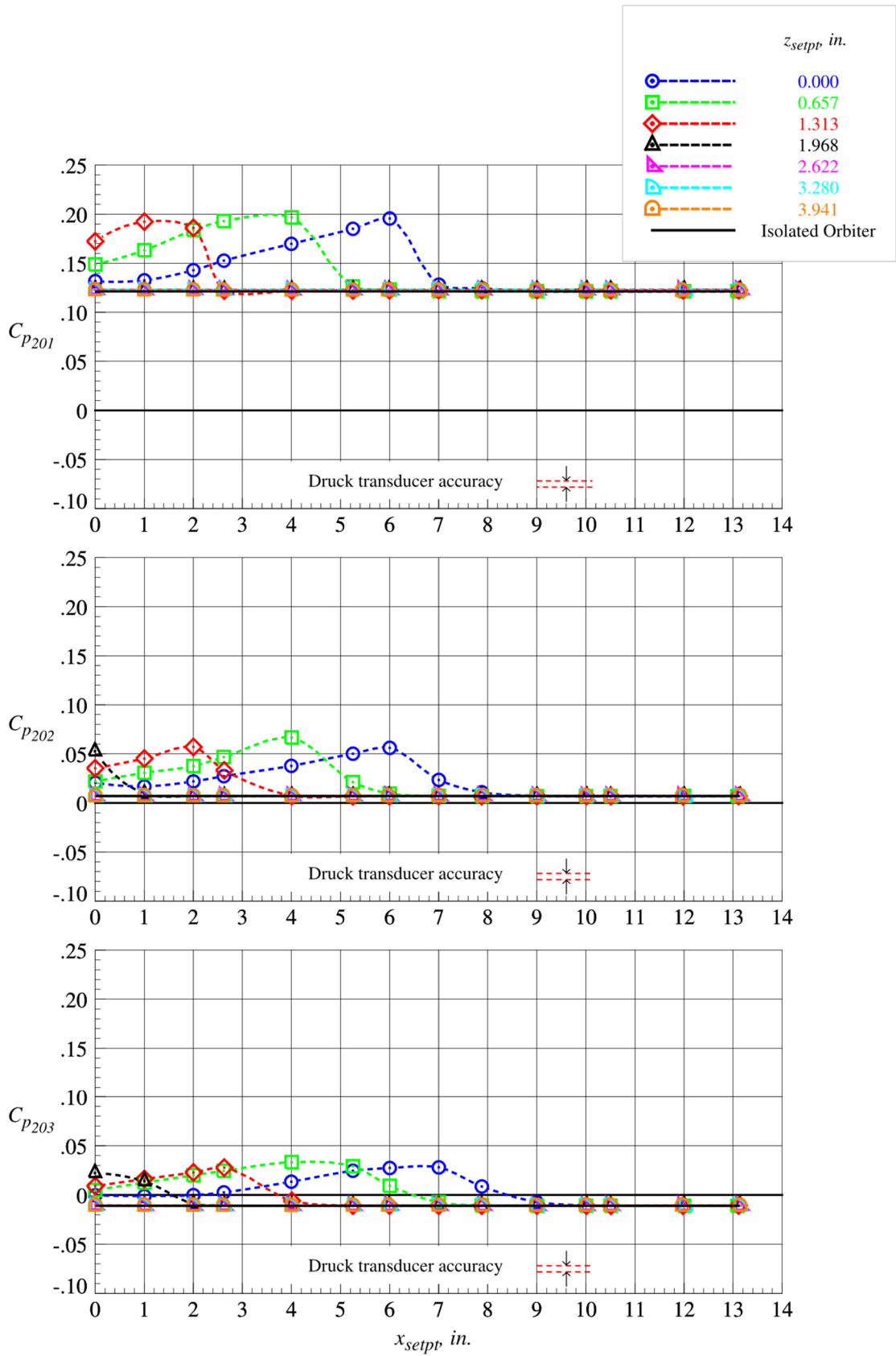
(b) fuselage centerline orifices 104, 105, and 106

Figure 76. Continued.



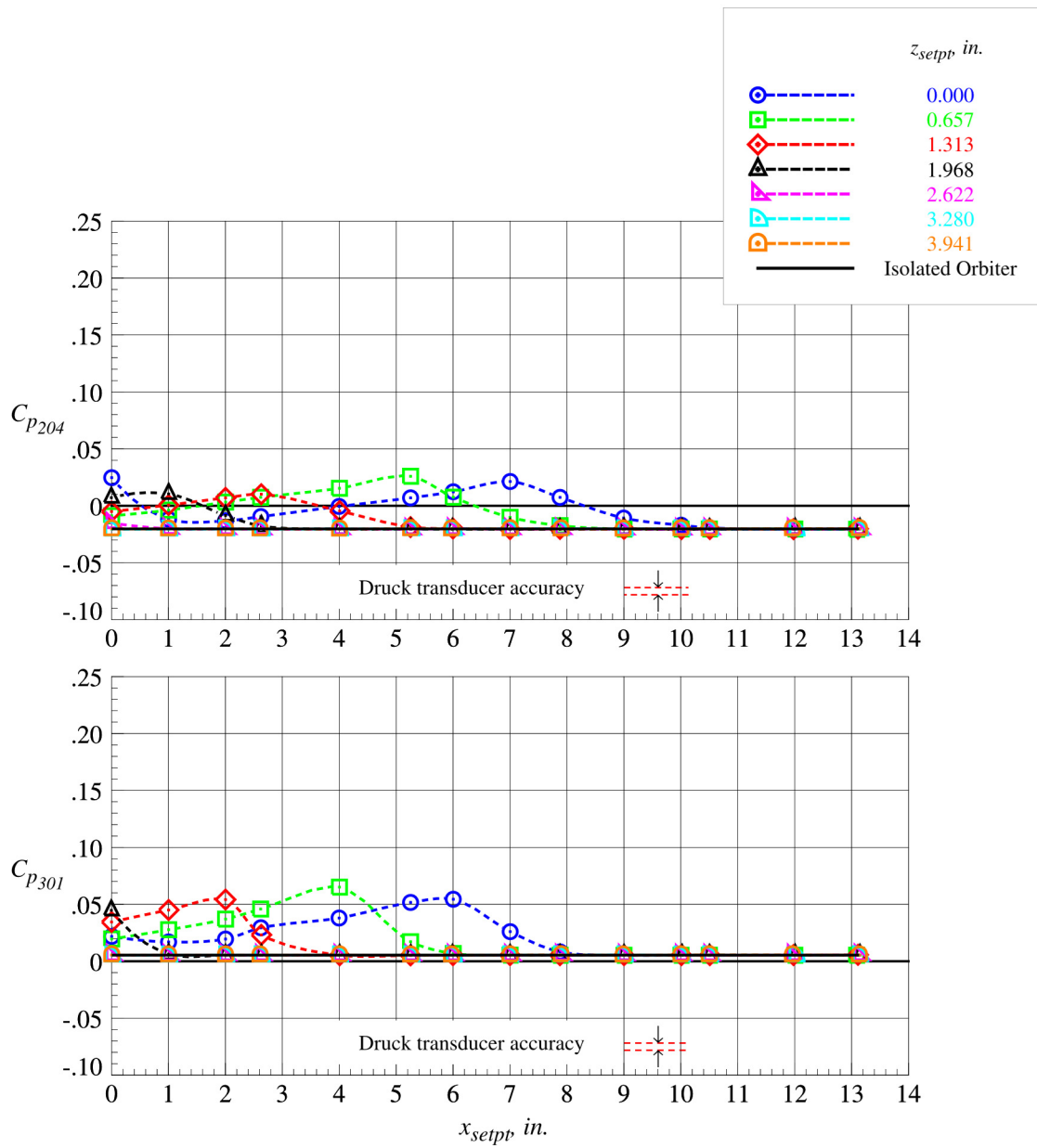
(c) fuselage centerline orifices 107 and 108

Figure 76. Concluded.



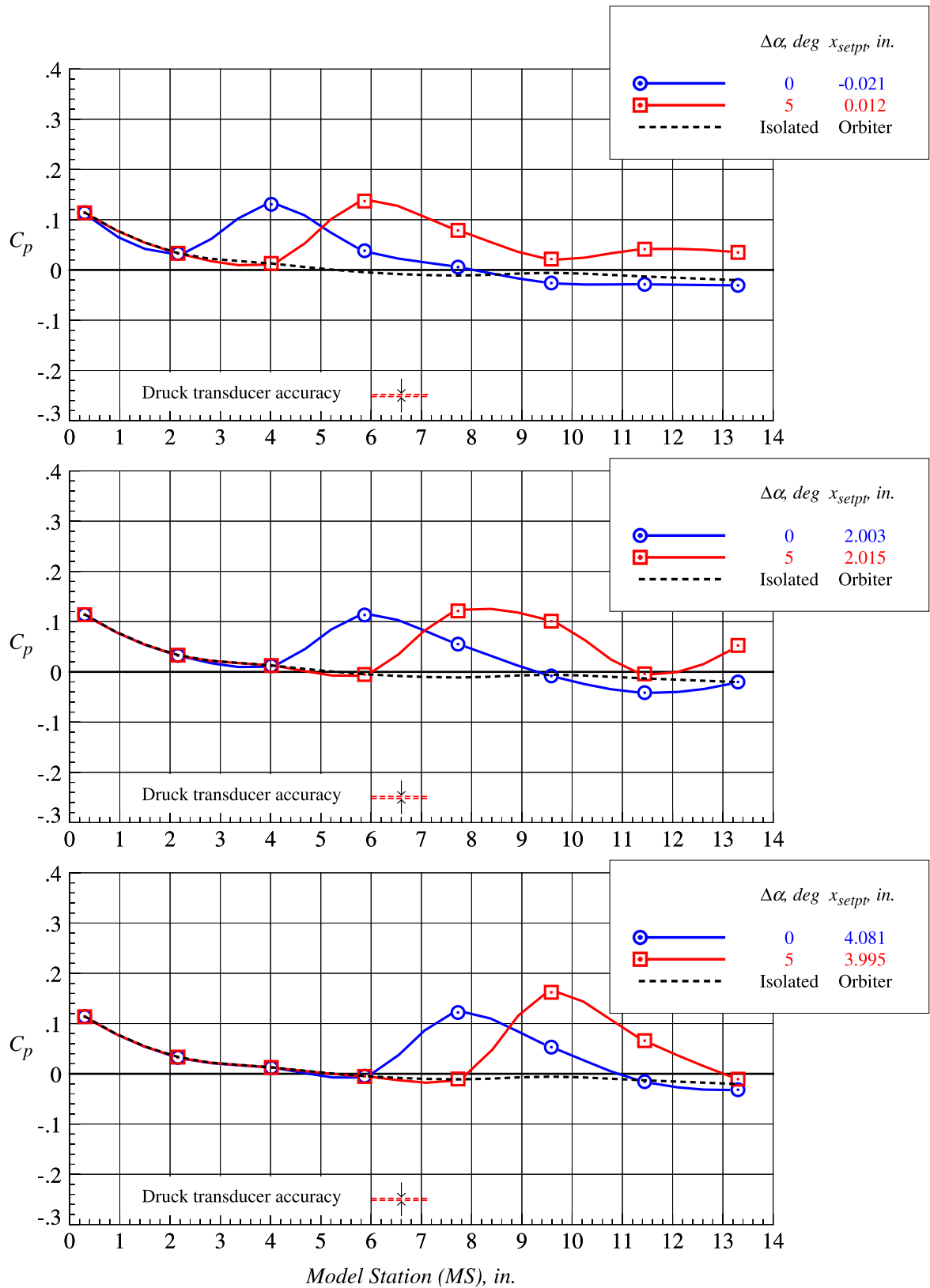
(a) right wing orifices 201, 202, and 203

Figure 77. Orbiter individual surface static pressure coefficients on wing lower surfaces at Mach = 4.5 and  $\Delta\alpha = 0^\circ$ .



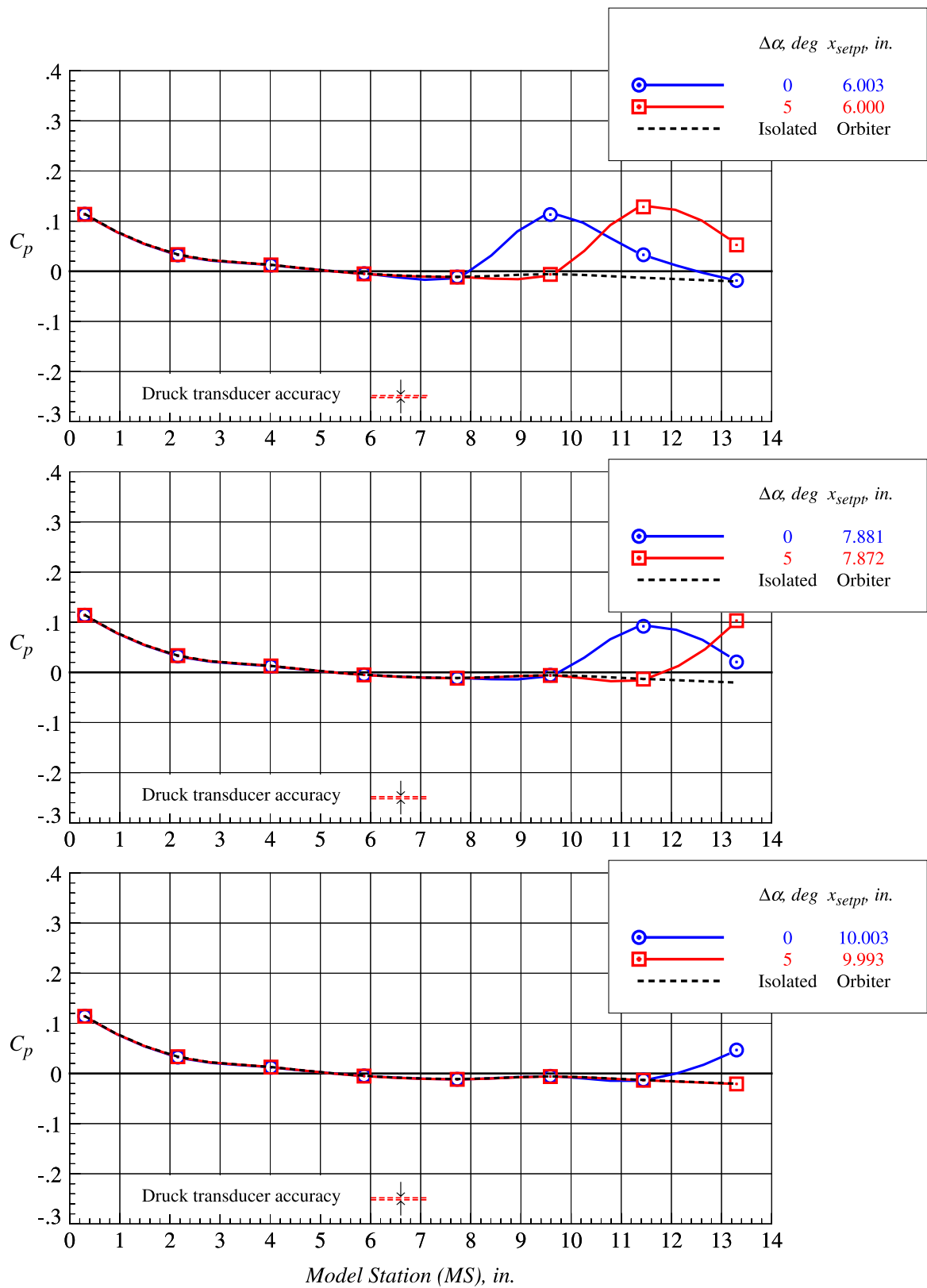
(b) left wing orifice 204 and right wing orifice 301

Figure 77. Concluded.



(a)  $z_{setpt} = 0.656$  in.,  $x_{setpt} = 0, 2$ , and  $4$  in.

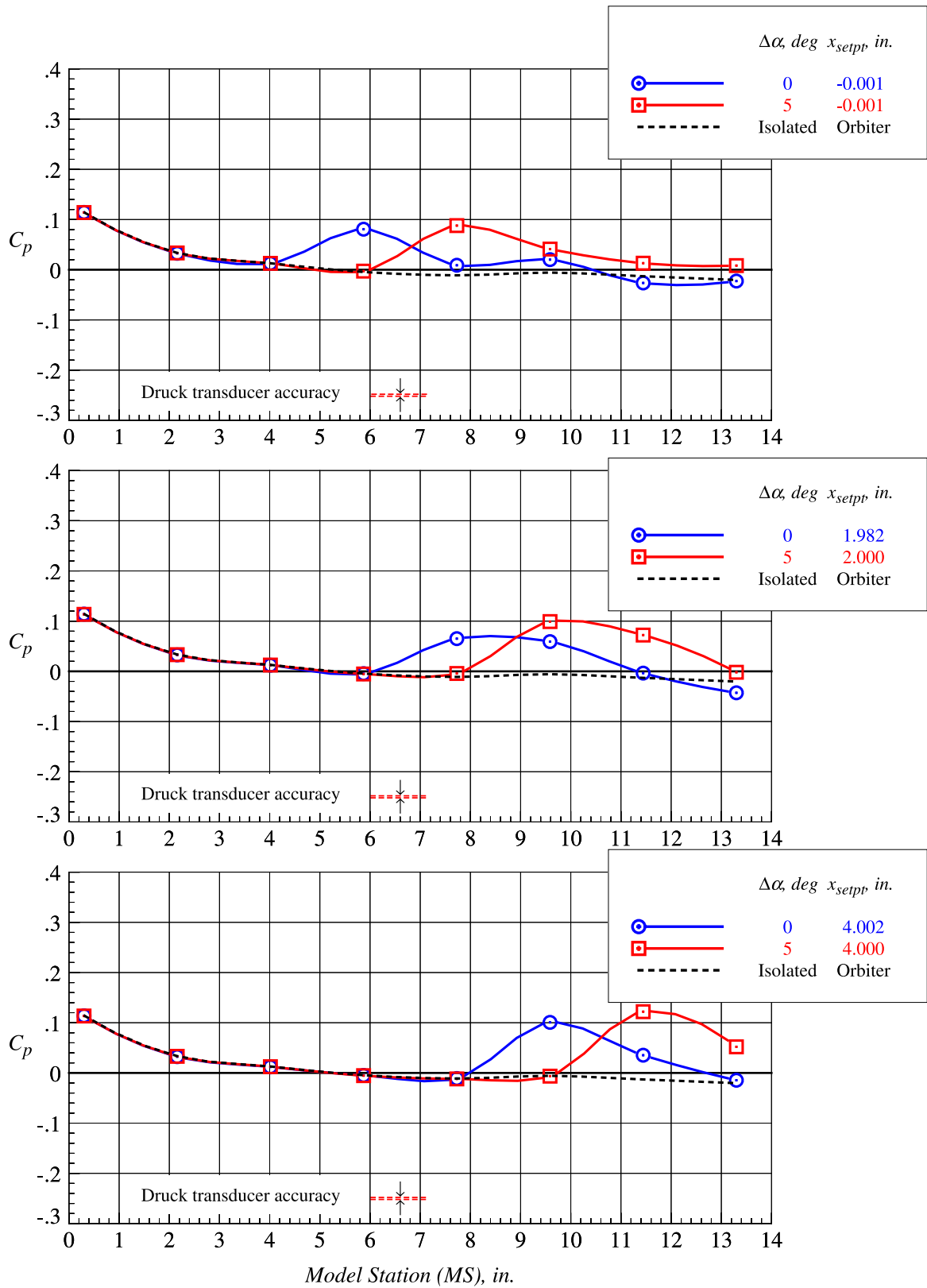
Figure 78. Orbiter proximity surface static pressure distributions on fuselage centerline lower surface at Mach = 3.0 and  $\Delta\alpha = 0^\circ$  and  $5^\circ$ .



(b)  $z_{setpt} = 0.656$  in.,  $x_{setpt} = 6, 8, \text{ and } 10$  in.

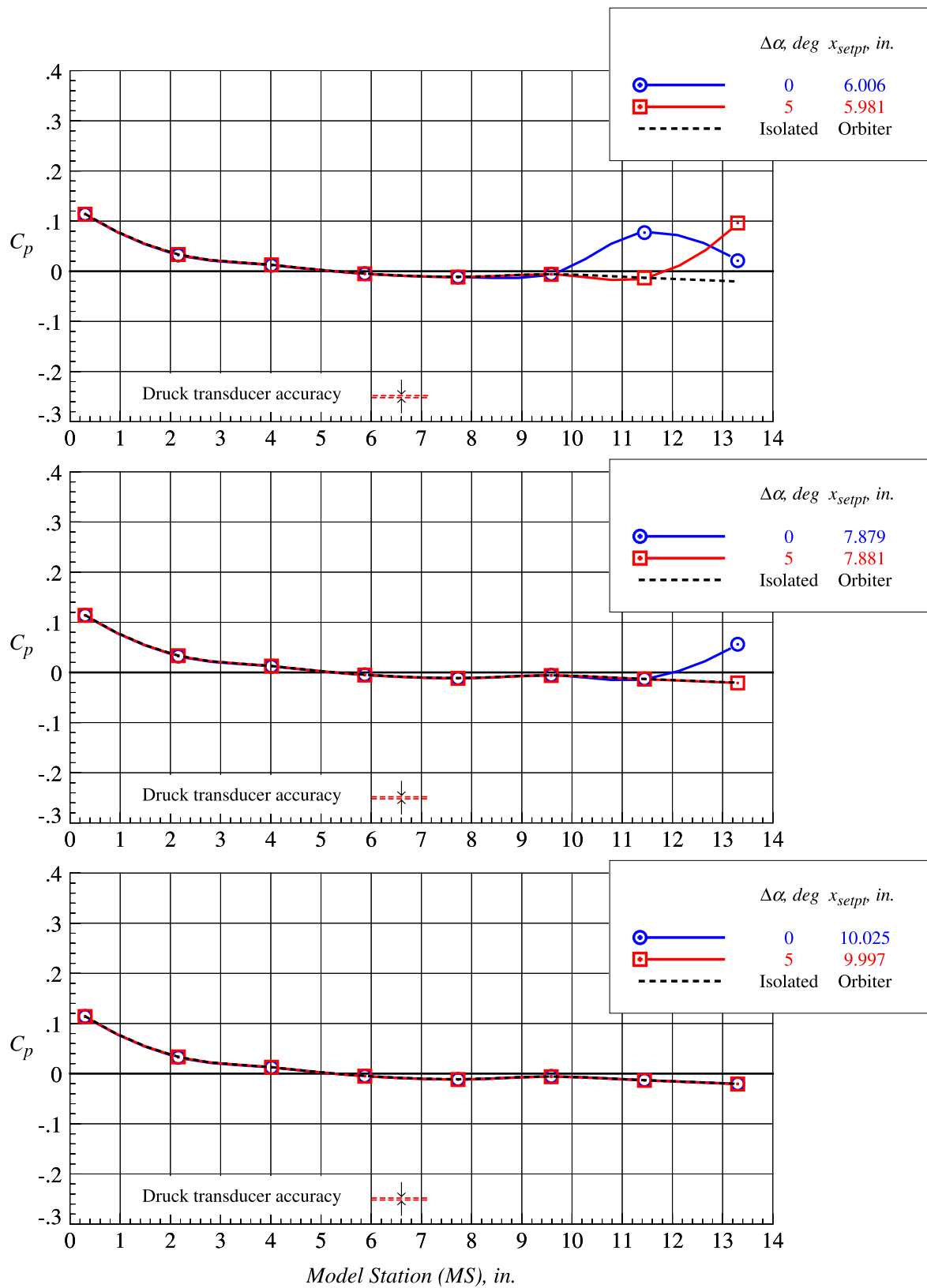
Figure 78. Continued.





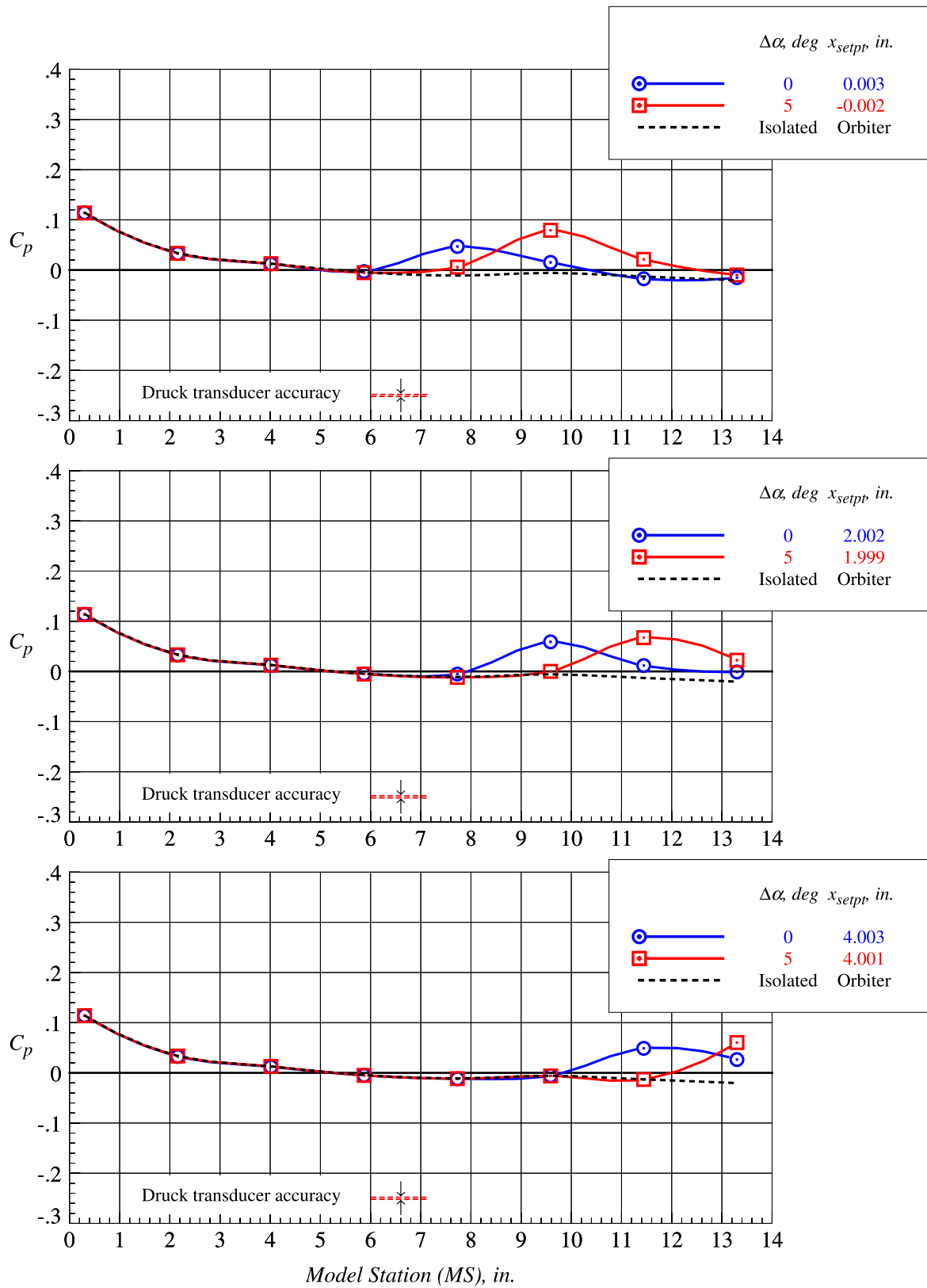
(c)  $z_{setpt} = 1.313$  in.,  $x_{setpt} = 0, 2$ , and 4 in.

Figure 78. Continued.



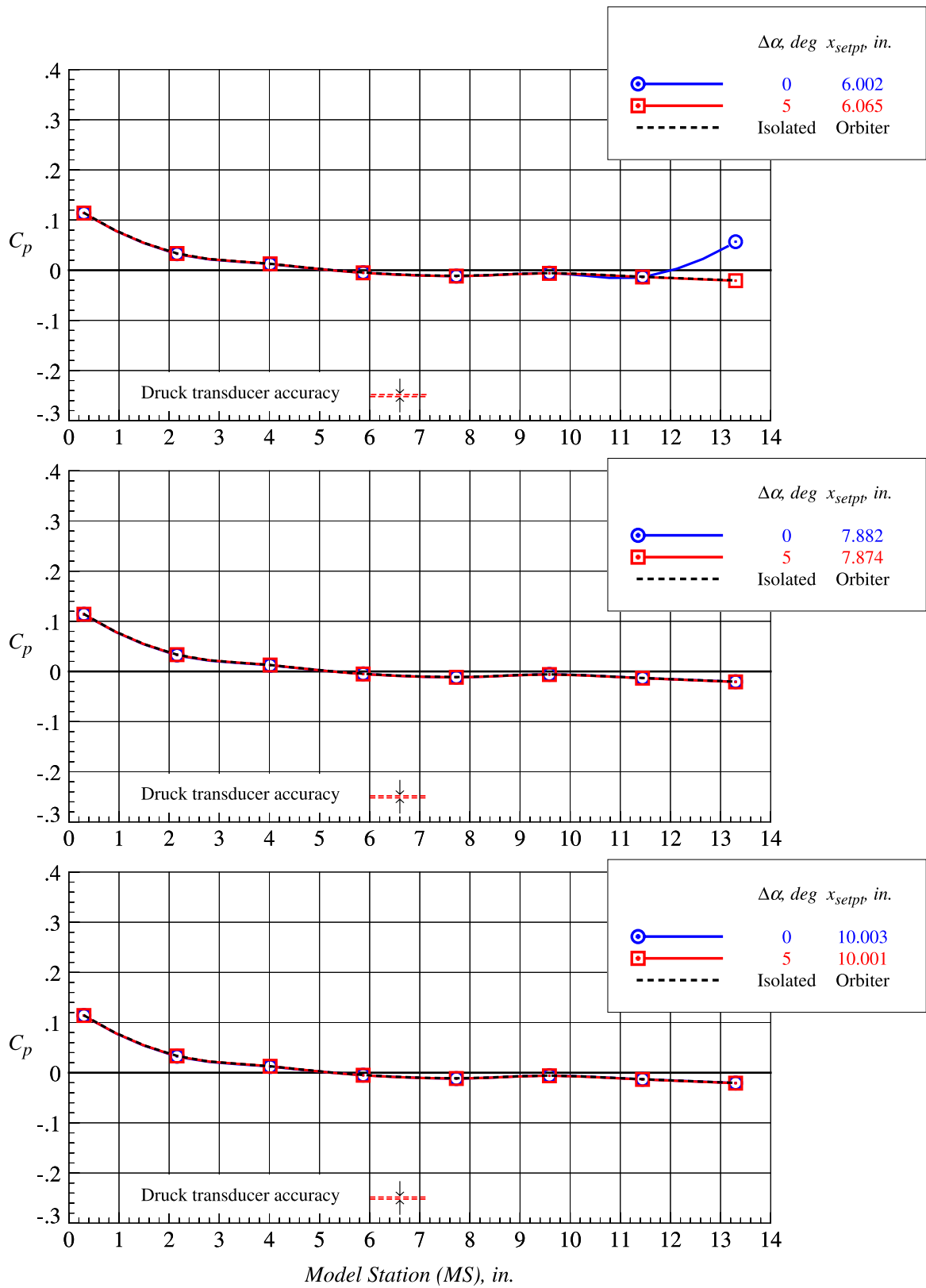
(d)  $z_{setpt} = 1.313$  in.,  $x_{setpt} = 6, 8,$  and  $10$  in.

Figure 78. Continued.



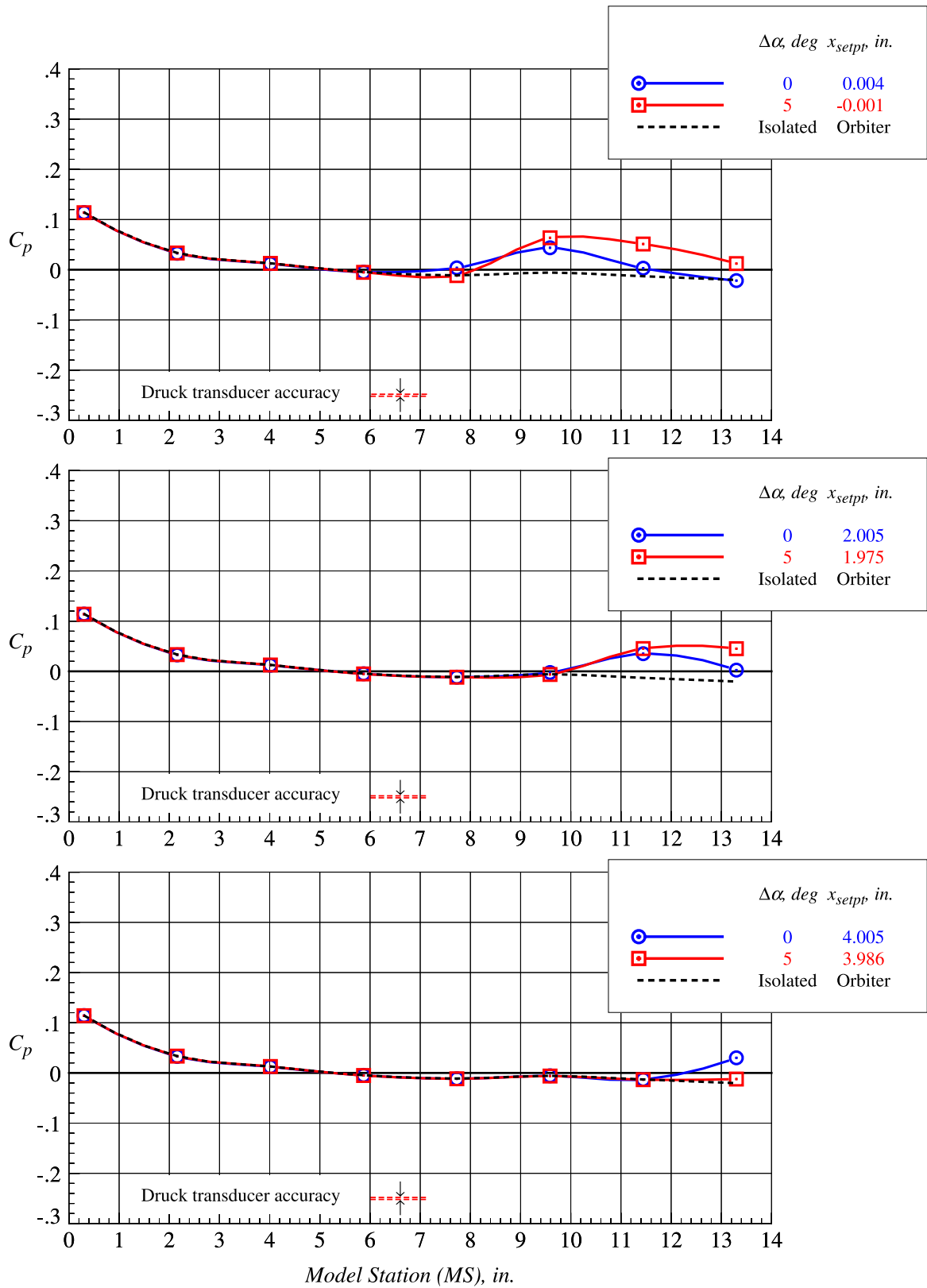
(e)  $z_{setpt} = 1.969$  in.,  $x_{setpt} = 0, 2$ , and 4 in.

Figure 78. Continued.



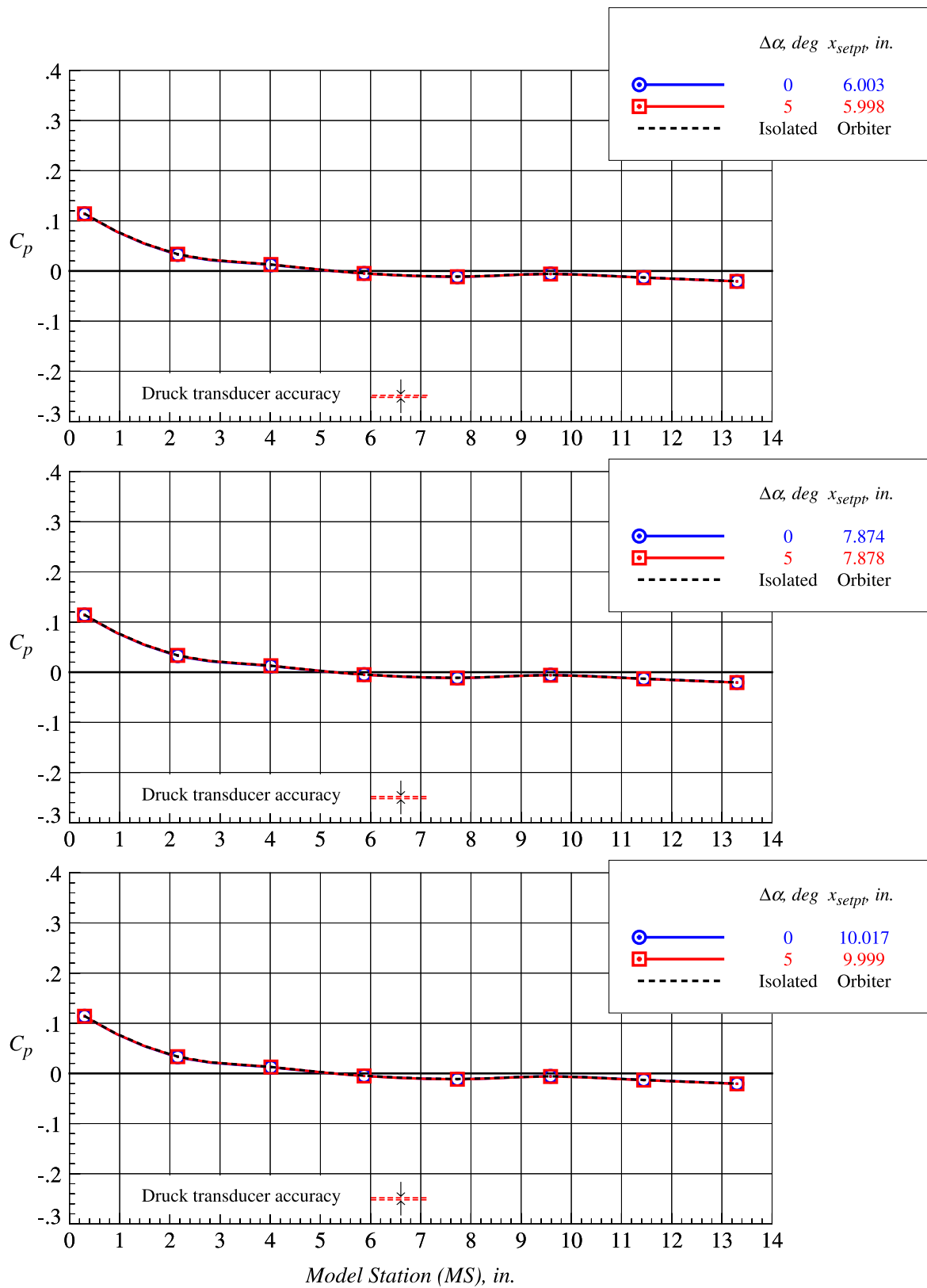
(f)  $z_{setpt} = 1.969$  in.,  $x_{setpt} = 6, 8$ , and  $10$  in.

Figure 78. Continued.



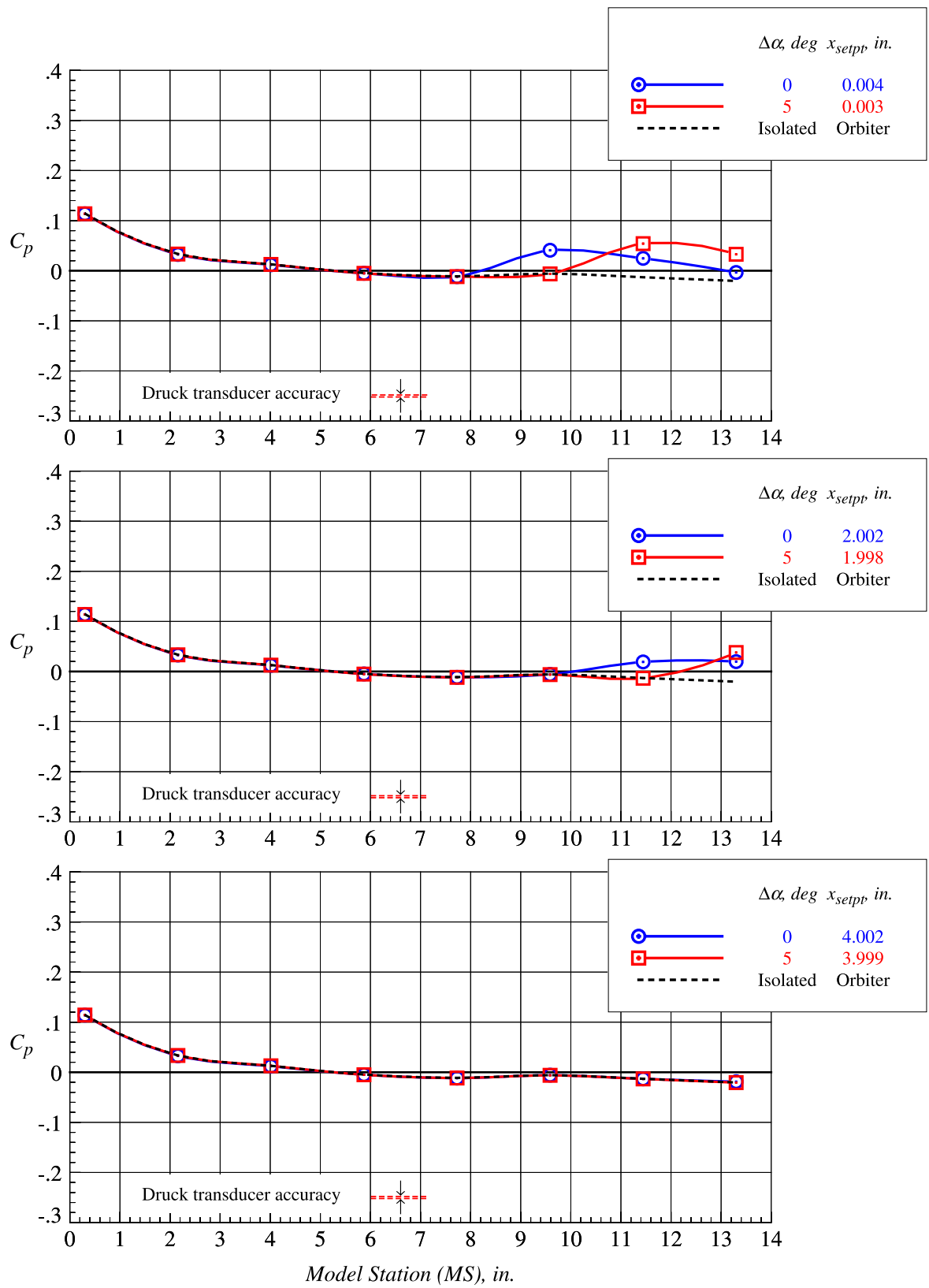
(g)  $z_{setpt} = 2.625$  in.,  $x_{setpt} = 0, 2$ , and  $4$  in.

Figure 78. Continued.



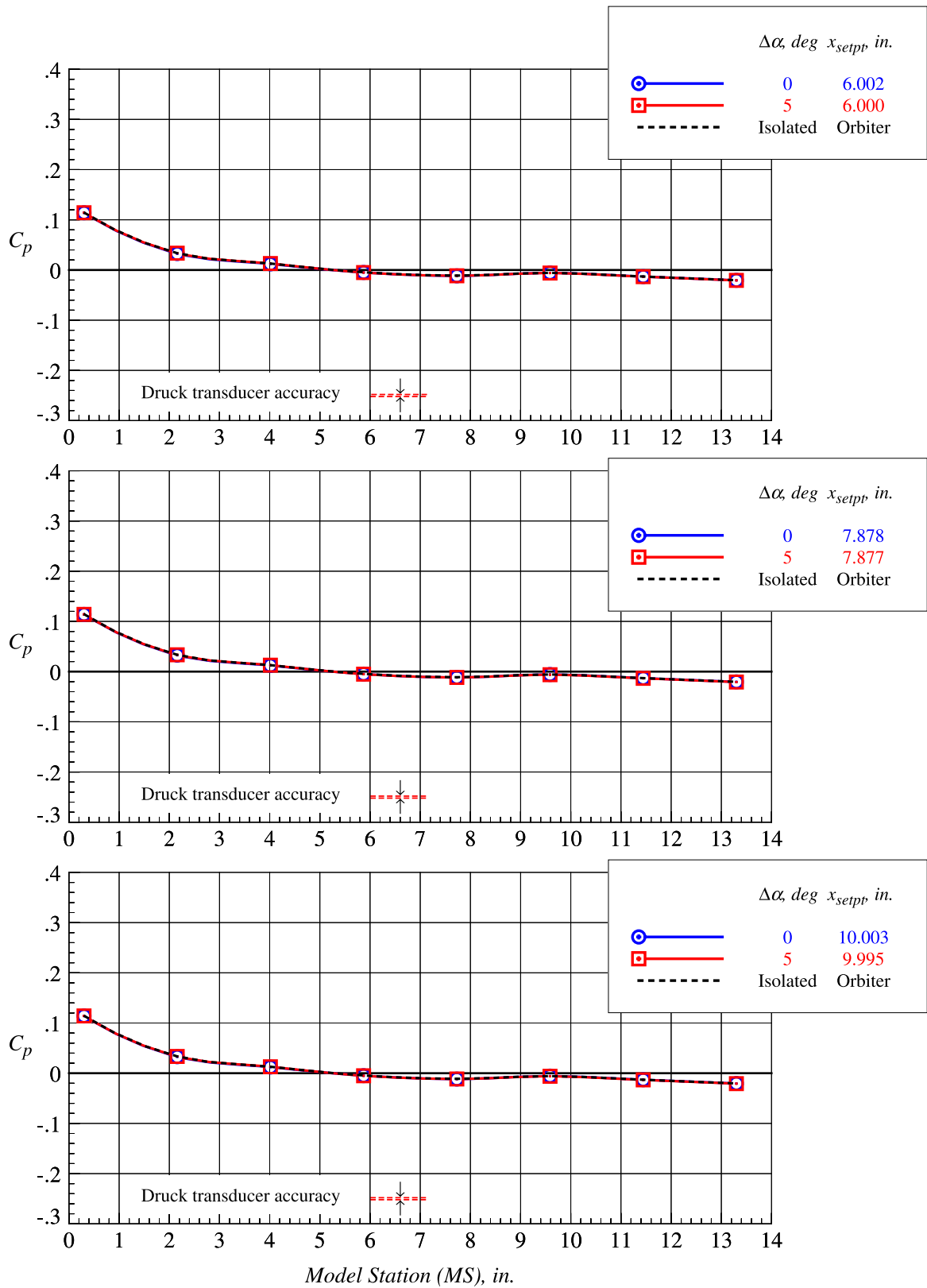
(h)  $z_{setpt} = 2.625$  in.,  $x_{setpt} = 6, 8$ , and  $10$  in.

Figure 78. Continued.



(i)  $z_{setpt} = 3.281$  in.,  $x_{setpt} = 0, 2$ , and 4 in.

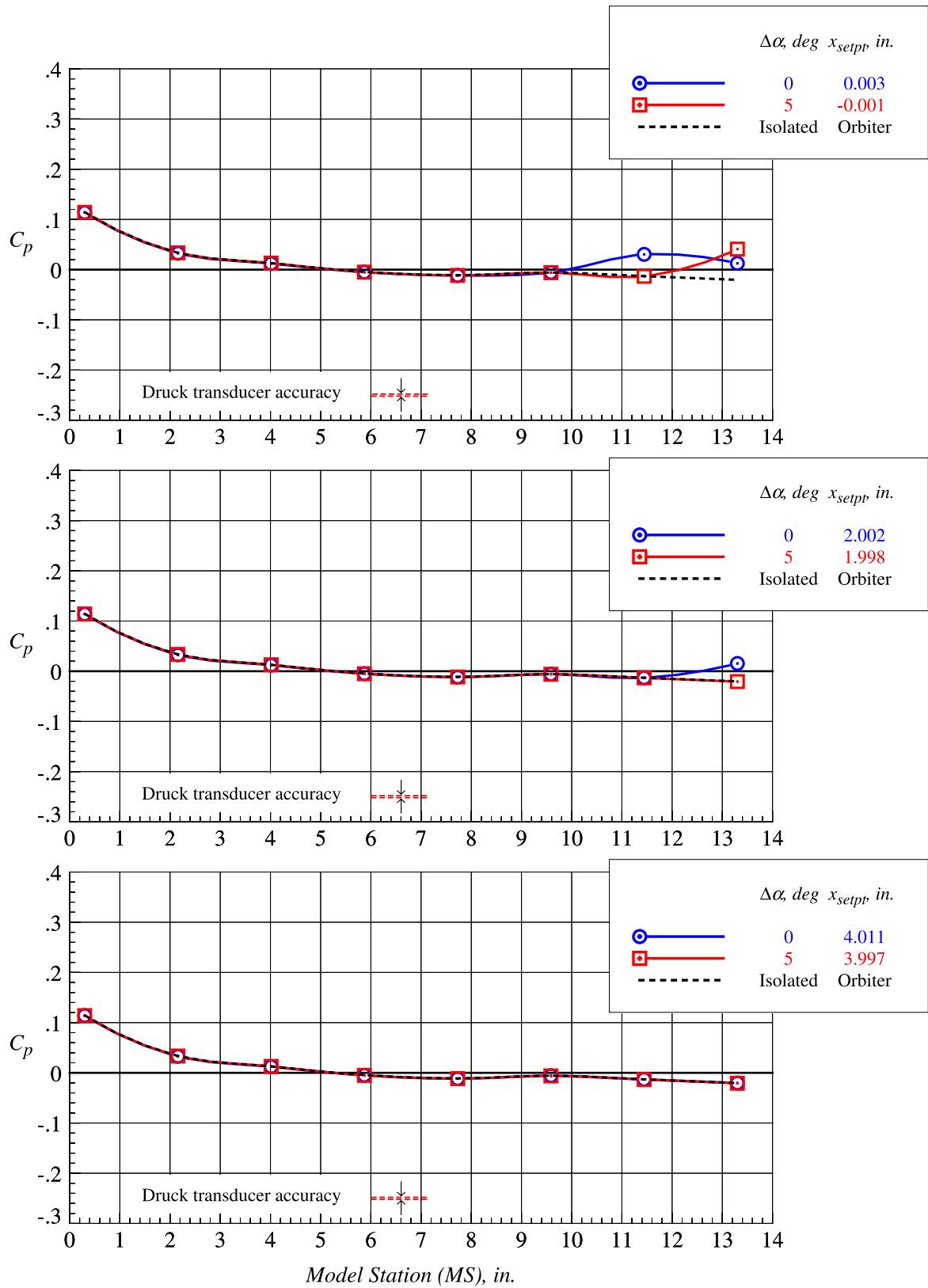
Figure 78. Continued.



(j)  $z_{setpt} = 3.281$  in.,  $x_{setpt} = 6, 8$ , and  $10$  in.

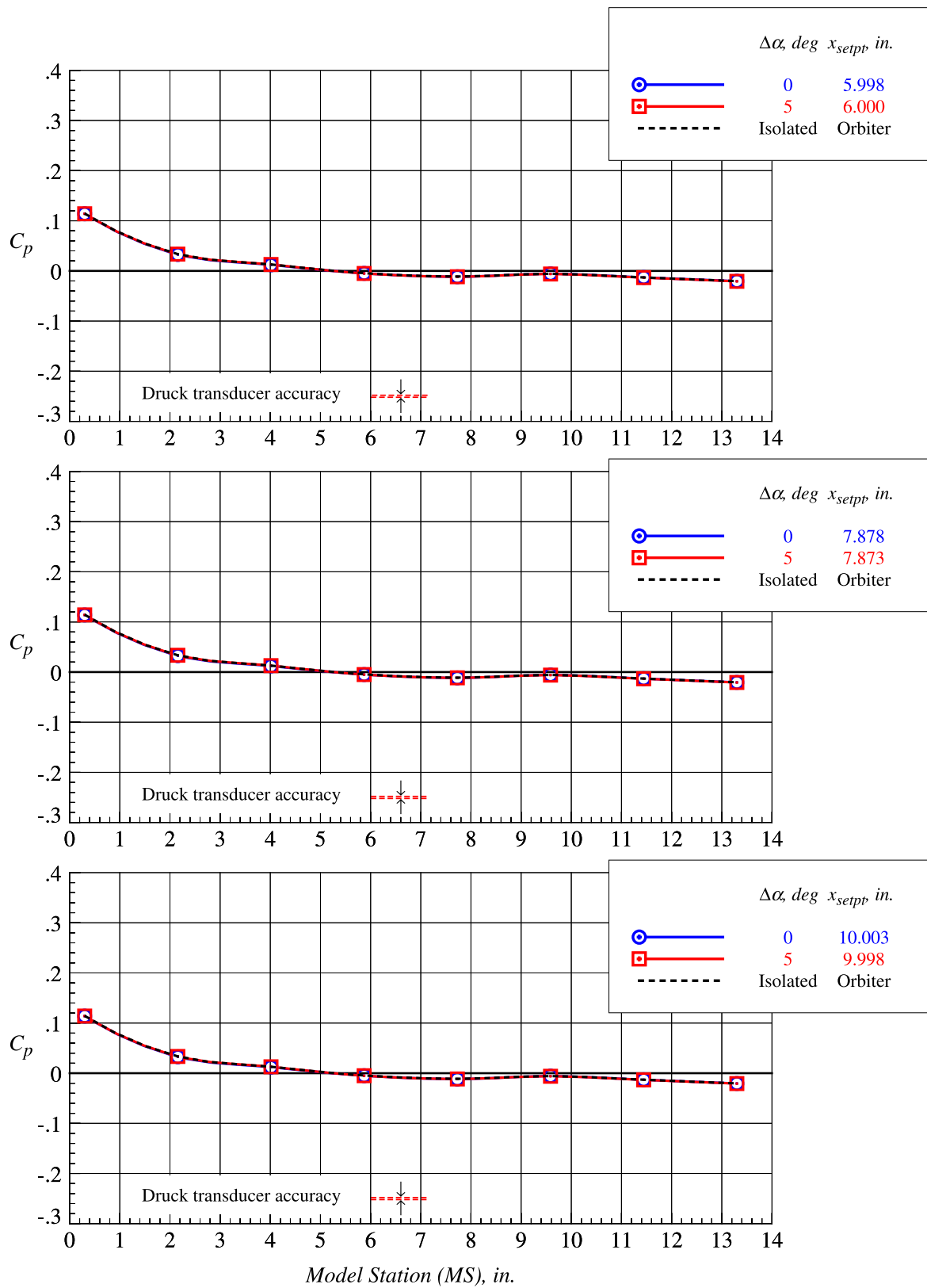
Figure 78. Continued.





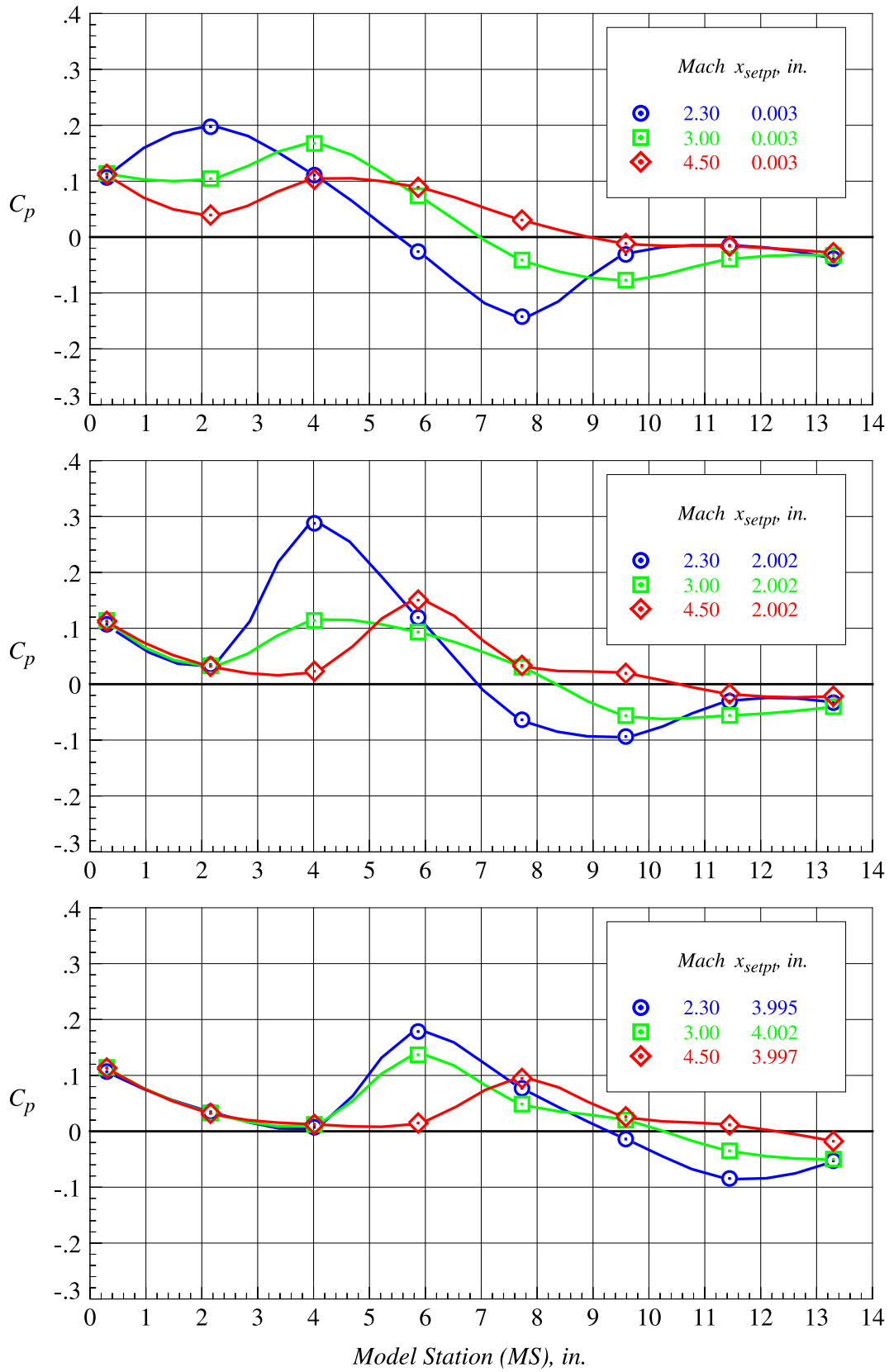
(k)  $z_{setpt} = 3.938$  in.,  $x_{setpt} = 0, 2$ , and 4 in.

Figure 78. Continued.



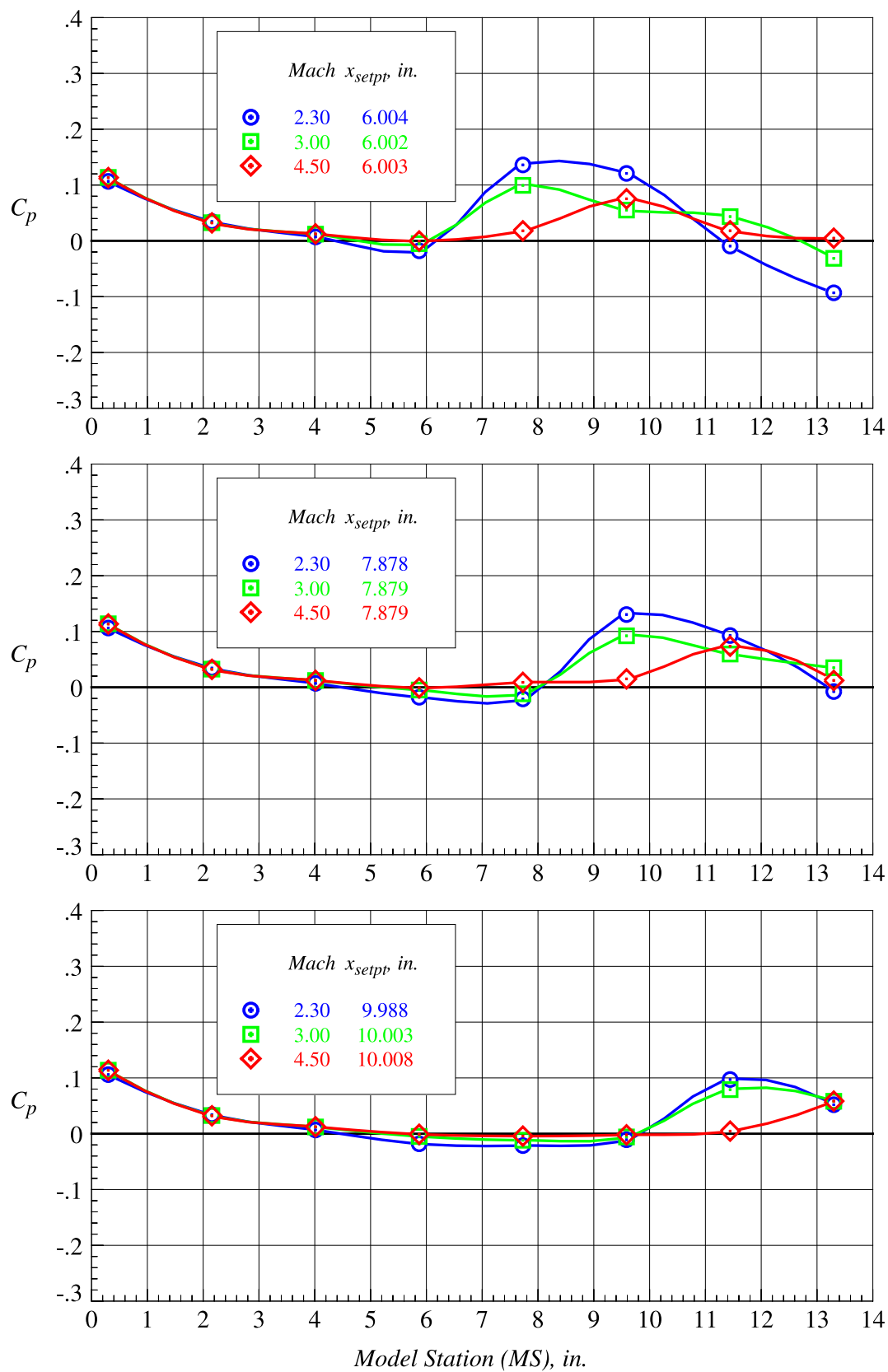
(l)  $z_{setpt} = 3.938$  in.,  $x_{setpt} = 6, 8$ , and  $10$  in.

Figure 78. Concluded.



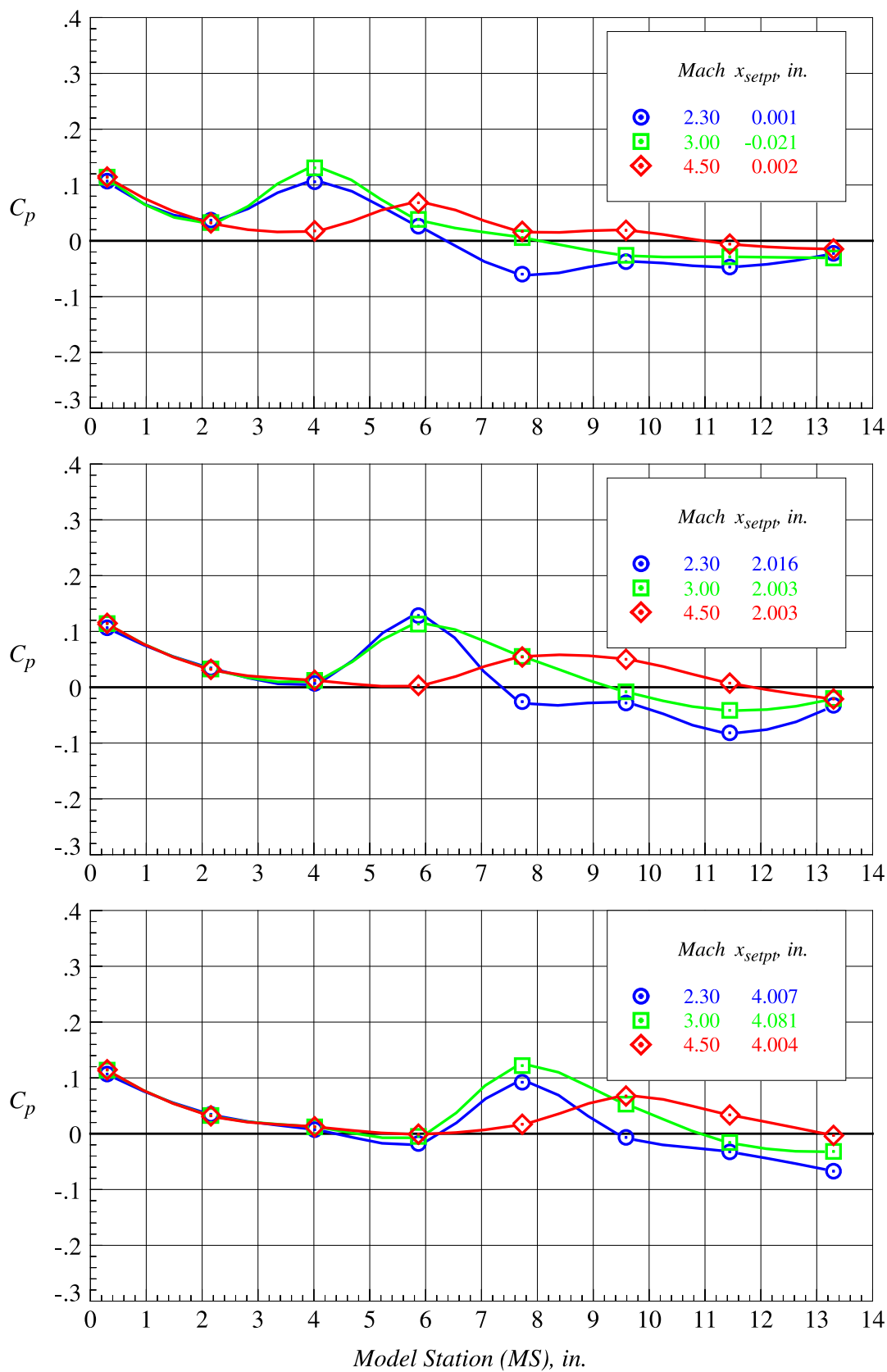
(a)  $z_{setpt} = 0$  in.,  $x_{setpt} = 0, 2$ , and  $4$  in.

Figure 79. Orbiter proximity surface static pressure distributions on fuselage centerline lower surface at Mach = 2.3, 3.0, and 4.5 and  $\Delta\alpha = 0^\circ$ .



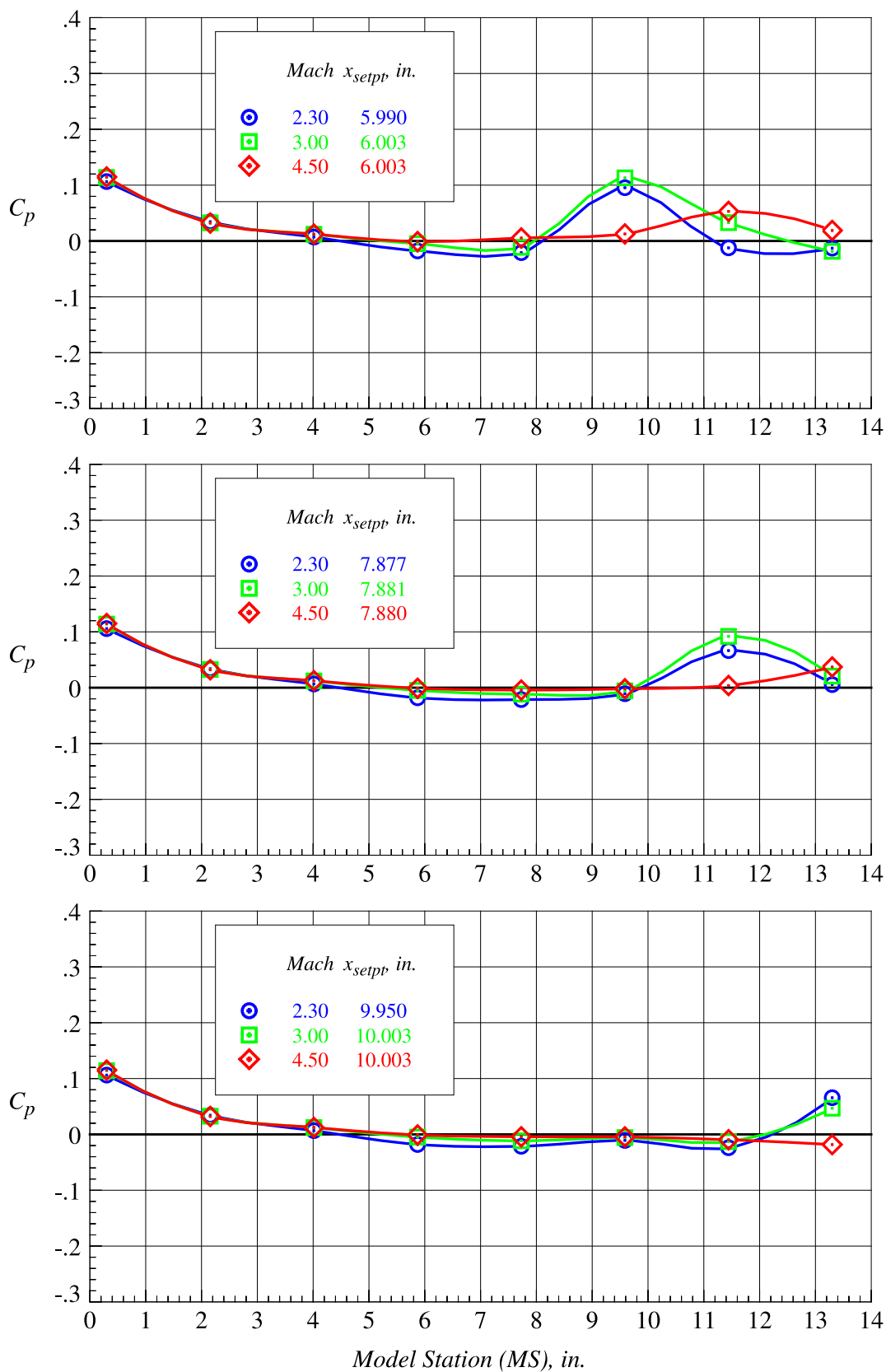
(b)  $z_{setpt} = 0$  in.,  $x_{setpt} = 6, 8,$  and  $10$  in.

Figure 79. Continued.



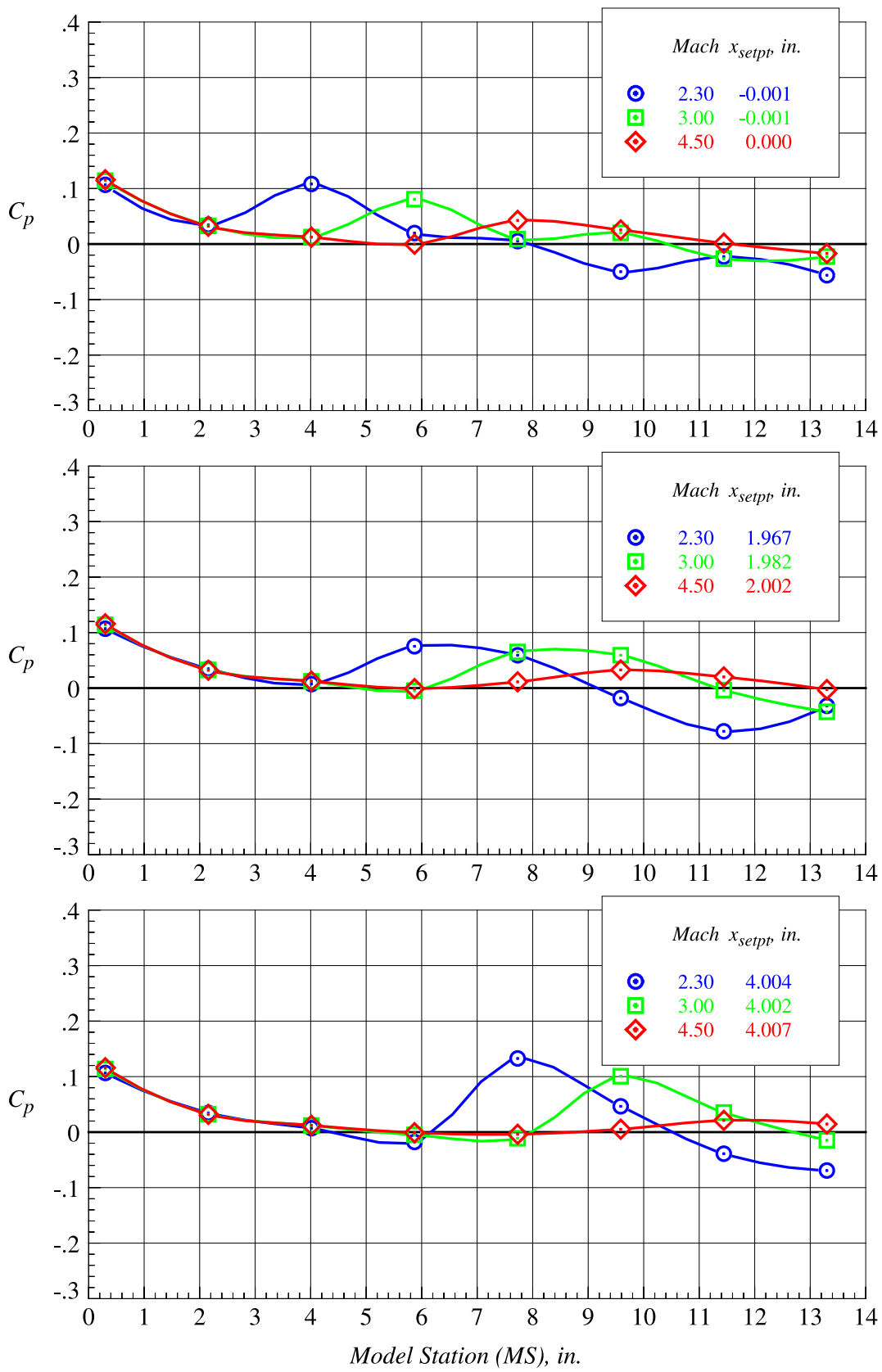
(c)  $z_{sept} = 0.656$  in.,  $x_{sept} = 0, 2$ , and  $4$  in.

Figure 79. Continued.



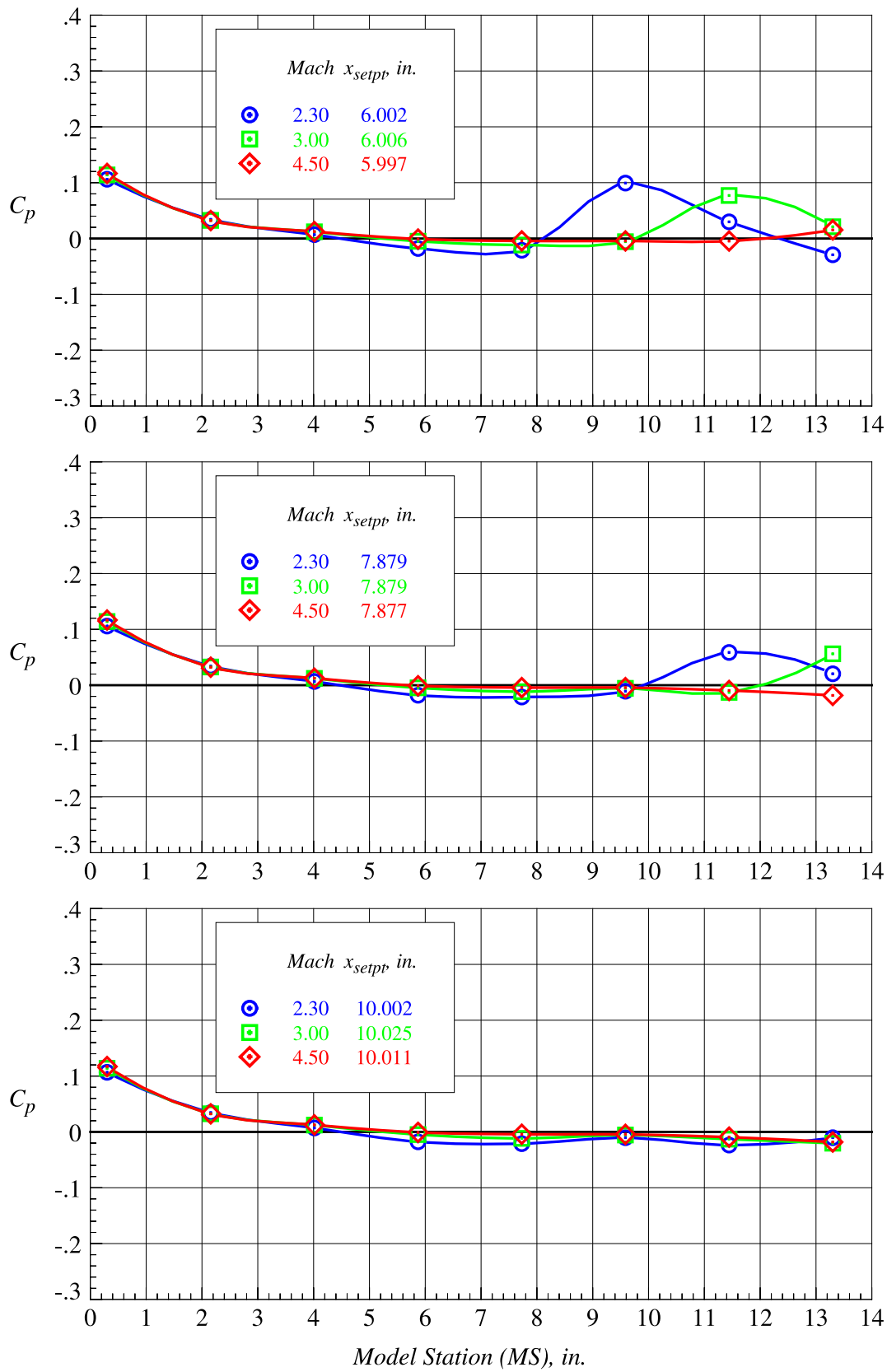
(d)  $z_{setpt} = 0.656$  in.,  $x_{setpt} = 6, 8,$  and  $10$  in.

Figure 79. Continued.



(e)  $z_{setpt} = 1.313$  in.,  $x_{setpt} = 0, 2$ , and  $4$  in.

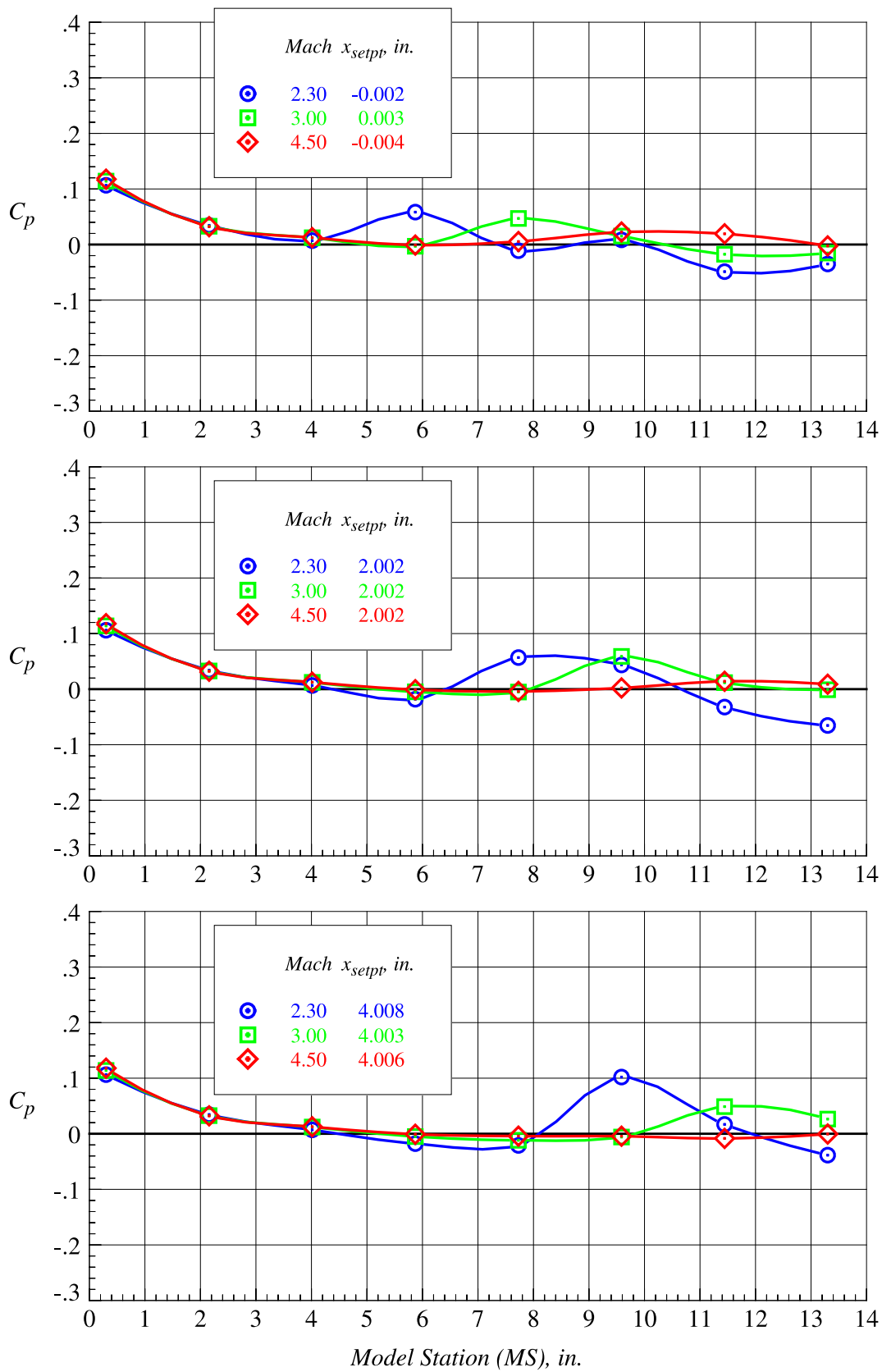
Figure 79. Continued.



(f)  $z_{setpt} = 1.313$  in.,  $x_{setpt} = 6, 8,$  and  $10$  in.

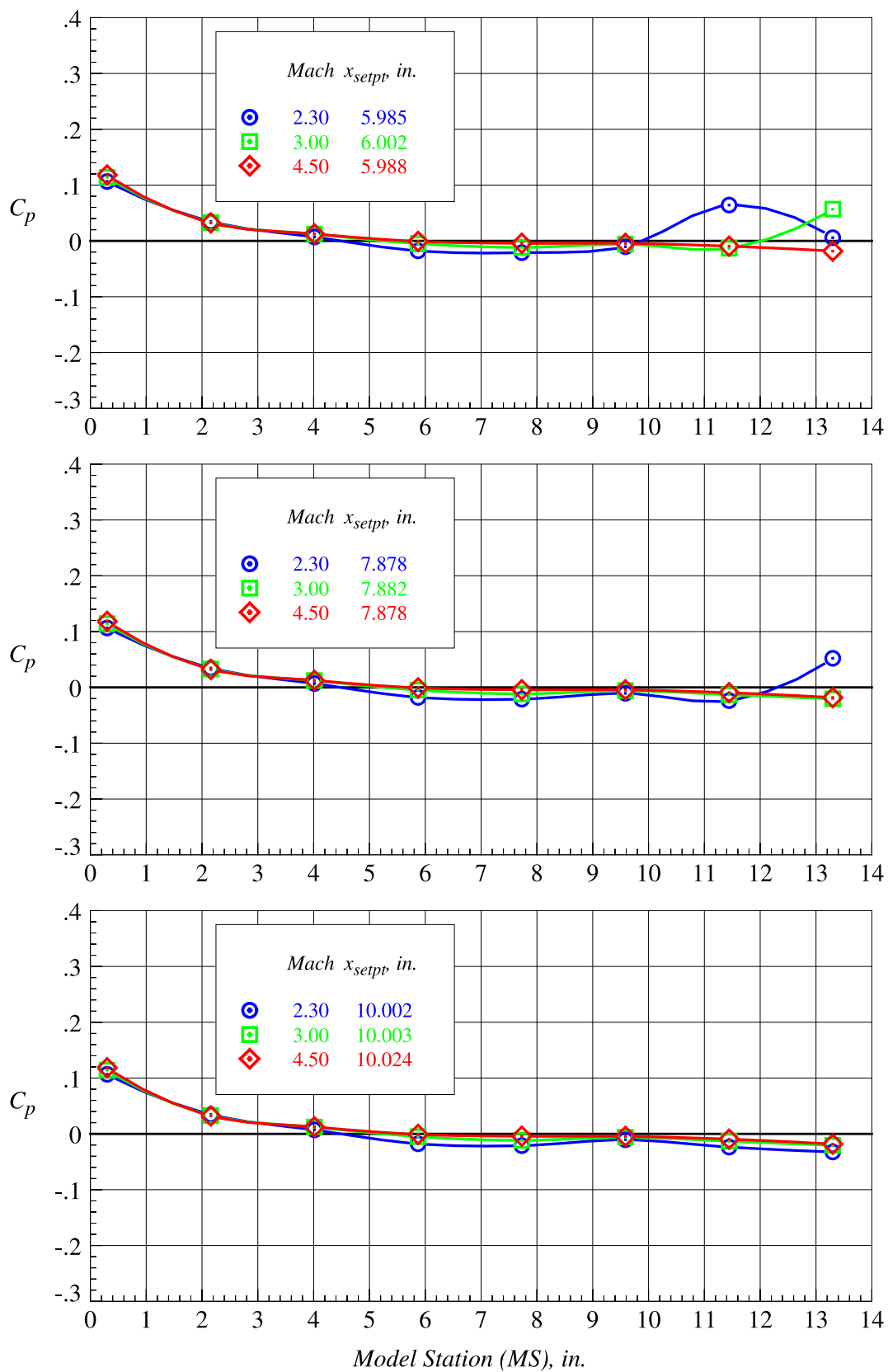
Figure 79. Continued.





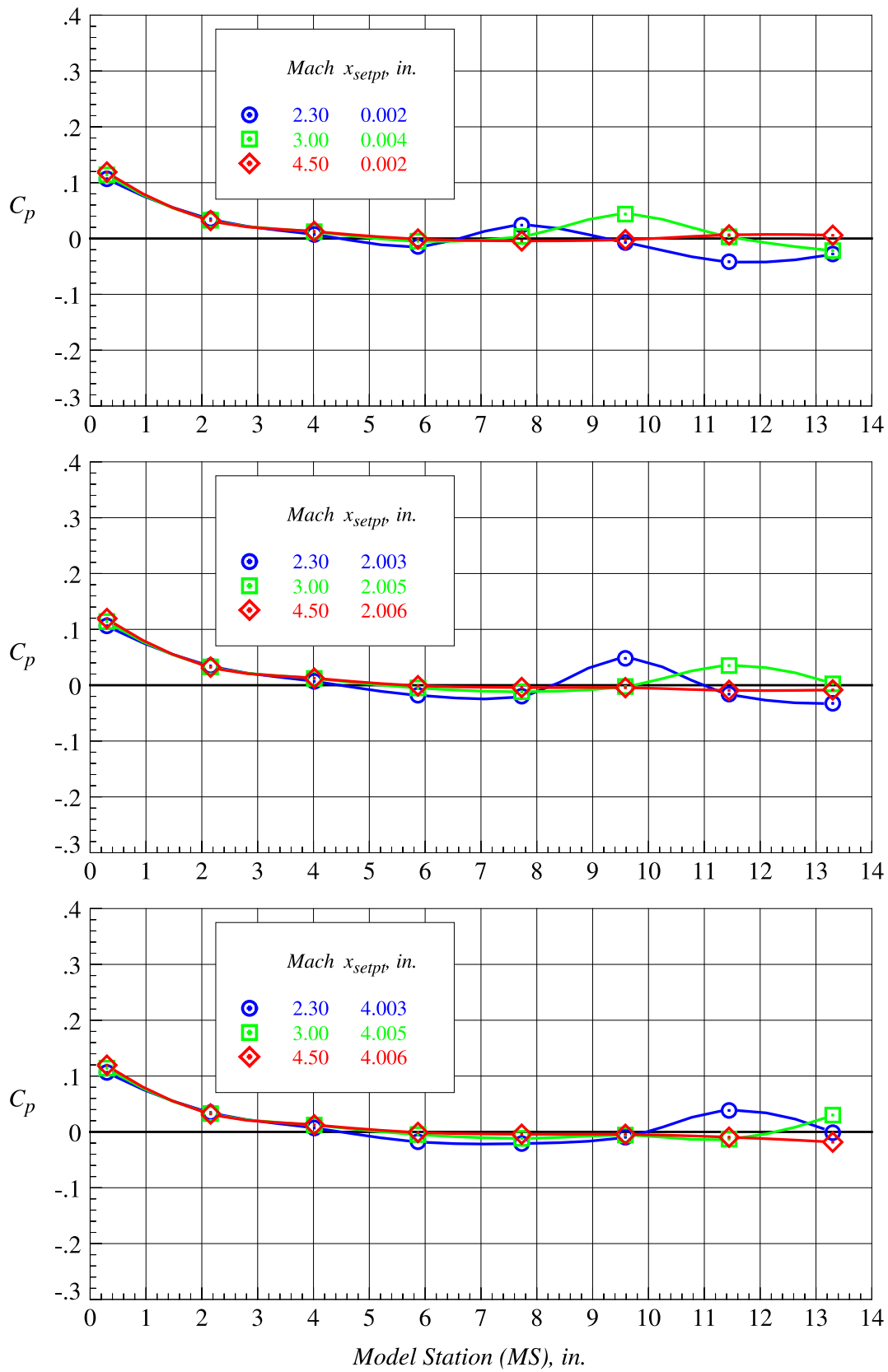
(g)  $z_{setpt} = 1.969$  in.,  $x_{setpt} = 0, 2$ , and 4 in.

Figure 79. Continued.



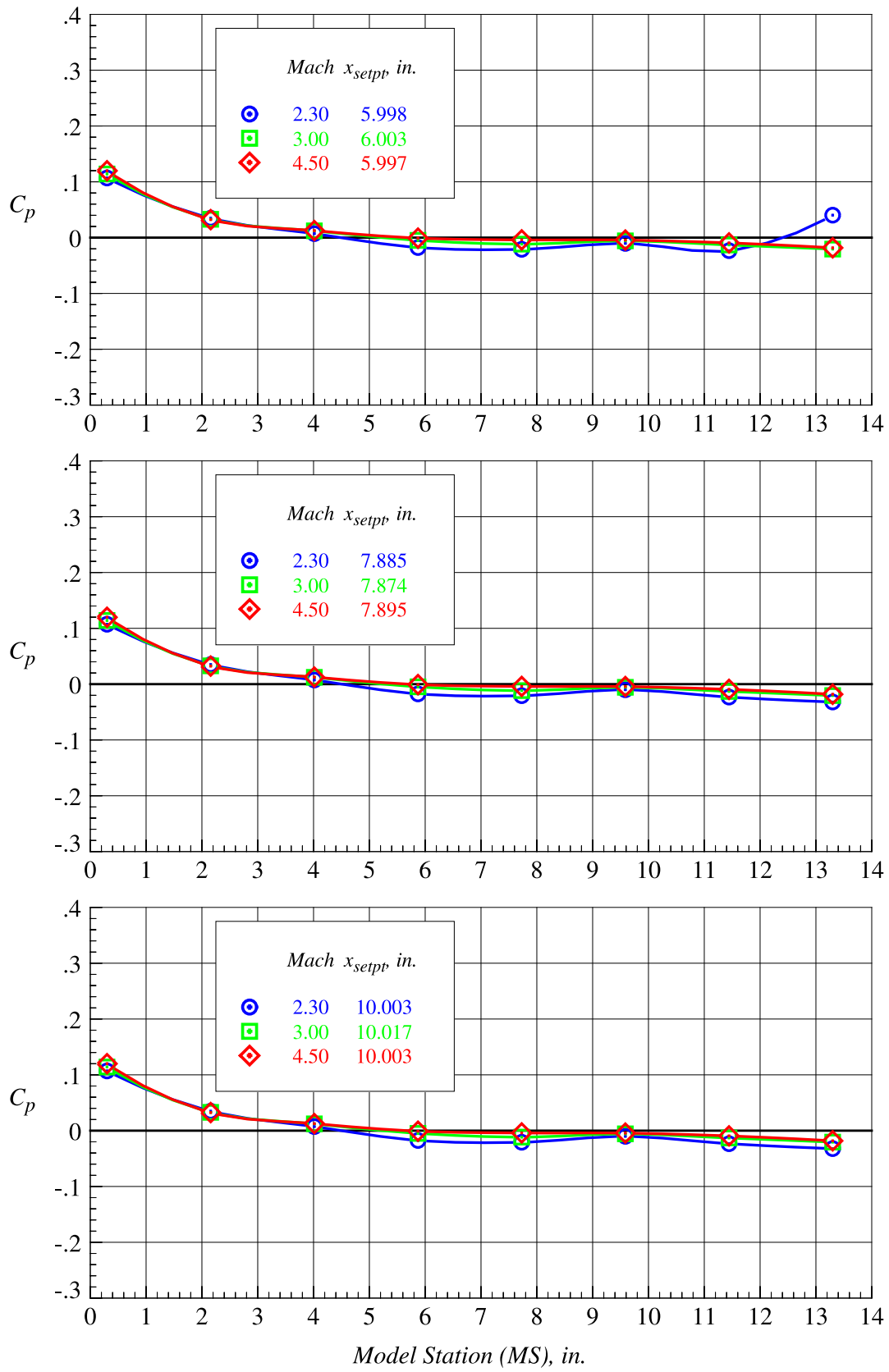
(h)  $z_{setpt} = 1.969$  in.,  $x_{setpt} = 6, 8,$  and  $10$  in.

Figure 79. Continued.



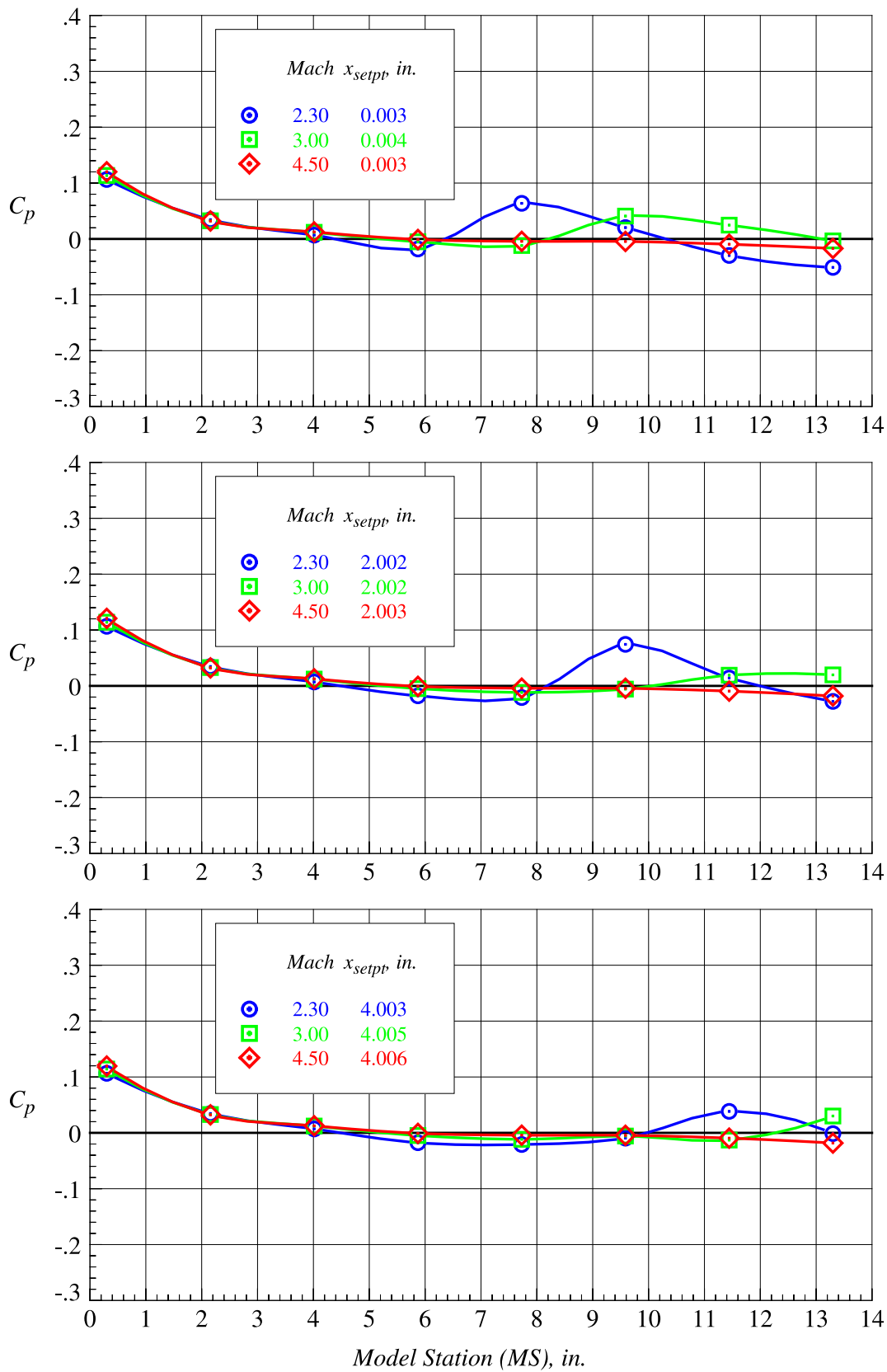
(i)  $z_{setpt} = 2.625$  in.,  $x_{setpt} = 0, 2$ , and 4 in.

Figure 79. Continued.



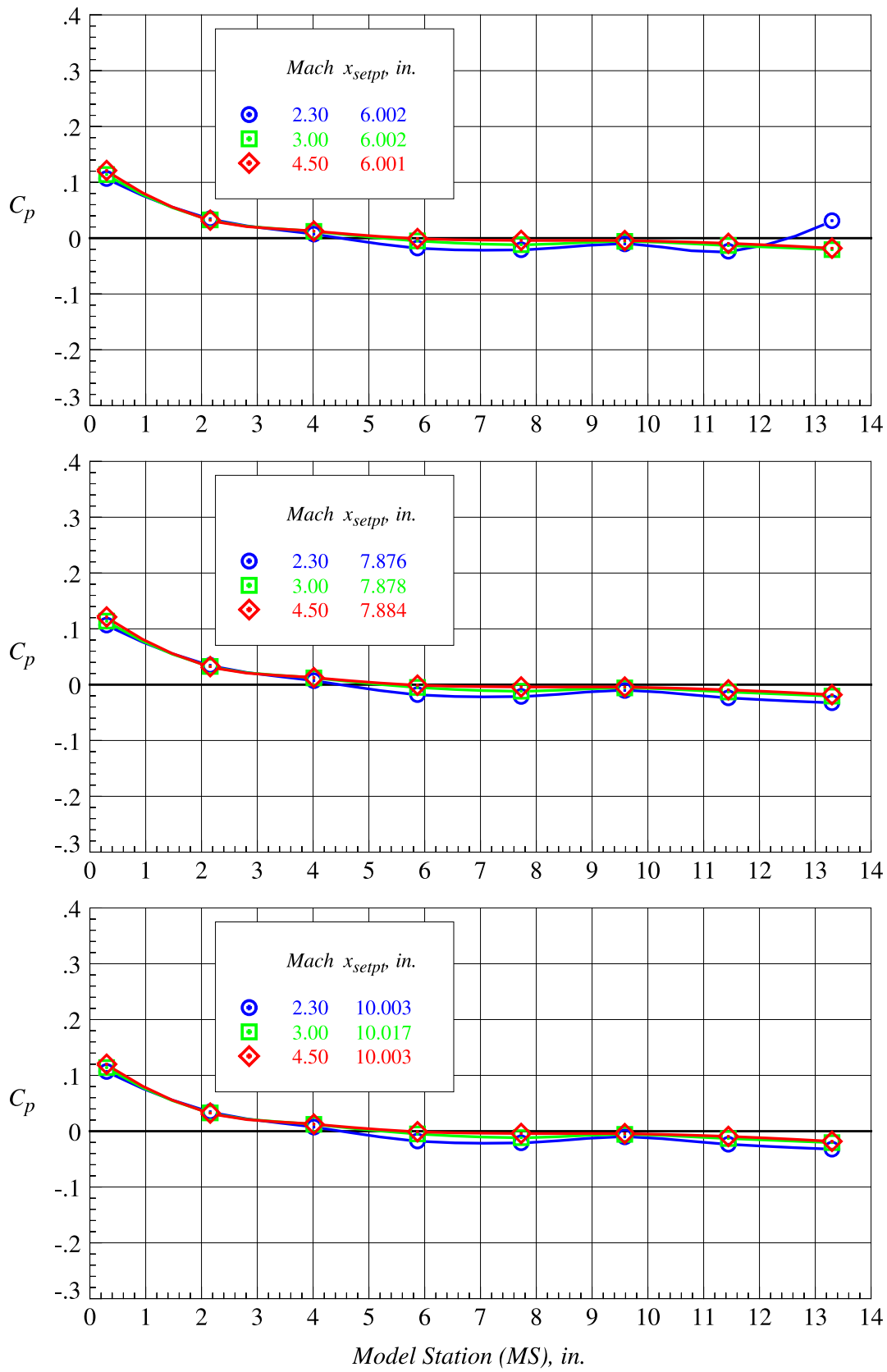
(j)  $z_{setpt} = 2.625$  in.,  $x_{setpt} = 6, 8,$  and  $10$  in.

Figure 79. Continued.



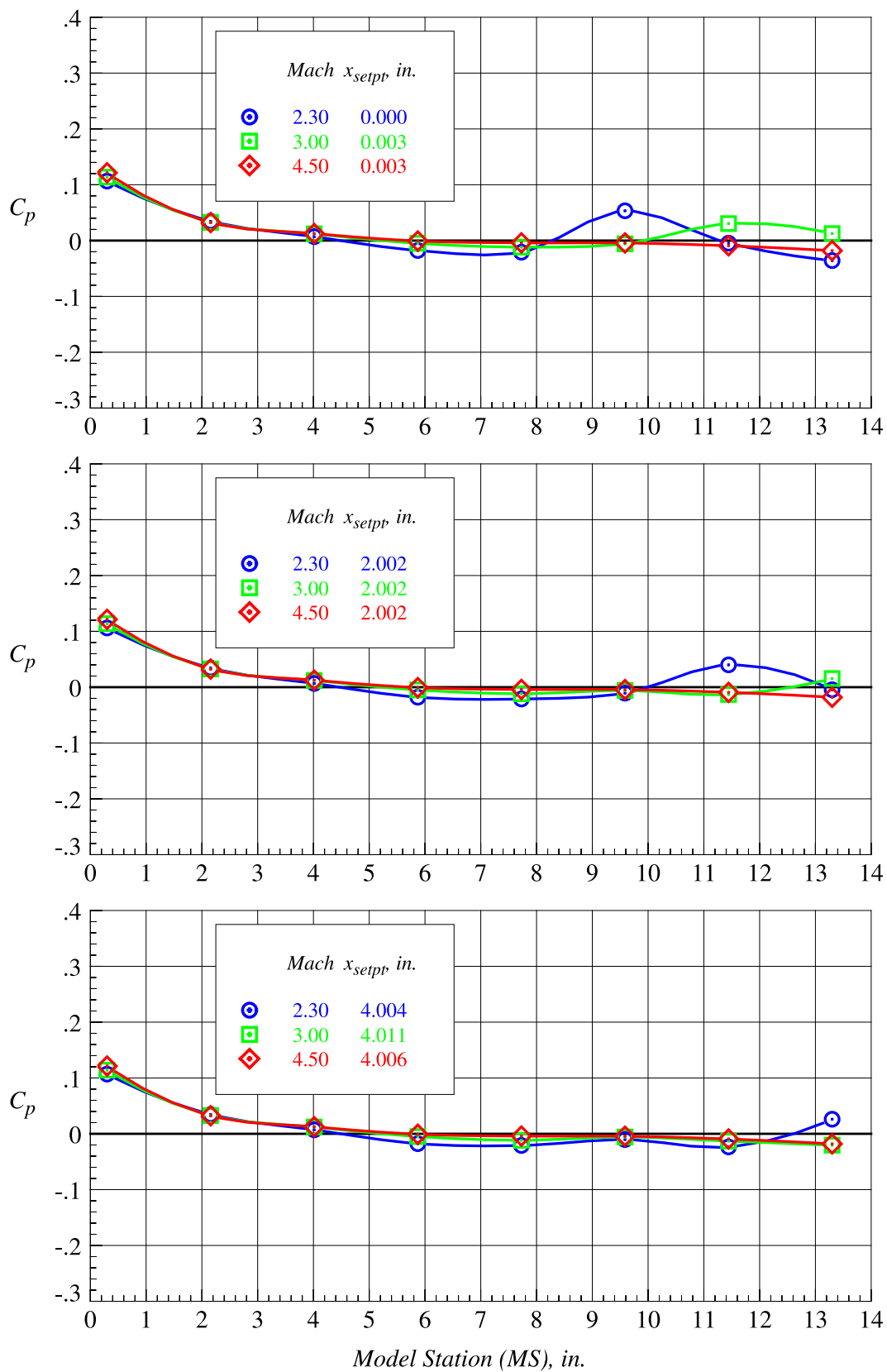
(k)  $z_{setpt} = 3.281$  in.,  $x_{setpt} = 0, 2$ , and  $4$  in.

Figure 79. Continued.



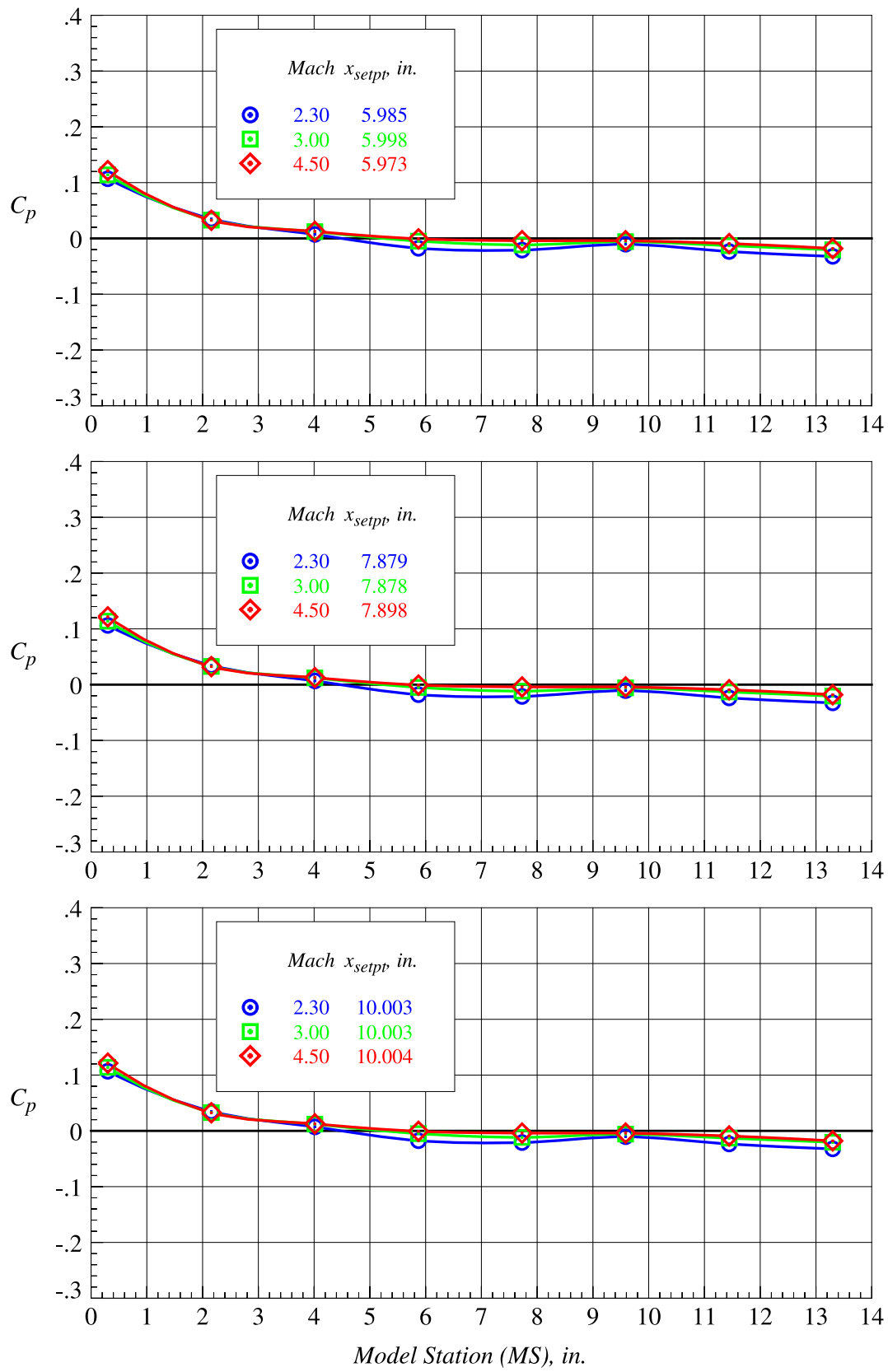
(l)  $z_{setpt} = 3.281$  in.,  $x_{setpt} = 6, 8,$  and  $10$  in.

Figure 79. Continued.



(m)  $z_{setpt} = 3.978$  in.,  $x_{setpt} = 0, 2$ , and  $4$  in.

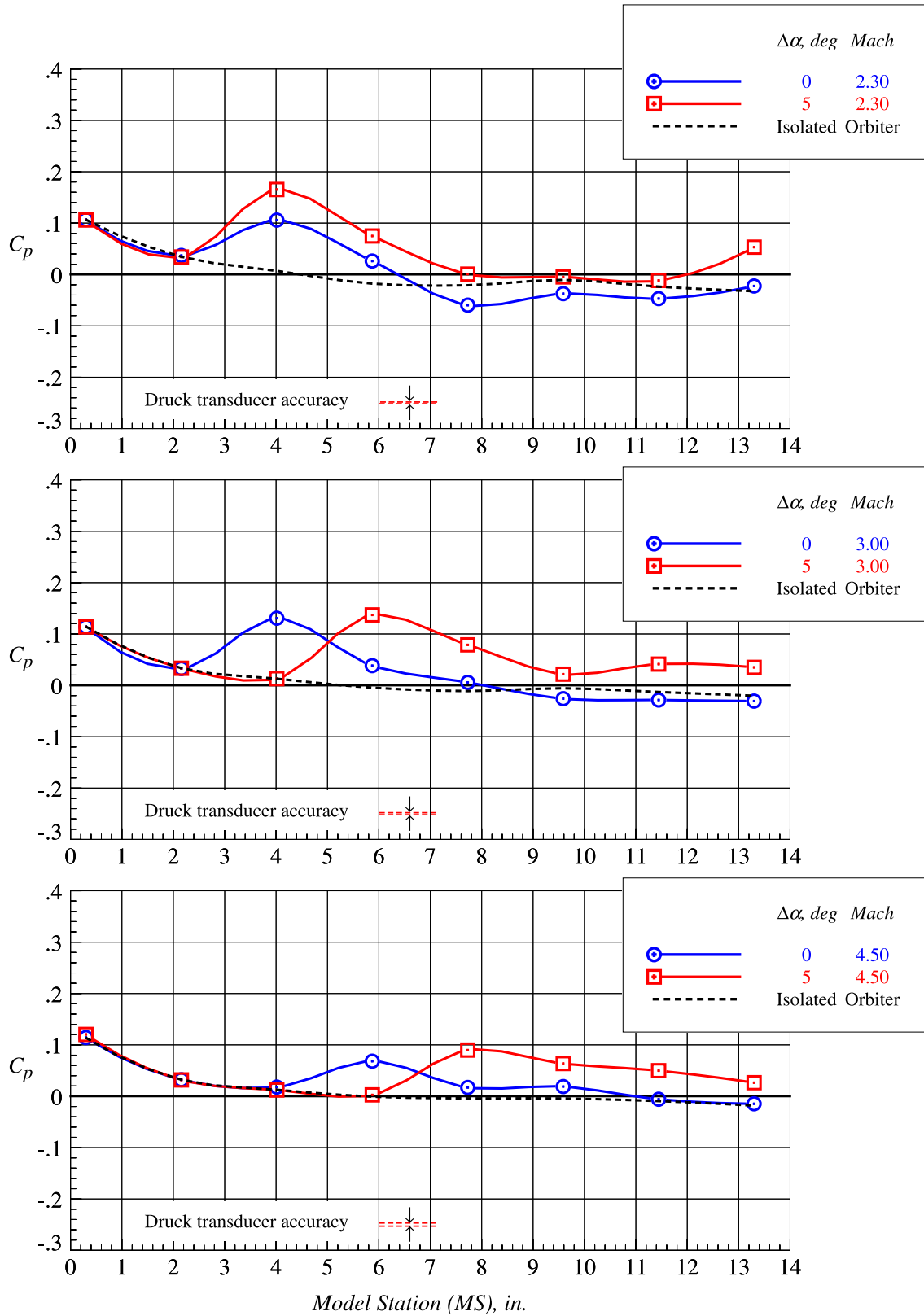
Figure 79. Continued.



(n)  $z_{setpt} = 3.978$  in.,  $x_{setpt} = 6, 8,$  and  $10$  in.

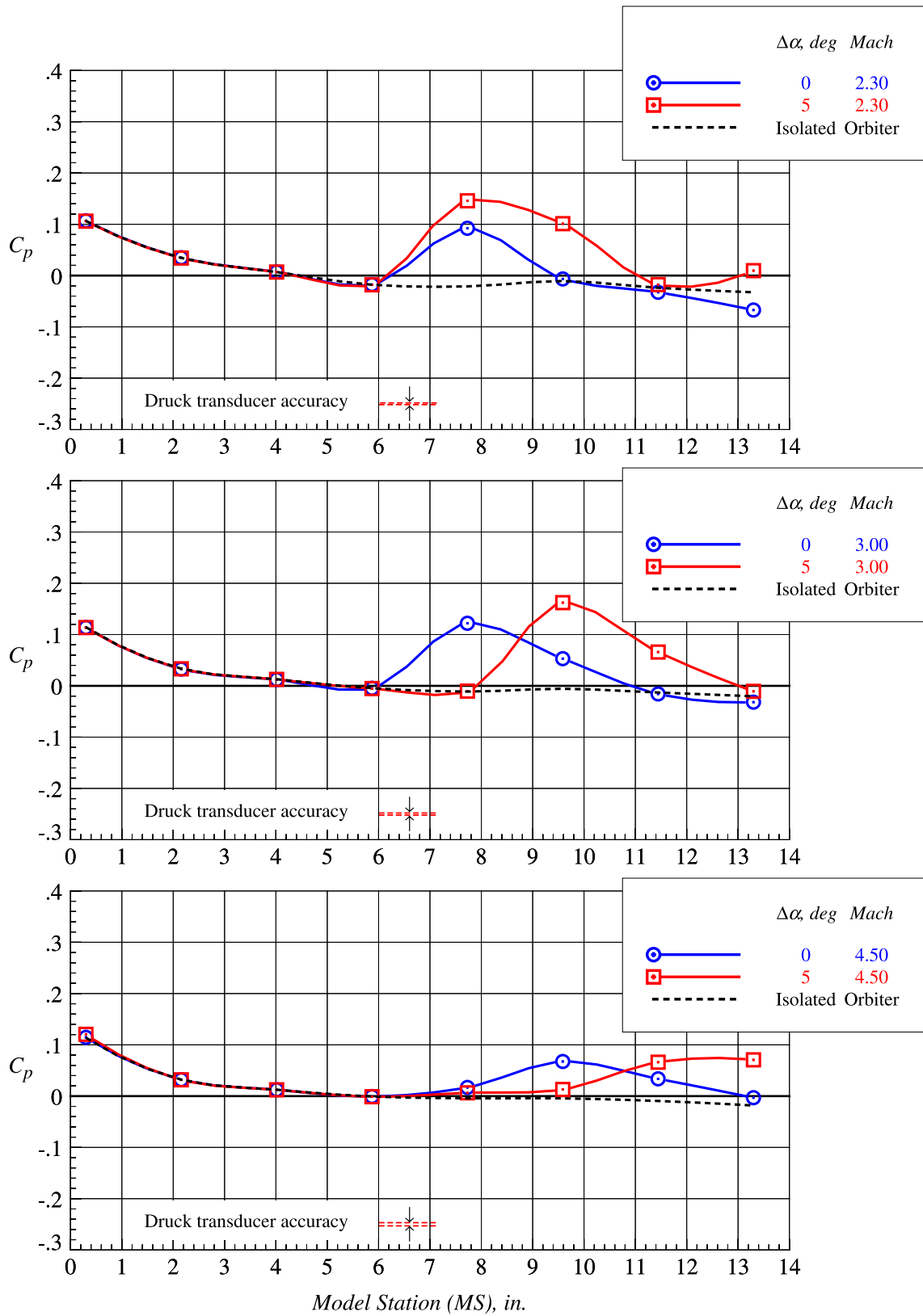
Figure 79. Concluded.





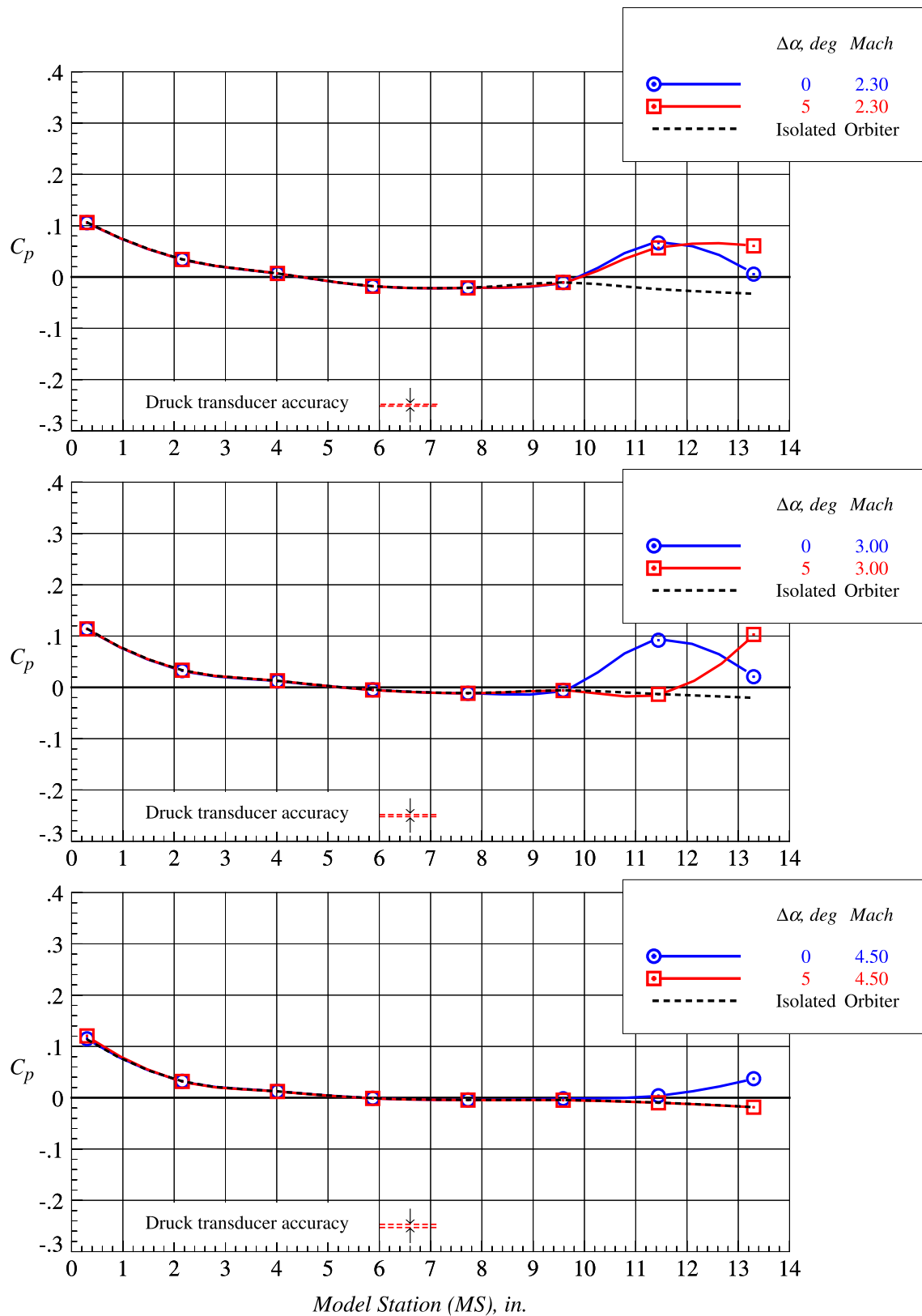
(a)  $z_{setpt} = 0.656$  in.,  $x_{setpt} = 0$  in.

Figure 80. Orbiter proximity surface static pressure distributions on fuselage centerline lower surface at  $\Delta\alpha = 0^\circ$  and  $5^\circ$  and  $Mach = 2.3, 3.0$ , and  $4.5$ .



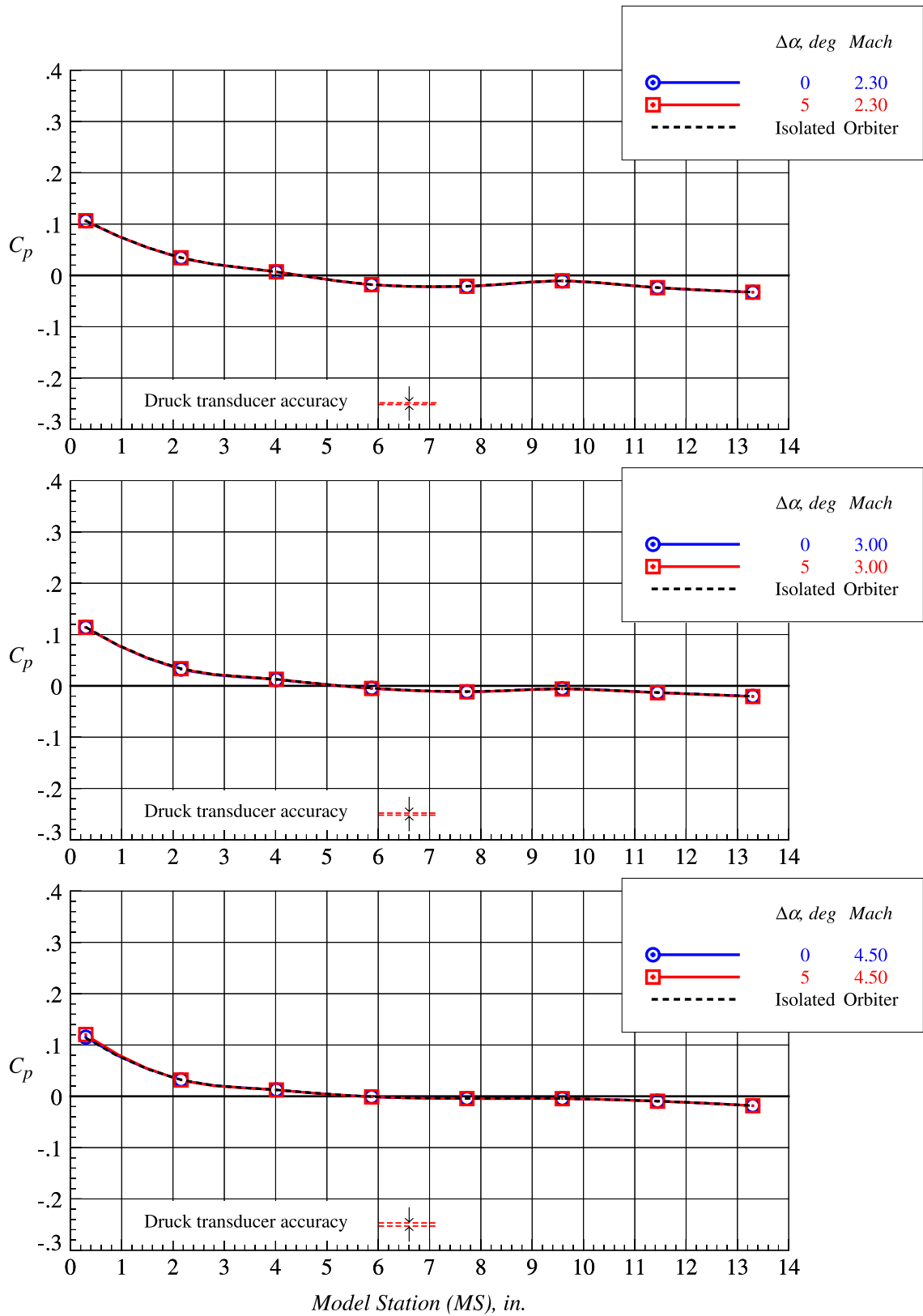
(b)  $z_{setpt} = 0.656$  in.,  $x_{setpt} = 4$  in.

Figure 80. Continued.



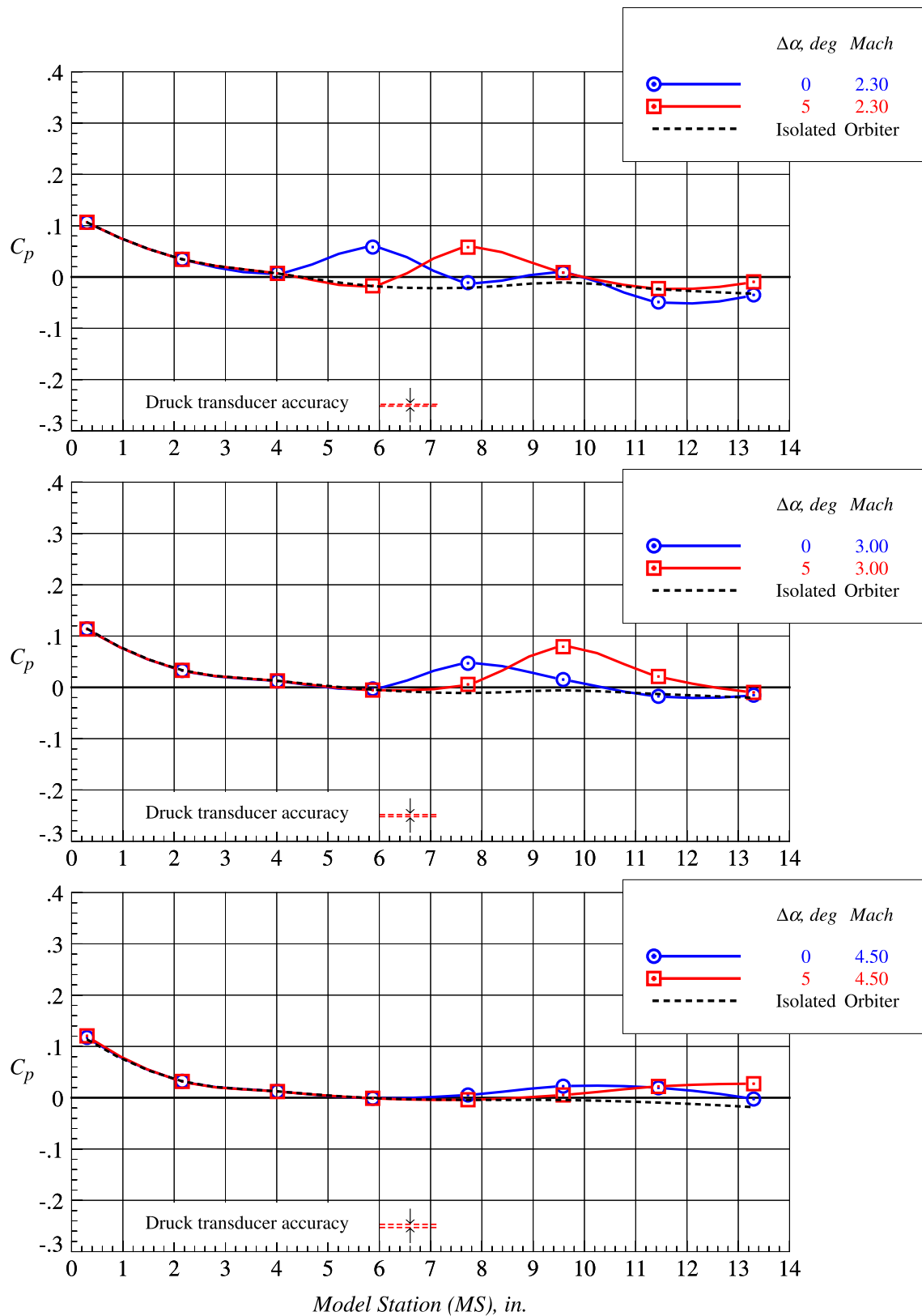
(c)  $z_{setpt} = 0.656$  in.,  $x_{setpt} = 8$  in.

Figure 80. Continued.



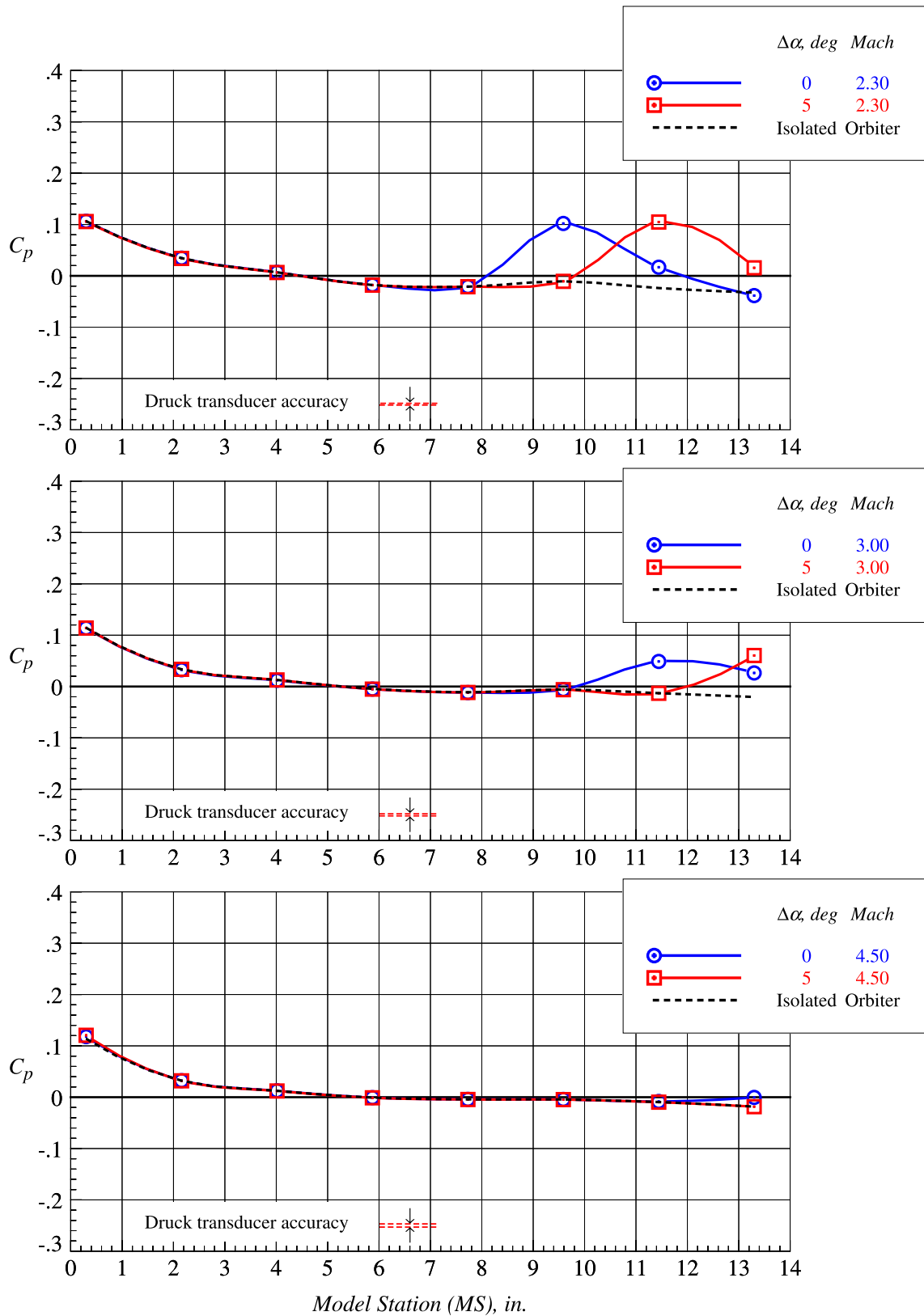
(d)  $z_{setpt} = 0.656$  in.,  $x_{setpt} = 12$  in.

Figure 80. Continued.



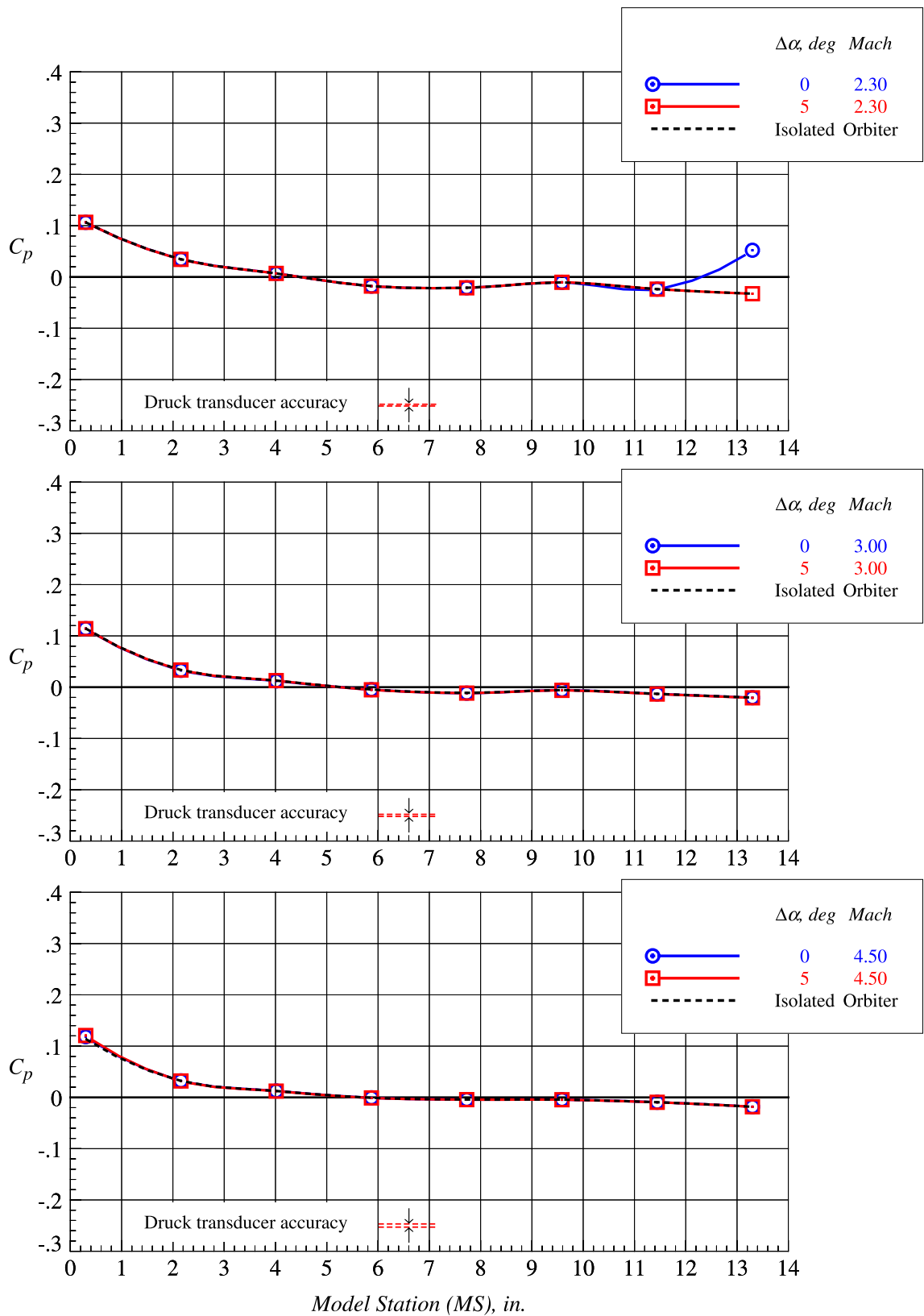
(e)  $z_{setpt} = 1.919$  in.,  $x_{setpt} = 0$  in.

Figure 80. Continued.



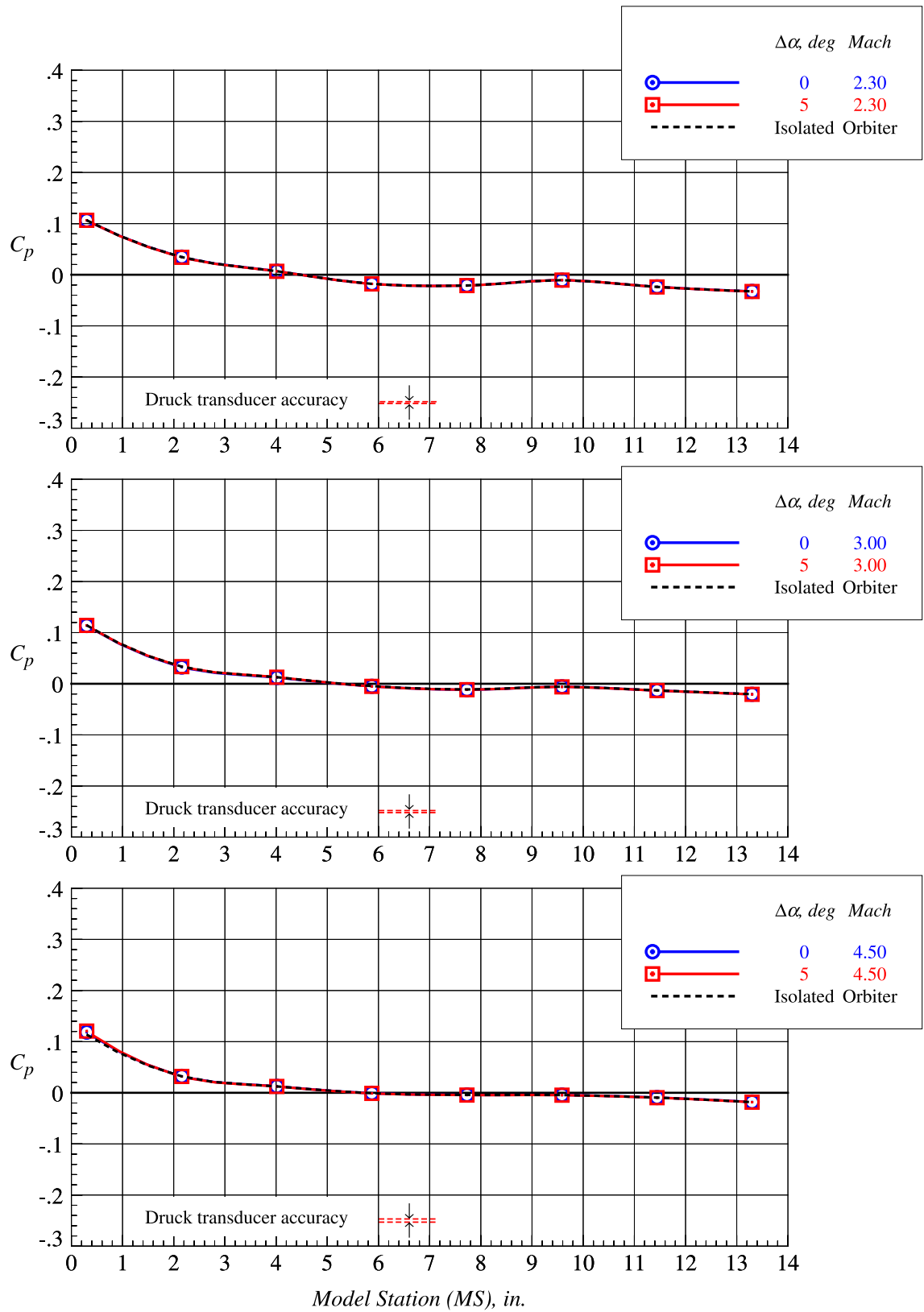
(f)  $z_{setpt} = 1.919$  in.,  $x_{setpt} = 4$  in.

Figure 80. Continued.



(g)  $z_{setpt} = 1.919$  in.,  $x_{setpt} = 8$  in.

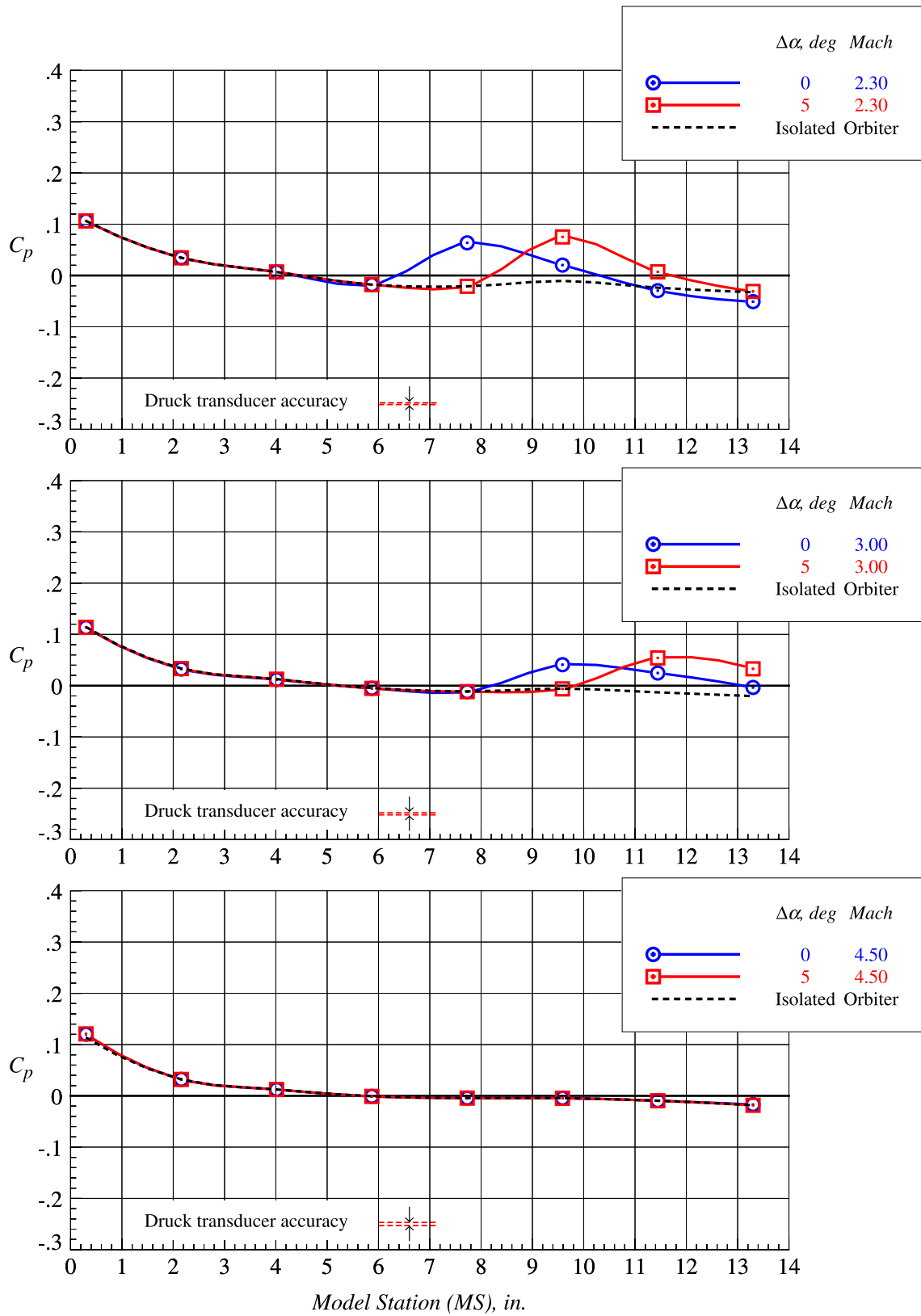
Figure 80. Continued.



(h)  $z_{setpt} = 1.919 \text{ in.}$ ,  $x_{setpt} = 12 \text{ in.}$

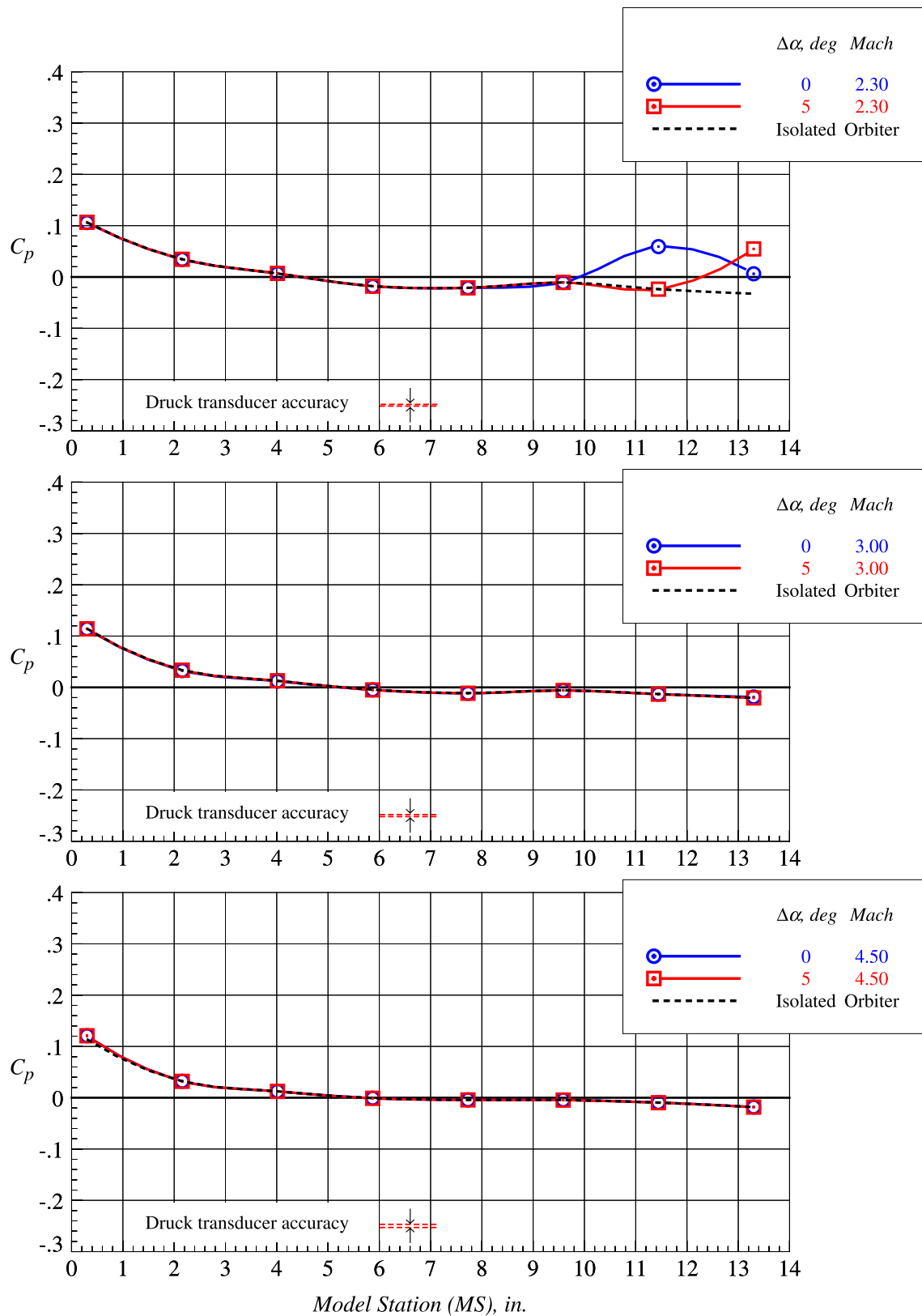
Figure 80. Continued.





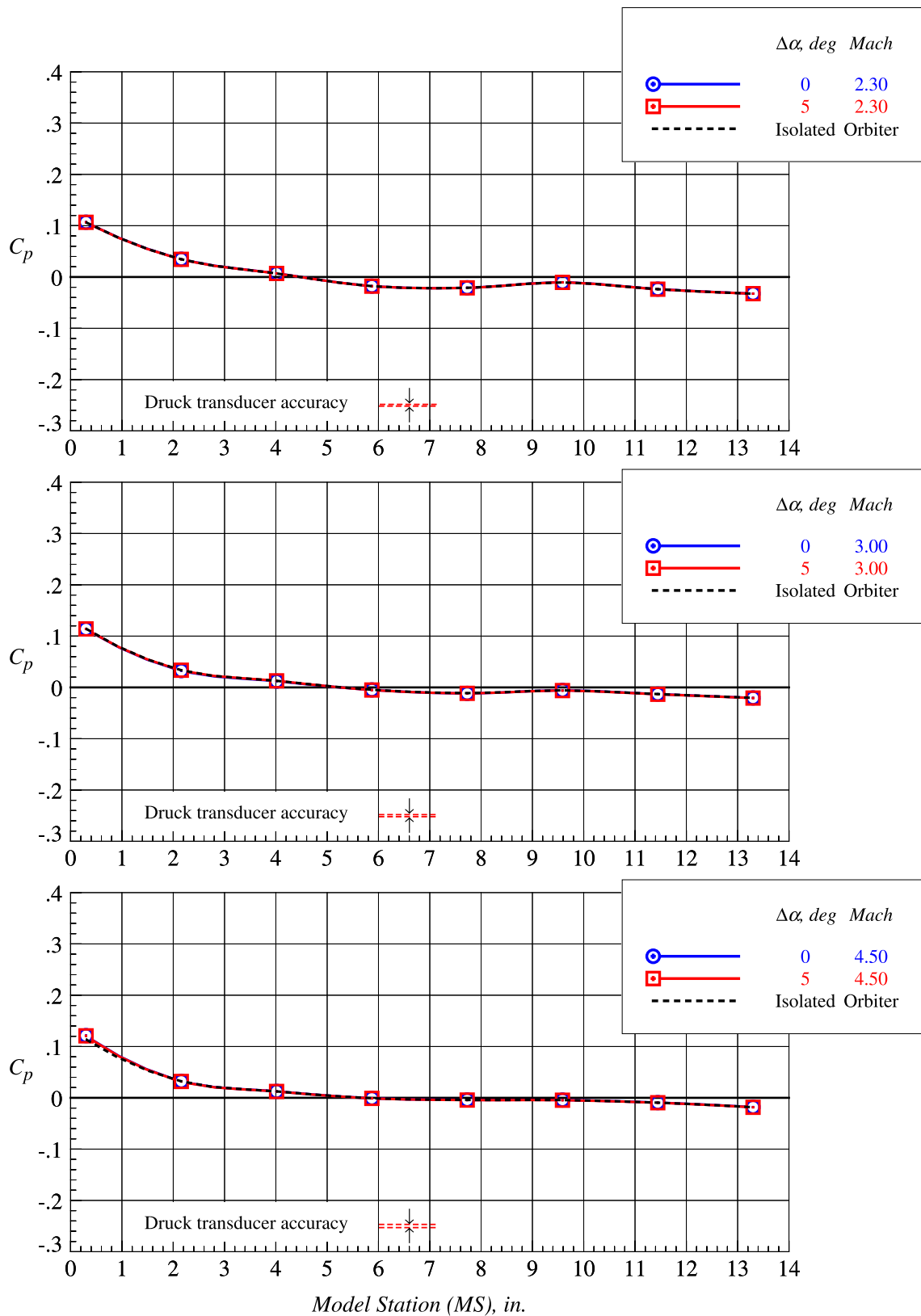
(i)  $z_{setpt} = 3.281$  in.,  $x_{setpt} = 0$  in.

Figure 80. Continued.



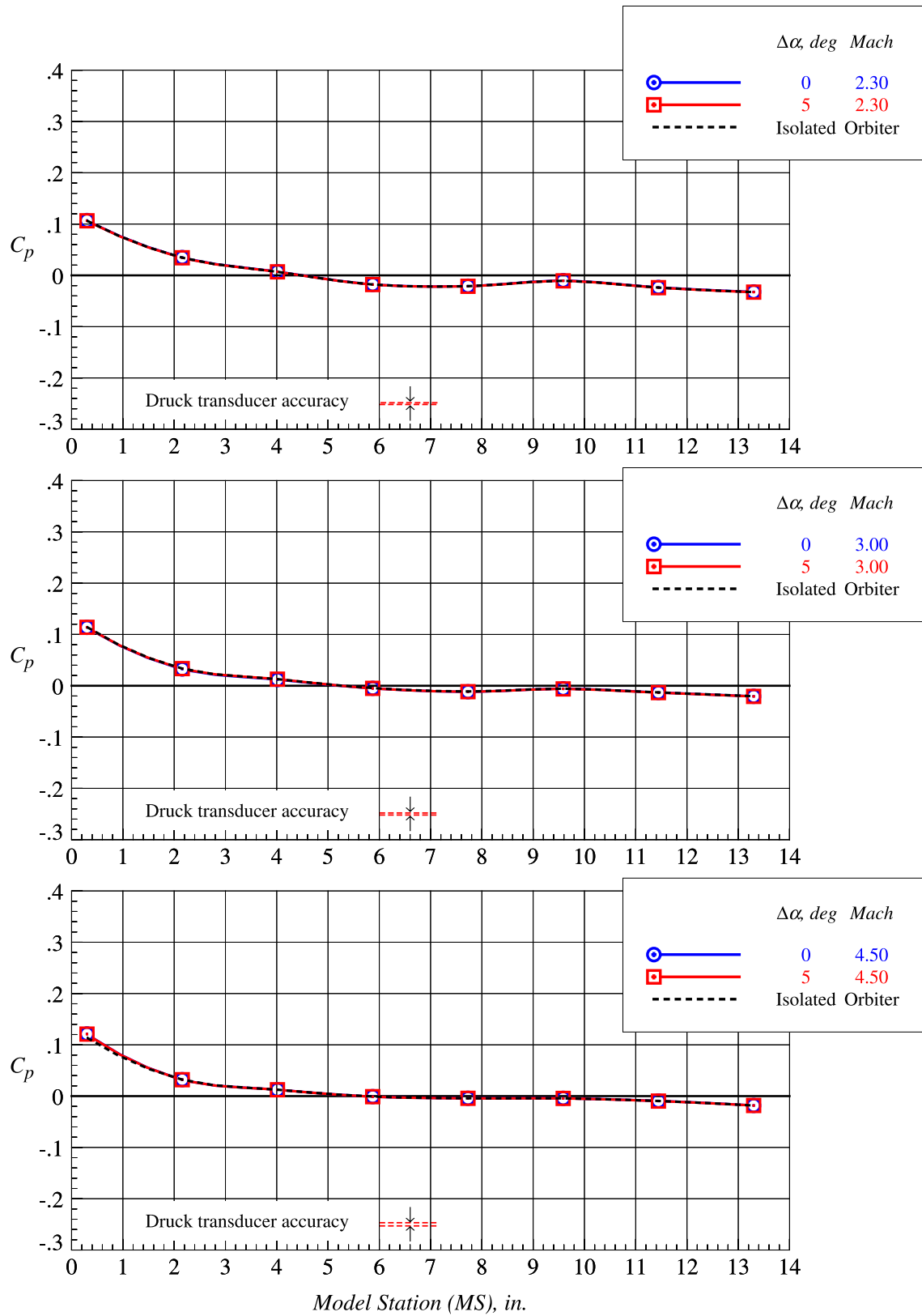
(j)  $z_{setpt} = 3.281$  in.,  $x_{setpt} = 4$  in.

Figure 80. Continued.



(k)  $z_{setpt} = 3.281$  in.,  $x_{setpt} = 8$  in.

Figure 80. Continued.



(l)  $z_{setpt} = 3.281$  in.,  $x_{setpt} = 12$  in.

Figure 80. Concluded.

# REPORT DOCUMENTATION PAGE

Form Approved  
OMB No. 0704-0188

The public reporting burden for this collection of information is estimated to average 1 hour per response, including the time for reviewing instructions, searching existing data sources, gathering and maintaining the data needed, and completing and reviewing the collection of information. Send comments regarding this burden estimate or any other aspect of this collection of information, including suggestions for reducing the burden, to Department of Defense, Washington Headquarters Services, Directorate for Information Operations and Reports (0704-0188), 1215 Jefferson Davis Highway, Suite 1204, Arlington, VA 22202-4302. Respondents should be aware that notwithstanding any other provision of law, no person shall be subject to any penalty for failing to comply with a collection of information if it does not display a currently valid OMB control number.

PLEASE DO NOT RETURN YOUR FORM TO THE ABOVE ADDRESS.

|   |                    |                     |   |                            |  |  |
|---|--------------------|---------------------|---|----------------------------|--|--|
| <b>1. REPORT DATE (DD-MM-YYYY)</b><br>1-04-2020   |                    |                     | <b>2. REPORT TYPE</b><br>Technical Memorandum |                            | <b>3. DATES COVERED (From - To)</b>                                  |  |
| <b>4. TITLE AND SUBTITLE</b><br><br>Wind Tunnel Investigation of the Supersonic Stage Separation Aerodynamics of a Generic 0.0175-Scale Bimane Two-Stage-to-Orbit Reusable Launch Vehicle Configuration   |                    |                     |   |                            | <b>5a. CONTRACT NUMBER</b>   |  |
|   |                    |                     |   |                            | <b>5b. GRANT NUMBER</b>  |  |
|   |                    |                     |   |                            | <b>5c. PROGRAM ELEMENT NUMBER</b>                                    |  |
| <b>6. AUTHOR(S)</b><br><br>Erickson, Gary E.  |                    |                     |   |                            | <b>5d. PROJECT NUMBER</b>  |  |
|   |                    |                     |   |                            | <b>5e. TASK NUMBER</b>   |  |
|   |                    |                     |   |                            | <b>5f. WORK UNIT NUMBER</b><br>081876.02.07.02.01.02                 |  |
| <b>7. PERFORMING ORGANIZATION NAME(S) AND ADDRESS(ES)</b><br><br>NASA Langley Research Center<br>Hampton, VA 23681-2199   |                    |                     |   |                            | <b>8. PERFORMING ORGANIZATION REPORT NUMBER</b><br><br>L-21129       |  |
| <b>9. SPONSORING/MONITORING AGENCY NAME(S) AND ADDRESS(ES)</b><br><br>National Aeronautics and Space Administration<br>Washington, DC 20546-0001  |                    |                     |   |                            | <b>10. SPONSOR/MONITOR'S ACRONYM(S)</b><br><br>NASA                  |  |
|   |                    |                     |   |                            | <b>11. SPONSOR/MONITOR'S REPORT NUMBER(S)</b><br>NASA-TM-2020-220582 |  |
| <b>12. DISTRIBUTION/AVAILABILITY STATEMENT</b><br><br>Unclassified-<br>Subject Category 02<br>Availability: NASA STI Program (757) 864-9658   |                    |                     |   |                            |  |  |
| <b>13. SUPPLEMENTARY NOTES</b>  |                    |                     |   |                            |  |  |
| <b>14. ABSTRACT</b><br>A wind tunnel investigation was conducted of the supersonic stage separation aerodynamics of a generic two-stage-to-orbit bimane wing-body configuration in the NASA Langley Research Center Unitary Plan Wind Tunnel. Proximity and isolated model testing was conducted at Mach numbers of 2.3, 3.0, and 4.5 and a unit Reynolds number of 2.0 million per foot using 0.0175-scale models of the Langley Glide-Back Booster concept designated as the orbiter and booster in belly-to-belly and back-to-belly configurations. Longitudinal forces and moments were obtained on both models and surface static pressure measurements were obtained on the orbiter model at 328 relative proximity locations and at relative angles of attack of 0 degrees and 5 degrees. The highly-nonlinear, shock-dominated aerodynamic characteristics of the orbiter and booster and their respective zones of influence and interference effects were identified from three-dimensional scatter plots, contour and influence maps, and two-dimensional plotting methods. This investigation led to upgrades in the facility stage separation hardware, calibration and testing techniques and capabilities, and data analysis and documentation methodologies that have been extended to recent NASA advanced launch vehicle test programs. |                    |                     |   |                            |  |  |
| <b>15. SUBJECT TERMS</b><br><br>aerodynamics; bow shock; flow separation; proximity aerodynamics; reusable launch vehicle; shock waves; stage separation; supersonic; two-stage-to-orbit; wind tunnel   |                    |                     |   |                            |  |  |
| <b>16. SECURITY CLASSIFICATION OF:</b>  |                    |                     | <b>17. LIMITATION OF ABSTRACT</b>             | <b>18. NUMBER OF PAGES</b> | <b>19a. NAME OF RESPONSIBLE PERSON</b>                               |  |
| <b>a. REPORT</b>  | <b>b. ABSTRACT</b> | <b>c. THIS PAGE</b> |   |                            | STI Help Desk (email: help@sti.nasa.gov)                             |  |
| U   | U                  | U                   | UU  | 552                        | <b>19b. TELEPHONE NUMBER (Include area code)</b><br>(757) 864-9658   |  |